


Failure Mechanisms, Prediction, and Risk Assessment of Natural and Engineering Disasters through Machine Learning and Numerical Simulation

Lead Guest Editor: Faming Huang

Guest Editors: Chi Yao, Haoyuan Hong, Jinsong Huang, Paraskevas Tsangaratos, and Shuihua Jiang





**Failure Mechanisms, Prediction, and Risk
Assessment of Natural and Engineering
Disasters through Machine Learning and
Numerical Simulation**

Advances in Civil Engineering

**Failure Mechanisms, Prediction,
and Risk Assessment of Natural and
Engineering Disasters through Machine
Learning and Numerical Simulation**

Lead Guest Editor: Faming Huang

Guest Editors: Chi Yao, Haoyuan Hong, Jinsong
Huang, Paraskevas Tsangaratos, and Shuihua Jiang



Copyright © 2021 Hindawi Limited. All rights reserved.

This is a special issue published in "Advances in Civil Engineering." All articles are open access articles distributed under the Creative Commons Attribution License, which permits unrestricted use, distribution, and reproduction in any medium, provided the original work is properly cited.






Chief Editor

Cumaraswamy Vipulanandan, USA









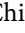




Associate Editors

Chiara Bedon , Italy
Constantin Chalioris , Greece
Ghassan Chehab , Lebanon
Ottavia Corbi, Italy
Mohamed ElGawady , USA
Husnain Haider , Saudi Arabia
Jian Ji , China
Jiang Jin , China
Shazim A. Memon , Kazakhstan
Hossein Moayedi , Vietnam
Sanjay Nimbalkar, Australia
Giuseppe Oliveto , Italy
Alessandro Palmeri , United Kingdom
Arnaud Perrot , France
Hugo Rodrigues , Portugal
Victor Yepes , Spain
Xianbo Zhao , Australia

Academic Editors

José A.F.O. Correia, Portugal
Glenda Abate, Italy
Khalid Abdel-Rahman , Germany
Ali Mardani Aghabaglou, Turkey
José Aguiar , Portugal
Afaq Ahmad , Pakistan
Muhammad Riaz Ahmad , Hong Kong
Hashim M.N. Al-Madani , Bahrain
Luigi Aldieri , Italy
Angelo Aloisio , Italy
Maria Cruz Alonso, Spain
Filipe Amarante dos Santos , Portugal
Serji N. Amirkhanean, USA
Eleftherios K. Anastasiou , Greece
Panagiotis Ch. Anastasopoulos , USA
Mohamed Moafak Arbili , Iraq
Farhad Aslani , Australia
Siva Avudaiappan , Chile
Ozgur BASKAN , Turkey
Adewumi Babafemi, Nigeria
Morteza Bagherpour, Turkey
Qingsheng Bai , Germany
Nicola Baldo , Italy
Daniele Baraldi , Italy

Eva Barreira , Portugal
Emilio Bastidas-Arteaga , France
Rita Bento, Portugal
Rafael Bergillos , Spain
Han-bing Bian , China
Xia Bian , China
Huseyin Bilgin , Albania
Giovanni Biondi , Italy
Hugo C. Biscaia , Portugal
Rahul Biswas , India
Edén Bojórquez , Mexico
Giosuè Boscato , Italy
Melina Bosco , Italy
Jorge Branco , Portugal
Bruno Briseghella , China
Brian M. Broderick, Ireland
Emanuele Brunesi , Italy
Quoc-Bao Bui , Vietnam
Tan-Trung Bui , France
Nicola Buratti, Italy
Gaochuang Cai, France
Gladis Camarini , Brazil
Alberto Campisano , Italy
Qi Cao, China
Qixin Cao, China
Iacopo Carnacina , Italy
Alessio Cascardi, Italy
Paolo Castaldo , Italy
Nicola Cavalagli , Italy
Liborio Cavaleri , Italy
Anush Chandrappa , United Kingdom
Wen-Shao Chang , United Kingdom
Muhammad Tariq Amin Chaudhary, Kuwait
Po-Han Chen , Taiwan
Qian Chen , China
Wei Tong Chen , Taiwan
Qixiu Cheng, Hong Kong
Zhanbo Cheng, United Kingdom
Nicholas Chileshe, Australia
Prinya Chindaprasirt , Thailand
Corrado Chisari , United Kingdom
Se Jin Choi , Republic of Korea
Heap-Yih Chong , Australia
S.H. Chu , USA
Ting-Xiang Chu , China

Zhaofei Chu , China
Wonseok Chung , Republic of Korea
Donato Ciampa , Italy
Gian Paolo Cimellaro, Italy
Francesco Colangelo, Italy
Romulus Costache , Romania
Liviu-Adrian Cotfas , Romania
Antonio Maria D'Altri, Italy
Bruno Dal Lago , Italy
Amos Darko , Hong Kong
Arka Jyoti Das , India
Dario De Domenico , Italy
Gianmarco De Felice , Italy
Stefano De Miranda , Italy
Maria T. De Risi , Italy
Tayfun Dede, Turkey
Sadik O. Degertekin , Turkey
Camelia Delcea , Romania
Cristoforo Demartino, China
Giuseppe Di Filippo , Italy
Luigi Di Sarno, Italy
Fabio Di Trapani , Italy
Aboelkasim Diab , Egypt
Thi My Dung Do, Vietnam
Giulio Dondi , Italy
Jiangfeng Dong , China
Chao Dou , China
Mario D'Aniello , Italy
Jingtao Du , China
Ahmed Elghazouli, United Kingdom
Francesco Fabbrocino , Italy
Flora Faleschini , Italy
Dingqiang Fan, Hong Kong
Xueping Fan, China
Qian Fang , China
Salar Farahmand-Tabar , Iran
Ilenia Farina, Italy
Roberto Fedele, Italy
Guang-Liang Feng , China
Luigi Fenu , Italy
Tiago Ferreira , Portugal
Marco Filippo Ferrotto, Italy
Antonio Formisano , Italy
Guoyang Fu, Australia
Stefano Galassi , Italy

Junfeng Gao , China
Meng Gao , China
Giovanni Garcea , Italy
Enrique García-Macías, Spain
Emilio García-Taengua , United Kingdom
DongDong Ge , USA
Khaled Ghaedi, Malaysia
Khaled Ghaedi , Malaysia
Gian Felice Giaccu, Italy
Agathoklis Giaralis , United Kingdom
Ravindran Gobinath, India
Rodrigo Gonçalves, Portugal
Peilin Gong , China
Belén González-Fonteboa , Spain
Salvatore Grasso , Italy
Fan Gu, USA
Erhan Güneyisi , Turkey
Esra Mete Güneyisi, Turkey
Pingye Guo , China
Ankit Gupta , India
Federico Gusella , Italy
Kemal Hacıfendioglu, Turkey
Jianyong Han , China
Song Han , China
Asad Hanif , Macau
Hadi Hasanzadehshooiili , Canada
Mostafa Fahmi Hassanein, Egypt
Amir Ahmad Hedayat , Iran
Khandaker Hossain , Canada
Zahid Hossain , USA
Chao Hou, China
Biao Hu, China
Jiang Hu , China
Xiaodong Hu, China
Lei Huang , China
Cun Hui , China
Bon-Gang Hwang, Singapore
Jijo James , India
Abbas Fadhil Jasim , Iraq
Ahad Javanmardi , China
Krishnan Prabhakan Jaya, India
Dong-Sheng Jeng , Australia
Han-Yong Jeon, Republic of Korea
Pengjiao Jia, China
Shaohua Jiang , China

MOUSTAFA KASSEM , Malaysia
Mosbeh Kaloop , Egypt
Shankar Karuppannan , Ethiopia
John Kechagias , Greece
Mohammad Khajehzadeh , Iran
Afzal Husain Khan , Saudi Arabia
Mehran Khan , Hong Kong
Manoj Khandelwal, Australia
Jin Kook Kim , Republic of Korea
Woosuk Kim , Republic of Korea
Vaclav Koci , Czech Republic
Loke Kok Foong, Vietnam
Hailing Kong , China
Leonidas Alexandros Kouris , Greece
Kyriakos Kourousis , Ireland
Moacir Kripka , Brazil
Anupam Kumar, The Netherlands
Emma La Malfa Ribolla, Czech Republic
Ali Lakirouhani , Iran
Angus C. C. Lam, China
Thanh Quang Khai Lam , Vietnam
Luciano Lamberti, Italy
Andreas Lampropoulos , United Kingdom
Raffaele Landolfo, Italy
Massimo Latour , Italy
Bang Yeon Lee , Republic of Korea
Eul-Bum Lee , Republic of Korea
Zhen Lei , Canada
Leonardo Leonetti , Italy
Chun-Qing Li , Australia
Dongsheng Li , China
Gen Li, China
Jiale Li , China
Minghui Li, China
Qingchao Li , China
Shuang Yang Li , China
Sunwei Li , Hong Kong
Yajun Li , China
Shun Liang , China
Francesco Liguori , Italy
Jae-Han Lim , Republic of Korea
Jia-Rui Lin , China
Kun Lin , China
Shibin Lin, China

Tzu-Kang Lin , Taiwan
Yu-Cheng Lin , Taiwan
Hexu Liu, USA
Jian Lin Liu , China
Xiaoli Liu , China
Xuemei Liu , Australia
Zaobao Liu , China
Zhuang-Zhuang Liu, China
Diego Lopez-Garcia , Chile
Cristiano Loss , Canada
Lyan-Ywan Lu , Taiwan
Jin Luo , USA
Yanbin Luo , China
Jianjun Ma , China
Junwei Ma , China
Tian-Shou Ma, China
Zhongguo John Ma , USA
Maria Macchiaroli, Italy
Domenico Magisano, Italy
Reza Mahinroosta, Australia
Yann Malecot , France
Prabhat Kumar Mandal , India
John Mander, USA
Iman Mansouri, Iran
André Dias Martins, Portugal
Domagoj Matesan , Croatia
Jose Matos, Portugal
Vasant Matsagar , India
Claudio Mazzotti , Italy
Ahmed Mebarki , France
Gang Mei , China
Kasim Mermerdas, Turkey
Giovanni Minafò , Italy
Masoomah Mirrashid , Iran
Abbas Mohajerani , Australia
Fadzli Mohamed Nazri , Malaysia
Fabrizio Mollaioli , Italy
Rosario Montuori , Italy
H. Naderpour , Iran
Hassan Nasir , Pakistan
Hossein Nassiraei , Iran
Satheeskumar Navaratnam , Australia
Ignacio J. Navarro , Spain
Ashish Kumar Nayak , India
Behzad Nematollahi , Australia

Chayut Ngamkhanong , Thailand
Trung Ngo, Australia
Tengfei Nian, China
Mehdi Nikoo , Canada
Youjun Ning , China
Olugbenga Timo Oladinrin , United Kingdom
Oladimeji Benedict Olalusi, South Africa
Timothy O. Olawumi , Hong Kong
Alejandro Orfila , Spain
Maurizio Orlando , Italy
Siti Aminah Osman, Malaysia
Walid Oueslati , Tunisia
SUVASH PAUL , Bangladesh
John-Paris Pantouvakis , Greece
Fabrizio Paolacci , Italy
Giuseppina Pappalardo , Italy
Fulvio Parisi , Italy
Dimitrios G. Pavlou , Norway
Daniele Pellegrini , Italy
Gatheeshgar Perampalam , United Kingdom
Daniele Perrone , Italy
Giuseppe Piccardo , Italy
Vagelis Plevris , Qatar
Andrea Pranno , Italy
Adolfo Preciado , Mexico
Chongchong Qi , China
Yu Qian, USA
Ying Qin , China
Giuseppe Quaranta , Italy
Krishanu ROY , New Zealand
Vlastimir Radonjanin, Serbia
Carlo Rainieri , Italy
Rahul V. Ralegaonkar, India
Raizal Saifulnaz Muhammad Rashid, Malaysia
Alessandro Rasulo , Italy
Chonghong Ren , China
Qing-Xin Ren, China
Dimitris Rizos , USA
Geoffrey W. Rodgers , New Zealand
Pier Paolo Rossi, Italy
Nicola Ruggieri , Italy
JUNLONG SHANG, Singapore

Nikhil Saboo, India
Anna Saetta, Italy
Juan Sagaseta , United Kingdom
Timo Saksala, Finland
Mostafa Salari, Canada
Ginevra Salerno , Italy
Evangelos J. Sapountzakis , Greece
Vassilis Sarhosis , United Kingdom
Navaratnarajah Sathiparan , Sri Lanka
Fabrizio Scozzese , Italy
Halil Sezen , USA
Payam Shafigh , Malaysia
M. Shahria Alam, Canada
Yi Shan, China
Hussein Sharaf, Iraq
Mostafa Sharifzadeh, Australia
Sanjay Kumar Shukla, Australia
Amir Si Larbi , France
Okan Sirin , Qatar
Piotr Smarzewski , Poland
Francesca Sollecito , Italy
Rui Song , China
Tian-Yi Song, Australia
Flavio Stochino , Italy
Mayank Sukhija , USA
Piti Sukontasukkul , Thailand
Jianping Sun, Singapore
Xiao Sun , China
T. Tafsirojjan , Australia
Fujiao Tang , China
Patrick W.C. Tang , Australia
Zhi Cheng Tang , China
Weerachart Tangchirapat , Thailand
Xiabin Tao, China
Piergiorgio Tataranni , Italy
Elisabete Teixeira , Portugal
Jorge Iván Tobón , Colombia
Jing-Zhong Tong, China
Francesco Trentadue , Italy
Antonello Troncone, Italy
Majbah Uddin , USA
Tariq Umar , United Kingdom
Muahmmad Usman, United Kingdom
Muhammad Usman , Pakistan
Mucteba Uysal , Turkey

Ilaria Venanzi , Italy
Castorina S. Vieira , Portugal
Valeria Vignali , Italy
Claudia Vitone , Italy
Liwei WEN , China
Chunfeng Wan , China
Hua-Ping Wan, China
Roman Wan-Wendner , Austria
Chaohui Wang , China
Hao Wang , USA
Shiming Wang , China
Wayne Yu Wang , United Kingdom
Wen-Da Wang, China
Xing Wang , China
Xiuling Wang , China
Zhenjun Wang , China
Xin-Jiang Wei , China
Tao Wen , China
Weiping Wen , China
Lei Weng , China
Chao Wu , United Kingdom
Jiangyu Wu, China
Wangjie Wu , China
Wenbing Wu , China
Zhixing Xiao, China
Gang Xu, China
Jian Xu , China
Panpan , China
Rongchao Xu , China
HE YONGLIANG, China
Michael Yam, Hong Kong
Hailu Yang , China
Xu-Xu Yang , China
Hui Yao , China
Xinyu Ye , China
Zhoujing Ye, China
Gürol Yildirim , Turkey
Dawei Yin , China
Doo-Yeol Yoo , Republic of Korea
Zhanping You , USA
Afshar A. Yousefi , Iran
Xinbao Yu , USA
Dongdong Yuan , China
Geun Y. Yun , Republic of Korea



Hyun-Do Yun , Republic of Korea
Cemal YİĞİT , Turkey
Paolo Zampieri, Italy
Giulio Zani , Italy
Mariano Angelo Zanini , Italy
Zhixiong Zeng , Hong Kong
Mustafa Zeybek, Turkey
Henglong Zhang , China
Jiupeng Zhang, China
Tingting Zhang , China
Zengping Zhang, China
Zetian Zhang , China
Zhigang Zhang , China
Zhipeng Zhao , Japan
Jun Zhao , China
Annan Zhou , Australia
Jia-wen Zhou , China
Hai-Tao Zhu , China
Peng Zhu , China
QuanJie Zhu , China
Wenjun Zhu , China
Marco Zucca, Italy
Haoran Zuo, Australia
Junqing Zuo , China
Robert Černý , Czech Republic
Süleyman İpek , Turkey

Contents




Microseismic Response Characteristics Induced by Mining Activities: A Case Study

Xuesong Bai, Zhi Tang, Tao Zhao, Xiaoyang Cheng , and Kai Chen
Research Article (18 pages), Article ID 9977589, Volume 2021 (2021)

Efficient Investigation of Rock Crack Propagation and Fracture Behaviors during Impact Fragmentation in Rockfalls Using Parallel DDA

Lu Zheng, Yihan Wu, Wei Wu, Hong Zhang , Xinyan Peng , Xuelue Zhang, and Xuezhen Wu
Research Article (17 pages), Article ID 5901561, Volume 2021 (2021)

Compression Load Tests on Composite Foundations of Spread Footing Anchored by Helical Anchors

Mingqiang Sheng , Zengzhen Qian , and Xianlong Lu 
Research Article (11 pages), Article ID 5531380, Volume 2021 (2021)



Phase-Field Modeling Fracture in Anisotropic Materials

Haifeng Li, Wei Wang , Yajun Cao , and Shifan Liu
Research Article (13 pages), Article ID 4313755, Volume 2021 (2021)

Seismic Performance and Risk Assessment of Traditional Brick-Wood Rural Buildings Based on Numerical Simulation

Baokui Chen , Li Fan, Jingang Xiong, Ming Wen, and Yaru Liu
Research Article (16 pages), Article ID 7648989, Volume 2021 (2021)


Stability Assessment of Dangerous Rock Mass of an Overhanging Slope in Puerdu Town, Southwestern China

Wen-Lian Liu, Jia-Xing Dong , Su-Gang Sui, Han-Hua Xu , Run-Xue Yang, and Zhen-Luo Shen
Research Article (12 pages), Article ID 6526417, Volume 2021 (2021)

FEA of Effects Induced by Diurnal Temperature Variation on Downstream Surface of Xiaowan Arch Dam

Huanhuan Li , Shaojun Fu , Gang Li , and Guofei Hu 
Research Article (11 pages), Article ID 6300387, Volume 2021 (2021)


Trajectory Analysis and Risk Evaluation of Dangerous Rock Mass Instability of an Overhang Slope, Southwest of China

Wen-lian Liu, Jia-xing Dong , Han-hua Xu, Su-gang Sui, Run-xue Yang, and Lun-shun Zhou
Research Article (15 pages), Article ID 7153535, Volume 2021 (2021)

The Prediction of Pile Foundation Buried Depth Based on BP Neural Network Optimized by Quantum Particle Swarm Optimization

Fei Yin , Yong Hao , Taoli Xiao , Yan Shao , and Man Yuan 
Research Article (15 pages), Article ID 2015408, Volume 2021 (2021)

A Constitutive Model of Sandy Gravel Soil under Large-Sized Loading/Unloading Triaxial Tests

Pengfei Zhang, Han Liu, Zhentu Feng, Chaofeng Jia, and Rui Zhou 
Research Article (11 pages), Article ID 4998351, Volume 2021 (2021)

Life-Cycle Seismic Fragility Assessment of Existing RC Bridges Subject to Chloride-Induced Corrosion in Marine Environment

Sicong Hu , Zheyang Wang, Yu Guo, and Gui Xiao


Research Article (18 pages), Article ID 9640521, Volume 2021 (2021)

Investigation of Factors Influencing the Construction Safety of High-Speed Railway Stations Based on DEMATEL and ISM

Feng Lin , Ping Wu , and Yidong Xu 



Research Article (12 pages), Article ID 9954018, Volume 2021 (2021)

Deformation Response and Safety Evaluation of Buildings Affected by Subway-Station Construction

Chunlei Feng , Dingli Zhang, Hualao Wang, and Xuan Zhang


Research Article (18 pages), Article ID 1694563, Volume 2021 (2021)

BP Neural Network Improved by Sparrow Search Algorithm in Predicting Debonding Strain of FRP-Strengthened RC Beams

Guibing Li , Tianyu Hu , and Dawei Bai




Research Article (13 pages), Article ID 9979028, Volume 2021 (2021)

Research on Landslide Warning Model Establishment and Disaster Space-Time Evolution Analysis

Zhen Wang 


Research Article (10 pages), Article ID 7496940, Volume 2021 (2021)

Hydrodynamic Performance and Cavitation Analysis in Bottom Outlets of Dam Using CFD Modelling

Omid Aminoroayaie Yamini , S. Hooman Mousavi , M. R. Kavianpour , and Ramin Safari Ghaleh


Research Article (14 pages), Article ID 5529792, Volume 2021 (2021)

Dynamic Wave-Induced Settlement Behavior of a Caisson Breakwater Built on a Sandy Seabed

Gichun Kang, Tae-Hyung Kim, Jiseong Kim, and Seong-Kyu Yun 



Research Article (16 pages), Article ID 5554530, Volume 2021 (2021)

A Displacement-Based Theory for Predicting the Support Force on the Shield Tunneling Surface in Sandy Soil Layers

Guang Sun, Han Liu, Zhiyuan Guo, Ranjie Li, and Tao Li 


Research Article (10 pages), Article ID 9980837, Volume 2021 (2021)

Stress Relief and Stimulation of Coal Reservoir by Hydraulic Slotting

Xiaoyang Cheng , Qinghua Zhang, Zhigang Zhang , Yunlong Zou, and Guo Junjie

Research Article (13 pages), Article ID 6664696, Volume 2021 (2021)


The Healing Process of the Joints between Buffer Material Blocks and the Influence on Solute Migration

Rui Zhou , Yuemiao Liu, Tao Xu, and Yufeng Gao

Research Article (15 pages), Article ID 5524346, Volume 2021 (2021)


Contents

Experimental Study on the Coupled Heat-Moisture-Heavy Metal Pollutant Transfer Process in Soils

Qingke Nie , Wei Wang, Wenkai Guo, and Huawei Li

Research Article (10 pages), Article ID 5510217, Volume 2021 (2021)

Numerical Analysis on Reinforcement Range of a Closed Steel Sleeve against Collapse

Qing-Feng Yin 



Research Article (10 pages), Article ID 5593657, Volume 2021 (2021)

Indirect Determination Approach of Blast-Induced Ground Vibration Based on a Hybrid SSA-Optimized GP-Based Technique

Zhaoxin Jiang, Hongyan Xu, Hui Chen , Bei Gao, Shijie Jia, Zhi Yu , and Jian Zhou 



Research Article (14 pages), Article ID 6694918, Volume 2021 (2021)

Experimental Study on Thermal Expansion Behavior of Concrete under Three-Dimensional Stress

Zhipeng Yu, Fan Zhang , Xiao Ma, Fujian Yang, Dawei Hu , and Hui Zhou

Research Article (8 pages), Article ID 5597918, Volume 2021 (2021)

Mechanical Properties of Sandstone Roof and Surrounding-Rock Control of Mining Roadways Subject to Reservoir Water Disturbance

Bin Ma, Zaiqiang Hu , Xingzhou Chen , Lili Chen, and Wei Du

Research Article (16 pages), Article ID 6656812, Volume 2021 (2021)


Study on the Mathematical Model and Propagation Characteristics of AE Waveform Signals during Rock Fracture

Xun You , Bin Gong , Xin Lv , and Longfei Hu 

Research Article (13 pages), Article ID 6685357, Volume 2021 (2021)

Research Article

Microseismic Response Characteristics Induced by Mining Activities: A Case Study

Xuesong Bai,^{1,2} Zhi Tang,^{1,2} Tao Zhao,^{1,2} Xiaoyang Cheng ,^{3,4} and Kai Chen^{1,2}

¹College of Safety Science and Engineering, Liaoning Technical University, Liaoning 123000, China

²School of Mechanical & Engineering, Liaoning Technical University, Liaoning 123000, China

³State Key Laboratory of the Gas Disaster Detecting, Preventing and Emergency Controlling, Chongqing 400037, China

⁴China Coal Technology and Engineering Group Chongqing Research Institute, Chongqing 400037, China

Correspondence should be addressed to Xiaoyang Cheng; cqmkyxcyang@163.com

Received 24 March 2021; Revised 17 August 2021; Accepted 30 August 2021; Published 23 September 2021

Academic Editor: Faming Huang

Copyright © 2021 Xuesong Bai et al. This is an open access article distributed under the Creative Commons Attribution License, which permits unrestricted use, distribution, and reproduction in any medium, provided the original work is properly cited.

For deep coal mines, geological disturbances or mining activities can cause damage to coal and rock masses, easily inducing dynamic disasters such as rock bursts or coal and gas outbursts, which seriously threaten the safety production of coal mine. In this paper, first, the Liyazhuang Coal Mine introduced the SOS MS (Sensor Observation Service Microseismic) monitoring system from the Polish Research Institute and verified the accuracy of its positioning. Then, to study the characteristics of MS signals induced by different mining activities, based on the field monitoring results, the waveform and frequency spectrum characteristics of MS signals at different energy levels induced by different mining activities are analyzed, and the energy levels of MS signals caused by different mining activities are classified. Studies have shown that there are large differences in the waveform and spectral characteristics of MS signals at different energy levels. High-level energy seismic signals are characterized by large amplitudes, low frequencies, relatively concentrated distribution, long vibration duration, and slow attenuation. In addition, the relationship between mining activities and MS events is also statistically analyzed based on the spatial and temporal distribution of MS events with the advancement of working face, and the results show that the increase of vibration frequency and energy can be precursor information for roof pressure. With the advance of the working face, the MS energy has the characteristic of periodic distribution, which is consistent with the periodic weighting revealed by the working resistance of the support. This study provides a reference for further revealing the energy release mechanism of rock burst.

1. Introduction

With the increase of mining depth, the occurrence conditions of coal seams are more and more complex. The frequency and damage degree of dynamic disasters such as rock burst and coal and gas outburst are increasing day by day [1–3]. Thus, there is an urgent need to develop new technologies and equipment to monitor coal and rock stability in real time. Under the action of ground stress, the formation and expansion of cracks in rock or coal body are accompanied by a large number of MS events. During crack initiation, propagation, and coalescence, the energy accumulated in the rock is dissipated in the elastic waveform, of which the signals can be captured by the MS monitoring

system [4]. To reveal the evolution law of MS activity in the process of rock fracture, the frequency spectrum of MS waveform was used to evaluate the danger intensity of rock fracture [5, 6]. Based on the analysis of field data, Zhang et al. [7] found that the minimum and maximum values of main frequency of MS events in heading face are 14 Hz and 515 Hz, and the maximum event duration is 1.78 s. Experimental results regarding the microseism signal time-frequency characteristics in the process of fault stick-slip instability indicate that the frequency band of the MS signal before the fault stick-slip is 0~100 Hz, and the main frequency is within 10 Hz [8]. The study on the typical intensive rock burst cases under different excavation methods, tunnel boring machine (TBM), and drilling and blasting method

(D&B) in deep marble tunnels of Jinping II hydropower station demonstrates that the single day lowest MS main frequency of both TBM and D&B is less than 200 Hz during the intensive rock burst development [9]. Wang and Zong [10] applied HHT method to analyze the vibration signals of deep-hole large-charge blasting. The results indicated that the vibration duration of blasting is about 150 ms, and the vibration energy is mainly concentrated in the frequency of 17.75 Hz. Li et al. [11] pointed out that the coal mining MS signals have lower dominant frequency (below 80 Hz) and longer vibration duration (more than 2 s) than the blasting signals (dominant frequency above 80 Hz and duration less than 2 s). And the following peak envelope curves of the two types of signals fit a power function. The VMD decomposition method is utilized by Zhang et al. [12] to analyze coal-rock fracturing and blasting vibration signals. The results show that the energy of the rock fracturing signals is mainly concentrated in the low-frequency modes, whereas the energy of the blasting vibration signals is mainly concentrated in the three high-frequency modes. The main frequency of microseismic signals during coal outflow, blasting, and coal wall collapse is 0.80, 0.50, and 1.00 kHz, respectively. The lower frequency part of microseismic signals is mainly contributed by the impact failure, and the higher frequency part is mainly contributed by the coal body caving; additionally, the greater the impact failure, the lower the low-frequency bound of its signal [13]. Scholars have analyzed the frequency spectrum characteristics of a large number of MS events caused by different mining activities and taken their variation laws as the precursor information to predict the occurrence of rock burst [14–16]. Field test results from 8935 working face in Xinzhouyao Coal Mine show that the main frequency spectrum of MS signals before the rock burst is mainly concentrated in 5–60 Hz, and the sharp decrease of the main frequency and the obvious increase of the amplitude of MS signals can be considered as one of the precursors characteristics of rock burst [17]. The S transform (ST) time-frequency analysis technique is introduced to MS signal analysis field by Jiang et al. [18], and the rock failure scale can be investigated based on the frequency characteristic of MS signal. The MS signal transforms from high frequency to low frequency before the obvious rock deformation. Thus, the frequency decrease of MS signal can be regarded as the precursory information of macroscopic deformation of rock mass.

Most of previous research mainly focuses on the distribution of main frequencies of MS signals induced by rock deformation. However, there has been a relative lack of research on the characteristics of MS signals generated by different disturbances with different energy levels. The relationship between energy levels and spectral characteristics of MS signals caused by different mining activities is also fuzzy. Taking the island working face of Liyazhuang Coal Mine (Shanxi Province, China) as the research object, a SOS MS monitoring system was established. Based on the real-time monitoring data of MS activities in the deep rock masses during the mining, this study explored the waveform and spectrum characteristics of MS signal generated by

different disturbances with different energy levels. And the MS response characteristics during different mining activities were also studied. And the flowchart of this study is shown in Figure 1.

2. Engineering Background

Liyazhuang Coal Mine is the second large-scale mine with design production capacity of 1.5 Mt./a coconstructed by China and Romania in Huozhou mining area (north area). The mine is located in Shizhuang District, Huozhou City, Shanxi province, 10 km away from southwest of Huozhou City (see Figure 2). It has mining area of 30.415 km², geological reserves of 2.4114 billion tons, and recoverable reserves of 2.1064 billion tons. There are 5 layers of mineable coal seam, and among them 2# coal seam is the current mining coal seam with average thickness of 3.16 m. Because the average dip angle of coal seam is 6°, the inclined-vertical shaft development is used.

The II228 working face being prepared is the isolated island working face with two completely mined out sections at the upper and lower sides, located in panel 2 of 2# coal seam with elevation of +355 m. The advance length and width of II228 working face are 630 m and 130 m, respectively. The dip angle of coal seam is 4 to 10°, average 6°. The thickness of coal seam is 2.82 m to 3.45 m, average 2.67 m. Meanwhile, as a complex structural coal seam, it generally contains 2 layers of gangue, mainly mudstone and carbonaceous mudstone.

After entering the deep part of the panel II, influenced by the hilly terrain, the mining depth reaches more than 600 m, leading to the large deformation of the roadway, serious floor heave, and frequent coal burst. The II228 working face currently being prepared is the isolated island working face, where the adjacent two sections have been mined out in the upper and lower sides (see Figure 3). It is noted that Figure 3 is a simplified excavation engineering plan of Liyazhuang coal mine, in which some roadways are not drawn, aiming to illustrate the current state and layout of the II228 working face. Affected by factors such as plateau rock stress, mining stress, and gas accumulation, etc., during the driving period, the coal burst occurred frequently, and the drills were frequently ejected or grabbed when drilling, as well as the phenomenon of borehole spraying, which poses serious threat to the underground safety production. According to the analysis of current mining technical conditions, there are multiple factors that may cause the aforementioned dynamic danger phenomena, including the energy accumulated in the coal seam due to high in situ stress, the large elastic energy accumulated in the hard roof of multiple layers, and the accumulated gas internal energy, etc. Therefore, the real-time Polish SOS MS monitoring system is introduced to determine and identify the energy source (hazard source) of the dynamic phenomenon based on the acquired MS signals and further formulate corresponding prediction and prevention methods to guarantee the safe production, meanwhile, providing useful guidance for other panels or mining areas with similar mining conditions.

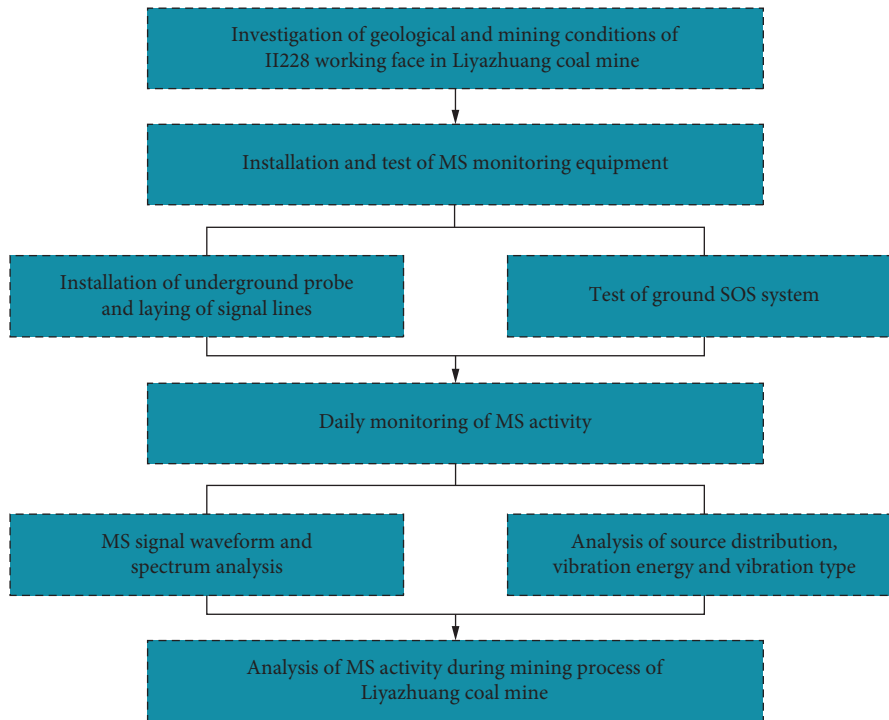


FIGURE 1: The flowchart of this study.

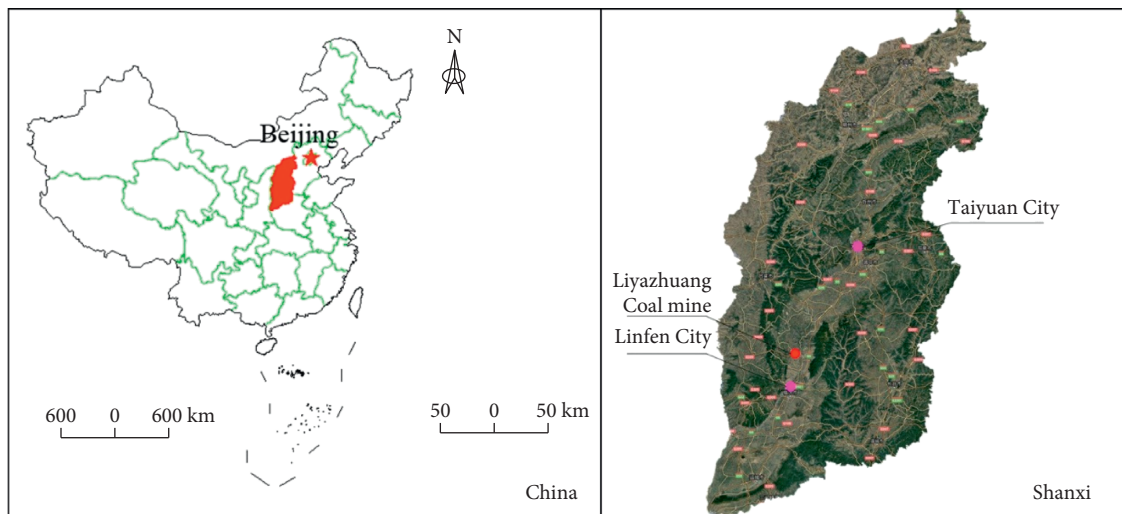


FIGURE 2: Geographical location of the Liyazhuang Coal Mine.

3. Establishment of the Polish SOS MS Monitoring System at Liyazhuang Coal Mine

3.1. Introduction to SOS MS Monitoring System. The SOS MS monitoring system is a new generation product developed and manufactured by the Polish Mining Research Institute. The hardware of this system is composed of three parts, namely, geophone (DLM-2001) with 20 sensors, signals acquisition station (DLM-SO) with 20 channels, and signals recorder (AS-1). DLM-2001 geophone has the function of MS pickup, magnetic transformer signals conversion, signal amplification, etc., of which the sensor is installed vertically

on the anchor bolt with a length of 1m or more on the bottom floor to facilitate construction, maintenance, and movement. Through the underground cables, the underground acquired signals will be transmitted to the DLM-SO signals acquisition station, of which the function is to rectify and filter the signals; besides, the DLM-SO acquisition station also powers to the geophone. Generally, a set of DLM-SO acquisition station works in conjunction with 16 DLM-2001 geophone sensors that isolate intrinsically safe signals from nonintrinsically safe signals. The current modulated signals in the measuring probe are transmitted through the underground cables into the acquisition station.

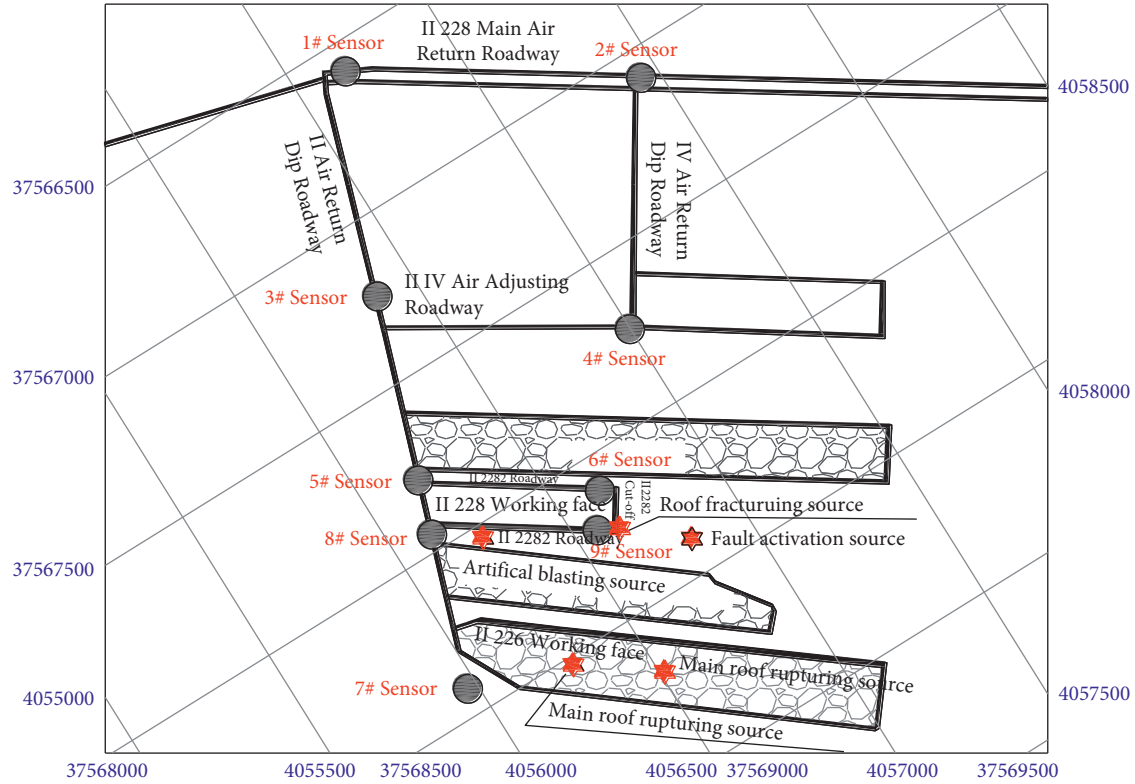


FIGURE 3: Arrangements of MS stations and partial typical MS events in the Liyazhuang Coal Mine.

In the acquisition station, the signals are accurately reproduced and converted into corresponding voltage signals. The distance between each acquisition station and geophone probe would not exceed 10 km. The AS-1 Seismogram signals recorder is designed based on the IBM PC computer embedded A/D conversion card with 32 channels. Its main function is to convert seismic signals into digital signals.

The software of this system is mainly divided into two parts, namely, Multilok and Seismogram. Multilok is mainly used to complete the three-dimensional position and relevant parameters calculation of the rock vibration source. And Seismogram is used to extract, visualize, and analyze useful MS signals and isolate and screen the wave groups, etc.

SOS MS system can continuously and automatically collect and filter shock signal and accurately calculate the occurrence time, energy, and space three-dimensional coordinates of shock event (>100 J). Its maximum sampling rate is 2500 Hz. The frequency bandwidth of MS signals that can be monitored by this system is 1–600 Hz.

3.2. Planning the MS Monitoring System

3.2.1. Basic Theory of MS Location. Effectively and accurately detecting and locating the MS events, which contain a large amount of information about rock and coal fracture, is of important significance to detect potential dangers and further mitigate hazards [19]. In terms of the range and scale of coal mine field, the P -wave is often chosen for locating the MS events because of its advantages of high accuracy. The

positioning principle of the MS monitoring system is to use the time difference of the P -wave under a specific wave velocity field to determine the rock failure point and further perform two-dimensional or three-dimensional MS source location. Besides, the energy released in the duration of the MS can be also calculated. In practical application, it is often assumed that the coal body is homogeneous and isotropic. That is, the velocity of P -wave in each direction is a constant. Thus, for homogeneous and isotropic velocity models, the time from the MS source $H = (X_0, Y_0, Z_0)^T$ to the sensor i can be calculated:

$$T_i(H, V, X_i) = \frac{\sqrt{(x_0 - x_i)^2 + (y_0 - y_i)^2 + (z_0 - z_i)^2}}{V_p}, \quad (1)$$

where $X = (x_i, y_i, z_i)$ is the coordinate of the sensor i ; t_0 is the time when the MS occurs; t_i is the time when the P -wave reaches the sensor i ; V_p is the velocity of P -wave; $i = 1, 2, \dots, n$, n is the number of sensors installed. From the above formula, it can be seen that at least four sensors are needed providing enough data to solve the equation.

3.2.2. Sensors Layout and Installation. The II228 working face in panel 2 is the key area for rock burst prevention and control, and it is also the important area for MS monitoring, which can provide useful information for rock burst prediction. Besides, the panel 2 in coal seam 2# has the risk of rock burst, so the monitoring stations should be arranged as close as possible to this area, and sufficient distribution density should be satisfied. Thus, based on the MS location

theory and MS monitoring principle [20, 21], 11 sensors were designed to install around the II228 working face, and the detailed coordinates for the 11 MS sensors are listed in Table 1. The map of the network topology of the MS monitoring system is shown in Figure 3. And the system diagram is shown in Figure 4.

Depending on the MS sensor used, the detector probe can be installed vertically on the drilling bolt with a depth of more than 1 m and an error of 10 degrees (the probe is fixed to the M20-bolt thread). To ensure the good operation of MS sensors, the transmission lines of MS network should be well and tightly connected. Therefore, under the condition that the positive and negative electrodes are correct, the probe output cable should be connected through the specially made explosion-proof sleeve or junction box. The schematic of MS sensors installation can be seen in Figure 5.

3.2.3. The Verification of Location Accuracy of Monitoring System. The location accuracy of MS monitoring system is the foundation of the prevention and early warning of rock burst. Thus, the precision of source positioning must be validated after installation of the MS monitoring system. A common approach is to compare positioning results with actual locations of blasting activities, which provide a useful assessment on the validity of sensor's spatial distribution and performance of the entire system. To ensure the calculation accuracy of the position and source parameters of MS events, we also performed a location accuracy test of the MS events. Their places in panel 2 were chosen as the blasting positions. The coordinates of the blasting points determined through three artificial explosions at 3 positions showed a maximum error of 5.93 m and a minimum error of 1.85 m against the actual points, which meets the requirement for studying MS activities in the field monitoring. The reliability of the equipment is verified through this test. On the other hand, the rationality of sensors layout is also validated. The detailed data of blasting location and estimated locations are listed in Table 2.

4. Results and Analysis

4.1. The Spectrum Characteristics of MS Signals of Mining Tremor with Different Energy Levels in Liyazhuang Coal Mine. Under the effect of external disturbances, dynamic failures would occur in the rock mass. In the process of rock failure, detectable acoustic and seismic signals would be produced, accompanied by the release of energy which can be monitored by the MS monitoring system. Due to the different failure mechanism of rock and coal, the monitored energy is in different magnitudes [22, 23]. According to the focal mechanisms of mine tremors, the characteristics of MS signals produced by various types of seismic sources are different, including energy, frequency spectrum, etc. [24, 25]. Previous studies have shown that there may be a relation between the MS energy and spectrum [26]. Thus, it is necessary to analyze the waveform and spectrum characteristics of MS signals with different energy levels and further provide the theoretical basis for identifying the types of mining-induced disturbances. It is also of important

significance to take corresponding preventive measures for the occurrence of the rock burst or other dynamic disasters induced by different mining disturbances. This section mainly aims at analyzing the spectrum characteristics of MS signals with different energy levels monitored and recorded in Liyazhuang Coal Mine.

The energy of MS events recorded by the MS monitoring system in Liyazhuang Coal Mine was mainly concentrated between 10^2 and 10^5 J. Figure 6 shows the waveform and spectrum variation characteristics of MS events with energy greater than 10^4 J. From Figures 6(a) and 6(c), it can be seen that the amplitudes (vibration velocity) of MS signals mainly concentrate in $(0.6-6.5) \times 10^{-4}$ m/s. The signal attenuation is fast, lasting from 800 ms to 1000 ms. Meanwhile, it also can be known that the MS signals monitored by sensors with different distances from the same vibration source have similar amplitudes. However, the closer the vibration source is, the longer the MS signals received by the sensor will last. From Figure 6(b), it can be seen that the main frequency is about 50 Hz and most of the amplitude is concentrated in the frequency bands between 25 Hz and 100 Hz, while from Figure 6(d), it can be known that the main frequency is about 60 Hz and most of the amplitude is concentrated in the frequency bands between 36 Hz and 90 Hz. They have similar characteristics of main frequency distributions. However, the closer the vibration source, the larger the amplitude spectrum of the signals. Generally, the seismic wave continuously attenuates along the rock medium, so that the MS signals monitored by the station closer to the vibration source may have more useful information.

Figure 7 shows the waveform and spectrum variation characteristics of MS events with energy of 1050.7183 J. It can be seen that the amplitudes (vibration velocity) of MS signals mainly concentrate in $(0.2-5) \times 10^{-4}$ m/s, and the MS signals last about 600 ms. In terms of the spectrum, the frequency band of the signal is 0-160 Hz. Besides, the main frequency bands range is about 10-75 Hz and most amplitude concentrates on the frequency bands of 10-50 Hz. Generally, the MS signals with such waveform characteristics and vibration energy of about 10^3 J are generated by the underground artificial blasting.

Figure 8 shows the waveform and spectrum variation characteristics of MS events with energy of 871.7724 J. Obviously, the amplitudes (vibration velocity) of MS signals mainly concentrate in $(0.2-0.6) \times 10^{-4}$ m/s, and the MS signals last about 550-750 ms. And the frequency band of the signal is 0-120 Hz, while the main frequency bands range is about 15-80 Hz.

As shown in Table 3, it can be concluded that the higher the vibration energy is, the longer the corresponding MS signals would last, and the larger the amplitude (vibration velocity) is. In addition, for the MS signals with high energy levels, the frequency is wide, but the main frequency band is narrow but centralized. Generally, the MS signals generated by strong vibration are characterized by large amplitude and low frequency, while the signals of vibration with low energy level have the characteristic of wide main frequency band. In most practical cases, the magnitude and the energy concentration degree of MS events were identified as the criteria

TABLE 1: The three-dimensional coordinates of MS sensors.

No.	Coordinate		
	X	Y	Z
1	37566700.00	4057296.00	-321.5
2	37567261.00	4058164.00	-363.8
3	37567733.00	4056877.00	-275
4	37568230.00	4057494.00	-294.5
5	37568281.00	4056688.00	-228
6	37568599.00	4057151.00	-235
7	37568911.00	4056468.00	-202
8	37568230.00	4057494.00	-294.5
9	37568911.00	4056468.00	-202

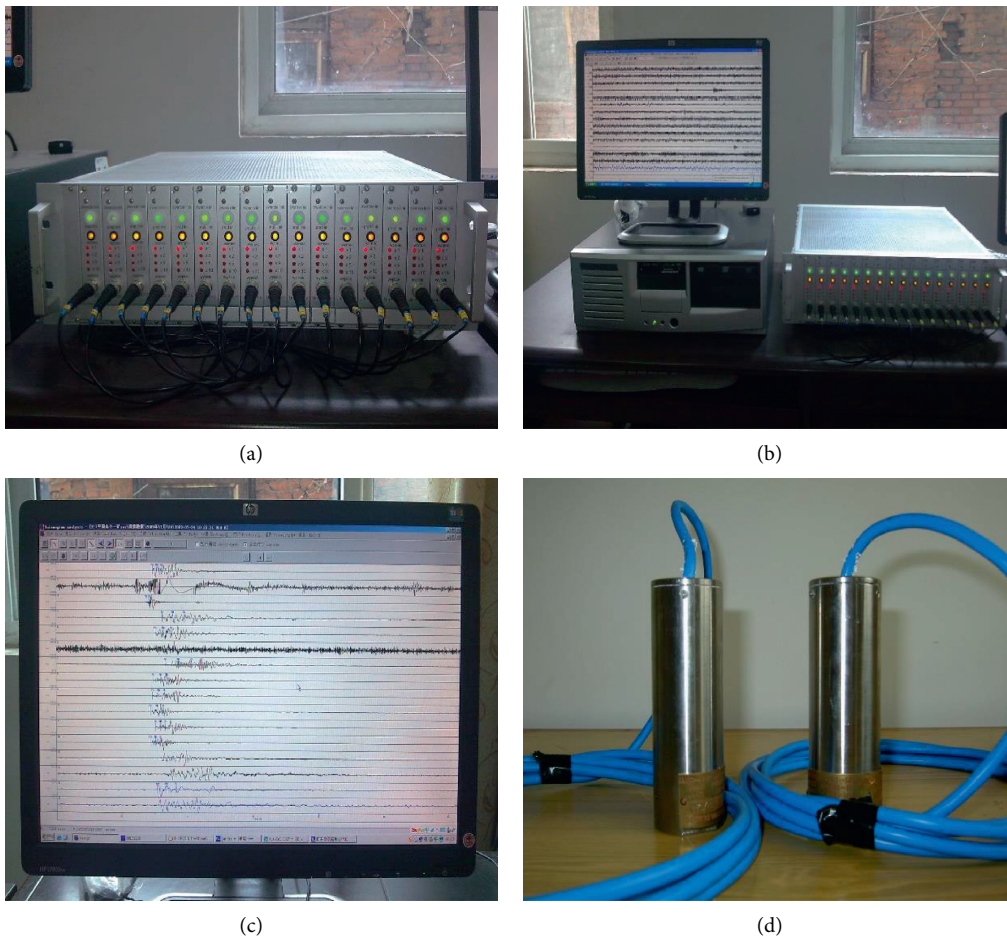


FIGURE 4: The schematic of MS sensors installation. (a) DLM-SO signal acquisition station (16 channels). (b) Recording instrument. (c) Analysis meter. (d) Detection and measurement probe.

for rock burst hazards [27]. Generally, the minimum energy at which the rock burst occurs is 10^3 J, and most rock bursts start from 10^5 J. The area where the MS events with the energy magnitude of 10^5 or above frequently occur can be considered as the high-risk area [28–30].

4.2. The Spectrum Characteristics of MS Signals Induced by Typical Underground Disturbances. Mining activity and tectonic activity are known to pose external disturbances

on the rock and coal mass, resulting in the damage of the rock and coal mass. Under different disturbances, the MS signals generated by the rock and coal failure have different characteristics due to the different failure mechanics of rock and coal mass [31–34]. Therefore, it is of practical significance to identify different focal sources and further make corresponding preventive measures by analyzing the waveform and spectrum characteristics of MS signals generated under different disturbance conditions.

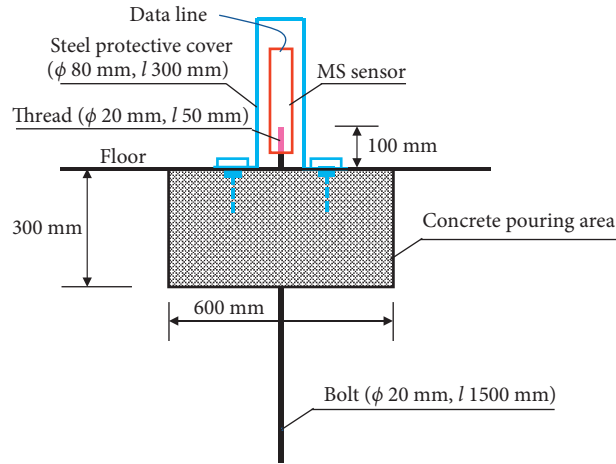
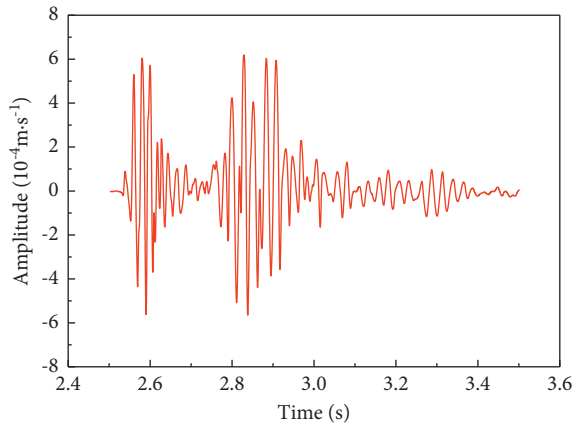


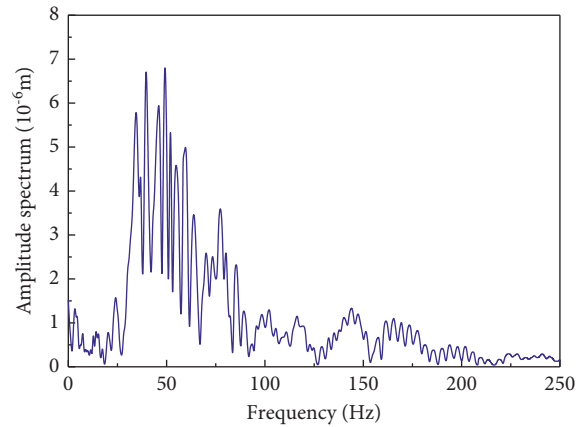
FIGURE 5: The schematic of MS sensors installation.

TABLE 2: The comparison of the three-dimensional coordinates of actual points and estimated location.

No.	Actual coordinate		Estimated coordinate		Error
1	X	37568453.68	X	37568448.32	5.36
	Y	4056695.32	Y	4056701.14	5.82
	Z	-224.52	Z	-227.08	2.56
2	X	37568613.02	X	37568608.87	4.3
	Y	4056939.97	Y	4056845.45	5.48
	Z	-231.1	Z	-233.26	1.85
3	X	37568673.14	X	37568677.23	4.09
	Y	4057176.65	Y	4057182.58	5.93
	Z	-233.54	Z	-236.31	2.77



(a)



(b)

FIGURE 6: Continued.

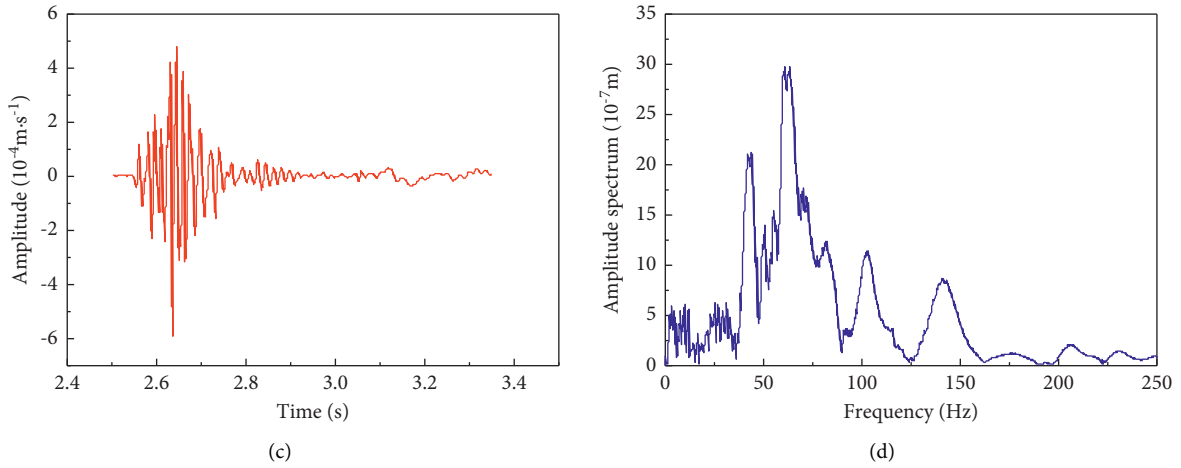


FIGURE 6: Curves of vibration velocity-time and amplitude spectrum-frequency with vibration energy = 39932.22 J. (a) Vibration velocity-time (sensor 6#). (b) Amplitude spectrum-frequency (sensor 6#). (c) Vibration velocity-time (sensor 9#). (d) Amplitude spectrum-frequency (sensor 9#).

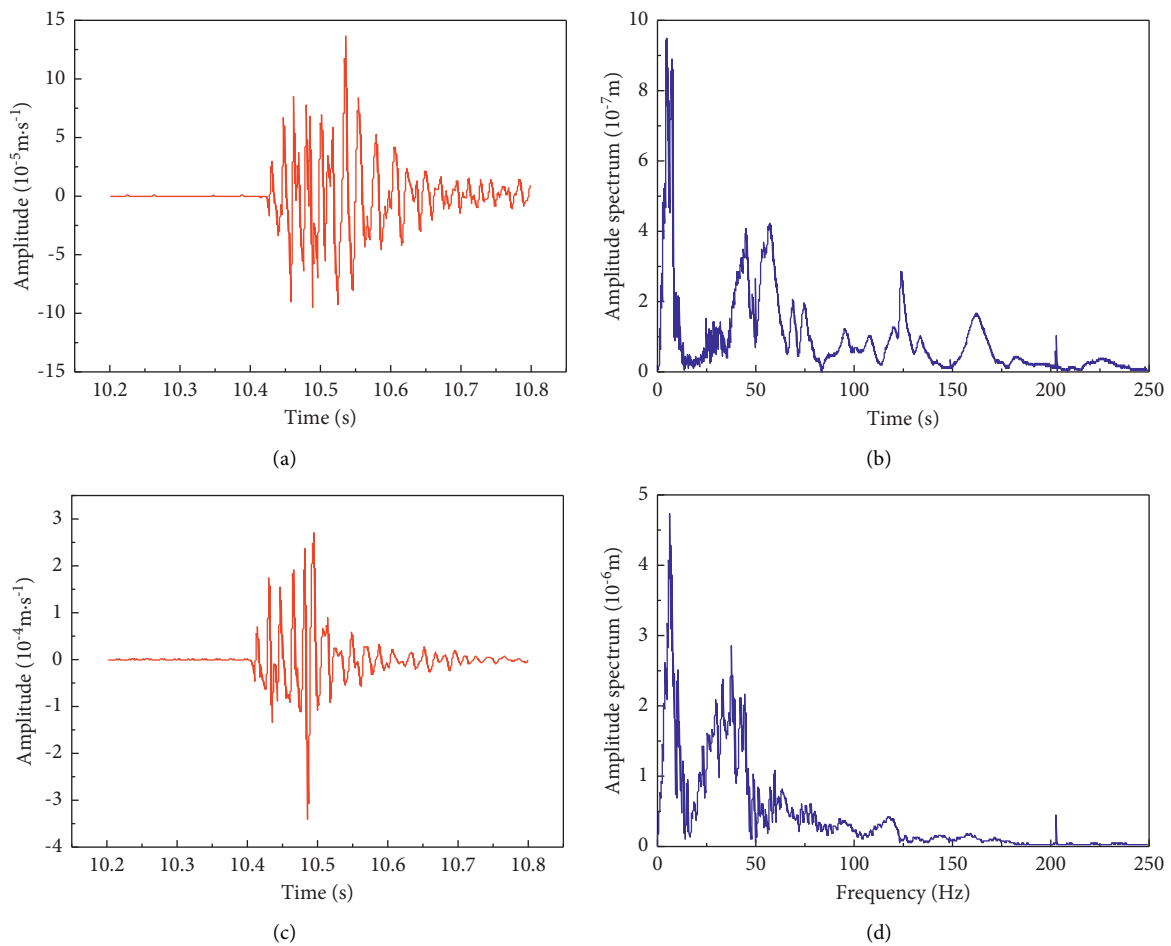


FIGURE 7: Curves of vibration velocity-time and amplitude spectrum-frequency with vibration energy = 1050.7183 J. (a) Vibration velocity-time (sensor 6#). (b) Amplitude spectrum-frequency (sensor 6#). (c) Vibration velocity-time (sensor 9#). (d) Amplitude spectrum-frequency (sensor 9#).

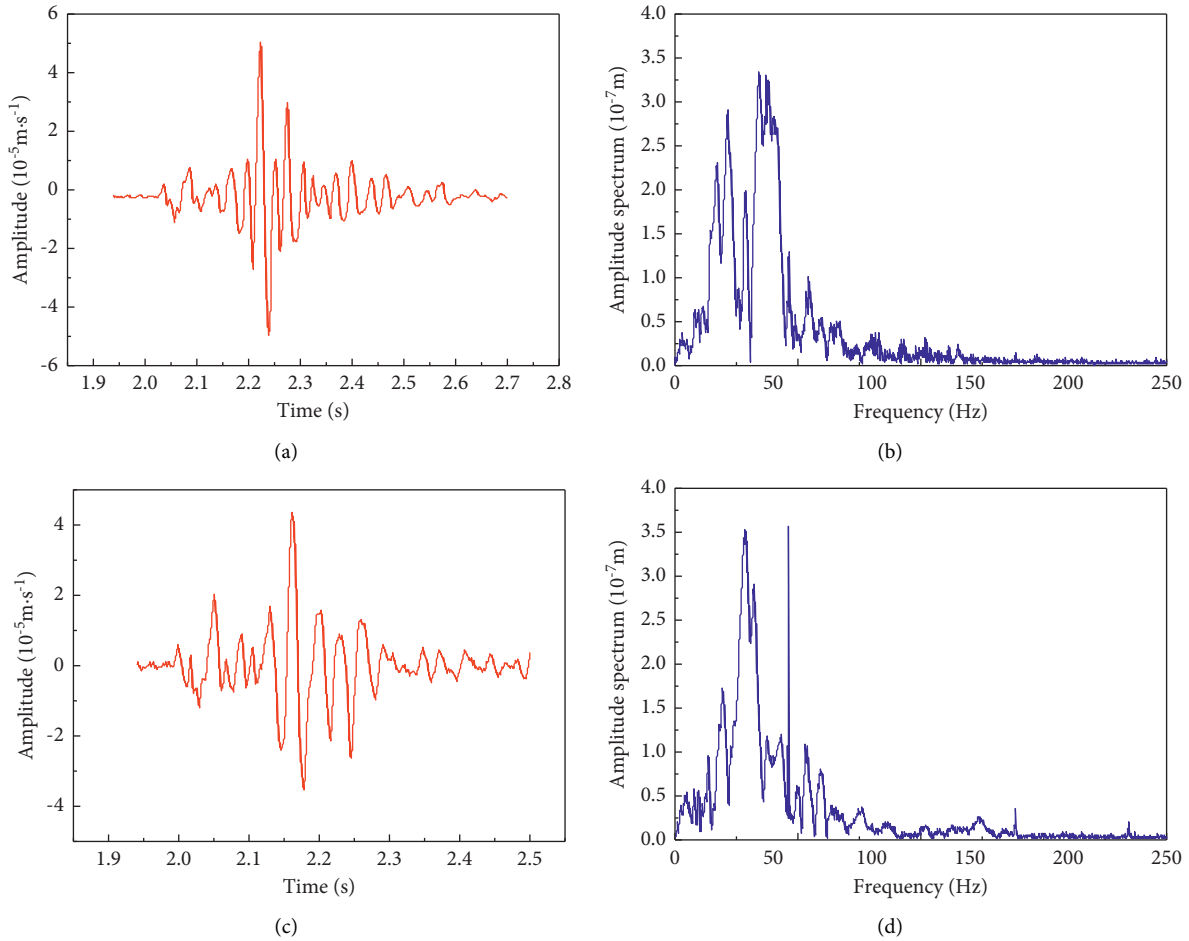


FIGURE 8: Curves of vibration velocity-time and amplitude spectrum-frequency with vibration energy = 871.7724 J. (a) Vibration velocity-time (sensor 6#). (b) Amplitude spectrum-frequency (sensor 6#). (c) Vibration velocity-time (sensor 9#). (d) Amplitude spectrum-frequency (sensor 9#).

TABLE 3: Comparison of MS signals with different energy levels monitored in Liyazhuang Coal Mine.

Energy levels (J)	Duration (ms)	Amplitude (m/s)	Attenuation rate	Frequency bands	Main frequency (Hz)
10 ⁴	800–1000	(0.6–6.5) × 10 ⁻⁴	Slow	0–200	40–70
10 ³	600–800	(0.2–0.5) × 10 ⁻⁴	Fast	0–160	10–75
10 ²	550–750	(0.2–0.6) × 10 ⁻⁴	Faster	0–120	15–80

By MS monitoring and analysis, in the advancement of working face, several typical shock events (Figure 3) occurred around the II228 working face. Figure 9 shows the waveforms of typical seismic signals and Figure 10 shows the corresponding curves of amplitude spectrum-frequency.

On May 5, 2011, a vibration was detected at the rear of 226 working face at 6:53:10 (Figure 3). According to the analysis of SEISGR and Multilok software, the geographical coordinates of the shock event were (37569200.00, 4057027.00, -220.14), and the vibration energy was 1.78 × 10³ J. And the vibration waveform was generated by the immediate roof falling in the gob (Figure 9(a)). From Figure 10(a), the main frequency bands range is about 0–100 Hz and the maximum energy concentrates on the frequency bands of 25–35 Hz.

On May 6, 2011, a vibration was detected at the rear of 226 working face at 16:51:36 (Figure 3). According to the analysis of SEISGR and Multilok software, the geographical coordinates of the shock event were (37569035.71, 4056781.66, -232.14), and the vibration energy was 2.72 × 10⁴ J. And the vibration waveform was a typical waveform of main roof rupturing (Figure 9(b)). From Figure 10(b), the main frequency bands range is about 0–140 Hz and the maximum energy concentrates on the frequency bands of 20–40 Hz.

On May 10, 2011, a major shock event appeared in a large fault near the cut-off of the II228 working face at 23:05:53 (Figure 3). It can be confirmed this shock event was induced by fault activation by signal waveform analysis and MS locating. And 7 sensors arranged in the II and IV mining

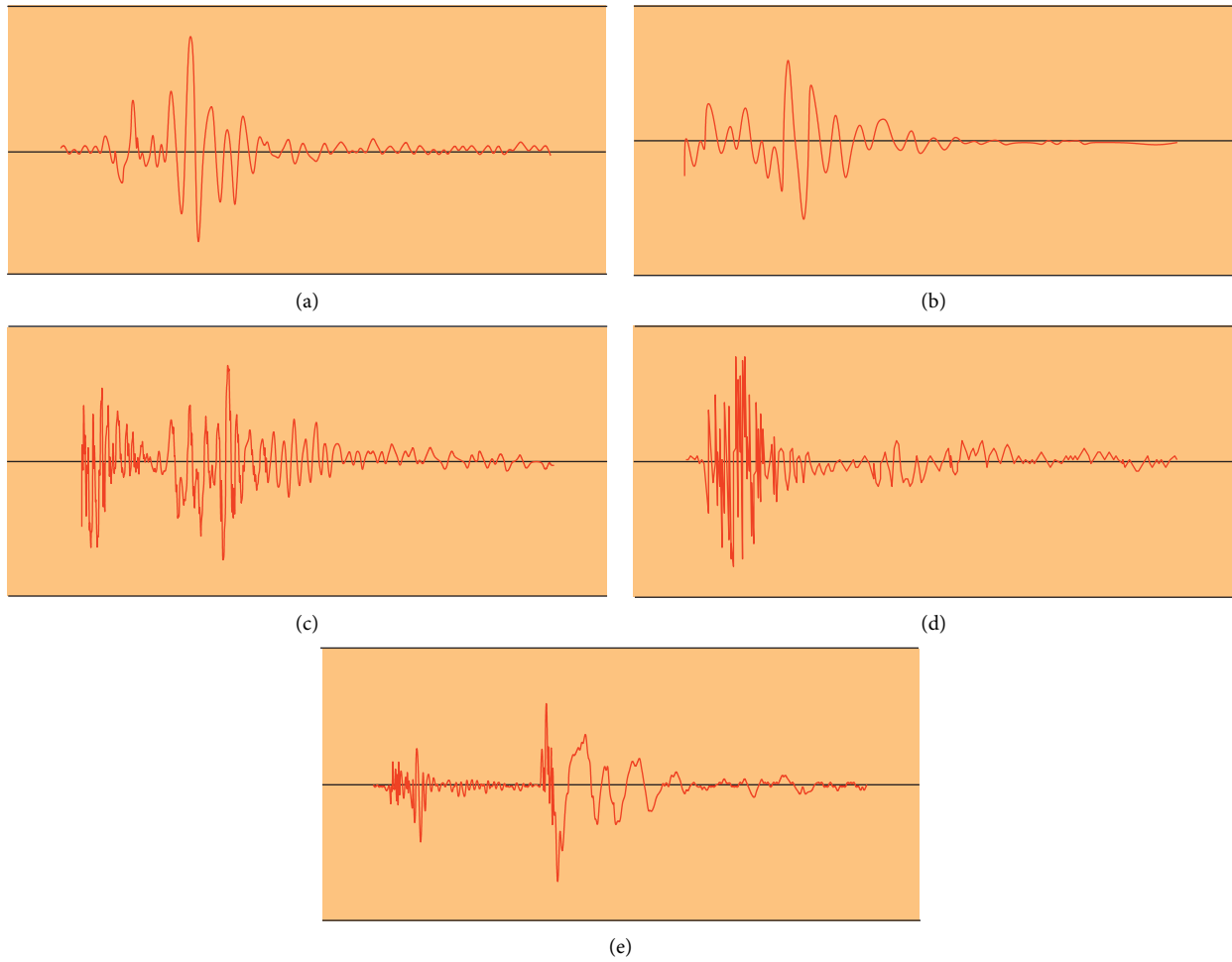


FIGURE 9: Waveforms of typical seismic signals. (a) Immediate roof rupturing in the gob. (b) Main roof rupturing in the gob. (c) Fault activation. (d) Roof fracturing in the cut-off. (e) Artificial blasting in the drilling site.

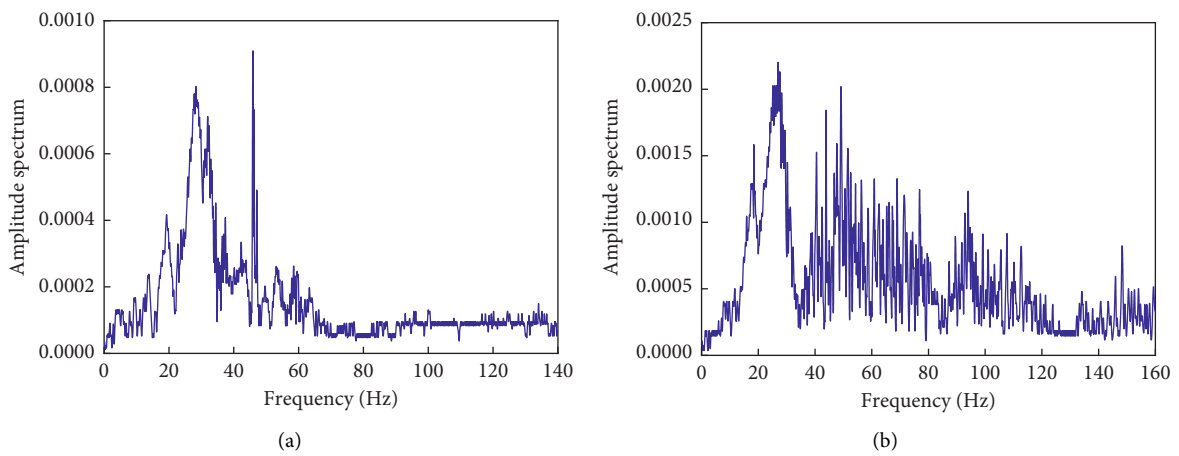


FIGURE 10: Continued.

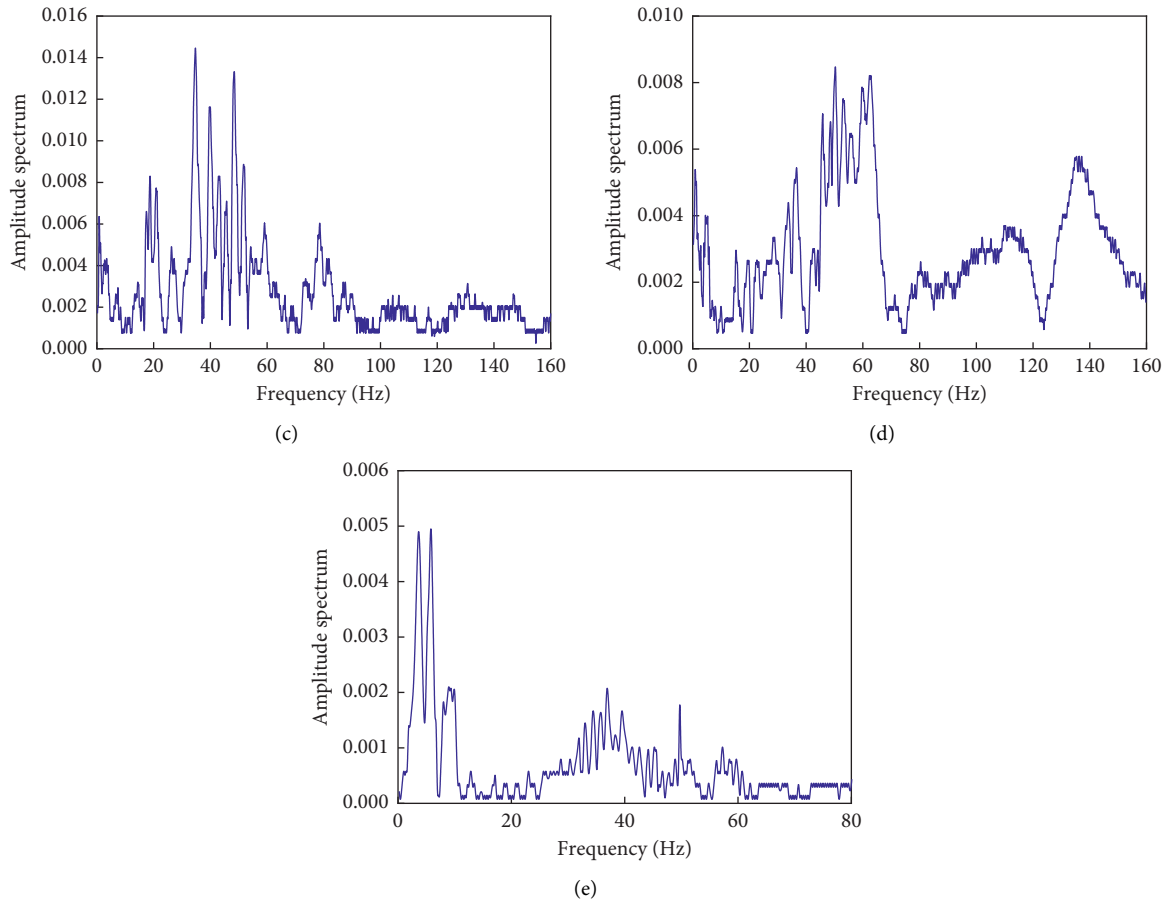


FIGURE 10: Curves of amplitude spectrum-frequency. (a) Immediate roof rupturing in the gob. (b) Main roof rupturing in the gob. (c) Fault activation. (d) Roof fracturing in the cut-off. (e) Artificial blasting.

areas have recorded the vibration information, indicating that the vibration energy is really large. According to the analysis of SEISGR and Multilok software, the geographical coordinates of the shock event were (3756889.84, 4057308.61, -217.87), and the vibration energy was 2.78×10^5 J. Figure 9(c) shows the waveform of this vibration. And the corresponding frequency spectrum is obtained by using the fast Fourier transform method, as shown in Figure 10(c). Obviously, the main frequency bands range is about 0–120 Hz and the maximum energy concentrates on the frequency bands of 35–55 Hz.

On May 15, 2011, a mine seismicity with high energy occurred near the cut-off of the II228 working face at 22:14:20 (Figure 3). According to the analysis of SEISGR and Multilok software, the geographical coordinates of the shock event were (37568718.80, 4057133.48, -240.56), and the vibration energy was 1.38×10^4 J. From the location and the vertical elevation of the epicenter source, the vibration was caused by the roof fracturing due to the high stress superimposing at the II228 cut-off. The vibration waveform was shown in Figure 9(d). After waveform attenuation, there are still large fluctuations in the tail, which is obviously different from roof fracturing in the gob and artificial blasting. From Figure 10(d), the main

frequency bands range is about 0–160 Hz and the maximum energy concentrates on the frequency bands of 40–80 Hz. Besides, the spectrum is relatively scattered. Although the amplitude and frequency of the wave caused by the vibration were relatively large, there was no rock burst occurring. This is because the vibration energy did not reach the average energy level required for the occurrence of rock burst under normal conditions; on the other hand, the location of the seismic source was deep, so the energy is attenuated to some extent during the propagation process.

On June 10, 2011, a vibration was detected at the NO.3 high-level drilling site near the II228 working face at 00:26:52 (Figure 3). According to the analysis of SEISGR and Multilok software, the geographical coordinates of the shock event were (37568545.00, 4056767.00, -224.06), and the vibration energy was 1.2×10^3 J. The vibration waveform was typical artificial blasting (Figure 9(e)), and the vibration information was recorded by 4 sensors arranged at II228 working face. Figure 10(e) shows the variation characteristics of corresponding frequency spectrum. It was found that the main frequency bands range is about 0–60 Hz and the maximum energy concentrates on the frequency bands of 0–10 Hz.

From above analysis, it also can be found that the vibration waveform caused by main roof fracturing is similar to that of the immediate roof fracturing, but their spectrum is different. The main frequency of the waveform generated by the main roof fracturing is lower than that of the immediate roof fracturing, and the energy generated by the former is generally much higher than that of the latter. The energy released by roof fracturing is basically the same as that of artificial blasting, but the waveform is obviously different. Besides, the frequency bands which the maximum energy concentrate on are also different.

4.3. MS Response Characteristics during Mining Activities and Roof Weighting

4.3.1. Variation of MS Events in the Normal Production Process. Generally, underground vibration caused by mining activities can be roughly divided into two categories. One type is directly caused by mining activities, including locomotive operation, loading loaders operation, artificial blasting, etc. The other is caused by the instability failure of surrounding rock due to mining activities. The SOS MS monitoring system can monitor, record, and preserve various vibration signals in real time, so as to locate the vibration source and calculate the magnitude of vibration energy.

(1) *Temporal Distribution of MS Events.* Figure 11 shows the variation of MS events near II226 working face in different periods of a day. More MS events occur in the period of normal production, while relatively less MS events occur in the period of handover and overhaul. Although the production time of Liyazhuang Coal Mine is not the same every day, in statistics, the frequency of MS events occurring near the working face in the period of normal production is twice that of the inspection time. For instance, during the shift period (14:00–16:00), as the mining activities reduce, the frequency of MS events is correspondingly reduced to a minimum. And after shift period (16:00–18:00), as mining activity increases, the frequency of MS events is also increased. Thus, it can be concluded that there exists a good correspondence between the frequency variation of MS events and mining activities, which validates the reliability of the SOS MS monitoring system from another perspective. Meanwhile, it also can be found that the MS events will not disappear immediately after stopping mining activities at working face, indicating that it would take some time for the surrounding rock to return to stability after the stopping of mining disturbance.

(2) *Spatial Distribution of MS Events.* Figure 12 shows the distribution of the MS events in daily production. The MS events are mainly concentrated in two zones: the first MS events concentration zone lies close to the II228 working face. In this zone, most MS events with high energy were mainly caused by the roof separation in front of the working face and roof fracturing and caving behind the working face. The second MS events concentration zone is the high-level drilling site, where most MS events were mainly generated

by the artificial blasting. In this zone, a high-level drainage roadway was being excavated. Thus, artificial blasting was carried out every day. On the other hand, the release of internal elasticity of rock strata due to the change of in situ stress caused by excavation may produce more MS events. In addition, it can be easily found that, with the advancement of II228 working face, the location of MS events also changed. Generally, the distribution of MS events is affected by mining activities, both spatially and temporally. The energy of these vibrations is generally below 10^3 J, which has no great influence on the occurrence of dynamic disasters.

4.3.2. Relationship between MS Events and Periodic Weighting of Working Face. To study the periodic weighting in the II226 working face, the real-time monitoring of hydraulic support working resistance was applied in the field. The measurement stations were arranged along the direction of working face. In the process of periodic pressure analysis, the sum of the average end-cycle resistance of the hydraulic support and its mean variance is taken as the main index to judge the periodic pressure. It can be calculated as

$$\sigma_p = \sqrt{\frac{1}{n} \sum_{i=1}^n (P_{ti} - \bar{P}_t)^2}, \quad (2)$$

$$\bar{P}_t = \frac{1}{n} \sum_{i=1}^n P_{ti},$$

where σ_p is the mean variance of the average end-cycle support resistance; n is the number of cycles; P_{ti} is the end-cycle support resistance in the i th cycle; \bar{P}_t is the average value of the end-cycle support resistance.

The criterion for the roof weighting can be expressed as

$$P'_t = \bar{P}_t + \sigma_p. \quad (3)$$

After calculation, the weighting criterion of each support is shown in Table 4.

Figure 13 shows the variation characteristics of periodic end-cycle support resistance of each support. The red lines indicate the weighting criterion, and the green lines indicate the weighting position.

Table 5 shows the statistics of periodic weighting time of each support in June, and Figure 14 shows the daily number and energy of MS events before and after three periodic weighting times in June. The column represents the daily total energy and the red line represents the daily numbers of MS events. The three times of periodic weighting of II226 working face were on June 5, 13, and 23, respectively. From Figures 13 and 14, with the breakage occurring in the main roof, the hydraulic support pressure increases periodically in the time of roof weighting. Two days before the period weighting, the daily average number of monitored vibrations was about 11 times, and the number of vibrations showed an increasing trend; the total energy of daily monitored vibrations was about 4500 J, of which the daily maximum vibration energy was 1800 J, and the overall vibration energy also showed an increasing trend. This increase of vibration

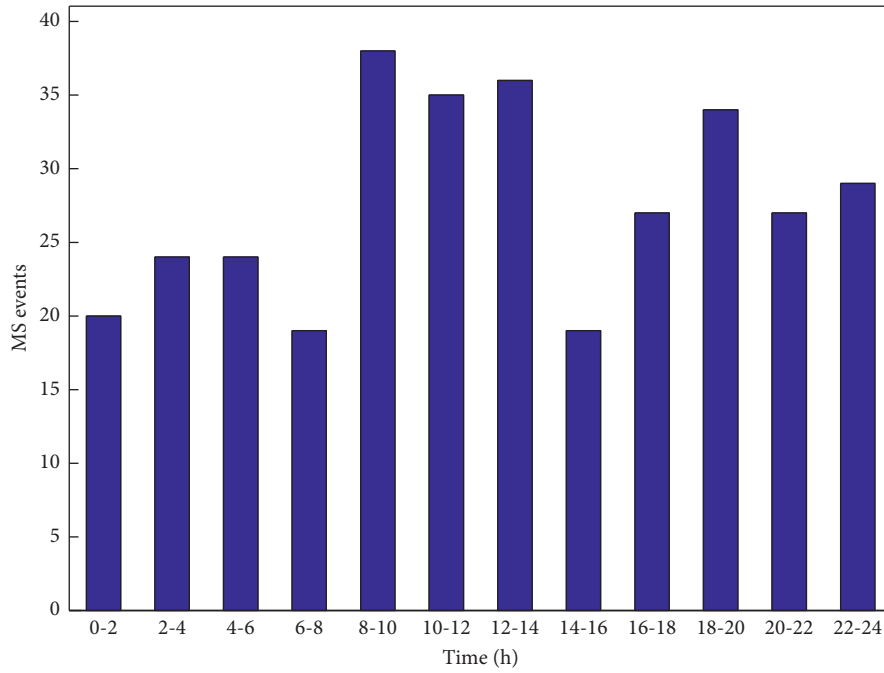


FIGURE 11: Temporal distribution of the MS events.

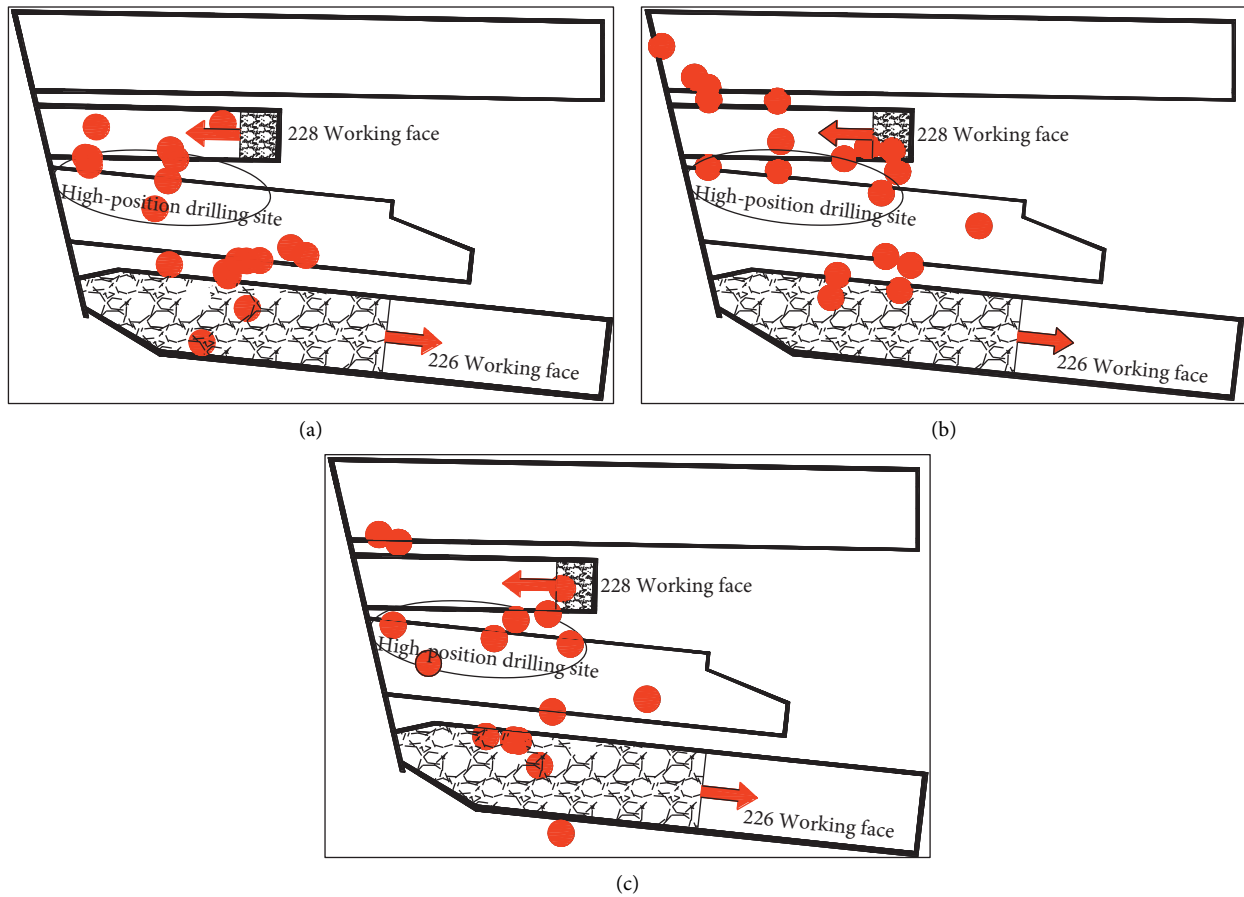
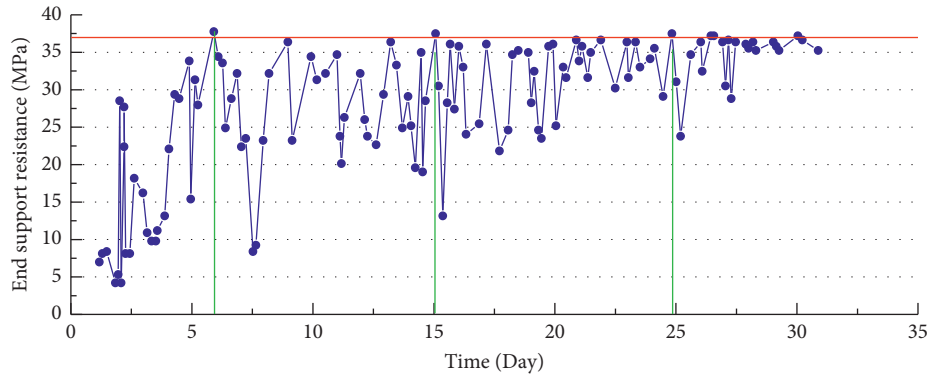


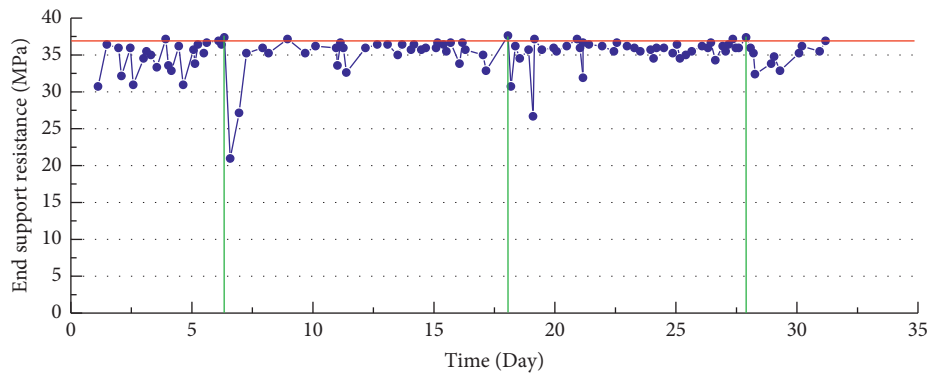
FIGURE 12: Spatial distribution of the MS events around II228 working face. (a) May 3, 2011; (b) May 11, 2011; (c) May 18, 2011.

TABLE 4: The weighting criterion of each support.

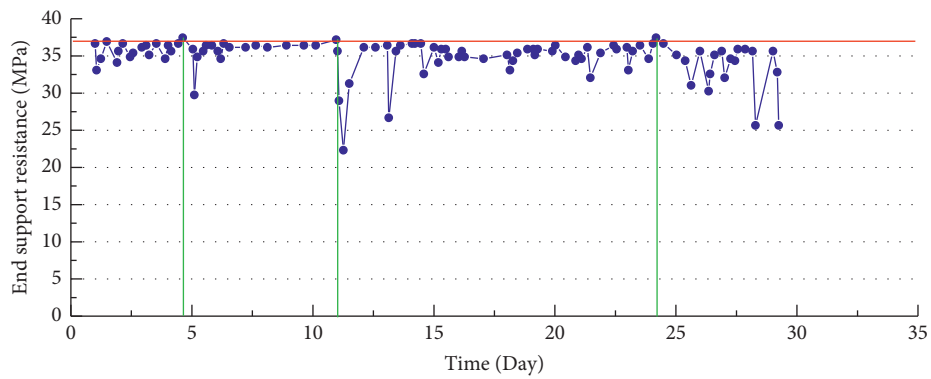
No.	End-cycle support resistance (MPa)		P_{ti}
	\bar{P}_t	σ_p	
3#	26.4	9.3	35.7
6#	27.7	9.3	37
8#	35	2.3	37.3
9#	34.8	2.4	37.2
13#	25.7	9.4	35.1
14#	29.5	5.7	35.2



(a)



(b)



(c)

FIGURE 13: Continued.

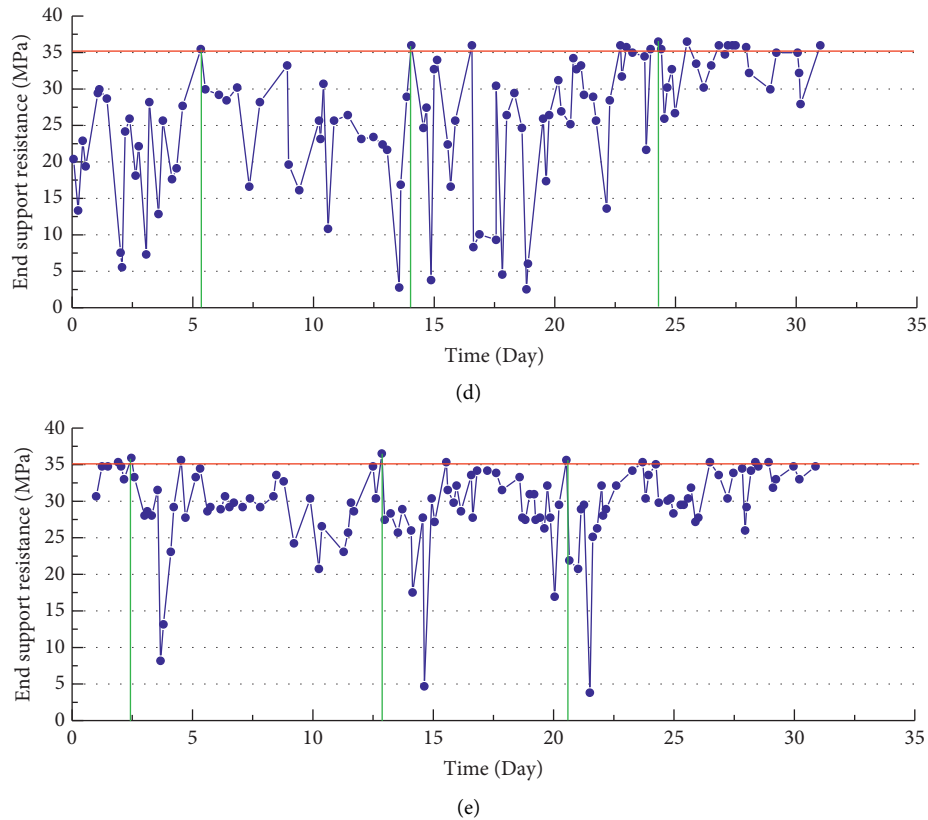


FIGURE 13: Variation characteristics of periodic end-cycle support resistance of each support. (a) 6# hydraulic support. (b) 8# hydraulic support. (c) 9# hydraulic support. (d) 13# hydraulic support. (e) 14# hydraulic support.

TABLE 5: The statistics of periodic weighting time of each support in June.

No.	Fist weighting	Second weighting	Third weighting
3#	3rd June	14th June	22th June
6#	5th June	15th June	24th June
8#	6th June	18th June	18th June
9#	4th June	10th June	24th June
13#	6th June	14th June	24th June
14#	2nd June	12th June	19th June

frequency and energy can be precursor information for roof pressure. With the advancement of the working face, the MS energy has the characteristic of periodic distribution, which is consistent with the periodic weighting revealed by the working resistance of the support.

5. Discussion

In the process of fracturing and sliding of coal and rock under the mining disturbances, microseismic waves with a certain frequency will propagate to the surrounding rock, which is also accompanied by the release of accumulated energy. The amplitude and frequency of the waves depend on the strength, stress state, fracture size, and the deformation speed of coal and rock [35]. The incubation process of rock burst is actually the process of the occurrence and expansion of cracks or secondary cracks in coal and rock

mass structure, which is the process of energy accumulation. And the occurrence of rock burst is the fracture and instability process of damage rock structure, which is the process of energy release [36]. The vibration energy of the roof pressure signals is large, and the amplitude of the signal is about 10^4 , which is due to the large deformation and failure area in the rock mass during the roof rupturing, and a large amount of elastic energy is released. Actually, for the process of fault activation, the initial instability of surrounding rock compaction fault is the initial stage of fault activation, and the single vibration energy generated is large, but the frequency is low. Then, the elastic stick-slip oscillation process of surrounding rock is the most important stage of the release of fault activation energy, and the vibration frequency is high. And the vibration frequency and energy are low in the process of plastic stick-slip failure. With the vibration energy and frequency of the surrounding rock in the stage of restabilization of the failure of the wall rock, the release of energy is large [37]. It can be seen that the analysis results of this paper are consistent with previous studies. Besides, the energy accumulated in coal and rock mass increases gradually, and the energy is in a stable release state. When the propulsion speed reaches a certain degree, this stable state will be destroyed, and the sudden release of energy will lead to the occurrence of large energy events. Thus, the distribution characteristic of MS energy and events can reflect the roof movement.

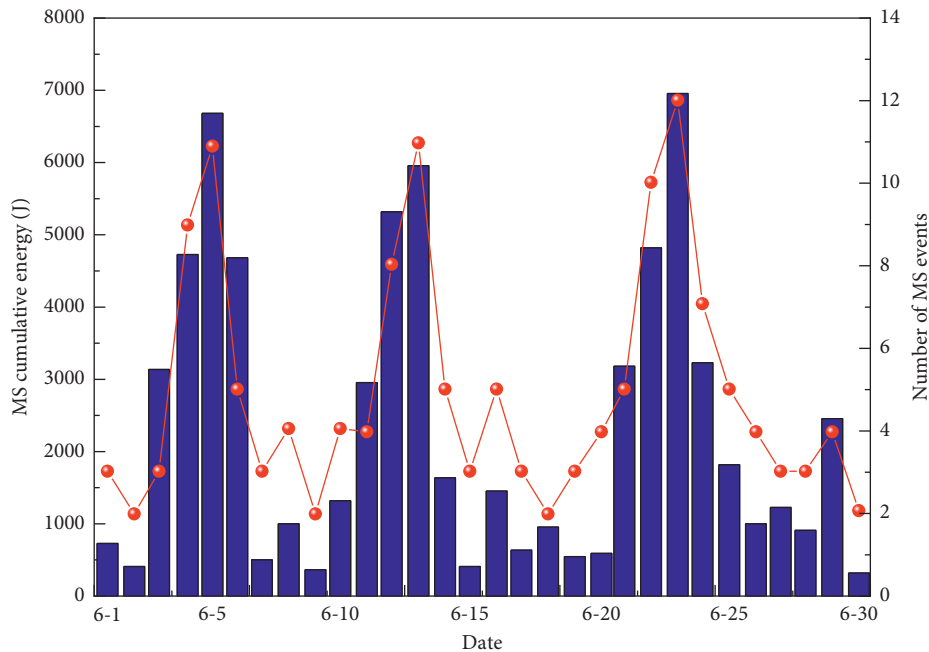


FIGURE 14: The daily number and total energy of MS events before and after three periodic weighting times in June.

6. Conclusion

- (1) There are large differences in the waveform and spectral characteristics of MS signals at different energy levels. High-level energy seismic signals are characterized by large amplitudes, low frequencies, relatively concentrated distribution, long vibration duration, and slow attenuation. As the energy decreases, the vibration attenuation rate gradually becomes faster, and the signal duration becomes shorter. Besides, the dominant frequency gradually develops from concentration to diffusion.
- (2) Due to the different fracture mechanisms of rock or coal mass, the different types of vibration induced by underground mining activities are different. There is a strong impact risk during fault activation because of its more released energy. In comparison, less energy would be released during roof falling.
- (3) With the advancement of the working face, the MS energy has the characteristic of periodic distribution, which is consistent with the periodic weighting revealed by the working resistance of the support. 1-2 days before the periodic weighting of working face, the MS events would increase. Combined with the real-time monitoring of hydraulic support, these MS characteristics can be regarded as precursory information of periodic weighting.

Data Availability

The data reported in this article are available from the corresponding author upon request.

Disclosure

Meanwhile, the sponsors had no role in the design of the study; in the collection, analyses, or interpretation of data; in the writing of the manuscript; and in the decision to publish the results.

Conflicts of Interest

The authors declare no conflicts of interest, and the manuscript is approved by all authors for publication.

Acknowledgments

This work was financially supported by Liaoning Revitalization Talents Program (Grant no. XLYC 1907168) and Natural Science Foundation of Liaoning Province (2019-MS-163).

References

- [1] M. Tutak, J. Brodny, D. Szurgacz, L. Sobik, and S. Zhironkin, "The impact of the ventilation system on the methane release hazard and spontaneous combustion of coal in the area of exploitation—a case study," *Energies*, vol. 13, no. 18, Article ID 4891, 2020.
- [2] B. Zhou, J. Xu, S. Peng et al., "Effects of geo-stress on the dynamic response of multi-physical field parameters during coal and gas outbursts under true triaxial stress," *International Journal of Rock Mechanics and Mining Sciences*, vol. 142, Article ID 104759, 2021.
- [3] J. Lu, C. Jiang, Z. Jin, W. Wang, W. Zhuang, and H. Yu, "Three-dimensional physical model experiment of mining-induced deformation and failure characteristics of roof and floor in deep underground coal seams," *Process Safety and Environmental Protection*, vol. 150, pp. 400–415, 2021.

- [4] X. Li, S. Chen, E. Wang, and Z. Li, "Rockburst mechanism in coal rock with structural surface and the microseismic (MS) and electromagnetic radiation (EMR) response," *Engineering Failure Analysis*, vol. 124, Article ID 105396, 2021.
- [5] R. Jiang, F. Dai, Y. Liu, and A. Li, "A novel method for automatic identification of rock fracture signals in microseismic monitoring," *Measurement*, vol. 175, Article ID 109129, 2021.
- [6] Y. Zhao, C. Cheng, Y. Liu, and G. Jing, "Study on microseismic and charge induction signal characteristics of different types of rock loading failure," *Journal of Water Resources & Water Engineering*, vol. 30, no. 5, pp. 199–203, 2021.
- [7] W. Zhang, T. Huo, C. Li, C. Wang, X. Qu, and C. Xin, "Characteristics of valuable microseismic events in heading face of an underground coal mine using microseismic system," *Shock and Vibration*, vol. 2021, Article ID 6683238, 2021.
- [8] Y. Zhao, G. Jing, Y. Fan, and Y. Pan, "Experimental study on the microseism and charge signal time-frequency characteristics in the process of fault stick-slip instability," *Chinese Journal of Rock Mechanics and Engineering*, vol. 39, no. 7, pp. 1385–1395, 2020.
- [9] Y. Xiao and X. Li, "Evolution of microseismic main frequency during intensive rockburst development in deep tunnel," *Journal of Shandong University of Science and Technology*, vol. 39, no. 4, pp. 14–19, 2020.
- [10] H. Wang and Q. Zong, "Study on safety of blasting vibration of super deep hole blasting in coal mine," *Journal of Safety and Environment*, vol. 15, no. 5, pp. 59–63, 2015.
- [11] B. Li, N. Li, E. Wang, X. Li, Y. Niu, and X. Zhang, "Characteristics of coal mining microseismic and blasting signals at Qianqiu coal mine," *Environ Earth Sci*, vol. 76, Article ID 722, 2017.
- [12] X. Zhang, R. Jia, X. Lu, Y. Peng, and W. Zhao, "Identification of blasting vibration and coal-rock fracturing microseismic signals," *Applied Geophysics*, vol. 15, no. 5, pp. 280–289, 2018.
- [13] J. Li, W. Lei, H. Zhao, T. Wang, Y. Liu, and H. Zhang, "Microseismic characteristics during impact failure of coal and rock under repetitive blast mining," *Journal of China University of Mining & Technology*, vol. 48, no. 5, pp. 966–974, 2018.
- [14] C. Zhang, G. Jin, C. Liu et al., "Prediction of rockbursts in a typical island working face of a coal mine through microseismic monitoring technology," *Tunnelling and Underground Space Technology*, vol. 113, Article ID 103972, 2021.
- [15] Z. Liang, R. Xue, N. Xu, and W. Li, "Characterizing rockbursts and analysis on frequency-spectrum evolutionary law of rockburst precursor based on microseismic monitoring," *Tunnelling and Underground Space Technology*, vol. 105, Article ID 103564, 2020.
- [16] Y. Wang, D. Lei, Y. Zheng, and T. Ma, "Study on response characteristics of surrounding rock rupture microseismic events during coal roadway excavation," *Tunnelling and Underground Space Technology*, vol. 2021, Article ID 9955994, 2021.
- [17] Y. Zhao, Y. Jiang, T. Wang, F. Gao, and S. Xie, "Features of microseismic events and precursors of rock burst in underground coal mining with hard roof," *Journal of China Coal Society*, vol. 37, no. 12, pp. 1960–1967, 2012.
- [18] P. Jiang, F. Dai, N. Xu, T. Li, and B. Li, "Analysis of correlation between fracture scale and frequency characteristic of rock mass and its engineering verification," *Rock and Soil Mechanics*, vol. 37, no. s2, pp. 483–492, 2016.
- [19] Z. Tang, X. Liu, Q. Xu, C. Li, and P. Qin, "Stability evaluation of deep-buried TBM construction tunnel based on microseismic monitoring technology," *Tunnelling and Underground Space Technology*, vol. 81, pp. 512–524, 2018.
- [20] Q. Qi and L. Dou, *Rock Burst Theory and Technology*, China University of Mining and Technology press, Xuzhou, China, 2008.
- [21] C. Liu, S. Li, C. Cheng, and X. Cheng, "Identification methods for anomalous stress region in coal roadways based on microseismic information and numerical simulation," *International Journal of Mining Science and Technology*, vol. 27, no. 3, pp. 525–530, 2017.
- [22] M. Ge, "Efficient mine microseismic monitoring," *International Journal of Coal Geology*, vol. 64, no. 1–2, pp. 44–56, 2005.
- [23] X. Li, Z. Li, E. Wang et al., "Analysis of natural mineral earthquake and blast based on Hilbert-Huang transform (HHT)," *Journal of Applied Geophysics*, vol. 128, pp. 79–86, 2016.
- [24] Y. Fujii and K. Sato, "Difference in seismic moment tensors between microseismic events associated with a gas outburst and those induced by longwall mining activity: proc 2nd International Symposium on Rockbursts and Seismicity in Mines, Minneapolis, 8–10 June 1988 P71–75. Publ Rotterdam: a A Balkema, 1990," *International Journal of Rock Mechanics and Mining Science & Geomechanics Abstracts*, vol. 28, no. 6, Article ID A397, 1991.
- [25] X. Luo, P. Hatherly, and M. Gladwin, "Application of microseismic monitoring to longwall geomechanics and safety in Australia," in *Proceedings of the 17th International Conference on Ground Control in Mining*, pp. 72–78, Morgantown, WV, USA, August 1988.
- [26] J. Liu, S. Xu, and Y. Li, "Analysis of rock mass stability according to power-law attenuation characteristics of acoustic emission and microseismic activities," *Tunnelling and Underground Space Technology*, vol. 83, pp. 303–312, 2019.
- [27] G. Wang, S. Gong, L. Dou, H. Wang, W. Cai, and A. Cao, "Rockburst characteristics in syncline regions and microseismic precursors based on energy density clouds," *Tunnelling and Underground Space Technology*, vol. 81, pp. 83–93, 2018.
- [28] F. Essrich, "Quantitative rockburst hazard assessment at Elandsrand gold mine," *Journal of the South African Institute of Mining and Metallurgy*, vol. 97, no. 7, pp. 319–324, 1997.
- [29] T. H. Ma, C. A. Tang, L. X. Tang, W. D. Zhang, and L. Wang, "Rockburst characteristics and microseismic monitoring of deep-buried tunnels for Jinping II hydropower station," *Tunnelling and Underground Space Technology*, vol. 49, pp. 345–368, 2015.
- [30] S. Zhu, Y. Feng, F. Jiang, and J. Liu, "Mechanism and risk assessment of overall-instability-induced rockbursts in deep island longwall panels," *International Journal of Rock Mechanics and Mining Sciences*, vol. 106, pp. 342–349, 2018.
- [31] X. Chen, W. Li, and X. Yan, "Analysis on rock burst danger when fully-mechanized caving coal face passed fault with deep mining," *Safety Science*, vol. 50, no. 4, pp. 645–648, 2012.
- [32] C.-P. Lu, L.-M. Dou, N. Zhang et al., "Microseismic frequency-spectrum evolutionary rule of rockburst triggered by roof fall," *International Journal of Rock Mechanics and Mining Sciences*, vol. 64, pp. 6–16, 2013.
- [33] A. Sainoki and H. S. Mitri, "Effect of slip-weakening distance on selected seismic source parameters of mining-induced fault-slip," *International Journal of Rock Mechanics and Mining Sciences*, vol. 73, pp. 115–122, 2015.
- [34] Y. Li, G. Lei, S. Xu, and D. Wu, "The spatial-temporal evolution law of microseismic activities in the failure process of

- deep rock masses,” *Journal of Applied Geophysics*, vol. 154, pp. 1–10, 2018.
- [35] S. Wang, G. Zhu, K. Zhang, and L. Yang, “Study on characteristics of mining earthquake in multicoal seam mining under thick and hard strata in high position,” *Shock and Vibration*, vol. 2021, Article ID 6675089, 2021.
- [36] Y. Zhang, “The different actions to the roof support of trusses and common bolts,” *Ground Pressure and Strata Control*, vol. 16, no. 3/4, pp. 159–161, 1999.
- [37] X. Guo, L. Dou, C. Lu, Z. Li, B. Liu, and C. Lv, “Research on the microseismic activity of fault reaction induced by coal mining,” *Safety In Coal Mines*, vol. 42, no. 1, pp. 26–30, 2011.

Research Article

Efficient Investigation of Rock Crack Propagation and Fracture Behaviors during Impact Fragmentation in Rockfalls Using Parallel DDA

Lu Zheng,^{1,2} Yihan Wu,¹ Wei Wu,³ Hong Zhang³ ,³ Xinyan Peng² ,² Xuelue Zhang,^{1,4} and Xuezen Wu¹

¹College of Civil Engineering, Fuzhou University, Fuzhou 350108, China

²Sichuan University-The Hong Kong Polytechnic University Institute for Disaster Management and Reconstruction, Sichuan University, Chengdu 610207, China

³College of Civil Engineering, Tongji University, Shanghai 200092, China

⁴Fujian Provincial Institute of Architectural Design and Research Co. Ltd., Fuzhou 350001, China

Correspondence should be addressed to Hong Zhang; hongzhang@tongji.edu.cn and Xinyan Peng; pengxinyan12321@my.swjtu.edu.cn

Received 23 April 2021; Accepted 31 July 2021; Published 31 August 2021

Academic Editor: Faming Huang

Copyright © 2021 Lu Zheng et al. This is an open access article distributed under the Creative Commons Attribution License, which permits unrestricted use, distribution, and reproduction in any medium, provided the original work is properly cited.

The study of the rock crack propagation and fracture behaviors during impact fragmentation is important and necessary for disaster evaluation of rockfalls. Discontinuous Deformation Analysis (DDA) incorporating virtual joints can offer a powerful tool to solve such a problem. In the analysis process, the computational efficiency is critical because the mesh must be very dense to make crack propagation more realistic. Thus, parallel DDA using OpenMP is applied. The flattened and precrack Brazilian disc tests are first reproduced, respectively, to verify the accuracy and efficiency of the parallel DDA with virtual joints. Then, the impact fragmentation process is simulated and validated with corresponding laboratory experiments in terms of crack propagation results. Furthermore, the effects of joint-slope angle, joint connectivity rate, and impact velocity on rock fracture behaviors are investigated. It is concluded that the peak number of cracks occurs when the joint-slope angle ranges between 30° and 45°; the higher impact velocity and joint connectivity rate tend to cause more cracks and larger damages to the specimen.

1. Introduction

Rockfall is one of the major geohazards in mountainous regions which is capable of threatening human life and properties [1, 2]. Since many infrastructures such as high-speed roads and railways are constructed inevitably through the area that is susceptible to rockfall, the investigation of development and mobility of rockfall is important [3–7].

Rockfall has been studied for decades [8, 9]. The researches of rockfall mechanics can be classified into two categories [1]: cause and motion. Rockfall can be triggered by weathering or fracturing of its surrounding [10, 11] and other factors like earthquakes [12]. When triggered, the rock will move in several modes of motion [13–15]. In addition,

researches about rockfall hazard assessment were also performed [16, 17]. Experiments are also served as an effective research approach about rockfall [18–20].

Compared to those aspects mentioned above, less attention has been paid to the fragmentation during rockfall [4]. Rockfall fragmentation is commonly observed in both in situ investigations and experimental tests [4, 21]. Fragmentation shows a great influence on the mechanical behaviors of rockfalls, which may greatly alter the trajectory and increase the probability of impact [22–24]. Because the physical fragmentation progress in rockfalls is complex, many computational codes adopted empirical or semiempirical models for the simulation [25]. Various fragmentation consideration approaches have been applied in rockfall

risk assessment, and most of them incorporate breakage models based on In Situ Block Size Distribution (IBSD) and Rockfall Block Size Distribution (RBSD) [26–29]. In recent years, some scholars tried to reveal the fragmentation mechanism in a physical way. The authors of [30] used the Discrete Element Method (DEM) to study the impact-induced fragmentation in rockfalls and claimed that large fragments are generated only when there are open preexisting fractures or when there are fully persistent closed fractures. De Blasio and Crosta [31] used DEM to study the fragmentation and boosting of rockfalls and rock avalanches. The authors of [32–34] used bond DEM particles to form an intact rock, and the simulation suggested that the collisions with the bottom floor produce fragmentations. Those studies yielded important and inspiring conclusions.

Nevertheless, the physical simulation of fragmentation in rockfalls still needs to be investigated. The rocks used are usually bonded by sphere particles, which can be different from real situations. The preexisting defects of the rock may affect the crack propagation and dynamic behavior of the fragments. Moreover, many studies were focused on the effects of impact loads on the fragmentation, but the internal factors such as preexisting crack have not been thoroughly investigated in mechanic manners. It is important because the existing cracks in rocks may significantly weaken the internal structure and dominate the fragmentation behavior.

To study the effect of preexisting cracks on rockfall fragmentation, two key issues need to be solved. First, a proper numerical tool needs to be selected, which can simulate the whole process of crack propagation, i.e., the continuity to discontinuity of medium, and the large deformation and displacement. Second, the computational efficiency should be sufficiently high because a careful investigation of crack propagation requires dense mesh. Based on those conditions, a parallel two-dimensional Discontinuous Deformation Analysis (2D DDA) on the OpenMP platform is a good choice. DDA was proposed by Shi [35]; it aims to analyze the evolution of blocky systems. Many studies involving DDA have been conducted since it has been proposed [36–43]. DDA has a complete theory about contacts and mechanics involving polygonal blocks, which is clearly suitable for crack propagation study. The virtual joint technique can be adopted to address the propagation of cracks. It refers to the joints that are not present in reality but do exist in models between blocks. The medium can be treated as continuous before cracking; when stress within the medium is great enough to create cracks, the blocks can detach each other through the virtual joints, and the virtual joints then become real joints. It has been introduced into DDA to simulate crack propagation [44–48]. When implementing virtual joints, the cracks extend through joints and the individual blocks keep intact. Apparently, to better describe the propagation of cracks in rockfalls, an intact rock should be meshed into blocks that are small enough. This brings the second issue, i.e., the computational efficiency. The authors have studied OpenMP-based parallel DDA, and the calculation can be significantly accelerated [49–51]. The parallel DDA is adopted in this study to facilitate the simulation of crack propagation in rockfalls.

In this paper, the effect of the preexisting crack in rocks on rockfall impact fragmentation is studied by using parallel DDA based on OpenMP. First, the theory of DDA and the involved methods of virtual joints and parallel techniques are briefly introduced. The implementation of the methods into DDA is also presented. Then, validation examples about flattened and precrack Brazilian disc tests are provided, respectively. After that, the effects of joint-slope angle, joint connectivity rate, and impact velocity on rock crack propagation in rockfall impact fragmentation are discussed in detail. Finally, conclusions are drawn.

2. Theory of DDA

Proposed by Dr. Shi [35], DDA has become a widely used tool in simulations involving discrete geological models such as landslides and rockfalls. The basic element in a DDA model is called block, which is an arbitrarily shaped polygon with constant stress and strain. The displacement variables are written into a vector form:

$$D_i = (u_0, v_0, r_0, \varepsilon_x, \varepsilon_y, \gamma_{xy}), \quad (1)$$

where D_i is the deformation matrix of block i in a blocky system; u_0 and v_0 are the x - and y -wise displacements at the centroid (x_0, y_0) , respectively; r_0 is the rotation of the block i ; ε_x and ε_y represent the x - and y -wise strains of the block, respectively; and γ_{xy} is the shear strain of the block i . The displacement of a point (x, y) within block i can be calculated by D_i using the following equation:

$$\begin{pmatrix} u \\ v \end{pmatrix} = T_i(x, y) \cdot D_i, \quad (2)$$

where $T_i(x, y)$ denotes displacement transformation matrix at $P(x, y)$, and it is calculated by

$$T_i(x, y) = \begin{bmatrix} 1 & 0 & -(y - y_0) & x - x_0 & 0 & (y - y_0)/2 \\ 0 & 1 & x - x_0 & 0 & y - y_0 & (x - x_0)/2 \end{bmatrix}. \quad (3)$$

The dynamic behavior of a system can be described by

$$M\ddot{D} + C\dot{D} + K D = F, \quad (4)$$

where D , \dot{D} , and \ddot{D} denote the matrices of displacement, velocity, and acceleration, respectively, and M , C , and K represent the matrices of mass, damping, and stiffness, respectively, of a system subject to the forcing matrix F . The damping matrix C takes the form of

$$C = \eta M, \quad (5)$$

where η is the viscosity. In this study, the viscosity η equals zero and thus no viscous damping is introduced. The energy loss is caused by the friction between blocks because the Mohr–Coulomb yield criterion is adopted to control the block sliding.

Equation (4) is solved by Newmark's β and γ method, with parameters $\gamma = 1.0$ for velocity weighting and $\beta = 0.5$ for acceleration weighting:

$$D^{n+1} = D^n + \Delta t \dot{D}^n + (\Delta t)^2 \frac{(1 - 2\beta)\ddot{D}^n + 2\beta\ddot{D}^{n+1}}{2}, \quad (6)$$

$$\dot{D}^{n+1} = \dot{D}^n + \Delta t \left[(1 - \gamma)\ddot{D}^n + \gamma\ddot{D}^{n+1} \right], \quad (7)$$

where superscript n denotes the calculation step. Taking $D^n = 0$ as the displacement at the start of the current calculation step and solving for the acceleration \ddot{D}^{n+1} from equation (6) result in

$$\ddot{D}^{n+1} = \frac{2}{(\Delta t)^2} D^{n+1} - \frac{2}{\Delta t} \dot{D}^n. \quad (8)$$

Substituting equations (8) into (7), the velocities at the end of the current calculation step are obtained as

$$\dot{D}^{n+1} = \frac{2}{\Delta t} D^{n+1} - \dot{D}^n. \quad (9)$$

Substituting equations (8) and (9) into (4) forms the global form

$$\tilde{K}D^{n+1} = \tilde{F}, \quad (10)$$

where \tilde{K} and \tilde{F} are generalized stiffness matrix and force matrix, respectively. Assuming that a blocky system contains n blocks, equation (10) can be rewritten as

$$\begin{bmatrix} K_{11} & K_{12} & \cdots & K_{1n} \\ K_{21} & K_{22} & \cdots & K_{2n} \\ \vdots & \vdots & \vdots & \vdots \\ K_{n1} & K_{n2} & \cdots & K_{nn} \end{bmatrix} \begin{bmatrix} D_1 \\ D_2 \\ \vdots \\ D_n \end{bmatrix} = \begin{bmatrix} F_1 \\ F_2 \\ \vdots \\ F_n \end{bmatrix}, \quad (11)$$

where K_{ij} is the stiffness submatrices and F_i is the loading submatrices of block n .

3. Parallel DDA with Virtual Joints and Its Verification

To model rock crack propagation during impact fragmentation in rockfalls, the domain of interest is generally discretized into a large number of triangular blocks using a triangular mesh generation method. Hence, a large-scale blocky system must be involved. To ensure efficiency, the parallel DDA with virtual joints is adopted to solve such problems.

3.1. Parallel DDA with Virtual Joints. The virtual joint in DDA is a general technique to study rock crack propagation, as shown in Figure 1. The essential of modeling rock crack propagation lies in the representation of an intact rock by gluing adjacent blocks through virtual joints and in the representation of the cracking by removing the linkage between the glued blocks. More specifically, the gluing of blocks can be realized by specifying strong strength parameters (friction, cohesion, and tensile strength) for virtual joints; meanwhile, the rock cracking is implemented by converting the virtual joints into real joints (with weak strength parameters). There are thus two kinds of interfaces

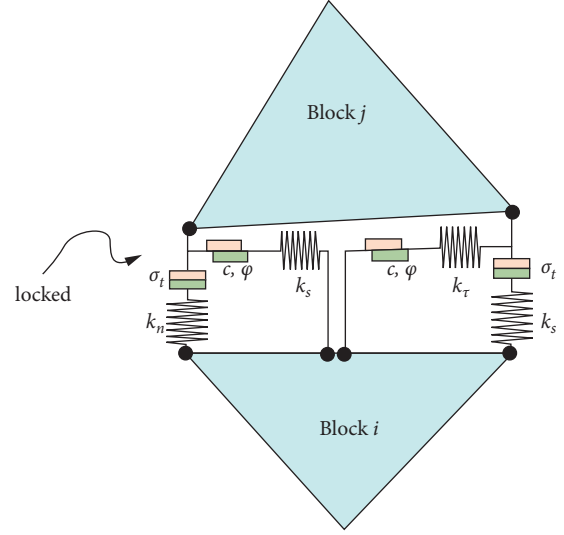


FIGURE 1: Schematic diagram of virtual joints.

between blocks: virtual and real interfaces. The real interfaces represent the real discontinuities (including the existing joints or fractures, the primary cracks, and the newly propagated cracks) whereas the virtual interfaces indicate the block boundaries that are artificially cut in the continuous domain [45]. The crack propagating paths in an intact rock are predetermined by the virtual joint system, and any crack propagates along the virtual interfaces.

With an aim to simulate continuous rock, a cohesive algorithm is applied to glue the adjacent blocks together through virtual interfaces for preventing their detachment. In DDA, when the contact between two blocks is in a locked contact state, both normal and shear contact springs are applied to prevent normal penetration and relative shear displacement. Once the contact force exceeds the joint strength, the corresponding contact spring is removed, and the contact state is changed. To ensure the bonding between adjacent blocks, the strength parameters of the virtual joints take the same values as those of the rock material. When the failure criterion is satisfied, the bonding between the adjacent blocks fails and the virtual interface becomes a real interface, which results in the crack initiation or propagation occurred at this interface. There are two types of failure: the tensile failure and the shear failure that are, respectively, along the normal and tangential directions. The tensile failure adopts the maximum tensile stress criterion while the shear failure employs the Mohr–Coulomb criterion. The maximum tensile and shear forces are, respectively, computed by

$$f_{t,\max} = \sigma_t l, \quad (12)$$

$$f_{s,\max} = cl + f_n \tan \varphi, \quad (13)$$

where φ , c , and σ_t are, respectively, the internal friction angle, cohesion, and tensile strength of the rock material; l is the contact length of the virtual joint; and f_n is the normal contact force. To determine the failure mode, two ratios (r_1 and r_2) are used and calculated as

$$r_1 = \frac{f_n}{f_{t,\max}}, \quad (14)$$

$$r_2 = \frac{f_s}{f_{s,\max}}, \quad (15)$$

where f_s is the shear contact force. If $r_1 > 1$ or $r_2 > 1$, the tensile failure or the shear failure occurs, leading to crack initiation or propagation along the virtual joint plane. When both r_1 and r_2 exceed 1, their values should be compared further: if $r_1 > r_2$, the tensile failure occurs; otherwise, the shear failure occurs. The flowchart of the cracking judgment process for virtual joints is presented in Figure 2.

Nevertheless, with the incorporation of virtual joints into DDA, the problem of computational ability becomes prominent because the mesh must be very dense to make crack propagation more realistic. In this case, a parallel technique based on OpenMP is adopted to accelerate the simulation. The previous work of [51] is followed in which a parallel framework for 2D DDA was developed and the parallel 2D DDA was applied to study a large-scale rockslide (containing numerous blocks) induced by earthquake. The parallelization for 2D DDA is briefly introduced here, and the interested readers are suggested to refer to [51].

A 2D DDA program can be regarded as an assembly of subroutines, and each of them has certain purposes and tasks. The main subroutines are contact detection, matrix assembly, equation solver, and contact post judgment. Those subroutines can consume as much as 96% of the total calculation time according to our previous research [51]. Therefore, by parallelizing the major subroutines, computational efficiency can be significantly improved, and the modeling of crack propagation will be easier. In this parallel strategy, independent tasks, for example, contact detection for every pair of blocks, are distributed to several threads that are forked by a master thread. These slave threads are then executed separately. However, for the tasks with data dependency or data race, some additional measures have to be implemented in advance, such as modifications of code structure or using atomic operation. Based on the previous work, the subroutine to complete the cracking judgment process for virtual joints is also executed in parallel. This is implemented by placing the compiler direction “#pragma omp parallel for” before the for loop that iterates every virtual joint, as shown in the upper shaded box in Figure 2.

3.2. Verification for Accuracy and Efficiency. The mechanical parameters such as tensile strength and fracture toughness of rock material can be determined by using the flattened Brazilian disc test. To verify the accuracy of the parallel DDA, the splitting process of the flattened Brazilian disc test is numerically studied. The Brazilian disc has a diameter of 100 mm and flats at each end with a central angle of 10° according to [52]. Three numerical models with different block quantities (2045, 4107, 6081) are constructed, as shown in Figure 3. The disc is placed between two platens each with a thickness of 20 mm. The top platen serves as the loading end and the bottom platen is fixed. The mechanical

properties for blocks to form the flattened Brazilian disc are the density of 2050 kg/m^3 , Young's modulus of 10.53 GPa, and Poisson's ratio of 0.12.

The strength parameters for virtual joints and real joints in the calculation are listed in Table 1. In the loading process, a time-dependent displacement constraint is applied at the loading platen at a loading rate of 2 mm/s. The calculation parameters in DDA are normal spring stiffness k_n of 10 GPa, maximum time step size Δt of 1×10^{-7} s, and maximum displacement ratio of 1×10^{-4} . In the simulation, gravity is not considered.

Under the diametrical compression, the crack initiation and propagation are reproduced. The cracks first initiate from the loading regions under the top platen and above the bottom platen. With the increasing loading, the cracks propagate along the vertical middle line, and finally, they coalesce to form a penetrative crack, dividing the specimen into two parts. The splitting process is similar to that in the experiment. The final splitting failure for the three numerical models is shown in Figure 4, compared with the experimental result [52]. The simulated results are in good agreement with the experiment one, suggesting the accuracy of the parallel DDA with virtual joints. In addition, a large number of microcracks appear in the top and bottom ends of the Brazilian disc, which may be attributed to the excessive stiffness of the platens.

On the other hand, the efficiency of the parallel DDA to analyze the rock crack propagation is investigated. The speedup ratio, defined as the ratio between serial and parallel CPU times, is calculated. The CPU times and the calculated speedup ratios for the three numerical models are compared in Figure 5. One can observe that the parallel DDA has approximately 5 times enhanced efficiency with 6 OpenMP threads used, compared with the serial computing.

In addition, the crack propagation of the precracked Brazilian disc (with a diameter of 100 mm) is also numerically studied. The single crack in the middle part of the disc has a length of 25 mm, and different values of the crack inclination (30° , 45° , 60° , 75°) are considered. By making a compromise between efficiency and accuracy, the domain of interest is discretized into around 4000 smaller blocks for each case [53]. The numerical model with a crack inclination of 45° is depicted in Figure 6.

The same mechanical properties and calculation parameters in DDA are adopted. The simulated final failure for the precracked Brazilian disc with different crack inclination angles is presented in Figure 7, compared with the experimental results [54]. It can be seen that both the crack propagation path and the fracture feature obtained by the parallel DDA accord well with the experiment results.

4. Study on Crack Propagation and Fracture Behaviors in Impact Fragmentation

In this section, the crack propagation of jointed rock mass under impact loads will be explored. The disc models of single jointed rock mass under different conditions are numerically analyzed. The fracturing behaviors during impact fragmentation as well as the effects of different factors on the impact fragmentation are studied.

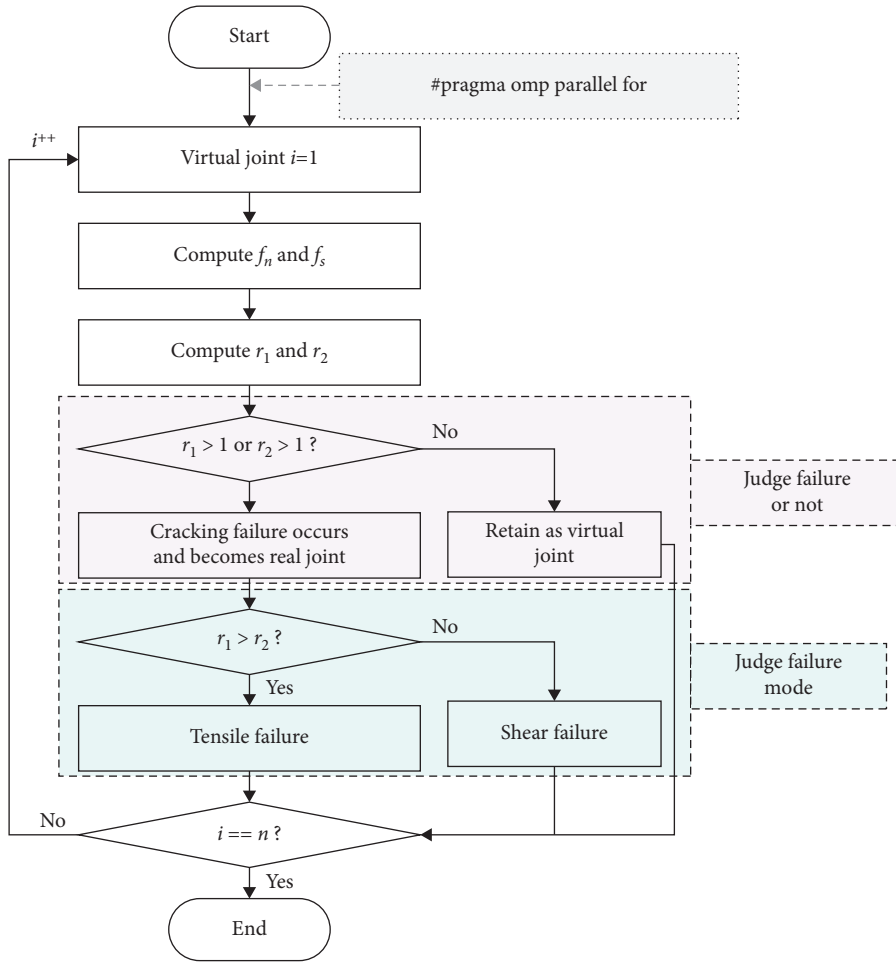


FIGURE 2: Flowchart of the cracking judgment process for virtual joints.

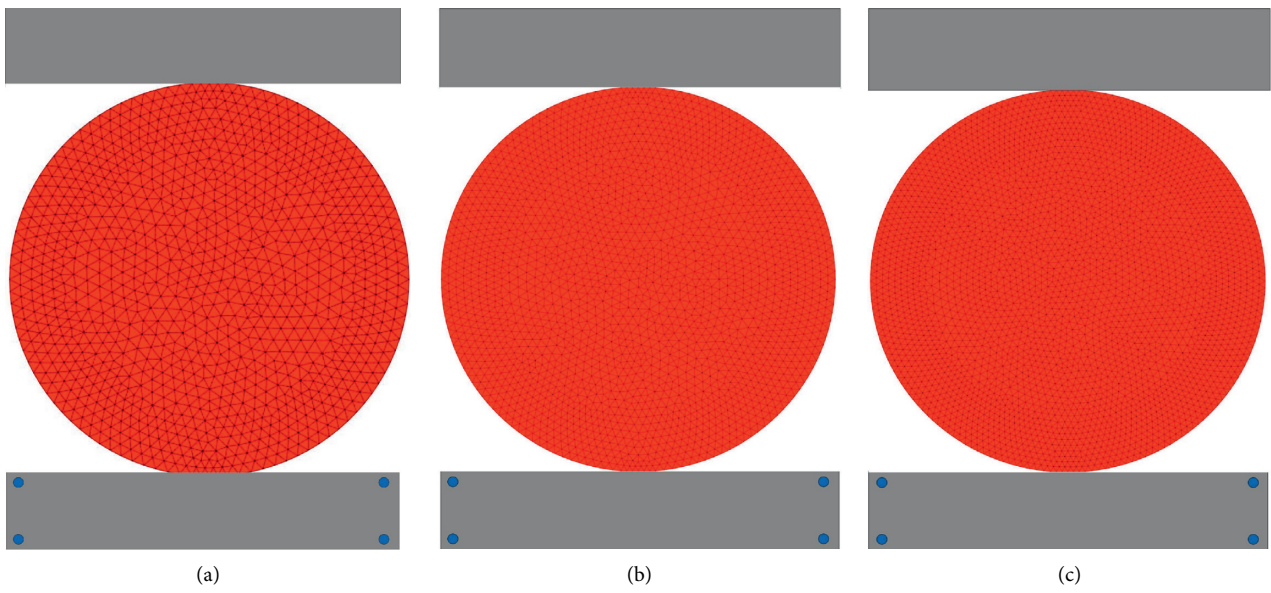


FIGURE 3: Three numerical models with different block quantities for the flattened Brazilian disc test. (a) 2045 blocks. (b) 4107 blocks. (c) 6081 blocks.

TABLE 1: Strength parameters for virtual joints and real joints when DDA simulating the flattened Brazilian disc test.

	Virtual joints	Real joints
Friction angle φ ($^{\circ}$)	38.5	20
Cohesion c (MPa)	8.29	1
Tensile strength σ_t (MPa)	7.86	1×10^{-5}

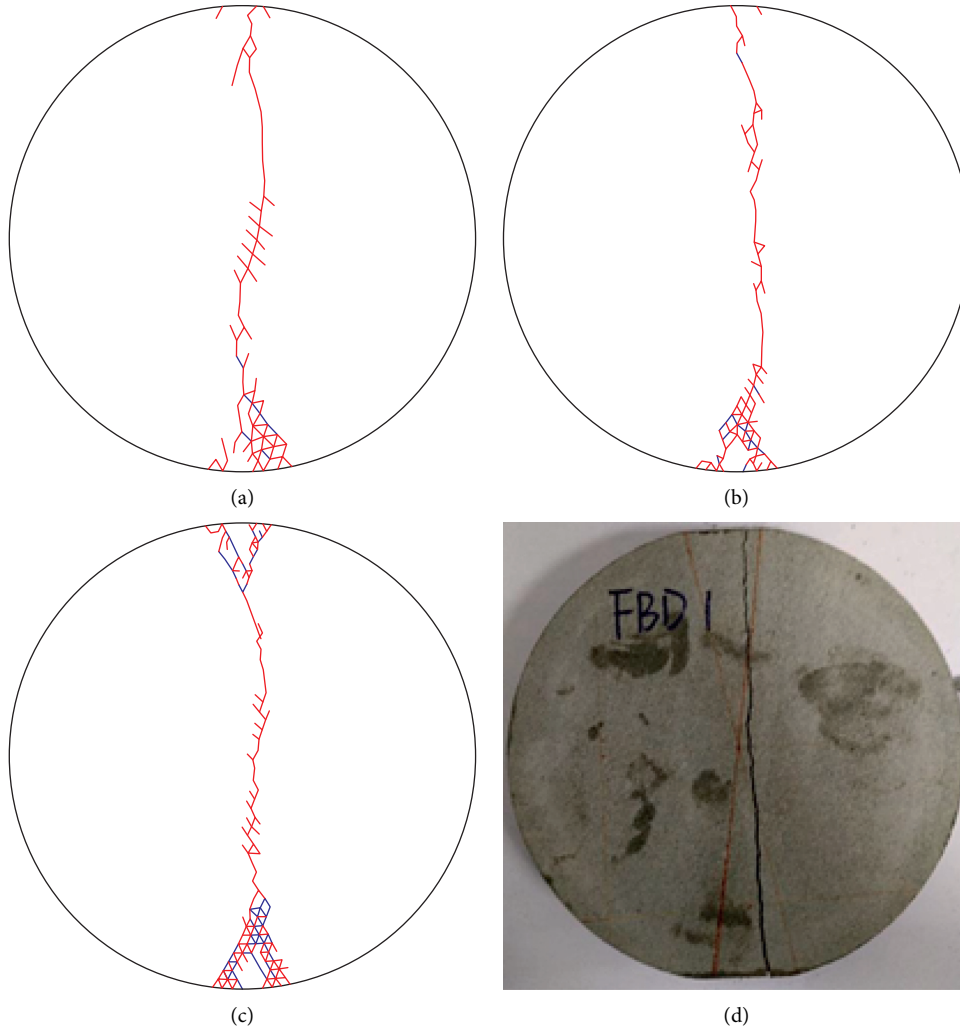


FIGURE 4: The final splitting failure for the three numerical models with different block quantities of blocks, compared with the experiment result [52]. (a) 2045 blocks. (b) 4107 blocks. (c) 6081 blocks. (d) experiment result.

The model for rockfall impact fragmentation comprises a rectangular collision plate ($100 \text{ mm} \times 20 \text{ mm}$) and a disc (with a diameter of 100 mm) formed by numerous smaller blocks (around $5500 \sim 5600$). The collision plate is placed at the bottom and keeps fixed in the whole simulation. The disc vertically impacts the collision plate. The disc contains a single crack with a width of 0.4 mm in the middle part. Different joint-slope angles θ (0° , 15° , 30° , 45° , 60° , 75° , and 90°) as well as different joint connectivity rates γ (0.25 , 0.50 , and 0.75) are considered. A representative numerical model is shown in Figure 8. To save time, the free fall process is not calculated, and instead, the disc with an initial velocity of v_0 impacts the collision plate as the simulation begins. The same mechanical properties listed in Section 3 are employed

for both blocks and joints. The calculation parameters in DDA for dynamic simulation are set as normal spring stiffness k_n of 0.35 GPa , maximum time step size Δt of $1 \times 10^{-7} \text{ s}$, and maximum displacement ratio of 1×10^{-4} . In the simulation, gravity is considered.

Considering different values of the joint-slope angle θ , the joint connectivity rate γ , and the initial impact velocity v_0 , various cases (as listed in Table 2) are studied.

4.1. Analysis of Fracture Behaviors in Impact Fragmentation. Figure 9(a) shows the failure states for the impact fragmentation modeling when different joint-slope angles θ (0° , 30° , 45° , 60° , 90°) are considered. In the different cases, the

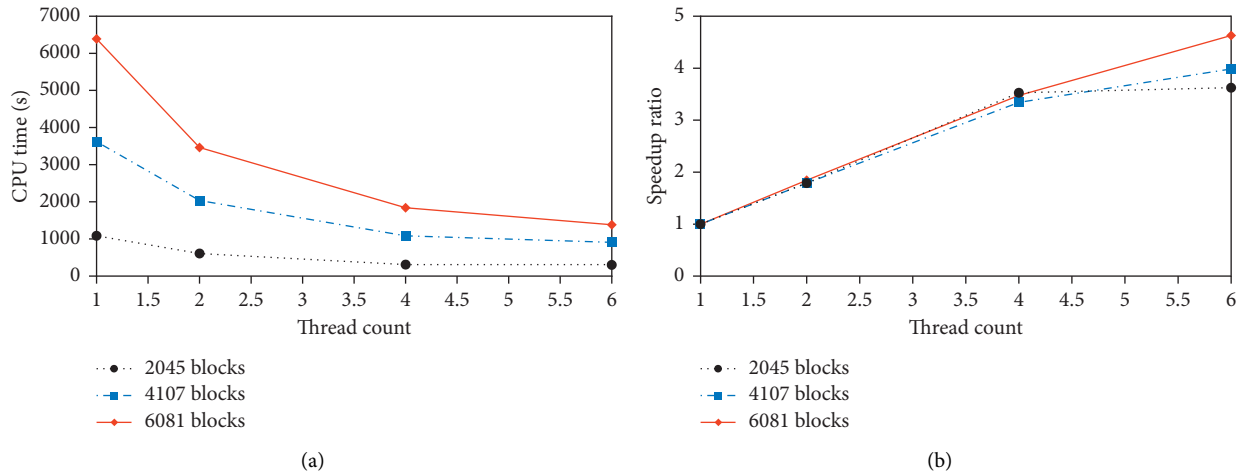


FIGURE 5: The CPU times and the calculated speedup ratios for the three numerical models of the flattened Brazilian disc test. (a) CPU times. (b) Calculated speedup ratios.

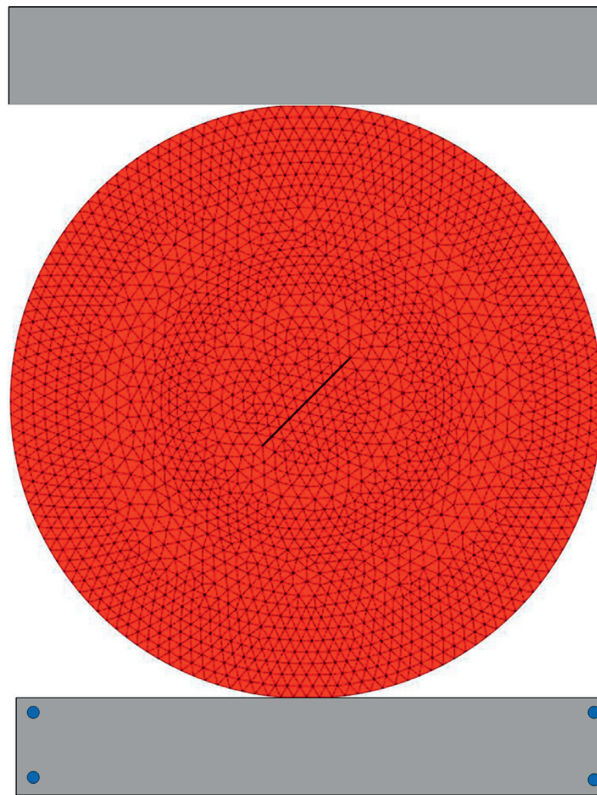


FIGURE 6: Numerical model of the precracked Brazilian disc with 45° crack.

joint connectivity rate γ is 0.25, and the initial impact velocity v_0 is 3.5 m/s. When $\theta = 0^\circ$, the fragmentation first occurs at the region near the impacting point, and individual blocks are cut out by the newly appeared cracks. The cracks then initiate from the middle of the joint and propagate radially toward the impact point and the top end of the specimen, and finally, they coalesce to form a penetrative crack. When $\theta = 45^\circ$, two wing cracks perpendicular to the

joint are first formed at the two ends of the prefabricated joint and gradually propagate toward the impact point and the top end of the specimen, and finally, two macrocracks are formed. When $\theta = 30^\circ$ or 60° , the crack initiation and propagation are similar to those in the case of $\theta = 45^\circ$. When $\theta = 90^\circ$, the stress wave is affected when it propagates from the impact point to the lower end of the joint, and it repeatedly oscillates between the impact point and the lower

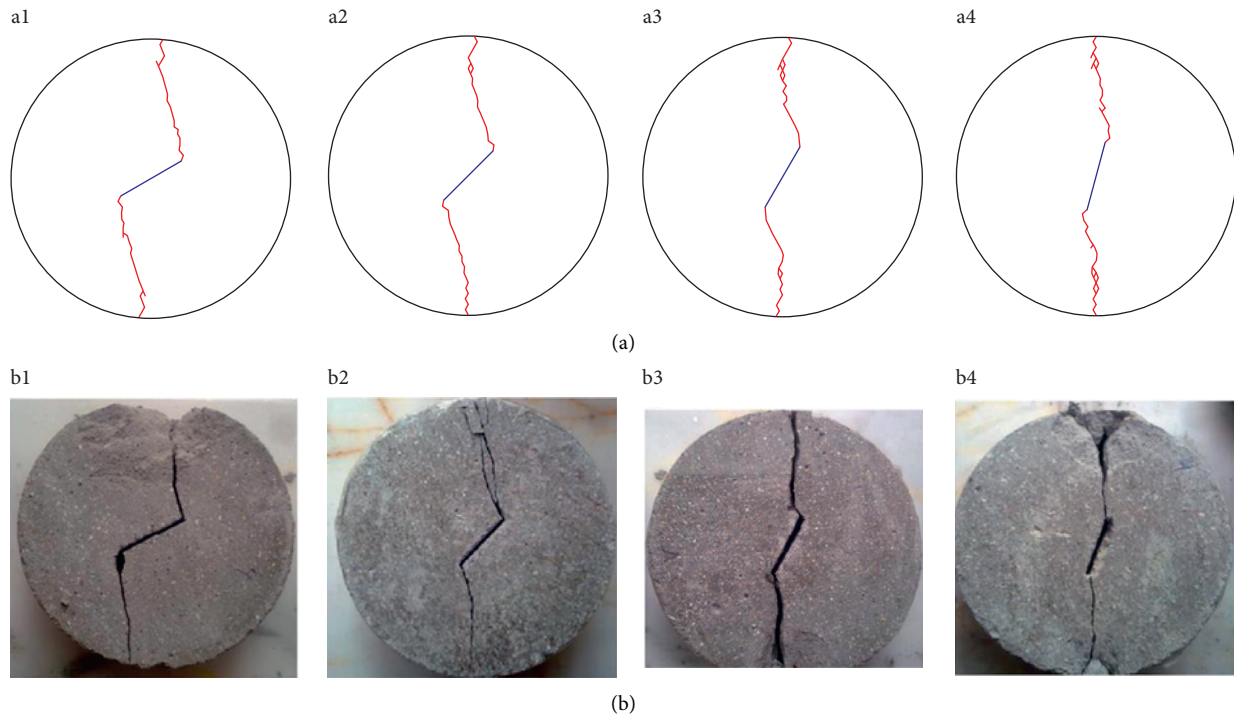


FIGURE 7: Comparison of the crack propagation paths from (a) the simulated and (b) the experimental results [54] for the precracked Brazilian disc with different crack inclination angles. a1 and b1 are 30 degrees, a2 and b2 are 45 degrees, a3 and b3 are 60 degrees, and a4 and b4 are 75 degrees.

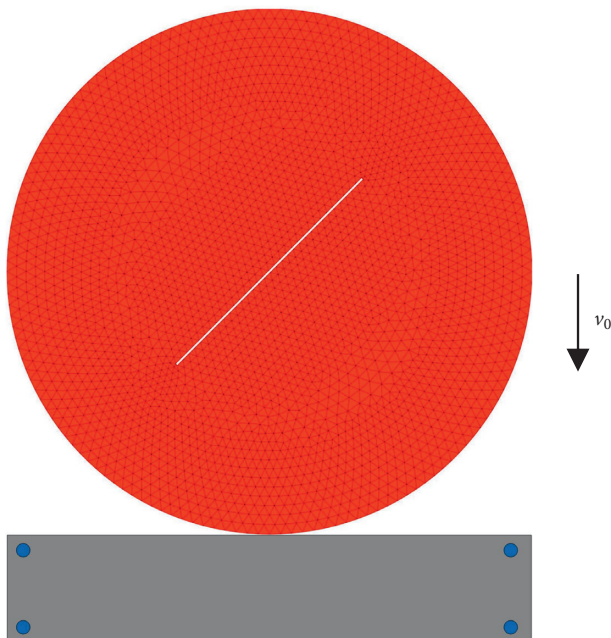


FIGURE 8: A representative numerical model ($\theta = 45^\circ$ and $\gamma = 0.50$) of rockfall impact fragmentation simulation.

end of the joint, resulting in a large amount of debris near the impact point. At the same time, the cracks propagate from the upper and lower ends of the joint toward the ends of the specimen in the vertical direction, finally leading to the

TABLE 2: Different values of the joint-slope angle θ , the joint connectivity rate γ , and the initial impact velocity v_0 for different cases.

Case no.	θ ($^\circ$)	γ	v_0 (m/s)	Case no.	θ ($^\circ$)	γ	v_0 (m/s)
1	0	0.25	3.5	8	45	0.25	3.5
2	15	0.25	3.5	9	45	0.50	3.5
3	30	0.25	3.5	10	45	0.75	3.5
4	45	0.25	3.5	11	45	0.25	3.0
5	60	0.25	3.5	12	45	0.25	3.5
6	75	0.25	3.5	13	45	0.25	4.0
7	90	0.25	3.5	14	45	0.25	5.0
				15	45	0.25	6.0

penetration failure of the specimen. By making a comparison between the simulated failure patterns presented in Figure 9(a) and the experiment results [55] shown in Figure 9(b), the fracturing behaviors are quite consistent.

In addition, the crack mechanism in impact fragmentation is clarified based on the calculation results in Case 4 ($\theta = 45^\circ$, $\gamma = 0.25$, and $v_0 = 3.5$ m/s). The penetrative crack formed in the specimen is the resultant failure mode of the stress distribution. In the simulation, the maximum principal stresses at different measurement points are recorded, as presented in Figure 10. The tensile stress is positive while the compressive stress is negative. It can be observed that after the specimen impacts the collision board, only the part near the impact point presents relatively large compressive stress whereas the tensile stress dominates the other parts. Measurement point A near the impact point shows gradually

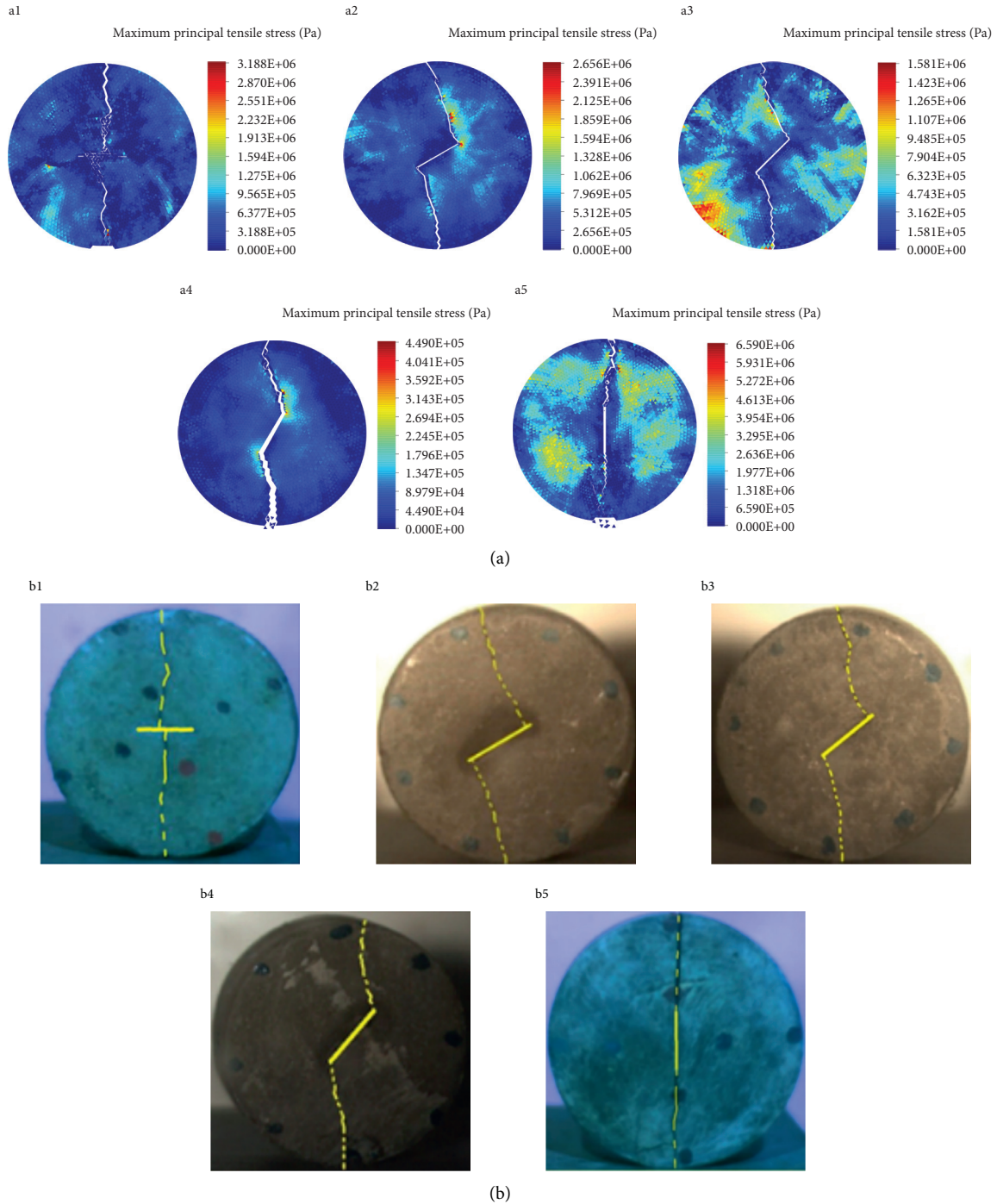


FIGURE 9: Comparison of failure states for the impact fragmentation modeling obtained from (a) the parallel DDA and (b) the experiment when the different joint-slope angles are considered ($\gamma = 0.25$ and $v_0 = 3.5\text{m/s}$). a1 and b1 are 0 degrees, a2 and b2 are 30 degrees, a3 and b3 are 45 degrees, a4 and b4 are 60 degrees, and a5 and b5 are 90 degrees.

decreasing compressive stress after reaching the maximum compressive stress peak, suggesting the occurrence of the plastic deformation inside the specimen. The measurement points (B, C, and D) placed along the vertical direction of the specimen successively attain the peak values from the bottom to the top. At about $265\ \mu\text{s}$, the measurement point E near the lower end of the joint first gets the peak stress and then rapidly decreases, which enables the stress

redistribution. At about $285\ \mu\text{s}$, the measurement point F near the upper end of the joint also reaches the peak stress. All the peak stresses of these two measurement points near the joint exceed the tensile strength of the specimen, and thus the tensile failure occurs. The peak values of stresses at the measurement points G and H placed near the middle of the joint are small so that the failure will not occur in the middle of the joint.

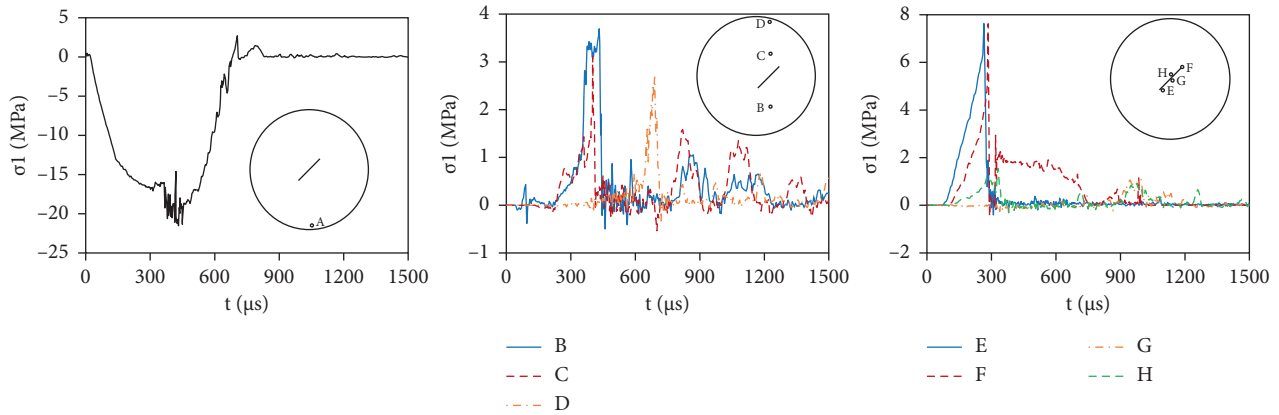


FIGURE 10: Time histories of the maximum principal stresses at different measurement points in Case 4 ($\theta = 45^\circ$, $\gamma = 0.25$, and $v_0 = 3.5\text{m/s}$).

Since the tensile strength of the rock material is much smaller than its compressive strength, the tensile failure typically occurs during the impact failure process. In order to reflect the failure of the specimen more clearly, the simulated maximum principal stress contours are plotted in Figure 11. One can also observe that relatively large compressive stresses appear in the area near the impact point of the specimen, but the compressive stress is only distributed in a small range near the impact point.

At about $300\mu\text{s}$, the maximum tensile stress exceeds the tensile strength of the specimen, causing the virtual joints of these blocks near the two ends of the preset joint to fail, and the cracks are thus initiated. At about $500\mu\text{s}$, the lower crack propagates toward the impact point, and the upper crack propagates toward the top end of the specimen. At about $800\mu\text{s}$, the cracks coalesce to form a penetrative crack, and the specimen is completely penetrated and destroyed. The failure of the specimen can be divided into three stages, namely, crack initiation, crack propagation, and crack penetration.

In addition, the simulated maximum principal stress contours in Case 1 ($\theta = 0^\circ$, $\gamma = 0.25$, and $v_0 = 3.5\text{m/s}$) and Case 7 ($\theta = 90^\circ$, $\gamma = 0.25$, and $v_0 = 3.5\text{m/s}$) are shown in Figure 12. In Case 1, many microcracks appear in the periphery of the preset joint at about $400\mu\text{s}$, and macrocracks sprout upward in the middle of the joint. The crack propagation gradually stagnates for a while. At about $900\mu\text{s}$, the radial cracks continue to propagate toward the impact point or the top end of the specimen. At $1400\mu\text{s}$, the upper cracks expand to the top end and the lower cracks expand to the impact point, causing the specimen to be completely penetrated and destroyed. In Case 7, at about $300\mu\text{s}$, the largest maximum principal stresses at the lower and upper ends of the joint, where the cracks initiate and propagate. At about $400\mu\text{s}$, the radial cracks continue to expand; due to the collision between the specimen and the collision board, stress superimposition is generated at the impact point and the lower end of the joint, resulting in fragmentation near the impact point of the specimen. At about $1200\mu\text{s}$, the cracks coalesce to form a penetrative crack, and the specimen is completely penetrated and destroyed.

4.2. Effect of Joint-Slope Angles. To study the effect of the joint-slope angle on the impact fragmentation, seven cases (Case 1–Case 7) with different joint-slope angles ($\theta = 0^\circ, 15^\circ, 30^\circ, 45^\circ, 60^\circ, 75^\circ$, and 90°) are considered. Some discussions have been conducted in Section 4.1. The cumulative number of cracks generated inside the specimen can reflect the internal damage: the more cracks in the specimen, the more serious the internal damage it suffers. Figure 13 shows the comparison of the cumulative crack number at about $1800\mu\text{s}$. It can be seen that the number of accumulated cracks in the specimen increases continuously in the range of $0^\circ \sim 30^\circ$ and reaches the maximum when the joint-slope angle θ is set to $30^\circ \sim 45^\circ$. After that, the number of accumulated cracks decreases with an increase of the joint-slope angle θ . This suggests that the internal damage of the specimen after impacting the collision plate is relatively large in the range of $30^\circ \sim 45^\circ$.

Figure 14 shows the comparison of the incremental crack number over time when different joint-slope angles are considered. The largest incremental number of cracks occurs at $150\mu\text{s} \sim 300\mu\text{s}$ for the specimens with the joint-slope angles of 0° and 15° , it occurs at $300\mu\text{s} \sim 450\mu\text{s}$ for the specimens with the joint-slope angles of $30^\circ, 45^\circ$, and 60° , and it occurs at $450\mu\text{s} \sim 600\mu\text{s}$ for the specimens with the joint-slope angles of 70° and 90° . One can conclude that, with the decrease of the joint-slope angle, the largest incremental number of cracks occurs earlier. Possibly because when the joint-slope angle is smaller, after being reflected by the joint surface, the stress wave is superimposed at the middle or the end of the joint to exceed the tensile strength, thereby initiating cracks and making the incremental number of cracks earlier reach the peak. When the joint-slope angle equals 90° , the joint will just slightly hinder the stress wave from propagating upwards and most of the stress wave will reflect downwards after reaching the top end of the specimen. Therefore, the incremental number of cracks will reach the peak later.

4.3. Effect of the Joint Connectivity Rate. To study the effect of the joint connectivity rate on the impact fragmentation, three cases (Case 8–Case 10) with different joint connectivity

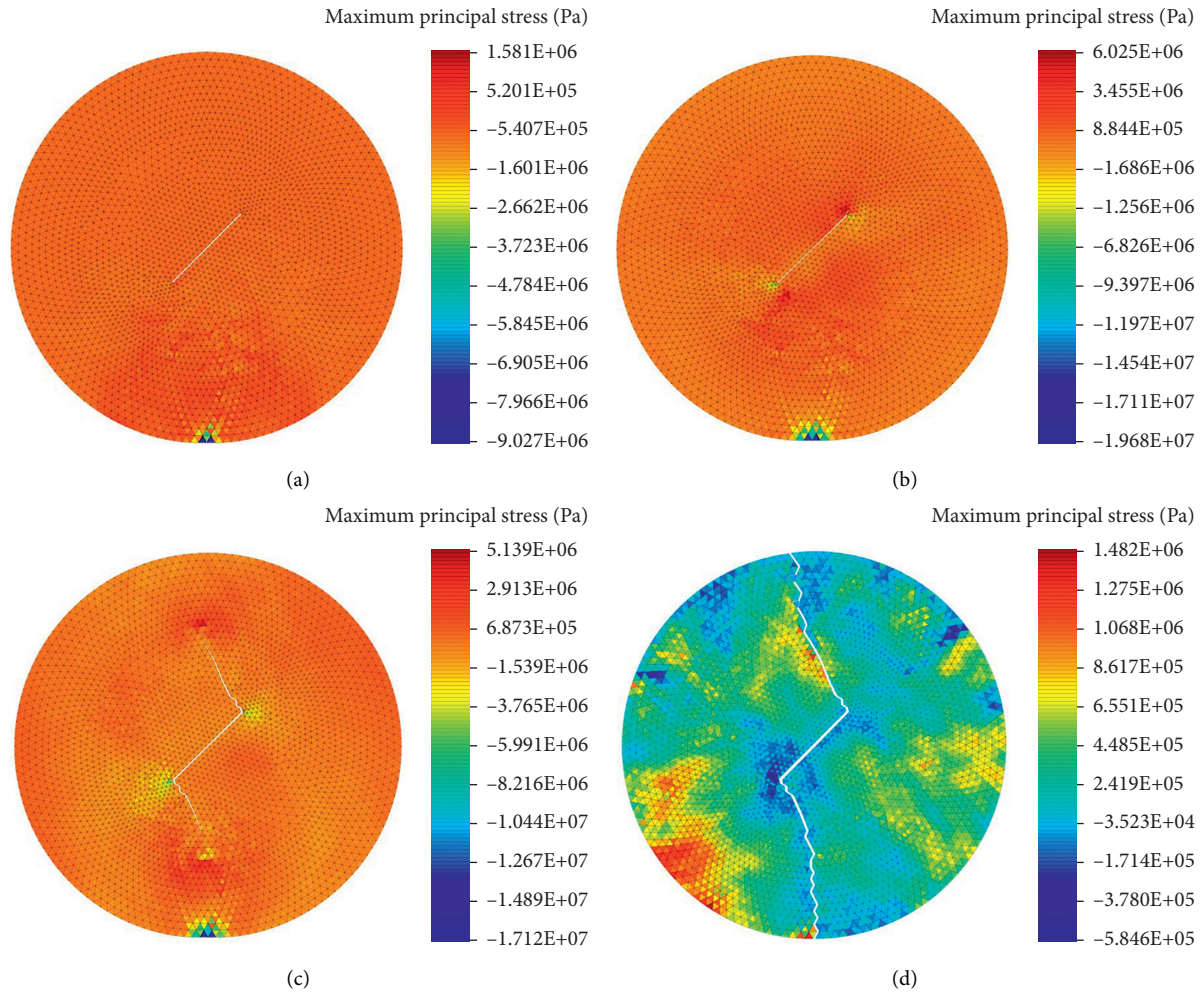


FIGURE 11: The simulated maximum principal stress contours in Case 4 ($\theta = 45^\circ$, $\gamma = 0.25$, and $v_0 = 3.5 \text{ m/s}$). (a) $100 \mu\text{s}$, (b) $300 \mu\text{s}$, (c) $500 \mu\text{s}$, and (d) $800 \mu\text{s}$.

rates ($\gamma = 0.25, 0.50, 0.75$) are considered. Figure 15 shows the simulated maximum principal stress contours in Case 8 ($\gamma = 0.25$) and Case 10 ($\gamma = 0.75$).

When the joint connectivity rate is smaller, the smaller damage of the specimen appears. This is because when its length is shorter, the joint shows less influence on the upward propagation of the stress wave. When the joint length is infinitely small, the specimen can be regarded as an intact rock mass without joints. The specimen damage increases with an increase in the joint connectivity rate. It can be seen from Figure 15(b) that the initial cracks appear at the upper position of the lower end of the preset joint, and the stress concentrates at the lower edge of the joint surface.

Figure 16 shows that, with the increasing joint connectivity rate, the cumulative crack number grows, leading to greater internal damage of the specimen. This result further confirms the analysis above. For the specimens with the joint connectivity rates of 0.25 and 0.50, the growth of the cumulative crack number is slower, and the incremental crack number (as shown in Figure 17) reaches the peak at about $450 \mu\text{s}$; after $1200 \mu\text{s}$, the crack propagation basically terminates. When the joint connectivity rate is 0.75, the joint has a greater influence on the stress wave. The cumulative

number of cracks in the specimen increases sharply, reaching the peak value at $600 \mu\text{s}$. After $1500 \mu\text{s}$, the crack propagation basically terminates. At $1800 \mu\text{s}$, the cumulative crack number of the specimen with the joint connectivity rate of 0.75 is 3.05 and 5.06 times that with the joint connectivity rate of 0.50 and 0.25, respectively. Therefore, the greater the joint connectivity rate, the greater the damage to the specimen.

4.4. Effect of Impact Velocity. To study the effect of the joint-slope angle on the impact fragmentation, five cases (Case 11–Case 15) with different impact velocities ($v_0 = 3.0 \text{ m/s}, 3.5 \text{ m/s}, 4.0 \text{ m/s}, 5.0 \text{ m/s}, 6.0 \text{ m/s}$) are considered.

Figure 18 shows the simulated maximum principal stress contours in Case 11 ($v_0 = 3.0 \text{ m/s}$), while Figure 19 shows those results in Case 14 ($v_0 = 5.0 \text{ m/s}$). When the impact velocity is smaller, the damage to the specimen is lower. As shown in Figure 18, the initial crack stops after extending for a certain distance, and the energy is completely consumed in the process of crack propagation, making the cracks unable to penetrate the specimen. When the specimen rebounds

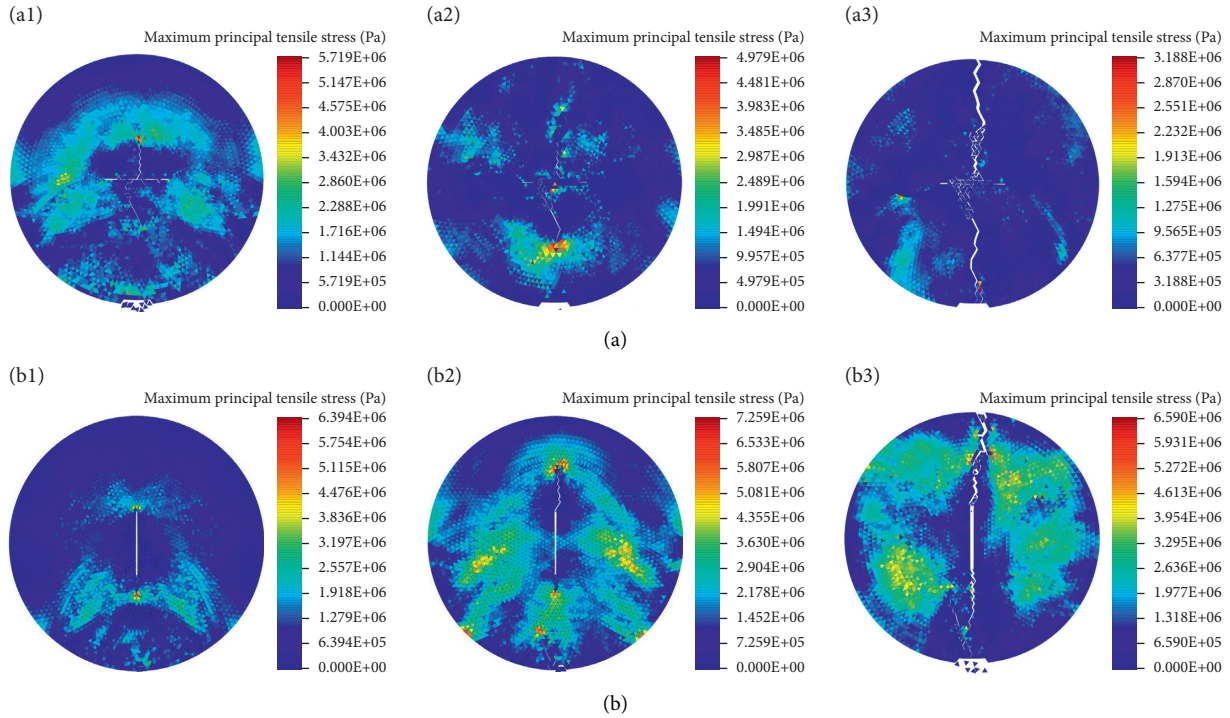


FIGURE 12: The simulated maximum principal tensile stress contours in (a) Case 1 and (b) Case 7 ($\gamma = 0.25$ and $v_0 = 3.5$ m/s). a1 is $400 \mu s$, a2 is $900 \mu s$, a3 is $1400 \mu s$, b1 is $300 \mu s$, b2 is $400 \mu s$, and b3 is $1200 \mu s$.

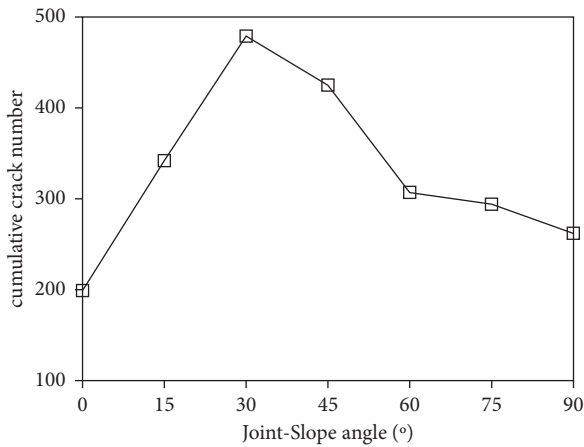


FIGURE 13: Comparison of the cumulative crack number at about $1800 \mu s$ when different joint-slope angles are considered.

upwards, the cracks shrink and become microcracks. As the impact velocity increases, the peak value of the stress also increases. As shown in Figure 19, affected by the impact stress wave, the specimen forms a high-stress zone at the joint end. The wing cracks are first generated at the joint ends, and then, secondary cracks also initiate at the joint ends. Specimen debris appears near the impact point after the collision. As the impact velocity increases, the specimen is more smashed.

Figure 20 compares the cumulative number of cracks in the specimen under different impact velocities. It can be seen

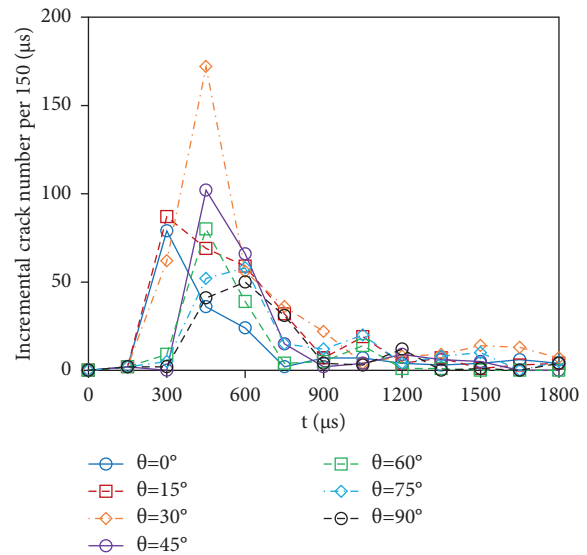


FIGURE 14: Comparison of the incremental crack number over time when different joint-slope angles are considered.

that when the impact velocity is 3.0 m/s or 3.5 m/s, the cumulative number of cracks hardly increases before $300 \mu s$. After $300 \mu s$, it begins to grow slowly, and the growth stops after $900 \mu s$, which indicates that the stress wave in the specimen is completely absorbed after $900 \mu s$ and the damage process ends. Meanwhile, when the impact velocity is greater than 4 m/s, the cumulative number of cracks grows

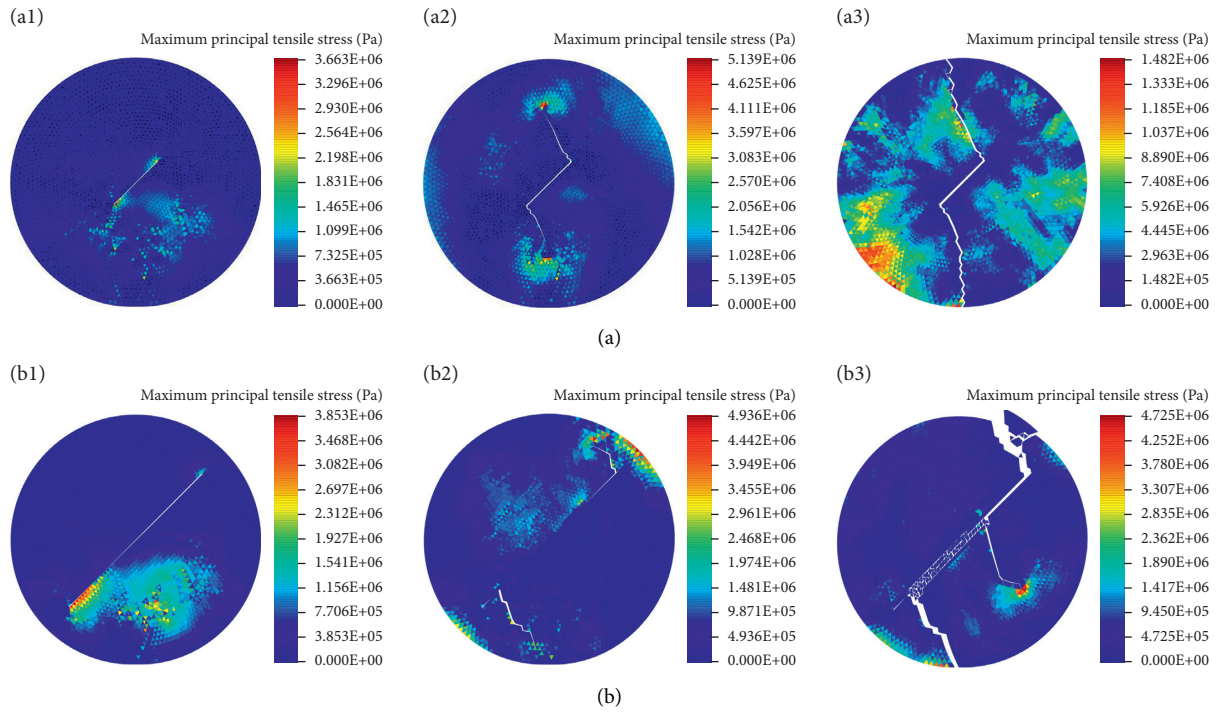


FIGURE 15: The simulated maximum principal tensile stress contours in (a) Case 8 and (b) Case 10 ($\theta = 45^\circ$ and $v_0 = 3.5\text{m/s}$). a1 and b1 are $200 \mu\text{s}$, a2 and b2 are $400 \mu\text{s}$, and a3 is $800 \mu\text{s}$ and b3 is $1000 \mu\text{s}$.

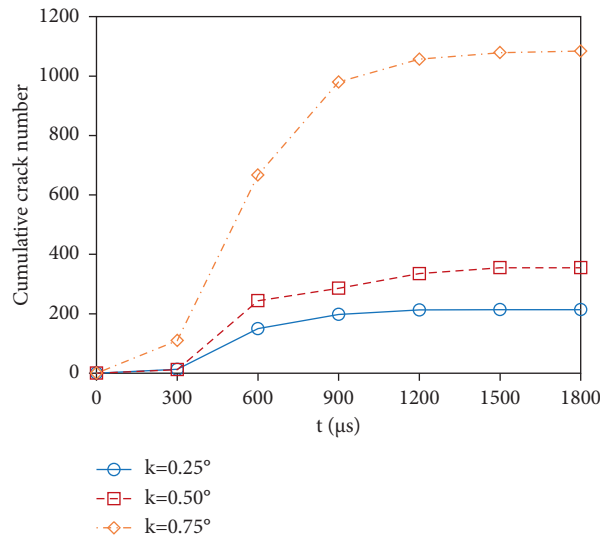


FIGURE 16: Comparison of the cumulative crack number over time when different joint connectivity rates are considered.

slowly before $300 \mu\text{s}$ but grows rapidly between $300 \mu\text{s}$ and $900 \mu\text{s}$. The growth of cracks continues even after $900 \mu\text{s}$, suggesting that the energy generated by the impact is not completely consumed when the specimen is penetrated, the stress wave is still propagating in the specimen, and the damage process is still continuing.

Figure 21 shows the comparison of the incremental number of cracks in the specimen under different impact velocities. It can be seen that, within the range of

$3.0 \sim 5.0 \text{ m/s}$, the number of cracks reaches the peak value at $300 \sim 450 \mu\text{s}$, and the crack grows the fastest in the whole process; after that, the number of cracks in the 3.0 m/s specimen drops rapidly, which indicates that the cracks no longer propagate. The greater the impact velocity is, the slower the decrease in the number of cracks is and the slower the energy dissipates. The comparison results suggest that the higher impact velocity leads to greater damage to the specimen.

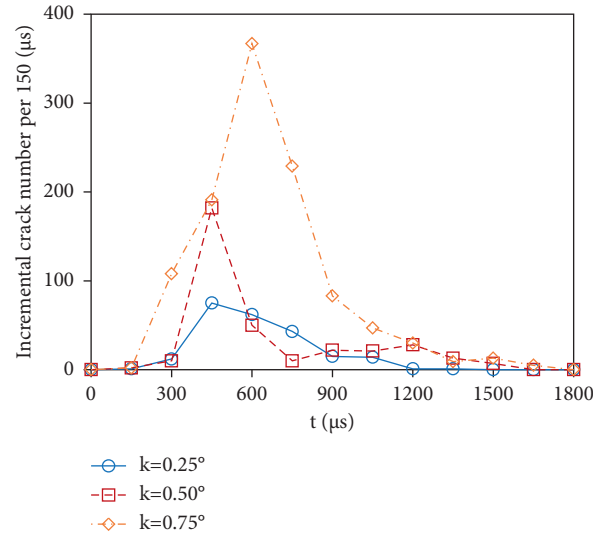


FIGURE 17: Comparison of the incremental crack number over time when different joint connectivity rates are considered.

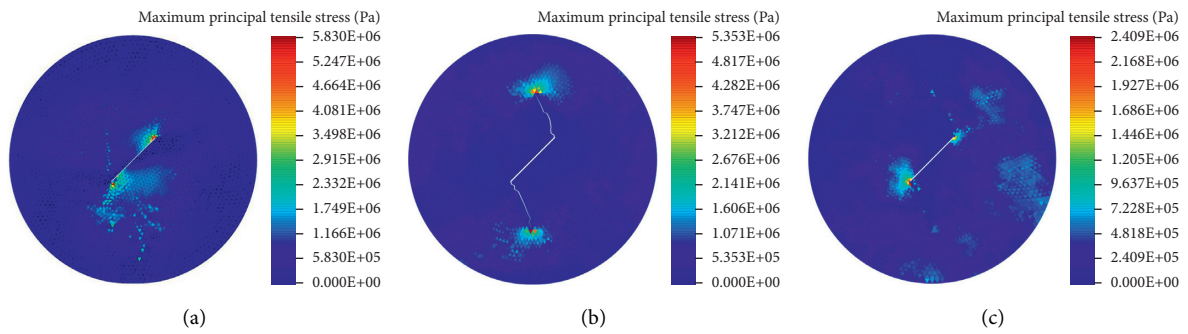


FIGURE 18: The simulated maximum principal stress contours in Case 11 ($\theta = 45^\circ$, $\gamma = 0.25$, and $v_0 = 3.0$ m/s). (a) $200 \mu s$, (b) $700 \mu s$, and (c) $900 \mu s$.

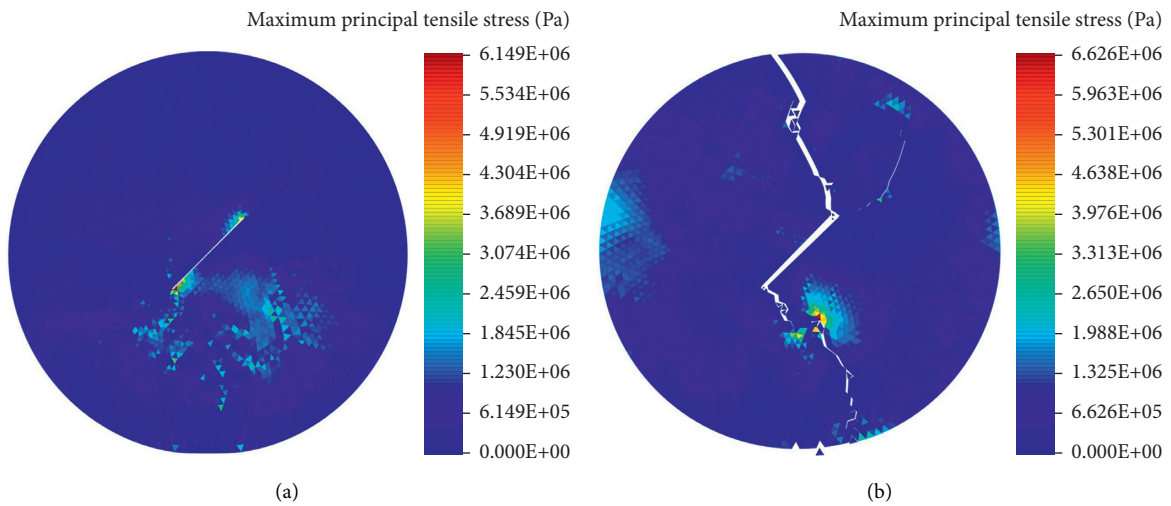


FIGURE 19: Continued.

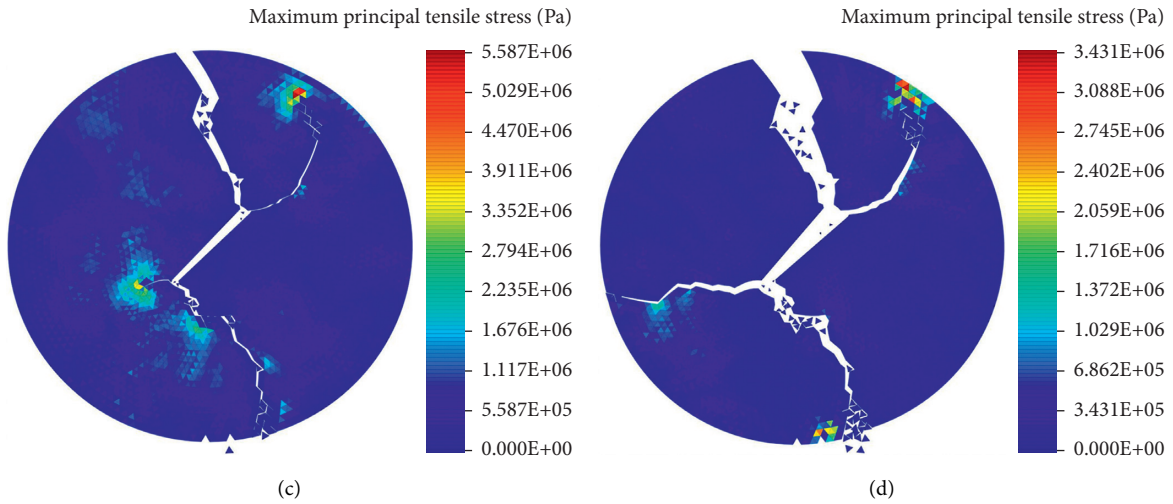


FIGURE 19: The simulated maximum principal stress contours in Case 14 ($\theta = 45^\circ$, $\gamma = 0.25$, and $v_0 = 5.0$ m/s). (a) $200 \mu\text{s}$, (b) $1200 \mu\text{s}$, (c) $1500 \mu\text{s}$, and (d) $3000 \mu\text{s}$

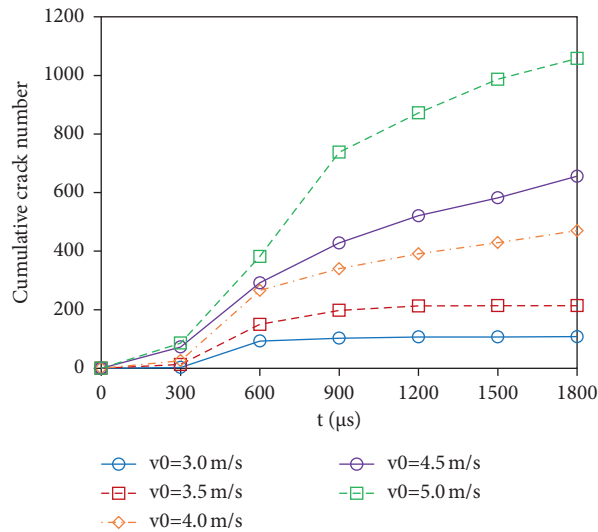


FIGURE 20: Comparison of the cumulative crack number over time when different impact velocities are considered.

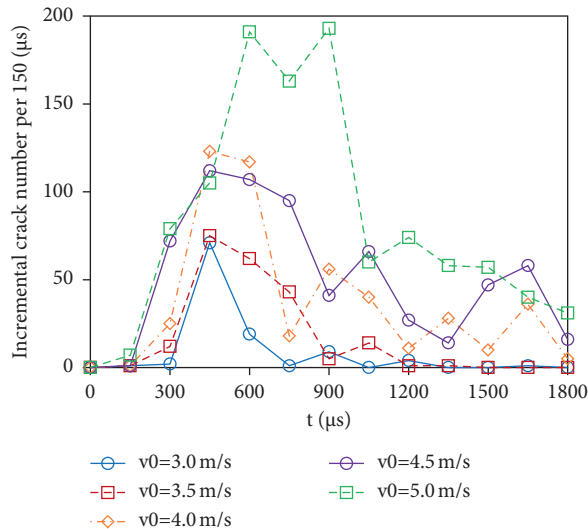


FIGURE 21: Comparison of the incremental crack number over time when different impact velocities are considered.

5. Conclusions

In this paper, the effect of the preexisting crack in rocks on rockfall fragmentation is studied by using parallel DDA with virtual joints based on OpenMP. Although fruitful research regarding rockfalls has been conducted, the influence of preexisting cracks in rocks on the fragmentation of rockfalls is still worth studying. First, the parallel DDA with virtual joints is presented. Then, validation examples about both flattened and precrack Brazilian disc tests are provided. Then, DDA simulation cases of the rockfall impact fragmentation process are performed and validated with corresponding laboratory experiments in terms of crack propagation results. Further, the effects of joint-slope angle, joint connectivity rate, and impact velocity on fracture behaviors during rockfall impact fragmentation are discussed in detail. It is concluded that the higher impact velocity and joint connectivity rate tend to cause larger damages to the specimen. When the joint-slope angle increases from 0° to 90°, the number of cracks tops in the range of 30° to 45°.

The study in this paper still has space to improve. The cases used in this study are in a 2D situation. As a future study, the 3D analysis is desired since the 3D motion and rotation obviously affect the dynamic behavior of the rockfalls. In addition, the damping effect is another factor that should be addressed, especially in rockfalls. Further studies will focus on those mentioned aspects.

Data Availability

The data used to support the findings of this study are included within the article and available from the corresponding author upon request.

Conflicts of Interest

The authors declare that they have no conflicts of interest.

Acknowledgments

This study was funded by the National Key R&D Program of China (No. 2017YFC1501001-03), the Natural Science Foundation of China (Nos. 41977233, 41902275, and 51708420, 41907251), and the Fuzhou Science and Technology Plan Project (No. 2019-G-45).

References

- [1] L. K. A. Dorren, "A review of rockfall mechanics and modelling approaches," *Progress in Physical Geography: Earth and Environment*, vol. 27, no. 1, pp. 69–87, 2016.
- [2] A. M. Ritchie, *Evaluation of Rockfall and its Control*, Washington State Highway Commission, Washington DC, USA, 1963.
- [3] S. Ferlisi, L. Cascini, J. Corominas, and F. Matano, "Rockfall risk assessment to persons travelling in vehicles along a road: the case study of the Amalfi coastal road (southern Italy)," *Natural Hazards*, vol. 62, no. 2, pp. 691–721, 2012.
- [4] O. Katz, P. Reichenbach, and F. Guzzetti, "Rock fall hazard along the railway corridor to Jerusalem, Israel, in the Soreq and Refaim valleys," *Natural Hazards*, vol. 56, no. 3, pp. 649–665, 2010.
- [5] B. Palma, M. Parise, P. Reichenbach, and F. Guzzetti, "Rockfall hazard assessment along a road in the Sorrento Peninsula, Campania, southern Italy," *Natural Hazards*, vol. 61, no. 1, pp. 187–201, 2011.
- [6] R. Salvini, M. Francioni, S. Riccucci, F. Bonciani, and I. Callegari, "Photogrammetry and laser scanning for analyzing slope stability and rock fall runout along the Domodossola-Iselle railway, the Italian Alps," *Geomorphology*, vol. 185, pp. 110–122, 2013.
- [7] A. Shirzadi, L. Saro, O. Hyun Joo, and K. Chapi, "A GIS-based logistic regression model in rock-fall susceptibility mapping along a mountainous road: s," *Natural Hazards*, vol. 64, no. 2, pp. 1639–1656, 2012.
- [8] S. G. Evans and O. Hungr, "The assessment of rockfall hazard at the base of talus slopes," *Canadian Geotechnical Journal*, vol. 30, no. 4, pp. 620–636, 1993.
- [9] S.-S. Wu, "Rockfall evaluation by computer simulation," *Transportation Research Record*, vol. 1031, pp. 1–5, 1984.
- [10] R. W. Day, "Case studies of rockfall in soft versus hard rock," *Environmental and Engineering Geoscience*, vol. III, no. 1, pp. 133–140, 1997.
- [11] S. A. Schumm and R. J. Chorley, "The fall of threatening rock," *American Journal of Science*, vol. 262, no. 9, pp. 1041–1054, 1964.
- [12] A. Valagussa, P. Frattini, and G. B. Crosta, "Earthquake-induced rockfall hazard zoning," *Engineering Geology*, vol. 182, pp. 213–225, 2014.
- [13] A. Azzoni, G. La Barbera, and A. Zaninetti, "Analysis and prediction of rockfalls using a mathematical model," *International Journal of Rock Mechanics and Mining Science & Geomechanics Abstracts*, vol. 32, no. 7, pp. 709–724, 1995.
- [14] D. Bozzolo and R. Pamini, "Simulation of rock falls down a valley side," *Acta Mechanica*, vol. 63, no. 1-4, pp. 113–130, 1986.
- [15] M. J. Kirkby and I. Statham, "Surface stone movement and scree formation," *The Journal of Geology*, vol. 83, no. 3, pp. 349–362, 1975.
- [16] K. T. Chau, R. H. C. Wong, J. Liu, and C. F. Lee, "Rockfall hazard analysis for Hong Kong based on rockfall i," vol. 36, no. 5, pp. 383–408, 2003.
- [17] G. B. Crosta and F. Agliardi, "A methodology for physically based rockfall hazard assessment," *Natural Hazards and Earth System Sciences*, vol. 3, no. 5, pp. 407–422, 2003.
- [18] V. Labiouse, F. Descoeurdes, and S. Montani, "Experimental study of rock sheds impacted by rock blocks," *Structural Engineering International*, vol. 6, no. 3, pp. 171–176, 2018.
- [19] D. Peila, S. Pelizza, and F. Sassudelli, "Evaluation of brockfall restraining nets by full scale tests," *Rock Mechanics and Rock Engineering*, vol. 31, no. 1, pp. 1–24, 1998.
- [20] M. Spadari, A. Giacomini, O. Buzzi, S. Fityus, and G. P. Giani, "In situ rockfall testing in New South Wales, Australia," *International Journal of Rock Mechanics and Mining Sciences*, vol. 49, pp. 84–93, 2012.
- [21] C. R. Ruiz, J. Corominas, and O. Mavrouli, "An empirical approach to rockfall fragmentation," in *Proceedings of the ISRM Regional Symposium-EUROCK 2015*, Salzburg, Austria, 2015.
- [22] Y. Okura, H. Kitahara, T. Sammori, and A. Kawanami, "The effects of rockfall volume on runout distance," *Engineering Geology*, vol. 58, no. 2, pp. 109–124, 2000.
- [23] J. Corominas, O. Mavrouli, D. Santana, and J. Moya, "Simplified approach for obtaining the block volume distribution

- of fragmental rockfalls,” in *Proceedings of the A International Symposium on Landslides. B Landslides and Engineered Slopes*, CRC Press, Taylor & Francis Group, Banff, Canada, June 2012.
- [24] J. Corominas, O. Mavrouli, and C. R. Ruiz, “Rockfall occurrence and fragmentation,” in *Proceedings of the Advancing Culture of Living with Landslides*, pp. 75–97, Ljubljana, Slovenia, May 2017.
- [25] F. Agliardi and G. B. Crosta, “High resolution three-dimensional numerical modelling of rockfalls,” *International Journal of Rock Mechanics and Mining Sciences*, vol. 40, no. 4, pp. 455–471, 2003.
- [26] J. Corominas, G. Matas, and C. R. Ruiz, “Quantitative analysis of risk from fragmental rockfalls,” *Landslides*, vol. 16, no. 1, pp. 5–21, 2018.
- [27] G. Matas, N. Lantada, J. Corominas, J. A. Gili, C. R. Ruiz, and A. Prades, “RockGIS: a GIS-based model for the analysis of fragmentation in rockfalls,” *Landslides*, vol. 14, no. 5, pp. 1565–1578, 2017.
- [28] C. R. Ruiz and J. Corominas, “Analysis of rockfalls by means of a fractal fragmentation model,” *Rock Mechanics and Rock Engineering*, vol. 53, no. 3, pp. 1433–1455, 2019.
- [29] C. R. Ruiz, J. Corominas, and O. Mavrouli, “A methodology to obtain the block size distribution of fragmental rockfall deposits,” *Landslides*, vol. 12, no. 4, pp. 815–825, 2015.
- [30] Y. Wang and F. Tonon, “Discrete element modeling of rock fragmentation upon impact in rock fall analysis,” *Rock Mechanics and Rock Engineering*, vol. 44, no. 1, pp. 23–35, 2010.
- [31] F. V. De Blasio and G. B. Crosta, “Fragmentation and boosting of rock falls and rock avalanches,” *Geophysical Research Letters*, vol. 42, no. 20, pp. 8463–8470, 2015.
- [32] T. Zhao, G. B. Crosta, S. Utili, and F. V. D. Blasio, “Investigation of rock fragmentation during rockfalls and rock avalanches via 3-D discrete element analyses,” *Journal of Geophysical Research: Earth Surface*, vol. 122, no. 3, pp. 678–695, 2017.
- [33] W. Shen, T. Zhao, G. B. Crosta, and F. Dai, “Analysis of impact-induced rock fragmentation using a discrete element approach,” *International Journal of Rock Mechanics and Mining Sciences*, vol. 98, pp. 33–38, 2017.
- [34] Y. Ye, K. Thoeni, Y. Zeng, O. Buzzzi, and A. Giacomini, “Numerical investigation of the fragmentation process in marble spheres upon dynamic impact,” *Rock Mechanics and Rock Engineering*, vol. 53, no. 3, pp. 1287–1304, 2020.
- [35] G. H. Shi, “Discontinuous Deformation Analysis: A New Numerical Model for the Statics and Dynamics of Block systems,” PhD Thesis, University of California, Berkeley, California, 1988.
- [36] G. Chen, L. Zheng, Y. Zhang, and J. Wu, “Numerical simulation in rockfall analysis: a close comparison of 2-D and 3-D DDA,” *Rock Mechanics and Rock Engineering*, vol. 46, no. 3, pp. 527–541, 2013.
- [37] Y. H. Hatzor, A. A. Arzi, Y. Zaslavsky, and A. Shapira, “Dynamic stability analysis of jointed rock slopes using the DDA method: k,” *International Journal of Rock Mechanics and Mining Sciences*, vol. 41, no. 5, pp. 813–832, 2004.
- [38] X. Peng, G. Chen, P. Yu, Y. Zhang, and J. Wang, “Improvement of joint definition and determination in three-dimensional discontinuous deformation analysis,” *Computers and Geotechnics*, vol. 110, pp. 148–160, 2019.
- [39] X. Peng, P. Yu, G. Chen, M. Xia, and Y. Zhang, “Development of a c method and its application to dynamic simulation of landslides involving solid-fluid i,” *Rock Mechanics and Rock Engineering*, vol. 53, no. 1, pp. 113–131, 2019.
- [40] J. Wu, C. H. Juang, and H. Lin, “Vertex-to-face contact searching algorithm for three-dimensional frictionless contact problems,” *International Journal for Numerical Methods in Engineering*, vol. 63, no. 6, pp. 876–897, 2005.
- [41] P. Yu, G. Chen, X. Peng, L. Guo, and Y. Zhang, “Extension and application of discontinuous deformation analysis with a damped contact spring model,” *International Journal of Rock Mechanics and Mining Sciences*, vol. 123, Article ID 104123, 2019.
- [42] P. Yu, Y. Zhang, X. Peng, G. Chen, and J. X. Zhao, “Distributed-spring edge-to-edge contact model for two-dimensional discontinuous deformation analysis,” *Rock Mechanics and Rock Engineering*, vol. 53, no. 1, pp. 365–382, 2019b.
- [43] H. Zhang, “A new algorithm to identify contact types between arbitrarily shaped polyhedral blocks for three-dimensional discontinuous deformation analysis,” *Computers and Geotechnics*, vol. 80, pp. 1–15, 2016.
- [44] L. Q. Choo, Z. Y. Zhao, H. M. Chen, and Q. Tian, “Hydraulic fracturing modeling using the discontinuous deformation analysis (DDA) method,” *Computers and Geotechnics*, vol. 76, pp. 12–22, 2016.
- [45] Y. Y. Jiao, X. L. Zhang, and J. Zhao, “Two-dimensional DDA contact constitutive model for simulating rock fragmentation,” *Journal of Engineering Mechanics*, vol. 138, pp. 199–209, 2012.
- [46] Q. Tian, Z. Y. Zhao, and H. R. Bao, “Block fracturing analysis using nodal-based discontinuous deformation analysis with the double minimization procedure,” *International Journal for Numerical and Analytical Methods in Geomechanics*, vol. 38, pp. 881–902, 2014.
- [47] Q. H. Wang, S. C. Li, L. P. Li, J. Wang, and Q. Zhang, “Crack propagation of jointed rock and application,” *Applied Mechanics and Materials*, vol. 651–653, pp. 1143–1146, 2014.
- [48] W. Zhu, Y. Chen, S. Li, F. Yin, S. Yu, and Y. Li, “Rock failure and its jointed surrounding rocks: a multi-scale grid meshing method for DDARF,” *Tunnelling and Underground Space Technology*, vol. 43, pp. 370–376, 2014.
- [49] X. Peng, “Parallel computing of three-dimensional discontinuous deformation analysis based on OpenMP,” *Computers and Geotechnics*, vol. 106, pp. 304–313, 2019.
- [50] X. Peng, G. Chen, P. Yu, Y. Zhang, H. Zhang, and L. Guo, “A full-stage parallel architecture of three-dimensional discontinuous deformation analysis using OpenMP,” *Computers and Geotechnics*, vol. 118, Article ID 103346, 2020.
- [51] P. Yu, X. Peng, G. Chen, L. Guo, and Y. Zhang, “OpenMP-based parallel two-dimensional discontinuous deformation analysis for large-scale simulation,” *International Journal of Geomechanics*, vol. 20, 2020.
- [52] Wang, *Test Method for Tensile Strength and Fracture Toughness of Sandstone*, Chengdu University of Technology, Chengdu, China, 2019.
- [53] K. S. Ni, “Study on DDA Method for Fracture Failure Simulation,” Master Thesis, Southwest University of Science and Technology, Mianyang, China, 2015.
- [54] H. Haeri, K. Shahriar, M. F. Marji, and P. Moarefvand, “Experimental and numerical study of crack propagation and coalescence in pre-cracked rock-like disks,” *International Journal of Rock Mechanics and Mining Sciences*, vol. 67, pp. 20–28, 2014.
- [55] X. L. Zhang, *Influence of Sing-Joint on the Impact-Fragmentation during rockfall-slope Interaction*, Master Thesis, Fuzhou University, Fuzhou, China, 2020.

Research Article

Compression Load Tests on Composite Foundations of Spread Footing Anchored by Helical Anchors

Mingqiang Sheng ¹, Zengzhen Qian ², and Xianlong Lu ³

¹School of Civil Engineering and Architecture, Nanchang University, Nanchang 330031, China

²School of Engineering and Technology, China University of Geosciences, Beijing 100083, China

³China Electric Power Research Institute, Beijing 100192, China

Correspondence should be addressed to Zengzhen Qian; zzqian@cugb.edu.cn

Received 26 February 2021; Accepted 12 July 2021; Published 31 July 2021

Academic Editor: Haoyuan Hong

Copyright © 2021 Mingqiang Sheng et al. This is an open access article distributed under the Creative Commons Attribution License, which permits unrestricted use, distribution, and reproduction in any medium, provided the original work is properly cited.

This study elucidates the compression behavior of a type of composite foundation of spread footing anchored by helical anchors. Three composite foundations were installed at a field site, and compression load testing was carried out on each foundation. Both the site conditions and the load tests were documented comprehensively. The compression load-settlement curves of composite foundations exhibit an initial linear-elastic segment, a curve transition, and a final linear region, and their capacities should be interpreted from the load-settlement curves. Five representative interpretation criteria (Chin, Terzaghi and Peck, slope tangent, tangent intersection, and L_1-L_2) were employed to determine the capacity of each foundation. Both the helical anchors and the footing share compression loadings on the composite foundation. Soil pressure cells at the center, near the edge, and at the corner of the footing represent a distribution from the lower, middle, and higher ranges of incremental soil pressures underneath the footing. Helical anchors underneath the footing approximately share 60%–80% of total load applied on the composite foundation pier, and higher compression resistance of a composite foundation can be obtained by increasing the footing embedment depth and the number of helical anchors underneath the footing.

1. Introduction

Spread footings have been widely designed to meet some unique soil conditions of geology and terrain such as in swampy grounds, flood plains, tropical areas, and thick residual deposits with reduced bearing capacities [1, 2]. Numerous investigations on the compression behavior of spread footings have been conducted based on theoretical and experimental analyses [3, 4]. As found in many practical applications, spread foundations are economical than piles under certain circumstances [5]. However, the solution for foundation designs using spread footings directly on the soil with reduced bearing capacity may result in low admissible pressure associated with remarkable settlement [6], and the employing of piles may lead to an excessive increase in cost. An alternative for such instance is therefore the proposal recommended in this study by designing a type of composite

foundation as shown in Figure 1, in which helical anchors are installed in the lower layer of soil and a spread footing at the top layer of soil will then be connected with these helical anchors. The helical anchors in such composite foundation can obtain instant load-carrying capacities upon installation and can be constructed through groundwater without casing, unaffected by caving soils.

Helical anchors have been recognized as a practical alternative to traditional pile foundations in construction industry because of their ease of installation and cost-effectiveness [7]. Experimental research findings have indicated that the performance of helical anchors under compressive and tensile loadings is similar, and the anchor plates can increase the anchor load-carrying capacity obviously, as does the underream in a underreamed cast-in-place pile [8]. Several design methods have been suggested to predict the helical pile load-carrying capacity under

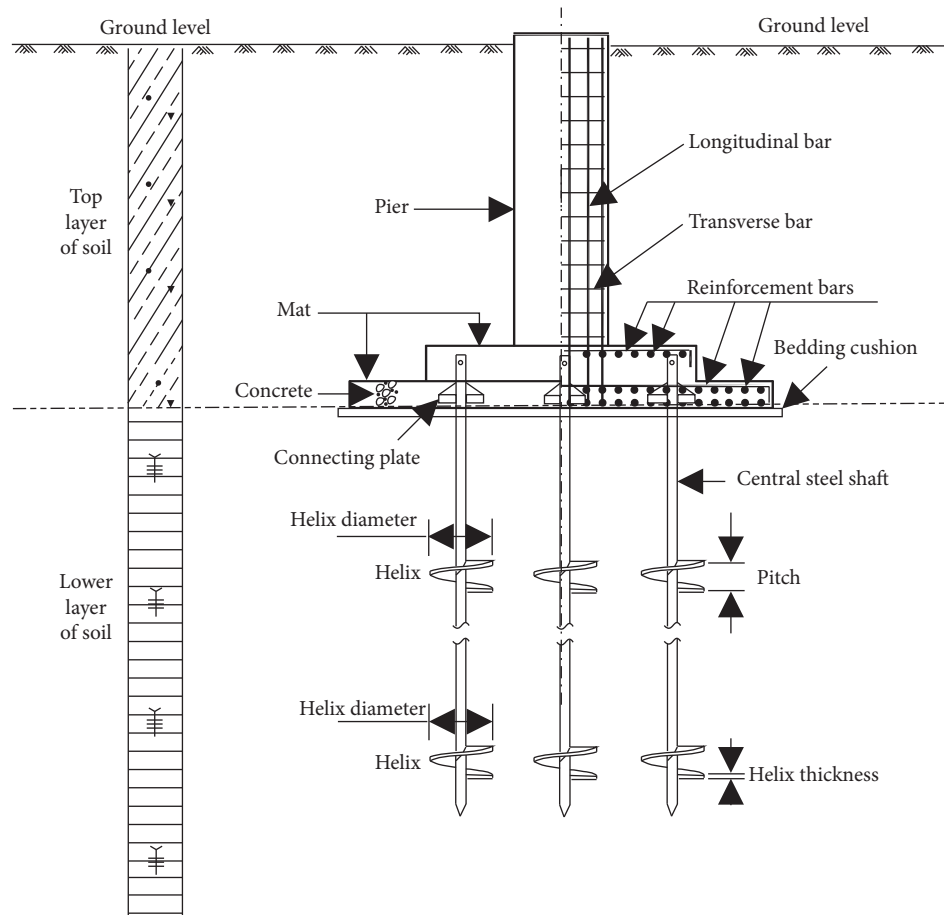


FIGURE 1: Design scheme of the composite foundation in this study.

compressive and tensile loads based on the individual plate anchor theories [9–14], whereas some methods are similar to those recommended for underreamed cast-in-place pile foundations [13, 15–17].

However, the composite foundation in Figure 1 makes the helical anchor-soil-footing interaction more complicated, and very insufficient experimental research findings are available for the justification of its design. This study has three objectives: (1) to examine the compression load-settlement behavior of the composite foundation as depicted in Figure 1; (2) to obtain the distribution of incremental soil pressures underneath the spread footing; and (3) to investigate the load-transfer mechanism when compression loads are applied to such composite foundation.

2. Test Site Conditions

The field test site is selected at Liaoyang City, Liaoning Province, China. From ground level to the foundation embedment depth in this study, the soil profile consists of a topsoil, silty clay, and sandy silt, categorized according to Chinese National Standard GB50007 [15]. Table 1 lists the detailed soil profile and properties at the testing site. Groundwater was not observed at the time that the test foundations were installed and tested.

As listed in Table 1, soil profile at the site comprises a surficial fill layer of sand and gravel mixed with some organics, which extends to about 1.0 m with SPT number ranging from 6 to 7 and moisture content ranging from 19% to 25%. Underlying this surficial layer is the soft plastic to plastic silty clay that extends to depths between 8.6 m and 8.8 m below ground surface with SPT number ranging from 9 to 23. Moisture content of this silty clay layer varies from 20% to 27%, with an average of 25.9%. Further down is a sandy clay with a thickness about 10 m with SPT number ranging from 33 to 48.

To investigate the on-site soil properties, a plate static loading test was carried out with a concrete plate (0.8 m in diameter and 0.55 m in height) on the silty clay at the depth of 1.5 m after topsoil was removed. Figure 2 demonstrates the load-settlement response from the plate loading test.

There is no peak load and asymptote value on the curve, and therefore, the maximum bearing capacity is difficult to determine from the test. There are two failure criteria generally recommended in China [18, 19]: (a) the load is held for 24 h but with the rate of increment settlement still exceeding 0.10 mm/h; and (b) the total settlement is greater than 10% of the diameter of the plate. The lesser of the loads corresponding to above two criteria is then defined as the failure load. The first criterion controlled the failure in this

TABLE 1: Test site soil conditions.

Layer	Soil layer thickness H (m)	SPT number N (blow counts/300 mm)	Moisture content w (%)	Unit weight γ (kN/m ³)
Topsoil (fill)	0.9–1.0	6–7	19–25	—
Silty clay	7.7–7.8	9–23	20–27	18.9
Sandy silt	10.2–10.8	33–48	—	19.3

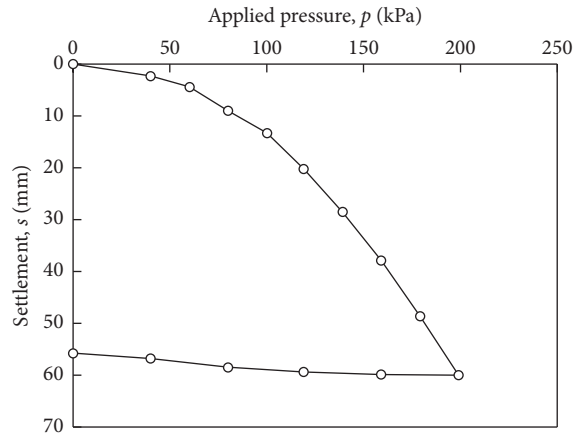


FIGURE 2: Load-settlement response in the plate loading test on silty clay at the depth of 1.5 m.

study, and the determined bearing capacity was 175 kPa with a settlement about 6% of the plate diameter.

3. Foundation Installation

Three composite foundations as shown in Figure 3, numbered from CF1 to CF3, were constructed and tested under compression load at the aforementioned site. As shown in Figure 3, all footings of the composite foundations in this study have two stepped mats, with upper mat having dimensions of length/width/thickness = 1.5 m/1.5 m/0.3 m compared to 2.1 m/2.1 m/0.3 m for the lower. The piers of the three footings have an identical cross section of 0.6 m by 0.6 m. The helical anchors were manufactured from a single cylindrical steel shaft with three welded helices, which served as triple-helix piles in a composite foundation. The central cylindrical shafts were manufactured of steel pipes of 108 mm outer diameter and 10 mm wall thickness. All helices had a dimension of 0.5 m diameter, 0.01 m thickness, and 0.25 m pitch, and they were welded at intervals of center-to-center spacing of 1.2 m along the steel shaft.

As listed in Figure 3, three field compression load tests were conducted on: (i) CF1, the footing with embedment depth of 1.5 m anchored by a four-helical-anchor group in square arrangement with spacing $s_p = 2.2D$ (where D is the helix diameter, and $D = 0.5$ m in this study) and $L = 4.85$ m (where L is the central steel shaft length); (ii) CF2, the spread footing with embedment depth of 2.0 m anchored by a four-helical-anchor group with $s_p = 2.2D$ and $L = 4.85$ m; and (iii) CF3, the footing with embedment depth of 2.0 m anchored by a five-helical-anchor group, with four 4.85 m long helical anchors being placed in square arrangement at the four

corners with $s_p = 2.2D$ and with a 3.85 m long helical anchor being placed at the core of the footing.

The construction of the composite foundations in Figure 3 was performed by three procedures. The first procedure was to excavate native topsoil to the designed footing embedment depth. Then, the second procedure was to install helical anchors in the excavated pit by screwing them into soil by trained operators with a special torque wrench equipment which had a safety link to prevent overtightening of the anchors and to avoid damage to the anchors and loss of soil. The helices advanced steadily at a rate of the pitch. Finally, the last procedure was to cast reinforced concrete pad and pier for footings, including the main progresses of binding steel bars, supporting wall framework, pouring concrete, removing template and maintenance, and back-filling soil.

All footings were made from sulfate-resistant concrete of nominally identical quality with a specified 28-day compressive strength of 25 MPa. Figure 4 shows the installed helical anchors and the footing with reinforcement prior to concrete placement.

4. Test Setup and Loading Procedure

Each of the compression load tests on the composite foundations was conducted after the footing concrete had cured for about four weeks. The same axial compression loading test setup, instrumentation, and data measurement system were employed for all tests. The compression load was axially applied through a system comprising a loading platform, a reaction beam, and a hydraulic jack in line with the central longitudinal axis of the composite foundation.

During each load test, pier-head settlements of the composite foundation were measured at four points with a 90° separation on the pier top head using four electronic displacement transducers with 50 mm range and 0.01 mm sensitivity. All the electronic displacement transducers were attached to the reference beams fixed over the pier head, and they were sufficiently stiff to sustain the instrumentation and to prevent excessive variations in the measurements.

Each compression load test was conducted using static monotonic loading with no unload-reload loops. The slowly maintained-load method was employed in all the tests; namely, the compression load was applied in increments of 10% of the predicted maximum resistance of each individual foundation, and the composite foundation was enabled to move under each maintained-load increment until a designated settlement rate was achieved. Each compression load increment was held after loading until two consecutive settlements within each hour were less than 0.10 mm. The next load increment was subsequently added. It is noted in

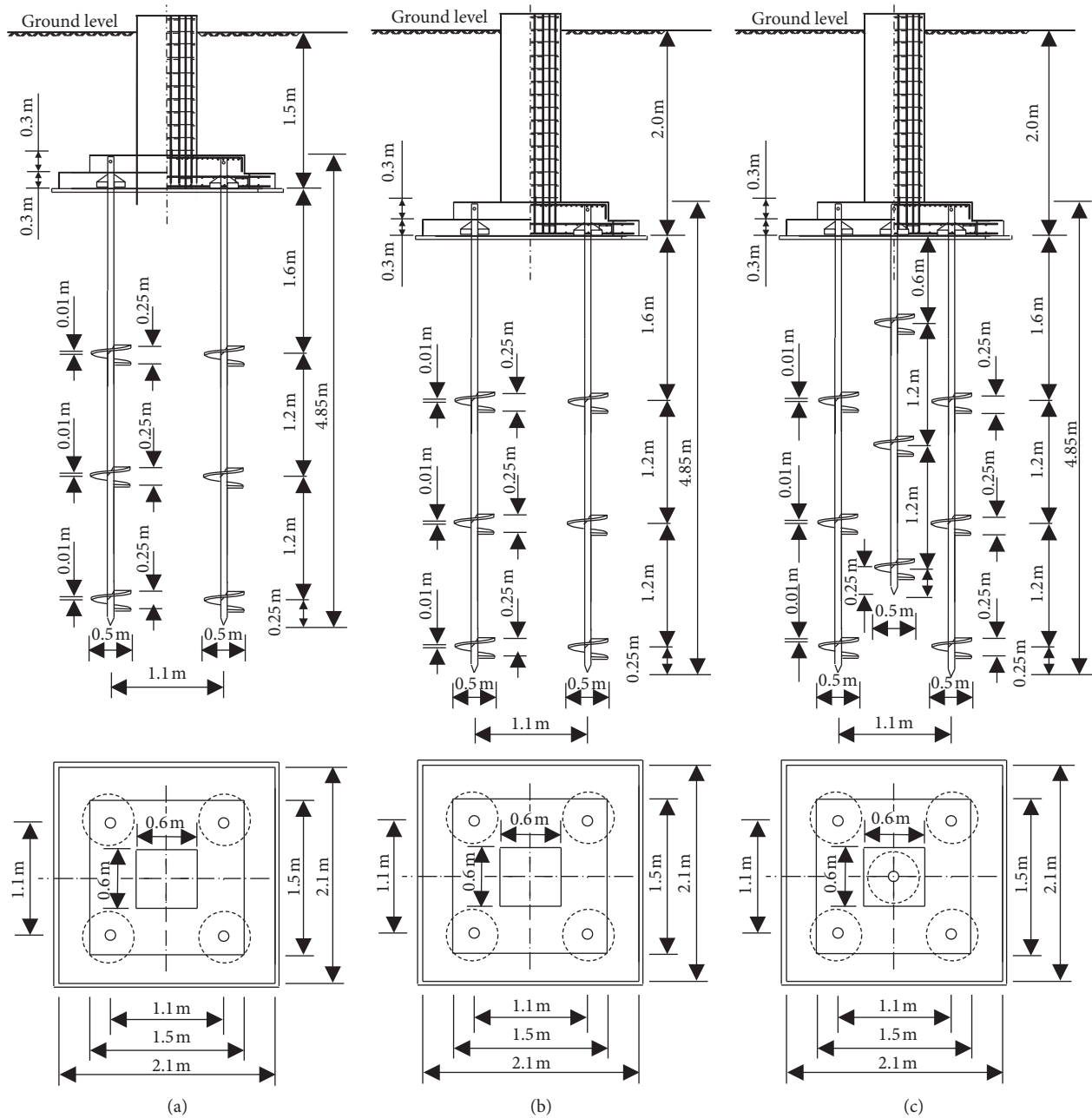


FIGURE 3: Details of composite foundations in the test: (a) CF1, (b) CF2, and (c) CF3.

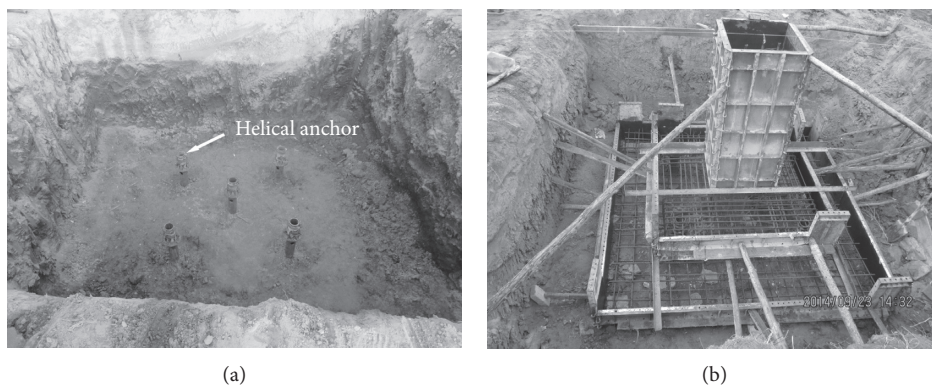


FIGURE 4: Photo of a composite foundation prior to concrete placement: (a) installed helical anchors and (b) the footing with reinforcement and supporting wall framework.

this study that the two consecutive settlement values were defined as the average of the vertical pier-head displacements within each hour from the four electronic displacement transducers on the pier head of the composite foundation. It is the typical procedure recommended by Chinese National Code GB50007 [18] and Local Code JGJ 94 [19–22].

5. Test Results and Discussion

5.1. Load-Settlement Response and Load Capacity. In limit state design, it is of great importance to consider the ultimate limit state (ULS) (addressing foundation capacity) and the serviceability limit state (SLS) (addressing foundation settlement) simultaneously [23–25]. Therefore, the load test results in this study are first analysed in terms of the load-settlement curves. Figure 5 shows the variation of compression load against pier-head vertical settlement for each composite foundation. It should be noted that the settlements in Figure 5 are the means of the output of the four electronic displacement transducers on the pier head.

It can clearly be seen that the compression load-settlement curves in Figure 5 are similar to those of drilled shafts [26, 27] and footings under compression loads [3], and they can generally be divided into three distinct segments: initial linear-elastic, curve transition, and final linear, as was suggested by Hirany and Kulhawy [28–30] in Figure 6. Various criteria have been recommended in the literature to interpret the failure load from this type of load-displacement curve. In this study, five criteria which employ varied interpretation bases, as noted in Table 2, were used to evaluate the capacity of each composite foundation. In general, these criteria can be considered as representative of existing criteria because they represent a distribution of interpreted failure loads from the lower, middle, and higher bounds, as identified in practice [20, 21]. The interpreted failure loads of the test foundations, as well as the corresponding settlements, are listed in Table 3. It should be noted that Q_{L1} is not an interpreted failure load, but the elastic limit, and it is listed for reference only.

Table 3 indicates that a significant scatter exists for the interpreted load capacities of the foundation using different criteria, and the interpreted failure loads vary from 475 to 1166 kN for CF1, from 479 to 1410 kN for CF2, and from 562 to 1435 kN for CF3. The slope tangent, tangent intersection, and Terzaghi and Peck methods yield compression capacities less than the L_1 – L_2 method and are therefore located within the curve transition segment between L_1 and L_2 . However, the Chin method always yields the highest load capacity, even greater than the applied maximum load. Therefore, defining the failure load as Q_{CHIN} yields a value that is too large, possibly because Q_{CHIN} is based on a hyperbolic mathematical model that corresponds to the asymptote of the load-settlement curve. In general, the L_1 – L_2 method could interpret all the load tests, and therefore Q_{L2} could be adopted as a base for comparison.

As shown in Table 3, the interpreted load capacity defined by L_1 – L_2 method, Q_{L2} , is 910 kN for CF2 and 813 kN for CF1, with a corresponding settlement of 29.57 mm for

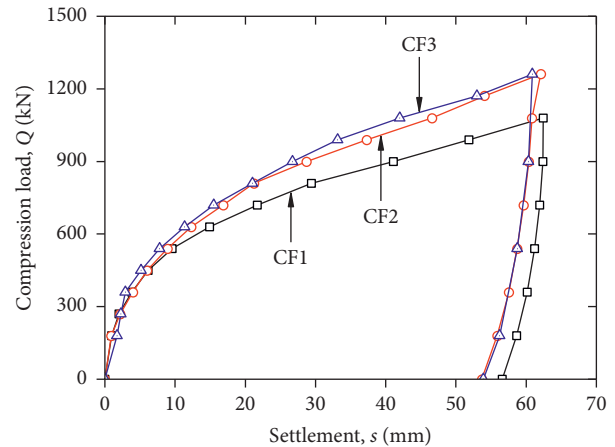


FIGURE 5: Variation of applied compression load against pier-head settlement.

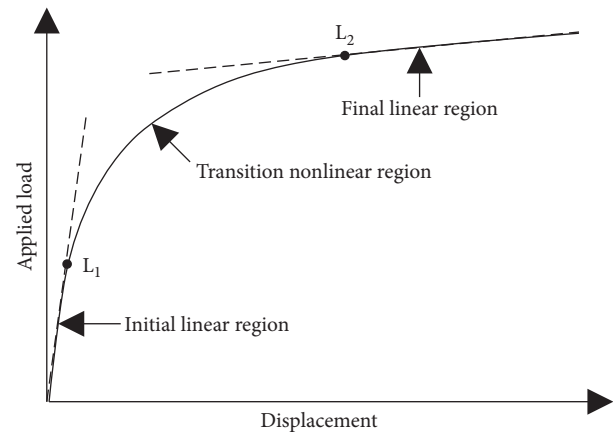


FIGURE 6: Sections of load-displacement curve for the L_1 – L_2 method [28–30].

CF2 and 30.22 mm for CF1. It can be seen that a 0.5 m increase of footing embedment depth for CF2 yields an increase of about 12% in the compression capacity. The interpreted load capacity, Q_{L2} , of CF3 is about 8% higher than that of CF2. This demonstrates that the compression capacity of a composite foundation as shown in Figure 1 depends on the dimension of footings and the layout of helical anchors. A higher compression load resistance can be obtained by increasing the footing embedment depth and the number of helical anchors underneath spread footing.

5.2. Soil Pressures underneath the Footing. When a composite foundation is subjected to compression loads, the steel-reinforced concrete footing may behave as a rigid body, and therefore, the soil underneath the footing becomes significant to resist the compression forces. To obtain a better understanding of the load-transfer mechanism, as illustrated in Figure 7, fifteen miniature vibrating-wire soil pressure cells, with a diameter of 0.10 m and a capacity of 500 kPa, were fixed underneath each footing of the composite

TABLE 2: Definitions of representative interpretation criteria examined in this study.

Method	Category	Definition of interpreted capacity, Q
Chin method [31]	Mathematical modeling	Q_{CHIN} is equal to the inverse slope, $1/m$, of the line, $s/Q = ms + c$, where Q is the load, s is the total displacement and m and c are the slope and intercept of the line, respectively.
Terzaghi and Peck method [32]	Displacement limitation	$Q_{T\&P}$ is the load that occurs at 1.0 inch (25.4 mm) total displacement.
Slope tangent method [33]	Graphical construction	Q_{ST} occurs at a displacement equal to the initial slope of the load-displacement curve plus 0.15 inch (3.8 mm).
Tangent intersection method [34, 35]	Graphical construction	Q_{TI} is determined as the intersection of two lines drawn as tangents to the initial linear and final linear portions of the load-displacement curve and projected to the load-displacement curve.
L_1 - L_2 method [28-30]	Graphical construction	Q_{L1} and Q_{L2} correspond to elastic limit and failure threshold loads, respectively, as shown in Figure 6.

TABLE 3: Interpreted compression load capacities and settlements for all three foundations.

Foundation number	Interpreted compression capacity, Q^a (kN), and the settlement, $s^{b,c}$ (mm)										
	Q_{L1}	s_{L1}	Q_{ST}	s_{ST}	Q_{TI}	s_{TI}	Q_{L2}	s_{L2}	$Q_{T\&P}$	Q_{CHIN}	s_{CHIN}
CF1	214	1.26	475	7.21	632	15.10	813	30.22	764	1166	$>62.43^d$
CF2	205	1.15	479	6.88	642	12.93	910	29.57	858	1410	>62.05
CF3	375	3.20	562	8.51	724	15.53	977	32.12	878	1435	>60.90

^aInterpreted load capacities for various methods: Q_{ST} , slope tangent method; Q_{TI} , tangent intersection method; Q_{L1} , L_1 method; Q_{L2} , L_2 method; $Q_{T\&P}$, Terzaghi and Peck method; and Q_{CHIN} , Chin method. ^bSettlements for the various methods: s_{ST} , slope tangent method; s_{TI} , tangent intersection method; s_{L1} , L_1 method; s_{L2} , L_2 method; $s_{T\&P}$, Terzaghi and Peck method; and s_{CHIN} , Chin method. ^cBy definition, $s_{T\&P} = 25.4$ mm, not included in the table. ^dThe symbol ($>$) expresses that the interpreted settlement is greater than the measured data.

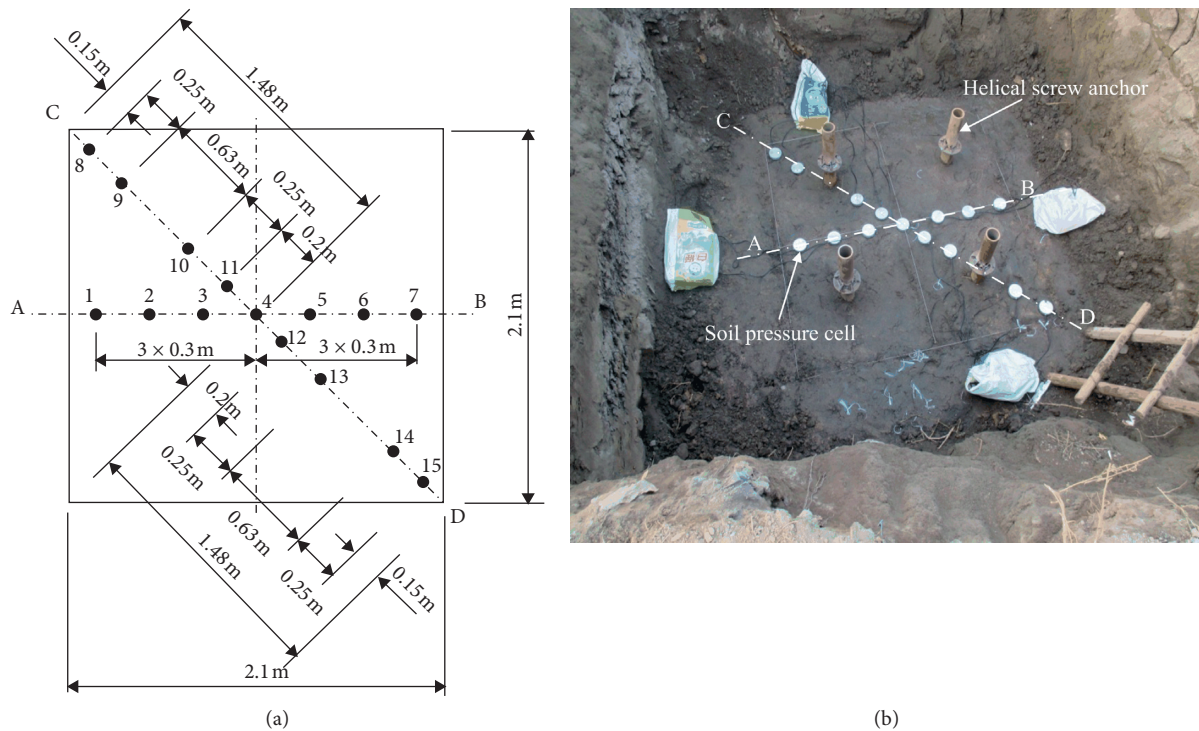
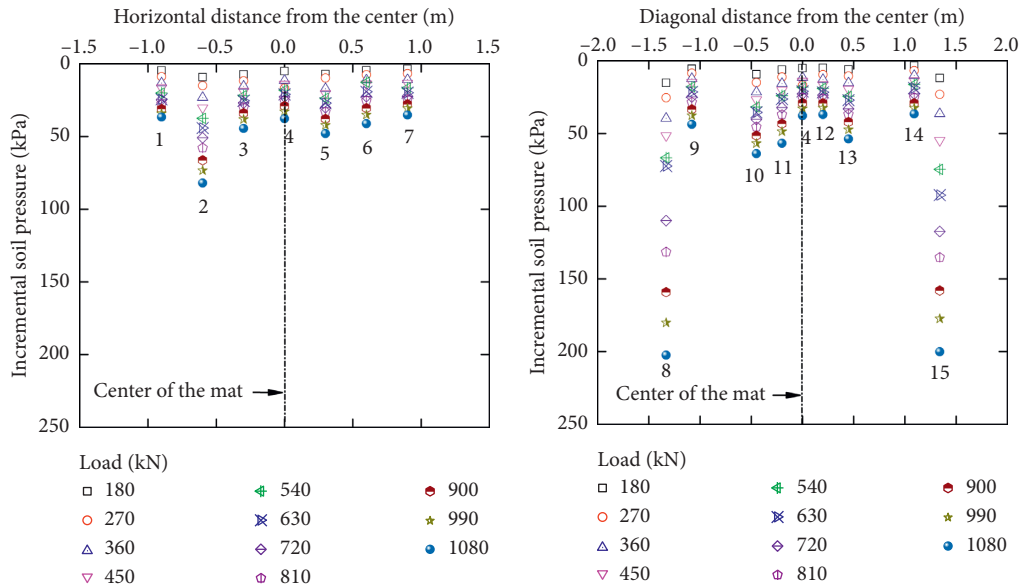


FIGURE 7: Details for (a) schematic diagram and (b) photograph of the arrangement of soil pressure cells.

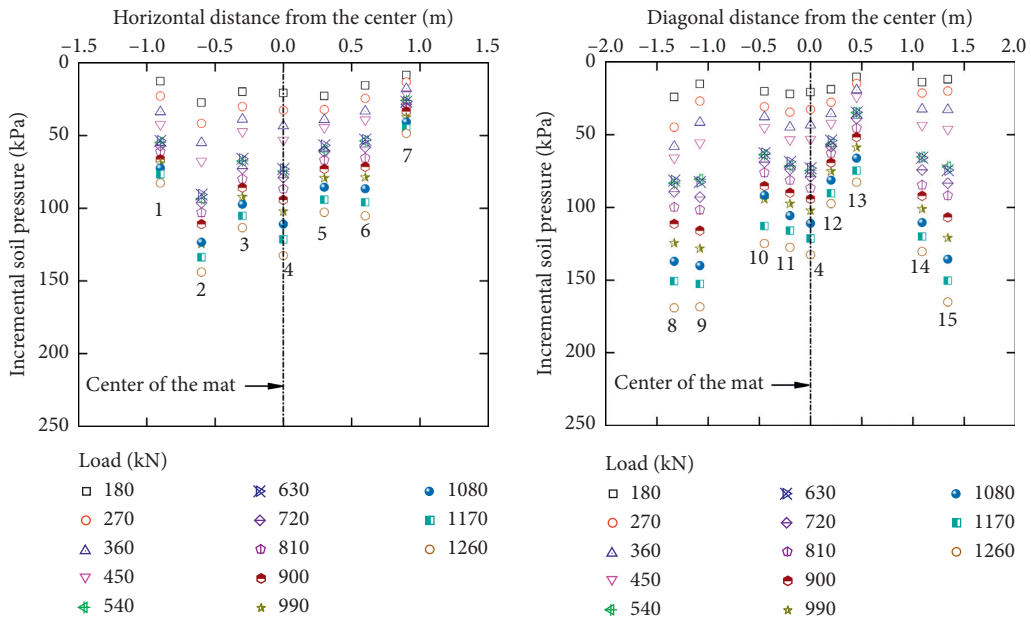
foundations after completion of the first two procedures during the installation.

As demonstrated in Figure 7, the soil pressure cells were arranged along the center line AB and diagonal line CD and

they were numbered 1 to 7 and 8 to 15 in sections AB and CD, respectively. All the soil pressure cells were calibrated and fixed within a 50 mm thick sand layer. Unfortunately, the soil pressure cell 4 of CF3 was damaged after installation.



(a)



(b)

FIGURE 8: Continued.

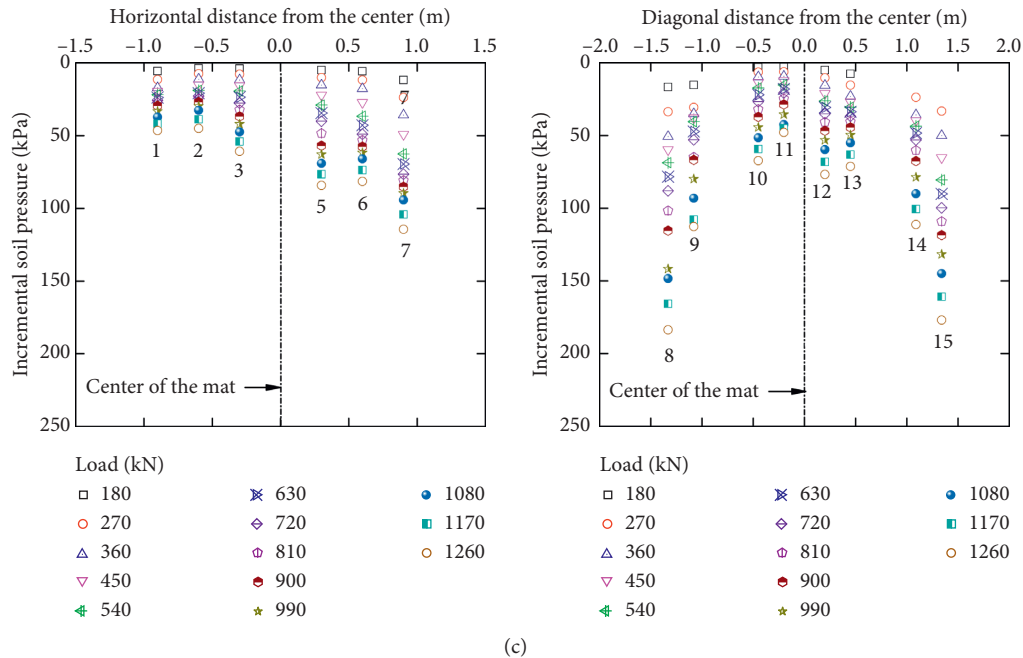


FIGURE 8: Distribution of incremental soil pressures underneath the footing during compression load testing for (a) CF1, (b) CF2, and (c) CF3.

TABLE 4: Average soil pressures and compression resistances from footing and helical anchors.

Applied load on footing pier head (kN)	Average soil pressure underneath footing (kPa)			Compression resistance from footing (kN)			Percentage of compression resistance from helical anchors (%)		
	CF1	CF2	CF3	CF1	CF2	CF3	CF1	CF2	CF3
180	6.6	17.7	7.0	29	78	31	83.8	56.6	83.0
270	11.8	28.0	14.0	52	123	62	80.8	54.3	77.2
360	16.7	37.7	21.0	74	166	93	79.5	53.8	74.3
450	21.3	46.1	26.8	94	203	118	79.1	54.8	73.8
540	26.2	54.9	32.5	115	242	144	78.6	55.7	73.4
630	30.3	63.0	37.0	134	278	163	78.8	55.9	74.1
720	36.7	68.9	41.4	162	304	183	77.5	57.8	74.6
810	41.9	75.9	46.4	185	335	205	77.2	58.7	74.7
900	48.7	83.8	51.3	215	370	226	76.2	58.9	74.8
990	54.6	92.3	58.0	241	407	256	75.7	58.9	74.2
1080	61.9	99.0	64.7	273	437	285	74.7	59.6	73.6
1170	—	109.4	72.9	—	482	321	—	58.8	72.5
1260	—	119.7	81.1	—	528	358	—	58.1	71.6

The measured results of the fifteen soil pressure cells along horizontal center line AB and the diagonal line CD for CF1, CF2, and CF3 are plotted in Figure 8.

Figure 8 indicates that the incremental soil pressures underneath the footing gradually increase with increasing of the applied compression loads, and a similar trend can be observed for distribution of the incremental soil pressures. Soil pressure cells at the center, near the edge, and at the corner represent a distribution from the lower, middle, and higher ranges of the incremental soil pressures underneath the footing. This phenomenon is similar to that of a foundation underpinned by micropiles reported by Han and Shu [36].

5.3. Percentage of Loads on Helical Anchors and Footing.

The distribution of incremental soil pressures underneath the footing in Figure 8 indicates that the helical anchors and the footing of the composite foundation both share the compression loads. As expected, a well-designed composite foundation to resist compression loadings will rely on how much of the compression resistance comes from the helical anchors and how much of that comes from the soil beneath the footing.

Based on the principle that the compression load applied on the composite foundation can be shared by the helical anchors and the soil beneath the footing, the compression resistance of the footing for each of composite foundations was estimated by the measured incremental soil pressures of the soil

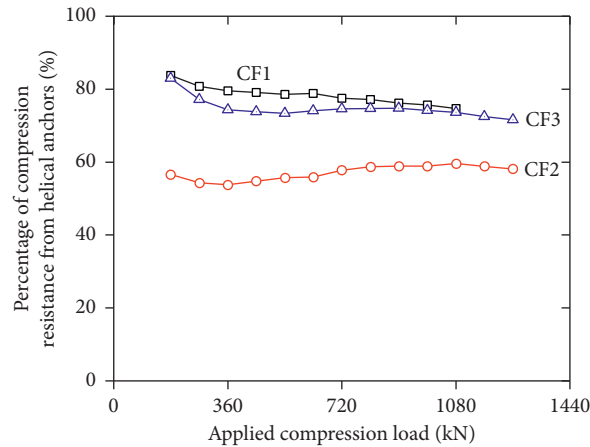


FIGURE 9: Variation in percentage of compression resistance from the helical anchors underneath footing.

pressure cells underneath the footing. As listed in Table 4, the average soil pressure underneath the footing corresponding to each compression load increment is calculated by each individual soil pressure cell. Then, the compression resistance from the footing is determined by using this average soil pressure to multiply the footing area. Finally, the corresponding compression resistance from the helical anchors can be obtained. For the purpose of analysis, as tabulated in Table 4, the compression resistance from helical anchors corresponding to each load increment is expressed as the percentage of the applied load on the composite foundation pier. Figure 9 shows the variation in the percentage of the compression resistance from the helical anchors for CF1, CF2, and CF3.

As shown in Figure 9, the percentage of the compression resistance from helical anchors during the loading fluctuates between 74.7% and 83.8% for CF1, between 53.8% and 59.6% for CF2, and between 72.5% and 83.0% for CF3. In general, the percentage tends to slightly decrease with the increase of the total load applied on the composite foundation pier. This reduction of the load on the helical anchors demonstrated that the screw anchors had started to yield, and more compression load was transferred onto the soil underneath the footing. The helical anchors carry approximately 60%–80% of the applied compression loads; in other words, the helical anchors share more loads than the footing.

6. Conclusions

Three axial compression load tests were carried out on a type of composite foundation of spread footing anchored by helical anchors. Based on the field load test results, the following conclusions can be reached:

- (1) The compression load-settlement responses of composite foundations approximately exhibit three distinct segments: initial linear-elastic, curve transition, and final linear, which are similar to those of drilled shafts and footings under compression loads, and their compression resistances should be interpreted employing an appropriate criterion as done in other studies.

- (2) Of the five representative interpretation criteria (Chin, Terzaghi and Peck, slope tangent, tangent intersection, and L_1-L_2) examined in this study, the slope tangent, tangent intersection, and Terzaghi and Peck methods are located within curve transition segment of the load-settlement curve, whereas the Chin method yields the highest load capacity, even greater than the measured data. According to L_1-L_2 method, L_1 is a definition for the elastic limit, while L_2 could be a useful definition for the interpreted load capacity and could be adopted as a base for comparison.
- (3) Under compression loads, the helical anchors and the footing both share the applied compression loadings on the composite foundation. However, the helical anchors generally share more compression loads than the footing, approximately 60%–80% of the applied loads. Higher compression resistance of a composite foundation can be obtained by increasing the footing embedment depth and the number of helical anchors underneath the footing.
- (4) When a composite foundation is subjected to compression loads, soil pressure cells at the center, near the edge, and at the corner represent a distribution from the lower, middle, and higher ranges of the incremental soil pressures underneath the footing. More load can be transferred onto the soils underneath the footing after the screw anchors start to yield.
- (5) It should be noted that the results shown in this study are general behaviors applicable for the composite foundations of spread footing anchored by helical anchors installed in silty clay and sandy silt only, and any extrapolation of these results to other different soil foundations is not recommended.

Data Availability

The data used to support the findings of this study can be obtained from the corresponding author upon request.

Conflicts of Interest

The authors declare that they have no conflicts of interest regarding the publication of this paper.

Acknowledgments

The authors gratefully acknowledge the financial support of the National Natural Science Foundation of China (52069013).

References

- [1] J. C. Huffman and A. W. Stuedlein, "Reliability-based serviceability limit state design of spread footings on aggregate pier reinforced clay," *Journal of Geotechnical and Geoenvironmental Engineering*, vol. 140, no. 10, Article ID 04014055, 2014.
- [2] J. C. Huffman, A. W. Strahler, and A. W. Stuedlein, "Reliability-based serviceability limit state design for immediate settlement of spread footings on clay," *Soils and Foundations*, vol. 55, no. 4, pp. 798–812, 2015.
- [3] S. O. Akbas and F. H. Kulhawy, "Axial compression of footings in cohesionless soils. I: load-settlement behavior," *Journal of Geotechnical and Geoenvironmental Engineering*, vol. 135, no. 11, pp. 1562–1574, 2009.
- [4] E. G. Diaz-Segura, "Assessment of the range of variation of N_y from 60 estimation methods for footings on sand," *Canadian Geotechnical Journal*, vol. 50, no. 7, pp. 793–800, 2013.
- [5] J.-L. Briaud, "Spread footings in sand: load settlement curve approach," *Journal of Geotechnical and Geoenvironmental Engineering*, vol. 133, no. 8, pp. 905–920, 2007.
- [6] N. C. Consoli, M. A. Vendruscolo, and P. D. M. Prietto, "Behavior of plate load tests on soil layers improved with cement and fiber," *Journal of Geotechnical and Geoenvironmental Engineering*, vol. 129, no. 1, pp. 96–101, 2003.
- [7] M. Elkasabgy and M. H. El Naggar, "Axial compressive response of large-capacity helical and driven steel piles in cohesive soil," *Canadian Geotechnical Journal*, vol. 52, no. 2, pp. 224–243, 2015.
- [8] S. N. Rao, Y. V. S. N. Prasad, and M. D. Shetty, "The behaviour of model screw piles in cohesive soils," *Soils and Foundations*, vol. 31, no. 2, pp. 35–50, 1991.
- [9] J. I. Adams and D. C. Hayes, "The uplift capacity of shallow foundations," *Ontario Hydro Research Quarterly*, vol. 19, pp. 1–13, 1967.
- [10] G. G. Meyerhof and J. I. Adams, "The ultimate uplift capacity of foundations," *Canadian Geotechnical Journal*, vol. 5, no. 4, pp. 225–244, 1968.
- [11] M. P. Mitsch and S. P. Clemence, "Uplift capacity of helix anchors in sand," in *Proceedings Of ASCE Convention, Uplift Behavior Of Anchor Foundations In Soil*, pp. 26–47, ASCE, Detroit, Michigan, USA, October 1985.
- [12] J. S. Mooney, S. J. Adamczak, and S. P. Clemence, "Uplift capacity of helix anchors in clay and silt," in *Proceedings Of ASCE Convention, Uplift Behavior Of Anchor Foundations In Soil*, pp. 48–72, ASCE, Detroit, Michigan, USA, October 1985.
- [13] Z. H. Elsherbiny and M. H. El Naggar, "Axial compressive capacity of helical piles from field tests and numerical study," *Canadian Geotechnical Journal*, vol. 50, no. 12, pp. 1191–1203, 2013.
- [14] K. Gavin, P. Doherty, and A. Tolooiyan, "Field investigation of the axial resistance of helical piles in dense sand," *Canadian Geotechnical Journal*, vol. 51, no. 11, pp. 1343–1354, 2014.
- [15] S. N. Rao, Y. V. S. N. Prasad, and C. Veeresh, "Behaviour of embedded model screw anchors in soft clays," *Géotechnique*, vol. 43, no. 4, pp. 605–614, 1993.
- [16] R. S. Merifield, "Ultimate uplift capacity of multiplate helical type anchors in clay," *Journal of Geotechnical and Geoenvironmental Engineering*, vol. 137, no. 7, pp. 704–716, 2011.
- [17] D. Wang, R. S. Merifield, and C. Gaudin, "Uplift behaviour of helical anchors in clay," *Canadian Geotechnical Journal*, vol. 50, no. 6, pp. 575–584, 2013.
- [18] CNS GB 50007, "Code for Design of Building Foundations" *Chinese National Standard*, China Architecture and Building Press, Beijing, China, 2011.
- [19] CLC JGJ 94, "Technical Code for Building Pile Foundations" *Chinese Local Standard*, China Architecture and Building Press, Beijing, China, 2008.
- [20] Z. Z. Qian, X. L. Lu, and W. Z. Yang, "Axial uplift behavior of drilled shafts in Gobi gravel," *Geotechnical Testing Journal*, vol. 37, no. 2, pp. 205–217, 2014.
- [21] Z.-Z. Qian, X.-L. Lu, X. Han, and R.-M. Tong, "Interpretation of uplift load tests on belled piers in Gobi gravel," *Canadian Geotechnical Journal*, vol. 52, no. 7, pp. 992–998, 2015.
- [22] X. L. Lu, Z. Z. Qian, and W. Z. Yang, "Axial uplift behavior of belled piers in sloping ground," *Geotechnical Testing Journal*, vol. 40, no. 4, pp. 579–590, 2017.
- [23] K. K. Phoon and F. H. Kulhawy, *Serviceability Limit State Reliability-Based Design* Chapter 9, *Reliability-Based Design in Geotechnical Engineering: Computations and Applications*, pp. 344–384, CRC Press, Florida, US, 2008.
- [24] M. Dithinde, K. K. Phoon, M. De Wet, and J. V. Retief, "Characterization of model uncertainty in the static pile design formula," *Journal of Geotechnical and Geoenvironmental Engineering*, vol. 137, no. 1, pp. 70–85, 2011.
- [25] X. L. Lu, Z. Z. Qian, W. F. Zheng, and W. Z. Yang, "Characterization and uncertainty of uplift load–displacement behaviour of belled piers," *Geomechanics and Engineering International Journal*, vol. 11, no. 2, pp. 211–234, 2016.
- [26] Y.-J. Chen and Y.-C. Fang, "Critical evaluation of compression interpretation criteria for drilled shafts," *Journal of Geotechnical and Geoenvironmental Engineering*, vol. 135, no. 8, pp. 1056–1069, 2009.
- [27] M. C. M. Marcos, Y.-J. Chen, and F. H. Kulhawy, "Evaluation of compression load test interpretation criteria for driven precast concrete pile capacity," *KSCE Journal of Civil Engineering*, vol. 17, no. 5, pp. 1008–1022, 2013.
- [28] A. Hirany and F. H. Kulhawy, "Conduct And Interpretation of Load Tests on Drilled Shaft Foundations: Detailed Guidelines," Report No. EL-5915, Electric Power Res. Inst., Palo Alto, California, US, 1988.
- [29] A. Hirany and F. H. Kulhawy, "Interpretation of Load Tests on Drilled Shafts. II: Axial Uplift" *Proc., Foundation Engineering: Current Principles and Practices*, F. H. Kulhawy, Ed., pp. 1150–1159, ASCE, New York, US, 1989.
- [30] A. Hirany and F. H. Kulhawy, "On the interpretation of drilled foundation load test results," in *Proceedings of International Deep Foundations Congress*, M. W. O'Neill and F. C. Townsend, Eds., pp. 1018–1028, ASCE, Orlando, Florida, February 2002.
- [31] F. K. Chin, "Estimation of the ultimate load of piles not carried to failure," in *Proceedings Of the 2nd Southeast Asian Conference On Soil Engineering*, pp. 81–90, Singapore, June 1970.
- [32] K. Terzaghi and R. B. Peck, *Soil Mechanics in Engineering Practice*, Wiley, New York, US, 2nd Ed. edition, 1967.

- [33] T. D. O'Rourke and F. H. Kulhawy, "Observations on Load Tests on Drilled Shafts" *Proc., Drilled Piers and Caissons II*, C. N. Baker, Ed., pp. 113–128, ASCE, New York, US, 1985.
- [34] W. S. Housel, "Pile load capacity: estimates and test results," *Journal of the Soil Mechanics and Foundations Division*, vol. 92, no. 4, pp. 1–30, 2002.
- [35] M. J. Tomlinson, *Pile Design and Construction Practice (A Viewpoint publication)*, Cement & Concrete Association of Great Britain, London, UK, 1977.
- [36] J. Han and S.-L. Ye, "A field study on the behavior of a foundation underpinned by micropiles," *Canadian Geotechnical Journal*, vol. 43, no. 1, pp. 30–42, 2006.

Research Article

Phase-Field Modeling Fracture in Anisotropic Materials

Haifeng Li,^{1,2} Wei Wang ,^{1,2} Yajun Cao ,^{1,2} and Shifan Liu^{1,2}

¹Geotechnical Research Institute, Hohai University, Nanjing, Jiangsu 210098, China

²Key Laboratory of Education for Geomechanics and Embankment Engineering, Hohai University, Nanjing, Jiangsu 210098, China

Correspondence should be addressed to Wei Wang; wwang@hhu.edu.cn and Yajun Cao; caoyajun@hhu.edu.cn

Received 21 April 2021; Revised 1 July 2021; Accepted 17 July 2021; Published 30 July 2021

Academic Editor: Faming Huang

Copyright © 2021 Haifeng Li et al. This is an open access article distributed under the Creative Commons Attribution License, which permits unrestricted use, distribution, and reproduction in any medium, provided the original work is properly cited.

The phase-field method is a widely used technique to simulate crack initiation, propagation, and coalescence without the need to trace the fracture surface. In the phase-field theory, the energy to create a fracture surface per unit area is equal to the critical energy release rate. Therefore, the precise definition of the crack-driving part is the key to simulate crack propagation. In this work, we propose a modified phase-field model to capture the complex crack propagation, in which the elastic strain energy is decomposed into volumetric-deviatoric energy parts. Because of the volumetric-deviatoric energy split, we introduce a novel form of the crack-driving energy to simulate mixed-mode fracture. Furthermore, a new degradation function is proposed to simulate crack processes in brittle materials with different degradation rates. The proposed model is implemented by a staggered algorithm and to validate the performance of the phase-field modelling, and several numerical examples are constructed under plane strain condition. All the presented examples demonstrate the capability of the proposed approach in solving problems of brittle fracture propagation.

1. Introduction

Crack propagation is an active research topic in mechanical, energy, and environmental engineering, such as underground excavation, oil drilling, and nuclear waste storage [1–3], during the past decades. In particular, predictive investigations of crack-induced failure in rocks or rock-like materials are a complex problem due to the presence of preexisting fractures and voids which impact the strength and other mechanical properties. For geological materials like concrete and gypsum at no/low confinement, the failure mode is brittle fracturing which can be explained by Griffith's theory [4] and assuming that the energy to create a fracture surface per unit area is equal to the critical energy release rate G_c . Based on the Griffith principle, many numerical computational methods have been developed. Numerical techniques for simulating crack propagation can be categorised into discrete and diffuse/smear methods depending upon how they handle the discontinuity.

Discrete methods attempt to capture the exact topology either in an explicit way or in an implicit manner. For

instance, the extended finite-element method (XFEM) [5, 6] has become a popular tool to consider the discontinuities. It enables the accurate approximation of solutions with jumps within elements through additional enrichment functions of discontinuous and asymptotic fields, thereby avoiding remeshing the cracked domain. Nevertheless, algorithmic tracking of the evolution of complex fracture surfaces is a tedious task in the numerical implementation. The cracking particles method (CPM) [7–9] is a pragmatic alternative to explicit modelling of crack surfaces in which a crack is represented by a set of cracking particles that can be easily updated when the crack propagates.

Diffuse methods for fracture modelling are based on the assumption that the discontinuity in the cracked material is not sharp but can be interpreted as smeared damage [10, 11]. Recently, the phase-field method [12, 13] has been attracting much attention because of its simplicity for numerical implementation. In the phase-field model, a smooth boundary of the phase-field is employed to approximate the internal discontinuity boundary of a crack. The use of the phase-field model for fracture can circumvent the

complexity of tracking crack propagation that is typically required in discrete models. In this research, we adopt the phase-field method and propose novel modifications in order to elegantly simulate complicated fracture processes in geological materials. The phase-field method was proposed by Bourdin et al. [14], and further developed by Borden et al. [15] and Miehe et al. [16, 17]. Due to its strong ability to simulate complex fracture processes such as nucleation, propagation, and branching, great efforts and extensions have also been done for brittle fracture [18–24], quasi-brittle fracture [25, 26], ductile fracture [27–30], dynamic fracture [15, 31], and multi-physicals fracturing problem [32, 33] for various materials.

The fundamental concept behind this model is the introduction of a scalar damage field, which ranges from 0 (undamaged material) to 1 (fully damage material), to represent the degree of fracture or damage of the material [13]. The crack propagation problem is sequentially recast as a standard multifield problem which can then be handled using the conventional finite-element method for both two-dimensional and three-dimensional cases. As a result, issues related to crack discontinuities are circumvented, and complex crack evolution can be treated naturally without difficulty. The phase-field model was developed within the framework of a variational principle of fracture [14], and this further enhances its attraction. The principle [12, 34] can be regarded as a generalization of Griffith's theory which enables it to predict not only crack initiation but also the crack propagation path. Furthermore, the solution of the variational principle is globally rather than locally optimal; thus, any new crack nucleation can be detected naturally without being specified in advance [14, 34].

Despite these contributions, these phase-field models assume that the critical energy release rates of different crack modes are the same, but in fact for many materials are not. In rock-like materials, such as concrete and gypsum, the critical energy release rate for Mode-I fracture is significantly lower than that for Mode-II fracture. This feature complicates the modelling of crack phenomena for rocks. In a rock specimen with a single inclined flaw under compression, wing cracks emerge first followed by secondary cracks. It has been reported [35, 36] that the wing crack is a Mode-I crack (tensile crack), while the secondary crack is usually Mode-II crack (shear crack). The sequential appearance of wing and secondary cracks can be attributed to the considerable difference in the critical energy release rates for different crack modes. Thus, it has been suggested [37] that this phenomenon cannot be captured by using the traditional critical energy release criterion, which does not account for the different critical energy release rates for mode-I and mode-II fractures.

In this paper, a modified phase-field model for brittle fracture is proposed to distinguish between the critical release rates for mode-I and mode-II cracks. This is achieved by partitioning the active energy density into distinct parts corresponding to different crack modes. The present paper is organized as follows: in Section 2, the fundamentals of the phase-field method are first briefly summarized. Section 3 presents the numerical implementation in detail. In Section 4, the accuracy of the numerical simulation is verified by

using one-element example; then a number of classical experimental tests are simulated. Finally, Section 5 concludes the paper.

2. Fundamentals of the Phase-Field Method

In this section, an arbitrary bounded computational domain $\Omega \subset \mathbb{R}^{n_{\text{dim}}}$ ($n_{\text{dim}} = 2, 3$) is considered with external boundary $\partial\Omega \subset \mathbb{R}^{n_{\text{dim}}-1}$ and internal discontinuity $\Gamma \subset \mathbb{R}^{n_{\text{dim}}-1}$ as illustrated in Figure 1. The external boundary $\partial\Omega$ is decomposed into two disjoint parts $\partial\Omega_u$ and $\partial\Omega_t$, i.e., $\partial\Omega_u \cap \partial\Omega_t = \emptyset$ and $\overline{\partial\Omega_u} \cup \overline{\partial\Omega_t} = \partial\Omega$. The domain Ω is subjected to the Dirichlet boundary conditions, $\mathbf{u}(\mathbf{x})$ for $\mathbf{x} \in \partial\Omega_u$, and the Neumann boundary $\partial\Omega_t \in \Omega$, with the corresponding outward unit normal vectors \mathbf{n}_u and \mathbf{n}_t . The Neumann conditions impose the traction $\mathbf{t}^*(\mathbf{x})$ on $\partial\Omega_t$.

2.1. Energy Functional. As already mentioned in Introduction, the phase-field approach to brittle fracture is based on the work of Bourdin et al. [13] and consists in the regularization of the variational formulation of Griffith's theory of brittle fracture, first proposed in 1998 by Francfort and Marigo [12]. Neglecting inertia effects and assuming quasi-static conditions, the total energy functional $\Psi(\mathbf{u}, \Gamma)$ of a solid is the sum of elastic energy $\psi(\boldsymbol{\varepsilon})$, fracture energy, and external work. Thus, the total power is written as

$$\Psi(\mathbf{u}, \Gamma) = \int_{\Omega} \mathbf{b} \cdot \mathbf{u} d\Omega + \int_{\partial\Omega_t} \mathbf{t}^* \cdot \mathbf{u} dS - \int_{\Gamma} G_c d\Gamma - \int_{\Omega} \psi_{\varepsilon}(\boldsymbol{\varepsilon}) d\Omega, \quad (1)$$

with the linear strain tensor $\boldsymbol{\varepsilon} = \boldsymbol{\varepsilon}(\mathbf{u})$ given by

$$\boldsymbol{\varepsilon} \equiv \nabla^s \mathbf{u} = \frac{1}{2} (\nabla \mathbf{u} + \nabla \mathbf{u}^T), \quad (2)$$

where \mathbf{u} denotes the displacement field of the body Ω and $\nabla(\cdot)$ and $\nabla^s(\cdot)$ denote the gradient and symmetric gradient operators, respectively, with $(\cdot)^T$ being the transpose operator.

Regarding the choice of the split of the energy density function, we introduce the volumetric-deviatoric energy split proposed by Lancioni and Royer-Carfagni [38]. Assuming the solid is isotropic and linear elastic, the elastic energy density $\psi_{\varepsilon}(\boldsymbol{\varepsilon}) = \psi^{\text{dev}}(\boldsymbol{\varepsilon}) + \psi^{\text{vol}}(\boldsymbol{\varepsilon})$ is written as

$$\psi^{\text{dev}}(\boldsymbol{\varepsilon}) = \mu (\boldsymbol{\varepsilon}^{\text{dev}} : \boldsymbol{\varepsilon}^{\text{dev}}) = \frac{1}{2} \boldsymbol{\varepsilon} : \mathbb{C}^{\text{dev}} : \boldsymbol{\varepsilon}, \quad (3)$$

$$\psi^{\text{vol}}(\boldsymbol{\varepsilon}) = \frac{1}{2} K \text{tr}^2(\boldsymbol{\varepsilon}) = \frac{1}{2} \boldsymbol{\varepsilon} : \mathbb{C}^{\text{vol}} : \boldsymbol{\varepsilon},$$

where $\boldsymbol{\varepsilon}^{\text{dev}} = \boldsymbol{\varepsilon} - (1/3)\text{tr}(\boldsymbol{\varepsilon})\mathbf{I}$ is the deviatoric component of the strain tensor $\boldsymbol{\varepsilon}$, $K = \lambda + (2/3)\mu$ is the bulk modulus of the material, λ and μ are the Lamé constants, \mathbf{I} the second-order unit tensor, and \mathbb{C}^{dev} and \mathbb{C}^{vol} are the deviatoric and volumetric parts of the elasticity tensor \mathbb{C} , and defined as follows:

$$\begin{cases} \mathbb{C}^{\text{vol}} = KI \otimes \mathbf{I}; \\ \mathbb{C}^{\text{dev}} = \mathbb{C} - \mathbb{C}^{\text{vol}}. \end{cases} \quad (4)$$

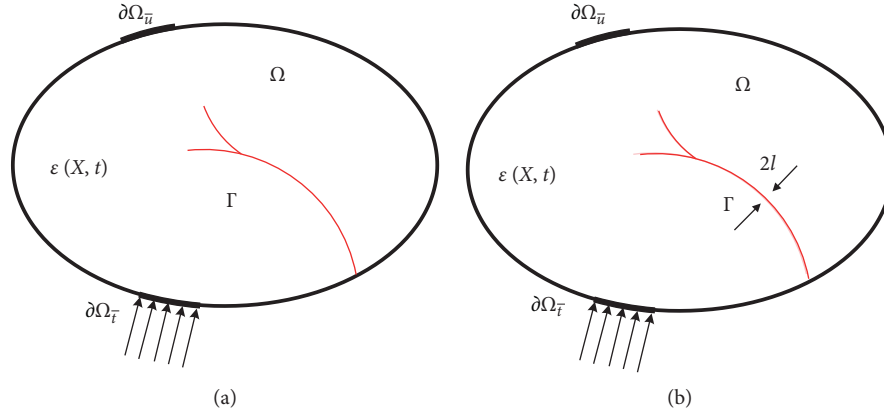


FIGURE 1: Schematic depiction of a solid body Ω with a strong discontinuity Γ (a), modeled by the phase-field fracture method (b). The parameter ℓ controls the width of the diffused fracture zone.

2.2. Phase-Field Approximation for Fracture Energy. In the phase-field model, a scalar field (phase-field) is used to diffuse the sharp crack topology [16, 17] over a certain domain which avoids complex crack tracking procedures and an explicit representation of the crack surface as in discrete crack approaches [39]. Therefore, a narrow transition band connects the fully fractured and intact domains with the displacement being still continuous. Within the context of quasi-static brittle fracture in elastic solids, the cracks are approximated as bands of finite thickness characterised by the phase-field $d(\mathbf{x}, t) \in [0, 1]$ as shown in Figure 1, which satisfies the following conditions:

$$d = \begin{cases} 0, & \text{if material is intact,} \\ 1, & \text{if material is cracked.} \end{cases} \quad (5)$$

This variable indicates the damage in the material. The material is fully broken for $d = 1$, and $d = 0$ represents the intact state. A typical one-dimensional phase-field is approximated with the exponential function:

$$d(x) = e^{-(|x|/\ell)}. \quad (6)$$

The length-scale parameter ℓ plays an important role which controls the transition region between the fracture and intact material.

For 2D and 3D problems, the crack surface density per unit volume of the solid is given by [17]

$$\gamma(d, \nabla d) = \frac{d^2}{2\ell} + \frac{\ell}{2} \frac{\partial d}{\partial x_i} \frac{\partial d}{\partial x_i}. \quad (7)$$

Thus, exploiting equation (6), the fracture energy in equation (1) can be rewritten as

$$\int_{\Gamma} G_c dS = \int_{\Omega} G_c \left[\frac{d^2}{2\ell} + \frac{\ell}{2} \frac{\partial d}{\partial x_i} \frac{\partial d}{\partial x_i} \right] d\Omega. \quad (8)$$

2.3. Governing Equations for Evolution of the Phase-Field. It is noticed that the phase-field formulation equation (1) does not distinguish fracture behaviour during tension and

compression. Therefore, based on the volumetric-deviatoric decomposition of the elastic energy, a more adequate choice for a split would be adopted [40]:

$$\psi^+ = \frac{1}{2} K \langle \text{tr}(\boldsymbol{\varepsilon}) \rangle_+^2 + \mu (\boldsymbol{\varepsilon}^{\text{dev}} : \boldsymbol{\varepsilon}^{\text{dev}}), \quad (9)$$

$$\psi^- = \frac{1}{2} K \langle \text{tr}(\boldsymbol{\varepsilon}) \rangle_-^2.$$

We follow Ambati et al. [41] and assume that the phase-field affects the positive part of the elastic energy:

$$\psi(\boldsymbol{\varepsilon}) = [(1-k)g(d) + k]\psi^+ + \psi^-, \quad (10)$$

where $0 < k \ll 1$ is the parameter that stabilizes the stiffness matrix to ensure the numerical convergence. Taking advantage of equations (8) and (10), equation (1) can be rewritten as

$$\begin{aligned} \Psi(\mathbf{u}, \Gamma) = & \int_{\Omega} \mathbf{b} \cdot \mathbf{u} d\Omega + \int_{\partial\Omega_t} \mathbf{t}^* \cdot \mathbf{u} dS - \int_{\Gamma} G_c \left[\frac{d^2}{2\ell} + \frac{\ell}{2} \frac{\partial d}{\partial x_i} \frac{\partial d}{\partial x_i} \right] d\Omega \\ & - \int_{\Omega} \{ [(1-k)g(d) + k]\psi^+ + \psi^- \} d\Omega. \end{aligned} \quad (11)$$

Following Miehe et al. [16], we obtain two coupled local equations:

$$\begin{cases} \text{div} \boldsymbol{\sigma} + \mathbf{b} = 0, \\ (1-k)g(d)\psi^+ + G_c \left[\frac{d}{\ell} - \ell \Delta d \right] = 0, \end{cases} \quad (12)$$

where $\boldsymbol{\sigma}$ is the stress tensor, defined as

$$\boldsymbol{\sigma} = g(d) \left[K \langle \text{tr}(\boldsymbol{\varepsilon}) \rangle_+ I + 2\mu \boldsymbol{\varepsilon}^{\text{dev}} \right] + K \langle \text{tr}(\boldsymbol{\varepsilon}) \rangle_- I. \quad (13)$$

The degradation function $g(d)$ characterizes the ratio of residual strain energy and total strain energy during the crack evolution. The degradation $g(d)$ function is a monotonically $g(0) = 1$ and $g(1) = 0$. Actually, the selection of degradation function depends on the

mechanical properties of materials. For this reason, inspired by the work of [42–44], a new degradation function is proposed in this study to describe a large range of failure processes:

$$g(d) = (1 - k) \frac{(1 - d)^2}{M + (M - 1)(1 - d)^2} + k. \quad (14)$$

In this degradation function, M is a nondimensional material parameter, which characterizes the degradation rate of strain energy with the evolution of the phase-field, as shown in Figure 2. To prevent crack healing, we take advantage of the definition of local history field proposed by Miehe and Schänzel [45] to set up relationship between phase-field variable and maximum reference energy in history, whereby the following relation is given:

$$\mathcal{H}(x, t) = \max_{s \in [0, t]} \psi_\varepsilon^+, \quad \text{in } \Omega \times (0, T], \quad (15)$$

where x is the material point in a reference body and t is the pseudotime. Thus the phase-field evolution equation is finally given as

$$l \Delta d = \frac{d}{\ell} + (1 - k) \dot{g}(d) \frac{\mathcal{H}}{G_c}. \quad (16)$$

The critical energy release rate for brittle tension fracture is significantly lower than that for the compressive-shear fracture. To capture this feature, in this work, the model incorporates different contributions of energy components to crack growth, which is able to capture tensile and shear cracks according to the strain states. Therefore, equation (16) can be rewritten as

$$l \Delta \phi = \frac{d}{\ell} + (1 - k) \dot{g}(d) \left(\frac{\mathcal{H}_{\text{vol}}^+}{G_t} + \frac{\mathcal{H}_{\text{dev}}^+}{G_t} + \frac{\mathcal{H}_{\text{dev}}^-}{G_s} \right), \quad (17)$$

where the parameters G_t and G_s are the critical energy rates for tensile and compressive-shear fracture, respectively. $\mathcal{H}_{\text{vol}}^+$ and $\mathcal{H}_{\text{dev}}^\pm$ represent parts of the volumetric-deviatoric split of the elastic strain energy:

$$\begin{cases} \mathcal{H}_{\text{vol}}^+ = \frac{1}{2} K \langle \text{tr}(\boldsymbol{\varepsilon}) \rangle_+, \\ \mathcal{H}_{\text{dev}}^+ = \mu (\boldsymbol{\varepsilon}^{\text{dev}} : \boldsymbol{\varepsilon}^{\text{dev}}) H(\text{tr}(\boldsymbol{\varepsilon})), \\ \mathcal{H}_{\text{dev}}^- = \mu (\boldsymbol{\varepsilon}^{\text{dev}} : \boldsymbol{\varepsilon}^{\text{dev}}) [1 - H(\text{tr}(\boldsymbol{\varepsilon}))], \end{cases} \quad (18)$$

where $H(\cdot)$ is the Heaviside function.

3. Numerical Algorithm

In this section, we describe the numerical algorithm on implementation of the phase-field modelling of fracture propagation in isotropic medium. We use the finite-element method to discretize the spatial domain and a staggered scheme to solve the coupling equations and for pursuing a higher convergence rate.

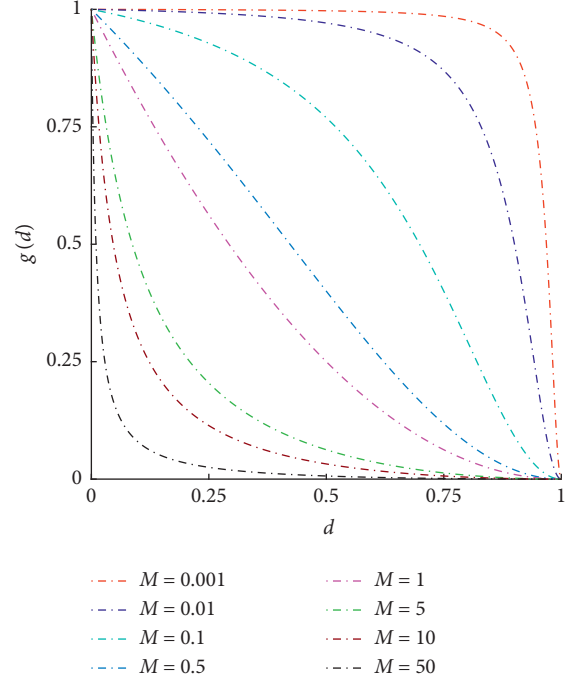


FIGURE 2: The evolution of degradation function for different M .

3.1. Finite-Element Discretization. The weak forms of the governing equations are given by

$$\begin{aligned} \int_{\Omega} -\boldsymbol{\sigma} : \delta \boldsymbol{\varepsilon} dV + \int_{\Omega} \mathbf{b} \cdot \delta \mathbf{u} dV + \int_{\partial \Omega_t} \mathbf{t}^* \cdot \delta \mathbf{u} dS &= 0, \\ \int_{\Omega} (1 - k) g'(d) \frac{\mathcal{H}}{G_c} \delta \phi d\Omega + \int_{\Omega} \left(\ell \nabla d \cdot \nabla \delta d + \frac{1}{\ell} d \delta d \right) d\Omega &= 0. \end{aligned} \quad (19)$$

The quadrilateral four-node element in 2D elements and the hexahedral eight-node in 3D elements are implemented to discretize the bulk domain Ω . The node values u_i and d_i are discretized as follows:

$$\begin{aligned} \mathbf{u} &= \sum_{i=1}^n N_i u_i, \\ d &= \sum_{i=1}^n N_i d_i, \end{aligned} \quad (20)$$

where n is the total number of nodes per element. N_i denotes the shape function associated with node i . The corresponding matrices of the spatial derivatives can be expressed as

$$\begin{aligned} B_i^u &= \begin{bmatrix} N_{i,x} & 0 \\ 0 & N_{i,y} \\ N_{i,y} & N_{i,x} \end{bmatrix}, \\ B_i^d &= \begin{bmatrix} N_{i,x} \\ N_{i,y} \end{bmatrix}. \end{aligned} \quad (21)$$

Then it is possible to express the gradients:

$$\begin{aligned}\boldsymbol{\varepsilon} &= \sum_{i=1}^n B_i^u u_i, \\ \nabla d &= \sum_{i=1}^n B_i^d d_i.\end{aligned}\quad (22)$$

According to 21) and (22), the contributions of one-element at node i to the residual of the overall systems of equations are given as

$$\begin{aligned}\mathbf{R}_i^u &= \mathbf{F}_i^{u,\text{ext}} - \mathbf{F}_i^{u,\text{int}} = \int_{\partial\Omega_i} N_i \mathbf{t}^* dS - \int_{\Omega} B_i^u \boldsymbol{\sigma} d\Omega, \\ R_i^d &= -F_i^{d,\text{int}} = \int_{\Omega} \left\{ (1-k)g'(d) \frac{\mathcal{H}}{G_c} N_i + \left(\ell [B_i^d]^T \nabla d + \frac{1}{\ell} d N_i \right) \right\} d\Omega,\end{aligned}\quad (23)$$

where $\mathbf{F}_i^{u,\text{ext}}$ and $\mathbf{F}_i^{u,\text{int}}$ denote the external forces and inner forces, respectively, which correspond to the displacement, whereas $F_i^{d,\text{int}}$ can be explained as inner forces to the phase-field. We used the Newton–Raphson procedure to obtain the

solutions by making $\mathbf{R}^u = 0$ and $R^d = 0$. The corresponding tangents on the element level can be obtained based on the inner forces:

$$\begin{aligned}K_{ij}^{uu} &= \frac{\partial \mathbf{F}_i^{u,\text{int}}}{\partial \mathbf{u}_j} = \int_{\Omega} [\mathbf{B}_i^u]^T \mathbf{D} [\mathbf{B}_j^u] d\Omega, \\ K_{ij}^{dd} &= \frac{\partial F_i^{d,\text{int}}}{\partial d_j} = \int_{\Omega} \left\{ [B_i^d]^T \ell [B_j^d] + N_i \left((1-k)g^{(2)}(d) \left(\frac{\mathcal{H}_{\text{vol}}^+}{G_t} + \frac{\mathcal{H}_{\text{dev}}^+}{G_t} + \frac{\mathcal{H}_{\text{dev}}^-}{G_s} \right) + \frac{1}{\ell} \right) N_j \right\} d\Omega,\end{aligned}\quad (24)$$

where \mathbf{D} is the fourth-order elasticity tensor given by

$$\mathbf{D} = \begin{cases} ((1-k)g(d) + k) [\mathbf{C}^{\text{vol}} + \mathbf{C}^{\text{dev}}], & \text{tr}(\boldsymbol{\varepsilon}) \geq 0, \\ \mathbf{C}^{\text{vol}} + ((1-k)g(d) + k) \mathbf{C}^{\text{dev}}, & \text{tr}(\boldsymbol{\varepsilon}) < 0. \end{cases} \quad (25)$$

3.2. Staggered Scheme. A staggered scheme is adopted here; where at each increment step, the governing equation (23) is solved for u by freezing d . After updating the elastic strains, we solve the phase-field evolution for d . The step is repeated until a convergence criterion is reached. A strong coupling between the displacement field and phase-field introduces a relatively complicated numerical process. Therefore, a N-R iteration procedure is needed for solving this nonlinear equation. For the sake of clarity, we show the flowchart of the N-R iterative scheme in Figure 3.

4. Verification of the Proposed Approach

In this section, starting with the simplest case where we compare different methods for one-element, more and more complex cases are introduced. In all cases, the relevant numerical parameters are summarized, then the results are shown and interpreted. In all cases (plane strain), the thickness of the element is 1 mm. The mesh is densified where the crack is expected to propagate, the size is specified in the text, and the mesh is shown in some of the figures. According to the results of Miehe et al. [17], the length-scale

parameter is always taken two times larger than the smallest element around the crack path.

4.1. One-Element. One 2D plane strain element is the simplest case, to verify the correctness of the proposed model. The geometry and the boundary conditions are illustrated in Figure 4(a). The bottom nodes are constrained in both directions, whereas we allow the top nodes to slide vertically. For the case of homogeneous materials, $E = 2.1 \times 10^5$ MPa, $\nu = 0.3$, $G_t = 5 \times 10^{-3}$ kN/mm, $G_s = 5 \times 10^{-2}$ kN/mm, and $\ell = 0.1$ mm as reported in [43, 46]. The loading history is divided into 1000 steps with a constant increment $\Delta u = 10^{-4}$ mm.

Figure 4(b) shows the comparisons of macroscopic stress-strain relation and damage evolution between the analytical solution and the proposed method. Obviously, these two solutions well recover each other as illustrated in this figure. This shows that the proposed phase-field method can well describe the damage process in homogeneous materials.

4.2. Three-Point Bending Test. In this section, an example of the problem of three-point bending test is presented performed by Perdikaris and Romeo [47] and widely taken as the benchmark model for numerical investigation on model-I fracture energy for plane concrete. Therefore, some previous experiences and results are available for comparison. The geometry and loading conditions of the specimen are

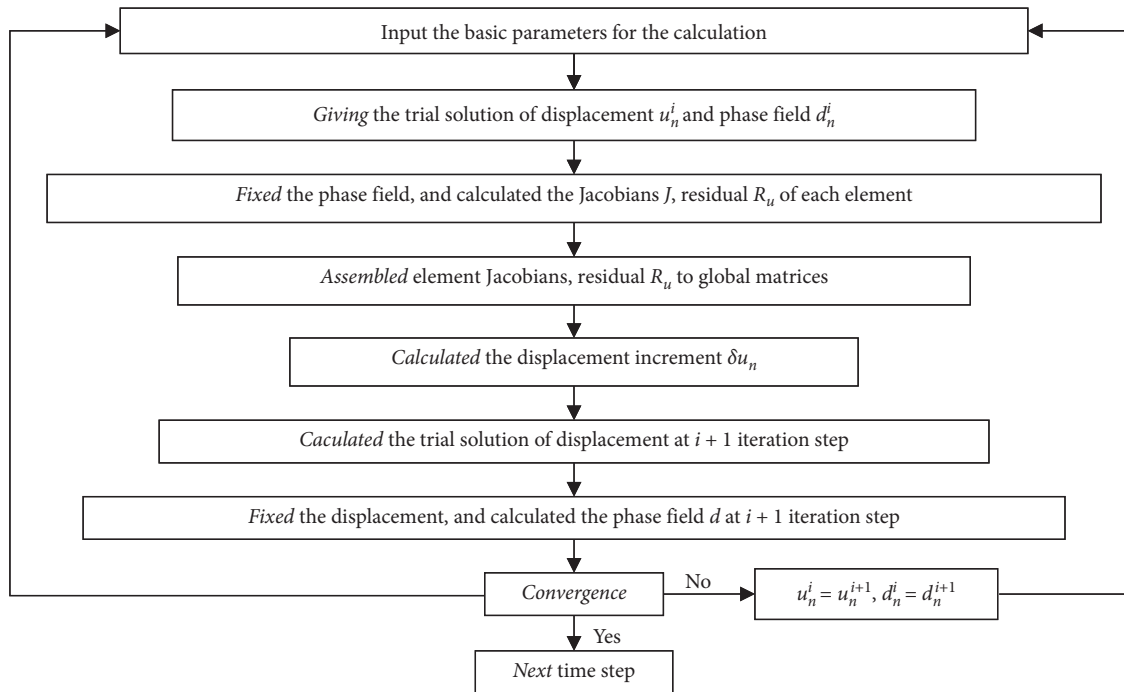


FIGURE 3: Flowchart of the staggered solution procedure.

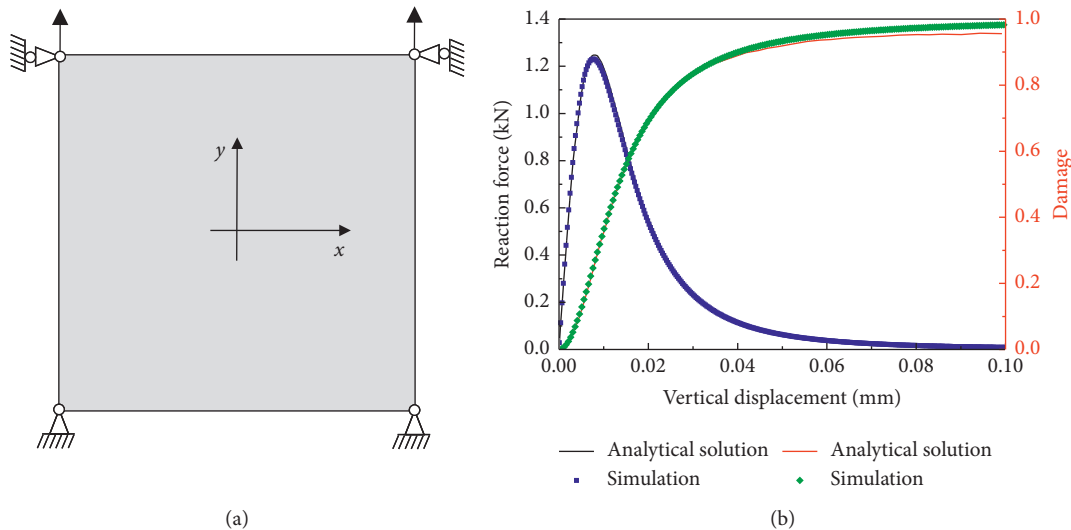


FIGURE 4: (a) Studied one-element and (b) comparisons of strain-force curves and macroscopic damage evolution between analytical solution and numerical results.

shown in Figure 5. Two different finite-element meshes are considered and shown in Figure 6. It amounts to 6252 elements in coarse mesh and 18474 elements in the fine mesh. The displacement imposed onto the notched beam is $\Delta u = 10^{-2}$ mm.

Young's modulus is taken as $E = 4.83 \times 10^4$ MPa. The parameter G_t on the one hand has been provided experimentally as $G_t = 0.0451$ N/mm and, on the other hand, can be calculated by the linear elastic fracture mechanics in consideration of size effect [48]. According to the work elaborated in [48], one takes $G_t = 0.029$ N/mm.

Figure 7 illustrates the crack evolution process predicted from the phase-field model. The crack initiates from the notch tip and propagates towards the top surface of the beam. Comparing the crack evolution processes in Figure 6, the speed of crack growth in the case of $G_t = 0.0290$ N/mm is faster than the other one, and the corresponding compressive-shear critical energy release rates are $G_s = 0.290$ N/mm and $G_s = 0.451$ N/mm, respectively.

Figure 8 compares the load-displacement response from this study to the experimental data. There is no detectable mesh dependency for the two meshes under consideration,

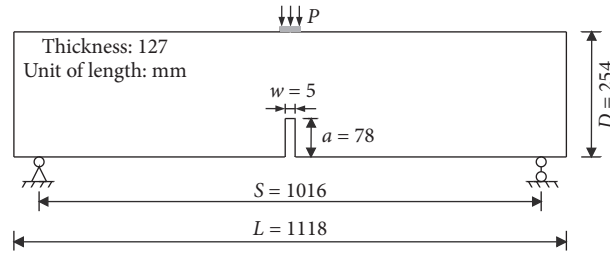


FIGURE 5: Symmetric three-point bending test: geometry and boundary conditions.

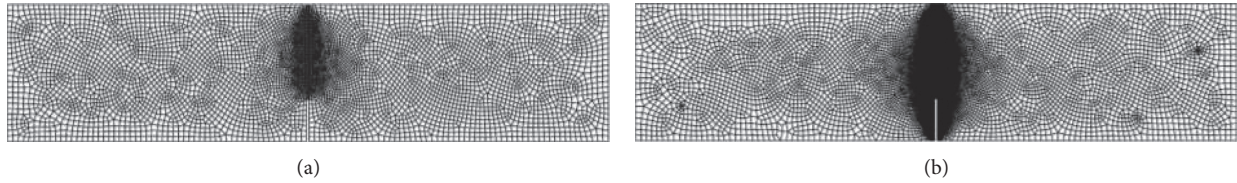


FIGURE 6: FE-meshes used for computation of three-point bending on notched beam: (a) coarse; (b) fine.

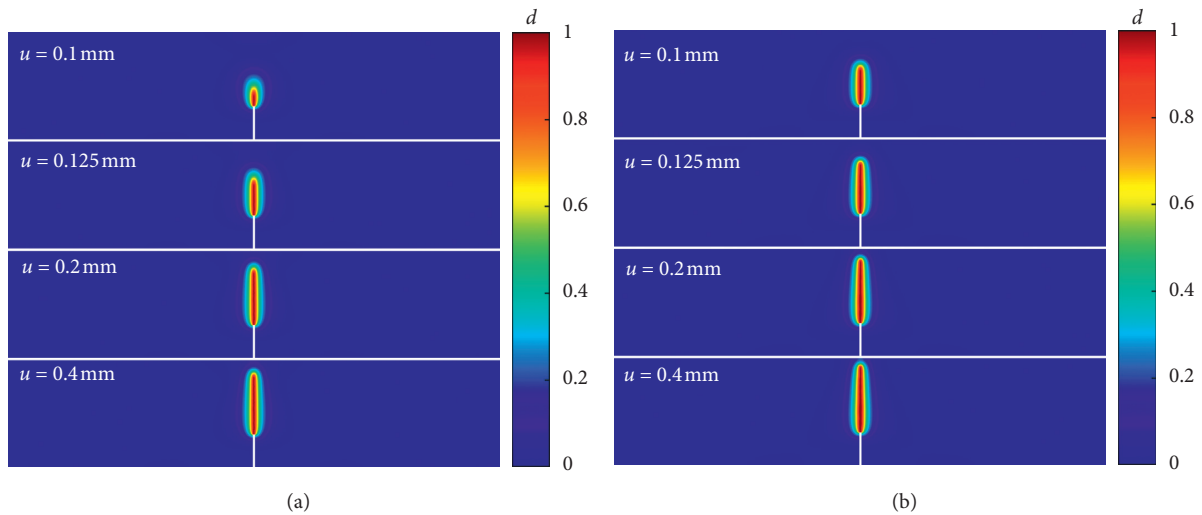


FIGURE 7: Predicted crack paths of the three-point bending test. (a) $G_t = 0.0451$ N/mm. (b) $G_t = 0.029$ N/mm.

and the beam is subject to noncyclic loading. In the case of $G_t = 0.0290$ N/mm and $G_s = 0.290$ N/mm, the maximum force that the beam can sustain from the simulation is 12.3 kN which is very close to the experimental data (12.0 kN). However, taking $G_t = 0.0451$ N/mm and $G_s = 0.451$ N/mm, the peak load is about 13 kN which is 8.3% higher than the experimental result.

The simulated forces both drop much faster than the experimental data after reaching the bearing capacity. These deviations on one aspect stem from the fact that a linear fracture model is used in the simulation, whereas the real fracture is nonlinear; the model neglects any plastic deformation. It can be clarified by examining the load-displacement curves from both cyclic and noncyclic loadings.

4.3. L-Shaped Panel Test. In this section, we simulate crack propagation in an L-shaped slab. The geometry and

boundary conditions of the problem are depicted in Figure 9(a). The experimental results are taken from [49], and Figure 9(b) illustrates the crack path obtained from the phase-field modelling and superimposes the range of experimentally obtained crack paths (shaded region). The material parameters are chosen as follows [50]: Young's modulus $E = 2.0 \times 10^4$ MPa, Poisson's ratio $\nu = 0.18$, $\ell = 10$ mm, tension fracture energy $G_t = 1.3 \times 10^{-4}$ kN/mm, and compressive-shear fracture energy $G_s = 1.3 \times 10^{-3}$ kN/mm [51]. The simulation is led with the step increment $\Delta u = 2 \times 10^{-3}$ mm.

The computational domain is discretized using a total of 51,766 elements with fine meshes assigned to the critical zone. Figure 10 illustrates the crack progression at several loading stages. The corresponding load-displacement curves are presented in Figure 11. For $\ell = 10$ mm, the crack path from the simulation is located at the path observed in the real test. The corresponding load-displacement curves are shown

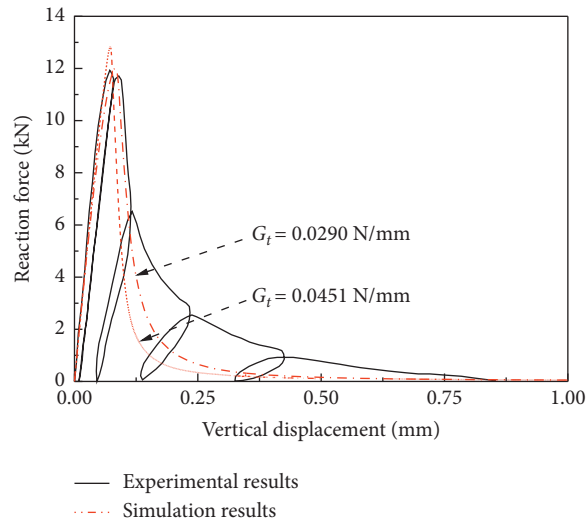


FIGURE 8: Calculated load-displacement curves of the three-point bending test.

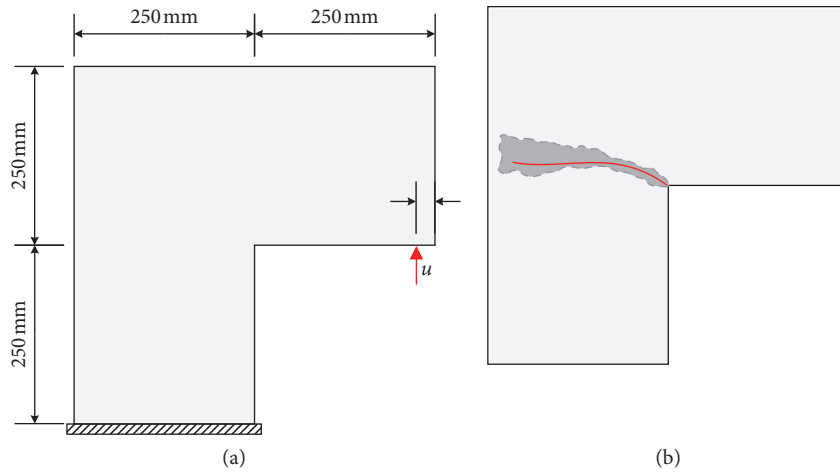


FIGURE 9: L-shaped panel test. (a) Geometry and boundary conditions. (b) Experimentally observed crack pattern.

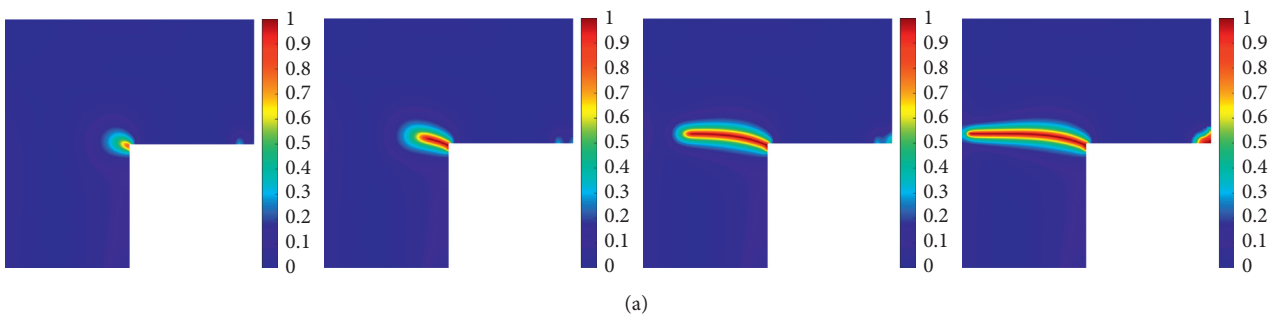


FIGURE 10: Continued.

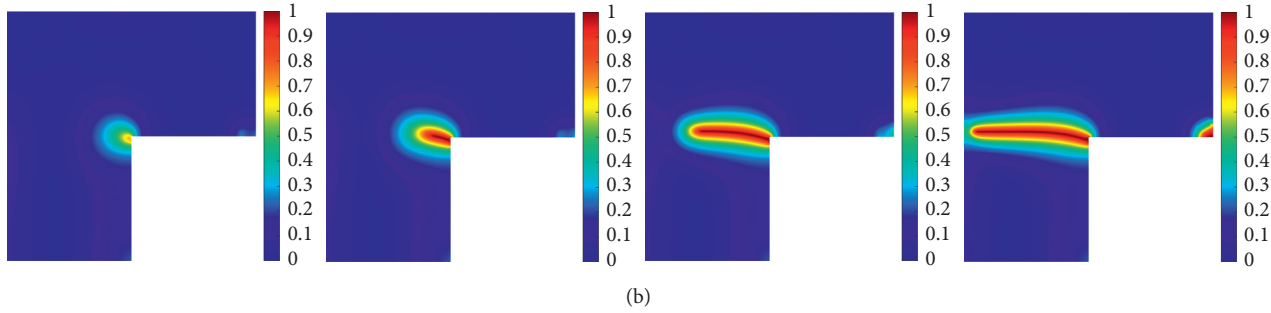


FIGURE 10: L-shaped panel test. Damage profiles for various length-scale parameters at displacements $u = 0.22$ mm, 0.30 mm, 0.45 mm, and 1.0 mm. (a) $\ell = 10$ mm. (b) $\ell = 20$ mm.

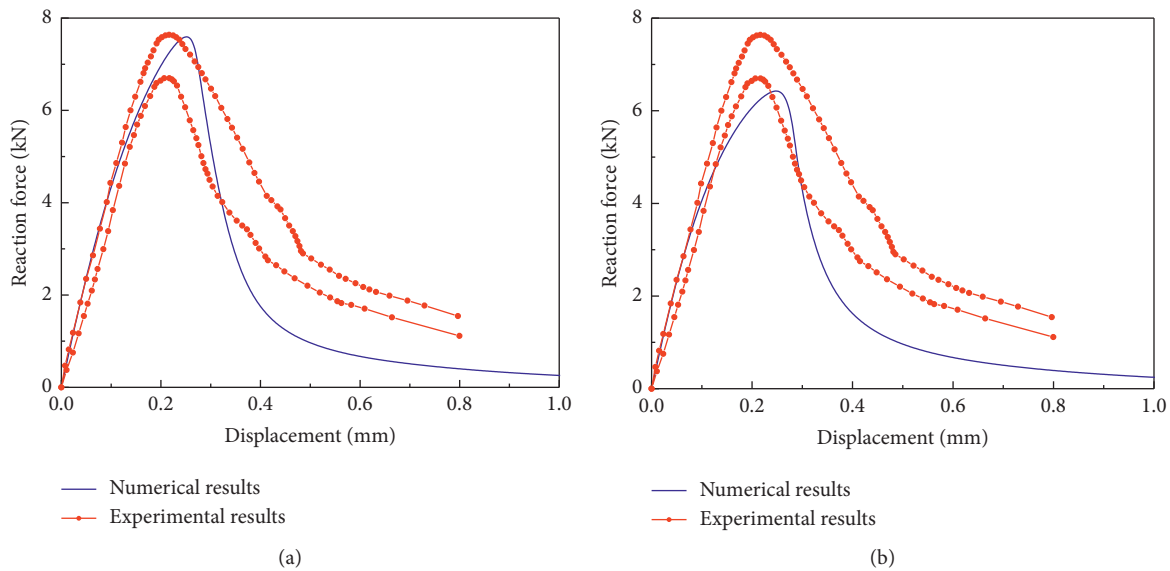


FIGURE 11: L-shaped panel: curves of load versus displacement for various length-scale parameters ℓ . (a) Length-scale parameter $\ell = 10$ mm. (b) Length-scale parameter $\ell = 20$ mm.

in Figure 11(a); the global response matches the experimental peak loads. The reaction force from the simulation increases steadily to a maximum value and then drops sharply. To further investigate the effect of the length scale, a second simulation is performed with a larger length scale ($\ell = 20$ mm). For $\ell = 20$ mm, a diffusive crack path is obtained due to the relatively large length scale. Although the maximum force obtained by using $\ell = 20$ mm is even lower as shown in Figure 11(b), the predicted crack path agrees well with the experimental data (Figure 10(b)). The proposed model is fairly in good agreement with the experimental results in terms of crack pattern.

4.4. Compression of a Rock Plate with Double Flaws. To further verify the modified phase-field model proposed and highlight its capabilities, crack propagation involving fracture coalescence is considered. Figure 12 shows a schematic illustration of the problem where a specimen with double inclined open flaws is loaded under uniaxial compression. Such a test has been widely investigated experimentally [35]

and numerically [52] by means of prefracture specimens of gypsum under uniaxial compression. In the test, the gypsum specimen is 76.2 mm long and 152.4 mm high. The length and the width for the flaws are 12.7 mm and 0.1 mm, respectively. The geometry of the flaws is represented by the terminology “ $\beta - s - c$,” as shown in Figure 12. Herein we consider the case of “45 - 2a - 2a” geometry ($2a = 12.7$ mm). Displacement increment $\Delta u = 0.002$ mm is prescribed in line with laboratory tests [35].

The mechanical properties of the material are $E = 5 \times 10^3$ MPa, Poisson’s ratio $\nu = 0.24$, $\ell = 0.5942$ mm, tension fracture energy $G_t = 5.0 \times 10^{-6}$ kN/mm, and compressive-shear fracture energy $G_s = 1.0 \times 10^{-2}$ kN/mm. The numerical simulation gives a crack pattern similar to the experimental observation, that is, the growth of four wing cracks and the coalescence of a secondary and one wing crack. The fracturing process is explained in more detail in Figure 13. Initially a stable growth of four wing cracks is seen (Figure 13(b)). The outer wing cracks continue to grow for a while, and a shear crack is subsequently initiated close to the inner tip of the upper notch; it coalesces with the inner wing

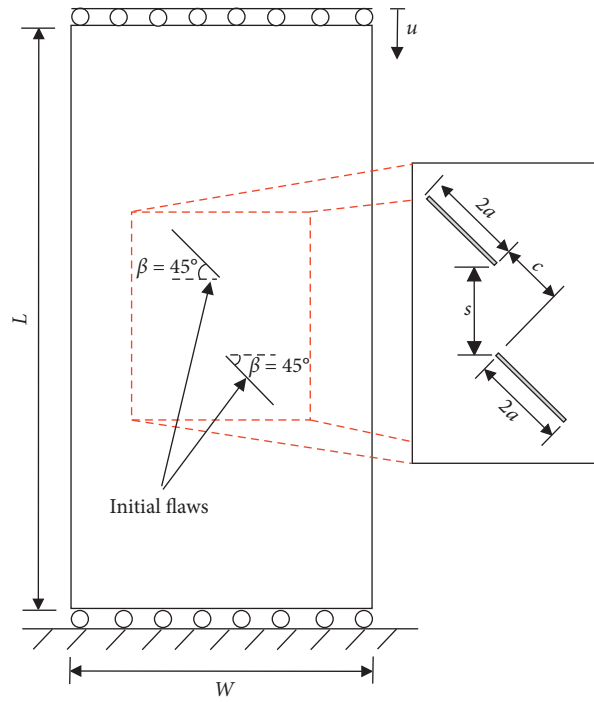


FIGURE 12: Geometries of the model rock specimen.

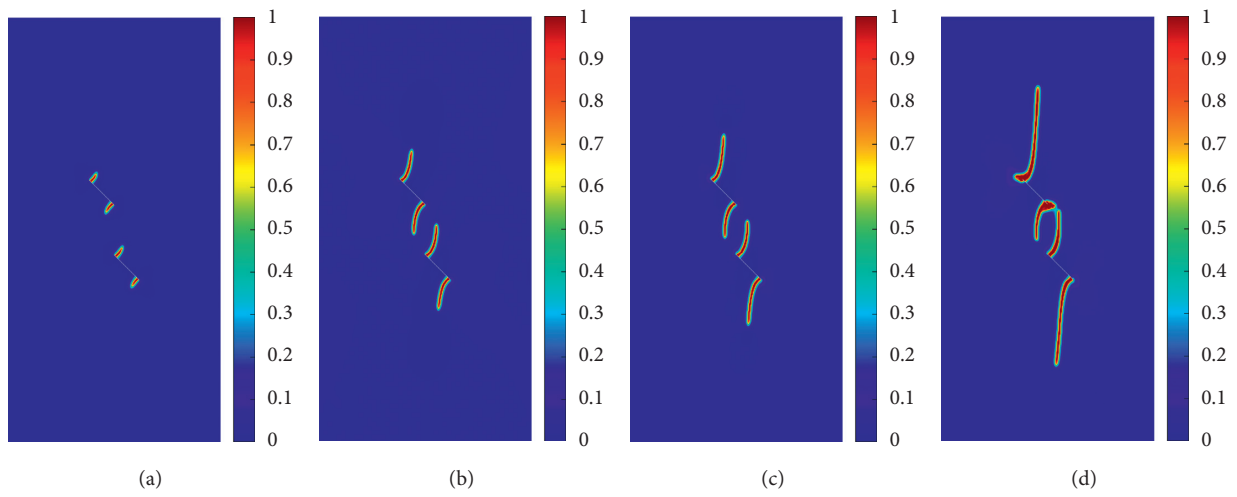


FIGURE 13: Continued.

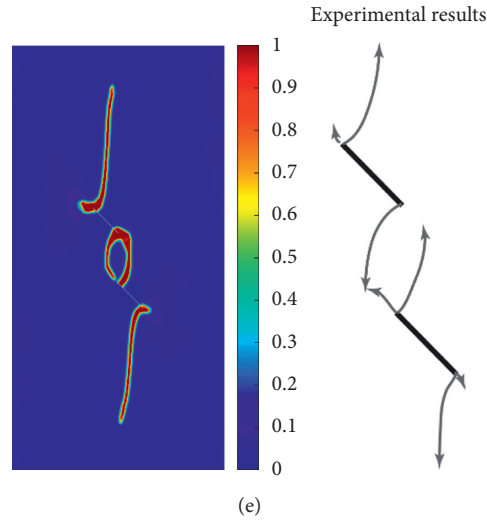


FIGURE 13: Crack evolution processes with displacement at (a) $u = 0.312$ mm; (b) $u = 0.632$ mm; (c) $u = 0.752$ mm; (d) $u = 0.856$ mm; (e) $u = 0.912$ mm.

crack of the lower notch (Figure 13(d)). Then, the inner wing crack of the upper notch is located in a strong shear stress state and approaches the preexisting flaw (Figure 13(e)). Eventually, they connect with each other. Up to this point, the simulated crack pattern is quite similar to the experimental [35].

5. Conclusions

This paper presents a new framework of the phase-field method based on the split of the fracture energy release rate for simulation of crack propagation in geotechnical materials. The critical release rate for tensile cracks is significantly lower than the energy release rate for shear cracks. In the proposed approach, the crack-driving energy is identified, and a new degradation function is introduced, in which a nondimensional parameter is used to describe crack propagation of brittle materials with different weakening rates.

Several numerical examples are carried out. Firstly, the modified phase-field model is validated by the widely used benchmark example, and the simulation results well agree with the analytical results. Furthermore, to demonstrate the capability of the modified phase-field model in simulation crack propagation and bifurcation in brittle materials, several numerical examples are presented. The presented phenomenon of crack propagation shows that the modified phase-field fracture model gives results in good agreement with the experimental observations both with respect to crack patterns and critical stress loads.

In summary, the modified model is capable of describing the failure behaviour for brittle and presenting the failure processes. Moreover, it is noteworthy that the effects of length parameter and critical energy release rate on simulation results need to be investigated further [53]. In future work, the proposed approach can be extended to predict crack propagation in multi-physics problems, for example, hydraulic fracture propagation and heat transfer.

Data Availability

The data used to support the findings of this study are available from the corresponding author upon request.

Conflicts of Interest

The authors declare that there are no conflicts of interest regarding the publication of this article.

Acknowledgments

This work was supported by the National Key Research and Development Program of China (No. 2017YFC1501100), National Natural Science Foundation of China (No. 12072102), Fundamental Research Funds for the Central Universities (No. B200203085), Postgraduate Research & Practice Innovation Program of Jiangsu Province (No. KYCX20_0440), China Postdoctoral Science Foundation (No. 2021M690047), and Scientific and Technological Innovation Projects for Overseas Scholars in Nanjing (B2004806). The authors also thank the support of the Six Talent Peaks Project in Jiangsu Province and the Program to Cultivate Middle-Aged and Young Science Leaders of Colleges and Universities of Jiangsu Province, China.

References

- [1] J. F. Shao, K. T. Chau, and X. T. Feng, "Modeling of anisotropic damage and creep deformation in brittle rocks," *International Journal of Rock Mechanics and Mining Sciences*, vol. 43, no. 4, pp. 582–592, 2006.
- [2] C.-H. Chen, C.-S. Chen, and J.-H. Wu, "Fracture toughness analysis on cracked ring disks of anisotropic rock," *Rock Mechanics and Rock Engineering*, vol. 41, no. 4, pp. 539–562, 2008.
- [3] K. Wu and J. E. Olson, "Simultaneous multifracture treatments: fully coupled fluid flow and fracture mechanics for

- horizontal,” *Journal of Petroleum Science and Engineering*, vol. 147, pp. 788–800, 2016.
- [4] A. A. Griffith, “The phenomena of rupture and flow in solids,” *Philosophical Transactions of the Royal Society of London. Series A, Containing Papers of a Mathematical or Physical Character (1896–1934)*, vol. 221, pp. 582–593, 1921.
 - [5] N. Moës, J. Dolbow, and T. Belytschko, “A finite element method for crack growth without remeshing,” *International Journal for Numerical Methods in Engineering*, vol. 46, no. 1, pp. 131–150, 1999.
 - [6] T. Belytschko, R. Gracie, and G. Ventura, “A review of extended/generalized finite element methods for material modelling,” *Modelling and Simulation in Materials Science and Engineering*, vol. 17, no. 4, 2009.
 - [7] T. Rabczuk and T. Belytschko, “A three-dimensional large deformation meshfree method for arbitrary evolving cracks,” *Computer Methods in Applied Mechanics and Engineering*, vol. 196, no. 29–30, pp. 2777–2799, 2007.
 - [8] T. Rabczuk and T. Belytschko, “Cracking particles: a simplified meshfree method for arbitrary evolving cracks,” *International Journal for Numerical Methods in Engineering*, vol. 61, no. 13, pp. 2316–2343, 2004.
 - [9] T. Rabczuk, G. Zi, S. Bordas, and H. Nguyen-Xuan, “A simple and robust three-dimensional cracking-particle method without enrichment,” *Computer Methods in Applied Mechanics and Engineering*, vol. 199, no. 37–40, pp. 2437–2455, 2010.
 - [10] R. d. Borst, J. J. C. Remmers, A. Needleman, and M.-A. Abellan, “Discrete vs. smeared crack models for concrete fracture: bridging the gap,” *International Journal for Numerical and Analytical Methods in Geomechanics*, vol. 28, no. 78, pp. 583–607, 2004.
 - [11] H. Mirzabozorg and M. Ghaemian, “Non-linear behavior of mass concrete in three-dimensional problems using a smeared crack approach,” *Earthquake Engineering & Structural Dynamics*, vol. 34, no. 3, pp. 247–269, 2005.
 - [12] G. A. Francfort and J.-J. Marigo, “Revisiting brittle fracture as an energy minimization problem,” *Journal of the Mechanics and Physics of Solids*, vol. 46, no. 8, pp. 1319–1342, 1998.
 - [13] B. Bourdin, G. A. Francfort, and J.-J. Marigo, “Numerical experiments in revisited brittle fracture,” *Journal of the Mechanics and Physics of Solids*, vol. 48, no. 4, pp. 797–826, 2000.
 - [14] B. Bourdin, G. A. Francfort, and J. J. Marigo, “The variational approach to fracture,” *Journal of Elasticity*, vol. 91, no. 1–3, pp. 5–148, 2008.
 - [15] M. J. Borden, C. V. Verhoosel, M. A. Scott, T. J. R. Hughes, and C. M. Landis, “A phase-field description of dynamic brittle fracture,” *Computer Methods in Applied Mechanics and Engineering*, vol. 217–220, pp. 77–95, 2012.
 - [16] C. Miehe, F. Welschinger, and M. Hofacker, “Thermodynamically consistent phase-field models of fracture: variational principles and multi-field FE implementations,” *International Journal for Numerical Methods in Engineering*, vol. 83, no. 10, pp. 1273–1311, 2010.
 - [17] C. Miehe, M. Hofacker, and F. Welschinger, “A phase-field model for rate-independent crack propagation: robust algorithmic implementation based on operator splits,” *Computer Methods in Applied Mechanics and Engineering*, vol. 199, no. 45–48, pp. 2765–2778, 2010.
 - [18] M. J. Borden, T. J. R. Hughes, C. M. Landis, and C. V. Verhoosel, “A higher-order phase-field model for brittle fracture: formulation and analysis within the isogeometric analysis framework,” *Computer Methods in Applied Mechanics and Engineering*, vol. 273, pp. 100–118, 2014.
 - [19] M. A. Msekh, J. M. Sargado, M. Jamshidian, P. M. Areias, and T. Rabczuk, “Abaqus implementation of phase-field model for brittle fracture,” *Computational Materials Science*, vol. 96, pp. 472–484, 2015.
 - [20] T. Gerasimov and L. De Lorenzis, “A line search assisted monolithic approach for phase-field computing of brittle fracture,” *Computer Methods in Applied Mechanics and Engineering*, vol. 312, pp. 276–303, 2016.
 - [21] S. Goswami, C. Anitescu, S. Chakraborty, and T. Rabczuk, “Transfer learning enhanced physics informed neural network for phase-field modeling of fracture,” *Theoretical and Applied Fracture Mechanics*, vol. 106, Article ID 102447, 2020.
 - [22] H. L. Ren, X. Y. Zhuang, C. Anitescu, and T. Rabczuk, “An explicit phase-field method for brittle dynamic fracture,” *Computers & Structures*, vol. 217, pp. 45–56, 2019.
 - [23] P. Areias, T. Rabczuk, and M. A. Msekh, “Phase-field analysis of finite-strain plates and shells including element subdivision,” *Computer Methods in Applied Mechanics and Engineering*, vol. 312, pp. 322–350, 2016.
 - [24] W. J. Li and Q. Z. Zhu, “Fully meshfree numerical analysis of nonlocal damage in voxel-based material models from microtomography,” *International Journal of Solids and Structures*, vol. 222–223, Article ID 111021, 2021.
 - [25] T. T. Nguyen, J. Yvonnet, M. Bornert, and C. Chateau, “Initiation and propagation of complex 3D networks of cracks in heterogeneous quasi-brittle materials: direct comparison between in situ testing-microCT experiments and phase-field simulations,” *Journal of the Mechanics and Physics of Solids*, vol. 95, pp. 320–350, 2016.
 - [26] T. Wick, “Modified Newton methods for solving fully monolithic phase-field quasi-static brittle fracture propagation,” *Computer Methods in Applied Mechanics and Engineering*, vol. 325, pp. 577–611, 2017.
 - [27] M. Ambati, T. Gerasimov, and L. De Lorenzis, “Phase-field modeling of ductile fracture,” *Computational Mechanics*, vol. 55, no. 5, pp. 1017–1040, 2015.
 - [28] M. J. Borden, T. J. R. Hughes, C. M. Landis, A. Anvari, and I. J. Lee, “A phase-field formulation for fracture in ductile materials: finite deformation balance law derivation, plastic degradation, and stress triaxiality effects,” *Computer Methods in Applied Mechanics and Engineering*, vol. 312, pp. 130–166, 2016.
 - [29] C. Miehe, F. Aldakheel, and A. Raina, “Phase field modeling of ductile fracture at finite strains: a variational gradient-extended plasticity-damage theory,” *International Journal of Plasticity*, vol. 84, pp. 1–32, 2016.
 - [30] T. You, Q.-Z. Zhu, P.-F. Li, and J.-F. Shao, “Incorporation of tension-compression asymmetry into plastic damage phase-field modeling of quasi brittle geomaterials,” *International Journal of Plasticity*, vol. 124, pp. 71–95, 2020.
 - [31] V. P. Nguyen and J.-Y. Wu, “Modeling dynamic fracture of solids with a phase-field regularized cohesive zone model,” *Computer Methods in Applied Mechanics and Engineering*, vol. 340, pp. 1000–1022, 2018.
 - [32] C. Miehe and S. Mauthe, “Phase field modeling of fracture in multi-physics problems. Part III. Crack driving forces in hydro-poro-elasticity and hydraulic fracturing of fluid-saturated porous media,” *Computer Methods in Applied Mechanics and Engineering*, vol. 304, pp. 619–655, 2016.
 - [33] S. Zhou, X. Zhuang, and T. Rabczuk, “Phase-field modeling of fluid-driven dynamic cracking in porous media,” *Computer Methods in Applied Mechanics and Engineering*, vol. 350, pp. 169–198, 2019.

- [34] A. Chambolle, G. A. Francfort, and J.-J. Marigo, "When and how do cracks propagate?" *Journal of the Mechanics and Physics of Solids*, vol. 57, no. 9, pp. 1614–1622, 2009.
- [35] A. Bobet and H. H. Einstein, "Fracture coalescence in rock-type materials under uniaxial and biaxial compression," *International Journal of Rock Mechanics and Mining Sciences*, vol. 35, no. 7, pp. 863–888, 1998.
- [36] L. N. Y. Wong and H. H. Einstein, "Systematic evaluation of cracking behavior in specimens containing single flaws under uniaxial compression," *International Journal of Rock Mechanics and Mining Sciences*, vol. 46, no. 2, pp. 239–249, 2009.
- [37] B. Shen and O. Stephansson, "Modification of the G-criterion for crack propagation subjected to compression," *Engineering Fracture Mechanics*, vol. 47, no. 2, pp. 177–189, 1994.
- [38] G. Lancioni and G. Royer-Carfagni, "The variational approach to fracture mechanics. A practical application to the French Panthéon in Paris," *Journal of elasticity*, vol. 95, no. 1-2, pp. 1–30, 2009.
- [39] N. Moës and T. Belytschko, "Extended finite element method for cohesive crack growth," *Engineering fracture mechanics*, vol. 69, no. 7, pp. 813–833, 2002.
- [40] H. Amor, J.-J. Marigo, and C. Maurini, "Regularized formulation of the variational brittle fracture with unilateral contact: Numerical experiments," *Journal of the Mechanics and Physics of Solids*, vol. 57, no. 8, pp. 1209–1229, 2009.
- [41] M. Ambati, T. Gerasimov, and L. De Lorenzis, "A review on phase-field models of brittle fracture and a new fast hybrid formulation," *Computational Mechanics*, vol. 55, no. 2, pp. 383–405, 2015.
- [42] J.-Y. Wu, "A unified phase-field theory for the mechanics of damage and quasi-brittle failure," *Journal of the Mechanics and Physics of Solids*, vol. 103, pp. 72–99, 2017.
- [43] Y. J. Cao, W. Q. Shen, J. F. Shao, and W. Wang, "A novel FFT-based phase-field model for damage and cracking behavior of heterogeneous materials," *International Journal of Plasticity*, vol. 133, p. 102786, 2020.
- [44] R. Alessi, J.-J. Marigo, and S. Vidoli, "Gradient damage models coupled with plasticity: variational formulation and main properties," *Mechanics of Materials*, vol. 80, pp. 351–367, 2015.
- [45] C. Miehe and L.-M. Schänzel, "Phase field modeling of fracture in rubbery polymers. Part I: finite elasticity coupled with brittle failure," *Journal of the Mechanics and Physics of Solids*, vol. 65, pp. 93–113, 2014.
- [46] G. Molnár and A. Gravouil, "2D and 3D abaqus implementation of a robust staggered phase-field solution for modeling brittle fracture," *Finite Elements in Analysis and Design*, vol. 130, pp. 27–38, 2017.
- [47] P. C. Perdikaris and A. Romeo, "Size effect on fracture energy of concrete and stability issues in three-point bending fracture toughness testing," *Materials Journal*, vol. 92, no. 5, pp. 483–496, 1995.
- [48] Z. P. Bazant and J. Planas, *Fracture and Size Effect in Concrete and Other Quasibrittle Materials*, CRC Press, Boca Raton, FL, USA, 1997.
- [49] B. J. Winkler, *Traglastuntersuchungen von Unbewehrten und Bewehrten Betonstrukturen auf der Grundlage eines Objektiven Werkstoffgesetzes für Beton*, Innsbruck University Press, Innsbruck, Austria, 2001.
- [50] J. Y. Wu, V. P. Nguyen, and C. T. Nguyen, "Phase field modeling of fracture," *Advances in Applied Mechanics: Multi-Scale Theory and Computation*, vol. 52, 2018.
- [51] J. F. Unger, S. Eckardt, and C. Könke, "Modelling of cohesive crack growth in concrete structures with the extended finite element method," *Computer Methods in Applied Mechanics and Engineering*, vol. 196, no. 41–44, pp. 4087–4100, 2007.
- [52] X. Zhang, S. W. Sloan, C. Vignes, and D. Sheng, "A modification of the phase-field model for mixed mode crack propagation in rock-like materials," *Computer Methods in Applied Mechanics and Engineering*, vol. 322, pp. 123–136, 2017.
- [53] K. M. Hamdia, M. Silani, X. Zhuang, P. He, and T. Rabczuk, "Stochastic analysis of the fracture toughness of polymeric nanoparticle composites using polynomial chaos expansions," *International Journal of Fracture*, vol. 206, no. 2, pp. 215–227, 2017.

Research Article

Seismic Performance and Risk Assessment of Traditional Brick-Wood Rural Buildings Based on Numerical Simulation

Baokui Chen , **Li Fan**, **Jingang Xiong**, **Ming Wen**, and **Yaru Liu**

School of Civil Engineering and Architecture, Nanchang University, Nanchang 33031, China

Correspondence should be addressed to Baokui Chen; baokui_2000@163.com

Received 22 April 2021; Revised 31 May 2021; Accepted 16 June 2021; Published 19 July 2021

Academic Editor: Meng Gao

Copyright © 2021 Baokui Chen et al. This is an open access article distributed under the Creative Commons Attribution License, which permits unrestricted use, distribution, and reproduction in any medium, provided the original work is properly cited.

The recent earthquakes have caused serious damage to Chinese rural houses. Research on the seismic performance and reinforcement for traditional rural houses is strongly needed. In this study, the seismic performance of traditional brick-wood structural houses in Jiangxi province and surrounding areas is analyzed and confirmed by site investigation and numerical simulation. And, the traditional constructions, such as the purlin roof and the cavity wall, are considered. These construction types can reduce the seismic behavior of rural houses, and limited research has been carried out. This study found that the structure will produce plastic deformation and local damage above 6-degree earthquake fortification action. The damage positions occurred in the walls close to purlins and the walls close to doors and windows. Given the above seismic safety problems, a reinforcement method of reinforced cement mortar strip and mesh surface is proposed, which is suitable for engineering applications for traditional rural houses. The seismic strengthening effect is analyzed by numerical simulation. Comparing the calculation results, it is found that the seismic performance of the structure after reinforcement is significantly enhanced, and the stress concentration of the walls is improved.

1. Introduction

Currently, there are many problems in rural buildings in China, such as unreasonable structural design and non-standard construction. There is a great earthquake risk due to a lack of corresponding seismic design code for rural houses. Different from urban buildings, the structural types of traditional rural buildings have obvious regional characteristics and unique styles. The seismic performance and safety problems of rural houses from the different areas are distinct. Therefore, the research on seismic performance of regional rural buildings and the seismic reinforcement methods of existing rural houses need to be supplemented urgently.

At the same time, it was found that the unreinforced masonry structure could not withstand the test of large earthquakes through the damage to the Xingtai earthquake in 1966, the Tangshan earthquake in 1976, and the Wenchuan earthquake in 2008. In particular, the self-built masonry structured houses in rural areas were seriously

damaged. For example, the walls of rural masonry buildings in the Wenchuan earthquake cracked a lot and even partially collapsed [1]. In the 8-degree area, most of the old rural houses were damaged, and some collapsed. Above the 6-degree area, most of the rural masonry buildings were seriously damaged or collapsed [2]. However, for areas with low fortification intensity and lack of seismic fortification awareness and measures, even under the action of medium and small earthquakes, the traditional rural buildings will be seriously damaged. For example, in 2005, regarding the Jiujiang earthquake with Ms5.7, the traditional brick-wood structured houses were severely damaged, with a damage ratio of 48.61% and a medium damage ratio of 26.22%, which was the highest among all kinds of buildings [3]. The traditional brick-wood structured farmhouse is also the main research object of this paper.

At present, the research on seismic performance of masonry structures of China mainly focused on three types of structures, namely, reinforced masonry structure, restrained masonry structure, and reinforced masonry

structure. Based on the earthquake damage analysis of the Tangshan earthquake, it is generally recognized that the structure of reinforced concrete rang beams and structural columns can effectively increase the deformation capacity of brick masonry buildings, make use of deformation energy, and enhance the seismic capacity of brick buildings, especially the collapse resistant capacity [4]. Based on the restrained masonry structure, researchers also put forward the reinforced masonry structure, and it has been proven by relevant tests [5] that the reinforced masonry has good seismic performance with high strength and strong deformation capacity. The form of masonry structured abroad is quite different from that in China. The main masonry structure is concrete or clay block, and the masonry method is mostly reinforced masonry structure [6–9].

The studies on masonry structure reinforcement methods mainly focus on the reinforcement of masonry walls, including experimental studies on traditional material reinforcement methods, such as adding ring beam to structural column, reinforced by steel bar-mortar [10] and reinforced by steel bar-mortar crossed strip method [11]. Moreover, in recent years, some new material reinforcement methods have been put forward, such as composite fiber sheet reinforcement method [12], high-performance composite mortar with steel mesh strip reinforcement method [13], high ductility fiber reinforced concrete surface layer reinforcement method [14], high strength wire cable mesh and polymeric mortar reinforcement method [15], and high ductility concrete reinforcement structure column restraint method [16]. Generally speaking, there are mature theories about seismic reinforcement of masonry structures, but there is little research on seismic reinforcement of traditional masonry structure buildings in specific areas.

Nowadays, numerical simulation technology has become the main method of structural seismic research. Dynamic analysis of masonry structured models in some cities and towns has been published. Ge et al. [17] used ABAQUS to analyze the seismic performance and collapse risk of old masonry buildings before and after reinforcement. Sun and Deng [18] analyzed the seismic behavior of bottom frame structure building. Hua et al. [19] and Wu et al. [20] analyzed the seismic performance and dynamic characteristics of rural brick-concrete structure buildings. Yu et al. [21] analyzed the effect of masonry strength on seismic performance of self-built dwellings through shaking table tests and numerical simulation method. Zhou et al. [22] analyzed the seismic performance of existing rural masonry buildings. Zhao et al. [23] tried to analyze the seismic vulnerability of rural buildings. The above results are mainly aimed at brick-concrete structured houses, but there are few studies on traditional brick-wood structured houses. Yao et al. [24] conducted seismic elastic-plastic analysis of brick-wood structured farmhouse, found that the strength of mortar has an important impact on the seismic capacity of the structure, and gave the weak spots of the structure. This study mainly focuses on low-rise rural houses in north China, whose structure is different from brick-wood structures in south China, and the cavity wall is not considered.

In summary, to master the seismic safety of traditional brick-wood structured buildings in Jiangxi Province and surrounding areas and cooperate with the national poverty alleviation and rural dilapidated houses reconstruction, this paper, combined with a large number of research studies and finite element numerical analysis, determined the seismic performance and seismic weak spots of this kind of structure and put forward the seismic reinforcement method suitable for this kind of buildings in this region. The seismic performance of the brick-wood structured model before and after reinforcement is compared to further verify the reinforcement effect.

2. Seismic Performance of Existing Brick-Wood Rural Structures in South China

The brick-wood rural buildings in Jiangxi were mostly built in the 1970s and 1980s. They are made of ordinary fire brick and built with lime mortar. The thickness of the exterior wall is generally 240 mm, and the interior wall is 120–240 mm. They are generally cavity walls, and there is a mixed-use of fire brick and adobe brick. The wall is high, without a ring beam and structure column. The purlin roof is usually of a double slope structure and consists of small green tiles or glazed tiles.

The survey found that the traditional brick-wood rural buildings in Jiangxi are highly seismic risk, and many safety problems are not conducive to earthquake resistance. First of all, due to the large bay and height of the frame, the bearing walls are generally cavity walls, which causes the load-carrying capacity and stability of the walls to decrease, and the walls are prone to cracking and skewing, which is not conducive to earthquake resistance, as shown in Figure 1. Secondly, there are many masonry quality problems of brick-wood rural buildings, such as the fact that the vertical and horizontal walls are not firmly overlapped, have inadequate mortar, and have mixed masonry of brick masonry and adobe brick (as seen in Figure 2). Thirdly, due to the high wall and unreasonable set of door and window openings, lintels or brick arched lintels are generally not set, resulting in cracks in the wall near the opening, as shown in Figure 3. In addition, the hard mountain purlin structure used in the roof has weak horizontal restraint ability to the house, and the timber purlin and the wall are not firmly connected and cannot form cooperative work between each other (as shown in Figure 4). Under the action of an earthquake, local damage is easy to occur, resulting in an overall collapse of the wall.

Moreover, such buildings have been built for a long time, the materials may be eroded and aged, and most of the existing buildings are still used for living. Therefore, the seismic risk of this kind of buildings is high, and it is easy to cause the loss of family property and even casualties under the action of an earthquake. So, it is urgent to quantify the seismic risk of the building and do seismic reinforcement.



FIGURE 1: Wall cracks.



FIGURE 2: Mixed masonry method.



FIGURE 3: Crack in the wall between the windows.

3. Seismic Performance of Brick-Wood Rural Buildings

Different from urban buildings, rural houses in China are basically constructed by farmers themselves based on traditional crafts in China, not designed and constructed according to architectural norms. Since there are a large number of self-built bricks and wood houses in rural China,

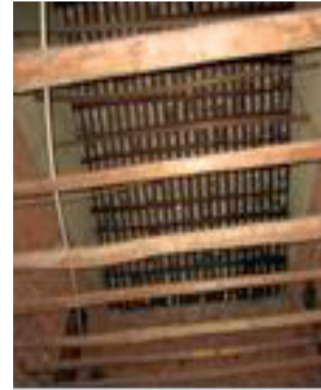


FIGURE 4: Roof truss structure.

these houses often lack the necessary seismic design. Therefore, this paper studies the specific seismic defects of these houses, which proves that this paper has good engineering application value. In addition, the study selected building examples of a household still living in Shangli County, Jiangxi Province. The converted house is a typical brick and wood structured house in the region. The research group has made reinforcement design and field construction with this building as an engineering example.

By using the finite element analysis software ADINA, a refined seismic response analysis model of buildings considering the structure of cavity wall and purlin roof is established. Firstly, through modal analysis, compare the natural vibration period calculated by the finite element model and the empirical formula to verify the rationality of the model. Then, through seismic response analysis, the seismic safety and seismic weak points of the structure under the earthquake action of 6 and 7 degrees are quantified.

3.1. Model Introduction. In this study, a numerical model is established by taking the traditional brick-wood rural buildings in Jiangxi Province as an example. The structure is a 2-story, 3-bay, and 4-room house. The story height is 3.6 m, there is no floor between the stories (it belongs to the common structure of brick-wood rural buildings in Jiangxi Province and surrounding areas), and the cavity wall thickness is 240 mm. The purlin roof is directly laid on the horizontal wall. The purlin diameter is 200 mm, without ring beam and structural column, and the model building design drawing is shown in Figure 5.

3.2. Model Simplification and Parameters. In this paper, the bearing brick wall adopts the overall modelling method to establish the finite element model of the brick-wood structure. In addition, through the equivalent method, the thickness of the model wall is adjusted to 190 mm to ensure the rationality of the cavity wall modelling, so that the model has the same dynamic characteristics as the original structure and meets the needs of dynamic analysis.

Masonry adopts the masonry constitutive relation expression put forward by Professor Liu [25] of Hunan University, which is shown in formula (1). According to the

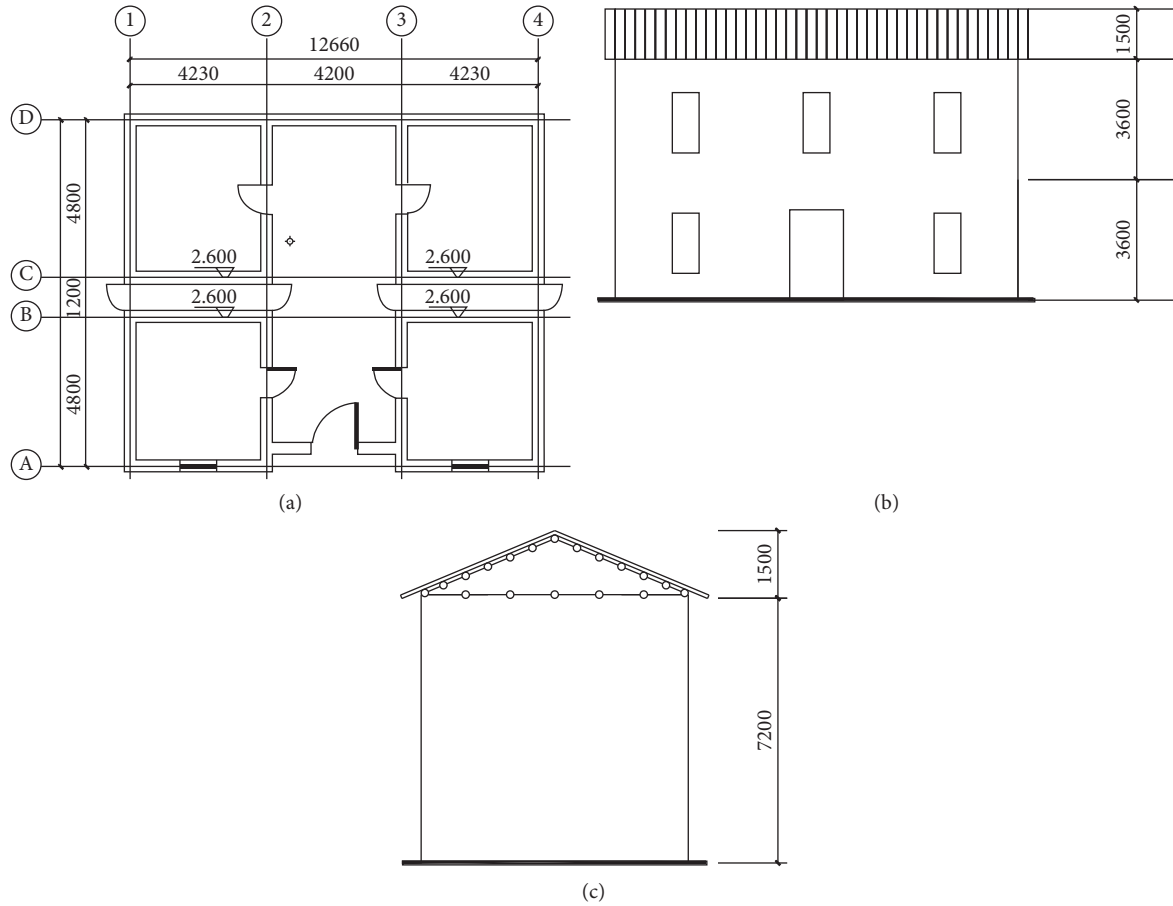


FIGURE 5: Architectural diagram of brick-wood structural house. (a) Layout plan of an engineering project. (b) Front elevation layout. (c) Model side elevation layout.

code for the design of masonry structures and related literature [26], the basic parameters of masonry materials can be calculated, as shown in Table 1.

$$\frac{\sigma_c}{f_m} = \begin{cases} 1.96 \frac{\varepsilon}{\varepsilon_0} - 0.96 \left(\frac{\varepsilon}{\varepsilon_0} \right)^2, & \frac{\varepsilon}{\varepsilon_0} \leq 1, \\ 1.2 - 0.2 \frac{\varepsilon}{\varepsilon_0}, & 1 \leq \frac{\varepsilon}{\varepsilon_0} \leq 1.6, \end{cases} \quad (1)$$

where σ_c and ε are the compressive stress and strain of masonry and f_m and ε_0 are the average axial compressive strength of masonry and their corresponding strain values.

As a natural growth material, the mechanical properties of the wood show obvious anisotropy. At the same time, affected by many factors such as growth environment and varieties, the performance varies greatly. Therefore, this paper adopts the mechanical properties of wood under the general ideal state. According to the relevant literature [27], the basic parameters of timber purlin material are listed in Table 2.

In the table, EL, ER, and ET are, respectively, the elastic modulus (MPa) of the timber purlins parallel to the grain, transverse grain tangential, and transverse grain radial; μ_{TL} , μ_{RT} , and μ_{LR} are, respectively, the Poisson ratios (MPa) of

TABLE 1: Basic parameters of masonry materials.

Elastic modulus (MPa)	Poisson ratio	Density (kg/m^3)
2218	0.15	2000

TABLE 2: Basic parameters of timber purlin material.

EL	ER	ET	μ_{TL}	μ_{RT}	μ_{LR}	GLR	GRT	GTL
1955	9702	1955	0.52	0.352	0.106	971	218	609

the timber purlin's parallel to grain radial, transverse grain tangential, and transverse grain radial; GLR, GRT, and GTL are, respectively, the shear modulus (MPa) of the timber purlin's longitudinal and tangential, radial and longitudinal, and tangential and radial.

3.3. *Seismic Waves.* Earthquake has great randomness. Under different seismic wave actions, the actual responses of the structure have obvious difference, so the seismic wave should be selected reasonably for analysis. The selection of seismic wave is mainly based on factors such as peak acceleration, duration, spectrum characteristics, and site conditions. The selected period of seismic wave should be close to the site characteristic period. At the same time, the

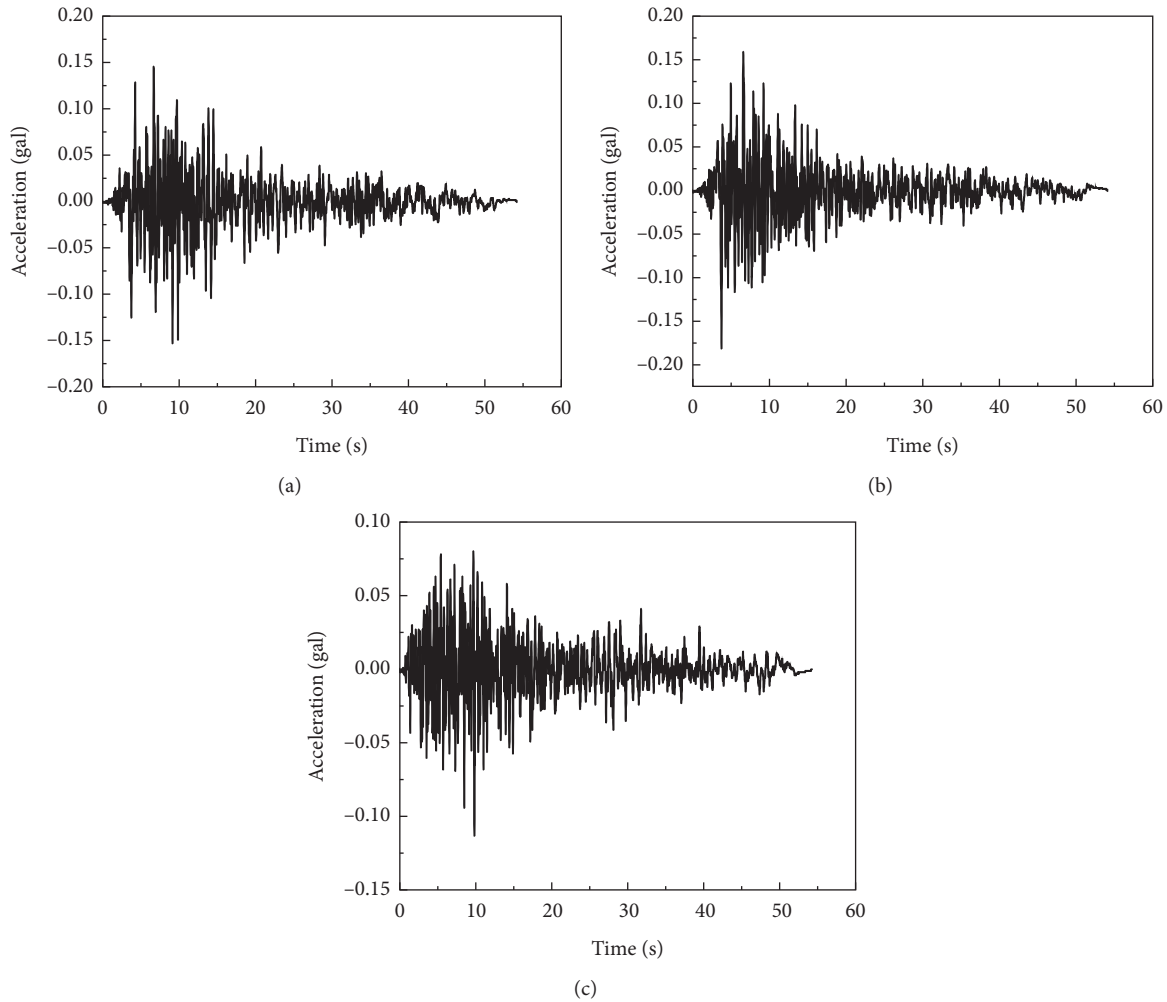


FIGURE 6: Taft wave source record. (a) X-direction. (b) Y-direction. (c) Z-direction.

reasonable duration of seismic wave is easy to cause the structure to be damaged by plastic deformation accumulation, so as to achieve the purpose of analysis. In addition, when the peak acceleration of the original seismic wave does not meet the requirements of the relevant codes or analysis needs, the seismic wave size should be adjusted proportionally.

In this paper, the site classification of brick-wood structure is class II, the classification of design earthquake is the first group, and seismic fortification intensity is 6 (7) degrees (only some areas in Jiangxi Province have seismic fortification intensity of 7 degrees). According to the above conditions, the Taft wave, EL-Centro wave, and Loma Prieta seismic wave are selected in this paper. Each seismic wave is intercepted at 12 s, the seismic wave is calculated according to the peak acceleration of 6 and 7 degrees, and the original acceleration record of Taft wave is shown in Figure 6.

The so-called “standard” in the standard seismic wave means that its response spectrum is more consistent with the code design spectrum or the “average spectrum” of multiple earthquakes. Therefore, it has many applications in the field of earthquake engineering. Among them, the spectra of EL-Centro wave and Taft wave combined with the “average

spectrum” are similar. Take the EL-Centro wave as an example and compare it with the average spectrum of 20 earthquakes as shown in Figure 7: comparison of EL-Centro wave and average spectrum of 20 earthquakes.

3.4. Numerical Results

3.4.1. Modal Analysis. Through modal analysis, the first 6 natural vibration periods of the structure are obtained, as shown in Table 3.

Yang et al. [28] put forward the empirical formula of the basic period of masonry structure, and the formula is as follows:

$$T_1 = 0.0168(H_0 + 1.2), \quad (2)$$

where T_1 is the basic period and H_0 is the height of the structure. According to empirical formula (2), $T_1 = 0.0168 \times (7.2 + 1.2) = 0.141$ s, which is close to the numerical simulation results with an error of less than 5%, proving that the brick-wood structure model is reasonable.

Different from other structures [29, 30], the shaking table tests of the brick-wood structured houses studied in

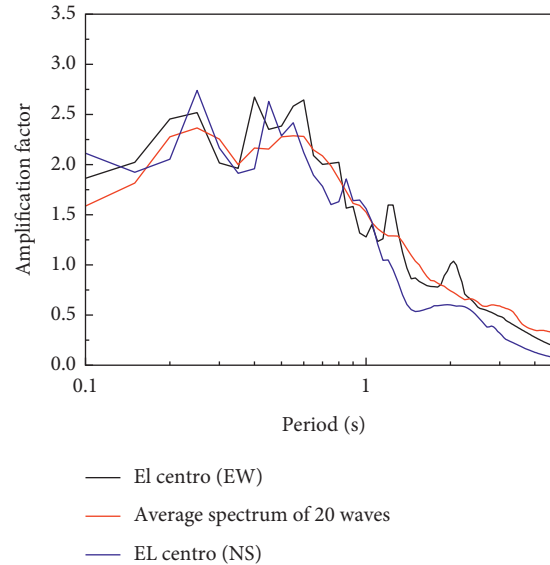


FIGURE 7: Comparison of the EL-Centro seismic response spectrum and the average spectrum of 20 seismic waves on medium-hard soil sites.

TABLE 3: The first 6 natural vibration periods of brick-wood structure.

Vibration	1	2	3	4	5	6
	order	order	order	order	order	order
Frequency (Hz)	7.285	8.029	8.382	8.656	8.876	8.929
Period (s)	0.137	0.125	0.119	0.1169	0.113	0.112

this research are relatively rare, and the numerical results in this study are compared with the theoretical solution of the natural vibration period of the masonry structure to verify the model.

3.4.2. Displacement Response. Under the action of an earthquake, the displacement response to each floor of the structure is shown in Figures 8–10. The failure degree of the masonry structure of this study takes the interval displacement angle as the evaluation standard, as shown in Table 4. Statistics of the displacement of each floor, the interval displacement angle, and the failure degree of brick-wood structured houses in the three earthquakes are shown in Table 5.

According to the structure displacement cloud diagram and the interval displacement angle statistics, it is found that under the action of an earthquake, the maximum displacement in the Y direction of the structure appears in the top of the gable, while the maximum displacement in the X-direction occurs in the top of the inner transverse wall and the opening of the second floor. In addition, the displacement response in the Y direction of the structure is significantly greater than that in the X-direction. Taking the Taft wave (0.2 g) as an example, the maximum displacement in the Y direction of the structure is 6.599 mm, the

maximum displacement in the X direction is 2.34 mm, and the maximum displacement in the Y direction is 2.82 times that in the X-direction. It can be seen that under the action of an earthquake, the purlin roof is not conducive to the seismic resistance of the structure, and the top of the gable is easy to generate a large displacement, and even cause local collapse.

The calculation results of the analysis model show that under the action of a 6-degree earthquake, the structure reached medium damage and the structure has reached serious damage under the action of a 7-degree earthquake. It can be seen that the seismic performance of brick-wood rural buildings is poor, which cannot resist the action of 6 and 7-degrees earthquakes.

At the same time, combined with the cloud diagram, it is found that the structure has a large displacement in the top of the gable, the opening and the top of the inner transverse wall, and it is the weak seismic position, which should be paid attention to as the key reinforcement location.

3.4.3. Stress Response. Under the earthquake loads, the statistics of the maximum shear stress of the wall bottom are shown in Table 6, and the cloud diagram of the maximum main tensile stress of the structure is shown in Figures 11–13.

According to the cloud diagram of the maximum main tensile stress of the structure and the statistics of the maximum shear stress of wall bottom, it can be seen that the main tensile stress of the wall has obvious stress concentration phenomenon in the top of the gable, the opening, the wall between windows, and the intersection of horizontal and vertical walls. The main tensile stress exceeds 0.23 MPa of the clay brick, indicating that the local wall has entered the plastic stage.

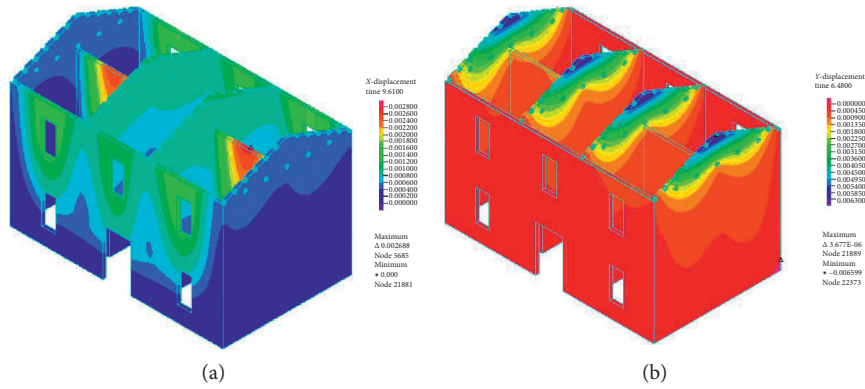


FIGURE 8: Cloud diagram of wall peak displacement under Taft earthquake with 7-degree fortification intensity. (a) X-direction. (b) Y-direction.

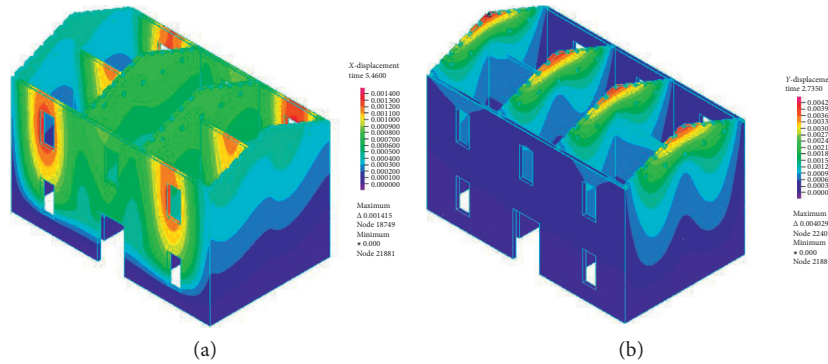


FIGURE 9: Cloud diagram of wall peak displacement under EL-Centro earthquake with 7-degree fortification intensity. (a) X-direction. (b) Y-direction.

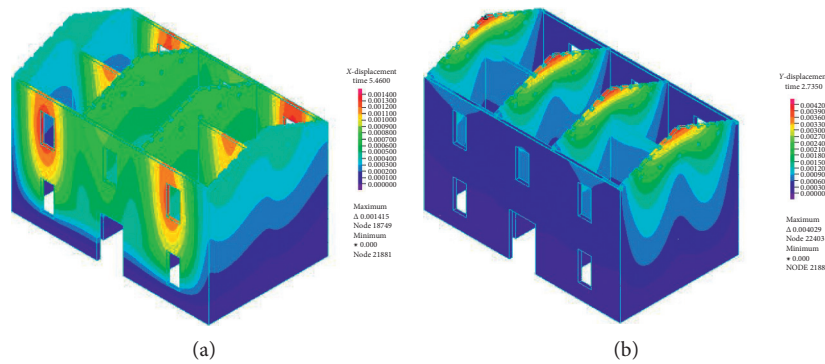


FIGURE 10: Cloud diagram of wall peak displacement under Loma Prieta earthquake with 7-degree fortification intensity. (a) X-direction. (b) Y-direction.

TABLE 4: Limiting values of interval displacement angle of masonry structure.

Seismic damage grade	Intact	Slight damage	Medium damage	Serious damage
Limiting values of the interval displacement angle	1/3000	1/2000	1/1100	1/350

TABLE 5: Structure maximum displacement (mm), maximum interval displacement angle, and failure degree.

Seismic waves	First-floor displacement	Second-floor displacement	Maximum interval displacement angle	Failure degree
Taft wave (0.1 g)	0.57	3.4	5.549×10^{-4}	Medium damage
Taft wave (0.2 g)	0.739	6.622	1.154×10^{-3}	Serious damage
EL-Centro wave (0.1 g)	0.733	3.63	5.68×10^{-4}	Medium damage
EL-Centro wave (0.2 g)	1.261	8.599	1.439×10^{-3}	Serious damage
Loma Prieta wave (0.1 g)	0.611	2.27	3.25×10^{-4}	Slight damage
Loma Prieta wave (0.2 g)	0.931	4.044	6.104×10^{-4}	Medium damage

TABLE 6: Maximum shear stress of wall bottom under each earthquake (Pa).

Seismic intensity	Taft wave	EL-Centro wave	Loma Prieta wave	Average
6 degree	182384	262260	229559	224734
7 degree	380692	468292	314878	387954

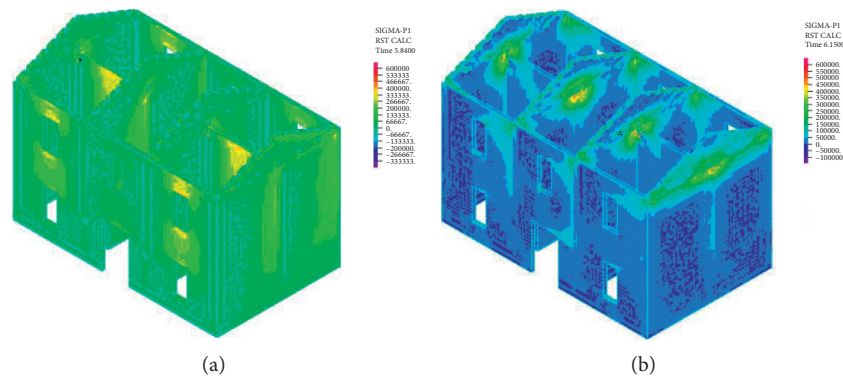


FIGURE 11: Cloud diagram of the maximum main tensile stress of the wall under Taft earthquake (0.2g). (a) X-direction. (b) Y-direction.

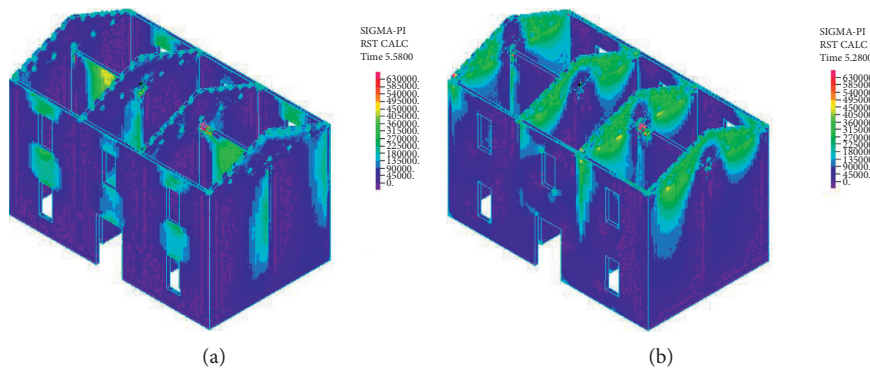


FIGURE 12: Cloud diagram of the maximum main tensile stress of the wall under EL-Centro earthquake (0.2g). (a) X-direction. (b) Y-direction.

Under the action of a 6-degree earthquake, the average shear stress of wall bottom is 0.225 MPa. And under the action of a 7-degree earthquake, the average shear stress of wall bottom is 0.388 MPa, which has greatly exceeded the shear strength of clay brick by 0.11 MPa, indicating that there is a risk of shear failure or even collapse of local walls.

4. Seismic Performance of Rural Buildings after Seismic Reinforcement

It is found that, under the action of 6-degree (0.1g) earthquake, the structure of brick-wood rural buildings in Jiangxi suffered medium damage. And under the action of 7-degree (0.2g) earthquake, the structure was seriously

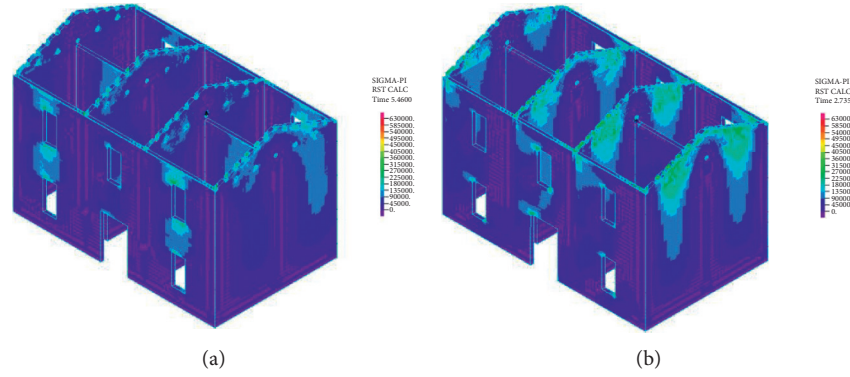


FIGURE 13: Cloud diagram of the maximum main tensile stress of the wall under the Loma Prieta earthquake (0.2 g). (a) X-direction. (b) Y-direction.

damaged. There is an obvious stress concentration phenomenon at locations, such as the intersection of horizontal and vertical walls, the opening, and the wall between windows, which are seismic weak spots. In a word, the seismic safety of the rural building is not enough to resist the strong earthquake load, which should add seismic reinforcement to improve the seismic performance of the rural house.

Most of the villages and towns in Jiangxi are distributed in mountainous areas, which are easy to use conventional materials and adopt simple construction methods to realize the reinforcement of rural houses. Therefore, referring to domestic and foreign research and the reinforcement methods that are easy to realize in local villages and towns [10, 11], the research proposes a reinforcement method of steel bar and wire mesh with cement mortar, adding steel mesh mortar surface layer on the outside of the house. Based on the needs of easy purchase and preparation of construction materials, cement mortar is used for the reinforcement of rural housing and add reinforced cement mortar strip at the junction of the vertical and horizontal walls of the external wall, the height of the first floor (3.6 m), and the eaves position to increase the integrity of the wall and improve the collapse ability of the house. By establishing the numerical model of the reinforced building, the effect of the reinforcement methods proposed in this paper is analyzed and compared.

The addition of reinforced mortar strips plays a role similar to ring beams and structural columns. It is an effective measure to strengthen the integrity of masonry buildings. It can restrain the development of cracks and greatly enhance the collapse resistance of the masonry walls. The house adopts the horizontal reinforced mortar belt as the ring beam at the elevation of the cornice (wall top), and the vertical reinforced mortar belt as the structural column at the junction of the vertical and horizontal walls of the outer wall of the house and the end of the wall.

The layout of the reinforced mortar belt is shown in Figure 14(a), and the mortar strength grade is M10. The

height of the horizontal reinforced mortar belt is 240 mm, the thickness is 50 mm, the reinforcement is 2 HRB300 steel bars with a diameter of 12 mm, and the spacing between the steel bars is 200 mm. The reinforcement of the horizontal reinforced mortar belt is shown in Figures 14(b)–14(e). The vertical reinforced mortar belt is arranged at the junction of the horizontal and vertical walls of the external wall and is mainly divided into “L-” and “T-” shaped vertical reinforced mortar belts. The “L-” shaped vertical reinforcement mortar belt uses two L-shaped wall-through steel wires to anchor the main reinforcement, and the “T-” shaped one uses U-shaped wall-through steel wires and in-line wall-through steel wires to anchor the main reinforcement (construction method: brick wall drilling, insert U Shaped steel wire, and bend and bind on another layer of the wall), the steel wire spacing is 500 mm, and the wire diameter is not less than 4 mm; see Figure 14(f) for details.

4.1. Structural Model after Reinforcement. In the reinforcement plan, the steel bars in the reinforced cement mortar are selected $\Phi 12$ steel bars and anchored through wall steel wires. The reinforced model and layout of steel bars are shown in Figure 15. In addition, the steel wire mesh mortar surface layer is modelled as a whole, and it is safe to use only the mortar layer material (without considering the parameters of steel wire mesh) for simulation.

4.2. Constitutive Relationship and Parameters of Reinforcement Materials. In this study, the constitutive relationship of cement mortar proposed by Du et al. [31] is selected, which is improved based on the concrete constitutive model and has passed the test verification. The constitutive relationship under compression is as follows (3):

$$y = \begin{cases} 2.1x - 1.2x^2 + 0.1x^3, & (x \leq 1), \\ \frac{x}{10(x-1)^2 + x}, & (x \geq 1), \end{cases} \quad (3)$$

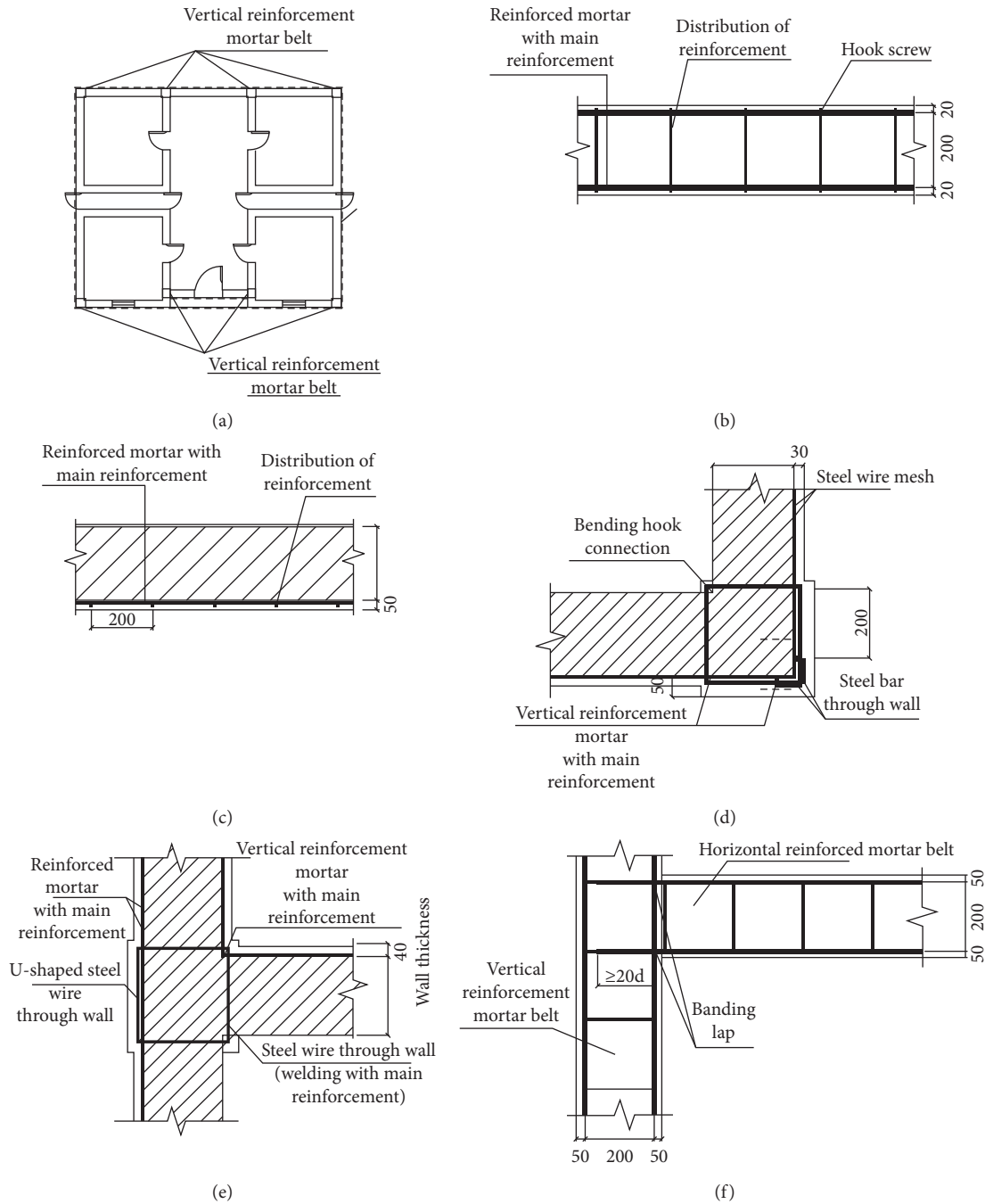


FIGURE 14: Schematic diagram of reinforced mortar belt. (a) Reinforced mortar belt layout drawing. (b) Brick masonry horizontal reinforcement mortar belt reinforcement map. (c) Sectional view of horizontally reinforced mortar belt of brick masonry. (d) Reinforcement diagram of “L”-shaped vertical reinforcement mortar belt. (e) Reinforcement diagram of “T”-shaped vertical reinforcement mortar with reinforcement. (f) Node diagram at the junction of vertically reinforced mortar belt and horizontally reinforced mortar belt.

where $x = \varepsilon/\varepsilon_m$, $y = \sigma/f_m$, ε and f are compressive stress and strain of cement, and f_m and ε_m are compressive strength and strain of cement mortar. Moreover, the Poisson ratio of cement mortar is 0.2, and the elastic modulus is calculated according to formula (4). The strength of the reinforced mortar is M10, which can be obtained by calculation. The material parameters of mortar are shown in Table 7.

$$E_m = 1057 f_2^{0.84}. \tag{4}$$

4.2.1. Constitutive Relationship of Steel Reinforcement. The ideal elastic-plastic constitutive relationship is adopted for steel reinforcement, and the material parameters are shown in Table 8.

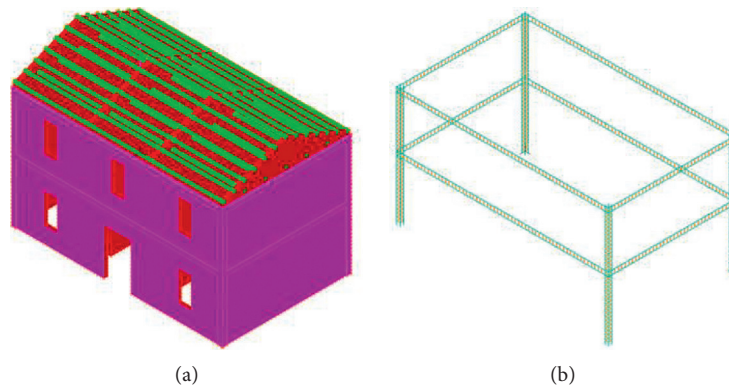


FIGURE 15: Numerical model of brick-wood structure after reinforcement. (a) House model. (b) Layout of steel bars.

TABLE 7: Material parameters of cement mortar.

Elastic modulus (MPa)	Poisson ratio	Density (kg/m ³)
7312	0.2	2000

TABLE 8: Steel material parameters.

Elastic modulus (MPa)	Poisson ratio	Yield strength (MPa)	Density (kg/m ³)
210000	0.3	300	7800

TABLE 9: The first 6 natural vibration periods.

Vibration	1 order	2 order	3 order	4 order	5 order	6 order
Frequency (Hz)	7.97	9.234	9.669	9.681	9.747	10.05
Period (s)	0.125	0.108	0.103	0.103	0.103	0.100

4.3. Numerical Results

4.3.1. *Modal Analysis of Reinforced Model.* Through modal analysis, the first 6 natural vibration periods of the structure are obtained, as shown in Table 9. And as shown in Figure 16, the comparison shows that the natural vibration period of each order of the model after reinforcement is smaller than that of the original model, which indicates that the stiffness of the model is significantly improved after reinforcement, and the integrity of the building is improved.

4.3.2. Displacement Response of the Reinforced Model.

Under the action of 6-degree and 7-degree earthquakes, the displacement response comparison of each layer before and after reinforcement is shown in Figures 17–19. Table 10 summarizes the maximum displacement, interval displacement angle, and damage degree of the reinforcement model under the action of an earthquake. The analysis found the following.

The maximum displacement of the structure after reinforcement is significantly reduced, which shows that the reinforcement method can effectively improve the seismic performance of the building and the displacement response of the structure under earthquake action.

According to the statistics of the interval displacement angle shown in Table 10, under the action of a 6-degree earthquake, the reinforced structure only suffered slight damage. Under the action of the 7-degree earthquake, the

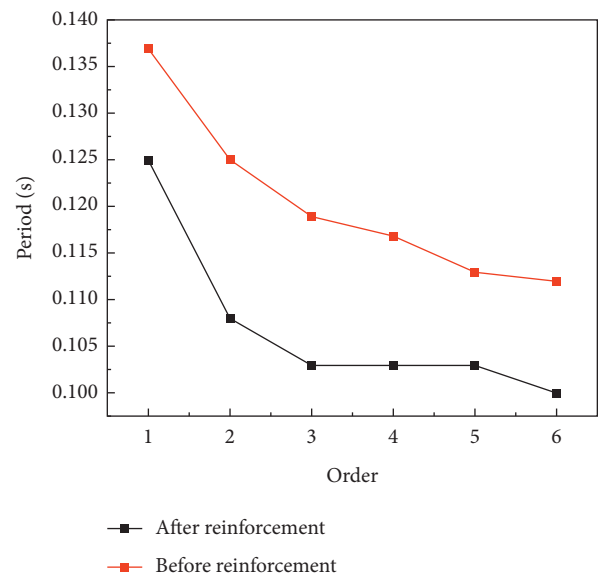


FIGURE 16: Comparison of natural vibration periods before and after reinforcement.

structure produces medium damage, which is significantly improved compared with the unreinforced structure. In the reinforced model, the maximum displacement still appears at the top of the gable. It can be seen that, under the action of an earthquake, due to the purlin roof structure, timber purlin and top of the gable are easy to be separated or collide, resulting in large displacement or damage. Therefore, in the reinforcement of the building, the wall should be added with other structures to

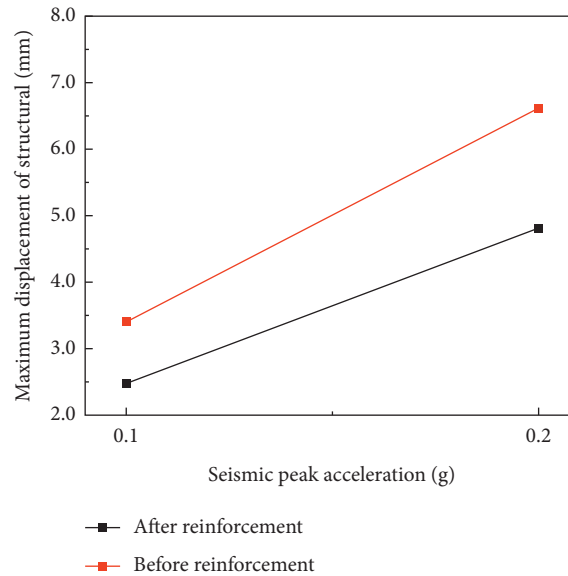


FIGURE 17: Comparison of the maximum displacement of the structure under Taft earthquake.

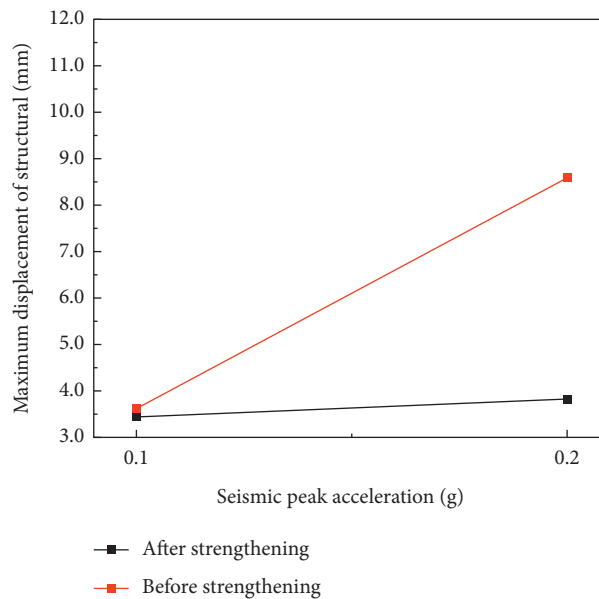


FIGURE 18: Comparison of the maximum displacement of the structure under EL-Centro earthquake.

strengthen the connection between the wall and the timber purlin, to form a whole, and to further improve the seismic performance of the house. In this model, the stable connection between the timber purlin and the wall is considered.

4.3.3. Stress Response of the Reinforced Model. Taking the stress response of the reinforced structure under the action of EL-Centro seismic wave as an example, the comparison of main tensile stress and shear stress before and after reinforcement is shown in Figures 20 and 21. It was found that, before reinforcement, there was an obvious stress

concentration in the wall near the opening and between the windows. After the reinforcement, the wall stress was significantly improved, and the shear stress of the gable and so on was greatly reduced.

Figure 22 shows the stress cloud diagram shared by the mortar layer and masonry structure after reinforcement. It can be found that, under the seismic action, the reinforced surface layer shares the main shear stress and the main tensile stress, which effectively improves the stress concentration at the opening and the intersection of horizontal and vertical walls. Adding reinforced mortar strips can also effectively improve the overall shear stress and local shear stress concentration of the wall.

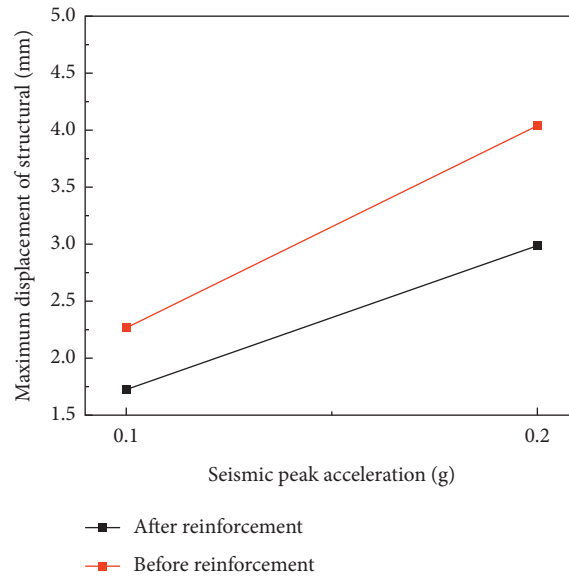


FIGURE 19: Comparison of the maximum displacement of the structure under the Loma Prieta earthquake.

TABLE 10: Maximum displacement (mm), maximum interval displacement angle, and failure degree of the structure after reinforcement.

Seismic wave	First-floor displacement	Second-floor displacement	Maximum interval displacement angle	Failure degree
Taft wave (0.1 g)	0.511	2.472	3.845×10^{-4}	Slight damage
Taft wave (0.2 g)	0.519	4.818	8.429×10^{-4}	Medium damage
EL-Centro (0.1 g)	0.594	3.459	5.618×10^{-4}	Medium damage
EL-Centro (0.2 g)	0.819	3.844	5.931×10^{-3}	Medium damage
Loma Prieta (0.1 g)	0.4393	1.726	2.523×10^{-4}	Slight damage
Loma Prieta (0.2 g)	0.770	2.990	4.353×10^{-4}	Slight damage

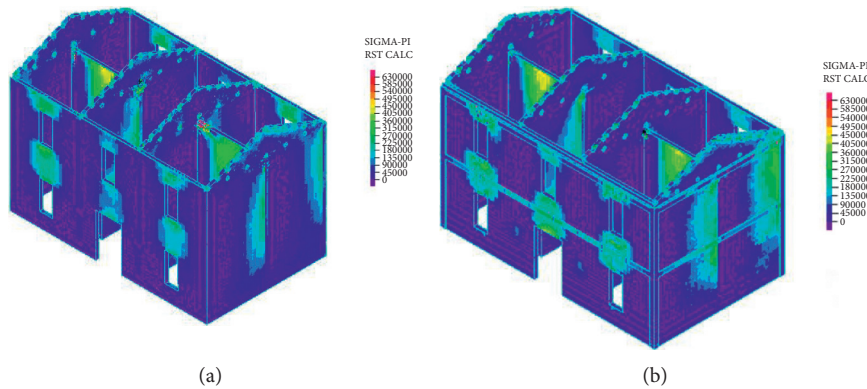


FIGURE 20: Comparison of main tensile stress of the structure before and after reinforcement. (a) Original structure (before reinforcement). (b) Structure after reinforcement.

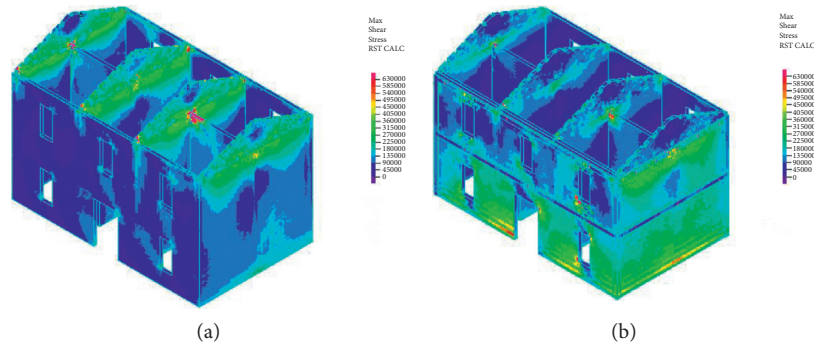


FIGURE 21: Comparison of shear stress of the structure before and after reinforcement. (a) Original structure. (b) Structure after reinforcement.

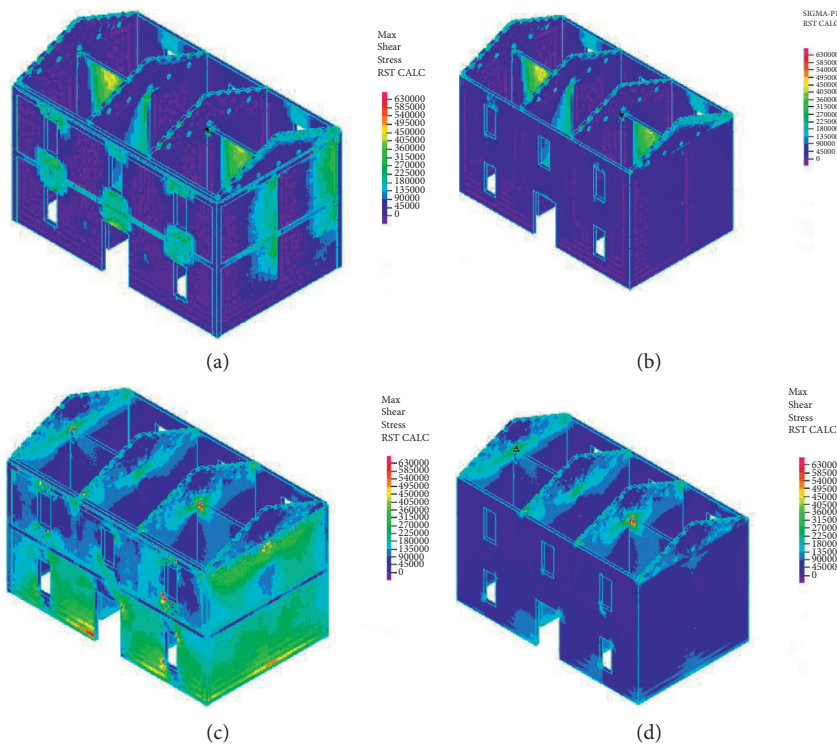


FIGURE 22: Comparison of stress cloud diagram between the mortar layer and masonry for structures after reinforcement. (a) Main tensile stress of mortar layer. (b) Main tensile stress of masonry. (c) Shear stress of mortar layer. (d) Shear stress of masonry.

5. Conclusion

Based on the earthquake investigation and numerical simulation, it is found that the seismic capacity of traditional brick-wood rural buildings in South China is insufficient. Under the earthquake action of 6-degree and 7-degree fortification intensity in China, the structures raise plastic deformation as the increase of the peak ground acceleration. The structure has medium damage under seismic load with 6-degree fortification intensity. The structure is seriously damaged under seismic load with 7-degree fortification intensity. Cracks often appeared at the contact position between timber purlin and gable, resulting in the maximum Y-direction displacement. This is mainly

due to the nonconnection of the traditional purlin roof structure, which is not conducive to the structural seismic resistance. In addition, the weak spots occurred in the opening of the wall, the wall between windows, the top of the inner transverse wall, and the junction of the transverse and longitudinal walls, and there is an obvious stress concentration phenomenon.

After reinforcement with a steel bar and wire mesh with cement mortar or other structures, the seismic response analysis shows that the structure displacement and stress response significantly reduced. Under the action of a 6-degree earthquake, the reinforcement model was only slightly damaged; under the action of a 7-degree earthquake, the reinforcement model has medium damage, and the damage generally occurs at

the contact position of the gable top with the timber purlin. This type of damage is mostly caused by the purlin roof structure. As far as the exterior wall is concerned, the original stress concentration position is transferred to the reinforced surface after reinforcement, and the damage mostly occurs in the reinforced surface. The overall stress and displacement of the wall are improved. At the same time, considering that the reinforcement effect of steel mesh has not been considered in the model, the simulation results tend to be conservative. Therefore, the reinforced buildings can ensure the safe use of the buildings under the action of 6- and 7-degree earthquakes.

Moreover, under the earthquake action, the stress concentration still exists in the junction of the inner and outer wall and the window and door holes after reinforcement. Therefore, these parts of the traditional brick-wood rural buildings should be regarded as the main objects for seismic reinforcement.

Data Availability

The data used to support the findings of this study are available from the corresponding author upon request.

Conflicts of Interest

The authors declare that there are no conflicts of interest regarding this study.

Acknowledgments

This work was financially supported by the National Science Foundation of China (Grant no. 51868048) and China Earthquake Administration Basic Research Project (Grant no. 2018D18).

References

- [1] L. I. Gang, X. Liu, and H. Li, "Seismic damage investigation and analysis on rural buildings in Wenchuan earthquake," *Journal of Dalian University of Technology*, vol. 49, no. 5, pp. 724–730, 2009.
- [2] G. Jia, Z. Yuan, X. Zhong, and K. Xia, "Study on characteristics of seismic damage to rural self-built brick masonry houses at different intensity zones," *World Earthquake Engineering*, vol. 26, no. 4, pp. 724–730, 2010.
- [3] Q. Su and C. Liu, "Analysis of characteristic ratio of the seismic wall of brick masonry buildings," *Journal of Building Structures*, vol. 38, no. 12, pp. 163–169, 2017.
- [4] X. Liu, H. Zhang, and J. Liu, "Study on strengthening the seismic performance of the brick building with reinforced concrete structural column," *Building Structure*, vol. 2, no. 6, pp. 47–55, 1981.
- [5] C. Cheng, Y. Zheng, and M. Wu, "Experimental study on a single-story reinforced masonry model house by vibration table," *Building Structure*, vol. 35, no. 9, pp. 28–33, 2005.
- [6] X. Li, "Several new forms of masonry building in the abroad," *Architectural Technology*, vol. 19, no. 2, pp. 114–115, 1992.
- [7] A. Ahamad, O. Ambrose, and M. Chukwunenye, "Compression behaviour of concrete masonry prisms," *Jamal of Structural Engineering*, vol. 112, no. 3, pp. 605–613, 1986.
- [8] J. J. Bommer, G. Magenes, J. Hancock, and P. Penazzo, "The influence of strong-motion duration on the seismic response of masonry structures," *Bulletin of Earthquake Engineering*, vol. 2, no. 1, pp. 1–26, 2004.
- [9] P. B. Lourenço, N. Mendes, L. F. Ramos, and D. V. Oliveira, "Analysis of masonry structures without box behavior," *International Journal of Architectural Heritage*, vol. 5, no. 4–5, pp. 369–382, 2011.
- [10] B. Zhu, M.-H. Wu, and Z. Jiang, "Study for seismic performance of masonry wall reinforced by steel bar-mortar method," *Earthquake Engineering and Engineering Vibration*, vol. 4, no. 1, pp. 70–81, 1984.
- [11] X. Zhou, W. Xie, and J. Jiang, "Application study for seismic performances of existing masonry wall reinforced by steel bar-mortar crossed strip method," *Building Structure*, vol. 49, no. 5, pp. 1–8, 2019.
- [12] L. Lin and L. Ye, "Experimental investigation on masonry wall strengthened with FRP," *Building Structure*, vol. 35, no. 3, pp. 21–27, 2005.
- [13] S. Shang and M. Lei, "Test study on seismic behavior and finite element analysis of row lock wall strengthened with HPFL," *Earthquake Engineering and Engineering Vibration*, vol. 33, no. 4, pp. 218–227, 2013.
- [14] M. Deng, X. Gao, X. Liang, and X. M. Fan, "Experimental investigation on seismic behavior of brick wall strengthened with ECC splint," *Engineering Mechanics*, vol. 30, no. 6, pp. 168–174, 2013.
- [15] Y. Wang, Q. Yao, and Z. Wang, "Test on brick walls strengthened by the composite cover of high strength wire cable mesh and polymeric mortar," *Building Structure*, vol. 35, no. 8, pp. 36–40, 2005.
- [16] M. Deng, S. Yang, and X. Liang, "Experimental studies on seismic behavior of confined masonry walls strengthened with single HDC layer," *China Civil Engineering Journal*, vol. 51, no. 4, pp. 10–19, 2018.
- [17] D. Ge, X. Chen, and W. Li, "Application of progressive-collapse numerical simulation of masonry structures under earthquake action," *Building Structure*, vol. 46, no. 17, pp. 88–92, 2016.
- [18] B. Sun and H. Deng, "Study on seismic behavior of bottom frame structure building," *Journal of Building Structures*, vol. 36, no. s2, pp. 131–137, 2015.
- [19] J. Hua, T. Wu, and M. Jiang, "Numerical analysis of seismic behaviors of masonry structures in village buildings during strong earthquakes," *China Earthquake Engineering Journal*, vol. 39, no. 1, pp. 52–57, 2017.
- [20] T. Wu, H. Wang, and M. Yi, "Dynamic characteristics of masonry structures in villages and towns," *China Earthquake Engineering Journal*, vol. 38, no. 6, pp. 877–882, 2016.
- [21] R. Yu, Z. Xie, and L. Peng, "Effect of masonry strength on seismic performance of self-built dwellings," *Earthquake Engineering and Engineering Vibration*, vol. 33, no. 11, pp. 6–11, 2014.
- [22] Q. Zhou, Q. Min, and Y. Xiong, "Seismic performance analysis of existing typical rural buildings in Jiangxi," *Journal of Natural Disasters*, vol. 27, no. 1, pp. 96–105, 2018.
- [23] G. Zhao, Y. Ma, and X. Chen, "Vulnerability analysis of performance-based seismic design criteria for rural buildings," *China Civil Engineering Journal*, vol. 47, no. 9, pp. 1–8, 2014.
- [24] X. Yao, B. Sun, and Y.-K. Chen, "Elastic-plastic finite element analysis of typical brick-wood rural buildings underground motions," *China Earthquake Engineering Journal*, vol. 40, no. 1, pp. 32–40, 2018.

- [25] G. Liu, *The Research on the Basic Mechanical Behavior of Masonry Structure*, Hunan University, Changsha, China, 2005.
- [26] T. Wu and R. Hou, "Experimental studies on elastic modulus and the Poisson ratio of fired perforated brick masonry," *Building Structure*, vol. 42, no. 12, pp. 117–138, 2012.
- [27] Y. Ding, *Study on Anti-seismic Performance of Brick Structures in Western Rural Areas*, Xi'an University of Architecture and Technology, Xi'an, China, 2015.
- [28] Y. Yang, L. Yang, and Y. Gao, "Method of damage prediction for existing militia-story brick buildings and its reliability," *Earthquake Engineering and Engineering Vibration*, vol. 2, no. 3, pp. 75–86, 1982.
- [29] B. Chen, D. Wang, S. Chen, and S. Hu, "Influence of site factors on offshore ground motions: observed results and numerical simulation," *Soil Dynamics and Earthquake Engineering*, vol. 145, Article ID 106729, 2021.
- [30] L.-Y. Xu, S. Cheng-Xiang, W.-Y. Chen, F. Cai, Y. Y. Li, and G.-X. Chen, "Liquefaction-induced settlement of the pile group under vertical and horizontal ground motions," *Soil Dynamics and Earthquake Engineering*, vol. 144, Article ID 106709, 2021.
- [31] X. Du, Y. Wang, D. Lu, and C. Ma, "Study on static and dynamic stress-strain in a relationship of cement mortar material," *China Journal of Civil Engineering*, vol. 43, no. s2, pp. 119–126, 2010.

Research Article

Stability Assessment of Dangerous Rock Mass of an Overhanging Slope in Puerdu Town, Southwestern China

Wen-Lian Liu,^{1,2} Jia-Xing Dong ,^{2,3} Su-Gang Sui,^{1,2} Han-Hua Xu ,^{1,2} Run-Xue Yang,³ and Zhen-Luo Shen³

¹Kunming Prospecting Design Institute of China Nonferrous Metals Industry Co., Ltd., Kunming 650051, Yunnan, China

²Yunnan Key Laboratory of Geotechnical Engineering and Geohazards, Kunming 650051, Yunnan, China

³Faculty of Electric Power Engineering, Kunming University of Science and Technology, Kunming 650500, Yunnan, China

Correspondence should be addressed to Jia-Xing Dong; dong1986@kust.edu.cn and Han-Hua Xu; 724767210@qq.com

Received 23 April 2021; Accepted 1 June 2021; Published 6 July 2021

Academic Editor: Faming Huang

Copyright © 2021 Wen-Lian Liu et al. This is an open access article distributed under the Creative Commons Attribution License, which permits unrestricted use, distribution, and reproduction in any medium, provided the original work is properly cited.

Dangerous rock mass in the overhanging slope of Puerdu town has good free-face condition, high position, and great potential energy, identification and stability evaluation of which is a difficult problem in the disaster prevention. In this paper, the limit equilibrium method was used to evaluate the dangerous rock mass stability in the overhanging slope. Firstly, geomorphic characteristics and the distribution of dangerous rock mass are determined by the field geological survey. Secondly, six dangerous rock masses which may cause more threat are studied, with defining their failure modes and characteristic parameters. Finally, a simplified geological model is established, the stability coefficient of dangerous rock mass under different conditions is calculated by the limit equilibrium method, at the same time, stability analysis of dangerous rock mass is carried out based on the stereographic projection, and the hazard probability is estimated by the empirical formula. Results show that joints obviously developed in the dangerous rock mass of W1, W2, W3, W4, W5, and W6, with falling-type and toppling-type failure modes. In the natural condition, the dangerous rock mass is understable and unstable under the rainstorm and earthquake conditions. Consequently, rainstorm and earthquake are the key triggering factors of the instability and collapse of dangerous rock mass.

1. Introduction

Rock mass collapse is a common geological disaster in mountainous areas. Most dangerous rock masses exist on the overhanging slope or steep cliff, and such rock masses are divided by multiple structural planes and have poor stability [1]. In June 2006, the overhanging slope of a highway in the southeastern Qinghai-Tibet Plateau, China, collapsed after more than ten consecutive days of rainstorm, and the loose dangerous rock mass fell about 400 m³. A large number of rock mass tumbled down the slope, and some houses at the foot of the slope were destroyed, forming a disaster. Meanwhile, it is also a serious threat to the highway project and the production and life of local residents, with extremely serious consequences [2]. In August 2017, a magnitude 7.0 earthquake occurred in Jiuzhaigou, Sichuan, China. Due to the impact of the earthquake on the rock mass cracking

damage, a large number of high or very high collapse hazards existed in the core scenic spots of Jiuzhaigou, which seriously threatened the life and property safety of tourists and local residents [3].

The stability evaluation of dangerous rock mass can be used as the basis for the design of support structure to prevent and control the disaster of dangerous rock mass scientifically and effectively. The Bishop method [4] considers the lateral force of the soil strip, but does not take into account the horizontal force; on the other hand, the tangent force is assumed to be equal, so the analysis results have certain limitations. Mithun et al. [5] used remote sensing technology to monitor glacier changes on the Bhutanese Himalayan Plateau and evaluate the stability of dangerous rock mass. Li et al. [6] also proposed that the unstable failure of dangerous rocks has obvious spatial characteristics. When Wang et al. [7] studied the stability of Jianchuandong

dangerous rock mass in the Three Gorges Reservoir area, they proposed that the instability mechanism was that the weight of the upper rock mass and the periodic change of the reservoir water level led to the weakening of the foundation rock mass and the increasing damage, which eventually led to the collapse of the bedrock, and carried out stability analysis on it. Li [8] proposed the collapse prevention method by strengthening the dangerous rock mass to slow down the development of unloading cracks. In a general way, the classification of deformation and failure modes is a necessary step for the stability analysis of the dangerous rock mass. According to the geological conditions of the study area. Dong et al. [9] classified the hazard sources in surrounding slope of a hydropower station into isolated stone, dangerous rock, dangerous rock mass and high position covering layer. Kuang [10] comprehensively considered the failure mechanism and stress state of unstable dangerous rock mass and classified the collapse types into shear-fall, tension-break, fall-fall, tipping-collapse, crushing and caving, etc. Huang and Deng [11] divided the dangerous rock mass into seven types according to the instability mechanism, including slope attachment type, suspension type, isolated type, slab crack type, cataclastic type, block type, and soft foundation type. When Zhang et al. [12] studied deformation and failure characteristics of Lianziya dangerous rock mass, they summarized 8 deformation and failure modes.

The stability evaluation of dangerous rock mass is mainly carried out from qualitative and quantitative methods. Li et al. [13] used the stereographic projection method and limit equilibrium method to analyze the stability of slipping Hesonglou dangerous rock mass in Hubei province of China. On this basis, the measure is put forward. Based on the key block theory, Zhang et al. [14] proposed the stability probability assessment method of the cataclastic rock masses. Tao et al. [15] analyzed stability of a cutting rock slope of a hydropower project located on Dadu river in Sichuan province of China using the SSPC method. Based on the limit equilibrium method and fracture mechanics theory, Gong [16] generalized the mechanical model of dangerous rocks in the Three Gorges Reservoir area, analyzed the maximum circumference stress fracture criterion and maximum shear stress fracture criterion, and deduced the stability coefficient expression of dangerous rocks. Xiao [17] used the limit equilibrium method to analyze the stability of dangerous rock mass in the Wanzhou Taibai rock slope and studied the influence of crack angle, vertical seismic force, and horizontal seismic force on the safety factor of dangerous rock mass. Chen [18] used the limit equilibrium theory to calculate and analyze the stability of slump-type dangerous rock mass in the Shouli Mountain, Wanzhou. When earthquakes and rainfall acted together, the decisive factor for the stability of dangerous rock mass was mainly horizontal seismic force. Li et al. [19] took the dangerous rock mass in a limestone area and granite area of Baoxing County, Yaan City, the “Wenchuan” earthquake zone, as the research object and made stability evaluation and analysis of the dangerous rock mass. The results showed the simplicity of the rigid body limit equilibrium method in the stability

analysis of the dangerous rock mass. Zhao and Bu [20] used the block limit equilibrium method to calculate the safety factor and sliding direction of dangerous rock mass and analyze its stability. By combining the Monte Carlo method and the block limit equilibrium method, the function of stability reliability was proposed, and the reliability index and instability probability were obtained. Taking Baiyanshan dangerous rock mass as the object, Liu et al. [21] used the limit equilibrium method to carry out quantitative checking calculation on the stability of the dangerous rock mass and comprehensively analyzed and evaluated the development characteristics and stability of the dangerous rock mass in Guilin.

The dangerous rock mass of the overhanging slope in Puerdu Town, Yanjin County, Zhaotong City, Yunnan Province, China, is a riparian slope area with a canyon landform that is intersected with structural erosion and river erosion. According to the terrain, the slope has already had the condition of collapse. Once the dangerous rock collapses, it will bring a great threat to the lives and property safety of the villagers. Therefore, the stability evaluation of dangerous rock mass in the study area will be beneficial to the geological disaster prevention and control planning of Yanjin County, and it provides the corresponding theoretical basis for disaster prevention and control, which has a very important practical significance. At present, there are many studies on the stability analysis of dangerous rock mass, but the stability evaluation of overhanging slope dangerous rock mass in mountainous areas is less. Based on the limit equilibrium method, this paper calculates the stability coefficient and hazard probability of the falling-type and tipping-type dangerous rock mass in the study area under different working conditions and evaluates the stability of six groups of dangerous rock mass with greater threat in the study area.

2. Geological Environment Background

2.1. Geographical Position. Puerdu town is located at the confluence of the Chuansi River, the Shangqing River, and the first-class tributary of the Jinsha River. The geographical coordinates are 104°10'E, 28°14'N. The straight-line distance from Zhaotong is about 110 km and from Yanjing is about 25 km. The location of the study area is shown in Figures 1 and 2.

2.2. Meteorological Hydrology. The average annual temperature in the region is 17°C, and the average annual rainfall in the area is 1226.2 mm. Rainfall is concentrated in June, July, August, and September, accounting for 82% of the annual precipitation. The average annual evaporation is 1083.5 mm, and the relative humidity is 81%.

2.3. Topographic Features. The topography and geomorphology of Puerdu town are mainly characterized by the flow geomorphology controlled by the geological structure. The basic geomorphologic units are mountains and canyons, in addition to the gentle slope geomorphology developed along the sedimentary rock level. Deep valley in the area is mainly

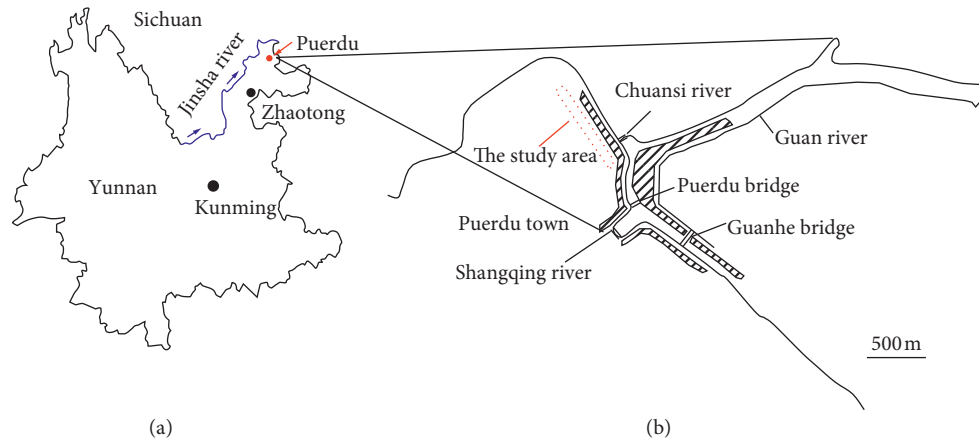


FIGURE 1: Location of the study area.



FIGURE 2: Location of the study area (satellite camera).

manifested as V-type valley and steep valley slope, slope is generally above 30, and vegetation coverage is high.

2.4. Stratigraphic Lithology. On the basis of field investigation and exploration, the stratigraphic lithology of this area is mainly composed of the quaternary residual slope layer (Q_4^{el+dl}) containing gravel silty clay, block stone soil, gravel soil, and pebble, and the underlying bedrock is the Jurassic Middle Series Shaximiao formation (J2S), including brown, purple gray sandstone interbedded with purplish red mudstone, silty mudstone, and argillaceous siltstone.

3. Engineering Geological Features of Dangerous Rock Areas

The occurrence of collapse is closely related to the scour cutting of the Guanhe River and Chuansi River and also to the slope rock mass structure. The regional geological history study shows that there is a belt distribution under the cliff, with a length of 100–1000 m, and a large collapse accumulation layer with a thickness of 10–20 m, which is a large-scale collapse in the Middle and Late Pleistocene. The scale of modern collapse is small, but the harm is serious. The dangerous rocks in this area have various forms, and their basic geometric forms are massive, columnar, plate-shaped, and inverted-cut cone-shaped. Other forms include arch

bridge and cantilever. According to their deformation characteristics and failure forms, dangerous rock collapse can be divided into collapse accumulation area and cliff dangerous rock area. According to the topographic features, the study area is divided into four levels of dangerous rocks from bottom to top, and each level of dangerous rocks is further divided into three microlandforms, including the upper gentle slope area, the steep cliff area, and the lower slope area. The landform map of the collapse accumulation area and cliff dangerous rock area is shown in Figure 3.

Grade 1 dangerous rock upper gentle slope area: it is located in the upper part of a steep cliff, the terrain slope is $20\text{--}34^\circ$, the average slope is 29° , the elevation difference is 51–104 m, and the average is 68 m; **steep cliff area:** the length of the cliff zone is 984 m, the slope of the cliff is $N62^\circ W$, the height difference is 8–25 m, most of the steep cliffs are upright, and some of the steep cliffs' angle is between 70 and 90° . The main slope area at the bottom of the Grade 1 dangerous rock steep cliff: from the lower part to the upper part of the Chuansi River, the elevation difference increases gradually from 58 m to 102 m. The topographic slope also increases gradually from the lower part to the upper part of the Chuansi River, from 26° to 38° . In the middle part of the country, the topography is mostly step-shaped due to the residential area cutting slope construction. The cut slope height is 10–15 m, and the cut slope degree is mostly in an upright state.

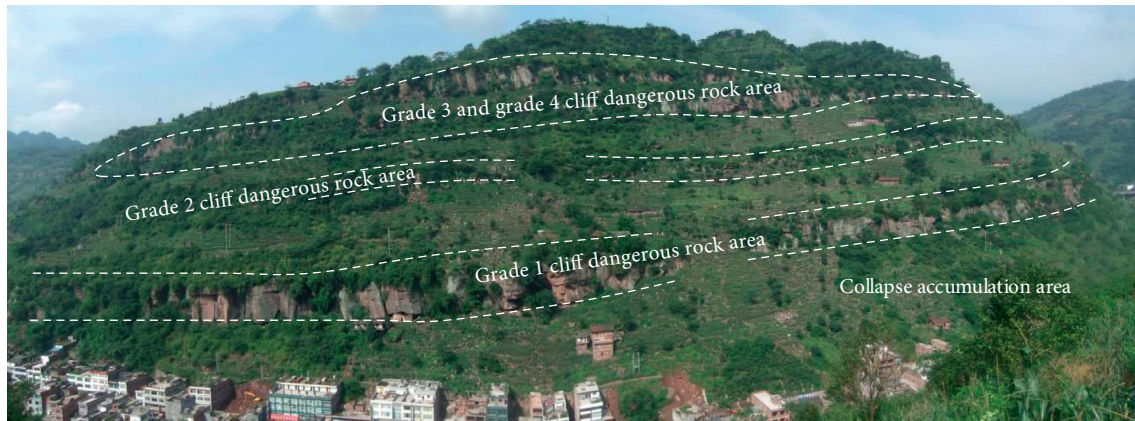


FIGURE 3: Geomorphologic map of the collapse and accumulation area and cliff dangerous rock area.

Grade 2 dangerous rock upper gentle slope area: it is located in the upper part of the secondary steep cliff, with a topographic slope of $25\text{--}34^\circ$, an average slope of 33° , an elevation difference of $30\text{--}50\text{ m}$, and an average of 39 m ; steep cliff area: the distribution is discontinuous, the length of the cliff is 497 m , the cliff line is $S63^\circ E$, the height difference is $6\text{--}13\text{ m}$, most of the cliffs are upright, and some of the cliffs' angle is between 70 and 90° . The lower slope of the grade 2 dangerous cliff is the upper gentle slope of the grade 1 steep cliff.

Most of the grade 3 and grade 4 dangerous rocks are connected together. The terrain is relatively slow from the upper part to the gentle slope area of the mountain top, and the slope of the terrain is $20\text{--}25^\circ$. The length of the steep cliff zone is 820 m , the cliff direction is $N62^\circ W$, and the height difference is $15\text{--}43\text{ m}$. The lower slope of the grade 3 and grade 4 dangerous rocks is the upper gentle slope of the grade 2 dangerous rocks.

3.1. Engineering Geological Characteristics in the Collapse Accumulation Area. The collapse accumulation area is located on the slope zone on the right bank of the Chuansi River. The slope and the steep cliff are in abrupt contact. The overall trend of the slope is $N25^\circ\text{--}30^\circ W$ and tends to NE. Generally belonging to the middle slope, due to artificial slope cutting, the terrain slope is almost verticle, the height of cutting slopes is $8\text{--}10\text{ m}$, with a height of 15 m in some areas. The collapse accumulation body has a transverse length of 750 m , a longitudinal length of $115\text{--}320\text{ m}$, a thickness of $2.3\text{--}18.2\text{ m}$, an average thickness of 8 m , an area of $111,660\text{ m}^2$, and a volume of $893,280\text{ m}^3$. It is a large collapse accumulation body with a large scale of collapse points.

3.2. Engineering Geological Characteristics in the Steep Cliff Dangerous Rock Area. The steep cliff dangerous rock area is located in the high-steep slope zone on the right bank of the Chuansi River. The high-steep slope can be divided into two sections. The upper section is the steep cliff, and the lower section is the moderate gentle slope. The slope height is mostly $100\text{--}200\text{ m}$. Most of the cliff walls are in the upright

state, the rock walls are smooth, and the dangerous rocks are well developed. The first level of the cliff dangerous rock area is $8\text{--}68\text{ m}$ away from the residential area, and the cliff dangerous rock belt is 976 m long. The strike of the wall is $S44^\circ E$ from the starting point to 350 m , from 400 m to 976 m , it is $S44^\circ E$ from 400 to 976 m , and it breaks off at $350\text{ m}\text{--}400\text{ m}$, and the height difference is $8\text{--}25\text{ m}$. Most of the cliffs are upright, and part of the cliff angle is between 70 and 90° . Joints cut the rock mass into blocks with different volumes of about $100\text{--}500\text{ m}^3$, and most of them are small collapses. In the distribution area of the steep cliff, there are many sections of soft rock weathering and denudation that have formed continuous cavities, the cavity rate is about 68% , and the cavity volume is mostly between 70 and 220 m^3 . The lithologic composition of the dangerous rock mass is mainly the Middle Jurassic Shaximiao Formation (J2S) sandstone, argillaceous siltstone, silty mudstone, mudstone, etc.

In a word, dangerous rock mass will be transformed into an unstable state under the combined action of self-weight, fissure water pressure (natural state), rainstorm, earthquake force, and other factors.

3.3. Characteristics of Dangerous Rocks. After the field investigation of W1, W2, W3, W4, W5, and W6, the basic characteristics of the dangerous rock mass are shown in Table 1.

The photographs of W1, W2, W3, W4, W5, and W6 fields are shown in Figure 4.

4. Analysis of the Formation Mechanism and Cause in Dangerous Rock Mass

Through geological survey, it is concluded that the steep cliff dangerous rock area is located in the high-steep slope zone on the right bank of the Chuansi River, and the slope height is mostly $100\text{--}200\text{ m}$. The unloaded rebound of dangerous rock mass, the deformation and failure of the slope, and the formation and development of dangerous rock mass are very favorable because of the good hanging conditions. The rock mass structure of the steep slope provides the material

TABLE 1: Basic parameters of the dangerous rock mass.

Characteristic parameters	W1	W2	W3	W4	W5	W6
The height of the dangerous rock mass (m)	5.0	23.0	2.0	17.0	18.0	17.0
The length of the dangerous rock mass (m)	32.7	23.0	20.0	24.0	23.0	30.0
The thickness of the dangerous rock mass (m)	4.0	8.0	7.0	6.0	8.0	5.0
Crack depth (m)	4.7	14.0	1.7	6.0	10.0	5.0
Dangerous rock mass volume (m ³)	654.0	4232.0	280.0	2448.0	3312.0	2550.0
Weight (kg)	1654.6	10,706.5	708.0	6192.0	8378.9	6450.0

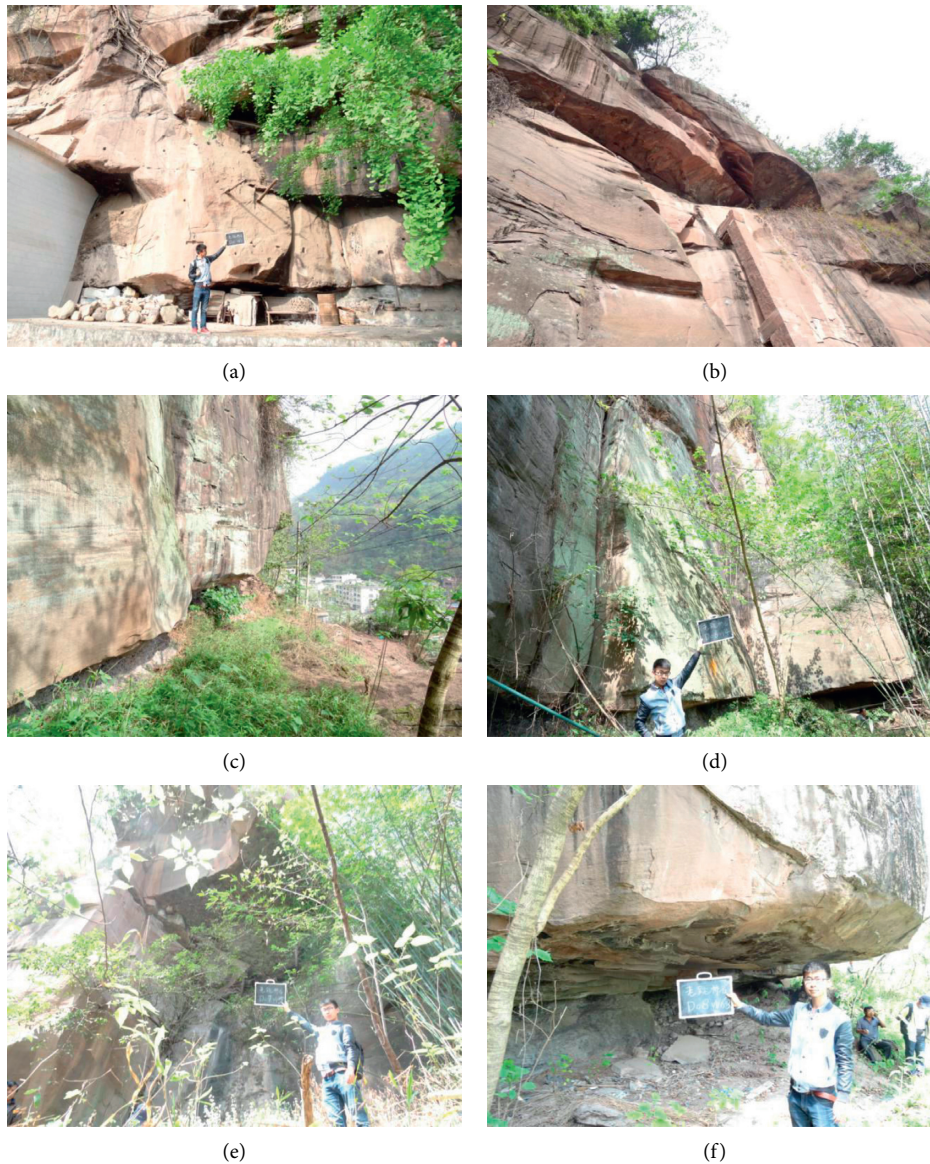


FIGURE 4: Photographs of dangerous rocks. (a) W1 dangerous rock mass. (b) W2 dangerous rock mass. (c) W3 dangerous rock mass. (d) W4 dangerous rock mass. (e) W5 dangerous rock mass. (f) W6 dangerous rock mass.

foundation for the formation of the dangerous rock, especially the interbedded sand and mudstone of the Middle Jurassic Shaximiao (J2S) Formation. The upper section of the slope is covered with sandstone, and the mudstone is under it, forming the step-like suspended slope with steep and slow phases. The sandstone layer is prone to brittle fracture, and

the mudstone layer is prone to plastic deformation, which aggravates the deformation and failure of the whole rock mass.

Comprehensive analysis shows that the cutting and separation of the joints is the internal reason for the formation of dangerous rock mass in the study area. The rock

blocks were formed with the intersecting of joints. In addition, under the action of hydrostatic pressure, water infiltrating into the fissure further promotes the fissure expansion, and the infiltration and immersion reduce the strength of the soft base of mudstone, strengthen the weathering effect, and intensify the plastic flow deformation. Meanwhile, they also increase the sliding force of dangerous rock mass and accelerate the formation of dangerous rocks.

Combined with the studies of many scholars on the instability failure modes of dangerous rock mass, it is concluded that the instability of dangerous rock mass of the overhanging slope in the study area is mainly falling type and tipping type, and its collapse formation mode is shown in Figure 5.

As shown in Figure 5, because the upper part of the cliff is hard and the lower part is soft, the mud layer in contact with the main slope begins to disintegrate under the action of pore water, the mudstone cavity appears, and the upper rock mass is unstable, resulting in the collapse of the dangerous rock body along the unloading joint.

5. Stability Analysis of Dangerous Rock Mass

5.1. Stability Analysis of Dangerous Rock Mass Based on the Stereographic Projection. The stability of the rock slope by the stereographic projection is based on the rigid assumption. The internal strain of the block is not considered; only the effect of sliding force and antisliding force of the block is considered. Through the stereographic projection, the structure surface and slope surface are projected to the plane, and the stability of the slope is evaluated. The basic attitude of the dangerous rock mass is shown in Table 2, and the stereographic projection is shown in Figure 6.

The dangerous rock mass was analyzed according to the stereographic projection, and the results are as follows:

In Figure 6(a), the angle between the slope surface and dip direction of the rock layer is 22° , with a similar dip direction, which is generally an unfavorable combination slope. There is little difference between the attitudes of $J1$ and b , both of $J1$ and b have a steep dip. Line represents $J2$ intersects with the layer as an unfavorable combination with the slope surface. Under the condition of “cavity” in the underlying mudstone, it is easy to cause the upper dangerous rock mass to “falling-type” failure.

In Figure 6(b), the angle between the slope surface and dip direction of the rock layer is 22° , with a similar dip direction, which is generally an unfavorable combination slope. The combination intersection of $J1$, $J2$, and st with the slope surface is unfavorable. Under the condition of “cavity” in the underlying mudstone, it is easy to cause the upper dangerous rock mass to “tipping-type” failure.

In Figure 6(c), the angle between the slope surface and dip direction of the rock layer is 7° , with a similar dip direction, which is generally an unfavorable combination slope. The combination intersection of $J1$, $J2$, and st with the slope surface is unfavorable. Under the

condition of “cavity” in the underlying mudstone, it is easy to cause the upper dangerous rock mass to “falling-type” failure.

In Figure 6(d), the angle between the slope surface and dip direction of the rock layer is 8° , with a similar dip direction, which is generally an unfavorable combination slope. The combination intersection of $J1$, $J2$, and st with the slope surface is unfavorable. $J1$ and $J2$ are rocks with cutting steep cliffs. Under the condition of “cavity” in the underlying mudstone, it is easy to cause the upper dangerous rock mass to “falling-type” failure. Similarly, stability and failure modes of $W5$ and $W6$ can be analyzed based on Figures 6(e) and 6(f).

5.2. Establishment of the Geological Model. Stability evaluation of dangerous rock mass is the foundation of the risk evaluation of dangerous rock mass. We analyzed the combination relationship of joints developed in dangerous rock mass, the degree of tension and closure, penetration, collapse direction of dangerous rock mass, and other factors. According to the field survey, six sections were selected to study the dangerous rock mass, and a generalized geological model was established according to the method proposed by Zhang et al. [21] and Doug Stead et al. [22]. They are numbered $W1$, $W2$, $W3$, $W4$, $W5$, and $W6$; among them, the failure mode of $W1$, $W3$, $W4$, and $W6$ is falling type. On the contrary, $W2$ and $W5$ are the tipping-type dangerous rock mass [24]. Their geological profiles are shown in Figures 7–12, respectively.

5.3. Stability Calculation

5.3.1. Calculation Method. The dangerous rock mass in the study area is divided into two categories, falling-type dangerous rock mass and tipping-type dangerous rock mass. This paper adopts the calculation model proposed by Chen et al. [25, 26] similar to the project. The calculation models and main formulas of falling-type and tipping-type dangerous rocks are as follows. The schematic diagram of the falling type is shown in Figure 13, and the schematic diagram of the tipping type is shown in Figure 14.

Normal force:

$$N = W \cos \beta - P \sin \beta. \quad (1)$$

Tangential force:

$$T = W \sin \beta + P \cos \beta, \quad (2)$$

$$\sigma = \frac{N}{H/\sin \beta}, \quad (3)$$

$$\tau = \frac{T}{H/\sin \beta}, \quad (3)$$

$$\tau_f = \sigma \tan \phi + c, \quad (4)$$

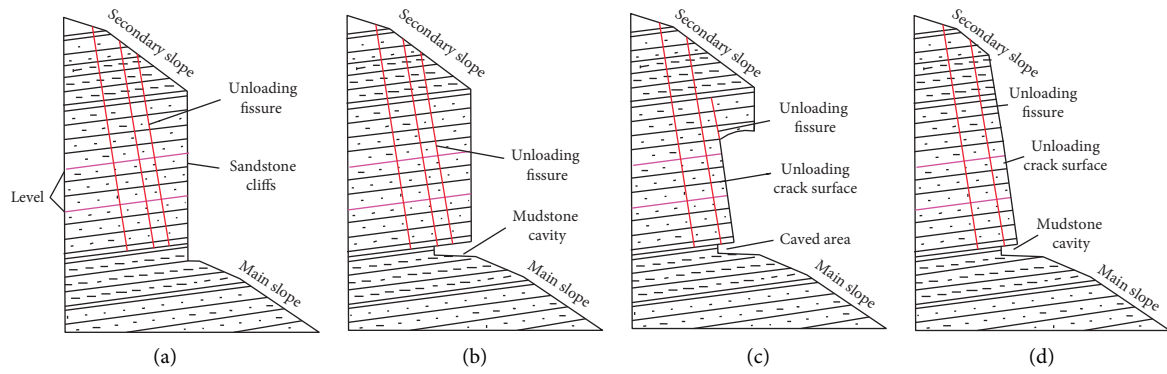


FIGURE 5: Collapse formation mode (the order of collapse is from (a) to (d)).

TABLE 2: The basic attitude of the dangerous rock mass.

Number	W1	W2	W3	W4	W5	W6	
General attitude of the slope surface	$N62^{\circ}W/NE\angle 84^{\circ}$						
Rock attitude	$N40^{\circ}W/SW\angle 8^{\circ}$	$N60^{\circ}W/SW\angle 12^{\circ}$	$N55^{\circ}W/SW\angle 10^{\circ}$	$N54^{\circ}W/SW\angle 11^{\circ}$	$N60^{\circ}W/SW\angle 13^{\circ}$	$N55^{\circ}W/SW\angle 9^{\circ}$	
Main joint	$J1$ $J2$	$N45^{\circ}W/NE\angle 89^{\circ}$ $N10^{\circ}E/SE\angle 86^{\circ}$	$N79^{\circ}W/NE\angle 89^{\circ}$ $N82^{\circ}E/NW\angle 71^{\circ}$	$N45^{\circ}W/NE\angle 80^{\circ}$ $N20^{\circ}E/SE\angle 85^{\circ}$	$N40^{\circ}W/NE\angle 87^{\circ}$ $N10^{\circ}E/SE\angle 86^{\circ}$	$N16^{\circ}W/NE\angle 88^{\circ}$ $N76^{\circ}E/NW\angle 87^{\circ}$	$N20^{\circ}W/NE\angle 74^{\circ}$ $N80^{\circ}E/NW\angle 56^{\circ}$

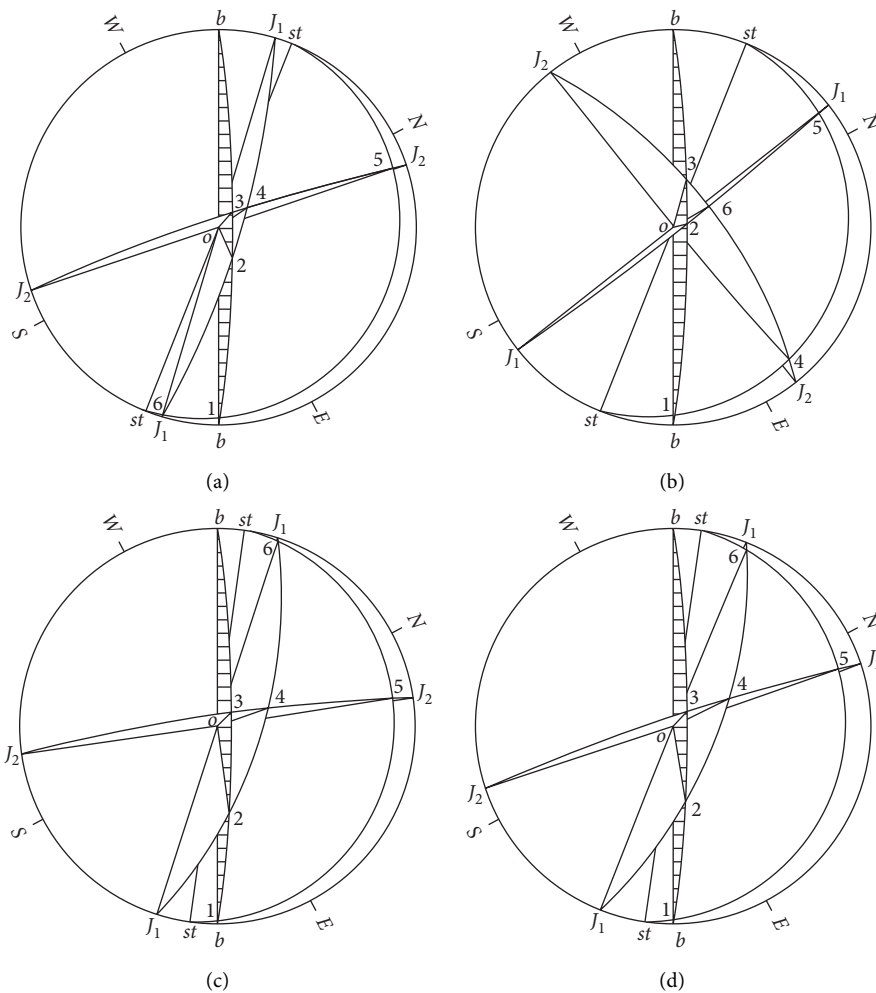


FIGURE 6: Continued.

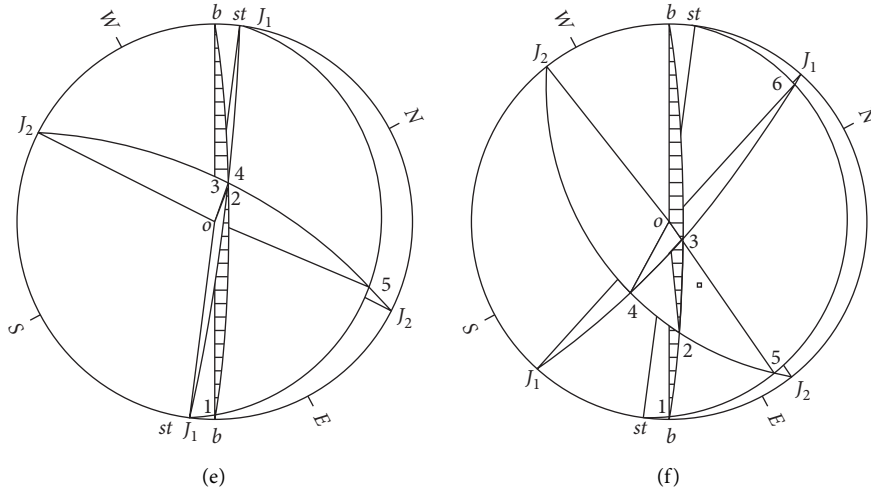


FIGURE 6: Analysis diagram of the stereographic projection. (a) W1. (b) W2. (c) W3. (d) W4. (e) W5. (f) W6.

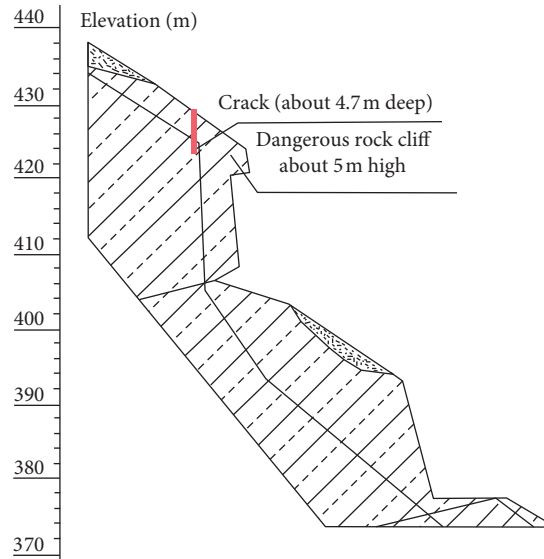


FIGURE 7: Falling-type dangerous rock mass of W1.

$$K = \frac{(W \cos \beta - P \sin \beta - Q) \tan \phi + C (H / \sin \beta)}{W \sin \beta + P \cos \beta}. \quad (5)$$

The above formulas (1)–(5) are about the calculation principle of the falling-type rock.

$$K = \frac{M_R}{M_O}, \quad (6)$$

$$M_O = Wa + Ph_0 + Q \left(\frac{1}{3} \frac{e_1}{\sin \beta} + \frac{H - e}{\sin \beta} \right), \quad (7)$$

$$\begin{aligned} M_R &= [\sigma_t] \frac{H - e}{\sin \beta} \frac{H - e}{2 \sin \beta} \\ &= \frac{1}{2} [\sigma_t] \frac{(H - e)^2}{\sin^2 \beta}. \end{aligned} \quad (8)$$

The above formulas (6)–(8) are about the calculation principle of the tipping-type rock.

In the above formula, W is the gravity of dangerous rock mass per unit length (kN); P is the horizontal seismic force (kN) borne by dangerous rock mass per unit length; Q is the hydrostatic pressure in the gap (kN); H is the vertical distance from the upper end of the edge fracture to the lower end of the incomplete segment (m); β is the dip angle ($^\circ$) of the fracture surface; c and ϕ , respectively, are the equivalent cohesive force (kPa) and internal friction angle ($^\circ$) of the fracture surface; e is the pore depth (m); e_1 is the pore water filling depth (m); a is the horizontal distance between the gravity action point and the overturning point (m); h_0 is the vertical distance between the seismic force and the overturning point (m); $[\sigma_t]$ is the standard value of tensile strength of dangerous rock mass (kPa); M_O is the overturning moment (kN·m); and M_R is the antioverturning moment (kN·m).

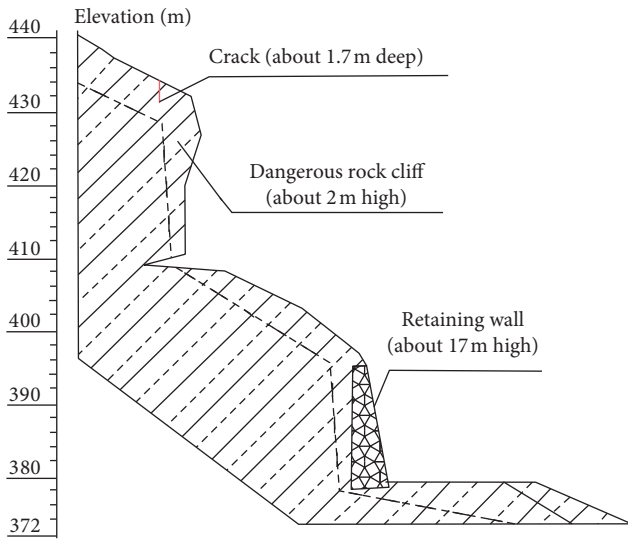


FIGURE 8: Falling-type dangerous rock mass of W3.

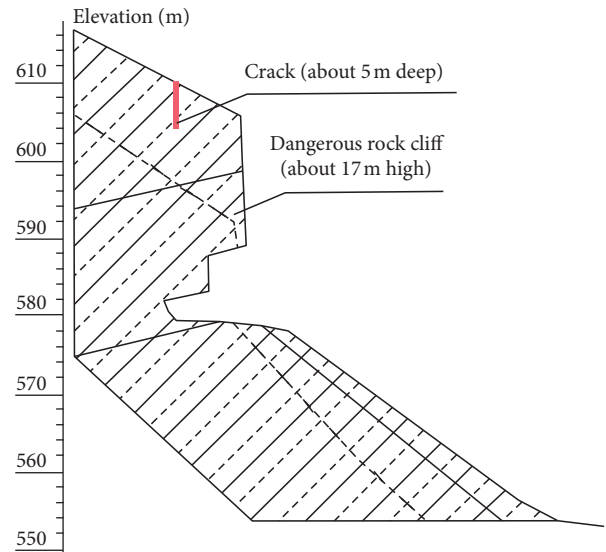


FIGURE 10: Falling-type dangerous rock mass of W6.

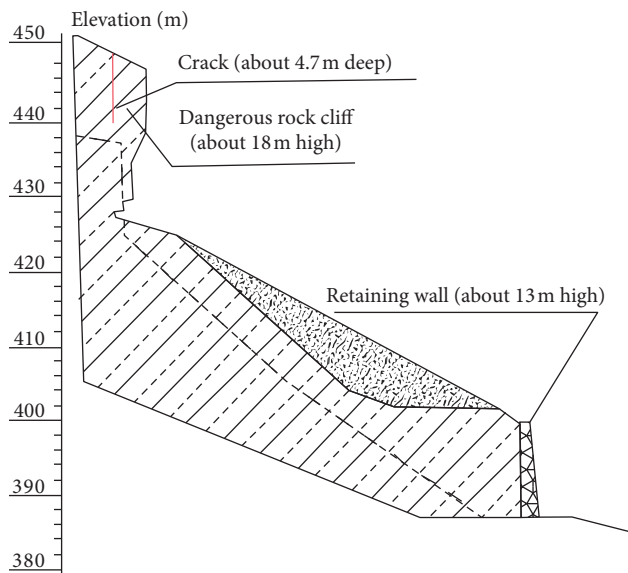


FIGURE 9: Falling-type dangerous rock mass of W4.

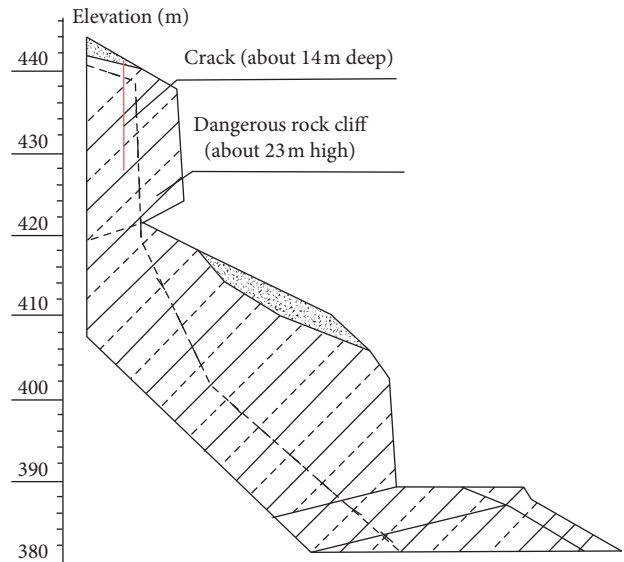


FIGURE 11: Tipping-type dangerous rock mass of W2.

5.3.2. *Load Combination.* The failure modes of dangerous rock mass in the study area are tipping type and falling type, and the main influencing factors of dangerous rock activities are rainstorm. The basic seismic intensity in the exploration area is 7°. Considering the influence of the earthquake on dangerous rocks, the following three working conditions are selected to evaluate the stability of dangerous rocks:

- Working condition I: self-weight (natural)
- Working condition II: self-weight + fissure water pressure (rainstorm)
- Working condition III: self-weight + fissure water pressure (rainstorm) + earthquake force

5.3.3. *Calculation Parameters of Dangerous Rocks.* The dangerous rock mass in the study area is mainly metamorphic sandstone. Suggested values and characteristic parameters of physical and mechanical parameters of the rock mass are shown in Tables 3–5.

5.4. *Stability Assessment of Dangerous Rock Mass*

5.4.1. *Stability Discrimination Basis of Dangerous Rock Mass.* Refer to the Landslide Industry Code in China “Specification of geological investigation for landslide stabilization (DZ/T0218-2006).” The stable state of dangerous rock mass can be divided into four states: stable, basically stable, understable, and unstable. The specific determination basis is shown in Table 6.

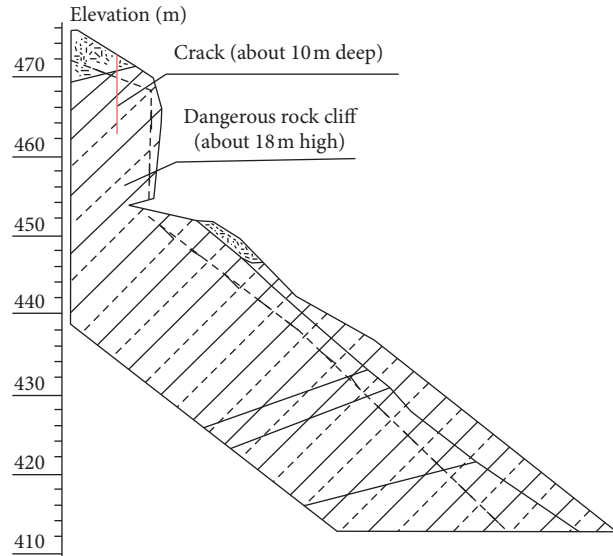


FIGURE 12: Tipping-type dangerous rock mass of W5.

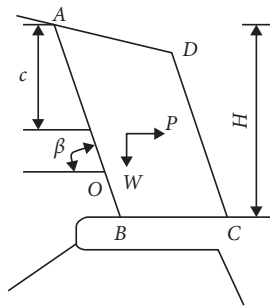


FIGURE 13: Calculation model for the unstable falling-type rock.

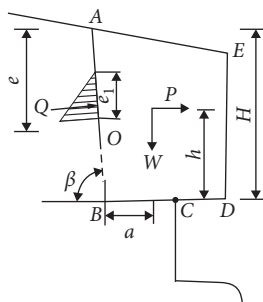


FIGURE 14: Calculation model for the unstable tipping-type rock.

TABLE 3: Suggested parameter values.

Physical and mechanical parameter	Suggested values
Natural gravity (kN/m ³)	2.00
Saturated unit weight (kN/m ³)	25.50
Natural compressive strength (MPa)	25.60
Saturated compressive strength (MPa)	18.80
Natural tensile strength (MPa)	1.60
Saturated tensile strength (MPa)	1.52

TABLE 4: Characteristic parameters of falling-type dangerous rocks.

Dangerous rock mass number	W1	W3	W4	W6
Characteristic parameters				
Weight per unit length (t)	50.6	35.4	258.0	215.0
Dip angle of the fracture surface (°)	89.0	80.0	87.0	74.0
Cohesive force of the rock mass (kPa)	700.0	700.0	700.0	700.0
Internal friction angle of the rock mass (°)	31.9	31.9	31.9	31.9
Cohesion of structural planes (kPa)	70.0	70.0	70.0	70.0
Internal friction angle of the structural plane (°)	28.0	28.0	28.0	28.0
Equivalent cohesion (kPa)	107.8	164.5	162.7	107.1
Equivalent angle of internal friction (°)	28.2	28.6	28.6	28.2
Earthquake force (kN)	60.7	42.5	309.6	258.0
Normal force (kN)	-51.9	19.64	-174.2	344.6
Tangential force (kN)	506.9	356.0	2592.6	2137.8

TABLE 5: Characteristic parameters of tipping-type dangerous rocks.

Dangerous rock mass number	W2	W5
Characteristic parameters		
Weight per unit length (t)	465.5	364.3
Dip angle of the fracture surface (°)	89.0	83.0
Hydrostatic pressure (kN)	106.7	54.8
Earthquake force (kN)	558.6	437.2
$[\sigma_t]$ (kPa)	390.8	390.8
$H - e$ (m)	9.0	8.0
Overturning moment	7550.6	11,723.9
Resistance moment	15,832.2	12,694.1

TABLE 6: Criteria for the stability evaluation of dangerous rocks.

Failure mode	Stable state			
	Unstable	Understable	Basically stable	Stable
Falling type	$K < 1.0$	$1.0 \leq K < 1.5$	$1.5 \leq K < 1.8$	$K \geq 1.8$
Tipping type	$K < 1.0$	$1.0 \leq K < 1.3$	$1.3 \leq K < 1.5$	$K \geq 1.5$

TABLE 7: Calculation results of dangerous rock stability.

Failure mode	Dangerous rock number	Working condition	Stability factor	Stable state	Hazard probability (%)
Falling type	W1	I	1.075	Understable	20.4
		II	0.950	Unstable	30.8
		III	0.928	Unstable	32.7
	W3	I	1.024	Understable	24.7
		II	0.980	Unstable	28.3
		III	0.953	Unstable	30.6
	W4	I	1.101	Understable	18.3
		II	0.953	Unstable	30.6
		III	0.909	Unstable	34.3
	W6	I	1.006	Understable	26.2
		II	0.863	Unstable	38.1
		III	0.833	Unstable	40.6
Tipping type	W2	I	1.026	Understable	24.5
		II	0.907	Unstable	34.4
		III	0.866	Unstable	37.8
	W5	I	1.168	Understable	12.7
		II	1.085	Understable	19.6
		III	1.040	Understable	23.3

5.4.2. *Safety Analysis Results.* Hazard probability reflects the general relationship between the disaster rate and the stability coefficient under different working conditions. The calculation formula adopts the empirical formula proposed by Zhang [27] and Deng [28].

$$P = 1.1 - \frac{k}{1.2}. \quad (9)$$

In the above formula (9), P is the hazard probability of the disaster; K is the stability coefficient of dangerous rock mass. When $K \geq 1.2$, $K = 1.2$ is taken. The calculation results of dangerous rock mass under different working conditions are shown in Table 7.

6. Conclusions

In this paper, six groups of dangerous rock mass with overhanging slope in Puerdu Town, Yanjin County, Zhao-tong City, Yunnan Province, China, were taken as the research objects. Field investigation was conducted to analyze the development characteristics of dangerous rock mass and define its failure and instability modes. According to the characteristics of dangerous rock mass, a simplified geological model is established. The influence of dead weight, rainstorm, and earthquake on dangerous rock mass is considered reasonably, and the stability state of dangerous rock mass under different working conditions of the overhanging slope is objectively reflected. The stability coefficient of dangerous rock mass under different working conditions is calculated by the limit equilibrium method, and the hazard probability is estimated by the empirical formula. The main conclusions are as follows:

- (1) According to the results of the engineering geological survey, the joints of dangerous rock mass (W1, W2, W3, W4, W5, and W6) in the study area are

obviously developed, with good hanging conditions and serious potential threats.

- (2) The failure mode of dangerous rock mass (W1, W3, W4, and W6) in the study area is falling type, and the failure mode of dangerous rock mass W2 and W5 is tipping type.
- (3) In dangerous rock mass (W1, W2, W3, W4, W5, and W6), under condition I, stability coefficient $K = 1.006$ – 1.101 , for the understable state, and the hazard probability is 18.3–26.2%; under condition II, stability coefficient $K = 0.863$ – 1.168 , which is an unstable state, and the hazard probability is 19.6–38.1%; under condition III, stability coefficient $K = 0.833$ – 1.040 , which is an understable state, and the hazard probability is 23.3–40.6%. In a word, the dangerous rock mass including W1, W2, W3, W4, W5, and W6 is mostly in the understable state. Under the conditions of rainstorm and earthquake, the stability coefficient decreases, and the hazard probability increases. Therefore, monitoring should be strengthened.

Data Availability

The data used to support the findings of this study are included within the article.

Conflicts of Interest

The authors declare that there are no conflicts of interest regarding the publication of this paper.

Acknowledgments

This study was sponsored by the Talent Development Program of Kunming University of Science and Technology

(nos. KKS201504022 and KKS201767034) and Kunming Prospecting Design Institute of China Nonferrous Metal Industry Co., Ltd. (Risk Assessment Method of Dangerous Rock High Slope in Northeast Yunnan Based on Engineering Geological Evolution).

References

- [1] H. Chen and X. Qin, "Status quo and trend of unstable rock stability analysis," *Journal of Chongqing Jiaotong University (Natural Science Edition)*, vol. 37, no. 10, pp. 49–60, 2018.
- [2] J. Wang, "Design of collapse control scheme for dangerous rock in overhanging slope," *Communications Science and Technology Heilongjiang*, vol. 33, no. 6, pp. 49–50, 2010.
- [3] Hu Gu, "Risk assessment of earthquake-induced collapse disaster in Jiuzhaigou scenic area," *Chengdu University of Technology*, 2019.
- [4] C. Li, T. Kang, X. Li, and L. Li, "Theoretical investigation of the sliding instability and caving depth of coal wall workplace based on the bishop strip method," *Advances in Civil Engineering*, vol. 2019, no. 1, 8 pages, 2019.
- [5] K. Mithun, M. F. A. Ayad, and M. Ismail, "Glacier changes monitoring in Bhutan high imalaya using remote sensing technology," *Environmental Engineering Research*, vol. 26, no. 1, pp. 38–50, 2021.
- [6] H. F. Li, G. X. Zhang, T. Huang, and Q. J. Zhou, "Stability analysis of dangerous rocks on the slope of a hydropower station," *Applied Mechanics and Materials*, vol. 405–408, pp. 621–629, 2013.
- [7] L. Wang, Y. Yin, B. Huang, and Z. Dai, "Damage evolution and stability analysis of the Jianchuandong dangerous rock mass in the three Gorges reservoir area," *Engineering Geology*, vol. 265, Article ID 105439, 2020.
- [8] P. Li, "Analysis of collapse deformation mechanism and prevention measures of Shiwei rock in Zhangkou, Chongqing," *Modern Mining*, vol. 36, no. 2, pp. 160–163+169, 2020.
- [9] J. Dong, G. Xu, Z. Li et al., "Classification and risk rating assessment of hazard sources in surrounding slope of Busigou hydropower project," *Journal of Engineering Geology*, vol. 20, no. 5, pp. 760–767, 2012.
- [10] Z. Kuang, "Study on characteristics, deformation mechanisms and control of dangerous rock and rock fall in central area of Chongqing city," *Journal of Geological Hazards and Prevention in China*, vol. 6, no. 3, pp. 51–56, 1995.
- [11] R. Huang, R. Deng et al., *Simulation of Whole Process of Material Movement in Overhanging Slope*, Chengdu University of Science and Technology Press, Chengdu, Sichuan, China, 1993.
- [12] Q. Zhang, G. Peng, S. Fu et al., "System identification of deformation-failure for the dangerous rock body of Lianzi cliff," *Chinese Journal of Rock Mechanics and Engineering*, vol. 17, no. 5, pp. 66–73, 1998.
- [13] Z. Li, W. Xiang, and M. Zhang, "Study on stability analysis and treatment plan of sliding dangerous rock mass," *Resource Environment and Engineering*, vol. 34, no. S2, pp. 83–89, 2020.
- [14] L. Zhang, D. Wang, G. Li, J. Dong, and J. Zhang, "Stability analysis and reliability evaluation in cataclastic loose rock mass blocks," *Advances in Civil Engineering*, vol. 2021, Article ID 5314937, 2020.
- [15] H. Tao, G. Xu, J. Meng, R. Ma, and J. Dong, "Stability assessment of high and steep cutting rock slopes with the SSPC method," *Advances in Civil Engineering*, vol. 2021, Article ID 8889526, 2021.
- [16] Y. Gong, "Study on the stability of dangerous rock based on limit equilibrium method and fracture mechanics method," *Gansu Water Resources and Hydropower Technology*, vol. 54, no. 9, pp. 48–51+65, 2018.
- [17] S. Xiao, "Stability analysis of dangerous rock based on limit equilibrium method," *Water Resources & Hydropower of Northeast China*, vol. 37, no. 12, pp. 52–72, 2019.
- [18] Y. Chen, "Stability analysis of slump dangerous rock mass," *Express Water Resources & Hydropower Information*, vol. 40, no. 7, pp. 23–26, 2019.
- [19] X. Li, P. Chen, and H. Shi, "Evaluating stability and its reliability of dangerous rock at abandoned Longsi mine in Jiaozuo," *Journal of Geological Hazards and Environment Preservation*, vol. 26, no. 3, pp. 92–97, 2015.
- [20] M. Zhao and X. Bu, "Analysis the application of rigid body limit equilibrium method to dangerous rock mass stability," *Journal of Changchun Institute of Technology (Natural Science Edition)*, vol. 14, no. 3, pp. 75–78+103, 2013.
- [21] B. Liu, Z. Pan, and J. Zheng, "Development characteristics and stability analysis of karst dangerous rock mass in Guilin city," *Journal of Natural Disasters*, vol. 22, no. 1, pp. 183–189, 2013.
- [22] Y. Zhang, W. Zhou, Z. Wu, F. Guo, and X. Zheng, "The development status of 3D geological modeling technology and modeling instances," *Journal of East China University of Technology (Social Science Edition)*, vol. 32, no. 3, pp. 403–409, 2013.
- [23] S. Doug and W. Andrea, "A critical review of rock slope failure mechanisms: the importance of structural geology," *Journal of Structural Geology*, vol. 74, pp. 1–23, 2015.
- [24] W. Liu, "Study on stability, movement characteristics and countermeasures of potential unstable rock mass in high-steep slope," *Chengdu University of Technology*, 2008.
- [25] H. Chen, H. Tang, and R. Wang, "Calculation method of stability for unstable rock and application to the three gorges reservoir," *Rock Mechanics and Engineering*, vol. 23, no. 4, pp. 614–619, 2004.
- [26] H. Chen, X. Xiang, H. Tang et al., "A massive development mechanism and countermeasures for perilous rocks in the Three Gorges Reservoir area of P. R. China: the example of the Taibaiyan cliff at Wanzhou," *Journal of Chongqing University*, vol. 31, no. 10, pp. 1178–1184, 2008.
- [27] Y. Zhang, *Study on the Risk Analysis of the Fenghuangshan's Landslides in Yan'an*, Chang'an University, Yanan, China, 2008.
- [28] G. Deng, *Study on Risk Assessment of Loess Landslide Disaster: A Case Study of Loess Landslide in Baota District, Yanan*, Chang'an University, Shaanxi, China, 2008.

Research Article

FEA of Effects Induced by Diurnal Temperature Variation on Downstream Surface of Xiaowan Arch Dam

Huanhuan Li ¹, Shaojun Fu ², Gang Li ¹ and Guofei Hu ³

¹Shaanxi Key Laboratory of Safety and Durability of Concrete Structures, Xijing University, Xi'an, China

²School of Civil Engineering, Wuhan University, Wuhan, China

³Anhui Institute of Building Research and Design, Hefei, China

Correspondence should be addressed to Shaojun Fu; sgjg@whu.edu.cn

Received 18 April 2021; Accepted 19 June 2021; Published 30 June 2021

Academic Editor: Chi Yao

Copyright © 2021 Huanhuan Li et al. This is an open access article distributed under the Creative Commons Attribution License, which permits unrestricted use, distribution, and reproduction in any medium, provided the original work is properly cited.

In order to make clear the cracking reasons in arch dam of Xiaowan Hydropower Station during operation period, the approach to combine ANSYS with finite element program COCE-3D is adopted. Firstly, the influence by element type and mesh size for the temperature field simulation result is analyzed. Subsequently, the three typical dam segments cut from Xiaowan arch dam are selected and the relevant finite element model is established; the effect of the measured diurnal air temperature on temperature field and temperature stress of arch dam is analyzed thoroughly. The results indicate that the temperature gradient in mass concrete becomes lower, whereas the affecting depth becomes deeper when the mesh size is too large. Therefore, it is advisable to use smaller size mesh to study the influence of the measured diurnal air temperature on the surface temperature distribution in mass concrete. The temperature of downstream zone in arch dam is significantly affected by air temperature; the changing laws of temperature field and temperature stress with the air temperature are basically consistent, which is sensitive to lower temperature. When the temperature sharply decreased, the temperature stress in the downstream zone is mainly in tensile stress state. The calculated results are basically consistent with the measured results, and the temperature stress induced by the day-night temperature difference is the important reason for the horizontal cracks on the downstream surface. The submodel analysis method is an important alternative approach to study the changing laws of temperature field of arch dam. The research results not only provide an evidence for temperature control and crack prevention of Xiaowan arch dam but also provide a reference for temperature field simulation of similar projects.

1. Introduction

It is acknowledged that thermal load is one of the important reasons for concrete arch dam cracking, both during construction and operation [1–4]. During the construction, due to the exothermic reactions, a lot of hydration heat cannot be released in time, resulting in the increase of internal temperature gradient and thermal stress, which leads to cracks. It is usually controlled by cooling water pipes or lowering concrete pouring temperature. Due to the influence of external environment, the cracking of arch dam during operation is still a difficult problem [5, 6]. As for the causes of cracks during the operation, Zhu proposed that the fundamental reason was that the influence of nonlinear temperature difference and cold wave was not considered in the

calculation of temperature load. Furthermore, he proposed that permanent surface thermal insulation was an effective method to prevent cracks occurring in arch dams during operation [7]. Temperature cracks problem was an important research topic in the field of high arch dam structure. To date, lots of achievements [3] related to thermal stress and temperature cracks of concrete dams mainly are focused on the influence of the diurnal temperature variation during the construction [8, 9], and the annual temperature [10], seasonal temperature variations [4, 11, 12], solar radiation [13, 14], and water temperature variations [1] during the operation. The results show that the cold wave or the diurnal temperature variation will affect the thermal field within a certain range below the concrete surface and lead to the surface cracks [15].

Xiaowan hydropower station, which is located in the middle reach of the Lancang River, is primarily for power generation and can also make other comprehensive utilization benefits such as flood control. Xiaowan arch dam is a parabolic double-curvature concrete dam, with the dam crest elevation of 1245 m, the maximum dam height of 294.5 m, the arc length of the crest centerline of 892.8 m, the bottom width of the crown cantilever of 69.49 m, and the crest width of the crown cantilever of 13 m. The dam includes 5 open surface spillways, 6 middle discharge holes, and 2 emptying bottom holes. During the service period of the arch dam, some horizontal and irregular cracks with different lengths are found on the arch dam downstream surface at the elevation of 1150 m to 1190 m through the field inspection. In order to find out the causes of cracks at the downstream side of Xiaowan arch dam, the temperature effect of concrete under the action of diurnal temperature variation is studied. It is necessary to establish a finite element model with smaller mesh size and select the calculation time step in hours. Due to the great difference between the size of the study area and that of the whole dam, it requires large computation scale and high request on computer hardware if establishing a finite element model for the whole dam. In order to better analyze the influence of the diurnal temperature variation on the thermal field and thermal stress field of the downstream-side concrete of Xiaowan arch dam, firstly, the sensitivity of element type and mesh size to the thermal field was analyzed. Subsequently, the 27#~29# typical segments of Xiaowan arch dam were taken as an example to establish 3-D finite element submodel, and the method of combining the whole model and the submodel [16] was adopted to simulate the changing law of thermal field and thermal stress field at the downstream side of arch dam under the action of diurnal temperature variation. Finally, the cause of cracks at downstream side of Xiaowan arch dam was revealed. It provides the guideline for temperature control and crack prevention of Xiaowan arch dam and reference for similar projects.

2. Computational Principles of Thermal Field and Thermal Stress

2.1. Thermal Field. According to the principle of thermal balance, the heat absorbed as the temperature rise is equal to the sum of the net heat flowing in from the outside and the heat of hydration inside. As for the isotropy, the basic equation of heat conduction in the 3-D transient thermal field is

$$a\left(\frac{\partial^2 T}{\partial x^2} + \frac{\partial^2 T}{\partial y^2} + \frac{\partial^2 T}{\partial z^2}\right) + \frac{\partial \theta}{\partial \tau} = \frac{\partial T}{\partial \tau}, \quad (1)$$

where θ is the adiabatic temperature rise of concrete ($^{\circ}\text{C}$), $\alpha = \lambda/c\rho$, λ is the thermal conductivity of concrete ($\text{kJ}/(\text{m} \cdot \text{h} \cdot ^{\circ}\text{C})$), c is the specific heat of concrete ($\text{kJ}/(\text{kg} \cdot ^{\circ}\text{C})$), ρ is the concrete density (kg/m^3), and τ is time (h).

For (1), the unique solution can be obtained by introducing corresponding initial conditions and boundary conditions [17]. According to the variation principle, the governing equation of finite element can be derived:

$$[H]\{T\} + \{F\} = 0, \quad (2)$$

where $[H]$ is the heat conduction matrix and $\{F\}$ is the thermal flow array.

2.2. Thermal Stress. From the elastomer hypothesis, it can be known that the coefficient of thermal expansion of a material is constant in all directions; that is to say, the positive strain does not change with direction or does not produce angular strain. Assuming the temperature variation on each node in the elastomer is ΔT , the coefficient of thermal expansion is α , and the produced free deformation is $\alpha\Delta T$, the corresponding initial strain arising therefrom shall be

$$\{\varepsilon^0\} = \{\varepsilon_x^0, \varepsilon_y^0, \varepsilon_z^0, \gamma_{xy}^0, \gamma_{yz}^0, \gamma_{zx}^0\} = \alpha\Delta T\{1, 1, 1, 0, 0, 0\}^T. \quad (3)$$

The total strain of elastomer is composed of the strain generated by temperature difference and the strain generated by other stresses, so the stress-strain relationship shall be

$$\{\sigma\} = [D](\{\varepsilon\} - \{\varepsilon^0\}) = [D][B]\{\delta\}^e - [D]\{\varepsilon^0\}. \quad (4)$$

And the relationship between node force and node displacement can be expressed as

$$\{F\}^e = [K]^e\{\delta\}^e + [F_{\Delta T}]^e, \quad (5)$$

where $\{\sigma\} = \{\sigma_x, \sigma_y, \sigma_z, \tau_{xy}, \tau_{yz}, \tau_{zx}\}^T$; $[D]$ is the elastic matrix of element; $[B]$ is the characteristic matrix of element; $\{\delta\}^e$ is the node displacement matrix of element; $[K]^e$ is the stiffness matrix of element; and $[F_{\Delta T}]^e = -\int \int \int_e [B]^T [D]\{\varepsilon^0\} dx dy dz$ is the equivalent nodal load generated by temperature variation.

3. Basic Information of the Project

3.1. Daily Temperature of Dam Site. According to the air temperature measured at the weather station (hourly variation), the process of temperature changes in the winter of 2014 (from 14 h on January 24 to 14 h on January 28) and in the summer of 2013 (from 14 h on June 11 to 14 h on June 15) is shown in Figure 1, where the maximum diurnal temperature variation is 19°C .

3.2. Water Temperature of the Reservoir. The normal impounding water level of Xiaowan is 1240 m during operation, and the water level of the corresponding downstream plunge pool is 1004 m. The average annual water temperature on the surface of Xiaowan reservoir is 20.6°C , and the annual amplitude of the water temperature on the surface (including the influence of sunlight) is 6.0°C . The water temperature under the elevation of 1120 m is constant at 10°C , while the water temperature in the elevation range from 1120 m to 1240 m is computed according to the following equations [17]:

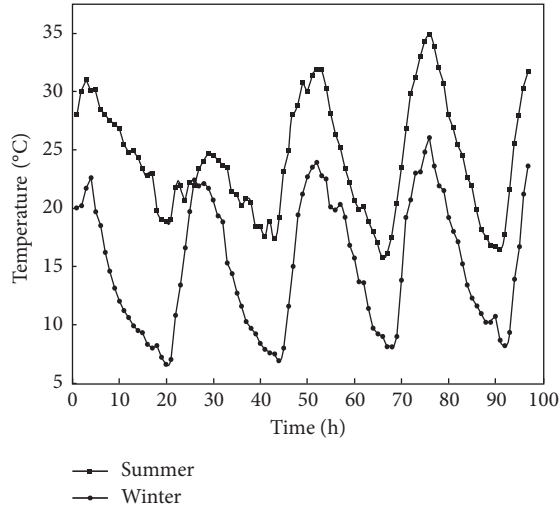


FIGURE 1: Temperature variation chart of typical time period.

$$T(y, t) = T_m(y) + A_0 e^{-0.048y} \cos \omega(t - t_0 - \varepsilon),$$

$$T_m(y) = \frac{T_b - T_s e^{-0.04H}}{1 - e^{-0.04H}} + \left(T_s - \frac{T_b - T_s e^{-0.04H}}{1 - e^{-0.04H}} \right) e^{-0.04y}, \quad (6)$$

where $T(y, t)$ is the temperature at depth y at time t (°C); A_0 is the average of the difference values of the monthly maximum and minimum temperatures; ω is the cycle of daily temperature change, taking $\pi/12$; ε is the phase difference between water temperature and air temperature; T_b is the average annual water temperature at the bottom of the reservoir (°C), taking 10°C; T_s is the monthly air temperature on the surface plus the sunlight (°C); t is the time when the calculation conducted (h); t_0 is the time of the highest temperature (h), generally taking 14 h; H is the reservoir depth (m); and y is the water depth (m).

3.3. Thermodynamic Property of Dam Concrete. The dam concrete was divided into A, B, and C; these three zones and the thermal and mechanical parameters of concrete could be found in Table 1.

4. Analysis Models and Analysis Methods

4.1. Sensitivity Analysis of Element Type and Mesh Size. The simulated calculation of thermal field [20] showed that the element type and mesh scale significantly influenced the precision of computation results. In general, to the mesh scale with the same element type, if the mesh scale is large, the calculation precision is low. Otherwise, the calculation precision is high but the efficiency is low. Therefore, the complex engineering problems could not even be realized on a microcomputer. Therefore, to investigate the influence of the element type and the mesh scale on the precision of simulating results of concrete thermal field, especially the influence of the external air temperature on the gradient of thermal field in the surface region of concrete, a simple

example should be first established to analyze the sensitivity of mesh scales and element types to the precision of computation.

To a rectangle model with size of $2m \times 2m \times 4m$, two element types and three mesh scales were adopted discretely (as shown in Table 2). C_{18040} is taken as the thermal parameter, the initial temperature is the uniform temperature of 20°C, and the air temperature boundary is the winter temperature curve as shown in Figure 1.

Figure 2 shows the cloud chart of the thermal field of above four schemes at 20h. From Figure 1, it could be known that the air temperature at 20h is 6.6°C, so by comparing the four schemes, the results are shown such that the range of temperature gradient of scheme 1 and scheme 4 is 12.8°C–20°C, and the influence depth is about 0.35 m. The temperature variation range of scheme 3 is 16.1°C–20°C, and the influence depth is about 0.8 m, roughly twice as much as options 1 and 2. Scheme 4 has the same temperature variation range as that in schemes 1 and 2 and has the same influence depth of air temperature as that in scheme 3.

Figure 3 is the temperature course curves of a node on the external surface of the models in four schemes. From Figure 3, it could be known that the trend and amplitude of temperature variations of schemes 1, 2, and 4 are the same, while the amplitude of temperature variation of scheme 3 is smaller and its peak time obviously lags behind that of its peak time of air temperature.

In conclusion, we have the following: (1) The temperature distribution law and the variation process of schemes 1 and 2 are consistent with the understanding of relevant literatures [1, 15]. (2) When the element type is the same, if the mesh size is too large, the surface temperature range of concrete is small, and the calculated value of temperature influence depth is large. (3) When the mesh size is the same, the calculation precision of surface temperature could be improved by using the high-order element, but the precision of the influence range is not improved. Therefore, an 8-node hexahedral element is applied in the paper, and the element scale in the direction of dam thickness is controlled within the range of 0.1 m–0.5 m.

4.2. Finite Element Mesh. By considering the element with small scale and its computation scale, 27#~29# dam segments of Xiaowan arch dam were selected as research objects (as shown in Figure 4(a)) to be conducted discretely by using 8-node hexahedral element. The element scale in the direction of dam thickness was controlled within 0.1 m–0.5 m, while the element scales in vertical direction and at right angle were controlled at about 10 times the element scale in the direction of thickness. The finite element mesh of submodels was shown in Figure 4(b), with total elements of 669,960 and with total nodes of 721,315.

4.3. Initial Conditions and Boundary Conditions. For stress and strain analysis, it was agreed in the coordinate system that the X -axis pointing to the left bank was positive, the Y -axis pointing to the upstream was positive, and the Z -axis upwards was positive.

TABLE 1: Thermal and mechanical parameters of dam concrete.

Parameter	Concrete grade			
	C ₁₈₀₄₀	C ₁₈₀₃₅	C ₁₈₀₃₀	
Thermal conductivity	kJ/(m·h°C)	8.479	8.227	8.016
Thermal diffusivity	m ² /h	0.003239	0.003116	0.002991
Density	kg/m ³		2500	
Specific heat	kJ/(kg°C)	1.047	1.056	1.072
Coefficient of linear expansion	10 ⁻⁶ /°C	8.26	8.15	8.1
Heat exchange coefficient	kJ/(m ² ·h°C)		47.1	
Elasticity modulus	10 ⁴ MPa	3.21	3.11	3.01
Poisson's ratio		0.24	0.167	0.167
Compressive strength	R _a /MPa	45.5	39.7	34.4
Tensile strength	R _t /MPa	3.52	3.36	3.07
Safety factor against cracking on the surface [18, 19]			1.4–1.5	

TABLE 2: Element types and mesh sizes.

Scheme	Element type	Mesh size (in the direction of thickness) (m)
1	8-node hexahedral element	0.1
2	8-node hexahedral element	0.2
3	8-node hexahedral element	1
4	20-node hexahedral element	1

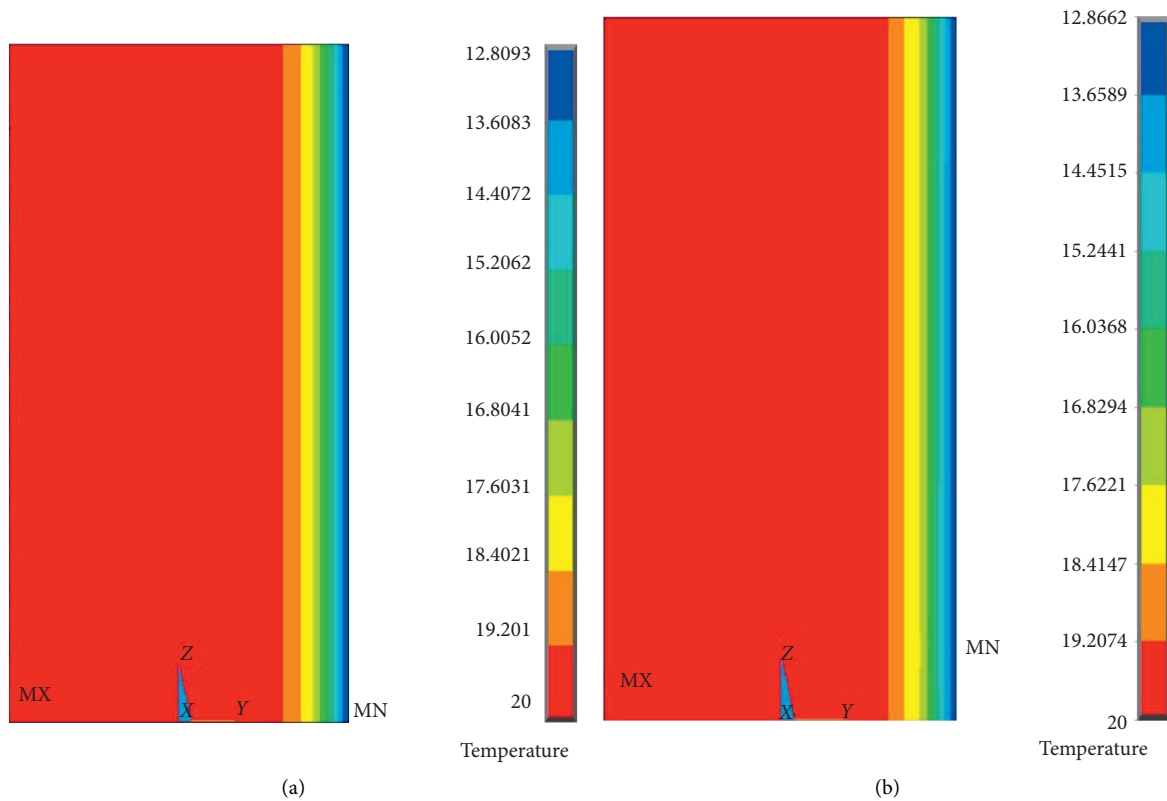


FIGURE 2: Continued.

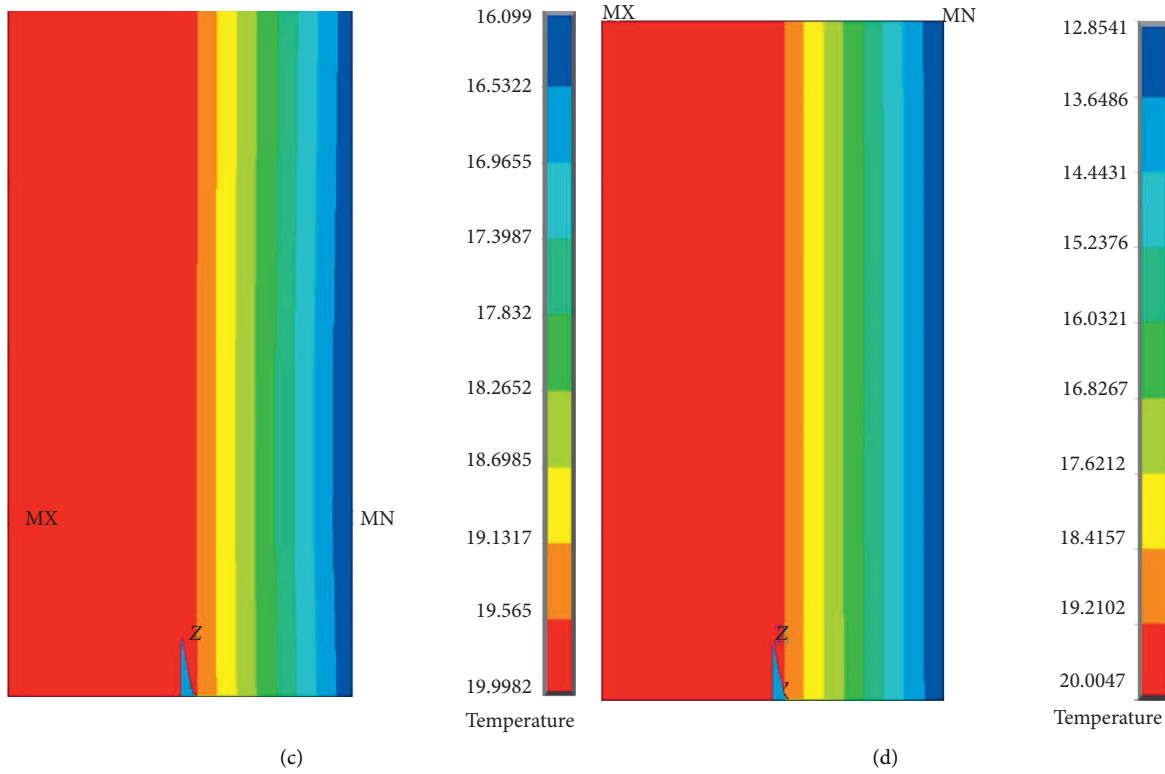


FIGURE 2: Cloud chart of thermal field at 20 h. (a–d) Temperature.

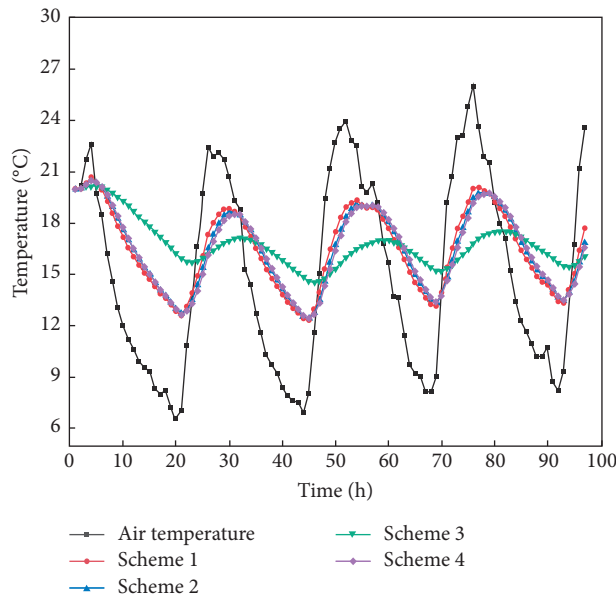


FIGURE 3: Temperature course curves of a node on outside surface.

Boundary conditions: in the computation of thermal field, the water temperature at the boundary between the dam and water was taken according to the first boundary condition, and the boundary between the dam and air was selected according to the third boundary condition, while the bottom and two sides of the foundation were treated according to the adiabatic condition. And in the

computation of stress field, the bottom of the foundation was fixed, the four sides of the foundation and the two sides of the dam were normal constraints, and the rest were free surfaces.

Initial conditions: for thermal field analysis, the diurnal temperature variation of typical days in winter and summer was investigated, respectively. According to the measured

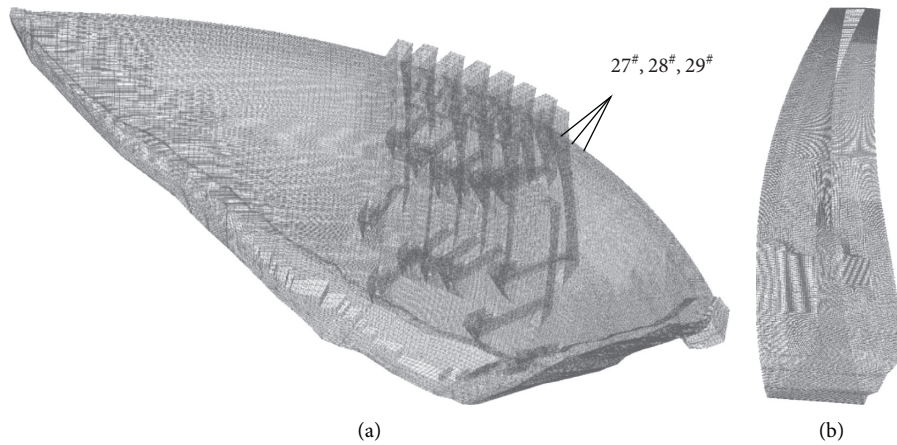


FIGURE 4: Finite element mesh of Xiaowan arch dam: (a) the whole model and (b) the submodel.

data, the time from 14:00 on January 24 to 14:00 on January 28 of 2014 was selected as winter period and the time from 14:00 on June 11 to 14:00 on June 15 of 2013 was selected as summer period. The thermal fields corresponding to 14:00 on January 24 of 2014 and 14:00 on June 11 of 2013 were respectively served as the initial condition. Since the stress-strain analysis only considered the increment caused by the diurnal temperature difference, the initial stress field was set as 0.

4.4. Analysis Methods

4.4.1. Thermal Field Analysis. The arch dam was closed by grouting to the dam crest on June 11, 2010, and by 2013, the internal temperature of the dam was stabilized and the temperature on the dam surface was mainly influenced by the external air temperature and the reservoir water temperature. In view of the calculation scale of the simulated analysis of thermal field for the whole dam section and the whole process, the mesh scale was larger than 1 m, and the time step was “day”. Therefore, when the results of the simulated analysis of thermal field for the whole dam section and the whole process were applied to analyze the effect of diurnal temperature variation of precise submodels (the time step was “hour”), the initial temperature conditions should be properly treated. And the effect of diurnal temperature variation on January 26, 2013 and June 13, 2014 was investigated respectively as winter and summer periods, so the initial value of node temperature of 27[#]~29[#] finite element mesh models could be obtained through the interpolation of the simulated analysis results of the whole dam section and the whole process in the thermal fields at 14:00 on January 24, 2013 and June 11, 2014. Subsequently, the boundary conditions of daily air temperature and water temperature were applied to 27[#]~29[#] submodels for simulated calculation, with 2 days apart from January 26, 2013 and June 13, 2014, respectively, not having obvious influence on the precision of typical daily thermal field results.

ANSYS software was applied to analyze the thermal field, with total computation time of 4 days, time step as “hour”, and 96 computation steps in total. The initial conditions

should be set according to the methods mentioned above, and the boundary conditions of air temperature and water temperature were simulated according to Sections 3.1 and 3.2.

4.4.2. Stress-Strain Analysis. This paper focused on the state of incremental stress generated by the diurnal temperature variation, so as to explain the possibility of cracking caused by the diurnal temperature variation. Therefore, the linear elastic finite element calculation was carried out on 27[#]~29[#] dam section models by considering the action of diurnal temperature variation, and the concrete was considered as a homogeneous isotropic elastomer.

The calculation of period and step length kept consistent with that of thermal field, and the temperature action was the difference between the simulated calculation of the thermal field results at a certain time and that at the previous time, and so on. The incremental method was adopted to calculate the stress and strain. Since the concrete pouring had been finished for about 3–4 years and the analysis time was short, the creep was not taken into account.

Self-developed finite program COCE-3D was adopted for the finite element calculation of stress-strain, the program was successfully applied in many large-scale hydropower projects such as the Three Gorges hydropower station, Longtan hydropower station, Xiluodu hydropower station, and Xiaowan hydropower station, [21, 22].

5. Results

5.1. Result Analysis of Thermal Field. For the convenience of analyzing, two points *P1* and *P2* at the downstream side of the dam were selected, where *P1* was located at the downstream side with elevation of 1190 m and *P2* was located at the downstream side with elevation of 1150 m, as shown in Figure 5.

Figure 6 shows the temperature-time curves of the two representative points, from which we could know the following: (1) The temperature on the downstream surface was significantly influenced by the air temperature variation, and its variation law was consistent with that of air temperature,

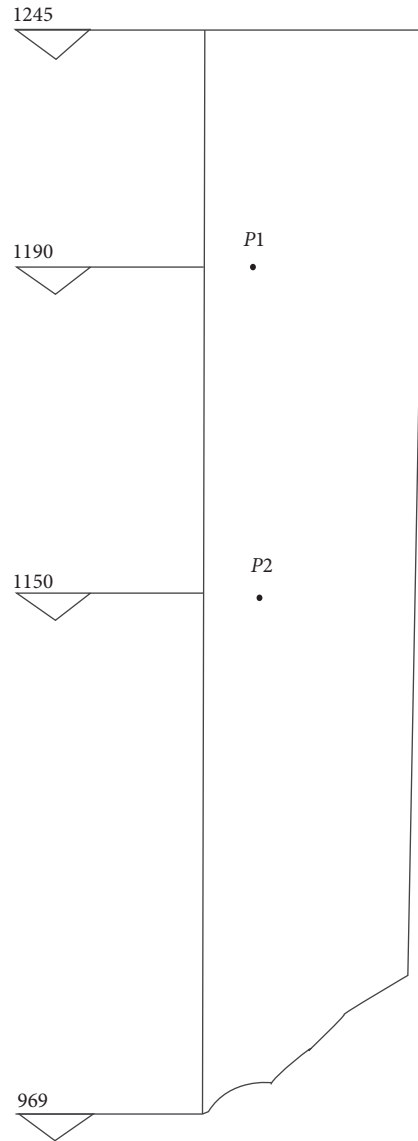


FIGURE 5: Position of representative points.

presented as a cosine curve, but the peak time of the dam surface temperature had an obvious hysteresis effect compared with that of the air temperature, about 2 hours lagging behind. This is consistent with the research rule in reference [1, 23]. (2) Under the same action of air temperature variation law, values of temperature variation at $P1$ and $P2$ were basically consistent with the variation law. (3) The temperature gradient of concrete surface was affected more obviously by the change of diurnal temperature variation in winter.

Figure 7 shows the temperature curves of two typical time periods in the direction of dam thickness, where 4 moments (24 h, 48 h, 72 h, and 96 h) were listed for each season. The compute node was taken every 0.15 m from the surface to the inside. From Figure 7, it could be found that a curve near the surface had a larger slope, which indicated that the temperature gradient in the region of this part was larger, and the air temperature had greater influence on the concrete of this part. When the distance

reached a certain depth, the slope of curve was very small, almost developing into a straight line, which showed that the temperature gradient in the deep region was very small, and air temperature changes had little influence on it; the influence law is consistent with reference [14, 24, 25]. In the region where the temperature gradient had larger changes, and if the distance kept unchanged, as the computation time increased, the slope of curve decreased; for example, the slope of temperature curve at 24 h was larger than that at 96 h, which explained that the shorter the action time of temperature changes, the larger the temperature gradient in the affected region.

When the influence depth of air temperature changes on concrete temperature was taken into consideration, the corresponding influence depth could be determined according to the difference of internal temperature variation amplitude; for example, the internal temperature variation was considered as 0.1, 0.05, and 0.01 times of the surface

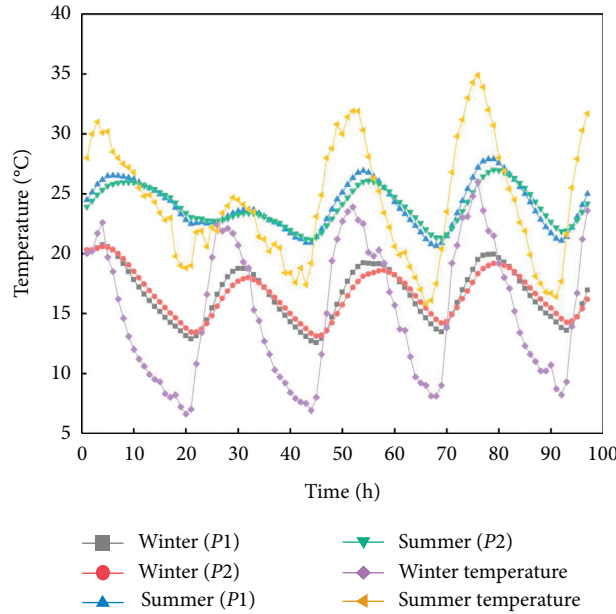


FIGURE 6: Temperature-time curves of two representative points at typical time.

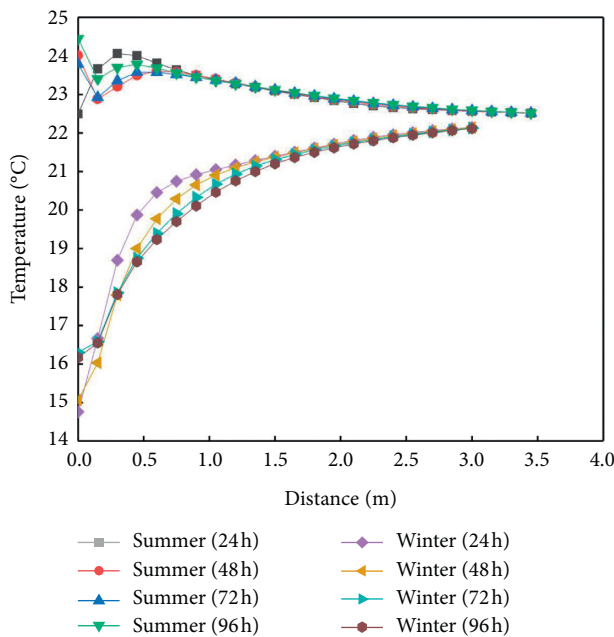


FIGURE 7: Temperature curves of typical time periods in the direction of dam thickness.

temperature variation amplitude of concrete. The influence depth of temperature at each condition is shown in Table 3, from which it could be known that the influence depth of temperature in winter was larger than that in summer.

In summary, the following conclusions could be drawn: (1) Air temperature changes in winter had greater influence on the thermal field of concrete; in other words, the concrete had sensitive temperature changes to temperature drop, a similar conclusion was obtained in reference [15]. (2) The longer the action time of the temperature difference, the greater depth of concrete affected by the temperature, but to

be kept unchanged after reaching a certain depth. (3) The shorter the action time of the temperature difference, the greater the change of temperature gradient of concrete surface in a certain range.

5.2. Result Analysis of Thermal Stress. According to the observation, the cracks at the downstream side of Xiaowan arch dam were mostly horizontal; therefore, the maximum main stress and changes of thermal stress in the Z direction were mainly discussed in this paper. Figure 8 shows the cloud charts of the maximum principal stress and the Z-direction stress at 68 h in winter (the external temperature of 8.1°C). From Figure 8, it could be known that the maximum principal stress and the Z-direction stress were almost the same in size and direction, both of which were tensile stress. Figure 9 shows the cloud charts of the maximum principal stress and the Z-direction stress at 76 h in winter (the external temperature of 23.6°C). From Figure 9, it could be known that the maximum principal stress and Z-direction stress were almost the same in size and direction, and a compressive stress appeared. The typical times in summer also had the similar laws, so it was not described in this paper.

Figure 10 shows the time curves of the normal stress in the Z-direction obtained at two representative points in two typical periods. From Figure 10, it could be known that the change law of Z-direction stress-time curves of the arch dam at P1 and P2 was consistent with that of temperature-time curves, both of which varied as cosine curve, which indicated that the stress state of concrete was greatly affected by the air temperature. The same rule was found in reference [23]. The Z-direction stress calculation results of both points at special moments are shown in Table 4.

In conclusion, under the action of diurnal temperature difference in winter, concrete at the downstream of arch dam

TABLE 3: Influence depth of air temperature.

Times of surface temperature variation amplitude	Time period			
	Winter		Summer	
	24 h	96 h	24 h	96 h
0.1	0.45	0.6	0.3	0.4
0.05	0.6	0.75	0.45	0.65
0.01	1.2	1.5	1.1	1.2

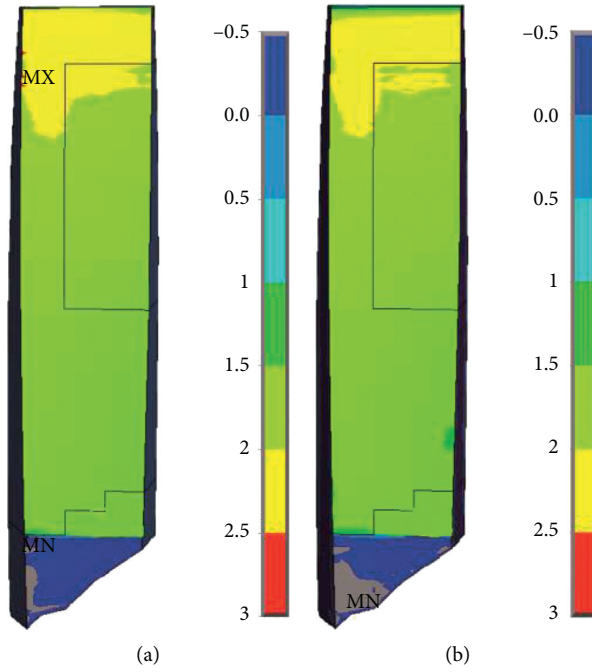


FIGURE 8: Stress contour at the downstream side of Xiaowan arch dam in winter (68 h): (a) the maximum principal stress and (b) the Z-direction stress.

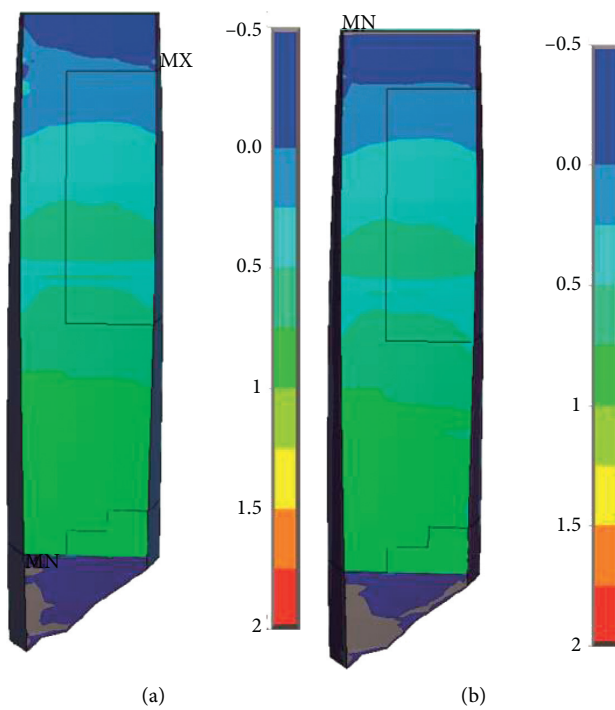


FIGURE 9: Stress contour at the downstream side of Xiaowan arch dam in winter (76 h): (a) the maximum principal stress and (b) the Z-direction stress.

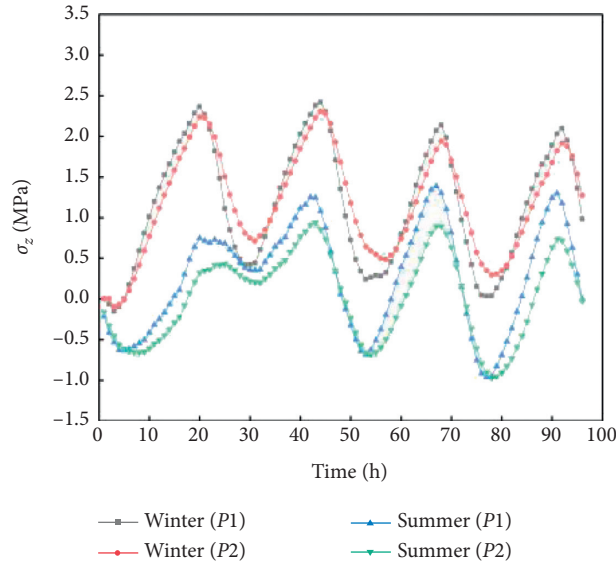


FIGURE 10: Z-direction stress-time curves of two representative points.

TABLE 4: Z-direction stress of two representative points at typical moments.

	Time (h)	External air temperature (°C)	P1 σ_z (MPa)	P2 σ_z (MPa)
Winter	20	6.6	2.35	2.20
	44	6.9	2.40	2.30
	68	8.1	2.20	1.90
	92	8.2	2.20	1.90
Summer	43	17.4	1.30	0.95
	67	16.1	1.40	0.90
	91	16.4	1.30	0.75

produced larger tensile stress, which indicated that the temperature variation of concrete was sensitive to the temperature drop. When the diurnal temperature variation was larger, the downstream side of arch dam generated larger tensile stress, about 2.4 MPa, and cracks occurred when the tensile stress caused by thermal stress and other loads exceeded the tensile strength of concrete. The measured positions of cracks were basically around the elevation of 1190 m and 1150 m, almost the same to calculated positions of tensile stress, so it showed that larger diurnal temperature variation was one of the main causes of horizontal cracking at the downstream side of Xiaowan arch dam.

6. Conclusions

Based on ANSYS and the self-developed COCE-3D finite element software and adopting the method of combing the integral model and submodel, the sensitivity of element types and mesh scales to the calculation results of thermal field were calculated and analyzed, and the change process of thermal field and thermal stress in three standard dam segments (27[#]~29[#]) during typical periods in winter and summer was also analyzed. The conclusions are as follows:

- (1) When the same element type and different mesh sizes were used to calculate the thermal field, the mesh size was too large, so that the temperature gradient of concrete surface changed slowly, and the influence depth by temperature was greatly deep. When the high-order element was used for calculation, yet the calculation precision of surface temperature was improved, the precision of the scope of influence had not.
- (2) The downstream side of arch dam was greatly affected by the air temperature, especially sensitive to the diurnal temperature variation in winter. The shorter the action time of air temperature, the greater the changes of temperature gradient of dam concrete surface; the longer the action time of air temperature, the greater the influence depth of concrete temperature, but to be kept unchanged after reaching a certain depth. As the air temperature changed, the temperature variation of concrete had different hysteresis effect.
- (3) The thermal stress of concrete at downstream side of arch dam was larger, and the change law of thermal stress was basically consistent with that of air temperature. The maximum principal stress

and Z-direction stress were almost the same in direction. When the temperature dropped sharply, the thermal stress was mainly a tensile stress, and when the temperature increases, a compressive stress appeared.

- (4) The calculation results of thermal stress was basically consistent with the positions of measured cracks, which indicated that the thermal stress generated by the diurnal temperature variation was one of the important causes of horizontal cracking at the downstream side of Xiaowan arch dam.
- (5) The combination of the integral model and submodel is an effective method to study the thermal field and the change law of thermal stress of dam concrete surface, so as to obtain satisfactory results.

Data Availability

The data used to support the findings of this study are available from the corresponding author upon request.

Conflicts of Interest

The authors declare that they have no conflicts of interest.

Acknowledgments

This study was supported by the Special Fund for Scientific Research by Shaanxi Provincial Education Department (20JK0962) and Special Fund for Natural Science Basic Research Program of Shaanxi Province (2021JQ-872).

References

- [1] F. Sheibany and M. Ghaemian, "Effects of environmental action on thermal stress analysis of Karaj concrete arch dam," *Journal of Engineering Mechanics*, vol. 132, no. 5, pp. 532–544, 2006.
- [2] F. Jin, Z. Chen, J. Wang, and J. Yang, "Practical procedure for predicting non-uniform temperature on the exposed face of arch dams," *Applied Thermal Engineering*, vol. 30, no. 14, pp. 2146–2156, 2010.
- [3] F. Salazar, D. J. Vicente, J. Irazábal, I. De-Pouplana, and J. San Mauro, "A review on thermo-mechanical modelling of arch dams during construction and operation: effect of the reference temperature on the stress field," *Archives of Computational Methods in Engineering*, vol. 27, no. 5, pp. 1681–1707, 2020.
- [4] F. Pettersson and F. Hjalmarsson, *Finite Element Analysis of Cracking of concrete Arch Dams Due to Seasonal Temperature Variation*, Lund University, Lund, Sweden, 2017.
- [5] M. Li, W. Si, S. Du, M. Zhang, Q. Ren, and Y. Shen, "Thermal deformation coordination analysis of CC-RCC combined dam structure during construction and operation periods," *Engineering Structures*, vol. 213, Article ID 110587, 2020.
- [6] S. J. Fu, T. He, G. J. Wang, S. H. Zhang, L. C. Zou, and S. H. Chen, "Evaluation of cracking potential for concrete arch dam based on simulation feedback analysis," *Science China*, vol. 54, no. 3, pp. 565–572, 2011.
- [7] B. F. Zhu, "On permanent superficial thermal insulation of concrete arch dams," *Water Power*, vol. 08, pp. 21–30, 2006.
- [8] E. Y. Sayed-Ahmed, A. A. Abdelrahman, and R. A. Embaby, "Concrete dams: thermal-stress and construction stage analysis," *Dams and Reservoirs*, vol. 28, no. 1, pp. 1–19, 2017.
- [9] C. Eloísa, S. Noemí, T. Carlos, and B. F. M. Luísa, "FEA model for the simulation of the hydration process and temperature evolution during the concreting of an arch dam," *Engineering Structures*, vol. 174, pp. 165–177, 2018.
- [10] D. Santillan, E. Salete, and M. A. Toledo, "A methodology for the assessment of the effect of climate change on the thermal-strain–stress behaviour of structures," *Engineering Structures*, vol. 92, no. 1, pp. 123–141, 2015.
- [11] J. Enzell and M. Tollsten, *Thermal Cracking of a concrete Arch Dam Due to Seasonal Temperature Variations*, Royal Institute of Technology (KTH), Stockholm, Sweden, 2017.
- [12] R. Malm, R. Hellgren, and J. Enzell, "Lessons learned regarding cracking of a concrete arch dam due to seasonal temperature variations," *Infrastructure*, vol. 5, no. 2, pp. 1–18, 2020.
- [13] H. Mirzabozorg, M. A. Hariri-Ardebili, and M. Shirkhan, "Impact of solar radiation on the uncoupled transient thermo-structural response of an arch dam," *Scientia Iranica*, vol. 22, no. 4, pp. 1435–1448, 2015.
- [14] D. Santillán, E. Salete, D. J. Vicente, and M. Á. Toledo, "Treatment of solar radiation by spatial and temporal discretization for modeling the thermal response of arch dams," *Journal of Engineering Mechanics*, vol. 140, no. 11, Article ID 05014001, 2014.
- [15] G. Liu, "Numerical simulation and analysis of the temperature effects on the fission of concrete," *Thermal Science*, vol. 23, no. 5A, pp. 2713–2720, 2019.
- [16] L. F. Song, M. X. Wu, J. T. Wang, and Y. J. Xu, "Seismic damage analysis of the outlet piers of arch dams using the finite element sub-model method," *Earthquake Engineering and Engineering Vibration*, vol. 03, pp. 617–626, 2016.
- [17] B. F. Zhu, *Temperature Stress and Temperature Control of Mass concrete*, China Electric Power Press, Beijing, China, 1999.
- [18] The Professional Standards Compilation Group of People's Republic of China, *Design Specification for concrete Arch Dams*, China Electric Power Press, Beijing, China, 2007.
- [19] The Professional Standards Compilation Group of People's Republic of China, *Design Specification for concrete Arch Dams*, China Electric Power Press, Beijing, China, 2018.
- [20] G. F. Hu, *Surface Crack Analysis of Xiaowan High Arch Dam during Operation Period*, Wuhan University, Wuhan, China, 2016.
- [21] X. Zhang, W. M. Wang, and S. H. Chen, "Research on reinforcement measure of embankment cracks of Xiaowan arch dam," *Chinese Journal of Rock Mechanics and Engineering*, vol. 30, no. 4, pp. 657–665, 2011.
- [22] S. J. Fu, S. H. Zhang, M. Xie, and S. H. Chen, "Dynamic analysis theory and practice for temperature control and cracking prevention of concrete arch dam," *Chinese Journal of Rock Mechanics and Engineering*, vol. 31, no. 1, pp. 113–122, 2012.
- [23] H. H. Zhang, P. Z. Wang, S. H. He, Y. Li, K. F. Chen, and N. N. Sun, "Research of thermal effect of cable-stayed bridge with a separated side-box steel-concrete composite girder under solar radiation," *Advances in Civil Engineering*, vol. 2021, Article ID 8812687, 17 pages, 2021.
- [24] S. R. Abid, N. Tayşi, and M. Ozakca, "Temperature records in concrete box-girder segment subjected to solar radiation and air temperature changes," *IOP Conference Series: Materials Science and Engineering*, vol. 870, no. 1, Article ID 012074, 2020.
- [25] B. Gu, Z. J. Chen, and X. D. Chen, "Temperature gradients in concrete box girder bridge under effect of cold wave," *Journal of Central South University*, vol. 21, no. 3, pp. 1227–1241, 2014.

Research Article

Trajectory Analysis and Risk Evaluation of Dangerous Rock Mass Instability of an Overhang Slope, Southwest of China

Wen-lian Liu,^{1,2} Jia-xing Dong ,³ Han-hua Xu,^{1,2} Su-gang Sui,^{1,2} Run-xue Yang,³ and Lun-shun Zhou³

¹Kunming Prospecting Design Institute of China Nonferrous Metals Industry Co., Ltd., Kunming, Yunnan 650051, China

²Yunnan Key Laboratory of Geotechnical Engineering and Geohazards, Kunming, Yunnan 650051, China

³Faculty of Electric Power Engineering, Kunming University of Science and Technology, Kunming, Yunnan 650500, China

Correspondence should be addressed to Jia-xing Dong; dong1986@kust.edu.cn

Received 23 April 2021; Accepted 28 May 2021; Published 24 June 2021

Academic Editor: Faming Huang

Copyright © 2021 Wen-lian Liu et al. This is an open access article distributed under the Creative Commons Attribution License, which permits unrestricted use, distribution, and reproduction in any medium, provided the original work is properly cited.

Analysis of the movement trajectory and risk assessment of the high-slope dangerous rock mass collapse are of great significance for preventing and controlling the geological disasters of collapse. This study firstly takes the dangerous rock mass of the high slope in Pu'erdu Town, Yanjin County, Zhaotong City, Yunnan Province, as the research object, calculates and analyzes the trajectory of collapse movement of several groups of dangerous rock mass with great threat, and RocFall are used to carry out numerical simulation analysis and verification. Secondly, the risk and vulnerability of the dangerous rock mass in the study area are analyzed, and the risk evaluation is carried out through the risk evaluation matrix to clearly define the risk level. Results show that if the dangerous rock mass collapses, the horizontal movement distance was approximately 53–88 m, and the maximum bounce height of the platform was approximately 3–18 m, which will seriously threaten the life and property safety of residents. There is little difference between the simulation of the collapse of dangerous rock mass by RocFall software and the calculation result of the formula. Although RocFall software is more intuitive and can be directly compared with charts, software cannot completely simulate the actual situation, and it is only suggested as a reference from design rather than a basis of design. The result of risk evaluation shows that there are 2 high-risk dangerous rocks, 3 medium-risk dangerous rocks, and 1 low-risk dangerous rock in this area. It is suggested that a reasonable and scientific engineering treatment scheme should be put forward as soon as possible in combination with the collapse trajectory of the collapsing movement.

1. Introduction

Pu'er Town, Yanjin County, Zhaotong City, Yunnan Province, is an area where the geological hazards are most developed in Yunnan Province, especially with landslides, collapses, debris flow, etc. For instance, on July 18, 2005, a landslide occurred in the residential area of the Pu'er branch of Yanjin Vocational Middle School. The crack was more than 30 meters long and the crack width was about 30 cm. The overall downward trend involved an area of more than 0.7 acres, which directly threatened 22 residents, two government agencies, 10 people in the family planning station, and a middle school, totally about 35 million yuan in property threatened. On August 29, 2007, a collapse

occurred above Shijie Community of Tiaoqiao, Pu'er Town, and a house was smashed, the stone weighing about 2 tons, endangering 21 people in 8 households and causing a direct economic loss of 800,000 yuan. On August 10, 2008, hit by heavy rain, a collapse occurred on the left side of Guanyinyan (Bench Rock) in Tiaoqiao Community, Pu'er Town, accompanied by debris flow, resulting in varying degrees of damage to 13 households; one person was injured, and 15 pigs washed away. The direct economic loss is more than 2 million yuan. The frequent occurrence of geological hazards threatens the life and property safety of the people in Pu'er Town, causing huge losses to the national economy and severely restricting the development of the local economy. Therefore, it is very urgent and necessary to analyze the

trajectory of the collapse of the dangerous rock mass in the disaster area and evaluate the risk to prevent the geological disaster from further causing casualties and property losses.

At present, the analysis methods of the falling path trajectory of the dangerous rock mass mainly include field test, empirical discrimination, and theoretical calculations. For example, the prediction formula for falling rock movement trajectory proposed by Bobbert et al. [1] and Dorren [2] has proposed the DOA model (reach angle model) of Angle and the shadow cone model (shallow angle model). Cui et al. [3], through the field test, obtained the overall flat, angle formulas for calculating local change linear slope rolling speed, and then estimated the speed of movement of the rolling stones and impact energy. Gu He and Wang [4] studied the analytical method of rockfall trajectory prediction, indoor rockfall experiment, and field experiment. Yang and Zhou [5] considered the influence of rockfall shape of rockfall trajectory and approximated rockfall to an ellipse; according to the common forms of rockfall motion, a theoretical method of calculation and prediction of rockfall trajectory was proposed. Based on the three stages of the whole process of rockfall movement, Fu et al. [6] obtained the velocity calculation formula for each stage by using the segmented cycle algorithm, established the model, and applied the theoretical formula for the prediction of rockfall movement trajectory. Cheng and Su [7] studied nearly 400 collapsing rock profiles in the Wenchuan earthquake through statistical analysis and obtained the movement characteristics and damage ranged parameters of the rock. RocFall software appeared with the development of computer technology, which can be used to assess the risk of a rockfall by two-dimensional statistical analysis [8]. Ye et al. [9] proposed a three-dimensional prediction method of rockfall trajectory combined with the characteristics of geotechnical materials. Qin et al. [10] proposed a three-dimensional analysis method of rockfall trajectory with the arbitrary shape of geotechnical slope; this method established rockfall and slope model with arbitrary shape, established rockfall motion equation according to the contact search algorithm and contact collision model between rockfall and slope, and simulated the three-dimensional motion trajectory of rockfall along a slope; the gap between the prediction results and the actual situation is narrowed. At present, despite the emergence of new methods, RocFall software is still most widely used. Based on RocFall software, many scholars have studied the kinetic energy, velocity, and bounce height envelope of the rockfall on the slope, the position of the endpoint of the rockfall rolling, the kinetic energy along the slope line, the velocity, the bounce height distribution, etc., which provide a reference for actual engineering [11–21].

Many institutions and scholars have put forward various definitions of geological hazard risks [22]. For example, Zhang [23], based on summarizing the risk assessment experience of developed countries and Hong Kong, China, put forward a basic concept of regional risk evaluation of geological hazards. RenQin [24] proposed to use the “product function” of hazard, vulnerability, and exposure to calculate risk. Yuan and Fang [25] proposed to evaluate the

risk and hazard risks matrix and take the Yan’an Baota District in Shaanxi as an example to conduct geological hazards risk evaluation research and exploration.

Based on the analysis of the stability of the dangerous rock mass in the treatment area, this paper conducts a study on the prediction of the trajectory of the dangerous rock mass collapse and verifies it by numerical simulation through RocFall. By judging the hazard and vulnerability of the dangerous rock mass, the risk assessment matrix is used to evaluate the risk to clarify the risk level.

2. Project Description

Pu’erdu Town is located in the northwest of Yanjin County, Zhaotong City, Yunnan Province, about 20 km away from Yanjin County and 140 km away from Zhaotong City. The town covers an area of 234 km² and has a population of about 60,000. The topography and geomorphology conditions in the treatment area are very complex, which mainly manifested as flowing water geomorphology controlled by geological structures, the basic geomorphic units are alpine and valleys, and there are also gentle slope landforms developed along with the sedimentary rock layer. The lowest elevation within 4 km² with Pu’er Town as the center is 355 m at the confluence of Chuansi River and Guan River, and the highest elevation is 699 m about 1 km northwest of Pu’er Town. The valley in the area is deep, mainly represented by V-shaped river valleys, and the slopes of the valleys are steep, generally above 30°. Pu’erdu Town has been affected by river erosion for a long time, the terrain is steep and the ravines crisscross, which is a typical mountainous terrain. The geographic location of the study area is shown in Figure 1.

In this paper, we selected six dangerous rock masses W1, W2, W3, W4, W5, and W6 in the control area for study. The plane distribution of each dangerous rock mass is shown in Figure 2, the field photos are shown in Figure 3, and joints developed in the dangerous rock mass are shown in Table 1. The characteristics of dangerous rock points and their descriptions are shown in Table 2.

3. Trajectory Analysis of Collapse Failure of Dangerous Rock Mass

3.1. Theoretical. The analysis methods of the falling path of dangerous rock can be basically classified into four categories: field test, empirical discrimination, theoretical calculation, and numerical simulation. The falling rock is simplified as a sphere or particle, and here falling rock is simplified as a sphere in the theoretical calculation [26]. The results show that only when the slope is less than a certain critical value (about 12°) with the increase in slope, it can be shown as sliding, rolling, jumping, and free cave, and part or all of it can be accumulated at the foot of slope or valley [27]. When the slope of the avalanche is between 12° and 45°, it will roll; when the slope is between 45° and 76°, it will roll and jump; and if the slope is greater than 76°, the avalanche will perform a free-fall motion. The falling angle is shown in Figure 4(a).

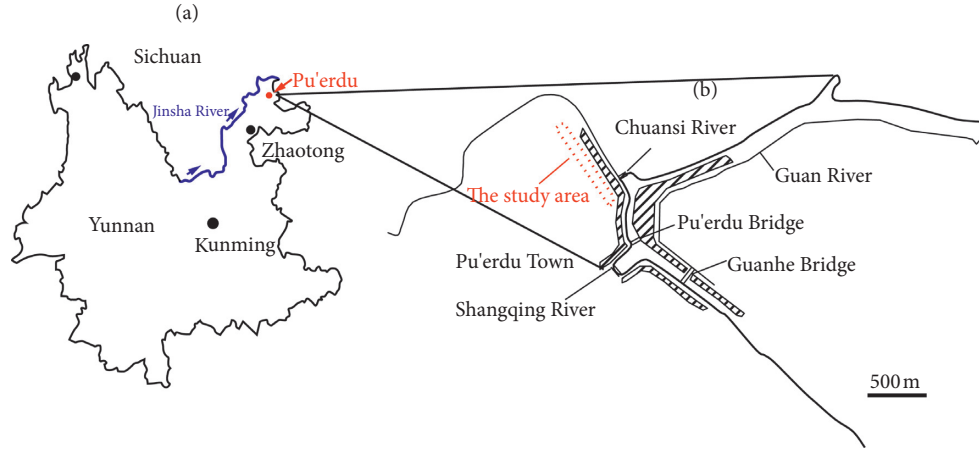


FIGURE 1: Geographical location of the study area.

Different types of dangerous rock blocks are unstable, and their collapse motion characteristics are different. The toppling dangerous rock mass is disintegrated at the foot of the cliff as the contact point and rolls down along the lower slope of $25^\circ \sim 40^\circ$, and the initial rolling velocity is small. The instability of falling dangerous rock mass all starts to fall from the upper or top of the cliff at about 80° , mainly due to the rotational fall of massive dangerous rock mass, rolls, and jumps on the lower slope at a high initial velocity until it stops. Through the investigation of the collapse block, the collapse distance of the dangerous rock in the exploration area is restricted by the terrain, and the shape of the block is similar to the dangerous rock block in the cliff zone.

Prediction and analysis of the movement distance of dangerous rock mass: as shown in Figure 4(b), when the falling rock falls on the slope surface for the first time, the energy changes due to collision, and part of the energy is consumed in the collision process.

According to the law of conservation of kinetic energy,

$$g \cdot h = \frac{1}{2} m V^2, \quad (1)$$

where g is the acceleration of gravity, h is the height of the object from the reference plane, m is the mass of the object, and V is the velocity of the object.

According to the above equation, the velocity V before the falling rock collision can be calculated. V_n (normal velocity) and V_t (tangential velocity) after the collision can be calculated by the following formula:

$$V_t = V \cdot \cos \beta, \quad (2)$$

$$V_n = V \cdot \sin \beta, \quad (3)$$

where V_t is the subvelocity of V perpendicular to the slope (m/s), V_n is the subvelocity of V parallel to the slope (m/s), β ($^\circ$) is the angle between V_t and V , and its value can be obtained according to the terrain contour.

3.2. Analysis of the Motion Trajectory of Dangerous Rock Mass. The terrain in the survey area has a steep slope and hard rock. After the collapse of the dangerous rock mass,

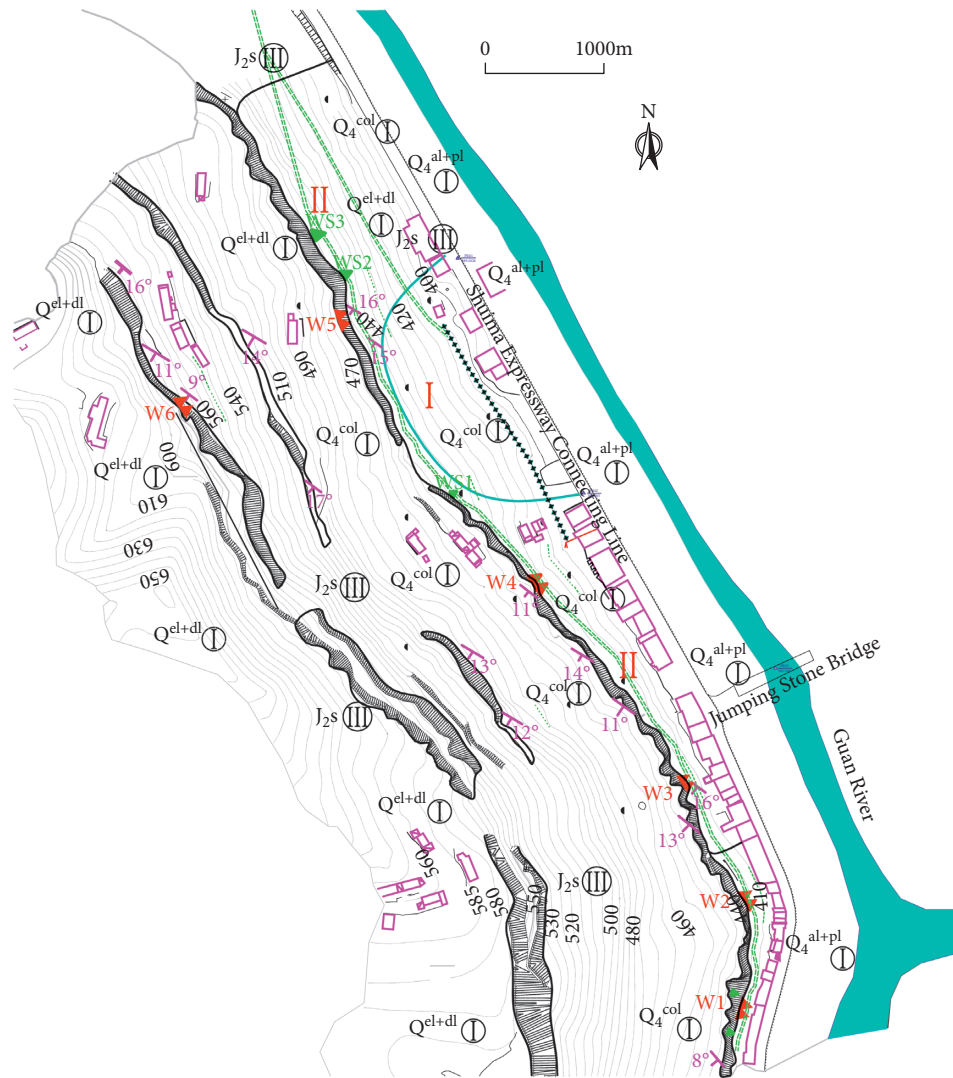
except along the joint surface and bedding plane, most of the rock blocks are maintained well, forming rock blocks of different sizes, and the rock blocks will jump and roll along the hillside when they are unstable, which has strong impact damage ability, with the schematic diagram of collapse damage movement of dangerous rock mass (Figure 4(b)), it can be seen that after the collapse of dangerous rock mass, movement way of the rock mass is mainly rolling and jumping down. Taking the geological section of dangerous rock mass W1 as an example, as shown in Figure 5, the normal collision between falling rock and a loose layer of the slope between the 4 and 3 section of the W1 dangerous falling rock path can be considered as the core plastic collision, so $V_n = 0$. In the tangential collision, the loss rate is 10%.

The kinetic energy of the first impact of the falling rock on the slope and its continuous motion is $0.5m(0.9V_t)^2$. The continuous movement towards falling rock on the slope is a comprehensive form of rolling and sliding, and for the convenience of calculation, it can be simplified to the comprehensive friction motion along the slope. According to the principle of function, the potential energy change of the falling rock is equal to the kinetic energy change and the work done to overcome friction:

$$\sum mg \cdot \Delta h_i = \frac{1}{2} m (V_i^2 - V_t^2) + \sum mg \cos a_i \cdot t g \Phi_r \cdot L_i, \quad (4)$$

where V_i is the velocity of falling rock at any position on the slope surface (m/s), a_i is the average slope ($^\circ$) of each straight line section, Δh_i is the vertical height of the slope of each straight line segment (m), Φ_r is the comprehensive friction angle between the falling rock and the slope ($^\circ$), and L_i is the length of each slope (m).

3.3. Calculation of Movement Distance. Since the cliff slope where the dangerous rock mass is located is greater than 76° , it can be considered that the dangerous rock is in free-fall motion during the fall. According to the law of conservation of kinetic energy, all the potential energy of the dangerous



- | | |
|--|---|
| 1. Geological structure | 4. Boundary lines and others |
| Occurrence | The area where dangerous rocks collapse |
| 2. Engineering geology rock group | Stream direction and name |
| Filling soil, silty clay containing gravel, block stone, gravel, bleached gravel multilayer soil | Control points and elevation |
| Extremely soft dispersive - cataclastic structure fully - strongly weathered rock group | Stability partition boundary |
| Clastic rock group with soft and hard interbedded structure | Unstable area (need to be treated) |
| 3. Geological hazards and undesirable geological phenomena | Stable area (need to be monitored) |
| Klint | Civil building |
| Dangerous rock mass and number | |
| Dangerous stones and their serial numbers | |

FIGURE 2: Plane distribution of dangerous rock mass.

rock mass is converted into kinetic energy immediately before the collision with the next slope section (without considering the air resistance). The maximum horizontal

movement distance to the dangerous rock mass can be calculated by the above formula. The calculation results are shown in Table 3.

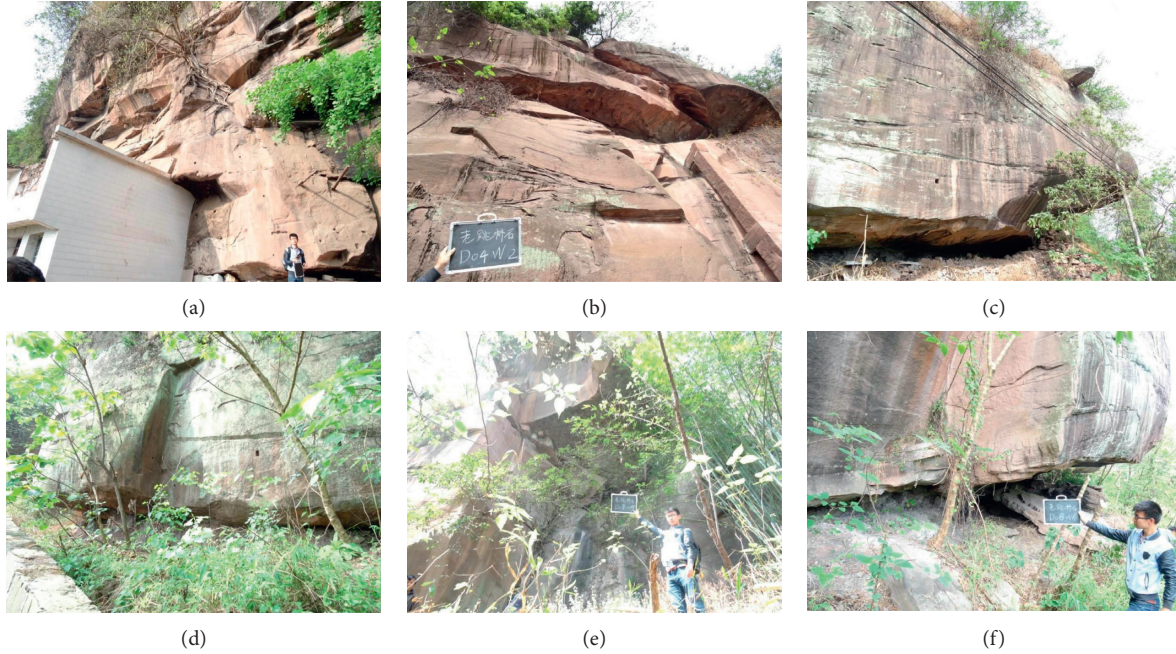


FIGURE 3: Field map of the investigated dangerous rock mass: (a) W1, (b) W2, (c) W3, (d) W4, (e) W5, and (f) W6, respectively.

TABLE 1: Main joint developed in the dangerous rock mass.

Dangerous rock mass	Joint		Attitude		Frequency (bar/m)	Strike extension length (m)	Tendency extension length (m)
	Code	Dip	Dip angle				
W1	J1	N45°E	89°	1/4~5	18~20	5~6	
	J2	S80°E	86°	1/18~20	4~5	15~20	
W2	J1	N80°E	89°	1/8~10	10	10~14	
	J2	S10°E	71°	1/23	8	20~23	
W3	J1	N45°E	80°	1/7~8	20	20~25	
	J2	S70°E	85°	1/10	7~8	15~20	
W4	J1	N50°E	87°	1/5~8	5~8	10~15	
	J2	S80°E	86°	3/20	6~8	14~16	
W5	J1	N35°E	83°	1/6~8	20~25	18~20	
	J2	S35°E	72°	1/20~25	6~8	10~15	
W6	J1	N70°E	74°	1/5~6	8~10	10~15	
	J2	N10°W	56°	3~30	6~8	14~16	

3.4. *Bouncing Calculation.* In this article, we only calculated the bounce height of W1, W2, W3, and W4, and the formula used is as follows.

Reflection speed after hitting the platform:

$$V_0 = (1 - \lambda)V_R \cdot \frac{\cos \gamma}{\sin \gamma} \quad (5)$$

The maximum height of the first bounce of the rock h_{\max} :

$$h_{\max} = \frac{V_0^2}{2g} \sin^2 \gamma \quad (6)$$

Total height of rock jumping:

$$h = h_s + h_{\max} \quad (7)$$

where λ is the coefficient of friction when hitting the platform, V_R is the velocity after hitting the platform, γ is the reflection angle after hitting the platform, and h_s is the safe value of jump height (generally 0.5 ~ 1.0). The calculation results are shown in Table 4.

4. The Numerical Simulation Verification Based on RocFall

4.1. *RocFall Software Introduction.* RocFall is statistical analysis software used to evaluate the risk of falling rocks on

TABLE 2: Characteristics of dangerous rock spots and economic losses caused by disasters.

Category	Destruction mode	Volume (m ³)	Stable state	Threat object	Economic loss
W1	Falling	654	Under stable	People, houses, highways, engineering facilities	Located above the concentration of residential houses, it seriously threatens the safety of life and property, and the economic loss caused by instability is huge
W2	Toppling	4323	Basically stable	People, houses, highways, engineering facilities	Located above the concentration of residential houses, it seriously threatens the safety of life and property, and the economic loss caused by instability is huge
W3	Falling	280	Unstable	People, houses, highways, engineering facilities	Located above the concentration of residential houses, it seriously threatens the safety of life and property, and the economic loss caused by instability is huge
W4	Falling	2448	Understable	People, houses, highways, engineering facilities	There are fewer houses under the dangerous rock mass, and the economic loss caused by instability is greater
W5	Toppling	3312	Understable	Houses, cultivated field, roads	The dangerous rock mass is far away from the house, and the economic loss caused by instability is not large
W6	Falling	2550	Unstable	Cultivated field, road	The economic loss caused is not big

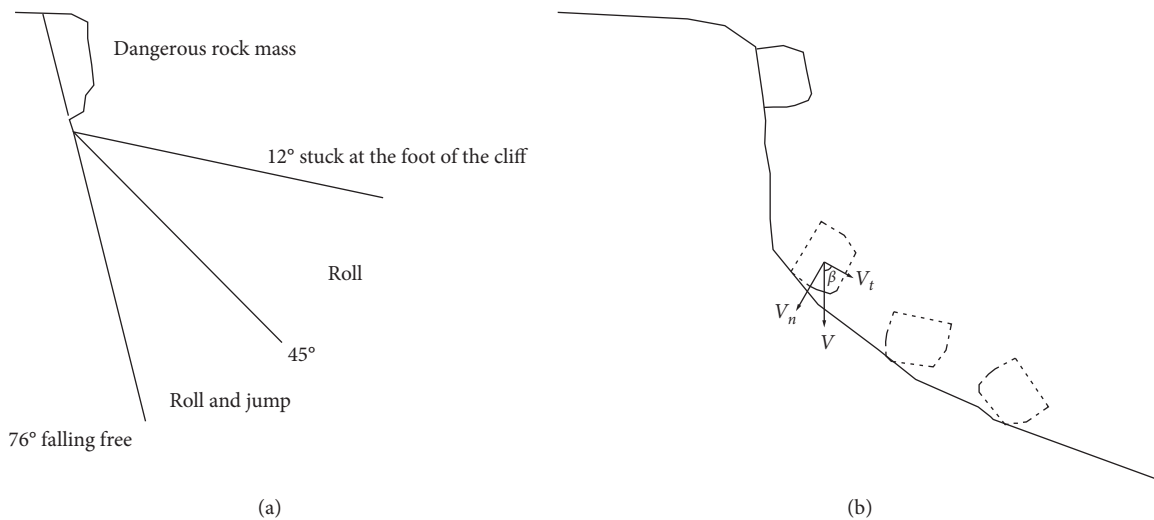


FIGURE 4: (a) Schematic diagram of the collapse and destruction movement of dangerous rocks. (b) The trajectory of dangerous rock collapse.

steep slopes. It stimulates the movement path, energy distribution, and bounce height changes of falling rocks on the slope by inputting basic parameters related to the slope and falling rocks. This software regards falling rocks as rigid mass points and the slope surface as isotropic plastic bodies, ignoring air resistance. The main parameters include the normal recovery coefficient, tangential recovery coefficient, dynamic friction coefficient, and the weight of the falling rock [28, 29]. The slope restitution coefficient range used in the numerical simulation is shown in Table 5.

Dangerous rock mass located on a high slope has a lot of potential energy; according to the law of potential energy, the heavier the dangerous rock mass, the greater the potential energy. If they are unable to maintain their stability due to some reasons like external forces, or due to weathering, earthquakes, these dangerous rock masses will lose their stability and fall from the mountain [30].

In the process of falling dangerous rock mass, according to the law of conservation of kinetic energy, the huge

potential energy of dangerous rock mass itself will be transformed into the kinetic energy of movement of dangerous rock mass [31]. The falling rock will collide with the slope body and consume part of the kinetic energy, because the normal recovery coefficient, tangential recovery coefficient, and inclination angle are different on different slopes [32].

When the rock falls to the bottom of the cliff, it collides with the gentle slope. After several jumps, most of the kinetic energy is consumed, and the rock begins to roll and slide into the gentle slope. Finally, with the kinetic energy under the action of the friction force of the gentle slope, the kinetic energy of the rock is consumed and the rock finally stops moving. Due to the difference in slope, friction coefficient and weight of falling rocks, the movement trajectory of falling rocks is also different, but in this process, the law of conservation of kinetic energy is still observed [33].

Numerical simulation software RocFall can directly analyze the trajectory of falling rock, which divides the

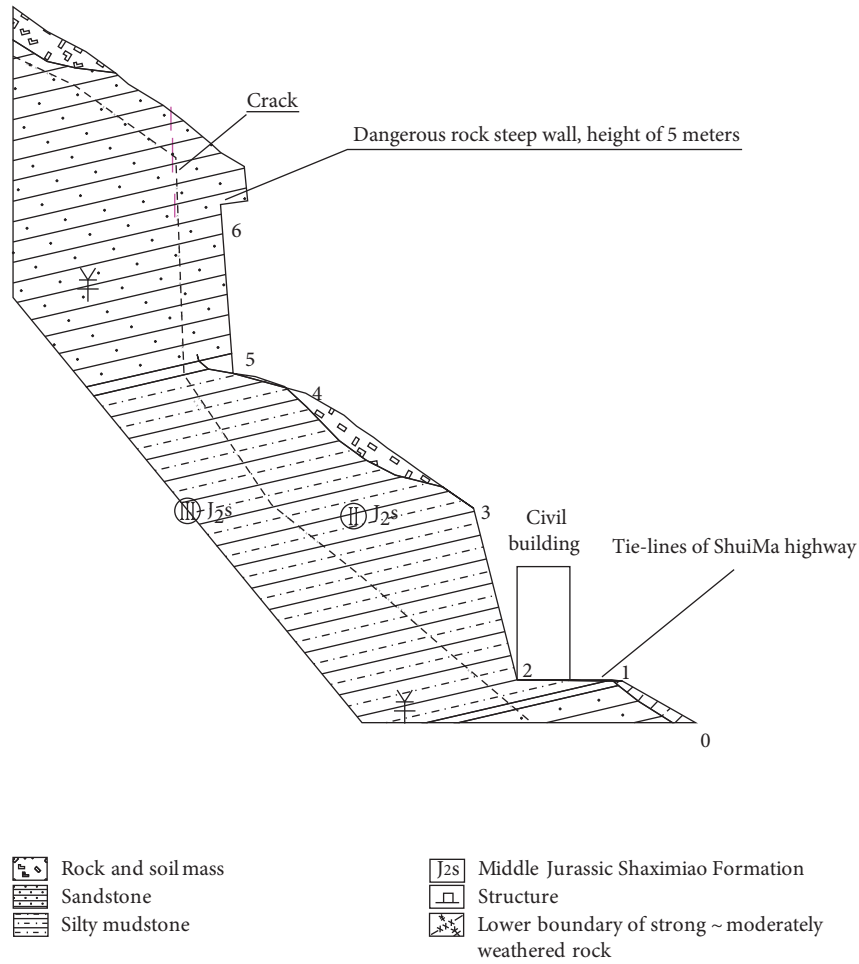


FIGURE 5: Geological section of dangerous rock mass W1.

TABLE 3: Maximum horizontal movement distance of dangerous rock mass.

Dangerous rock mass number	Destruction mode	Horizontal movement distance X (m)
W1	Falling	52.91
W3		57.99
W4		84.85
W6		52.49
W2	Toppling	61.25
W5		66.61

TABLE 4: Calculation results of the jumping height of dangerous rock mass.

Serial number	Jump safety value h_s (m)	Jumping height h_{max} (m)	Total high jump h (m)
W1	1	8.964	9.964
W2	1	2.697	3.697
W3	1	7.133	8.133
W4	1	17.930	18.930

TABLE 5: Range of restitution coefficient (according to Chen et al. [27]).

Slope characteristics	R_n (normal recovery coefficient)	R_t (tangential recovery coefficient)
Smooth hard rock surface, paved concrete surface	0.25~0.75	0.88~0.98
Soft rock face, strong weathered hard rock face	0.15~0.37	0.78~0.95
Rock pile slope	0.15~0.37	0.75~0.95
Rubble dense, hard surface slope, the vegetation growth, to shrub	0.12~0.33	0.30~0.95
Dense gravel pile, hard soil slope, no or little vegetation development	0.12~0.32	0.65~0.95
Loose gravel piles, soft soil slopes, well-developed vegetation, mainly shrubs	0.10~0.25	0.30~0.80
Soft soil slope, no or little vegetation development	0.10~0.30	0.50~0.80

trajectory of falling rock into two processes: parabolic motion in the air and impact motion between falling rock and ground [34].

The equation of parabolic motion:

$$\left(\frac{1}{2}g\right)t^2 + (V_{Y_0} - qV_{X_0})t + [Y_0 - Y_1 + q(X_1 - X_0)] = 0, \quad (8)$$

$$q = \frac{Y_2 - Y_1}{X_2 - X_1}, \quad (9)$$

where X_1 , Y_1 represent the starting point coordinate of the straight line segment (m), g is the acceleration of gravity (m/s^2), and V_{X_0} , V_{Y_0} are the fall velocity of rock (m/s), generally taking 0.

Impact time equation:

$$t = \frac{-b + \sqrt{b^2 - 4ac}}{2a}, \quad (10)$$

where $a = g/2$, $b = V_{Y_0} - qV_{X_0}$, $c = Y_0 - Y_1 + q(X_1 - X_0)$.

4.2. Numerical Simulation of the Motion Trajectory of the Falling Rock. When using RocFall software, we should first clarify the location, initial speed, and mass of the falling rock. Secondly, the two-dimensional model of the slope should be drawn according to a certain scale.

4.2.1. Determine the Initial State of the Falling Rock. In this simulation, without considering the influence of random factors, it is considered that when the rock mass leaves the ground, it is a free-fall motion with an initial velocity of zero. Regardless of the shape and size of the rock, treat it as a mass point.

4.2.2. Determine the Mechanical Parameters of the Slope. The rock will be affected by the slope friction during the falling process. During this process, the speed attenuation depends on parameters such as R_n (normal recovery coefficient) and R_t (tangential recovery coefficient). Table 6 lists the reference values of R_n and R_t for different geological slopes.

4.3. Simulation Calculation of the Falling Rock Trajectory. On the slope section where the dangerous rock is unstable, it is assumed that the near-spherical falling rock of the dangerous rock mass starts to move, and it moves in a combination of rolling, collision, bounce, and air flight.

Usually, the falling rock first falls freely, dumps and falls, then collides and rebounds or rolls down along the slope, rolls to the edge of the cliff, enters the next level of cliff, and continues to roll down until it stops or does projectile motion, or flies in the air, does projectile movement, and then collides again. Repeat this until it stops.

The independent motion simulations of 60 groups of single rolling rocks are performed randomly and the results are statistically analyzed to determine the most dangerous rolling rocks stagnation zone and maximum bouncing height. Through this numerical simulation, the results we want to obtain are the following items: the motion trajectory diagram of dangerous rock mass displayed in Figure 6. The bounce height envelope diagram of the dangerous rock mass is shown in Figure 7. The horizontal location of rock end-points is shown in Figure 8.

The figure lists the parameters of each slope, the X coordinate represents the relative horizontal distance between the falling rock and the instability point B.

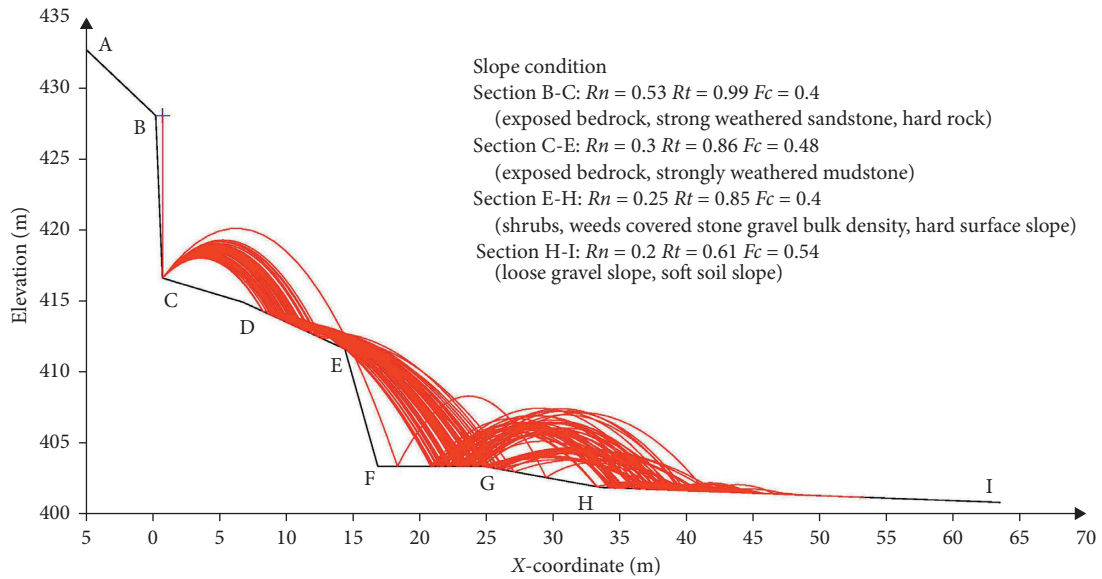
W1 falls freely from point B, most of the falling rocks hit section D-E, and they begin to roll and fall into section F-G and continue to bounce. Eventually, they stop at $X = 53.93$ m. W2 falls freely from point B, it begins to roll at section C-E, then falls into section F-G, and continues to bounce. Eventually, it stops at $X = 65.33$ m. W3 falls freely from point B, after the jumping movement of section C-D, it will fall into section D-F and begins to roll, and then it falls into section G-H. Finally, it stops at $X = 57.03$ m. W4 falls freely from point B, rolls along section C-E, then falls into section F-G, and finally stops at $X = 86.27$ m.

It can be seen that the shape of the slope is an important factor that affects the trajectory of falling rock. When the slope remains the same and the height increases, the potential energy of the rock is greater. After being converted into kinetic energy, the speed also increases. Its horizontal movement distance will be farther. In addition, due to the existence of the platform, the falling rock with a certain speed produces a greater bounce height.

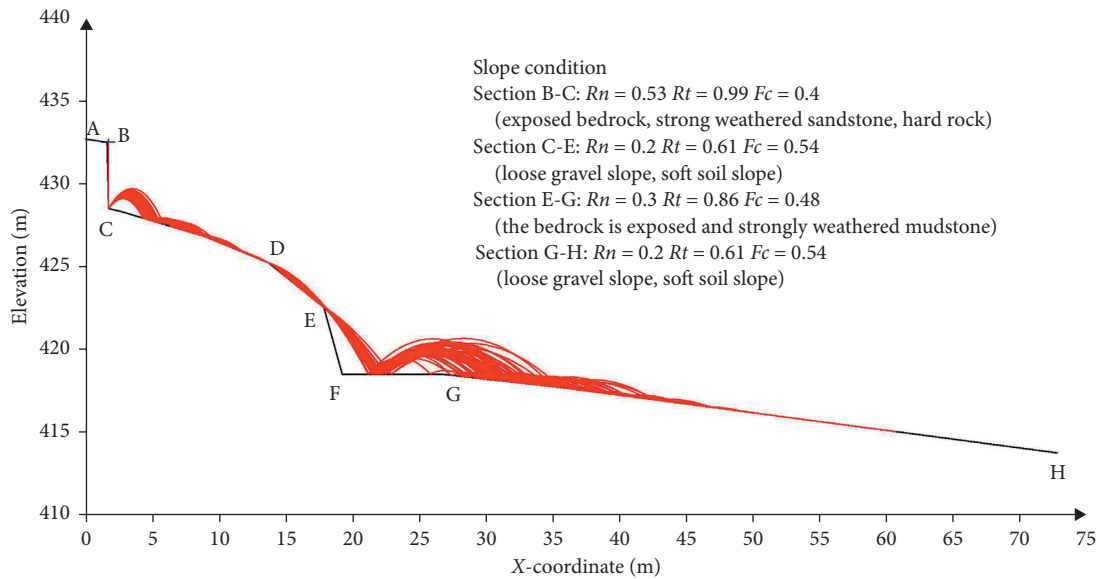
As shown in Figure 7, the maximum bounce height of W1 is 9.68 m, and the horizontal movement distance at this

TABLE 6: Reference values of different geological slope sections [35, 36].

Slope section of lithology	R_n	R_t	Coefficient of rolling friction
The bedrock is exposed, the strong weathering sandstone, the rock quality is hard	0.53	0.99	0.4
The bedrock is exposed and strongly weathered mudstone	0.3	0.86	0.48
Weeds and shrubs covered by dense gravel piles, hard soil slope	0.25	0.84	0.58
Gravel soil and blocks of stone piled up	0.28	0.85	0.4
Loose gravel slope, soft soil slope	0.2	0.61	0.54

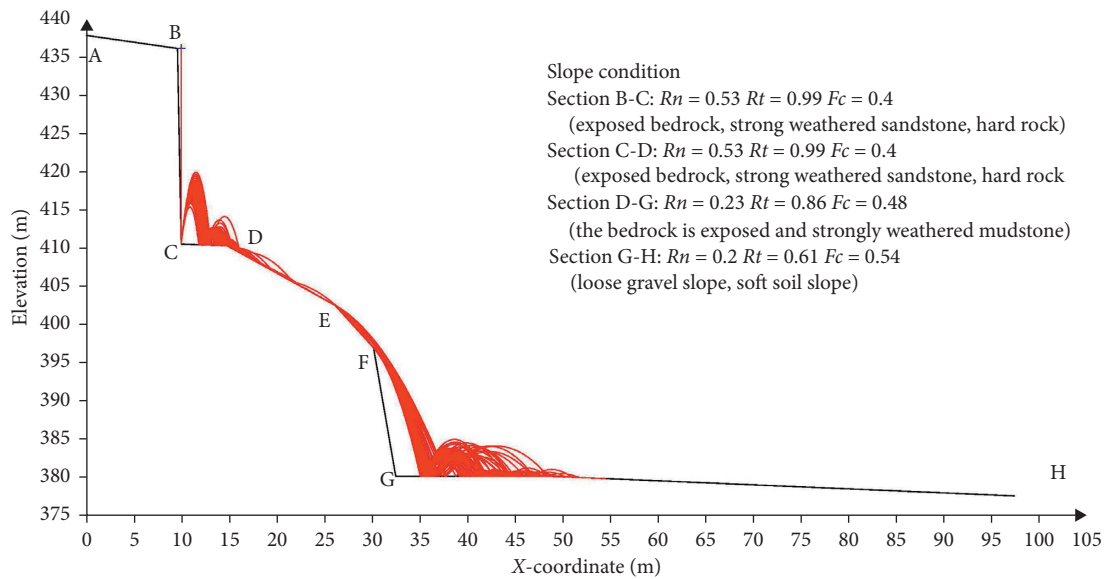


(a)

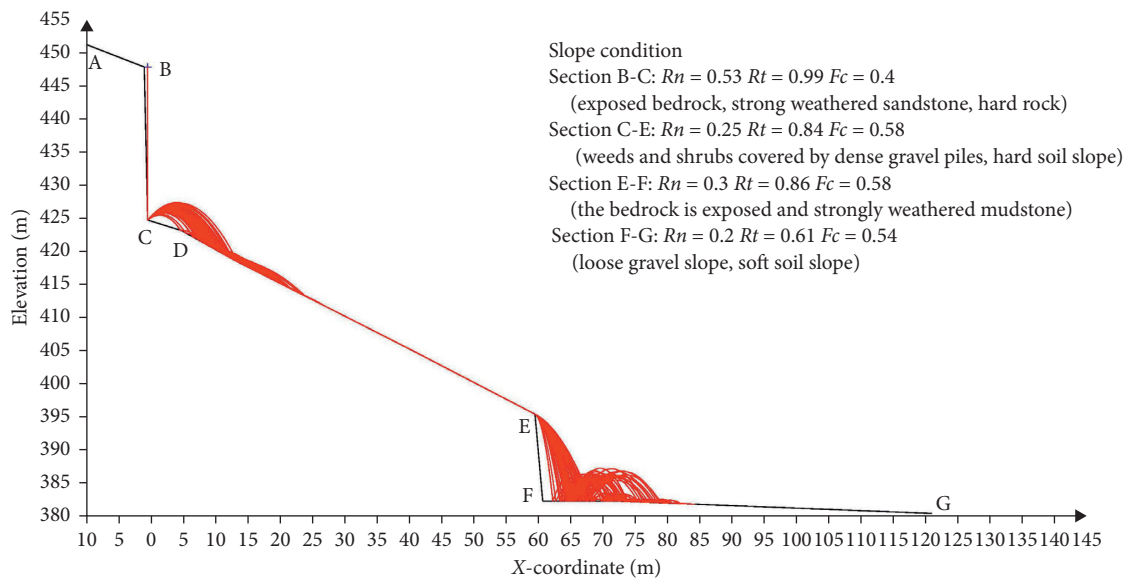


(b)

FIGURE 6: Continued.



(c)



(d)

FIGURE 6: Motion trajectory diagram of the dangerous rock mass. (a) Motion trajectory diagram of W1. (b) Motion trajectory diagram of W2. (c) Motion trajectory diagram of W3. (d) Motion trajectory diagram of W4.

time is 19.13 m, which is located in section F-G. The maximum bounce height of W2 is 3.71 m, and the horizontal movement distance at this time is 20.59 m, which is located in section F-G. The maximum bounce height of W3 is 8.13 m, and the horizontal movement distance at this time is 34.22 m, which is located in section G-H. The maximum bounce height of W4 is 18.86 m, and the horizontal movement distance at this time is 62.18 m, which is located in section F-G.

As shown in Figure 8, the farthest horizontal movement distance from W1 dangerous rock masses is 53.93 m, and the falling rocks are mainly distributed at coordinates 37.5~48 m. The farthest horizontal movement distance of W2 dangerous rock masses is 65.33 m, and the falling rocks are mainly distributed at coordinates 41.3~63.8 m. The farthest horizontal distance of W3 dangerous rock masses is 57.84 m, and the falling rocks are mainly distributed at coordinates 44.8~58.8 m. The farthest horizontal distance of

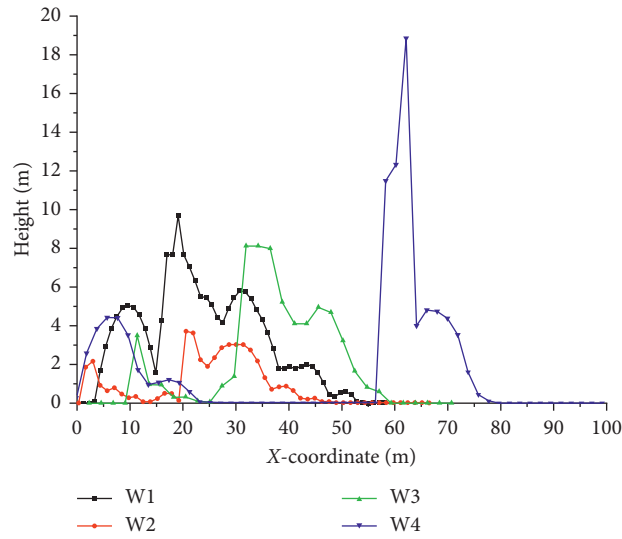


FIGURE 7: Bounce height envelope diagram of the dangerous rock mass.

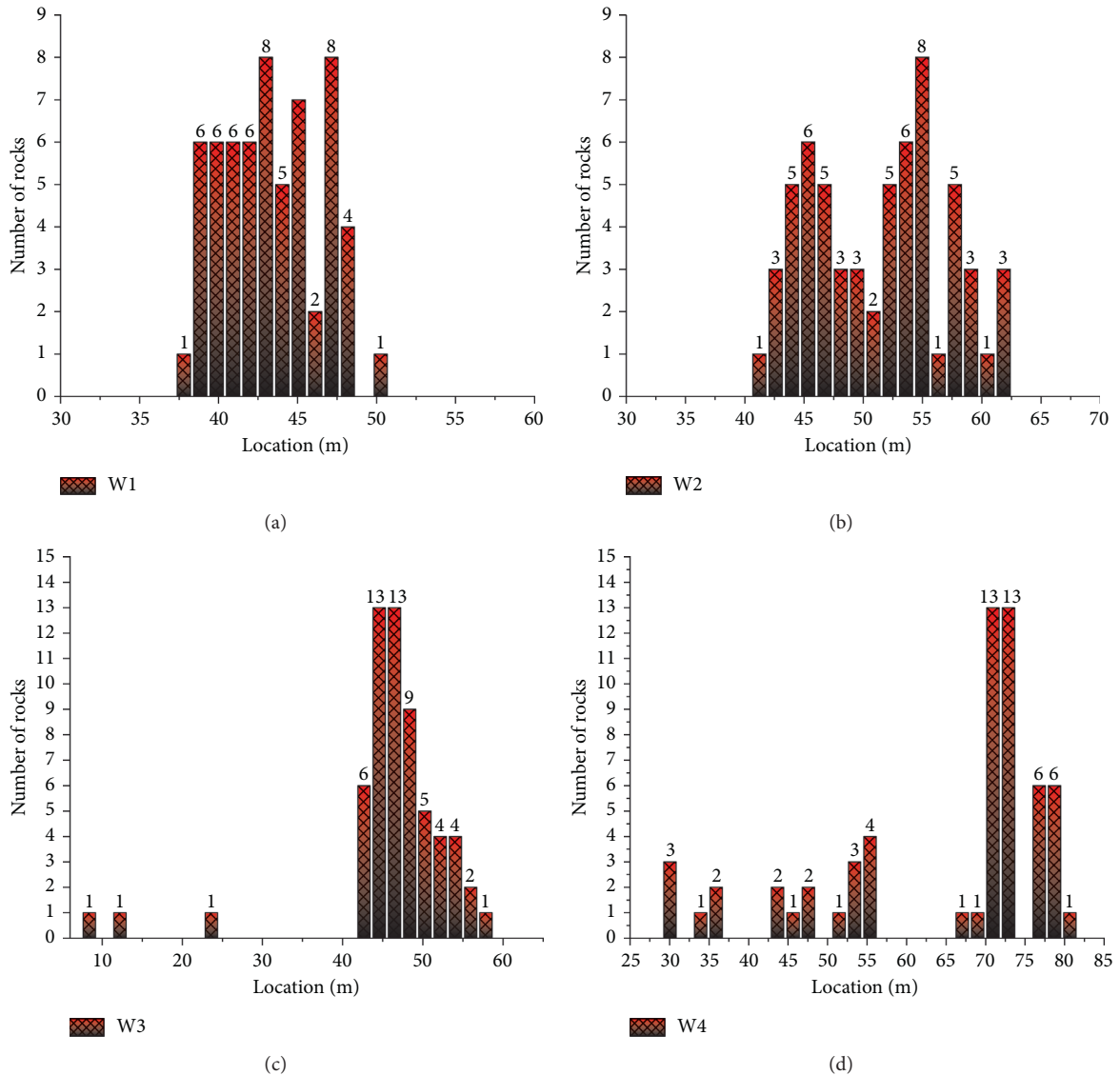


FIGURE 8: Horizontal location of rock end-points. (a) Rockfall distribution of W1. (b) Rockfall distribution of W2. (c) Rockfall distribution of W3. (d) Rockfall distribution of W4.

TABLE 7: Comparison of results of two calculation methods of motion trajectory.

Serial number	Calculation method			
	The formula to calculate		RocFall simulation	
	Horizontal distance X (m)	Maximum bounce height of falling rocks H (m)	Horizontal distance X (m)	Maximum bounce height of falling rocks H (m)
W1	52.91	9.96	53.93	9.682
W2	61.25	3.70	65.33	3.714
W3	57.99	8.13	57.03	8.135
W4	84.85	18.93	86.27	18.863

W4 dangerous rock masses is 86.27 m, and the falling rocks are mainly distributed at coordinates 70.1~81.3 m.

4.4. Analysis of Calculation Results. Comparing the calculation result with the RocFall software simulation result, it is found that the two results are relatively close. It can be seen from Table 7 that the results of calculating the trajectory of the dangerous rock mass by the two methods are not much different, indicating that the RocFall simulation can be used as a reference from the prediction of the trajectory of the dangerous rock mass.

5. Risk Evaluation of Dangerous Rock Mass

Pu'erdu Town was built close to the mountain. The instability of dangerous rock is a great threat to the safety of people or property. According to geological survey data, the total volume of collapsed and dangerous cliffs in the study area is 893,300 m³. The threats are mainly residents, streets, bridges, and so forth. Once the dangerous rocks become collapse, they will seriously threaten the lives of 2,685 people below and cause economic damage. The loss was as high as 120 million RMB Yuan. At present, the cliff rock is basically in an unstable state. Therefore, it is necessary to evaluate the instability risk of dangerous rock mass and provide data support for disaster prevention and mitigation in the study area. In this paper, risk assessment of dangerous rock mass of high slope is carried out from two aspects of risk and vulnerability.

5.1. Risk Assessment of Dangerous Rock Mass. According to the scale and stability of dangerous rock masses, the risk levels are classified, which is the semiquantitative method. The risk of dangerous rock mass is classified according to technical requirements for geological hazard evaluation of construction land, as shown in Table 8.

When categorizing the risk of dangerous rock masses, it is necessary to make a comprehensive judgment based on factors such as its scale, stability, instability failure type, and topography. The danger grade in dangerous rock mass in the study area is divided, and the results are as follows: I level dangerous rock mass: W3, W6; II level dangerous rock mass: W1, W4, W5; III level dangerous rock mass: W2.

5.2. Vulnerability Evaluation of Dangerous Rock Mass. Analyzing the damage degree of hazard-bearing bodies after the collapse of rock is the vulnerability evaluation of dangerous rock mass, which is an indispensable factor to study

TABLE 8: Hazard source level of the dangerous rock mass.

Steady state	Large scale ($\geq 100 \text{ m}^3$)	Medium scale (10~100 m ³)	Small scale (<10 m ³)
Basically stable	III	III	III
Less stable	II	II	III
Unstable	I	I	I

the instability risk of the dangerous rock mass. The vulnerability evaluation is mainly to count the types, quantity, and loss value of the hazard-bearing bodies within the range of collapse threat of dangerous rock mass. The unstable dangerous rock mass may produce many different disasters bearing bodies, especially near the market town. In this paper, different hazard-bearing bodies were classified into the following four categories for statistics, as shown in Table 9.

The paper divides the severity of the losses suffered by the above four types of disaster-bearing bodies into three levels: mild, moderate, and severe. The degree of injury received by people is expressed as a minor injury, severe injury, and death. Combining the historical damage caused by the collapse of dangerous rock masses and the disaster resistance capacity of the disaster-bearing bodies of the study area, the vulnerability is classified into 3 levels in total. Aiming to quantitatively analyze the vulnerability of hazard-bearing bodies of the study area, a dimensionless assignment was made to the levels. The results are shown in Table 10.

According to the plan of the study area, the vulnerability evaluation of dangerous rock mass disaster in the study area is carried out, and the results are as follows: I level vulnerability: W1, W2, W3; II level vulnerability: W4; III level vulnerability: W5, W6.

5.3. Instability Risk Estimation of Dangerous Rock Mass. As the United Nations' definitions and formulas for geological hazard risk evaluation [37] to assess the risk of dangerous rock masses, the formula is as follows:

$$R = HV = (1 \ 2 \ 3) \begin{pmatrix} 3 \\ 2 \\ 1 \end{pmatrix} = \begin{pmatrix} 3 & 2 & 1 \\ 6 & 4 & 2 \\ 9 & 6 & 3 \end{pmatrix}, \quad (11)$$

where R is the risk index of dangerous rock mass, H is the hazard score of the dangerous rock mass, and V is the

TABLE 9: Type of disaster-bearing body.

Serial number	Type	Possible damage
1	People	Injuries, deaths
2	Arable land	Destroyed, buried
3	Housing, engineering facilities	Collapse, cracking
4	Highway	Damaged

TABLE 10: Vulnerability grade of disaster-bearing body.

Level	Grade	Consequences	Score
I	Severe	A small number of people died or a large number of people were seriously injured, and the damage to property was huge	3
II	Moderate	A small number of serious injuries or more minor injuries, resulting in partial property damage	2
III	Mild	There were no or a few minor injuries and little property damage	1

TABLE 11: Failure risk evaluation matrix of dangerous rock mass.

Score	Serious vulnerability	Moderate vulnerability	Slight vulnerability
Small risk	3	2	1
Medium risk	6	4	2
High risk	9	6	3

TABLE 12: Risk grade of dangerous rock mass.

Serial number	Risk level	Risk index
I	High	$6 \leq R_i \leq 9$
II	Medium	$3 \leq R_i < 6$
III	Low	$1 \leq R_i < 3$

TABLE 13: Risk grade of dangerous rock mass.

Dangerous rock number	Hazard score	Vulnerability score	Risk index	Risk classification
W1	2	3	6	High
W2	1	3	3	Medium
W3	3	3	9	High
W4	2	2	4	Medium
W5	2	1	2	Low
W6	3	1	3	Medium

vulnerability score of the dangerous rock mass. After determining the two major factors of hazard and vulnerability of dangerous rock mass, a matrix is formed to evaluate the risk of dangerous rock mass with the hazard as the column and the vulnerability as the row. Among them, each value of the matrix is the risk index of dangerous rock mass disaster. Table 11 is the evaluation level of instability risk of the dangerous rock mass.

According to the calculation results, the instability risk of dangerous rock mass is classified according to Table 12.

According to the risk classification and vulnerability classification of dangerous rock mass in the study area, the

risk grade classification of rock was carried out, and the results are shown in Table 13.

6. Conclusion

Based on the study of the stability of the dangerous rock mass in the treatment area, this paper predicts the movement trajectory of rock after the collapse. Based on the RocFall simulation verification, the risk evaluation of dangerous rock masses is carried out, and the following conclusions are drawn:

- (1) Through the comparison of formula calculation and numerical simulation analysis, the furthest horizontal movement distance, bounce height, and main distribution range of falling rocks can be determined, and RocFall software has a good effect on the prediction of falling rocks trajectory.
- (2) Through dimensionless assignment and risk assessment matrix, W1 and W3 can be determined as high-risk dangerous rock mass, W2, W4, and W6 are medium-risk rocks, W5 is the low-risk rock mass. It is suggested that a reasonable and scientific engineering treatment scheme should be put forward in combination with the collapse trajectory and risk assessment results of dangerous rock mass, to eliminate the hidden danger of dangerous rock mass in the high slope of the treatment area as soon as possible.
- (3) The trajectory calculated by the calculation formula is more accurate and the calculation results are more reliable. However, the calculation process is more complex and requires more process geological parameters to be prepared for the early stage, which consumes a lot of manpower and material resources and leads to high cost. At the same time, simulation by Rockfall software is convenient as fewer parameters are needed.

With the current study, the calculation method of collapse motion trajectory of dangerous rock mass and risk evaluation theory are not perfect for the prevention and control of geological disasters. The calculation method used in this article is just an attempt. And the effectiveness still needs to be verified and improved by generations of engineers and technicians in future engineering examples.

Data Availability

The data used to support the findings of this study are included within the article.

Conflicts of Interest

The authors declare that there are no conflicts of interest regarding the publication of this paper.

Acknowledgments

This study was sponsored by the Kunming Prospecting Design Institute of China Nonferrous Metal Industry Co., Ltd. (Risk Assessment Method of Dangerous Rock High Slope in Northeast Yunnan Based on Engineering Geological Evolution) and the Talent Development Program of Kunming University of Science and Technology (no. KKS201767034).

References

- [1] M. Bobbert, P. Huijing, and G. Schenau, "Instantaneous torque-angular velocity relationships during jumping," *Journal of Biomechanics*, vol. 18, no. 6, p. 553, 1985.
- [2] L. K. A. Dorren, "A review of rockfall mechanics and modelling approaches," *Progress in Physical Geography: Earth and Environment*, vol. 27, no. 1, pp. 69–87, 2003.
- [3] S. Cui, X. Pei, and R. Huang, "Study on velocity characteristics of rolling stone on straight slope," *Journal of Engineering Geology*, vol. 21, no. 5, pp. 912–915, 2013.
- [4] T. Z. Gu He and T. W. Wang, "Study on prediction method of rockfall trajectory," *Railway Architecture*, vol. 8, pp. 8–13, 1992.
- [5] H. Q. Yang and X. P. Zhou, "New method for calculating rockfall trajectory of slope," *Geotechnical Mechanics*, vol. 11, pp. 3411–3416, 2009.
- [6] F. J. Fu, Z. Jun Hong, Z. bin, and C. Yu Long, "Segmented cycle algorithm of rockfall trajectory of slope," *Chinese Journal of Geological Hazards and Prevention*, vol. 4, pp. 96–101, 2011.
- [7] Q. Cheng and S. Su, "Characteristics of rolling slope movement in Wenchuan earthquake collapse," *Rock and Soil Mechanics*, vol. 35, no. 2, pp. 772–776, 2014.
- [8] W. Douglas Stevens, *Rockfall: A Tool for Probabilistic Analysis, Design of Remote Measures and Prediction of Rockfalls*, University of Toronto, Toronto, Canada, 1998.
- [9] S. Ye, K. Li, and C. Lin, "A method for three-dimensional prediction and analysis of rockfall trajectory combined with characteristics of geotechnical materials," Chinese patent: cn111737871a, 2020.
- [10] F. Qin, Y. Peng, K. Xiangzhen, and Z. Jinhua, "Three dimensional analysis method of rockfall trajectory with arbitrary shape on geotechnical slope," Chinese patent: cn112258643a, 2021.
- [11] C. Zhong, "Rocfall is used to simulate the influence of slope topography on rockfall motion characteristics," *China Metal Bulletin*, vol. 8, pp. 148–150, 2020.
- [12] H. Zhu, Z. Yang, L. Cheng, R. Luo, and Z. Liu, "Study on rockfall trajectory of dangerous rocks based on rockfall numerical simulation: a case study of a section of dangerous rocks in the three gorges reservoir area," *Scientific and Technological Innovation*, vol. 19, pp. 45–46, 2020.
- [13] H. Jianqun, "Application of Rocfall software in engineering design of geological disaster prevention and control of collapse," *Engineering Construction and Design*, vol. 12, pp. 33–34, 2020.
- [14] S. Zhang and Y. Luo, "Discussion on prevention and control method of boulder falling in high and steep building slope based on rockfall simulation," *Guangdong Civil Engineering and Architecture*, vol. 26, no. 2, pp. 54–63, 2019.
- [15] C. Luo, Z. Xiang, and R. Chen, "Rockwall design based on Rocfall," *Nonferrous Metal Design*, vol. 45, no. 4, pp. 12–23, 2018.
- [16] X. Fu, Q. Sheng, Y. Zhang, J. Chen, and X. Leng, "Extension of discontinuous deformations analysis method to simulate seismic response of large rock cavern complex," *International Journal of Geomechanics (ASCE)*, vol. 17, no. 5, 2017.
- [17] L. Wang, C. Yongfeng, and N. Xingxin, "Calculation and application of blasting force transport distance based on rockfall numerical simulation," *Mining Research and Development*, vol. 35, no. 4, pp. 8–11, 2015.
- [18] X. Fu, Q. Sheng, H. Tang et al., "Seismic stability analysis of a rock block using the block theory and Newmark method," *International Journal for Numerical and Analytical Methods in Geomechanics*, vol. 43, no. 7, 2019.
- [19] S. Zeng, "Application of rockfall software in the design of dangerous rock collapse," *China Water Transport (Second Monthly)*, vol. 11, no. 1, pp. 211–212, 2011.

- [20] J. Xu, M. Zhang, and W. Fan, "A review of geological hazard risk evaluation," *Disaster*, vol. 30, no. 4, pp. 130–134, 2015.
- [21] X. Xiang and R. Huang, "Risk evaluation and risk management of geological hazards," *Geological Hazards and Environmental protection*, vol. 11, no. 1, pp. 38–41, 2000.
- [22] Y. Han, P. Cui, and H. Liu, "Study on risk evaluation method and application of debris flow disaster," *China Safety Science Journal*, vol. 18, no. 12, pp. 141–147, 2008.
- [23] M. Zhang, *Geological Disaster of Landslide Collapse in Bota District of Yanan*, Geological Publishing House, Beijing, China, 2008.
- [24] J. RenQin, *Stability Analysis and Treatment Method of Dangerous Rock in High Highway Slope in Chongqing Area*, Chongqing Jiaotong University, Chongqing, China, 2014.
- [25] J. Yuan and C. Fang, "Stability analysis and prevention of a dangerous rock belt in Chongqing," *Western Exploration Project*, vol. 5, pp. 121–124, 2008.
- [26] S. Zeng, "Application of rockfall software in dangerous rock collapse treatment design," *China Water Transport (second Half)*, vol. 11, no. 1, pp. 211–212, 2011.
- [27] H. Chen, X. Xian, H. Tang, and L. Wang, "Stability analysis method of dangerous rock," *Chinese Journal of Applied Mechanics*, vol. 26, no. 2, pp. 278–407, 2009.
- [28] C. Zhong, "Based on rockfall to simulate the influence of slope topography on the characteristics of falling rocks," *China Metal Bulletin*, vol. 8, pp. 148–150, 2020.
- [29] H. Zhu, Z. Yang, L. Cheng, K. Luorong, and Z. Liu, "Research on the trajectory of dangerous rock caving based on rockfall numerical simulation——taking a certain section of dangerous rock in the three gorges reservoir area as an example," *Science and Technology Innovation*, vol. 19, pp. 45–46, 2020.
- [30] H. Jianqun, "Application of rockfall software in the design of geological collapse prevention and control engineering," *Engineering Construction and Design*, vol. 12, pp. 33–34, 2020.
- [31] S. Zhang and Y. Luo, "Discussion on the prevention method of boulder roll-off on the slope of high and steep rock building based on rockfall simulation," *Guangdong Civil Engineering and Construction*, vol. 26, no. 2, pp. 54–63, 2019.
- [32] C. Luo, Z. Xiang, and R. Chen, "Design of stone barrier based on rockfall," *Nonferrous Metal Design*, vol. 45, no. 4, pp. 12–23, 2018.
- [33] Z. Lin, H. Wang, K. Gong, and G. Chen, "Research on the protection design of spherical weathered granite slope rolling rock disaster," *Journal of Fuzhou University (Natural Science Edition)*, vol. 44, no. 5, pp. 760–766, 2016.
- [34] C. Luo, X. Zhiqun, and C. Renquan, "Rock retaining wall design based on rockfall," *Design of Nonferrous Metals*, vol. 45, no. 4, pp. 12–23, 2018.
- [35] S. Ye, H. Tang, and H. Zhu, "Design concept of rock-blocking net based on analysis of rockfall motion characteristics," *Chinese Journal of Geotechnical Engineering*, vol. 4, pp. 566–571, 2007.
- [36] X. Wang, L. Pai, and H. Wu, "Simulation analysis and experimental study on the failure of bridge structure caused by slope collapse and rock fall of Lalin railway," *Chinese Journal of Rock Mechanics and Engineering*, vol. 39, no. 8, pp. 1622–1633, 2020.
- [37] United Nations. Department of Humanitarian Affairs, *Mitigating Natural Disasters: Phenomena, Effects and Options. A Manual for Policy Maker and Planners*, United Nations, New York, NY, USA, 1991.

Research Article

The Prediction of Pile Foundation Buried Depth Based on BP Neural Network Optimized by Quantum Particle Swarm Optimization

Fei Yin , Yong Hao , Taoli Xiao , Yan Shao , and Man Yuan 

School of Urban Construction, Yangtze University, Jingzhou, Hubei, China

Correspondence should be addressed to Yong Hao; 518004@yangtzeu.edu.cn

Received 19 April 2021; Revised 28 May 2021; Accepted 16 June 2021; Published 24 June 2021

Academic Editor: Faming Huang

Copyright © 2021 Fei Yin et al. This is an open access article distributed under the Creative Commons Attribution License, which permits unrestricted use, distribution, and reproduction in any medium, provided the original work is properly cited.

Due to the fluctuation of the bearing stratum and the distinct properties of the soil layer, the buried depth of the pile foundation will differ from each other as well. In practical construction, since the designed pile length is not definitely consistent with the actual pile length, masses of piles will be required to be cut off or supplemented, resulting in huge cost waste and potential safety hazards. Accordingly, the prediction of pile foundation buried depth is of great significance in construction engineering. In this paper, a nonlinear model based on coordinates and buried depth of piles was established by the BP neural network to predict the samples to be evaluated, the consequence of which indicated that the BP neural network was easily trapped in local extreme value, and the error reached 31%. Afterwards, the QPSO algorithm was proposed to optimize the weights and thresholds of the BP network, which showed that the minimum error of QPSO-BP was merely 9.4% in predicting the depth of bearing stratum and 2.9% in predicting the buried depth of pile foundation. Besides, this paper compared QPSO-BP with three other robust models referred to as FWA-BP, PSO-BP, and BP by three statistical tests (RMSE, MAE, and MAPE). The accuracy of the QPSO-BP algorithm was the highest, which demonstrated the superiority of QPSO-BP in practical engineering.

1. Introduction

Pile foundation is one of the oldest foundation forms. With the development of history, pile foundation has become the most commonly used foundation form of high-rise buildings, significant structures, tunnels, bridges, offshore platforms, and other structures on soft ground [1]. Pile, as a member of foundation structure, is vertically or aslant set in the soil and has certain stiffness and bending shear capacity. It allows itself to pass through the soft compressible soil layer, compact the weak soil, and transmit part or all of the load from the superstructure to the soil layer or rock below with low compressibility and certain bearing capacity, thus avoiding the excessive settlement of the foundation and improving the bearing capacity of the soil layer [2]. As one of the most important steps in foundation construction, the construction of pile foundation is a large-scale project; meanwhile, there is also a problem of waste of materials. It is

usually found that the designed length of pile is much higher or lower than the required value in actual engineering, which can be seen from Figure 1

Each pile to be bored would be surveyed in advance according to current construction technique. There is a construction technique of “one pile with one investigation” or “one pile with lots of investigation” [3], namely, each pile to be driven will be investigated in advance, and the pile length is designed by the elevation of pile bottom which is estimated by the most unfavorable principle, but this technique is not adopted in every project [4]. Only a few survey boreholes are arranged to predict the soil distribution of the whole site in general engineering.

When the irregular fluctuation of the bearing stratum changes greatly, it may result in a large elevation difference between the undrilled area and the nearby drilled area. Therefore, in the area where the bearing stratum is relatively shallow, the pile will reach the bearing stratum too early and



FIGURE 1: The buried depth of piles in the site varied greatly.

cannot continue going deeper. At this time, the pile head will extend too long from the soil and needs to be cut off, which can be seen from Figure 2 below. On the contrary, in the area where the bearing stratum is deeply distributed, the pile length will be insufficient and needs to be supplemented. The reason for this situation is that the variety of pile length is limited, especially the prefabricated pile. If the construction is carried out according to the designed pile length, a large number of piles will be cut off or supplemented, resulting in unnecessary waste in pile foundation engineering. Therefore, this paper predicted the buried depth of pile foundation and bearing stratum, then made targeted technical scheme preparation and construction deployment in practical engineering according to the prediction results.

At present, there are few research studies on predicting the buried depth of pile foundation and the fluctuation of bearing stratum; however, in the field of pile foundation engineering, many scholars have made some achievements. In the static load test of pile foundation finished by Qi et al. [5], a first-order linear dynamic differential equation was derived by studying the settlement of pile under various loads. On the basis of gray system theory, the GM (1, 1) model of load-settlement relationship of single pile was established and employed to predict the ultimate bearing capacity and the complete load-settlement relationship. Despite the accurate prediction results obtained by this method, the uniformity of original data should be ensured. According to the measured data, Gao et al. [6] adopted the hyperbolic method to predict the bearing capacity of squeezed branch pile. Although the error between the predicted results and the measured curve was not great, the values predicted by this method were generally too large and had certain limitations. Deng et al. [7] used the superlong and large-diameter cast-in-place pile foundation of the Sutong Yangtze River Bridge as an example to calculate its settlement amount by adopting different specifications, and then a new empirical formula considering pile compression and modifying additional stress of the pile tip was proposed

by comparing with the settlement value of the large-scale centrifugal model test. Afterwards, this formula was applied to verify the settlement value of a super large-scale pile group foundation on the Nei-Kun Line, and the calculation result of which was relatively consistent with the measured data. However, this formula was not suitable for the analysis of single pile settlement, which had certain limitations as well.

Most of the forecasting methods mentioned above rely on a fixed knowledge framework and can only be adopted under certain preconditions, which are rigid and not flexible enough. As a consequence, an intelligent technology that can deal with various problems flexibly and has self-learning awareness will be needed. Machine learning, as a technology that computers build models based on data to simulate human activities, can meet this condition. It possesses the strong generalization ability and has been applied in different aspects. Methods of machine learning were used by Ahmadi et al. [8] to successively predict the solubility of carbon dioxide (CO_2) in brines, porosity and permeability of petroleum reservoirs, the amount of dissolved calcium carbonate concentration throughout oil field brines, condensate-to-gas ratio in retrograded condensate gas reservoirs, solubility of hydrogen sulfide (H_2S) in ionic liquids, etc. The prediction of pile foundation depth belongs to a highly nonlinear problem, which can also be analyzed by this method. The artificial neural network (ANN) is a kind of machine learning, which is a powerful intelligent learning tool with functions [9, 10] such as mapping nonlinear relations, information processing, optimization calculation, classification, and recognition. It has been widely applied in the fields of model prediction, content prediction, cost control, fault diagnosis, information processing, construction engineering, mechanical engineering, medicine, etc., and the results were great as expected. Hamid et al. [11] built an ANN model based on the critical pressure (P_c), critical temperature (T_c), and molecular weight (M_w) of pure ionic liquids to predict the solubility of hydrogen sulfide (H_2S) in different temperature, pressure, and concentration ranges.

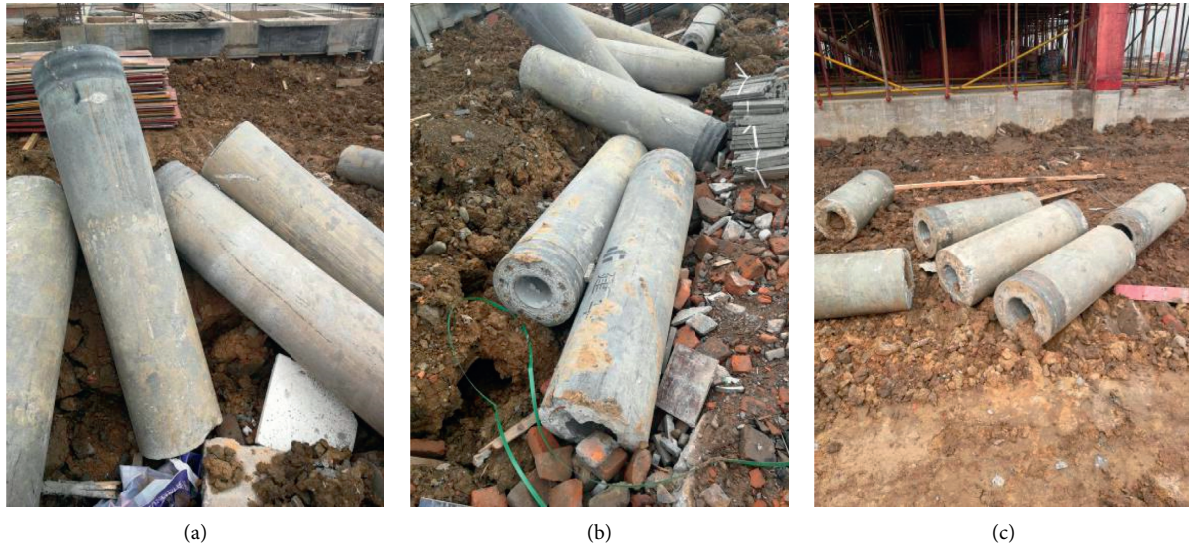


FIGURE 2: The section of the pile that has been cut off.

Moosavi et al. established an ANN model based on 214 data records of published CO₂-foam injection tests into oil-reservoir cores to predict the CO₂-foam flooding performance for improving oil recovery. Shang et al. [12] proposed two kinds of ANN models to analyze the content and types of heavy metals in the soil based on the complex permittivity of materials, so as to determine whether the soil is contaminated. The first ANN model was adopted to confirm the presence of heavy metals in the site, and the second model was employed to classify the presence of heavy metals in the site. Alias et al. [13] completed the cost of the skeletal system of a building project through the ANN model. Sorsa et al. [14] detected and diagnosed the faults in the testing process based on three different ANN structures. Jin et al. [15] established an ANN model with water-cement ratio, specimen shape, and section size as input parameters based on the size effect of concrete compressive strength, then predicted the compressive strength with different section sizes. Suzuki [16] found it feasible to apply the improved ANN to reduce false positives in computer detection of pulmonary nodules in low-dose computed tomography images, and the results turned out to be great.

The emergence of ANN provides a more convenient and intelligent prediction way for many fields. It no longer needs a large amount of statistical data to predict the future trend but can achieve a good prediction effect based on limited data. Therefore, in this paper, the highly nonlinear problem of the prediction of pile foundation burial depth can be solved by relying on ANN.

Among them, the backpropagating (BP) neural network is the most widely used artificial neural network, which is a multilayer feedforward neural network trained according to the error backpropagation algorithm. It has a certain ability of summary and extension. Some mathematical analysis has demonstrated its ability to deal with any nonlinear problem to solve complex internal mechanisms [17]. However, there are still some shortcomings of the traditional BP network at present. (1) It is a complex process for the BP neural network

to optimize the objective function by using the gradient descending method, and when the output of neurons is in the vicinity of 0 and 1, the weight error only changes within a small range. This phenomenon causes training to almost stop, so that the efficiency of the BP neural network is low and the speed of the BP neural network is at a slow pace [18]. (2) From the mathematical point of view, the algorithm used by the BP neural network is mainly to search the local area, which will easily fall into the local extreme value. The final training curve presented is almost going to be a straight line, as a result of which the training of the network will fail [19]. (3) The prediction ability of the network is proportional to the learning ability within a certain range, but once beyond this range, the prediction ability of the BP neural network will decline with the improvement of the learning ability, which leads to the phenomenon of “overfitting.” At this time, even if the network has learned a large sample, it cannot directly and correctly reflect its rules [20]. To sum up, there will be plenty of deficiency when the BP neural network is solely used for prediction; as a result, it is necessary to apply some algorithms to optimize the BP neural network and then establish a more accurate training model.

In recent years, several swarm intelligence optimization algorithms have emerged in an endless stream. This kind of algorithm is also one of the optimization algorithms that scholars pay the most attention to, which has the characteristics of simplicity and high efficiency when compared with others [21]. So that they have been also widely adopted in various fields. The swarm intelligence algorithm uses the group relations among some animals or individuals in the society, such as interaction, heredity, variation, cooperation, and other behaviors, to achieve the purpose of searching for optimal solution.

Fireworks algorithm (FWA) is a new swarm intelligence optimization algorithm proposed by Tan et al. [22] in recent years, which simulates the mechanism of the simultaneous explosion and diffusion of the firework explosion operator. It introduces the idea of concentration suppression in the

immune algorithm and the mechanism of distributed information sharing, thus having stronger global search capabilities [23]. Compared with traditional algorithms, the population of FWA is more diverse, and its characteristics have also attracted the attention of many scholars. However, the FWA still has several shortcomings. For example, when the explosion point range is large and there are many explosion operators, the targets generated by the explosion will overlap, resulting in irrelevant searches. Then, it will greatly affect the optimization efficiency of FWA, which is the major cause of slower convergence speed and lower search accuracy [24].

Particle swarm optimization (PSO) algorithm [25], as one of the most classic optimization algorithms, is inspired by the foraging behavior of birds. It seeks the optimal value in the stochastic solution of particle swarm through constant iteration. Compared with FWA, it has the advantages of simple operation and fewer parameters to be adjusted [26]. Ahmadi et al. [27] used the neural network model optimized by the PSO algorithm to predict asphaltene precipitation due to natural depletion. Wang et al. [28] predicted the mechanical properties of hot rolled strip steel in material processing based on the PSO-BP model. Likewise, this PSO-BP model was applied by Ismail et al. [29] in the field of soil-structure composite interaction to predict the load-deformation characteristics of axially loaded piles as well. Shafiei et al. [30] predicted the solubility of hydrogen sulfide in different temperature, pressure, and concentration ranges in the same way. Ahmadi et al. used the PSO-ANN model to predict the dew point pressure of condensate gas reservoir. In another paper by the same author, estimation of efficiency of chemical flooding in oil reservoirs was predicted. Although the above literature studies have achieved relatively good prediction results, the PSO algorithm still has plenty of problems, and it has been proved that it is not a globally convergent algorithm [31]. In the meantime, it also has some problems to be solved, such as premature convergence, lack of dynamic adjustment of velocity, easy to fall into local extreme value, lack of randomness in particle position change, inability to effectively deal with discrete and combinatorial optimization, and limitation of search space [32]. From the perspective of dynamics, there is a point with potential energy field in the search area that attracts the particle swarm, causing the surrounding particles to constantly approach this point. When the velocity decreases to 0, the particles converge to this point as well. Therefore, the motion of each particle in the traditional PSO algorithm is carried out along a fixed orbit, the velocity of the particle is always a finite value, and the search area of its feasible solution is also small [33]. In order to improve the global optimization capability of PSO, this algorithm needs to be optimized. As a result, the concept of quantum particle swarm algorithm (QPSO) was proposed by Sun [34].

Based on the traditional PSO algorithm, the QPSO algorithm randomizes the velocity of the particle. In the quantum space, the state of the particle is not represented by position and velocity vector any more, but by wave function. In this way, within the feasible region, the probability of particles appearing at a position is random, and the motion

of particles is no longer along a fixed orbit. Their updated position in the next second has no correlation with the previous position; that is, the search can be carried out in the whole feasible solution region, which improves the global optimization performance of particles. Chen et al. [35] took the gear reducer of belt conveyor as the research object and optimized the parameters such as modulus, tooth width coefficient, and helical angle of the gear reducer based on the QPSO and PSO algorithm. The results showed that the optimization effect of QPSO was obviously better than that of PSO. Genetic algorithm (GA) and ANN, PSO, and QPSO algorithms were used by Lu et al. [36] to predict the parameters of the batch fermentation kinetic model. The results demonstrated that the prediction effect of QPSO in all aspects was superior to that of other algorithms. Therefore, on the basis of the BP neural network, this paper used the QPSO algorithm to optimize the BP model and then predicted the buried depth of pile foundation. Finally, three error analysis tools, RMSE, MAE, and MAPE, were, respectively, employed to analyze its reliability and uncertainty.

Based on the above, this paper provides the following contributions. (1) In this paper, the ANN in machine learning was used to predict the buried depth of pile foundation. However, there were very few research studies on this topic before; as a result, it can be applied as a new field in practical engineering. (2) In this paper, the samples of piles were collected on the spot based on engineering examples. The relevant parameters of pile samples in this area were sorted out and summarized, which were X -coordinate, Y -coordinate, Z -coordinate, thickness of miscellaneous fill h_1 , thickness of silty clay h_2 , thickness of silt h_3 , thickness of fine sand h_4 , and pile buried depth H . Some samples were selected as training models. (3) In this paper, the steps of predicting test objects after optimizing the BP neural network by the QPSO algorithm were described in detail. (4) This paper used the QPSO algorithm to optimize the BP neural network for modeling training and then predicted the remaining samples in step (2). The great global optimization of the QPSO algorithm successfully made up for the defect that the traditional PSO algorithm was easy to fall into the local extreme value, and the prediction results were very close to the measured results, indicating that this method had achieved a good prediction effect in the research objects. (5) This paper compared the errors of the QPSO algorithm with other robust models: PSO algorithm, FWA, and BP neural network. The results showed that QPSO had higher prediction accuracy.

This paper also introduces the following parts. Section 2 introduces training parameters based on project example. Section 3 describes the concept of BP neural network and the optimization methods of PSO and QPSO algorithms. Section 4 is the error analysis after using different algorithms to optimize the BP neural network for prediction. Section 5 is the conclusion of the above description and the analysis of the predicted results. At the same time, this paper also gives an overview of how to apply this method in engineering examples with similar soil propriety.

2. Project Example

2.1. Project Profile. The project is located in the East Campus of Yangtze University in Jingzhou District, Jingzhou City, Hubei Province, which was to build dormitory and canteen in this area. According to the design document, this investigation site with pile location layout is shown in Figures 3–5 below.

The distribution of boreholes and piles can be obtained from the figure. Each long black dotted line, such as “11-11’,” represents “11-11’ section” of boreholes from K64 to K67. According to the section drawings, the soil stratification at each borehole from K64 to K67 can be known. First of all, the piles at the boreholes were selected as the data of the network model, X -coordinate, Y -coordinate, and Z -coordinate of each pile were taken according to the coordinate information provided by layout drawings, and the length of the bearing stratum and the buried depth of pile were obtained from the section drawings. In order to make the selected data representative, 43 piles were randomly selected as the training samples and 10 piles were randomly selected as the prediction samples from the boreholes of investigation in the figure. With the difference of the geographical location, the fluctuation of the bearing stratum of the site will have a certain trend of change as well. The process of driving the pile into the bearing stratum needs to pass through different soil layers on the upper side. However, the thickness of each soil layer at the undetected coordinates is an uncertain unknown. As the thickness of the soil layer is different, the depth of the bearing layer changes to another number, which will affect the buried depth of the pile. According to the field data, the piles were all driven into the fine sand layer, which indicated that the fine sand layer was the bearing stratum. The depth of the sample pile into the first layer of soil called miscellaneous fill is h_1 , the depth of the sample pile into the second layer of soil called silty clay is h_2 , the depth of the sample pile into the third layer of soil called silt is h_3 , and the depth of the sample pile into the fourth layer of soil called fine sand is h_4 which presents the bearing stratum. H is the sum of h_1 , h_2 , h_3 , and h_4 , which represents the buried depth of pile. The depth of the sample pile into different layers of soil can be calculated by combining the geological profile and the data of pile buried depth H measured from actual engineering. Based on the above, the X -coordinate, Y -coordinate, and Z -coordinate of each pile were collected as input parameters for model training. In this training, to predict the fluctuation of the bearing stratum is to predict the depth of h_4 , to predict the buried depth of pile is to predict the depth of H , and the thickness of h_4 is less than the thickness of fine sand layer. In addition, $H = h_1 + h_2 + h_3 + h_4$, H and h_4 are output parameters. The schematic diagram is shown in Figure 6.

2.2. Geological Overview. The terrain of the site is relatively flat, and the absolute elevation value of the ground is in the range of 31.5 m–32.88 m, which belongs to the first-grade terraced geomorphic unit on the north bank of the Yangtze River. There is no adverse geological action such as landslide,

soil collapse, and debris flow. According to the detailed investigation report of the site, the area within this depth range can be divided into artificial fill soil layer, Quaternary Holocene alluvium and Quaternary Upper Pleistocene alluvium and diluvium according to its genetic type and sedimentary age [37].

According to their properties and composition, the geotechnical layers can be classified into the following parts, which are distributed as follows: (1) artificial fill soil layer (Q^{ml}), miscellaneous fill, brown, moist, and loose. The main component is clay, containing a small amount of plant rhizomes. This layer is distributed in the whole field, and the soil uniformity is poor. The thickness is 0.4 m–1.7 m. (2) Quaternary Holocene alluvium (Q_4^{al}), silty clay, yellowish-brown to grayish-brown, soft to plastic, saturated, full-field distribution. This layer contains a small amount of ferromanganese nodules and medium compressibility. The thickness is 4.5 m–14.8 m. (3) Quaternary Holocene alluvium (Q_4^{al}), silt, gray, slightly density to medium density, saturated, full-field distribution, medium compressibility.

The thickness is 1.9 m–12.4 m. (4) Quaternary Holocene alluvium (Q_4^{al}), fine sand, gray, medium density, saturated, full-field distribution, mainly composed of quartz and feldspar, and low compressibility. The thickness is 3.9 m–16.5 m. (5) Quaternary Upper Pleistocene alluvium and diluvium (Q_3^{al+pl}), pebbles, gray, white and other colors, medium dense to dense state, low compressibility, and full-field distribution. The main component is quartzite, with good roundness and poor sorting. The particle size is generally 3~5 cm, and the larger particle size is greater than 7 cm, of which the particle size greater than 2 cm accounts for about 51%. The filling material between pebbles is fine silty sand.

It can be seen from the above data that the thickness and uniformity of each layer are greatly different.

3. Optimization Algorithms for Pile Depth Prediction

3.1. Implementation of BP Neural Network Algorithm. As the name suggests, the neural network is an artificial intelligence algorithm to simulate the human brain nervous system, which has a strong self-learning ability and can deal with complex nonlinear models [9, 10]. Through the connections of countless neurons, it can carry out huge parallel processing and analysis on the information of the previous input layer and then pass it to the next layer. A large amount of training can constantly update the weights of the neuronal connections in the front and rear layers, so as to achieve the goal of reducing error and meeting people’s expectations.

X -coordinate, Y -coordinate, and Z -coordinate of pile were regarded as input parameters for model training of the BP algorithm. Besides, the depth of bearing stratum h_4 and buried depth of pile H were regarded as output parameters. The detailed process can be described as the following steps. (1) A training model based on X -coordinate, Y -coordinate, Z -coordinate, h_4 , and H of 43 training samples was established. (2) The h_4 and H of 10 remaining samples were predicted. (3) The values of output parameters were compared with measured values. (4)

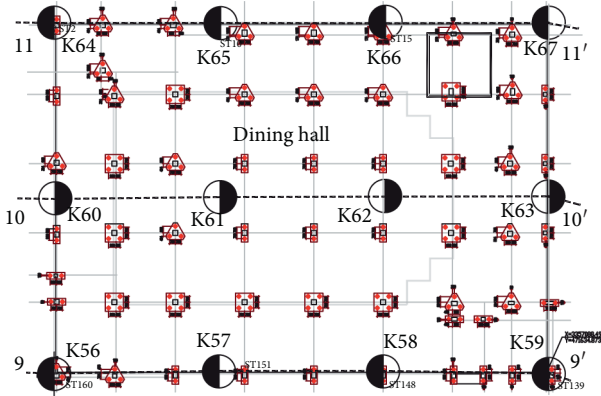


FIGURE 3: The investigation site with pile location layout of dining hall.

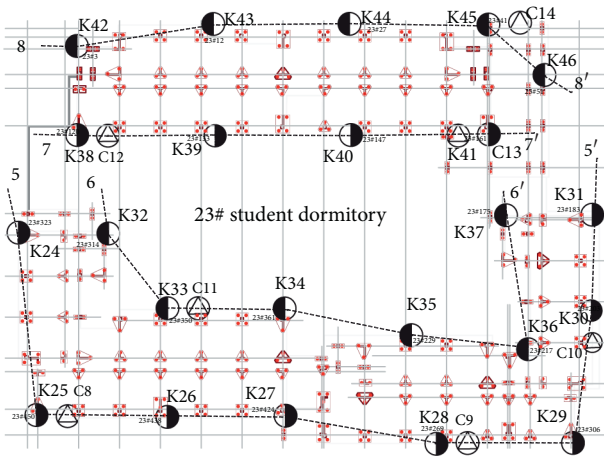


FIGURE 4: The investigation site with pile location layout of 23# student dormitory.

The error between predicted values and measured values was analyzed. During the process of prediction, there was no correlation between the input and output parameters, which was a nonlinear function. As a result, the three-layer network for nonlinear function can meet the training requirements in the BP algorithm [17]. The diagram is shown in Figure 7.

The S-type action function shown in (1) is its activation function [38]:

$$f(x) = \frac{1}{1 + e^{-x}}, \quad (1)$$

where x_k is the input parameter of the input layer; v_j is the output parameter of hidden layer; y_k is the output parameter of output layer; w_{jk} is the connection weight of neurons between the input layer unit and the hidden layer unit; and w_{ij} is the connection weight of neurons between hidden layer unit to output layer unit. The number of neurons of input layer, hidden layer, and output layer is, respectively, n , m , and l .

The training process was as follows:

- (1) Since the activation function of the neural network is a logarithmic S-type function, it may have the

problem of convergence; that is, the infinite or infinitesimal results appear in the calculation process. Therefore, the input data of X-coordinate, Y-coordinate, and Z-coordinate and output data h_4 and H of the samples should be normalized first, which was to make these values vary from 0 to 1.

- (2) The values randomly generated in the interval $[-1, 1]$ were taken, and the initial values were assigned to the weights.
- (3) The independent variable parameters of the processed sample data were input at the corresponding nodes of the input layer, and the output values of the BP neural network were calculated at the corresponding nodes of the output layer through the action of weight and activation function.
- (4) The output values of the BP neural network training were compared with the expected values, and then the error between them was calculated.
- (5) The error obtained was propagated back from the output layer, and the weight was corrected according to the gradient method when it reached the first layer, and then step (3) was repeated and recalculated.
- (6) The above steps (1)–(5) were repeated until the error function satisfied equation:

$$E = \frac{1}{2} \sum_{i=1}^m (y_i - o_i)^2 \leq \varepsilon. \quad (2)$$

After the BP neural network had been trained according to the above steps, the trained network model could be used to predict the samples. Based on the measured data from engineering project, 43 and 10 piles were, respectively, selected as input and test vectors, and each pile was determined by three parameters.

The BP algorithm with single hidden layer was adopted in this paper. It was difficult to determine the number of neurons in the hidden layer, and the neurons affected the determination of accuracy to a certain degree. If the number of neurons was too small, the algorithm had almost no ability to train. On the contrary, if the number of neurons was too large, the training time would be extended, which was easy to fall into the local optimal solution. As a result, the normal predicted values were not available to obtain. Generally, there are three methods to identify hidden layer neurons [39]: (1) For FangfaGorman theory, the relation between the number of neurons S and the input parameter N is $S = \log_2 N$; (2) for Kolmogorov theory, the relation between the number of neurons S and the input parameter N is $S = 2N + 1$; (3) the relation between the number of neurons S and the input parameter N and the output parameter M is $S = \sqrt{0.43MN + 0.12NN + 2.54M + 0.77N + 0.35} + 0.51$. The input parameter N was 3, and the output parameter M was 2 in this BP training; thus, the calculated S using the above three method was, respectively, 1.58, 7, and 3.45. Since the number of neurons needed to be an integer,

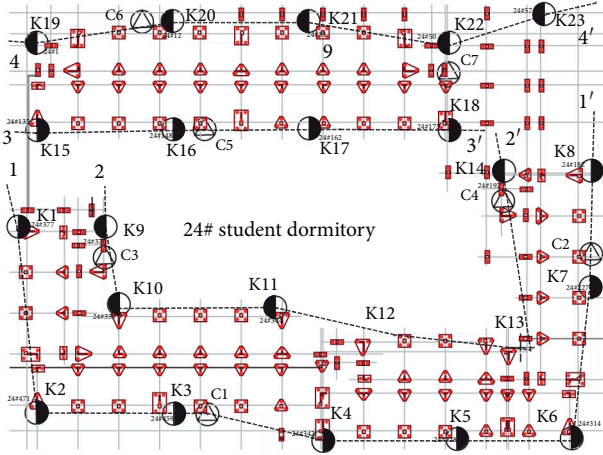


FIGURE 5: The investigation site with pile location layout of 24# student dormitory.

three values of 2, 4, and 7 were selected for prediction and the errors of them were compared in the later section.

The transfer function in hidden layer and output layer was S-type tangent function and logarithmic function, respectively. The network training function was “traingdx,” gradient descent method was used during learning process, and the learning rate was adaptive.

3.2. Implementation of PSO-BP Algorithm. The process of the BP algorithm optimized by PSO is shown as follows [40]:

- (1) Firstly, the maximum number of iterations required, the number of independent variables required by the objective function, the maximum particle velocity, and the position information of particles were set as the whole search space. In addition, the velocity and position coordinates were initialized randomly in the velocity interval and search space, and each particle was given an initialized random flight velocity.
- (2) The fitness function was defined, and each particle would have an extreme value, which was the individual extreme value and the optimal solution of the unit particle. Then, a global value was found from the optimal solution of all particles, that was, the global optimal solution. Finally, this optimal solution was updated after comparing with the global optimal solution obtained in history.
- (3) The updating velocity and position [41] were, respectively, shown in equations:

$$V_{id} = \omega V_{id} + C_1 \text{random}(0, 1)(P_{id} - X_{id}) + C_2 \text{random}(0, 1)(P_{gd} - X_{id}), \quad (3)$$

$$X_{id} = X_{id} + V_{id}, \quad (4)$$

where ω is inertial factor and a nonnegative value. When ω is large, the ability to find the global optimal solution is strong, but the ability to find the local

optimal solution is weak. When ω is small, the ability to find the global optimal solution is weak, but the ability to find the local optimal solution is strong. Therefore, the ability to find the global and local optimal solution can be adjusted by different values of ω . C_1 and C_2 are learning factors, and current research studies [42] have investigated that a better solution can be obtained when C_1 and C_2 are constants. The values of C_1 and C_2 are between [0, 4], which are equal to 2 in general. The random (0, 1) is a random value on the interval [0, 1]. P_{id} is the individual extremum of i -th variable at d -dimension; P_{gd} is the global optimal solution at d -dimension.

The weights and thresholds optimized by PSO can be assigned as initial value for training and prediction of the BP algorithm [40]. The detailed process is shown in Figure 8.

The PSO-BP algorithm can be realized in two methods. (1) By combining the powerful global searching ability of the PSO algorithm with the local searching ability of the BP neural network, the global searching performance of the PSO algorithm is used to compensate for the topological structure, weight, and threshold of the BP neural network, so as to optimize the generalization and training ability, and the overall searching performance of the BP neural network. (2) The BP algorithm is added to the PSO algorithm, and the optimization performance of the PSO algorithm is improved through the powerful training and learning skills of the neural network, which can reduce the huge required workload and accelerate the convergence of the PSO algorithm. In this paper, the first method was adopted to obtain the optimal initial threshold through the PSO algorithm, and it was assigned to the BP algorithm to improve the efficiency and accuracy.

However, in the PSO algorithm, the convergence form of the particle is along the orbit, and the maximum velocity of the particle is always a finite value, which leads to certain limitations in the search area of the PSO, which cannot guarantee that it can search the whole feasible space, and the global convergence will be affected [33].

3.3. Implementation of QPSO-BP Algorithm. Based on the traditional PSO algorithm, the QPSO algorithm randomizes the velocity of the particle. In the quantum space, the state of the particle is not represented by position and velocity vector, but by wave function. Due to the uncertainty principle, the probability of a particle appearing at a certain place x is expressed by a probability density function, and no longer along a fixed orbit. As a result, the position of the particle has no relationship with the previous position [43]. The evolution equations of each dimension of the particle state are shown by the following equations:

$$P_{id}(t) = \varphi_{id} P_{id}(t) + (1 - \varphi_{id}(t)) P_{gd}(t), \quad (5)$$

$$X_{id}(t+1) = P_{id}(t) \pm \frac{1}{2} L_{id}(t) \times \text{In} \left[\frac{1}{u_{id}(t)} \right], \quad (6)$$

where P_{id} is the attractor of the i -th particle in the evolutionary iteration, X_{id} is the current position of the i -th

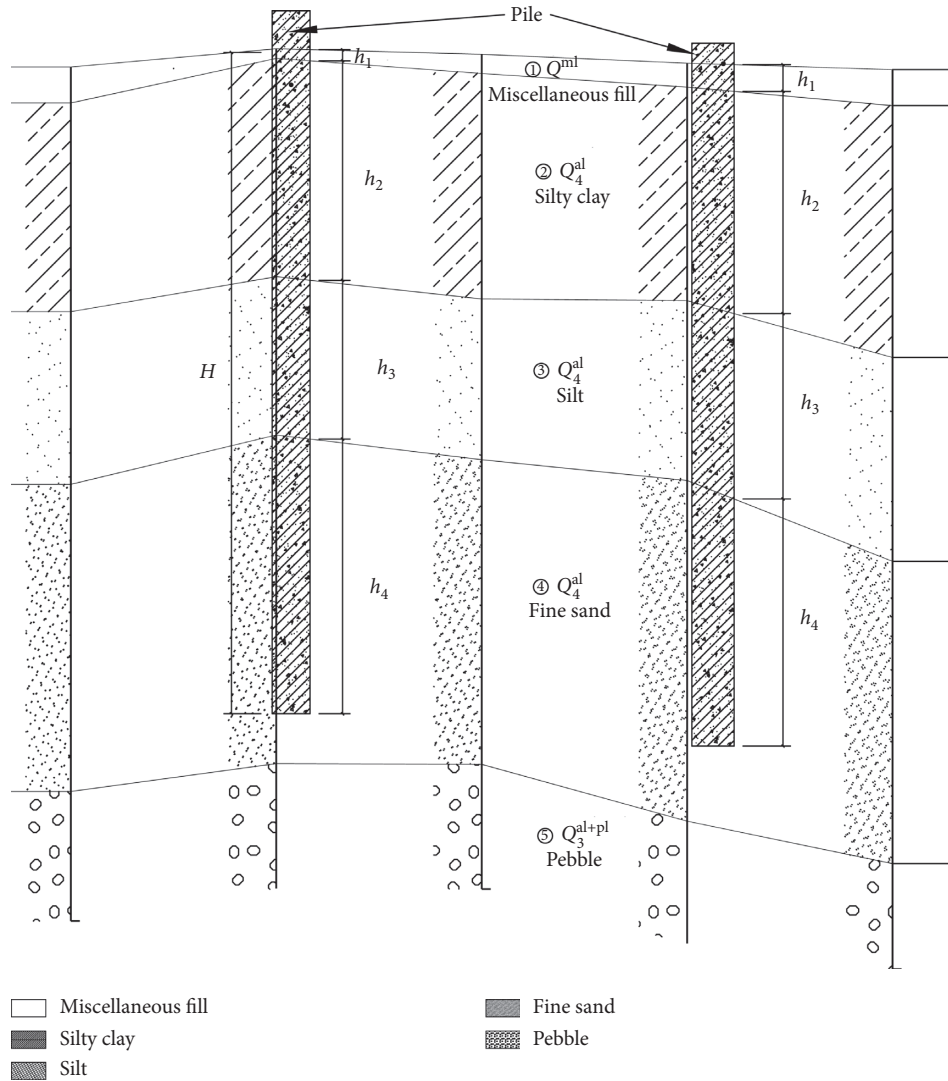


FIGURE 6: Schematic diagram of h_1 , h_2 , h_3 , h_4 , and H .

particle, φ_{id} and u_{id} are uniformly distributed random numbers on $[0, 1]$, and L_{id} represents the characteristic length of the attractor and potential well, which is used to describe the search range of a particle, and L_{id} can be shown in the following equation [43]:

$$L_{id}(t) = 2\alpha \times |MBP_{id}(t) - X_{id}(t)|, \quad (7)$$

where $MBP_{id}(t)$ is the mean best position, and α is the compression-expansion factor.

By substituting equations (7) into (6), the iterative equation (8) below of quantum group evolution can be obtained:

$$X_{id}(t+1) = p_{id}(t) \pm \alpha \times |MBP_{id}(t) - X_{id}(t)| \times \ln \left[\frac{1}{u_{id}(t)} \right]. \quad (8)$$

The size of the particle swarm is set as M . The implementation of its specific steps is as follows. (1) Initialize the particle swarm and set the maximum number of iterations.

(2) Determine and initialize the individual optimal extremum and global optimal extremum of the particle swarm. (3) The fitness value of each particle is calculated. (4) The individual optimal extremum of each particle and global optimal extremum of the particle swarm are updated. (5) The new position of the particle swarm is calculated according to equation (8), and then the original particle swarm is updated. (6) Repeat steps (2)–(5) until the fitness values of the particle swarm meet the convergence condition.

The above is the principle and realization of QPSO, and the method of using the QPSO algorithm to optimize the BP neural network is similar to that of PSO. The explanation in Section 3.2 above can be used as a reference.

4. Analysis of Results

4.1. Prediction Results of Different Models. The original 43 groups of data for training were shown in Table 1, which were prepared to form a database to predict the other 10

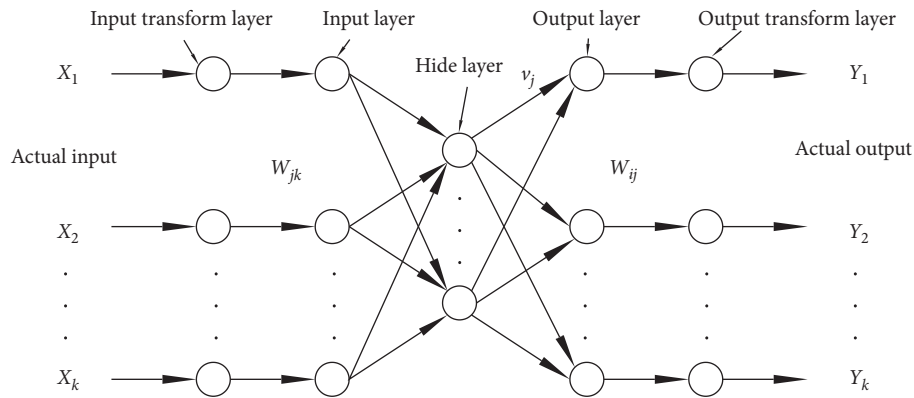


FIGURE 7: Schematic diagram of three-layer neural network transmission.

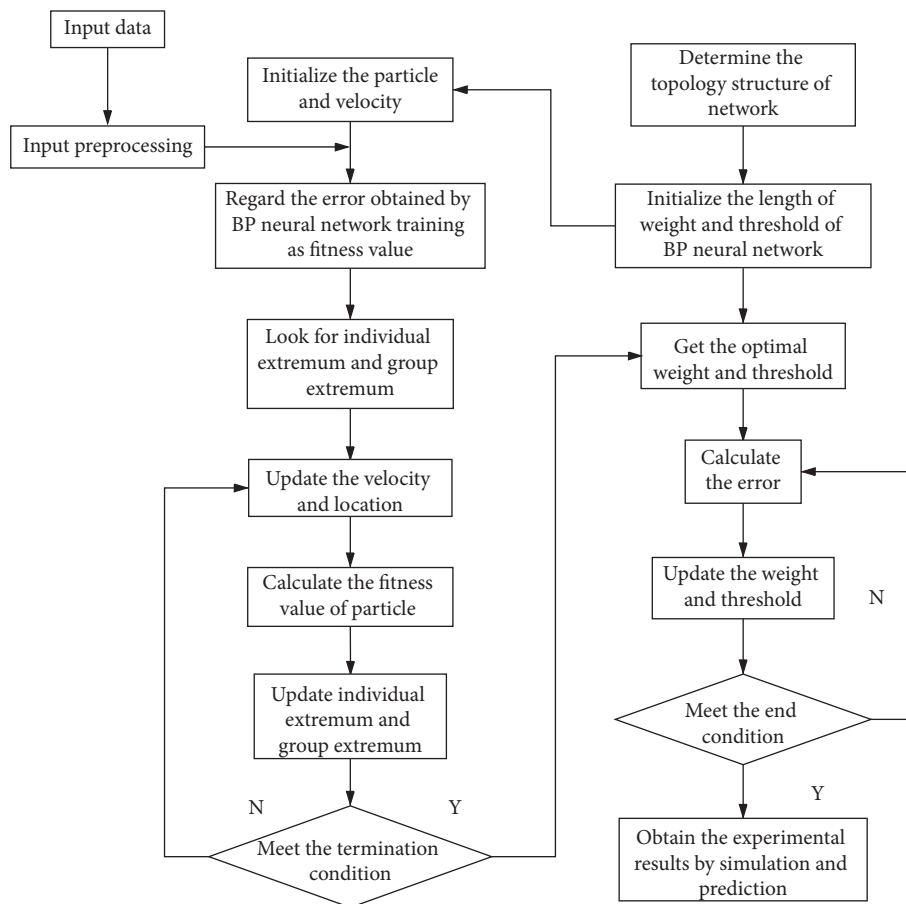


FIGURE 8: Flowchart of the PSO-BP algorithm.

groups of samples to be evaluated, where X -coordinate, Y -coordinate, and Z -coordinate were input parameters and h_4 and H were output parameters.

The original 10 groups of data to be evaluated are shown in Table 2.

The first was the prediction result of the BP neural network. As mentioned above, the number of hidden layer neurons was calculated by three different methods, which were 2, 4, and 7, respectively. Therefore, three different prediction results and error comparison for h_4 and H based on the number of neurons

in the hidden layer were obtained, which are shown in Figures 9–12.

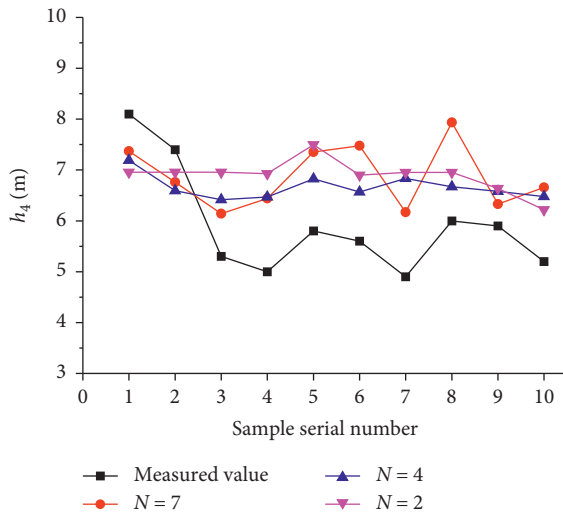
It can be known from the above figures that different numbers of hidden layer neurons can affect the forecast results. When the number of neurons in the hidden layer was 7, the errors of the BP neural network in predicting h_4 and H were smaller than that of the other two neurons. This phenomenon indicated the forecast result of the second method mentioned in Section 3.1 named Kolmogorov theorem was the best. In addition, no matter how many neurons there were, the errors

TABLE 1: 43 groups of data for training.

No.	Pile number	Borehole number	X-coordinate	Y-coordinate	Z-coordinate	h_1 (m)	h_2 (m)	h_3 (m)	h_4 (m)	H (m)
1	3	K42	11.7510	171.2880	31.9300	0.40	12.60	3.80	6.60	23.40
2	12	K43	32.2510	174.2880	31.7000	0.70	12.10	4.50	5.90	23.20
3	27	K44	59.6510	174.2880	31.9600	1.30	12.60	3.10	6.70	23.70
4	41	K45	82.4510	175.6380	31.9200	0.80	14.20	2.70	6.90	24.60
5	51	K46	91.7000	164.9380	31.9700	0.90	12.70	3.30	7.60	24.50
⋮	⋮	⋮	⋮	⋮	⋮	⋮	⋮	⋮	⋮	⋮
39	15	K66	53.0730	246.5240	31.7400	1.40	12.30	2.70	6.80	23.20
40	160	K56	12.7330	204.0270	31.6100	1.30	9.00	5.50	7.60	23.40
41	151	K57	36.2730	204.9410	31.5900	1.30	11.90	3.00	7.10	23.30
42	148	K58	53.0730	203.5410	31.8600	1.20	13.30	2.10	6.80	23.40
43	139	K59	73.5230	204.9410	31.9400	1.30	4.50	9.90	7.70	23.40

TABLE 2: 10 groups of data for prediction.

No.	Pile number	Borehole number	X-coordinate	Y-coordinate	Z-coordinate	h_1 (m)	h_2 (m)	h_3 (m)	h_4 (m)	H (m)
1	314	K32	14.4510	136.7880	31.9800	0.50	11.00	4.90	8.10	24.50
2	350	K33	25.0510	124.4880	31.8700	1.20	10.60	5.20	7.40	24.40
⋮	⋮	⋮	⋮	⋮	⋮	⋮	⋮	⋮	⋮	⋮
9	306	K29	97.5713	103.1992	32.0300	0.40	14.30	3.90	5.90	24.50
10	269	K28	74.0510	102.5880	31.9100	1.10	13.10	5.00	5.20	24.40

FIGURE 9: The prediction curve of h_4 when the number of BP neural network neurons was 2, 4, and 7, respectively.

between the prediction results of the sample using the BP neural network algorithm and the actual values were still very large. Especially, for the prediction results of h_4 , the maximum error was up to about 41% when the number of neurons was 2 and was up to about 31% when the number of neurons was 7. Besides, it was found in Figures 9 and 10 that the curves of prediction results of the BP neural network were all relatively gentle and the basic trend was a straight line, which proved that the BP network is easy to fall into the characteristics of searching for local optimal solution. Therefore, in order to compensate the lack of global search capacity of the BP network, the QPSO algorithm was going to be employed to optimize the BP network model when the number of neurons in the hidden layer was 7.

The linear fitting formula for predicting h_4 and H had been calculated. The calculation results indicated that the deviation between the prediction values and the actual values reached 58.8%, which demonstrated the necessity of using the QPSO-BP algorithm. In order to intuitively observe the error comparison between different algorithms, relative error was adopted to compare the accuracy of QPSO-BP, PSO-BP, and FWA-BP. The formula can be seen in the following equation:

$$E_R = \frac{|x_p - x_a|}{x_a}, \quad (9)$$

where x_p is the predicted value and x_a is the actual value.

The parameter settings of the BP neural network and QPSO algorithm were as described below. The number of iterations of the BP network was 1000, the training goal of the BP network was 0.01, the learning rate of the BP network was 0.001, the population size of the QPSO algorithm was 20, the dimension of the QPSO algorithm was 30, and the iteration termination error of QPSO was 10^{-7} . Compared with other models, QPSO was simple to operate and had fewer parameters to set.

The predicted curves of different models are shown in Figures 13 and 14. The predicted error curves of different models are shown in Figures 15 and 16.

According to Figures 15 and 16, a conclusion can be confirmed that the relative error of QPSO-BP was the smallest compared with that of PSO-BP, FWA-BP, and linear fitting. In the process of predicting h_4 , the minimum relative error was 9.4%, the maximum relative error was only 14.7%, and all of the errors were basically around 11%; in the process of predicting H , the maximum relative error was merely 2.9%, which confirmed the powerful prediction accuracy of QPSO. Furthermore, the prediction curve of

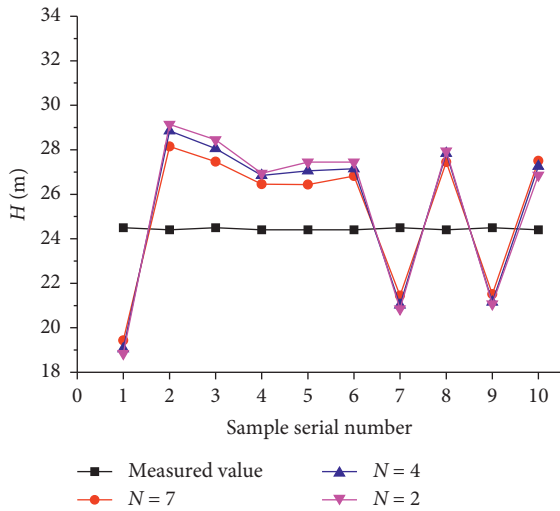


FIGURE 10: The prediction curve of H when the number of BP neural network neurons was 2, 4, and 7, respectively.

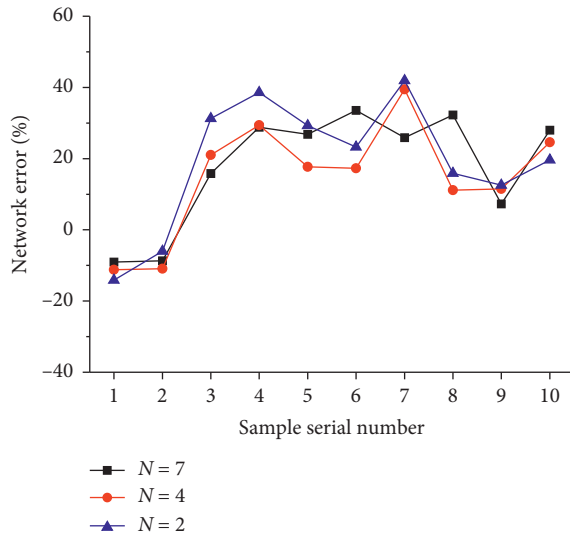


FIGURE 11: The prediction error curve of h_4 when the number of BP neural network neurons was 2, 4, and 7, respectively.

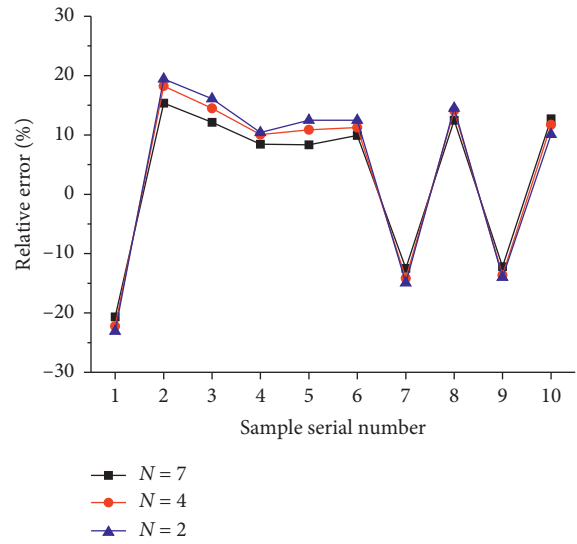


FIGURE 12: The prediction error curve of H when the number of BP neural network neurons was 2, 4, and 7, respectively.

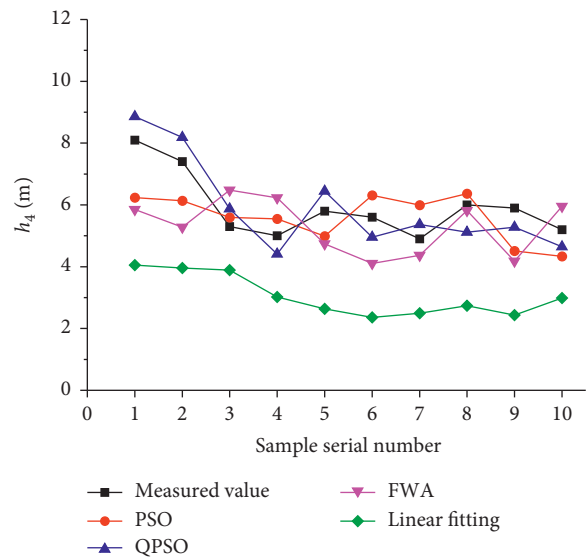


FIGURE 13: The prediction curve of h_4 by using different models.

QPSO-BP possessed the characteristic of fluctuation, rather than an almost flat straight line like the BP network. This showed that QPSO successfully compensated for the lack of global search characteristics of BP and was not easy to fall into the endless loop of finding local optimal solution. After comparison and analysis, the accuracy of these models in descending order was QPSO-BP > PSO-BP > FWA-BP > linear fitting.

Figure 17 shows the convergence curves of QPSO-BP, PSO-BP, and FWA-BP. It can be seen from the figure that the curve of decreasing fitness of QPSO-BP started to be very smooth and tended to a fixed value after iterating for about 25 times, and then the program stopped iterating when the number of iterations was around 143, which presented the optimal value of QPSO-BP had been discovered. Besides, from the comparison of the iterative curves of the other two

algorithms, it can be seen that the decline rate of QPSO in the early stage was the fastest, and it was the first of the three models to converge in the subsequent iterative process, which demonstrated the capability of fast search and convergence of QPSO.

The above conclusions indicated that it was feasible to use the QPSO-BP method in machine learning to predict the buried depth of pile foundation and the fluctuation of bearing stratum, and the particle swarm optimization algorithm was already a relatively mature optimization algorithm compared with many other algorithms, which was not difficult to implement. QPSO-BP has the advantages of fast search and fast convergence speed, simple operation, and high precision; therefore, it was more reasonable to apply this algorithm in this paper.

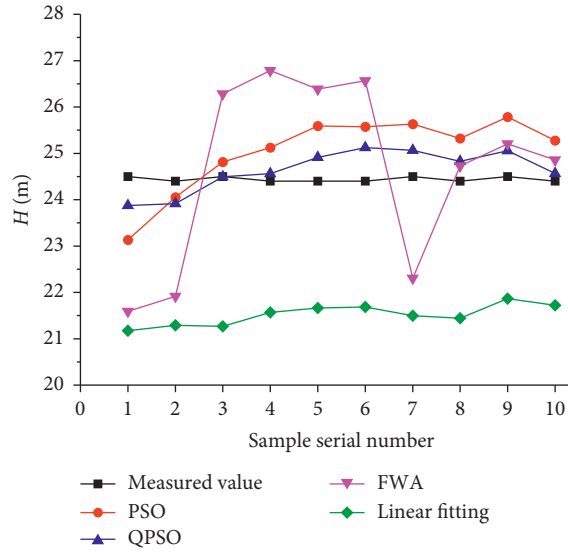


FIGURE 14: The prediction curve of H by using different models.

4.2. Error Analysis of Different Models. In order to further prove the powerful prediction accuracy of QPSO, three statistical test methods were, respectively, used [44–46], namely, RMSE, MAE, and MAPE. The three formulas can be obtained from equations (10)–(12), and the error comparison of different algorithms can be seen in Table 3 in detail.

RMSE is root mean square error, which represents the square root of the ratio of the square deviation between the actual value and the predicted value to the number of test sets. It evaluates the model by the following criteria: the smaller the value of RMSE, the smaller the error of the model and the higher the accuracy. When the actual value is completely consistent with the predicted value, it means this model is a perfect model:

$$\text{RMSE} = \sqrt{\frac{1}{n} \sum_{i=1}^n (x_{ai} - x_{pi})^2}, \quad (10)$$

where x_{ai} is the actual value, x_{pi} is the predicted value, and n is the number of test sets.

MAE is mean absolute error, which represents the average of the absolute values of the deviations of all predicted values and the arithmetic mean. It evaluates the model by the following criteria: the smaller the value of MAE, the smaller the error of the model and the higher the accuracy. Similar to RMSE, when the actual value is exactly the same as the predicted value, it is also a perfect model:

$$\text{MAE} = \frac{1}{n} \sum_{i=1}^n |x_{ai} - x_{pi}|. \quad (11)$$

MAPE is mean absolute percentage error, which measures the relative errors between the average predicted value and the actual value on the test set [40]. It evaluates the model by the following criteria, the smaller the value of MAE, the smaller the error of the model and the higher the accuracy. Similar to RMSE and MAE, it is also an ideal

model when the actual value is consistent with the predicted value:

$$\text{MAPE} = \frac{100\%}{n} \sum_{i=1}^n \left| \frac{x_{ai} - x_{pi}}{x_{ai}} \right|. \quad (12)$$

According to the statistical tests, the minimum RMSE of QPSO-BP was only about 0.48, that of PSO-BP was about 0.99, and that of FWA was about 1.94, while the maximum RMSE of BP reached 3.16. Similarly, the MAE and MAPE values of QPSO were the minimum values compared with those of the other three models, which confirmed our checking calculation above. Furthermore, by separately comparing the prediction results of h_4 and H , the accuracy of these models was as the following orders, QPSO-BP > PSO-BP > FWA-BP > BP, which was also echoed above.

Because of its high accuracy, fast convergence, and few parameters, QPSO successfully demonstrates its advantages in practical application.

4.3. Application of QPSO-BP in Practical Engineering. In a practical project similar to the geological condition of the project in Section 2.2, the method proposed in this paper can be adopted to predict the distribution of bearing stratum and the buried depth of pile foundation. The specific implementation steps are as follows: (1) it is necessary and the most critical step for professional personnel to conduct geotechnical investigation, which determine whether the soil properties in the area meet the predicted conditions or not. (2) The designers should determine the specific location of each pile foundation in AutoCAD based on the pile foundation design drawings and geotechnical investigation report, and then sort out the X -coordinate, Y -coordinate, and Z -coordinate, which must be based on the geodetic origin. (3) The QPSO-BP model is employed to predict the indicators to be predicted with a method similar to that in this paper. (4) According to the prediction results, the length of the precast pile in the area with different bearing depth can be determined, and then the pile number and

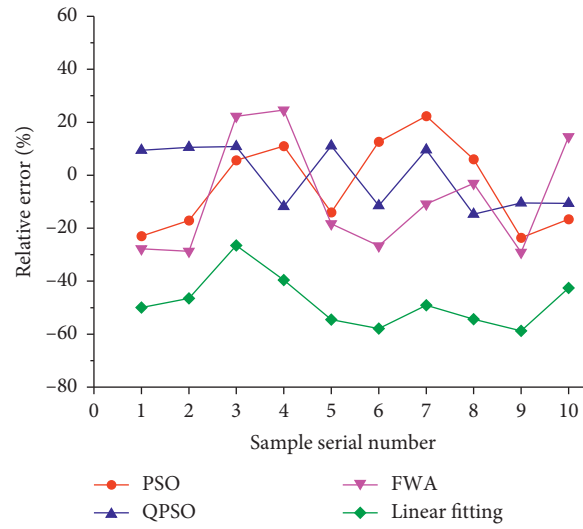


FIGURE 15: The prediction error curve of h_4 by using different models.

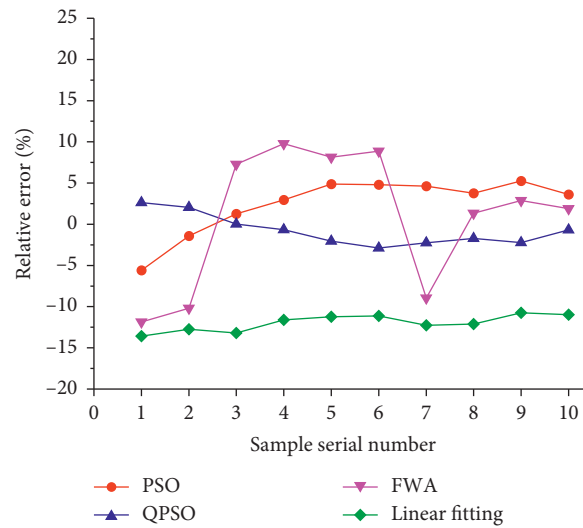


FIGURE 16: The prediction error curve of H by using different models.

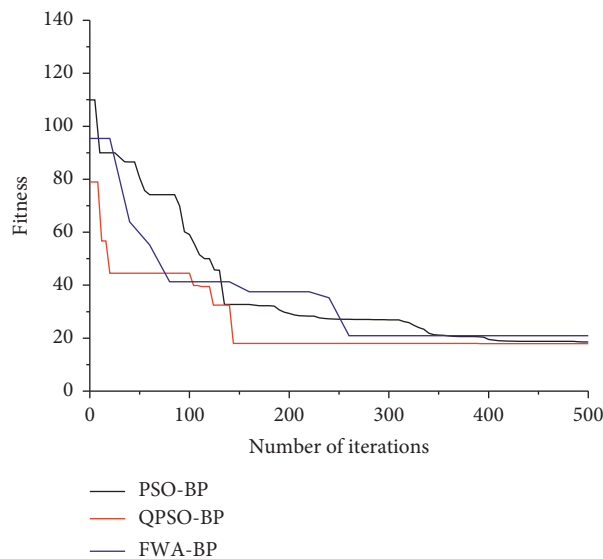


FIGURE 17: Convergence curves of the QPSO-BP, PSO-BP, and FWA-BP models.

TABLE 3: Statistical tests of the different models.

Model		RMSE	MAE	MAPE (%)
BP	h_4	1.317045	1.218072	21.6218
	H	3.159338	3.047166	12.4648
FWA-BP	h_4	1.403003	1.253222	20.5951
	H	1.943137	1.739423	7.1161
PSO-BP	h_4	1.030985	0.920521	15.1887
	H	0.998472	0.93352	3.819
QPSO-BP	h_4	0.662284	0.65193	11.0622
	H	0.478191	0.423976	1.7347

corresponding coordinates are recorded. Finally the piles will be driven into the soil layer one by one in the actual engineering.

5. Conclusion

It is of great significance to determine the fluctuation of bearing stratum and the buried depth of pile foundation before construction, which can effectively reduce the project cost and avoid unnecessary losses. The QPSO-BP model was adopted to deal with this highly nonlinear problem, and the following part is a summary of the specific work completed in this paper:

- (1) Based on engineering examples, the BP network model was used to predict the fluctuation of bearing stratum and the buried depth of pile foundation in this paper. Besides, when the number of neurons S in the hidden layer and the input parameters N meet $S = 2N + 1$, the error of prediction results was the minimum.
- (2) The prediction results indicated that the BP network would easily fall into the local optimal solution, and the error between the predicted value and the actual value was quite large; the maximum error of which reached about 41% when the number of neurons was 2 and 31% when the number of neurons was 7. Therefore, although the predicted value of the BP neural network could be used as a reference, its algorithm still had shortcomings and disadvantages. Therefore, it needed to be optimized.
- (3) The QPSO algorithm was adopted to optimize the BP network, and then the model of QPSO-BP was no longer trapped in the infinite loop of searching for local optimal solution. The relative error was merely 9.4% in predicting h_4 and 2.9% in predicting H . Besides, two other optimization algorithms (FWA and PSO) were used to optimize the BP model, and the results demonstrated the high accuracy of QPSO-BP. The error of QPSO-BP was the smallest of the three algorithms.
- (4) Three different statistical tests (RMSE, MAE, and MAPE) were further employed to evaluate the accuracy of the three models. The calculation results of the three statistical tests were consistent with the above, and the accuracy followed the order of QPSO-BP > PSO-BP > FWA-BP.
- (5) All the evidence demonstrated the superiority of the QPSO-BP model in engineering application.

Data Availability

The case analysis data used to support the findings of this study are available from the corresponding author upon request.

Conflicts of Interest

The authors declare that there are no conflicts of interest regarding the publication of this paper.

Acknowledgments

This study was supported by the Science and Technology Project of Jingzhou (2019AC27), China.

References

- [1] M. F. Randolph, "Science and empiricism in pile foundation design," *Geotechnique*, vol. 53, no. 10, pp. 847–876, 2003.
- [2] J. R. Meyer, *Analysis and Design of Pile Foundations*, ASCE, Virginia, NV, USA, 2015.
- [3] Z. M. Zhang, "Achievements and problems of geotechnical engineering investigation in china," *Journal of Zhejiang University-Science*, vol. 12, no. 2, pp. 87–102, 2011.
- [4] W. Fleming, A. J. Weltman, M. F. Randolph, and K. Elson, *Piling Engineering*, CRC Press, Boca Raton, FL, USA, 3rd edition, 2009.
- [5] K. J. Qi, M. J. Xu, and J. M. Zai, "Gray prediction of ultimate bearing capacity of single pile," *Chinese Journal of Rock Mechanics and Engineering*, vol. 23, no. 12, p. 2069, 2004.
- [6] X. J. Gao and X. R. Zhu, "Forecasting ultimate bearing capacity of single squeezed branch pile by hyperbola method," *Rock and Soil Mechanics*, vol. 27, no. 9, pp. 1596–1600, 2006.
- [7] Y. S. Deng, W. M. Gong, and A. M. Yuan, "Research on calculating methods for settlement of extra-long large-diameter pile group," *Journal of the China Railway Society*, vol. 29, no. 4, pp. 87–90, 2007.
- [8] M. Ali Ahmadi, "Applying a sophisticated approach to predict CO₂ solubility in brines: application to CO₂ sequestration," *International Journal of Low Carbon Technologies*, vol. 11, no. 3, pp. 325–332, 2016.
- [9] E. Másson and Y. J. Wang, "Introduction to computation and learning in artificial neural networks," *European Journal of Operational Research*, vol. 47, no. 1, pp. 1–28, 2007.
- [10] M. D. Himmelblau, "Accounts of experiences in the application of artificial neural networks in chemical engineering," *Industrial & Engineering Chemistry Research*, vol. 47, no. 16, pp. 5782–5796, 2008.
- [11] H. R. Amedi, A. Baghban, M. A. Ahmadi et al., "Evolving machine learning models to predict hydrogen sulfide solubility in the presence of various ionic liquids," *Journal of Molecular Liquids*, vol. 216, pp. 411–422, 2016.
- [12] J. Q. Shang, W. Ding, R. K. Rowe, and L. Josic, "Detecting heavy metal contamination in soil using complex permittivity and artificial neural networks," *Canadian Geotechnical Journal*, vol. 41, no. 6, pp. 1054–1067, 2004.
- [13] M. Alias, R. Dhanya, and G. Ramasamy, "Study on factors affecting the performance of construction projects and developing a cost prediction model using," *Annals of Forestry*, vol. 8, pp. 2189–2194, 2015.

- [14] T. Sorsa and H. N. Koivo, "Application of artificial neural networks in process fault diagnosis," *IFAC Proceedings Volumes*, vol. 24, no. 6, pp. 423–428, 1991.
- [15] L. Jin, R. Zhao, and X. L. Du, "Neural network prediction model for size effect of concrete compressive strength," *Journal of Beijing University of Technology*, vol. 47, no. 3, pp. 260–268, 2021.
- [16] K. Suzuk, S. G. Armato, F. Li, S. Sone, and K. Doi, "Massive training artificial neural network (MTANN) for reduction of false positives in computerized detection of lung nodules in low-dose computed tomography," *Medical Physics*, vol. 30, no. 7, pp. 1602–1617, 2003.
- [17] S. Ding, H. Li, C. Su, J. Yu, and F. Jin, "Evolutionary artificial neural networks: a review," *Artificial Intelligence Review*, vol. 39, no. 3, pp. 251–260, 2013.
- [18] T. He, S. Zheng, P. Zhang, and M. Zou, "Input values function for improving generalization capability of BP neural network," in *Proceedings of the Asia-Pacific Conference on Wearable Computing Systems*, pp. 228–231, Shenzhen, China, April 2010.
- [19] H. Ai and S. Guo, "Bridge health evaluation system based on the optimal BP neural network," *International Journal of Control & Automation*, vol. 7, no. 1, pp. 331–338, 2014.
- [20] J. H. Wang, J. H. Jiang, and R. Q. Yu, "Robust back propagation algorithm as a chemometric tool to prevent the overfitting to outliers," *Chemometrics and Intelligent Laboratory Systems*, vol. 34, no. 1, pp. 109–115, 1996.
- [21] C. C. Shi, Y. Y. Zeng, and S. M. Hou, "Application of swarm intelligence algorithm in image segmentation," *Computer Engineering and Applications*, vol. 57, no. 08, pp. 36–47, 2021.
- [22] Y. Tan and Y. C. Zhu, "Fireworks algorithm for optimization," in *Proceedings of the Advances in Swarm Intelligence (ICSI 2010)*, vol. 6145, pp. 355–364, Beijing, China, June, 2010.
- [23] Y. Tan, *FWA Application on Non-Negative Matrix Factorization*, Springer, Berlin, Germany, 2015.
- [24] S. Zheng, A. Janecek, and Y. Tan, "Enhanced fireworks algorithm," in *Proceedings of the IEEE Congress on Evolutionary Computation*, IEEE, Cancun, MX, USA, June 2013.
- [25] J. Kennedy, "Particle swarm optimization," in *Proceedings of the 1995 IEEE International Conference Neural Networks*, Perth, Australia, December 2011.
- [26] A. Khare and S. Rangnekar, "A review of particle swarm optimization and its applications in solar photovoltaic system," *Applied Soft Computing Journal*, vol. 13, no. 5, pp. 2997–3006, 2013.
- [27] M. A. Ahmadi and S. R. Shadzadeh, "New approach for prediction of asphaltene precipitation due to natural depletion by using evolutionary algorithm concept," *Fuel*, vol. 102, 2012.
- [28] P. Wang, Z. Y. Huang, M. Y. Zhang, and X.-W. Zhaoi, "Mechanical property prediction of strip model based on PSO-BP neural network," *Journal of Iron & Steel Research International*, vol. 15, no. 3, pp. 87–91, 2008.
- [29] A. Ismail, D.-S. Jeng, and L. L. Zhang, "An optimised product-unit neural network with a novel PSO-BP hybrid training algorithm: applications to load-deformation analysis of axially loaded piles," *Engineering Applications of Artificial Intelligence*, vol. 26, no. 10, pp. 2305–2314, 2013.
- [30] A. Shafiei, M. A. Ahmadi, S. H. Zaheri et al., "Estimating hydrogen sulfide solubility in ionic liquids using a machine learning approach," *The Journal of Supercritical Fluids*, vol. 95, pp. 525–534, 2014.
- [31] J. Kennedy and R. Eberhart, "Particle swarm optimization," in *Proceedings of ICNN'95-International Conference on Neural Networks*, pp. 1942–1948, Perth, WA, Australia, December 1995.
- [32] W. Fang, J. Sun, Y. Ding, X. Wu, and W. Xu, "A review of quantum-behaved particle swarm optimization," *IETE Technical Review*, vol. 27, no. 4, pp. 336–348, 2010.
- [33] J. Li, J. Q. Zhang, C. J. Jiang, and M. Zhou, "Composite particle swarm optimizer with historical memory for function optimization," *IEEE Transactions on Cybernetics*, vol. 45, no. 10, pp. 2350–2363, 2017.
- [34] J. Sun, B. Feng, and W. Xu, "Particle swarm optimization with particles having quantum behavior," in *Proceedings of the 2004 Congress on Evolutionary Computation (IEEE Cat. No. 04TH8753)*, pp. 325–331, Portland, OR, USA, June 2004.
- [35] Y. T. Chen and Q. Zhang, "Optimization design and simulation of belt conveyor gear based on levy flight quantum particle swarms," *Machinery Design & Manufacture*, vol. 4, no. 4, pp. 54–57, 2020.
- [36] K. Lu and R. Wang, "Application of PSO and QPSO algorithm to estimate parameters from kinetic model of glutamic acid batch fermentation," in *Proceedings of the 2008 7th World Congress on Intelligent Control and Automation*, pp. 8968–8971, Choungqing, China, June 2008.
- [37] Q. P. Zuo and L. Huang, "Evaluation factors of overburden thickness and site type in Jingzhou urban area," *Resources Environment & Engineering*, vol. 29, no. 6, pp. 940–944, 2015.
- [38] Z. B. Xu, R. Zhang, and W. F. Jing, "When does online BP training converge?" *IEEE Transactions on Neural Networks*, vol. 20, no. 10, pp. 1529–1539, 2009.
- [39] S. X. Xu and L. Chen, "A novel approach for determining the optimal number of hidden layer neurons for FNN's and its application in data mining," in *Proceedings of the 5th International Conference on Information Technology and Applications (ICITA)*, pp. 683–686, Cairns, Australia, June 2008.
- [40] L. J. Liu, D. H. Liu, H. Wu, and X. Y. Wang, "The prediction of metro shield construction cost based on a backpropagation neural network improved by quantum particle swarm optimization," *Advances in Civil Engineering*, vol. 2020, Article ID 6692130, 15 pages, 2020.
- [41] Y. Shi and R. Eberhart, "A modified particle swarm optimizer," in *Proceedings of the IEEE International Conference on Evolutionary Computation. IEEE World Congress on Computational Intelligence (Cat. No.98TH8360)*, pp. 69–73, Anchorage, AK, USA, May 1998.
- [42] H. Li, Q. Zhang, and Y. Zhang, "Improvement and application of particle swarm optimization algorithm based on the parameters and the strategy of co-evolution," *Applied Mathematics & Information Sciences*, vol. 9, no. 3, pp. 1355–1364, 2015.
- [43] D. Z. Pan and Y. J. Chen, "Quantum-behaved particle swarm optimization algorithm based on reverse random-weighted mean best position," *Journal of China West Normal University (Natural Sciences)*, vol. 33, no. 3, pp. 281–285, 2012.
- [44] M. Najafzadeh and G. A. Barani, "Comparison of group method of data handling based genetic programming and back propagation systems to predict scour depth around bridge piers," *Scientia Iranica*, vol. 18, no. 6, pp. 1207–1213, 2011.
- [45] M. Najafzadeh and F. Saberi-Movahed, "GMDH-GEP to predict free span expansion rates below pipelines under waves," *Marine Georesources & Geotechnology*, vol. 37, no. 3, pp. 1–18, 2018.
- [46] F. Saberi-Movahed, M. Najafzadeh, and A. Mehrpooya, "Receiving more accurate predictions for longitudinal dispersion coefficients in water pipelines: training group method of data handling using extreme learning machine conceptions," *Water Resources Management*, vol. 34, pp. 529–561, 2020.

Research Article

A Constitutive Model of Sandy Gravel Soil under Large-Sized Loading/Unloading Triaxial Tests

Pengfei Zhang,¹ Han Liu,¹ Zhentu Feng,² Chaofeng Jia,² and Rui Zhou³ 

¹Hebei Research Institute of Construction and Geotechnical Investigation Co. Ltd., Shijiazhuang 050031, China

²Luoyang Rail Transit Group Co Ltd., Luoyang 471000, Henan, China

³School of Civil Engineering, Beijing Jiaotong University, Beijing 100044, China

Correspondence should be addressed to Rui Zhou; 18121179@bjtu.edu.cn

Received 23 April 2021; Accepted 2 June 2021; Published 14 June 2021

Academic Editor: Faming Huang

Copyright © 2021 Pengfei Zhang et al. This is an open access article distributed under the Creative Commons Attribution License, which permits unrestricted use, distribution, and reproduction in any medium, provided the original work is properly cited.

Based on large-scale triaxial tests of sandy gravel materials, the strength and deformation characteristics under loading/unloading conditions are analyzed. At the same time, the applicability of the hyperbolic constitutive model to sandy gravel is studied using experimental data. The results indicate that sandy gravel under low confining pressures (0.2 and 0.4 MPa) shows a weak softening trend; the higher the confining pressure, the more obvious the hardening tendency (0.6 and 0.8 MPa) and the greater the peak strength. During unloading tests, strain softening occurs, and the peak strength increases with increasing confining pressure. During loading tests, dilatancy appears when the confining pressure is low (0.2 MPa). With increasing confining pressure (0.4, 0.6, and 0.8 MPa), the dilatancy trend gradually weakens, and the cumulative volumetric strain increases, which reflects the relevance of the stress paths. Through research, it is found that the hyperbolic constitutive model has good applicability to sandy gravel soils, and the corresponding model parameters are obtained.

1. Introduction

With the rapid development of rail transit, shield tunnel construction has encountered many severe challenges in sandy gravel strata in China. For example, the first phase of the Luoyang Urban Rail Transit Line 2 project under construction uses the shield method to cross the sandy gravel stratum, which is particularly important for the ground settlement, seepage damage, and the stability of the excavation surface [1–3]. In addition to a large number of field tests, the mechanical characteristics and description of the stress-strain relationship of coarse-grained soil are hot topics [4, 5], which can provide necessary conditions for numerical calculations in practical engineering.

The mechanical properties of soils are determined by many factors, including externally applied stress, soil type, microstructure damage [6], density, matrix suction caused by surface tension passing through the air in unsaturated environments [7], and temperature [8–10]. To date, many constitutive models of saturated/unsaturated soil have been

proposed, but there are still many controversies regarding some basic problems [9, 11], such as the selection of state variables of stress and strain and the theoretical framework of hydraulic coupling processes [12, 13]. Alonso et al. [14] established a constitutive model of unsaturated soil materials by utilizing the double-stress variables of net stress and matrix suction. Many scholars [15, 16] have discussed the hydraulic coupling characteristics of saturated/unsaturated soil and even some basic thermo-hydromechanical coupling characteristics [17, 18]. These theoretical studies considered the influence of the volume water content on mechanical properties, such as irreversible compression during drying and changes in the water content during loading/unloading. Based on the principle of thermodynamics, some researchers [19–21] established the hydraulic coupling effects of three-phase unsaturated soil by analyzing the thermodynamic potential of the solid-liquid-gas phase and dissipated energy. Recently, Bai et al. [22] proposed a thermo-hydromechanical constitutive model for geomaterials in view of the concept of particle rearrangement during the thermodynamic process

of porous granular materials, which is contributed to understand the mechanical properties of the particle movement of sandy gravel soils from the microscopic point of view.

For subway tunnel projects in sandy gravel strata [23–25], when discussing settlement control and deformation characteristics, the constitutive relationship of sandy gravel is rarely mentioned, and the commonly used Mohr–Coulomb relationship is still utilized [26]. The actual sandy gravel is a kind of coarse-grained soil; however, it is not reasonable to use the Mohr–Coulomb relationship. Therefore, it is particularly important to study the deformation characteristics of shield tunneling in sandy gravel formations and to determine the appropriate constitutive model and parameters [27, 28]. It has important engineering significance in stratum settlement control and station foundation pit excavation [29].

In this paper, a large-sized laboratory triaxial shear test is carried out on sandy gravel soil taken from the Luoyang subway site, and then triaxial shear tests on sandy gravel under different confining pressures are carried out to determine the appropriate sandy gravel constitutive model as well as the model parameters accordingly. This work can help with engineering design and practice. The established constitutive model can well reflect the loading process and unloading process of sandy gravel soil, which is also used for the numerical calculation during the unloading process in the shield tunnel excavation process.

2. Experiments of Large Sandy Gravel Soil under a Complex Stress Path

2.1. Test Schemes. This paper selects sandy gravel soil samples from the first phase of the project of Luoyang Urban Rail Transit Line 2 to conduct a large-scale triaxial test. The purpose is to investigate two typical stress state change processes (namely, loading and unloading stress paths) and then determine the stress-strain relationship characteristics and volumetric strain-axial strain characteristics, as well as the seepage effect [30, 31] and damage mechanism of the soil layer [24, 32, 33].

Actually, the stress and deformation state changes of the surrounding stratum are very complicated during the shield tunnel excavation process [34, 35], even related to the effect of environmental temperature [36, 37] and the thermal-mechanical behavior of tunnel lining segments [38, 39]. For simplicity, this test simulates two extreme stress path change processes, namely, active failure and passive failure of the excavation surface. The specific test scheme is shown in Table 1, including 2 groups of tests. Among them, the sample size is 30 cm in diameter and 70 cm in height, and the test confining pressure is determined by the actual stress state at the site to be 200, 400, 600, and 800 kPa. The loading/unloading tests were accomplished by the stress-controlled method, and the shear rate was 0.2 kPa/s. This test primarily studies the strength and deformation characteristics of sandy gravel under triaxial compression and unloading conditions.

2.2. Preparation of Soil Samples. The soil layer in the project area is composed of silty clay, silt soil, a sand layer, and a gravel soil layer, which is a multilayer structure. According to the actual situation of the project, samples were taken at a depth of 10 m, and the dry density was controlled to be 2.27 g/cm^3 .

Through particle analysis, the maximum particle size of sandy gravel tested was 80 mm, and its characteristic particle size is shown in Table 2. The inhomogeneity coefficient of the soil is greater than 10, and the curvature coefficient is between 1 and 5. It belongs to coarse-grained soil with good gradation.

The test equipment was an SJ70 large-scale high-pressure triaxial shear tester. The test specimen has a diameter of 300 mm and a height of 700 mm. According to the sampling and sieving situation, the gravels that exceed the particle size limit of 60 mm account for only approximately 5%, so a particle size of 40–60 mm was used instead. The sample was prepared by splitting the soil into 5 layers. The sample preparation method uses a vibrator to vibrate. The static pressure of the vibrator bottom plate is 14 kPa, and the vibration frequency is 40 Hz. The vibration time is determined according to the dry density of the sample.

According to the actual engineering conditions and the high water permeability of sandy gravel, this test adopts the consolidated drained shear (i.e., CD) test. The sample saturation method adopts the suction saturation method.

3. Test Results and Analysis

3.1. Stress-Strain-Strength Characteristics. From the stress-strain relationship curves of sandy gravel in Figures 1 and 2, under the condition of the same shear rate, sandy gravel is loaded under low confining pressure (0.2 and 0.4 MPa), showing a weak softening trend. The higher the confining pressure, the more obvious the hardening tendency (0.6 and 0.8 MPa) and the greater the peak strength. For the unloading test, there is a more obvious softening phenomenon, and as the confining pressure increases, the peak value becomes more obvious. The deviator stress-strain curves of the two groups of sandy gravels show a strong nonlinear relationship when the stress and strain reach a certain value.

3.2. Volume Deformation Characteristics. Figures 3 and 4 give the $\varepsilon_v - \varepsilon_a$ relationship of sandy gravel when loading and unloading under different confining pressures. From Figure 3, under conditions of low confining pressure (0.2 MPa), sandy gravels exhibit shear shrinkage first and then dilatancy. As the confining pressure increases (0.4, 0.6, and 0.8 MPa), the dilatancy trend gradually weakens, and the cumulative body strain increases. Under unloading conditions (Figure 4), the main manifestation is dilatancy, and with increasing confining pressure, the dilatancy phenomenon becomes more obvious, which fully reflects the relevance of the stress path.

TABLE 1: Test schemes for large-size specimens.

Test number	Load path	Loading/unloading	Confining pressure (kPa)	Number of soil samples
1	$\sigma_3 = \text{constant}$, $\sigma_1 = \text{increases}$	Loading	200, 400, 600, 800	4
2	$\sigma_1 = \text{constant}$, $\sigma_3 = \text{decreases}$	Unloading	200, 400, 600, 800	4

TABLE 2: Particle gradation of sandy gravel samples.

Particle size (mm)	80	60	20	10	5	1	0.5	0.25	0.1
Cumulative percentage (%)	100	96.9	58.9	42.9	34.5	30.5	29.1	16.85	0

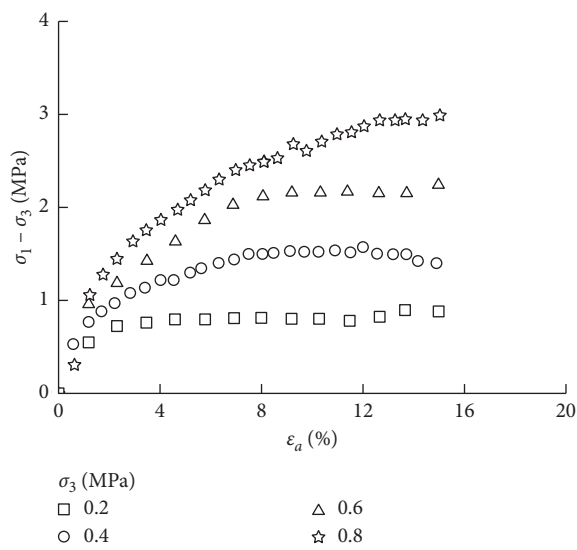


FIGURE 1: Axial stress-strain curve of sandy gravel soil under loading conditions.

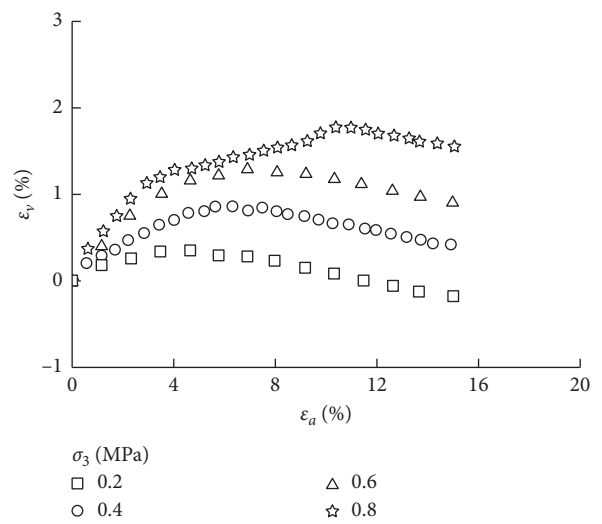


FIGURE 3: Curve of volumetric strain-axial strain under loading conditions.

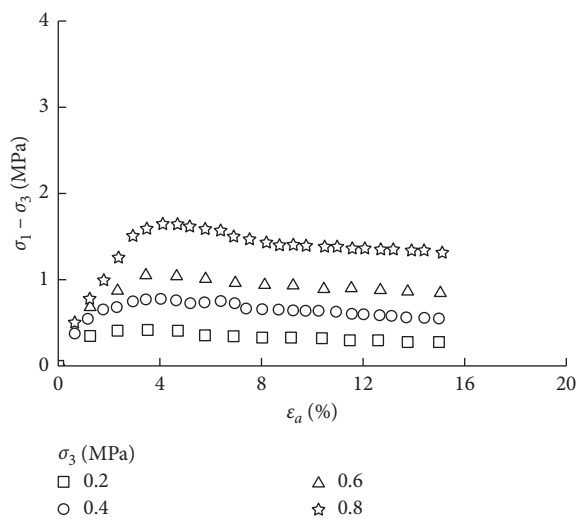


FIGURE 2: Axial stress-strain curve of sandy gravel soil under unloading conditions.

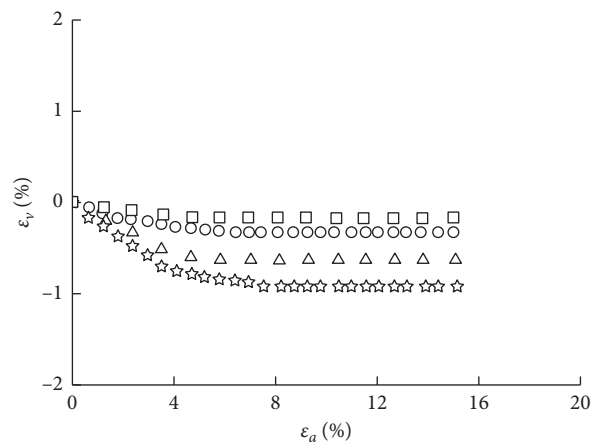


FIGURE 4: Curve of volumetric strain-axial strain under unloading conditions.

4. Constitutive Model of Sandy Gravel Considering the Loading/Unloading Process

Kondner [40] thought that the hyperbola can be used to fit the general triaxial test $(\sigma_1 - \sigma_3) - \varepsilon_1$ curve, namely,

$$(\sigma_1 - \sigma_3) = \frac{\varepsilon_a}{a + b\varepsilon_a}, \quad (1)$$

where a and b are test constants.

For the conventional triaxial shear test, $\varepsilon_a = \varepsilon_1$. Later, Duncan and Chang [41] proposed a widely used nonlinear elastic model, namely, the Duncan–Chang model, which was developed widely [42].

4.1. Conventional Triaxial Loading Test. Under conventional triaxial loading conditions, (1) can be written as

$$\frac{\varepsilon_1}{(\sigma_1 - \sigma_3)} = a + b\varepsilon_1, \quad (2)$$

where a is the intercept of the line and b is the slope of the line.

Obviously, there is an approximately linear relationship between $\varepsilon_1/(\sigma_1 - \sigma_3)$ and ε_1 . In the conventional triaxial shear test, the tangent elastic modulus can be expressed as

$$\begin{aligned} E_t &= \frac{d(\sigma_1 - \sigma_3)}{d\varepsilon_1}, \\ &= \frac{a}{(a + b\varepsilon_1)}. \end{aligned} \quad (3)$$

When $\varepsilon_1 = 0$ and $E_t = E_i$, the combination of (3) leads to

$$E_i = \frac{1}{a}. \quad (4)$$

When $\varepsilon_1 \rightarrow \infty$, from (1), we can get

$$(\sigma_1 - \sigma_3)_{\text{ult}} = \frac{1}{b}. \quad (5)$$

In (4) and (5), a represents the reciprocal of the initial elastic modulus E_i , and b represents the reciprocal of the ultimate deviator stress $(\sigma_1 - \sigma_3)_{\text{ult}}$ corresponding to the asymptote of the hyperbola.

In the conventional triaxial test, the shear strength $(\sigma_1 - \sigma_3)_f$ is determined according to the stress value corresponding to the strain value $\varepsilon_1 = 15\%$; for the stress-strain curve with a peak value, it generally takes its strength, that is, $(\sigma_1 - \sigma_3)_f = (\sigma_1 - \sigma_3)_{\text{peak}}$.

In this way, the damage ratio R_f can be defined as

$$R_f = \frac{(\sigma_1 - \sigma_3)_f}{(\sigma_1 - \sigma_3)_{\text{ult}}}. \quad (6)$$

Considering (5), one has

$$\begin{aligned} b &= \frac{1}{(\sigma_1 - \sigma_3)_{\text{ult}}}, \\ &= \frac{R_f}{(\sigma_1 - \sigma_3)_f}. \end{aligned} \quad (7)$$

Consider E_t as a function of stress, which can be obtained by transforming (2):

$$\varepsilon_1 = \frac{a(\sigma_1 - \sigma_3)}{1 - b(\sigma_1 - \sigma_3)}. \quad (8)$$

Substituting (8) into (3), we get

$$E_t = \frac{1}{a[1/(1 - b(\sigma_1 - \sigma_3))]^2}. \quad (9)$$

Substituting (4) and (7) into (9), we can get

$$E_t = E_i \left[1 - R_f \frac{(\sigma_1 - \sigma_3)}{(\sigma_1 - \sigma_3)_f} \right]^2. \quad (10)$$

According to the Mohr–Coulomb strength criterion, there is

$$(\sigma_1 - \sigma_3)_f = \frac{2c \cos \varphi + 2\sigma_3 \sin \varphi}{1 - \sin \varphi}. \quad (11)$$

The expression of the initial elastic modulus E_i with consolidation pressure σ_3 can be described as

$$E_i = K p_a \left(\frac{\sigma_3}{p_a} \right)^n, \quad (12)$$

where p_a is the atmospheric pressure ($p_a = 101.4$ kPa) and K and n are experimental parameters, representing the intercept and slope of the straight line between $\log(E_i/p_a)$ and $\log(\sigma_3/p_a)$.

Substituting (11) and (12) into (10), we can obtain

$$E_t = K p_a \left(\frac{\sigma_3}{p_a} \right)^n \left[1 - R_f \frac{(\sigma_1 - \sigma_3)(1 - \sin \varphi)}{2c \cos \varphi + 2\sigma_3 \sin \varphi} \right]^2. \quad (13)$$

In (13), the tangent elastic modulus E_t contains five material parameters (K , n , c , φ , and R_f). There is a hyperbolic relationship between the axial strain ε_1 and the confining strain $-\varepsilon_3$ based on the conventional triaxial loading test data of the soil (Figure 5).

The hyperbolic equation shown in Figure 5(a) can be written as

$$\varepsilon_1 = \frac{-\varepsilon_3}{f + D(-\varepsilon_3)}. \quad (14)$$

The linear equation in Figure 5(b) can be written as

$$\begin{aligned} -\left(\frac{\varepsilon_3}{\varepsilon_1} \right) &= f + D(-\varepsilon_3) \\ &= f - D(\varepsilon_3). \end{aligned} \quad (15)$$

When $\varepsilon_3 = 0$, $-\varepsilon_3/\varepsilon_1 = f = \nu_i$ is initial Poisson's ratio; when $-\varepsilon_3 \rightarrow \infty$, $D = 1/(\varepsilon_1)_{\text{ult}}$. The triaxial shear test shows that

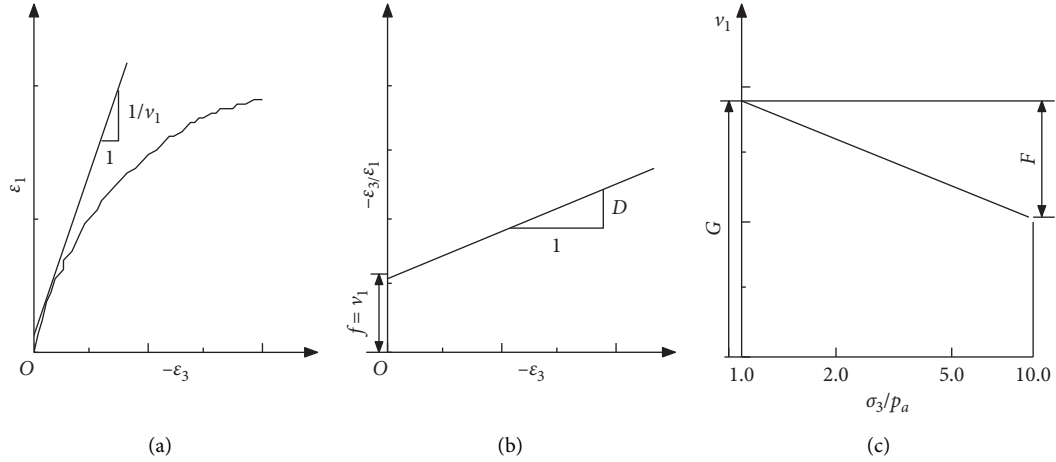


FIGURE 5: Determination of the relevant parameters of tangent Poisson's ratio: (a) ε_1 and $-\varepsilon_3$, (b) $-\varepsilon_3/\varepsilon_1$ and $-\varepsilon_3$, and (c) ν and $\log(\sigma_3/p_a)$.

initial Poisson's ratio is related to the confining pressure [9, 12]. As shown in Figure 5(c), it is assumed that

$$\begin{aligned} \nu_i &= f, \\ &= G - F \lg\left(\frac{\sigma_3}{p_a}\right), \end{aligned} \quad (16)$$

where G and F are test constants.

The difference of (14) induces

$$\begin{aligned} \nu_t &= \frac{-d\varepsilon_3}{d\varepsilon_1}, \\ &= \frac{\nu_i}{(1 - D\varepsilon_1)^2}. \end{aligned} \quad (17)$$

Substituting (8) and (16) into (17), we get

$$\nu_t = \frac{G - F \lg(\sigma_3/p_a)}{\left\{1 - D(\sigma_1 - \sigma_3)/(Kp_a(\sigma_3/p_a)^n [1 - R_f((\sigma_1 - \sigma_3)(1 - \sin \varphi))/(2c \cos \varphi + 2\sigma_3 \sin \varphi)]\right\}^2}. \quad (18)$$

4.2. Conventional Triaxial Unloading Test. Assuming that the soil is an isotropic medium, according to the generalized Hooke's law, the stress-strain relationship can be written as

$$E_t = \frac{\Delta\sigma_a(\Delta\sigma_a + \Delta\sigma_r) - 2\Delta\sigma_r^2}{\Delta\varepsilon_a(\Delta\sigma_a + \Delta\sigma_r) - 2\Delta\varepsilon_r\sigma_r}, \quad (19)$$

where $\Delta\sigma_a = \Delta\sigma_1$ is the axial stress increment, $\Delta\sigma_r = \Delta\sigma_3$ is the lateral stress increment, $\Delta\varepsilon_a = \Delta\varepsilon_1$ is the axial strain increment, and $\Delta\varepsilon_r = \Delta\varepsilon_3$ is the lateral strain increment.

When $\Delta\sigma_a = 0$ and $\Delta\sigma_r \neq 0$, the tangent elastic modulus E_t can be written as

$$\begin{aligned} E_t &= \frac{12\Delta\sigma_r}{\Delta\varepsilon_a - 2\Delta\varepsilon_r}, \\ &= \frac{\partial[2(\sigma_a - \sigma_r)]}{\partial(\varepsilon_a - 2\varepsilon_r)}. \end{aligned} \quad (20)$$

Referring to the derivation process of the triaxial loading test, under the condition of lateral unloading, the

relationship curve of $2(\sigma_{rc} - \sigma_r) - (\varepsilon_a - 2\varepsilon_r)$ is still satisfied with a hyperbolic relationship, namely, $(\varepsilon_a - 2\varepsilon_r)/2(\sigma_{rc} - \sigma_r) - (\varepsilon_a - \varepsilon_r)$.

Use (12) to establish the relationship between the initial tangent elastic modulus E_i and the axial consolidation pressure σ_{ac} . Here, E_i is actually the slope of the curve between $2(\sigma_{rc} - \sigma_r)$ and $(\varepsilon_a - 2\varepsilon_r)$ at the origin of the curve. Hence,

$$E_i = Kp_a \left(\frac{\sigma_{ac}}{p_a}\right)^n. \quad (21)$$

During lateral unloading, the failure deviator stress can be deduced:

$$(\sigma_a - \sigma_r)_f = \frac{2c \cos \varphi + 2\sigma_{ac} \sin \varphi}{1 + \sin \varphi}. \quad (22)$$

Because $\sigma_a = \sigma_{ac}$ is a constant during lateral unloading, it can be obtained from (20):

$$E_t = K p_a \left(\frac{\sigma_{ac}}{p_a} \right)^n \left\{ 1 - R_f \frac{(\sigma_{rc} - \sigma_r)(1 + \sin \varphi)}{2c \cos \varphi + 2\sigma_{ac} \sin \varphi - (\sigma_{ac} - \sigma_{rc})(1 + \sin \varphi)} \right\}. \quad (23)$$

The tangential elastic modulus E_t of the triaxial unloading test still contains 5 material constants (i.e., K , n , c , φ , and R_f). Comparing the unloading and loading paths, it can be seen that the axial strain ε_1 increases and ε_3 decreases. That is, the two effects on the test results are the same. From

this point of view, the calculation formula of Poisson's ratio for loading and unloading tests is the same. Therefore, the final expression of tangent Poisson's ratio in the unloading test is

$$\nu_t = \frac{G - F \lg(\sigma_3/p_a)}{\left\{ 1 - D(\sigma_1 - \sigma_3) / \left(K p_a (\sigma_3/p_a)^n \left[1 - r_f ((\sigma_1 - \sigma_3)(1 - \sin \varphi)) / (2c \cos \varphi + 2\sigma_3 \sin \varphi) \right] \right) \right\}^2}. \quad (24)$$

5. Determination of Loading/Unloading Parameters

5.1. Parameters of the Triaxial Loading. According to the stress-strain relationship shown in Figure 2, three groups of confining pressures and corresponding failure stresses $(\sigma_1 - \sigma_3)_f$ are obtained, as shown in Table 3. Thus, we can obtain the cohesive force $c = 19.2$ kPa and the friction angle $\varphi = 40^\circ$. In the coordinates of ε_1 and $\varepsilon_1/(\sigma_1 - \sigma_3)$, the relationship between the two is approximately linear (Figure 6). In Figure 6, a and b are the intercept and slope obtained by fitting a straight line. Combining equation (24), the E_i value can be obtained as shown in Table 4.

Figure 6 indicates that ε_1 and $\varepsilon_1/(\sigma_1 - \sigma_3)$ of sandy gravel have a good linear relationship, which means a hyperbolic relationship between shear stress and strain. The determination parameter R^2 values are all greater than 0.98, and the hyperbolic model has better applicability. Combining (7) can calculate the values of R_f to be 0.91, 0.93, and 0.92, and the average value is 0.92.

According to (12), the following expression can be obtained:

$$\lg\left(\frac{E_i}{p_a}\right) = \lg k + n \lg\left(\frac{\sigma_3}{p_a}\right). \quad (25)$$

From the results in Table 4, three sets of E_i and σ_3 values can be obtained. According to the fitting results, we can obtain the intercept $K=97$ and the slope $n=0.538$. According to the relationship between the axial strain of sandy gravel and the volume tric strain, the relationship of $-\varepsilon_3/\varepsilon_1$ and $-\varepsilon_3$ can be obtained as shown in Figure 7. Figure 7 indicates that there is a good linear relationship between $-\varepsilon_3/\varepsilon_1$ and $-\varepsilon_3$. By fitting the result to a straight line, the average value of the slope D is 0.07.

According to the three groups of values of ν_i and σ_3 in Figure 7, the relationship between ν_i and $\lg(\sigma_3/p_a)$ is shown in Figure 8. Due to $\nu_i = G - F \lg(\sigma_3/p_a)$, the parameters $G=0.49$ and $F=0.186$ can be obtained.

5.2. Parameters for Triaxial Unloading. A large number of experimental studies [13–15] show that the cohesion c and

the friction angle φ in the unloading test are equal to those in the load test, that is, the cohesion c is 19.2 kPa and the friction angle φ is 40° . The damage ratio R_f of the unloading test is consistent with (26). In the coordinates $(\varepsilon_1 - 2\varepsilon_3)/2(\sigma_1 - \sigma_3) - (\varepsilon_1 - 2\varepsilon_3)$ (Figure 9), the linear fitting results are poor. This is because high or low stress levels will cause the test point to deviate from the straight line.

The relevant values obtained according to this method are shown in Table 5, and the fitted straight line relationship is shown in Figure 10. Combining the stress paths of the unloading test, there are

$$E_i = \frac{1}{a}, \quad (26)$$

$$2(\sigma_1 - \sigma_3)_{\text{ult}} = \frac{1}{b}, \quad (27)$$

where a and b are the intercepts and slopes obtained by fitting in Figure 4.

Combining the results in Figure 4, the relevant parameters of the unloading test and E_i and R_f can be obtained (Table 6). Finally, the average value of R_f in the sandy gravel unloading test can be obtained from Table 6, namely, $R_f=0.43$. Using (21), the following equation can be obtained:

$$\lg\left(\frac{E_i}{p_a}\right) = \lg K + \lg\left(\frac{\sigma_1}{p_a}\right), \quad (28)$$

where K represents the intercept and n represents the slope.

According to Table 6, three groups of E_i and σ_1 values can be obtained to fit a straight line, and the expression is

$$\lg\left(\frac{E_i}{p_a}\right) = 1 \cdot 6322 + 0 \cdot 759 \lg\left(\frac{\sigma_1}{p_a}\right). \quad (29)$$

Comparing (28) and (29), we can obtain that intercept $K=43$ and slope $n=0.759$. Finally, the parameters G , F , and D related to tangent Poisson's ratio are determined. Figure 5 shows the relationship between the axial strain and the body strain and the relationship between $-\varepsilon_3/\varepsilon_1$ and $-\varepsilon_3$ (Figure 11).

TABLE 3: Failure stress under loading conditions.

σ_3 (kPa)	$(\sigma_1 - \sigma_3)_f$ (kPa)	$(\sigma_1)_f$ (kPa)
200	800	1000
400	1529	1929
600	2238	2838

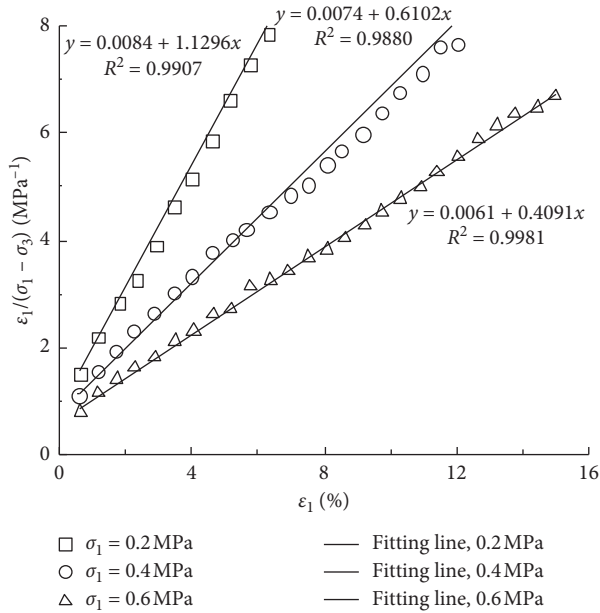


FIGURE 6: Relationship between ϵ_1 and $\epsilon_1/(\sigma_1 - \sigma_3)$.

TABLE 4: Model parameters of the triaxial loading test (unit: MPa).

σ_3	a	b	E_i
0.2	0.0084	1.1296	119.05
0.4	0.0074	0.6102	135.14
0.6	0.0061	0.4091	163.93

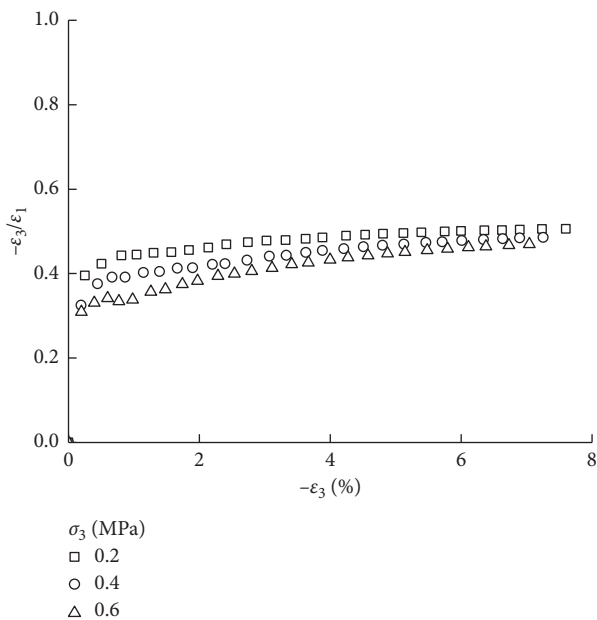


FIGURE 7: Relationship between $-\epsilon_3/\epsilon_1$ and $-\epsilon_3$.

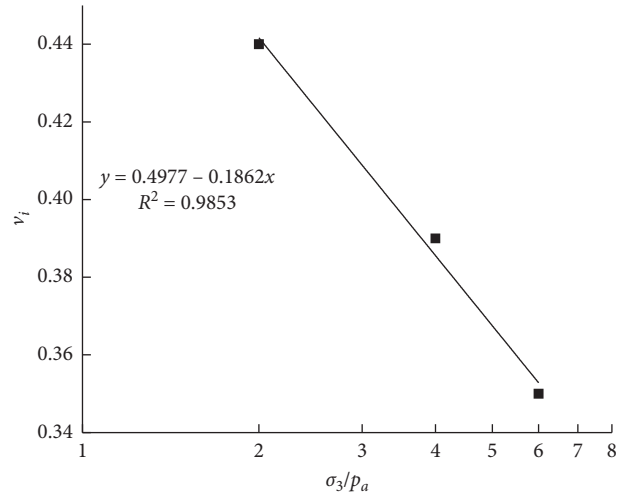


FIGURE 8: Relationship between ν_i and $\log(\sigma_3/Pa)$.

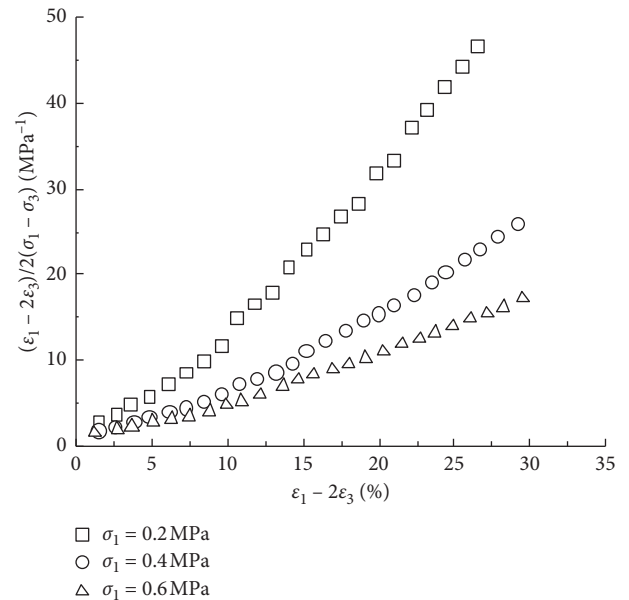


FIGURE 9: Relationship between $(\epsilon_1 - 2\epsilon_3)/2(\sigma_1 - \sigma_3)$ and $(\epsilon_1 - 2\epsilon_3)$.

TABLE 5: Failure stress under unloading conditions.

ϵ_1	$\epsilon_1 - \epsilon_3$		$\epsilon_1 - 2\epsilon_3$		$(\epsilon_1 - 2\epsilon_3)/2(\epsilon_1 - \epsilon_3)$	
	70%	90%	70%	90%	70%	90%
0.2	0.29	0.37	1.9	3.8	3.3	5.2
0.4	0.55	0.7	2.48	5.2	2.2	3.7
0.6	0.75	0.97	3.4	6.2	2.0	3.14

Figure 11 indicates that there is an obvious linear relationship between $-\epsilon_3/\epsilon_1$ and $-\epsilon_3$, indicating that the assumption that the axial strain ϵ_1 and the lateral strain ϵ_3 are hyperbolic in the unloading test is applicable. The average value of the slope D of the fitted straight line is -0.015 . According to Figure 11, three groups of values of ν_i and σ_3

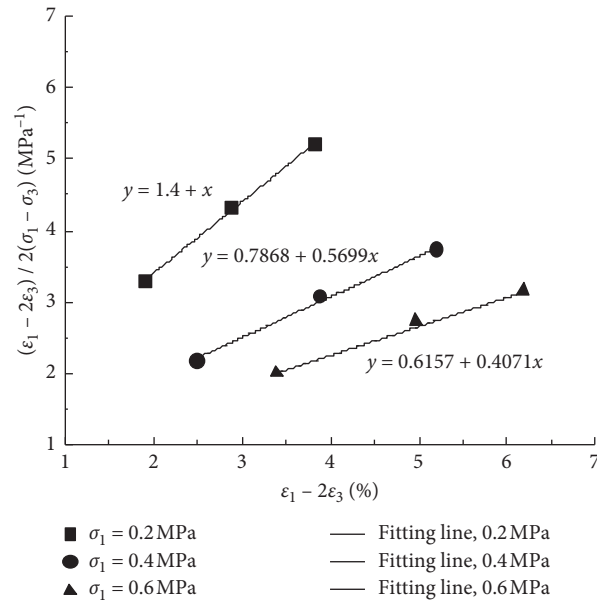


FIGURE 10: Relationship between $(\epsilon_1 - 2\epsilon_3)/2(\sigma_1 - \sigma_3)$ and $(\epsilon_1 - 2\epsilon_3)$.

TABLE 6: Model parameters of the triaxial unloading test (unit: MPa).

σ_1	a	b	E_i	R_f
0.2	0.014	1	71.43	0.42
0.4	0.0078	0.56	128.21	0.43
0.6	0.0062	0.41	162.60	0.43

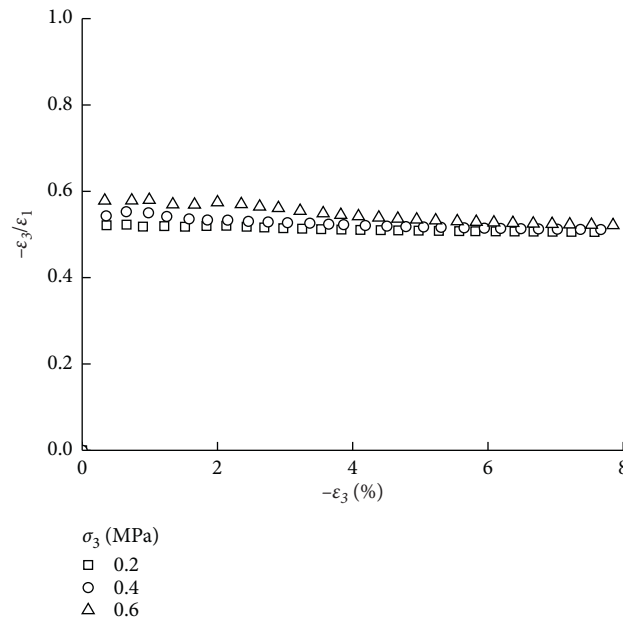
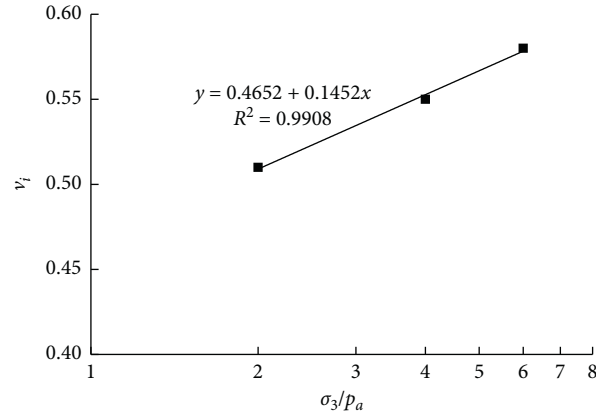


FIGURE 11: Relationship between $-\epsilon_3/\epsilon_1$ and $-\epsilon_3$.

FIGURE 12: Relationship between v_t and $\log(\sigma_3/p_a)$.

can be obtained, and the corresponding relationship between v_t and $\log(\sigma_3/p_a)$ can be drawn, as shown in Figure 12.

Due to

$$v_t = G - F \lg\left(\frac{\sigma_3}{p_a}\right), \quad (30)$$

the equation of the fitted straight line in Figure 12 is

$$v_t = 0.47 + 0.145 \lg\left(\frac{\sigma_3}{p_a}\right). \quad (31)$$

Comparing (30) and (31), the value of G is 0.47, and the value of F is -0.145 .

5.3. The Tangent Elastic Modulus and Tangent Poisson's Ratio.

For triaxial loading, according to the relevant parameters determined above, the tangent elastic modulus E_t and tangent Poisson's ratio v_t of sandy gravel under triaxial loading can be obtained as

$$E_t = 97 p_a \left(\frac{\sigma_3}{p_a}\right)^{0.538} \left[1 - 0.92 \frac{(\sigma_1 - \sigma_3)(1 - \sin \varphi)}{38 \cdot 4 \cos 40^\circ + 2\sigma_3 \sin 40^\circ} \right], \quad (32)$$

$$v_t = \frac{0.49 - 0.186 \lg(\sigma_3/p_a)}{\left\{ 1 - (0.07(\sigma_1 - \sigma_3)/97 p_a (\sigma_3/p_a)^{0.538} [1 - 0.92((\sigma_1 - \sigma_3)(1 - \sin \varphi))/(38 \cdot 4 \cos 40^\circ + 2\sigma_3 \sin 40^\circ)]) \right\}^2}. \quad (33)$$

For triaxial unloading, E_t and v_t during the unloading test are

$$E_t = 43 p_a \left(\frac{\sigma_3}{p_a}\right)^{0.759} \left[1 - 0.43 \frac{(\sigma_1 - \sigma_3)(1 - \sin \varphi)}{38 \cdot 4 \cos 40^\circ + 2\sigma_3 \sin 40^\circ} \right]^2, \quad (34)$$

$$v_t = \frac{0.47 + 0.145 \lg(\sigma_3/p_a)}{\left\{ (-0.015(\sigma_1 - \sigma_3))/43 p_a (\sigma_3/p_a)^{0.759} [1 - 0.43((\sigma_1 - \sigma_3)(1 - \sin \varphi))/(38 \cdot 4 \cos 40^\circ + 2\sigma_3 \sin 40^\circ)] \right\}^2}. \quad (35)$$

6. Conclusions

Consolidation and drainage shear tests of sandy gravel under different confining pressures under loading/unloading conditions are carried out. The differences in the strength and deformation of sandy gravel are analyzed. In using the proposed model, the parameters are few and can be obtained

from normal geotechnical tests, which has high application value in practical engineering. The main conclusions drawn are as follows:

- (1) The relationships between $\sigma_1 - \sigma_3$ and ε_1 and ε_v and ε_a of sandy gravel soil under loading conditions are all nonlinear. The smaller the confining pressure, the

weaker the stress-strain relationship. The stress-strain relationship exhibits a softening phenomenon, and the bulk strain undergoes dilatancy deformation. In contrast, it shows strain hardening and shear shrinkage deformation.

- (2) Under unloading conditions, the sandy gravel soil softens significantly with increasing confining pressure, and the peak strength increases. In the meantime, the tric strain response exhibits dilatancy characteristics. The strength and deformation characteristics of sandy gravel soil have a high dependence on the stress path.
- (3) The Duncan–Chang hyperbolic model has good applicability for simulating sandy gravel soils, and the model parameters are calculated according to the test results, which can provide help for engineering design and practice.

Abbreviations

$\varepsilon_1, \varepsilon_3$:	Principal strains
ε_r :	Lateral strain
ε_v :	Bulk strain
σ_1, σ_3 :	Principal stresses
σ_{rc} :	Lateral consolidation pressure
σ_r :	Lateral pressure
E_t :	Tangent elastic modulus
E_i :	Initial modulus of elasticity
c :	Cohesion
φ :	Internal friction angle
p_a :	Atmospheric pressure
K, n, G, F :	Material test constants
ν_i :	Initial Poisson's ratio.

Data Availability

The data used to support the findings of this study are available from the corresponding author upon request.

Conflicts of Interest

The authors declare that they have no conflicts of interest.

Acknowledgments

This research was supported by the Hebei Province Postdoctoral Research Project Merit-Based Funding Program (B2020005008).

References

- [1] X. Li, T. Li, and L. Peng, "Elastoplastic two-surface model for unsaturated cohesive soils under cyclic loading," *International Journal of Geomechanics*, vol. 20, no. 8, Article ID 04020122, 2020.
- [2] L. Zhu, G. Wang, F. Huang, Y. Li, W. Chen, and H. Hong, "Landslide susceptibility prediction using sparse feature extraction and machine learning models based on GIS and remote sensing," *IEEE Geoscience and Remote Sensing Letters*, vol. 15, pp. 1–5, 2021.
- [3] B. Bai, S. Jiang, L. Liu, X. Li, and H. Wu, "The transport of silica powders and lead ions under unsteady flow and variable injection concentrations," *Powder Technology*, vol. 387, pp. 22–30, 2021.
- [4] M. Aslani, J. Nazariafshar, and N. Ganjian, "Experimental study on shear strength of cohesive soils reinforced with stone columns," *Geotechnical and Geological Engineering*, vol. 37, no. 3, pp. 2165–2188, 2019.
- [5] A. M. Deganutti, P. R. Tecca, and R. Genevois, "The measure of friction angles for different types of granular material," *Journal of Mountain Science*, vol. 16, no. 4, pp. 769–777, 2019.
- [6] B. Bai, D. Rao, T. Chang, and Z. Guo, "A nonlinear attachment-detachment model with adsorption hysteresis for suspension-colloidal transport in porous media," *Journal of Hydrology*, vol. 578, Article ID 124080, 2019.
- [7] B. Bai, T. Xu, Q. Nie, and P. Li, "Temperature-driven migration of heavy metal Pb²⁺ along with moisture movement in unsaturated soils," *International Journal of Heat and Mass Transfer*, vol. 153, Article ID 119573, 2020.
- [8] M. Sánchez, A. Gens, M. V. Villar, and S. Olivella, "Fully coupled thermo-hydro-mechanical double-porosity formulation for unsaturated soils," *International Journal of Geomechanics*, vol. 16, no. 6, pp. 1–38, 2016.
- [9] E. Gholizadeh and M. Latifi, "A coupled hydro-mechanical constitutive model for unsaturated frictional and cohesive soil," *Computers and Geotechnics*, vol. 98, pp. 69–81, 2018.
- [10] B. Bai, D. Rao, T. Xu, and P. Chen, "SPH-FDM boundary for the analysis of thermal process in homogeneous media with a discontinuous interface," *International Journal of Heat and Mass Transfer*, vol. 117, pp. 517–526, 2018.
- [11] G. Yang and B. Bai, "Thermo-hydro-mechanical model for unsaturated clay soils based on granular solid hydrodynamics theory," *International Journal of Geomechanics*, vol. 19, no. 10, Article ID 04019115, 2019.
- [12] F. Huang, Z. Ye, S.-H. Jiang, J. Huang, Z. Chang, and J. Chen, "Uncertainty study of landslide susceptibility prediction considering the different attribute interval numbers of environmental factors and different data-based models," *Catena*, vol. 202, Article ID 105250, 2021.
- [13] F. Huang, Z. Cao, S.-H. Jiang, C. Zhou, J. Huang, and Z. Guo, "Landslide susceptibility prediction based on a semi-supervised multiple-layer perceptron model," *Landslides*, vol. 17, no. 12, pp. 2919–2930, 2020.
- [14] E. E. Alonso, A. Gens, and A. Josa, "A constitutive model for partially saturated soils," *Géotechnique*, vol. 40, no. 3, pp. 405–430, 1990.
- [15] B. Bai, L. Guo, and S. Han, "Pore pressure and consolidation of saturated silty clay induced by progressively heating/cooling," *Mechanics of Materials*, vol. 75, pp. 84–94, 2014.
- [16] S. L. Houston, "It is time to use unsaturated soil mechanics in routine geotechnical engineering practice," *Journal of Geotechnical and Geoenvironmental Engineering*, vol. 145, no. 5, Article ID 02519001, 2019.
- [17] B. Bai and Z. Su, "Thermal responses of saturated silty clay during repeated heating-cooling processes," *Transport in Porous Media*, vol. 93, no. 1, pp. 1–11, 2012.
- [18] B. Bai and X. Shi, "Experimental study on the consolidation of saturated silty clay subjected to cyclic thermal loading," *Geomechanics and Engineering*, vol. 12, no. 4, pp. 707–721, 2017.
- [19] K. S. Wong and D. Mašin, "Coupled hydro-mechanical model for partially saturated soils predicting small strain stiffness," *Computers and Geotechnics*, vol. 61, pp. 355–369, 2014.

- [20] B. Bai, F. Long, D. Rao, and T. Xu, "The effect of temperature on the seepage transport of suspended particles in a porous medium," *Hydrological Processes*, vol. 31, no. 2, pp. 382–393, 2017.
- [21] H. Ghasemzadeh and S. A. Ghoreishian Amiri, "A hydro-mechanical elastoplastic model for unsaturated soils under isotropic loading conditions," *Computers and Geotechnics*, vol. 51, pp. 91–100, 2013.
- [22] B. Bai, G.-C. Yang, T. Li, and G.-S. Yang, "A thermodynamic constitutive model with temperature effect based on particle rearrangement for geomaterials," *Mechanics of Materials*, vol. 139, Article ID 103180, 2019.
- [23] A. Hamrouni, D. Dias, and B. Sbartai, "Probability analysis of shallow circular tunnels in homogeneous soil using the surface response methodology optimized by a genetic algorithm," *Tunnelling and Underground Space Technology*, vol. 86, pp. 22–33, 2019.
- [24] Z. Zizka, B. Schoesser, M. Thewes, and T. Schanz, "Slurry shield tunneling: new methodology for simplified prediction of increased pore pressures resulting from slurry infiltration at the tunnel face under cyclic excavation processes," *International Journal of Civil Engineering*, vol. 17, no. 1, pp. 113–130, 2019.
- [25] L. Flessati and C. Di Prisco, "Deep tunnel faces in cohesive soils under undrained conditions: application of a new design approach," *European Journal of Environmental and Civil Engineering*, vol. 32, Article ID 1785332, 2018.
- [26] H. R. Huang, J. G. Zhu, and Z. R. Fang, "Triaxial test study of deformation and strength behavior of sand-gravel materials," *Water Resources and Power*, vol. 30, no. 7, pp. 87–89, 2012.
- [27] M. C. Liu, X. M. Huang, and Y. F. Gao, "Research on strength-deformation characteristics and nonlinear elastic model of rockfills," *Rock and Soil Mechanics*, vol. 25, no. 5, pp. 798–802, 2004.
- [28] G. Zhang and J. M. Zhang, "Study on behavior of coarse-grained soil and its modeling," *Rock and Soil Mechanics*, vol. 25, no. 10, pp. 1587–1591, 2004.
- [29] B. Indraratna, D. Ionescu, and H. D. Christie, "Shear behavior of railway ballast based on large-scale triaxial tests," *Journal of Geotechnical and Geoenvironmental Engineering*, vol. 124, no. 5, pp. 439–449, 1998.
- [30] P. Zhang, B. Bai, S. Jiang, P. Wang, and H. Li, "Transport and deposition of suspended particles in saturated porous media: effect of hydrodynamic forces and pore structure," *Water Science and Technology: Water Supply*, vol. 16, no. 4, pp. 951–960, 2016.
- [31] B. Bai, Q. Nie, Y. Zhang, X. Wang, and W. Hu, "Cotransport of heavy metals and SiO₂ particles at different temperatures by seepage," *Journal of Hydrology*, vol. 597, Article ID 125771, 2021.
- [32] D. Rao and B. Bai, "Study of the factors influencing diffusive tortuosity based on pore-scale SPH simulation of granular soil," *Transport in Porous Media*, vol. 132, no. 2, pp. 333–353, 2020.
- [33] W. Li, X. Fan, F. Huang et al., "Uncertainties analysis of collapse susceptibility prediction based on remote sensing and GIS: influences of different data-based models and connections between collapses and environmental factors," *Remote Sensing*, vol. 12, no. 24, p. 4134, 2020.
- [34] B. Mi and Y. Xiang, "Analysis of the limit support pressure of a shallow shield tunnel in sandy soil considering the influence of Seepage," *Symmetry*, vol. 12, no. 6, p. 1023, 2020.
- [35] S. Zingg and G. Anagnostou, "Tunnel face stability and the effectiveness of advance drainage measures in water-bearing ground of non-uniform permeability," *Rock Mechanics and Rock Engineering*, vol. 51, no. 1, 2017.
- [36] B. Bai, "Thermal response of saturated porous spherical body containing a cavity under several boundary conditions," *Journal of thermal Stresses*, vol. 36, no. 11, pp. 1217–1232, 2013.
- [37] B. Bai and T. Li, "Irreversible consolidation problem of a saturated porothermoelastic spherical body with a spherical cavity," *Applied Mathematical Modelling*, vol. 37, no. 4, pp. 1973–1982, 2013.
- [38] T. Qiu, C. Liu, X. Zhong, and Y. Zhu, "Experimental research on the impact of temperature on the adhesion characteristics of soil–structure interface," *Geofluids*, vol. 2020, Article ID 6675576, 9 pages, 2020.
- [39] Z.-G. Yan, Y. Zhang, Y. Shen, H.-H. Zhu, and Y. Lu, "A multilayer thermo-elastic damage model for the bending deflection of the tunnel lining segment exposed to high temperatures," *Tunnelling and Underground Space Technology*, vol. 95, Article ID 103142, 2020.
- [40] R. L. Kondner, "Hyperbolic stress-strain response: cohesive soils," *Journal of Soil Mechanics and Foundation Engineering*, vol. 89, no. 1, pp. 115–143, 1963.
- [41] J. M. Duncan and C.-Y. Chang, "Nonlinear analysis of stress and strain in soils," *Journal of Soil Mechanics and Foundation Engineering*, vol. 96, no. 5, pp. 1629–1653, 1970.
- [42] B. O. Hardin and V. P. Drnevich, "Shear modulus and damping in soils: design equations and curves," *Journal of the Soil Mechanics and Foundation Division*, vol. 98, no. 7, pp. 667–692, 1972.

Research Article

Life-Cycle Seismic Fragility Assessment of Existing RC Bridges Subject to Chloride-Induced Corrosion in Marine Environment

Sicong Hu , Zheyang Wang, Yu Guo, and Gui Xiao

School of Civil Engineering and Architecture, Nanchang University, Nanchang, China

Correspondence should be addressed to Sicong Hu; eric731hu@ncu.edu.cn

Received 7 April 2021; Accepted 19 May 2021; Published 14 June 2021

Academic Editor: Haoyuan Hong

Copyright © 2021 Sicong Hu et al. This is an open access article distributed under the Creative Commons Attribution License, which permits unrestricted use, distribution, and reproduction in any medium, provided the original work is properly cited.

Bridges in a marine environment have been suffering from the chloride attack for a long period of time. Due to the fact that different sections of piers may be exposed to different conditionals, the chloride-induced corrosion not only affects the scale of the deterioration process but also significantly modifies over time the damage propagation mechanisms and the seismic damage distribution. In order to investigate the seismic damage of existing RC bridges subject to spatial chloride-induced corrosion in a marine environment, Duracrete model is applied to determine the corrosion initiation time of reinforcing steels under different exposure conditionals and the degradation models of reinforcing steels, confined concrete, and unconfined concrete are obtained based on the previous investigation. According to the seismic fragility assessment method, the damage assessment approach for the existing RC bridges subject to spatial chloride-induced corrosion in a marine environment is present. Moreover, a case study of a bridge under two kinds of water regions investigated the influence of spatial chloride-induced corrosion on the seismic damage of piers and other components. The results show that the spatial chloride-induced corrosion may result in the section at the low water level becoming more vulnerable than the adjacent sections and the alteration of seismic damage distribution of piers. The corrosion of pier will increase the seismic damage probability of itself, whereas it will result in a reduction of seismic damage probability of other components. Moreover, the alteration of seismic damage distribution of piers will amplify the effect. Due to the fact that the spatial chloride-induced corrosion of piers may alter the yield sequence of cross section, it then affects the seismic performance assessment of piers. A method to determine the evolution probability of yield sequence of corroded piers is proposed at last. From the result, the evolution probability of yield sequence of piers in longitudinal direction depends on the relationship between the height of piers and submerged zone. Moreover, the height of piers, submerged zone, and tidal zone have a common influence on the evolution of yield sequence of piers in transversal direction.

1. Introduction

In the past decades, many coastal bridges have been built in different countries with long coastlines to meet the growing requirement of fast transport and economic development. Overall, most of these bridges are reinforced concrete structures and are located in the severe marine environments. Under such environments, chloride-induced corrosion is a major environmental stressor for RC bridges, because it may result in the decrease of the effective cross-sectional area of the reinforcing steels and the deterioration of the mechanical properties of reinforcing steels and concrete. Obviously, the performance of coastal bridges is expected to be significantly affected by chloride-induced corrosion. Therefore, it is of interest to investigate the effects

of chloride-induced corrosion on the performance of aging RC bridges in marine environments and to improve the performance level of these bridges with the corrosion effects.

On the other hand, chloride-induced corrosion may also result in the decrease of the seismic performance of aging RC bridges; thereby bridges exhibit different seismic damage probability as time increases. In this respect, many studies have focused on the seismic damage assessment of RC bridges with chloride-induced corrosion. Choe et al. [1] developed the probabilistic drift and shear force capacity models for corroding reinforced concrete columns to predict the service-life and life-cycle cost of the columns. Kumar et al. [2] assessed the seismic damage probability of the aging bridges with the cumulative seismic damage and chloride-induced corrosion. Alipour et al. [3] investigated the effects

of reinforcement corrosion on the seismic damage probability of the aging bridge in California with different structural parameters. Thanapol et al. [4] developed the seismic fragility curves of the deteriorating piers through the field instrumentation of the corrosion measurements. Cui et al. [5] applied an improved deterioration model of the reinforced concrete steel to carry out the seismic fragility analysis of the reinforced concrete bridges with the marine chloride-induced corrosion. Panchireddi and Ghosh [6] proposed an analytical strategy to consider the deterioration of the damaged bridge through updating the pier section properties. Zhang et al. [7] proposed a seismic risk assessment method for the corrosion RC bridges with shear-critical columns. Crespi [8] presented a procedure for the collapse mechanism evaluation of the existing reinforced concrete motorway bridges under horizontal loads.

Overall, the previous studies have enriched the knowledge of the seismic damage assessment of aging RC bridges. However, only uniform exposure condition was considered in these studies when performing the seismic damage assessment of aging RC bridges with the corrosion effects. In fact, exposure conditions exhibit significant spatial variation characteristic along the pier direction for many coastal bridges, and the nonuniform degradation phenomenon occurs in the corroded piers, resulting in the nonuniform distribution of seismic damage of piers. Obviously, these studies may be inappropriate and/or inadequate to completely investigate probabilistic seismic damage of aging RC bridges and to reveal the effects of spatial chloride-induced corrosion. On the other hand, the knowledge of plastic hinges of piers will contribute to the ductile seismic design of RC bridges. Recently, Yuan et al. [9] investigated the damage characteristics of the coastal bridge piers suffering non-uniform corrosion by the shaking table tests. However, the yield characteristic of piers subject to the spatial chloride-induced corrosion has not been comprehensively investigated in the previous studies, and the evolution mechanism of yield sequence of corroded piers has not been clarified.

In this study, the probabilistic seismic damage assessment of aging RC bridges subject to spatial chloride-induced corrosion in marine environments is presented. Overall, the major objectives of this study are threefold: (1) to develop a probabilistic seismic damage assessment procedure for aging RC bridges suffering spatial chloride-induced corrosion, (2) to reveal the effects of spatial chloride-induced corrosion on the seismic damage characteristics of piers and other components, and (3) to discuss the evolution probability of yield sequence of piers subject to spatial chloride-induced corrosion. The paper is organized as follows: In Section 2, we describe the corrosion process of reinforcing steels and degradation properties of various materials under different marine exposure conditions. Section 3 presents the probabilistic seismic damage assessment procedure for aging RC bridges subject to spatial chloride-induced corrosion. Subsequently, details of the case study bridge are described in Section 4, and the finite element models are developed. In Section 5, the corrosion level and seismic capacity of RC piers in different exposure conditions are investigated. Moreover, the seismic damage of piers and other components is discussed in Section 6. Furthermore, a method to determine the

evolution probability of yield sequence of piers subject to spatial chloride-induced corrosion is proposed in Section 7. A brief summary of the results is presented in Section 8.

2. Chloride-Induced Corrosion Effects

The coastal bridges are often exposed to high concentrations of chloride ions. The concentration gradient between the exposed surface and the pore solution of the cement makes the chloride ions penetrate from the external environment through the concrete cover and reach the surface of reinforcing steels. Moreover, the chloride ions decrease the pH in the concrete and break down the passive film of reinforcing steels, resulting in the corrosion of reinforcing steels and the damage of concrete. In this section, the corrosion processes of reinforcing steels and the deterioration mechanism of RC members are presented.

2.1. Corrosion Initiation Time. The corrosion initiation time is an important parameter during the chloride-induced corrosion process of RC members, which can be defined as the time when the chloride ions concentration near reinforcing steels reaches a threshold concentration C_{cr} . To calculate the corrosion initiation time, it is necessary to describe the diffusion process of chloride ions and determine the chloride ions concentration at different depths of RC members. In this respect, Duracrete provided a probabilistic model to predict the chloride concentration in the concrete by taking into account the time-dependent characteristics of chloride diffusion, as well as the different types of uncertainties associated with the modelling of these complex processes [10]. The chloride concentration at depth x after time t can be expressed as follows:

$$C(x, t) = C_{cs} \left[1 - \operatorname{erf} \left(\frac{x}{2\sqrt{k_e k_t k_c D_0 (t_0)^n (t)^{1-n}}} \right) \right], \quad (1)$$

where $\operatorname{erf}(\theta) = (2/\sqrt{\pi}) \int_0^\theta e^{-t^2} dt$ is the error function; D_0 is the empirical diffusion coefficient; k_e is an environmental coefficient; k_t represents the influence of test methods on determining D_0 ; k_c is a coefficient that accounts for the influence of curing; t_0 is the reference period for D_0 ; n is the age factor; C_{cs} is the chloride concentration at concrete surface and can be represented as

$$C_{cs} = A_{cs} \left(\frac{w}{b} \right) + \varepsilon_{cs}, \quad (2)$$

where w/b is the water binder ratio and A_{cs} and ε_{cs} are the model parameters.

If the cover depth of reinforcing steels d_c is known, the corrosion initiation time can be determined as follows:

$$T_{\text{cor}} = \left\{ \frac{d_c^2}{4k_e k_t k_c D_0 (t_0)^n} \left[\operatorname{erf}^{-1} \left(\frac{C_{cs} - C_{cr}}{C_{cs}} \right) \right]^2 \right\}^{(1/(1-n))}. \quad (3)$$

For many coastal bridges, the bottom of piers may be submerged in the water, whereas the middle and top of piers are exposed to chloride dry-wet cycle and atmosphere environment, respectively. The discrepancies of humidity,

temperature, oxygen, and chloride concentration will cause the different corrosion initiation time of reinforcing steels in various marine exposure conditions. Therefore, the corrosion level of reinforcing steels is highly dependent on the type of exposure conditions. Overall, four categories of exposure conditions are included in the Duracrete model: (a) submerged zone, (b) tidal zone, (c) splash zone, and (d) atmospheric zone. Table 1 summarizes the statistical parameters for corrosion coefficients in the Duracrete model.

2.2. Corrosion Propagation. Generally, the corrosion form of reinforcing steels can be divided into two types: uniform corrosion and pitting corrosion (Figure 1). The former is caused by carbonation, whereas the latter is caused by chloride penetration [11]. Therefore, the pitting corrosion is considered during the corrosion analysis in this study.

The classical model proposed by Val and Melchers simplified the geometry of pitting into a quadrilateral form approximately to consider the reduction of reinforcement area [12]. The time-dependent residual cross-sectional area of a reinforcing steel with pitting corrosion $A_{\text{res}}(t)$ can be represented as follows:

$$A_{\text{res}}(t) = [1 - Q_{\text{cor}}(t)]A_0 = [A_0 - A_{\text{cor},p}(t)], \quad (4)$$

where $Q_{\text{cor}}(t)$ is the time-dependent percentage mass loss of corroded reinforcing steels; A_0 is the initial cross-sectional area of reinforcing steels; $A_{\text{cor},p}(t)$ is the time-dependent pitting area of reinforcing steels and it can be calculated as follows:

$$A_{\text{cor},p}(t) = \begin{cases} A_1 + A_2, & P(t) \leq \frac{d_{s0}}{\sqrt{2}}, \\ \frac{\pi d_{s0}^2}{4} - A_1 + A_2, & \frac{d_{s0}}{\sqrt{2}} < P(t) \leq d_{s0}, \\ \frac{\pi d_{s0}^2}{4}, & P(t) \geq d_{s0}, \end{cases} \quad (5)$$

$$A_1 = \frac{1}{2} \left[\theta_1 \left(\frac{d_{s0}}{2} \right)^2 - \frac{b}{2} \sqrt{d_{s0}^2 - b^2} \right], \quad (6)$$

$$A_2 = \frac{1}{2} \left[\theta_2 P(t)^2 - \frac{bP(t)^2}{d_{s0}} \right],$$

$$\begin{aligned} \theta_1 &= 2\arcsin\left(\frac{b}{d_{s0}}\right), \\ \theta_2 &= 2\arcsin\left(\frac{b}{2P(t)}\right), \\ b &= 2P(t) \sqrt{1 - \left(\frac{P(t)}{d_{s0}}\right)^2}, \end{aligned} \quad (7)$$

where d_{s0} is the initial diameter of reinforcing steels; $P(t)$ is the time-dependent pitting depth, and it can be expressed by

$$P(t) = R \int_{T_{\text{cor}}}^t \lambda(t) dt, \quad (8)$$

where $\lambda(t)$ is uniform corrosion rate; R is pitting factor, which represents the ratio of maximum pit depth to average depth considering uniform corrosion.

A Gumbel (Extreme Value Type I) distribution can be applied to predict the pitting factor of reinforcing steels [13]. Consequently, the statistical parameters of R can be calculated as

$$\mu = \mu_0 + \frac{1}{\alpha_0} \ln\left(\frac{A_U}{A_0}\right), \quad (9)$$

$$\alpha = \alpha_0, \quad (10)$$

where μ_0 and α_0 are the scale and location parameters in the Gumbel distribution, respectively; A_0 is taken as the surface area of reinforcing steels with 125 mm length and 8 mm diameter; A_U is the surface area of reinforcing steels with other sizes.

In theory, the uniform corrosion rate of reinforcing steels $\lambda(t)$ is related to the corrosion current density. The corrosion current density will reduce and approach a constant level with the development of corrosion. Moreover, the unconfined concrete cracking will lead to easier ingress of chlorides, oxygen, and water, entailing the corrosion rate of reinforcement undergoing a large continuous increase after crack initiation and subsequent crack growth [14, 15]. To fully consider these effects, an improved time-dependent uniform corrosion rate model is proposed by Cui et al. [5] based on the Vu and Stewart model [16]:

$$\lambda(t) = \begin{cases} \lambda'(t), & T_{\text{cor}} < t < T_{\text{cr}}, \\ \frac{(t - T_{\text{cr}})[4.5 - 26\lambda'(T_{\text{Wcr}})]\lambda'(T_{\text{Wcr}}) + (T_{\text{Wcr}} - t)\lambda'(T_{\text{cr}})}{T_{\text{Wcr}} - T_{\text{cr}}}, & T_{\text{cr}} < t < T_{\text{Wcr}}, \\ [4.5 - 26\lambda'(t)]\lambda'(t), & T_{\text{Wcr}} < t, \end{cases} \quad (11)$$

$$\lambda'(t) = 0.0116 \times 0.85 \times \frac{37.8(1 - w/c)^{-1.64}}{d_c} \times (t - T_{\text{cor}})^{-0.29}, \quad (12)$$

where w/c is the water cement ratio; T_{cr} and T_{Wcr} are initial cracking time and initiation of severe cracking time,

respectively. The detailed calculation method is illustrated in [5].

TABLE 1: Statistical parameters for corrosion coefficients in the Duracrete model.

Parameter	Distribution type	Atmospheric		Splash		Tidal		Submerged	
		Mean	Std.	Mean	Std.	Mean	Std.	Mean	Std.
$D_0 (w/b = 0.4)$	Normal	220	25.4	220	25.4	220	25.4	220	25.4
$D_0 (w/b = 0.45)$	Normal	315.6	32.5	315.6	32.5	315.6	32.5	315.6	32.5
$D_0 (w/b = 0.5)$	Normal	473	43.2	473	43.2	473	43.2	473	43.2
n	Beta ($A = 0.0, B = 0.98$)	0.362	0.245	0.362	0.245	0.362	0.245	0.362	0.245
A_{cs}	Normal	2.565	0.356	7.758	1.36	7.758	1.36	10.348	0.714
ε_{cs}	Normal	0	0.58	0	1.105	0	1.105	0	0.405
C_{cr}	Normal	0.9	0.15	0.9	0.15	0.9	0.15	1.6	0.2
k_t	Normal	0.832	0.024	0.832	0.024	0.832	0.024	0.832	0.024
k_e	Gamma	0.676	0.114	0.265	0.045	0.924	0.155	0.325	0.223
$k_c (t = 1 \text{ days})$	Beta ($A = 1.0, B = 4.0$)	2.4	0.7	2.4	0.7	2.4	0.7	2.4	0.7
$k_c (t = 3 \text{ days})$	Beta ($A = 1.0, B = 4.0$)	1.5	0.3	1.5	0.3	1.5	0.3	1.5	0.3
$k_c (t = 7 \text{ days})$	Determined value	1	-	1	-	1	-	1	-
$k_c (t = 28 \text{ days})$	Beta ($A = 0.4, B = 1.0$)	0.8	0.1	0.8	0.1	0.8	0.1	0.8	0.1

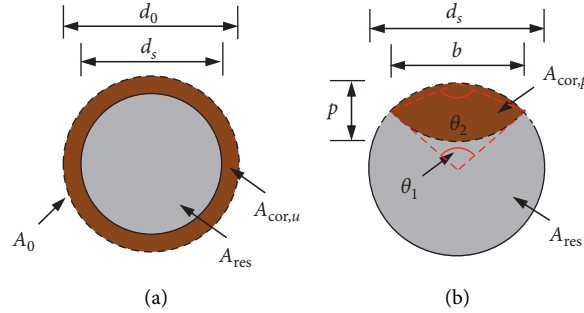


FIGURE 1: (a) Uniform corrosion and (b) pitting corrosion of reinforcing steels.

2.3. Material Properties. As stated, chloride-induced corrosion will affect the effective sectional area and mechanical properties of reinforcing steels. Moreover, the expansive pressure localized at the interface between reinforcing steels and concrete can also result in the cracking and spalling of concrete cover. At the same time, the deterioration of transverse reinforcement may reduce the lateral confinement of core concrete, resulting in the decrease of strength and ultimate strain of confined concrete. To fully consider the overall performance of corroded RC members, the degradation properties of reinforcing steels, concrete cover, and confined concrete should be determined.

2.3.1. Reinforcing Steels. Du et al. [17] proposed a linear strength reduction model as a function of the percentage mass loss Q_{cor} of corroded reinforcing steels:

$$f = [1 - \beta Q_{cor}] f_0, \quad (13)$$

where f_0 and f are the strength of uncorroded and corroded reinforcing steels, respectively; β is coefficient of strength degradation, which is taken as 0.49 for the yield strength and 0.65 for the ultimate strength.

2.3.2. Concrete Cover. The reduction in concrete cover strength f_c can be calculated as follows [18]:

$$f_c = \frac{f_{c0}}{1 + K \varepsilon_1 / \varepsilon_0}, \quad (14)$$

where f_{c0} is the peak compressive strength of the undamaged concrete; K is a coefficient related to the roughness and diameter of reinforcing steels, which can be 0.1 for medium diameter ribbed reinforcing steels [19]; ε_0 is the strain at peak stress in compression; ε_1 is the average tensile strain of cracked concrete perpendicular to the direction of stress, which can be calculated as follows:

$$\varepsilon_1 = \frac{n_{bars} \kappa_w (\Delta A_s - \Delta A_{s0})}{b_0}, \quad (15)$$

where b_0 is the width of pristine cross section; n_{bars} is the amount of longitudinal reinforcement in compressed regions; κ_w is the empirical coefficient, which is taken as 0.0575 mm^{-1} ; ΔA_s is the area loss of reinforcing steels; ΔA_{s0} is the critical area loss of reinforcing steels for cracking initiation, which can be evaluated as [20]

$$\Delta A_{s0} = A_s - A_s \left[1 - \frac{\delta (7.53 + 9.32 d_c / d_{s0})}{1000 d_{s0}} \right]^2, \quad (16)$$

where δ is the pitting concentration factor, which is taken as 4 to 8; A_s is the area of pristine cross section.

2.3.3. *Confined Concrete.* The Mander stress-strain relationship is utilized to simulate the behaviour of confined concrete after corrosion [21]. For a circular cross section, the confined strength f'_{cc} and ultimate strain ϵ_{cu} of core concrete are estimated as

$$f'_{cc} = f_{c0} \left(2.254 \times \sqrt{1 + \frac{7.94 \times 0.5K_e \rho_h f_{yh}}{f_{c0}}} - 2 \times \frac{0.5K_e \rho_h f_{yh}}{f_{c0}} - 1.254 \right), \quad (17)$$

$$\epsilon_{cu} = 0.004 + \frac{1.4 \rho_h f_{yh} \epsilon_u}{f_{c0}}, \quad (18)$$

where K_e is the effective confined coefficient of section; ρ_h is the residual volumetric ratio of corroded transverse reinforcement; f_{yh} and ϵ_u are the yield strength and ultimate strain of corroded transverse reinforcement, respectively.

3. Time-Dependent Fragility Method

In this study, the analytical seismic fragility is applied to quantify the seismic damage probability of bridges. Fragility functions describe the conditional damage probability of a component or structure exceeding a specific damage state (DS) for a given ground motion intensity measure (IM) [22]. Considering the time-dependent effect, the damage probability of aging bridges at t year after construction can be described as follows:

$$P[DS(t) > ds(t) | IM = im] = P \left[\frac{S_D(t)}{S_{C|ds}(t)} | IM = im \right], \quad (19)$$

where $S_D(t)$ is a time-dependent structural seismic demand for the specific IM; $S_{C|ds}(t)$ is the time-dependent structural seismic capacity corresponding to the given DS.

For a specific service time, $S_D(t)$ and $S_{C|ds}(t)$ can be assumed to follow lognormal distributions. Therefore, the time-dependent seismic fragility functions take the following form:

$$P[DS(t) > ds(t) | IM = im] = P \left[\frac{\mu(t)}{\sigma(t)} | IM = im \right], \quad (20)$$

where $\mu(t)$ and $\sigma(t)$ are the median estimate and standard deviation of $\ln[S_D(t)/S_{C|ds}(t)]$, respectively; $\Phi(\cdot)$ is the standard normal cumulative distribution function.

Generally, $\mu(t)$ can be predicted by a power model using the least-square method as follows:

$$\mu = a(t) \cdot \ln(IM) + b(t), \quad (21)$$

where $a(t)$ and $b(t)$ are the time-dependent regression coefficients.

Moreover, the standard deviation $\sigma(t)$ is determined as follows:

$$\sigma(t) = \sqrt{\frac{\sum_{i=1}^N [y_i(t) - \mu_i(t)]^2}{N - 2}}, \quad (22)$$

where $y_i(t)$ and $\mu_i(t)$ are the actual and predicted values of $\ln[S_D(t)/S_{C|ds}(t)]$, respectively; $N - 2$ represents the freedom degree of simulations when the log-linear model is adopted in the probabilistic seismic demand analysis.

Combining the above corrosion analysis method and the time-dependent seismic fragility method, we can perform the probability seismic damage assessment of aging RC bridges subject to spatial chloride-induced corrosion. Overall, Figure 2 summarizes the analysis procedure, and the critical steps are included as follows:

- (1) *Corrosion Analysis.* For given details of piers (e.g., the thickness of concrete cover, the diameter of piers, the arrangement of reinforcing steels, the water binder ratio of concrete, the properties of materials, etc.), the corrosion initial time of reinforcing steels under different exposure conditions can be calculated (equations (2) and (3)). Subsequently, the time-dependent percentage mass loss of reinforcing steels is determined by using the pitting corrosion model (equations (4)~(10)) and time-dependent uniform corrosion rate model (equations (11) and (12)). On this basis, the time-dependent properties of reinforcing steels, concrete cover, and confined concrete in the corroded piers are determined (equations (13)~(18)).
- (2) *Bridge Model Updated.* The exposure conditions of each part of piers should be first determined according to the layout of bridge and the hydrological data (e.g., high level, low level, height of marine splash, etc.). Subsequently, the finite element model of bridge at pristine condition is developed. Moreover, elements of piers should be divided reasonably to ensure that each element of piers is located in the same exposure condition. For a specified time, the degeneration properties of various materials are obtained from step (1) and are associated with each part of piers.
- (3) *Time-Dependent Seismic Fragility Analysis.* The nonlinear time history and nonlinear static analysis are performed to obtain seismic demand and seismic capacity of components, respectively. By comparing the seismic demand and seismic capacity of components, the seismic demand capacity ratio can be determined, and the median estimate and standard deviation in seismic fragility function are calculated by using the regression fitting (equations (21) and (22)). By repeating step (2) and step (3), the time-dependent seismic fragility functions can be developed (equation (20)).

4. Case Study

4.1. *Bridge Description.* To investigate the seismic damage of aging bridges, a four-span continuous RC bridge is taken as the case study, as shown in Figure 3(a). Each span of the bridge is 30 m. The deck consists of four box-shaped concrete girders. The width and height of deck are 13.25 m and 1.6 m, respectively. Each pier bent consists of two circular

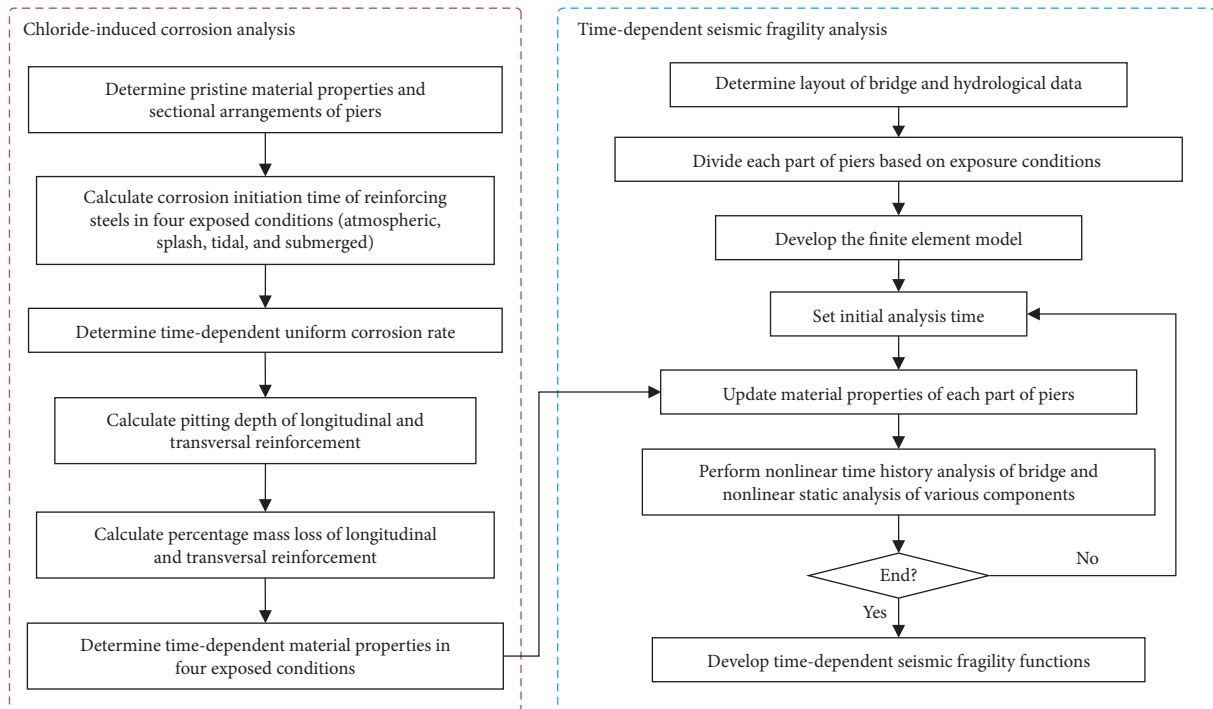


FIGURE 2: Flowchart of probabilistic seismic damage assessment for aging RC bridges subject to spatial chloride-induced corrosion.

columns with 1.5 m diameter. The heights of three piers are 6 m, 10 m, and 8 m, respectively. The concrete strengths of the substructure and superstructure are 30 MPa and 50 MPa, respectively. Each column consists of 48 longitudinal reinforcements with a diameter of 28 mm and yield stress of 335 MPa. The longitudinal reinforcement ratio is 1.67%. Moreover, rebars with a diameter of 12 mm and yield stress of 335 MPa are used as circular stirrups with a spacing of 80 mm (corresponding to a volumetric ratio of 0.6%). The thickness of concrete cover is 50 mm. Four rubber bearings are installed at the top of each bent, and four PTFE elastomeric bearings are located on the top of each abutment. In this study, two analysis cases are considered: (a) the bridge located in shallow water and (b) the bridge located in deep water. The high water level and low water level of two analysis cases are present in Figures 3(b) and 3(c). The height of marine splash is assumed to be 1 m.

4.2. Finite Element Modelling. The finite element model is developed by OpenSees (Open System for Earthquake Engineering Simulation), the PEER Center's finite element platform [23]. Figure 3(a) shows the three-dimensional finite element model of bridge. Overall, the girder is modelled by the linear elastic beam-column elements and the nonlinear beam-column element with fiber cross sections is used to simulate the piers. The element of piers is divided based on the different exposure conditions. The piers fibers use Concrete04 and Steel02 for concrete and longitudinal reinforcement, respectively. The zero-length element with the elastic and elastic PP materials is used to simulate the rubber bearings and the PTFE bearings, respectively. Shear keys are simulated in parallel with the hysteretic and elastic PP gap

materials. Furthermore, the interaction effects of abutments and backfill soil are considered by using hyperbolic gap material. The expansion joints at the deck end are modelled through the gap elements. In order to consider the effects of spatial chloride-induced corrosion, five group time-dependent finite element models of bridge under different time after construction (i.e., pristine, 20, 40, 60, 80, and 100 years, etc.) are developed according to the above modelling approach. The Monte Carlo approach is used to fully consider the uncertainties in the development of seismic fragility curves. Based on the finite element model, modal analysis of the bridge at pristine condition is performed to determine the fundamental periods. The result shows that the fundamental periods of model in longitudinal and transverse directions are 1.67 s and 1.35 s, respectively.

4.3. Ground Motions. To fully consider the uncertainties of ground motions, a broad range of intensities should be included in a reasonable ground motion suite. In this respect, 100 ground motions are selected to perform nonlinear time history analysis [24]. The selected ground motions include different source-to-site distances and magnitudes (Figure 4(a)): small magnitude and small epicentre distances (SMSR), small magnitude and large epicentre distances (SMLR), large magnitude and small epicentre distances (LMSR), large magnitude and large epicentre distances (LMLR), and near field (NF). Moreover, the spectra acceleration at the geometric mean of the periods with 5% damping SA_{GM} is chosen as intensity measure in this study [25]. The linear acceleration spectra and the distribution of SA_{GM} of 100 ground motions are present in Figure 4(b).

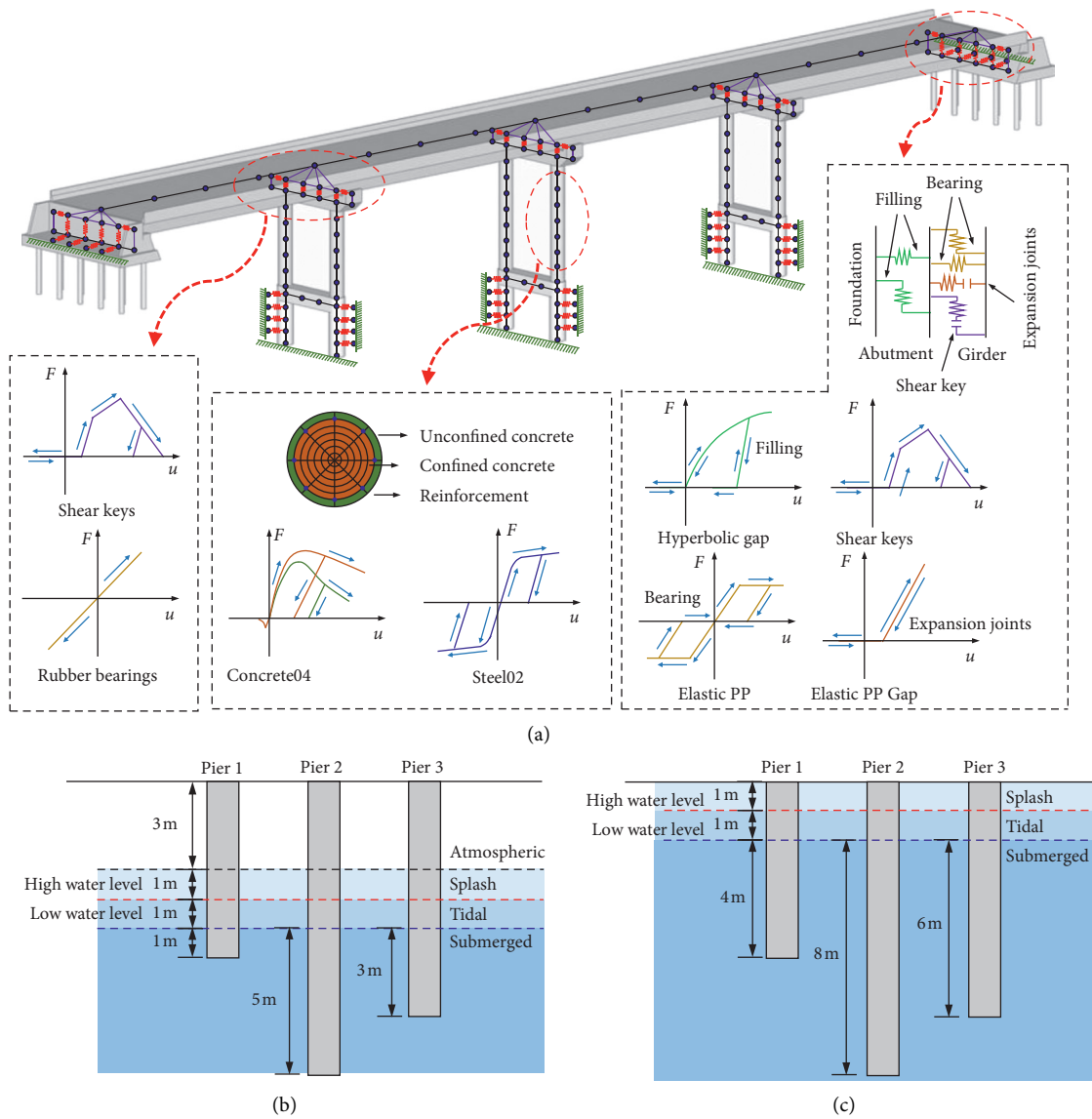


FIGURE 3: Schematic and finite element model of case study bridge.

5. Corrosion Process and Seismic Capacity Analysis

5.1. Corrosion Process of Reinforcing Steels. To consider the uncertainties during the corrosion process, 10000 samples are randomly generated using the Monte Carlo simulation method. Figure 5 illustrates the probability density of corrosion initiation time of transverse and longitudinal reinforcement. Overall, the significant dispersions of corrosion initiation time can be observed owing to the uncertainty of chloride ions diffusion process and outside environment. The corrosion initiation time of reinforcing steels can be well described by the lognormal distributions. Given that the distance varies in the outside environment, the transverse reinforcement presents a relatively smaller corrosion initiation time than the longitudinal reinforcement. Moreover, the corrosion of reinforcing steels exposure in tidal zone is most likely to be corroded, followed by the splash zone,

atmospheric zone, and submerged zone. Furthermore, it should be noted that the general thickness of concrete cover (i.e., 50 mm) is unlikely to effectively prevent the corrosion of reinforcing steels of bridges in a marine environment during the lifetime.

Based on the corrosion initiation time, the time-dependent corrosion level of reinforcing steels can be determined. Figure 6 presents the distribution and mean value of the percentage mass loss of corroded transverse and longitudinal reinforcement at different time. As expected, the corrosion level of reinforcing steels also exhibits significant dispersions. From the mean of the percentage mass loss, we can observe that the corrosion level of transverse reinforcement is obviously larger than that of the longitudinal reinforcement due to its smaller diameter and shorter corrosion initiation time. Similar to the corrosion initiation time, the corrosion of reinforcing steels in tidal zone is more serious than that in other exposure conditions.

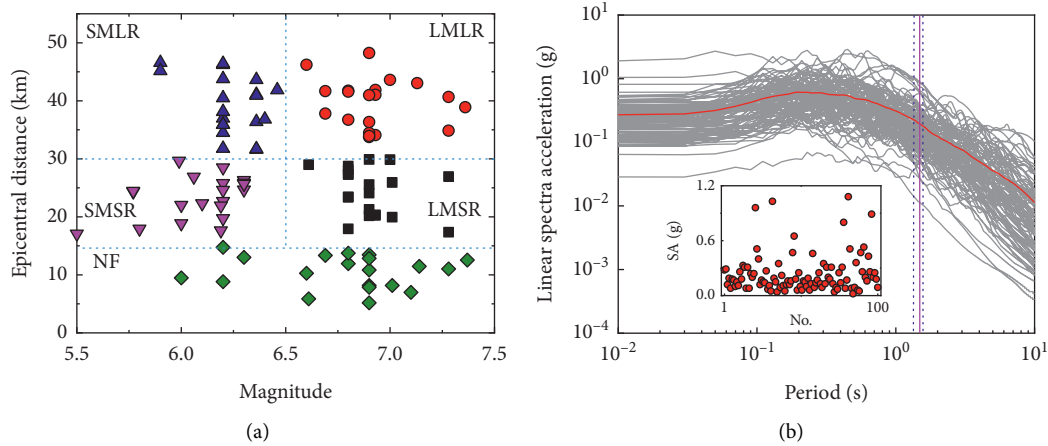


FIGURE 4: (a) R-M distribution and (b) acceleration response spectra of 100 ground motions ($\xi = 0.05$).

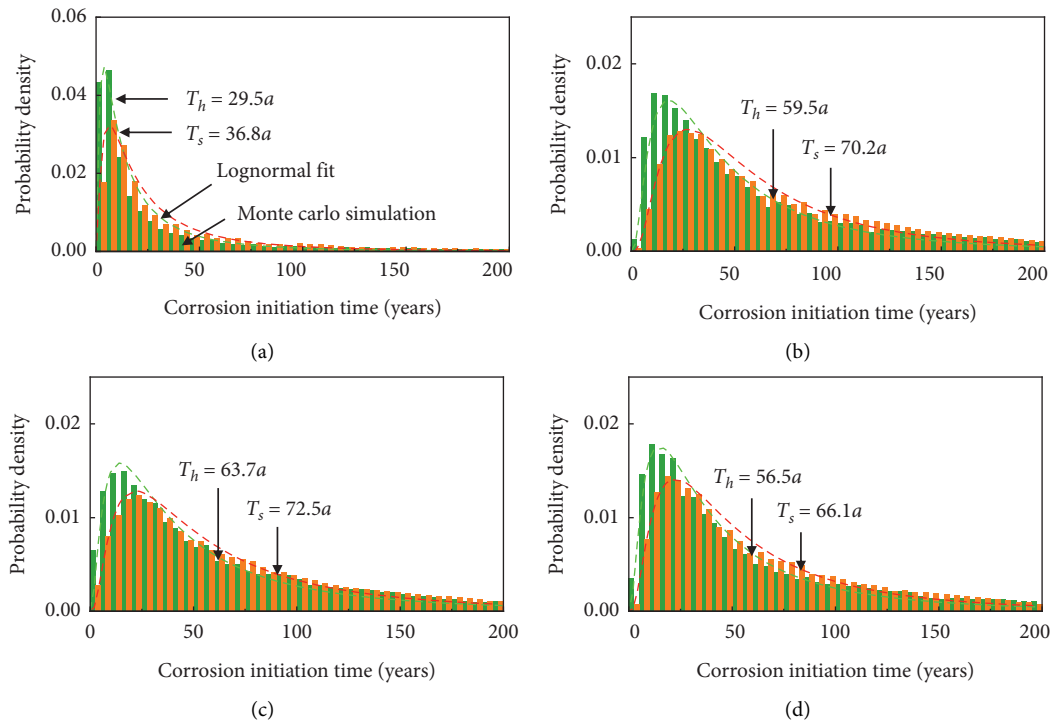


FIGURE 5: Probability distribution of corrosion initiation time in (a) tidal zone, (b) atmospheric zone, (c) submerged zone, and (d) splash zone.

On the other hand, a nonlinear relationship between time and the mean of percentage mass loss of reinforcing steels can be observed. In particular, the increase rate of the percentage mass loss is relatively small at initial years. One reason is that most of samples will not be corroded at the initial years, and another reason is that the influence of corrosion depth on the pitting corrosion area is relatively slight when the corrosion level is low. Meanwhile, the percentage mass loss has a remarkable increase as time increases, and the increase rate keeps an approximate constant value. Moreover, the increase rate of the percentage mass loss of transverse reinforcements decreases when the corrosion level exceeds a threshold value (about

50% percentage mass loss). It is because the sensitivities of pitting corrosion area to the corrosion depth decrease when the corrosion level is high.

5.2. Seismic Capacity of Piers. To investigate the influence of chloride-induced corrosion on the seismic capacity of piers, the properties of degradation materials should be determined. Table 2 shows the time-dependent properties of reinforcing steels and concrete. Based on the material properties and nonlinear static analysis, the time-dependent moment-curvature relationships of cross section of piers are obtained, as shown in Figure 7.

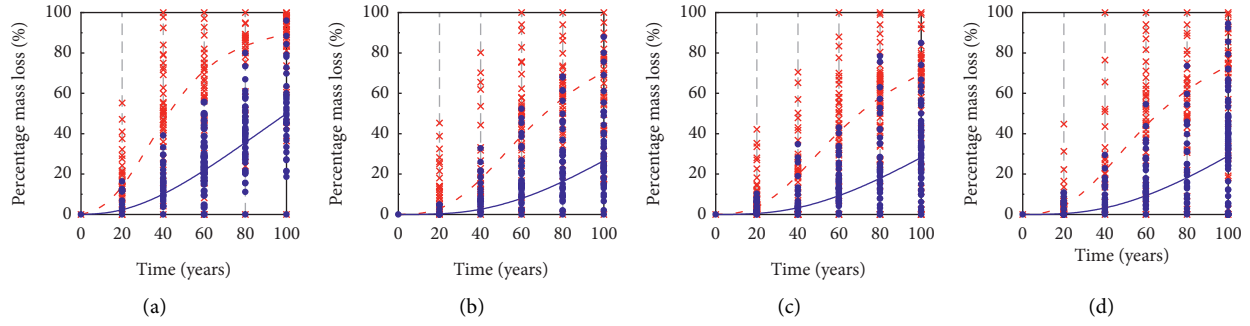


FIGURE 6: Distribution and mean value of the percentage mass loss of reinforcement at different years in (a) tidal zone, (b) atmospheric zone, (c) submerged zone, and (d) splash zone.

TABLE 2: Time-dependent material properties under four categories of exposure conditions.

Material parameters	0	20	40	60	80	100
<i>Tidal zone</i>						
Yield strength of longitudinal reinforcement	335	332	319	288	267	252
Compressive strength of unconfined concrete	30.0	20.4	12.8	8.7	6.3	4.7
Compressive strength of confined concrete	37.5	34.0	32.8	31.9	31.5	31.3
Ultimate strain of confined concrete	0.0116	0.0077	0.0061	0.0052	0.0048	0.0047
<i>Submerged zone</i>						
Yield strength of longitudinal reinforcement	335	335	331	322	308	291
Compressive strength of unconfined concrete	30.0	28.7	23.6	18.7	14.7	11.7
Compressive strength of confined concrete	37.5	34.7	34.0	33.3	32.6	32.1
Ultimate strain of confined concrete	0.0116	0.0087	0.0076	0.0066	0.0059	0.0054
<i>Atmospheric zone</i>						
Yield strength of longitudinal reinforcement	335	334	330	320	306	289
Compressive strength of unconfined concrete	30.0	28.1	22.9	18.6	15.1	12.3
Compressive strength of confined concrete	37.5	34.6	34.0	33.3	32.7	32.2
Ultimate strain of confined concrete	0.0116	0.0087	0.0076	0.0067	0.0060	0.0055
<i>Splash zone</i>						
Yield strength of longitudinal reinforcement	335	334	330	320	305	287
Compressive strength of unconfined concrete	30.0	28.1	22.7	17.7	13.9	11.1
Compressive strength of confined concrete	37.5	34.6	33.9	33.0	32.4	32.0
Ultimate strain of confined concrete	0.0116	0.0086	0.0074	0.0064	0.0057	0.0053

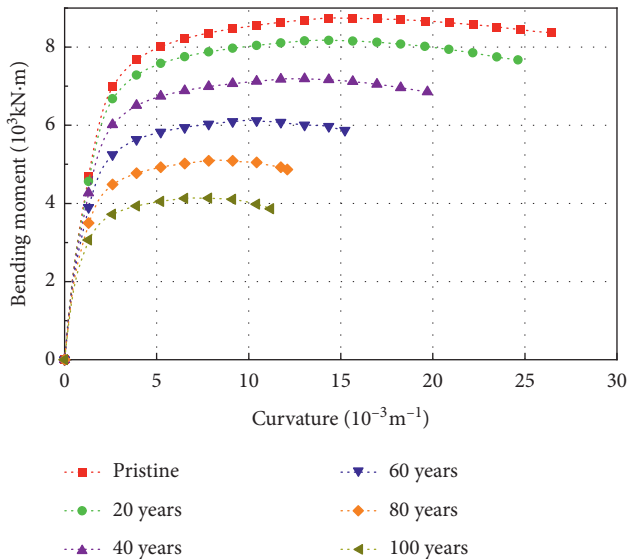


FIGURE 7: Time-dependent moment-curvature relationships of piers in tidal zone.

Referring to Figure 7, it is seen that the effects of corrosion on the initial stiffness of cross section are relatively slight. Meanwhile, the moment capacities and the ultimate curvatures of cross section exhibit a remarkable degradation. The phenomenon is consistent with the findings from some experiments [26, 27]. However, an increase in the ultimate curvature of cross section after corrosion can be observed in some previous studies [28, 29]. The main reason is that these studies ignore the degradation effect of confined concrete on the seismic capacity of corroded piers. In fact, the corrosion of longitudinal reinforcement will decrease the compression area of cross section of piers. Had the reduction of ultimate compression strain of confined concrete not been considered, the ultimate curvature of corroded piers would have increased slightly rather than decreasing significantly.

To further investigate seismic capacity of corroded piers, the curvatures of cross section in various exposure conditions at four-level damage states (i.e., slight, moderate, extensive, and complete [30]) are shown in Figure 8. Overall, two different variation trends of the curvature

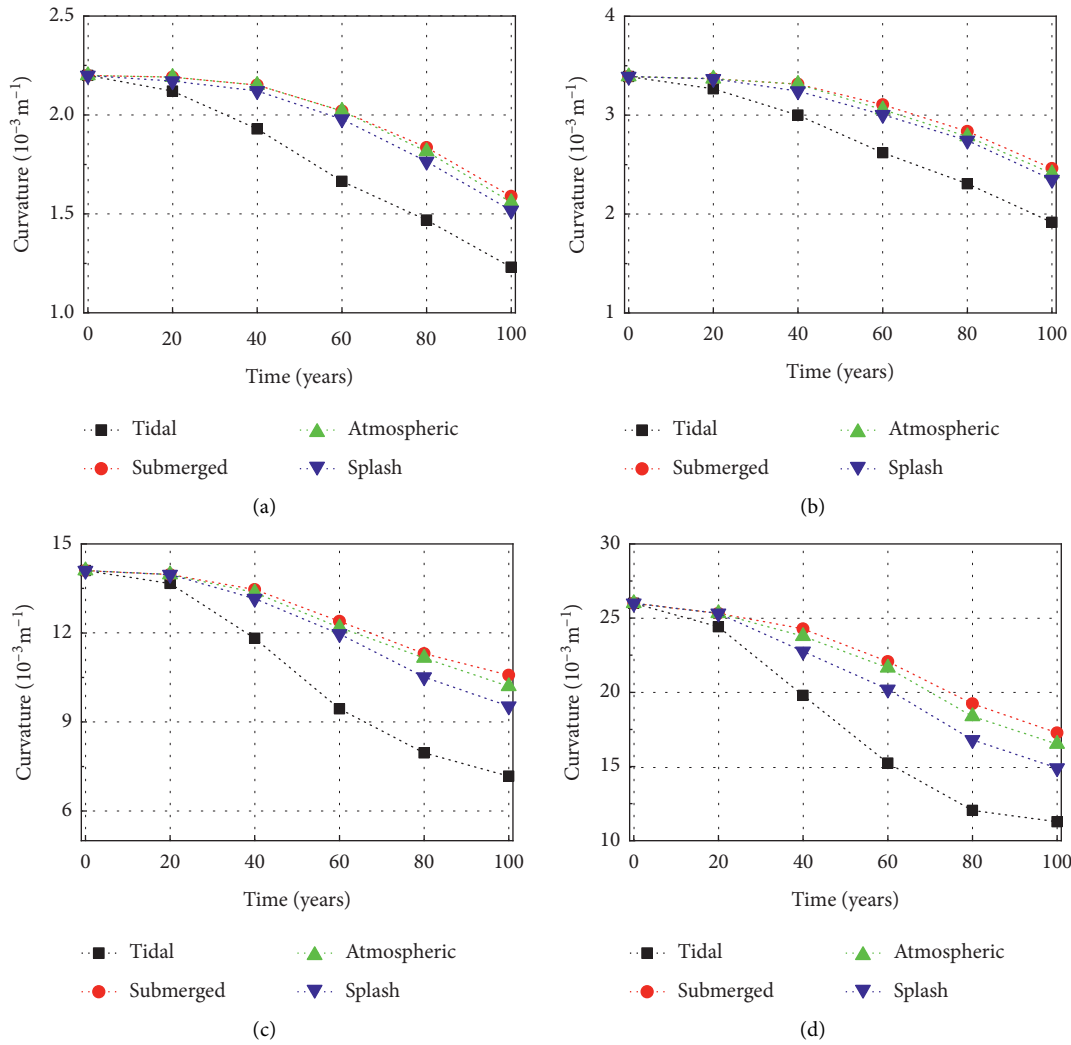


FIGURE 8: Curvature capacity of piers at (a) slight, (b) moderate, (c) extensive, and (d) complete damage states.

capacities at four damage states can be observed. As the slight and moderate damage states are defined as the first longitudinal reinforcement yields and the fully formed plastic hinge of section, respectively, the corresponding curvatures highly depend on the properties of longitudinal reinforcement. In consequence, the curvature capacities of piers at these two damage states exhibit a similar variation trend to the percentage mass loss of corroded longitudinal reinforcement. Meanwhile, the compressive strength and ultimate strain of confined concrete play an important role in the curvature capacity of piers at extensive and complete damage states. Therefore, the variation trend of curvature capacity of piers at these two damage states is similar to that of the percentage mass loss of corroded transverse reinforcement. Moreover, the curvature capacity of piers in tidal zone is significantly lower than that of other exposure conditions, as expected. In particular, the maximum reduction ratios of curvatures capacity in various exposure conditions at extensive damage states are 49%, 25%, 28%, and 32%, respectively.

6. Seismic Damage Assessment of Aging Bridge

6.1. Fragility Analysis of Piers. According to the damage assessment procedure, the time-dependent seismic fragility functions of bridges can be obtained. Figure 9 presents the time-dependent fragility surfaces of three piers in longitudinal direction when the bridge is located in shallow water. Due to the stiffness discrepancy of piers, the fragility surfaces of various piers exhibit significant different. With the increase of service time, the fragility surfaces of each pier at four damage states present upward trends. This is particularly seen in the fragility surfaces at extensive and complete damage states. For example, for an SA value of 0.3 g, the probabilities of pier 1 exceeding four damage states increase by 12%, 20%, 73%, and 195%, respectively. It is indicated that the corrosion has negative effects on the seismic damage of piers. Moreover, the different variation degrees result in the decrease of gap between fragility surfaces at each damage state. It is revealed that the ductility level of piers will significantly decrease, entailing the damage state of corroded

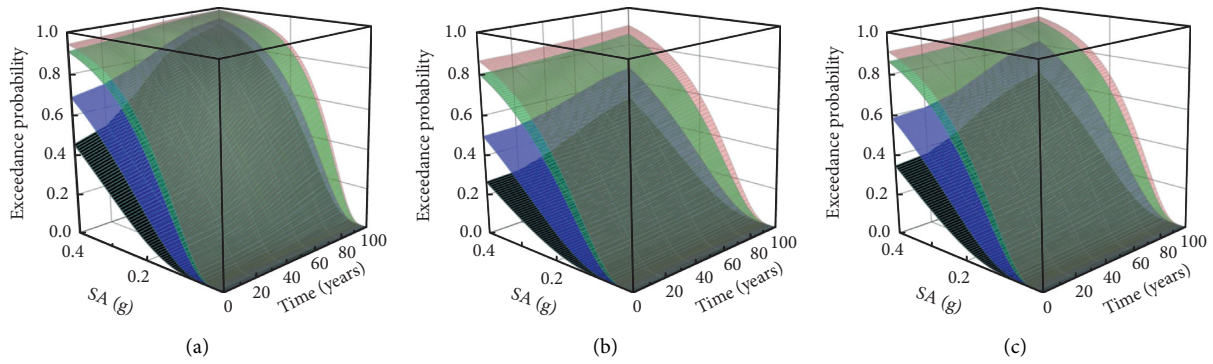


FIGURE 9: Time-dependent fragility surfaces of (a) pier 1, (b) pier 2, and (c) pier 3 in longitudinal direction.

piers much easier to transform from a low level to a high level during earthquakes.

On the other hand, it can be observed from Figure 9 that the damage probabilities of piers at various damage states demonstrate nonlinear variation trends with the increase of time. Specifically, the damage probabilities of piers at 20 years are close to those at pristine condition because the degradation of piers mainly occurs at 30~40 years after construction. Moreover, the damage probabilities of piers at slight and moderate damage states steadily increase after 40 years. Meanwhile, the increase rates of damage probabilities at extensive and complete damage states reduce after 80 years. Overall, the phenomenon is similar to the variation trends of curvature capacities (see Figure 8). It can be inferred that the seismic capacities of piers strongly affect the seismic fragility of piers.

In order to investigate the effects of spatial chloride-induced corrosion on the damage distribution of piers, Figure 10 shows the seismic fragility contour maps of pier 1 at pristine condition and 100 years after construction. Depending on the inertia force distributions of piers during earthquakes, the damage probability distribution of piers in longitudinal direction at pristine condition follows an approximate linear triangle pattern, whereas the damage in transverse direction forces on the two ends of piers and decreases from two ends to the middle of piers. However, a jaggedness damage probability distribution of piers can be observed in some cases after spatial chloride-induced corrosion. In particular, the section at the low and/or high water levels may become more vulnerable than the adjacent sections in two directions. The reason is that seismic capacities of the sections exposed in the tidal zone between the low water level and high water level will exhibit more significant degradation. Therefore, the spatial chloride-induced corrosion not only increases the seismic damage probability of piers but also may alter the damage probability distribution of piers.

To clearly illustrate the damage distribution of various piers, Figure 11 presents the distribution of the median SA (corresponding to a 50% damage probability) exceeding moderate damage state of each pier at pristine condition and 100 years after construction. A visible alteration of damage distribution in two directions can be observed from the pier located in shallow water. Meanwhile, the damage

distribution of pier in transverse direction will be altered when it is located in shallow water. Moreover, the movement of inflection points in piers can be found after alteration of damage distribution. It should be noted that the probability exceeding moderate damage state of section at the low water level may exceed that of sections at two ends of piers after corrosion. It can be inferred that the formation of plastic hinges of section at the low water level will be earlier than that of two-end sections. In other words, the spatial chloride-induced corrosion may alter the yield sequence of piers during earthquakes. On the other hand, the alteration of damage distribution is the most significant in pier 1 followed by pier 3 and pier 2 when the bridge is located in shallow water. Meanwhile, an opposite trend can be found from the bridge located in deep water. It is indicated that the height of piers and water level will commonly affect the damage distribution of piers. A further discussion in this regard is presented in Section 7.

6.2. Fragility Analysis of Other Components. Previous investigation mainly focused on the effects of corrosion on the seismic damage of piers. In fact, the degradation of piers will affect the dynamic characteristics and seismic response of the whole bridge. To fully investigate the seismic damage of aging bridge, the seismic fragility functions of shear keys, rubber bearings, and PTFE sliding bearings are developed. Table 3 shows the seismic capacities of these components at different damage states.

Figure 12 shows the time-dependent fragility curves of components at moderate and complete damage states when the bridge is located in shallow water. Due to the stiffness discrepancy between various piers and abutments, the damage of components at abutment is always more serious than that of components at piers. Moreover, the components at pier 1 are the most vulnerable followed by the components at pier 3 and pier 2. On the other hand, a decrease in damage probability of various components with increasing time can be observed from the figure, which is opposite to that of piers. When $SA = 0.2$ g, the probabilities of shear keys at abutment, PTFE sliding bearings at abutment, and rubber bearings at pier 1 exceeding moderate damage reduce by 24.1%, 35.1%, and 29.0%, respectively. The main reason is that the corrosion of piers will decrease the inertia force in

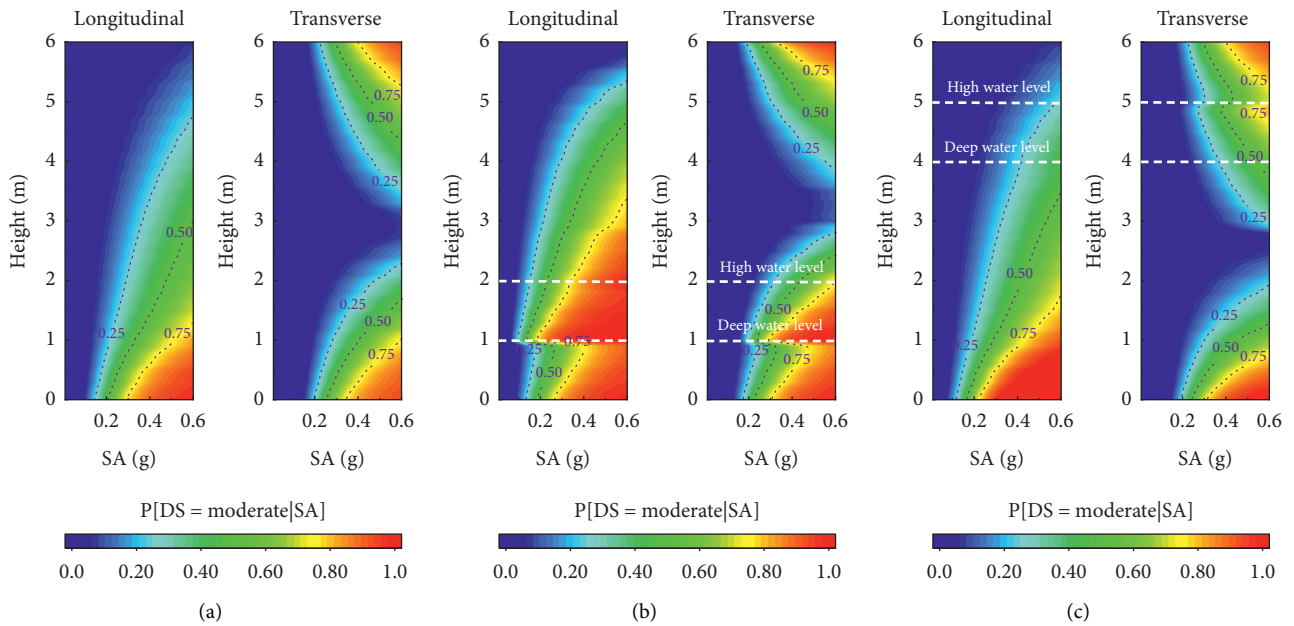


FIGURE 10: Fragility contour maps of pier 1 (a) at pristine condition, (b) at 100 years after construction in shallow water, and (c) at 100 years after construction in deep water.

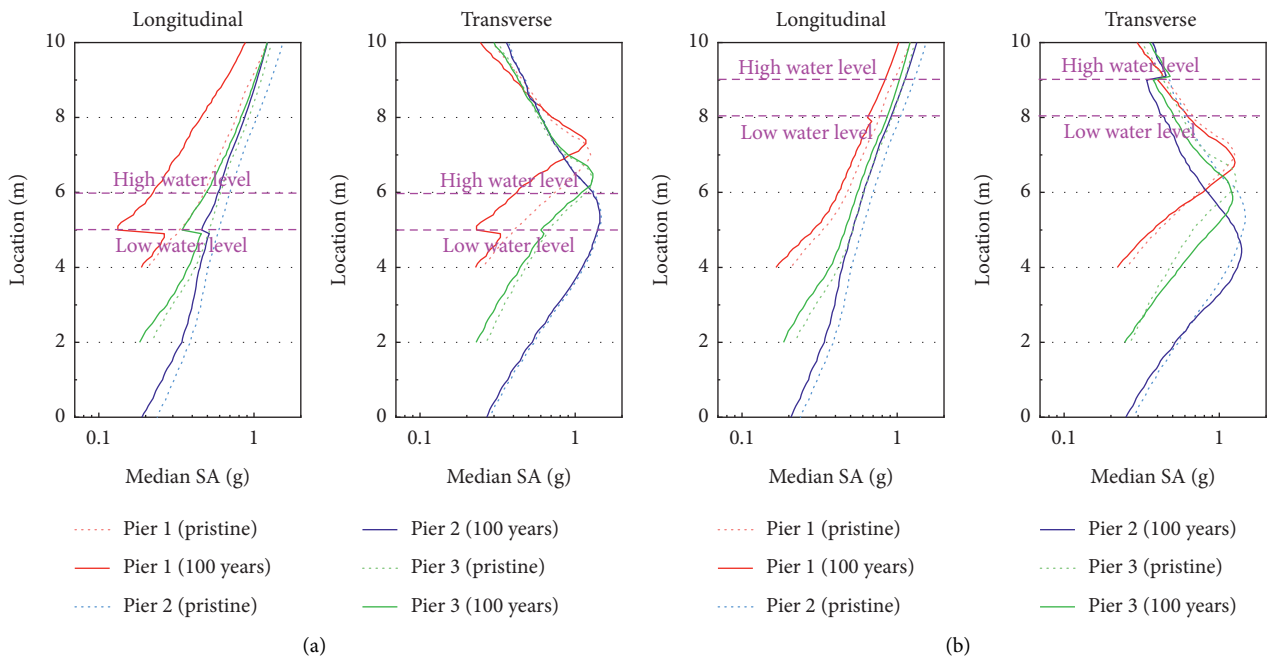


FIGURE 11: Distribution of median SA of piers at moderate damage state: (a) in shallow water and (b) in deep water.

TABLE 3: Definition of damage states of different components.

Component	EDP	Slight	Moderate	Extensive	Complete
Shear keys	Deformation (mm)	5.2	51	70	130
PTFE sliding bearings	Deformation (mm)	80	150	200	300
Rubber bearings	Deformation (mm)	80	120	160	200

the bridge, resulting in a decrease of seismic response of other components. In this case, the corrosion of piers may have a beneficial effect on the seismic damage of these

components. Because only the variation of seismic demand is considered in the development of seismic fragility of these components, the variation degree of fragility curves is

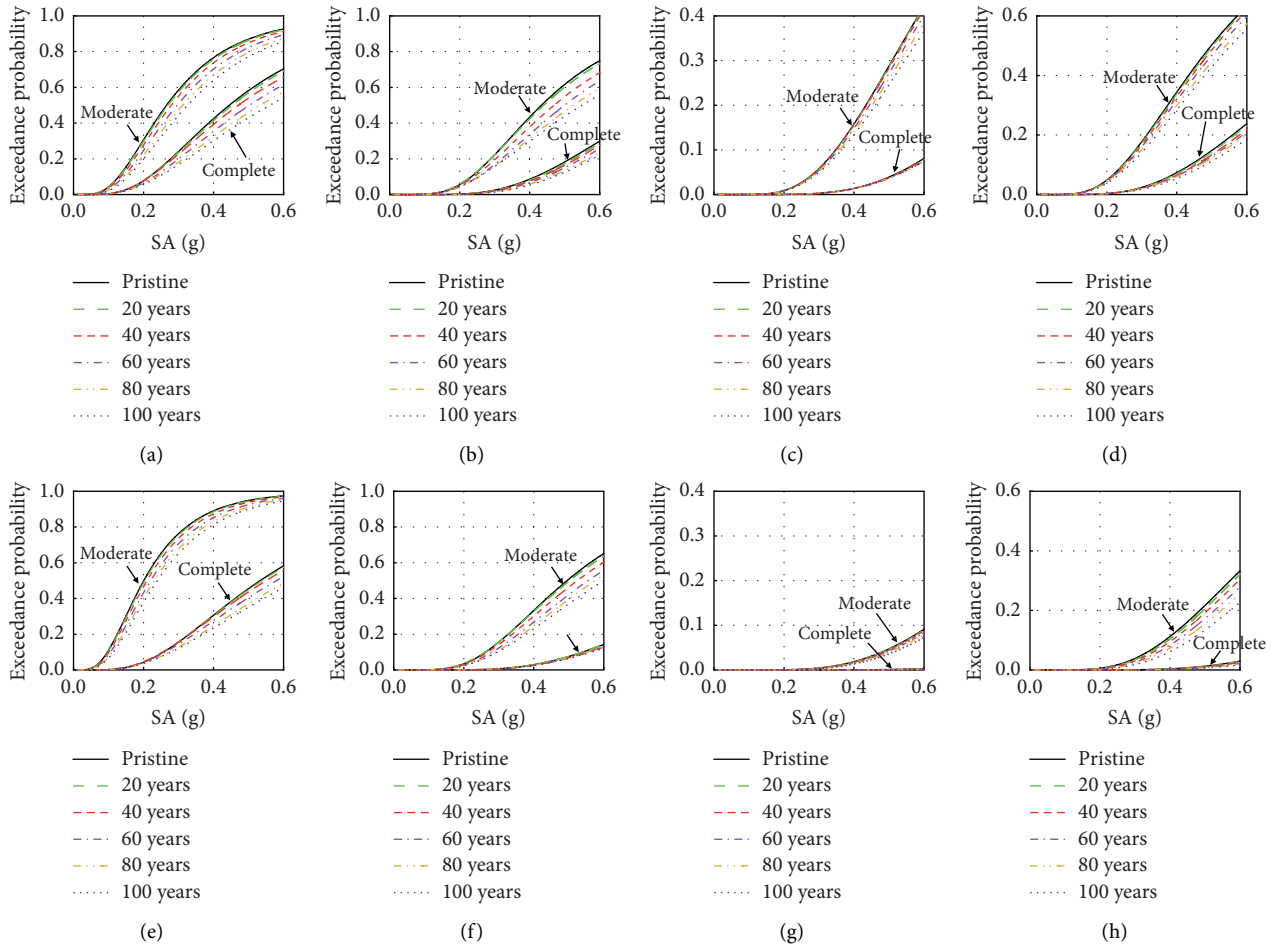


FIGURE 12: Time-dependent fragility curves of (a) shear keys at abutment, (b) shear keys at pier 1, (c) shear keys at pier 2, (d) shear keys at pier 3, (e) PTFE sliding bearings at abutment, (f) rubber bearings at pier 1, (g) rubber bearings at pier 2, and (h) rubber bearings at pier 3.

relatively slighter than that of piers. Additionally, Table 4 lists the median SAs of some critical components. By comparing the seismic fragility of piers in Figure 11(a), we can observe that the PTFE sliding bearing at abutment is the most vulnerable component at slight damage state at pristine condition. Meanwhile, pier 1 tends to dominate the vulnerability of the bridge at 100 years after construction. It is indicated that the opposite degradation trends between piers and other components may change the most vulnerable component in the whole bridge.

Figure 13 presents the fragility curves of various components at extensive damage state. The difference between fragility curves in deep water and shallow water indicates that the water level will affect the damage probability of other components. For the components at abutment and pier 1, the damage probability in shallow water is relatively smaller than that in deep water. On the contrary, the damage probability of components at pier 3 in shallow water is relatively larger than that in deep water. Combined with the previous analysis, it seems that the alteration of damage distribution of piers seems to aggravate the variation degree of damage probability of other components.

7. Evolution Probability of Yield Sequence of Corroded Piers

Modern RC piers are generally designed to dissipate energy during strong earthquakes by permitting the controlled formation of plastic hinges. In this aspect, detailed design of the plastic hinges is necessary to ensure that piers have enough dissipation of energy. Meanwhile, the displacement ductility capacity of piers should be determined according to the distribution of plastic hinges. Therefore, the plastic hinges of piers should be predetermined during the ductile seismic design. In general, the plastic hinges are expected to form at the bottom and/or top of piers. However, as mentioned, the spatial chloride-induced corrosion may alter the yield sequence of corroded piers. In this case, it is important to determine the yield sequence of the corroded piers during the ductile seismic design.

In this section, we propose a method to determine the evolution probability of yield sequence of piers. Based on the results in Section 6, the plastic hinges of corroded piers may appear at four sections: (1) the bottom section of piers, (2) the top section of piers, (3) the section at low water level, and

TABLE 4: Median SAs of various components.

Components	Damage states	Pristine	20 years	40 years	60 years	80 years	100 years
<i>Shear keys at abutment</i>	Slight	0.171	0.173	0.179	0.188	0.197	0.205
	Moderate	0.266	0.27	0.28	0.296	0.312	0.326
	Extensive	0.307	0.312	0.324	0.344	0.363	0.38
	Complete	0.445	0.452	0.471	0.503	0.533	0.561
<i>PTFE bearings at abutment</i>	Slight	0.122	0.123	0.126	0.131	0.136	0.141
	Moderate	0.201	0.203	0.209	0.22	0.23	0.239
	Extensive	0.339	0.344	0.356	0.376	0.395	0.412
	Complete	0.533	0.542	0.563	0.598	0.632	0.663
<i>Rubber bearings at pier 1</i>	Slight	0.28	0.287	0.293	0.31	0.33	0.35
	Moderate	0.495	0.51	0.53	0.56	0.58	0.6
	Extensive	0.743	0.77	0.8	0.83	0.86	0.9
	Complete	0.99	1.04	1.08	1.113	1.16	1.2

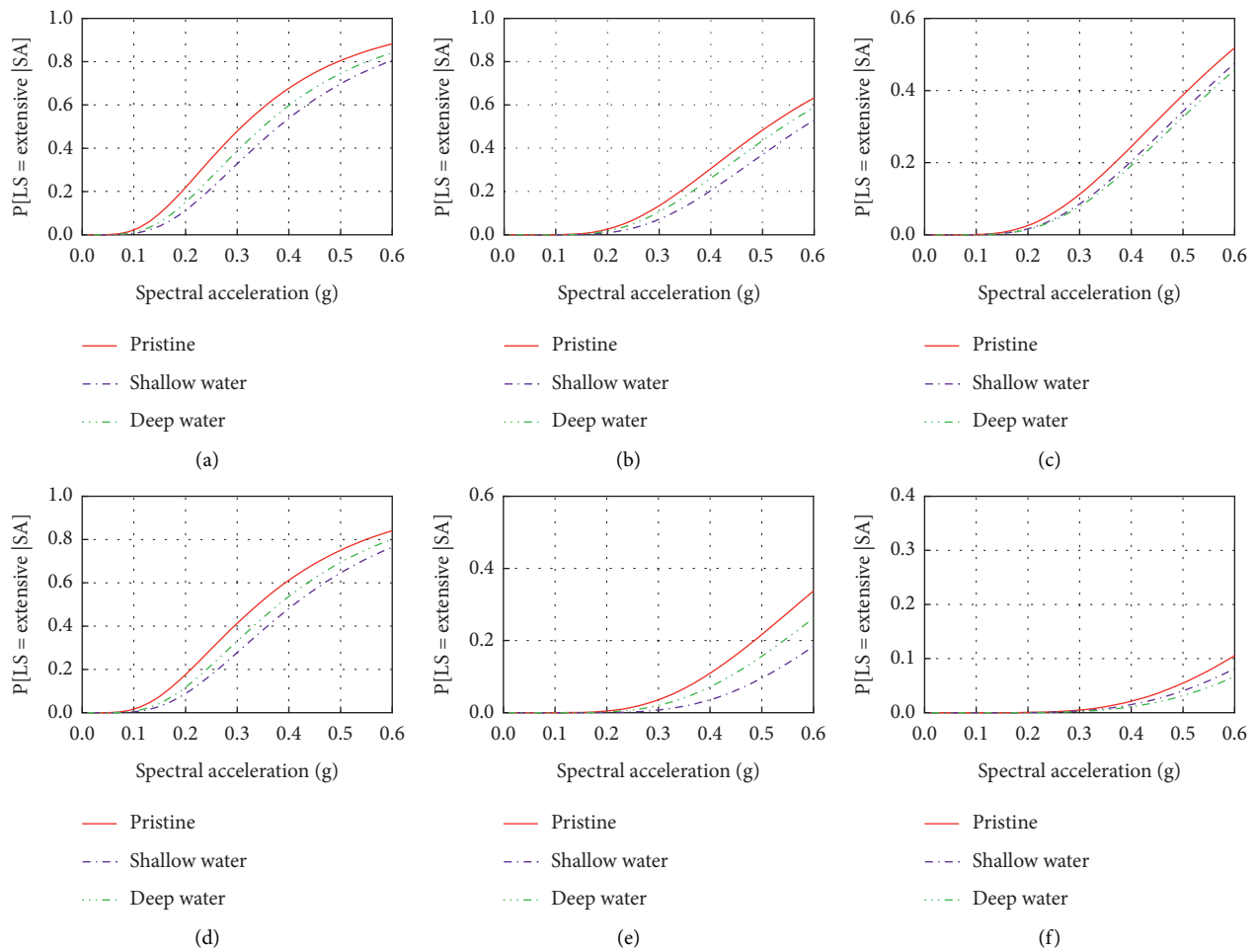


FIGURE 13: Time-dependent fragility curves of (a) shear keys at abutment, (b) shear keys at pier 1, (c) shear keys at pier 3, (d) PTFE sliding bearings at abutment, (e) rubber bearings at pier 1, and (f) rubber bearings at pier 3 under different water region.

(4) the section at high water level. In theory, the yield sequence of piers can be determined by comparing the curvature demand during earthquakes and yield curvature capacity (corresponding curvature capacity at moderate damage state), as shown in Figure 14.

Theoretically, the double-column pier can be regarded as a cantilever column in longitudinal direction. Therefore, the

distribution of longitudinal curvature demand of piers before yielding can be simplified to a linear relationship (Figure 14(a)). On the contrary, the framing effects between the columns and the bents result in the distribution of curvature demand of piers in transverse direction presenting the double triangle curves before the pier yields (Figure 14(b)) [31]. On the other hand, the yield curvature

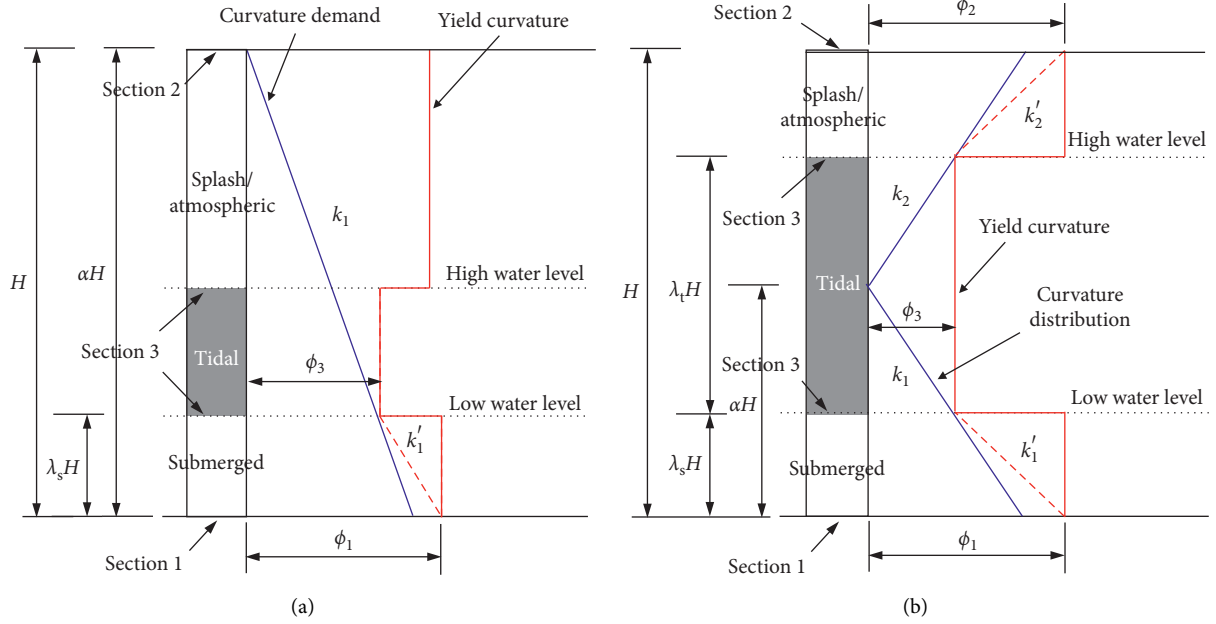


FIGURE 14: Evolution condition of yield sequence of corroded piers in (a) longitudinal direction and (b) transverse direction.

capacity of piers presents a stepped distribution due to the nonuniform degradation. By comparing the slope of curvature demand distribution and curvature capacity

distribution, the evolution probability of yield sequence of piers can be described as follows:

$$\begin{cases} P = P(k'_1 \leq k_1), & \text{longitudinal direction,} \\ P = P[(k'_1 \leq k_1) \cup (k'_2 \leq k_2)] = 1 - P[(k'_1 > k_1) \cap (k'_2 > k_2)], & \text{transverse direction,} \end{cases} \quad (23)$$

$$\begin{aligned} k_1 &= (\alpha - \lambda_s) \frac{H}{\varphi_3}, \\ k'_1 &= \lambda_s \frac{H}{(\varphi_1 - \varphi_3)}, \end{aligned} \quad (24)$$

$$\begin{aligned} k_2 &= (\lambda_t + \lambda_s - \alpha) \frac{H}{\varphi_3}, \\ k'_2 &= (1 - \lambda_s - \lambda_t) \frac{H}{(\varphi_2 - \varphi_3)}, \end{aligned} \quad (25)$$

where α is the ratio between the distance from inflection points to the bottom of piers and the height of piers, which can be assumed to be 1 and 0.5 in longitudinal and transverse directions, respectively; λ_s is the ratio between the depth of submerged zone and the height of piers; λ_t is the ratio

between the depth of tidal zone and the height of piers; H is the height of pier; φ_1 , φ_2 , and φ_3 are the yield curvatures of section 1 (bottom section), section 2 (top section), and section 3 (section at low or high water level), respectively.

Thus, equation (23) can be rewritten as follows:

$$\begin{cases} P = P[\alpha_{31} \leq (1 - \lambda_s)], & \text{longitudinal direction,} \\ P = 1 - P\{[\alpha_{31} > (1 - 2\lambda_s)] \cap [\alpha_{32} > (2\lambda_s + 2\lambda_t - 1)]\}, & \text{transverse direction,} \end{cases} \quad (26)$$

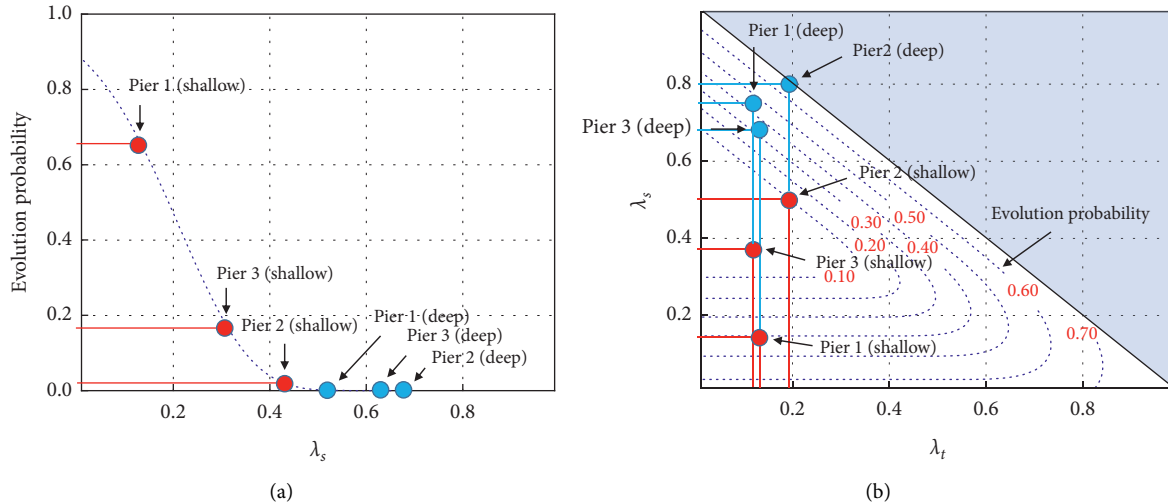


FIGURE 15: Effects of λ_s and λ_t on the evolution probabilities of yield sequence of corroded piers in (a) longitudinal direction and (b) transverse direction.

where α_{31} is the yield curvature ratio between sections 1 and 3; α_{32} is the yield curvature ratio between sections 2 and 3.

Subsequently, the Monte Carlo simulation method is applied to obtain the evolution probability of yield sequence based on equation (26). Figure 15(a) shows the influences of λ_s on the evolution probability of yield sequence of corroded piers in longitudinal direction. From the figure, it can be seen that the evolution probability of yield sequence rapidly decreases with the increase in λ_s . For the case study of bridge, the evolution probabilities of pier 1 in shallow water and deep water are 66.4% and 0.1%, respectively. In addition, the evolution probabilities of pier 1 and pier 2 in shallow water are 66.4% and 0.3%, respectively. It is indicated that the yield sequence of corroded piers in longitudinal direction is more likely to evolve in shallow water than in deep water. Moreover, the yield sequence of short pier is more likely to evolve than that of tall pier in a bridge.

On the other hand, Figure 15(b) represents the influences of λ_s and λ_t on the evolution probability of yield sequence of corroded piers in transverse direction. For a constant λ_t , the evolution probability will first decrease and then increase with the growth of λ_s . For example, the evolution probability of piers will reduce from 49.0% to 9.9% for λ_s in the range from 0.1 to 0.3 when λ_t is equal to 0.3. Next, the evolution probability increases to 33.2% with λ_s reaching 0.8. It can be inferred that the evolution of yield sequence in transverse direction will be easy to happen in both the shallow water and the deep water. Moreover, higher λ_t is more likely to cause the evolution of the yield sequence of corroded piers in transverse direction.

8. Conclusion

This study assessed the seismic damage of aging RC bridges subject to spatial chloride-induced corrosion in marine environments. Moreover, a method is proposed to determine the evolution probability of yield sequence of corroded

piers, and the influence factors are further investigated. Generally, the following conclusions can be obtained:

- (1) The corrosion level of reinforcing steels in tidal zone is the most serious, followed by the splash zone, atmospheric zone, and submerged zone. Moreover, the transverse reinforcement experiences more remarkable corrosion than the longitudinal reinforcement. The chloride-induced corrosion will significantly decrease the moment capacity and curvature ductility of piers. Meanwhile, the influence of corrosion on the initial stiffness of piers is relatively slight.
- (2) The seismic damage probability will present non-linear increase trends with the increase of time when the piers suffer spatial chloride-induced corrosion. Moreover, the corroded pier is easy to turn from low damage states to high damage states during earthquakes because of its poor ductility level. Furthermore, the nonuniform degradation along the pier direction may result in the sections at the low water level and/or high water level becoming more vulnerable than the adjacent sections, entailing the alteration of damage distribution of corroded piers or even the yield sequence of corroded piers in some cases.
- (3) The spatial chloride-induced corrosion of piers will decrease the seismic response of other components, resulting in a reduction of seismic damage probability of various components. Moreover, the alteration of seismic damage distribution of piers will aggravate the variation degree of damage probability of components. It should be noted that the opposite degradation trends between piers and other components may change the most vulnerable component in the whole bridge.
- (4) The evolution probabilities of yield sequence of corroded piers are dependent on the relationships

among the height of piers and the depths of submerged zone and tidal zone. A lower ratio between the depth of submerged zone and the height of piers will increase the evolution probabilities of yield sequence of corroded piers in longitudinal and transverse directions. Moreover, the yield sequence of corroded piers in transverse direction is also more likely to evolve in a higher ratio between the depth of submerged zone and the height of piers. Meanwhile, a lower ratio between the depth of tidal zone and the height of piers will relieve the evolution of yield sequence of piers.

Data Availability

The data used to support the findings of this study are available from the corresponding author upon request.

Conflicts of Interest

The authors declare that they have no conflicts of interest.

Acknowledgments

This study was supported by the Natural Science Foundation of Jiangxi Province of China (no. 20192BAB216033), the China Postdoctoral Science Foundation (no. 2020M671972), and the National Innovation and Entrepreneurship Training Program for Undergraduate Students of China (no. 201910403021).

References

- [1] D. E. Choe, P. Gardoni, D. Rosowsky, and T. Haukaas, "Probabilistic capacity models and seismic fragility estimates for RC columns subject to corrosion," *Reliability Engineering & System Safety*, vol. 93, no. 3, pp. 383–393, 2008.
- [2] R. Kumar, P. Gardoni, and M. Sanchez-Silva, "Effect of cumulative seismic damage and corrosion on the life-cycle cost of reinforced concrete bridges," *Earthquake Engineering & Structural Dynamics*, vol. 38, no. 7, pp. 887–905, 2009.
- [3] A. Alipour, B. Shafei, and M. Shinozuka, "Performance evaluation of deteriorating highway bridges located in high seismic areas," *Journal of Bridge Engineering*, vol. 16, no. 5, pp. 597–611, 2011.
- [4] Y. Thanapol, M. Akiyama, and D. M. Frangopol, "Updating the seismic reliability of existing RC structures in a marine environment by incorporating the spatial steel corrosion distribution: application to bridge piers," *Journal of Bridge Engineering*, vol. 21, no. 7, Article ID 04016031, 2016.
- [5] F. Cui, H. Zhang, M. Ghosn, and Y. Xu, "Seismic fragility analysis of deteriorating RC bridge substructures subject to marine chloride-induced corrosion," *Engineering Structures*, vol. 155, pp. 61–72, 2018.
- [6] B. Panchireddi and J. Ghosh, "Cumulative vulnerability assessment of highway bridges considering corrosion deterioration and repeated earthquake events," *Bulletin of Earthquake Engineering*, vol. 17, no. 3, pp. 1603–1638, 2019.
- [7] Y. Zhang, R. DesRoches, and I. Tien, "Impact of corrosion on risk assessment of shear-critical and short lap-spliced bridges," *Engineering Structures*, vol. 189, pp. 260–271, 2019.
- [8] P. Crespi, M. Zucca, and M. Valente, "On the collapse evaluation of existing RC bridges exposed to corrosion under horizontal loads," *Engineering Failure Analysis*, vol. 116, Article ID 104727, 2020.
- [9] W. Yuan, A. Guo, W. Yuan, and H. Li, "Shaking table tests of coastal bridge piers with different levels of corrosion damage caused by chloride penetration," *Construction and Building Materials*, vol. 173, pp. 160–171, 2018.
- [10] DuraCrete, "Statistical quantification of the variables in the limit state functions," DuraCrete Inc., Salt Lake City, UT, USA, The European Union-Brite EuRam III-Contract BRPR-CT95-0132-Project BE95-1347/R9, 2000.
- [11] Y. C. Ou and N. D. Nguyen, "Plastic hinge length of corroded reinforced concrete beams," *ACI Structural Journal*, vol. 111, no. 5, pp. 1049–1058, 2014.
- [12] D. V. Val and R. E. Melchers, "Reliability of deteriorating RC slab bridges," *Journal of Structural Engineering*, vol. 123, no. 12, pp. 1638–1644, 1997.
- [13] M. G. Stewart and A. Al-Harthy, "Pitting corrosion and structural reliability of corroding RC structures: experimental data and probabilistic analysis," *Reliability Engineering & System Safety*, vol. 93, no. 3, pp. 373–382, 2008.
- [14] M. B. Otieno, M. G. Alexander, and H.-D. Beushausen, "Corrosion in cracked and uncracked concrete - influence of crack width, concrete quality and crack reopening," *Magazine of Concrete Research*, vol. 62, no. 6, pp. 393–404, 2010.
- [15] C. Cao, M. M. S. Cheung, and B. Y. B. Chan, "Modelling of interaction between corrosion-induced concrete cover crack and steel corrosion rate," *Corrosion Science*, vol. 69, pp. 97–109, 2013.
- [16] K. A. T. Vu and M. G. Stewart, "Structural reliability of concrete bridges including improved chloride-induced corrosion models," *Structural Safety*, vol. 22, no. 4, pp. 313–333, 2000.
- [17] Y. G. Du, L. A. Clark, and A. H. C. Chan, "Residual capacity of corroded reinforcing bars," *Magazine of Concrete Research*, vol. 57, no. 3, pp. 135–147, 2005.
- [18] D. Coronelli and P. Gambarova, "Structural assessment of corroded reinforced concrete beams: modeling guidelines," *Journal of Structural Engineering*, vol. 130, no. 8, pp. 1214–1224, 2004.
- [19] F. J. Vecchio and M. P. Collins, "The modified compression-field theory for reinforced concrete elements subjected to shear," *ACI Journal*, vol. 83, no. 2, pp. 219–231, 1986.
- [20] T. Vidal, A. Castel, and R. François, "Analyzing crack width to predict corrosion in reinforced concrete," *Cement and concrete Research*, vol. 34, no. 1, pp. 165–174, 2004.
- [21] J. B. Mander, M. J. N. Priestley, and R. Park, "Theoretical stress-strain model for confined concrete," *Journal of Structural Engineering*, vol. 114, no. 8, pp. 1804–1826, 1988.
- [22] L. Li, S. Hu, and L. Wang, "Seismic fragility assessment of a multi-span cable-stayed bridge with tall piers," *Bulletin of Earthquake Engineering*, vol. 15, no. 9, pp. 3727–3745, 2017.
- [23] S. Mazzoni, F. McKenna, M. H. Scott, and G. L. Fenves, "OpenSees command language manual," *Pacific Earthquake Engineering Research (PEER) Center*, vol. 264, 2006.
- [24] N. Shome, C. A. Cornell, P. Bazzurro, and J. E. Carballo, "Earthquakes, records, and nonlinear responses," *Earthquake Spectra*, vol. 14, no. 3, pp. 469–500, 1998.
- [25] J. E. Padgett, B. G. Nielson, and R. DesRoches, "Selection of optimal intensity measures in probabilistic seismic demand models of highway bridge portfolios," *Earthquake Engineering & Structural Dynamics*, vol. 37, no. 5, pp. 711–725, 2008.

- [26] Z. Yuan, C. Fang, M. Parsaeimaram, and S. Yang, "Cyclic behavior of corroded reinforced concrete bridge piers," *Journal of Bridge Engineering*, vol. 22, no. 7, Article ID 04017020, 2017.
- [27] A. S. Rajput and U. K. Sharma, "Corroded reinforced concrete columns under simulated seismic loading," *Engineering Structures*, vol. 171, pp. 453–463, 2018.
- [28] H. Yalciner, S. Sensoy, and O. Eren, "Time-dependent seismic performance assessment of a single-degree-of-freedom frame subject to corrosion," *Engineering Failure Analysis*, vol. 19, pp. 109–122, 2012.
- [29] D. Sobhani, S. Zarei, H. Savoj, and M. Shayanfar, "Investigation on corrosion effects of reinforcement on the moment-curvature diagram of reinforced concrete sections," *Mapta Journal of Architecture, Urbanism and Civil Engineering (MJAUCE)*, vol. 1, no. 3, pp. 11–22, 2018.
- [30] FEMA, *Multi-hazard Loss Estimation Methodology: Earthquake Model*, Department of Homeland Security, FEMA, Washington, DC, USA, 2003.
- [31] Transportation Officials Subcommittee on Bridges, *AASHTO Guide Specifications for LRFD Seismic Bridge Design*, AASHTO, Washington, DC, USA, 2011.

Research Article

Investigation of Factors Influencing the Construction Safety of High-Speed Railway Stations Based on DEMATEL and ISM

Feng Lin ¹, Ping Wu ², and Yidong Xu ²

¹School of Civil Engineering and Architecture, Jiangsu University of Science and Technology, Zhenjiang 212003, China

²School of Civil Engineering and Architecture, NingboTech University, Ningbo 315100, China

Correspondence should be addressed to Ping Wu; wuping@nit.zju.edu.cn

Received 24 March 2021; Revised 17 May 2021; Accepted 30 May 2021; Published 12 June 2021

Academic Editor: Faming Huang

Copyright © 2021 Feng Lin et al. This is an open access article distributed under the Creative Commons Attribution License, which permits unrestricted use, distribution, and reproduction in any medium, provided the original work is properly cited.

To explore the influencing factors and mutual influence mechanism of the construction safety of China's high-speed railway stations, this study takes the Hanghuang high-speed railway Fuyang station as the subject and studies 17 risk factors in 4 categories affecting construction safety based on system safety theory, and the interaction relationship and degree among the factors were analysed. Based on DEMATEL (Decision-making Trial and Evaluation Laboratory) and ISM (Interpretative Structural Modelling) methods, through a questionnaire survey, the logical relationship among the influencing factors is quantified. Then, the influencing degree, influenced degree, centrality, and causality of the influencing factors were calculated, and a multilevel hierarchical hybrid model is established to systematically analyse the influencing factors and the mechanism of high-speed railway station construction. The results show that the factors of construction safety risk are summarized as 3 main factors, 6 important factors, and 7 direct factors and personnel factors and management factors need to be controlled with emphasis. In addition, some measures are proposed. This research provides a theoretical basis and method for preventing accidents and improving the safety of high-speed railway station construction.

1. Introduction

With the rapid development of China's high-speed railway, its construction scale and speed of development have ranked first in the world [1]. At the same time, high-speed railway construction has been subject to safety issues due to its long production cycle, many working high above the ground in open air, complicated construction techniques, and many other factors. Construction safety accidents can cause serious casualties and heavy economic losses. According to the Ministry of Housing and Urban-Rural Development of the People's Republic of China, there were 4,100 construction and municipal engineering production safety accidents, with 5,011 deaths, in China (excluding Hong Kong, Macau, and Taiwan) from 2012 to 2018 [2]. Even in a developed country such as the United States, construction workers are twice as likely to be injured and have a death rate three and a half times higher than that of workers in production industries [3]. The death rate for construction workers in the UK is 5

times the average death rate of workers in the production industry [4]. Therefore, construction safety is a worldwide problem.

In the study of safety accidents, safety accident theories such as human error theory [5, 6], causal linkage theory [7], energy transfer theory [8, 9], and disturbance theory [10] have emerged successively. These theories analyse the relationship between safety accident factors and safety accidents from different perspectives and at different levels. With the recent increase in safety accident analysis in safety system engineering theory, system engineering technology was introduced into safety accident analysis in [11, 12]. However, previous studies have not examined the factors influencing safety accidents and safety accident causation, have not deepened the theory of accident causation, and have not identified safety accident factors for further systematic analysis from the perspective of the accidents.

There are two types of risk assessment research: qualitative and quantitative [13]. Qualitative research mainly

includes the safety checklist method, expert consultation method, and prerisk analysis method [14–18]. Quantitative research mainly includes the analytic hierarchy process (AHP), operating condition risk evaluation method (LEC), neural network and support vector machine method (SVM), and fuzzy comprehensive evaluation (FCE) method [19–24]. However, the existing security risk assessment methods usually focus on a single indicator and do not consider the interactions or coupling of the indicators [25]. In fact, accidents are usually caused by a combination of many factors.

In the 1960s, Tavistock institute proposed the complex social technology system, referring to an industrial organization that is technology-intensive and capital-intensive and accumulates large amounts of energy [26]. With the increasing scale of a project, the increase in participants and stakeholder groups, and the expanded interaction between the project and the environment, it increasingly presents richer and more profound complex system characteristics and connotations [17]. The construction of a high-speed railway station has the characteristics of a typical complex social technology system: nonlinearity, emergence, feedback loops, and so forth [27]. From a system perspective, safety and actual accidents are emerging attributes of nonlinear interactions between different components of complex sociotechnical systems. Leveson established a system theory accident model (STAMP) based on the belief that an accident is an emergent phenomenon caused by the interaction of various elements in a complex system [28]. The lack of control behaviour that imposes constraints on these interactions will lead to accidents [29]. Security is a control problem that can be managed through the control structure embedded in the social technology system [29].

To determine how to control a complex system, we must first study the relationship of the factors. Existing methods for complex system factor analysis include ISM [30], DEMATEL [31], SEM [32], ANP [33], and complex network [34]. In this study, we combine DEMATEL and ISM to establish the relationship among factors affecting the construction safety of high-speed railway stations and establish a multilevel hierarchical structural model. Then, the importance of the influencing factors and their hierarchical relationship is determined, and the influence of these factors on high-speed railway station accidents is determined. Finally, some countermeasures are proposed. This study provides a theoretical basis and method for preventing accidents in the construction of high-speed railway stations.

2. Methodology

2.1. Extraction of Influencing Factors of Construction Safety. Various factors affecting the safety of complex systems interact. The influencing factors of high-speed railway station construction systems have an extraordinarily complex relationship and interactions, showing strong nonlinearity and reverse feeding. From 2012 to 2018, the types of accidents that frequently occurred in China's construction industry were falling from a height, structural collapse, lifting injuries, object attack, vehicle injuries, mechanical injuries, electric shock, poisoning and suffocation, fire and explosion, and

other injuries. These accidents were the result of the interaction of multiple factors, including humans, machines, the environment, and management, rather than each case having a single cause.

Hamid believed that the cause of an accident is a multifactor phenomenon mainly involving worker negligence and bad attitudes towards safety, lack of safety devices, unskilled workers, etc. [35]. Haslam et al. investigated accidents in the UK and found that they were caused by workers, the working environment, equipment defects, and inadequate risk management [36]. When implementing safety control of complex systems based on control theory, the following are usually considered: human factors, organizational factors, management factors, and physical systems [37]. Du et al. studied an underground transportation system and concluded that it is a complex and enormous system with many factors affecting safety. The causes of accidents were defects in humans, machines, and the environment [38].

Through the analysis and summary of the relevant literature [35–42], in this research, we summarize four aspects of construction safety risk factors: human, mechanical, environmental, and management. In total, 17 risk factors are identified. The human aspect includes cognitive deficits, poor physical or mental health, and illegal operations. The mechanical aspect includes unreasonable equipment selection and layout, lack of equipment maintenance and overhaul, mechanical equipment failure, failure of construction monitoring equipment, and numerous large-scale equipment cross-operations. The management aspect includes imperfect safety management systems, inadequate safety disclosure, inadequate acceptance of key procedures, inadequate supervision of safety behaviours, inadequate safety protection measures, and errors in construction safety operational guidelines. The environmental aspect includes unforeseeable natural factors, complex hydrogeological environments, and complex construction site environments. The definitions are shown in Table 1.

2.2. Risk Coupling Model Based on SD Model Causality Diagram. In the construction safety risk of high-speed railway station, personnel factors, mechanical factors, environmental factors, and management factors interact and influence each other. The direct objects of management are human, machine, and environment; people have subjective initiative which will have an impact on things, environment, and management; mechanical equipment is affected by the environment, and the state of the equipment depends on personnel operation and reasonable and effective management; the environment has direct or indirect influence on people, things, and management. The interaction and mutual influence of human, material, environment, and management factors finally form human-material-environment-pipe coupling risk.

System Dynamics (SD) is the subject of information feedback systems. It is a combination of system theory, control theory, and information theory and provides a way to understand and solve system problems [43]. The SD

TABLE 1: Construction safety risk factors and their interpretation.

Factor	Interpretation
Cognitive deficits R1	Managers and workers cannot recognize the possibility of safety accidents. Safety awareness is a prerequisite for operational safety.
Poor physical or mental health R2	Personality traits such as impulsiveness, emotional response, and carelessness. Physiological conditions such as illness and fatigue.
Illegal operations R3	During the construction process, the construction is not carried out according to the construction safety operation guidelines.
Unreasonable equipment selection and layout R4	The equipment model does not meet the needs of the project, the site layout is not conducive to the construction, and there are potential safety hazards.
Lack of equipment maintenance and overhaul R5	The equipment lacks daily maintenance and professional overhaul assessment.
Mechanical failure R6	During the construction process, for various reasons, equipment malfunctions, stops operating, and even causes chain accidents.
Numerous large-scale equipment cross-operations R7	The operations of large-scale mechanical equipment such as tower cranes and construction vehicles are complex.
Failure of construction monitoring equipment R8	Construction monitoring such as foundation pit monitoring, mass concrete pouring temperature monitoring, steel structure stress monitoring, and equipment monitoring fails or is performed incorrectly.
Unforeseeable natural factors R9	Earthquakes, typhoons, floods, and so forth occur.
Complex hydrogeological environment R10	The natural conditions of construction and harsh geological conditions may cause foundational engineering accidents.
Complex construction site environments R11	The combination of ventilation, lighting, temperature, humidity, noise, dust, and harmful gases affects the physical and psychological conditions of construction workers.
Imperfect safety management systems R12	Relevant safety regulations are lacking or unreasonable.
Incomplete safety disclosure R13	The construction leader does not train the direct production workers on safety operational rules and precautions before beginning the production operation.
Inadequate acceptance of key processes R14	As a necessary condition for the acceptance of a branch project, key process acceptance is an effective quality control measure that highlights the key points of supervision.
Inadequate supervision of safety behaviours R15	Leaders and management personnel at all levels do not sufficiently inspect and supervise the workplace to correct improper behaviour and ensure the safety of production.
Inadequate safety protection measures R16	The arrangement of devices to prevent operators from generating risks in the production process is not in place.
Errors in construction safety operational guidelines R17	Operational sequences and operational instructions are not specified in the method and safety regulations for technical operations.

cause-and-effect diagram theory is used to discuss and study the risk coupling relationship among various risk factors in the construction safety system of high-speed railway station. As shown in Figure 1, taking the starting point of management factors as an example, inadequate supervision of safety behaviours of management factor indirectly leads to unreasonable equipment selection and layout of mechanical factors, unreasonable equipment selection and layout indirectly lead to complex construction site environments of environmental factors, and complex construction site environments lead to poor physical or mental health of human factors. Taking the starting point of human factors as an example, illegal operations of human factors lead to mechanical failure of mechanical factors, mechanical failure leads to complex construction site environments of environmental factors, and complex construction site environments lead to inadequate supervision of safety behaviours of management factors.

2.3. Principles for the DEMATEL and ISM Method. DEMATEL, a method proposed by Bottel in 1971, uses matrix operations to calculate the direct or indirect causality and degree of influence of the elements. By using the causal

diagram to determine the basic nature of the complex problem, the core problem is determined and solutions are suggested. DEMATEL can be used to divide factors into causal and influencing factors. In addition, by ranking or prioritizing causal factors, core problems can be solved quickly and effectively to improve performance [44]. ISM is a method developed by John N. Warfield in the United States in 1973 to analyse systems with numerous factors and complex and unclear structures based on graph theory and Boolean function. Multivariable, complex, and unstructured systems are transformed into multilevel explanatory structural models to show the influence paths and hierarchical structure of complex factors. ISM has the advantages of system operation, effectiveness, low data dependence, and clear handling of problems [45]. The DEMATEL-ISM hybrid has two advantages. First, the DEMATEL model can simplify the calculation process of the ISM model and provide convenience for the system. By directly adding thresholds λ to DEMATEL's overall influence matrix, the reachable matrix required by ISM model is obtained. The process of ISM's adjacency matrix to reachable matrix is omitted. Second, the DEMATEL causality and centrality analysis can further use the unique advantages of the ISM model to clarify the structural hierarchical relationship.

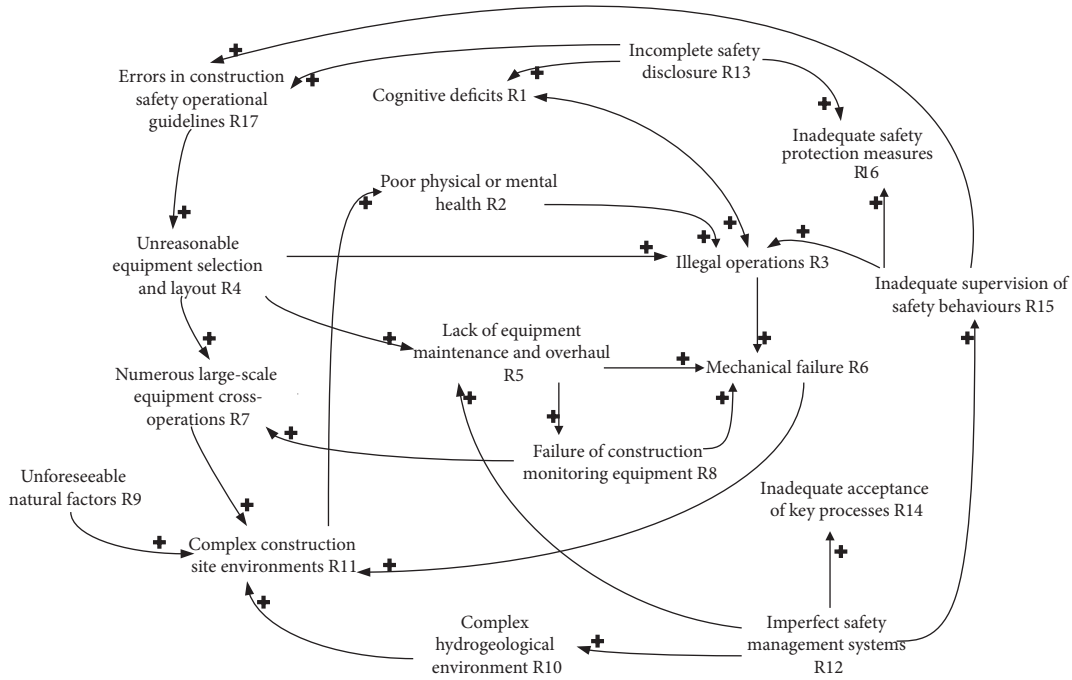


FIGURE 1: SD model causality diagram.

2.4. *Modeling Process.* The process of using DEMATEL-ISM model as shown in Figure 2 and the basic steps are as follows:

- (1) Determine the construction safety risk factors r_1, r_2, \dots, r_n , $r_i \in R (i = 1, 2, \dots, n)$, where n is the number of construction safety risk factors and R is the total set of construction safety risk factors.
- (2) Generate the direct impact matrix of construction safety risk factors. According to the experience of experts and construction site personnel $k (k = 1, 2, \dots, m)$, process the arithmetic mean value to eliminate the subjective error of experts as much as possible; then, obtain the direct impact matrix $X (X = [x_{ij}]_{n \times n})$ between factors as follows:

$$X = \frac{1}{M} \sum_{k=1}^m X^k. \quad (1)$$

- (3) Obtain a new normalized impact matrix from the direct impact matrix $G (G = [g_{ij}]_{n \times n})$:

$$G = [g_{ij}]_{n \times n} = \frac{1}{\max_{1 \leq i \leq n} \sum_{j=1}^n r_{ij}} X, \quad (2)$$

where $\max_{1 \leq i \leq n} \sum_{j=1}^n r_{ij}$ is the maximum value obtained by adding each row. After normalized treatment, obtain $0 \leq g_{ij} \leq 1$.

- (4) Calculate the comprehensive impact matrix $T (T = [t_{ij}]_{n \times n})$:

$$T = G^1 + G^2 + \dots + G^n = \sum_{i=1}^n G^i. \quad (3)$$

Since $0 \leq g_{ij} \leq 1$, when $n \rightarrow \infty$, $G^{n-1} \rightarrow 0$, the following formula can be used for approximate calculation:

$$T = G(I - G)^{-1}. \quad (4)$$

- (5) Calculate the influencing degree f_i and the influenced degree e_i . The influencing degree f_i is obtained by adding the row elements of the matrix T , and the influenced e_i degree is obtained by adding the column elements of matrix T . The calculation formulas for the influencing degree f_i and the influenced degree e_i are as follows:

$$f_i = \sum_{j=1}^n t_{ij}, \quad i = 1, \dots, n, \quad (5)$$

$$e_i = \sum_{j=1}^n t_{ji}, \quad i = 1, \dots, n.$$

The greater the centrality, the more important the factor.

- (6) Calculate centrality and causality. Centrality m_i is obtained by adding the influencing degree and the influenced degree of the system, and the causality n_i is obtained by subtracting the influencing degree and the influenced degree of the system. The formulas for calculating centrality m_i and causation n_i are as follows:

$$m_i = f_i + e_i, \quad i = 1, \dots, n, \quad (6)$$

$$n_i = f_i - e_i, \quad i = 1, \dots, n.$$

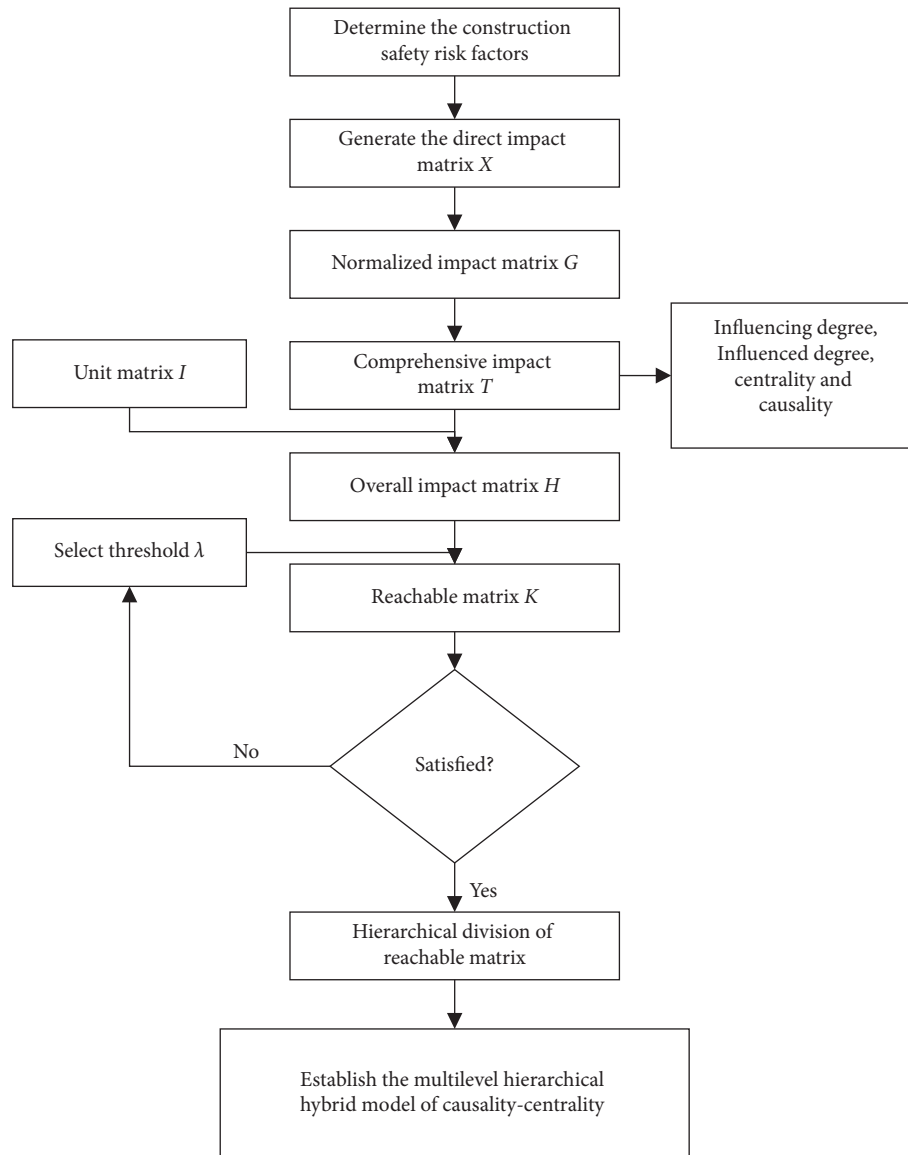


FIGURE 2: Basic flow of DEMATEL-ISM model.

(7) Establish the causality-centrality diagram of the influence factor, the causality is the ordinate, centrality is the abscissa, and the diagram is drawn on the Cartesian coordinate system.

(8) Calculate the overall impact matrix H ($H = [h_{ij}]_{n \times n}$):

$$H = I + T, \tag{7}$$

where I is the identity matrix.

(9) Calculate the reachable matrix, K ($K = [K_{ij}]_{n \times n}$). Given a threshold λ , calculate the reachable matrix K ($K = [K_{ij}]_{n \times n}$):

$$\begin{aligned} k_{ij} &= 1, & \text{if } h_{ij} \geq \lambda, & \quad i, j, 2, \dots, n, \\ k_{ij} &= 0, & \text{if } h_{ij} < \lambda, & \quad i, j, 2, \dots, n. \end{aligned} \tag{8}$$

The key to establishing the reachable matrix is to determine the threshold λ . If the degree of influence of one factor on another factor exceeds λ , the factor will directly affect the other factor. If the reverse is true, then this factor does not affect the other factor. Since the purpose of the value of λ is to highlight the main causes of accidents in the complex system and at the same time not to oversimplify the relationship among the factors, the value is selected multiple times and optimized on the basis of expert suggestions and actual needs.

(10) Determine the reachable set A_i and the antecedent set B_i of each factor.

(11) Verify that the following formula holds. If so, the corresponding factor is the bottom factor and the i row and i column are crossed out in matrix K .

$$A_i = A_i \cap B_i, \quad i = 1, \dots, n. \quad (9)$$

- (12) Repeat steps 10 and 11 until all factors are crossed out.
- (13) According to the order in which the factors are crossed out, combined with the causality and centrality, the multilevel hierarchical hybrid model of causality-centrality is established.

3. Case Study and Result Analysis

3.1. Study Subject and Data Collection. This study takes the Fuyang station of Hanghuang high-speed railway as the subject. Fuyang station is located in Fuyang District, Hangzhou City, Zhejiang Province. The station house has three floors, one underground and two above ground. The underground is reinforced concrete frame structure, and the above-ground part is steel structure. The location of Fuyang station is shown in Figure 3.

The excavation depth of the foundation pit is 6.8~14.4 meters, which is the first level foundation pit. Fuyang District has abundant rainfall and high groundwater level. According to the above-determined construction safety risk factor set, we adopt the method of expert consultation to study the relevant influence relations of the 17 factors that affect construction safety. Twenty-four questionnaires were distributed to professors and associate professors of the



FIGURE 3: The location of Fuyang station (from Google Maps).

School of Civil Engineering and Architecture of Ningbo Institute of Technology, Zhejiang University, and safety managers of China Railway Fourth Bureau, and twenty-two questionnaires were recovered (the recovery rate was 92%). The influence of a factor is represented by a five-point scale, where 0 means no influence, 1 means weak influence, 2 means general influence, 3 means strong influence, and 4 means extremely strong influence.

Arithmetic mean processing of the data in the questionnaire is carried out to eliminate expert error as much as possible, and the direct impact matrix $X = [x_{ij}]_{17 \times 17}$ is formed:

$$X = \begin{bmatrix} 0 & 1.17 & 3.42 & 2.67 & 2.42 & 1.5 & 1.75 & 1.5 & 0.42 & 0.5 & 1 & 2.5 & 2.5 & 2.67 & 2.75 & 3.25 & 3.08 \\ 1.75 & 0 & 2.33 & 1.17 & 1.42 & 0.75 & 0.92 & 0.92 & 0.17 & 0 & 0.5 & 0.75 & 1 & 1.25 & 1.33 & 1.33 & 1.83 \\ 0.58 & 0.75 & 0 & 1.75 & 1.58 & 2.42 & 1.75 & 2.5 & 0.08 & 0.71 & 0.92 & 0.75 & 1.67 & 2 & 2 & 2.17 & 2.58 \\ 0.17 & 0.33 & 1.02 & 0 & 1.67 & 2.25 & 2.58 & 2.08 & 0 & 0 & 1 & 0.75 & 1.75 & 1.75 & 1.67 & 1.83 & 2.08 \\ 0.33 & 0.17 & 1.25 & 1.08 & 0 & 3 & 1.67 & 2.42 & 0 & 0 & 0.25 & 0.58 & 1.17 & 1.25 & 1.25 & 1.42 & 1.75 \\ 0.08 & 0.42 & 1.17 & 1 & 1.67 & 0 & 1.17 & 2 & 0 & 0 & 0.42 & 0.42 & 1.17 & 1.25 & 1.67 & 1.92 & 1.83 \\ 0.58 & 0.33 & 2 & 1.83 & 1.75 & 2.5 & 0 & 2.08 & 0 & 0 & 1.92 & 1.08 & 1.42 & 1.58 & 1.67 & 1.42 & 1.75 \\ 0.17 & 0.58 & 1.58 & 1 & 2 & 2.08 & 1.75 & 0 & 0.33 & 0.33 & 0.75 & 1.17 & 1.75 & 1.92 & 2 & 2.33 & 2 \\ 0.33 & 1.17 & 1.42 & 0.92 & 0.92 & 1.92 & 0.67 & 1.75 & 0 & 2.25 & 2.17 & 0.83 & 0.83 & 1.17 & 1.17 & 1.5 & 1.5 \\ 0.5 & 0.75 & 1.08 & 1.5 & 1 & 1.5 & 1.25 & 1.58 & 1.42 & 0 & 2.5 & 1.42 & 0.92 & 1.08 & 1.17 & 1.25 & 1.25 \\ 1.42 & 1.33 & 2.58 & 2.42 & 0.83 & 1.67 & 2.17 & 1.92 & 0.42 & 0.08 & 0 & 1.67 & 1.08 & 1.75 & 1.58 & 1.92 & 1.75 \\ 1.5 & 0.83 & 2.5 & 1.75 & 1.83 & 1.92 & 1.58 & 1.83 & 0.17 & 0 & 0.67 & 0 & 2.25 & 2.42 & 2.67 & 2.58 & 2.67 \\ 0.92 & 0.67 & 2.25 & 1.75 & 1.42 & 1.5 & 1.25 & 1.5 & 0.33 & 0.25 & 0.58 & 0.92 & 0 & 2.42 & 2.17 & 2.42 & 2.5 \\ 0.67 & 0.83 & 1.5 & 1.92 & 1 & 1.08 & 1.08 & 0.92 & 0 & 0 & 0.17 & 0.5 & 1.17 & 0 & 1.5 & 1.33 & 1.75 \\ 1.33 & 0.67 & 2.92 & 1.75 & 1.58 & 1.58 & 1.42 & 1.83 & 0 & 0 & 0.25 & 1.42 & 2 & 2.25 & 0 & 2.33 & 2.42 \\ 0.83 & 1.17 & 2.42 & 1.17 & 0.83 & 1.08 & 0.42 & 0.92 & 0 & 0 & 0.25 & 0.58 & 0.75 & 1 & 1.17 & 0 & 2 \\ 0.67 & 0.92 & 1.92 & 0.75 & 0.75 & 1.42 & 0.42 & 1 & 0.25 & 0.17 & 0.33 & 0.67 & 1 & 1.17 & 1.33 & 1 & 0 \end{bmatrix}. \quad (10)$$

3.2. Calculation of the Integrated DEMATEL/ISM Method

3.2.1. DEMATEL Analysis. According to step 3, normalize the direct influence matrix to obtain the normalized influence matrix $G = [g_{ij}]_{17 \times 17}$:

$$G = \begin{bmatrix} 0 & 0.03 & 0.09 & 0.07 & 0.07 & 0.04 & 0.05 & 0.04 & 0.01 & 0.01 & 0.03 & 0.07 & 0.07 & 0.07 & 0.08 & 0.09 & 0.09 \\ 0.05 & 0 & 0.06 & 0.03 & 0.04 & 0.02 & 0.03 & 0.03 & 0 & 0 & 0.01 & 0.02 & 0.03 & 0.03 & 0.04 & 0.04 & 0.05 \\ 0.02 & 0.02 & 0 & 0.05 & 0.04 & 0.07 & 0.05 & 0.07 & 0 & 0 & 0.03 & 0.02 & 0.05 & 0.06 & 0.06 & 0.06 & 0.07 \\ 0 & 0.01 & 0.05 & 0 & 0.05 & 0.06 & 0.07 & 0.06 & 0 & 0 & 0.03 & 0.02 & 0.05 & 0.05 & 0.05 & 0.05 & 0.06 \\ 0.01 & 0.01 & 0.03 & 0.03 & 0 & 0.08 & 0.05 & 0.07 & 0 & 0 & 0.01 & 0.02 & 0.03 & 0.03 & 0.03 & 0.04 & 0.05 \\ 0 & 0.01 & 0.03 & 0.03 & 0.05 & 0 & 0.03 & 0.06 & 0 & 0 & 0.01 & 0.01 & 0.03 & 0.03 & 0.05 & 0.05 & 0.05 \\ 0.02 & 0.01 & 0.06 & 0.05 & 0.05 & 0.07 & 0 & 0.06 & 0 & 0 & 0.05 & 0.03 & 0.04 & 0.04 & 0.05 & 0.04 & 0.05 \\ 0 & 0.02 & 0.04 & 0.03 & 0.06 & 0.06 & 0.05 & 0 & 0.01 & 0.01 & 0.02 & 0.03 & 0.05 & 0.05 & 0.06 & 0.06 & 0.06 \\ 0.01 & 0.03 & 0.04 & 0.03 & 0.03 & 0.05 & 0.02 & 0.05 & 0 & 0.03 & 0.06 & 0.02 & 0.02 & 0.03 & 0.03 & 0.04 & 0.04 \\ 0.01 & 0.02 & 0.03 & 0.04 & 0.03 & 0.04 & 0.03 & 0.04 & 0.04 & 0 & 0.07 & 0.04 & 0.03 & 0.03 & 0.03 & 0.03 & 0.03 \\ 0.04 & 0.04 & 0.07 & 0.07 & 0.02 & 0.05 & 0.06 & 0.05 & 0.01 & 0 & 0 & 0.05 & 0.03 & 0.05 & 0.04 & 0.05 & 0.05 \\ 0.04 & 0.02 & 0.07 & 0.05 & 0.05 & 0.05 & 0.04 & 0.05 & 0 & 0 & 0.02 & 0 & 0.06 & 0.07 & 0.07 & 0.07 & 0.07 \\ 0.03 & 0.02 & 0.06 & 0.05 & 0.04 & 0.04 & 0.03 & 0.04 & 0.01 & 0.01 & 0.02 & 0.03 & 0 & 0.07 & 0.06 & 0.07 & 0.07 \\ 0.02 & 0.02 & 0.04 & 0.03 & 0.03 & 0.03 & 0.03 & 0.03 & 0 & 0 & 0 & 0.01 & 0.03 & 0 & 0.04 & 0.04 & 0.05 \\ 0.04 & 0.02 & 0.08 & 0.05 & 0.04 & 0.04 & 0.04 & 0.05 & 0 & 0 & 0.01 & 0.04 & 0.06 & 0.06 & 0 & 0.06 & 0.07 \\ 0.02 & 0.03 & 0.07 & 0.03 & 0.02 & 0.03 & 0.01 & 0.03 & 0 & 0 & 0.01 & 0.02 & 0.02 & 0.03 & 0.03 & 0 & 0.06 \\ 0.02 & 0.03 & 0.05 & 0.02 & 0.02 & 0.04 & 0.01 & 0.03 & 0.01 & 0 & 0.01 & 0.02 & 0.03 & 0.03 & 0.04 & 0.03 & 0 \end{bmatrix} \quad (11)$$

According to step 4, calculate the comprehensive influence matrix $T = [t_{ij}]_{17 \times 17}$:

$$T = \begin{bmatrix} 0.05 & 0.08 & 0.22 & 0.16 & 0.16 & 0.15 & 0.13 & 0.15 & 0.02 & 0.02 & 0.07 & 0.13 & 0.16 & 0.18 & 0.19 & 0.21 & 0.22 \\ 0.07 & 0.02 & 0.13 & 0.08 & 0.09 & 0.08 & 0.07 & 0.8 & 0.01 & 0 & 0.03 & 0.05 & 0.08 & 0.09 & 0.09 & 0.1 & 0.12 \\ 0.05 & 0.05 & 0.08 & 0.1 & 0.1 & 0.14 & 0.1 & 0.14 & 0.01 & 0.01 & 0.05 & 0.06 & 0.11 & 0.13 & 0.13 & 0.14 & 0.16 \\ 0.03 & 0.04 & 0.13 & 0.05 & 0.1 & 0.13 & 0.12 & 0.12 & 0 & 0 & 0.05 & 0.06 & 0.11 & 0.12 & 0.11 & 0.12 & 0.14 \\ 0.03 & 0.03 & 0.09 & 0.07 & 0.05 & 0.13 & 0.09 & 0.12 & 0 & 0 & 0.03 & 0.05 & 0.08 & 0.09 & 0.09 & 0.1 & 0.11 \\ 0.02 & 0.03 & 0.09 & 0.07 & 0.09 & 0.05 & 0.07 & 0.1 & 0 & 0 & 0.03 & 0.04 & 0.08 & 0.09 & 0.1 & 0.11 & 0.11 \\ 0.05 & 0.04 & 0.13 & 0.11 & 0.11 & 0.14 & 0.06 & 0.12 & 0.01 & 0 & 0.08 & 0.07 & 0.10 & 0.11 & 0.12 & 0.14 & 0.13 \\ 0.03 & 0.04 & 0.12 & 0.08 & 0.11 & 0.13 & 0.1 & 0.07 & 0.01 & 0.01 & 0.05 & 0.07 & 0.11 & 0.12 & 0.12 & 0.14 & 0.14 \\ 0.04 & 0.06 & 0.11 & 0.08 & 0.08 & 0.12 & 0.07 & 0.11 & 0.01 & 0.07 & 0.09 & 0.06 & 0.08 & 0.09 & 0.1 & 0.11 & 0.12 \\ 0.04 & 0.05 & 0.1 & 0.09 & 0.08 & 0.11 & 0.09 & 0.11 & 0.04 & 0.01 & 0.09 & 0.08 & 0.08 & 0.09 & 0.1 & 0.11 & 0.11 \\ 0.07 & 0.07 & 0.16 & 0.13 & 0.09 & 0.13 & 0.12 & 0.13 & 0.02 & 0.01 & 0.03 & 0.09 & 0.1 & 0.13 & 0.13 & 0.14 & 0.15 \\ 0.08 & 0.06 & 0.17 & 0.12 & 0.12 & 0.14 & 0.11 & 0.13 & 0.01 & 0.01 & 0.05 & 0.05 & 0.14 & 0.16 & 0.16 & 0.17 & 0.18 \\ 0.06 & 0.05 & 0.14 & 0.1 & 0.1 & 0.11 & 0.09 & 0.11 & 0.01 & 0.01 & 0.04 & 0.07 & 0.06 & 0.14 & 0.13 & 0.14 & 0.15 \\ 0.04 & 0.04 & 0.1 & 0.06 & 0.07 & 0.08 & 0.07 & 0.07 & 0 & 0 & 0.02 & 0.04 & 0.07 & 0.05 & 0.09 & 0.09 & 0.11 \\ 0.07 & 0.05 & 0.17 & 0.11 & 0.11 & 0.12 & 0.1 & 0.12 & 0.01 & 0.01 & 0.04 & 0.08 & 0.12 & 0.14 & 0.08 & 0.15 & 0.16 \\ 0.04 & 0.05 & 0.12 & 0.07 & 0.06 & 0.08 & 0.05 & 0.07 & 0 & 0 & 0.02 & 0.04 & 0.06 & 0.08 & 0.08 & 0.05 & 0.11 \\ 0.04 & 0.04 & 0.1 & 0.06 & 0.06 & 0.08 & 0.05 & 0.07 & 0.01 & 0.01 & 0.03 & 0.04 & 0.07 & 0.08 & 0.08 & 0.08 & 0.05 \end{bmatrix} \quad (12)$$

Calculate the influencing degree, influenced degree, centrality, and causality, as shown in Table 2.

As shown in Table 2, influencing factors can be divided into reason factors and result factors according to the centrality (centrality greater than 0 is reason factors, while centrality less than 0 is result factors). Centrality determines the importance of the factor in the system. To visualise the degree of influence of factors, establish the quartile of the influence factor, and use the centrality and causality of the factor as Cartesian coordinates, as shown in Figure 4. The detailed analysis is in Section 3.3.

3.2.2. *ISM Analysis.* According to step 9, select multiple thresholds λ for comparative analysis, as listed in Table 3.

Finally, determine the selected threshold, $\lambda = 0.11$, and convert the specification influence matrix G into the reachable matrix $K = [k_{ij}]_{17 \times 17}$ by MATLAB programming.

$$K = \begin{bmatrix} 1 & 0 & 1 & 1 & 1 & 1 & 1 & 1 & 0 & 0 & 0 & 1 & 1 & 1 & 1 & 1 & 1 \\ 0 & 1 & 1 & 0 & 0 & 1 & 0 & 1 & 0 & 0 & 0 & 0 & 1 & 1 & 1 & 1 & 1 \\ 0 & 0 & 1 & 0 & 0 & 1 & 0 & 1 & 0 & 0 & 0 & 0 & 1 & 1 & 1 & 1 & 1 \\ 0 & 0 & 1 & 1 & 0 & 1 & 1 & 1 & 0 & 0 & 0 & 0 & 1 & 1 & 1 & 1 & 1 \\ 0 & 0 & 1 & 0 & 1 & 1 & 0 & 1 & 0 & 0 & 0 & 0 & 1 & 1 & 1 & 1 & 1 \\ 0 & 0 & 0 & 0 & 0 & 1 & 0 & 0 & 0 & 0 & 0 & 0 & 0 & 0 & 0 & 0 & 1 \\ 0 & 0 & 1 & 0 & 0 & 1 & 1 & 1 & 0 & 0 & 0 & 0 & 1 & 1 & 1 & 1 & 1 \\ 0 & 0 & 1 & 0 & 0 & 1 & 0 & 1 & 0 & 0 & 0 & 0 & 1 & 1 & 1 & 1 & 1 \\ 0 & 0 & 1 & 0 & 0 & 1 & 0 & 1 & 1 & 0 & 0 & 0 & 1 & 1 & 1 & 1 & 1 \\ 0 & 0 & 0 & 0 & 0 & 0 & 0 & 0 & 0 & 1 & 0 & 0 & 0 & 0 & 0 & 0 & 1 \\ 0 & 0 & 1 & 1 & 0 & 1 & 1 & 1 & 0 & 0 & 1 & 0 & 1 & 1 & 1 & 1 & 1 \\ 0 & 0 & 1 & 1 & 1 & 1 & 1 & 1 & 1 & 0 & 0 & 0 & 1 & 1 & 1 & 1 & 1 \\ 0 & 0 & 1 & 0 & 0 & 1 & 0 & 1 & 0 & 0 & 0 & 0 & 1 & 1 & 1 & 1 & 1 \\ 0 & 0 & 0 & 0 & 0 & 0 & 0 & 0 & 0 & 0 & 0 & 0 & 0 & 1 & 0 & 0 & 0 \\ 0 & 0 & 1 & 0 & 0 & 1 & 0 & 1 & 0 & 0 & 0 & 0 & 1 & 1 & 1 & 1 & 1 \\ 0 & 0 & 1 & 0 & 0 & 1 & 0 & 1 & 0 & 0 & 0 & 0 & 1 & 1 & 1 & 1 & 1 \\ 0 & 0 & 0 & 0 & 0 & 0 & 0 & 0 & 0 & 0 & 0 & 0 & 0 & 0 & 0 & 0 & 1 \end{bmatrix} \quad (13)$$

According to steps 9–11, process the reachable matrix, and, finally, obtain the factor set Cq ($q = 1, 2, \dots, n$) of each layer. Finally, establish the multilevel hierarchical hybrid model, as shown in Figure 5.

3.3. *Construction Safety Risk Factors and Related Influence Mechanisms.* According to the DEMATEL analysis, the factors can be divided into cause factors and result factors. In the actual construction process, more attention should be paid to the causes, and effective control should be carried out to improve the safety of the construction site. As Table 2 shows, the influencing degree of these factors varies greatly, ranging from 0.98 to 2.435.

The eight factors with high impact include cognitive defects R1, imperfect safety management systems R12, complex construction site environments R11, inadequate supervision of safety behaviours R15, illegal operations R3, inadequate safety disclosure R13, numerous large-scale equipment cross-operations R7, and failure of construction monitoring equipment R8. Therefore, management factors and human factors can be classified as factors that potentially affect construction safety by influencing other factors. The influenced degree indicates the comprehensive influence of other factors on the factor R_i . At the level of impact, errors in construction safety operational guidelines R17, illegal operations R3, inadequate safety protection measures R16, mechanical failure R6, inadequate supervision of safety behaviours R15, inadequate acceptance of key processes R14, failure of construction monitoring equipment R8, and inadequate safety disclosure R13 are the leaders, which shows that the security level can be improved by increasing influencers. Inadequate supervision of safety behaviours R15, inadequate safety disclosure R13, and failure of construction monitoring equipment R8 are all important influencing factors and affected factors; improving these factors will help improve the circulatory effects in the system.

Centrality reflects the importance of factors in the system. As shown in Table 2, illegal operations R3 is the most important, followed by inadequate supervision of safety behaviours R15, failure of construction monitoring equipment R8, errors in construction safety operational guidelines R17, inadequate safety disclosure R13, cognitive defects R1, inadequate safety protective measures R16, mechanical equipment failure R6, imperfect safety management systems R12, unreasonable equipment selection and layout R4, multiple cross-operations of large equipment R7, inadequate acceptance of key processes R14, lack of maintenance and repair of equipment R5, construction site complex environment R11, poor physical or mental health status R2, complex hydrogeological environments R10, and unforeseen natural factors R9. Among all the factors, illegal operations R3, inadequate supervision of safety behaviours R15, failure of construction monitoring equipment R8, errors in construction safety operational guidelines R17, inadequate safety disclosure R13, cognitive defects R1, inadequate safety protection measures R16, mechanical failure R6, and imperfect safety management systems R12 are especially important. However, complex construction site environment R11, poor physical or mental health R2, complex hydrogeological environments R10, and unforeseen natural factors R9 also play important roles that cannot be ignored. Safety issues must be analysed from a systematic perspective. In the human-machine-environmental-management system, management factors closely related to people are the most important factors affecting construction safety.

In the multilevel hierarchical hybrid model, cognitive defects R1, imperfect safety management systems R12, and complex construction site environments R11 are deep factors, and unforeseeable natural factors R9, numerous large-scale equipment cross-operations R7, lack of maintenance

TABLE 2: DEMATEL parameter table.

Factor	Influencing degree	Influenced degree	Centrality	Causality	Centrality ranking	Factor attribute
R1	2.435	0.868	3.303	1.567	6	Reason factor
R2	1.267	0.855	2.122	0.412	15	Reason factor
R3	1.613	2.317	3.929	-0.704	1	Result factor
R4	1.512	1.629	3.141	-0.117	10	Result factor
R5	1.194	1.669	2.862	-0.475	14	Result factor
R6	1.140	2.043	3.183	-0.902	8	Result factor
R7	1.546	1.580	3.126	-0.034	11	Result factor
R8	1.516	1.926	3.442	-0.410	3	Result factor
R9	1.421	0.191	1.612	1.230	17	Reason factor
R10	1.440	0.186	1.626	1.253	16	Reason factor
R11	1.798	0.832	2.630	0.966	14	Reason factor
R12	1.977	1.170	3.147	0.807	9	Reason factor
R13	1.600	1.729	3.330	-0.129	5	Result factor
R14	1.061	2.029	3.090	-0.968	12	Result factor
R15	1.691	2.032	3.723	-0.341	2	Result factor
R16	1.047	2.218	3.265	-1.171	7	Result factor
R17	0.980	2.419	3.399	-1.438	4	Result factor

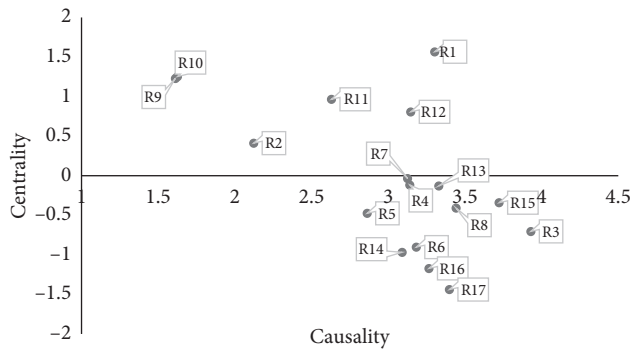


FIGURE 4: Causal diagram of influencing factors of construction safety risk.

TABLE 3: Comparison of different threshold λ .

Factor	0.09	0.1	0.11	0.15
R1	13	13	13	10
R2	5	3	2	0
R3	27	24	18	5
R4	18	17	11	1
R5	15	11	5	1
R6	18	16	13	1
R7	19	14	11	0
R8	22	21	15	0
R9	7	5	3	0
R10	9	5	1	0
R11	14	10	9	1
R12	15	13	13	5
R13	19	16	10	2
R14	15	11	10	3
R15	23	18	16	5
R16	17	16	12	3
R17	18	18	16	6

and overhaul of equipment R5, inadequate supervision of safety behaviours R15, unreasonable equipment selection and layout R4, and poor physical or mental health R2 are

middle factors. Mechanical failure R6, errors in construction safety operational guidelines R17, complex hydrogeological environments R10, inadequate acceptance of key processes R14, failure of construction monitoring equipment R8, inadequate safety disclosure R13, inadequate safety protection measures R16, and illegal operations R3 are surface factors.

Human-related factors, such as cognitive deficits R1, are deep factors; illegal operations R3 ranks second in centrality; and poor physical or mental health R2 belongs to the middle factors. These findings show that human-related factors play a pivotal role in construction safety risks and must be taken seriously. Factors related to management, such as imperfect safety management systems R12, are surface factors, and poor supervision of safety behaviours R15, inadequate safety disclosure R13, and inadequate safety protection measures R16 are ranked 2nd, 5th, and 7th in centrality, respectively. The system has an important impact.

According to Figure 5, the key factors are cognitive defects R1, illegal operations R3, failure of construction monitoring equipment R8, imperfect safety management systems R12, inadequate safety disclosures R13, and inadequate supervision of safety behaviours R15. However, in the multilevel hierarchical hybrid model, key factors exist in the three-layer structure, which indicates that, in security risk control, we must not only pay attention to the proximal causes but also comprehensively consider the overall perspective. In addition, except for the failure of construction monitoring equipment, all the factors are related to the human or management aspects.

As the above analysis shows, the human and management aspects need to focus on control. In addition, the following corresponding measures are proposed:

- (1) Strengthen safety education. Personnel training and education can be provided through multimedia resources such as Virtual Reality (VR) equipment and on-site teaching simultaneously. On-site self-help and self-protection training should be conducted.

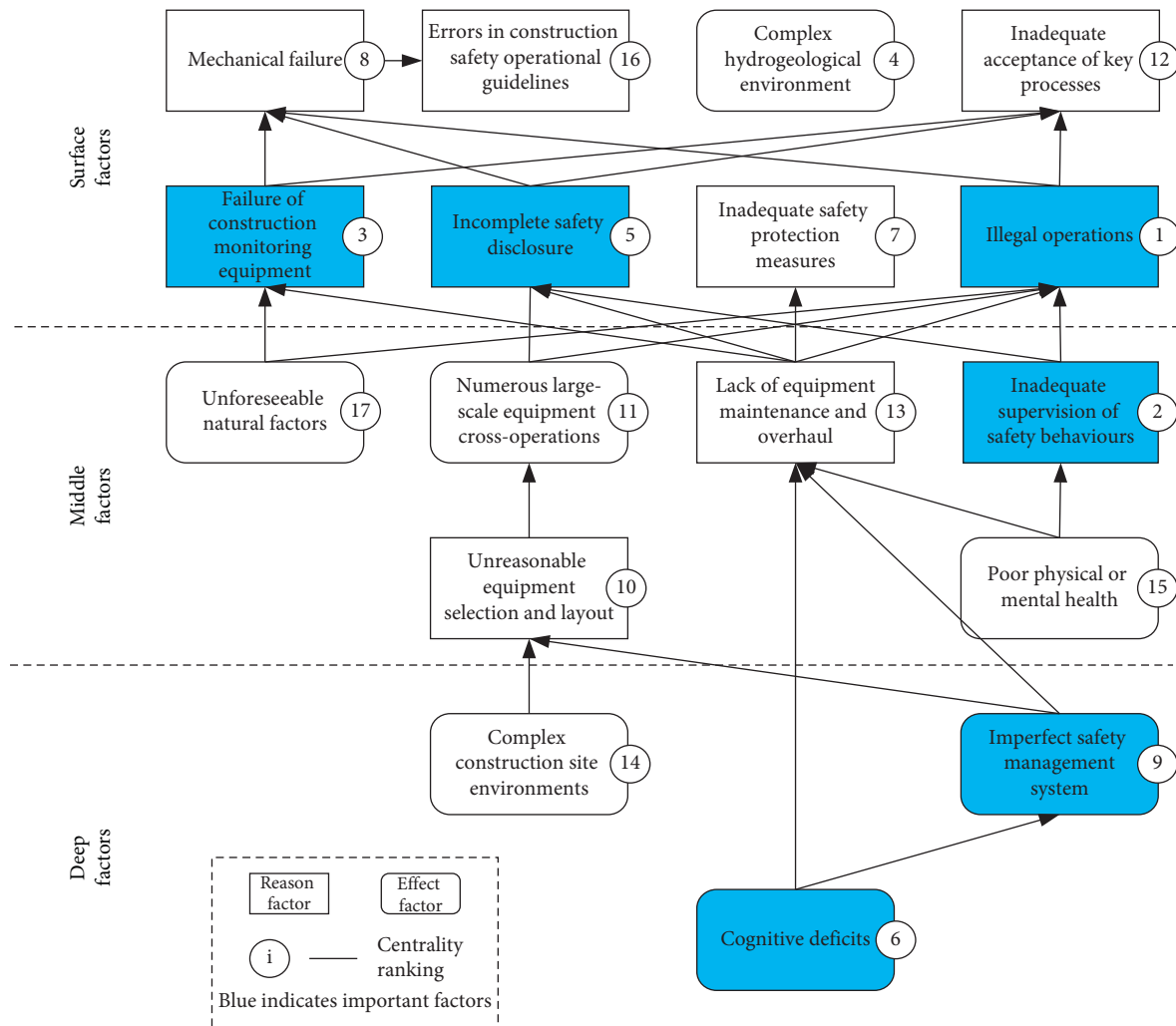


FIGURE 5: Multilevel hierarchical hybrid model.

- (2) Improve safety and protection measures. Safety protection measures should be taken for major hazards to avoid safety accidents.
- (3) Scientifically arrange the construction sequence to reduce environmental uncertainty.
- (4) Improve rules and regulations. Enterprises should improve the responsibility system for production safety and establish various rules and regulations for safety inspection and on-site management.
- (5) Focus on the production management of key processes, master the construction status in advance, eliminate safety hazards, and formulate effective preventive measures.
- (6) Develop a special safety plan. It is necessary to combine the characteristics of the project to prepare specialized, targeted, and operable special safety programmes and technical measures.
- (7) Strengthen the implementation of safety supervision. Strengthen the enforcement capacity of safety supervision, and timely discover to solve safety problems in production.

- (8) Master professional skills and knowledge. Ensure that workers master relevant practices. Check for related knowledge and skills, reward and update them, and retest regularly.
- (9) Perform good safety technical clarification. The construction technology department and the safety risk management agency should cooperate to implement construction safety.

4. Conclusion

Construction accidents in high-speed railway station construction are the result of the joint actions of humans, machines, the environment, and management. Based on system safety theory, an index system of the influencing factors of construction safety is established with human-machine-environment management aspects, and the influencing mechanism among the influencing factors is analysed. The main conclusions are as follows:

- (1) DEMATEL and ISM can be combined to analyse the relationship among various factors affecting

construction safety. DEMATEL is used to analyse the centrality and causation of construction safety risk factors and to determine the key factors. According to the results, causation was divided into 6 causes and 11 results. ISM is used to divide construction safety risk factors into three hierarchical structures and to obtain a multilevel hierarchical hybrid model of influencing factors.

- (2) The conclusion is that personnel factors and management factors need to be controlled with emphasis. Three main factors, six important factors, and seven direct factors are obtained by analyzing the risk factors affecting the construction safety of high-speed railway station.
- (3) The factors that affect the construction safety of high-speed railway stations are extraordinarily complex and have classification modes. In security risk control, we should not only pay attention to the proximal cause but also start from the overall situation and consider all factors comprehensively.

Data Availability

The data used to support the findings of this study are included within the article.

Conflicts of Interest

The authors declare that there are no conflicts of interest regarding the publication of this paper.

Acknowledgments

The authors acknowledge the financial support of Science and Technology Project of Ningbo Transportation Bureau (Grant no. 202007) and Science and Technology Research and Development Project of China Railway Construction Group Co., Ltd. (2020-12).

References

- [1] J. Zhang and J. Zhang, "Comprehensive evaluation of operating speeds for high-speed railway: a case study of China high-speed railway," *Mathematical Problems in Engineering*, vol. 2021, Article ID 8826193, 16 pages, 2021.
- [2] General Office of the Ministry of Housing and Urban-Rural Development, *Circular of the General Office of the Ministry of Housing and Urban-Rural Development on the Special Action to Address Production Safety Accidents and Construction Safety in Housing and Municipal Projects in 2018* General Office of the Ministry of Housing and Urban-Rural Development, Beijing, China, 2019.
- [3] BLS, "Injuries, illnesses, and fatalities," 2021, http://www.mohurd.gov.cn/wjfb/201903/t20190326_239913.html.
- [4] Health and Safety Executive, "Workplace fatal injuries in Great Britain," 2020, <https://www.hse.gov.uk/statistics/>.
- [5] E. C. Wigglesworth, "Human factors in level crossing accidents," *Accident Analysis & Prevention*, vol. 10, no. 3, pp. 229–240, 1978.
- [6] A. Lawrence, "Human error as a cause of accidents in gold mining," *Journal of Safety Research*, vol. 6, no. 2, pp. 78–88, 1974.
- [7] H. W. Heinrich, *Industrial Accident Prevention. A Scientific Approach*, *Industrial Accident Prevention. A Scientific Approach*, McGraw-Hill Education, New York, NY, USA, 2nd edition, 1941.
- [8] W. Haddon Jr., "The changing approach to the epidemiology, prevention, and amelioration of trauma: the transition to approaches etiologically rather than descriptively based," *American Journal of Public Health and the Nations Health*, vol. 58, no. 8, pp. 1431–1438, 1968.
- [9] W. Haddon Jr., "A logical framework for categorizing highway safety phenomena and activity," *The Journal of Trauma: Injury, Infection, and Critical Care*, vol. 12, no. 3, pp. 193–207, 1972.
- [10] F. P. McKenna, "Accident proneness: a conceptual analysis," *Accident Analysis & Prevention*, vol. 15, no. 1, pp. 65–71, 1983.
- [11] N. G. Leveson, "A new approach to hazard analysis for complex systems," in *Proceedings of the 2003 International Conference of the System Safety Society*, Ottawa, Canada, 2003.
- [12] E. Hollnagel and O. Goteman, "The functional resonance accident model," *Proceedings of Cognitive System Engineering in Process Plant*, vol. 2004, pp. 155–161, 2004.
- [13] Z. Guo, L. Chen, K. Yin, D. P. Shrestha, and L. Zhang, "Quantitative risk assessment of slow-moving landslides from the viewpoint of decision-making: a case study of the Three Gorges reservoir in China," *Engineering Geology*, vol. 273, Article ID 105667, 2020.
- [14] M. O. Sanni-Anibire, A. S. Mahmoud, M. A. Hassanain, and B. A. Salami, "A risk assessment approach for enhancing construction safety performance," *Safety science*, vol. 121, pp. 15–29, 2020.
- [15] M. R. Hollowell and J. A. Gambatese, "Qualitative research: application of the Delphi method to CEM research," *Journal of Construction Engineering and Management*, vol. 136, no. 1, pp. 99–107, 2010.
- [16] O. Rozenfeld, R. Sacks, Y. Rosenfeld, and H. Baum, "Construction job safety analysis," *Safety science*, vol. 48, no. 4, pp. 491–498, 2010.
- [17] E. E. Ameyaw, Y. Hu, M. Shan, A. P. C. Chan, and Y. Le, "Application of Delphi method in construction engineering and management research: a quantitative perspective," *Journal of Civil Engineering and Management*, vol. 22, no. 8, pp. 991–1000, 2016.
- [18] K. Alomari, J. Gambatese, C. Nnaji, and N. Tymvios, "Impact of risk factors on construction worker safety: a Delphi rating study based on field worker perspective," *Arabian Journal for Science and Engineering*, vol. 45, no. 10, pp. 8041–8051, 2020.
- [19] G. Zhang, C. Wang, Y. Jiao et al., "Collapse risk analysis of deep foundation pits in metro stations using a fuzzy Bayesian network and a fuzzy AHP," *Mathematical Problems in Engineering*, vol. 2020, Article ID 4214379, 18 pages, 2020.
- [20] D. A. Patel and K. N. Jha, "Evaluation of construction projects based on the safe work behavior of co-employees through a neural network model," *Safety Science*, vol. 89, pp. 240–248, 2016.
- [21] W. Z. Taffese and E. Sistonen, "Neural network based hygrothermal prediction for deterioration risk analysis of surface-protected concrete façade element," *Construction and Building Materials*, vol. 113, pp. 34–48, 2016.
- [22] Y. Kim and S. S. Lee, "Application of artificial neural networks in assessing mining subsidence risk," *Applied Sciences*, vol. 10, no. 4, p. 1302, 2020.

- [23] A. Nieto-Morote and F. Ruz-Vila, "A fuzzy approach to construction project risk assessment," *International Journal of Project Management*, vol. 29, no. 2, pp. 220–231, 2011.
- [24] W. Zhang, B. Li, Z. Liu, and B. Zhang, "Application of improved fuzzy comprehensive evaluation method in karst groundwater quality evaluation: a case study of Cengong county," *Earth Science Informatics*, vol. 14, pp. 1101–1109, 2021.
- [25] Z. Guo, K. Yin, F. Huang, S. Fu, and W. Zhen, "Evaluation of landslide susceptibility based on landslide classification and weighted frequency ratio model," *Chinese Journal of Rock Mechanics and Engineering*, vol. 38, no. 2, pp. 287–300, 2019.
- [26] A. Rice, *The Enterprise and Its Environment*, Routledge, London, UK, 1991.
- [27] S. Bertelsen, "Construction as a complex system," in *Proceedings for the 11th Annual Conference of the International Group for Lean Construction*, Blacksburg, VA, USA, 2003.
- [28] N. Leveson, "A new accident model for engineering safer systems," *Safety Science*, vol. 42, no. 4, pp. 237–270, 2004.
- [29] J. Rasmussen, "Risk management in a dynamic society: a modelling problem," *Safety Science*, vol. 27, no. 2, pp. 183–213, 1997.
- [30] D. q. Zhou, L. Zhang, and H.-w. Li, "A study of the system's hierarchical structure through integration of DEMATEL and ISM," in *Proceedings of the 2006 International Conference on Machine Learning and Cybernetics*, IEEE, Dalian, China, 2006.
- [31] Q. Zhou, W. Huang, and Y. Zhang, "Identifying critical success factors in emergency management using a fuzzy DEMATEL method," *Safety Science*, vol. 49, no. 2, pp. 243–252, 2011.
- [32] A. Medina-Borja and K. S. Pasupathy, "Uncovering complex relationships in system dynamics modeling: Exploring the use of CART, CHAID and SEM," in *Proceedings of the 25th International Conference of the System Dynamics Society*, pp. 1–24, Boston, MA, USA, 2007.
- [33] T. L. Saaty, "Making and validating complex decisions with the AHP/ANP," *Journal of Systems Science and Systems Engineering*, vol. 14, no. 1, pp. 1–36, 2005.
- [34] C. Zhou, L. Y. Ding, M. J. Skibniewski, H. Luo, and H. T. Zhang, "Data based complex network modeling and analysis of shield tunneling performance in metro construction," *Advanced Engineering Informatics*, vol. 38, pp. 168–186, 2018.
- [35] S. Ahmed, "Causes of accident at construction sites in Bangladesh," *Organization, Technology and Management in Construction: An International Journal*, vol. 11, no. 1, pp. 1933–1951, 2019.
- [36] R. A. Haslam, S. A. Hide, A. G. F. Gibb et al., "Contributing factors in construction accidents," *Applied ergonomics*, vol. 36, no. 4, pp. 401–415, 2005.
- [37] L. Wang, Q. Cao, and L. Zhou, "Research on the influencing factors in coal mine production safety based on the combination of DEMATEL and ISM," *Safety Science*, vol. 103, pp. 51–61, 2018.
- [38] W. Du, G. Jing, and Q. Shi, "Preliminary study on safety analysis of man-machine-environment system in underground transportation," *Chinese Journal of Safety Science*, vol. 3, pp. 37–40, 1997.
- [39] J. Zhang, K. Xu, G. You et al., "Causation analysis of risk coupling of gas explosion accident in chinese underground coal mines," *Risk Analysis*, vol. 39, no. 7, pp. 1634–1646, 2019.
- [40] H. Kim, H. S. Lee, M. Park et al., "Influence factor-based safety risk assessment methodology for construction site," in *Proceedings of the Construction Research Congress 2010: Innovation for Reshaping Construction Practice*, Banff, Canada, 2010.
- [41] W. Qiao, "Analysis and measurement of multifactor risk in underground coal mine accidents based on coupling theory," *Reliability Engineering & System Safety*, vol. 208, Article ID 107433, 2021.
- [42] C. M. Tam, S. X. Zeng, and Z. M. Deng, "Identifying elements of poor construction safety management in China," *Safety Science*, vol. 42, no. 7, pp. 569–586, 2004.
- [43] Z. Ding, M. Zhu, V. W. Y. Tam, G. Yi, and C. N. N. Tran, "A system dynamics-based environmental benefit assessment model of construction waste reduction management at the design and construction stages," *Journal of Cleaner Production*, vol. 176, pp. 676–692, 2018.
- [44] S.-B. Tsai, J. Zhou, Y. Gao et al., "Combining FMEA with DEMATEL models to solve production process problems," *PLoS One*, vol. 12, no. 8, Article ID e0183634, 2017.
- [45] S. Tong, J. Liu, L. Zhao et al., "Impact on water traffic environment based on ISM model," in *Proceedings of the 2019 5th International Conference on Transportation Information and Safety (ICTIS)*, IEEE, Liverpool, UK, 2019.

Research Article

Deformation Response and Safety Evaluation of Buildings Affected by Subway-Station Construction

Chunlei Feng ¹, Dingli Zhang,² Hualao Wang,¹ and Xuan Zhang¹

¹Bridge and Tunnel Research Center, Research Institute of Highway, Ministry of Transport, Beijing 100088, China

²Key Laboratory for Urban Underground Engineering of Ministry of Education, Beijing Jiaotong University, Beijing 100044, China

Correspondence should be addressed to Chunlei Feng; fclbjtu@163.com

Received 22 April 2021; Accepted 24 May 2021; Published 8 June 2021

Academic Editor: Faming Huang

Copyright © 2021 Chunlei Feng et al. This is an open access article distributed under the Creative Commons Attribution License, which permits unrestricted use, distribution, and reproduction in any medium, provided the original work is properly cited.

Based on the sand and pebble stratum in the Beijing area, this paper studies the interaction between deep-foundation-pit excavation for subway stations and surrounding buildings using an orthogonal test. Moreover, it considers the relative position relationship between buildings and how the foundation pit is set up as well as different design schemes for foundation pits and the surrounding buildings. Results show that the horizontal distance s between the building and foundation pit and stiffness of the building itself have a clear impact on the differential settlement δ_{ij} and relative deflection Δ , and the degree of deformation of the building near the corner of the foundation pit is complex. Simultaneously, based on numerical simulation results, the deformation characteristics and degree of deformation of the building under different relative position relationships with the foundation pit are analyzed. Finally, by establishing a relationship among the comprehensive deformation index D_j , surrounding environmental safety evaluation index S_j , and scheme safety grade L_j , a multiangle safety evaluation method for buildings affected by foundation-pit construction is formed, which can provide a reference for the research and design of similar projects.

1. Introduction

Deep-foundation-pit engineering is accompanied by different degrees of environmental impact in construction processes, which causes a change in the stress field of surrounding soil, resulting in foundation soil deformation within a certain range that affects surrounding buildings and structures. If foundation-pit excavation deformation is not properly controlled, it can threaten the safety of the surrounding environment because the deformation of the surrounding soil leads to uneven settlement or even damage caused by cracking in the building and structure, and the building can then no longer be used for its normal purpose. However, damage to or the destruction of the surrounding buildings also has an impact on deep-foundation-pit engineering. For example, the excessive settlement of the adjacent buildings exacerbates the deformation of the surrounding soil, which may lead to a further increase in the deformation of the retaining structure. Moreover, cracks and

leaks in underground pipelines may cause water bubbles at the bottom of the foundation pit and threaten the stability of its basement [1]. Therefore, with the increasing depth of foundation-pit excavation and increasingly complex surrounding environment, the foundation-pit support system should not only be appropriate for its own strength and stability but should also meet the requirements of the surrounding environment for deformation control.

At present, existing research on the environmental response of deep-foundation-pit excavation mostly focuses on the influence of foundation-pit deformation on surrounding structures, including actual deformation statistics [2–4] and numerical simulations and model test [5–7]. Li and Yan [8] numerically simulated ground surface settlement using auxiliary planes perpendicular and parallel to the excavation and angled auxiliary planes at the excavation corner; thereafter, they analyzed the bending and torsional deformation regularities of the surrounding buildings and developed an estimation method for building settlement. Liang

et al. [9] investigated building settlement near excavations in soft clay and proposed a simplified theoretical method to predict the additional settlements and axial forces of excavation adjacent to existing building floating piles in soft clay. Combined with the deep-foundation-pit engineering for subway stations in their respective regions, many scholars [10–13] have conducted in-depth research on deformation characteristics and influencing factors. Moreover, many studies [14, 15] have reported the response of surrounding buildings to foundation-pit excavation using field measurements, which provides a basis for studying the deformation mode and allowable deformation of buildings. According to the research of Skempton and MacDonald [16] and later scholars, damage to buildings can be roughly divided into architectural, functional, and structural damages. On the basis of previous research, Burland [17] proposed a classification standard for the levels of damage to buildings according to the degree of reparability of the largest cracks in masonry walls. To clearly and accurately quantify the impact of foundation-pit excavation on the surrounding environment, Burland and Wroth [18] provided a definition for various building-deformation variables, which has been widely recognized by related research.

Through a broad review of the relevant literature, it can be established that existing studies have the following limitations: first, foundation-pit engineering and the surrounding environment are an interactive system; therefore, accurately analyzing the interaction relationship between them depending only on measured analyses and theoretical research is difficult; second, a finite-element method can establish a variety of working conditions, and the influence of different factors on results can be further analyzed using calculation results. However, existing studies have only established the relative displacement relationship between the surrounding buildings and foundation pit. Because foundation pits for subway stations are long and narrow, the deformation of a building at a particular location can hardly represent the entirety of the deformation around the foundation pit; third, in the research process, the influence of the foundation pit itself and the surrounding environment on the deformation results has not been fully considered, and the calculation results have not been further combined with multiple factors to form a specific impact evaluation.

In this study, a sandy pebble stratum formed the basis of the investigation, and related engineering data were used to establish stratigraphic distribution and a standardized model for a subway-station deep-foundation pit. Starting from the influence of foundation-pit excavation on building deformation, the interaction between foundation-pit excavation and adjacent buildings is analyzed and evaluated in many aspects, so as to give feedback about the influence of foundation-pit excavation on the environment. Secondly, starting from the design scheme of the foundation-pit support system and the relative displacement relationship between the building and the foundation pit, the distance between the building and the foundation pit, the stiffness of the building itself, the stiffness of the retaining structure of the foundation pit, and the stiffness of the inner support are set as the main influencing factors. An orthogonal test and

research into the deformation of the different test schemes were then used to analyze the degree of influence of the various factors on building deformation. A comprehensive evaluation method for the influence of multiangle foundation-pit excavations on surrounding buildings was then developed, which provides a reference for subsequent related research and design.

2. Project Overview

2.1. Project Introduction. The project is located in Beijing, China, and its geographical location is shown in Figure 1. As the political and cultural center of China with a long history, Beijing has a varied construction style, which is complex and spans a large area; thus, given the complex urban environmental conditions, the requirements for environmental protection in relation to foundation-pit engineering are high, especially with regard to foundation-pit engineering for subway stations. As a form of urban construction, these foundation pits are excavated in considerably populated areas and can therefore cause a serious engineering accident if sufficient care is not taken. In this study, foundation-pit engineering for the first and second phase of the subway-station construction of Beijing Metro Line 6 is taken as the focus, and 16 open-cut foundation-pit projects are selected as the main research objects. The support system adopts the form of “internal support + bored pile.” The specific dimensions and characteristic values of the foundation-pit excavation are shown in Table 1, where, L , B , H_e , and H are the length, width, excavation depth, and depth of the foundation pit’s retaining structure. The diagram of subway lines is shown in Figure 2 in which the pink line is the first phase of the project, and the green line is the second. The serial numbers of each station in the figure correspond to the serial numbers in Table 1.

2.2. Geological and Hydrological Conditions of the Project. The first and second phases of Beijing Metro Line 6 are located in central and eastern Beijing, where the soil is mainly cohesive, silty, sandy, and with pebbles. Based on the summary of the geological survey data for the Beijing Metro Line 6 project, the stratigraphic sequence of the whole area from top to bottom is shown in Table 2, and the main types of soil in each layer are shown in Figure 3.

The Line 6 subway stations are mainly located at a depth of 15–25 m underground, and they are all built in the Quaternary clay, sand, and pebble layer. Therefore, the influence of strata conditions on subway construction in Beijing mainly includes the following two aspects [19]:

- (1) The sand and pebble stratum in Beijing are a typical mechanical unstable stratum, which is characterized by loose structure, lack of cementation, and different sized granulation. Once this kind of stratum is excavated, the original state of relative stability or equilibrium is easily destroyed so that the excavation face and wall of the foundation pit lose their constraints, leading to instability. Large pores are present among the grains of the sandy pebble



FIGURE 1: Schematic of the project location.

TABLE 1: Basic statistics of the excavation for Beijing Metro Line 6 open-cut station.

Project number	L (m)	B (m)	H_e (m)	H (m)
1	381	34.2	24.4	27.7
2	245.3	22.3	28.7	34.9
3	291.1	28.8	18.5	30.7
4	323.8	23	17.4	30.4
5	219.1	20.9	19.8	23.3
6	564.9	19.7	21.1	25.4
7	358.3	21.1	17.5	22.5
8	256	19.5	18.5	21
9	394	34.9	18.6	21
10	357.5	20.9	13.3	17.8
11	473	43.9	22.2	26.6
12	219.6	21.9	17.6	33.6
13	314.2	21.1	17.9	42.5
14	326.4	20.9	20	24.2
15	286.4	20.8	17.4	22.4
16	523.6	29.7	18.2	22.4
Average	319.5	25.44	20.12	27.16

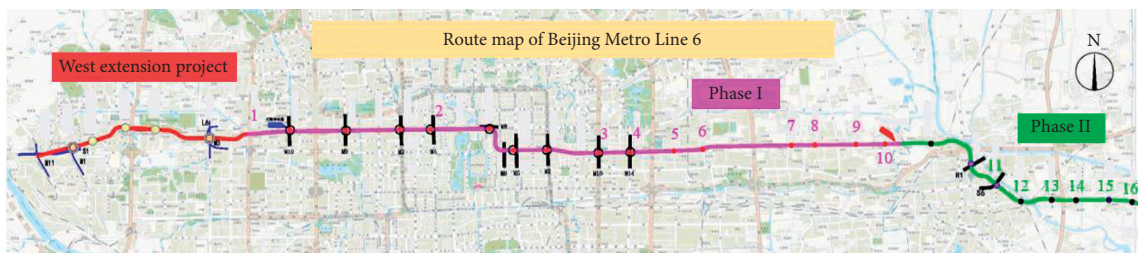


FIGURE 2: Diagram of Beijing Metro Line 6 and project numbers.

TABLE 2: Strata along Beijing Metro Line 6.

Number	Name of the soil	Type of soil
1	Artificial filled soil	It mainly contains silt filling soil and miscellaneous filling soil, in which the miscellaneous filling soil is 6–8 m below the ground
2	Recently deposited soil	It mainly contains silty soil layer, silty clay layer, and fine sand
3	Quaternary Holocene alluvial and diluvial deposits	It mainly contains silty soil, silty clay, clay, fine silty sand, and medium coarse sand
4	Quaternary late Pleistocene alluvial and diluvial deposits	It mainly contains boulder, medium coarse sand, fine silty sand, silty clay, clay, silt, and fine medium sand

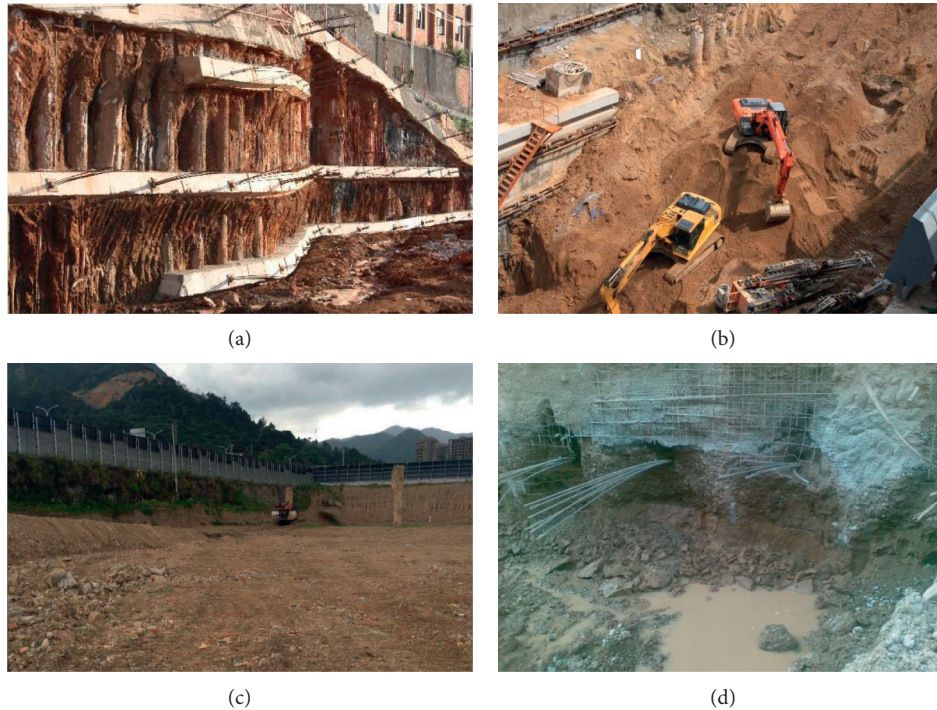


FIGURE 3: Longitudinal geological profile of the K0 + 600–K1 + 074 section of the Gongchang road project. (a) Silty clay. (b) Fine powder sand. (c) Sandy pebble. (d) Sandy pebbles are interlaced with silty clay.

formation, and the cohesive force among the grains is almost zero. During the excavation of the foundation pit, the stratum can easily collapse. In particular, the spalling of large pebbles in the wall of the foundation pit may cause a sudden subsidence of the overlying strata.

- (2) Beijing strata also contain a large number of sand layers, which are generally dense but have poor self-stabilizing ability, and these layers are prone to collapse. In the presence of water, sand flow occurs easily. If precipitation construction is adopted, the surrounding groundwater level decreases, and the silty sand layer becomes loose as a result of water loss, which makes it unstable when disturbed by an excavation operation.

Therefore, studying the influence of subway-station construction on the surrounding buildings in dense urban areas with these strata characteristics is necessary to establish a set of construction safety evaluation methods.

3. Basic Information on the Foundation Pits and Surrounding Buildings

A large number of engineering design data pieces were collected to standardize the design parameters of the subway-station foundation pits in the Beijing area, and the finite-element calculation method was adopted to analyze the interaction between the existing design scheme for foundation-pit excavation and the surrounding buildings.

3.1. The Establishment of a Foundation-Pit Standard Model. After assigning an average weighting to all the parameters of the open-cut foundation pit, as shown in Table 1, the main parameters of the standardized model of the subway-station foundation pit were obtained (Table 3), where d , l , H , and E are the diameter, spacing, depth, and stiffness, respectively, of the bored piles. The excavation conditions of the standardized foundation pit are shown in Table 4.

3.2. Main Building Parameters and Relative Position Relationship. The overall stiffness of most multistory masonry structures, compared to reinforced concrete shear frame structure, is weaker due to its shallow depth and overall stiffness, making it relatively more vulnerable to environmental impact in the excavation of foundation pits. Therefore, this paper focuses primarily on the deformation of multistory masonry structures to evaluate the environmental impact of foundation-pit excavations.

To study the influence of foundation-pit excavation on surrounding buildings, the setting parameters mainly include the position relationship between the building and envelope structure and the size and stiffness of the building itself. The size of the building is shown in Figure 4. The outer contour is a strip 27 m long and 4.5 m wide. Four floors are present, and each layer is 3 m high, with a total height of 12 m. The main structure of the building includes a horizontal wall, vertical wall, partition wall, and floor slab. The foundation is in the form of a strip foundation under the wall, and the openings for doors and windows have been considered. The thickness of the wall and floor slab is 0.24 m

TABLE 3: Main parameters of the normalized model of the Beijing Metro Line 6 open-cut foundation pit.

<i>Basic dimensions</i>	L (m)	319.5
	B (m)	25.44
	H_e (m)	20.12
<i>Bored pile</i>	d (m)	0.8/1.5
	l (m)	27.16
	H (m)	3.0×10^4
	E (MPa)	Q235
<i>Inner support</i>	Material	Q235
	Layer number	4
	Section size (mm)	$\Phi 609 \times 14$ $\Phi 609 \times 16$
	Horizontal spacing (m)	3

TABLE 4: Main excavated conditions of the foundation pit.

Construction step	Construction content	Excavation depth
I	Initial ground stress	—
II	Retaining structure construction	—
III	Excavate the first layer of soil and set up the first steel support	2 m
IV	Excavate the second layer of soil and set up the second steel support	4.5 m
V	Excavate the third layer of soil and set up the third steel support	4.5 m
VI	Excavate the fourth layer of soil and set up the fourth steel support	4.5 m
VII	Excavation to the bottom	4.5 m

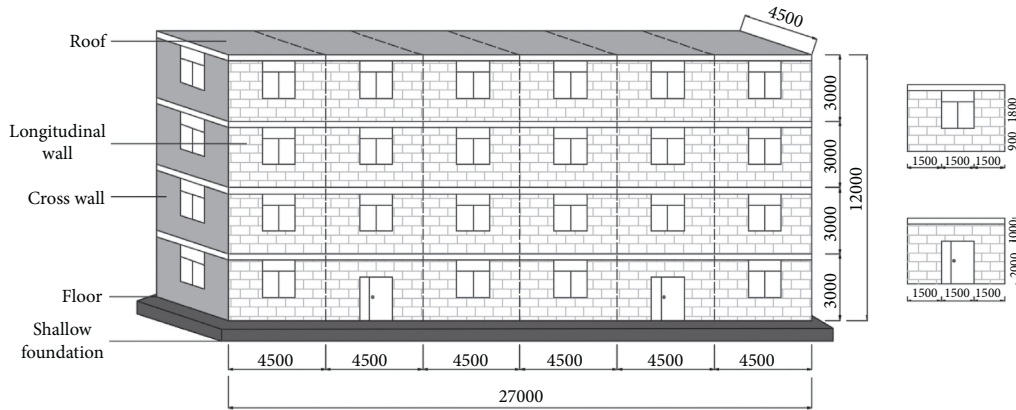


FIGURE 4: Dimensions of surrounding buildings.

and 0.1 m, respectively. Considering that the stiffness of most masonry structures gradually degrades with age, the impact of earthquakes, and other factors [20, 21], the elastic modulus of the wall is set at 220 MPa, and Poisson's ratio is 0.1. The elastic modulus of the floor is set at 30 GPa, and Poisson's ratio is 0.2.

Since the subway-station foundation pit is long and narrow, the deformation in the length direction of the foundation pit is more complicated [22, 23]. The location of the maximum deformation of the foundation-pit excavation was determined using the design, construction scheme, and complexity of the surrounding environment, of which the influencing factors relating to the deformation of the surrounding buildings include the structural form, buried depth of the foundation, and relative position relationship with the foundation pit.

Therefore, the deformation situation between the building and the foundation pit at different relative positions is compared and analyzed by using three different relative position relations: on one side of the foundation pit near the center, at a quarter of the length, and at an angle to the pit, as shown in Figure 5. The comparative analysis in relation to the different relative positions between the buildings and foundation pit depending on the location parameter is given in the subsequent calculations.

When setting the horizontal distance between the building and envelope, ensuring that the building was located in the main impact area of the foundation-pit excavation was necessary, as shown in Figure 6. When the longitudinal wall of the building is parallel to the foundation pit, the horizontal wall crosses the position where the maximum settlement occurs on the surface. When the

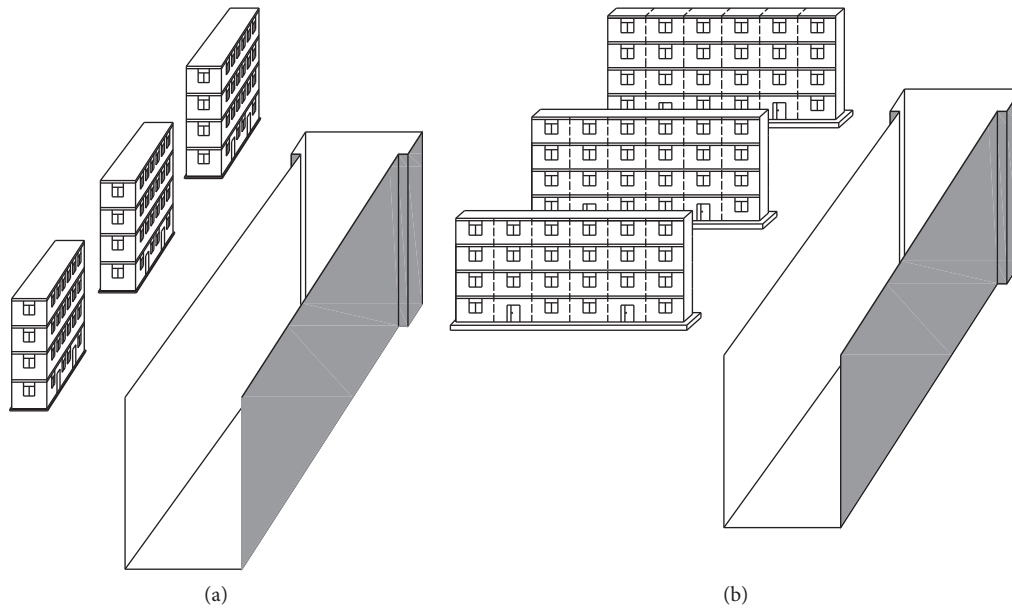


FIGURE 5: Schematic of the relative position relationship between the building and foundation pit. (a) The longitudinal walls of the building are parallel to the foundation pit. (b) The longitudinal walls of the building are perpendicular to the foundation pit.

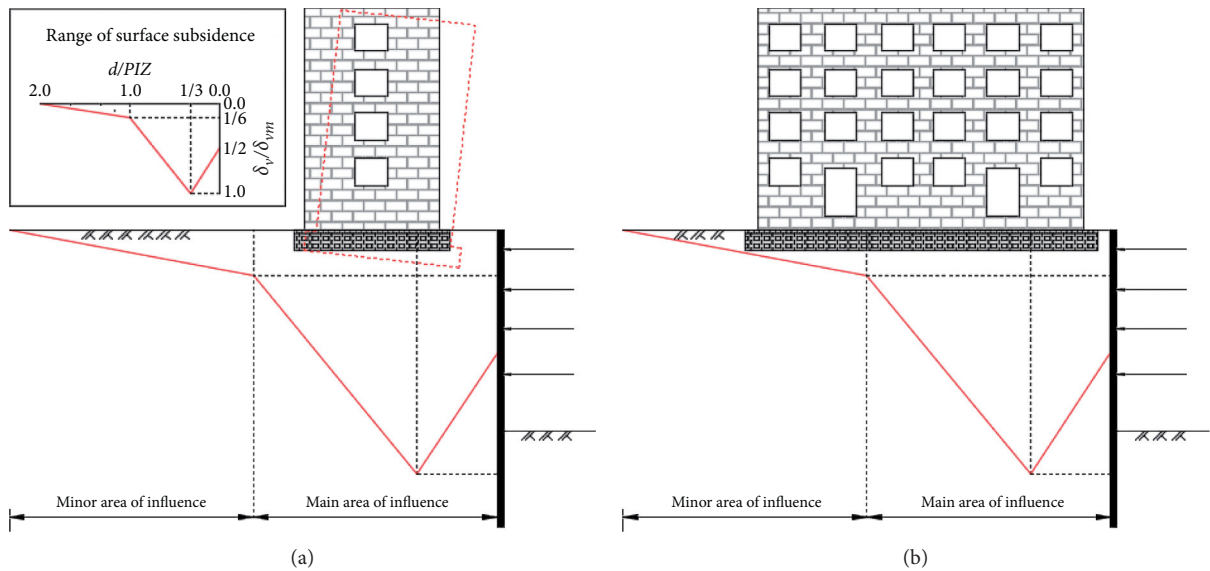


FIGURE 6: The relationship between the location of the building and influence range of ground subsidence during excavation [24]. (a) The longitudinal walls of the building are parallel to the foundation pit. (b) The longitudinal walls of the building are perpendicular to the foundation pit.

longitudinal wall of the building is perpendicular to the foundation pit, the longitudinal wall crosses the position where the maximum settlement occurs.

3.3. Selection of a Constitutive Model. To describe the stress-strain relationship of soil accurately, scholars have proposed various models to consider the small-strain stiffness of soil. These models can distinguish the

deformation characteristics of soil in relation to loading and unloading. Among them, the hardening soil small-strain model proposed by Benz [5], used with small-strain stiffness, has been widely used and recognized by scholars in the field of foundation-pit engineering. Therefore, this paper adopted this constitutive model to simulate and analyze the excavation process of a standardized foundation pit in the Beijing strata. Moreover, considering the calculation efficiency of the finite-element software and symmetry of the foundation

pit, a half-section of the central axis along the long side of the foundation pit was used for the simulation in the numerical calculation.

4. Deformation of the Retaining Structure and Surrounding Buildings after Excavation of a Foundation Pit

To facilitate the description of the deformation under different relative position relationships between buildings and foundation pits, the foundation pits and buildings are numbered using the plane coordinate system as viewed from above. Starting from the pit corner, the order of buildings is stipulated in the direction of the x -axis, as shown in Figure 7. In the calculation process, the deformation in the floor and roof of the building was monitored. The deformation results were summarized by the deformation at the intersections of each partition wall with the baseplate and roof. The positions and numbers of the monitoring points are shown in Figure 8: a monitoring point on the roof is m , and the number of the monitoring point on the bottom plate perpendicular to the roof is m' .

When the longitudinal wall of the building is parallel to the foundation pit, as shown in Figure 9, based on the size of the foundation pit, the distance between two adjacent buildings is set as 30 m, and the horizontal distance from the foundation pit is 5 m. Because the width of the foundation-pit shield shaft is larger than the shield interwell section, the distance between building A and the foundation pit is closer than that between building B and building C, and the horizontal distance is approximately 3 m.

The calculation results are shown in Figure 10. By comparing the soil deformation on the left and right sides of the foundation pit in Figures 10(a) and 10(b), it can be seen that the size and range of horizontal and vertical deformation of the soil with a building on one side of the foundation pit are significantly larger than that without a building. At the same time, further analysis can obtain the deformation of the building, as shown in Figures 11 and 12.

By comparing the floor settlement of the three buildings in Figure 11, it can be seen that: ① building A, which is closer to the shield shaft, has the largest settlement, and its maximum settlement is approximately -32.5 mm; the settlement of buildings B and C is small, and the maximum settlement is approximately -25.9 mm. The settlement of buildings B and C is in the form of synchronous subsidence and symmetrical depression on both sides of the floor, and the settlement of building A is due to the settlement on the left side of the floor being greater than the asymmetric depression on the right side; ② the length of the red line on the right side of the deformation curve in Figure 11 is the differential settlement of buildings A, B, and C, which is 24.8, 18.4, and 25 mm, respectively. The relative deflections are 12.55, 9.8, and 14.35 mm, respectively. The corresponding deflection ratios are 1/2151, 1/2755, and 1/1881, respectively; ③ the settlement of the front edge of the floor of the three buildings is greater than that of the back edge, and the settlement difference between the front and back sides of the

floor is between 5 and 7.5 mm. Based on the previous assumptions on building deformation, it is speculated that the whole building may be inclined toward the foundation pit.

Figure 12 shows the horizontal deformation of the top and bottom monitoring points of the longitudinal wall in front of the building in the direction of the foundation pit. The maximum horizontal displacement of the top and bottom of building A is 7.5 and 5.5 mm, respectively. The maximum horizontal displacements at the top and bottom of the longitudinal walls of buildings B and C are similar, approximately 5.45 and 3.85 mm, respectively. Compared with buildings B and C, the maximum horizontal displacement of building A in the direction of the foundation pit appears on the left side of the building, i.e., the side near the shield shaft, and the bottom presents a slightly concave deformation. However, the deformation of buildings B and C is generally shown as an overall forward tilt, without prominent deformation in any position. Therefore, the forms of deformation of the buildings located near shield shafts are relatively complex compared with those in other locations.

4.1. Deformation of Buildings with Longitudinal Walls Perpendicular to the Foundation Pit. As shown in Figure 13, when the longitudinal wall of the building is perpendicular to the foundation pit, with the three buildings still in a horizontal position, the horizontal spacing between the adjacent buildings is 65 m, the horizontal distance between the transverse walls of the building near the foundation pit is 5 m, and horizontal distance between building A and the foundation pit is 3 m due to its proximity to where the shield shaft and shield interwell section connect.

As can be seen from Figure 14, when the longitudinal wall of the building is perpendicular to the foundation pit, the deformation range of horizontal and vertical soil displacement on the side of the foundation pit with the building increases compared with that on the side without the building. The maximum horizontal displacement is within the range of 30–40 mm, and the maximum vertical settlement is within the range of 40–50 mm.

When the longitudinal wall of the building is perpendicular to the foundation pit, the horizontal displacement of the building toward the foundation pit can be ignored because the moment of inertia along the vertical wall of the building is much larger than that along the horizontal wall. As shown in Figure 15, through further analysis of the settlement deformation at the bottom of the building, it can be seen that the left and right sides of the floor of the building at the three locations show synchronous settlement deformation, and the maximum settlement is similar at approximately 30 mm. The three largest settlement points are all located near monitoring points no. 6 (or no. 12) and no. 7 (or no. 13). This means that the horizontal distance from the ipsilateral retaining structure of the foundation pit is approximately $0.7\text{--}0.8 H_c$ within the range of 12–14 m.

In summary, when the longitudinal wall of the building is perpendicular to the foundation pit, the horizontal displacement of the building toward the foundation pit is

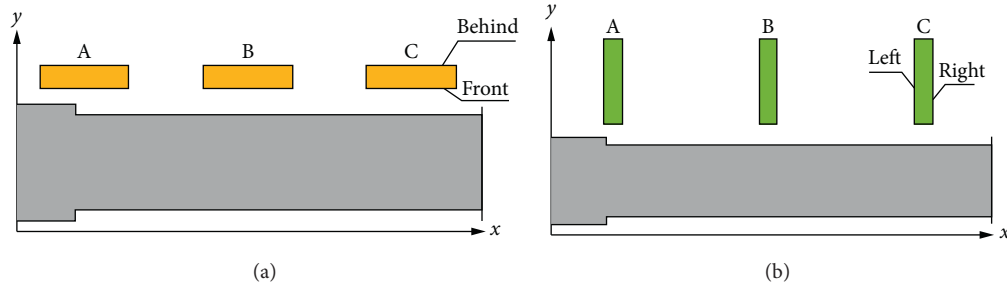


FIGURE 7: The position relationship between the foundation pit and building, as viewed from above, in plane coordinate and building number.

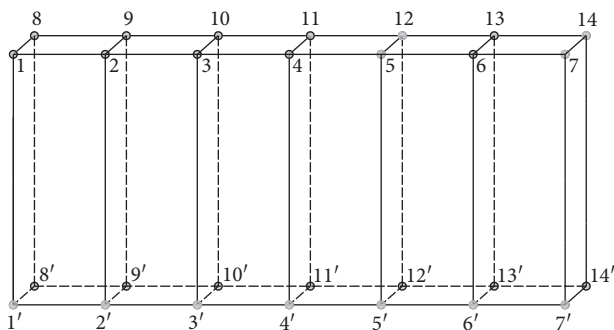


FIGURE 8: Diagram of building-deformation monitoring points.

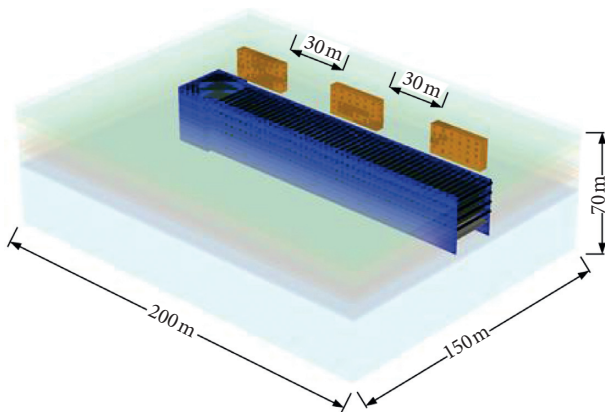


FIGURE 9: Three-dimensional numerical model of the longitudinal wall of buildings parallel to the foundation pit.

ignored due to the greater stiffness of the vertical wall. Therefore, the settlement deformation of the floor of the building is mainly analyzed herein. It can be seen from the building settlement deformation curve that the position of the maximum settlement of the building is consistent with the position of the maximum settlement of the surface outside the pit obtained from the measured data statistics [18]. Therefore, further studies on the influence of various factors on building deformation can be conducted in subsequent studies based on the above 3D model.

5. Environmental Response and Safety Evaluation of Foundation-Pit Construction

To obtain the degree of influence of the excavation of the foundation pit on the surrounding buildings accurately, this section combines the main parameters of the buildings and foundation-pit support scheme and analyzes the influence of different support schemes and the state of the surrounding buildings on the deformation of the building in the process of foundation-pit excavation from multiple angles.

According to the deformation described in the previous section, the forms of deformation in the buildings are primarily uneven settlement δ_{ij} , overall deflection Δ , inclination toward the pit (angle α), and torsion (angle β), as shown in Figure 16. Uneven settlement δ_{ij} in Figure 16(a) is the absolute value of the difference between the settlement value of the monitoring point j with the largest settlement and that of the monitoring point i with the smallest settlement of the monitoring points on the floor.

5.1. Deformation Response Analysis of the Surrounding Buildings Affected by Foundation-Pit Construction. In this section, the foundation-pit supporting scheme is represented by two main factors E^c and E^s , while the relative position relationship between the building and the foundation pit, s and E^c , is mainly considered for the surrounding buildings, as shown in Table 5, where s is the horizontal distance between the building and foundation pit; E^c is the stiffness of the building wall; E^e is the stiffness of the retaining structure; and E^s is the stiffness of the internal support. Three levels are set for each factor. The relative position relationship between the building and foundation pit is consistent with that in Section 4.

Through the analysis and study of different foundation-pit retaining design schemes and the deformation of the surrounding buildings in the previous section, the specific degree of influence of the different factors on the deformation of buildings with the three relative positions can be obtained, as shown in Figure 17. The vertical coordinate in the figure is the absolute value of the difference between the maximum and minimum mean values of the deformation parameters obtained at the three different levels under the

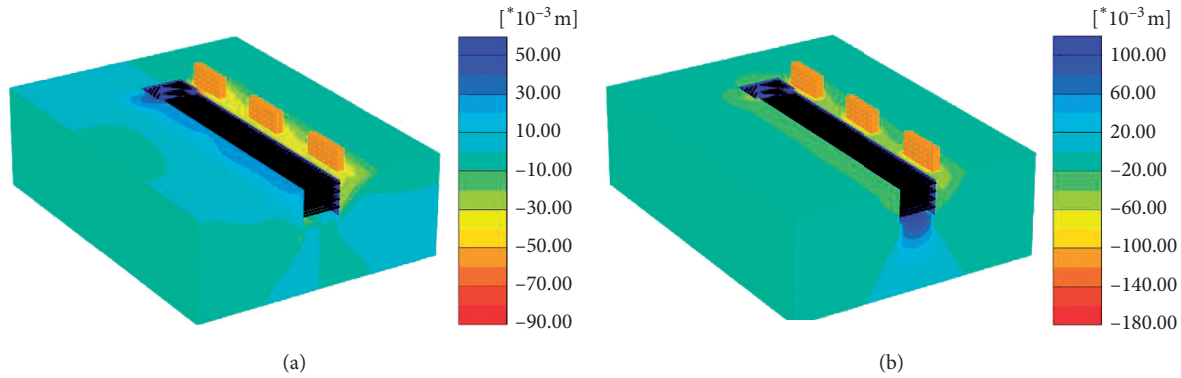


FIGURE 10: Displacement cloud image of surrounding environment after completion of foundation-pit excavation parallel to the foundation pit. (a) Horizontal displacement of soil. (b) Vertical displacement of soil.

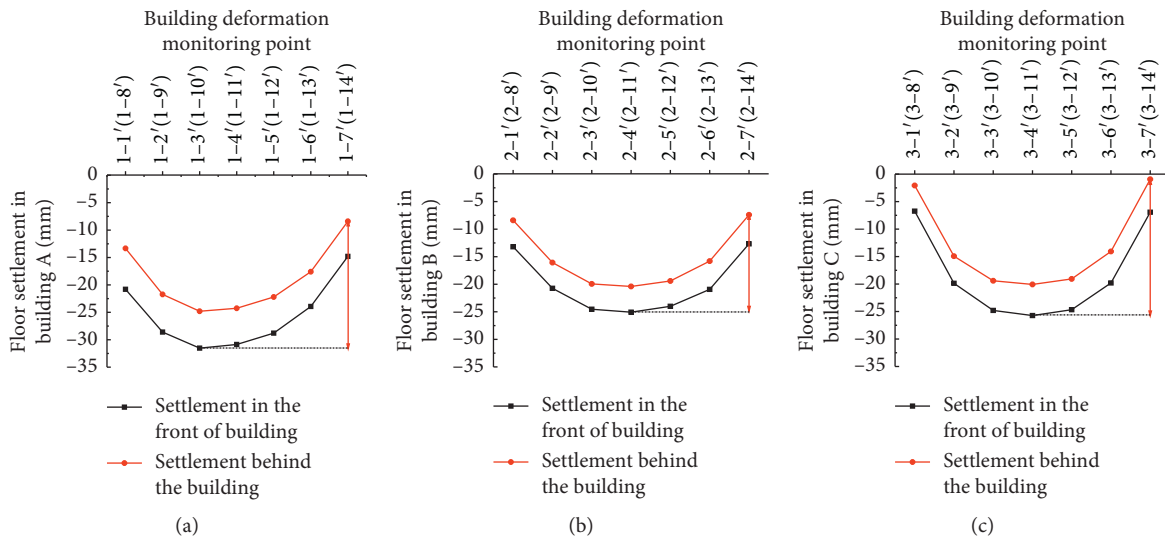


FIGURE 11: Floor settlement of the three buildings when the longitudinal wall of the building is parallel to the foundation pit. (a) Building A. (b) Building B. (c) Building C.

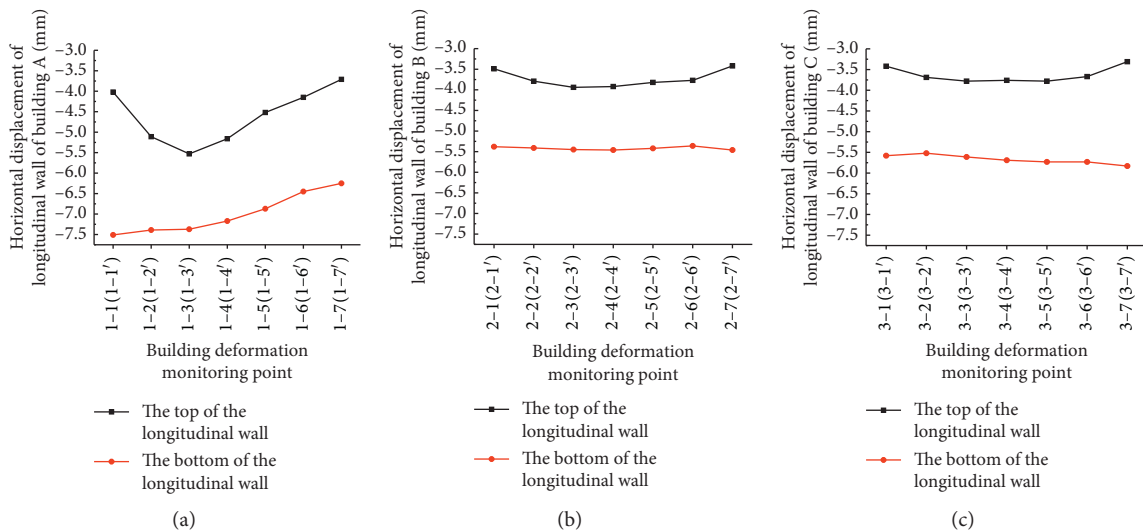


FIGURE 12: Horizontal displacement of the roof and floor of the three buildings when the longitudinal wall of the building is parallel to the foundation pit. (a) Building A. (b) Building B. (c) Building C.

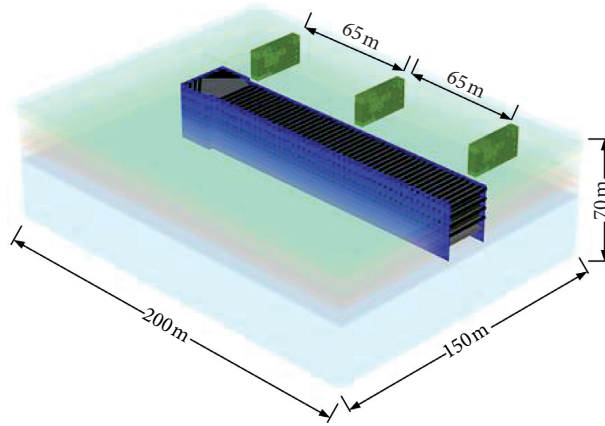


FIGURE 13: Three-dimensional numerical model of the longitudinal wall of buildings perpendicular to the foundation pit.

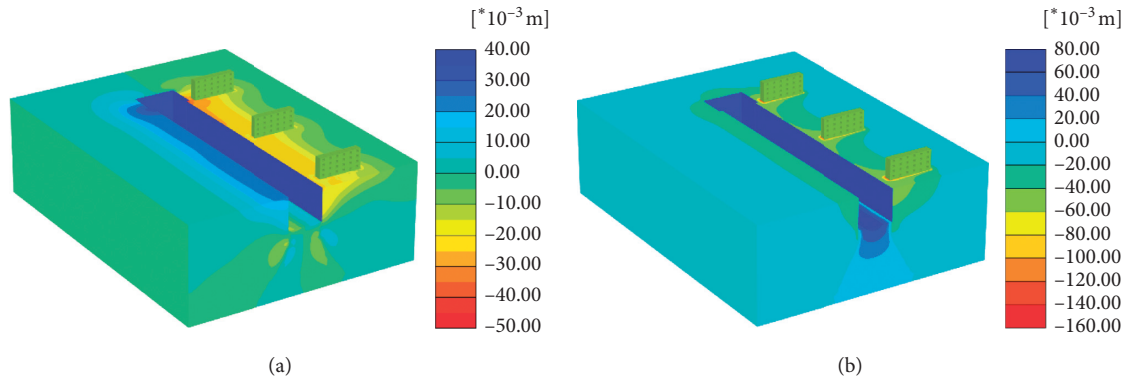


FIGURE 14: Displacement cloud image of surrounding environment after completion of foundation-pit excavation (perpendicular to the foundation pit). (a) Horizontal displacement of soil. (b) Vertical displacement of soil.

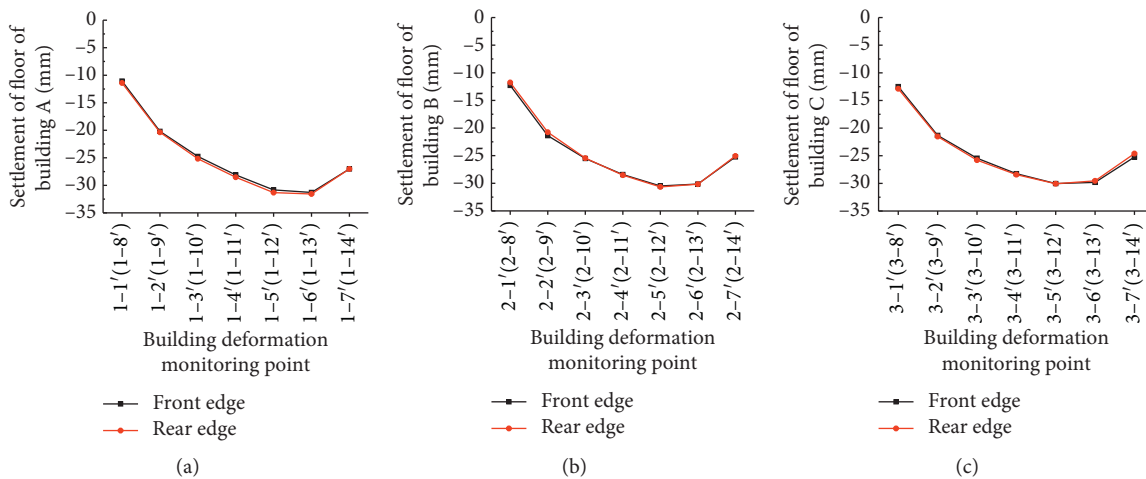


FIGURE 15: Floor settlement of the three buildings when the longitudinal wall of the building is perpendicular to the foundation pit. (a) Building A. (b) Building B. (c) Building C.

same influence factor. It is a dimensionless index and is only used to consider the degree of influence of different factors on the same deformation parameter; the larger the

difference, the greater the influence of this factor on the deformation parameters. In each figure, the left curve is the degree of impact of the longitudinal walls of buildings A, B,

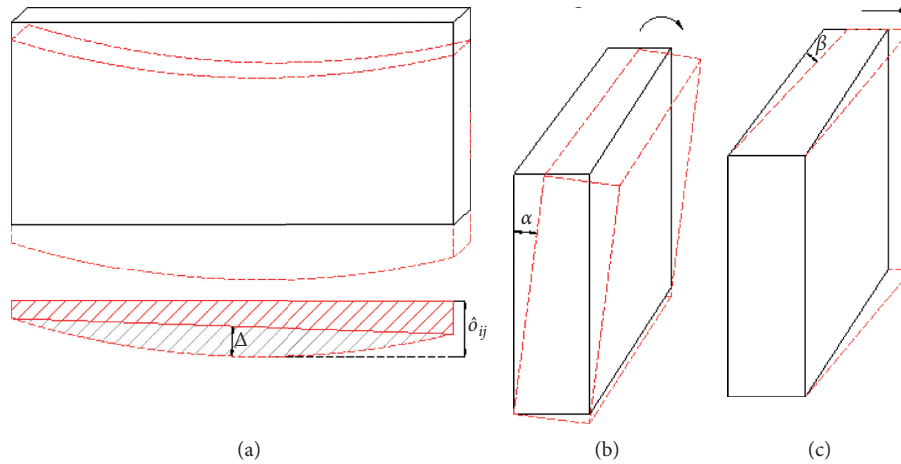


FIGURE 16: Diagram of building-deformation forms. (a) Relative deflection and differential settlement. (b) Tilt deformation. (c) Torsional deformation.

TABLE 5: Orthogonal test factors for a deformation response analysis of the buildings.

Main influencing factors	Test conditions		
	Standard 1	Standard 2	Standard 3
s (m)	5	10	15
E^c (10^3 MPa)	0.2	0.4	0.6
E^s (10^3 MPa)	30	15	7.5
E^s (10^3 MPa)	200	100	50

and C parallel to the foundation pit, and the right curve is the degree of impact of the longitudinal walls of buildings A, B, and C perpendicular to the foundation pit.

The comprehensive analysis set out in Figure 17 shows the following: ① of the four influencing factors, the horizontal distance between the building and foundation pit and the stiffness of the building itself have a relatively clear influence on the deformation of the building, especially the differential settlement and relative deflection of the building; ② regardless of whether the longitudinal wall of the building is parallel or perpendicular to the foundation pit, the degree of influence of the four deformation parameters of building A is larger than that of the other two locations, which is related to the complexity of the deformation near the connection between the shield shaft and the shaft section; ③ for the inclined and torsional deformation of the building in the direction of the foundation pit, in addition to the factors of the building itself, the influence of the stiffness on the bracing in the foundation pit cannot be ignored, as shown in Figures 17(a) and 17(c). The second influence is the stiffness of the foundation-pit retaining structure.

From the perspective of the relative position relationship between the building and the foundation pit, the deformation parameters of the building vary greatly with its location, and the position of building A is still the most clearly affected.

5.2. Interaction between Foundation-Pit Construction and Surrounding Buildings. In addition to the influence of the foundation-pit excavation on the building described above,

there will also be some interaction between the building and foundation pit in the process of the foundation-pit excavation, and the degree of interaction between the two will differ because of the different design schemes of foundation-pit support structures and surrounding environmental conditions. Through further analysis of the 54 testing schemes of deformation parameter trends along with the change in the main influencing factors, establishing the most and least favorable excavation and surrounding environmental conditions is possible. In this way, it is possible to not only optimize the design scheme but also design a subway-station foundation-pit engineering and safety risk assessment targeted at taking effective control measures.

Figures 18 and 19 show building deformation under the influence of different design schemes for foundation-pit support systems and the relative position relationship, respectively. Because the differential settlement and relative deflection of the building are five orders of magnitude larger than the tilt and torsion angles, to identify the four deformation parameters simultaneously and then determine the comprehensive deformation of the building, the calculated results are normalized in the figure; i.e., the ordinate is the degree of deformation after the normalization of the four deformation parameters.

As shown in Figures 18 and 19, when the longitudinal wall of the building is parallel to the foundation pit, the scheme with the minimum comprehensive deformation of buildings A, B, and C is no. 3, no. 2, and no. 3, respectively, the distance between the building and foundation pit is at the minimum, stiffness of the building is medium or above, and stiffness of the retaining structure and inner support is medium or below. The maximum comprehensive deformation is no. 7, no. 8, and no. 7, respectively. At this point, the distance between the building and foundation pit is the largest, building stiffness is medium or below, stiffness of the envelope structure is at the maximum or minimum, and stiffness of the inner support is medium or below.

When the longitudinal wall of the building is perpendicular to the foundation pit, the minimum comprehensive deformations of buildings A, B, and C are no. 8, no. 3, and

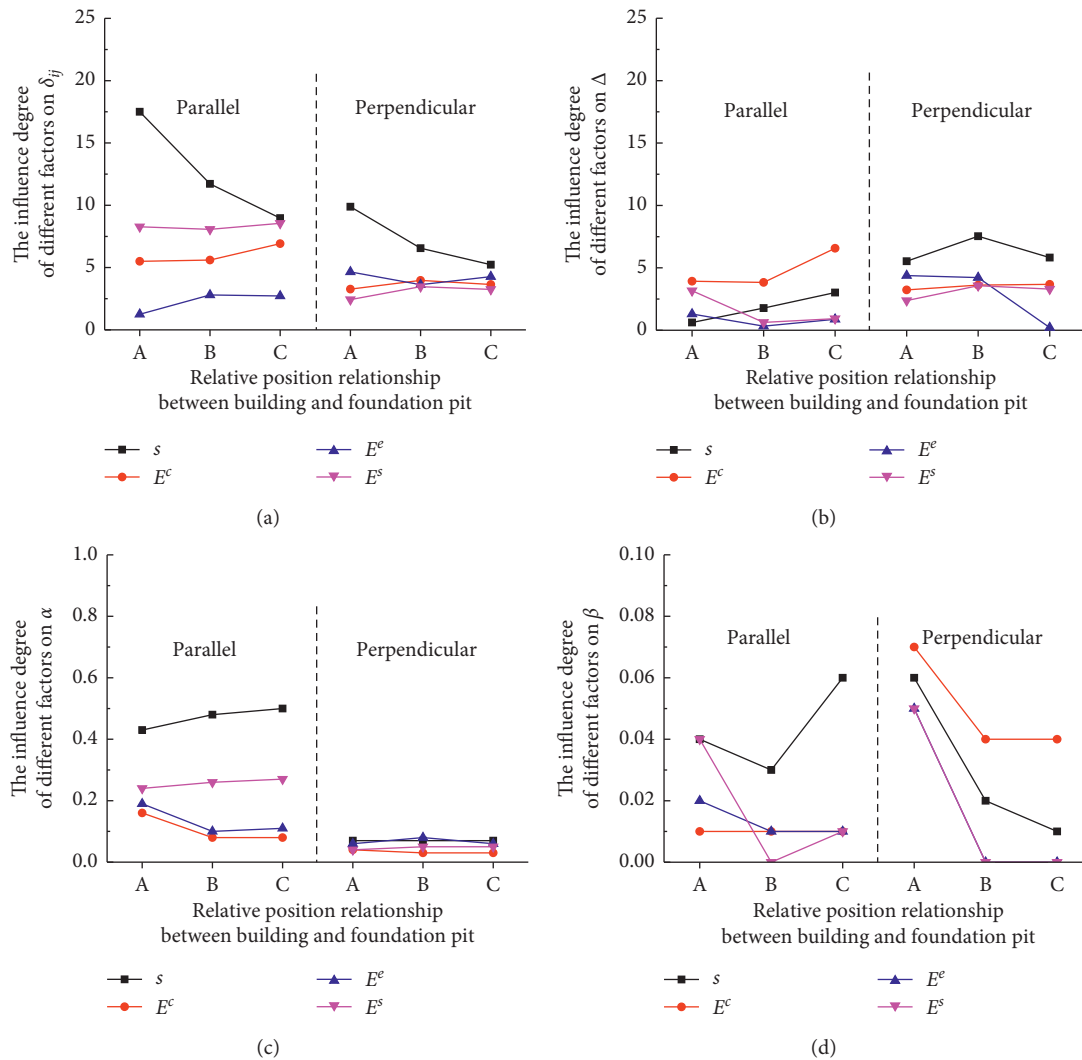


FIGURE 17: Influence of different factors and relative position on building deformation. (a) δ_{ij} . (b) Δ . (c) α . (d) β .

no. 8, respectively. At this point, the distance between the building and foundation pit is at the maximum and minimum, stiffness of the building is medium and above, stiffness of the retaining structure of the foundation pit is at the maximum and minimum, and stiffness of the inner support is medium and below. The maximum comprehensive deformations are no. 4, no. 7, and no. 7. In this case, the distance between the building and foundation pit is medium or above, building stiffness is at the minimum, and stiffness of the retaining structure and inner support of the foundation pit is medium or below.

Through the above analysis, it can be seen that the maximum or minimum comprehensive deformation of buildings with different relative position relationships is determined through various influencing factors. When the distance between the building and foundation pit is small, the deformation of the building may be smaller than when the distance is large. The deformation of a building with greater stiffness may also be greater than that of a building with less stiffness. Due to the diversity in forms of building deformation and influencing factors, judging the impact of

foundation-pit excavation on buildings using only a single deformation or factor may lead to incomplete results. Therefore, a comprehensive evaluation method that can integrate a variety of influencing factors and deformation forms is needed.

5.3. Comprehensive Evaluation of the Deformation Response of Surrounding Buildings. This section continues the corresponding systematic evaluation of building deformation as a result of foundation-pit excavation from two perspectives: the influence of various deformation indexes and influencing factors on comprehensive deformation and the interaction between foundation-pit excavation and buildings.

5.3.1. Influence of Various Deformation Indexes on the Comprehensive Deformation of Buildings. By calculating the average value of the proportion of normalized deformation parameters in the comprehensive deformation index in the 54 schemes, the degree of influence of the four kinds of deformation on the comprehensive deformation index of the

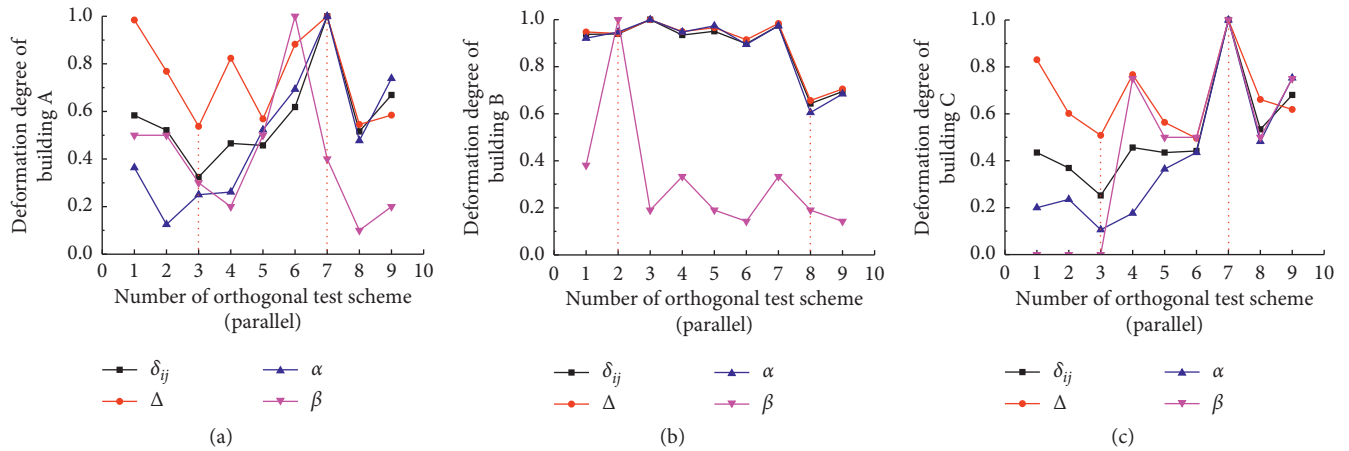


FIGURE 18: The variation trend of four deformation parameters in different test schemes (parallel to the foundation pit). (a) Building A. (b) Building B. (c) Building C.

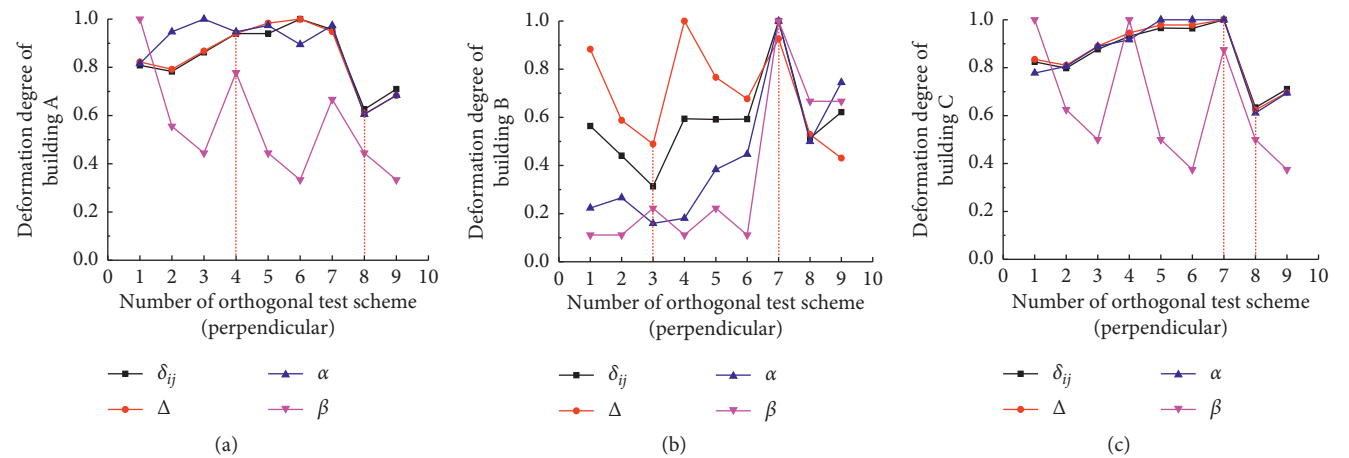


FIGURE 19: The variation trend of four deformation parameters in different test schemes (perpendicular to the foundation pit). (a) Building A. (b) Building B. (c) Building C.

building under different relative position relationships can be obtained, as shown in Figure 20. When the longitudinal wall of the building is parallel to the foundation pit, the relative deflection of the building has the greatest influence on the comprehensive deformation, followed by the differential settlement deformation. When the longitudinal wall of the building is perpendicular to the foundation pit, differential settlement, relative deflection, and inclined angle have an almost equal effect on the comprehensive deformation, and the torsion angle has the least effect.

In this paper, the sum of the normalized values of the four deformation indexes of the building is called the comprehensive deformation index D_j , which is used to measure the overall degree of deformation of the surrounding buildings after foundation-pit excavation. Figure 21 shows the distribution range and proportion of the comprehensive deformation index of all buildings in the 54 schemes under different relative position relationships between the buildings and foundation pits. When the

longitudinal wall of the building is parallel to the foundation pit, the ratio of the comprehensive deformation index of the surrounding buildings between 1 and 3 is the largest; of these, the comprehensive deformation index between 1 and 2 accounted for 51.8%, and that between 2 and 3 accounted for 29.6%. The comprehensive deformation index of the building between 0 and 1 is less than 5%, and that of more than 3 accounts for 14.8%. When the longitudinal wall of the building is perpendicular to the foundation pit, the distribution of the building comprehensive deformation index between 0 and 2 is approximately zero, and the proportion between 2 and 3 accounts for 25.9%; the proportion greater than 3 is the largest, accounting for 74.1%.

When Figures 20 and 21 are combined, the comprehensive influence of foundation-pit excavation on the deformation of surrounding buildings under different relative position relationships can be accurately judged, as can the degree of influence of the various deformation indexes on the comprehensive deformation of the surrounding

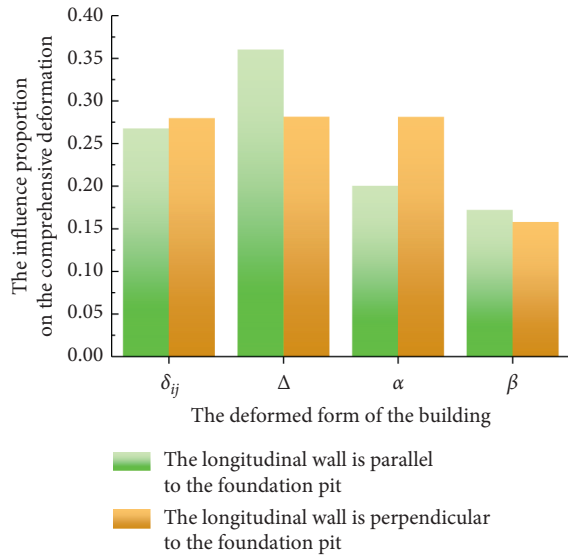


FIGURE 20: Influence of building-deformation parameters on the comprehensive deformation index.

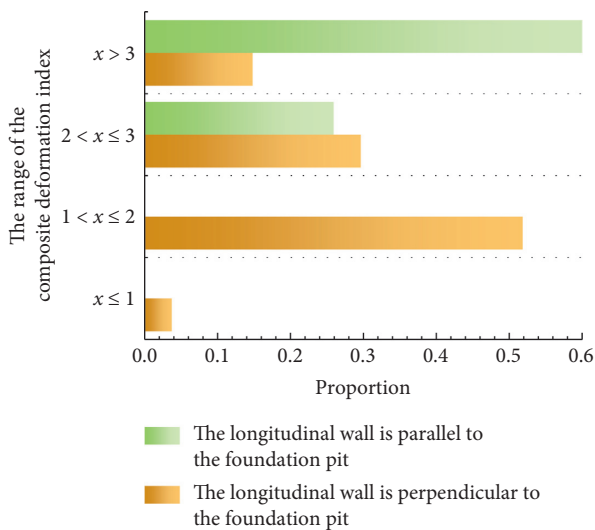


FIGURE 21: The distribution of the composite deformation index under different relative position relationships of buildings.

environment. To a certain extent, this can provide the basis for deformation prediction and the safety evaluation of similar projects.

5.3.2. The Influence of Various Factors from the Surrounding Environment on Comprehensive Deformation. To express the degree of influence of the four factors more intuitively, the degree of each influence factor was assigned to I, II, and III according to the order of the calculation parameters from small to large, and specific values were assigned to each level, as shown in Table 6. The average value of each deformation parameter was then calculated according to the calculation results of the 54 experimental schemes using three grades: low, medium, and high. Finally, the absolute value of the difference between the maximum and minimum values of

the three average values was taken as the criterion to judge the degree of influence of the factor on each deformation parameter.

Taking differential settlement, one of the deformation parameters, as an example, in Table 7, $\bar{a}_i(\delta^v)$, $\bar{b}_i(\delta^v)$, $\bar{c}_i(\delta^v)$, and $\bar{d}_i(\delta^v)$ represent the average values of the differential settlement calculated at each level ($I = 1, 2, 3$) of the four influencing factors, i.e., the distance between the building and foundation pit S_j , building stiffness E_j^c , stiffness of the retaining structure of the foundation pit E_j^e , and stiffness of the internal support E_j^s . The values $r_s(\delta^v)$, $r_{Ec}(\delta^v)$, $r_{Ee}(\delta^v)$, and $r_{Es}(\delta^v)$ represent the degree of influence of the four influencing factors on the differential settlement, respectively: the distance between the building and the foundation pit S_j , stiffness of the building E_j^c , stiffness of the retaining structure of the foundation pit E_j^e , and stiffness of the internal support E_j^s . The calculation method considers the influence of the distance between the building and foundation pit on differential settlement as an example, as shown in equations (1) and (2). The calculation method for the degree of influence of each factor on other deformation parameters can be referred to and will not be described here.

$$\bar{a}_i(\delta^v) = \frac{\sum_{i=1}^3 s_i(\delta^v)}{3}, \quad (1)$$

$$r_s(\delta^v) = \text{Max}\{\bar{a}_i(\delta^v)\} - \text{Min}\{\bar{a}_i(\delta^v)\}. \quad (2)$$

After the degree of influence of each factor on the different deformation parameters is obtained, the average value of the degree of influence of this factor on all deformation parameters is calculated, and the comprehensive influence index R of each factor on building deformation is obtained. For example, the comprehensive influence index of the distance between the building and foundation pit on building deformation is shown in equation:

$$R_s = \frac{r_s(\delta^v) + r_s(\Delta) + r_s(\alpha) + r_s(\beta)}{4}, \quad (3)$$

where $r_s(\Delta)$, $r_s(\alpha)$, and $r_s(\beta)$ are the degree of influence of the distance between the building and foundation pit on the relative deflection, tilt angle, and torsion angle of the building, respectively. The calculation method for the comprehensive degree of influence of other factors on building deformation can be conducted using references and will not be repeated herein. Thus, the comprehensive degree of influence of the various factors on building deformation when the longitudinal wall of the building is parallel and perpendicular to the foundation pit is obtained, as shown in Table 8.

When the assigned value of each influencing factor in Table 6 is multiplied by the comprehensive degree of influence of each influencing factor in Table 8, the safety evaluation index S_j of each scheme can be obtained. To verify the reliability of the safety evaluation index, the comprehensive deformation of the 54 schemes was sorted, as shown in Figure 22. The comprehensive deformation index is the sum of the normalized values of the deformation parameters

TABLE 6: The grade division and assignment of influencing factors.

Influencing factor level	s (m)	$E^c 10^3$ (MPa) ^c	$E^e 10^3$ (MPa) ^c	$E^s 10^3$ (MPa) ^c	Graphics and assignment
I (low)	5	0.2	7.5	50	1
II (medium)	10	0.4	15	100	2
III (high)	15	0.6	30	200	3

TABLE 7: Calculation table of the degree of influence of the four factors on δ_{ij} .

Level i	δ_{ij}			
	s	E^c	E^e	E^s
1	$\bar{a}_1(\delta^v)$	$\bar{b}_1(\delta^v)$	$\bar{c}_1(\delta^v)$	$\bar{d}_1(\delta^v)$
2	$\bar{a}_2(\delta^v)$	$\bar{b}_2(\delta^v)$	$\bar{c}_2(\delta^v)$	$\bar{d}_2(\delta^v)$
3	$\bar{a}_3(\delta^v)$	$\bar{b}_3(\delta^v)$	$\bar{c}_3(\delta^v)$	$\bar{d}_3(\delta^v)$
$r(\delta^v)$	$r_s(\delta^v)$	$r_{E^c}(\delta^v)$	$r_{E^e}(\delta^v)$	$r_{E^s}(\delta^v)$

TABLE 8: The comprehensive degree of influence of various factors on building deformation.

Relative position relation	s	E^c	E^e	E^s
Parallel to the foundation pit	0.40	0.25	0.12	0.23
Perpendicular to the foundation pit	0.34	0.30	0.20	0.17

L_j	s	E^c	E^e	E^s	D_j	S_j
9	3	3	2	3	1.41	2.91
8	3	2	3	1	1.64	2.34
7	2	3	3	2	1.75	2.39
6	2	2	1	3	1.91	2.12
5	2	1	2	1	2.05	1.55
4	1	1	3	3	2.19	1.69
3	3	1	1	2	2.43	2.07
2	1	2	2	2	3.19	1.6
1	1	3	1	1	3.40	1.51

L_j	s	E^c	E^e	E^s	D_j	S_j
9	3	2	3	1	2.10	2.36
8	3	3	2	3	2.23	2.78
7	1	2	2	2	2.85	1.63
6	1	3	1	1	3.08	1.57
5	2	3	3	2	3.16	2.46
4	2	2	1	3	3.19	1.95
3	1	1	3	3	3.19	1.69
2	3	1	1	2	3.27	1.85
1	2	1	2	1	3.83	1.53

(a)

L_j	s	E^c	E^e	E^s	D_j	S_j
9	3	3	2	3	0.87	2.91
8	2	3	3	2	1.21	2.39
7	3	2	3	1	1.47	2.34
6	3	1	1	2	1.86	2.07
5	2	2	1	3	1.87	2.12
4	1	2	2	2	2.15	1.6
3	1	1	3	3	2.18	1.69
2	2	1	2	1	2.80	1.55
1	1	3	1	1	4.0	1.51

L_j	s	E^c	E^e	E^s	D_j	S_j
9	3	3	2	3	2.28	2.78
8	2	3	3	2	2.41	2.46
7	3	2	3	1	3.08	2.36
6	2	2	1	3	3.17	1.95
5	3	1	1	2	3.23	1.85
4	1	1	3	3	3.34	1.69
3	1	2	2	2	3.45	1.63
2	2	1	2	1	3.55	1.53
1	1	3	1	1	3.61	1.57

(b)

FIGURE 22: Continued.

L_j	s	E^c	E^e	E^s	D_j	S_j
9	3	3	2	3	1.18	2.91
8	3	2	3	1	1.41	2.34
7	2	3	3	2	1.78	2.39
6	3	1	1	2	1.83	2.07
5	2	2	1	3	1.89	2.12
4	1	1	3	3	1.96	1.69
3	1	2	2	2	2.21	1.6
2	2	1	2	1	2.46	1.55
1	1	3	1	1	3.93	1.51

(c)

FIGURE 22: Comprehensive deformation index (D_j) and safety evaluation index (S_j) of surrounding buildings under different schemes. (a) Building A. (b) Building B. (c) Building C.

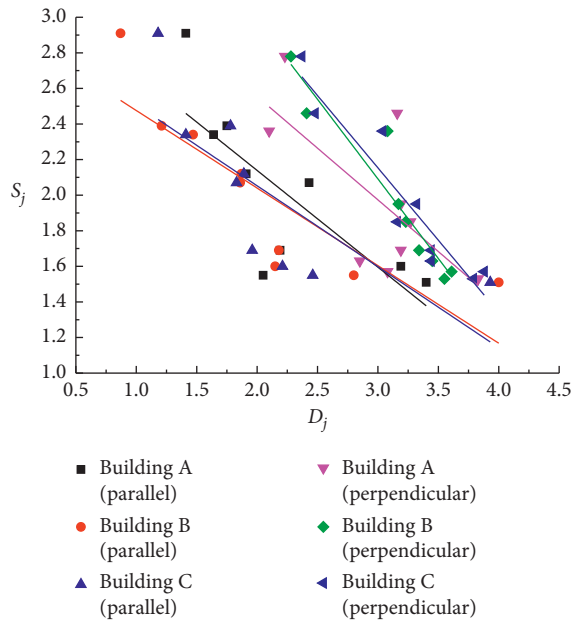


FIGURE 23: Relationship between the comprehensive deformation index (D_j) and safety evaluation index (S_j) of surrounding buildings.

corresponding to each scheme in Figures 18 and 19: the larger the sum, the greater the comprehensive deformation index; the smaller the sum, the lower the comprehensive deformation index; and the smaller the comprehensive deformation index, the higher the safety level of the scheme.

Therefore, the comprehensive deformation index is sorted from small to large, and the corresponding safety level of each scheme is ranked from high to low, as shown in columns 1 and 6 of each table in Figure 22. Columns 2 to 5 are the grades of the four influencing factors corresponding to each scheme and are multiplied by the comprehensive degree of influence of each influencing factor on building deformation under the corresponding relative position

L_j	s	E^c	E^e	E^s	D_j	S_j
9	3	3	2	3	2.37	2.78
8	2	3	3	2	2.48	2.46
7	3	2	3	1	3.04	2.36
6	3	1	1	2	3.16	1.85
5	2	2	1	3	3.32	1.95
4	1	1	3	3	3.44	1.69
3	1	2	2	2	3.44	1.63
2	2	1	2	1	3.79	1.53
1	1	3	1	1	3.88	1.57

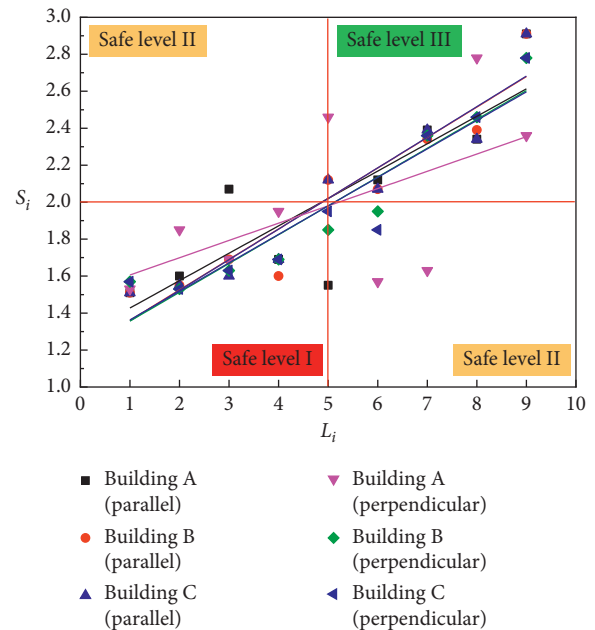


FIGURE 24: The relationship between the safety grade (L_j) of the scheme and safety evaluation index (S_j) of the surrounding buildings.

relationship set out in Table 8; the corresponding safety evaluation index S_j can be obtained for each scheme.

As can be observed, with an increase in the comprehensive deformation index of each table in Figure 22, the corresponding safety evaluation index shows a downward trend. This rule can be expressed intuitively, as in Figure 23. The relationship between the building comprehensive deformation index D_j and safety evaluation index S_j can be expressed by (4), where $-0.89 < m \leq -0.43$, $2.9 < n \leq 4.8$:

$$D_j = mS_j + n. \tag{4}$$

Moreover, according to Figure 22, the relationship between the scheme safety level L_j and safety evaluation index S_j can be obtained, as shown in Figure 24. A certain linear

TABLE 9: Safety evaluation of building-deformation response during foundation-pit excavation and corresponding grade description.

Safety level evaluation	Basis of evaluation		Description of basis	Description of the safety degree
	S_j	L_j		
Level III	2~3	5~9	Both the safety evaluation index and the safety grade of the scheme are high	The safety reserve of the foundation-pit design scheme is larger or the surrounding environment deformation is less affected by the excavation of the foundation pit
Level II	2~3	1~5	The safety evaluation index is higher, but the safety grade of the scheme is lower	The safety reserve of the foundation-pit design scheme is small or the surrounding environment deformation is less affected by the foundation-pit excavation
	1~2	5~9	The safety level of the scheme is higher, but the safety evaluation index is lower	The design of the foundation pit has a high safety reserve or the surrounding environment or the deformation of the surrounding environment is greatly affected by the excavation of the foundation pit
Level I	1~2	1~5	Both the safety evaluation index and the safety grade of the scheme are lower	The safety reserve of the foundation-pit design is lower or the surrounding environment or the deformation of the surrounding environment is greatly affected by the excavation of the foundation pit

relationship exists between the two, as shown in equation (5), where $0.09 < a \leq 0.17$, $1.2 < b \leq 1.5$:

$$S_j = aL_j + b. \quad (5)$$

Figure 24 can be further divided to clarify the criterion for the environmental impact of the relationship between the environmental safety evaluation index around foundation pit and the safety level of the scheme. In this figure, the relationship between the safety evaluation index of the building and safety level of the scheme has a common intersection point, which is roughly located at the positions of $S_j=2$ and $L_j=5$. With this intersection point as the center, the horizontal and vertical symmetrical middle lines and red line segments in Figure 24 can be drawn. The two lines divide the diagram into four parts so that the environmental safety situation can be judged simultaneously according to the safety evaluation index and safety level of the scheme, as shown in Table 9.

6. Conclusion

- (1) The horizontal distance between the building and foundation pit and stiffness of the building itself are the factors that have a clear influence on the deformation of the building, especially the difference settlement and relative deflection of the building. Regardless of whether the longitudinal wall of the building is perpendicular or parallel to the foundation pit, the influence of the four deformation parameters of the building near the pit angle is greater than that of the building at the other two locations. For the tilt and torsion of the building toward the foundation pit, in addition to the factors relating to the building itself, the influence of the stiffness of the bracing in the foundation pit cannot be ignored.
- (2) When the longitudinal wall of the building is parallel to the foundation pit, the relative deflection of the building has the greatest influence on the

comprehensive deformation, followed by the differential settlement deformation. The proportion of distribution of the building comprehensive deformation index is the largest between 1 and 3. When the longitudinal wall of the building is perpendicular to the foundation pit, the differential settlement, relative deflection, and inclined-angle deformation of the building have the same effect on the comprehensive deformation, and the torsion angle has the least effect; the proportion of the comprehensive deformation index greater than 3 is the largest.

- (3) The influence of various factors relating to the surrounding environment on the comprehensive deformation can be determined by defining the comprehensive deformation index D_j , peripheral environmental safety evaluation index S_j , and scheme safety levels L_j ; then further analysis of the relationship among the three indexes is based on the above three indicators. By combining the comprehensive deformation arrangement scheme safety grade with the degree of influence of the various factors on comprehensive deformation, an environmental response evaluation method of the multiangle safety evaluation index can be obtained.

Glossary

- L : Length of the foundation pit's retaining structure
 B : Width of the foundation pit's retaining structure
 H_c : Excavation depth of the foundation pit's retaining structure
 H : Depth of the foundation pit's retaining structure
 d : Diameter of the bored pile
 l : Spacing of the bored pile
 H : Depth of the bored pile
 E : Stiffness of the bored pile
 δ_{ij} : Primarily uneven settlement
 Δ : Overall deflection
 α : Inclination toward the pit
 β : Torsion

- s : The horizontal distance between the building and foundation pit
 E_c : The stiffness of the building wall
 E^e : The stiffness of the retaining structure
 E^s : The stiffness of the internal support
 D_j : The comprehensive deformation index
 R : The comprehensive influence index
 S_j : The corresponding safety evaluation index
 L_j : The scheme safety level.

Data Availability

The measured data used to support the findings of this study are included within the article.

Conflicts of Interest

The authors declare that they have no conflicts of interest.

Acknowledgments

This research was supported by the National Natural Science Foundation of China, Grant no. 51278233, and Science and Technology Project of China Communications First Bureau Group Co. Ltd, Grant no. 4GS(J)-GUD-GCL-01-JS-016.

References

- [1] H. Bin, X. Li, and L. Zheng, "Influences of urban viaduct pier caps on uneven settlement of roadbed," *Advances in Civil Engineering*, vol. 2019, Article ID 4151278, 20 pages, 2019.
- [2] H. Li, E. Ma, J. Lai et al., "Tunnelling-Induced settlement and treatment techniques for a loess metro in Xi'an," *Advances in Civil Engineering*, vol. 2020, Article ID 1854813, 20 pages, 2020.
- [3] X. Weng, R. Zhou, W. Rao, and D. Wang, "Research on subway shield tunnel induced by local water immersion of collapsible loess," *Natural Hazards*, vol. 2021, 2021.
- [4] Q. Fang, J. Du, J. Li, D. Zhang, and L. Cao, "Settlement characteristics of large-diameter shield excavation below existing subway in close vicinity," *Journal of Central South University*, vol. 28, no. 3, pp. 882–897, 2021.
- [5] H. Zheng, P. Li, and G. Ma, "Stability analysis of the middle soil pillar for asymmetric parallel tunnels by using model testing and numerical simulations," *Tunnelling and Under-ground Space Technology*, vol. 108, Article ID 103686, 2020.
- [6] S. He, J. Lai, Y. Zhong et al., "Damage behaviors, prediction methods and prevention methods of rockburst in 13 deep traffic tunnels in China," *Engineering Failure Analysis*, vol. 121, Article ID 105178, 2021.
- [7] S. Xu, H. Lei, C. Li, H. Liu, J. Lai, and T. Liu, "Model test on mechanical characteristics of shallow tunnel excavation failure in gully topography," *Engineering Failure Analysis*, vol. 119, Article ID 104978, 2021.
- [8] D. Li and C. Yan, "Building deformation prediction based on ground surface settlements of metro-station deep excavation," *Advances in Civil Engineering*, vol. 2018, Article ID 6050353, 14 pages, 2018.
- [9] Y.-Y. Liang, N.-W. Liu, F. Yu, X.-N. Gong, and Y.-T. Chen, "Prediction of response of existing building piles to adjacent deep excavation in soft clay," *Advances in Civil Engineering*, vol. 2019, Article ID 8914708, 11 pages, 2019.
- [10] J. Zhang, R. Zhang, L. Ding, Q. Chen, and D. Zhao, "Displacement control effects and parameter analysis of passive zone improvement of foundation pits," *Chinese Journal of Rock Mechanics and Engineering*, vol. 29, no. 5, pp. 1042–1051, 2010.
- [11] Q. Cheng, G. Liu, and W. Zhang, "Deformation analysis of subway ultra-deep and deep excavation in Shanghai by FEM," *Chinese Journal of Under-ground Space and Engineering*, vol. 5, no. 2, pp. 1497–1502, 2009.
- [12] Z. Li, W. Lin, Y. Zhu et al., "Field test and analysis of controlling metro excavations deformation by foundation reinforcement," *Journal of Zhejiang University (Engineering Edition)*, vol. 51, no. 8, pp. 1475–1481, 2017.
- [13] X. Ren, *Analysis of the Effect of Deformation on the Shanghai Subway Station Foundation Pit Basement Reinforcement*, Tongji University, Shanghai, China, 2009.
- [14] E. J. Cording, T. D. O'Rourke, and M. Boscardin, "Ground movements and damage to structures," in *Proceedings of the International Conference on Evaluation and Prediction of Subsidence*, S. K. Saxena, Ed., ASCE, New York, NY, USA, pp. 516–537, November 1978.
- [15] S. J. Boone, J. Westland, and R. Nusink, "Comparative evaluation of building responses to an adjacent braced excavation," *Canadian Geotechnical Journal*, vol. 36, no. 2, pp. 210–223, 1999.
- [16] A. W. Skempton and D. H. MacDonald, "The allowable settlements of buildings," *Proceedings of the Institution of Civil Engineers*, vol. 5, no. 6, pp. 727–768, 1956.
- [17] J. B. Burland, "Assessment of risk of damage to buildings due to tunneling and excavations. Invited special lecture," in *Proceedings of the First International Conference on Earthquake Geotechnical Engineering, IS-Tokyo'95*, Tokyo, Japan, November 1995.
- [18] J. B. Burland and C. P. Wroth, "Settlement of buildings and associated damage," in *Proceedings of the Conference on Settlement of Structures*, pp. 611–654, Pentech Press, Cambridge, UK, January 1974.
- [19] S. Li, D. Zhang, Q. Fang, and W. Lu, "Research on characteristics of ground surface deformation during deep excavation in Beijing subway," *Chinese Journal of Rock Mechanics and Engineering*, vol. 31, no. 1, pp. 189–198, 2012.
- [20] Z. Li and G. Zheng, "Finite element analysis of response of building with different stiffnesses adjacent to excavation," *Rock and Soil Mechanics*, vol. 34, no. 6, pp. 1807–1814, 2013.
- [21] G. Zheng and Z. Li, "Finite element analysis of adjacent building response to corner effect of excavation," *Journal of Tianjin University*, vol. 45, no. 8, pp. 688–699, 2012.
- [22] G. B. Liu, R. J. Jiang, C. W. W. Ng, and Y. Hong, "Deformation characteristics of a 38 m deep excavation in soft clay," *Canadian Geotechnical Journal*, vol. 48, no. 12, pp. 1817–1828, 2011.
- [23] N. Liu, Y. Chen, X. Gong et al., "Analysis of deformation characteristics of foundation pit of metro station and adjacent buildings induced by deep excavation in soft soil," *Rock and Soil Mechanics*, vol. 40, no. 4, pp. 1515–1525, 2019.
- [24] P. G. Hsieh and C.-Y. Ou, "Shape of ground surface settlement profiles caused by excavation," *Canadian Geotechnical Journal*, vol. 35, no. 6, pp. 1004–1017, 1998.
- [25] T. Benz, *Small Strain Stiffness of Soils and its Numerical consequences*, Institute of Geotechnical Engineering, University of Stuttgart, Stuttgart, Germany, 2007.

Research Article

BP Neural Network Improved by Sparrow Search Algorithm in Predicting Debonding Strain of FRP-Strengthened RC Beams

Guibing Li ¹, Tianyu Hu ¹ and Dawei Bai²

¹School of Management Science and Engineering, Shandong Technology and Business University, Yantai 264005, Shandong, China

²School of Civil Engineering and Transportation, Hohai University, Nanjing 210024, Jiangsu, China

Correspondence should be addressed to Guibing Li; leegb@sina.com

Received 15 March 2021; Accepted 18 May 2021; Published 28 May 2021

Academic Editor: Faming Huang

Copyright © 2021 Guibing Li et al. This is an open access article distributed under the Creative Commons Attribution License, which permits unrestricted use, distribution, and reproduction in any medium, provided the original work is properly cited.

To prevent debonding failure of FRP- (fiber reinforced polymer-) strengthened RC (reinforced concrete) beams, most codes proposed models for debonding strain limitation of FRP reinforcements. However, only a few factors that affect debonding failure are considered in the models. The experimental results show that these models cannot accurately evaluate debonding strain and have a large variability. In order to improve the accuracy of predicting the debonding strain of FRP-strengthened RC beams, a BP neural network model was developed based on the sparrow search algorithm (SSA). To predict the debonding strain of FRP reinforcements, the established neural network model was trained and simulated through experimental data. The results show that the coefficient of variation of the present SSA-BP neural network model is 13%. The main factors affecting debonding strain are the longitudinal reinforcement ratio, stirrup reinforcement ratio, and concrete strength, which are not considered in the code models. The present model has better prediction accuracy and more robustness than the traditional BP neural network and the code models.

1. Introduction

In the past decades, FRP (fiber reinforced polymer) reinforcements have been widely used in the rehabilitation and strengthening of existing reinforced concrete (RC) structures due to their lightweight, high strength, and good corrosion resistance [1]. Many researchers have conducted experimental and numerical studies on the flexural performance of FRP-strengthened RC beams [2–6]. Intermediate crack-induced debonding failure is the dominant failure mode of FRP-strengthened RC beams. Most of the codes have proposed different models of debonding strain limitation for prevention of debonding failure [7–10]. ACI440.2R [7] corrected the model of Teng [11] based on the maximum tensile strain of the FRP-strengthened RC beams with intermediate crack-induced debonding failure and proposed a model to limit the debonding strain of FRP reinforcements. Kim and Harries [12] proposed a statistical model of FRP effective strain based on the Monte Carlo

method. Oller et al. [13] established the model of FRP-concrete interface ultimate tensile based on nonlinear fracture mechanics and the bilinear constitutive relationship of the FRP-concrete interface. Lu et al. [14] proposed a model of FRP ultimate tensile strain based on the shear test and finite element analysis. Bilotta et al. [15] established the standard value and design value calculation model of the maximum tensile strain of FRP reinforcements. However, the experimental results and statistical analysis [13, 16–18] show that these models cannot evaluate debonding strain accurately and have a large coefficient of variation as only a few factors that affect the debonding strain are considered in these models.

In the recent decades, the BP neural network has been applied in various fields of civil engineering, including the assessment of compressive strength of ultrahigh-performance concrete [19], the study of material intrinsic model [20], and prediction of shear strength and behavior of RC beams strengthened with externally bonded FRP sheets [21],

but the research on the debonding strain of FRP-strengthened RC beams is still relatively rare [22]. Since many factors are affecting the debonding failure, such as the mechanical properties of materials, the geometry of the member, deformation and cracks of the specimen, etc., and there are complex nonlinear relationships between the debonding strain and each parameter, the calculation formulas established based on theoretical and experimental results usually have low accuracy and large variability, which cannot prevent the debonding failure of FRP-strengthened beams. The BP neural network has the characteristics of nonlinear mapping theoretically and can provide a better simulation of complex nonlinear relationships. However, in the determination of weights and thresholds using the gradient descent method, the BP neural network is easy to lead the model into the local optimum and make convergence speed slow; it needs to be improved by a better algorithm [23]. This paper introduced the sparrow search algorithm (SSA) to optimize the weights and thresholds of the network [24] and the nonlinear mapping relationship between each parameter and the debonding strains of FRP-strengthened RC beams.

2. BP Neural Network and Sparrow Search Algorithm

2.1. BP Neural Network. BP (backpropagation) neural network is a multilayer forward neural network trained according to the error backpropagation algorithm, including the input layer, hidden layer, and output layer. It uses gradient descent to adjust the weights and thresholds for each layer of the neuron to reduce errors in the network output until the errors reach a given error convergence level before training the network. The BP neural network can perform arbitrary nonlinear mapping of input and output and realize self-learning and simple structure, but the disadvantage of the BP neural network is that it is easy to drop to a local minimum and has poor stability [22–24]. The basic structure of the BP neural network is shown in Figure 1.

The rules for the collection of experimental data are as follows:

2.2. Sparrow Search Algorithm. The sparrow search algorithm (SSA) is a novel swarm intelligence optimization algorithm proposed in 2020, mainly inspired by the foraging and antipredatory behavior of sparrows [25, 26].

In the sparrow search algorithm, the priority to obtain food is the sparrow with a higher fitness value. Besides, the sparrow as a discoverer searches for a target for the whole population and directs the joiners to search for food (target), i.e., the sparrow as a discoverer has a larger search range compared with the joiners. As the iteration proceeds, the location of the sparrow as a discoverer is described in the following equation:

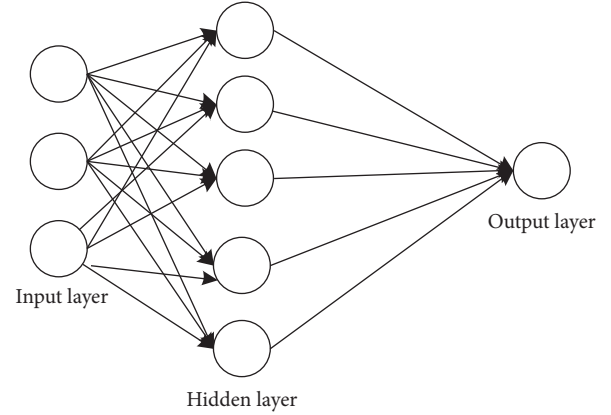


FIGURE 1: Structure diagram of neural network.

$$X_{i,j}^{t+1} = \begin{cases} X_{i,j}^t \cdot \exp\left(\frac{-i}{\alpha \cdot \text{iter}_{\max}}\right), & \text{if } R_2 < ST, \\ X_{i,j}^t + Q \cdot L, & \text{if } R_2 \geq ST, \end{cases} \quad (1)$$

where t is the current number of iterations and iter_{\max} is a constant representing the maximum number of iterations. $X_{i,j}$ is the position information of the i -th sparrow in the j -th dimension. $\alpha \in (0,1]$ is a random number. R_2 ($R_2 \in [0,1]$) and ST ($ST \in [0.5,1]$) represent the warning value and safety value, respectively. Q is a random number that obeys the normal distribution. L is a $1 \times d$ matrix; each element in the matrix is 1. When $R_2 < ST$, it means that there are no predators around the foraging environment at this time, and the discoverer can perform extensive search operations. When $R_2 \geq ST$, it means that some sparrows in the population have found a predator and have issued an alarm to other sparrows in the population. At this time, all sparrows need to fly to other safe places quickly for food.

The update of the joiner's position is shown in the following equation:

$$X_{i,j}^{t+1} = \begin{cases} Q \cdot \exp\left(\frac{X_{\text{worst}}^t - X_{i,j}^t}{i^2}\right), & \text{if } i > n/2, \\ X_p^{t+1} + |X_{i,j}^t - X_p^{t+1}| \cdot A^+ \cdot L, & \text{otherwise,} \end{cases} \quad (2)$$

where X_p is the best position currently occupied by the discoverer while X_{worst} is the current worst position globally. A is a $1 \times d$ matrix, where each element is randomly assigned a value of 1 or -1, and $A^+ = AT(AAT) - 1$. When $i > n/2$, this indicates that the i -th joiner with a lower fitness value has no food and is in a very hungry state. At this time, it needs to fly to other places to find food to obtain more energy.

When it is aware of the danger, the sparrow population will make antipredation behavior. The mathematical expression is shown in the following equation:

$$X_{i,j}^{t+1} = \begin{cases} X_{\text{best}}^t + \beta \cdot |X_{i,j}^t - X_{\text{best}}^t|, & \text{if } f_i > f_g, \\ X_{i,j}^t + K \cdot \left(\frac{X_{i,j}^t - X_{\text{worst}}^t}{(f_i - f_w) + \varepsilon} \right), & \text{if } f_i = f_g, \end{cases} \quad (3)$$

where X_{best}^t is the current global optimal position. As the step control parameter, β is a random number that obeys the normal distribution with a mean value of 0 and a variance of 1. $K \in [-1, 1]$ is a random number; f_i is the fitness value of the current individual sparrow; and f_g and f_w are the current global best and worst fitness values, respectively. ε is the smallest constant to avoid zero in the denominator.

For the sake of simplicity, when $f_i > f_g$, it means that the sparrow is at the edge of the population and is extremely vulnerable to predators. When $f_i = f_g$, this indicates that the sparrows in the middle of the population are aware of the danger and need to be close to other sparrows to minimize their risk of predation. K is the direction in which the sparrow moves and is also a parameter to control the step length.

The flow chart of the BP neural network optimized by SSA is shown in Figure 2.

3. Determination of Parameters and Collection of Experimental Data

3.1. Determination of Parameters. The FRP-strengthened RC beams mainly consist of FRP sheets, concrete, and steel bars. According to codes and related experimental studies [8–18, 27], the parameters affecting the debonding strain are concrete strength (f_c), FRP stiffness ($E_f t_f$), the ratio of FRP to the length of the strengthened beam (L_f/L), the ratio of FRP to the width of the strengthened beam (b_f/b), the ratio of shear span to the depth of the strengthened beam (λ), longitudinal reinforcement ratio (ρ_s), stirrup reinforcement ratio (ρ_v), and yield strain of steel bars (ε_{sy}).

3.2. Collection of Experimental Data. In order to study the debonding strain of FRP-strengthened RC beams and train the neural network better, this study has collected 60 experimental data from different literatures. The literatures are shown in Table 1.

- (1) The failure mode of the strengthened beams is intermediate crack-induced debonding
- (2) The strengthened beams are under four-point loading
- (3) The end of the FRP is not anchored, and there is no preload before bonding FRP
- (4) The geometric characteristics of the strengthened beams and FRP reinforcements are determined
- (5) The material properties of the test beam and FRP are determined
- (6) The FRP bonding on the soffit of the RC beam is continuous

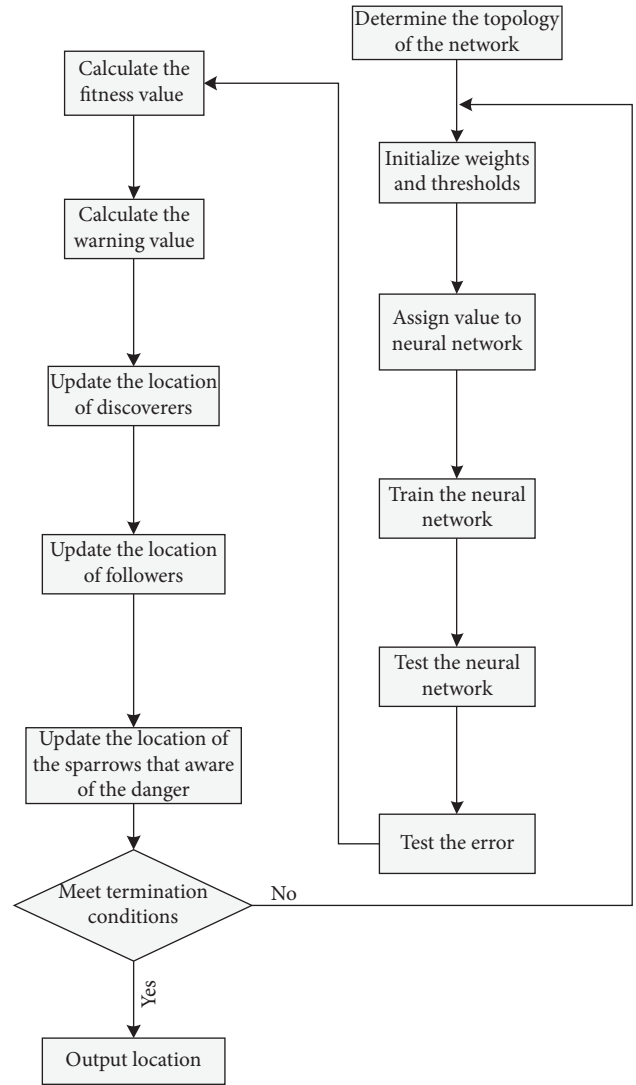


FIGURE 2: Flow chart of SSA-BP.

TABLE 1: Sources of the data.

Reference	Number
[28]	10
[29]	6
[30]	1
[31]	1
[32]	3
[33]	2
[34]	4
[35]	2
[16]	2
[36]	2
[37]	9
[38]	4
[39]	4
[40]	1
[41]	3
[42]	6

The detailed proportion of each parameter is shown in Figure 3.

From Figure 3, the following information can be found:

- (1) The concrete strength (f'_c) is distributed in the range of 10–70 MPa; most of them are 40–50 MPa. The proportion of concrete strength greater than 40 MPa is 73%.
- (2) The FRP stiffness ($E_f t_f$) is between 40 and 210 kN/mm; the distribution of each interval is relatively uniform. The largest segment interval is 150–200 kN/mm that accounts for about 33%.
- (3) The ratio of FRP to the length of the strengthened beam (L_f/L) is between 0.4 and 1.0; most of them are in the range of 0.8–0.9, which accounts for about 70%. This indicates that in most tests, the length of the FRP sheet is close to the length of the beam.
- (4) The ratio of FRP to the width of the strengthened beam width (b_f/b) is between 0.1 and 0.9. There are about 63% of all the beams with ratios greater than 0.7. Most of the sheet width is close to the width of the beam.
- (5) The interval of the ratio of shear span to depth (λ) is 2–5. The ratios are greater than 4, which accounts for 78%, which indicates that most of the test beams have large spans.
- (6) The longitudinal reinforcement ratio (ρ_s) is between 0.3% and 1.8%; the distribution in each interval is relatively even.
- (7) The stirrup reinforcement ratio (ρ_v) is between 0.1% and 1.6%; the distribution in each interval is relatively even.
- (8) The yield strains of steel bars (ε_{sy}) are between 0.0016% and 0.0032; the strains are 0.0024–0.0028 accounting for 84%.

4. Model Design and Simulation

4.1. Design of the Model. Considering the parameters affecting the debonding strain of FRP-strengthened RC beams and the characteristics of neural networks, the design of the model of debonding strain of FRP-strengthened RC beams is as follows:

- (i) Firstly, the concrete strength (f'_c), FRP stiffness ($E_f t_f$), the ratio of FRP to the length of the strengthened beam (L_f/L), the ratio of FRP to the width of the strengthened beam (b_f/b), the ratio of shear span to depth (λ), longitudinal reinforcement ratio (ρ_s), stirrup reinforcement ratio (ρ_v), and the yield strain of steel bars (ε_{sy}) are taken as the input layer of the neural network, and the hidden layer is selected as one layer. The number of neurons in the hidden layer is determined through trials according to the empirical formula. The empirical formula is shown in the following equation:

$$L = \sqrt{m + n} + a, \quad (4)$$

where L is the number of neurons in the hidden layer; m is the number of neurons in the input layer; n is the number of neurons in the output layer; a takes an integer between 1 and 10. Considering the over- and underfitting problems, L is taken as 10 after repeated debugging.

- (ii) Secondly, the debonding strain is taken as the output layer. The topology of the SSA-BP model is shown in Figure 4.

4.2. Model Training and Simulation. The number of samples is 60. The distributions of the training set, validation set, and testing set are freely controlled by the neural network. The results of the SSA-BP neural network and BP neural network are shown in Figures 5–8.

It can be seen from Figures 5 and 6, the SSA-BP model has a higher regression coefficient than BP in the training and testing sets. Also, the overall regression coefficient of the SSA-BP is greater than 0.96, indicating that the present model has high accuracy. Besides, it can be seen from Figures 7 and 8 that the best root-mean-square error of the SSA-BP is 0.0061269 that is greatly lower than that of the BP (0.014484). However, the SSA-BP needs eight iterations to achieve convergence, and the BP only needs six times. This indicates that the SSA-BP needs to be improved in terms of the rate of convergence. To further compare the robustness of SSA-BP and BP, the models were trained and simulated twenty times, and the error comparison is shown in Figure 9.

It can be seen from Figure 9 that the coefficient of variation of SSA-BP is between 13% and 25%, and the coefficient of variation of BP is between 15% and 45%. This indicates that compared with the traditional BP neural network, the neural network optimized by SSA does not only have a relatively small error but also has stronger robustness.

4.3. Correlation Analysis of Parameters. The influence of each parameter on debonding strain is derived by the connection weights between neurons in each layer, where the input layer neurons are represented by $X_1 \sim X_8$; implied layer neurons are represented by $H_1 \sim H_{10}$; and output layer neurons are represented by Y . The connection weights of interlayer neurons are shown in Tables 2 and 3, and the degree of influence of $X_1 \sim X_8$ on Y is calculated in Equation (2), and the calculation results are shown in Figure 10:

$$P_x = \sum_{i=1}^{10} w_{xi} \times h_i, \quad (5)$$

where P_x is the degree of influence of the parameter of the X -th on the debonding strain; w_{xi} is the connection weight between X -th parameter and the i -th implied layer; and h_i is the connection weight between the i implied layer and the output layer, respectively.

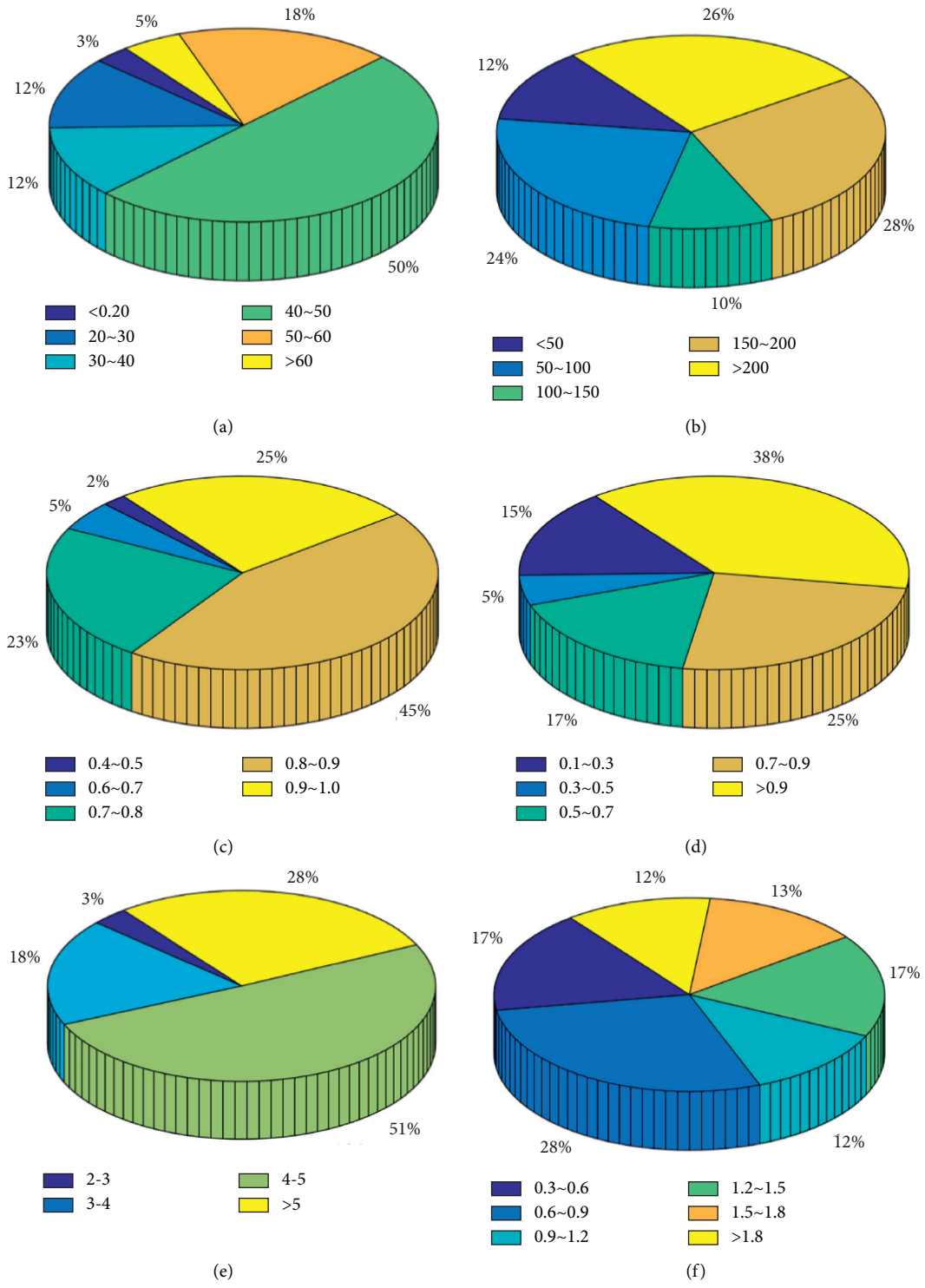


FIGURE 3: Continued.

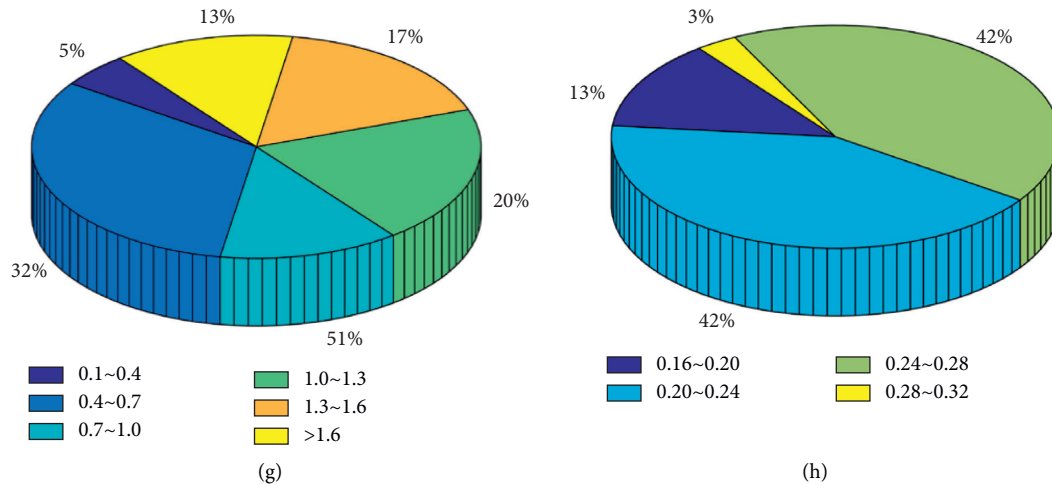


FIGURE 3: Distribution of each parameter: (a) the distribution of concrete strength, (b) the distribution of FRP stiffness, (c) the ratio of sheet length to beam length, (d) the ratio of sheet width to beam width, (e) the shear-to-span ratio, (f) longitudinal reinforcement ratio, (g) stirrup reinforcement ratio, and (h) the yield strain of steel bars.

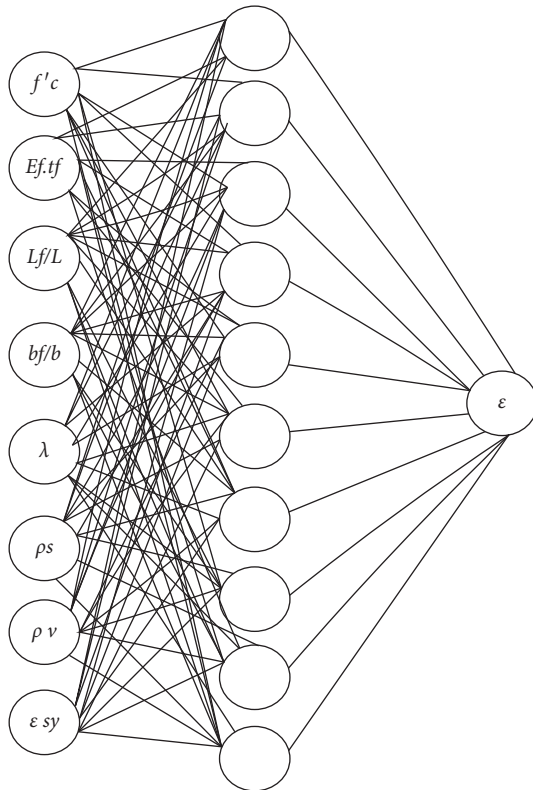


FIGURE 4: Topology of SSA-BP.

From Figure 10, it can be seen that X_1 , X_5 , and X_6 , which are the concrete strength, shear-to-span ratio, and longitudinal reinforcement ratio, respectively, have a greater effect on the debonding strain; they can make the debonding strain of the strengthened beams increase. However, the FRP stiffness, X_2 , is negatively correlated with the debonding strain, indicating that the increase of FRP stiffness will accelerate the debonding of the strengthened beams.

5. Model Evaluation

To further study the effectiveness of the SSA-BP model, the SSA-BP regression value was compared with several current international codes.

The ACI440.2R modified the maximum tensile strain of the FRP reinforcements of flexurally strengthened specimens with intermediate crack-induced debonding failure [7] and proposed the debonding strain limitation of FRP-strengthened RC beams:

$$\varepsilon_{fd} = 0.41 \sqrt{\frac{f'_c}{nE_f t_f}} \leq 0.9\varepsilon_{fu} \quad (6)$$

where ε_{fd} is the debonding strain of FRP-strengthened RC beams; f'_c is the compressive strength of concrete; n is the number of layers of FRP reinforcements; E_f is the elastic modulus of FRP; t_f is the thickness of the single layer of FRP; and ε_{fu} is the ultimate tensile strain of FRP.

The JSCE [8], according to the model proposed by Wu [27], taking into account the degree of crack propagation after the debonding failure of the FRP and concrete interface, recommended that the debonding strain of FRP-strengthened RC beams is calculated as follows:

$$\varepsilon_{fd} \leq \sqrt{\frac{2G_f}{E_f t_f}} \quad (7)$$

where G_f is the fracture energy of the bonding interface between FRP and concrete; it should be determined by testing the strengthened members; and the value is generally taken as 0.5 N/mm.

The debonding strain of FRP-strengthened RC beams in the "Guidelines for the Design of Reinforced Concrete Structures with Fiber Composite Materials" [9] (TR55) issued by the Advisory Committee of Building Technical Regulations of the Italian National Research Council is calculated as follows:

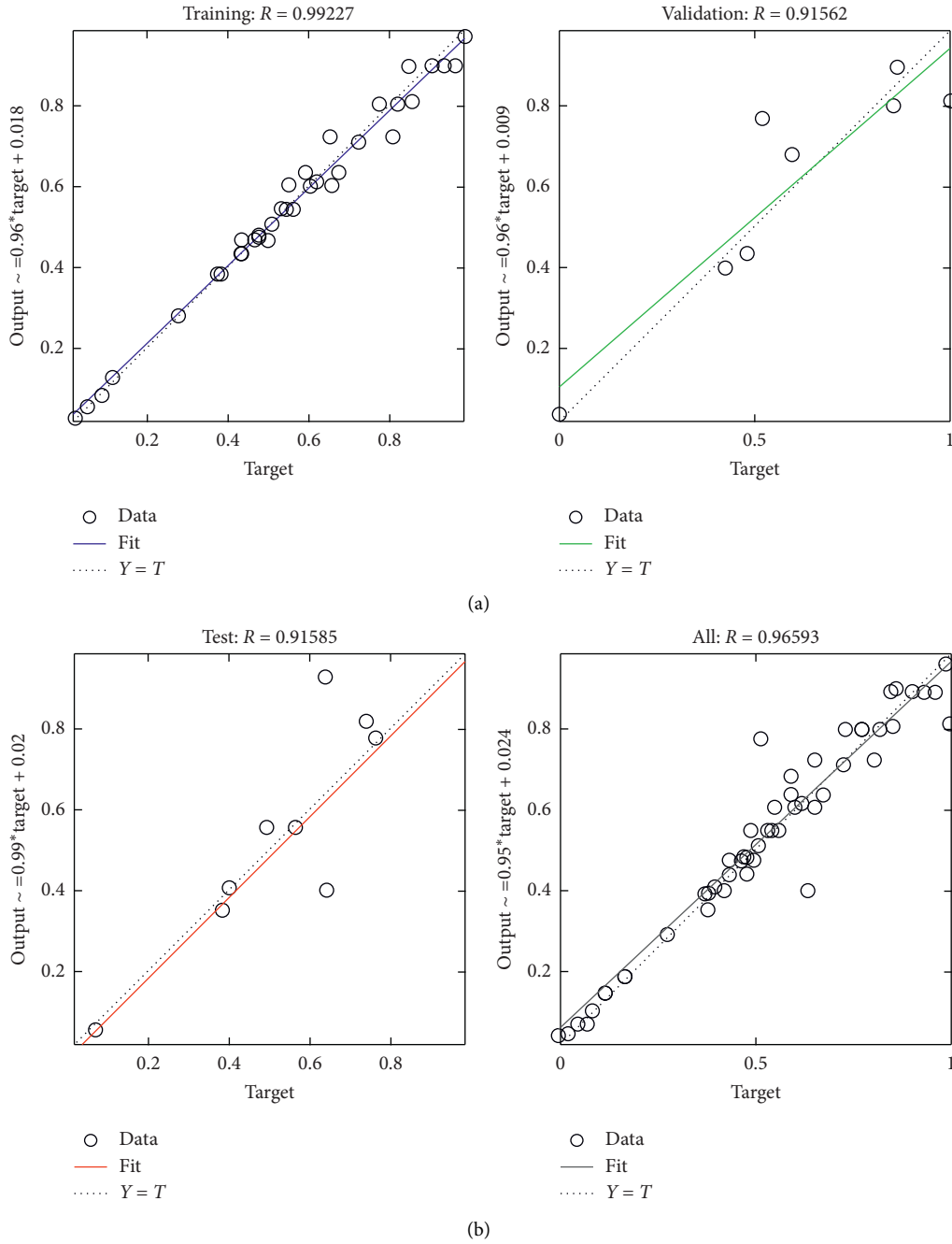


FIGURE 5: Simulation results of SSA-BP.

$$\varepsilon_{fd} = 0.484 \sqrt{\frac{k_b \sqrt{f'_c f_{ct}}}{n E_f t_f}} \quad (8)$$

$$\varepsilon_{fd} = 0.5kb \sqrt{\frac{f_{ct}}{E_f t_f}} \quad (9)$$

where k_b is the width coefficient of FRP reinforcements. The formula for the debonding strain of FRP-strengthened RC beams recommended by the “Fiber Reinforced Materials Reinforced Concrete Structures” [10] (CNR) issued by the British Concrete Association is given in the following equation:

The calculated values by the code models and the predicted value by SSA-BP are shown in Figure 11.

It can be seen from Figure 11 that the model calculation value distribution proposed by the codes is relatively discrete, and SSA-BP is significantly better than JSCE, ACI, CNR, and TR55 in terms of model fit. In addition, Table 4

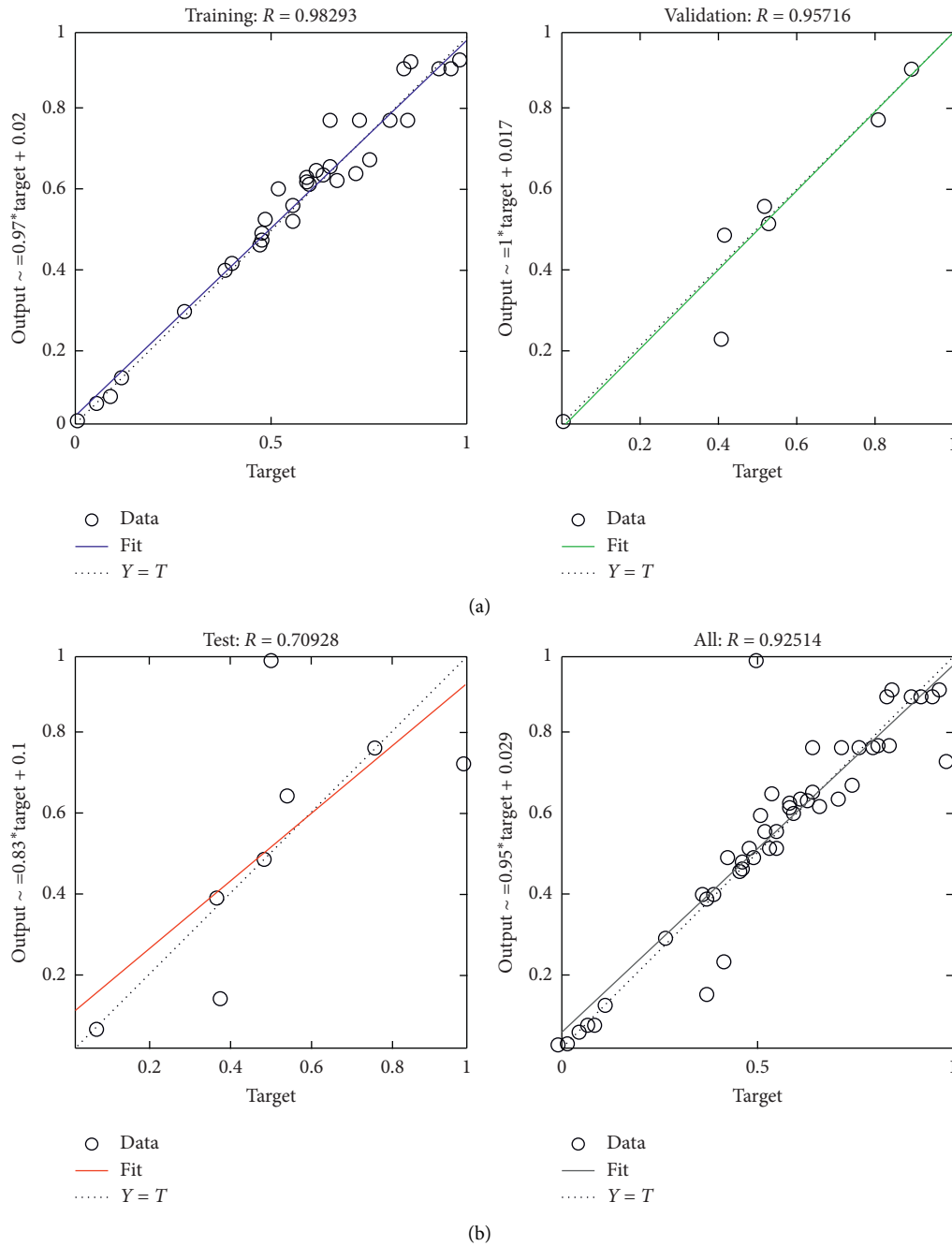


FIGURE 6: Simulation results of BP.

further analyzes the prediction accuracy and robustness of the model built in this study and national codes.

From Table 4, the model values of JSCE, ACI, CNR, TR55, and SSA-BP are 0.22–1.63, 0.50–4.24, 0.24–1.48, 0.20–1.42, and 0.35–1.17 times of the experimental value, respectively. The coefficient of variation of all the code models is greater than 45%. However, the coefficient of

variation of SSA-BP is only 13%. Compared with the codes, SSA-BP has a smaller degree of dispersion. The JSCE, TR55, and CNR models are very conservative with an average less than 0.55; there are about 92%, 93%, and 95% of all the specimens with the predicted value underestimated. The ACI model is significantly overestimated the debonding strain with an average of 1.39, and about 68% of all the

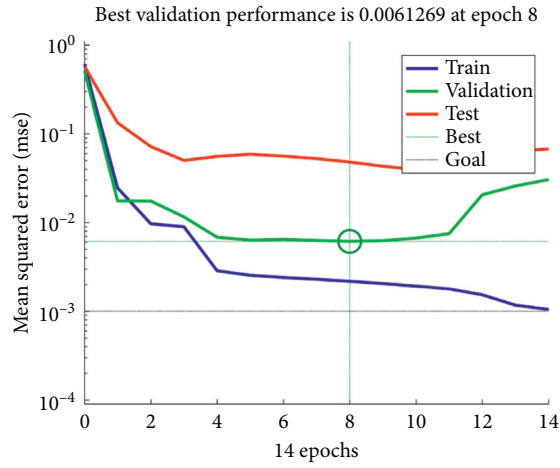


FIGURE 7: Performance of SSA-BP.

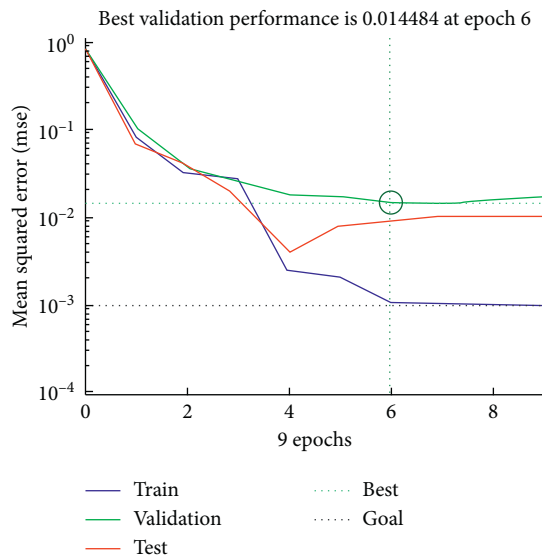


FIGURE 8: Performance of BP.

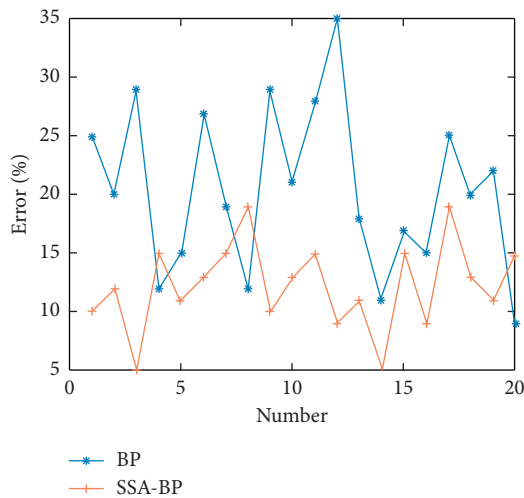


FIGURE 9: Error comparison of SSA-BP and BP.

TABLE 2: Connection weights of the input layer and the hidden layer.

	X_1	X_2	X_3	X_4	X_5	X_6	X_7	X_8
H_1	-0.39	0.20	-0.53	0.34	-0.46	0.62	-0.37	0.44
H_2	0.61	-0.66	0.41	-0.77	0.00	-0.46	-0.34	-0.31
H_3	-0.57	0.49	-0.19	-1.37	-0.70	-1.04	-0.88	-0.10
H_4	-0.16	-0.28	0.11	0.66	0.11	0.02	-0.36	-0.37
H_5	-0.52	-0.58	-0.01	-0.63	0.19	-0.68	-0.08	-0.25
H_6	0.10	-0.49	0.11	-0.21	-0.05	0.26	0.09	-0.45
H_7	-0.60	-0.67	-1.33	0.59	-0.24	0.02	-0.92	-0.22
H_8	-0.22	-0.28	0.01	0.13	0.09	-0.59	-0.04	0.02
H_9	-0.35	-0.13	-0.01	0.03	0.52	-0.18	-0.55	-0.69
H_{10}	0.14	0.06	-0.44	0.05	0.13	0.06	-0.17	-0.03

TABLE 3: Connection weights of the hidden layer and the output layer.

	H_1	H_2	H_3	H_4	H_5	H_6	H_7	H_8	H_9	H_{10}
Y	-0.04	0.28	-0.40	-0.16	0.24	-0.51	0.09	-0.57	0.19	-0.17

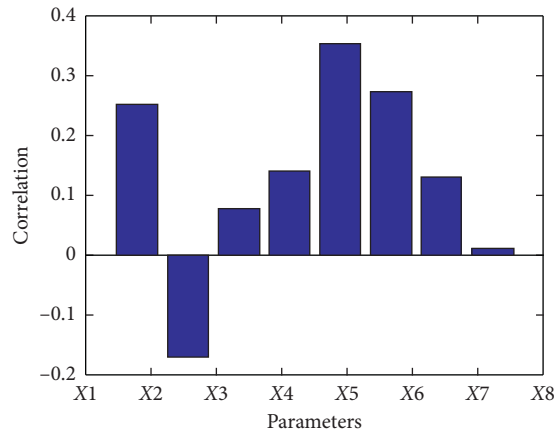


FIGURE 10: Effect of parameters on debonding strain.

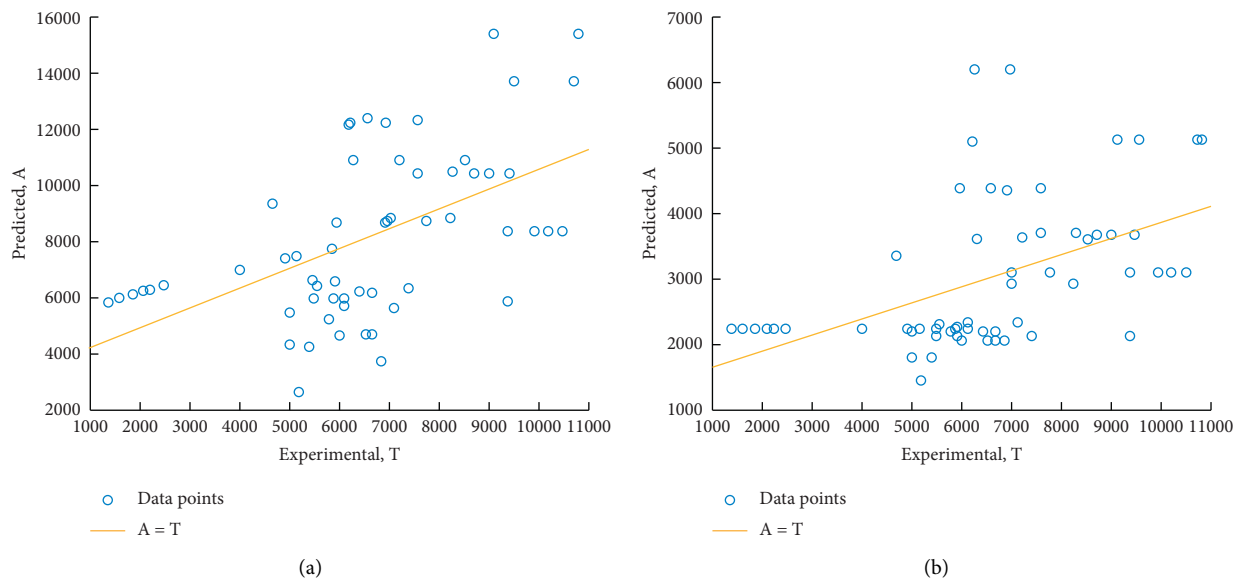


FIGURE 11: Continued.

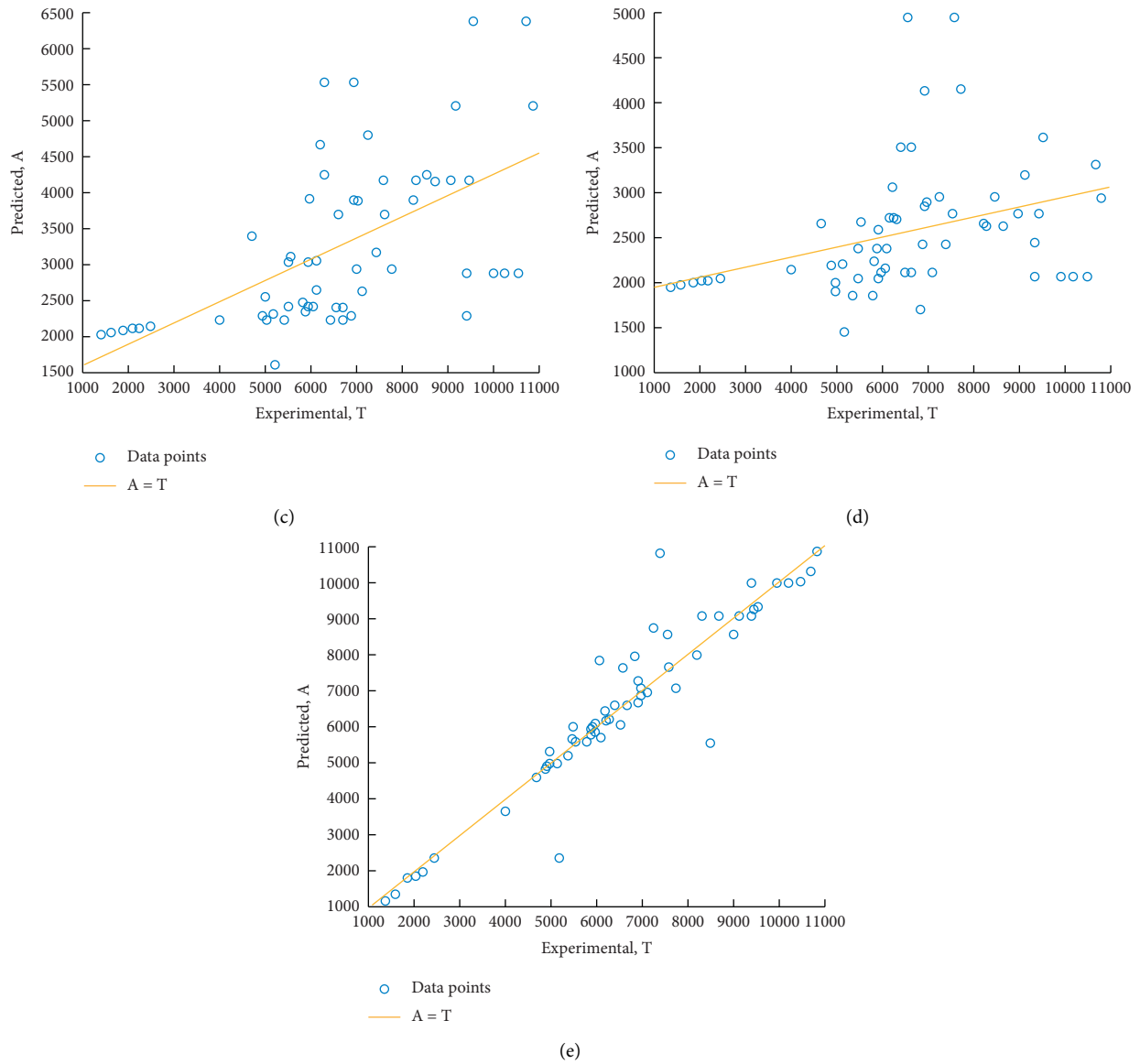


FIGURE 11: Predicted values and experimental values: (a) ACI, (b) JSCE, (c) TR55, (d) CNR, and (e) SSA-BP.

TABLE 4: Statistical results of each model.

	JSCE	ACI	CNR	TR55	SSA-BP
Min	0.22	0.5	0.24	0.2	0.35
Max	1.63	4.24	1.48	1.42	1.17
AV	0.52	1.39	0.55	0.45	0.99
STD	0.29	0.75	0.24	0.24	0.13
CV	55%	54%	45%	54%	13%
C	92%	32%	93%	95%	50%
N-C	8%	68%	7%	5%	50%

specimens are overestimated. However, the conservative and nonconservative values calculated by the SSA-BP model account for 50%; the SSA-BP is more stable than the codes.

6. Conclusions

- (1) The SSA-BP model is better than the traditional BP neural network in terms of its accuracy and robustness. The concrete strength, shear-to-span ratio, and longitudinal reinforcement ratio have a great effect on the debonding strain of FRP-strengthened RC beams; the debonding strain of FRP-strengthened RC beams can be improved with the increase of them. The FRP stiffness is negatively correlated with the debonding strain; the debonding strain will be reduced with the increased FRP stiffness.
- (2) The present model developed based on the SSA-BP neural network has a coefficient of variation of 13%.

Compared with JSCE, ACI, TR55, CNR, and other codes, it has higher accuracy and robustness.

- (3) There are still some shortcomings in experimental data collection and model convergence speed. In the future, these two aspects need to be improved to establish a better prediction model of debonding strain of FRP-strengthened RC beam.

Data Availability

The data for the study were collected from articles by different researchers and have been marked in the article.

Additional Points

Research Highlights. The influence of different parameters on debonding strain of FRP-strengthened RC beams is comprehensively considered. The sparrow search algorithm has been used to optimize the weights and thresholds of the BP neural network and establish a more accurate prediction model.

Conflicts of Interest

The authors declare no conflicts of interest.

Acknowledgments

The authors are grateful for the financial support from the Shandong Provincial Natural Science Foundation (Project no. ZR2017MEE019).

References

- [1] M. Z. Naser, R. A. Hawileh, and J. A. Abdalla, "Fiber-reinforced polymer composites in strengthening reinforced concrete structures: a critical review," *Engineering Structures*, vol. 198, Article ID 109542, 2019.
- [2] N. A. Nuaimi, "Durability of reinforced concrete beams externally strengthened with CFR Plaminates under harsh climatic conditions," *Journal of Composites for Construction*, vol. 25, no. 2, Article ID 04021005, 2021.
- [3] R. Abokwiek, T. E. Maadday, RC columns strengthened with NSM-CFRP strips and CFRP wraps under axial and uniaxial bending: experimental investigation and capacity models," *Journal of Composites for Construction*, vol. 25, no. 2, Article ID 04021009, 2021.
- [4] K. Helal, S. Yehia, R. Hawileh, and J. Abdalla, "Performance of preloaded CFRP-strengthened fiber reinforced concrete beams," *Composite Structures*, vol. 244, Article ID 112262, 2020.
- [5] N. Al Nuaimi, M. G. Sohail, R. A. Hawileh, J. A. Abdalla, and K. Douier, "Durability of reinforced concrete beams strengthened by galvanized steel mesh-epoxy systems under harsh environmental conditions," *Composite Structures*, vol. 249, Article ID 112547, 2020.
- [6] H. A. Rasheed, J. Abdalla, R. Hawileh, and A. K. Al-Tamimi, "Flexural behavior of reinforced concrete beams strengthened with externally bonded aluminum alloy plates," *Engineering Structures*, vol. 147, pp. 473–485, 2017.
- [7] ACI-440.2R, *Guide for the Design and Construction of Externally Bonded FRP Systems for Strengthening Concrete Structures*, ACI-440, Farmington Hills, MI, USA, 2017.
- [8] Japan Society of Civil Engineers (JSCE), *Recommendations for upgrading of concrete structures with use of continuous fiber sheets. Concrete Engineering Series*, Japan Society of Civil Engineers, Nagaoka, Japan, 2001.
- [9] Concrete Society, *Design Guidance for Strengthening Concrete Structures using Fibre Composite Materials*, Concrete Society, Crowthorne, UK, 2012.
- [10] National Research Council, *Guide for the design and construction of externally bonded FRP systems for strengthening existing structures (CNR-DT 200 R1)*, CNR, Rome, Italy, 2013.
- [11] J.G. Teng, "Intermediate crack-induced debonding in RC beams and slabs," *Construction and Building Materials*, vol. 17, no. 6-7, pp. 447–462, 2003.
- [12] Y. J. Kim and K. A. Harries, "Statistical characterization of reinforced concrete beams strengthened with FRP sheets," *Journal of Composites for Construction*, vol. 17, no. 3, pp. 357–370, 2013.
- [13] E. Oller, D. Cobo, and A. R. Mari, "Laminate debonding process of FRP-strengthened beams," *Structure and Infrastructure Engineering*, vol. 7, no. 1-2, pp. 131–146, 2011.
- [14] X. Z. Lu, J. G. Teng, L. P. Ye, and J. J. Jiang, "Intermediate crack debonding in FRP-strengthened RC beams: FE analysis and strength model," *Journal of Composites for Construction*, vol. 11, no. 2, pp. 161–174, 2007.
- [15] A. Bilotta, F. Ceroni, E. Nigro, and M. Pecce, "Efficiency of CFRPNSM strips and EBR plates for flexural strengthening of RC beams and loading pattern influence," *Composite Structures*, vol. 124, pp. 163–175, 2015.
- [16] P. Rusinowki and B. Täljsten, "Intermediate crack induced debonding in concrete beams strengthened with CFRP plates - an experimental study," *Advances in Structural Engineering*, vol. 12, no. 6, pp. 793–806, 2009.
- [17] J. Y. Xu, B. B. Zheng, and G. B. Li, "Study on allowable peeling strain of reinforced concrete beams with externally bonded CFRP," *China Safety Science Journal*, vol. 28, no. 7, pp. 70–75, 2018.
- [18] O. R. Abuodeh, J. A. Abdalla, and R. A. Hawileh, "Assessment of compressive strength of ultra-high performance concrete using deep machine learning techniques," *Applied Soft Computing*, vol. 95, 2020.
- [19] P. Gao, Y. H. Zhao, L. Hong et al., "Effect of corner radius on axial compressive performance of steel reinforced concrete rectangular short columns confined by CFRP," *ActaMateriaeCompositaeSinica*, vol. 37, 2020.
- [20] O. R. Abuodeh, J. A. Abdalla, and R. A. Hawileh, "Prediction of shear strength and behavior of RC beams strengthened with externally bonded FRP sheets using machine learning techniques," *Composite Structures*, vol. 234, 2020.
- [21] F. Yu and X. Xu, "A short-term load forecasting model of natural gas based on optimized genetic algorithm and improved BP neural network," *Applied Energy*, vol. 134, pp. 102–113, 2014.
- [22] T. Hu, *IOP Conference Series Earth Environmental Science*, vol. 719, Article ID 022028, 2021.
- [23] G. Ayea, "Forecasting the Price of Gold Using Dynamic Model Averaging," *International Review Of Financial Analysis*, vol. 41, pp. 257–266, 2015.
- [24] Y. Shi, R. M. Liu, Y. Luo, and K. Yang, "The temporal and spatial process of PM_(2.5) pollution evolution in China in the past 20 years," *Environmental Science*, vol. 41, no. 1, pp. 1–13, 2020.

- [25] J. K. Xue, *Research and Application of a New Type of Swarm Intelligence Optimization Technology*, Donghua University, Shanghai, China, 2020.
- [26] Y. L. Li, S. Q. Wang, Q. R. Chen, and X. G. Wang, "Comparative study of several new swarm intelligence optimization algorithms," *Computer Engineering and Applications*, vol. 56, no. 22, pp. 1–12, 2020.
- [27] Z. Wu and H. Niu, "Prediction of crack-induced debonding failure in R/C structures flexurally strengthened with externally bonded FRP composites," *Doboku Gakkai Ronbunshuu E*, vol. 63, no. 4, pp. 620–639, 2007.
- [28] R. Bakay, E. Y. Sayed-Ahmed, and N. G. Shrive, "Interfacial debonding failure for reinforced concrete beams strengthened with carbon-fibre-reinforced polymer strips," *Canadian Journal of Civil Engineering*, vol. 36, no. 1, pp. 103–121, 2009.
- [29] H.B. Pham and R. Al-Mahaidi, "Assessment of available prediction models for the strength of FRP retrofitted RC beams," *Composite Structures*, vol. 66, no. 1–4, pp. 601–610, 2004.
- [30] F. Ceroni, M. Pecce, S. Matthys, and L. Taerwe, "Debonding strength and anchorage devices for reinforced concrete elements strengthened with FRP sheets," *Composites Part B: Engineering*, vol. 39, no. 3, pp. 429–441, 2008.
- [31] J. M. Sena-Cruz, J. A. O. Barros, M. R. F. Coelho, and L. F. F. T. Silva, "Efficiency of different techniques in flexural strengthening of RC beams under monotonic and fatigue loading," *Construction and Building Materials*, vol. 29, pp. 175–182, 2012.
- [32] O. Gunes, O. Buyukozturk, and E. Karaca, "A fracture-based model for FRP debonding in strengthened beams," *Engineering Fracture Mechanics*, vol. 76, no. 12, pp. 1897–1909, 2009.
- [33] G. Spadea, F. Bencardino, and R.N. Swamy, "Optimizing the performance characteristics of beams strengthened with bonded CFRP laminates," *Materials and Structures*, vol. 33, no. 226, pp. 119–126, 2000.
- [34] J. Pan, C. K. Y. Leung, and M. Luo, "Effect of multiple secondary cracks on FRP debonding from the substrate of reinforced concrete beams," *Construction and Building Materials*, vol. 24, no. 12, pp. 2507–2516, 2010.
- [35] T. W. White, K. A. Soudki, and M.-A. Erki, "Response of RC beams strengthened with CFRP laminates and subjected to a high rate of loading," *Journal of Composites for Construction*, vol. 5, no. 3, pp. 153–162, 2001.
- [36] Y.-C. You, K.-S. Choi, and J. Kim, "An experimental investigation on flexural behavior of RC beams strengthened with prestressed CFRP strips using a durable anchorage system," *Composites Part B: Engineering*, vol. 43, no. 8, pp. 3026–3036, 2012.
- [37] S. F. Brena, "Increasing flexural capacity of reinforced concrete beams using carbon fiber-reinforced polymer composites," *ACI Structural Journal*, vol. 100, no. 1, pp. 36–46, 2003.
- [38] A.-H. Zhang, W.-L. Jin, and G.-B. Li, "Behavior of preloaded RC beams strengthened with CFRP laminates," *Journal of Zhejiang University-SCIENCE A*, vol. 7, no. 3, pp. 436–444, 2006.
- [39] R. Kotynia and S. Cholostiakow, "New proposal for flexural strengthening of reinforced concrete beams using CFRP T-shaped profiles," *Polymers*, vol. 7, no. 11, pp. 2461–2477, 2015.
- [40] J. Aidoo, K. A. Harries, and M. F. Petrou, "Fatigue behavior of carbon fiber reinforced polymer-strengthened reinforced concrete bridge girders," *Journal of Composites for Construction*, vol. 8, no. 6, pp. 501–509, 2004.
- [41] M. Ali-Ahmad, K. Subramaniam, and M. Ghosn, "Experimental investigation and fracture analysis of debonding between concrete and FRP sheets," *Journal of Engineering Mechanics*, vol. 132, no. 9, pp. 914–923, 2006.
- [42] T.-K. Lee, A. D. E. Pan, and M. J. L. Ma, "Ductile design of reinforced concrete beams retrofitted with fiber reinforced polymer plates," *Journal of Composites for Construction*, vol. 8, no. 6, pp. 489–500, 2004.

Research Article

Research on Landslide Warning Model Establishment and Disaster Space-Time Evolution Analysis

Zhen Wang 

School of Engineering, Huanghe Science and Technology College, Zhengzhou, Henan, China

Correspondence should be addressed to Zhen Wang; hhstu_wz@163.com

Received 7 April 2021; Revised 28 April 2021; Accepted 3 May 2021; Published 20 May 2021

Academic Editor: Faming Huang

Copyright © 2021 Zhen Wang. This is an open access article distributed under the Creative Commons Attribution License, which permits unrestricted use, distribution, and reproduction in any medium, provided the original work is properly cited.

As important methods to avoid landslide disasters, velocity monitoring and early warning are significant research topics in slope engineering at the present stage. This paper combines the randomness of velocity data in evolution process of landslide disasters, using Markov chain theory with no aftereffect to describe the randomness process, and introduces it into landslide warning. The research collects velocity monitoring data before landslide occurrence and applies average standard deviation method which can reflect statistical characteristics of the classification data to carry out state division of the velocity data. Then, it proposes landslide warning criteria and establishes landslide warning model based on dynamic prediction of future velocity status by Markov chain theory. Meanwhile, it puts forward the evaluation standard of landslide warning model from the aspects of timeliness, anti-interference, and credibility. At the same time, it takes typical open-pit mine landslide disaster as the engineering background and gradually optimizes and evaluates the landslide warning model from the above three evaluation standards. The results show that the landslide warning model can realize the landslide early warning of multiple monitoring points; it has good effects in both time warning and regional warning. On the other hand, the landslide warning model has high accuracy in timeliness, anti-jamming, and credibility, and it can reveal space-time evolution law of landslide occurrence, so this research has important theoretical significance and engineering promotion value.

1. Introduction

The frequency of large geological disasters has increased significantly with the severe climate changing, the continuous increasing of global population, the gradual expansion of human living areas, the increase geological disturbances of engineering activity, and other influencing factors since the 20th century [1–3]. Among them, the quantity of landslide disasters accounted for more than 70% of the total amount of geological disasters, and it is becoming the highest occurrence frequent and the maximum economic losses of geological disasters [4, 5].

As important methods to avoid landslide disasters, velocity monitoring and early warning are significant research topics in slope engineering; its core is monitoring data collection and landslide warning analysis. In recent years, with the development of slope monitoring technology, monitoring data collection has been effectively solved, but

how to establish a landslide warning model based on monitoring data is still an important problem in the field of slope engineering at this stage. The research on landslide warning began in the 1960s. Japanese scholar Saito proposed an empirical formula for landslide warning, creating a precedent for landslide warning research [6]. In the next few decades, scholars from various countries have successively proposed dozens of landslide warning models and have experienced development stages such as qualitative landslide warning, quantitative landslide warning, and comprehensive landslide warning [7–11]. Qualitative landslide warning established the slope catastrophic evolution model based on engineering experience, and then analyzed catastrophic stage and stability state of the slope [12]. Guo counted 119 landslide cases in Wenchuan earthquake and established a landslide warning model from the perspectives of horizontal peak, slope angle, ground acceleration, rock type, geological structure, and so on by qualitative analysis method [13].

Wang used qualitative analysis methods to establish a landslide warning model which comprehensively considered rainfall, river erosion, human activities, and other factors and evaluated the typical loess slope stability in Baoji City, Shaanxi Province [14]. Quantitative landslide warning is a method which numericalizes geological features and external environment in the process of slope catastrophe evolution and then analyzes and forecasts the slope stability by mathematical and physical methods [15]. Ciervo analyzed the change law of soil mechanics parameters in rainfall-induced landslide evolution by mathematical statistical method and proposed a landslide warning model based on the evolution of soil mechanics parameters. At the same time, he applied the model to the landslide warning on the Amalfi coast in southern Italy and achieved good prediction results [16]. Yan quantified the influence of external environment on slope stability through sensitivity analysis and established a quantitative landslide warning model which considered the influence of external environment [17]. Comprehensive landslide warning is a method which applied physical simulation, numerical simulation, and other means to establish a geological, mechanical, and deformation coupling model that comprehensively reflects internal mechanism and external performance in the process of landslide disasters [18]. Tiranti established a landslide warning model that comprehensively considers strength conditions and deformation constraints through physical simulation method, and applied the model into Piemonte regional landslide warning, which achieved good warning results [19]. Canli established a coupled hydromechanical model to describe the evolution process of landslide disasters in rainfalls and applied it into slope warning with rainfalls [20]. The majority of scholars have done lots of research on landslide warning model, but the research results are still not very ideal. First of all, landslide warning models are hysteresis and warning information is not timely enough; it is to say there is not enough time to prepare for the disaster before landslides occur [21]. Secondly, a large number of landslides occur outside the warning area, that is to say, the failure rate of landslide area is very high. Lastly, the error warning rate is high, that means the warning information is provided when there is no risk of landslides, and this error warning information will have a serious impact on the normal productions and lives of residents [22]. The reason is

that, due to the complexity, randomness, and uncertainty of landslide disasters evolution, a warning model is only suitable for a certain type or a certain stage of landslide prediction, and various landslide warning models have certain limitations. In addition, landslide warning should include landslide time warning and landslide area warning, the previous research focused on landslide time warning, and the landslide area warning is insufficient, but these two aspects should be in mutual unity in fact [23].

In the evolution process of landslide disasters, the anti-sliding force changing with time can be regarded as a random process, and the velocity data obtained by slope monitoring can also be regarded as a random process correspondingly [24]. Using the theories and methods of random process analyzed data and forecast warning have solid theoretical foundation and realistic practical requirements. Markov chain theory, as a method to describe the law of transition between system states, describes a process that the probability regularity of future state has been determined if the current state of the system is known; that is to say, future state of the system has nothing to do with past state under the condition that current state is known [25]. This memoryless feature is consistent with the practice of predicting future stability of the slope based on current stability in landslide warning, and it reflects the feasibility of Markov chain theory in landslide warning [26]. Therefore, this paper made an intensive research of landslide warning method based on Markov chain theory and established a reasonable and accurate landslide warning model to provide scientific means and theoretical basis for landslide disasters warning.

2. Landslide Warning Method

Markov chain theory is a method that describes the law of transition between system states; applying the method can obtain the transfer probability between different states and thus can predict the future state change trend of the system.

2.1. Markov Chain Theory. Assume random process $X(n)$, $\{X(n), n \in N\}$, where N is the set of nature numbers, and all values of $X(n)$ make up the discrete state I , $I = \{i_0, i_1, i_2, i_3, \dots\}$, if the conditional probability satisfies formula (1) for any arbitrary $n \in N$ and $i \in I$,

$$P\{X(n+1) = i_{n+1} | X(n) = i_n, X(n-1) = i_{n-1}, X(n-2) = i_{n-2}, \dots, X(0) = i_0\} = P\{X(n+1) = i_{n+1} | X(n) = i_n\}. \quad (1)$$

Then, we call $\{X(n), n \in N\}$ as a Markov chain. The process of $X(t)$, $\{X(t), t \in T\}$, is a random vector that

satisfies Markov chain and contains time factors when the set of nature numbers in formula (1) is ended to time attribute.

$$\begin{aligned}
& P\{X(t) = i_t, X(t-1) = i_{t-1}, X(t-2) = i_{t-2} \dots X(0) = i_0\} \\
& = P\{X(t) = i_t | X(t-1) = i_{t-1}, X(t-2) = i_{t-2}, X(t-3) = i_{t-3} \dots X(0) = i_0\} \\
& \quad \cdot P\{X(t-1) = i_{t-1}, X(t-2) = i_{t-2}, X(t-3) = i_{t-3} \dots X(0) = i_0\} \\
& = P\{X(t) = i_t | X(t-1) = i_{t-1}\} \cdot P\{X(t-1) = i_{t-1}, X(t-2) = i_{t-2}, X(t-3) = i_{t-3} \dots X(0) = i_0\} \\
& = \dots \\
& = P\{X(t) = i_t | X(t-1) = i_{t-1}\} \cdot P\{X(t-1) = i_{t-1} | X(t-2) = i_{t-2}\} \\
& \quad \cdot P\{X(t-2) = i_{t-2} | X(t-3) = i_{t-3}\} \dots P\{X(1) = i_1 | X(0) = i_0\}.
\end{aligned} \tag{2}$$

In formula (2), $X(t)$ is the state of moment t , and finite moment t forms a time set $T, T = \{0, 1, 2, 3 \dots\}$. It is obvious from formula (2) that the statistical properties of Markov chain are determined by the conditional probability $P\{X(t+1) = i_{t+1} | X(t) = i_t\}$. The conditional probability means the probability of system state is i_{t+1} at moment $t+1$ under the condition that system state is i_t at moment t . Therefore, the probability distribution of future states can be determined under the premise that initial state probability vector and transition probability matrix are known, so that reasonable predictions can be made of future states.

2.2. Markov Chain Prediction Method. For a data sequence composed of multiple data $\{x_1, x_2, x_3 \dots x_n\}$, the data is divided into r states according to a specific standard, and q_{ij} represents the times of state sequence transitions from state i to state j by $k-1$ steps (k is the number of statistical steps, $k = 1, 2, 3 \dots m$). Obviously, q_{ij} can form an $n \times n$ state transition frequency matrix $q^{(k)}$. Formula (3) can be used to calculate the state transfer probability matrix $p^{(k)}$ according to the state transition frequency matrix $q^{(k)}$.

$$p_{ij} = q_{ij} \cdot \left(\sum_{i=1}^{i=r} q_{ij} \right)^{-1}. \tag{3}$$

For an arbitrary state $l, l \in \{1, 2, 3 \dots r\}$, p_l is 1 when the state of x_{n-k+1} is l . On the other side, p_l is 0 when the state of x_{n-k+1} is not l . Thus, the initial state probability vector A_k^T ,

$A_k^T(n) = (p_1, p_2, p_3 \dots p_l \dots p_r)$, can be determined when the step length is k . So the state distribution matrix $B_k^{(n+1)}$ of x_{n+1} can be expressed as formula (4) in the condition of the step length being k .

$$B_k^{(n+1)} = A_k^T(n) \cdot p^{(k)}. \tag{4}$$

For the different values of $k, B_k^{(n+1)}$ consists of matrix $B, B = (B_1^{(n+1)}, B_2^{(n+1)}, B_3^{(n+1)} \dots B_m^{(n+1)})^T$. The calculation formula of self-correlation coefficient r_k can be expressed as formula (5) when the step length is k .

$$\begin{aligned}
r_k = & \left[\sum_{t=1}^{t=n-k} (x_t - x)(x_{t+k} - x) \right] \\
& \cdot \left[\sum_{t=1}^{t=n-k} (x_t - x)^2 \cdot \sum_{t=1}^{t=n-k} (x_{t+k} - x)^2 \right]^{-1/2}.
\end{aligned} \tag{5}$$

In formula (5), x is average value of the data $\{x_1, x_2, x_3 \dots x_n\}$. Accordingly, the weight vector w_k with step length m can be calculated by

$$w_k = |r_k| \cdot \left(\sum_{k=1}^{k=m} |r_k| \right)^{-1}. \tag{6}$$

Different step weights form an $m \times m$ weight matrix $w, w = (w_1, w_2, w_3 \dots w_k \dots w_m)$. The probability distribution vector C of next day prediction state through weighted Markov chain can be expressed as

$$C^{(n+1)} = (c_1, c_2 \dots c_r) = (w_1, w_2 \dots w_k \dots w_m) \cdot (B_1^{(n+1)}, B_2^{(n+1)} \dots B_m^{(n+1)})^T. \tag{7}$$

In the probability distribution vector C , the state corresponding to the column where the largest element is located is the most probable state for x_{n+1} predicted by the weighted Markov chain.

2.3. Markov Chain Landslide Warning Model. According to Markov chain prediction method, the state sequence contains time information of velocity data change if velocity data obtained by slope monitoring is divided into several states through certain criteria. Then, we can establish statistical laws of the slope stability state changes over time. Combined with velocity monitoring data and future state

prediction characteristics, the model can determine whether to provide warning information. The establishment of landslide warning model can be expressed as follows.

2.3.1. Status Classification of Velocity Data. Landslide warning model should make a clear judgment on safety states of the slope stability. At the same time, states division should follow the principle of concise and clear. Therefore, velocity data was divided into two states of safe and dangerous. For the monitoring velocity data, the average value x and standard deviation s were calculated, and the boundary point D was determined according to $D = x + b \cdot s$ (b is a

variable parameter and it represents standard deviation multiple). It was defined as safe and represented by “1” when the velocity data was in the interval $[x_{min}, D)$. Conversely, it was defined as dangerous and represented by “2” when the velocity data was in the interval $[D, x_{max}]$.

2.3.2. Dynamic Prediction of Future Velocity. In order to effectively reduce the error warning rate of landslide warning model, the comprehensive prediction results are defined dangerous only in the condition that future states prediction results for the step length 1, 2, 3, 4, 5 of Markov chain prediction method are all dangerous. At the same time, the importance of current data is highlighted and the influence of historical data is gradually diminishing with the continuous update of monitoring data. As a result, the warning model should eliminate early historical data while incorporating new data opportunely and predicts the future

velocity state constantly through Markov chain prediction method.

2.3.3. Establishment of Landslide Warning Criteria. The warning model should also make clear whether to provide warning information while predicting the future velocity state. In the phase of constant velocity deformation, the dangerous velocity is rare and the prediction results will inevitably show a large number of safe states. Even if the dangerous state occurs, it will gradually revise and restore to safe state in dynamic data updating. On the other side, in the phase of accelerated velocity deformation before landslide, dangerous velocity appears in large numbers and the prediction results will continue to show dangerous values. The prediction will usually not revise and restore to safe state in the dynamic data updating due to the irreversible of landslides. Therefore, the landslide warning criteria of Markov chain landslide warning model can be described as follows:

The actual velocity state of yesterday was dangerous

The actual velocity state of today is dangerous Landslide warning \longrightarrow Landslide warning. (8)

The prediction velocity state of next day is safe

2.4. Evaluation Index of Landslide Warning Model. In order to provide necessary emergency preparation time for people evacuation and property transfer, the basic requirement of landslide warning model is to give frequent warning information before the occurrence of landslides. At the same time, to ensure normal production and life of residents, the landslide warning model should not give warning information when there is no risk of landslide. Aiming at the above goals, this paper evaluates the landslide warning model from three aspects: timeliness, anti-interference, and credibility.

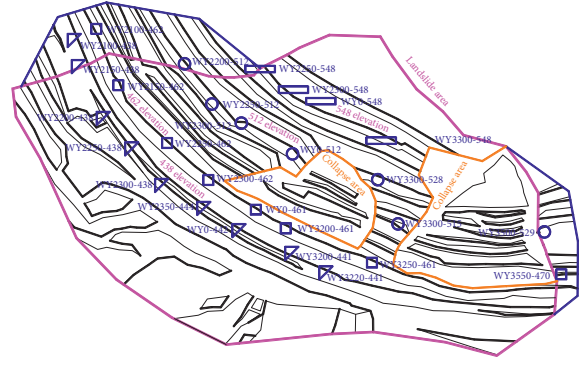
Apply warning intensity I to evaluate the index of timeliness. It is defined that, in R times of warning judgments within landslide emergency preparation time, warning model gives $R *$ times of warning information; then, the warning intensity $I = R * /R$. Apply error warning rate W to evaluate the index of anti-interference. It is defined that, in M times of warning judgments before landslide emergency preparation time, warning model gives $M *$ times of warning information; then, the error warning rate $W = M * /M$. Apply prediction consistency rate Y to evaluate the index of credibility. It is defined that, in Q times of warning judgments, $Q *$ times are consistent with the actual state among them; then, the prediction consistency rate $Y = Q * /Q$. Among the above three indexes, timeliness is the most significant evaluation index, anti-interference is an optimization index under the premise of satisfying timeliness, and credibility is an evaluation of model accuracy accumulation under the premise of satisfying timeliness and anti-interference. There is no need to pursue excessive credibility in engineering practice.

3. Engineering Case

3.1. Slope Engineering Overview. A large-scale landslide occurred in an open-pit mine on April 17. For the landslide body, the length is more than 700 m, the width is nearly 400 m, the height is nearly 200 m, and the volume is more than 3 million m^3 . There are 28 velocity monitoring points at 438, 462, 512, and 548 levels near the landslide area. Among them, 21 monitoring points are located in the landslide area and 7 monitoring points are located outside the landslide area [27]. The prospect of landslide area and the layout of monitoring points are shown in Figure 1.

3.2. Landslide Warning Analysis. This paper selected 5 January to 17 April as monitoring period. At the same time, due to the huge amount of data, we selected WY3250-461 monitoring point and used sample size of 20 and standard deviation multiple of 0.4 to illustrate the prediction process. The velocity monitoring data of WY3250-461 monitoring point in sample size of 20 is shown in Table 1.

The minimum velocity is 0.44 mm d^{-1} and the maximum velocity is 3.02 mm d^{-1} for the 20 velocity data in Table 1. At the same time, the average value x is 1.745 and the standard deviation s is 0.675. It can determine that the boundary point D is 2.015 in the condition of standard deviation multiple is 0.4 based on the formula $D = x + b \cdot s$. Therefore, it is defined safe and represented by “1” when the velocity data is in the interval $[0.44, 2.015)$, and it is defined dangerous and represented by “2” when the velocity data is in the interval $[2.015, 3.02]$. The state transition probability matrix with step length of 1, 2, 3, 4, 5 can be calculated according to



- Boundary lines of landslide area
- Boundary lines of collapse area
- Top lines of step slope
- Bottom lines of step slope
- Monitoring points at 438 elevation
- Monitoring points at 462 elevation
- Monitoring points at 512 elevation
- Monitoring points at 548 elevation

(a)

(b)

FIGURE 1: Engineering overview of landslide area. (a) Prospect of landslide area. (b) Layout of monitoring points.

TABLE 1: WY3250-461 monitoring point velocity data.

Date	5 Jan	6 Jan	7 Jan	8 Jan	9 Jan	10 Jan	11 Jan	12 Jan	13 Jan	14 Jan
Velocity/mm·d ⁻¹	1.53	1.37	2.24	2.58	1.54	2.43	0.44	1.59	1.78	1.93
Date	15 Jan	16 Jan	17 Jan	18 Jan	19 Jan	20 Jan	21 Jan	22 Jan	23 Jan	24 Jan
Velocity/mm·d ⁻¹	1.68	1.34	1.98	1.39	0.68	3.00	0.98	1.66	1.74	3.02

formula (3). For this example, the 20th velocity data state is 2, and the initial state vector A_1^T is (0, 1). Similarly, the 19th, 18th, 17th, and 16th velocity data state are, respectively, 1, 1, 1, 2, and the initial state vectors are, respectively, $A_2^T = (1, 0)$, $A_3^T = (1, 0)$, $A_4^T = (1, 0)$, $A_5^T = (0, 1)$. The self-correlation coefficient and weight vector with step length of 1, 2, 3, 4, 5 can be calculated through formulas (5) and (6). On this basis, the probability distribution vector of future velocity state with each step length can be obtained. It can be known that the probability of predicting future velocity state as safe is 0.833 with step length of 1, the probability of predicting future velocity state as safe is 0.758 with step length of 2, the probability of predicting future velocity state as safe is 0.672 with step length of 3, the probability of predicting future velocity state as safe is 0.695 with step length of 4, and the probability of predicting future velocity state as safe is 0.743 with step length of 5. Therefore, Markov chain prediction method predicts that the future velocity state is safe.

Dynamically update data and implement Markov chain prediction process after acquiring new data so that we can obtain the state prediction sequence. According to actual velocity state information and predicted velocity state information, a warning judgment can be made based on landslide warning criteria. For WY3250-461 monitoring point, landslide warning model gives continuous warning information within 7 days before the occurrence of

landslide. If emergency preparation time is set to 7 days, warning intensity is 100% and error warning rate is 0 of the warning model which indicate the model has good timeliness and anti-interference. At the same time, prediction consistency rate is 61%; the model can gradually accumulate confidence in the forecast process while satisfying the above two criteria.

3.3. Optimization of Warning Model. The average value and standard deviation are unchanged for a specific data sample, so the boundary point is only determined by standard deviation multiple. The larger the standard deviation multiple, the stricter the requirements for judging as dangerous. The model responds slowly to abnormal data, and timeliness of the warning model is poor correspondingly. On the contrary, the smaller the standard deviation multiple, the looser the requirements for judging as dangerous. The model responds sensitively to abnormal data, and error warning rate of the warning model is high correspondingly. For a specific standard deviation multiple, the generalization of transition matrix will be insufficient if the sample size is too small. Correspondingly, it cannot fully reflect recent state transition law and will lead to increased prediction sensitivity and error warning rate. On the contrary, abnormal data will impact weakly on prediction if the sample size is too large. But it reduces the sensitivity of the

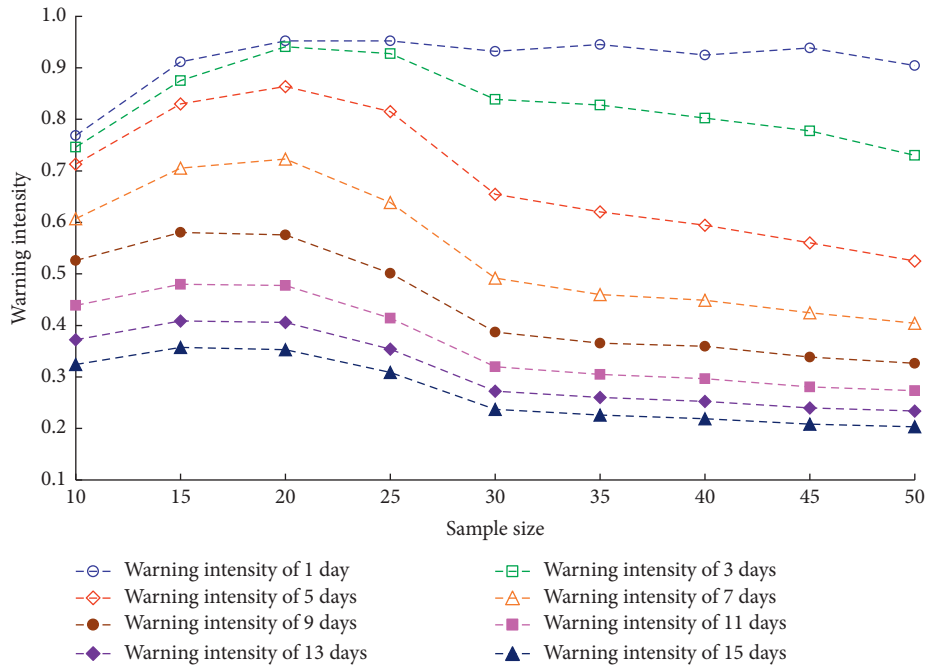


FIGURE 2: Warning intensity with different sample sizes.

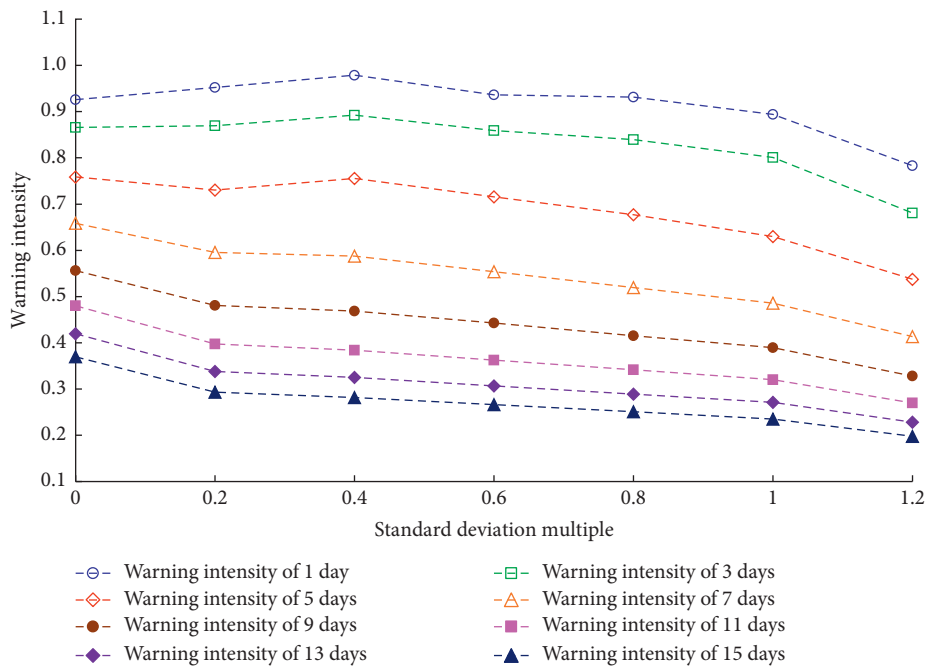


FIGURE 3: Warning intensity with different standard deviation multiples.

model and will lead to expressing poor timeliness of the warning model. In order to determine optimization parameters of the warning model, use prediction method to analyze each monitoring point in landslide area and optimize sample size and standard deviation multiple from three aspects of timeliness, anti-interference, and reliability. The curves of warning intensity under different sample sizes and standard deviation multiples are shown in Figures 2 and 3; the curves of prediction consistency are shown in Figure 4.

It can be seen from Figure 2 that warning intensity shows a trend of early increasing and then decreasing with increasing of sample size when the standard deviation multiple is unchanged. The optimization sample size is selected to be 20 according to the law of curve fitting. It can be seen from Figure 3 that warning intensity of 1 day, 3 days, and 5 days increases only with increasing of standard deviation multiple from 0.2 to 0.4, and the others all decrease in the condition of increasing standard deviation multiple. Therefore, alternative options of standard deviation multiple are 0, 0.2, and 0.4.

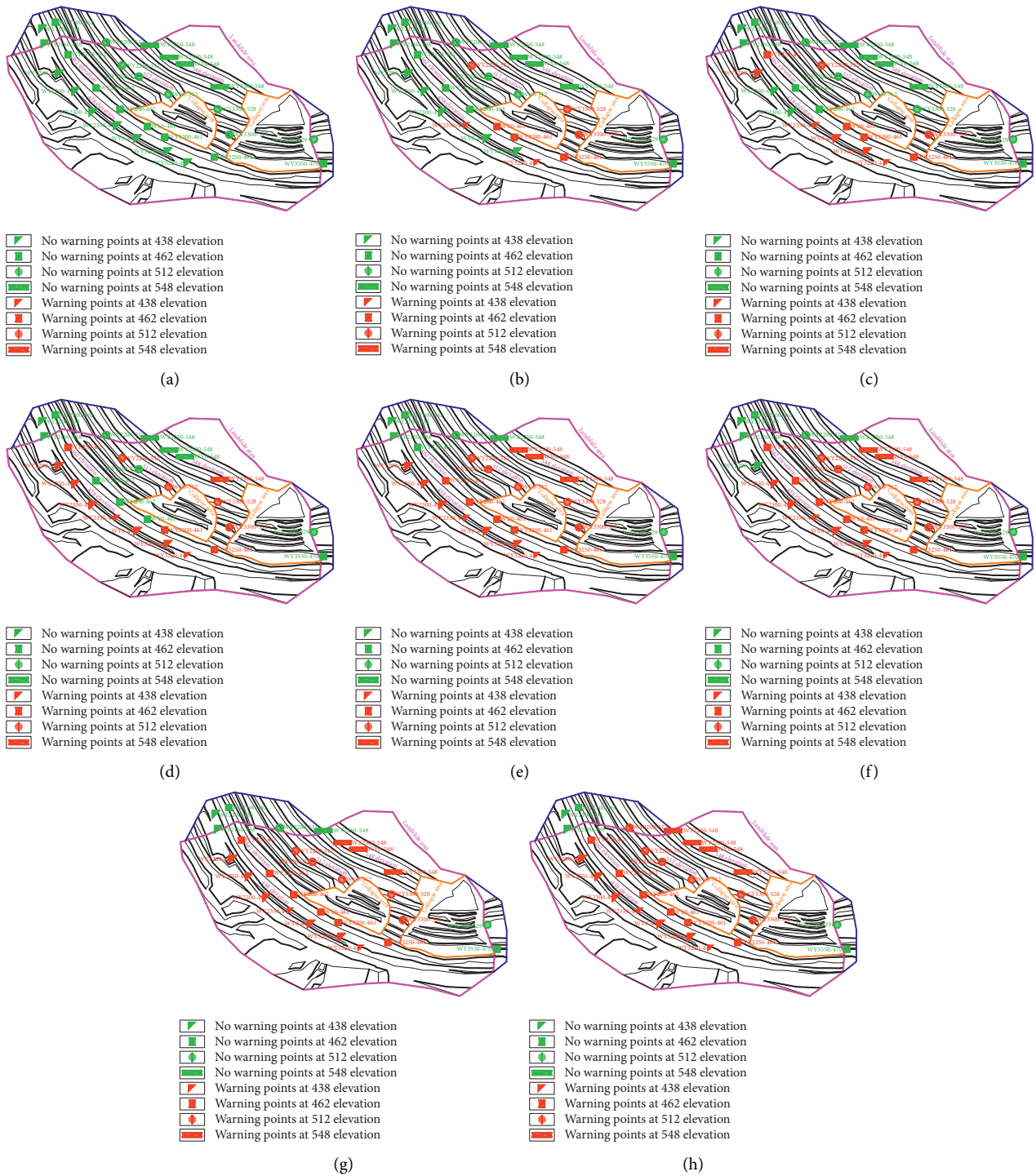


FIGURE 5: Warning information of each monitoring point before landslide. (a) 8 days before landslide. (b) 7 days before landslide. (c) 6 days before landslide. (d) 5 days before landslide. (e) 4 days before landslide. (f) 3 days before landslide. (g) 2 days before landslide. (h) 1 day before landslide.

It can be seen from Figure 4 that prediction consistency rate gradually increases with increasing of standard deviation multiple when standard deviation multiple is greater than 0.2. This is because increasing of standard deviation multiple leads to respond slowly to abnormal data of the warning model, so the warning model does not need to pursue too high prediction consistency rate. The optimization parameters of the warning model are determined to be sample size of 20 and standard deviation multiple of 0.4.

3.4. Analysis of Disaster Space-Time Evolution. Warning effect of the model for all monitoring points in the condition of sample size of 20 and standard deviation multiple of 0.4 is shown in Table 2.

The gray in Table 2 indicates that the model gives warning information. It can be seen that warning rate on 4 days and 3 days before occurrence of landslide is as high as 95% and warning rate on 2 days and 1 day before occurrence of landslide reaches 100% in the landslide area, which indicates the warning model has good timeliness. On the contrary, warning rate on 1 day before occurrence of landslide is only 29% and warning rate is 0 for the rest of the time outside the landslide area, which indicates the warning model has good anti-interference. The warning situations of all monitoring points in the slope area before occurrence of landslide are shown in Figure 5.

Figure 5 reveals the space-time evolution of landslide disaster. It can be seen from Figure 5 that the landslide disaster starts at 438 level, upper sliding body loses its support and landslide occurs due to lower sliding, and it belongs to a typical traction landslide.

4. Conclusion

This paper established a landslide warning model based on Markov chain theory and optimized parameters, evaluated accuracy of the landslide warning model through a typical landslide disaster case, and revealed the space-time evolution of landslide disaster. The main conclusions are as follows:

- (1) This paper analyzed Markov chain theory and proposed a prediction method by assigning time characteristics to the sample and then established a landslide warning model based on Markov chain theory and slope engineering practice.
- (2) In order to evaluate accuracy of the landslide warning model, this paper proposed warning model evaluation indicators from the aspects of timeliness, anti-interference, and credibility combined with practical requirements of slope engineering.
- (3) The landslide warning model was applied to practice of typical landslide. The model parameters are optimized in combination with evaluation indicators. The optimization parameters of the warning model were determined to be of a sample size of 20 and standard deviation multiple of 0.4.

- (4) In the condition that the warning model obtained optimization parameters, warning results before landslide of each monitoring point have been described, and space-time evolution of landslide disaster has been revealed based on warning situation of each monitoring point.

Data Availability

The data used to support the findings of this study are available from the corresponding author upon request.

Conflicts of Interest

The author declares no conflicts of interest.

Acknowledgments

This paper was supported by research funding of Huanghe Science and Technology College (02032293) and Scientific and Technological Project in Henan Province (202102310567).

References

- [1] N. Bar, M. Kostadinovski, M. Tucker et al., "Rapid and robust slope failure appraisal using aerial photogrammetry and 3D slope stability models," *International Journal of Mining Science and Technology*, vol. 30, no. 5, pp. 651–658, 2020.
- [2] H. Zhao, Y. Tian, Q. Guo, M. Li, and J. Wu, "The slope creep law for a soft rock in an open-pit mine in the Gobi region of Xinjiang, China," *International Journal of Coal Science & Technology*, vol. 7, no. 2, pp. 371–379, 2020.
- [3] Q.-X. Meng, W.-Y. Xu, H.-L. Wang, X.-Y. Zhuang, W.-C. Xie, and T. Rabczuk, "DigiSim - an open source software package for heterogeneous material modeling based on digital image processing," *Advances in Engineering Software*, vol. 148, Article ID 102836, 2020.
- [4] Z. Tao, C. Zhu, M. He, and M. Karakus, "A physical modeling-based study on the control mechanisms of Negative Poisson's ratio anchor cable on the stratified toppling deformation of anti-inclined slopes," *International Journal of Rock Mechanics and Mining Sciences*, vol. 138, Article ID 104632, 2021.
- [5] Y. Wang, W. K. Feng, R. L. Hu, and C. H. Li, "Fracture evolution and energy characteristics during marble failure under triaxial fatigue cyclic and confining pressure unloading (FC-CPU) conditions," *Rock Mechanics and Rock Engineering*, vol. 54, no. 2, pp. 799–818, 2021.
- [6] M. Saito, "Forecasting the time of occurrence of a slope failure," *Proceedings of the 6th International Conference on Soil Mechanics and Foundation Engineering*, vol. 6, no. 24, pp. 537–541, 1965.
- [7] Z. Wang, X. Yang, and A. Li, "Upper bound limit stability analysis for soil slope with nonuniform multiparameter distribution based on discrete algorithm," *Advances in Civil Engineering*, vol. 2020, no. 4, 9 pages, 2020.
- [8] B. Li, R. Bao, Y. Wang et al., "Permeability evolution of two-dimensional fracture networks during shear under constant normal stiffness boundary conditions," *Rock Mechanics and Rock Engineering*, vol. 54, no. 3, pp. 1–20, 2021.
- [9] W.-D. Wu, J.-B. Bai, X.-Y. Wang, S. Yan, and S.-X. Wu, "Numerical study of failure mechanisms and control techniques for a gob-side yield pillar in the sijiazhuang coal mine,

- China," *Rock Mechanics and Rock Engineering*, vol. 52, no. 4, pp. 1231–1245, 2019.
- [10] C. Zhu, M. He, M. Karakus, X. Zhang, and Z. Tao, "Numerical simulations of the failure process of anaclinal slope physical model and control mechanism of negative Poisson's ratio cable," *Bulletin of Engineering Geology and the Environment*, vol. 80, no. 4, pp. 3365–3380, 2021.
- [11] W. Pan, W. Pan, J. Luo et al., "Slope stability of increasing height and expanding capacity of south dumping site of Heshoula coal mine: a case study," *International Journal of Mining Science & Technology*, vol. 30, 2020.
- [12] R. Supper, D. Ottowitz, B. Jochum et al., "Goelectrical monitoring: an innovative method to supplement landslide surveillance," *Near Surface Geophysics*, vol. 12, no. 1, pp. 133–150, 2015.
- [13] D. Guo and M. Hamada, "Qualitative and quantitative analysis on landslide influential factors during Wenchuan earthquake: a case study in Wenchuan County," *Engineering Geology*, vol. 152, no. 1, pp. 202–209, 2013.
- [14] H. B. Wang, S. R. Wu, J. S. Shi, and B. Li, "Qualitative hazard and risk assessment of landslides: a practical framework for a case study in China," *Natural Hazards*, vol. 69, no. 3, pp. 1281–1294, 2013.
- [15] A. Smith and N. Dixon, "Quantification of landslide velocity from active waveguide-generated acoustic emission," *Canadian Geotechnical Journal*, vol. 52, no. 4, pp. 413–425, 2015.
- [16] F. Ciervo, G. Rianna, P. Mercogliano, and M. N. Papa, "Effects of climate change on shallow landslides in a small coastal catchment in southern Italy," *Landslides*, vol. 14, no. 3, pp. 1043–1055, 2016.
- [17] F. Yan, Q. Zhang, S. Ye, and B. Ren, "A novel hybrid approach for landslide susceptibility mapping integrating analytical hierarchy process and normalized frequency ratio methods with the cloud model," *Geomorphology*, vol. 327, no. 2, pp. 170–187, 2019.
- [18] I. Emanuele, B. Federica, F. Riccardo et al., "Big data managing in a landslide early warning system: experience from a ground-based interferometric radar application," *Natural Hazards & Earth System Sciences*, vol. 17, no. 10, pp. 1–22, 2017.
- [19] D. Tiranti and D. Rabuffetti, "Estimation of rainfall thresholds triggering shallow landslides for an operational warning system implementation," *Landslides*, vol. 7, no. 4, pp. 471–481, 2010.
- [20] E. Canli, B. Loigge, and T. Glade, "Spatially distributed rainfall information and its potential for regional landslide early warning systems," *Natural Hazards*, vol. 91, no. S1, pp. 103–127, 2018.
- [21] C. Lian, Z. Zeng, W. Yao, and H. Tang, "Ensemble of extreme learning machine for landslide displacement prediction based on time series analysis," *Neural Computing and Applications*, vol. 24, no. 1, pp. 99–107, 2014.
- [22] V. Tofani, C. Del Ventisette, S. Moretti, and N. Casagli, "Integration of remote sensing techniques for intensity zonation within a landslide area: a case study in the northern apennines, Italy," *Remote Sensing*, vol. 6, no. 2, pp. 907–924, 2014.
- [23] R. Supper, D. Ottowitz, B. Jochum et al., "Goelectrical monitoring: an innovative method to supplement landslide surveillance and early warning," *Near Surface Geophysics*, vol. 12, no. 1, pp. 133–150, 2014.
- [24] D. G. Sutherland, M. Hansler Ball, S. J. Hilton, and T. E. Lisle, "Evolution of a landslide-induced sediment wave in the navarro river, California," *Geological Society of America Bulletin*, vol. 114, no. 8, pp. 1036–1048, 2002.
- [25] F. Dammeier, J. R. Moore, C. Hammer, F. Haslinger, and S. Loew, "Automatic detection of alpine rockslides in continuous seismic data using hidden Markov models," *Journal of Geophysical Research Earth Surface*, vol. 121, no. 2, pp. 351–371, 2016.
- [26] M. Peng, X. Y. Li, D. Q. Li, S. H. Jiang, and L. M. Zhang, "Slope safety evaluation by integrating multi-source monitoring information," *Structural Safety*, vol. 49, pp. 65–74, 2014.
- [27] G. J. Dick, E. Eberhardt, A. G. Cabrejoievano et al., "Development of an early-warning time-of-failure analysis methodology for open-pit mine slopes utilizing ground-based slope stability radar monitoring data," *Canadian Geotechnical Journal*, vol. 52, no. 4, pp. 1–15, 2014.

Research Article

Hydrodynamic Performance and Cavitation Analysis in Bottom Outlets of Dam Using CFD Modelling

Omid Aminoroayaie Yamini , S. Hooman Mousavi , M. R. Kavianpour ,
and Ramin Safari Ghaleh

Department of Civil Engineering, K. N. Toosi University of Technology, Tehran, Iran

Correspondence should be addressed to Omid Aminoroayaie Yamini; o.aminoroaya@mail.kntu.ac.ir

Received 11 January 2021; Revised 25 April 2021; Accepted 6 May 2021; Published 18 May 2021

Academic Editor: Faming Huang

Copyright © 2021 Omid Aminoroayaie Yamini et al. This is an open access article distributed under the Creative Commons Attribution License, which permits unrestricted use, distribution, and reproduction in any medium, provided the original work is properly cited.

Bottom outlets are significant structures of dams, which are responsible for controlling the flow rate, operation, or removal of reservoir sedimentation. The service gate controls the outlet flow rate, and whenever this gate is out of order, the emergency gate which is located at upstream is utilized. The cavitation phenomenon is one of the common bottom outlets' problems due to the rapid flow transfer. The present research is a numerical study of the flow pattern in a dam's bottom outlet for different gate openings by the use of Flow-3D software and RNG $k-\epsilon$ turbulence model. The investigation is carried out on the Sardab Dam, an earth dam in Isfahan (Iran). The maximum velocity for 100% opening of the gate and Howell Bunger valve is about 18 m/s in the section below the gate, and the maximum velocity for 40% opening of the gate is equal to 23.1 m/s. For 50% opening of the service and emergency gate in the valve's upstream areas, the desired pressure values are reduced. Moreover, in the areas between the two emergency and service gates, the pressure values are reduced. The possibility of cavitation in this area can be reduced by installing aerators. The flow pattern in Sardab Dam's bottom outlet has relatively stable and proper conditions, and there are no troublesome hydraulic phenomena such as local vortices, undesirable variations in pressure, and velocity in the tunnel, and there is no flow separation in the critical area of flow entering into the branch.

1. Introduction

Bottom outlets are utilized as one of the dam's hydraulic structures to control the reservoir impoundment, the reservoir evacuation in case of emergency, and the removal of the sediments entering the reservoir. Hence, they require careful design and harmful factors identification [1]. On the other hand, to ensure the channel's proper operation, its associated hydraulic and hydromechanical installations, including gates and valves, the flow discharge capacity should be carefully examined along with performing hydraulic model tests [2]. By studying failure causes of dams' terminal gates, it has been determined that the cavitation phenomenon and gate vibration are the chief reasons for damages, because, in the areas where air bubbles collapse, pressure fluctuations intensity raises [3–8]. At the bottom outlets, the two-phase air-water flow is transmitted at high

speed. Due to the division of the flow and its impromptu conversion from the pressurized flow to the free-surface flow, a sharp loss in pressure values downstream of the gate occurs. Cavitation is one of the destructive phenomena that happen because of such negative pressure. Aeration by aerator tube is usually employed in order to control this phenomenon [9–12].

Sadat Helbar et al. (2021) studied on the size and shape of bottom outlet gates, which affect the outflow discharge, and flushing efficiency. The purpose of their study was to investigate the effect of the area, shape, and number of the bottom outlet gates on the velocity and concentration of the sediments [13].

In these structures, due to the high-velocity flow and the channel's water level fluctuation, the flow may separate from the channel's wall, and flow pressure may reduce locally. If the flow pressure is less than the water vapor pressure, the

water state shifts from a liquid to a gas, and air bubbles form. The flow may carry air bubbles to a higher pressure area in order to collapse, and a negative pressure wave enters the flow. If air bubbles explode near the wall's surface, they can damage the channel's wall [14–16]. Yang et al. (2020) worked on a 3D CFD modeling to show the water-air flow behavior. Air demand varies considerably between flow cases. It is not the simultaneous discharge of all openings that results in the largest air demand [17].

The service gate's downstream area and the area between the emergency gate and the service gate, as well as the gate slots that create an uneven surface against the flow hold the highest risk of cavitation [18, 19]. The cavitation index, a function of local pressure and flow velocity, is used as an essential parameter to assess the potential for cavitation [20]. Daneshmand et al. (2007) experimentally studied flow's hydraulic characteristics at different service gate openings in Sivand Dam's bottom outlet. Their study showed an increase in the amount of flow turbulence in the emergency gate slit with the service gate opening from 85% above, and also the cavitation index in all openings is more than the critical limit [21]. Two cavitation index control methods can control cavitation damage by modifying the structure geometry and flow aeration [22]. Kavianpour (1997) performed experiments to determine aeration's effect on slopes downstream pressure fluctuations. They concluded that air intake lessens severe pressure fluctuations and raises its mean, which in turn reduces cavitation likelihood. They also studied flow aeration's effect on the pressure field's structure, including the energy spectrum of fluctuations, skewness, the sharpness of fluctuations, and negative pressure fluctuations' risk reduction. This study showed that aeration changes the pressure field's structure [23]. Khazaei et al. (2015) studied the cavitation phenomenon in Rudbar Lorestan Dam's bottom intake numerically and in the laboratory. They showed that changing the channel's slope by 10 to 12%, changing the channel's length by 1 to 3.5 meters, and reducing the channel walls' slope by 1 to 2 degrees can be a good option to eliminate the risk of cavitation [24].

Ruan et al. (2007) examined the hydraulic performance of aerators used at the base of Goupitan Dam's bottom discharge channel in a laboratory. The results indicate an increase in the inlet air flow rate into the stream in case of a decrease in the channel's slope after aeration. This correction has an effective role in protecting the discharge channel against cavitation damage [25]. Wu et al. (2007) studied hydraulic parameters such as flow pressure, water conductivity coefficient, and downstream flow profile at various service gate openings and diverse upstream channel heads in the Longtan Dam's bottom outlet in a laboratory. The results showed that the flow bottom's pressure values in channel gate's downstream rise with an increase in service gate opening, and the water conductivity coefficient in small and large is higher than the middle openings [26]. Li et al. (2020) investigated control gate opening's effect on pressure distribution and cavitation index with numerical and laboratory models. With basic assumptions such as a 45-degree edge angle and a value of 2 for the length to width ratio of the gate (by keeping the gate height constant), they conducted

their research on 10, 30, 50, and 100% opening of control gate with different 2-, 3-, and 4-meter heads. The result is that the cavitation index is high in 10% and 100% openings of the control gate, so that in 30%, 50%, and 70% gate openings, the probability of cavitation is higher [27].

Nikseresht et al. (2012) simulated the bottom intake No. 5 of Sefidrud Dam using a three-dimensional limited volume method and showed that the lowest pressure inside the tunnel occurs at 20% opening of the emergency gate, in which case the cavitation index is lower than the critical value. The use of aeration was proposed to eliminate the risk of cavitation. It is attempting to separate the high-velocity flow along the tunnel by using the appropriate system of aeration. Then, flow can be achieved in the tunnel lining when the risk of cavitation is decayed [28]. In this project, the channel's hydraulic performance and its geometry correction are evaluated for the proper functioning of the deep removal gates in different states of their opening. Since the deep removal gate divides the flow into two parts, the controller with agricultural irrigation valve and the controller with sliding valves through a branch, the study of different functional states has been considered. Single valve operation, single service gate function, and Howell Bungler valve and service gate's simultaneous operation are this project's objectives. Next, the channel's hydraulic operation in different agreed cases with the numerical model will be done, and the conclusion will be made.

1.1. Flow-3D Model and Governing Equations. Numerical simulation of the flow field in the bottom outlets and hydraulic structures in general, spillways, and energy dissipation systems are crucial for designing such structures. The experience of researchers in such simulations has shown that Flow-3D software has a better capability in modeling this type of hydraulic structures among the existing software packages. Flow-3D provides a complete and versatile CFD simulation platform for engineers investigating the dynamic behavior of liquids and gas in a wide range of industrial applications and physical processes. One of the significant features of the Flow-3D for hydraulic analysis is its ability to model free-surface flows, which are modeled using the VOF (volume of fluid) technique reported by Hirt and Nichols (1981) [29]. VOF is an advection scheme, a numerical recipe that allows the programmer to track the shape and position of the interface, but it is not a standalone flow solving algorithm. On the other hand, the equations governing fluid motion can be considered, which include the continuity equation for a control volume assuming incompressible flow and constant flow (equation (1)) and the momentum equation within a control volume considering turbulent (equation (2)) [30].

$$\frac{\partial U_i}{\partial x_i} = 0, \quad (1)$$

$$\frac{\partial U_i}{\partial t} + U_j \frac{\partial U_i}{\partial x_j} = -\frac{1}{\rho} \frac{\partial P}{\partial x_i} + \frac{\partial}{\partial x_i} \left(\nu \frac{\partial U_i}{\partial x_j} - \overline{u_i' u_j'} \right), \quad (2)$$

where ρ is the density of the fluid; x_i and x_j are the Cartesian coordinates; U_i and U_j are the Cartesian components of the velocity vector v ; P is the pressure; and $\overline{u_i u_j}$ mean Reynolds stress tensor.

The two-equation model renormalization group (RNG) k - ε is used to determine the Reynolds stress tensor in the momentum equation for turbulent flow. This model's equations are as follows:

The turbulent kinetic energy equation K :

$$\frac{\partial}{\partial t}(\rho k) + \frac{\partial}{\partial x_i}(\rho k U_i) = \frac{\partial}{\partial x_j} \left(\alpha_k \mu_{eff} \frac{\partial k}{\partial x_j} \right) + G_k - \rho \varepsilon. \quad (3)$$

The turbulent kinetic energy consumption rate equation:

$$\begin{aligned} \frac{\partial}{\partial t}(\rho \varepsilon) + \frac{\partial}{\partial x_i}(\rho \varepsilon U_i) = & \frac{\partial}{\partial x_j} \left(\alpha_\varepsilon \mu_{eff} \frac{\partial \varepsilon}{\partial x_j} \right) + C_{1\varepsilon} \frac{\varepsilon}{k} G_k \\ & - C_{2\varepsilon} \rho \frac{\varepsilon^2}{k} - R_\varepsilon. \end{aligned} \quad (4)$$

In the above equations, α_k and α_ε are the inverse effective Prandtl numbers for k and ε , respectively. $C_{1\varepsilon}$ and $C_{2\varepsilon}$ are constants with values of 1.42 and 1.68, respectively; μ_{eff} is the effective viscosity. The major difference between the RNG k - ε model and the standard k - ε model is that the RNG model has an additional term, R_ε , that significantly improves the accuracy for rapidly strained flows.

2. Material and Methods

2.1. Case Study of Sardab Dam's Outlet Channel with Howell Bunger Valve. Sardab Dam has been built on Sardab River in Iran. The dam site's height is 2712 meters above sea level; the dam's reservoir area is 270 hectares with a total reservoir capacity of 48 million cubic meters (Table 1).

Two sliding gates (service and emergency) with dimension (height * width) 1.4×1.1 m are located in a row inside the dam's bottom channel. Geometric details of Sardab Dam's bottom outlet is shown in Figure 1.

2.2. The Flow Rate Passing through the Channel during Gate Operation. In order to calculate the channel flow rate, assuming the gates are fully open, with the help of Bernoulli's equation and considering the channel loss, we have

$$Q = V_d A_d = A_d \sqrt{\frac{2gH}{\sum \xi + \xi_{out}}}, \quad (5)$$

where Q (m^3/s) is the volume flow rate; V_d (m/s) is the velocity in reference area; A_d (m^2) is the cross-sectional reference area; g (m/s^2) is the gravitational acceleration; H (m) is the head; ξ is the loss coefficient; and ξ_{out} is the loss coefficient in outflow section.

In different parts of the channel, to calculate the total head loss and the total flow rate, a section should be selected as the reference, and the location under the gate is considered a reference section.

Head loss is the potential energy that is converted to kinetic energy. Head losses are due to the frictional resistance of the bottom outlet system (valves, gates, fittings, pipe, entrance, exit losses, etc.). To calculate the total head loss, we have

$$\sum \xi \frac{V_i^2}{2g} = \sum h_{fi} = 1.4224 \frac{V_o^2}{2g}, \quad (6)$$

where V_i (m/s) is the velocity in each section; V_o (m/s) is the velocity in reference area; and h_{fi} (m) is head loss.

The contraction coefficient due to the constriction for the 45-degree angle will be about 0.95.

$$\xi_{out} = 1.05 \left(\frac{A_d}{\varepsilon A_e} \right)^2. \quad (7)$$

In the above equation, A_e (m^2) is the output cross-sectional area, A_d (m^2) is the cross-sectional reference area, and ε is the contraction coefficient of the cross-section compression function.

According to the theoretical issues stated and equations (5)–(7), the maximum volume flow rate passing through the channel is estimated to be $26 m^3/s$ (velocity in reference area is $18.9 m/s$). Table 2 and Figure 2 show the flow rate at different openings and heads.

2.3. Numerical Model. The first feature of Flow-3D is that it employs a highly variable rectangular gridding system for gridding. This characteristic makes the grid or geometry separable from each other. In simpler terms, it does not utilize a fixed grinding system connected to geometry or finite elements. It is also possible to use multiple gridding systems to increase efficiency and flexibility in gridding. The entire outlets flow rigid body is designed with all its details in three dimensions by SolidWorks software to model the bottom outlets' hydraulic conditions flow in Flow-3D software (Figures 3 and 4). It should be noted that five times the tunnel's diameter (7 meters) was added to the length and upstream of the tunnel to create a fully developed flow.

In order to cover the entire rigid body of the outlet with the branch valve, the mesh should be selected so that there is as little space as possible in the channel area as empty space. The following figures show the grid's details (12825258 cells), the computational cells, and the bottom outlet boundary conditions. It should be noted that the elements of the Flow-3D numerical model are of the cuboid element type. Size of the cells in mesh block 1, 2, 3, and 4 in each direction (X , Y , and Z) is 2.3, 2.3, 3.7, and 2.1 cm, respectively. One of the issues that significantly affect the increasing calculation accuracy is determining the appropriate boundary conditions. There are six distinct aspects for defining boundary conditions in Cartesian coordinates, which according to the positive direction of the axes include X_{Min} , X_{Max} , Y_{Min} , Y_{Max} , Z_{Min} , and Z_{Max} . It is worth noting that all these specifications are defined in one block, and separate boundary conditions must be defined for each in the case of several blocks (Figures 5 and 6). The mechanism of applying boundary conditions to each aspect is such that after assigning each of

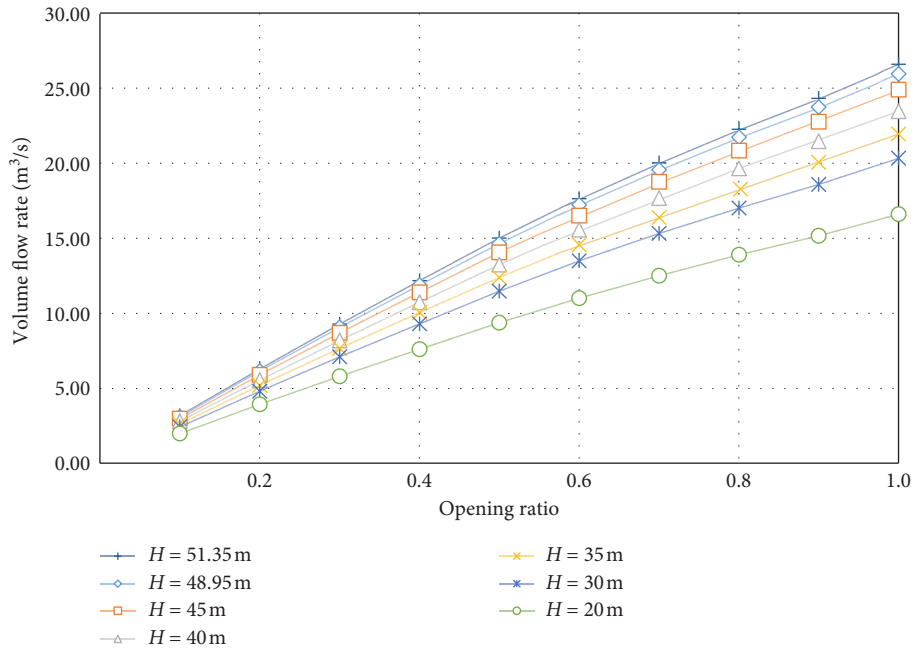


FIGURE 2: The volume flow rate at different openings and heads.

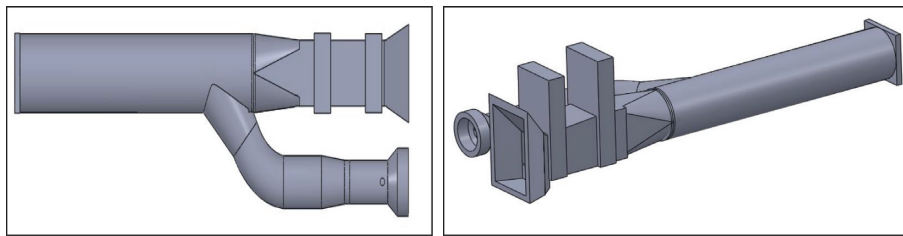


FIGURE 3: Complete bottom outlet geometry with Howell Bunger valve, aerator, and butterfly valve made in SolidWorks software.

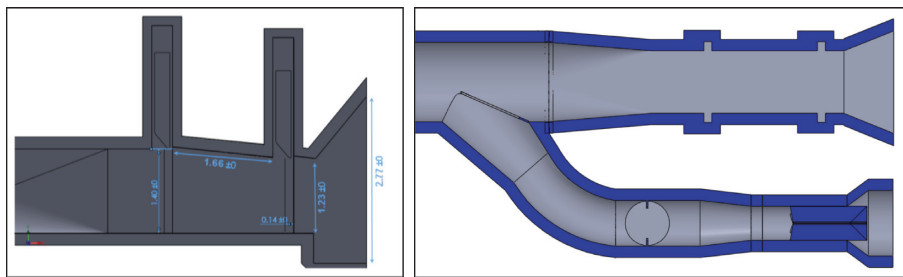


FIGURE 4: Details of construction of 3D geometry of Sardab Dam's bottom outlet (all dimensions are in m).

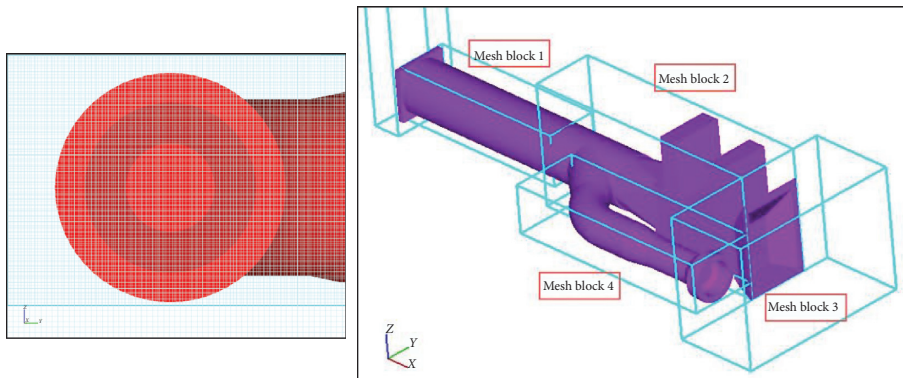


FIGURE 5: Numerical model's gridding and meshing blocks for bottom outlets and branch in Flow-3D numerical model.

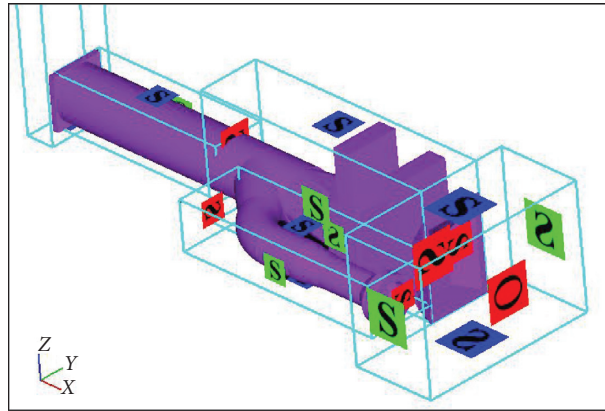


FIGURE 6: Boundary conditions applied in flow simulation in the bottom outlets.

TABLE 3: Mesh sensitivity analysis.

Parameters	Type of mesh				
	Cell size 20% smaller	Cell size 10% smaller	Main	Cell size 10% larger	Cell size 20% larger
Velocity (m/s)	18.21	18.13	18.05	17.42	17.1
Analytical velocity (m/s)	18.9	18.9	18.9	18.9	18.9
Error (%)	3.65	4.07	4.49	7.83	9.52

(Figure 7). In the mentioned destructive phenomena, parameters such as flow rate, velocity, water’s hydrodynamic pressure, air velocity entering the flow, and water depth are effective. By measuring some of these parameters, they can be prevented from happening before failure [34]. Furthermore, due to the governing equations’ nature, it is essential to start the flow analysis with fixed boundary conditions so that eventually the flow reaches a steady state after a suitable time in the model. The output flow rate values of the steady flow state in the numerical model are compared with the analytical solution results in Figure 8. It is noteworthy that the numerical model’s head is considered based on the standard head of 48.95 meters, and the branch valve’s opening is considered 100% open [35].

As indicated in Figure 8, by calculating the mean relative error, the numerical model’s output flow rate in different openings of Sardab Dam’s bottom outlet gate is about 4%, which is an acceptable and petite amount. Hence, based on these conditions, Flow-3D numerical modeling is calibrated and validated, and other required hydraulic parameters, including pressure values, velocity, and hydraulic field of flow in the bottom outlet’s sensitive points, can be investigated. Figures 9 and 10 show the Sardab Dam’s bottom outlet’s output flow rate values at different openings with the analytical solution results.

3.2. Numerical Modeling Results for 5 Modes of Gate and 100% Branch Valve Opening. The results manifested in Table 4 are for openings including 20, 40, 60, 80, and 100% at a standard head height of 48.95 meters. Table 4 presents the changes’ values in the bottom outlet’s output flow rate for different gate openings.

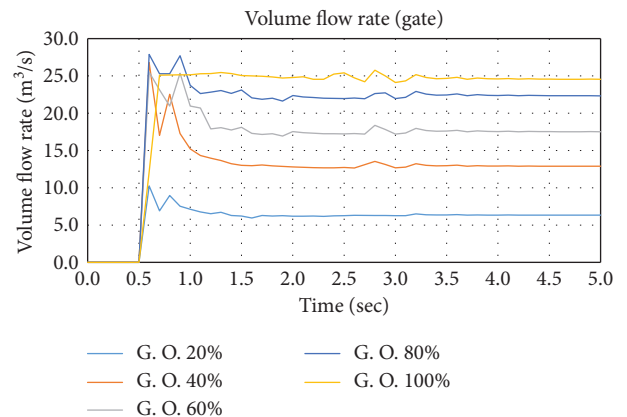


FIGURE 7: Numerical model results for output flow rate at various gate openings during Flow-3D numerical model implementation.

3.3. Velocity Changes in Different Gate Conditions. The hydraulic parameter modeling results show that the velocity value at 100% opening in the section below the gate is about 18 m/s (Figure 11). The maximum velocity under the gate for 40% opening is 23.1 m/s (Figure 12). The velocity values at 80%, 60%, and 20% can be found in Figures 13–15, respectively. Velocity values examination in sensitive points, including gate slots, in the input flow areas to the branch valve, shows that undesirable hydraulic changes do not occur, and severe changes in velocity increase are not observed in these areas [36].

The gate slot’s velocity values are about 2-3 m/s, in which case no flow separation and undesirable circular flow are observed in the slot. These conditions function almost the

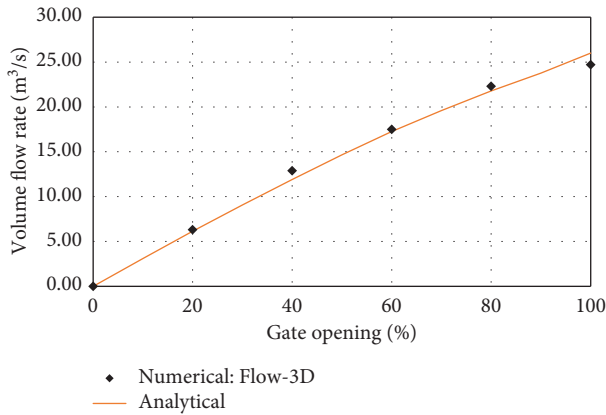


FIGURE 8: Comparison of analytical solution results and numerical modeling of output flow rate in varying valve openings.

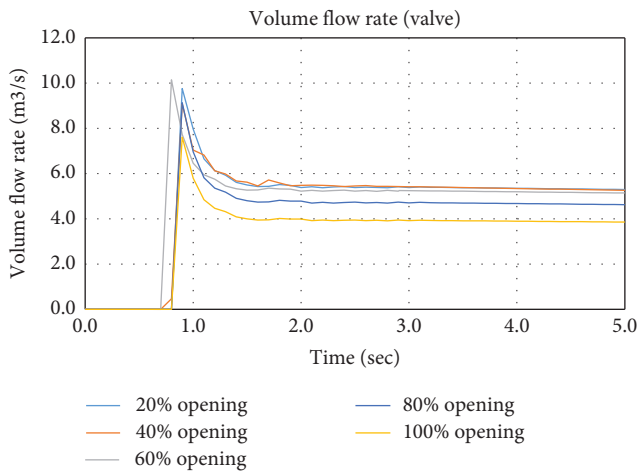


FIGURE 9: Results of Flow-3D numerical model for the valve's output flow rate at the service gate's different openings during model execution.

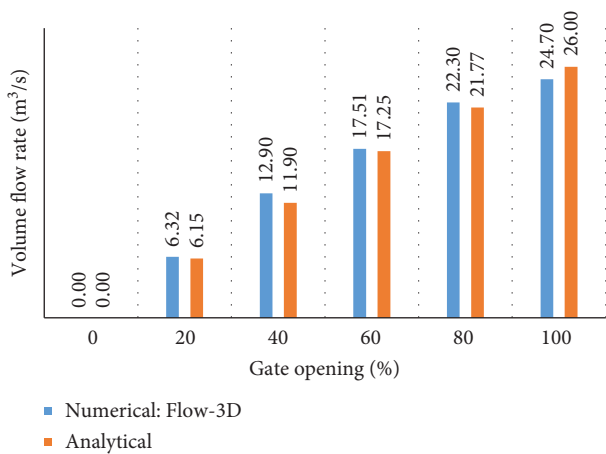


FIGURE 10: Comparison of analytical solution results and numerical modeling of output flow rate in different gate openings.

TABLE 4: Changes in bottom outlet's output flow rate for different gate openings.

Gate openings (%)	Flow rate (gate) (m ³ /s)	Flow rate (valve) (m ³ /s)
0	0.00	0.00
20	6.32	5.30
40	12.90	5.26
60	17.51	5.14
80	22.30	4.63
100	24.70	3.86

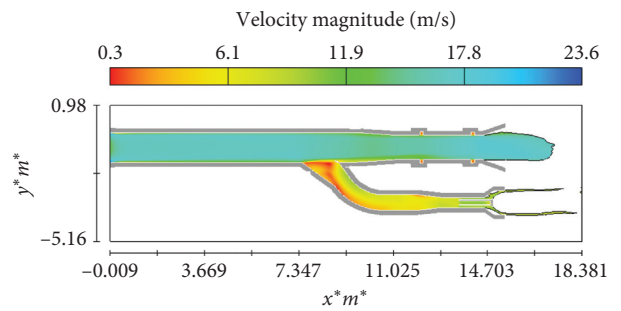


FIGURE 11: Output velocity of the gate and valve in 100% gate and valve opening.

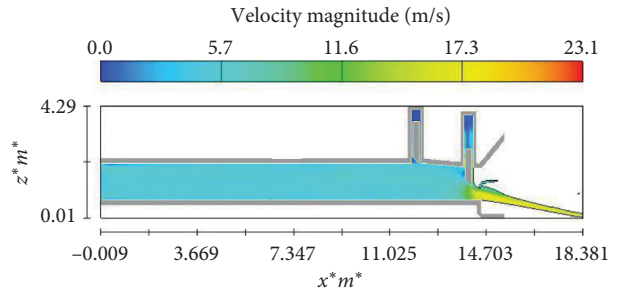


FIGURE 12: Output velocity of the gate and valve in 40% gate and 100% valve opening.

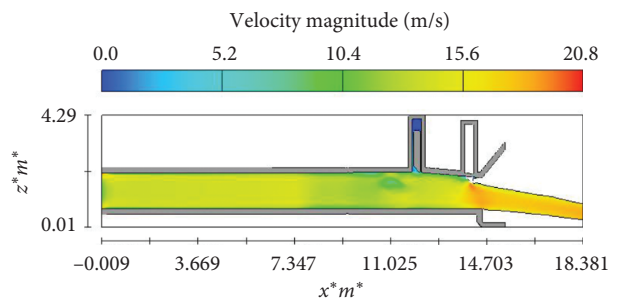


FIGURE 13: Output velocity of the gate and valve in 80% gate and 100% valve opening.

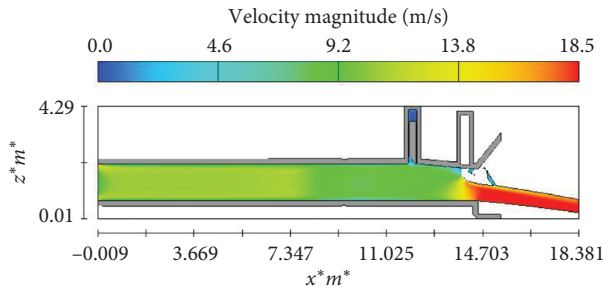


FIGURE 14: Output velocity of the gate and valve in 60% gate and 100% valve opening.

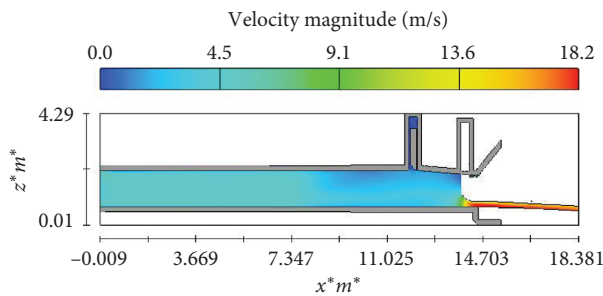


FIGURE 15: Output velocity of the gate and valve in 20% gate and 100% valve opening.

same for all openings. Figure 16 shows the velocity change's size and vectors in the gate slots at 100% gate opening.

Investigation of velocity values in the branch and stiffener area is presented in Figure 17. There is no flow separation and other adverse conditions in this area, and the velocity values at the branch entrance are variable, 2-5 m/s. The velocity values increase after passing through the branch entrance.

3.4. Changes in the Pressure Parameter under Different Gate Openings. In outlet tunnels, the fluid movement may increase the pressure in the flow direction in the face of an obstacle. Such a pressure change is called the inverse pressure gradient. The fluid in this flow boundary layer area is affected by this increasing pressure so that this fluid velocity also slows down. However, because the fluid's kinetic energy within the boundary layer is low, it will likely stagnate and be reversed, causing the boundary layer to separate and deviate from it. The separation of the main stream from the boundary is called the separation phenomenon, which is caused by the reverse pressure gradient. A reverse pressure gradient is a necessary condition and not a sufficient condition for the separation of the flow. In other words, there can be a reverse pressure gradient without separation, while separation without a reverse pressure gradient cannot occur. The pressure amount in the channel area in different gate openings can be seen in Figures 18–21.

The flow under the gate creates a circular flow downstream, the main feature of which is a sharp pressure loss. This pressure loss is a function of the gate's opening, the

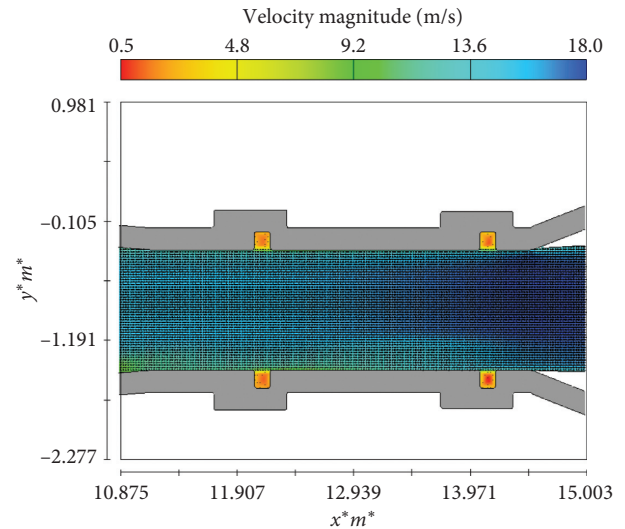


FIGURE 16: Velocity change's size and vectors in the gate slots at 100% gate and valve opening.

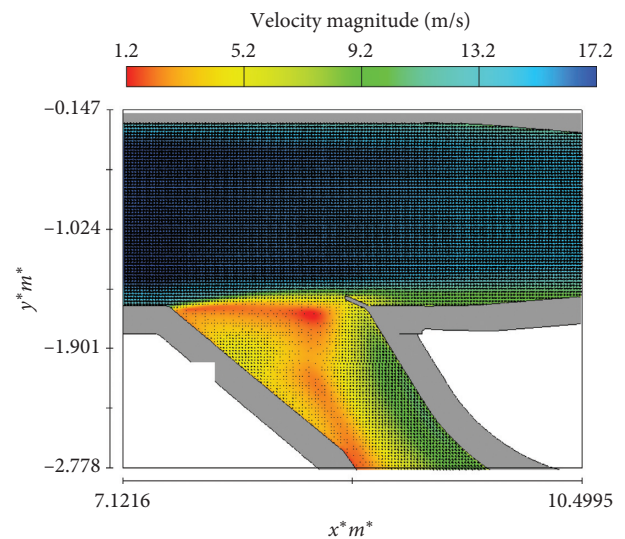


FIGURE 17: Velocity change's size and vectors in the branch area at 100% gate and valve opening.

water head behind the gate, and the channel's geometry. On the other hand, severe pressure fluctuations lessen that area's local pressure, and the potential for cavitation increases due to the high-velocity [37]. As can be seen in Figures 22–25, along the tunnel and in gate areas, gate slots, and branch area, undesirable severe pressure reduction did not occur, and there are no undesirable hydraulic phenomena such as flow separation and local vortices.

3.5. Numerical Modeling Results for 50% Emergency Gate and Service Gate Opening

3.5.1. Fluid Volume Fraction Values per 50% Service and Emergency Gates Opening.

According to Figure 26, part of

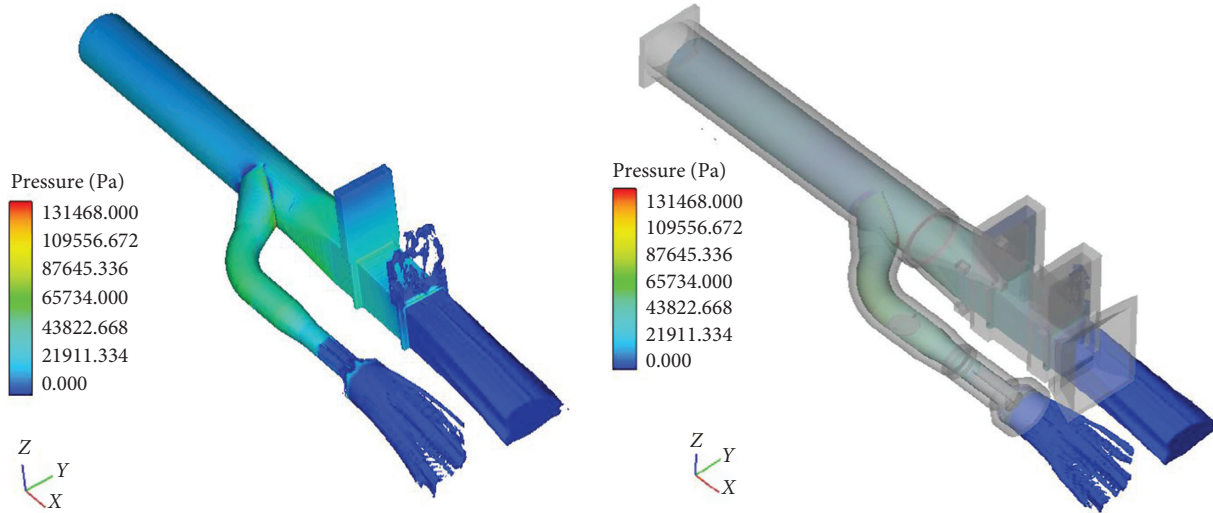


FIGURE 18: Three-dimensional view of the pressure in the whole model.

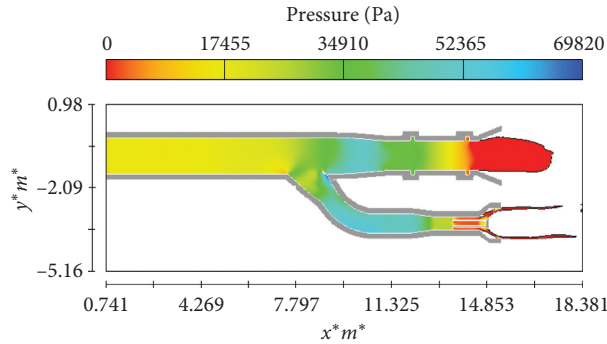


FIGURE 19: The pressure amount in the channel area leading to the gate and the branch in the state of 100% opening (100% valve opening).

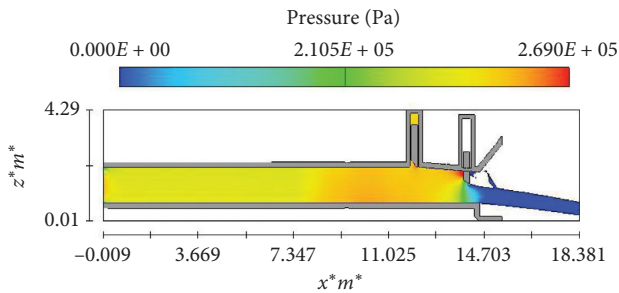


FIGURE 20: The pressure amount in the channel area leading to the gate and the branch in the state of 60% opening (100% valve opening).

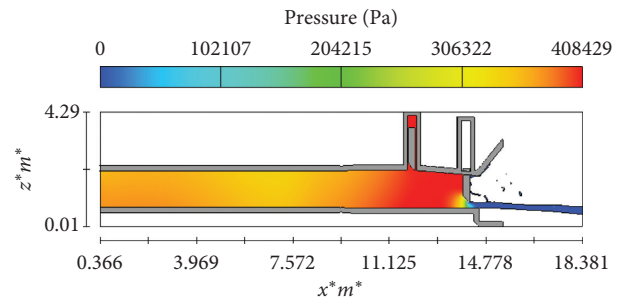


FIGURE 21: The pressure amount in the channel area leading to the gate and the branch in the state of 20% opening (100% valve opening).

the aeration between the two gates is provided through the service gate.

values are reduced. The possibility of cavitation in this area is reduced with the installation of aerators.

3.5.2. *Pressure Changes Values per 50% Service and Emergency Gates Opening.* As can be seen in Figures 27, in the gate's upstream areas, the desired pressure values are decreased, and in the areas between the two gates, the pressure

3.5.3. *Numerical Modeling Results for Fully Closed Gate Mode and 100% Open Branch Valve.* The flow's hydraulic conditions are checked for the completely closed valve state and 100% open branch valve using numerical modeling in this case.

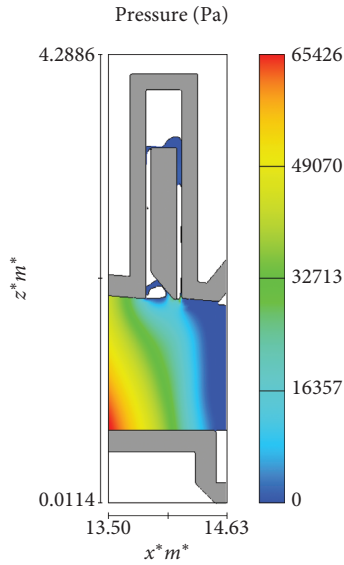


FIGURE 22: Pressure distribution under the gate for 100% opening mode (100% valve opening).

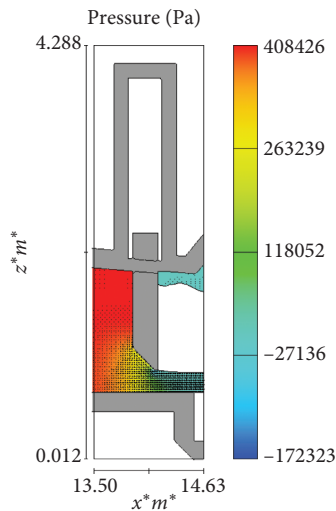


FIGURE 23: Pressure distribution under the gate for 20% opening mode (100% valve opening).

3.5.4. *Pressure Values in the Bottom Outlet’s Tunnel of Sardab Dam and the Branch Area.* As can be seen in Figures 28 and 29, when the valve is completely closed, there is no circular flow and undesirable pressure changes in the tunnel.

3.5.5. *Velocity Values in the Bottom Outlet’s Tunnel of the Sardab Dam and the Branch Area.* As can be seen in Figure 30, the velocity behind the gates is zero in the fully closed state, and the velocity values at the branch entrance are 5-6 m/s. The velocity at the valve output has increased by about 36% compared to when the valves are fully open. Based on these conditions, the branch valve’s output flow rate is estimated to be about 5.3 m³/s.

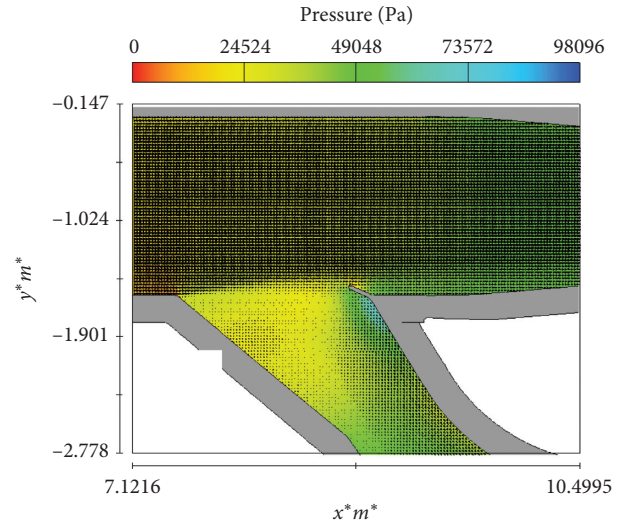


FIGURE 24: Flow pattern around the stiffener and no flow separation in this area (100% valve opening).

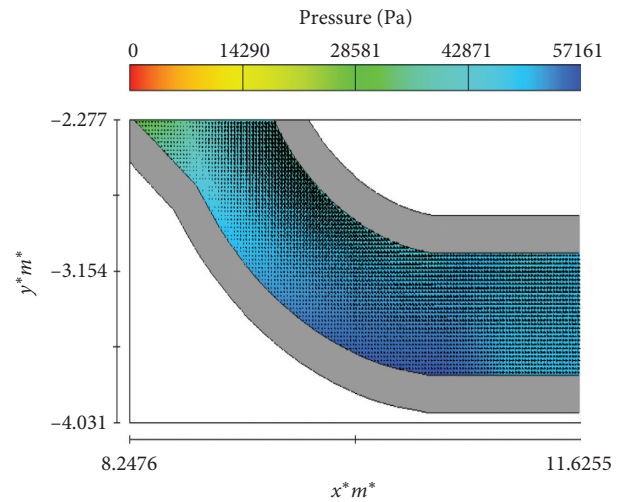


FIGURE 25: Flow pattern around the siphon and no flow separation in this area (100% valve opening).

3.5.6. *Investigation of Cavitation Phenomenon in Channel and Slot.* Cavitation along the channel is usually checked based on a dimensionless number called the cavitation index (σ).

The cavitation index is a function of local pressure and fluid velocity, and this index’s critical value is (0.2–0.25) along the channels and 0.2 inside the slots [38].

In the bottom outlet channels, when the gate opening is 100%, the maximum velocity and, as a result, the maximum discharge capacity is created in the channel. Subsequently, the study and control of cavitation index in 100% opening is considered for this channel. Since the Sardab Dam will be built at an altitude of approximately 2500 meters above sea level and with an ambient temperature of approximately 20 degrees Celsius, to calculate the cavitation index, we will have

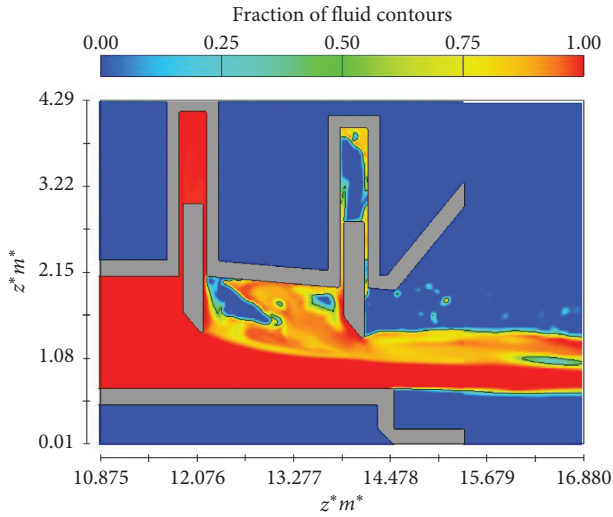


FIGURE 26: Fluid volume fraction contour between two gates in 50% opening state.

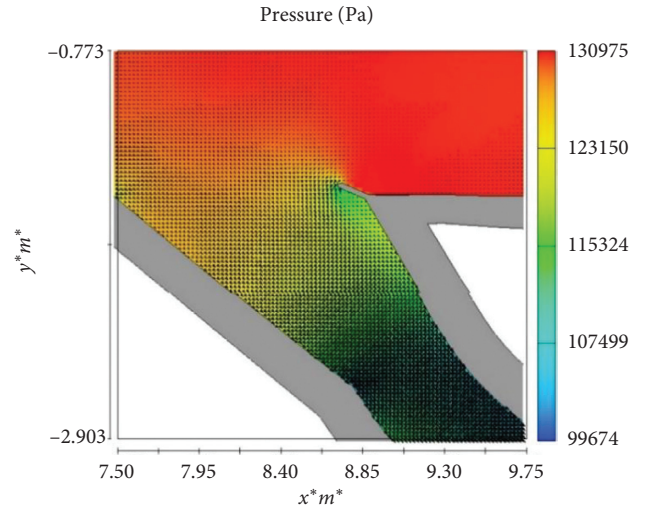


FIGURE 29: Pressure changes in the bottom outlet's branch area of the Sardab Dam for a fully closed gate and 100% open branch valve.

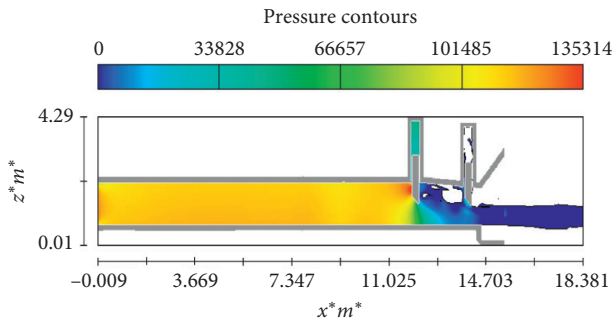


FIGURE 27: Pressure changes in the bottom outlet's tunnel of Sardab Dam at the time of 50% opening of service and emergency gates.

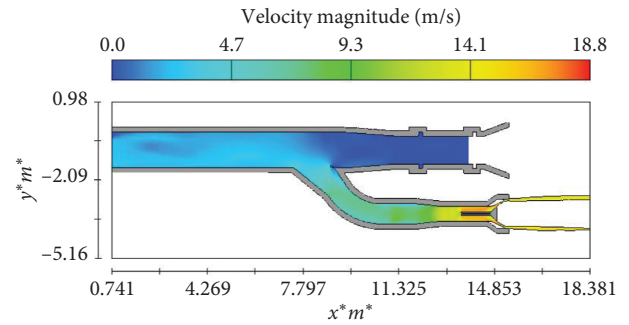


FIGURE 30: Velocity changes in the branch area for fully closed gate mode and 100% open branch valve.

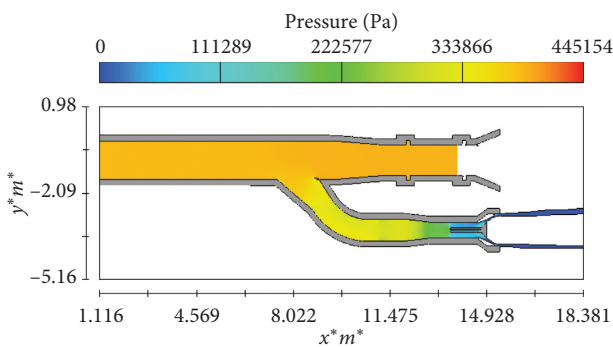


FIGURE 28: Pressure changes in the bottom outlet's tunnel of Sardab Dam for a fully closed gate and 100% open branch valve.

$$\sigma = \frac{P_{\text{abs}} - P_v}{(1/2)\rho.V^2}, \quad (8)$$

where σ is the cavitation index; $P_{\text{abs}} = P_i + P_{\text{bar}}$, in which P_{bar} (Pa) is the atmosphere pressure; and P_i (Pa) is the relative pressure and P_v is the vapor pressure of fluid.

Equation (9) is used to calculate atmospheric pressure:

$$P_{\text{bar}} = P_a \left(1 - \frac{BZ}{T_0} \right)^{g/RB}. \quad (9)$$

The parameters' values of the above equation are defined as follows:

$$\begin{aligned} \frac{g}{RB} &= 5.26, \\ T_0 &= 293.1 \text{ K}, \\ B &= 0.0065 \frac{\text{K}}{\text{m}}, \\ Z &= 2500 \text{ m}, \\ P_a &= \text{Sea level pressure.} \end{aligned} \quad (10)$$

For air-fluid, the value of $P_{\text{bar}} = 74 \text{ kPa}$ is considered using equation (9).

It should be noted that the fluid vapor pressure will be equal to $P_v = 2.337 \text{ kPa}$ at this temperature. The cavitation index can be calculated with the help of pressure and velocity

values in different conditions using the above parameters' values.

To calculate the relative pressure values of P_i , according to the specific values of the 51.35 m head, the velocity V_i can be calculated with the help of the following equation. The loss values sum is based on the velocity values in the reference cross-section V , which has a cross-section equal to $A = 1.25 \times 1.10 = 1.375 \text{ m}^2$:

$$P_i = \rho g \left(H - \frac{V_o^2}{2g} - \sum h_i \right), \quad (11)$$

$$\sum h_o = \sum \xi \frac{V^2}{2g}.$$

Considering the flow head equal to 51.35 m for the two sections of the gate slot and the output section, there will be a flow (in the output section, the relative pressure is equal to zero, and the velocity is equal to 18.9 m/s).

At the output section,

$$\sigma = \frac{P_i + P_{\text{bar}} - P_v}{(1/2)\rho.V^2} \approx 0.4. \quad (12)$$

Also, the cavitation values in the service gate slot, as one of the most critical points for cavitation occurrence, are calculated as follows:

$$P_i = \rho g \left(H - \frac{V_o^2}{2g} - \sum h_i \right) \approx 71 \text{ kPa}, \quad (13)$$

$$\sigma = \frac{P_i + P_{\text{bar}} - P_v}{(1/2)\rho.V^2} \approx 0.79.$$

The gate slot should be checked using the slot characteristics in order to examine the possibility of cavitation. Considering that the slot's retraction angle is 1:12 and $W/D = 140/162 = 0.86$ and $\Delta/W = 25/140 = 0.18$, the allowable index value is about 0.2, and this index is about 0.79 in Sardab Dam's gate slot. Accordingly, cavitation will not happen in the slot [39–42].

Dam bottom outlets which contain valves and pumps play a vital role in dam operation and safety, as they allow controlling the water surface elevation below the spillway level. Probability of the formation of cavitation due to the concentrated vortices is too high. The vorticity distribution near the branch entrance exhibited high values due to the cylindrical shape of the bottom outlet which contributed to high amount of flow separation [43, 44]. The transient flow features associated with a moving gate were successfully captured as well as the discharge characteristic for partial opening of the gate. For partial openings, water flows under the gate lip at high-velocity and drags the air downstream of the gate, which may cause damages due to cavitation and vibration. The results suggest that the Flow-3D can be useful for calculating the air demand in dam bottom outlets. In the case study presented, the appropriateness of the existing design was verified. For partial gate opening, the discharge varies with the square of gate opening, whereas for a fully opened gate, discharge varies with $H^{1/2}$. For new facilities,

the possibilities of the Flow-3D for identifying the flow patterns and for computing the pressure and velocity fields should be helpful for designing the aeration system.

4. Conclusion

In the present study, Sardab Dam's bottom outlet and Howell Bunger valve's hydraulic performance in different opening conditions, including 20, 40, 60, 80, and 100%, with different flow rates, was investigated. These examinations comprise the service gate's single operation, the service gate and the Howell Bunger valve's simultaneous operation, and the Howell Bunger valve's single operation. The results presented for different opening conditions for velocity values with 100% opening in the section below the gate is about 18 m/s, and the maximum velocity under the gate for 40% opening is equal to 23.1 m/s. The velocity values in the gate slot are about 2–3 m/s, in which case no flow separation and undesirable circular flow are observed in the slot. This condition is true for all gate openings. The velocity values at the branch entrance are variable 2–5 m/s, no flow separation and other adverse conditions occur in this area, and the velocity values increase after passing through the branch entrance. There is no undesirable change in the distribution of pressure along the tunnel and in the gate areas, and there is no drastic reduction of pressure in this area. It should be noted that there are no undesirable hydraulic phenomena in these sections, including flow separation and local vortices. For 50% opening of the gates in the gate's upper areas, the desired pressure values are reduced, and in the areas between the two gates, the pressure values are reduced. Moreover, with the installation of aerators, the possibility of cavitation in this area is reduced. For fully closed gate mode and 100% open branch valve, no circular flow and undesirable pressure changes are created in the tunnel. Also, the velocity behind the valves in the fully closed state is zero, and at the branch entrance point, it is 5–6 m/s. At the valve output, the velocity has increased by about 36% compared to when the gates are fully open. Based on these conditions, the branch valve's output flow rate is estimated to be about 5.3 m/s. The presented results show that due to the bottom outlet operation in the reservoir's maximum head condition, the probability of cavitation in the area between the two gates is very high. This analysis suggests that numerical modeling with the Flow-3D can be helpful for the design of this kind of hydraulic works.

Data Availability

All data used to support the findings of the study are included within the article.

Disclosure

This research received no specific grant from any funding agency in the public, commercial, or not-for-profit sectors.

Conflicts of Interest

The authors declare that there are no conflicts of interest regarding the publication of this paper.

References

- [1] F. Salazar, J. San-Mauro, M. Á. Celigueta, and E. Oñate, "Air demand estimation in bottom outlets with the particle finite element method," *Computational Particle Mechanics*, vol. 4, no. 3, pp. 345–356, 2016.
- [2] M. Zounemat-Kermani and M. Scholz, "Computing air demand using the Takagi-Sugeno model for dam outlets," *Water*, vol. 5, no. 3, pp. 1441–1456, 2013.
- [3] G. H. Chen, G. Y. Wang, C. L. Hu, B. Huang, and M. D. Zhang, "Observations and measurements on unsteady cavitating flows using a simultaneous sampling approach," *Experiments in Fluids*, vol. 56, no. 2, 2015.
- [4] M. Karalar and M. Çavuşlı, "Seismic effects of epicenter distance of earthquake on 3D damage performance of CG dam," *Earthquakes and Structures*, vol. 18, no. 2, pp. 201–213, 2020.
- [5] M. Moradi, S. M. Aghajanzadeh, H. Mirzabozorg, and M. Alimohammadi, "Underwater explosion and its effects on nonlinear behavior of an arch dam," *Coupled Systems Mechanics*, vol. 7, no. 3, pp. 333–351, 2018.
- [6] M. Karalar and M. Çavuşlı, "Examination of 3D long-term viscoplastic behaviour of a CFR dam using special material models," *Geomechanics and Engineering*, vol. 17, no. 2, pp. 119–131, 2019.
- [7] M. Karalar and M. Çavuşlı, "Evaluation of 3D nonlinear earthquake behaviour of the Ilisu CFR dam under far-fault ground motions," *Advances in Civil Engineering*, vol. 2019, Article ID 7358710, 15 pages, 2019.
- [8] O. A. Yamini, M. R. Kavianpour, and S. H. Mousavi, "Wave run-up and rundown on ACB Mats under granular and geotextile filters' condition," *Marine Georesources & Geotechnology*, vol. 36, no. 8, pp. 895–906, 2017.
- [9] J. Speerli and W. H. Hager, "Air-water flow in bottom outlets," *Canadian Journal of Civil Engineering*, vol. 27, no. 3, pp. 454–462, 2000.
- [10] B. Fazelabdolabadi and M. H. Golestan, "Towards bayesian quantification of permeability in micro-scale porous structures-the database of micro networks," *HighTech and Innovation Journal*, vol. 1, no. 4, pp. 148–160, 2020.
- [11] R. Touaibi, H. Koten, and O. Boydak, "Parametric study of an organic rankine cycle using different fluids," *Emerging Science Journal*, vol. 4, no. 2, pp. 122–128, 2020.
- [12] G. Innella and P. A. Rodgers, "The benefits of a convergence between art and engineering," *HighTech and Innovation Journal*, vol. 2, no. 1, pp. 29–37, 2021.
- [13] M. Sadat Helbar, A. Parvaresh Rizi, J. Farhoudi, and A. Mohammadi, "3D flow simulation to improve the design and operation of the dam bottom outlets," *Arabian Journal of Geosciences*, vol. 14, no. 2, 2021.
- [14] B. K. Sreedhar, S. K. Albert, and A. B. Pandit, "Cavitation damage: theory and measurements-a review," *Wear*, vol. 372–373, pp. 177–196, 2017.
- [15] A. R. Sengupta, R. Gupta, and A. Biswas, "Computational fluid dynamics analysis of stove systems for cooking and drying of muga silk," *Emerging Science Journal*, vol. 3, no. 5, pp. 285–292, 2019.
- [16] I. Ntintakis, G. E. Stavroulakis, and N. Plakia, "Topology optimization by the use of 3D printing technology in the product design process," *HighTech and Innovation Journal*, vol. 1, no. 4, pp. 161–171, 2020.
- [17] J. Yang, P. Teng, Q. Xie, and S. Li, "Understanding water flows and air venting features of spillway-a case study," *Water*, vol. 12, no. 8, p. 2106, 2020.
- [18] K. Kramer, W. H. Hager, and H.-E. Minor, "Development of air concentration on chute spillways," *Journal of Hydraulic Engineering*, vol. 132, no. 9, pp. 908–915, 2006.
- [19] J. Lewin, *Hydraulic Gates and Valves: In Free Surface Flow and Submerged Outlets*, Thomas Telford, London, UK, 2001.
- [20] R. Shilpakar, Z. Hua, B. Manandhar et al., "Numerical simulation on tunnel spillway of Jingping-I hydropower project with four aerators," *IOP Conference Series: Earth and Environmental Science*, vol. 82, Article ID 012013, 2017.
- [21] F. Daneshmand, E. A. Yazdi, and Y. B. Lari, "Hydraulic model test of the bottom outlet of Sivand dam," in *Proceedings of the 5th ISME/WSEAS International Conference on Fluid Mechanics and Aerodynamics*, pp. 269–275, Athens, Greece, 2007.
- [22] D. L. Vischer and W. H. Hager, *Dam Hydraulics*, John Wiley & Sons, London, UK, 1999.
- [23] M. R. Kavianpour, *The Reattaching Flow Downstream of Deflectors Including the Effect of Air Injection*, Ph.D. dissertation, University of Manchester, Manchester, UK, 1997.
- [24] S. Khazaei, R. Ellahi, E. Niknami, and K. Shahverdy, "Hydraulic analysis and cavitation cavitation phenomenon in physical and numerical models of the bottom outlet in Rudbar dam, Lorestan province, Iran," in *Proceedings of the 36th IAHR World Congress*, The Hague, the Netherlands, 2015.
- [25] S.-P. Ruan, J.-H. Wu, W.-W. Wu, and R.-Z. Xi, "Hydraulic research of aerators on tunnel spillways," *Journal of Hydrodynamics*, vol. 19, no. 3, pp. 330–334, 2007.
- [26] J.-H. Wu, S.-R. Feng, W.-W. Wu, and S.-P. Ruan, "Hydraulic characteristics of partial opening of the working gate for a discharge tunnel," *Journal of Hydrodynamics*, vol. 19, no. 4, pp. 488–493, 2007.
- [27] J.-Y. Li, Z.-X. Gao, H. Wu, and Z.-J. Jin, "Numerical investigation of methodologies for cavitation suppression inside globe valves," *Applied Sciences*, vol. 10, no. 16, p. 5541, 2020.
- [28] A. H. Nikseresht, N. Talebneydokhti, and H. Khorshidi, "Three-dimensional numerical modeling of cavitation and aeration system in dam outlets," *Journal of Fluids Engineering*, vol. 134, no. 9, Article ID 091302, 2012.
- [29] C. W. Hirt and B. D. Nichols, "Volume of fluid (VOF) method for the dynamics of free boundaries," *Journal of Computational Physics*, vol. 39, no. 1, pp. 201–225, 1981.
- [30] J. H. Ferziger and M. Perić, "Computational methods for fluid dynamics," *Computational Methods for Fluid Dynamics*, Springer, Berlin, Germany, 2002.
- [31] Flow Science, Inc., FLOW-3D User Manual Version 10.0.1.
- [32] M. Nazari-Sharabian, A. Nazari-Sharabian, M. Karakouzian, and M. Karami, "Sacrificial piles as scour countermeasures in river bridges a numerical study using flow-3D," *Civil Engineering Journal*, vol. 6, no. 6, pp. 1091–1103, 2020.
- [33] N. J. H. Al-Mansori and L. S. A. Al-Zubaidi, "One-dimensional hydrodynamic modeling of the euphrates river and prediction of hydraulic parameters," *Civil Engineering Journal*, vol. 6, no. 6, pp. 1074–1090, 2020.
- [34] T. M. Taher and A. O. Anwar, "Effects of gate lip orientation on bottom pressure coefficient of dam tunnel gate," *Arabian Journal for Science and Engineering*, vol. 41, no. 12, pp. 4927–4936, 2016.
- [35] B. Dargahi, "Flow characteristics of bottom outlets with moving gates," *Journal of Hydraulic Research*, vol. 48, no. 4, pp. 476–482, 2010.
- [36] H. Wang, "Turbulence and air entrainment in hydraulic jumps," Ph.D. dissertation, The University of Queensland, Brisbane, Australia, 2014.
- [37] R. Narayanan, "The role of pressure fluctuations in hydraulic modelling," in *Proceedings of the Symposium on Scale Effects in*

- Modelling Hydraulic Structures, Congress IAHR, Esslingenam Neckar, Germany, September 1984.*
- [38] H. T. Falvey, *Cavitation in Chutes and Spillways, Engineering Monograph 42*, Water Resources Technical Publication, US Printing Office, Bureau of Reclamation, Washington, DC, USA, 1990.
 - [39] M. Ghaderi, "Study of rehabilitation plan of bottom outlet service and emergency gates of Karun 1 dam," *Dams and Reservoirs*, vol. 30, no. 3, pp. 91–96, 2020.
 - [40] C. Liu, Q. Yan, and H. G. Wood, "Numerical investigation of passive cavitation control using a slot on a three-dimensional hydrofoil," *International Journal of Numerical Methods for Heat & Fluid Flow*, vol. 30, no. 7, pp. 3585–3605, 2019.
 - [41] T. Smajdorová and D. Noskievičová, "Methodology for the application of nonparametric control charts into practice," *Emerging Science Journal*, vol. 4, no. 4, pp. 272–282, 2020.
 - [42] C. V. Davis and K. E. Sorensen, *Handbook of Applied Hydraulics*, vol. 22, pp. 22–66, McGraw-Hill Book Company, New York, NY, USA, 1969.
 - [43] X. Song and C. Liu, "Experimental investigation of floor-attached vortex effects on the pressure pulsation at the bottom of the axial flow pump sump," *Renewable Energy*, vol. 145, pp. 2327–2336, 2020.
 - [44] T. A. Norizan, E. Reda, and Z. Harun, "Enhancement of vorticity reduction by floor splitter in pump sump to improve pump efficiency," *Sustainable Energy Technologies and Assessments*, vol. 26, pp. 28–36, 2018.

Research Article

Dynamic Wave-Induced Settlement Behavior of a Caisson Breakwater Built on a Sandy Seabed

Gichun Kang,¹ Tae-Hyung Kim,² Jiseong Kim,³ and Seong-Kyu Yun ⁴

¹Department of Civil Engineering, College of Engineering, Gyeongsang National University, 501 Jinjudae-ro, Jinju, Gyeongsangnam-do 52828, Republic of Korea

²Department of Civil Engineering, Korea Maritime and Ocean University, 727 Taejong-ro, Youngdo-gu, Busan 49112, Republic of Korea

³Department of Cadastre & Civil Engineering, Vision College of Jeonju, 235 Cheonjam-ro, Wansan-gu, Jeonju, Jeollabuk-do 55069, Republic of Korea

⁴Engineering Research Institute, Gyeongsang National University, 501 Jinjudae-ro, Jinju, Gyeongsangnam-do 52828, Republic of Korea

Correspondence should be addressed to Seong-Kyu Yun; tjdrb330@gnu.ac.kr

Received 21 February 2021; Accepted 23 April 2021; Published 11 May 2021

Academic Editor: Faming Huang

Copyright © 2021 Gichun Kang et al. This is an open access article distributed under the Creative Commons Attribution License, which permits unrestricted use, distribution, and reproduction in any medium, provided the original work is properly cited.

Monitored breakwater settlements taken from an actual breakwater structure over an extended period of time (more than five years) were analyzed. The analysis revealed that the waves clearly affect the settlement of the breakwater, especially during high wave conditions such as typhoons. Breakwater settlement is caused by a decrease of effective stress of seabed during partial liquefaction due to wave-induced cyclic loads, which occurs due to an increase in excess pore pressure and the combination of oscillatory and residual pore water pressures. A new combined numerical model was suggested that allows the storm wave-induced seabed settlement underneath the caisson breakwater to be examined qualitatively. The technique uses a combined wave model (2D-NIT) and soil model (FLIP). The dynamic wave load calculated by the 2D-NIT was used as the input data for the soil model. This soil model can simulate both oscillatory and residual pore water pressures at the same time. There is a different feature to other previous studies adopting similar techniques.

1. Introduction

Two key calculations are required to design a breakwater on sand layers: an assessment of the ultimate bearing capacity and an estimation of the settlement under working loads. Settlements are considered tolerable if they do not impair the functionality or serviceability of the foundations or the supported superstructures under the design loads [1–3].

Figure 1 shows the schematic diagram from the settlement data measured at the edge of the caisson breakwater placed at the west breakwater in Jeju's outer harbor. As shown in this figure, a settlement occurs not only immediately after loading but also continually over time. Soil strata from the top layer at this site contain layers of marine sediment, sandy soil, and weathered rock. According to the soil profile, there is not a soft clay layer at this site. Kim et al.

[4] studied this long-term compressional settlement problem. They conducted compression tests to assess the compression characteristics of the sands and found that the settlement issues are due to the high compressibility and particle crushing and shattering of the sand materials at the site, about 50% of which includes carbonate sands derived from shell. The carbonate sand is weaker than silicate sand and has many pores on the particle's surface and an angular shape [5].

Another interesting phenomenon in Figure 1 is the rapid and abruptly large settlement at intervals A and B. This settlement is not related to the carbonate sands because its magnitude is fairly large, and it occurs over a very short period of time. The settlement at interval A occurred after Typhoon Maemi passed, as shown in Figure 1. Typhoon Maemi had a maximum wave height of 11.38 m and

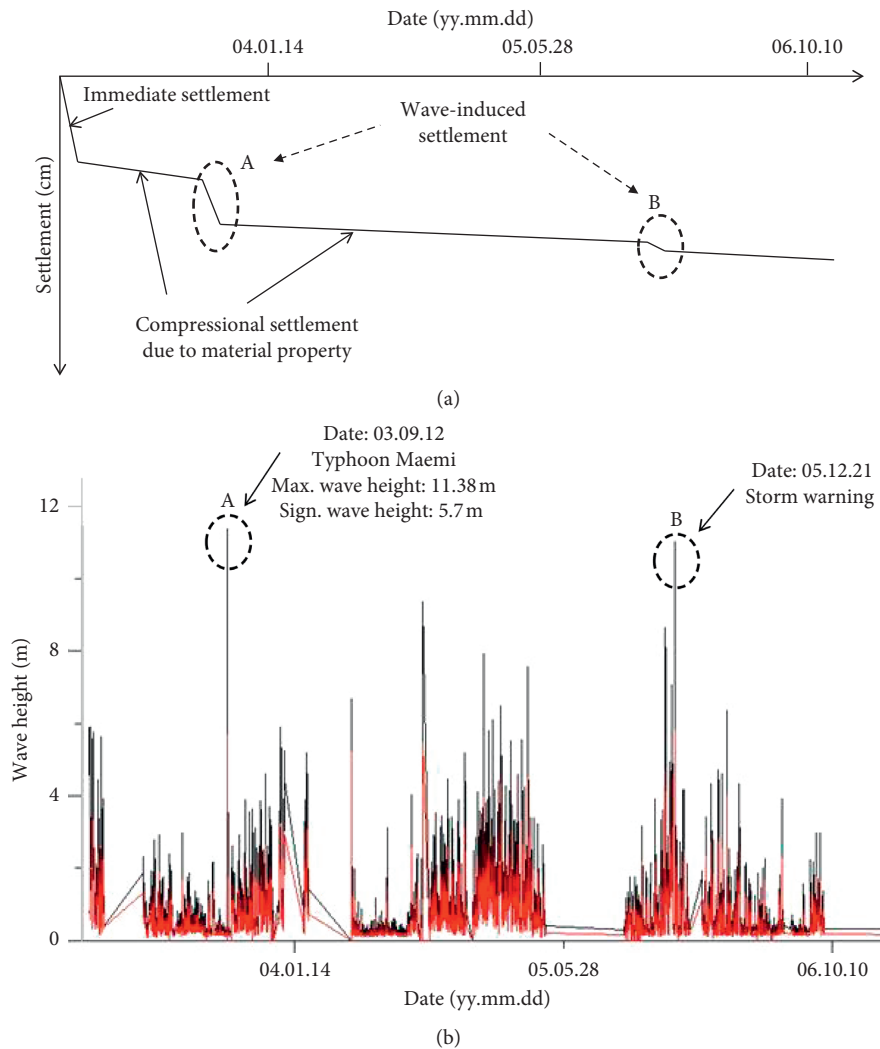


FIGURE 1: (a) Schematic diagram of caisson breakwater settlement history and (b) wave height history measured in the west breakwater of Jeju Outer Harbor.

a maximum wave period of 7.8 sec. It was the first big storm after the caisson was placed on the site. Interval *B* indicates another big wave that attacked the caisson, similar to Typhoon Maemi. Some settlements also occurred here, but the magnitude was smaller than that of interval *A*. Based on the settlement record data, the structure built on sand was also exposed to wave-induced settlements. This phenomenon also has been captured by previous research done by Ye et al. [6].

Many numerical and experimental studies for wave-induced soil responses around breakwater have been carried out since the 1970s. Zen and Yamazaki [7], Mase et al. [8], Mizutani et al. [9], Ulker et al. [10], Li and Jeng [11], and Jeng et al. [12] used a poroelastic model for the seabed, and the dynamic Biot equation [13], known as “u-p” approximation, was proposed by Zienkiewicz et al. [14] to govern the dynamic response of the porous medium under wave loading. Ye and Jeng had conducted milestone work in this field. Ye et al. [15] developed a semicoupled numerical mode FSSI-CAS 2D to investigate the complicated interaction between

ocean waves, offshore structures, and their loose seabed foundations. They further extended the 2D package to form FSSI-CAS 3D for the same purpose [16].

Oumeraci [17] analyzed many breakwater failures and concluded that the partial or complete liquefaction risk must be considered in the case of wave loading, which is especially relevant with a vertical breakwater or an offshore gravity platform. de Groot et al. [18,19] indicated that the foundation of the vertical breakwater, or an offshore gravity platform built in sandy soil, may fail due to wave-induced partial liquefaction. Kudella [20] conducted large-scale model experiments in a wave flume to study the generation of transient, instantaneous, and residual pore pressure in a seabed beneath a caisson breakwater that has been subjected to wave loads. These experiments showed that the residual pore pressure is essentially generated by the caisson’s movements when breaking the wave loads and that they are closely related to residual soil deformation. These previous studies clearly show the effect of waves on seabed deformation underneath the breakwater.

Like previous studies done by other researchers, this study focused on the dynamic response of a sandy seabed and the liquefaction in the sand seabed's foundation under typhoon-generated wave loading. Two subjects were studied. First, the settlement data from the actual caisson breakwaters, measured over a time span greater than five years, were analyzed to determine the characteristics of the wave-induced settlement. The data obtained from the caissons were selected to build the west breakwater at the Jeju Outer Harbor. Secondly, a new numerical model consisting of two submodels: the wave and soil models, was proposed to simulate the wave-induced settlement of a caisson built on a sandy seabed. The dynamic wave load calculated by the wave model (2D-NIT) was used as the input data for the soil model (FLIP). This soil model can simulate both oscillatory and residual pore water pressures at the same time.

2. Characteristics of the Soil and Waves at the Site

2.1. Properties of the Soil and Waves at the Site. The results of a boring investigation conducted at the west breakwater construction site in the Jeju Outer Harbor indicated the seabed ground level was DL (datum level) (-) 12.78~(-) 22.62 m. The bedding in this region consists of marine alluvial deposits, weathered bedrock deposits, and soft rock from the face of the seabed surface. The marine alluvial deposits, the main subject of this study, consist of fine to medium sand and silty sand, based on USCS (unified soil classification systems) guidelines. It has been transported by waves and distributed between 0.3 and 17.5 m, with an average of approximately 10 m. This sediment sand contains a significant amount of carbonate sand formed by fish bones and shellfish. The N value of the standard penetration test ranged from 9 to 25, which indicates a generally dense or very dense relative density. The variations were based on the location and the depth. Interestingly enough, according to the soil profile in Figure 2, no soft clay layer exists in this area.

A self-recording wave gauge was installed to observe the height and direction of the waves at the west breakwater construction site. The impact of the wave reflection, due to the structure of the caisson body, was minimized because the measuring point was 500 m from the front of the breakwater. This space between the gauge and the breakwater was large enough to eliminate the wave reflection effect. Table 1 summarizes the observation of waves over 5 m from 2002 to 2006. During the monitoring period, one mega typhoon, Maemi, occurred. Maemi produced waves with a maximum height of 11.38 m (max. significant wave height of 5.7 m) and a maximum wave period of 7.8 sec (max. significant wave period of 8.4 sec). Additionally, as shown in Table 1, after Typhoon Maemi, more than 14 times the average number of waves over 5 m in height passed this area. On Dec 21, 2005, a storm hit this area, producing waves with a height of 11.01 m, with a maximum wave period of 9.7 sec.

2.2. Measurement of the Caisson Settlement Results and Discussion. A total of 84 caissons were installed in the west breakwater. Caisson #5 was the first to be installed, followed

by caissons #1, 2, 3, and 4, which were installed to connect to caisson #5. They were installed in the eastbound direction in sequence, from caisson #6. The caissons installed in the west breakwater can be classified into four groups: nonperforated, curved slit, enlarged slit, and different shapes curved slit.

When constructing a caisson breakwater, the stability must be judged, which is why it is important to establish a plan to measure its settlement. In the case of the Jeju Outer Harbor, only level measurements were conducted. Jeju TBM (No. 7) was used as a reference point. The caisson's settlement was recorded after it was installed at the reference point. The settlement was measured at four edges, and those edges were numbered from one to four—starting from the seaward edge of the caisson.

Of the 84 total caissons installed in the west breakwater, Figure 3 shows the selected caissons' (#4, 5, 7, 8, and 9) settlement data. These selected caissons were installed from approximately 2003 through 2006 and have experienced wave actions. The vertical dotted lines in Figure 3, which are very important, represent the date of the occurrence of a high wave that could have affected the caisson's settlement. As shown in Figure 3, the final settlement varied for each caisson, but the settlement trend was very similar across all the caissons. The initial immediate settlement occurred after the installation of the caisson due to its weight. Then, creep settlement occurred steadily due to the properties of the sand in this area. Then, on particular dates, such as September 12, 2003, a significant amount of settlement occurred rapidly. It is unlikely that this rapid, significant settlement was caused by the material properties of the sand because the settlement progressed greatly in a short period of time. Rather, this settlement may have been induced by wave actions. The settlement occurred at the same time that a large wave hit.

The settlement of caisson #8, which was installed just three months before the typhoon, increased from 26 cm to 42 cm after the typhoon. The settlement of caisson #9, which was installed just one month before the typhoon, increased dramatically from 14 cm to 45 cm after the typhoon. Other caissons also exhibited a significant amount of wave-induced settlement, though of a lesser magnitude than caisson #9, because they were installed much earlier.

3. Present Numerical Model

3.1. Wave Model (2D-NIT). To determine the dynamic wave force (including breaking waves) on the seabed and the breakwater, the present study used a program called the 2D-NIT (two-dimensional numerical irregular wave tank) model [21,22]. The model used the solutions to the viscous and incompressible Navier-Stokes equations for a two-phase flow (water and air) model, and the volume of the fluid (VOF) method was used to treat the free surface of the water. The numerical wave tank that was adopted in the 2D-NIT model is shown in Figure 4. As for the open boundary conditions, fictitious dissipation zones (L_a) were added to the left and right sides of the computational domain. Their thickness is $2L$, with L being the wavelength, in order to absorb the wave energy. The internal wavemaker is located in front of the fictitious dissipation zone on the left side of the computational domain.

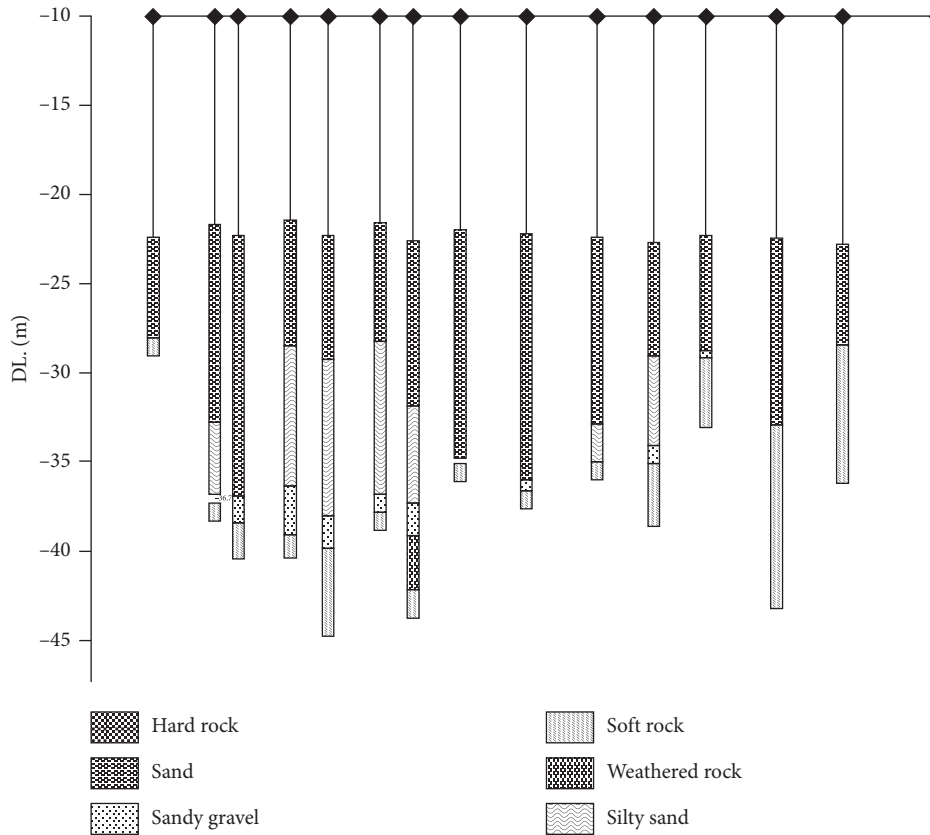


FIGURE 2: Boring results at the west breakwater in Jeju Outer Harbor.

TABLE 1: Real monitored data measured by a wave gauge installed in front of the west breakwater.

Date (yy.mm.dd)	Time	Maximum wave height (m)	Maximum wave period (s)	Significant wave height (m)	Significant wave period (s)
02.12.30	0:00	5.91	5.6	0.80	4.5
03.01.05	8:00	5.76	7.3	3.12	7.0
03.01.20	18:00	5.63	9.3	2.55	6.4
03.09.12 ¹	18:00	11.38	7.8	5.70	8.4
03.12.19	12:00	5.90	6.5	3.01	6.6
03.12.26	20:00	5.23	5.8	2.61	6.5
04.02.05	4:00	5.18	6.7	3.03	7.2
04.11.26	18:00	5.20	8	3.08	7.7
04.12.31	20:00	7.91	8	3.97	8.5
05.01.16	8:00	6.10	17.2	2.88	6.8
05.02.01	2:00	6.49	8.2	4.30	8.6
05.02.19	18:00	5.53	6.3	3.02	7.2
05.03.12	6:00	5.56	5.9	3.09	7.1
05.03.24	18:00	7.57	7.1	4.51	8.9
05.12.04	18:00	8.64	11.6	4.60	9.9
05.12.17	20:00	7.07	9.1	4.46	9.3
05.12.21 ²	22:00	11.01	9.7	5.50	10.4
06.03.28	16:00	6.35	7.2	4.00	7.7

¹Typhoon Maemi. ²Storm.

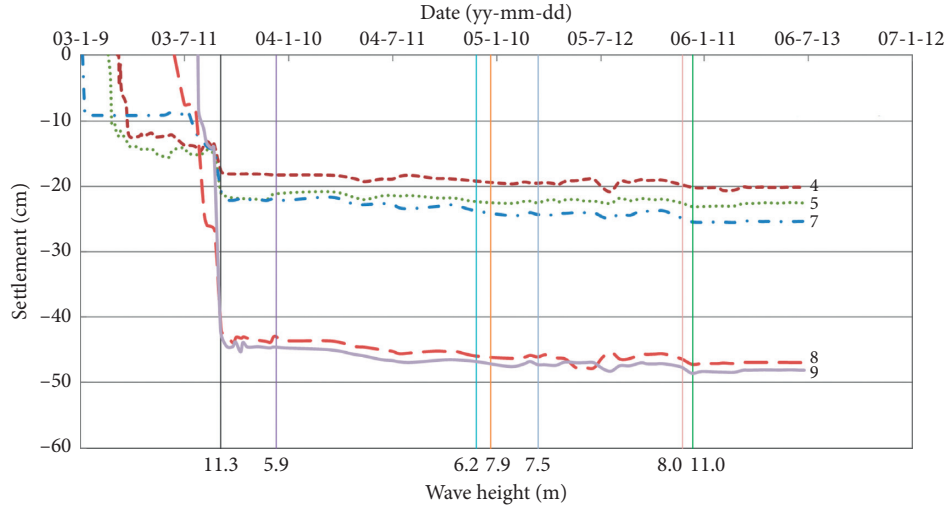


FIGURE 3: Settlement time history of caissons #4, 5, 7, 8, and 9.

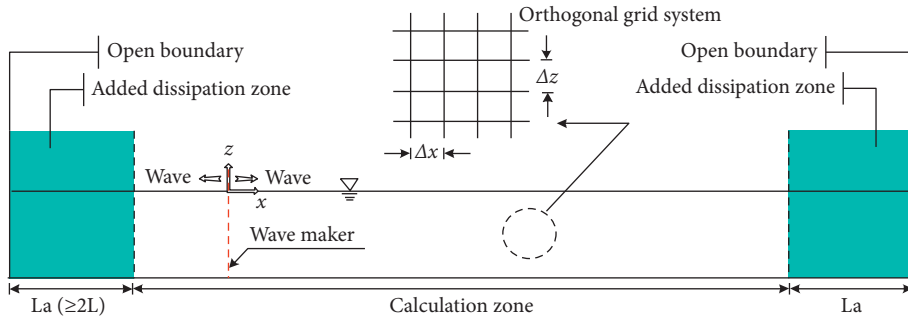


FIGURE 4: Schematic diagram of the numerical wave tank used in the 2D-NIT model.

The basic equation of the 2D-NIT model consists of the continuity equation (1) and Navier-Stokes' equations of

motions 2 and 3, which were expanded to a porous media by Sakakiyama and Kajima [23] described as follows:

$$\frac{\partial \gamma_x u}{\partial x} + \frac{\partial \gamma_z w}{\partial z} = \gamma_v S_p, \tag{1}$$

$$\begin{aligned} \lambda_v \frac{\partial u}{\partial t} + \frac{\partial \lambda_x u u}{\partial x} + \frac{\partial \lambda_z w u}{\partial z} = & -\frac{\gamma_v}{\rho} \frac{\partial p}{\partial x} + \frac{\partial}{\partial x} \left\{ \gamma_x \nu_e \left(2 \frac{\partial u}{\partial x} \right) \right\} \\ & + \frac{\partial}{\partial z} \left\{ \gamma_z \nu_e \left(\frac{\partial u}{\partial z} + \frac{\partial w}{\partial x} \right) \right\} - D_x u - R_x + S_u, \end{aligned} \tag{2}$$

where t is time; x and z are the horizontal and vertical coordinates; u and w are the horizontal and vertical components of flow velocity; ρ is the density of the fluid; p is the pressure; ν_e is the sum of the dynamic viscosity coefficient and the eddy viscosity coefficient; g is the acceleration of gravity; λ_v is the volume porosity; λ_x and λ_z are the directional area porosity; D_x and D_z are the wave energy dissipation coefficients for directions x and z ; S_p , S_u , and S_w are the source terms to generate a wave in the computational domain.

The 2D-NIT program uses the VOF method to trace the free surface. In the VOF method, the interface between

the water and the air phase is modeled according to the VOF function; i.e., the VOF method evolves the volume of water in each cell over time instead of directly tracking the free surface itself. The VOF function F is the volume fraction of a fluid that is a constant physical quantity and has a value of $0 \leq F \leq 1$.

3.2. Soil Model. The FLIP program, a finite element analysis program for the liquefaction process that is based on the effective stress analysis method Iai et al. [24], was adopted to

analyze the storm wave-induced settlement behavior of the caisson breakwater. This program was originally developed for the dynamic soil response under earthquake loading. The effective stress model for these soils is the multiple shear mechanism model that was originally proposed by Towata and Ishihara [25]. As shown in Figure 5, this model is represented by a movable point located within the circular fixed boundary. It is defined in the shear strain space and connected to the boundary with an infinite number of virtual springs. Each spring corresponds to a virtual simple shear mechanism and has one of a number of various orientations. The relationship between the force and the displacement of each spring follows the hyperbolic-type load-displacement pattern. The displacement of the movable point from the center represents the mobilized shear strain, and the resulting forces acting on the point represent the shear stress that is induced in the soil.

The excess pore water pressure is generated as a function of the cumulative shear work [24]. Equation (3) considers the effect of positive dilatancy when taking the cyclic mobility behavior into account using the concept of a liquefaction front, as shown in Figure 6:

$$S = S_0, \quad (\text{if } r < r_3),$$

$$S = S_2 + \sqrt{(S_0 - S_2)^2 + \frac{(r - r_3)^2}{m_1}}, \quad (\text{if } r > r_3), \quad (3)$$

in which

$$r_2 = m_2 S_0,$$

$$r_3 = m_3 S_0, \quad (4)$$

$$S_2 = \frac{S_0 - (r_2 - r_3)}{m_1},$$

where S_0 is a parameter to be defined by a function of shear work; m_1 is the inclination of the failure line, defined by the shear resistance angle ϕ_f' as $m_1 = \sin \phi_f'$; m_2 is the inclination of the phase transformation line, defined by the phase transformation angle ϕ_p' as $m_2 = \sin \phi_p'$; $m_3 = 0.67 m_2$. The auxiliary parameter, m_3 , is introduced to ensure a smooth transition from one zone to the other and is determined as a balance of the smoothness and the realism of the stress path shape.

In Figure 6, S is a state variable ($S = \sigma_m' / \sigma_{m0}'$) under undrained conditions with a constant total confining pressure, and r is the shear stress ratio ($r = \tau / (-\sigma_{m0}')$). The initial effective mean stress and deviatoric stress are defined by $\sigma_{m0}' = (\sigma_{x0}' + \sigma_{y0}')/2$ and $\tau = (\sigma_1' - \sigma_3')/2 = (\tau_{xy}' + ((\sigma_x' - \sigma_y')/2))^{0.5}$, respectively. The model can simulate a rapid or gradual increase in the cyclic strain amplitude to the order of several percentage points under undrained cyclic loading. The program has been verified in many numerical simulations of structure damage induced by earthquakes and liquefaction [26–29].

3.3. Verification of the Present Numerical Model. Verification of the present numerical model is a necessary process before applying it. To verify the present numerical

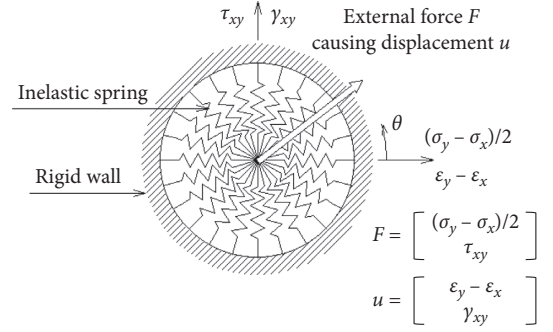


FIGURE 5: Schematic figure for multiple simple shear mechanisms [25, 26].

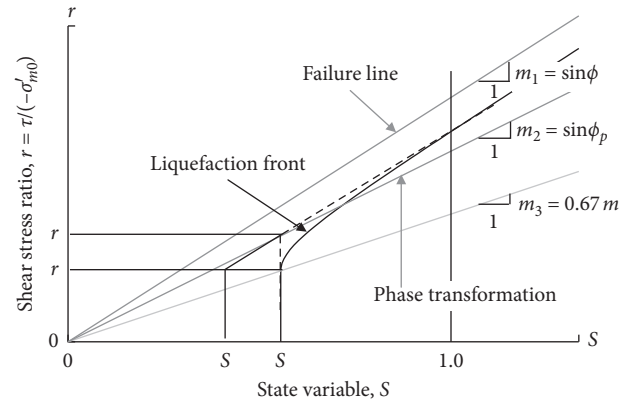


FIGURE 6: Schematic figure of liquefaction front, state variable S , and shear stress ratio γ [24, 26].

model, two previous studies available in the literature, Mizutani et al. [9] and Jeng et al. [12] were used. Mizutani et al. [9] conducted a series of experiments for regular waves to investigate the wave-seabed-structure (submerged breakwater) interaction. The water-free surface elevation and the dynamic pore water pressure inside the sandy seabed foundation under the breakwater were recorded during experiments. Mizutani et al. [9] also developed a combined BEM-FEM model. Modified Navier-Stokes equations were used to solve the flow inside the porous media, and Biot's equation was applied to solve the poroelastic media. Jeng et al. [12] developed the integrated model (PORO-WSSI II) for wave-seabed-structure (WSSI) by combining the Volume-Averaged Reynolds-Averaged Navier-Stokes (VAR-ANS) equation for wave motions in a fluid domain and the porous media flows in structures, and the dynamic Biot's equations for a porous elastic seabed. Jeng et al. [12] applied their model to investigate the dynamic response of a composite breakwater on a seabed.

The properties of the sand and breakwater provided by Mizutani et al. [9] and Jeng et al. [12] listed in Table 2 were used for simulation of the present numerical model. The soil model (FLIP) in the present model needs more parameters related to the liquefaction process. But in this verification, those parameters were assumed as zero because (i) sand has no fines, and (ii) Mizutani et al. [9] and Jeng et al. [12] only considered oscillatory pore water pressure in seabed based

TABLE 2: Soil properties and wave characteristics in verification case.

Medium	Shear modulus (kPa)	Bulk modulus (kPa)	Poisson's ratio	Porosity	Internal friction angle (°)
Seabed	5×10^5	1.304×10^5	0.33	0.30	38
Breakwater	1×10^6	1.590×10^5	0.24	0.33	45

on Biot's equation. The regular wave of height 3.0 cm and period of 1.4 sec in a still water depth 30 cm above the sand bed provided by Mizutani et al. [9] and Jeng et al. [12] were used for simulation.

Figure 7 shows a schematic sketch of the numerical wave-soil tank used for verification of the present model. Four locations for the value of η/H (η = water surface elevation above SWL and H = wave height) were selected and named as "a, b, c, and d." Location "a" is in front of the breakwater, "d" is behind the breakwater, and "b" and "c" are edges of the breakwater crown. Four locations for the pore water pressure selected and named as *A, B, C, and D*. Location "A" was used for recording the pore water pressure in the middle of the submerged breakwater and "B, C, and D" for recording the pore water pressure inside the seabed in front of, middle of, and behind the breakwater.

Figure 8 shows the computed dimensionless water surface elevation (the value of η/H) with the 2D-NIT model in the present model together with Mizutani et al.'s experiment [9] and Jeng et al.'s numerical result [12]. The circle, blue line, and red line indicated Mizutani's experiment, Jeng's numerical result, and the computed one with the 2D-NIT model, respectively. As illustrated in Figure 8, the agreements at "a" and "b" are good, while little differences are observed at "c" and "d" that are located behind the breakwater in between the computed and Mizutani's experiment values. This may be accounted to the boundary condition at the seabed. In the experiment of Mizutani, it is assumed as permeable, whereas in the numerical analysis, it is assumed as an impermeable rigid surface. Anyway, the difference is small enough, and the wave model used in this study can successfully simulate wave propagation in a viscous fluid.

Figure 9 shows the computed dimensionless pore water pressure ($p_s/\rho gH$, in which p_s = pore water pressure and ρ = density) with the FLIP in the present model together with Mizutani et al.'s experiment in Mizutani et al. [9] and Jeng et al.'s numerical result [12]. The circle, blue line, and red line indicated Mizutani et al.'s experiment, Jeng et al.'s numerical result, and the computed one with the 2D-NIT model, respectively. The numerical prediction of the pore water pressure overall agrees well with the results of Mizutani's and Jeng's works. From this result, it can be stated that the present soil model can simulate the wave-induced pressure breakwater and its seabed accurately.

3.4. Application of the Present Numerical Model to Caisson Breakwater

3.4.1. Modeling of the Target Breakwater. The caisson breakwater shown in Figure 10 was modeled for the numerical analysis, as shown in Figure 11. The rubble mound is 6 m in height and 72 m in width with a slope of 1:1.5. The

caisson is 26 m in height and 24 m in width. The thickness of the wave dissipation block (tripod) is about 1~2 m. The sandy soil layer is with 16 m thick. It is placed as close to the target site ground (Figure 2) as possible, and it is located under the rubble mound. A layer of weathered rock is placed below the sandy layer.

Figure 12 shows the modeled meshes of the composite breakwater and the seabed. The seabed underneath the caisson breakwater is modeled with a smaller mesh. Figure 13 indicates the results of the mesh convergence test. It is the relationship between displacements of the caisson breakwater and the number of elements. The displacement was increased with the number of elements and they were converged when the number of elements was more than approximately 2,300. Therefore, 2,326 elements were used to make the mesh in this study.

Dynamic wave pressures acting at the boundary of the caisson breakwater and the seabed are calculated at all points. The dynamic responses of the caisson breakwater and the seabed are also estimated at all locations. As a matter of convenience, several points were selected to represent the general behavior of the caisson breakwater structure and the seabed. In Figure 12, *N1* and *N2*, at the top of the caisson, mark the locations of caisson settlement. Element numbers 1~30 indicate the representative wave pressure output points. Elements *E1* ~ *E4* indicate the representative output elements of seabed behavior.

3.4.2. Wave Pressure Estimation Using 2D-NIT. The northern direction of an irregular wave with a maximum height of 7 m and a maximum period of 11.0 sec was used as the source wave in this analysis. This source wave was selected after the characteristics of Typhoon Maemi (Table 1) were considered. A water depth of 13.3 m was used. This water depth was determined by integrating the tide level for the duration of the wave in this area and then adding the depth to the mean.

The numerical wave channel used in the present study is 1,750 m long and 60 m tall. Fictitious dissipation zones of 500 m are located to the left and right sides of the computational domain in order to absorb the wave energy. The lattice distance Δx is 0.5 m at the section where the breakwater was installed and 1.0 m at the other sections, while Δz chooses to be 0.5 m. The interval of time is $\Delta t = 0.01 \sim 0.20$ sec. The total calculation time is set at 600 sec. This given time is ample enough to study how the seabed's behavior changes in response to the wave.

Dynamic wave pressures were obtained for all of the points on the breakwater structure and its surrounding seabed. This pressure data was used for the input data (the external force) in the seabed analysis program (FLIP). Figure 14 shows a typical wave load history: (a) at point No. 3

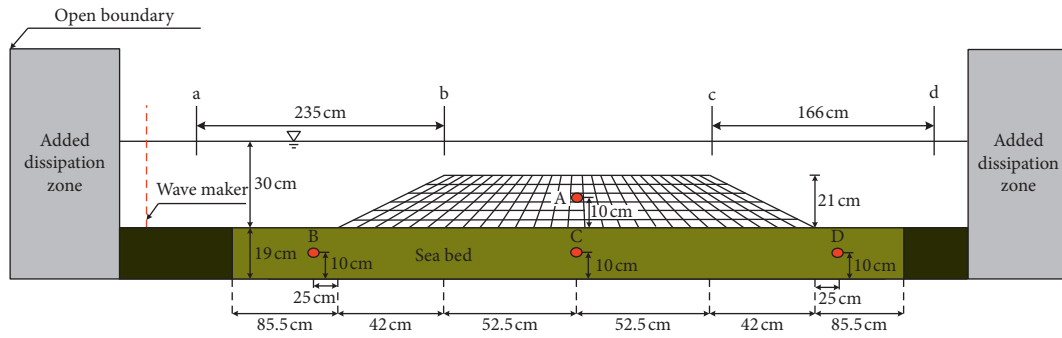
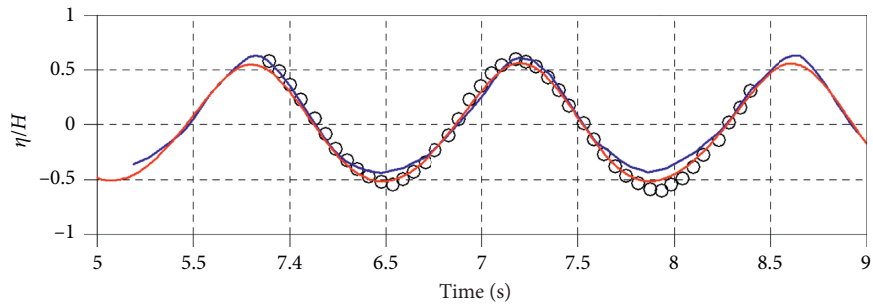
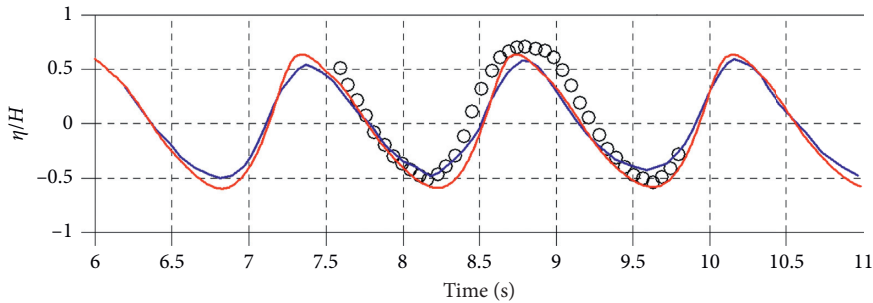


FIGURE 7: Schematic figure of the numerical wave-soil tank used in 2D-NIT and FLIP model.



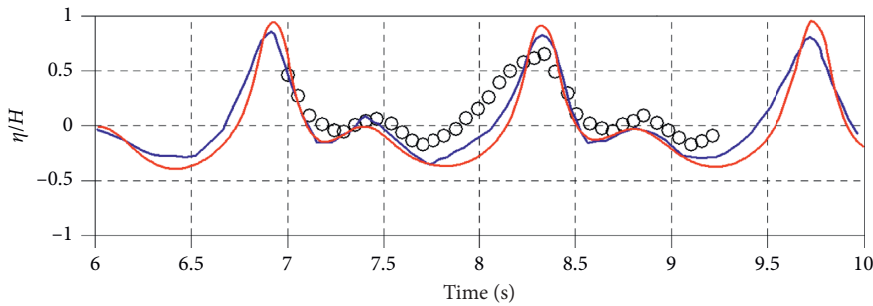
Gage a
 ○ ○ ○ Mizutani et al., 1988
 — Jeng et al., 2013
 — This study

(a)



Gage b
 ○ ○ ○ Mizutani et al., 1988
 — Jeng et al., 2013
 — This study

(b)



Gage c
 ○ ○ ○ Mizutani et al., 1988
 — Jeng et al., 2013
 — This study

(c)

FIGURE 8: Continued.

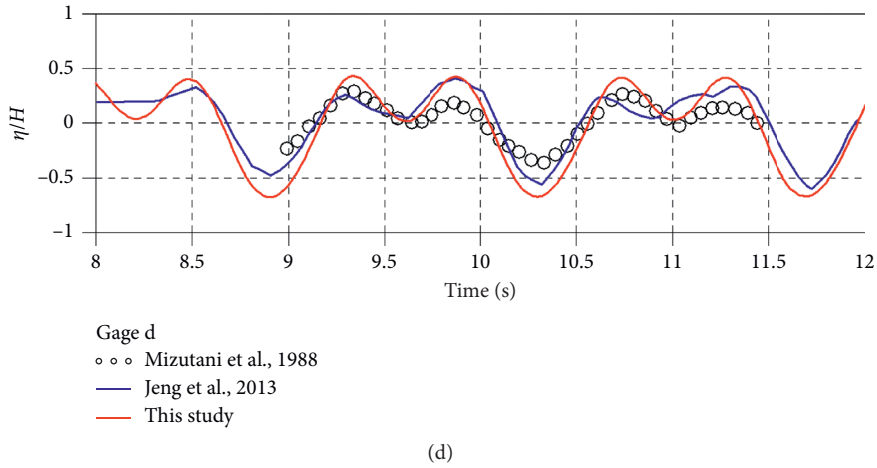


FIGURE 8: Comparison between measured and calculated dimensionless water surface elevations. (a) Location a; (b) location b; (c) location c; (d) location d.

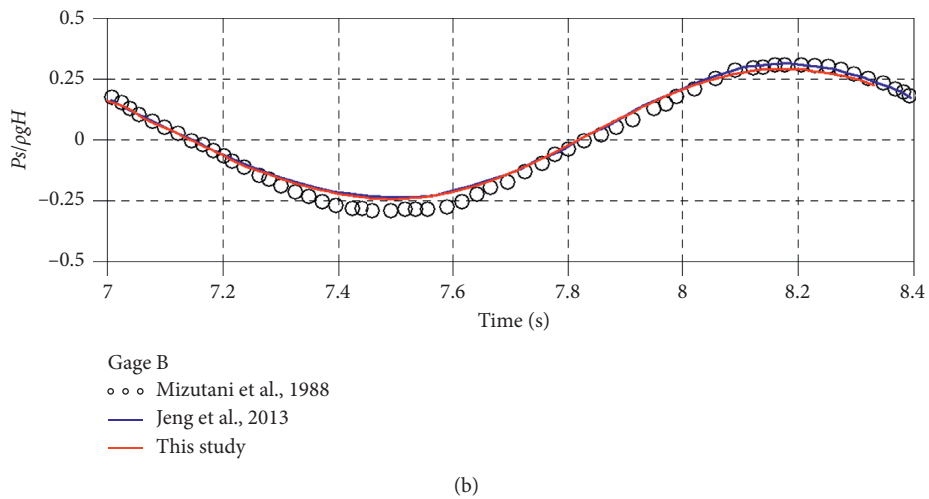
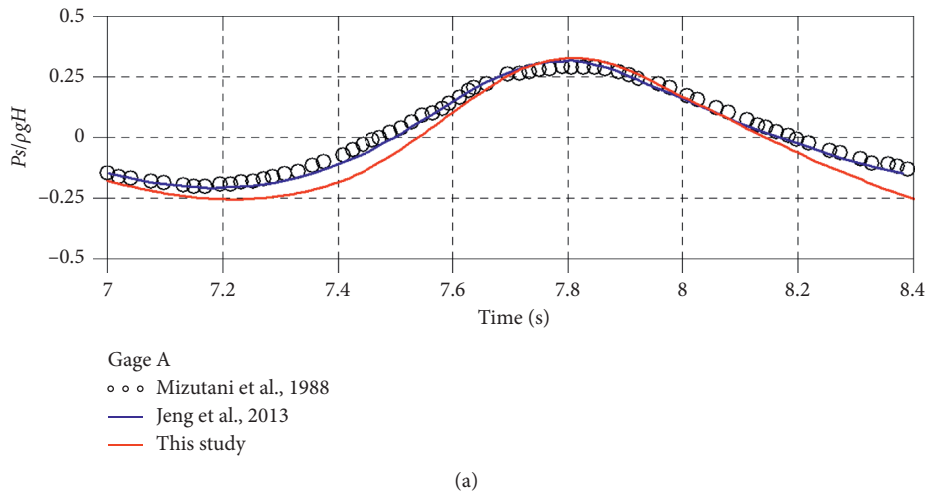
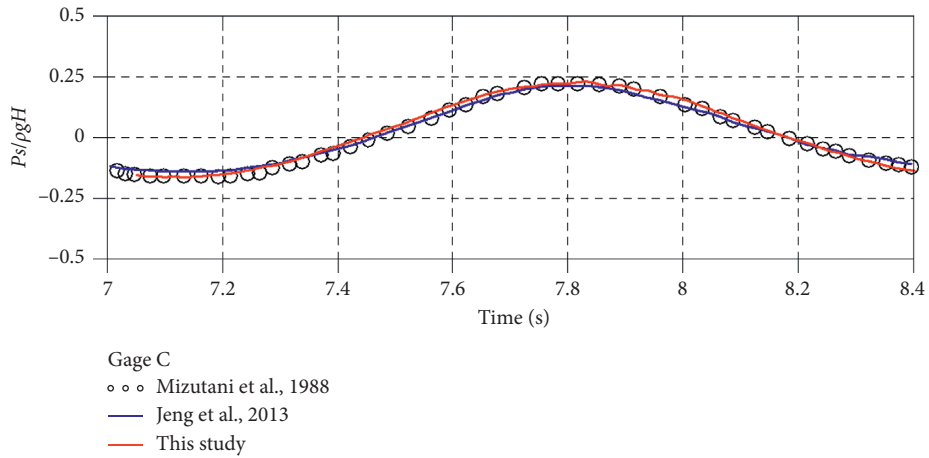
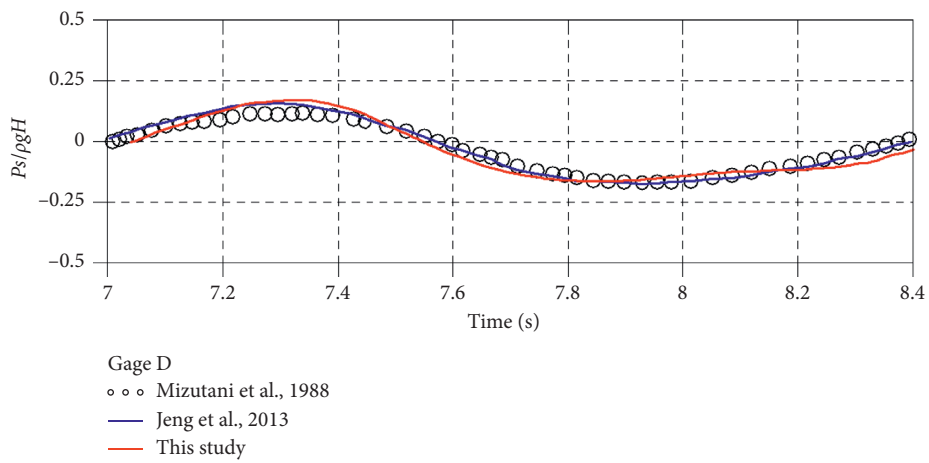


FIGURE 9: Continued.

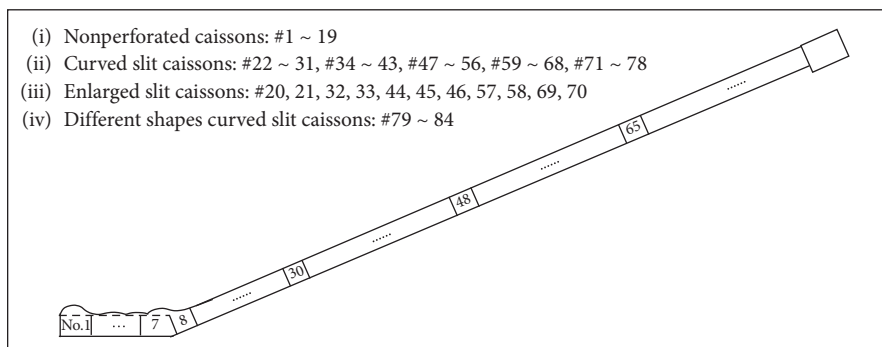


(c)



(d)

FIGURE 9: Comparison between measured and calculated dimensionless pore water pressures. (a) Location A; (b) location B; (c) location C; (d) location D.



(a)

FIGURE 10: Continued.

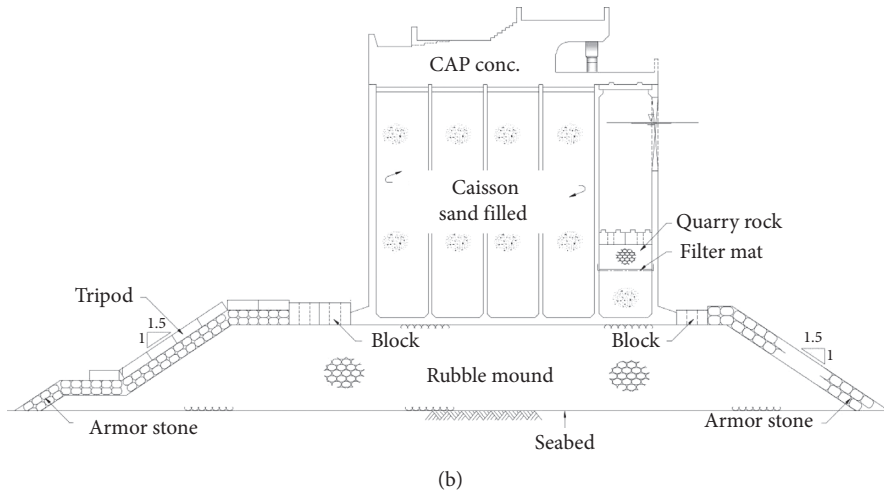


FIGURE 10: Schematic diagram of (a) layout of caissons in the west breakwater and (b) a composite nonperforated caisson.

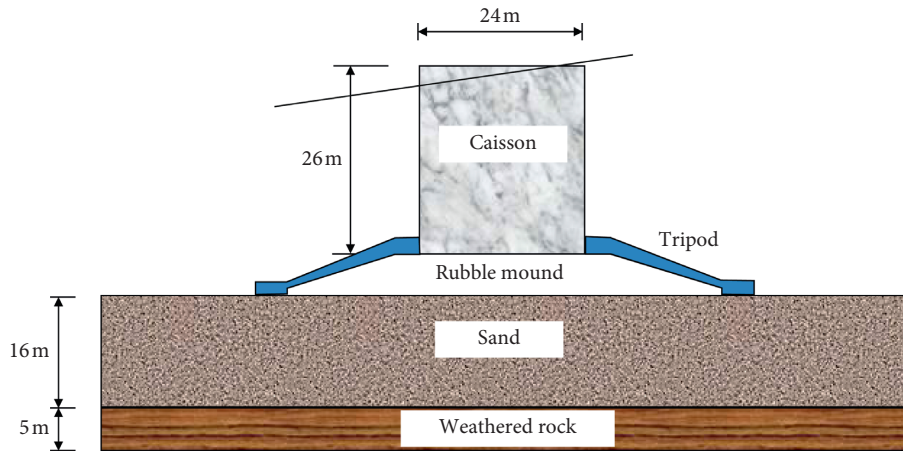


FIGURE 11: Cross-sectional view of the composite breakwater and its surround seabed formation for numerical analysis (unit: m).

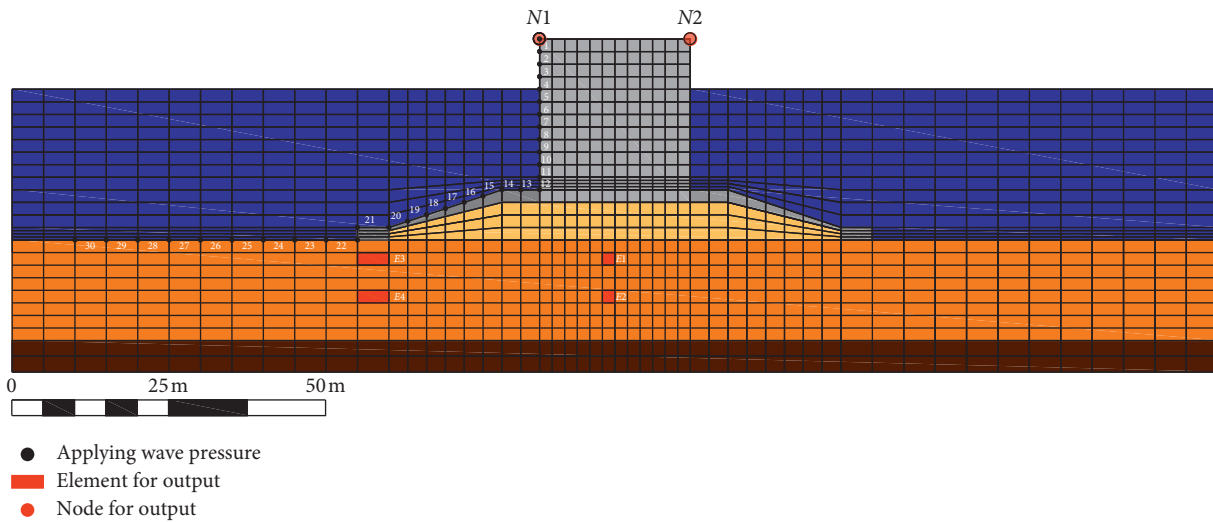


FIGURE 12: Modeled meshes of the composite breakwater and the seabed.

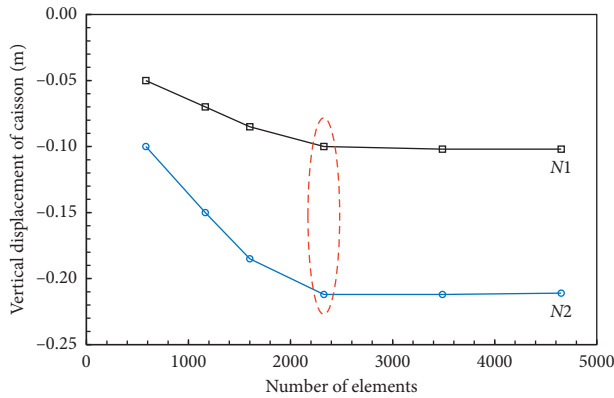


FIGURE 13: Mesh convergence test.

on the caisson side above the water level, (b) at point No. 10 on the caisson side below the water level, (c) at point No. 16 on the rubble mound, and (d) at point No. 25 on the seabed.

As seen in Figure 14, a significant number of non-uniform dynamic wave pressures are repeatedly acting on the breakwater except at the part over the hydrostatic water level, such as point No. 3. Additionally, a significant number of dynamic wave pressures are acting non-uniformly on the seabed (point No. 25) in front of the breakwater. These wave pressure distributions reveal some very important information. Some cases of breakwater design only consider the dynamic wave pressure on the breakwater structure itself and assume the wave pressure is uniform. There is a considerable difference between making assumptions about the wave pressure and actually studying it. Thus, the present study considered the real dynamic wave pressure acting on the seabed and the breakwater structure.

3.4.3. Seabed Behavior Analysis Using FLIP. Before the dynamic wave loading response analysis was performed, static analysis was conducted where gravity was used to simulate the initial stresses acting on the seabed. The wave pressures obtained by 2D-NIT were assigned at the boundary of the domain as the input motion. The shear stress induced by the wave velocity on the surface of the seabed was also incorporated as part of the input source. The seabed was analyzed in an undrained condition. The peak period of an earthquake may vary over the range 0.1s~1s smaller than the range of wave period. Owing to the smaller periods in the earthquakes, pore water pressure accumulates faster than in the case of waves. Mutlu Sumer [30] mentioned that the cyclic shear stresses cause the soil to undergo cyclic shear deformations, in exactly the same way as in the case of waves leading to pressure buildup, if the soil is undrained. It was assumed that the vertical and horizontal displacements were fixed on the bottom boundary. The vertical displacement was only allowed on the side boundary. The material parameters used for the analysis are shown in Table 3. They were determined based on field and laboratory test results.

(1) *Excess Pore Pressure Ratio.* The excess pore pressure ratio is the ratio between the initial effective stress and the excess pore pressure (hereinafter EPP). When the EPP ratio reaches up to 1, and we can define the soil element, it becomes liquefied. Figure 15 shows the EPP ratio in seabed elements E1, E2, E3, and E4. The EPP ratio of all elements increases with time. This is especially true for element E3, as it shows a relatively high increase in its EPP ratio. The EPP ratio of element E3 increases up to 0.9, while the other elements are around 0.5. These values are not 1, so the sand layer may not liquefy completely. However, it is close to reaching a value of 1, so we can expect the effective strength of the sand layer to decrease without completely vanishing. This is called “partial liquefaction” [18,19].

The buildup of EPP on the seabed and underneath the caisson may be caused by the combination of both the wave and the caisson’s movements [17,20]. Oumeraci’s [17] study suggested an especially interesting result for the pore pressure of the seabed where the breakwater was placed during the wave tank model that was undertaken in the condition of wave height $H = 0.4$ m, wave period $T = 6.5$ sec, and water depth $hs = 1.6$ m. The behavior of the seabed ground layer is the same in accordance with the behavior of the wave, crest, and trough. However, the wave does not directly trigger the excess pore pressure in the lower ground area beneath the caisson. Alternately, the behavior of the seabed underneath the caisson breakwater was essentially governed by the wave-induced caisson motion. If the caisson moves upward, the ground shows a negative oscillatory excess pore pressure, while it shows a positive oscillatory excess pore pressure in cases where the caisson moves downward. During the caisson’s movements, due to the wave, the excess pore pressures in the ground underneath the caisson keep increasing.

Figure 16 shows the final state (after 600 seconds of wave motion) of the EPP distribution. The critical part of the EPP ratio is the edge of the rubble mound on the seaward and shoreward sides. This may be related to the location, which is on the border of the seabed and the breakwater structure. In this area, the EPP had significant buildup due to the wave and the breakwater motions. Generally, near the edges, the shear stress can be much higher.

(2) *Effective Stress Path.* Figure 17 shows the effective stress path in the $p' - q'$ diagram. The effective stress path is a very useful way to track the stress changes in the ground. During a wave, the downward propagation of the wave force through the seabed generates shear stresses and strains that are cyclic in nature [31]. If a cohesionless soil is saturated, excess pore pressures may accumulate during wave shearing, and the effective stress path moves toward failure. As shown in Figure 16, as the EPP increases, the effective stress path moves toward the Mohr-Coulomb failure line for all of the soil elements. Element E3 in the seabed, related to the EPP ratio shown in Figure 15, has a relatively high increase in its EPP ratio and is closer to the failure line than any other element. A higher increase in the EPP results in a higher decrease in effective stress.

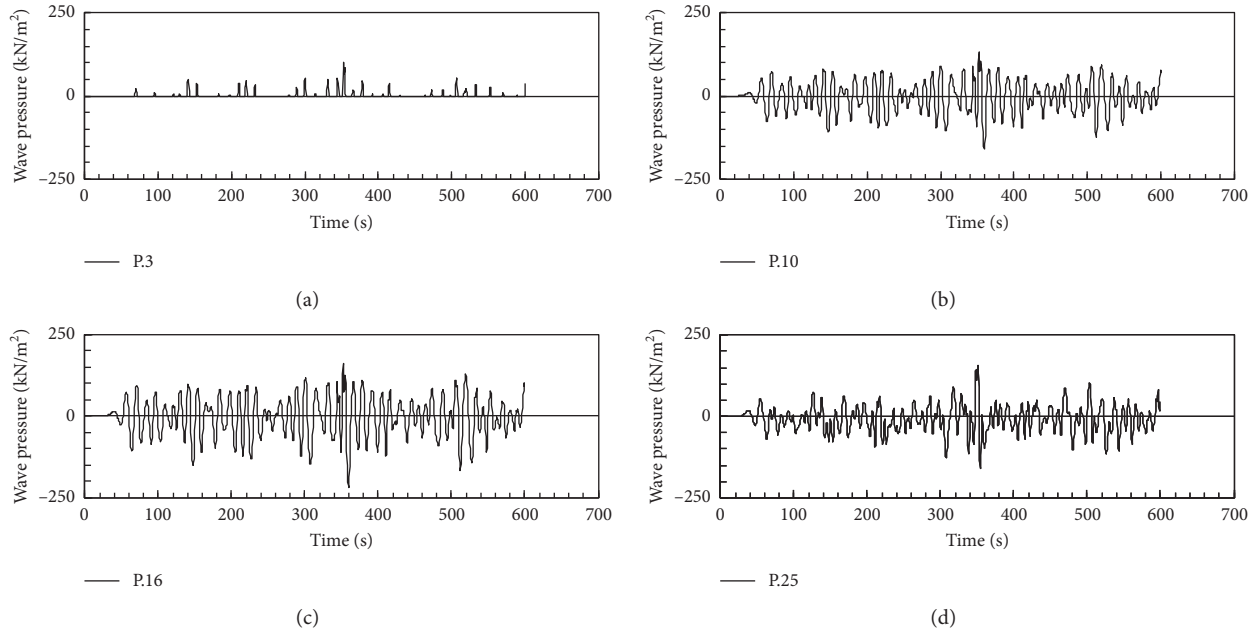


FIGURE 14: Time history of wave pressure on the breakwater system: (a) 3, (b) 10, (c) 16, and (d) 25 points.

TABLE 3: Medium parameters used for the analyses by FLIP model.

Medium	Unit weight (kN/m ³)	Poisson's ratio	Elastic modulus (kN/m ²)	Internal friction angle (°)
Sand	19.0	0.35	10000	31
Rock	25.0	0.22	3900000	40
Rubble	18.0	0.25	90000	40
Tripod	23.0	0.25	25000000	—
Concrete	23.0	0.25	25000000	—

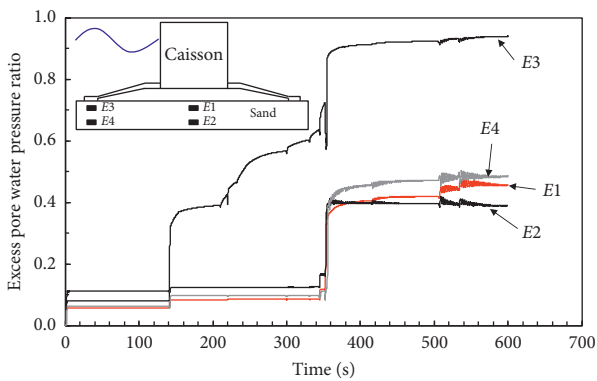


FIGURE 15: Time history of excess pore water pressure ratio.

(3) *Settlement of Caisson Breakwater.* Figure 18 shows the settlement deformation of the caisson breakwater and the area around the seabed at the end of the analysis, after 600 seconds. For a better view, this figure was magnified twenty times. The settlement deformation mainly occurs in the top soil layer beneath the caisson breakwater. This settlement was caused by the effective stress decrease in the soil layer, which stems from the EPP increase. When a sand layer is subjected to cycles of shear strains under undrained conditions, excess pore pressure may be generated in each load cycle leading to softening and accumulated deformation

[32]. An increase in the pore pressures leads to a transfer of stress from the soil skeleton to the pore pressure. This precipitates a decrease in the effective stress and shear resistance of the soil. If the shear resistance of the soil becomes less than the driving shear stress, the soil can undergo large deformations [31].

In this numerical simulation, the EPP ratio increases and the effective stress decreases in the seabed sand layer when it is subjected to cyclic shearing stress induced by the wave force (Figures 15 and 17). A decrease in the wave-induced effective stress is a result of the seabed ground's tendency to decrease in volume (settlement). Castro [33] classified settlement deformation into two categories depending on the shear stress and shear strength: (1) when the driving shear loads are greater than the residual shear strength of a liquefied soil deposit, a loss of stability can result in extensive ground failures or flow slides, and (2) when the driving shear stress is less than the residual shear strength, limited shear distortion and settlement occur without the soil mass losing its stability. This present study is corresponding to the latter because the EPP values do not reach 1, so the sand layer is not completely liquefied.

Figure 19 shows the combined actions of the wave pressure on element No. 10 in the caisson (above) and the settlement behavior of the caisson (below) over time. From this figure, evidence of the effect of a wave on the settlement

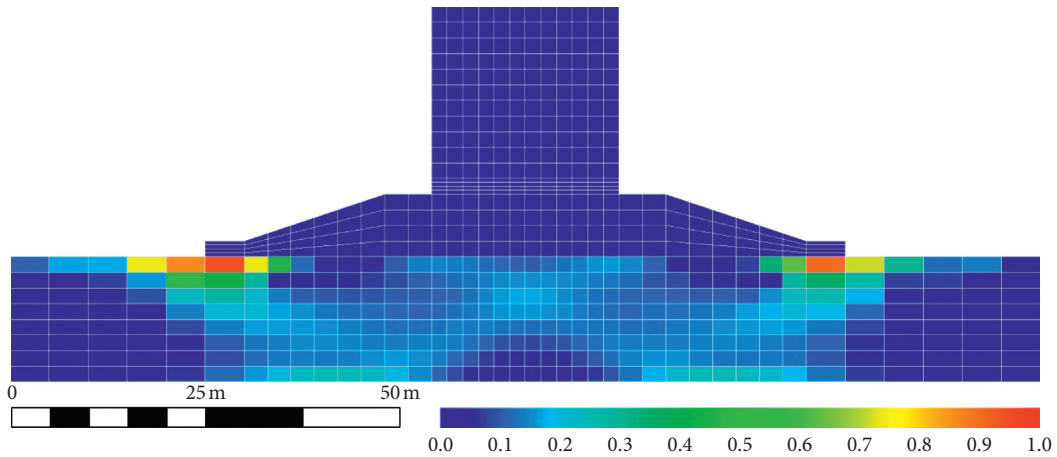


FIGURE 16: Final distribution state of excess pore water pressure ratio.

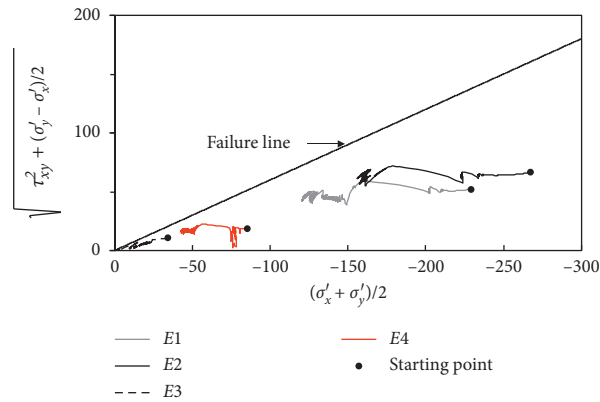


FIGURE 17: Effective stress path of soil elements in seabed during wave loading.

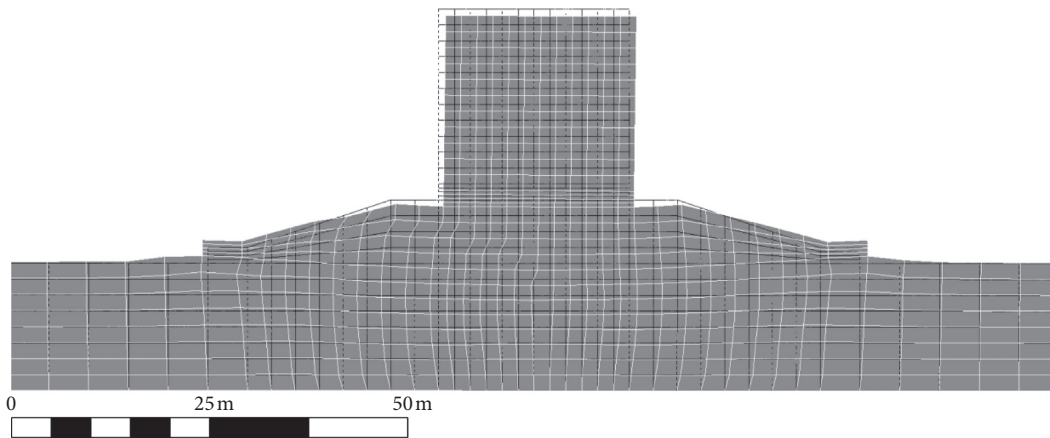


FIGURE 18: Deformation of whole breakwater system ($\times 20$ magnitude).

of the caisson breakwater is clearly visible. The settlement of the caisson has not happened at the initial start time ($t < 40$ sec) because there was no wave pressure acting on the caisson. As time goes on, the wave pressure starts acting on the caisson wall and induces the settlement of the caisson due to the increase in the excess pore pressure on the seabed. The settlement continuously accumulates under the wave pressure and at around 340 sec, the time where the

maximum amount of wave pressure is acting on the caisson; the maximum settlement has occurred. After that, the settlement is less significant because the pressure is less significant.

$N1$ and $N2$ are points on the top of the caisson. As seen in Figure 19, the trends of settlement at $N1$ and $N2$ are similar. The settlement of $N2$ (landward) is bigger than that of $N1$ (seaward). Figure 20 shows the settlement measured at four

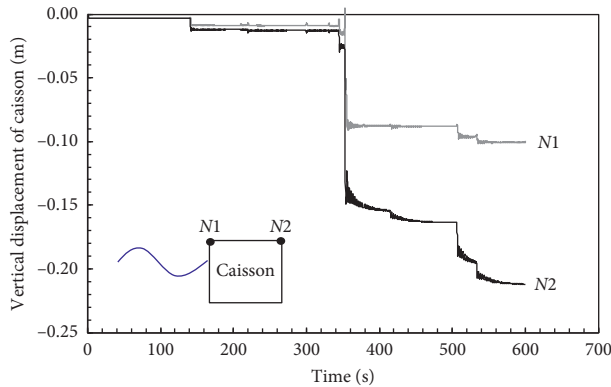


FIGURE 19: Time history of caisson's settlement.

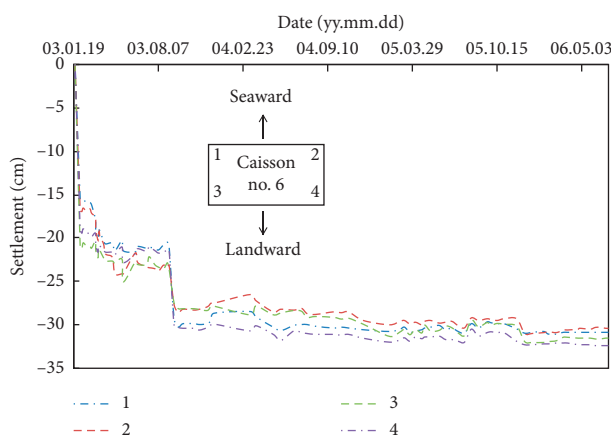


FIGURE 20: Time history of caisson's settlement at seaward (numbered as 1 and 2) and landward sides (numbered as 3 and 4) of caisson #6.

edges of caisson No. 6 that was installed in the west breakwater of the Jeju Outer Harbor. Coincidentally, the settlements at the edges of the landward side (numbered as 3 and 4) are bigger than those at the edges of the seaward side (numbered as 1 and 2). This may be related to the stress concentration at the landward seabed due to the high wave pressure acting on the seaward side of the caisson.

4. Conclusion

This study was conducted to characterize wave-induced settlement in coastal structures (including the ground underneath these structures) by analyzing the settlement data measured in actual breakwaters over a long period of time (more than 5 years). To determine the effect that the waves have on seabed settlement, the wave history that was recorded during the construction period was also analyzed. These analyses show that waves clearly influence the settlement of caisson breakwaters. Wave-induced settlement in the breakwaters becomes very significant and rapid when large waves attack, such as during a typhoon.

A new numerical model was also suggested to simulate the storm wave-induced seabed settlement underneath the caisson breakwater, which could be simulated qualitatively.

The new model combines the wave model (2D-NIT) and the soil model (FLIP). The dynamic wave load calculated by the 2D-NIT was used as the input data for the soil model. The model can simulate the oscillatory and residual pore pressures increase and the effective stress decrease in the seabed sand layer when the layer is subjected to cyclic shearing stress induced by wave force. The decrease in the wave-induced effective stress results from the seabed ground's tendency to decrease in volume (settlement). The numerical analysis and field measured data both show clear evidence of the effect of waves on the settlement of the caisson breakwater.

Data Availability

The research data used to support the findings of this study were supplied by 2D-NIT and FLIP under license and so cannot be made freely available. Requests for access to these data should be made to the corresponding author.

Conflicts of Interest

The authors declare that there are no conflicts of interest regarding the publication of this article.

Acknowledgments

This research was supported by the Basic Science Research Program through the National Research Foundation of Korea (NRF) funded by the Ministry of Education (No. 2020R1I1A3067248).

References

- [1] J. Burland, M. Burbidge, and E. Wilson, "Settlement of foundations on sand and gravel," *Proceedings of the Institution of Civil Engineers*, vol. 78, no. 6, pp. 1325–1381, 1985.
- [2] R. Berardi, M. Jamiolkowski, and R. Lancellotta, "Settlement of shallow foundations in sands selection of stiffness on the basis of penetration resistance," *Proceedings of the Geotechnical Engineering Congress-1991*, pp. 185–200, ASCE, New York, NY, USA, 1991.
- [3] J. Lee and R. Salgado, "Estimation of footing settlement in sand," *International Journal of Geomechanics*, vol. 2, no. 1, pp. 175–192, 2002.
- [4] T.-H. Kim, J.-M. Nam, L. Ge, and K.-I. Lee, "Settlement characteristic of beach sands and its evaluation," *Marine Georesources & Geotechnology*, vol. 26, no. 2, pp. 67–85, 2008.
- [5] J. Sinkankas, *Mineralogy*, Van Nostrand, Princeton, NJ, USA, 1966.
- [6] J. Ye, D. Jeng, R. Wang, and C. Zhu, "Numerical simulation of the wave-induced dynamic response of poro-elastoplastic seabed foundations and a composite breakwater," *Applied Mathematical Modelling*, vol. 39, no. 1, pp. 322–347, 2015.
- [7] K. Zen and H. Yamazaki, "Mechanism of wave-induced liquefaction and densification in seabed," *Soils and Foundations*, vol. 30, no. 4, pp. 90–104, 1990.
- [8] H. Mase, T. Sakai, and M. Sakamoto, "Wave-induced pore-water pressures and effective stresses around breakwater," *Ocean Engineering*, vol. 21, no. 4, pp. 361–379, 1994.

- [9] N. Mizutani, A. M. Mostafa, and K. Iwata, "Nonlinear regular wave, submerged breakwater and seabed dynamic interaction," *Coastal Engineering*, vol. 33, no. 2-3, pp. 177–202, 1998.
- [10] M. B. C. Ulker, M. S. Rahman, and M. N. Guddati, "Wave-induced dynamic response and instability of seabed around caisson breakwater," *Ocean Engineering*, vol. 37, no. 17-18, pp. 1522–1545, 2010.
- [11] J. Li and D. S. Jeng, "Response of a porous seabed around breakwater heads," *Ocean Engineering*, vol. 35, no. 8-9, pp. 864–886, 2008.
- [12] D.-S. Jeng, J.-H. Ye, J.-S. Zhang, and P. L.-F. Liu, "An integrated model for the wave-induced seabed response around marine structures: model verifications and applications," *Coastal Engineering*, vol. 72, pp. 1–19, 2013.
- [13] M. A. Biot, "General theory of three-dimensional consolidation," *Journal of Applied Physics*, vol. 12, no. 2, pp. 155–164, 1941.
- [14] O. C. Zienkiewicz, C. T. Chang, and P. Bettess, "Drained, undrained, consolidating and dynamic behaviour assumptions in soils," *Géotechnique*, vol. 30, no. 4, pp. 385–395, 1980.
- [15] J. Ye, D. Jeng, R. Wang, and C. Zhu, "Validation of a 2-D semi-coupled numerical model for fluid-structure-seabed interaction," *Journal of Fluids and Structures*, vol. 42, pp. 333–357, 2013.
- [16] J. Ye, D. Jeng, R. Wang, and C. Zhu, "A 3-D semi-coupled numerical model for fluid-structures-seabed-interaction (FSSI-CAS 3D): model and verification," *Journal of Fluids and Structures*, vol. 40, pp. 148–162, 2013.
- [17] H. Oumeraci, "Review and Analysis of vertical breakwater failure-lessons learned," *Coastal Engineering*, vol. 22, no. 1-2, pp. 3–29, 1994.
- [18] M. B. de Groot, M. D. Bolton, P. Foray et al., "Physics of liquefaction phenomena around marine structures," *Journal of Waterway, Port, Coastal, and Ocean Engineering*, vol. 132, no. 4, pp. 227–243, 2006.
- [19] M. B. de Groot, M. Kudella, P. Meijers, and H. Oumeraci, "Liquefaction phenomena underneath marine gravity structures subjected to wave loads," *Journal of Waterway, Port, Coastal, and Ocean Engineering*, vol. 132, no. 4, pp. 325–335, 2006.
- [20] M. Kudella, H. Oumeraci, M. B. de Groot, and P. Meijers, "Large-scale experiments on pore pressure generation underneath a caisson breakwater," *Journal of Waterway, Port, Coastal, and Ocean Engineering*, vol. 132, no. 4, pp. 310–324, 2006.
- [21] K.-H. Lee, S.-S. Beom, D.-S. Kim, J.-B. Park, and S.-W. An, "A study on the control of short-period waves by resonator," *Journal of Korean Society of Coastal and Ocean Engineers*, vol. 24, no. 1, pp. 36–47, 2012.
- [22] K. H. Lee, J. H. Park, S. Cho, and D. S. Kim, "Numerical simulation of irregular airflow in OWC wave generation system considering sea water exchange," *Journal of Korean Society of Coastal and Ocean Engineers*, vol. 25, no. 3, pp. 128–137, 2013.
- [23] T. Sakakiyama and R. Kajima, "Numerical simulation of nonlinear wave interaction with permeable breakwater," in *Proceedings of the 23rd ICCE*, pp. 1517–1530, ASCE, Venice, Italy, January 1992.
- [24] S. Iai, Y. Matsunaga, and T. Kameoka, "Strain space plasticity model for cyclic mobility," *Soils and Foundations*, vol. 32, no. 2, pp. 1–15, 1992.
- [25] I. Towata and K. Ishihara, "Modeling soil behavior under principal stress axes rotation," in *Proceeding of the Fifth International Conference on Numerical Method in Geomechanics I*, pp. 523–530, CRC Press, Rotterdam, Netherlands, April 1985.
- [26] G.-C. Kang, T. Tobita, and S. Iai, "Seismic simulation of liquefaction-induced uplift behavior of a hollow cylinder structure buried in shallow ground," *Soil Dynamics and Earthquake Engineering*, vol. 64, pp. 85–94, 2014.
- [27] S. Sawada, O. Ozutsumi, and S. Iai, "Analysis of liquefaction induced residual deformation for two types of quay walls: analysis by "FLIP"" in *Proceedings of the 12th World Conference on Earthquake Engineering*, no. 2486, September 2000.
- [28] O. Ozutsumi, S. Sawada, S. Iai, and Y. Takeshima, "Effective stress analyses of liquefaction-induced deformation in river dikes," *Soil Dynamics and Earthquake Engineering*, vol. 22, no. 9–12, pp. 1075–1082, 2002.
- [29] S. Iai and O. Ozutsumi, "Yield and cyclic behaviour of a strain space multiple mechanism model for granular materials," *International Journal for Numerical and Analytical Methods in Geomechanics*, vol. 29, no. 4, pp. 417–442, 2005.
- [30] B. Mutlu Sumer, "Liquefaction around marine structures," *Advanced Series on Ocean Engineering*, vol. 39, p. 472.
- [31] H. B. Seed and I. M. Idriss, *Ground Motions and Soil Liquefaction during Earthquakes*, Earthquake Engineering Research Institute, Oakland, CA, USA, 1982.
- [32] A. F. Rauch, *Soil liquefaction in earthquakes*, Ph.D. thesis, Virginia Polytechnic Institution and State University, Blacksburg, Virginia, 1997.
- [33] G. Castro, "On the behavior of soils during earthquakes-liquefaction," *Developments in Geotechnical Engineering*, vol. 42, pp. 169–204, 1987.

Research Article

A Displacement-Based Theory for Predicting the Support Force on the Shield Tunneling Surface in Sandy Soil Layers

Guang Sun,¹ Han Liu,¹ Zhiyuan Guo,² Ranjie Li,² and Tao Li¹ 

¹Hebei Research Institute of Construction and Geotechnical Investigation Co. Ltd., Shijiazhuang 050031, China

²School of Civil Engineering, Beijing Jiaotong University, Beijing 100044, China

Correspondence should be addressed to Tao Li; taoli-bj@bjtu.edu.cn

Received 19 March 2021; Revised 6 April 2021; Accepted 8 April 2021; Published 20 April 2021

Academic Editor: Faming Huang

Copyright © 2021 Guang Sun et al. This is an open access article distributed under the Creative Commons Attribution License, which permits unrestricted use, distribution, and reproduction in any medium, provided the original work is properly cited.

Due to the poor stability of the loose sandy soil layer, if the support force is not properly controlled during the construction process of the shield tunnel using the earth pressure balance method, it is easy to cause the ground to collapse or uplift. Therefore, understanding the support force of the excavation surface of shield tunneling in sandy soil layer is very vital to ensure the stability of the excavation surface. Firstly, it is assumed that the damaged soil is a three-dimensional wedge and a modified three-dimensional wedge in the active and passive failure modes, respectively. The shallow soil pressure theory and the soil plastic limit equilibrium theory are derived by analyzing the stress distribution on the damaged soil. The equation for revealing the inner essence between the support force of the shield excavation surface and excavation surface displacement under the condition of sand-covered soil is used. Secondly, the numerical simulation method analyzes the displacement of the excavation surface when the support force changes under different working conditions, and the relationship curve between the excavation surface support force and the shield tunneling displacement is obtained. The comparison and analysis between the numerical simulation calculation and the theoretical analysis indicate that the deduced calculation equation for the excavation surface support force based on the displacement earth pressure is reasonable.

1. Introduction

With the acceleration of China's urbanization process and the increasing urban population, the subway has become the first choice to relieve traffic pressure and promote urban development. Shield tunneling is extensively utilized in subway construction owing to its advantages of small environmental impact [1, 2] and a high degree of automation. The earth pressure balance shield is widely used because of the advantages of minor site impact and low cost. The support force required to ensure the excavation surface's stability for shield tunneling is an urgent problem to be solved. When the support force is too large, it may lead to the front soil uplift. When the support force is insignificant, it may lead to soil collapse. When shield tunneling is carried out in the sandy soil layer, the slag is not easy to be discharged, the cutter is seriously worn, and the equipment load is large. Simultaneously, sand is an extremely unstable soil layer, and its

cohesion is minimal, which is easy to cause ground collapse. Therefore, the research on the support force on shield excavation surface in sandy soil layer has important engineering application value in reducing soil instability, controlling construction risk, and reducing construction cost.

Many theories have been made on the support force of the shield excavation surface, which have formed a variety of analysis methods such as the limit analysis method, and plastic balance theory, even considering the grouting reinforcement effect [3], drainage condition [4–6], migration of soil particles caused by infiltration [7, 8], and consolidation deformation caused by temperature disturbance during excavation [9–11]. The upper limit value of the active limit earth pressure of the shield excavation surface was usually used to analyze the double logarithm spiral model. Lee and Nam [12, 13] obtained the upper limit value of the excavation surface's support force under the condition of groundwater seepage in view of the upper limit theorem while the

infiltration problem and its effect become a hot topic [6, 14]. Soubri and Wong [15] assume that the soil's sliding surface before the construction excavation surface can be considered as a given logarithmic spiral surface and studied the maximum support force by the limit analysis method.

In the limit equilibrium method, the soil's sliding surface located before the excavation surface is assumed first, and then the solution is obtained by the equilibrium of each isolation body in the sliding surface. There are many models using limit equilibrium theory, and the three-dimensional wedge model is the most widely used. Vermeer et al. [16] assumed that the failure surface was a two-dimensional semicircle, a quarter circle, or a three-dimensional sphere and calculated the support force of the excavation surface according to the limit equilibrium method. Some scholars [15, 17] modified the three-dimensional wedge model and revised the prism form above the wedge body to a trapezoid. The calculated results are closer to the centrifugal experiment results, but the effect of groundwater is not considered. Dai et al. [18] thought that the buried depth ratio manifests a noticeable action on the excavation surface instability of a tunnel and, therefore, improved the so-called "wedge-prism" limit equilibrium model.

Liang et al. [19] used the finite difference calculation software FLAC3D in a numerical simulation to analyze the shield excavation surface stability in the sandy soil layer and obtained the soil failure mechanism in front of the excavation surface. Mi and Xiang [20] explored the support force of the excavation surface by considering the seepage action in simulating shield construction. Some results show that groundwater is an essential factor affecting the force applied on ground structure, and generally, the support force becomes large when there exists groundwater in the soil layer. Liang et al. [21] numerically investigated the limit support pressure, mode of limit failure, inherit of instability, and failure pattern of the excavation surface in the loose granular stratum. Besides, similar researches also explored the induced pore water pressure in a saturated loose granular stratum during the construction of a shield tunnel using a coupled water-solid finite element model. Many scholars have studied the coupling effect of multiple physical fields to consider the influence of various complex factors on soil stress, such as the loading-unloading effect, seepage force, and the environmental temperature change caused by seasonal variation or in the process of excavation [22, 23] and established relevant constitutive laws as well as the soil particle movement models by seepage [24–26]. Overall, the existing research shows that there is rarely a complete calculation theory of excavation surface support force based on displacement evolution.

In view of the concept of displacement earth pressure and the plastic limit equilibrium theory of soil, this paper deduces the theoretical equation between the support force and the displacement of shield excavation surface under the shallow sandy soil layer's condition. A numerical simulation method is then utilized to reveal the displacement of the excavation surface when the support force changes under different working conditions. The relationship curve between the support force and the corresponding displacement (i.e., deformation) of the excavation surface is deduced, and the equations are analyzed. The results are helpful to

understand the relationship between the induced displacement and the corresponding support force and to guide the selection of the suitable support force.

2. Displacement Earth Pressure Theory

Actually, the theory of displacement earth pressure means that there is a close association between the earth pressure (i.e., the stress in soil) and the induced displacement during the movement of the retaining structure, which also involves the coupling process of external force, seepage action [27, 28], soil microstructure damage [7, 29], and even thermal loading [23, 30]. In the existing theory, the relationship between displacement and earth pressure is generally described from three aspects: (a) the displacement earth pressure curve is fitted according to the experimental data to obtain a certain functional relationship between earth pressure and displacement [31]; (b) the association between the internal friction angle and the displacement is obtained from the backfilling of retaining structure, to obtain the variation of earth pressure with the corresponding displacement; (c) in view of the stress-strain constitutive law of the soil behind the retaining structure, the calculation model of the relationship between displacement and earth pressure is established.

Terzaghi [32] carried out experimental research on the soil layer behind the retaining structure and acquired the relationship curve of earth pressure and corresponding displacement when the retaining structure moved. According to this theory, the soil takes on a static state at the beginning. Due to the external disturbance and the change of soil microstructure [29, 30], a certain deformation occurs. The deformation can be close to the structure or far away from the structure. At this time, the soil stress increases or decreases until the active/passive limit equilibrium state is reached. At this time, the soil pressure does not change, but the deformation can continue to change.

In the light of the theory of displacement earth pressure, it is clear that the earth pressure of the retaining structure changes with its displacement. When the retaining structure moves in the direction of filling, the earth pressure increases, and it decreases when it moves away from the soil until the deformation of the soil body achieves the limit state. The retaining structure is defined as the nonlimit state from an initial static state to a continuous sliding surface (reaching limit state).

The displacement ratio is defined to describe the non-limit state of shield tunneling as follows:

$$W = \frac{S}{S_a}, \quad (1)$$

$$\text{or } W = \frac{S}{S_p},$$

where S is the displacement of excavation, S_a is the displacement when reaching the active limit state, and S_p is the displacement when reaching the passive limit state.

When the internal friction angle (φ_m) and external friction angle (δ_m) reach the maximum values of φ and δ with the change of displacement, the soil reaches the failure

limit state. It is assumed that there is a linear relationship between the induced displacement and the internal friction angle (or external friction angle). As indicated in Figure 1, the general relationship between φ_m and δ_m and displacement ratio can be established.

It is evident from Figure 1 that when the retaining structure is at rest, $S=0$, $\varphi_m=\varphi_0$, $\delta_m=\delta_0$; when the displacement of the retaining structure reaches the limit displacement, that is, $S \geq S_a(S_p)$, $\varphi_m=\varphi$, $\delta_m=\delta$.

When $0 \leq S \leq S_a(S_p)$, the calculation equations of φ_m and δ_m are written as follows, respectively:

$$\tan \varphi_m = \tan \varphi_0 + K_d (\tan \varphi - \tan \varphi_0), \quad (2)$$

$$\tan \delta_m = \tan \delta_0 + K_d (\tan \delta - \tan \delta_0), \quad (3)$$

$$K_d = \frac{4 \arctan(S/S_a(S_p))}{\pi} = \frac{4 \arctan W}{\pi}. \quad (4)$$

From the above equations that when in the static state, $S=0$, displacement ratio $W=0$, $K_d=0$; when in the limit state, $S=S_a$ (or S_p), displacement ratio $W=1$, $K_d=1$. When the action of the initial external friction angle (δ_0) of the retaining structure is not considered, the initial internal friction angle (φ_0) is simply expressed as

$$\varphi_0 = \arctan\left(\frac{(1-K_0)}{(1+K_0)}\right), \quad (5)$$

where K_0 is the static earth pressure coefficient, namely, $K_0=1-\sin\varphi$.

When considering the influence of the initial internal friction angle (δ_0) of retaining structure, Chang [33] suggested a modified Coulomb earth pressure coefficient equation to obtain the following equation:

$$\frac{1}{K_0} = \left[\frac{1}{\cos \varphi_0} + \sqrt{\tan^2 \varphi_0 + \tan \varphi_0 \tan \delta_0} \right], \quad (6)$$

where δ_0 is generally taken as $\varphi_0/2$.

3. Theory of Support Force on Shield Excavation Surface

3.1. Basic Assumptions. Because the interaction between the shield and excavation surface is very complex in practical engineering [17, 33, 34], the problem is simplified to facilitate mathematical derivation. It is assumed that (a) when the displacement of the center location of the excavation surface changes as a result of the change of support force, it is considered that the soil has wedge-shaped sliding and developed to the top of the shield; (b) in view of the existence of soil arch effect, the soil sliding is gradually developing upward; (c) the sandy soil layer is uniform and isotropic ideal rigid-plastic material, which obeys the so-called Mohr-Coulomb yield criterion; (d) the shape of the excavation surface is rectangular, and its area is equivalent to the area of the excavation surface, and the height of the rectangle is equivalent to the diameter D of the excavation tunnel; (e) the seepage problem in the soil layer and the influence of hydrostatic pressure [35–37] are not

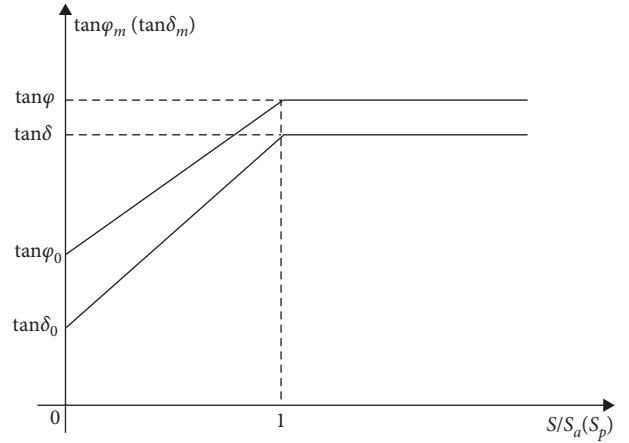


FIGURE 1: The evolution of internal friction angle with displacement.

considered due to the complexity of the interfering factors such as groundwater, ambient temperature, and even the existence of gas phase in unsaturated soil.

3.2. Calculation of Active Support Force of Excavation Surface. Based on the three-dimensional wedge model composed of two parts, this section deduces the equation of excavation surface support force owing to the concept of displacement-based earth pressure. Thus, the stress analysis mode of the wedge is shown in Figure 2.

According to the basic assumption, the area of the middle surface ($abcd$) of the discussed wedge is equal to the area of the circular excavation surface, and the height (ad) is equivalent to the diameter (D) of the construction tunnel. Let B be the width of the rectangle ($abcd$); then,

$$BD = \frac{\pi D^2}{4}. \quad (7)$$

If the perimeter of the rectangle ($cdef$) on the top of the wedge is U and the area is A , and the angle of the inclined plane ($abef$) of the wedge ($abcdef$) is α , then there is

$$\frac{U}{A} = \frac{2(B+D) \cot \alpha}{B D \cot \alpha}. \quad (8)$$

Substituting equation (6) into equation (7), we obtain

$$\frac{U}{A} = \frac{2}{D} \left(\tan \alpha + \frac{4}{\pi} \right). \quad (9)$$

The static equilibrium in the Z direction is as follows:

$$G + Q_1 - (2T_3 + 2C_3 + T_2 + C_2) \sin \alpha - T_p - C_p - Q_2 \cos \alpha = 0, \quad (10)$$

where G is the gravity of wedge ($abcdef$); Q_3 , T_3 , and C_3 are the supporting force, sliding friction, and cohesive friction of wedge side (ade) and (bcf), respectively; Q_2 , T_2 , and C_2 are the supporting force, sliding friction, and cohesive friction of the wedge inclined plane ($abef$), respectively; T_p and C_p are the wedge sliding and cohesive friction, respectively; and α is the included angle between the wedge and the horizontal level.

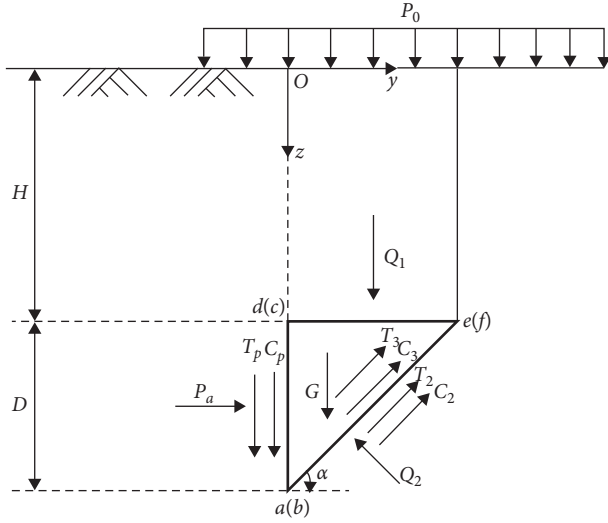


FIGURE 2: Force analysis of actively damaged wedge.

$$\begin{aligned} T_3 &= Q_3 \tan \varphi_m, \\ T_2 &= Q_2 \tan \varphi_m, \\ T_p &= P_a \tan \delta_m. \end{aligned} \quad (11)$$

From the static equilibrium in the Y direction, it can be seen that

$$P_a + (2T_3 + 2C_3 + T_2 + C_2) \cos \alpha - Q_2 \sin \alpha = 0, \quad (12)$$

where P_a is the shield support force to the excavation surface.

By substituting equations (10) and (11) into equation (12), the calculation equation of active support force of excavation surface can be acquired:

$$\begin{aligned} P_a &= \frac{-(2Q_3 \tan \varphi_m + 2C_3 + C_2) [\sin \alpha \tan(\alpha - \varphi_m) + \cos \alpha]}{1 + \tan \delta_m \tan(\alpha - \varphi_m)} \\ &+ \frac{(G + Q_1 - C_p) \tan(\alpha - \varphi_m)}{1 + \tan \delta_m \tan(\alpha - \varphi_m)}. \end{aligned} \quad (13)$$

The value of the internal friction angles φ_0 and φ_m and the external friction angles δ_0 and δ_m can be obtained by equations (1)–(6), which are related to displacement ratio W . Other parameters are calculated as follows:

$$\begin{aligned} C_2 &= \frac{c\pi D^2}{4 \sin \alpha}, \\ C_3 &= c \frac{D^2}{2 \tan \alpha}, \\ G &= \frac{1}{2} \gamma B D^2 \cot \alpha, \\ C_p &= \frac{c\pi D^2}{8}. \end{aligned} \quad (14)$$

Assuming that the support force and earth pressure are balanced during shield tunneling, the active support force at the center point of the excavation surface can be obtained as follows:

$$P'_a = \frac{4P_a}{\pi D^2}. \quad (15)$$

3.2.1. The Inclination Angle of Wedge Slope α . Generally, the inclination angle of the sliding surface of the wedge can be assumed as $45^\circ + \varphi/2$ for the active limit support force in the three-dimensional wedge model. The slope angle of the wedge-shaped sliding surface gradually decreases as the support force and the soil displacement reduce. Therefore, the inclination angle of wedge sliding surface is defined as

$$\alpha = 45^\circ + \varphi - \varphi_m/2. \quad (16)$$

3.2.2. Overburden Earth Pressure Q_1 . The calculation methods of overburden earth pressure include the proctor's earth pressure theory, the loose pressure estimation method proposed by Terzaghi (1923), and the standard calculation method. Among these, the loose earth pressure theory given by Terzaghi is extensively utilized because of its rationality. Therefore, the calculation of overburden earth pressure is acquired by

$$Q_1 = \sigma_v(H)A. \quad (17)$$

3.2.3. Force on Both Sides of Wedge Q_3 . The stress analysis of the wedge is shown in Figure 3. In the light of Rankine's theory, the expression of earth pressure at z' is as follows:

$$\sigma_h(z') = K\sigma_{v0} + K\gamma z'. \quad (18)$$

The force on both sides of the wedge (Q_3) is

$$Q_3 = \int \sigma_h(z') dA = \int \sigma_h(z') l(z') dz'. \quad (19)$$

In equation (19),

$$l(z') = D \cot \alpha - z' \cot \alpha. \quad (20)$$

Substituting equation (20) into equation (19), then

$$Q_3 = \int \sigma_h(z') (D \cot \alpha - z' \cot \alpha) dz'. \quad (21)$$

The integral of equation (21) leads to

$$Q_3 = \frac{K}{2} \sigma_{v0} D^2 \cot \alpha + \frac{1}{6} K \gamma D^3 \cot \alpha. \quad (22)$$

3.3. Calculation of Passive Support Force of Excavation Surface. Based on the three-dimensional wedge model, the failure pattern of the excavation surface is still assumed as a wedge, and the top of the wedge is changed into an inverted

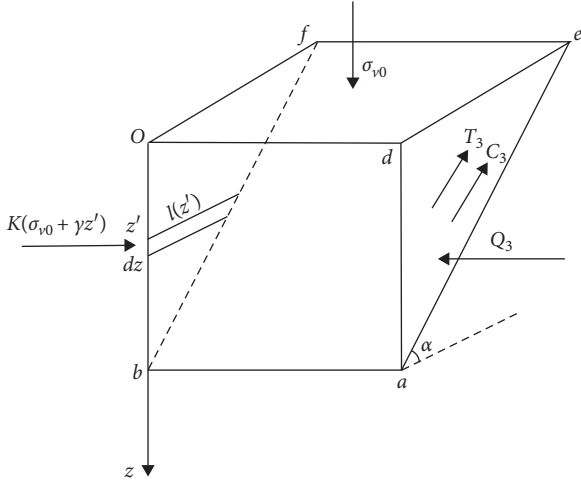


FIGURE 3: Force analysis of wedge.

prism. The stress analysis of the wedge in front of the excavation surface is indicated in Figure 4.

The calculation process of the passive support force is similar to that of the active support force. Therefore, in view of the equilibrium state in y and z directions, the total passive support force can be obtained as follows:

$$P_p = \frac{(2Q_3 \tan \varphi_m + 2C_3 + C_2) [\sin \beta \tan(\beta + \varphi_m) + \cos \beta]}{1 - \tan \delta_m \tan(\beta + \varphi_m)} + \frac{(G_1 + Q_1 + C_p) \tan(\beta + \varphi_m)}{1 - \tan \delta_m \tan(\beta + \varphi_m)}. \quad (23)$$

In equation (23), the values of internal friction angles φ_0 and φ_m and external friction angles δ_0 and δ_m can be seen from equations (1) to (6), which are related to displacement ratio δ_m ; other parameters are calculated as follows:

$$\lambda = \frac{1}{\sin \beta \cos(\beta + \varphi_m + \delta_m) / \cos \beta \cos \delta_m \sin(\beta - \varphi_m) + 2 \tan \delta_m \tan \beta} \quad (28)$$

The stress analysis of the inverted prism above the wedge is shown in Figure 5.

The geometric parameters of the inverted prism are defined: the lower surface of the inverted prism or the upper wedge surface is E in length, B in width, and A in the area; the upper surface of the inverted prism is E' , B' in width, and A' in area; the side area of the inverted prism is A_1 , and the volume of the inverted prism is V .

Based on the mechanical equilibrium of the inverted prism, the force Q_1 of the inverted wedge prism is obtained as follows:

$$Q_1 = Q_5 + G_1 + (T_4 + C_4) \sin \omega, \quad (29)$$

where Q_5 is the force of the soil above the inverted prism in the failure height; T_4 and C_4 are the sliding friction and cohesive friction of the inverted prism, respectively; and G_1

$$\begin{aligned} C_2 &= \frac{c\pi D^2}{4 \sin \beta}, \\ C_3 &= \frac{c\pi D^2}{2 \tan \beta}, \\ G &= \frac{1}{2} BD^2 \cot \beta, \\ Q_3 &= \frac{\lambda \gamma (H + D/2) D^2}{2 \tan \beta}, \\ T_3 &= Q_3 \tan \varphi_m, \\ C_s &= \frac{c\pi D^2}{8}. \end{aligned} \quad (24)$$

Similarly, the passive support force at the center point of the excavation surface can be obtained as follows:

$$P'_p = \frac{4P_p}{\pi D^2}. \quad (25)$$

On the basis of the theory of displacement-based earth pressure in this paper, the inclination angle of the wedge sliding surface (β) is calculated by

$$\tan \beta = \tan \varphi_m \left[\sqrt{1 + \cot \varphi_m \cot(\varphi_m + \delta_m)} - 1 \right]. \quad (26)$$

The inclination angle of the inverted prism (ω) above the wedge is calculated by the angle of the sliding surface under the active failure model:

$$\omega = \frac{\pi}{4} + \varphi - \varphi_m/2. \quad (27)$$

Thus, the displacement-based lateral pressure coefficient is given by

is the gravity of the inverted prism in the failure height of the soil.

The corresponding calculation equations are as follows:

$$\begin{aligned} Q_5 &= \gamma (H - X) A', \\ T_4 &= \lambda \gamma A_1 \left(H - \frac{X}{2} \right) \cos \omega \tan \varphi_m, \\ G_1 &= \gamma V, \\ C_4 &= c A_1. \end{aligned} \quad (30)$$

By substituting equation (30) into equation (29), the overburden earth pressure Q_1 can be obtained.

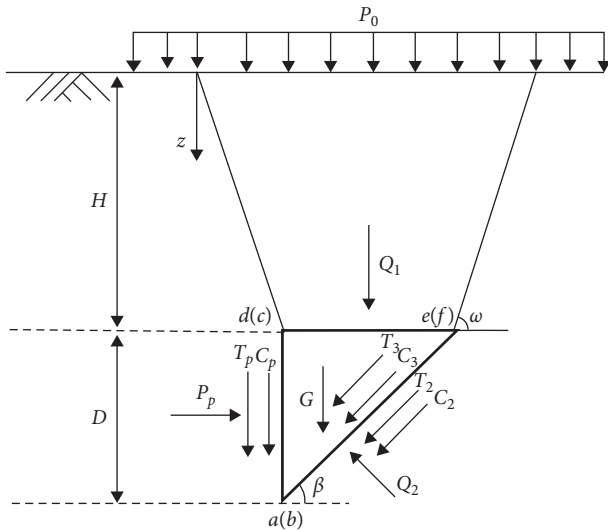


FIGURE 4: Force analysis of passively damaged wedge.

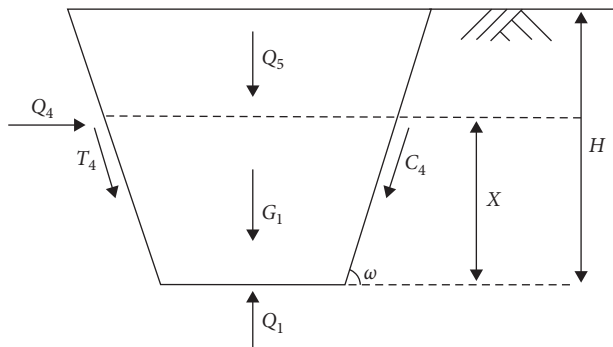


FIGURE 5: Stress analysis of chamfered cylinder.

4. Comparison of the Proposed Model with Numerical Simulation

4.1. Numerical Calculation and Parameters. A numerical calculation based on the program FLAC3D is used to verify the established theoretical model in this paper. The FLAC3D is a numerical simulation software based on the difference method (Itasca company, USA). The geometric model scale is $20 \times 30 \times 24$ m. Here, the diameter size of the tunnel section is 6 m. Due to the symmetry of the geometric model, half of the models are selected for calculation (Figure 6). The model has a free surface, horizontal side direction constrained, and bottom fixed. As a typical example, for the tunnel model with buried depth ratio $H/D = 1$, there are 66871 elements and 66920 nodes.

The shield segment is assumed to be made of C50 reinforced concrete. The thickness of the segment is 35 cm and is considered a linear elastic material. Mohr–Coulomb's yield criterion is used to describe the sandy soil layer. Shell element is used for the contact surface between segment and concrete, and the specific material parameters are shown in Table 1.

The sand soil layers with two buried depth ratios (i.e., $H/D = 0.5$ and $H/D = 1$) and four internal friction angles

(i.e., $\varphi = 25^\circ, 30^\circ, 35^\circ, 40^\circ$) are numerically simulated. Table 2 shows the calculation cases and conditions.

4.2. Influence of Shield Tunneling Displacement on Support Force. Case 1–Case 4 are taken as an example to obtain the influence of shield tunneling displacement on the active support force. The material calculation parameters and displacement ratio are substituted into equations (13) and (30), respectively, and the above same conditions and material parameters are numerically simulated. The results of theoretical calculation and numerical simulation are shown in Figure 7.

According to Figure 7, the theoretical and numerical results are consistent and demonstrate that the active support force changes with an increased displacement ratio. When the ratio of internal friction angle to buried depth is certain, the active support force decreases with the displacement ratio increase. Moreover, the difference between theoretical and numerical simulation is between 0 and 5 kPa, and the error is minimal.

The same method is adopted to obtain the influence of shield tunneling displacement on the passive support force. The theoretical and numerical results shown in Figure 8 are consistent and represent the changing trend of passive support force with increasing displacement ratio. Figure 8 indicates that, as the internal friction angle and buried depth ratio are fixed, the passive support force increases with increasing the displacement ratio. Moreover, the divergence between the theoretical values and the numerical simulation results is between 0 and 0.1 MPa, and the error is also minor.

4.3. Comparison of Ultimate Support Force. Using equations (13) and (23), the active and passive ultimate supporting forces of the excavation surface under 8 cases are obtained. The calculation results are shown in Table 3.

The excavation surface support force is gradually increased or decreased with the same conditions and material parameters mentioned above until the center displacement of the tunnel excavation surface develops rapidly and reaches the limit state. The corresponding support force is selected as the limit support force calculated by numerical method. The ultimate support force calculated by theoretical and numerical methods is compared, as manifested in Figure 9.

From Figure 9, the changing trend of the ultimate support force with increasing the internal friction angle is consistent between the theoretical and numerical simulation under different buried depth ratio conditions. Therefore, the active limit support force decreases with increasing the internal friction angle, and on contrary, the passive limit support force increases. From another perspective, as the internal friction angle is fixed, the active and passive limit support forces increase with increasing the buried depth ratio. In addition, the difference between the theoretical and the numerical results is not significant. The differences between the active limit support force and the passive limit support force are

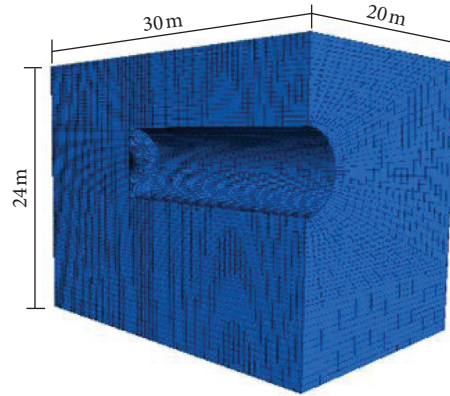


FIGURE 6: Numerical calculation model.

TABLE 1: Computational parameter.

Materials	Elastic modulus (MPa)	Poisson's ratio	Density (kg/m ³)	Cohesion (kPa)	Tensile strength (kPa)
Soil	20	0.35	1800	1	1
Shield segment	30000	0.25			

TABLE 2: Cases of numerical simulation.

Case	H/D	φ (°)
1	0.5	25
2	0.5	30
3	0.5	35
4	0.5	40
5	1	25
6	1	30
7	1	35
8	1	40

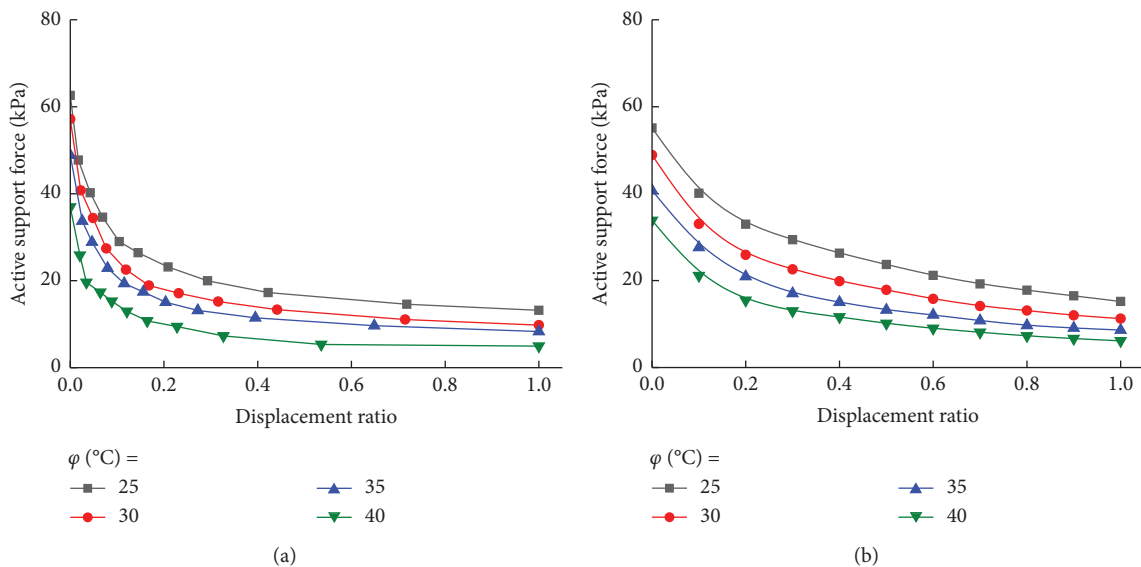


FIGURE 7: Comparison of the influence of shield driving displacement on active support force: (a) theoretical results and (b) numerical results.

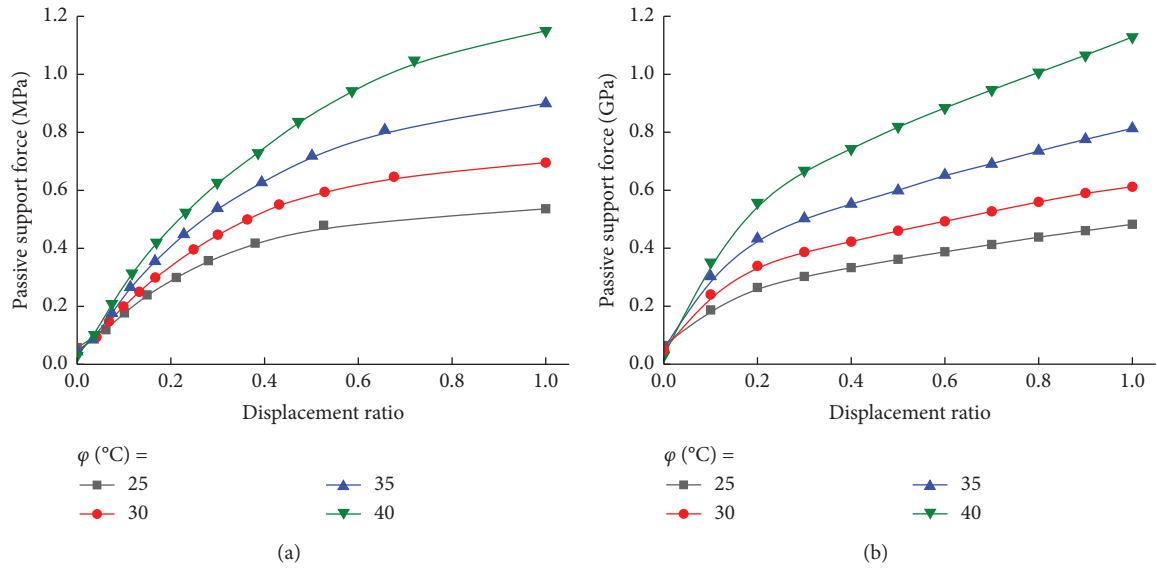


FIGURE 8: Comparison of the influence of shield driving displacement on the passive supporting force: (a) theoretical results and (b) numerical results.

TABLE 3: Theoretical results of the ultimate supporting force.

H/D	ϕ ($^\circ$)	Active ultimate support force (kPa)	Passive ultimate support force (kPa)
0.5	25	14.51	480
0.5	30	11.65	630
0.5	35	8.4	820
0.5	40	6.12	1120
1	25	17.77	850
1	30	12.56	950
1	35	9.57	1420
1	40	6.6	1880

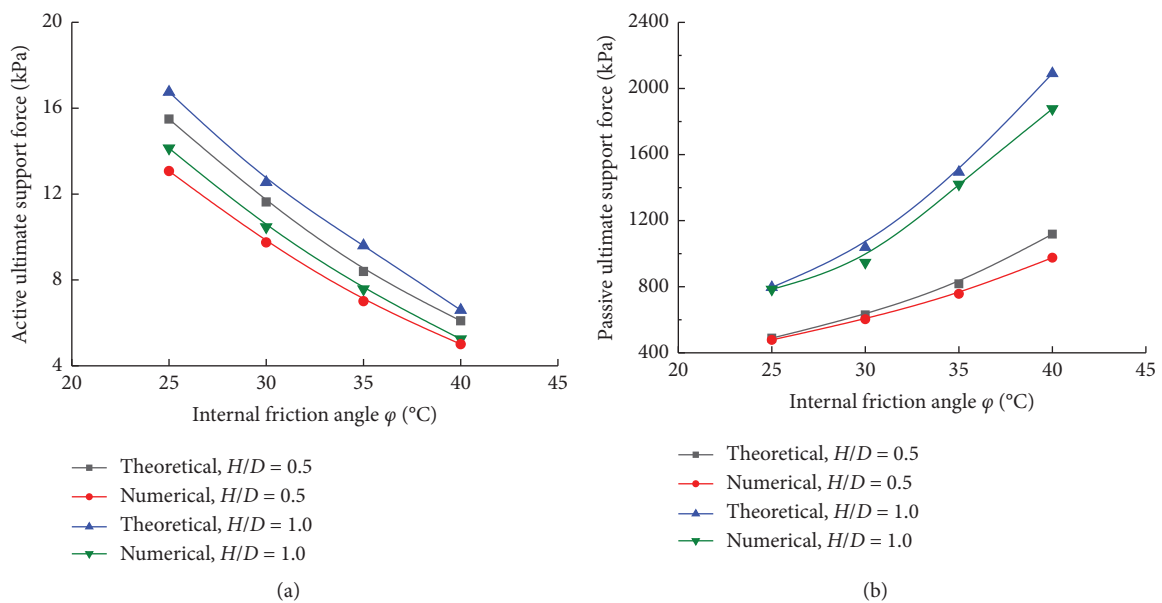


FIGURE 9: Comparison of ultimate support force obtained from theoretical and numerical calculation: (a) active ultimate support force and (b) passive ultimate support force.

0–4 kPa and 0–3 kPa, respectively, which is within the acceptable range proving the rationality of the theoretical equation.

5. Conclusions

Based on the three-dimensional wedge assumption, the relationship of the support force and the corresponding displacement on the excavation surface of the shield in the shallow sandy soil layer is derived using the displacement earth pressure and the plastic limit equilibrium theories.

When the ratio of internal friction angle to buried depth is certain, the active support force decreases with increasing the displacement ratio, while the passive support force decreases with increasing the displacement ratio. Moreover, the difference between the theoretical calculation and the numerical simulation is very small.

When the buried depth ratio is constant, the active ultimate support force decreases with increasing the internal friction angle, while the passive ultimate support force increases with increasing the internal friction angle. From another perspective, as the internal friction angle is fixed, the active and passive ultimate support forces increase with the rise in the buried depth ratio. Overall, the above analyses indicate the rationality of the proposed displacement-based calculation theory for predicting the support force.

Data Availability

The data used to support the findings of this study are available from the corresponding author upon request.

Conflicts of Interest

The authors declare that they have no conflicts of interest.

Acknowledgments

This work was supported by the National Natural Science Foundation of China (52078031).



References

- [1] X. Hu, C. He, G. Walton, Y. Fang, and G. Dai, "Laboratory model test of EPB shield tunneling in a cobble-rich soil," *Journal of Geotechnical and Geoenvironmental Engineering*, vol. 146, no. 10, Article ID 04020112, 2020.
- [2] B. Bai, D. Rao, T. Xu, and P. Chen, "SPH-FDM boundary for the analysis of thermal process in homogeneous media with a discontinuous interface," *International Journal of Heat and Mass Transfer*, vol. 117, pp. 517–526, 2018.
- [3] L. Li, S. Sun, J. Wang, W. Yang, S. Song, and Z. Fang, "Experimental study of the precursor information of the water inrush in shield tunnels due to the proximity of a water-filled cave," *International Journal of Rock Mechanics and Mining Sciences*, vol. 130, Article ID 104320, 2020.
- [4] B. Bai, T. Xu, Q. Nie, and P. Li, "Temperature-driven migration of heavy metal Pb^{2+} along with moisture movement in unsaturated soils," *International Journal of Heat and Mass Transfer*, vol. 153, Article ID 119573, 2020.
- [5] L. Flessati and C. di Prisco, "Deep tunnel faces in cohesive soils under undrained conditions: application of a new design approach," *European Journal of Environmental and Civil Engineering*, vol. 51, Article ID 1785332, 2018.
- [6] S. Zingg and G. Anagnostou, "Tunnel face stability and the effectiveness of advance drainage measures in water-bearing ground of non-uniform permeability," *Rock Mechanics and Rock Engineering*, vol. 51, no. 1, pp. 187–202, 2017.
- [7] B. Bai, D. Rao, T. Chang, and Z. Guo, "A nonlinear attachment-detachment model with adsorption hysteresis for suspension-colloidal transport in porous media," *Journal of Hydrology*, vol. 578, Article ID 124080, 2019.
- [8] K.-H. Park, J.-G. Lee, and A. Owatsiriwong, "Seepage force in a drained circular tunnel: an analytical approach," *Canadian Geotechnical Journal*, vol. 45, no. 3, pp. 432–436, 2008.
- [9] T. Qiu, C. Liu, X. Zhong, and Y. Zhu, "Experimental research on the impact of temperature on the adhesion characteristics of soil-structure interface," *Geofluids*, vol. 2020, Article ID 6675576, 9 pages, 2020.
- [10] B. Bai, L. Guo, and S. Han, "Pore pressure and consolidation of saturated silty clay induced by progressively heating/cooling," *Mechanics of Materials*, vol. 75, pp. 84–94, 2014.
- [11] B. Bai and Z. Su, "Thermal responses of saturated silty clay during repeated heating-cooling processes," *Transport in Porous Media*, vol. 93, no. 1, pp. 1–11, 2012.
- [12] I.-M. Lee and S.-W. Nam, "The study of seepage forces acting on the tunnel lining and tunnel face in shallow tunnels," *Tunnelling and Underground Space Technology*, vol. 16, no. 1, pp. 31–40, 2001.
- [13] I. Lee, S. Nam, and J. Ahn, "Effect of seepage forces on tunnel face stability," *Canadian Geotechnical Journal*, vol. 40, no. 2, pp. 342–350, 2002.
- [14] B. Bai, H. Li, T. Xu, and X. Chen, "Analytical solutions for contaminant transport in a semi-infinite porous medium using the source function method," *Computers and Geotechnics*, vol. 69, pp. 114–123, 2015.
- [15] D. Soubirin and H. Wong, "Tunnel face stability in frictional material: a new 3D failure mechanism," *Comptes Rendus Mecanique*, vol. 330, no. 7, pp. 513–519, 2002.
- [16] P. A. Vermeer, P. G. Bonnier, and S. C. Mollen, "On a smart use of 3D-FEM in tunneling," in *Proceedings of the 8th International Symposium on Numerical Models in Geomechanics*, Rome, Italy, April 2002.
- [17] X. Lü, S. Zeng, Y. Zhao, M. Huang, S. Ma, and Z. Zhang, "Physical model tests and discrete element simulation of shield tunnel face stability in anisotropic granular media," *Acta Geotechnica*, vol. 15, no. 10, pp. 3017–3026, 2020.
- [18] C. Dai, H. Sui, and C. Ma, "Study on the ultimate supporting force of shield excavation face based on anisotropic strength theory," *Applied Sciences*, vol. 10, no. 15, p. 5222, 2020.
- [19] X. Liang, F. Ye, A. Ouyang, X. Han, and X. Qin, "Theoretical analyses of the stability of excavation face of shield tunnel in Lanzhou metro crossing beneath the yellow river," *International Journal of Geomechanics*, vol. 20, no. 11, Article ID 04020200, 2020.
- [20] B. Mi and Y. Xiang, "Analysis of the limit support pressure of a shallow shield tunnel in sandy soil considering the influence of seepage," *Symmetry*, vol. 12, no. 6, p. 1023, 2020.
- [21] Y. Liang, Y. Xiao, and Y. Lin, "Pore water pressure responses in sand stratum during shield tunnelling: a case study," *Advances in Civil Engineering*, vol. 2020, Article ID 6139246, 9 pages, 2020.
- [22] X.-Y. Wang, D.-J. Yuan, D.-L. Jin, and W.-L. Su, "Thermal and mechanical response of soil and tunnel during replacement of

- shield tail brush by freezing method,” *KSCE Journal of Civil Engineering*, vol. 24, no. 5, pp. 1632–1640, 2020.
- [23] B. Bai and X. Shi, “Experimental study on the consolidation of saturated silty clay subjected to cyclic thermal loading,” *Geomechanics and Engineering*, vol. 12, no. 4, pp. 707–721, 2017.
- [24] X. Li, T. Li, and L. Peng, “Elastoplastic two-surface model for unsaturated cohesive soils under cyclic loading,” *International Journal of Geomechanics*, vol. 20, no. 8, Article ID 04020122, 2020.
- [25] G. C. Yang and B. Bai, “Thermo-hydro-mechanical model for unsaturated clay soils based on granular solid hydrodynamics theory,” *International Journal of Geomechanics*, vol. 19, no. 10, Article ID 04019115, 2019.
- [26] B. Bai, Q. Nie, Y. Zhang, X. Wang, and W. Hu, “Cotransport of heavy metals and SiO₂ particles at different temperatures by seepage,” *Journal of Hydrology*, vol. 51, Article ID 125771, 2020.
- [27] Y. Wang, Z. Li, H. Jing, Y. Li, and M. Wang, “Study on the seepage characteristics of deep buried tunnels under variable high-pressure water heads,” *Bulletin of Engineering Geology and the Environment*, vol. 80, no. 2, pp. 1477–1487, 2021.
- [28] Y. Wang, F. Chen, X. Li, X. Yin, and Y. Lei, “The variable-mass seepage law of broken porous rock: an experimental study,” *Geomatics, Natural Hazards and Risk*, vol. 11, no. 1, pp. 1991–2005, 2020.
- [29] Z. Zizka, B. Schoesser, M. Thewes, and T. Schanz, “Slurry shield tunneling: new methodology for simplified prediction of increased pore pressures resulting from slurry infiltration at the tunnel face under cyclic excavation processes,” *International Journal of Civil Engineering*, vol. 17, no. 1, pp. 113–130, 2019.
- [30] B. Bai, F. Long, D. Rao, and T. Xu, “The effect of temperature on the seepage transport of suspended particles in a porous medium,” *Hydrological Processes*, vol. 31, no. 2, pp. 382–393, 2017.
- [31] A. Hamrouni, D. Dias, and B. Sbartai, “Probability analysis of shallow circular tunnels in homogeneous soil using the surface response methodology optimized by a genetic algorithm,” *Tunnelling and Underground Space Technology*, vol. 86, pp. 22–33, 2019.
- [32] K. Terzaghi, “Record earth pressure testing machine,” *Engineering News Record*, vol. 109, no. 29, pp. 365–369, 1932.
- [33] M.-F. Chang, “Lateral earth pressures behind rotating walls,” *Canadian Geotechnical Journal*, vol. 34, no. 4, pp. 498–509, 1997.
- [34] J. Xu and Q. Pan, “Analysis of the upper limit of the shield tunnel excavation surface support force,” *Journal of Railway Science and Engineering*, vol. 11, no. 4, p. 80, 2014.
- [35] B. Bai, “Fluctuation responses of saturated porous media subjected to cyclic thermal loading,” *Computers and Geotechnics*, vol. 33, no. 8, pp. 396–403, 2006.
- [36] G. Mollon, D. Dias, and A.-H. Soubra, “Probabilistic analysis of pressurized tunnels against face stability using collocation-based stochastic response surface method,” *Journal of Geotechnical and Geoenvironmental Engineering*, vol. 137, no. 4, pp. 385–397, 2011.
- [37] L. Wang, K. Han, T. Xie, and J. Luo, “Calculation of limit support pressure for EPB shield tunnel face in water-rich sand,” *Symmetry*, vol. 11, no. 9, p. 1102, 2019.

Research Article

Stress Relief and Stimulation of Coal Reservoir by Hydraulic Slotting

Xiaoyang Cheng ^{1,2}, Qinghua Zhang,^{1,2} Zhigang Zhang ^{1,2}, Yunlong Zou,^{1,2} and Guo Junjie³

¹China Coal Technology Engineering Group Chongqing Research Institute, Chongqing 400037, China

²State Key Laboratory of Gas Disaster Monitoring and Emergency Technology, Chongqing 400037, China

³School of Safety Engineering, Henan Institute of Engineering, Zhengzhou 451191, China

Correspondence should be addressed to Zhigang Zhang; zgz-2@163.com

Received 20 December 2020; Revised 23 January 2021; Accepted 27 February 2021; Published 20 April 2021

Academic Editor: Chi Yao

Copyright © 2021 Xiaoyang Cheng et al. This is an open access article distributed under the Creative Commons Attribution License, which permits unrestricted use, distribution, and reproduction in any medium, provided the original work is properly cited.

Coal seam permeability is one of the key factors influencing the gas extraction efficiency, which is of great significance to reduce coal and gas dynamic disasters in gassy coal mines. Hydraulic slotting technique is an effective method to stimulate the coal reservoir, but the selection of slotting key parameters has great impact on gas extraction efficiency. For this reason, the hydraulic slotting model was established by using FLAC^{3D} software to analyze the stress distribution before and after slotting. Then, the influence of borehole diameter, slotting width, and slotting length on coal seam stress relief is also discussed. The results show that the slotting width has a great influence on the stress relief of the coal seam, while the borehole diameter and slotting length have no obvious influence on that. Based on the results of numerical simulation, field tests were carried out in Sangshuping NO.2 coal mine. The results show that the coal seam stress can be fully released, resulting in the improvement of coal seam permeability. The gas extraction efficiency can be highly enhanced by hydraulic slotting. This research achievement provides the guidance basis for high-stress water jet slotting technology with adaptive selection of slotting parameters in different geological conditions.

1. Introduction

As the most important energy in China, coal plays an important role in promoting China's economic development [1]. In order to realize the maximum utilization of resources in the coal production process, the resource exploitation model of "coal-gas coexploitation" has been formed in China [2, 3]. However, China's coal reservoir has common characteristics such as high gas content, high gas stress, and low permeability, which also results in low production of coalbed methane and difficulties in large-scale development. In addition, the low efficiency of gas drainage is also the direct cause of increasing the frequency of gas dynamic disasters [4, 5]. To improve the efficiency of gas extraction, experts and scholars at home and abroad have been putting lots of effort in permeability improvement in the coal reservoir. The widely applied techniques to improve the permeability of the coal seam include deep-hole split blasting [6–8], hydraulic

slotting [9–12], hydraulic fracturing [13, 14], hydraulic flushing [15–17], CO₂ fracturing [18–20], and gas injection [21, 22]. Different techniques are all able to create a large number of fractures, forming a network of fractures that can promote the gas migration. However, the adaptability of different techniques to the occurrence conditions of the coal seam is different to some extent.

Hydraulic slotting technology is being developed rapidly in recent years, which cannot only weaken or eliminate the danger of gas disasters but also change the physical property of the coal reservoir to realize the double effect of stress relief and permeability enhancement in the coal seam. Therefore, this technology has been widely used in coal mines. Yang et al. [23] have put forward a method using high-pressure water jet technology to control rock burst in roadway and analyzed the theory of controlling rock burst in roadway by the weak structure zone mode. Then, the influence law of the weak structure zone under dynamic and static-combined

load is analyzed by the numerical simulation method. The results show that the distressed zone formed by high-pressure water jet cutting seam can effectively prevent rock burst. Zhang et al. [24] and Yin et al. [25], respectively, used experimental and simulation methods to study the prevention and control mechanism of high-pressure water jet slicing on rock burst. Feng [26] and Lu et al. [27] studied the application of hydraulic slotting technology in rock cross-cut uncovering coal. The results show that hydraulic slotting technology has significant advantages in improving the gas drainage effect and shortening the time of coal uncovering at cross-cut, and the application of hydraulic slotting technology in tunnel coal uncovering engineering also proves this conclusion [28]. Lin et al. [29] and Chen et al. [30] applied the hydraulic slotting technology to the outburst prevention in the excavation working face, and the field test proved that the hydraulic slotting technology has good pressure relief and permeability increasing effect and has a positive role in reducing or eliminating the outburst risk of the coal mine. These research results provide a large number of reference examples for the promotion and application of hydraulic slotting technology in coal mines.

For hydraulic slotting technology, the selection of slotting parameters has a significant effect on the stress relief effect of the coal seam. Wei [31] simulated the formation of the stress relief area by hydraulic slotting utilizing PFC2D software and concluded that the effective slotting radius of the coal seam was 0.5 m and optimal hole spacing was 5 m. Lu et al. [32] pointed out that, in the same seam, the optimal distance between the slots is 4 m. Zhang and Zou [33] and Cheng et al. [34] established the prediction model of slotting depth and verified its precision in the field test. Si et al. [35] discussed the influence of geological mechanical property, in situ stress, slotting shape, slotting spacing, and other key parameters on slotting performance. Lu et al. [36, 37] studied the influence of slotting parameters on fracture closure of soft and hard coal after slotting. The spacing between boreholes is also an important part of slotting parameters, and the spacing between boreholes is directly related to the gas extraction radius after slotting. Xue et al. [38] adopted a thermo-hydro-mechanical coupled model to study the influence of hydraulic slotting technology on the gas extraction radius. Ge et al. [39] used COMSOL software to study the drainage influence radius of the slotted borehole in different coal seam conditions, and field tests were carried out.

The hydraulic slotting technology first increases the fracture opening generated by the release of the stress of the coal seam. Then, under the effect of stress, the fracture gradually closes, which results in the reduction of permeability of the coal seam [40]. How to preserve the high permeability of the coal seam and how to extend the period of high gas extraction efficiency are the core issues of the development of hydraulic slotting technology. Thus, the scientific selection of slotting parameters is crucial. In this paper, FLAC^{3D} numerical simulation software is used to simulate hydraulic slotting. Firstly, the stress relief effect of the coal around the borehole before and after the slotting is discussed. Secondly, the influence of the slotting parameters

on the stress relief effect of the coal seam is analyzed. Finally, based on the guidance of numerical simulation results, the hydraulic slotting field test is carried out to verify the improvement of gas extraction by hydraulic slotting. This study provides the theoretical support for the optimization of slotting process and high-efficiency gas extraction.

2. The Influence of Hydraulic Slotting on Stress Relief of the Coal Seam

2.1. Model Establishment and the Governing Equation. After the formation of the slotting borehole, stress concentration will happen around the borehole. After slotting, the coal around the borehole damages and deforms, which results in the stress relief. In order to study the influence of slotting on the stress relief of the coal seam around the borehole, this paper chooses the coal seam as the research object and adopts Fast Lagrangian Analysis of Continuous numerical simulation to study the stress distribution around the borehole before and after slotting and then study the impact of different slotting parameters on the stress relief effect by hydraulic slotting. The simulation parameters are based on the test results of physical and mechanical parameters of No. 3 coal in Sangshuping NO.2 coal mine, as shown in Table 1.

The simulation adopts the two-dimensional model, with size 8 m × 5 m and a diameter of 100 mm. Symmetrical slotting is conducted along the center of the borehole to both sides, with division into 3538 units in total by 58 × 61, and all units are quadrilateral equal units. The grid around the slots is refined. Taking the far-field effect into consideration, the grid is divided with a combination of equal and unequal spacing. The left edge of the model adopts the symmetric boundary, and the right edge adopts the displacement boundary. The left and right edges only allow the boundary nodes to move along the vertical direction. The lower edge is set as the displacement boundary, of which the horizontal and vertical displacements are both zero. The upper edge adopts the stress boundary, and the applied vertical stress is 0.6 MPa. In order to simulate the effect of hydraulic slotting, a flat slotting with a length of 90 mm and a width of 60 mm is formed along the center of the borehole. The grid model is shown in Figure 1. After the model is established, the center of the borehole is marked as the origin of coordinates, and the stress and displacement value of all the points on X = 2 cm and Y = 2 cm measuring lines are recorded by using the FLAC print command. The calculation process of the model can be seen from Figure 2. Firstly, the appropriate mathematical model and geometric model should be established according to the problem and then mesh the geometric model. Then, the model boundary conditions should be initialized. Then, calculate the initial conditions to see if the results are reasonable. If the calculation result is not reasonable, then return to Step 1 to find the problem. If the result is reasonable, then calculate the problem under predetermined conditions to see if the result is reasonable. If not, return to Step 1, and gradually check whether there is a problem in each step and modify it. If reasonable, the calculation is completed, and the data can be exported and postprocessed.

TABLE 1: Simulation parameters' form.

Parameter	Minimum-maximum value	Mean value
Wave velocity (m/s)	1974~2245	2105
Vision density (kN/m ³)	13.40~14.13	13.36
Uniaxial compression strength (MPa)	12.74~16.00	14.64
Uniaxial elastic modulus (GPa)	3.64~3.91	3.79
Uniaxial deformation modulus (GPa)	2.61~2.92	2.81
Poisson's ratio	0.37~0.42	0.39
Consistent coefficient	1.3~1.6	1.5
Cohesive force (MPa)	—	10.13
Internal friction angle (°)	—	30.7

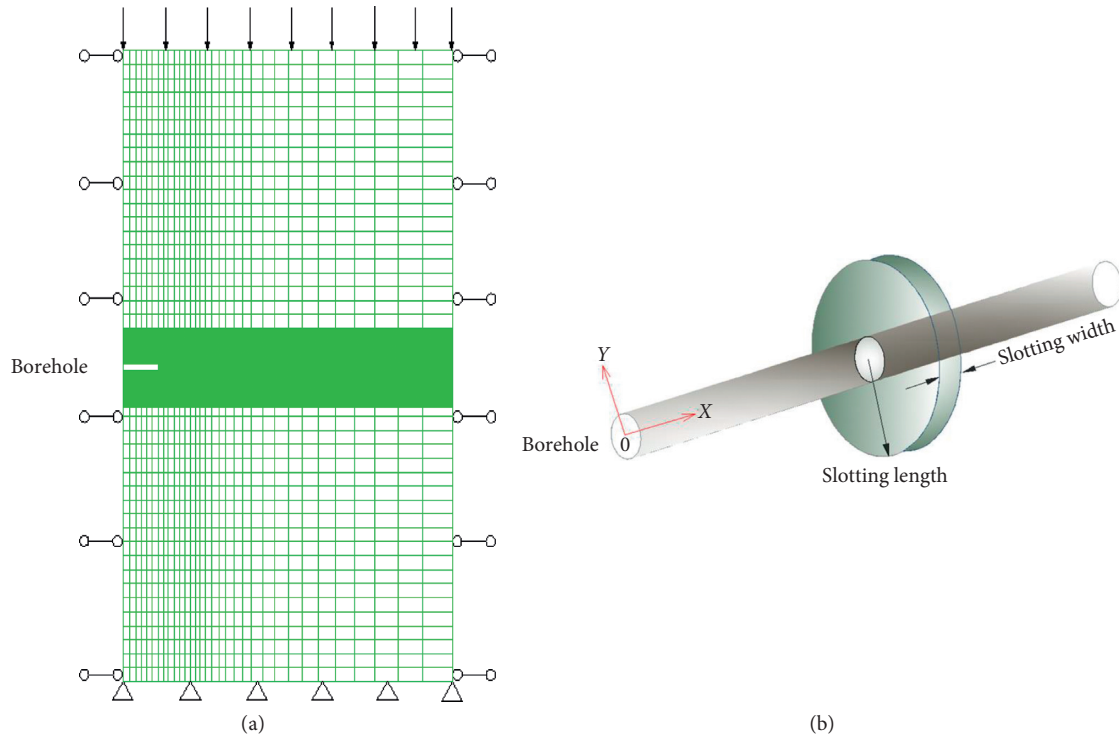


FIGURE 1: Grid model and slotting schematic.

The calculation of the model needs to consider the following assumptions: (1) the model is subject to three-dimensional static equilibrium conditions; (2) the rock is a homogeneous isotropic elastic-plastic continuum medium; (3) the rock mass in the plastic zone meets the Mohr-Coulomb strength criterion. The governing equation calculated by the model is as follows [41].

2.1.1. Stress-Strain Equation. When the model causes small plastic strains, the stress-strain relationship is then written as

$$\sigma = \sigma_0 + C': (\varepsilon - \varepsilon_0 - \delta\theta), \quad (1)$$

where σ is the Cauchy stress tensor, σ_0 and ε_0 are the stress and strain tensors, ε is the total strain tensor, δ is the thermal expansion tensor, and C' is the fourth-order elasticity tensor. Due to the thermal effect being neglected, $\delta\theta = 0$.

According to the deformation continuity condition, the total strain tensor is written in terms of the displacement gradient:

$$\varepsilon = \frac{1}{2} \left[\left(\frac{\partial s}{\partial x} + \frac{\partial s}{\partial y} \right) + \left(\frac{\partial s}{\partial x} + \frac{\partial s}{\partial y} \right)^T \right], \quad (2)$$

where s is the displacement.

2.1.2. Mohr-Coulomb Strength Criterion.

$$|\tau| = C + \sigma \tan \varphi, \quad (3)$$

where τ is the shear stress, C is the cohesive force, and φ is the angle of internal friction.

2.2. The Stress Distribution of the Surrounding Rock around the Borehole before and after Slotting. Figure 3 shows the vertical stress distribution on $X = 2$ cm and $Y = 2$ cm measured lines before and after slotting. From Figure 3(a), after the formation of the borehole, the vertical stress on $X = 2$ cm measured line will decrease gradually in radiation from the

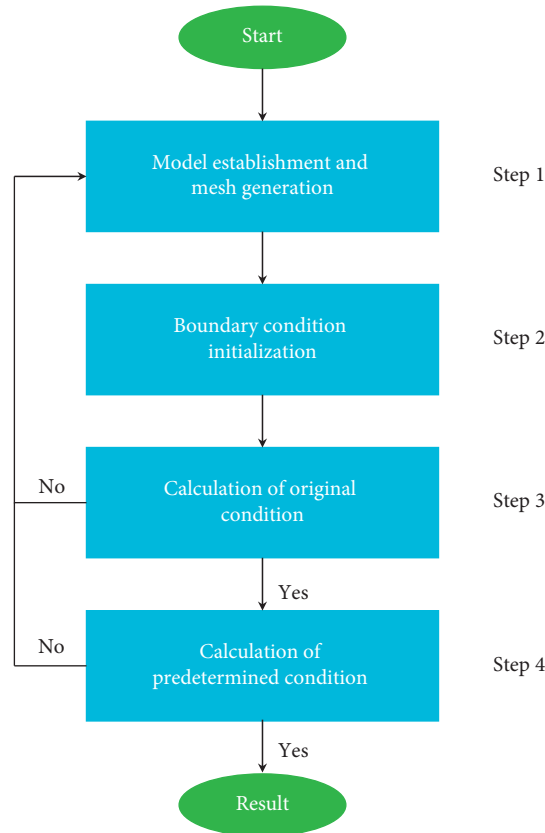


FIGURE 2: Calculation process of FLAC3D.

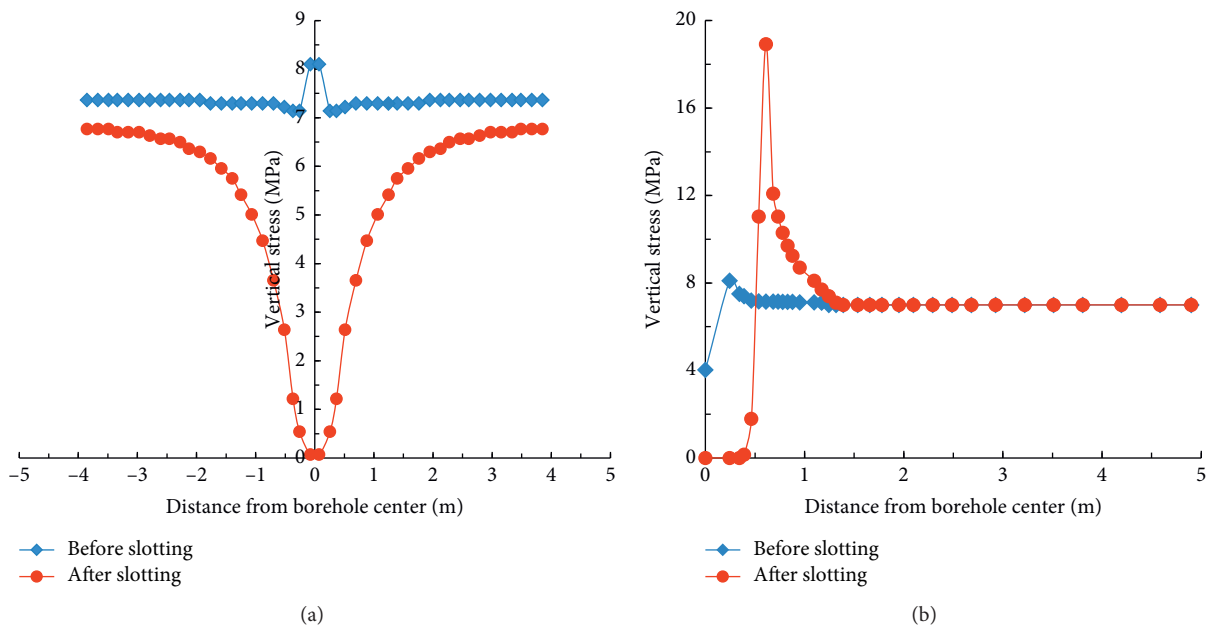


FIGURE 3: Vertical stress distribution on (a) $X = 2$ cm and (b) $Y = 2$ cm measured lines before and after slotting.

center of the slotting borehole to around in the vertical direction. The stress concentration occurs on the top of the borehole, and the maximum stress is 8.1 MPa, and the stress concentration factor is 1.1. After being slotted, a large-area stress relief appears with the influence scope of 6.4 m. From

Figure 3(b), the vertical stress on $Y = 2$ cm measured line will increase gradually in radiation in the horizontal direction. A stress relief zone appears, of which the influence scope is 24 cm. After being slotted, a stress concentration area was formed in the horizontal direction. Under the effect of

concentrated stress, a certain yield zone appears at the end of slots, with maximum stress at 18.92 MPa.

Figure 4 shows the horizontal stress distribution on $X=2\text{ cm}$ and $Y=2\text{ cm}$ measured lines before and after slotting. From Figure 4(a), after the formation of the borehole, a small stress relief area with diameter of 9 cm appears around the borehole, and the minimum stress is 4.06 MPa. After being slotted, the diameter of the stress relief area increases to 1.2 m. From Figure 4(b), there also exists a stress relief area in the horizontal direction. Therefore, an obvious stress relief area with $6.4\text{ m} \times 1.2\text{ m}$ will be formed around the borehole after slotting.

2.3. The Influence of Slotting Parameters on Stress Relief of the Coal Seam

2.3.1. The Influence of Borehole Diameter on Stress Relief of the Coal Seam. To study the influence of borehole diameter on stress relief of the coal seam after slotting, the diameters of 84 mm, 100 mm, 120 mm, and 150 mm were selected for simulation, respectively. The stress distribution of the coal seam after slotting is shown in Figures 5 and 6.

From Figures 5 and 6, the distribution of vertical stress and horizontal stress of the coal seam around the borehole with different diameters after slotting is basically same, which indicates that the diameter of the borehole has a small effect on the stress relief effect by hydraulic slotting. On the contrary, in the field gas extraction work, it is not necessary to drill large-diameter slotting boreholes, which can also reduce the drilling cost.

2.3.2. The Influence of Slotting Width on Stress Relief of the Coal Seam. To study the influence of slotting width on stress relief of the coal seam, the slotting widths of 40 mm, 60 mm, 80 mm, and 100 mm are selected for simulation, respectively. The stress distribution of the coal seam around slots with different slotting widths is shown in Figures 7 and 8. And, the corresponding stress relief area is shown in Table 2.

It can be seen that, the larger the slotting width, the larger the stress relief area. So, if the slotting width increases to a certain value, the coal seam can be fully stress relieved so as to generate a fully connected fracture network, which provides excellent conditions for high-efficiency gas extraction. Therefore, the increase of slotting width is the key parameter to evaluate the performance of the high-pressure water jet slotting device. However, in the field work, the slotting width is restrained by many conditions, such as the pressure of the pump, slotting nozzle performance, and coal and rock strength. Therefore, the selection of slotting width should depend on the geological conditions and device performance, so as to achieve the best stress relief effect.

2.3.3. The Influence of Slotting Length on Stress Relief of the Coal Seam. To study the influence of slotting length on stress relief of the coal seam, the slotting lengths of 60 cm, 90 cm, and 120 cm are selected for simulation, respectively. The stress distribution of the coal seam around slots with

different slotting lengths is shown in Figures 9 and 10. It can be seen that, within a small range of variation, the slotting length has little influence on the stress relief effect of the coal seam by using hydraulic slotting. Besides, the slotting length is also related to slotting system performance. And, the higher slotting length may trigger coal and gas outburst. So, it is not necessary to purely improve the slotting length.

3. Field Experiments

3.1. Test Location and Scheme

3.1.1. Test Equipment. The hydraulic slotting equipment mainly contains drilling bit, shallow spiral-integral drill rod, high-stress rotary aqua tail, water pump, remote operation floor, stress conversion slotter, high-stress hose, safety protection accessories, etc., and it can be seen in Figure 11. The device can realize the integration of drilling and slotting. The remote control is over 100 meters away from the slotting site, ensuring the safety and efficiency of the slotting process.

3.1.2. Hydraulic Slotting Process. The hydraulic slotting process mainly includes three stages: slotting preparation stage, borehole construction stage, and slotting stage. The operation process of hydraulic slotting can be seen from Figure 12. (1) Slotting preparation stage: before slotting, the water supply and power supply system should meet the requirement of the slotting operation. At the same time, the pumping pipe network and pumping metering device should be installed and completed in advance, and the hole sealing material should be prepared. In addition to this, drilling bit, slotting device drilling pipe, etc. are also assembled into the hydraulic slotting system in turn. All of this work is for the smooth operation of the slotting equipment. (2) Borehole construction stage: in this stage, low-pressure water is used to drill the borehole to the design depth. It is important to note that the sealing ring should be installed when connecting the drill pipe, and the thread of the drill pipe and its inner cavity should be cleaned. (3) Slotting stage: after the completion of drilling construction, it is necessary to remove the low-pressure water tail manually, connect the high-pressure water tail and high-pressure pipeline, and set up the warning line. Then, the water pump is turned on until water overflows through the borehole, at which time the drilling machine is turned on. Finally, slowly and uniformly adjust the pressure valve to the specified pressure value. At this time, the water flows through the high-pressure hose into the drill pipe, and the jet is formed by the nozzle on the slitter to cut the coal. The time of cutting the coal body is about 20–25 min each time. After the end of each knife slit, the pump is pressed back to zero and then shut down. According to the set slit spacing, the backward slit operation method is used to continue until the slit is completed.

3.1.3. Test Location and Scheme. The test mine selected is Sangshuping NO.2 coal mine in Hancheng City, Shanxi Province, which is a coal and gas outburst mine. This extraction seam is 3# coal seam, with average thickness of

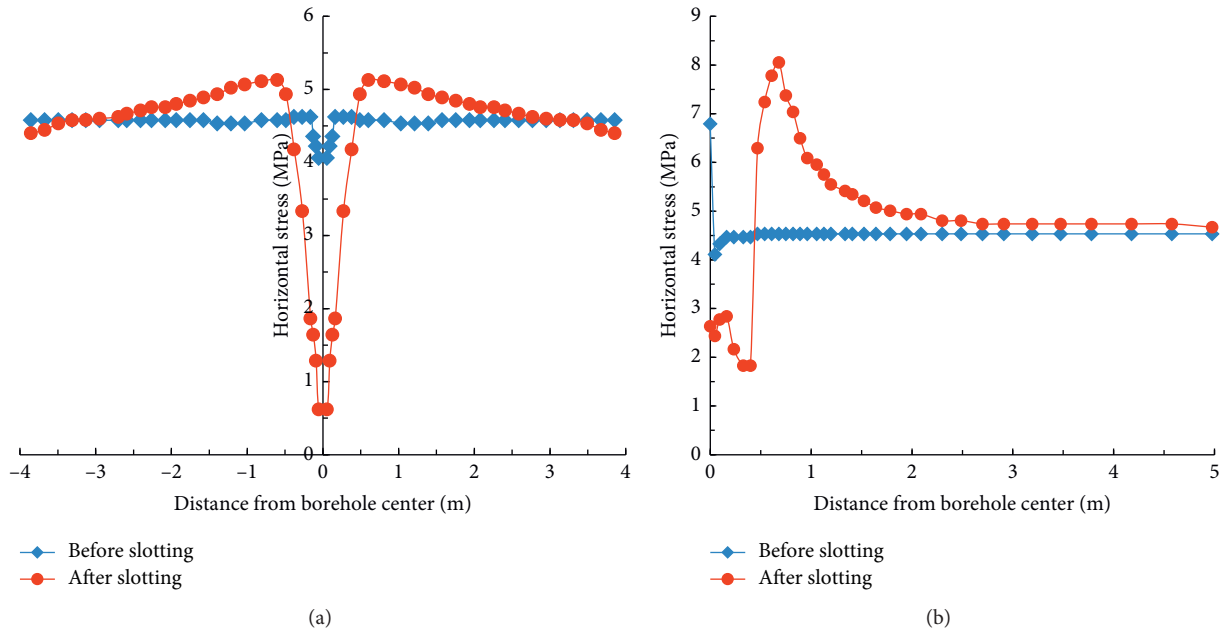


FIGURE 4: Horizontal stress distribution on (a) $X=2$ cm and (b) $Y=2$ cm measured lines before and after slotting.

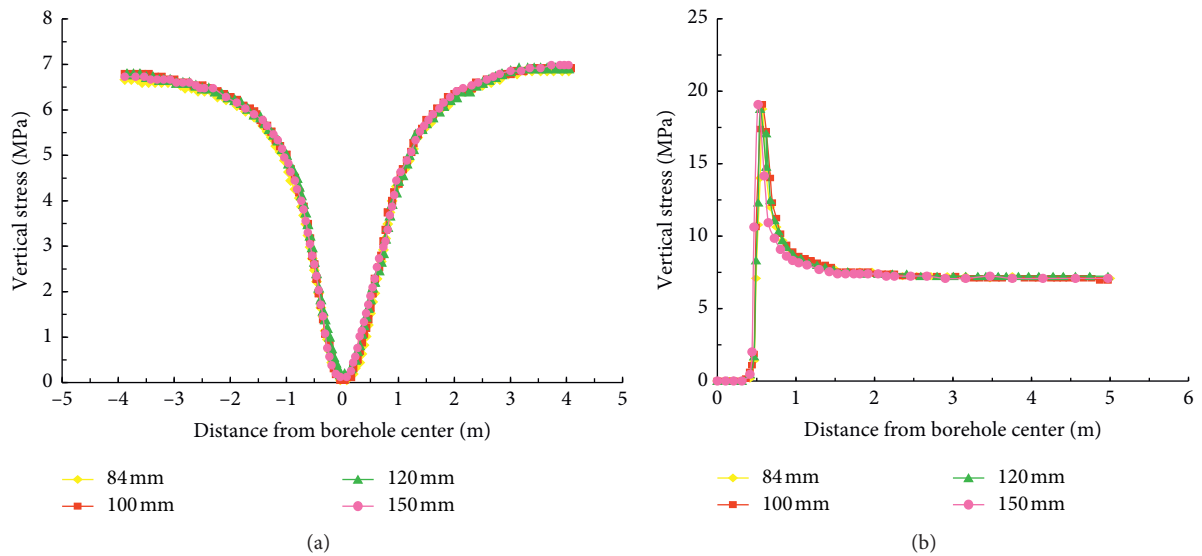


FIGURE 5: Vertical stress distribution on (a) $X=2$ cm and (b) $Y=2$ cm measured lines after slotting.

5.97 m, gas pressure of 0.4-0.94 MPa, and gas content of 8–14.57 m³/t. The mine mainly adopted gas preextraction by bedding boreholes. However, due to the high gas content and poor permeability of the coal seam, the gas extraction efficiency cannot reach the expected effect. And, there are still some dynamic phenomena occurring in the drilling process, such as spraying hole and clamping drill, which seriously restrict the safe and efficient production of the mine.

The test site is located in the 3306 working face, where the coal seam thickness is 4.35 m~6.16 m, the coal seam sturdiness coefficient is 0.4~0.5, and the destruction of the coal type is class II. The maximum original gas content of

No.3 coal seam measured in the test area is 12.24 m³/t, which indicates that the test area has a high risk of coal and gas outburst. The coal seam geological conditions of the working face improve the favorable conditions for the hydraulic slotting test [42].

16 bedding boreholes were drilled in this test. The boreholes are divided into two groups for comparison of the test results, where S_1-S_8 are slotting boreholes and D_1-D_8 are ordinary boreholes. Through the comprehensive consideration of the numerical simulation research and the actual conditions on-site, the optimized hydraulic slotting technological parameters were determined, that is, the drilling diameter was 90 mm, the drilling depth was 80 m, the

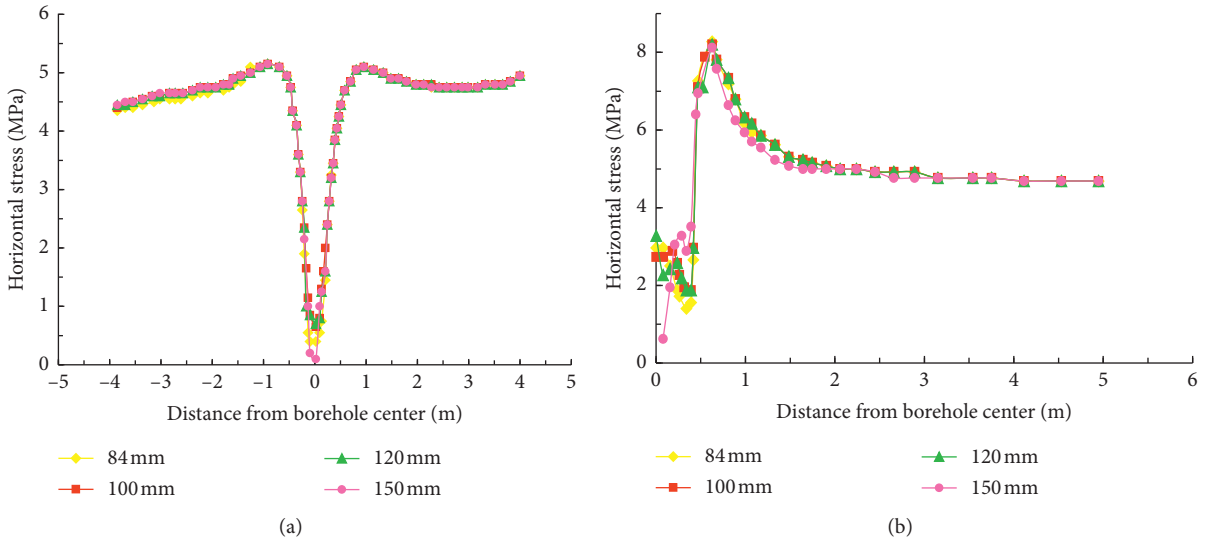


FIGURE 6: Horizontal stress distribution on (a) $X=2$ cm and (b) $Y=2$ cm measured lines after slotting.

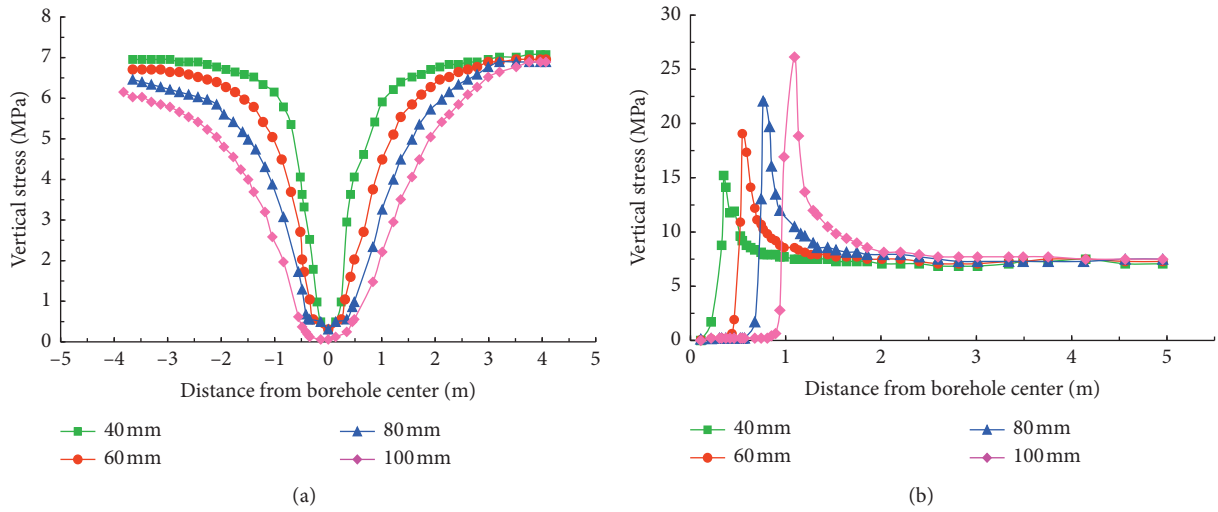


FIGURE 7: Vertical stress distribution after slotting. (a) $X=2$ cm. (b) $Y=2$ cm.

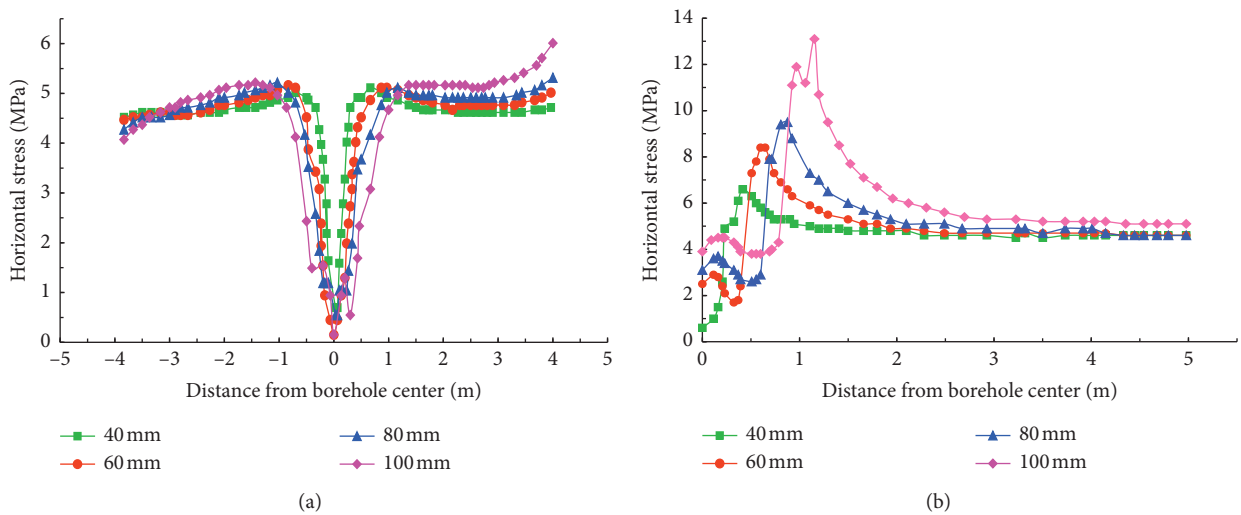


FIGURE 8: Horizontal stress distribution after slotting. (a) $X=2$ cm. (b) $Y=2$ cm.

TABLE 2: Stress relief area around slotting.

Slotting width (mm)	Stress relief area of vertical stress		Stress relief area of horizontal stress	
	Slotting up-down side (cm)	Slotting end (cm)	Slotting up-down side (cm)	Slotting end (cm)
40	2.2	0.4	0.4	0.4
60	3.2	0.6	0.6	0.6
80	3.5	0.8	0.9	0.8
100	3.8	1.0	1.2	1.0

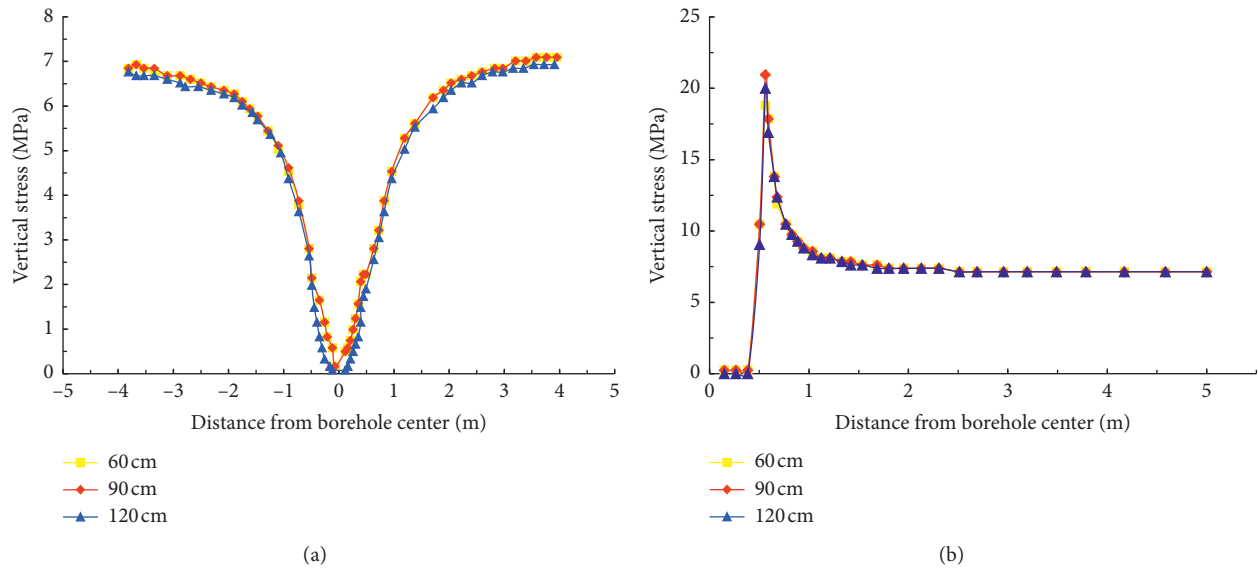


FIGURE 9: Vertical stress distribution after slotting. (a) X = 2 cm. (b) Y = 2 cm.

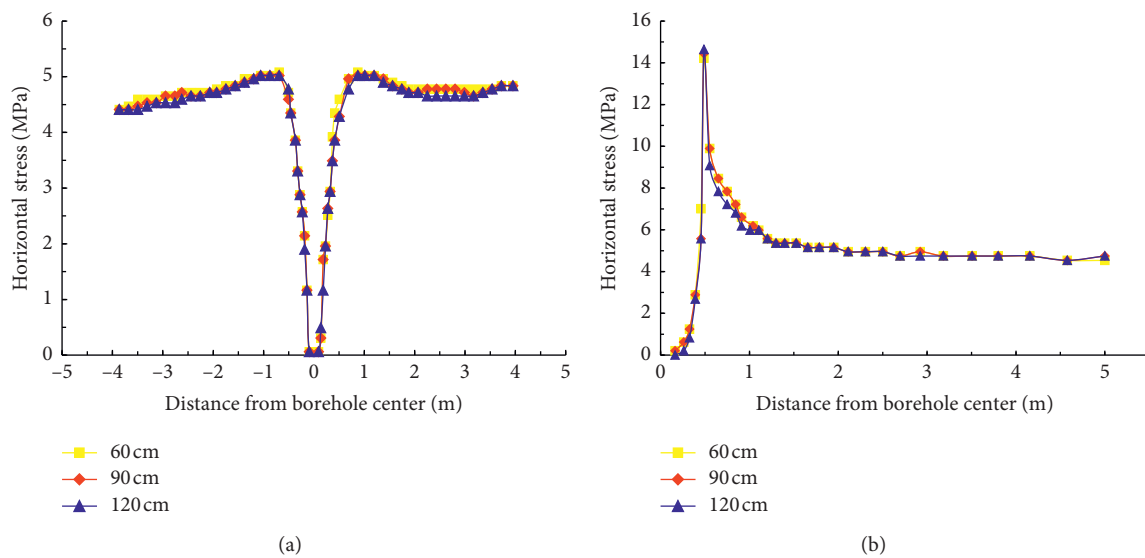


FIGURE 10: Horizontal stress distribution after slotting. (a) X = 2 cm. (b) Y = 2 cm.

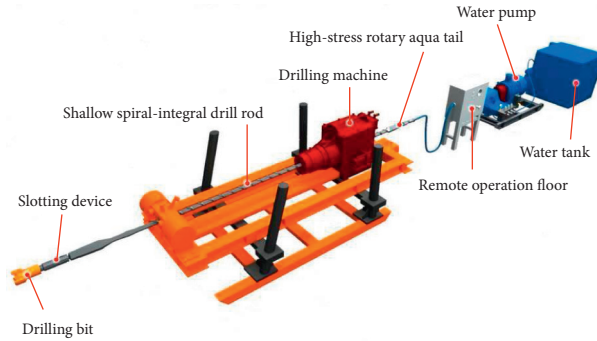


FIGURE 11: High-stress water jet slotting set device diagram.

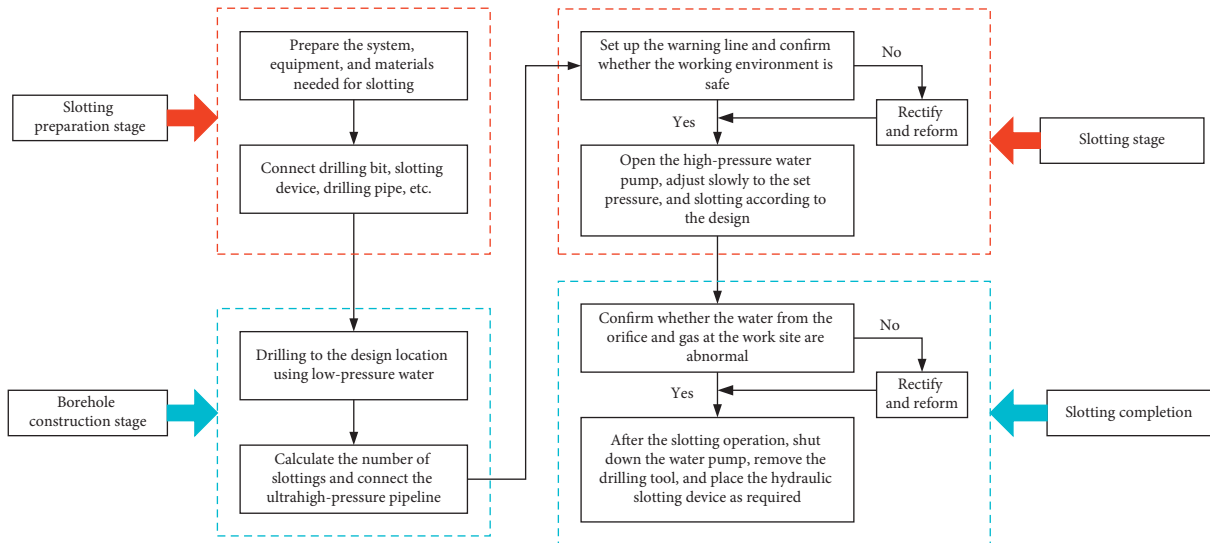


FIGURE 12: Operation process of hydraulic slotting.

drilling spacing was 12 m, the hole sealing depth was 12 m, the slotting length was 1.2 m, the slotting width was 6 cm, and the slotting spacing was 1 m [43]. The test site and boreholes' arrangement can be seen in Figure 13.

3.2. Results and Analysis

3.2.1. The Natural Gas Flow and Attenuation Coefficient in Boreholes. The better the cutting effect of hydraulic slotting, the greater the permeability of the coal seam, the greater the initial gas flow of the borehole. The natural gas flow is an important index to characterize the initial gas permeability. Therefore, before connecting the drainage pipeline with the borehole, the natural gas flow of the slotted borehole and the ordinary borehole was measured, respectively. The measurement results are shown in Figure 14.

Figure 14 shows that natural gas flow in drill holes $S_1 \sim S_8$ is $0.0203\text{--}0.0813 \text{ m}^3/(\text{min}\cdot\text{hm})$; natural gas flow in drill holes $D_1 \sim D_8$ is $0.0052\text{--}0.0363 \text{ m}^3/(\text{min}\cdot\text{hm})$. The natural gas flow in drill holes rises 3-4 times averagely after hydraulic slotting. It can be seen that the permeability of the coal seam has been significantly improved in the initial stage after the completion of hydraulic slotting. On the one hand, the

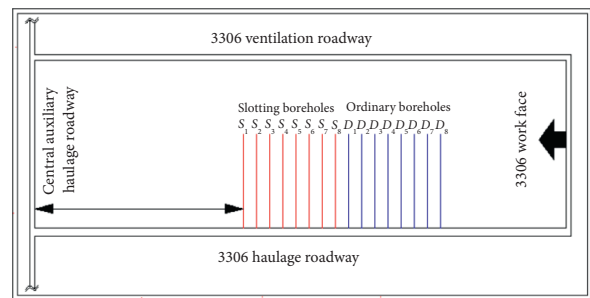


FIGURE 13: Test site and borehole arrangement.

hydraulic slotting causes the pressure relief of coal around the borehole, resulting in a large number of new fractures and secondary fractures. On the other hand, slotted stress in the coal body around the borehole is reduced, and the compression of the original coal crack opening increases. Both of them jointly promote the connection of the fracture network around the borehole and provide favorable conditions for gas migration. In addition, the slotting increases the exposed area of coal and accelerates the gas desorption speed, which is also an important reason for increasing the gas flow in the borehole.

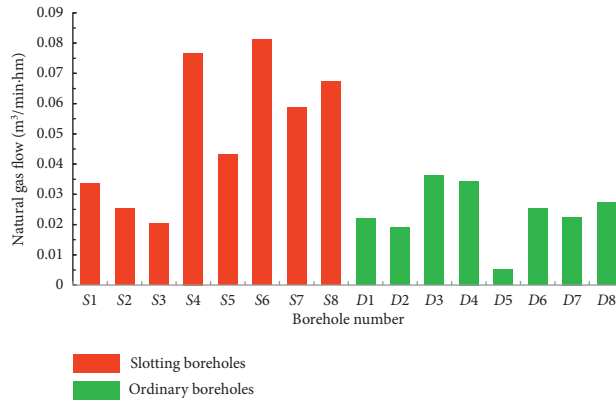
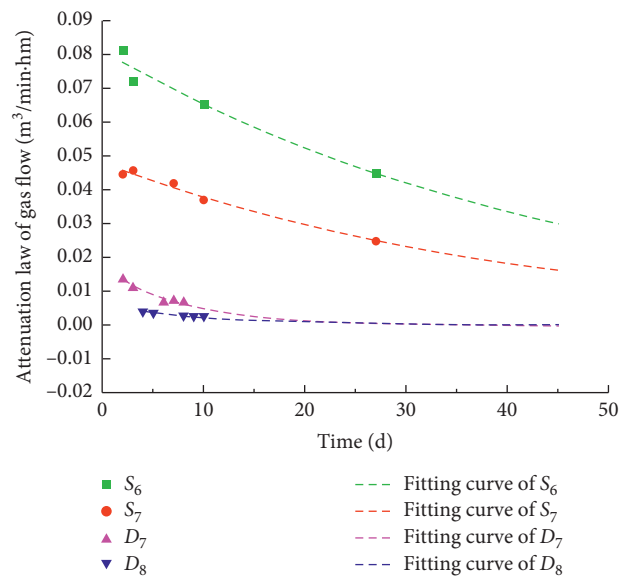


FIGURE 14: Comparison graph of the natural gas flow in slotting boreholes and ordinary boreholes.

The attenuation coefficient of the gas flow in the borehole is an important index to evaluate the difficulty of gas extraction in the coal seam. The larger the attenuation coefficient is, the harder gas exhausting and mining may be. This paper selects S_6 and S_7 and D_7 and D_8 drill holes, respectively, to measure gas emission initial velocity and obtain the attenuation coefficient of drill holes' gas flow by mathematical fitting. The results are shown in Figure 15.

From Figure 15, it can be seen that, with the extension of time, the gas emission initial velocity of each borehole shows a decreasing trend, but the extent of reduction of the slotted borehole is significantly higher than that of the ordinary drilling hole. In addition, the attenuation coefficients of the gas flow of slotting boreholes S_6 and S_7 are 0.0215 d^{-1} and 0.0237 d^{-1} , respectively. And, the attenuation coefficients of the gas flow of ordinary boreholes D_7 and D_8 are 0.0763 d^{-1} and 0.1231 d^{-1} , respectively. That is, the attenuation coefficient of the gas flow of slotting boreholes is 1/6-1/3 times smaller than that of ordinary boreholes. This is because, under the action of effective stress, the opening degree of slotted fracture gradually decreases or even closes, and the permeability of the coal seam is restrained. However, for ordinary boreholes, the number of cracks produced by coal relief around boreholes is limited, and the closure of cracks under effective stress is also small. It also shows that the effect of hydraulic slotting on coal seam permeability is more significant than that of borehole pressure relief.



Borehole number	$Y = a * \exp(b * X)$		
	a	b	R^2
S_6	0.0814	-0.0221	0.9396
S_7	0.0438	-0.024	0.9802
D_7	0.0169	-0.1259	0.9268
D_8	0.0056	-0.0817	0.981

FIGURE 15: The attenuation law of the gas flow of slotting and ordinary boreholes.

3.2.2. Improvement Effect of Gas Extraction Quantity by Hydraulic Slotting. The gas extraction purity is an important parameter to indicate the gas extraction effect. The higher the gas extraction purity is, the lower the residual gas content of the coal seam will be, which is of great significance to reduce or even eliminate the coal seam outburst risk. To analyze the improvement effect of gas extraction quantity by hydraulic slotting, the maximum and average values of daily gas extraction quantity of slotting boreholes and ordinary boreholes are counted, as shown in Figure 16. The maximum and average gas extraction quantities of slotting boreholes are $133.1 \text{ m}^3/\text{d}$ and $93.0 \text{ m}^3/\text{d}$, respectively. And, the maximum and average gas extraction quantities of ordinary boreholes are $66.7 \text{ m}^3/\text{d}$

and $40.4 \text{ m}^3/\text{d}$, respectively. Thus, the gas quantity of slotting boreholes is 2-3 times higher than that of ordinary boreholes.

3.2.3. Effective Gas Extraction Radius by Hydraulic Slotting. Before the high-pressure hydraulic slotting test, the maximum original gas content measured in the test area was $12.24 \text{ m}^3/\text{t}$. According to the requirements of China's coal industry, the gas content in the test area should be reduced to less than $8 \text{ m}^3/\text{t}$ to meet the drainage standard, which is also

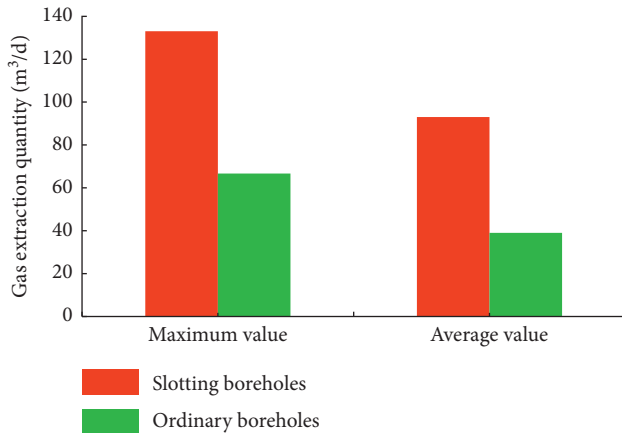


FIGURE 16: Daily gas extraction quantity of slotting boreholes and ordinary boreholes.

the criterion for determining the effective drainage radius. According to the measured data, the steps to calculate the extraction radius are as follows:

- (1) Calculate the total amount of gas extraction in the test area, and the formula is as follows:

$$Q_t = L_1 \times L_2 \times h \times \gamma \times W \times \eta, \quad (4)$$

where L_1 is the length of the extraction hole control area, m , L_2 is the width of the extraction hole control area, m , h is average thickness of the coal seam, m , γ is volume density of coal, t/m^3 , W is coal seam gas content, m^3/t , and η is the gas extraction rate, %

- (2) Calculate the number of boreholes required to reach the standard of extraction under a certain time, and the formula is as follows:

$$N = \frac{Q_t}{Q_s}, \quad (5)$$

where Q_2 is the total amount of single-hole gas extraction in a certain time, m^3

- (3) Calculate the effective radius of drilling drainage, and the formula is as follows:

$$r = \frac{L}{2NK}, \quad (6)$$

where L is the equivalent extraction length of the extraction area, m , and K is the unbalance coefficient of the borehole layout, and the value ranges from 1.0 to 1.3

According to the above calculation process, the results of the extraction radius of the slotted hole and the ordinary hole are shown in Figure 17. It can be seen that the effective gas extraction radius of ordinary boreholes after 30 days, 60 days, 90 days, and 180 days is 0.32 m, 0.6 m, 0.84 m, and 1.36 m, respectively; while, the effective gas extraction radius of slotting boreholes after 30 days, 60 days, 90 days, and 180 days is 0.8 m, 1.25 m, 1.75 m, and 1.36 m. Therefore, the effective gas extraction radius of slotting boreholes is 2-3 times larger than that of ordinary boreholes.

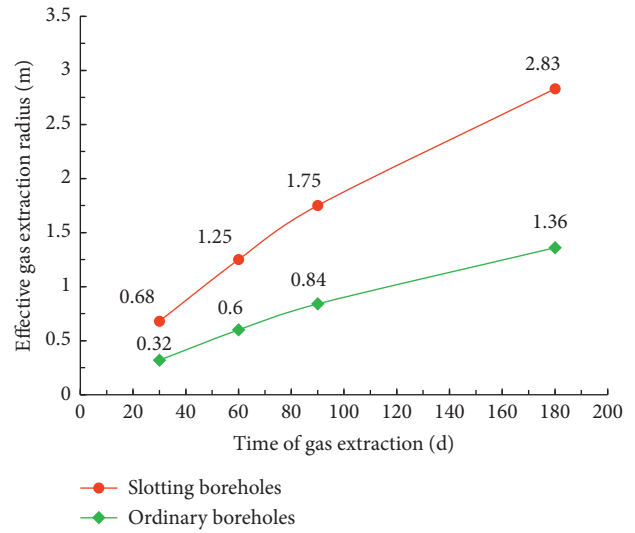


FIGURE 17: Effective gas extraction radius of slotting boreholes and ordinary boreholes.

4. Conclusion

- (1) The stress distribution around the borehole before and after slotting is analyzed. Before slotting, a small area of stress relief appeared around the boreholes, and a circle caused by stress concentration was formed. After slotting, the stress of the coal seam around the borehole is fully released, and even though the slotting width is only 6 cm, an obvious stress relief area with $6.4\text{ m} \times 1.2\text{ m}$ would be formed around boreholes.
- (2) The influence of slotting parameters on the stress relief of the coal seam was studied. The slotting width has great influence on the stress relief effect, while the borehole diameter and slotting length have little influence on the stress relief effect.
- (3) Field results showed that the gas extraction efficiency was highly enhanced by hydraulic slotting. The natural gas flow of slotting boreholes rises 3-4 times averagely. The attenuation coefficient of the gas flow of slotting boreholes is 1/6-1/3 times smaller than that of ordinary boreholes. And, the gas extraction quantity and effective gas extraction radius are improved 2-3 times by hydraulic slotting, respectively.

Data Availability

The data used to support the findings of the study are included within this article.

Conflicts of Interest

The authors declare that they have no conflicts of interest.

Acknowledgments

This work was supported by the National Key R&D Program of China (2018YFC0808305).


References

- [1] H. Xie, L. Wu, and D. Zhang, "Prediction on the energy consumption and coal demand of China in 2025," *Journal of China Coal Society*, vol. 44, no. 7, pp. 1949–1960, 2019, in Chinese.
- [2] L. Yuan, "Control of coal and gas outbursts in huainan mines in China: a review," *Journal of Rock Mechanics and Geotechnical Engineering*, vol. 8, no. 4, pp. 559–567, 2016.
- [3] L. Yuan, "Strategic thinking of simultaneous exploitation of coal and gas in deep mining," *Journal of China Coal Society*, vol. 44, no. 1, pp. 1–6, 2016, in Chinese.
- [4] H. Chen, Z. Wang, X. Chen, X. Chen, and L. Wang, "Increasing permeability of coal seams using the phase energy of liquid carbon dioxide," *Journal of CO₂ Utilization*, vol. 19, pp. 112–119, 2017.
- [5] F. Yan, J. Xu, S. Peng, Q. Zou, Q. Long, and Z. Zhao, "Effect of capacitance on physicochemical evolution characteristics of bituminous coal treated by high-voltage electric pulses," *Powder Technology*, vol. 367, pp. 47–55, 2020.
- [6] X. Gao, J. Liu, C. Zhang, and C. Zhang, "Experimental study on permeability improvement of deep hole pre-splitting cumulative blasting in low permeability coal seam," *Safe in Coal Mines*, vol. 60, no. 4, pp. 23–26, 2019, in Chinese.
- [7] Z. Ti, F. Zhang, J. Pan, X. Ma, and Z. Shang, "Permeability enhancement of deep hole pre-splitting blasting in the low permeability coal seam of the Nanting coal mine," *PLoS One*, vol. 13, no. 6, Article ID e0199835, 2018.
- [8] C. G. Huang, Y. B. Zhang, J. F. He, Y. Luo, and Z. G. Sun, "Permeability improvements of an outburst-prone coal seam by means of presplitting and blasting with multiple deep boreholes," *Energy Science & Engineering*, vol. 7, no. 5, pp. 2223–2236, 2019.
- [9] C. Shen, B. Lin, C. Sun, Q. Zhang, and Q. Li, "Analysis of the stress-permeability coupling property in water jet slotting coal and its impact on methane drainage," *Journal of Petroleum Science and Engineering*, vol. 126, pp. 231–241, 2015.
- [10] T. Lu, H. Yu, T. Zhou, J. Mao, and B. Guo, "Improvement of methane drainage in high gassy coal seam using waterjet technique," *International Journal of Coal Geology*, vol. 79, no. 1–2, pp. 40–48, 2009.
- [11] H. Chi, G. Li, H. Liao, S. Tian, and X. Song, "Effects of parameters of self-propelled multi-orifice nozzle on drilling capability of water jet drilling technology," *International Journal of Rock Mechanics and Mining Sciences*, vol. 86, pp. 23–28, 2016.
- [12] B. Lin and C. Shen, "Coal permeability-improving mechanism of multilevel slotting by water jet and application in coal mine gas extraction," *Environmental Earth Sciences*, vol. 73, no. 10, pp. 5975–5986, 2015.
- [13] F. Yan, B. Lin, C. Zhu et al., "A novel ECBM extraction technology based on the integration of hydraulic slotting and hydraulic fracturing," *Journal of Natural Gas Science and Engineering*, vol. 22, pp. 571–579, 2015.
- [14] W. Lu and B. Huang, "Mathematical model of methane driven by hydraulic fracturing in gassy coal seams," *Adsorption Science & Technology*, vol. 38, no. 3–4, pp. 127–147, 2020.
- [15] J. Jiang, W. Yang, Y. Cheng, B. Lv, K. Zhang, and K. Zhao, "Application of hydraulic flushing in coal seams to reduce hazardous outbursts in the mengjin mine, China," *Environmental and Engineering Geoscience*, vol. 24, no. 4, pp. 425–440, 2018.
- [16] W. Feng, X. Su, J. Wang, J. Qin, and X. Li, "The mechanism and field test of permeability improvement by hydraulic flushing in three-soft and single coal seam," *Coal Geology & Exploration*, vol. 43, no. 1, pp. 100–103, 2015, in Chinese.
- [17] Y. Tao, C. Zhang, J. Xu, S. Peng, and D. Feng, "Effect evaluation on stress relief and permeability improvement of hydraulic flushing physical experiment," *Journal of Chongqing University*, vol. 41, no. 10, pp. 69–77, 2018, in Chinese.
- [18] X. Wei, P. Massarotto, G. Wang, V. Rudolph, and S. D. Golding, "CO₂ sequestration in coals and enhanced coalbed methane recovery: new numerical approach," *Fuel*, vol. 89, no. 5, pp. 1110–1118, 2010.
- [19] X. Zhang and P. G. Ranjith, "Experimental investigation of effects of CO₂ injection on enhanced methane recovery in coal seam reservoirs," *Journal of CO₂ Utilization*, vol. 33, pp. 394–404, 2019.
- [20] Z. Hong, C. Wang, and Z. Xiong, "Research on CO₂ phase-transition fracturing technology for permeability improvement in high gas and low permeability coal seam," *Journal of Safety Science and Technology*, vol. 13, no. 1, pp. 39–45, 2017, in Chinese.
- [21] X. Yang, G. Wen, H. Sun et al., "Environmentally friendly techniques for high gas content thick coal seam stimulation—multi-discharge CO₂ fracturing system," *Journal of Natural Gas Science and Engineering*, vol. 61, pp. 71–82, 2019.
- [22] H. Yang, *Study on Mechanism and Characteristics Laws of Displacement Coalbed Methane by Underground Gas Injection*, Henan Polytechnic University, Jiaozuo, China, 2010.
- [23] Z. Yang, L. Dou, C. Liu, M. Xu, Z. Lei, and Y. Yao, "Application of high-pressure water jet technology and the theory of rock burst control in roadway," *International Journal of Mining Science and Technology*, vol. 26, no. 5, pp. 929–935, 2016.
- [24] X. Zhang, Y. Pan, and Z. Li, "A study of rock burst prevention by high-pressure water jet applied to cutting coal seam," *Science Technology and Engineering*, vol. 10, no. 6, pp. 1514–1516, 2010, in Chinese.
- [25] L. Yin, Y. Pan, Z. Li, and S. Wang, "Numerical simulation of rock burst prevention by high-pressure water jet applied to cutting coal seam," *Science Technology and Engineering*, vol. 10, no. 5, pp. 1225–1230, 2010, in Chinese.
- [26] K. Feng, "Research on the application of hydraulic pressure relieved and permeability enhanced technology in cross-cut rapid uncovering coal," *Mining Safety & Environmental Protection*, vol. 47, no. 4, pp. 62–65, 2020, in Chinese.
- [27] Y. Lu, Z. Ge, X. Li, J. Chen, and Y. Liu, "Investigation of a self-excited pulsed water jet for rock cross-cutting to uncover coal," *Journal of China University of Mining & Technology*, vol. 39, no. 1, pp. 55–58, 2010, in Chinese.
- [28] W. Xiong, "Numerical study and application of pressure relief and permeability enhancement technology for hydraulic cutting of tunnel uncovering coal," *China Journal of Underground Space and Engineering*, vol. 16, no. S1, pp. 291–296, 2020, in Chinese.
- [29] B. Lin, F. Yan, C. Zhu et al., "Cross-borehole hydraulic slotting technique for preventing and controlling coal and gas outbursts during coal roadway excavation," *Journal of Natural Gas Science and Engineering*, vol. 26, pp. 518–525, 2015.
- [30] M. Chen, B. Li, C. Li, and X. Pang, "Application of hydraulic slotting as an outburst prevention technology in driving face," *China Coal*, vol. 36, no. 5, pp. 96–98, 2010, in Chinese.
- [31] J. Wei, *Study on Hydraulic Gas Control Technology of Roadway Tunneling*, Chongqing University, Chongqing, China, 2017, in Chinese.
- [32] Y. Lu, C. Huang, Y. Jia, Y. You, and J. Tang, "Analysis on rock cross-cut coal uncovering using high stress water jet slotting

- in close distance seam group,” *Journal of Chongqing University*, vol. 37, no. 3, pp. 95–100, 2014, in Chinese.
- [33] Y. Zhang and Q. Zou, “A prediction model for the slot depth of high pressure water jet,” *Results in Physics*, vol. 11, pp. 1105–1109, 2018.
- [34] Y. Cheng, J. Zhao, C. Guo, X. Zhang, and W. Zhang, “Study on deep forecasting model of ultra high stress abrasive water jet drilling,” *Coal Mine Machinery*, vol. 37, pp. 66–68, 2016.
- [35] G. Si, S. Durucan, J. Shi, A. Korre, and W. Cao, “Parametric analysis of slotting operation induced failure zones to stimulate low permeability coal seams,” *Rock Mechanics and Rock Engineering*, vol. 1, no. 52, pp. 163–182, 2019.
- [36] T.-K. Lu, F.-T. Chang, Z.-F. Wang, and P.-J. Yuan, “Numerical modeling of time-dependent closure of coal seam artificial fractures,” *Journal of Coal Science and Engineering (China)*, vol. 19, no. 4, pp. 441–453, 2013.
- [37] T. Lu, Z. Wang, H. Yang, P. Yuan, Y. Han, and X. Sun, “Improvement of coal seam gas drainage by under-panel cross-strata stimulation using highly pressurized gas,” *International Journal of Rock Mechanics and Mining Sciences*, vol. 77, pp. 300–312, 2015.
- [38] Y. Xue, F. Gao, Y. Gao, X. Liang, Z. Zhang, and Y. Xing, “Thermo-hydro-mechanical coupled mathematical model for controlling the pre-mining coal seam gas extraction with slotted boreholes,” *International Journal of Mining Science and Technology*, vol. 27, no. 3, pp. 473–479, 2017.
- [39] Z. Ge, X. Mei, Y. Jia, Y. Lu, and B. Xia, “Influence radius of slotted borehole drainage by high pressure water jet,” *Journal of Mining & Safety Engineering*, vol. 31, no. 4, pp. 657–664, 2014.
- [40] Y. Xue, T. Teng, F. Dang, Z. Ma, S. Wang, and H. Xue, “Productivity analysis of fractured wells in reservoir of hydrogen and carbon based on dual-porosity medium model,” *International Journal of Hydrogen Energy*, vol. 45, pp. 20240–20249, 2020.
- [41] X. Kong, E. Wang, X. Liu et al., “Coupled analysis about multi-factors to the effective influence radius of hydraulic flushing: application of response surface methodology,” *Journal of Natural Gas Science and Engineering*, vol. 32, pp. 538–548, 2016.
- [42] W. Long, S. Sun, K. Zheng, B. Wang, and X. Hei, “Probe into geological condition adaptability in coal seam high pressure hydraulic slotting permeability enhancement,” *Coal Geology of China*, vol. 29, no. 3, pp. 37–40, 2017.
- [43] Y. Zhang, Z. Huang, and C. Li, “Investigation and application of high pressure water jet annularity slotting self pressure release mechanism,” *Journal of China Coal Society*, vol. 43, no. 11, pp. 3016–3022, 2018.

Research Article

The Healing Process of the Joints between Buffer Material Blocks and the Influence on Solute Migration

Rui Zhou ¹, Yuemiao Liu,² Tao Xu,¹ and Yufeng Gao²

¹Key Laboratory of Urban Underground Engineering of Ministry of Education, Beijing Jiaotong University, Beijing 100044, China

²Beijing Research Institute of Uranium Geology, Beijing 100029, China

Correspondence should be addressed to Rui Zhou; 18121179@bjtu.edu.cn

Received 22 January 2021; Revised 11 March 2021; Accepted 1 April 2021; Published 14 April 2021

Academic Editor: Haoyuan Hong

Copyright © 2021 Rui Zhou et al. This is an open access article distributed under the Creative Commons Attribution License, which permits unrestricted use, distribution, and reproduction in any medium, provided the original work is properly cited.

A set of thermo-hydro-mechanical coupling control equations was established, and the healing process of the joints between Gaomiaozi bentonite (GMZ01) buffer material blocks and the influence of the joint parameters were numerically simulated. The calculations consider the effect of joints on solute migration, the permeability and thermal conductivity of the buffer material, and the evolution of the healing effect. The effects of the joint design parameters, including the type, number, width, splicing form, and average dry density of the joint, are investigated. Studies show that, under an external water head, the joints will become hydraulic priority channels due to their higher permeability, which will shorten the saturation time of the blocks. As the bentonite gradually saturates, the swelling force compresses the joint material. This action improves the overall uniformity of the buffer material and reduces the priority channel effect. Meanwhile, the final average permeability and diffusion coefficient of the buffer material are found to mainly depend on the average dry density of the buffer material. The higher the average dry density of the buffer material is, the lower the final average permeability and diffusion coefficient are, whereas the distribution of joints and the block splicing are less affected by the average dry density of the buffer material. The findings of this study can provide a reference for the design of bentonite buffer material blocks in the repository.

1. Introduction

In the geological disposal of high-level radioactive waste, highly compacted bentonite blocks are often used to fill the space between waste canister and the surrounding rock because bentonite has low permeability, good thermal conductivity, high sorption capacity, and durability in a natural environment [1, 2]. Joints inevitably occur during construction between the canister and blocks, between the surrounding rock and blocks, and between blocks [3, 4]. These joints accelerate the propagation of groundwater and decrease the effectiveness of high-level nuclear waste repository. Therefore, studying the self-sealing process and permeability characteristics of bentonite blocks and joints is the key to testing the reliability of bentonite as an engineering barrier.

Researchers have carried out experimental studies to elucidate the mechanism of joint action. Imbert and Villar

[5] studied the hydraulic response of bentonite particle mixtures: during the saturation process, the microstructure of bentonite is rearranged, the swelling force reaches a steady state, and the mixture becomes homogeneous after full saturation. A study by the FEBEX project [6] in Europe shows that the presence of joints delays the action of the expansion force and produces a preferential flow hydraulic channel. Marcial et al. [7] varied the sample density and joint width in a gap sealing experiment to determine the water transmission law between metal canister and bentonite blocks. Some researchers have suggested backfilling construction joints with clay material [8, 9]: the swelling pressure of the blocks compacts the joint material, thus healing joints between bentonite blocks. Chijimatsu et al. [10] found that joints affect the mechanical properties, permeability properties, and water solute nuclide migration law of blocks. However, the experimental study on the multiphysical field evolution

law of the blocks and joints and their influence on solute migration is still limited.

The long research cycle of buffer material necessitates the use of numerical calculations for repository design. A large-scale test device named China-Mock-Up was used to investigate transfer and swelling during the THM process of buffer material in [11, 12], and the study results were analysed. In addition, the application of new methods improves the accuracy of numerical calculation. Samaniego et al. [13] presented an alternative approach to treat the coupled problems purely based on the deep energy method (DEM). In order to further quantify the influence of input parameters on the model output, Vu et al. [14] proposed a sensitivity analysis method. Morteza [15, 16] revealed that the Damköhler number in the finite fracture affects the breakthrough of the solute much more considerably compared to that in the matrix and presented an analytical expression for the shear dispersion during solute transport in a coupled system comprised of a capillary tube and a porous medium. However, few studies have been performed on how joints between blocks affect the THM coupling process and their influence on solute migration.

In the present study, the use of GMZ01 bentonite buffer material with joints and bentonite powder as a joint filling material [17] was investigated. A framework for integrated analysis of the thermal, hydraulic, solute migration, and mechanical behaviors is presented in Figure 1. First, by establishing a set of thermo-hydro-mechanical coupling control equations, the healing process of the joints between Gaomiaozi bentonite (GMZ01) buffer material blocks is simulated. Second, the influence of the joint design parameters, such as the type, number, width, splicing form, and dry density, on the properties of the bentonite buffer material was analysed. Then, the quantitative relational expressions of the influence of the joint design parameters on the working performance of buffer materials are summarized. The present study aims to reveal the healing process of the joints and the influence of the joint parameters on the buffer material, which can provide a reference for the design of the repository.

2. THM Coupled Governing Equation

The same convection control equation is used to model the blocks and joints, which are both composed of Gaomiaozi bentonite (GMZ01). However, different dry densities are used to model the blocks and joints, resulting in different calculation parameters. Two assumptions are made in this study: heat transfer induced by air flow is neglected, and the temperature of the soil particles and water are considered to reach equilibrium, such that there is only one temperature variable T . The heat transfer equation for unsaturated soil can be written as [3, 11]

$$H \frac{\partial T}{\partial t} = \nabla(\lambda_k \nabla T) - \rho_l C_l u \nabla T + q, \quad (1)$$

where ∇ is the Hamiltonian operator, H is the heat capacity per unit volume, λ_k is the heat transfer coefficient, ρ_l is the density of liquid water, C_l is the specific heat capacity of

water, u is the water flow rate vector, and q is the heat source intensity.

The thermal conductivity of bentonite, λ_k (W/(m·°C)), is approximately linear in the dry density ρ_d (g/cm³) and the saturation S_w [18, 19]:

$$\lambda_k(\rho_d, S_w) = \lambda_{k,d0} + \lambda_{k,d1} \rho_d + \lambda_{k1} S_w. \quad (2)$$

Bentonite is characterized by a high density and slow seepage and can therefore be modelled by the Richards equation for seepage [11, 20]:

$$\frac{\partial \theta_l}{\partial t} = \frac{K_l}{\rho_l g} \nabla(\nabla p - \rho_l g) - E_l + Q_v, \quad (3)$$

where θ_l is the water volume fraction, g is the gravity acceleration vector, E_l is an evaporation term, Q_v is a source term, p is the water pressure, and K_l is the permeability coefficient.

At a constant air pressure, the suction s depends on the saturation, temperature, and dry density of the soil, i.e., [21–23]

$$s = s_r(S_w) \sigma(T) \left(\frac{\rho_d}{\rho_{d0}} \right)^l. \quad (4)$$

3. Stress Path Analyses

The Barcelona basic model is used to analyse the stress paths for the blocks and joints during soil wetting. The maximum swelling force at constant volume produced by bentonite after complete saturation depends on the dry density, initial moisture content, montmorillonite content, and test methods. The result from a test carried out by Ye et al. [8] for the relationship between the swelling pressure and dry density of GMZ01 bentonite with an initial water content of 11% and an initial temperature of 20°C is given below:

$$P_{sM} = 19.4 \exp(7.4197 \rho_d) \times 10^{-6} \text{ MPa}. \quad (5)$$

The dry densities of the block and joint are 1.7 g/cm³ and 1.1 g/cm³, respectively. Using Equation (5), P_{sMj} of the joint material and P_{sMb} of the block are 0.068 MPa and 5.83 MPa, respectively.

The deformation of the block caused by the change in the suction under low confining pressures is always elastic and can be written as [18, 24]

$$d\nu_b = -\kappa_s \frac{ds}{(s + P_{v0})}, \quad (6)$$

where s is the suction, κ_s is the elastic deformation index for the suction, and P_{v0} is a fitting parameter.

Equation (7) is the fitted relationship between the free swelling ratio and the suction of a block with a dry density of 1.7 g/cm³, as measured by Niu et al. [24], from which $\kappa_s = 0.10$ and $P_{v0} = 5.0$ MPa are obtained. Increasing the external pressure reduces the amount of swelling. Denoting the average external pressure on the soil by P and replacing P_s with $P_s - P$ in equation (7) yields the stress-strain

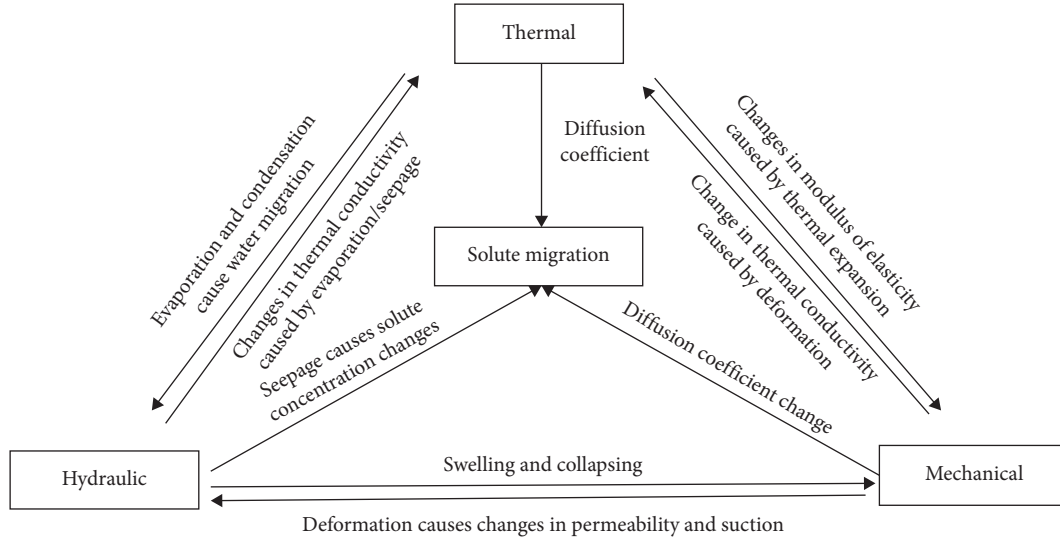


FIGURE 1: Thermal-hydraulic-mechanical coupled behaviors of the joints between the bentonite blocks.

relationship for the block during the swelling process under load as [11]

$$v_b = v_{b0} + \kappa_s \ln \left(\frac{s_{b0} + P_{v0}}{s_0 (1 - (P_s - P)/P_{sM}) + P_{v0}} \right), \quad v_b > v_{b0}, \quad (7)$$

where v_{b0} and s_{b0} are the specific volume and the suction, respectively, of the block in the initial state.

The compression index of the joint material is taken as $\lambda(0)$ in the numerical calculation, yielding the stress-strain relationship of the joint material during compression as

$$v_j = N(0) - \lambda(0) \ln \left(\frac{p'}{p_{ref}^*} \right), \quad v_j \leq v_{jpc}, \quad (8)$$

where p_{ref}^* is the reference stress, $N(0)$ is the reference specific volume, which can be measured in compression tests [25], and v_{jpc} is the specific volume corresponding to the preconsolidation pressure.

Assuming that the soil is linearly elastic for $v > v_{jpc}$,

$$v_j = v_{jpc} - \lambda(0) \frac{p' - p_{cj}}{p_{cj}}, \quad v_j \leq v_{jpc}, \quad (9)$$

where p_{cj} is the preconsolidation pressure of the joint material.

Setting $p' = 0$ in Equation (9) results in $v_j = v_{j0}$. The following result is thus obtained:

$$v_{jpc} = v_{j0} - \lambda(0). \quad (10)$$

Denoting the elastic compression index of the block as κ yields [26, 27],

$$v_b = N(0) - \kappa \ln \left(\frac{p'}{p_{ref}^*} \right), \quad v_b \leq v_{b0}. \quad (11)$$

The values of the parameters used in the diffusion and mechanical models are shown in Table 1 and the specific derivation process can be seen in Appendix A. The symbols used in the calculation are listed in Table 2.

4. Solute Migration Governing Equation

Assuming that solute migration is affected by the THM field but that solute migration does not affect the THM field corresponds to a unidirectional coupling process. The governing equation for solute migration in unsaturated soil is as follows:

$$\frac{\partial(\theta_l C)}{\partial t} = \nabla(\theta_l D_{eff} \nabla C) - u \nabla C - \frac{\partial}{\partial t}(\rho_d C_s) + q C_R - \xi_1 + \xi_2, \quad (12)$$

where θ_l is the volumetric water content of the porous medium, $\nabla(\theta_l D_{eff} \nabla C)$ is a diffusion term, $u \nabla C$ is a convection term, u is the water flow rate vector, $(\partial/\partial t)(\rho_d C_s)$ represents an adsorption term, ρ_d is the dry density, C is the solute concentration (mol/m³), C_s is the quantity of solute adsorbed on the solid framework (mol/kg), $q C_R$ is a source term, q is the source volume flow rate per unit volume, C_R is the concentration of the source solution (mol/kg), ξ_1 denotes the rate of reaction degradation or decay of the considered substance (mol/m²s), and ξ_2 is the rate at which other substances form the considered substance through reaction or decay (mol/m²s):

$$\frac{\partial C}{\partial t} = \frac{\nabla(\theta_l D_{eff} \nabla C) - u \nabla C - \rho_d (\partial C_s / \partial T) (\partial T / \partial t) + C_s (\partial \rho_d / \partial t) - \xi_1 + \xi_2}{\theta_l + \rho_d (\partial C_s / \partial C)}. \quad (13)$$

TABLE 1: Value of parameters in diffusion and mechanical models.

Parameters	Parameters of diffusion models		Parameters	Parameters of mechanical models	
	Values	Source		Values	Source
Initial water content	0.11	[8]	Compression index $\lambda(0)$	0.133	[26]
Density of water $\rho_l/(kg/m^3)$	1000	[25]	Reference stress P_{ref}^* (MPa)	1	[25]
Specific gravity of soil particles ρ_s	2.7	[25]	Reference specific volume $N(0)$	1.9	[25]
Specific heat of water $C_{pl}/(J/(kg \cdot ^\circ C))$	4200	[25]	Initial specific volume of joints v_{j0}	2.455	Calculation
Specific heat of soil particles $C_{ps}/(J/(kg \cdot ^\circ C))$	900	[25]	Initial specific volume of blocks v_{b0}	1.588	Calculation
Coefficient of permeability k_0	3.51	[1, 11]	Elastic deformation index of suction κ	0.0244	[26]
Coefficient of permeability k_1	6	[1, 11]	Elastic deformation index of suction κ_s	0.1	[26]
Reference temperature $T_0/^\circ C$	20	Assumption	Maximum swelling force of blocks $P_{sMb}/(MPa)$	5.83	[8]
Reference dry density $\rho_{d0}/(g/cm^3)$	1.7	[25]	Swelling deformation parameters $P_{s0}/(MPa)$	5	[24]
Heat transfer coefficient $\lambda_{k d0}/(W/m \cdot ^\circ C)$	-0.5	[14]	Poisson ratio between blocks and joints μ	0.3	[25]
Heat transfer coefficient $\lambda_{k d1}/(W/m \cdot ^\circ C)$	0.6	[14]	Thermal swelling coefficient $\alpha_s/^\circ C^{-1}$	$\rho_d \times 10^{-5}$	[27]
Heat transfer coefficient $\lambda_{k1}/(W/m \cdot ^\circ C)$	1.07	[14]	Temperature correction factor $E_T/(\circ C^{-1})$	1.1×10^{-3}	[28]
Parameters in VG model $a/(m^{-1})$	0.009	[9]	Parameters of cohesion $c_0/(MPa)$	-0.5	[29]
Parameters in VG model b	1.3386	[9]	Parameters of cohesion $c_d/(MPa)$	0.59	[29]
Parameters of suction l	2	[19]	Parameters of cohesion $c_T/ (MPa/^\circ C)$	0.0012	[29]
Parameters of suction σ_0	1	[19]	Parameters of internal friction angle $\varphi_0/(deg)$	40	[29]
Parameters of suction $\sigma_1/(\circ C^{-1})$	0.004	[19]	Parameters of internal friction angle $\varphi_T/ (deg/^\circ C)$	25	[29]
Indoor temperature $T_{rm}/(^\circ C)$	20	Assumption	Parameters of internal friction angle $\varphi_T/ (deg/^\circ C)$	25	[29]

TABLE 2: List of symbols.

Parameters	Definition (unit)
a	Parameters in VG model (m^{-1})
b	Parameters in VG model
C_l	The specific heat capacity ($J/(kg \cdot ^\circ C)$)
C_{ps}	The specific heats of the soil particles ($J/(kg \cdot ^\circ C)$)
C_{pl}	The specific heats of water ($J/(kg \cdot ^\circ C)$)
c	The cohesion
C	The solute concentration (mol/m^3)
C_s	The quantity of solute adsorbed on the solid framework (mol/kg)
C_R	The concentration of the source solution (mol/kg)
D_{eff}	The effective diffusion coefficient
D_m	The mechanical diffusion coefficient
D_e	The molecular diffusion coefficient
D_{e0}	The reference value of the molecular diffusion coefficient (m^2/s)
D	The diffusion coefficient
E_t	The evaporation term
g	The gravity acceleration vector
H	The heat capacity per unit volume ($J/(m^3 \cdot ^\circ C)$)
K_l	The permeability coefficient
K_{into}	The reference permeability (m^2)
k_r	The relative permeability
κ_s	The elastic deformation index for the suction
k_d	The adsorption coefficient (m^3/kg)
n	The porosity
$N(0)$	The reference specific volume
P_s	The swelling pressure (MPa)
P_{ref}^*	The reference stress (MPa)
P_{cj}	The preconsolidation pressure of the joint material (MPa)
p	The water pressure (Pa)
Q_v	The source term
q	The heat source intensity
S_w	The saturation

TABLE 2: Continued.

Parameters	Definition (unit)
s	The suction
s_{b0}	The suction of the block in the initial state
T_{rm}	The laboratory room temperature ($^{\circ}\text{C}$)
u	The water flow rate vector
∇	The Hamiltonian operator
λ_k	The heat transfer coefficient ($\text{W}/(\text{m}^{\circ}\text{C})$)
ρ_l	The density of liquid water (g/cm^3)
ρ_d	The dry density (g/cm^3)
θ_l	The water volume fraction
μ_l	The dynamic viscosity of water
$\sigma(T)$	The effect of the surface tension coefficient of water on the suction
v_{b0}	The specific volume of the block in the initial state
v_{jpc}	The specific volume corresponding to the preconsolidation pressure
φ	The internal friction angle (deg)
θ_l	The volumetric water content of the porous medium
ξ_1	The rate of reaction degradation or decay of the considered substance ($\text{mol}/\text{m}^2\text{s}$)
ξ_2	The rate at which other substances form the considered substance through reaction or decay ($\text{mol}/\text{m}^2\text{s}$)

Under ideal conditions, that is, a constant temperature, a saturated porous medium, a steady-state porosity, and no reaction or decay of the solute, $(\partial T/\partial t) = (\partial \rho_d/\partial t) = \xi_1 = \xi_2 = 0$; in addition, $(\partial C_s/\partial C) = K_f(C)$ can be defined in the adsorption model, and a retardation coefficient can be introduced as $R_d = 1 + (\rho_d/n)K_f(C)$. Equation (13) can be used to obtain the following equation for isothermal solute migration in saturated porous media [30]. The specific derivation process can be seen in Appendix A and the symbols are listed in Table 2:

$$\frac{\partial C}{\partial t} = \nabla \left(\frac{D_{\text{eff}}}{R_d} \nabla C \right) - \frac{u}{R_d n} \nabla C. \quad (14)$$

5. THM Coupling Calculations and Results

5.1. Physical Model and Boundary Conditions. Referring to the China-Mock-Up experiment [1, 8], the overall repository model is a cylinder with a radius of 450 mm, and the central section comprises a heat source with a radius of 150 mm that is surrounded by rock. The buffer material is formed by splicing blocks and joint material. The initial dry densities of the block and the joint material are $1.70 \text{ g}/\text{cm}^3$ and $1.10 \text{ g}/\text{cm}^3$, respectively. As the blocks are placed at equal intervals, a 1/6 model is used for the calculation. Symmetrical boundary conditions are used at the left and right sides and the upper and lower sides of the model. The model is 300 mm high, and the temperature of the central section is 90°C ; the initial temperature of the buffer layer and the ambient temperature are both 20°C . The initial water content of the blocks and joints are both 0.11 and the inner side is set to “no flow.” The deformation of the heat source and the surrounding rock are not considered, and the inner and outer sides of the soil are set to “roller support.” The program COMSOL is used for numerical calculation and the model mesh contains 3456 domain elements, 3480 boundary elements, and 1208 edge elements.

Figure 2 illustrates the specific size of the physical model and the points used to record data during the calculation,

where B1, B2, B3, and B4 are points in the block, J1 and J2 are points in a transverse joint, and J3 and J4 are points in a radial joint. In the numerical calculation, the block material is modelled by a nonlinear elastic stress-strain relation, in which the Poisson ratio is fixed and the swelling force is applied as an external stress; the joint material is modelled using an elastoplastic model, the Mohr–Coulomb yield criterion, and an associated flow rule. Table 1 shows the values of the material parameters obtained from the literature. Each physical field is discretized by the quadratic method. The “MUMPS” solver is applied to solve the transient problem. The backward difference formula is used for time stepping with an initial step size of 10^{-8} d.

During the calculation, the outer boundary of the material is set as the normal fixed boundary, and the risk factors such as shear failure and hydraulic fracturing are not considered. Meanwhile, the time effects such as creep and stress relaxation are not taken into consideration.

5.2. Healing Process. The strain in bentonite is directly reflected by the dry density, which determines the thermal conductivity, seepage, and strength characteristics of soil. The calculated results show that, under an external water head, both the joint and block materials gradually saturate from the outside to the inside, as evidenced by the increased rate of saturation at B2 and B4 compared to that at B1 and B3. The final saturation of the block at B1 is 0.72 without joints, which is lower than the corresponding value with joints (0.99). Water absorption by the block creates a swelling pressure that squeezes the joint. After complete saturation of the buffer material, the dry density of both the inner and outer layers of the block reaches $1.62 \text{ g}/\text{cm}^3$, the dry density of the joint material after compression reaches approximately $1.47 \text{ g}/\text{cm}^3$, and the final dry densities of blocks at B1 and B2 without joints are $1.71 \text{ g}/\text{cm}^3$ and $1.69 \text{ g}/\text{cm}^3$, respectively, which are higher than the corresponding values with joints ($1.62 \text{ g}/\text{cm}^3$ and $1.61 \text{ g}/\text{cm}^3$, respectively). The dry density of the joint material increases significantly

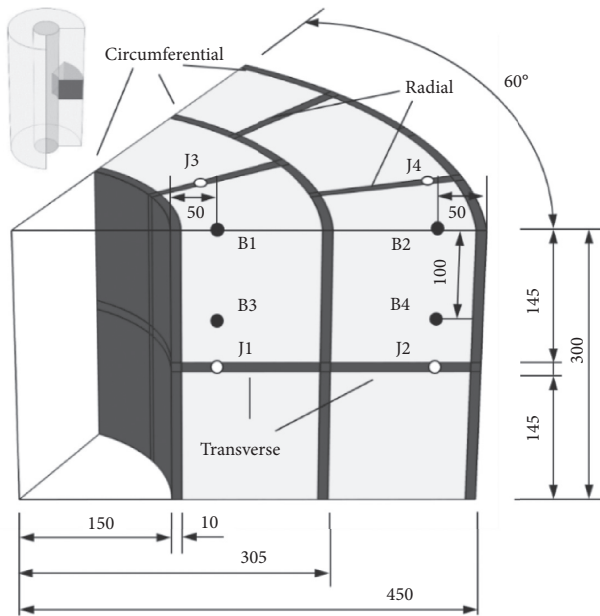


FIGURE 2: Model size (mm).

compared to that of the initial state (1.1 g/cm^3), and the overall buffer material becomes more uniform.

The analysis presented above shows that the presence of joints shortens the saturation time of blocks for the following reasons: the joint has a considerably higher permeability than the block, resulting in the formation of a hydraulic channel, and swelling increases the porosity permeability coefficient of the block. The calculation results also show that the permeability of the joint is reduced from $8.0 \times 10^{-18} \text{ m}^2$ in the initial state to approximately $5.0 \times 10^{-20} \text{ m}^2$ after saturation, and the outer joints heal before the inner joints. The permeability of the block is increased from $2.0 \times 10^{-21} \text{ m}^2$ in the initial state to approximately $6.0 \times 10^{-21} \text{ m}^2$ after saturation. The function of the buffer material is to delay the penetration of pollutants [31]. Therefore, there should be less than an order of magnitude difference in the permeability between the joint and the block for effective healing. The data analysis shows that the joint has a significant healing effect and the overall average permeability of the block is considerably reduced after the joints are healed.

The calculated results presented in Figure 3 show that although the joint has a slightly smaller thermal conductivity than the block, the joints do not significantly affect the overall temperature distribution. The heat transfer coefficients of the block and joint both increase with the saturation, and the considerable increase in the thermal conductivity of the joints meets the International Atomic Energy Agencies recommended requirement of exceeding $1 \text{ W/m}^2\text{C}$.

5.3. Effect of Joints on the Seepage Process. The analysis presented above shows that joints significantly affect the overall permeability of the buffer material, which is the key factor affecting the solute migration rate. The design parameters of the buffer material include the number and

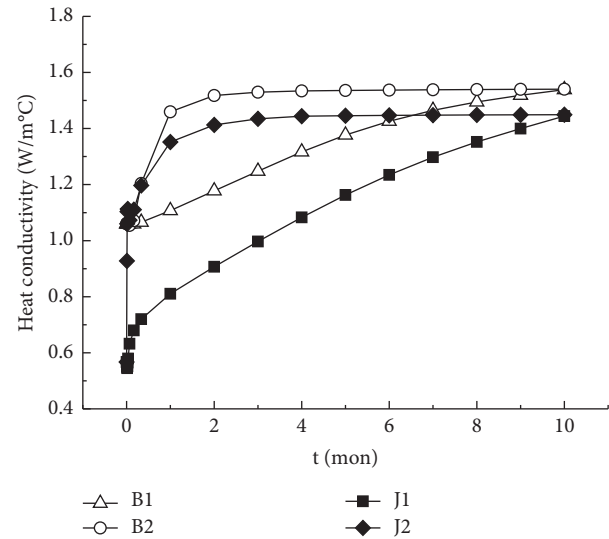


FIGURE 3: Evaluation of heat conductivity with time.

width of joints, the splicing form of the blocks, and the dry density of the materials used. An analysis of the influence of the joint design parameters on heat water migration and solute migration is useful for the design of the geological disposal schemes for high-level radioactive waste. The same initial and boundary conditions are used in this section, which were also presented in Section 5.1.

Figure 2 shows three types of joints (circumferential, radial, and transverse) in the buffer material. The effect of the joint type on seepage is assessed by building models with only one joint type and the same overall size of the buffer material: the calculation results are shown in Figure 4. In these models, the width of the circumferential (a) joint is 10 mm, the width of the circumferential (b) joint has a width of 5 mm, the radial joint angle is 2° , and the transverse joint width is 10 mm. A comparative analysis of the calculation results for different joint widths shows that the samples with wider joints require a relatively short time for the centre of the block to reach 95% saturation and have a lower dry density. The average permeability of the block at $S_w = 95\%$ is similar for the radial and transverse joints but less than that of the circumferential (a) joint. It can be concluded that the main function of the circumferential joint is to provide space for the block to swell, which reduces the dry density of the block and thus increases the permeability. The radial and transverse joints lie perpendicular to the surface of the tank. Consequently, these joints act as hydraulic channels, in addition to providing space for the block to swell. The normal joints have a larger influence on seepage than the circumferential joints.

The influence of the number of joints on the permeability was investigated: considering the widespread use of circumferential joints, only the number of radial joints is changed in the calculations, and the influence of transverse joints is neglected. The calculations are performed for 3, 6, 8, and 12 radial joints. A plan view of the buffer layer with 6 radial joints is shown in Figure 5. ρ_{aj} and ρ_{db} are the dry densities of the joints and blocks at $r = 0.2 \text{ m}$ after saturation,

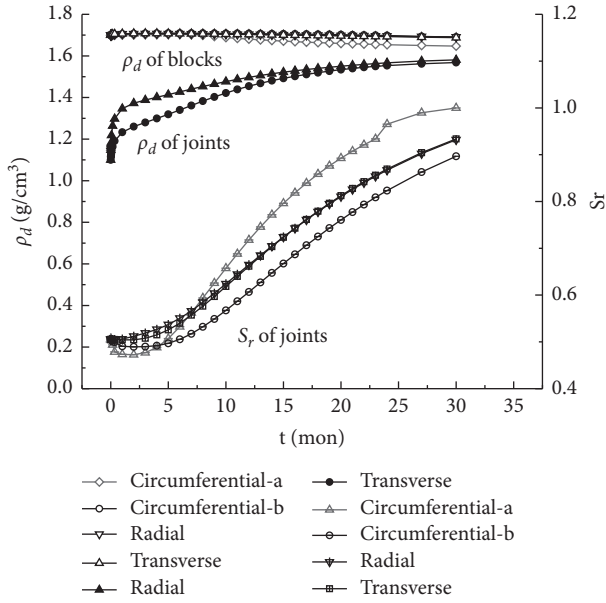


FIGURE 4: Influence of joint type on seepage.

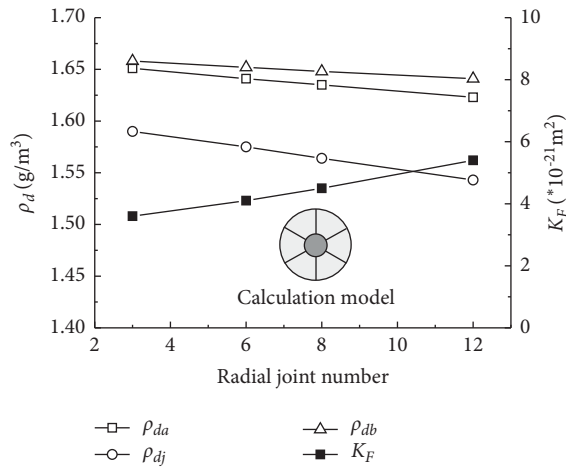


FIGURE 5: Models with different numbers of radial joints.

respectively. ρ_{da} is the average dry density of the buffer material, which is obtained as a volume-weighted average of the dry densities of the joints and blocks. K_I and K_F represent the average permeability of the section at $r=0.2\text{ m}$ in the initial state and after full saturation, respectively, where K_F reflects the overall permeability of the block. Figure 5 shows the calculated results for a radial joint angle of 2° : as the number of joints increases, the joint dry density decreases and the average permeability increases. Therefore, the number of radial joints should be minimized to ensure the barrier performance of the buffer material. Figure 6 shows the calculation model used to investigate the influence of the radial joint width on the permeability. The influence of the radial joint width is investigated by changing the radial joint angle for 6 radial joints and a constant circumferential joint width. Figure 6 shows that, as the radial joint angle increases, the final dry density of the joints decreases and the average

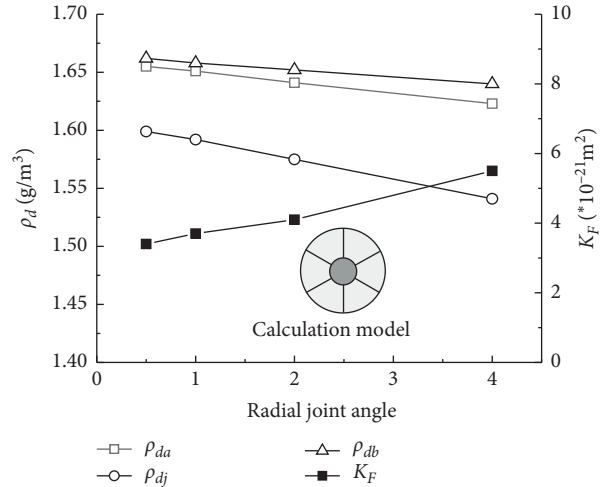


FIGURE 6: Influence of radial joint angle on seepage.

permeability increases. Therefore, the precision during construction should be carefully controlled to ensure that the joints are not overly wide.

Figure 7 shows the results obtained using a model with a constant number and width of joints while varying the dry density of the blocks and joints to simulate the effect of a buffer material with a variable dry density. As the joint has a significantly higher permeability than the block, the joint dry density has a more important effect on the initial average permeability K_I of the buffer layer than the block dry density. The higher the joint dry density is, the lower the initial average permeability is. During self-healing, the block dry density determines the average permeability K_F after full saturation, that is, the average permeability K_F decreases as the dry density increases. The expansion force increases with the block dry density, thus squeezing the joint material into a denser state and significantly reducing the overall permeability. Therefore, increasing the dry density of the block can significantly enhance the antiseepage characteristic of the buffer layer.

The data for the average dry density ρ_{da} and average permeability K_F presented in Section 5.3 are regressed to yield the following correlation:

$$\log_{10}(K_F) = -6.58\rho_{da} - 9.58. \quad (15)$$

The calculated results presented in Figure 8 show that the final average permeability is approximately exponential in the average dry density in the presence of multiple types of joints. The average permeability decreases as the average dry density increases, which is similar to the trend observed for the existing test results.

6. Effect of Joints on the Solute Migration

An important function of the buffer material is to block the migration of pollutant solutes. This study is based on the assumptions that solute migration does not affect the THM field (via a one-way coupled process) and occurs on a considerably longer time scale than heat conduction and

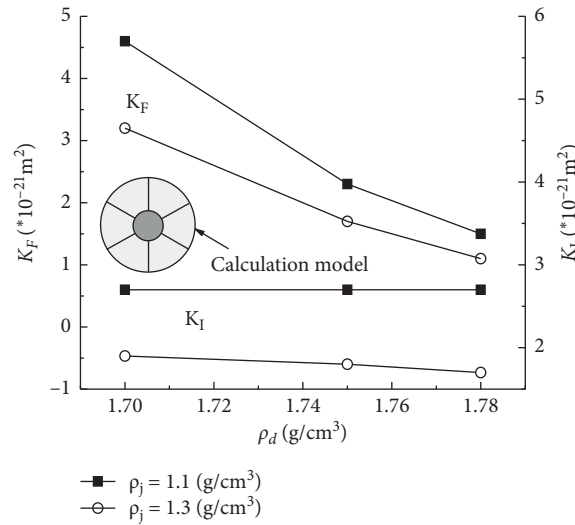


FIGURE 7: Influence of dry density of buffer material on seepage.

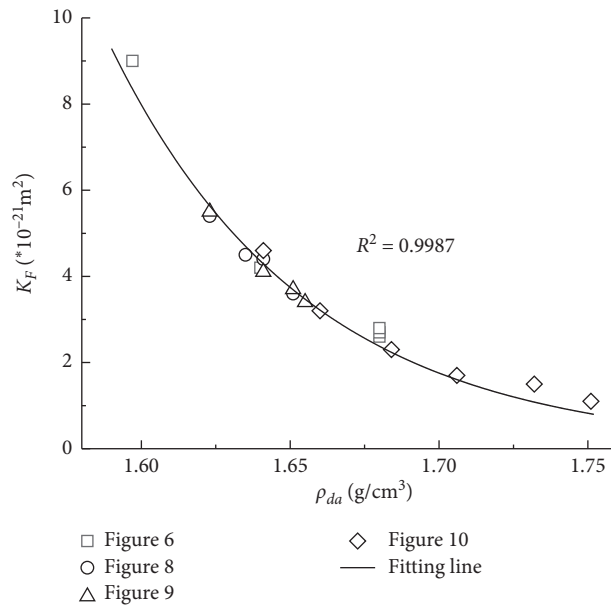


FIGURE 8: Relationship between the final permeability and average dry density of the buffer material.

seepage [32, 33]. Therefore, the calculated results for solute migration are analysed in a separate section. The governing equations used in the calculation are shown in Section 3, and the calculation parameters are shown in Table 3.

The splicing mode of the block and dry density of the material are changed, the law of solute migration after self-healing is analysed, and the relationship between the design parameters and the final average diffusion coefficient is determined.

6.1. Evolution of Solute Migration. Figure 9 shows a calculation model based on the following assumptions: when the waste container is damaged, the bentonite is completely saturated under the long-term action of groundwater and the external water head, the temperature of the waste

container and the solute concentration at the inner boundary remain constant [28], $C_0 = 1 \text{ mol/m}^3$, and the initial soil saturation is 1.

Figure 10 shows the solute concentration distribution along the radial joint at different times, where the time unit is years (denoted as a). The solute concentration diffuses from the inside to the outside, and the solute concentration at the same distance gradually increases with increasing diffusion time. These results are in line with expectations.

6.2. Influence of the Block Splicing Form on Solute Migration. Figure 11 is a plan view of the block splicing, in which the inner and outer radial joints have an average width of 10 mm. The staggered and aligned arrangement corresponds to the scheme used for the FEBEX project [8]. A transverse

TABLE 3: Parameters of migration models.

Parameters	Value	Source
Reference value of molecular diffusion coefficient $D_{c0}/(m^2/s)$	1.62×10^{-12}	[34]
Adsorption coefficient $k_d/(cm^3/g)$	55.86	[34]
Reference permeability $K_{int0}/(m^2)$	2.0×10^{-21}	[35]

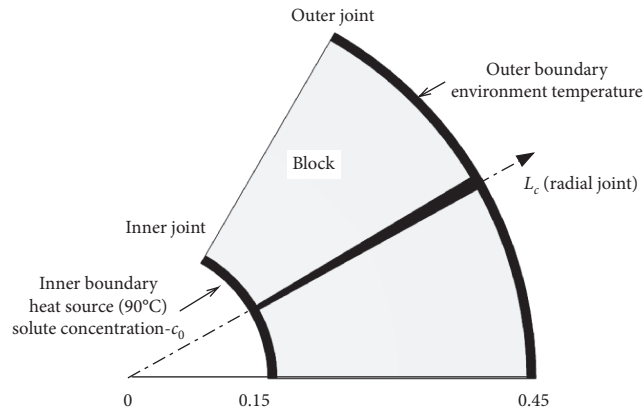


FIGURE 9: Diagram of solute migration calculation model.

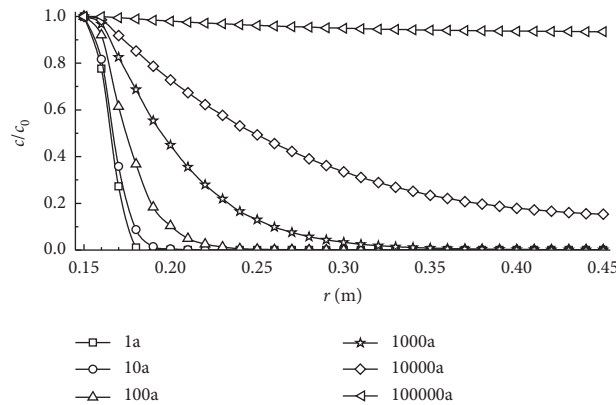


FIGURE 10: Solute distribution of the radial joint L_c line at different times.

joint has a similar effect as a radial joint and is therefore not considered in this section. The calculated results are shown in Table 4.

D_j and D_b are the diffusion coefficients of the joints and blocks at $r=0.2\text{ m}$ after deformation, where D_f is the final average diffusion coefficient for the section at $r=0.2\text{ m}$, and the diffusion coefficient D is given by Equation (A.25) in Appendix A. t_{c10} is the time for the average solute concentration in the outer seam of $R=0.45\text{ m}$ to reach $0.1c_0$, which reflects the overall barrier performance of the buffer material. An analysis of the data in Table 4 shows that the alignment of the outer and inner joints has little effect on solute migration for a fixed joint volume proportion. This result shows that, as the soil is fully saturated at the beginning of the calculation, the joints on the inner and outer sides have healed, the diffusion coefficient of the material is

relatively uniform, and the concentration distribution during solute migration is relatively uniform.

6.3. *Effect of Dry Density of Joints and Blocks on Solute Migration.* The results presented in Figure 12 show that increasing the dry density of the block or joint decreases the diffusion of the solute concentration to the outer boundary, indicating that increasing the dry density of the material can enhance the barrier performance. The data presented in Table 5 are regressed to obtain the correlation for the average dry density ρ_{da} and the final average diffusion coefficient D_f shown in Figure 13. The logarithm of the final average diffusion coefficient decreases approximately linearly with increasing average dry density. The fitting relationship is as follows:

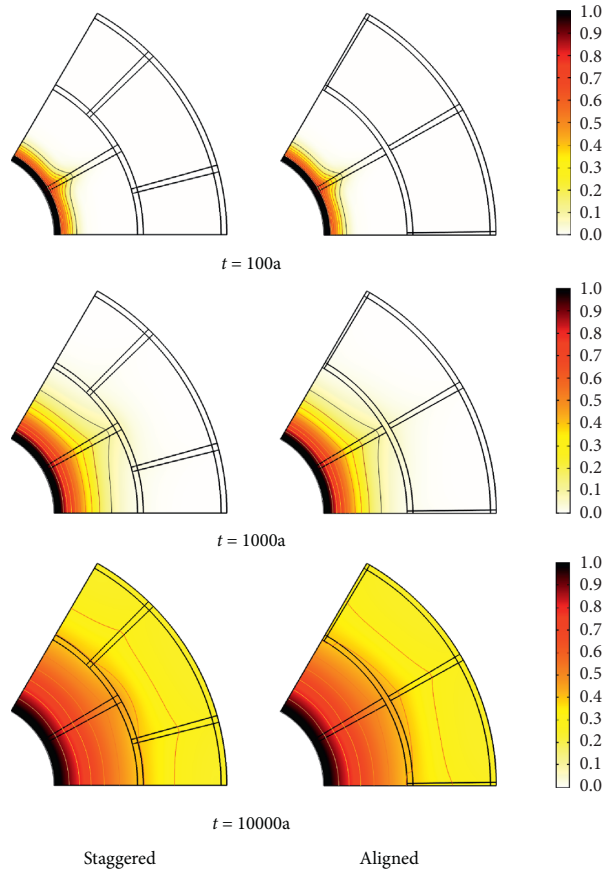


FIGURE 11: Solute distribution in blocks' splicing forms.

TABLE 4: Influence of the splicing form on solute migration.

Splicing form	ρ_{da} g/cm ³	D_j m ² /s	D_b m ² /s	D_F m ² /s	t_{c10} a
Staggered	1.614	1.83×10^{-13}	2.09×10^{-14}	2.63×10^{-14}	5500
Aligned	1.614	1.84×10^{-13}	2.09×10^{-14}	2.64×10^{-14}	5500

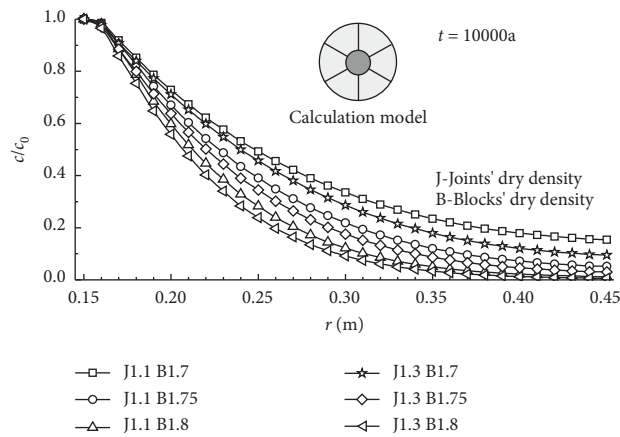


FIGURE 12: Solute distribution along the Lc line at different times.

TABLE 5: Influence of material dry density on solute migration.

Dry density g/cm ³		ρ_{da} g/cm ³	D_j m ² /s	D_b m ² /s	D_f m ² /s	t_{c10} a
Joints	Blocks					
1.1	1.70	1.641	1.2×10^{-13}	1.5×10^{-14}	1.8×10^{-14}	8800
	1.75	1.684	5.8×10^{-15}	7.4×10^{-15}	9.1×10^{-15}	16800
	1.80	1.732	2.8×10^{-14}	3.7×10^{-15}	4.5×10^{-15}	32500
1.3	1.70	1.660	9.1×10^{-14}	1.4×10^{-14}	1.1×10^{-14}	11900
	1.75	1.706	4.6×10^{-14}	5.6×10^{-15}	6.9×10^{-15}	22300
	1.80	1.751	2.2×10^{-14}	2.8×10^{-15}	3.4×10^{-15}	43300

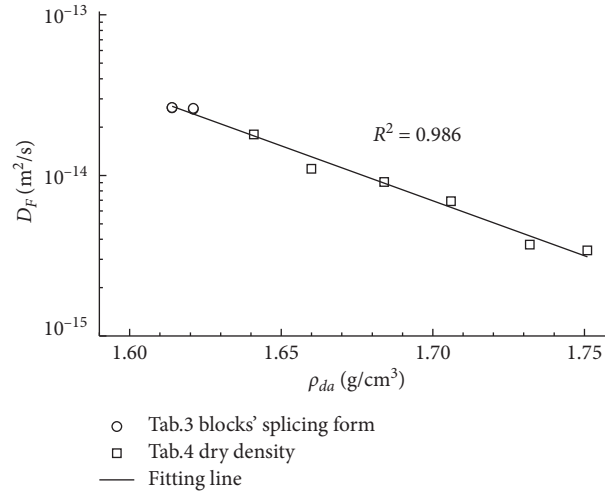


FIGURE 13: Relationship between the joint final diffusion coefficient and average dry density.

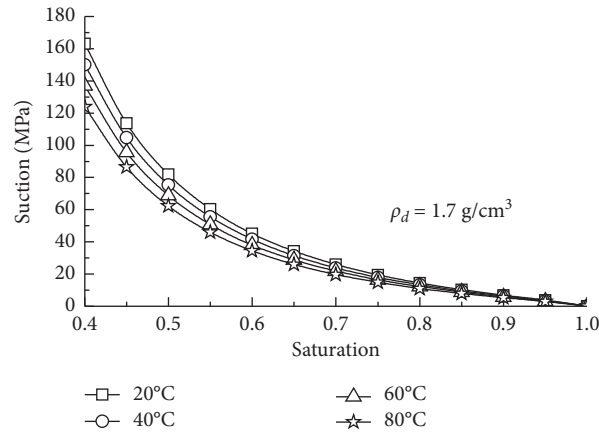


FIGURE 14: SWCC of compacted bentonite at different temperatures.

$$\log_{10}(D_F) = -6.86\rho_{da} - 2.50 \cdot R^2 = 0.986. \quad (16)$$

7. Summary and Conclusions

Through the establishment of THM coupling model, the healing process of the joints, and the influence of different joint design parameters, such as joint type, number, width, splicing form, dry density of block, and joint, on the heat

transfer, seepage and solute migration of buffer material are studied. The main conclusions drawn are as follows:

- (1) The presence of joints in the buffer material significantly increases the overall material permeability and reduces the swelling stress to some extent but has little influence on the thermal conductivity.
- (2) The high swell ability of bentonite facilitates healing by joints during the saturation process and improves the uniformity of the buffer material.

- (3) Radial and transverse joints considerably affect the permeability of the buffer material; thus, these joints should be excluded from designs to the greatest possible extent.
- (4) The dry densities of the block and joint determine the final average permeability and diffusion coefficient of the buffer material. At a fixed average dry density, the splicing pattern of the blocks has little effect on the overall permeability and solute migration.

Appendix

A. The Specific Derivation Process of the Governing Equation

1.1. THM Coupled Governing Equation. The same convection control equation is used to model the blocks and joints, which are both composed of GMZ01 bentonite. However, different dry densities are used to model the blocks and joints, resulting in different calculation parameters. Two assumptions are made in this study: heat transfer induced by air flow is neglected and the temperature of the soil particles and water are considered to reach equilibrium, such that there is only one temperature variable T . The heat transfer equation for unsaturated soil can be written as [3, 11]

$$H \frac{\partial T}{\partial t} = \nabla (\lambda_k \nabla T) - \rho_l C_l u \nabla T + q, \quad (\text{A.1})$$

where ∇ is the Hamiltonian operator, H is the heat capacity per unit volume, λ_k is the heat transfer coefficient, ρ_l is the density of liquid water, C_l is the specific heat capacity of water, u is the water flow rate vector, and q is the heat source intensity.

The thermal conductivity of bentonite, λ_k (W/(m°C)), is approximately linear in the dry density ρ_d (g/cm³) and the saturation S_w [18, 19]:

$$\lambda_k(\rho_d, S_w) = \lambda_{k,d0} + \lambda_{k,d1} \rho_d + \lambda_{k1} S_w. \quad (\text{A.2})$$

The heat capacity per unit volume H (J/(m³•C)) is given as follows:

$$H(S_w) = (1 - n) \rho_s C_{ps} + S_w n \rho_l C_{pl}, \quad (\text{A.3})$$

where n is the porosity and C_{ps} and C_{pl} represent the specific heats of the soil particles and water, respectively.

Bentonite is characterized by a high density and slow seepage and can therefore be modelled by the Richards equation for seepage [11, 20]:

$$\frac{\partial \theta_l}{\partial t} = \frac{K_l}{\rho_l g} \nabla (\nabla p - \rho_l g) - E_l + Q_v, \quad (\text{A.4})$$

where θ_l is the water volume fraction, g is the gravity acceleration vector, E_l is an evaporation term, Q_v is a source term, p is the water pressure, and K_l is the permeability coefficient [11, 36]:

$$K_l(S_w, T, \rho_d) = k_r \frac{K_{\text{int}}(\rho_d)}{\mu_l(T)} \rho_l g, \quad (\text{A.5})$$

where $k_r = S_w^4$ is the relative permeability.

The permeability K_{int} is approximately exponential in the bentonite dry density [11]:

$$\log_{10}(K_{\text{int}}) = -k_1 \rho_d - k_0 - \log_{10} \left(\frac{\rho_l g}{\mu_l(T_{rm})} \right), \quad (\text{A.6})$$

where T_{rm} is the room temperature in the laboratory and μ_l is the dynamic viscosity of water, which depends on the temperature (°C) as given below [21, 37].

$\mu_l(T) = 0.666 \times (T + 46)^{-1.55} \times 10^{-6} \text{MPa} \cdot \text{s}$ at a constant air pressure, and the suction s depends on the saturation, temperature, and dry density of the soil, i.e., [21–23]

$$s = s_r(S_w) \sigma(T) \left(\frac{\rho_d}{\rho_{d0}} \right)^l, \quad (\text{A.7})$$

where $\sigma(T)$ reflects the effect of the surface tension coefficient of water on the suction and can be expressed as

$$\sigma(T) = \sigma_0 - \sigma_1 (T - T_{rm}). \quad (\text{A.8})$$

Here, the relation between s_r and S_w can be described by the Van Genuchten model:

$$s_r(S_w) = -(-1 + S_w^{(b/1-b)})^{1/b} \left(\frac{\rho_l g}{a} \right). \quad (\text{A.9})$$

The model parameters a and b are obtained by fitting the test results of a soil-water characteristic curve for a compacted bentonite block at 20°C obtained by Bai et al. [38]. The change in the air pressure is neglected. Figure 14 shows the bentonite SWCC curve for different temperatures calculated using Equation (A.9).

1.2. Stress Path Analyses. The Barcelona basic model is used to analyse the stress paths for the blocks and joints during soil wetting. The maximum swelling force at constant volume produced by bentonite after complete saturation depends on the dry density, initial moisture content, montmorillonite content, and test methods. The result from a test by Ye et al. [8] for the relationship between the swelling pressure and dry density of GMZ01 bentonite with an initial water content of 11% and an initial temperature of 20°C is given below:

$$P_{sM} = 19.4 \exp(7.4197 \rho_d) \times 10^{-6} \text{MPa}. \quad (\text{A.10})$$

The dry densities of the block and joint are 1.7 g/cm³ and 1.1 g/cm³, respectively. Using Equation (A.10), P_{sMj} of the joint material and P_{sMb} of the block are 0.068 MPa and 5.83 MPa, respectively.

The swelling pressure P_s of bentonite increases with decreasing suction and reaches a maximum P_{sM} at a suction force of 0 [39–41]:

$$P_s = P_{sM} \left(1 - \left(\frac{s}{s_0} \right) \right). \quad (\text{A.11})$$

The deformation of the block caused by the change in the suction under low confining pressures is always elastic and can be written as [18, 24]

$$dv_b = -\kappa_s \frac{ds}{(s + P_{v0})}, \quad (\text{A.12})$$

where s is the suction, κ_s is the elastic deformation index for the suction, and P_{v0} is a fitting parameter.

Equation (A.13) is the fitted relationship between the free swelling ratio and the suction of a block with a dry density of 1.7 g/cm^3 , as measured by Niu et al. [24], from which $\kappa_s = 0.10$ and $P_{v0} = 5.0 \text{ MPa}$ are obtained. Increasing the external pressure reduces the amount of swelling. Denoting the average external pressure on the soil by P and replacing P_s with $P_s - P$ in Equation (A.13) yields the stress-strain relationship for the block during the swelling process under load as [11]

$$v_b = v_{b0} + \kappa_s \ln \left(\frac{s_{b0} + P_{v0}}{s_0 (1 - (P_s - P)/P_{sM}) + P_{v0}} \right), \quad v_b > v_{b0}, \quad (\text{A.13})$$

where v_{b0} and s_{b0} are the specific volume and the suction, respectively, of the block in the initial state.

The compression index of the joint material is taken as λ (0) in the numerical calculation, yielding the stress-strain relationship of the joint material during compression as

$$v_j = N(0) - \lambda(0) \ln \left(\frac{p'}{p_{ref}^*} \right), \quad v_j \leq v_{jpc}, \quad (\text{A.14})$$

where p_{ref}^* is the reference stress, $N(0)$ is the reference specific volume, which can be measured in compression tests [25], and v_{jpc} is the specific volume corresponding to the preconsolidation pressure.

Assuming that the soil is linearly elastic for $v > v_{jpc}$ yields

$$v_j = v_{jpc} - \lambda(0) \frac{p' - p_{cj}}{p_{cj}}, \quad v_j \leq v_{jpc}, \quad (\text{A.15})$$

where p_{cj} is the preconsolidation pressure of the joint material.

Setting $p' = 0$ in Equation (A.15) results in $v_j = v_{j0}$. The following result is thus obtained.

$v_{jpc} = v_{j0} - \lambda(0)$ denoting the elastic compression index of the block as κ yields [26, 27]:

$$v_b = N(0) - \kappa \ln \left(\frac{p'}{p_{ref}^*} \right), \quad v_b \leq v_{b0}. \quad (\text{A.16})$$

The modulus of elasticity of bentonite varies with the temperature. Zhang et al. [30] correlated the elastic modulus with the temperature. Zhang et al. [42] carried out a saturated expansion test of bentonite at different temperatures and found that the expansion rate decreases as the temperature increases: this behavior can be modelled by modifying the elastic modulus in the calculation model.

Introducing a temperature correction factor E_T into the model yields [9, 11]

$$E(T) = [1 + E_T(T - T_{rm})]E(T_{rm}). \quad (\text{A.17})$$

The Mohr–Coulomb yield criterion can be used to determine when the material yields based on the principal stress, cohesion c , and internal friction angle φ . Wood [29] reported that the cohesion c is proportional to the temperature and the dry density, whereas the internal friction angle φ mainly depends on the saturation. Thus, the following relationships can be written:

$$c = c_0 + c_d \rho_d + c_T (T - T_{rm}), \quad (\text{A.18})$$

$$\varphi = \varphi_0 - \varphi_T S_w, \quad (\text{A.19})$$

where C_0 , C_d , C_T , φ_0 , and φ_T are obtained by fitting the test results of pure GMZ01 bentonite samples with high water contents [29]. The values of the parameters used in the diffusion and mechanical models are shown in Table 1.

1.3. Solute Migration Governing Equation. Assume that solute migration is affected by the THM field, but that solute migration does not affect the THM field corresponds to a unidirectional coupling process. The governing equation for solute migration in unsaturated soil is as follows:

$$\frac{\partial(\theta_l C)}{\partial t} = \nabla(\theta_l D_{eff} \nabla C) - u \nabla C - \frac{\partial}{\partial t}(\rho_d C_s) + q C_R - \xi_1 + \xi_2, \quad (\text{A.20})$$

where θ_l is the volumetric water content of the porous medium, $\nabla(\theta_l D_{eff} \nabla C)$ is a diffusion term, $u \nabla C$ is a convection term, u is the water flow rate vector, $(\partial/\partial t)(\rho_d C_s)$ represents an adsorption term, ρ_d is the dry density, C is the solute concentration (mol/m^3), C_s is the quantity of solute adsorbed on the solid framework (mol/kg), $q C_R$ is a source term, q is the source volume flow rate per unit volume, C_R is the concentration of the source solution (mol/kg), ξ_1 denotes the rate of reaction degradation or decay of the considered substance ($\text{mol/m}^2\text{s}$), and ξ_2 is the rate at which other substances form the considered substance through reaction or decay ($\text{mol/m}^2\text{s}$).

In the absence of the injection of additional solution into the solution domain, q in the source term can be considered to be the change in the pore water volume caused by seepage, that is, $q = (\partial(\theta_l)/\partial t)$, for a sufficiently small unit, and $C_R = C$. The quantity of solute adsorbed on the solid framework [29] can be expressed as $C_s = C_s(C, T)$, considering the effect of temperature. Then, Equation (A.20) can be written as follows:

$$\frac{\partial C}{\partial t} = \frac{\nabla(\theta_l D_{eff} \nabla C) - u \nabla C - \rho_d (\partial C_s / \partial T) (\partial T / \partial t) + C_s (\partial \rho_d / \partial t) - \xi_1 + \xi_2}{\theta_l + \rho_d (\partial C_s / \partial C)}. \quad (\text{A.21})$$

Under ideal conditions, that is, a constant temperature, a saturated porous medium, a steady-state porosity, and no reaction or decay of the solute, $(\partial T/\partial t) = (\partial \rho_d/\partial t) = \xi_1 = \xi_2 = 0$; in addition, $(\partial C_s/\partial C) = K_f(C)$ can be defined in the adsorption model, and a retardation coefficient can be introduced as $R_d = 1 + (\rho_d/n)K_f(C)$. Equation (A.21) can be used to obtain the following equation for isothermal solute migration in saturated porous media [30]:

$$\frac{\partial C}{\partial t} = \nabla \left(\frac{D_{\text{eff}}}{R_d} \nabla C \right) - \frac{u}{R_d n} \nabla C. \quad (\text{A.22})$$

The effective diffusion coefficient D_{eff} is composed of a mechanical diffusion coefficient D_m and a molecular diffusion coefficient D_e . As the velocity of seepage in bentonite is low, the influence of mechanical diffusion can be neglected, that is, $D_m = 0$. Molecular diffusion occurs via the random thermal motion of molecules and is positively correlated with the thermodynamic temperature [20]; thus, the saturation of the porous medium and the permeability K_{int} [34] can be written as follows:

$$D_e = D_{e0} \frac{K_{\text{int}}}{K_{\text{int}0}} S_w \frac{T + 273.15}{T_{\text{rm}} + 273.15}, \quad (\text{A.23})$$

where D_{e0} is the reference value of the molecular diffusion coefficient and $K_{\text{int}0}$ is the reference permeability.

Sodium-based GMZ bentonite adsorbs radionuclides through ion exchange reactions and surface coordination reactions [43, 44]; the adsorption of Eu(III) in GMZ can be described by the Freundlich equation:

$$C_s = k_d C, \quad (\text{A.24})$$

where k_d is an adsorption coefficient (m^3/kg) that can be obtained by fitting experimental data [35].

The diffusion coefficient D is often normalised by R_d to produce a direct input parameter for numerical calculation [11]. The expression for D is

$$D = \frac{D_{\text{eff}}}{R_d}. \quad (\text{A.25})$$

Data Availability

The data used to support the findings of this study are available from the corresponding author upon request.

Conflicts of Interest

The authors declare that there are no conflicts of interest regard this paper.

Acknowledgments

The authors would like to thank the National Natural Science Foundation of China (52078031) for financially supporting this study.

References

- [1] L. Chen, Y. M. Liu, J. Wang et al., "Investigation of the thermal-hydro-mechanical (THM) behavior of GMZ bentonite in the China-Mock-up test," *Engineering Geology*, vol. 172, no. 8, pp. 57–68, 2014.
- [2] A. Idiart, M. Laviña, B. Cochepin, and A. Pasteau, "Hydro-chemo-mechanical modelling of long-term evolution of bentonite swelling," *Applied Clay Science*, vol. 195, Article ID 105717, 2020.
- [3] B. Bai, "Thermal consolidation of layered porous half-space to variable thermal loading," *Applied Mathematics and Mechanics*, vol. 27, no. 11, pp. 1531–1539, 2006.
- [4] B. Bai and Z. Su, "Thermal responses of saturated silty clay during repeated heating-cooling processes," *Transport in Porous Media*, vol. 93, no. 1, pp. 1–11, 2012.
- [5] C. Imbert and M. V. Villar, "Hydro-mechanical response of a bentonite pellets/powder mixture upon infiltration," *Applied Clay Science*, vol. 32, no. 3–4, pp. 197–209, 2006.
- [6] P. L. Martin and J. M. Barcala, "Large scale buffer material test: mock-up experiment at CIEMAT," *Engineering Geology*, vol. 81, no. 3, pp. 298–316, 2005.
- [7] D. Marcial, P. Delage, and Y. J. Cui, "A laboratory study of the self sealing behaviour of a compacted sand-bentonite mixture," *Geomechanics and Geoengineering*, vol. 1, no. 1, pp. 73–85, 2006.
- [8] W. M. Ye, Y. J. Cui, L. X. Qian, and B. Chen, "An experimental study of the water transfer through confined compacted GMZ bentonite," *Engineering Geology*, vol. 108, no. 3–4, pp. 169–176, 2009.
- [9] B. Chen, L. Qian, M. Ye, Y. Cui, and J. Wang, "Soil–water characteristic curves of Gaomiaozi bentonite," *Chinese Journal of Rock Mechanics and Engineering*, vol. 25, no. 4, pp. 788–793, 2006.
- [10] M. Chijimatsu, T. Fujita, A. Kobayashi, and M. Nakano, "Experiment and validation of numerical simulation of coupled thermal," *hydraulic and mechanical behaviour in the engineered buffer materials. International Journal for Numerical and Analytical Methods in Geomechanics*, vol. 24, no. 4, pp. 403–424, 2000.
- [11] B. Bai and T. Li, "Irreversible consolidation problem of a saturated porothermoelastic spherical body with a spherical cavity," *Applied Mathematical Modelling*, vol. 37, no. 4, pp. 1973–1982, 2013.
- [12] B. Bai, L. Guo, and S. Han, "Pore pressure and consolidation of saturated silty clay induced by progressively heating/cooling," *Mechanics of Materials*, vol. 75, pp. 84–94, 2014.
- [13] E. Samaniego, C. Anitescu, S. Goswami et al., "An energy approach to the solution of partial differential equations in computational mechanics via machine learning: concepts, implementation and applications," *Computer Methods in Applied Mechanics and Engineering*, vol. 362, Article ID 112790, 2020.
- [14] N. Vu, T. Lahmer, X. Zhuang, T. Nguyen, and T. Rabczuk, "A software framework for probabilistic sensitivity analysis for computationally expensive models," *Advances in Engineering Software*, vol. 100, pp. 19–31, 2016.
- [15] D. Morteza, "Advective–diffusive–reactive solute transport due to non–Newtonian fluid flows in a fracture surrounded by a tight porous medium," *International Journal of Heat and Mass Transfer*, vol. 128, pp. 1307–1321, 2019.
- [16] D. Morteza, H. Hassan, and Z. Chen, "Shear dispersion in a capillary tube with a porous wall," *Journal of Contaminant Hydrology*, vol. 185–186, pp. 87–104, 2016.

- [17] B. Bai, "Thermal response of saturated porous spherical body containing a cavity under several boundary conditions," *Journal of Thermal Stresses*, vol. 36, no. 11, pp. 1217–1232, 2013.
- [18] Y. Liu, M. Cai, and J. Wang, "Thermal properties of buffer material for high-level radioactive waste disposal," *Chinese Journal of Rock Mechanics and Engineering*, vol. 26, pp. 3891–3896, 2017.
- [19] N. Mokni, A. Molinero Guerra, Y.-J. Cui et al., "Modelling the long-term hydro-mechanical behaviour of a bentonite pellet/powder mixture with consideration of initial structural heterogeneities," *Géotechnique*, vol. 70, no. 7, pp. 563–580, 2020.
- [20] B. Bai, J. Zhang, L. Liu, and Y. Ji, "The deposition characteristics of coupled lead ions and suspended silicon powders along the migration distance in water seepage," *Transport in Porous Media*, vol. 134, no. 3, pp. 707–724, 2020.
- [21] B. Bai, G.-C. Yang, T. Li, and G.-S. Yang, "A thermodynamic constitutive model with temperature effect based on particle rearrangement for geomaterials," *Mechanics of Materials*, vol. 139, Article ID 103180, 2019.
- [22] Q. Nie, Y. Li, G. Wang, and B. Bai, "Physicochemical and microstructural properties of red muds under acidic and alkaline conditions," *Applied Sciences*, vol. 10, no. 9, p. 2993, 2020.
- [23] Y. Wang, Z. Li, H. Jing, Y. Li, and M. Wang, "Study on the seepage characteristics of deep buried tunnels under variable high-pressure water heads," *Bulletin of Engineering Geology and the Environment*, vol. 80, no. 2, pp. 1477–1487, 2021.
- [24] W. Niu, W. Ye, and B. Chen, "Experimentally derived model for suction-induced permeability, swell and microstructure behaviour of unsaturated compacted bentonite," *Rock and Soil Mechanics*, vol. 30, pp. 88–92, 2009.
- [25] Y. Liu, M. Cai, J. Wang, and Z. Wen, "Compressibility of buffer material for HLW disposal in China," *Uranium Geology*, vol. 23, no. 2, pp. 91–95, 2007.
- [26] J. Zhao, L. Chen, F. Collin, Y. Liu, and J. Wang, "Numerical modeling of coupled thermal-hydro-mechanical behavior of GMZ bentonite in the China-Mock-up test," *Engineering Geology*, vol. 214, no. 30, pp. 116–126, 2016.
- [27] B. Bai and X. Shi, "Experimental study on the consolidation of saturated silty clay subjected to cyclic thermal loading," *Geomechanics and Engineering*, vol. 12, no. 4, pp. 707–721, 2017.
- [28] P. Zhang, B. Bai, S. Jiang, P. Wang, and H. Li, "Transport and deposition of suspended particles in saturated porous media: effect of hydrodynamic forces and pore structure," *Water Supply*, vol. 16, no. 4, pp. 951–960, 2016.
- [29] E. Wood, "A mechanistic model for the thermal conductivity of planetary regolith: 1. The effects of particle shape, composition, cohesion, and compression at depth," *Icarus*, vol. 352, 2020.
- [30] Y. Zhang, Y. Lu, S. Liu, and M. Yang, "Influence of temperature and gravel content on uniaxial compressive characteristics of frozen gravel-mixed clays," *Chinese Journal of Rock Mechanics and Engineering*, vol. 38, no. 11, pp. 2357–2364, 2019.
- [31] B. Bai, "Fluctuation responses of saturated porous media subjected to cyclic thermal loading," *Computers and Geotechnics*, vol. 33, no. 8, pp. 396–403, 2006.
- [32] B. Bai, Q. Nie, Y. Zhang, X. Wang, and W. Hu, "Cotransport of heavy metals and SiO₂ particles at different temperatures by seepage," *Journal of Hydrology*, vol. 18, 2020.
- [33] G. Yang and B. Bai, "Thermo-hydro-mechanical model for unsaturated clay soils based on granular solid hydrodynamics theory," *International Journal of Geomechanics*, vol. 19, no. 10, Article ID 04019115, 2019.
- [34] L. Zhou, H. Zhang, H. Chen, and M. Yan, "Laboratory research on migration of EU(III) in compacted GMZ bentonite-sand mixtures," *Journal of Rock Mechanics and Geotechnical Engineering*, vol. 33, pp. 4163–4167, 2014.
- [35] L. Chen, J. Wang, Y. Liu, F. Collin, and J. Xie, "Numerical thermo-hydro-mechanical modeling of compacted bentonite in China-mock-up test for deep geological disposal," *Journal of Rock Mechanics and Geotechnical Engineering*, vol. 4, no. 2, pp. 183–192, 2012.
- [36] X.-X. Dong, Y.-G. Chen, W.-M. Ye, and Y.-J. Cui, "Effect of initial suction on the stiffness and strength of densely compacted Gaomiaozi bentonite," *Applied Clay Science*, vol. 194, Article ID 105696, 2020.
- [37] L. Changsoo, L. Jaewon, P. Seunghun, K. Sangki, C. Wonjin, and K. Geonyoung, "Numerical analysis of coupled thermo-hydro-mechanical behavior in single- and multi-layer repository concepts for high-level radioactive waste disposal," *Tunnelling and Underground Space Technology Incorporating Trenchless Technology Research*, vol. 103, Article ID 103452, 2020.
- [38] B. Bai, D. Rao, T. Chang, and Z. Guo, "A nonlinear attachment-detachment model with adsorption hysteresis for suspension-colloidal transport in porous media," *Journal of Hydrology*, vol. 578, Article ID 124080, 2019.
- [39] E. E. Alonso, J. Vaunat, and A. Gens, "Modelling the mechanical behaviour of expansive clays," *Engineering Geology*, vol. 54, no. 1-2, pp. 173–183, 1999.
- [40] D. Rao and B. Bai, "Study of the factors influencing diffusive tortuosity based on pore-scale SPH simulation of granular soil," *Transport in Porous Media*, vol. 132, no. 2, pp. 333–353, 2020.
- [41] E. E. Alonso, A. Gens, and A. Josa, "A constitutive model for partially saturated soils," *Géotechnique*, vol. 40, no. 3, pp. 405–430, 1990.
- [42] F. Zhang, Z. Fang, B. Qin, and S. Li, "Study on bentonite's swelling strain behaviour at different temperatures," *Journal of Logistical Engineering University*, vol. 33, no. 2, pp. 23–27, 2017.
- [43] F. Liu, Y. Yuanlv, N. Guo, R. Zhang, Y. Wu, and Z. Guo, "The adsorption of Eu(III) on Gaomiaozi Na-bentonite: experimental and modeling study," *Scientia Sinica Chimica*, vol. 43, no. 02, pp. 242–252, 2013.
- [44] Y. Wang, F. Chen, X. Li, X. Yin, and Y. Lei, "The variable-mass seepage law of broken porous rock: an experimental study," *Geomaterials, Natural Hazards and Risk*, vol. 11, no. 1, pp. 1991–2005, 2020.

Research Article

Experimental Study on the Coupled Heat-Moisture-Heavy Metal Pollutant Transfer Process in Soils

Qingke Nie ^{1,2}, Wei Wang,¹ Wenkai Guo,³ and Huawei Li^{1,2}

¹Hebei Research Institute of Construction and Geotechnical Investigation Co. Ltd., Shijiazhuang 050031, China

²Center for Geotechnical Engineering Technology of Hebei Province, Shijiazhuang 050031, China

³School of Civil Engineering, Beijing Jiaotong University, Beijing 100044, China

Correspondence should be addressed to Qingke Nie; niealex@126.com

Received 1 March 2021; Revised 14 March 2021; Accepted 22 March 2021; Published 29 March 2021

Academic Editor: Faming Huang

Copyright © 2021 Qingke Nie et al. This is an open access article distributed under the Creative Commons Attribution License, which permits unrestricted use, distribution, and reproduction in any medium, provided the original work is properly cited.

The coupled physical mechanism of heat conduction, moisture migration, and heavy metal transfer in a kaolin soil was studied by one-dimensional column tests. Two cyclic temperature tests show that, during the second cycle, the temperature close to the heat source of the soil column is lower than that during the first cycle and the temperature far away from the heat source is low, which reflects the influence of heating path. Correspondingly, the moisture content distribution during the second cycle is quite different from that during the first cycle. The higher the soil dry density is, the better the heat conduction is. The lower the dry density is, the more favorable the moisture migration is. The placement direction of the soil column and the set of temperature boundaries affect the moisture distribution of the soil column through the difference in the temperature, gravity, and solid matrix potentials. The temperature-driven liquid water movement effectively promotes the transfer of heavy metal contaminant in unsaturated soils; it is closely correlated with the convection of the heavy metal substances easily dissolved in liquid water. However, the transfer of heavy metal substances in unsaturated soil is not obvious without a thermal driving force. The test results for the different heavy metal ions indicate that the thermally induced transfer distance of the heavy metal pollutants with low adsorption properties (e.g., Cu^{2+}) to soil particles is much larger than that of the heavy metal pollutants with high adsorption properties (e.g., Cd^{2+}).

1. Introduction

Rapid industrial and agricultural production has caused the extensive occurrence of pollutants in soil layers due to contaminant transport, such as organic and inorganic matter and even heavy metal ions [1–3], causing widespread ecosystem damage in environmental engineering [4, 5]. Among these pollutants, the transfer mechanism and treatment measures of heavy metal contaminants (e.g., Cd^{2+} , Pb^{2+} , Cu^{2+} , Cr^{2+} , and Zn^{2+}) have become the focus issue of geoenvironmental research [6–8]. The interactions between soil particles and heavy metal contaminants can differ substantially [9–11], which depends on their deposition mechanism and the imposed external conditions [12], including the aspects such as the pH value and ionic concentration of solutions, van der Waals forces, double layer repulsive force, presence of colloidal particles [13, 14], and even the temperature effect [15, 16].

The transfer of contaminants has been largely investigated through experimental research, theoretical analyses, and numerical simulations [17, 18]. Its application fields include industrial pollutant treatment in groundwater exploitation and recharge, geothermal resource development, and waste disposal in metal mining [19]. Lee et al. [5] discovered that the concentrations of Cr^{2+} and Pb^{2+} in soil pores increase with increasing the colloidal concentration; as a result, the release of Cd^{2+} and Cu^{2+} lags behind that of colloidal particles. Cui et al. [20] discussed the detachment processes of previously deposited silicon powders in soils and reported that the seepage direction of water is more important than the seepage rate. Monged et al. [21] investigated the differences in the occurrence state, adsorption concentration, migration law, and migration speed of heavy metal contaminants (i.e., Cd^{2+} , Cu^{2+} , Pb^{2+} , Zn^{2+} , and Ni^{2+}) located in a geothermal resource development area and nearby strata and evaluated the safety of the polluted strata.

Overall, the present research on the retardation mechanism and transfer process of contaminants was accomplished mainly considering a hydraulic/chemical gradient [22]. However, the thermally induced transfer of heavy metal contaminants in porous media widely occurs in the protection of buildings, the treatment of metal iron ore, landfill leachate diffusion, thermal energy storage, and nuclear waste disposal. Funk and Wakili [23] proposed a thermodynamic transport model to describe the contaminant transfer induced by temperature. Miracapillo and Ferroni [24] numerically calculated the radionuclide transfer in a geological repository site and analyzed the transfer process of contaminants. Nguyen and Amiri [25] assessed the transfer process of some typical ions (e.g., cation Na^+ , anion Cl^- , and OH^-) in soils caused by heating. Tang and Cui [26] elaborated the temperature influence in the deformation of bentonite and investigated the transfer of radioactive matters.

For unsaturated soils, the matric suction and temperature effect are generally interacted, which greatly changes the thermal and hydraulic properties of soils [27, 28]. Heat conduction induces notable changes in the temperature potentials of soils and makes moisture migrate from high-temperature locations to low-temperature locations [29, 30]. Bai et al. [31] proposed a theoretical model of the soil-water characteristic curve (SWCC) taking into account the influence of water flow as well as thermal conduction using the so-called nonequilibrium thermodynamics theory. Cui et al. [32] studied the desorption process of already adsorbed particles on the surfaces of porous media matrix by laboratory experiments, which showed that both increasing the flow velocity and changing the flow direction alter the detachment rate of the deposited particles. Bai and Shi [33] considered the transition between gas and liquid phases by the temperature and established a relationship for the content of bound water in pores measured by the volume density technique.

In this study, the physical mechanism of heat transfer in unsaturated soil (i.e., kaolin soil) is investigated by column tests, along with the moisture migration and heavy metal transfer. To this end, the changes in temperature and moisture content and the steady-state distribution characteristics are studied, and the influence of the soil dry density, soil column placement direction, and temperature boundary on the heat and moisture transfer process is analyzed. In addition, experiments are also performed to elucidate the temperature influence on the transfer mechanism of heavy metal pollutants. This study has important applications for the evaluation and prediction of environmental impacts.

2. Materials and Methods

2.1. Test Apparatus. The test equipment is a hollow cylindrical chamber, which is constructed of organic glass with heat-resisting temperature (Figure 1). The size of the specimen is $L = 102$ cm in length and $D = 14.8$ cm in the inner diameter, and their ratio is 6.9. Hence, the test soil column is herein considered as a one-dimensional case. This device consists of two cylinders each with a length of 51 cm.

The two parts are fixed by bolts and sealed by rubber rings on their cross sections. The sidewall of the cylinder is covered with thick insulation materials. The heat source of the chamber is connected by a circulating water tank with a controlled constant temperature in the range of 20°C to 100°C (HH-601 Model, Shanghai city, China). The interface between the soil column end and the heat source is connected with a thin steel plate to guarantee excellent heat conduction. Small holes are made on the cylinder wall to install moisture and temperature sensors. The distances of the holes from the heat source are 2, 7, 17, 27, 42, 57, 72, and 88 cm, respectively.

The temperature is measured with small platinum resistance sensors (PT100 Mode, JY Company, Beijing, China) and a JY-DAM-TC16 collector. The measurement accuracy is 0.5°C in the test range of 0 to 100°C . The moisture content is measured with small capacitive sensors (EC-5 Mode, Decagon Company, USA) and an Em50 collector. The test results of moisture content in the experiment are very sensitive, and careful calibration should be guaranteed.

2.2. Test Materials. Kaolin clay has low permeability and good adsorption property, which has been widely used in environment pollution control in soil layers. The selected kaolin clay utilized in this study was collected from in Hebei Province of China (Lingshou County). A laser diffraction instrument (LA-950 Mode, HORIBA, Ltd., Japan) was used to measure the particle size distribution of the sample (wet method). The median particle size of the sample is $D_{50} = 15.7 \mu\text{m}$, and the particle size ranges from 1 to $90 \mu\text{m}$. The soil particle density is $\rho_s = 2.56 \text{ g/cm}^3$. The composition of the sample measured by X-ray diffraction produced by Bruker Corporation (D8 Advance Mode, Germany) mainly includes quartz (SiO_2 , 35.5%), albite ($\text{NaAlSi}_3\text{O}_8$, 47.9%), and sanidine ($\text{KNaAlSi}_3\text{O}_8$, 16.6%).

Generally, the adsorption capacity of copper ions (Cu^{2+}) to soil particles is much lower than that of cadmium ions (Cd^{2+}), which is a typical heavy metal pollutant in geo-environmental engineering [3,4,34]. For comparison, these two heavy metal ions are selected to examine the temperature-driven transfer process in this paper. Here, copper nitrate solution (i.e., $\text{Cu}(\text{NO}_3)_2$) and cadmium nitrate solution (i.e., $\text{Cd}(\text{NO}_3)_2$) were employed as heavy metal contaminants. Disodium ethylenediaminetetraacetate (EDTA-2Na) with high solubility was used as an extractant to separate the Cu^{2+} and Cd^{2+} ions adsorbed onto the soil particles [7, 11, 35].

2.3. Test Procedures. Soil samples with specified moisture content were prepared at an ambient temperature of $T = 22^\circ\text{C}$ for laboratory testing. For the convenience of operation, the test cylinder is placed vertically, and afterwards, the soil material is filled in layers. The filling is divided into 20 layers, so the thickness of each layer is about 5 cm. During the filling process, the corresponding sensors should be carefully placed in the predetermined position and compacted with soil. Then, the sensor wire is led out through the preset cylinder wall hole and connected with the data acquisition system (Figure 1).

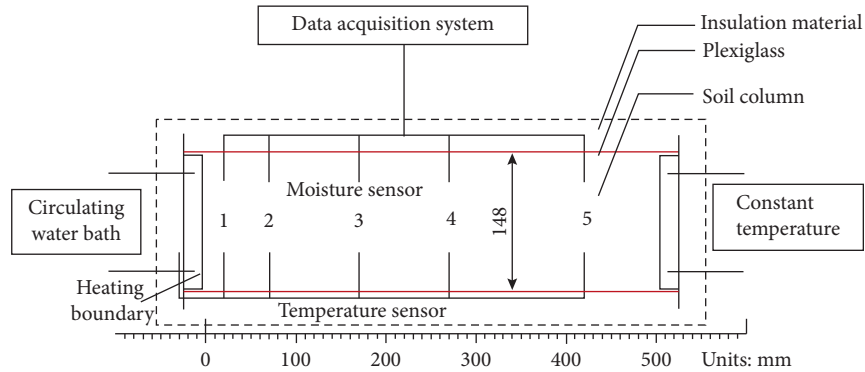


FIGURE 1: Experimental apparatus (half of the length).

During the test, the heat loss of the cylinder sidewall cannot be ignored. In order to correct the temperature boundary, the corresponding temperature at the sidewall and both ends of the cylinder are also measured.

Moisture migration tests of the soil column under cyclic temperature loading are executed, including 5 test schemes (Table 1). The initial mass moisture content of the specimen is set to 18.0%, including three different initial dry densities (i.e., $\rho_d = 1.4, 1.3,$ and 1.2 g/cm^3) and two placement directions of the soil columns (i.e., horizontal and vertical with different heating ends). Moreover, the initial volume moisture content and saturation degree are different, as summarized in Table 1, where the volume moisture content refers to the ratio of the volume occupied by moisture to the soil column volume. The temperature at the heating end is controlled at approximately 73°C during the heating stage (Figure 1) or 25°C during the cooling stage. In fact, the control of boundary temperature is very sensitive due to the heat dissipation effect. The temperature range herein is given by the actual measured value of the tests. In addition, the low-temperature end of the soil column is always maintained at 22°C .

The transfer of heavy metal ions Cu^{2+} and Cd^{2+} caused by heating is investigated. Therefore, a certain thickness of contaminated soil (i.e., pollution source, and thickness of 5 mm) should be filled near the heating end of the cylinder. The standard copper nitrate ($\text{Cu}(\text{NO}_3)_2$) or lead nitrate ($\text{Cd}(\text{NO}_3)_2$) solutions were prepared to the required concentration and then mixed with the kaolin sample of a certain quality. Then, according to the filling method and density requirements similar to the previous clean soil sample, the pollutant soil layer is filled. Finally, the concentration of pollution source (C_0) was calculated (Table 2) for the subsequent evaluation of the pollutant migration process. For convenience, the concentration of the pollution source refers to the mass of heavy metal pollutants in the water contained in unit mass soil particles.

In these tests, the soil column is placed horizontally. The location of the heating end is set to the left end except for case 9 (no thermal driving force). The temperature of the heat source can remain at 73°C . Thus, the moisture content is set to $\theta_0 = 18.0\%$ in the initial state, and the measured Cu^{2+} and Cd^{2+} concentrations in the solution are $C_0 = 1 \text{ mg/g}$.

In the above transfer tests of heavy metal ions, when the heating experiment is completed, the samples are taken at

different positions of the test soil column to determine the concentration of copper (Cu^{2+}) or lead ions (Pb^{2+}) in the contaminated soil caused by temperature. Three soil samples at the same section of the soil column are taken out for parallel measurement, and finally, their average values were adopted. For this, a small amount of soil samples (about 3 g) was dried, and 0.15 mol/L EDTA solution was added to extract the heavy metal ions adsorbed on the soil particles. The mixed solution is placed on the oscillator for vibration (HZQ-F160, Shanghai city, China) and centrifuged using a high-speed centrifuge (Sigma 3K15, Germany). Then, the supernatant is taken out for the measurement of the concentration of heavy metal substances which was determined by a graphite furnace spectrophotometer (TAS-990G Mode, Puxi Co., China) [36,37].

3. Results and Discussion

3.1. Temperature Evolution Process. As a typical cyclic heating process, case 1 (Table 1) is selected as an example to illustrate the evolution process of the temperature over time at different distances of the soil column under the action of cyclic temperature loading (two cycles). Figure 2 shows that, during the heating stage, the temperature at the measuring points close to the heat source (i.e., at $x = 2$ and 7 cm) starts to rise at first, and the temperature at the measuring points farther away (e.g., at $x = 27$ and 42 cm) also gradually increases due to the effect of heat conduction. When the temperature stabilizes, the difference in the temperature gradient between every two measuring points is obvious. During the subsequent cooling, the temperature at each measuring point decreases as the temperature near the heat source (i.e., the heating boundary; Figure 2) decreases and compared to the heating stage, the temperature gradient between the measuring points greatly decreases. During the second temperature cycle, the change process also reveals a similar law.

Figure 2 indicates that, during the first heating stage, the maximum temperature at measuring point 1 ($x = 2 \text{ cm}$) nearest to the heating end reaches 71.5°C , while that during the second heating stage is 70.3°C . After the first cooling step, the minimum temperature at this point is 26.5°C , and the lowest temperature after the second cooling is 26.0°C . It is observed that, under the action of cyclic temperature loading, the temperature of the column section away from

TABLE 1: Test schemes for cyclic temperature loading.

Case	Dry density (g/cm^3)	Volume moisture content (%)	Saturation	Placement direction	Heating end
1	1.4	25.2	0.557	Horizontal	Left
2	1.4	25.2	0.557	Vertical	Top
3	1.4	25.2	0.557	Vertical	Bottom
4	1.3	23.4	0.476	Vertical	Top
5	1.2	21.6	0.407	Horizontal	Left

TABLE 2: Test schemes for heavy metal transfer.

Case	Dry density (g/cm^3)	Volume moisture content (%)	Saturation	Heavy metal contaminant
6	1.4	25.2	0.557	Cu^{2+}
7	1.3	23.4	0.476	Cu^{2+}
8	1.2	21.6	0.407	Cu^{2+}
9	1.4	25.2	0.557	Cu^{2+}
10	1.4	25.2	0.557	Cd^{2+}

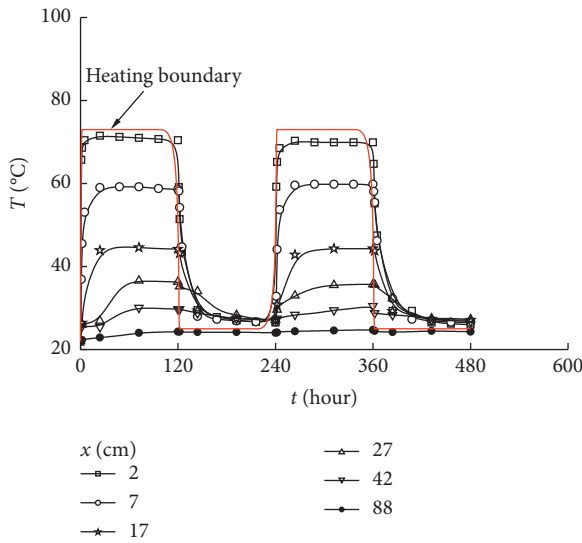


FIGURE 2: Temperature evolution processes over time for the two heating cycles.

the heat source (viz., at measuring point 8, $x = 88$ cm) is generally maintained at approximately $24.3^\circ\text{C} (\pm 1^\circ\text{C})$, which indicates that the length of the soil column used in the tests suitably maintains a constant temperature at the other end (i.e., the low-temperature end).

On the whole, the other four cases (i.e., cases 2 to 5 in Table 1) also exhibit similar laws, but their magnitudes are quite different. In addition, the stable temperature values during the two cycles are different. The main difference is that after the second temperature cycle, the temperature at the measuring points near the higher-temperature end (at $x = 2$ cm) is lower than that during the first cycle. In contrast, the temperature of the column section away from the heat source is low (at $x = 42$ cm). This phenomenon shows that the cooling process during the first cycle imposes an obvious impact on the temperature evolution of the second heating process, which reflects the influence of the heating path. Now, certain factors are examined below, such as the dry density of the soil column and its placement direction.

Figure 3 shows the distribution curves along the heat conduction distance for the different dry densities and placement directions of the soil column during the first temperature cycle when the heating process has stabilized (i.e., at $t = 120$ h). Figure 3(a) indicates that, for the same placement direction (e.g., cases 1 and 5 with the horizontal direction; cases 2 and 4 with the vertical direction and top heating; Table 1), the greater the dry density is, the larger the steady-state temperature at the same location of the soil column is. For example, the dry density in case 1 is set to $\rho_d = 1.4 \text{ g}/\text{cm}^3$ and that in case 5 is set to $\rho_d = 1.2 \text{ g}/\text{cm}^3$. At this time, the difference in the temperature distribution between these two cases can thus be clearly observed. However, the difference in temperature decreases for cases 2 and 4 because the difference in dry density between these two cases is slightly smaller (i.e., $\rho_d = 1.4$ and $1.3 \text{ g}/\text{cm}^3$ for cases 2 and 4, resp.). In fact, the dry density reflects the soil compactness. Therefore, the higher the soil dry density is, the larger the contact area between the soil particles is, and the thermal conductivity of soil with three-phase properties is closer to that of continuous solid particles [29, 31]; hence, the thermal conductivity increases with increasing dry density.

In fact, with increasing dry density, the soil column temperature rises faster (see Figure 3(a)). In addition, with increasing dry density, the specific heat capacity of soil increases with increasing moisture content [29, 33, 38]. This is closely related to the saturation degree of soils and also to the phase transition process between bound water and free water. As a result, more thermal energy is absorbed and subsequently released when the temperature stabilizes, which delays temperature stabilization. In other words, the heat conduction property and heat capacity are mutually restrained during the process of soil temperature stabilization [39]. For the different dry densities, it is generally considered that the heat conductivity is the fundamental factor influencing the temperature, while the impact of the specific heat capacity is relatively slight.

Figure 3(b) shows the influence of the placement direction of the soil column in the steady state, which indicates that the stable temperature value of the vertical soil column (cases 2 and 3) during heating is lower than that of the

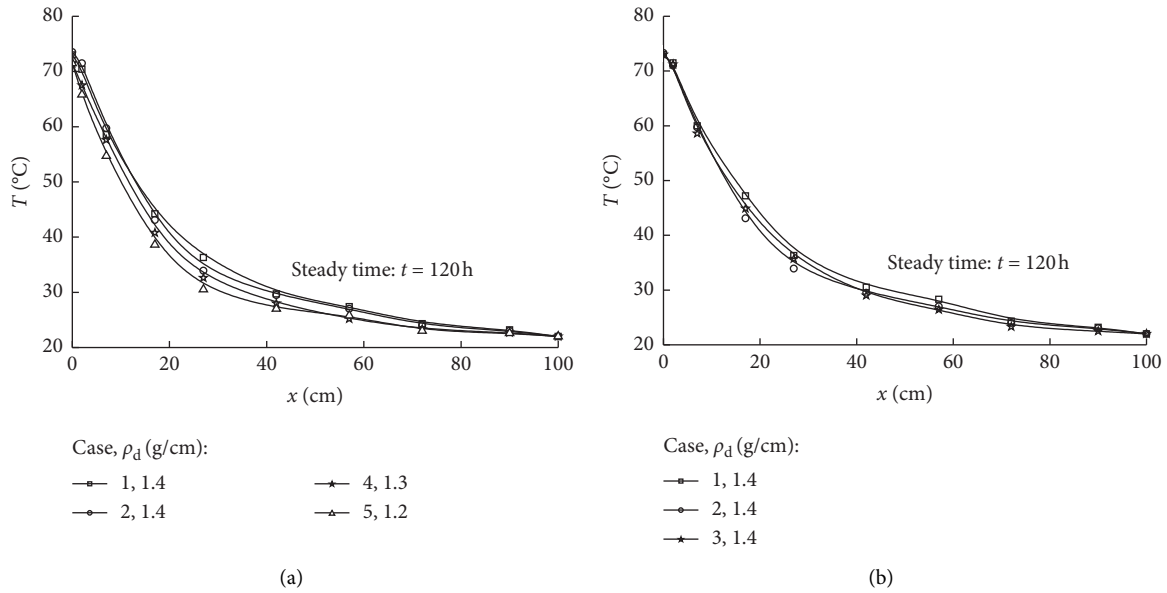


FIGURE 3: Steady-state temperature distribution along the distance: (a) effect of the dry density and (b) effect of the placement direction.

horizontally placed column (case 1). This is attributed to the effect of gravity, namely, for the vertical soil column with the heating end at the top, the amount of high-temperature vapor migrating to the low-temperature end is very small, while for the vertical soil column with the heating end at the bottom (case 3), the directions of the temperature and gravity potentials are opposite, and the amount of liquid water near the heat source is also small. When the soil column is horizontal (case 1), the influence of the gravity potential on moisture migration (including liquid and gaseous water) is weaker than that when the soil column is vertical. Moreover, the driving effect of the temperature potential leads to more moisture transferring heat from the heating end to the low-temperature end. Generally, compared to heat conduction, the influence of heat convection on the temperature distribution of unsaturated soils is limited [31].

3.2. Moisture Evolution Process. Under the action of the temperature gradient at both ends of the soil column, heat transfer will cause temperature redistribution in the unsaturated soil and then cause moisture migration in the soil pores. Figure 4 shows the evolution processes of moisture migration caused by the temperature over time under three different soil column placement direction conditions (cases 1 to 3). Figure 4 indicates that the moisture content at the measuring points close to the heat source (viz., at $x = 2$ and 7 cm) gradually decreases as the heating time increases. In the meantime, the moisture content away from the heat source (viz., at $x = 57$ and 72 cm) increases, resulting in an obvious reverse moisture content gradient. In contrast, when the temperature drops (i.e., during the cooling process), the moisture content at the points close to the cooling end (viz., at $x = 2$ and 7 cm) gradually increases. Nevertheless, at the points away from the cooling end (viz., at $x = 57$ and 72 cm),

it gradually decreases. During the second temperature cycle, the moisture evolution also presents a similar phenomenon. For example, in case 1 (Figure 4(a)), the point at $x = 2$ cm is the closest to the heating end. During the first temperature cycle, the moisture reduction caused by the temperature reaches $\Delta\theta = -4.9\%$ in the steady state, and during the second temperature cycle, the moisture reduction is $\Delta\theta = -2.0\%$. During the cooling stage, the moisture content at this point increases by 1.3% in the first temperature cycle and 0.5% in the second temperature cycle. In addition, the point at $x = 88$ cm is close to the low-constant-temperature end, and its moisture increase is $\Delta\theta = 2.4\%$ during the first cycle and 1.4% during the second cycle. The moisture change is $\Delta\theta = 1.2\%$ in the process of cooling stage in the first cycle and it is $\Delta\theta = -1.0\%$ in the process of cooling in the second cycle.

Due to the difference in the dry density, the placement direction of the soil column, and the location of the heating boundary (top or bottom), the moisture distribution inside the soil column is also distinct (Figure 5), and the moisture distribution caused by the two temperature cycles also varies. Comparing the two cases (cases 1 and 5, or cases 2 and 4; Figure 5(b)) with the same placement direction of the soil column, it is found that when the dry density decreases, the change range of the moisture content increases along the soil column. This occurs because when the dry density is low, the soil porosity correspondingly increases, the soil is loose, and the connectivity between the particle pores is good.

However, the lower the soil dry density is, the lower the saturation degree is (please refer to Table 1). There are more open migration channels and larger storage spaces in the process of moisture migration, which eventually leads to a larger change in the moisture content.

Figure 5(a) also demonstrates that, in the case of the horizontal displacement direction (cases 1 and 5), the variation of moisture content in the soil column is generally

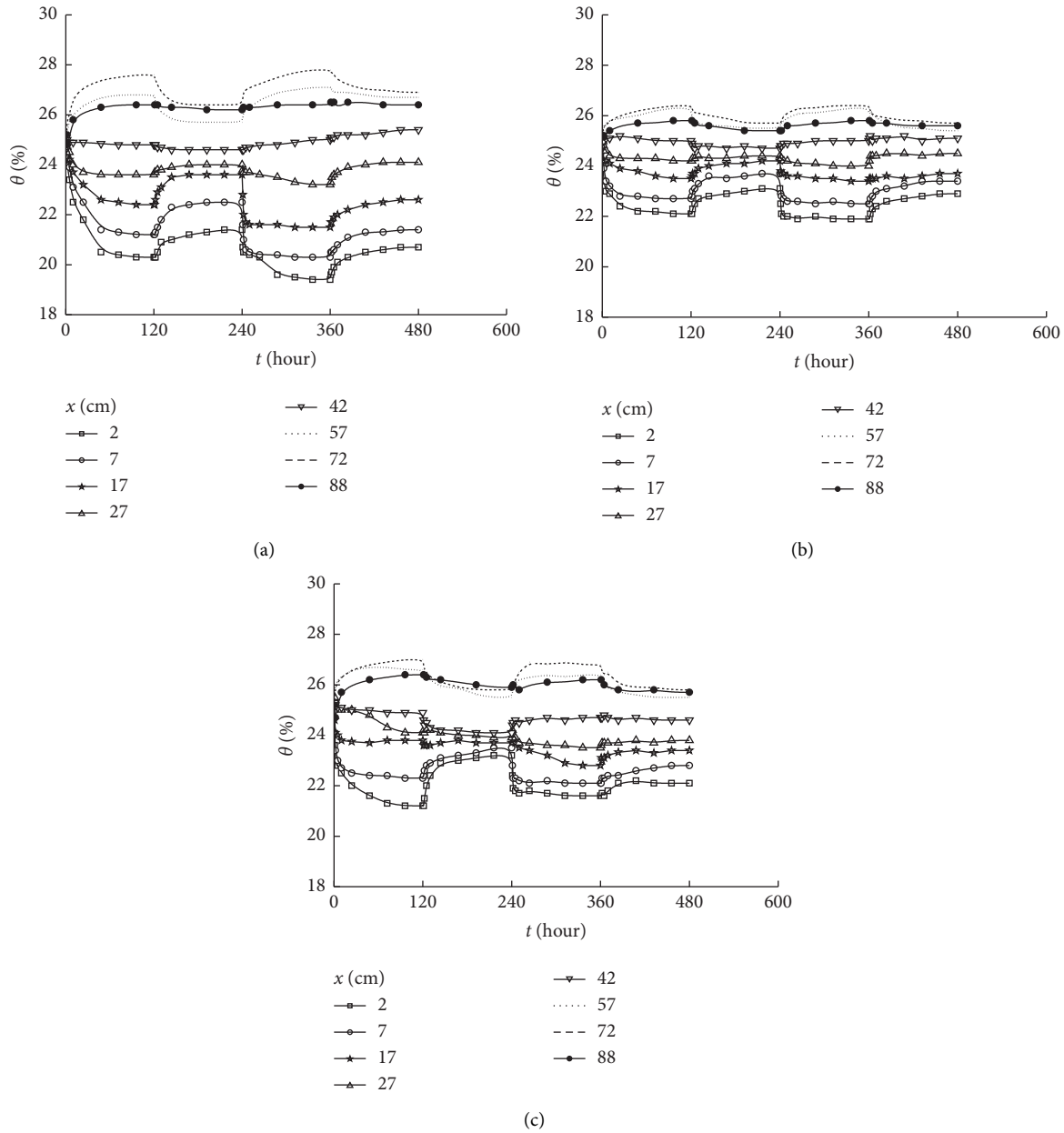


FIGURE 4: Moisture evolution processes over time for the two heating cycles: (a) horizontal placement, (b) vertical placement and top heating, and (c) vertical placement and bottom heating.

greater than that of the soil column placed vertically (cases 2 and 4; also see Figures 4(b) and 4(c)), and in addition, the effect of the gravity potential can be ignored (Figure 5(a)). When the soil column is vertical (cases 2 and 3 in Figure 5(b)), the soil moisture travels in the state of gaseous water and liquid free water under the action of the temperature potential. However, when the upper boundary temperature is higher than the lower boundary temperature (case 2), the directions of the temperature and gravity potentials are consistent, but due to the low density of gaseous water, in the soil near the heating end, less gaseous water and more liquid water move downward. However, when the temperature of the lower boundary is higher than that of the upper boundary (case 3), the direction of the temperature

potential is the opposite to that of the gravity potential. As a result, less liquid water migrates due to gravity, but gaseous water notably migrates due to the thermal diffusion effect. Finally, the moisture content change in the soil column under vertical heating (cases 2 and 3; Figure 5(b)) is greater than that in the soil column under horizontal heating (case 1).

At the completeness of the heating stage, the gradient of the temperature inside the soil column greatly decreases due to the latter cooling process (Figure 6), and the effect of the solid matrix potential becomes prominent. When the soil column is placed horizontally, the influence of the gravity potential can be ignored. When the soil column is placed vertically and the top boundary temperature is higher than the lower boundary temperature,

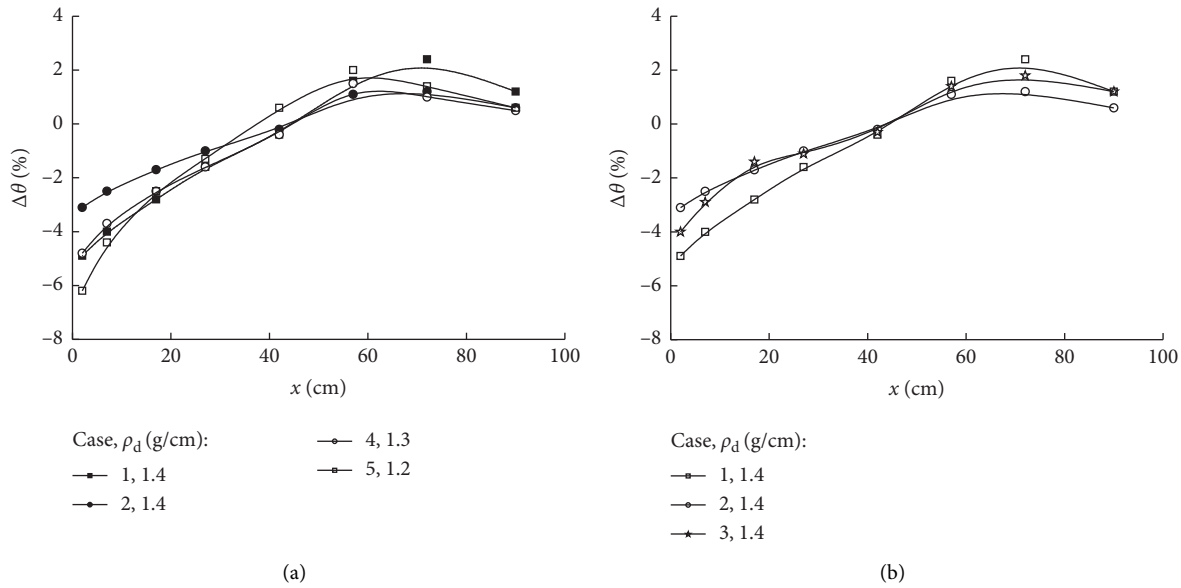


FIGURE 5: The moisture content variations caused by heating in the different cases ($t = 120$ h): (a) effect of the dry density and (b) effect of the placement direction.

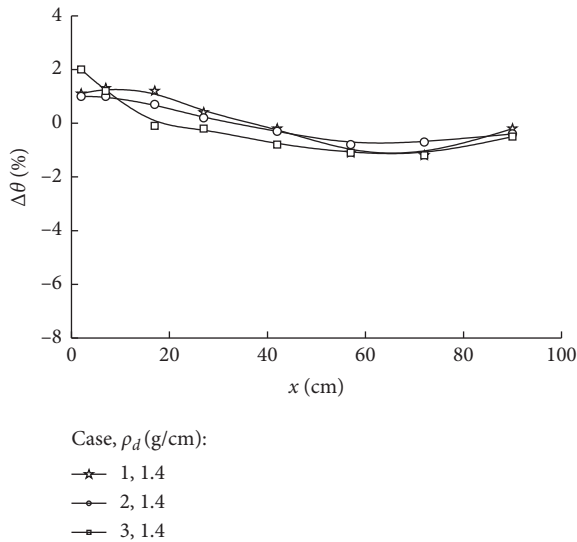


FIGURE 6: The moisture content variations caused by cooling in the different cases ($t = 120$ h).

the moisture content gradient direction is upward (i.e., the matrix potential direction is upward), and the direction of the matrix potential is the opposite to that of the gravity potential. Moreover, less liquid water migrates. When the temperature at the lower boundary of the soil column is higher than the temperature at the upper boundary, the direction of the matrix potential caused by the moisture content gradient is consistent with that of the gravity potential, and the liquid water migration caused by gravity increases. In addition, a comparison of Figures 2 and 4(a) indicates that the change in moisture and the time required to reach stability lag behind the temperature.

3.3. Heavy Metal Pollutant Evolution Process. Figure 7 shows the concentration distributions of the two heavy metal ions (Cu^{2+} and Cd^{2+}) in the soil column after 240 h of temperature-driven action by monotonous heating on the left end of the soil column. These experiments consider different initial moisture contents, dry densities, and heavy metal ions (Table 2). The experimental results reveal that, without temperature-driven action (case 9; Figure 7(a)), the migration amount of Cu^{2+} is very small due to the possible molecular diffusion of heavy metal ions. The presence of a temperature gradient effectively promotes the transfer of heavy metal ions in the kaolin soil column (Figure 7(a), cases 6 to 8), which can be attributed to the significant convection of liquid free water in soil pores caused by the temperature variation and, of course, mechanical dispersion. Moreover, the maximum migration distance of the Cu^{2+} ions reaches 20 cm, which indicates that the migration distance of Cu^{2+} increases due to the temperature-driven action. In fact, as the moisture in the soil column moves from high- to low-temperature locations, the heavy metal ions in the pollution source dissolve in the liquid water and migrate from the heating end to the low-temperature end mainly with the liquid water movement. In addition, the movement of gaseous water hardly carries any heavy metal ions.

The higher the dry density is, the smaller the migration distance of the heavy metals is, which is related to the small pores and limited liquid water migration. In particular, the smaller the pores between the solid soil particles are, the less liquid water there is functioning as a carrier of the heavy metal ions, and the more unfavorable the convection and diffusion of heavy metals are. As mentioned above, the temperature gradient increases with increasing dry density, the proportion of liquid water to the total amount of transferred water is low, and the migration amount of the heavy metals is small.

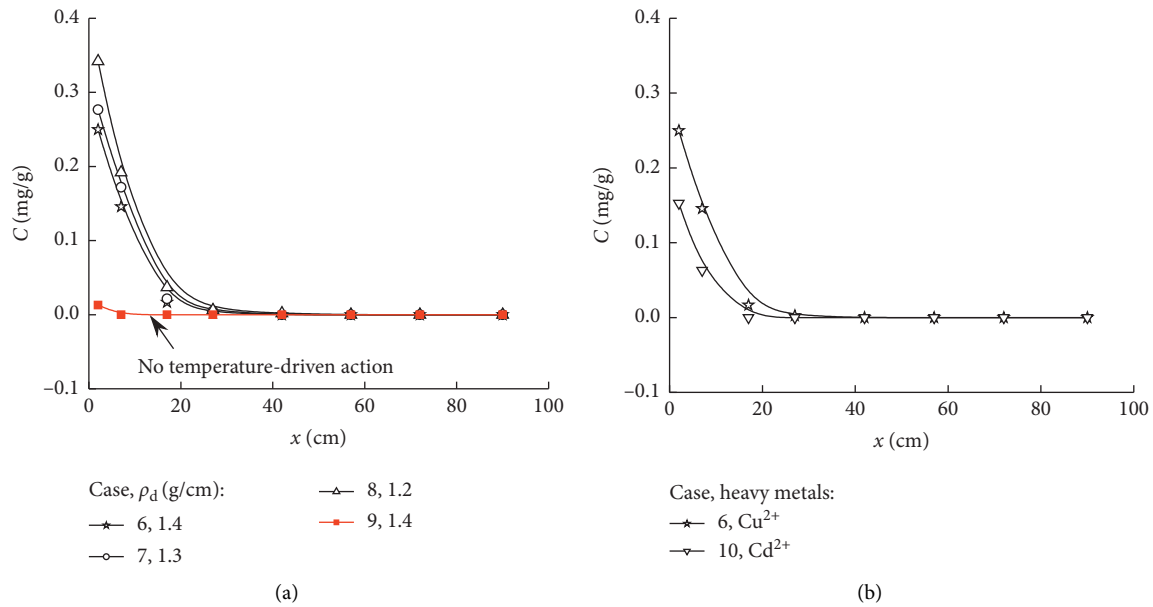


FIGURE 7: Concentration distributions of the heavy metal ions caused by the temperature: (a) effect of the dry density and (b) the different heavy metals.

Figure 7(b) also depicts a comparison of the migration amounts of Cu^{2+} and Cd^{2+} ions in the soil column. Moreover, the concentrations of the two heavy metal ions near the heating end are the same; namely, the concentrations of the pollutant source are both 1 mg/g. The results show that the migration amount and distance of the two heavy metals are quite different due to the temperature-driven action. Because the adsorption capacity of Cd^{2+} ions to soil is much higher than that of Cu^{2+} ions, the migration amount and concentration distance of the Cu^{2+} ions are greater than those of the Cd^{2+} ions. Notably, the difference in adsorption mode between these two heavy metal ions leads to different migration rules. Certainly, the adsorption effect of heavy metal ions by soil particles is closely related to the type of soil. That is, the physicochemical interaction between soil particles and water on the migration process of heavy metal ions has an important impact, which is worthy of further discussion.

4. Conclusions

The physical mechanism of heat transfer, moisture migration, and heavy metal transfer in kaolin soils was studied by one-dimensional column tests. Heat energy was mainly transferred in the form of heat conduction in the unsaturated soils, and moisture was transferred in the form of gaseous and liquid water. The change in moisture and time required to reach stability lagged behind the temperature change on the whole.

The cyclic temperature tests indicate that, during the second cycle, the temperature of the soil column near the heat source is lower than that during the first cycle. In contrast, the temperature of the soil column far away from the heat source is low, which reflects the influence of the heating path. Correspondingly, the moisture distribution during the second cycle is quite different from that during the first cycle due to the difference in the initial moisture content conditions between the two cycles.

The initial soil dry density, placement direction of the soil column, and set of temperature boundaries greatly affect heat conduction, moisture migration, and heavy metal transfer. The higher the dry density is, the better the heat transfer is. The lower the dry density is, the more favorable the moisture migration is. The placement direction of the soil column and the set of temperature boundaries influence the moisture distribution through the difference in the temperature, gravity, and solid matrix potentials.

Temperature-driven liquid water movement could effectively promote the transfer of heavy metals in kaolin soils, which is closely correlated with the convection of liquid free water. However, the transfer of heavy metal ions in soils induced by molecular diffusion is not obvious due to the absence of a thermal driving force. The higher the soil dry density is, the smaller the migration distance of the heavy metal pollutants is, which is related to the small pores and limited liquid water movement. In view of the obvious adsorption difference of copper ions (Cu^{2+}) and lead ions (Cd^{2+}), the transfer distance and deposited concentration values of Cu^{2+} are much greater than those of Cd^{2+} .

Data Availability

The data used to support the findings of this study are available from the corresponding author upon request.

Conflicts of Interest

The authors declare that there are no conflicts of interest.

Acknowledgments

This work was supported by the National Natural Science Foundation of China (51979002).

References

- [1] Y. Wang, F. Chen, X. Li, X. Yin, and Y. Lei, "The variable-mass seepage law of broken porous rock: an experimental study," *Geomatics, Natural Hazards and Risk*, vol. 11, no. 1, pp. 1991–2005, 2020.
- [2] C. Yu, R. Liao, X. Cai, and X. Yu, "Sodium polyacrylate modification method to improve the permeant performance of bentonite in chemical resistance," *Journal of Cleaner Production*, vol. 213, pp. 242–250, 2019.
- [3] B. Bai and T. Li, "Irreversible consolidation problem of a saturated porothermoelastic spherical body with a spherical cavity," *Applied Mathematical Modelling*, vol. 37, no. 4, pp. 1973–1982, 2013.
- [4] B. Bai, J. Wang, Z. Zhai, and T. Xu, "The penetration processes of red mud filtrate in a porous medium by seepage," *Transport in Porous Media*, vol. 117, no. 2, pp. 207–227, 2017.
- [5] S. Lee, I.-W. Ko, I.-H. Yoon, D.-W. Kim, and K.-W. Kim, "Colloid mobilization and heavy metal transport in the sampling of soil solution from duckum soil in South Korea," *Environmental Geochemistry and Health*, vol. 41, no. 1, pp. 469–480, 2019.
- [6] Y.-J. Du, M.-L. Wei, K. R. Reddy, Z.-P. Liu, and F. Jin, "Effect of acid rain pH on leaching behavior of cement stabilized lead-contaminated soil," *Journal of Hazardous Materials*, vol. 271, pp. 131–140, 2014.
- [7] B. Bai, T. Xu, and Z. Guo, "An experimental and theoretical study of the seepage migration of suspended particles with different sizes," *Hydrogeology Journal*, vol. 24, no. 8, pp. 2063–2078, 2016.
- [8] D. Rao and B. Bai, "Study of the factors influencing diffusive tortuosity based on pore-scale SPH simulation of granular soil," *Transport in Porous Media*, vol. 132, no. 2, pp. 333–353, 2020.
- [9] S. Raikova, M. Piccini, M. K. Surman, M. J. Allen, and C. J. Chuck, "Making light work of heavy metal contamination: the potential for coupling bioremediation with bioenergy production," *Journal of Chemical Technology & Biotechnology*, vol. 94, no. 10, pp. 3064–3072, 2019.
- [10] R. Valsala and S. K. Govindarajan, "Co-colloidal BTEX and microbial transport in a saturated porous system: numerical modeling and sensitivity analysis," *Transport in Porous Media*, vol. 127, no. 2, pp. 269–294, 2019.
- [11] B. Bai, J. Zhang, L. Liu, and Y. Ji, "The deposition characteristics of coupled lead ions and suspended silicon powders along the migration distance in water seepage," *Transport in Porous Media*, vol. 134, no. 2, pp. 1–18, 2020.
- [12] B. Bai, D. Rao, T. Chang, and Z. Guo, "A nonlinear attachment-detachment model with adsorption hysteresis for suspension-colloidal transport in porous media," *Journal of Hydrology*, vol. 578, Article ID 124080, 2019.
- [13] B. Abbar, A. Alem, A. Pantet et al., "Effect of natural geotextile on the cotransport of heavy metals (Cu^{2+} , Pb^{2+} , and Zn^{2+}) and kaolinite particles," *Environmental Technology*, vol. 42, no. 4, pp. 558–570, 2019.
- [14] X. Chen and B. Bai, "Experimental investigation and modeling of particulate transportation and deposition in vertical and horizontal flows," *Hydrogeology Journal*, vol. 23, no. 2, pp. 365–375, 2015.
- [15] B. Bai, F. Long, D. Rao, and T. Xu, "The effect of temperature on the seepage transport of suspended particles in a porous medium," *Hydrological Processes*, vol. 31, no. 2, pp. 382–393, 2017.
- [16] X. Cui, Y. Fan, H. Wang, and S. Huang, "Experimental investigation of suspended particles transport in porous medium under variable temperatures," *Hydrological Processes*, vol. 33, no. 7, pp. 1117–1126, 2019.
- [17] X. Chen, Z. Wu, Q. Cai, and W. Cao, "Effect of ultrasonic stimulation on particle transport and fate over different lengths of porous media," *Journal of Hydrology*, vol. 559, pp. 972–983, 2018.
- [18] S. Taghipour, S. M. Hosseini, and B. Ataie-Ashtiani, "Engineering nanomaterials for water and wastewater treatment: review of classifications, properties and applications," *New Journal of Chemistry*, vol. 43, no. 21, pp. 7902–7927, 2019.
- [19] K. Bär, W. Rühaak, B. Welsch, D. Schulte, S. Homuth, and I. Sass, "Seasonal high temperature heat storage with medium deep borehole heat exchangers," *Energy Procedia*, vol. 76, pp. 351–360, 2015.
- [20] X. Cui, Q. Liu, C. Zhang, Y. Huang, Y. Fan, and H. Wang, "Land subsidence due to groundwater pumping and recharge: considering the particle-deposition effect in ground-source heat-pump engineering," *Hydrogeology Journal*, vol. 26, no. 3, pp. 789–802, 2018.
- [21] M. H. E. Monged, M. T. Hussein, and A. E. M. Khater, "Elemental and radiological aspects of geothermal springs and nearby soil and sediment of Al-Lith area: concentration and risk assessment," *Environmental Earth Sciences*, vol. 77, no. 12, p. 427, 2018.
- [22] C. Yu, M. Zhou, J. Ma, X. Cai, and D. Fang, "Application of the homotopy analysis method to multispecies reactive transport equations with general initial conditions," *Hydrogeology Journal*, vol. 27, no. 5, pp. 1779–1790, 2019.
- [23] M. Funk and K. G. Wakili, "Driving potentials of heat and mass transport in porous building materials: a comparison between general linear, thermodynamic and micromechanical derivation schemes," *Transport in Porous Media*, vol. 72, no. 3, pp. 273–294, 2008.
- [24] C. Miracapillo and L. Ferroni, "Numerical simulation of radionuclides migration in the far field of a geological repository," *Energy Procedia*, vol. 82, pp. 848–854, 2015.
- [25] P. T. Nguyen and O. Amiri, "Study of the chloride transport in unsaturated concrete: highlighting of electrical double layer, temperature and hysteresis effects," *Construction and Building Materials*, vol. 122, pp. 284–293, 2016.
- [26] A. M. Tang and Y. J. Cui, "Effects of mineralogy on thermo-hydro-mechanical parameters of MX80 bentonite," *Journal of Rock Mechanics and Geotechnical Engineering*, vol. 2, no. 1, pp. 91–96, 2010.
- [27] H. A. Basha and A. P. S. Selvadurai, "Heat-induced moisture transport in the vicinity of a spherical heat source," *International Journal for Numerical and Analytical Methods in Geomechanics*, vol. 22, no. 12, p. 969, 1998.
- [28] H. R. Thomas, Y. He, and C. Onofrei, "An examination of the validation of a model of the hydro/thermo/mechanical behaviour of engineered clay barriers," *International Journal for Numerical and Analytical Methods in Geomechanics*, vol. 22, no. 1, pp. 49–71, 1998.
- [29] F. Lindner, M. Pfitzner, and C. Mundt, "Experimental and numerical study of multiphase, multicomponent flow in porous media with a multiphase mixture model," *Transport in Porous Media*, vol. 116, no. 1, pp. 143–161, 2017.
- [30] B. Bai, D. Rao, T. Xu, and P. Chen, "SPH-FDM boundary for the analysis of thermal process in homogeneous media with a discontinuous interface," *International Journal of Heat and Mass Transfer*, vol. 117, pp. 517–526, 2018.

- [31] B. Bai, G.-C. Yang, T. Li, and G.-S. Yang, "A thermodynamic constitutive model with temperature effect based on particle rearrangement for geomaterials," *Mechanics of Materials*, vol. 139, Article ID 103180, 2019.
- [32] X. Cui, Q. Liu, and C. Zhang, "Detachment characteristics of deposited particles in porous medium: experimentation and modeling," *Transport in Porous Media*, vol. 119, no. 3, pp. 633–647, 2017.
- [33] B. Bai and X. Shi, "Experimental study on the consolidation of saturated silty clay subjected to cyclic thermal loading," *Geomechanics and Engineering*, vol. 12, no. 4, pp. 707–721, 2017.
- [34] Y.-J. Du, J. Wu, Y.-L. Bo, and N.-J. Jiang, "Effects of acid rain on physical, mechanical and chemical properties of GGBS-MgO-solidified/stabilized Pb-contaminated clayey soil," *Acta Geotechnica*, vol. 15, no. 4, pp. 923–932, 2020.
- [35] N. Finzgar and D. Lestan, "Advanced oxidation for treatment of aqueous extracts from EDTA extraction of Pb and Zn contaminated soil," *Journal of Environmental Engineering*, vol. 132, no. 10, pp. 1376–1380, 2006.
- [36] P. Zhang, B. Bai, S. Jiang, P. Wang, and H. Li, "Transport and deposition of suspended particles in saturated porous media: effect of hydrodynamic forces and pore structure," *Water Supply*, vol. 16, no. 4, pp. 951–960, 2016.
- [37] G. C. Yang and B. Bai, "Thermo-hydro-mechanical model for unsaturated clay soils based on granular solid hydrodynamics theory," *International Journal of Geomechanics*, vol. 19, no. 10, Article ID 04019115, 2019.
- [38] Y. Wang, Z. Li, H. Jing, Y. Li, and M. Wang, "Study on the seepage characteristics of deep buried tunnels under variable high-pressure water heads," *Bulletin of Engineering Geology and the Environment*, vol. 80, no. 2, pp. 1477–1487, 2021.
- [39] B. Bai, "Fluctuation responses of saturated porous media subjected to cyclic thermal loading," *Computers and Geotechnics*, vol. 33, no. 8, pp. 396–403, 2006.

Research Article

Numerical Analysis on Reinforcement Range of a Closed Steel Sleeve against Collapse

Qing-Feng Yin ^{1,2}

¹China Construction Communications Construction Group Co. Ltd., Beijing 100142, China

²School of Civil Engineering, Huaqiao University, Xiamen, Fujian 361021, China

Correspondence should be addressed to Qing-Feng Yin; 1106244363@qq.com

Received 28 January 2021; Revised 18 February 2021; Accepted 7 March 2021; Published 19 March 2021

Academic Editor: Faming Huang

Copyright © 2021 Qing-Feng Yin. This is an open access article distributed under the Creative Commons Attribution License, which permits unrestricted use, distribution, and reproduction in any medium, provided the original work is properly cited.

Before the shield machine begins to excavate, the end of the station structure often requires extensive soil reinforcement to ensure construction safety. Closed steel sleeve can prevent water leakage, sand leakage, and cave door collapse by balancing the water and soil pressure on the tunnel surface, thereby reducing the reinforcement range. In this study, a launching project of a closed steel sleeve is investigated; the Madis GTS finite element analysis software is used to simulate the triple-tube high-pressure jet-grouting pile to reinforce the water-rich sand layer. Soil displacement and stress after opening of the tunnel door are studied in detail at different longitudinal reinforcement lengths and transverse reinforcement scopes. The results show that, as the longitudinal reinforcement length increases, the displacement of the soil shows a decreasing trend, and the greater the length of the reinforced soil, the smaller the reduction in displacement. Furthermore, with the decrease of the lateral reinforcement range, though the soil settlement area has increased, the displacement remains unchanged. However, changing the end reinforcement range has no effect on the soil stress. In general, based on the strength and stability of the soil after the gate is cut out, the reinforcement range of the closed steel sleeve can be appropriately reduced compared to traditional reinforcement methods.

1. Introduction

Steel sleeve can form a confined space by injecting cement mortar to provide water and soil pressure on the face of the tunnel to prevent the risk of water leakage, sand leakage, and ground collapse, thereby reducing the end reinforcement range or even eliminating reinforcement requirement [1–4]. The high-pressure jet-grouting pile uses nozzles that extend into the underground soil to spray high-pressure cement slurry and mix it with the soil to form a columnar reinforcement. It has the advantages of simple construction and controllable grout injection range and is widely used in China and other countries [5–7].

Many scholars have conducted numerical simulation studies on the end reinforcement range. Hu et al. [8] numerically simulated the development and distribution of the temperature field on a large-diameter cup-shaped frozen soil wall and analyzed the influence of different factors on the temperature field. In addition to the physical reinforcement methods mentioned above, Hu et al. [9] also studied the

initial reinforcement range of the shield when using chemical reinforcement (such as high-pressure jet grouting) and compared the soil deformation strength and surface settlement under different reinforcement ranges. Zhou et al. [10] introduced the process of grouting construction when the shield was started and received in detail and analyzed the stability of the excavation face of the shield under different horizontal and longitudinal reinforcement scopes using a numerical simulation method. Wu [11] performed a numerical simulation of the shield machine passing through a starting working well and compared the simulation data of the unreinforced end with the surface settlement value calculated according to the Peak formula. In terms of theoretical calculations, Luo et al. [12] studied the determination of the end soil reinforcement range and the establishment of a sand-soil composite stratum end sliding model and proposed a load equivalent model on the theory of soil strength and a sliding model of sandy soil according to the stability theory. Based on the slab strength theory, Lei et al. [13] simplified the mechanical model of simply

supported rectangular slabs, divided the equivalent loads into uniformly distributed loads and triangular antisymmetric loads, and discussed the conditions of different reinforced soil thicknesses. Jiang and Jain [14] conducted end reinforcement effect statistics on a variety of layers and analyzed the relationship between longitudinal reinforcement length and shield diameter. It can be seen that the conventional numerical simulation and theoretical calculation of the end reinforcement range need to comprehensively analyze the strength, stability, and impermeability of the soil under the conditions of tunnel gate removal and end excavation. When the closed steel sleeve starts, the end reinforcement range only needs to ensure the strength and stability of the soil after the tunnel door is cut out. The end reinforcement range determined according to the existing research results is no longer applicable. Therefore, the reasonable range of end reinforcement at the beginning of the launch of the closed steel sleeve still needs further study.

In this study, through a closed steel sleeve project, the Madis GTS finite element analysis software is used to simulate the triple-tube high-pressure jet-grouting pile to strengthen the end soil. According to the survey report and drilling data, a three-dimensional numerical model is established, and the displacement and stress of the soil mass at different longitudinal reinforcement lengths and lateral reinforcement ranges after the gate is cut out are analyzed in detail to determine the economical and reasonable end reinforcement range.

2. Project Overview

The enclosed steel sleeve launching project is located in a water-rich sand layer. The end reinforcement and precipitation are necessary to meet the launching conditions. The outer diameter of the tunnel shield is 6.2 m, and the depth of the tunnel gate is 21.6 m. Due to the dense underground pipelines at the starting end and the limited location of the construction site, it is easy to cause damage to the underground pipelines. Therefore, the design of the three-axis mixing pile reinforcement plan failed to be implemented; instead, it is strengthened by high-pressure rotary jet grouting. Furthermore, before cutting out the tunnel door to install the steel sleeve, we use triple pipe $\Phi 850@600$ high-pressure jet-grouting pile reinforcement (empty pile cement 8% and solid pile cement 30%) outside the station enclosure structure. Simultaneously, three dewatering wells are arranged at the starting end, two dewatering wells are set at 1 m from the starting end, and one dewatering well is set at the middle of the reinforcement area on the left and right lines. From top to bottom, the beginning soil layer is mainly composed of plain fill, silty clay, organic clay, silty sand, and fine sand. The suggested parameter values of each soil layer are shown in Table 1.

3. Numerical Model

Madis GTS, a three-dimensional finite element analysis software, was used to simulate the soil at the end of the triple-tube high-pressure jet-grouting pile. Then, the

simulation results of soil displacement and stress after opening the portal was used to study the appropriate reinforcement range. The numerical model is presented in Figure 1. Based on practical experience and Saint-Venant's principle, the area affected by tunnel excavation is basically concentrated within 5 times the tunnel diameter [15–17]. Dimensions of the model used in this study were 100 m \times 53 m \times 70 m. The Mohr–Coulomb elastoplastic model was adopted for soil, and the shear expansion effect was neglected. The suggested values of the soil parameters are listed in Table 1. The mechanical parameters of cement-soil are related to factors such as the cement mixing ratio, spray pressure, and age. When the unconfined compressive strength of the reinforced soil is 1.0 MPa, the cohesion and internal friction angle can be considered as 250 MPa and 25°, respectively [18]. Furthermore, panel units were used for the station enclosure and the tunnel doors. A hybrid grid generator was in the model to obtain the grids, and the number of generated units was 142512, comprising 90601 nodes. To simulate a semi-infinite space, the top of the model is set as a free boundary, then the lower part of the model is set as a fixed boundary, and, finally, the rest of the parts are set with displacement constraints in the normal direction. In the construction phase, the properties of soil elements are altered to simulate the reinforcement afforded by high-pressure jet-grouting piles. The procedures involved in construction are as follows: initial ground stress analysis, station foundation excavation and construction of enclosure, high-pressure jet-grouting pile reinforcement, and one-time excavation of tunnel door. To evaluate the influence of the longitudinal reinforcement length on the soil after the excavation of the portal, a lateral reinforcement range of 3 m is set at the top and bottom of the shield tunnel. Thereafter, the longitudinal reinforcement lengths are set as 3, 4, 5, 6, 7, and 8 m. To study the influence of the lateral reinforcement range on the soil after the excavation of the portal, a longitudinal reinforcement length of 3 m is fixed behind the portal; then, the lateral reinforcement range is set as 1, 2, and 3 m, respectively.

4. Analysis of Calculation Results

4.1. Result Analyses for Different Longitudinal Reinforcement Lengths. Figures 2 and 3 show the displacement and stress under different longitudinal reinforcement lengths. It can be seen from Figure 2 that the three curves of total displacement, X-direction displacement, and Y-direction displacement have the same changing trend. As the length of the reinforced soil increases, the displacement continues to decrease. When the length increases to 5 m, the slope of the curve decreases noticeably; the greater the length of reinforced soil, the smaller is the contribution to the reduction of displacement. When the length of the longitudinal reinforcement increases, the displacement along the Z-direction increases, which is due to the corresponding increase in settlement caused by the increase in the soil weight stress. Figure 3 shows that when the length of reinforced soil increases, the compressive stress of the soil

TABLE 1: Soil physical and mechanical parameter values.

Name of soil layers	Soil thickness (m)	Elastic modulus (MPa)	Poisson ratio	Natural gravity (kN/m ²)	Cohesion (kPa)	Internal friction angle (°)
① ₁ Plain fill	1.6	16	0.20	16.0	5	10
② ₃₁ Silty clay	3.9	39	0.30	15.7	12	22
② ₃₂ Silty clay	4.0	39	0.31	15.9	11	22
② ₂₁ Silty clay	1.6	20	0.30	15.6	23	14
② ₃₃ Silty clay	2.7	43	0.31	15.8	11	21
② _{22F} Organic clay	6.2	15	0.33	12.4	26	13
② ₅₃ Fine sand	10.0	25	0.30	20.0	0	30
③ ₂₁ Silty clay	40.0	27	0.31	16.4	24	13

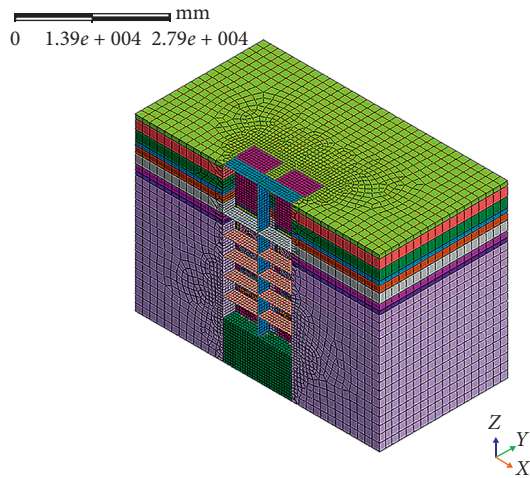


FIGURE 1: Three-dimensional numerical model.

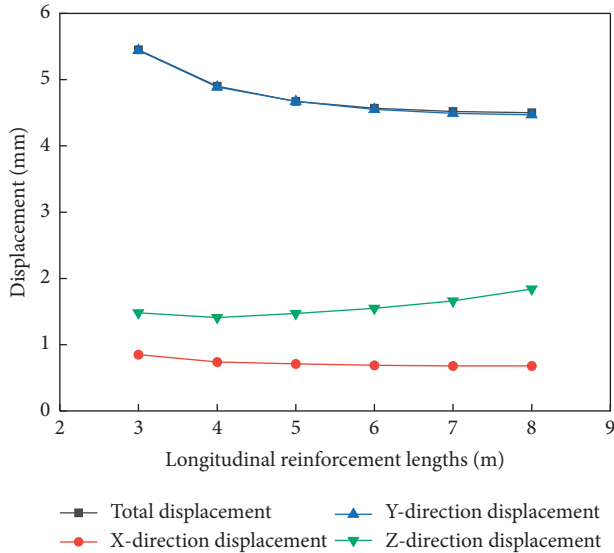


FIGURE 2: Displacement under longitudinal reinforced lengths of 3 m, 4 m, 5 m, 6 m, 7 m, and 8 m.

fluctuates in the range of 0.47 ~ 0.49 MPa, the shear stress fluctuates in the range of 0.15 ~ 0.17 MPa, and the tensile stress fluctuates in the range of 0.014 ~ 0.017 MPa. It can be seen that increasing the length of reinforcement has no significant effect on soil stress.

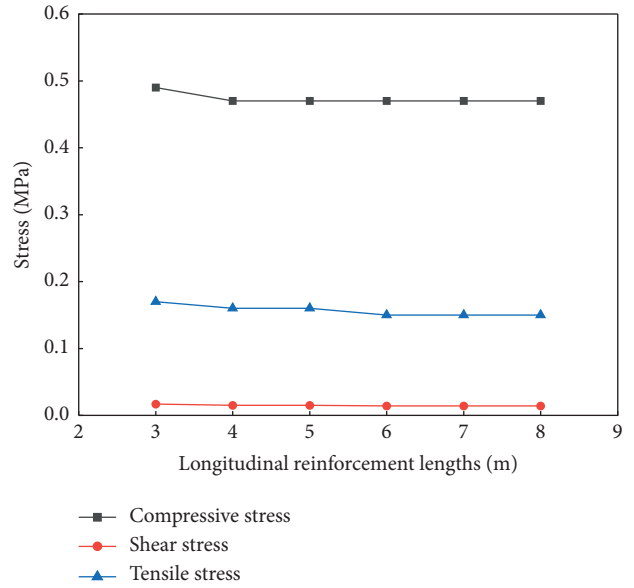


FIGURE 3: Stresses under longitudinal reinforced lengths of 3 m, 4 m, 5 m, 6 m, 7 m, and 8 m.

In order to determine the feasibility when the longitudinal reinforcement length is 3 m, the soil displacement, stress, and surface settlement are analyzed in detail. Figure 4 depicts a cloud diagram of soil displacement. From Figure 4(a), it can be seen that the maximum displacement along the X-direction is 0.85 mm, which shows that the soil in the middle of the portal is squeezed toward the edges on both sides. It can be seen from Figure 4(b) that the maximum displacement along the Y-direction is 5.44 mm, which occurs at the center of the portal; this shows that the soil behind the door moves toward the exposed surface of the tunnel. According to the technical code for building foundation pit inspection [19], the horizontal displacement control depth of the foundation pit supported by the diaphragm wall is 6.48 mm, when the design depth of the foundation pit is 21.6 m. Hence, the Y-direction displacement meets the safety requirement. As shown in Figure 4(c), the maximum displacement in the Z-direction is 0.67 mm, while the minimum is -1.48 mm, which shows that the soil above the portal slides downward and the soil below the portal bulges upward. According to the technical specifications for subway construction and inspection [20], when the safety status of the rail transit structure is Class I, the vertical displacement

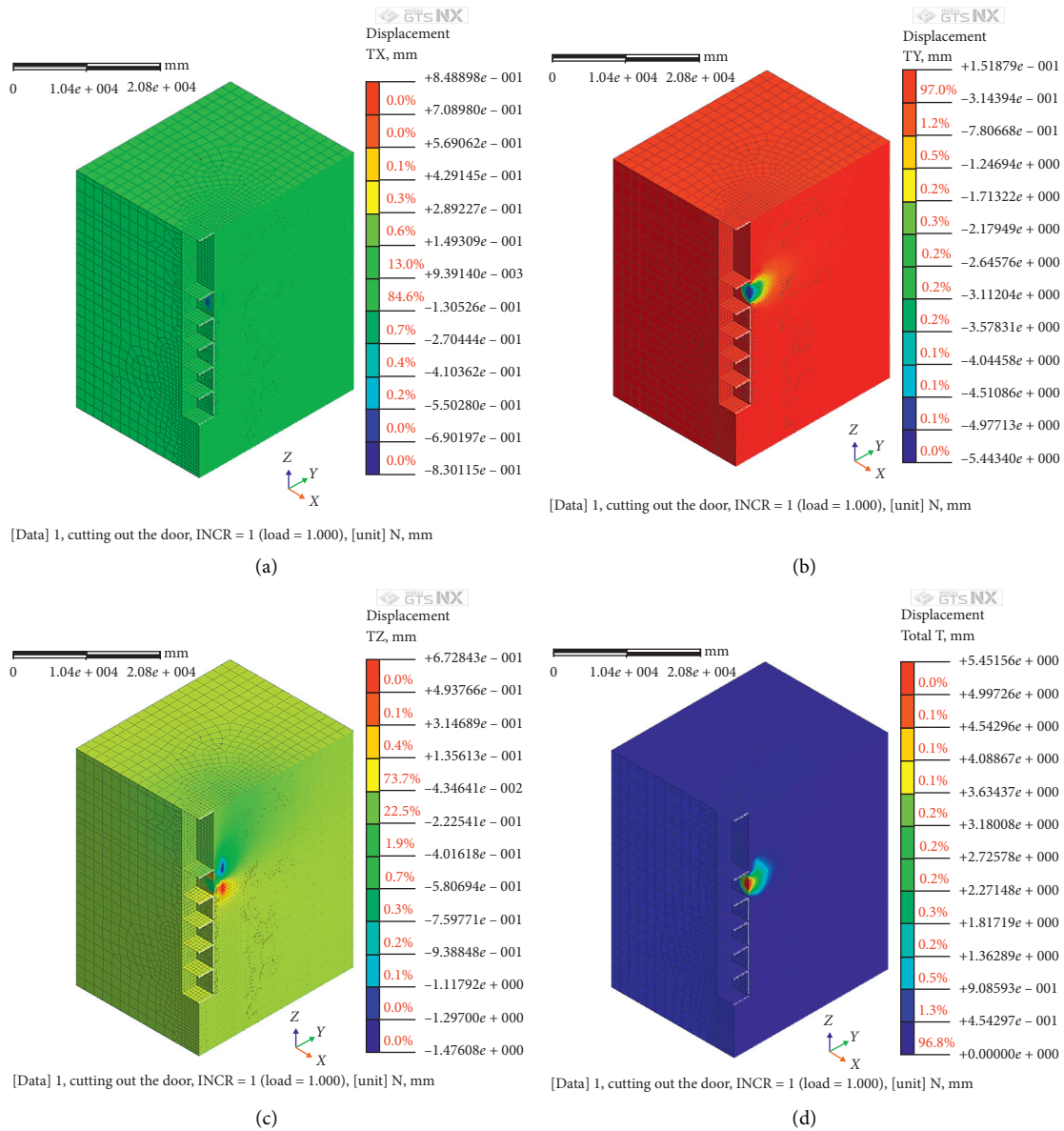


FIGURE 4: Soil displacement nephogram. (a) X-direction displacement. (b) Y-direction displacement. (c) Z-direction displacement. (d) Total displacement.

safety value of the structural safety control index is 5 mm. Hence, the Z-direction displacement is within the safe limits. From Figure 4(d), it can be seen that the maximum total displacement is 5.45 mm, which appears on the exposed face; this is basically the same as the displacement in the Y-direction. Therefore, soil deformation is mainly composed of the horizontal displacement along the longitudinal direction of the tunnel; the displacements along the other two directions have limit effect on portal stability.

Figure 5 shows the reinforced soil stress. It can be seen from Figure 5(a) that the maximum compressive stress, σ_x , is 0.35 MPa, which occurs on both sides of the portal. Figure 5(b) shows that σ_y involves tensile and compressive stresses; the maximum compressive stress is 0.45 MPa, which occurs at the top of the portal, and the maximum tensile stress is 0.017 MPa, which occurs at the edges of both

sides of the portal. It can be seen from Figure 5(c) that the compressive stress, σ_z , induces delamination, and the maximum compressive stress is 0.48 MPa, which occurs at the bottom of the portal. The unconfined compressive strength of the soil reinforced by high-pressure jet-grouting piles for 28 days is generally required to be no less than 0.8 MPa. Therefore, the maximum compressive stress in the reinforced soil caused by the removal of the portal is less than its compressive strength. According to the Griffith strength criterion, the compressive strength is 8 times the tensile strength, that is, $\sigma_c = 8\sigma_t$, and the tensile strength of the reinforced soil is 0.1 MPa. Hence, the maximum tensile stress is considerably smaller than its tensile strength. From Figures 5(d) and 5(e), it can be seen that the maximum shear stress is 0.17 MPa, which appears on both sides of the portal. Based on the Coulomb formula, that is,

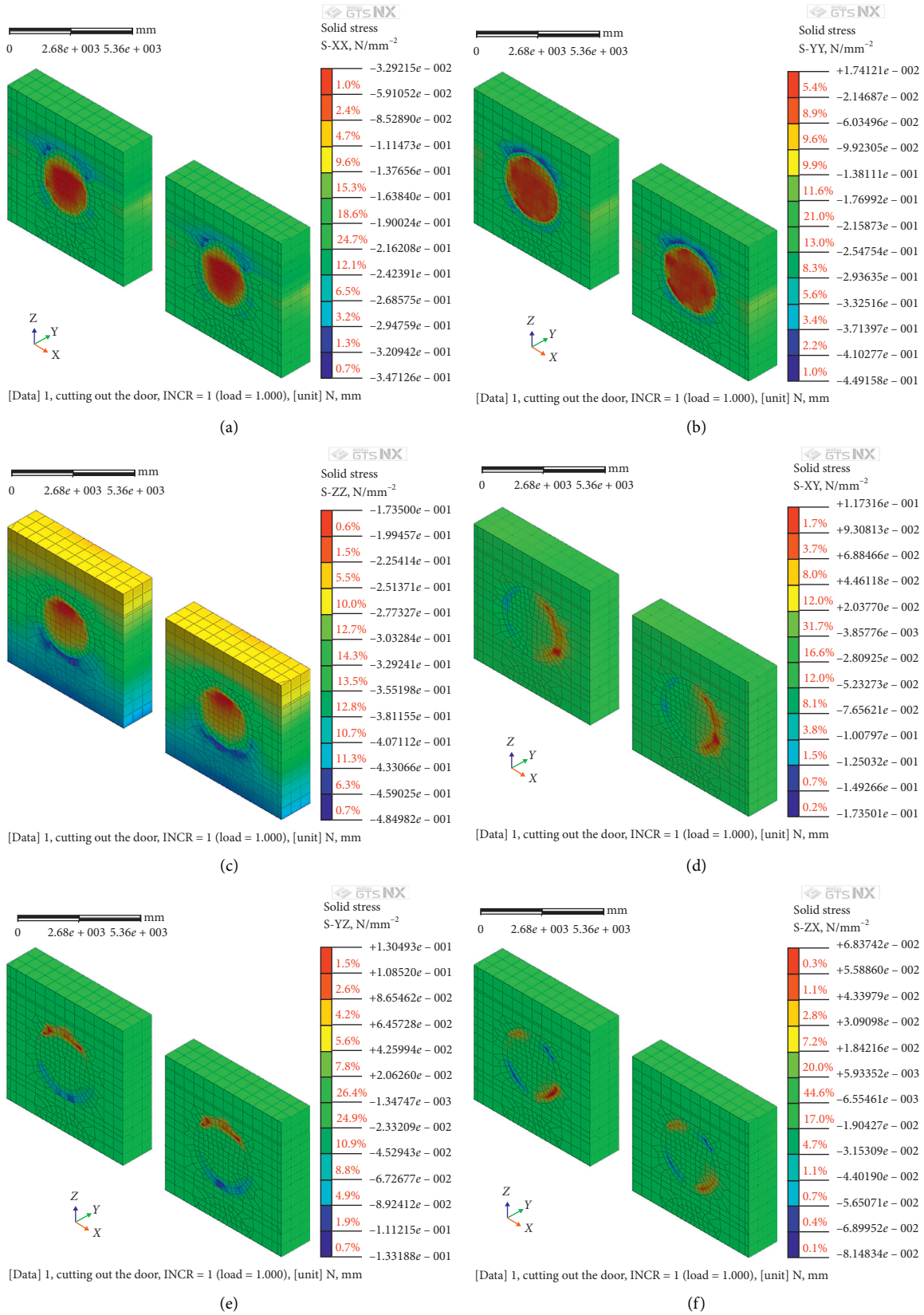


FIGURE 5: Stresses of reinforcement soil. (a) Stress of σ_x . (b) Stress of σ_y . (c) Stress of σ_z . (d) Stress of τ_{xy} . (e) Stress of τ_{yz} . (f) Stress of τ_{xz} .

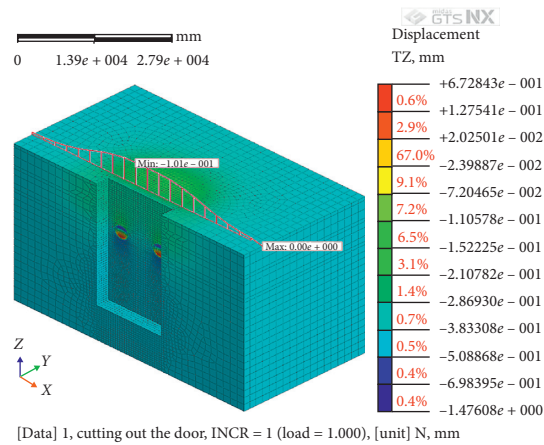


FIGURE 6: Surface subsidence diagram at 3 m of longitudinal reinforcement length.

$\tau_f = \sigma \tan \phi + c$, the shear strength of the reinforced soil is 0.31 MPa. Therefore, the maximum shear stress of the reinforced soil caused by the removal of the tunnel door is less than its shear strength.

Figure 6 shows the surface settlement. It can be seen from Figure 6 that the surface settlement trough caused by the simultaneous removal of the left and right portals has a “V” shape, which is approximately a normal distribution curve, and the maximum settlement is less than 1 mm, which appears on the central axis of the two portals. According to the technical specifications for subway construction and inspection [20], the vertical displacement safety value of the structure is 5 mm; therefore, the surface settlement meets the safety requirements.

4.2. Result Analysis of Different Lateral Reinforcement Ranges.

Figures 7 and 8 show the displacement and stress under different lateral reinforcement ranges. It can be seen from the figures that, with the reduction in the lateral reinforcement range, the soil displacement and stress do not change, which indicates that the effective reinforcement range of high-pressure jet-grouting piles is limited. The strength and stability of soil are not affected by changing the transverse reinforcement scope.

To further study the feasibility when the lateral reinforcement range is 1 m, the soil displacement, stress, and ground settlement are analyzed in detail. Figure 9 shows a cloud diagram of soil displacement. It can be seen from Figure 9(a) that the maximum displacement in the X-direction is 0.89 mm, which appears on both sides of the portal. It can be seen from Figure 9(b) that the maximum displacement in the Y-direction is 5.51 mm, and the deformation area and displacement are unchanged. It can be seen from Figure 9(c) that the maximum displacement in the Z-direction is 1.50 mm, and the settlement range has been significantly expanded but the value has not changed. It can be seen from Figure 9(d) that the maximum total displacement is 5.52 mm, with only a small increase of 0.07 mm. Generally, although the reduction in the lateral reinforcement range increases the soil settlement area, the displacement remains unchanged.

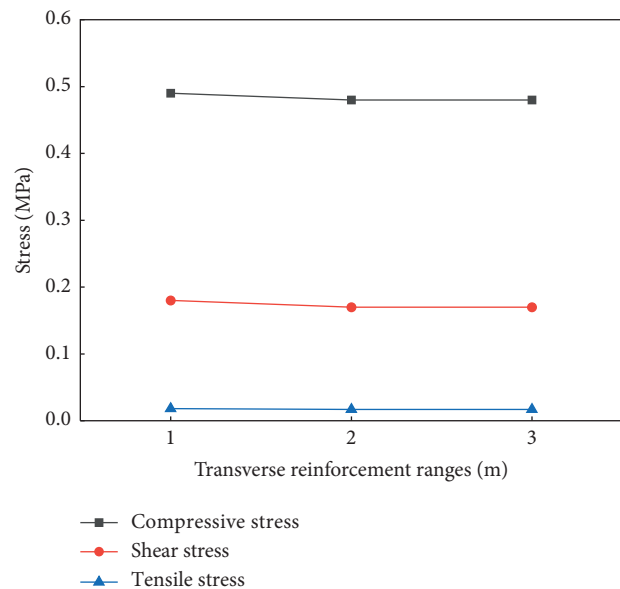


FIGURE 7: Stresses under transverse reinforcing ranges of 1 m, 2 m, and 3 m.

Figure 10 shows the reinforced soil stress. It can be seen from Figure 10(a) that the maximum compressive stress of σ_x is 0.35 MPa, which shows that the soil in the middle of the portal is squeezed to the edges on both sides. It can be seen from Figure 10(b) that the maximum compressive stress of σ_y is 0.47 MPa, which appears on top of the portal, and the maximum tensile stress of σ_y is 0.017 MPa, which appears at the edges of both sides of the portal. From Figure 10(c), it can be seen that the maximum compressive stress of σ_z is 0.49 MPa, with a small increase of 0.01 MPa. From Figures 10(d) and 10(e), it can be seen that the maximum shear stress is 0.18 MPa, which remains unchanged. In general, the various stresses of the reinforced soil meet the strength requirements.

Figure 11 shows the surface settlement. It can be seen from Figure 11 that although the reduction in the lateral reinforcement range leads to an increase in the settlement area, the maximum settlement is still less than

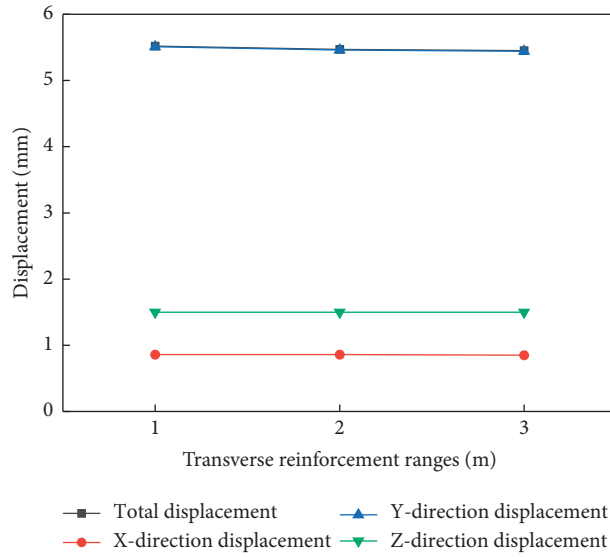


FIGURE 8: Displacement under transverse reinforcing ranges of 1 m, 2 m, and 3 m.

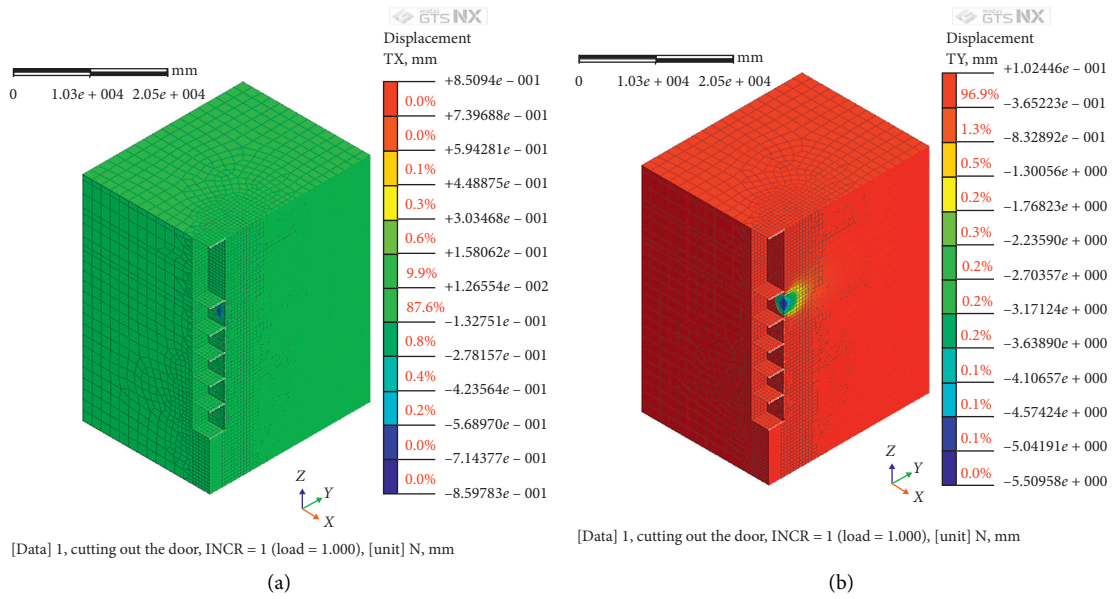


FIGURE 9: Continued.

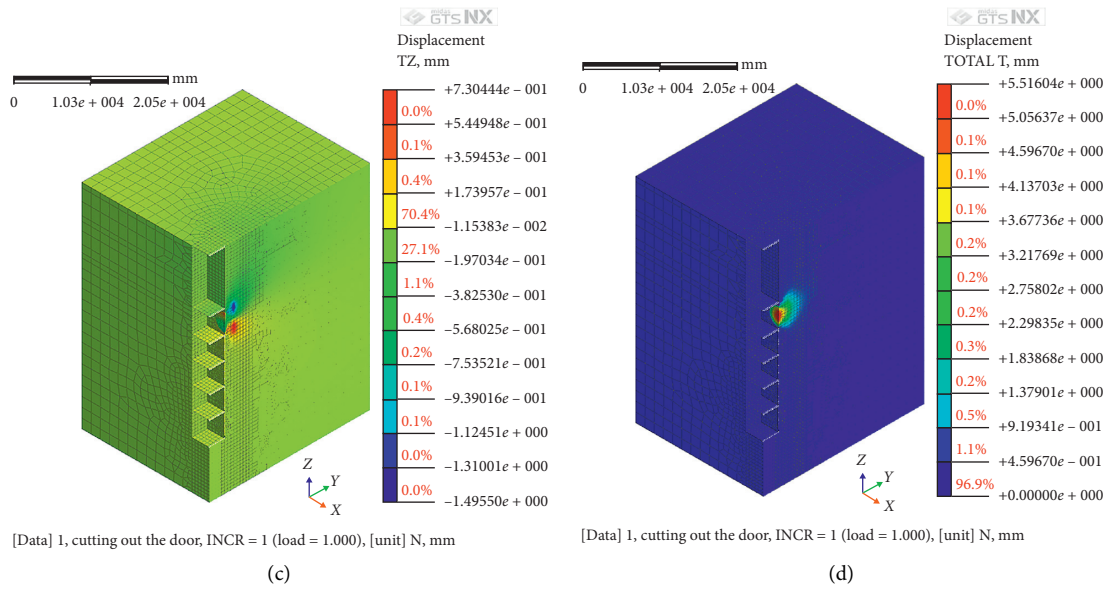


FIGURE 9: Soil displacement nephogram. (a) X-direction displacement. (b) Y-direction displacement. (c) Z-direction displacement. (d) Total displacement.

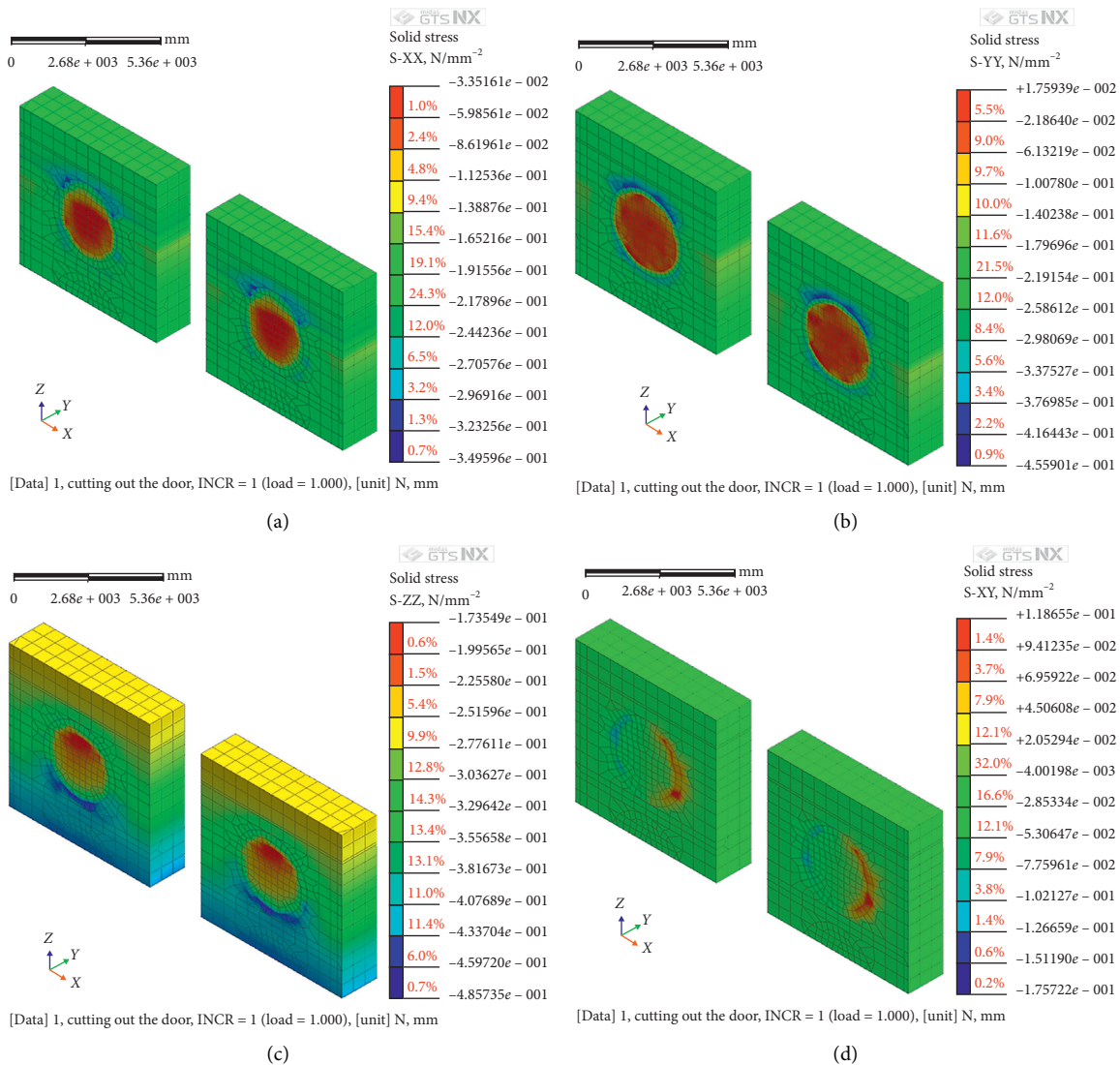


FIGURE 10: Continued.

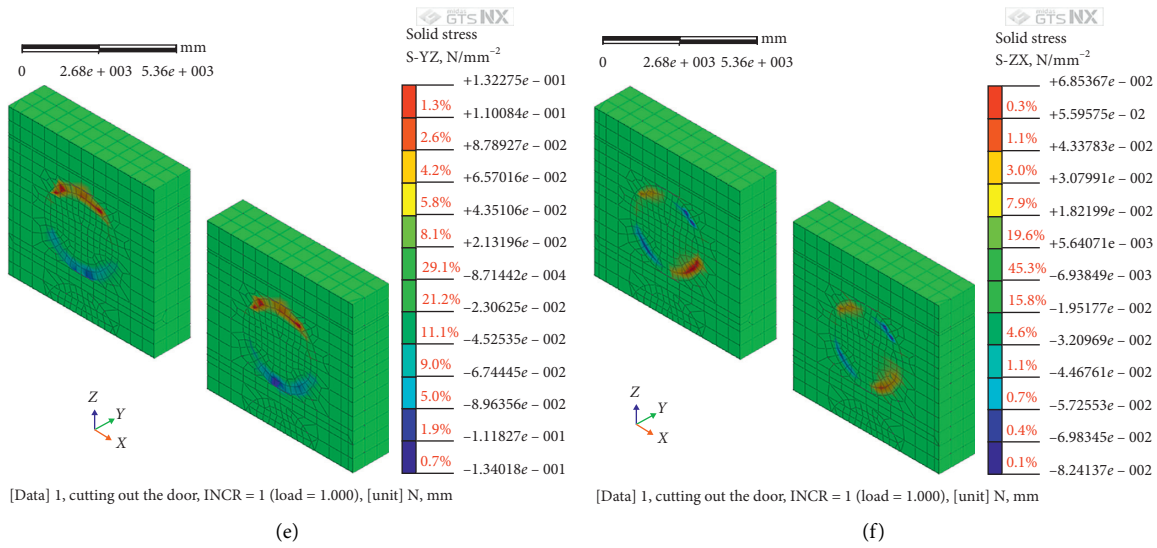


FIGURE 10: Stresses of reinforcement soil. (a) Stress of σ_x . (b) Stress of σ_y . (c) Stress of σ_z . (d) Stress of τ_{xy} . (e) Stress of τ_{yz} . (f) Stress of τ_{xz} .

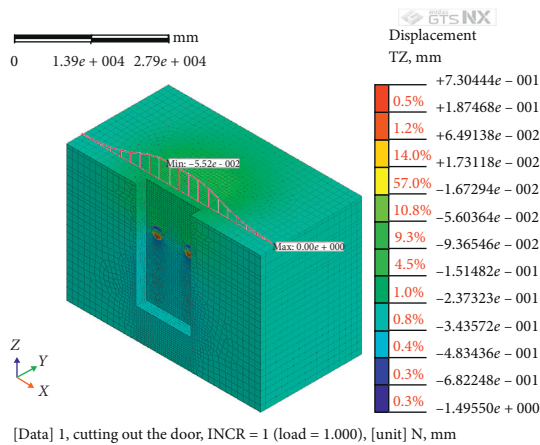


FIGURE 11: Surface subsidence diagram at 1 m of lateral reinforcement.

1 mm, which meets the requirements of rail transit regulations.

5. Conclusions and Discussion

Based on a sealed steel sleeve launching project, this study uses Madis GTS to simulate the triple-tube high-pressure jet-grouting pile to reinforce the water-rich sand layer. The changes in soil displacement and stress at different longitudinal reinforcement lengths and lateral reinforcement ranges were studied in detail. The following conclusions are drawn from the study:

- (1) The overall displacement of the soil tends to decrease with an increase in the length of the longitudinal reinforcement, and the greater the length of the reinforced soil, the smaller the reduction in displacement. With the decrease in the lateral reinforcement range, the soil settlement area increases; however, the displacement remains unchanged.

- (2) Irrespective of whether the reinforcement length or the transverse reinforcement scope changes, the soil stress remains unchanged after the hole door is removed.
- (3) The soil deformation is mainly composed of horizontal displacement along the longitudinal direction of the tunnel; the displacement in other directions has little effect on portal stability. The compressive stress σ_z is the largest among the various stresses of the soil, and the tensile stress and shear stress are generally small.
- (4) When the reinforcement range is reduced, although the settlement area increases, the maximum surface settlement is still less than 1 mm, appearing between the central axis of the left and right portals.

Based on the strength and stability of the soil, the longitudinal reinforcement length and the lateral reinforcement range of the end can be taken as 3 m and 1 m, respectively, which is greatly reduced compared to the traditional reinforcement range. However, if the construction control of high-pressure jet-grouting piles does not meet the requirements, it is difficult to guarantee the effect of preventing the cave door from collapsing. Common construction quality defects include broken piles, necking piles, clogging nozzle, and pile head cavities. When the borehole slope deviation is large, the antiseepage effect of the water-stop curtain composed of piles is not good. Therefore, the design of the end reinforcement range should be appropriately designed based on the actual construction situation. On the other hand, the scope of application of high-pressure jet-grouting piles is limited. For example, if the groundwater flow rate is too high in a water-rich sand layer, the sprayed grout will not be able to solidify around the grouting pipe. The reinforcement method of plain underground continuous wall suitable for this complex condition needs further study.

Data Availability

The data used to support the findings of this study are available from the corresponding author upon request.

Conflicts of Interest

The author declares no conflicts of interest.

Acknowledgments

The author wishes to thank China Construction Communications Construction Group Co. Ltd. for offering field data. This study was funded by the Promotion Program (Grant No. ZQN-PY513).

References

- [1] W. L. Wu, H. H. Zhu, Y. Zhou et al., "Study of key technologies of steel sleeve launching and receiving of shield," *Chinese Journal of Tunnel Construction*, vol. 37, pp. 872–877, 2017.
- [2] S. S. Lv, W. Liu, S. H. Zhai et al., "Influence of water inrush from excavation surface on the stress and deformation of tunnel-forming structure at the launching-arrival stage of subway shield," *Advances in Civil Engineering*, vol. 2019, p. 20, Article ID 6989730, 2019.
- [3] X. Chen, M. Fang, P. Chen, Q. Cai, and L. Guo, "Effects of ultrasonic stimulation on the transport of different-sized particles in porous media," *Hydrogeology Journal*, vol. 28, no. 4, pp. 1403–1417, 2020.
- [4] B. Bai, D. Y. Rao, T. Chang et al., "A nonlinear attachment-detachment model with adsorption hysteresis for suspension-colloidal transport in porous media," *Journal of Hydrology*, vol. 578, Article ID 124080, 2019.
- [5] W. Li, X. Fan, F. Huang et al., "Uncertainties analysis of collapse susceptibility prediction based on remote sensing and GIS: influences of different data-based models and connections between collapses and environmental factors," *Remote Sensing*, vol. 12, no. 24, p. 4134, 2020.
- [6] X. L. Nguyen, L. Wu, and K. T. Nguyen, "Application research of high pressure jet grouting pile in an underground engineering in Vietnam," *Archives of Civil Engineering*, vol. 66, pp. 575–593, 2020.
- [7] X. Chen, Z. Wu, Q. Cai, and W. Cao, "Effect of ultrasonic stimulation on particle transport and fate over different lengths of porous media," *Journal of Hydrology*, vol. 559, pp. 972–983, 2018.
- [8] J. Hu, H. Zeng, and X. B. Wang, "Numerical analysis of temperature field of cup-shaped frozen soil wall reinforcement at shield shaft," *Applied Mechanics and Materials*, vol. 341–342, pp. 1467–1471, 2013.
- [9] J. Hu and P. Yang, "A numerical simulation study on the chemical reinforcement area at shield start shaft," in *Proceedings of the International Conference on Electric Technology and Civil Engineering (ICETCE)*, Lushan, China, April 2011.
- [10] X. J. Zhou, J. H. Wang, X. B. Wang et al., "Study on launching and receiving technology of shield tunnel," in *Proceedings of the International Conference on Pipelines and Trenchless Technology 2011: Sustainable Solutions for Water, Sewer, Gas, and Oil Pipelines*, Beijing, China, October 2011.
- [11] Y. W. Wu, *Analysis of the Ground Settlement Caused by the Construction of the Portal of the Shield Starting Shaft in the East Huai'an Station*. Master, Anhui Jianzhu University, Hefei, China, 2020.
- [12] F. R. Luo, Y. S. Jiang, and H. Jiang, "Theoretical modeling and sensitivity analysis of improved sandy strata at TBM portal areas with strength and stability theories," *Chinese Journal of Engineering Geology*, vol. 19, pp. 364–369, 2011.
- [13] J. S. Lei, L. M. Yin, X. Z. Yang et al., "Study on reinforcement scope at TBM launching and breaking through area in sandy pebble stratum," in *Proceedings of the International Conference on Pipelines & Trenchless Technology*, Xi'an, China, October 2013.
- [14] Y. S. Jiang and H. Jian, "Study on soil reinforcement for the launching and arrival ends of large-diameter EPB shields in Beijing metro," *Chinese Journal of Urban Rapid Rail Transit*, vol. 26, pp. 93–96, 2013.
- [15] L. Zhu, L. Huang, L. Fan et al., "Landslide susceptibility prediction modeling based on remote sensing and a novel deep learning algorithm of a cascade-parallel recurrent neural network," *Sensors*, vol. 20, no. 6, p. 1576, 2020.
- [16] J. Lai, H. Zhou, K. Wang et al., "Shield-driven induced ground surface and Ming Dynasty city wall settlement of Xi'an metro," *Tunnelling and Underground Space Technology*, vol. 97, Article ID 103220, 2020.
- [17] F. Huang, Z. Cao, S.-H. Jiang, C. Zhou, J. Huang, and Z. Guo, "Landslide susceptibility prediction based on a semi-supervised multiple-layer perceptron model," *Landslides*, vol. 17, no. 12, pp. 2919–2930, 2020.
- [18] K. H. Gu and Y. F. Zhang, "Parametric study on soil reinforcement in front of lattice shaped diaphragm wall revetment on soft ground," *Chinese Journal of Port & Waterway Engineering*, vol. 4, pp. 134–139, 2018.
- [19] Ministry of Housing and Urban-Rural Development of the People's Republic of China, *State Administration for Market Regulation*, China Planning Press, Beijing, China, 2019.
- [20] Ministry of Housing and Urban-Rural Development of the People's Republic of China, *General Administration of Quality Supervision, Inspection and Quarantine of the People's Republic of China*, China Building Industry Press, Beijing, China, 2017.

Research Article

Indirect Determination Approach of Blast-Induced Ground Vibration Based on a Hybrid SSA-Optimized GP-Based Technique

Zhaoxin Jiang,¹ Hongyan Xu,² Hui Chen ,^{3,4,5} Bei Gao,² Shijie Jia,² Zhi Yu ,⁵
and Jian Zhou ⁵

¹Xinjiang Xuefeng Sci-Tech (Group) Co., Ltd., Urumqi, Xinjiang 830047, China

²Xinjiang Xuefeng Blasting Engineering Co., Ltd., Urumqi, Xinjiang 830047, China

³School of Geology and Mines Engineering, Xinjiang University, Urumqi, Xinjiang 830047, China

⁴Key Laboratory of Environmental Protection Mining for Minerals Resources at Universities of Education Department of Xinjiang Uygur Autonomous Region, Urumqi, Xinjiang 830047, China

⁵School of Resources and Safety Engineering, Central South University, Changsha 410083, China

Correspondence should be addressed to Hui Chen; xjuchenhui@126.com

Received 23 December 2020; Revised 22 February 2021; Accepted 9 March 2021; Published 17 March 2021

Academic Editor: Haoyuan Hong

Copyright © 2021 Zhaoxin Jiang et al. This is an open access article distributed under the Creative Commons Attribution License, which permits unrestricted use, distribution, and reproduction in any medium, provided the original work is properly cited.

The accurate determination of blast-induced ground vibration has an important significance in protecting human activities and the surrounding environment. For evaluating the peak particle velocity resulting from the quarry blast, a robust artificial intelligence system combined with the salp swarm algorithm (SSA) and Gaussian process (GP) was proposed, and the SSA was used to find the optimal hyperparameters of the GP here. In this regard, 88 datasets with 9 variables including the ratio of bench height to burden (H/B) and the ratio of spacing to burden (S/B) were selected as the input variables, while peak particle velocity (PPV) was measured. Then, an ANN model, an SVR model, a GP model, an SSA-GP model, and three empirical models were established, and the predictive performance was evaluated by using the root-mean-square error (RMSE), determination coefficient (R^2), value account for (VAF), Akaike Information Criterion (AIC), Schwarz Bayesian Criterion (SBC), and the run time. After comparing, it is found that the proposed SSA-GP yielded a superior performance and the ratio of bench height to burden (H/B) was the most sensitive variable.

1. Introduction

With the development of science and technology, many rock fragmentation technologies have been invented and applied in the engineering area, but the blasting technique is still the method with the best economic benefit and the highest rock fragmentation efficiency both in the open-pit mines and underground mines [1]. However, a previous study [2] showed that more than half of the explosive energy was wasted, and blast-induced vibration, flyrock, blast-induced overpressure, etc. were caused during the blasting operation. Among them, blast-induced vibration is considered to be the most serious and most common blast-induced environment issue, so it is of great significance to predict and control the blast-induced vibration for avoiding the undesirable effects on the neighboring building and human activities, etc.

Usually, the blast-induced ground vibration is evaluated and measured by using peak particle velocity, frequency, and duration time. Among these three indexes, peak particle velocity (PPV) is the most common and widely used index in the previous literature [3–5]. Aiming at the accurate prediction of the peak particle velocity, some empirical equations were proposed and utilized in many cases such as Sungun Copper Mine, Iran [6], Miduk Copper Mine, Iran [7], Bakhtiari Dam, Iran [8], and Sinagreni Collieries Company Limited, India [9]. But, some research studies [10, 11] show that the predictive performance of these empirical models is not high when being utilized in peak particle velocity prediction.

Nowadays, artificial intelligence (AI) technology is developing rapidly and many new artificial intelligence technologies such as ANN, SVR, and RF are being

proposed and applied in practical cases such as predicting the field capacity in disaster management problems [12–18], mining production problems [19], etc. In practice, artificial intelligence (AI) technology is also being used to predict PPV values in many studies. For example, Arthur et al. [20] checked the efficiency of the Wavelet Neural Network (WNN) in predicting peak particle velocity, and satisfying prediction results were obtained, which proves the strong prediction capability of the Wavelet Neural Network (WNN). Monjezi et al. [21] used an artificial neural network (ANN) model which includes an input layer, two hidden layers, and an output layer to evaluate the ground vibration based on the Siahbیشهh project, which demonstrates the effectiveness of using an ANN to predict the blast-induced ground vibration. Li et al. [22] proposed two hybrid models using biogeography-based optimization (BBO), deterministic optimization algorithm (DIRECT), and artificial neural network, namely, BBO-ANN and DIRECT-ANN, and the generalization capability was found to be better than other prediction models. This study shows the use of an optimization algorithm to improve the prediction performance of the prediction model. Sheykhi et al. [23] combined the fuzzy C-means clustering (FCM) and support vector regression (SVR) to develop an accurate prediction model based on a database from the Sarcheshmeh copper mine, and the model performance of this new proposed hybrid model is introduced in this paper. In addition to the abovementioned research studies, many studies [24–30] were conducted by using artificial intelligence (AI) technology to predict the PPV for vibration control.

Although many studies were conducted previously, there is not a model that is suitable for all areas because every engineering site has its characteristics. Meanwhile, artificial intelligence (AI) technology is an evolving technology, and the predictive models in the artificial intelligence (AI) area are gradually updated and developed. The salp swarm algorithm (SSA) is a newly proposed metaheuristic algorithm, and this algorithm was checked using 7 unimodal test functions and 6 multimodal benchmark functions. Comparing with particle swarm optimization (PSO), gravitational search algorithm (GSA), bat algorithm (BA), firefly algorithm (FA), and genetic algorithm (GA), SSA shows superior and steady performance on average. Meanwhile, the successful application in solving the classical engineering design problem [31], airfoil design for aero vehicles problem [31], the strength of fiber-reinforced cemented paste backfill [32], and the compressive strength of concretes [33] also proves the high capacity of SSA. Besides, the Gaussian process was found to be an effective prediction technique after be used in landslide cases [34], broken rock zone prediction [35], carbon dioxide emission prediction [36], etc. Meanwhile, the conclusion that the GP performance can be improved after using the metaheuristic algorithm has been proved after many combinations such as PSO-GP [35] and GA-PSO [34] were proposed and tested. However, as far as the authors know, the combination of the SSA and Gaussian

process (GP) has not to be proposed and tried in predicting PPV.

This paper proposes a new machine learning model, namely, SSA-GP, the Gaussian process (GP) model was optimized by the salp swarm algorithm (SSA), and the modeling process and the application of using the SSA-GP to predict the blast-induced ground vibration were introduced. This is an innovative work as the SSA-GP has not been analyzed and tried in predicting PPV before. The model development process and this application will promote the application of the artificial technique in solving mining and geotechnical problems and will be helpful for blast-induced ground vibration controlling.

2. Materials and Methods

2.1. Collected Database. To develop a high-precision evaluation method, a database generated by Hudaverdi [37] was used here for constructing the empirical, ANN, SVR, GP, and SSA-GP model. A total of 88 sets of data were monitored at the Akdaglar Quarry in northern Istanbul, Turkey, and several parameters including burden (B), spacing (S), bench height (H), stemming (T), subdrilling (U), hole diameter (D), power factor (PF), the distance between the monitoring station and blasting point (D), the weight of explosive charge detonated per delay (W), and peak particle velocity (PPV) were recorded. Among these parameters, burden is the distance between each explosive charge or the distance between the explosive charge to free face. Spacing is the distance between the two blastholes in a row. Bench height is the distance from the surface to hole bottom. Stemming is the distance from the top of the charging section to the surface. Subdrilling is the distance from the bottom of the bench to the bottom of blasthole. Power factor means the explosive charge per cubic meter. After reviewing the study of Hudaverdi [37], the ratio of bench height to burden (H/B), the ratio of spacing to burden (S/B), the ratio of burden to hole diameter (B/D), the ratio of subdrilling to burden (U/B), the ratio of stemming to burden (T/B), power factor (PF), the distance between the monitoring station and blasting point (D), and the weight of explosive charge detonated per delay (W) were selected as the input variables, while PPV was selected as the output variable. To describe the collected database, a scatter plot which shows the data distribution using diagonal, the bivariate scatter plots using the bottom of diagonal, the correlation, and significance level using the top of diagonal was plotted as shown in Figure 1. It should be noted that the symbol of “***,” “**,” and “*” are, respectively, corresponding to the p values with the range of [0, 0.001], [0.001, 0.01], and [0.01, 0.05]. Meanwhile, the coefficient of relationship between the B/D and PF was found to be -0.91 , so PF was removed from the input variable after reviewing the study of Rovini et al. [38].

Before the model development, both the input variables and output variables should be scaled into the range of 0 to 1 for avoiding the effect of the variable with the large number on the variable with the small number [12]. After scaling, 80% of the database which is normally called training datasets will be utilized to train and validate the prediction

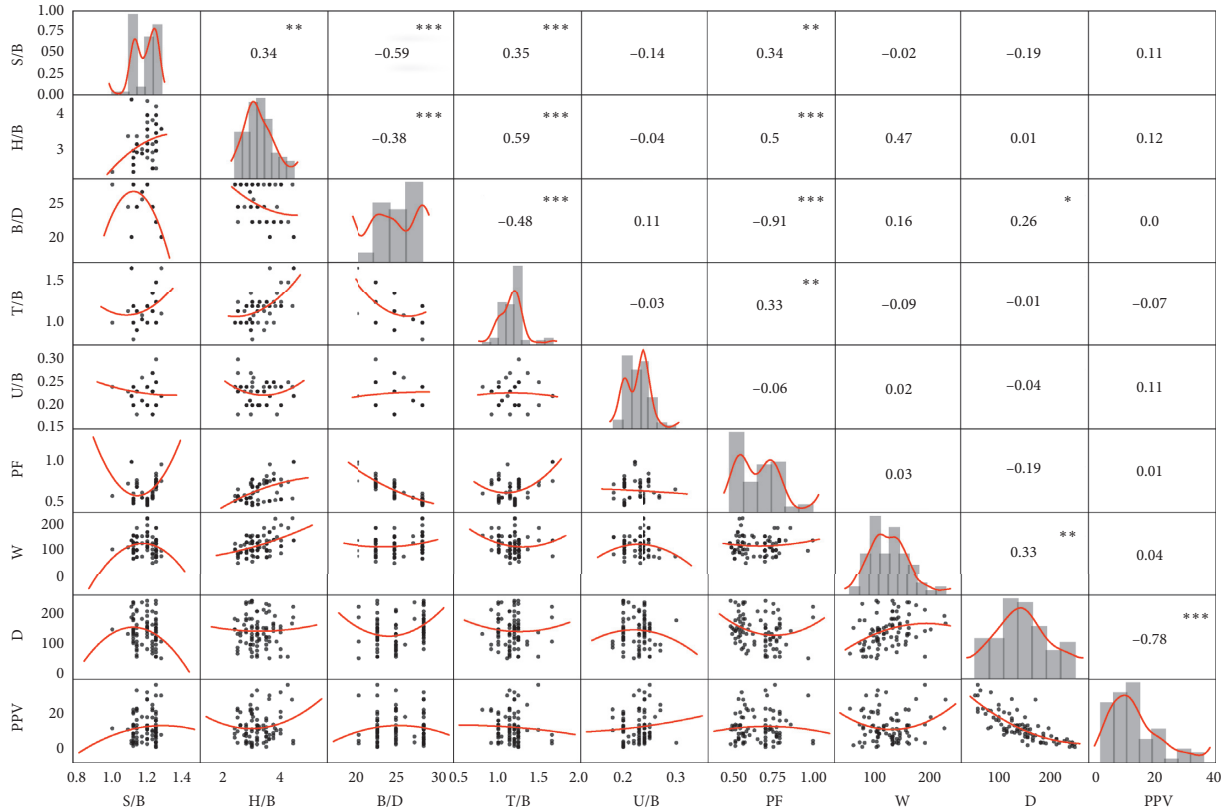


FIGURE 1: Scatter plot of the established database.

model, the remained 20% of the database which is normally called testing datasets will be used to check the model performance [39, 40], and the consistency of data distribution of these two datasets can reduce the impact of the data partitioning process on model performance.

2.2. Empirical Techniques. The empirical equation of the United States Bureau of Mines (USBM) [41, 42] is the most common and widely used technique for PPV prediction, and that equation can be described as

$$PPV = a \left(\frac{D}{\sqrt{W}} \right)^{-b}, \quad (1)$$

where a and b are the constants that are affected by the mine geology; D is the distance between the monitoring station and blasting point; and W is the weight of explosive charge detonated per delay.

In addition to the abovementioned empirical formula, two equations proposed by Davies et al. [43] and the Bureau of Indian Standard [44] were also selected.

Davies et al.:

$$PPV = aD^{-b}W^c. \quad (2)$$

Bureau of Indian Standard:

$$PPV = a \left(\frac{W}{D^{2/3}} \right)^b. \quad (3)$$

2.3. Artificial Neural Network (ANN). The ANN model is an important branch of the machine learning (ML) technique and is inspired by the human brain [45, 46]. With the help of computer calculation, many problems including blast-induced rock movement [47–49], blast-induced overpressure [50], rockburst [51], flyrock [52], and rock fragmentation [53, 54] can be solved by learning message from the input variables and using these messages to predict the output variables. After reviewing previous studies [55, 56], multi-layer perception (MLP) which is composed of input layers, hidden layers, and output layers is the best type of neural network among many artificial neural networks. In the multilayer perception model, the layer in the multilayer perception consists of one or more nodes, and the line between the nodes show the information exchange.

To train the neural network, an efficient learning algorithm should be selected. According to the study of Jahed Armaghani et al. [57], Dreyfus [58], and Pedrycz et al. [59], the back-propagation (BP) algorithm is the most competent learning algorithm for MLP neural networks. During the process of the BP algorithm, the message learned from the input variables is used to predict the output variables, then the predicted values of the output variable will be compared with the actual values, and the error will be calculated [60]. After that, the error will be sent back for updating the individual weights in the neural network, and that process will be repeated until the error of the predict value and actual value reach a defined level [61].

2.4. Support Vector Regression (SVR). SVR was successfully applied in solving engineering problems including hydrocarbon reservoir prediction [62], the thermal conductivity of frozen soil prediction [63], and rock mass parameter [64] prediction. That algorithm is developed from the statistical learning theory, and the input variables were reflected into a high-dimensional space by using the kernel function [65, 66].

The kernel function provided by support vector regression (SVR) mainly includes three types such as the linear kernel, polynomial kernel, and radial primary kernel function [67]. Among these kernel functions, the radial primary kernel function was found to be the most efficient kernel function for higher predictive performance [68].

2.5. SSA-GP

2.5.1. Salps Swarm Algorithm (SSA). Normally, the hyperparameter of the prediction model such as ANN, RF, SVR, and GP is obtained from the trial-and-error method, but this method is time consuming and it is hard to find the optimal hyperparameter combination when there are several in the prediction model. The emergence of a metaheuristic algorithm provides a good way to solve this problem, and by using these algorithms, the optimal hyperparameter combination can be found after hundreds of iterations. In this area, many metaheuristic algorithms were inspired by the natural phenomenon such as animal behavior (Harris Hawks Optimization Algorithm (HHO) [69], Grey Wolf Optimizer Algorithm (GWO) [70, 71], etc.) and evolutionary behavior (Differential Evolution Algorithm (DE) [72], Genetic Algorithm (GA) [73, 74], etc.). The salp swarm algorithm is a metaheuristic algorithm inspired by the behavior of the salp swarm in the ocean [31]. Like the behavior of jellyfish, the salp moves forward by pumping water from the salp body. Meanwhile, the salp always forms a swarm in the deep ocean, and some research studies [31, 75] show that the swarm behavior (shown in Figure 2) of the salp can help the salp determine the location of food resource fastly and accurately. According to the research of Mirjalili et al. [31], Faris et al. [76], and Sayed et al. [77], the salp chains consist of a leader salp (the first salp in the salp chain) and follower salps (rest of the salps in the salp chain). The lead salp controls the moving direction, and the follower salps will follow the leader salp during the movement of the salp chain.

The updating rule of the position of the leader and follower salp is given by [31]

$$x_j^1 = \begin{cases} F_j + c_1((ub_j - lb_j)c_2 + lb_j), & c_3 \geq 0, \\ F_j - c_1((ub_j - lb_j)c_2 + lb_j), & c_3 < 0, \end{cases} \quad (4)$$

with

$$c_1 = 2 \exp\left(-\left(\frac{4l}{L}\right)^2\right), \quad (5)$$

where x_j^1 and F_j are, respectively, the position of the leader salp in the salp chain and the position of food resource; ub_j and lb_j are, respectively, the upper bound and lower bound

of j^{th} dimensional; c_1 , c_2 , and c_3 are random numbers; and l and L are, respectively, the current and maximum number of iteration.

After obtaining the position of the leader salp in the salp chain, the position of the following salps can be expressed as follows:

$$x_j^i = \frac{1}{2}(x_j^i + x_j^{i-1}), \quad (6)$$

where x_j^i represents the position of i^{th} salp in the j dimension and i is the number greater than or equal to 2.

2.5.2. Gaussian Process (GP). The Gaussian process (GP) can find a relationship between the input variable value and the output variable value of the training datasets, and the predicted output variable value of the testing datasets can be calculated using the created relationship. According to the study of Yu et al. [35], Arthur et al. [79], and Fang et al. [36], a GP model can be determined by the mean function $m(x)$ and covariance function $k(x, x')$, and that model $f(x)$ is defined as follows:

$$f(x) \sim \text{GP}(m(x), k(x, x')), \quad (7)$$

subjected to

$$\begin{cases} m(x) = E[f(x)], \\ k(x, x') = E\{[f(x) - m(x)][f(x') - m(x')]\}. \end{cases} \quad (8)$$

Assume $D = (x_i, y_i)$ is the training dataset of the Gaussian model, where x_i and y_i are, respectively, the input and output vector.

Then, the standard linear regression model is determined using the following formula:

$$y = f(X) + \varepsilon, \quad (9)$$

where ε is an independent random variable, $\varepsilon \sim N(0, \sigma_n^2)$, where σ_n is the variance.

Given the new testing input x^* and the training set D , the goal of the GP model is to calculate the y^* using the posterior probability formula.

The parameters in the mean function $m(x)$ and covariance function $k(x, x')$ constitute the hyperparameters of the Gaussian process model, which are the only parameters to be determined in the Gaussian process.

2.5.3. Hybrid of the SSA and GP. During the development of the GP model, the combination of hyperparameters is a very important issue for achieving higher predictive performance. Normally, the optimal combination of hyperparameters in the Gaussian process was found by using the conjugate gradient algorithm, but it is easy to fall into local optimum and that algorithm is strongly dependent on the initial value.

After scaling the collected datasets into the range of 0 to 1, the collected database will be randomly split into the training (80%) and testing datasets (20%). The SSA algorithm was used to find the optimal combination of

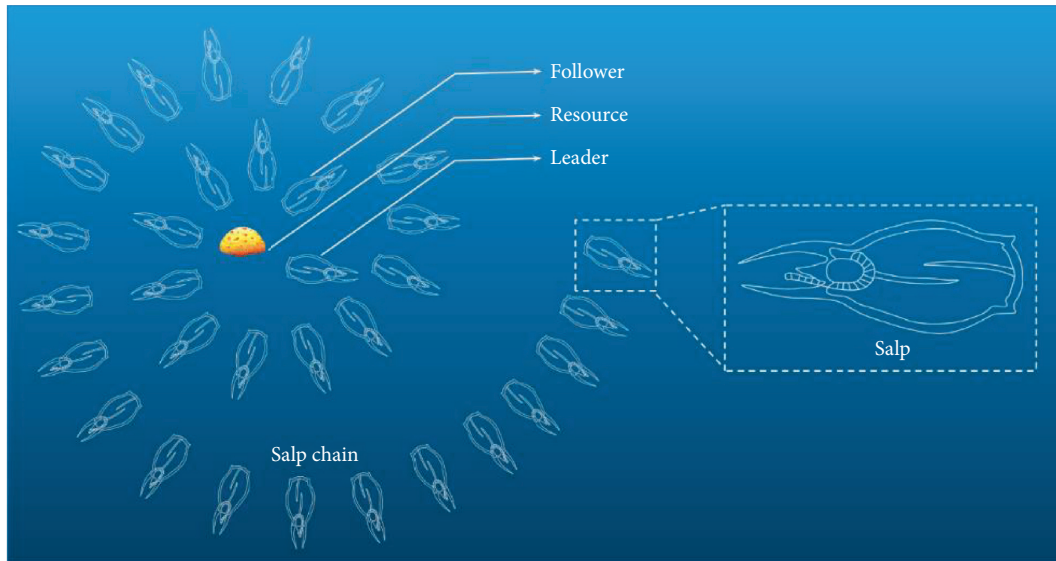


FIGURE 2: Swarm behavior of the slaps in the deep ocean (picture of the salp modified from [78]).

hyperparameters by learning knowledge from training datasets, and the obtained hyperparameter combination will be used to establish the optimal GP model (see Figure 3). In this process, the 10-fold cross-validation method was applied to calculate the fitness value for hyperparameter searching and optimal GP model development. During the 10-fold cross-validation method, the training datasets were split into 10 folds; 9 of them will be utilized to develop the prediction model, and the remained one will be used to test the performance of that model. After 10 runs, each dataset will have the opportunity to be learned and tested, and the overfitting and underfitting phenomenon can be avoided. Finally, the testing datasets will be used to evaluate the established optimal GP model by using performance evaluation metrics.

In this study, the blast-induced ground vibration models were developed in the MATLAB environment, and the computation code was programmed using MATLAB language and implemented on the computer with Intel (R) Core (TM) i7-7500U CPU running at 2.70 GHz and 2.90 GHz.

3. Results and Discussion

3.1. Results of Empirical Models. For the empirical model, two constants are determined by using the MATLAB code based on 70 training datasets which are the same as those used in the proposed ANN, SVR, GP, and SSA-GP model. After regressing, these fitted equations were obtained and are as follows:

$$PPV = 167.8 \times \left(\frac{D}{\sqrt{W}} \right)^{-0.9846}, \quad (10)$$

$$PPV = 370.6 \times D^{-1.21} \times W^{0.5221}, \quad (11)$$

$$PPV = 1.901 \times \left(\frac{W}{D^{2/3}} \right)^{1.215}. \quad (12)$$

After formula regression, the testing datasets (18 blasting datasets) were predicted using the abovementioned evolution formula, the model performance of equation (10) was found to be an R^2 of 0.64 and 0.67, RMSE of 4.92 and 3.94, and VAF of 70.45 and 75.36, the model performance of equation (11) was found to be an R^2 of 0.70 and 0.75, RMSE of 4.44 and 3.43, and VAF of 70.44 and 74.74, and the model performance of equation (12) was found to be an R^2 of 0.46 and 0.47, RMSE of 6.00 and 4.97, and VAF of 45.92 and 47.67.

3.2. Results of the ANN Model. To check the performance of using the ANN model to forecast the peak particle velocity, various ANN models should be built for optimal ANN model development. In the ANN model, the number of hidden layers and hidden nodes significantly affect the model performance due to the different weights and biases. An ANN model with too many hidden layers and hidden nodes may lead to the excessive learning of the training datasets, while too few of them will lead the ANN model to not be able to effectively learn the knowledge from the training datasets. Here, we constructed 17 ANN models with 1 hidden layer and a different number of hidden nodes ranging from 1 to 17 after following the suggestion of Mohamad et al. [80] and Hecht-Nielsen [81]. With the help of the 10-fold cross-validation method, an ANN model with 1 hidden layer and 3 hidden neurons in this hidden layer shows the best results (R^2 of 0.85 and 0.83, RMSE of 3.14 and 2.78, and VAF of 85.29 and 83.86 for training and testing datasets) and determined as the prediction model to evaluate peak particle velocity in this research.

3.3. Results of the SVR Model. Similar to the development of the ANN model, the blast datasets were converted, and then, a grid search method (GSM) was used to search the optimal hyperparameter combination for PPV prediction. In the SVR

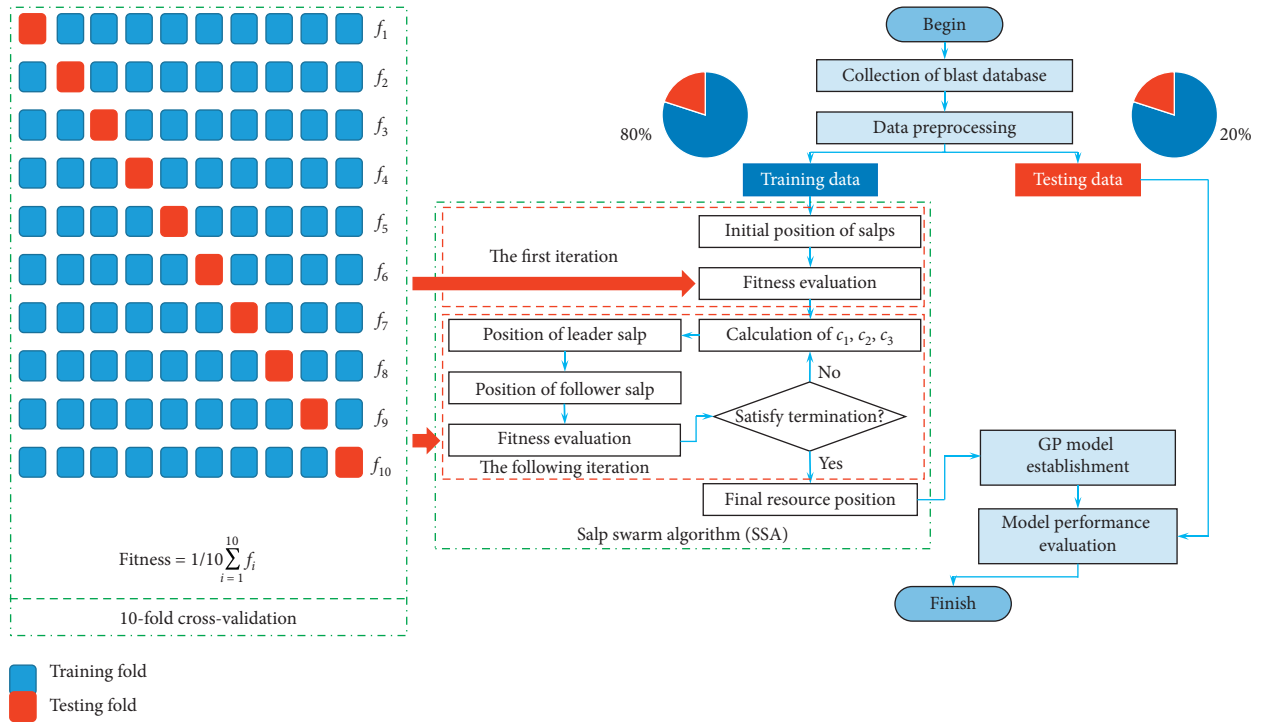


FIGURE 3: Flowchart of the SSA-GP model.

model, two hyperparameters including penalty factor (C) and gamma (g) in the RBF kernel should be determined. Here, the search scope of $\log_2(C)$ and $\log_2(g)$ are -10.0 to 10.0 , the cross-validation method was applied to guide hyperparameter selection, and the hyperparameter is optimal when the fitness value is the smallest. As a result, the optimal combination of C and g was found with $C = 10.556$ and $g = 0.435$. It is found that the R^2 values are 0.87 and 0.84 , the RMSE values are 2.91 and 2.71 , and the VAF values are 87.32 and 84.34 for training and testing datasets, respectively.

3.4. Results of the GP Model. Using the conjugate gradient algorithm, the hyperparameter combination of an original Gaussian process model was searched after learning knowledge from the training datasets. After training, the Gaussian process model yielded a prediction performance of $R^2 = 0.86$, RMSE = 3.00 , and VAF = 86.46 for training datasets and $R^2 = 0.87$, RMSE = 2.43 , and VAF = 87.40 for testing datasets.

3.5. Results of the SSA-GP Model. For developing the SSA-GP model, the number of salps in the salp chain and the maximum iteration should be determined first. Then, 9 SSA-GP models with the number of salps ranging from 20 to 300 and maximum iteration of 500 were established, the fitness curve calculated from the 10-fold cross-validation method of each SSA-GP model was recorded, and the hyperparameter combination is the best when the fitness value is smallest. After setting parameters for the SSA algorithm, the salps find the optimal location for the GP models with the corresponding parameters. Model results show that the number

of salps does not have a significant effect on the fitness curve, and then, 20 and 500 were selected to be the optimal number of salps and a maximum number of iterations.

After determining the hyperparameters of the SSA-GP model, the optimal SSA-GP model was established and evaluated by using R^2 , RMSE, and VAF. After predictive performance evaluation, the results show that the measured PPV values agree well with the predicted PPV values with $R^2 = 0.88$, RMSE = 2.78 , and VAF = 88.38 for the training datasets and $R^2 = 0.89$, RMSE = 2.25 , and VAF = 89.37 for testing datasets.

3.6. Performance of Various Models. For the comparison of the model performance, three performance metrics including R^2 , RMSE, and VAF were applied, and a prediction model can be considered as the best model when $R^2 = 1$, RMSE = 0 , and VAF = 100 . Meanwhile, the value of these performance metrics can be calculated using the following formula [32, 82–87]:

$$R^2 = 1 - \frac{\sum_{i=1}^N (y - y_{\text{pre}})^2}{\sum_{i=1}^N (y - \bar{y})^2}, \quad (13)$$

$$\text{RMSE} = \sqrt{\sum_{i=1}^N \frac{(y - y_{\text{pre}})^2}{N}}, \quad (14)$$

$$\text{VAF} = 100 \times \left(1 - \frac{\text{var}(y - y_{\text{pre}})}{\text{var}(y_{\text{pre}})} \right), \quad (15)$$

where N , \bar{y} , y , and y_{pre} are the number of datasets, the average PPV values, the actual PPV values, and the predicted PPV values, respectively.

Besides the statistical criteria shown above, the Akaike Information Criterion (AIC) and Schwarz Bayesian Criterion (SBC) were also utilized after reviewing the study of Agoubi and Kharroubi [88] and Phiri et al. [89].

$$\begin{aligned} \text{AIC} &= \ln \left[\sum_{i=1}^N \frac{\varepsilon_i^2}{N} \right] + \frac{2k}{N}, \\ \text{SBC} &= \ln \left[\sum_{i=1}^N \frac{\varepsilon_i^2}{N} \right] + k \ln \frac{(N)}{N}, \end{aligned} \quad (16)$$

where ε is the residual value and k is the number of estimated coefficients.

For comparing the prediction performance of the empirical model 1, empirical model 2, empirical model 3, ANN model, SVR model, GP model, and SSA-GP model, the datasets (88 measured PPV datasets) were compared with the 88 predicted PPV datasets, as shown in Figure 4. It shows that the predicted blast-induced ground vibration value obtained from the empirical model 1, empirical model 2, empirical 3, ANN model, SVR model, GP model, and SSA-GP model and the measured blast-induced ground vibration shows the same data distribution trend. Meanwhile, the errors between these measured 88 datasets and the predicted 88 PPV datasets obtained from the empirical model 1, empirical model 2, empirical 3, ANN model, SVR model, GP model, and SSA-GP model were plotted in Figure 5. It can be seen that error of the SSA-GP in each sample is smaller. The performance shows that the predicted PPV values provided by SSA-GP are closer to the measured PPV values than the PPV values provided by the other 6 prediction models, while the difference between the measured PPV value and the value predicted by the empirical model 3 is the biggest.

By comparing the results shown in Table 1, the proposed SSA-GP model yield better prediction performance in PPV prediction due to the higher R^2 and VAF value, lower RMSE value, and higher summing ranking value obtained from the ranking method proposed by Zorlu et al. [90]. Meanwhile, the prediction performance of empirical model 3 is the worst among these 7 prediction models. Notably, the VAF value of the empirical model 3 in PPV prediction was only 45.92 and 47.67 for training datasets and testing datasets, whereas these values of the proposed SSA-GP model were 88.38 and 89.37. The values of those performance metrics prove that the proposed SSA-GP model is the most dominant model for PPV prediction.

Also, the PPV value compassion shown in Figure 6 expresses that the errors between the actual PPV value and the value predicted by the SSA-GP model are smaller, which also means that the difference between actual PPV values and the predicted values obtained from the ANN model, SVR model, GP model, empirical model 1, empirical model 2, and empirical model 3 is greater. Besides the prediction model provided in this study, the same database was studied by Hudaverdi [37] using multivariate analysis, and the prediction performance of SSA-GP was found to be superior.

Besides R^2 , RMSE, and VAF, the AIC and SBC values were also calculated using equations (12) and (13), the AIC value of the empirical model 1, empirical model 2, empirical model 3, ANN, SVR, GP, and SSA-GP is 6.13, 1.04, -1.09, 2.45, 1.15, -2.80, and -3.46, and the BIC value of the empirical model 1, empirical model 2, empirical model 3, ANN, SVR, GP, and SSA-GP is 6.33, 1.23, -0.89, 2.65, 1.35, -2.60, and -3.26, respectively. Normally, the smaller the AIC and SBC value, the better the suitability of the prediction model. Therefore, SSA-GP was found to be the best prediction model among these 7 models.

The run time of developing a prediction model was recorded to check the time complexity of the prediction model. In this investigation, the run time from data preprocessing to dataset prediction was recorded, and the run time of the ANN model, SVR model, GP model, and SSA-GP model was 0.20, 31.57, 0.46, and 405.24 seconds, respectively. It is found that the SVR model and SSA-GP model take a longer time than ANN model and GP model, and the reason for this is that the hyperparameter optimization process of the SVR model and SSA-GP model was contained in the model development process. Although more time needs to be used in SSA-GP development, it can be accepted when comparing with the model performance improvement.

3.7. Performance of Dependency Analysis. After model development and performance comparison, a performance dependency analysis was carried out to analyze the effect of the number of training datasets (NTD) on the model performance. In this analysis, 7 ANN models, 7 SVR models, 7 GP models, and 7 SSA-GP models with the NTD equal to 10, 20, 30, 40, 50, 60, and 70 were developed, and 10 unused datasets in the collected database were used to check the model performance. It can be seen from Figure 7 that the prediction accuracy evaluated by the R^2 value of these models gradually increases and finally tend to be stable when NTD is large than 40. This phenomenon shows that the developed prediction model can provide stable results when used in the engineering site.

3.8. Sensitivity Analysis. To identify the most sensitive parameter, a sensitivity analysis was carried out and a cosine amplitude method [91] was utilized. In this method, the sensitive value is 0 when that variable is least important and is 1 when that variable is most important. After calculating, the sensitive value of the ratio of bench height to burden (H/B), the ratio of spacing to burden (S/B), the ratio of burden to hole diameter (B/D), the ratio of subdrilling to burden (U/B), the ratio of stemming to burden (T/B), the distance between the monitoring station and blasting point (D), and the weight of explosive charge detonated per delay (W) is 0.8519, 0.8503, 0.8459, 0.8379, 0.8514, 0.8249, and 0.6712, respectively. The results show that the ratio of bench height to burden (H/B) is the most sensitive parameter among these variables. Meanwhile, there is little difference between the ratio of bench height to burden (H/B), the ratio of spacing to burden (S/B), the ratio of burden to hole diameter (B/D), the ratio of subdrilling to burden (U/B), the ratio of stemming to

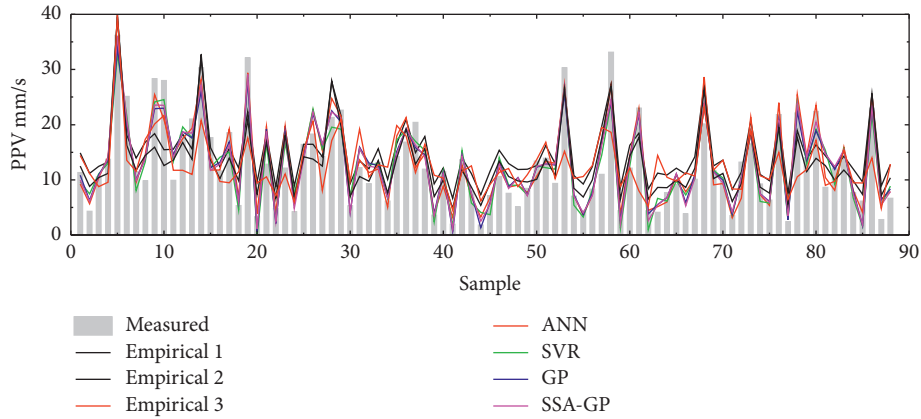


FIGURE 4: Measured and predicted PPV value obtained from various models.

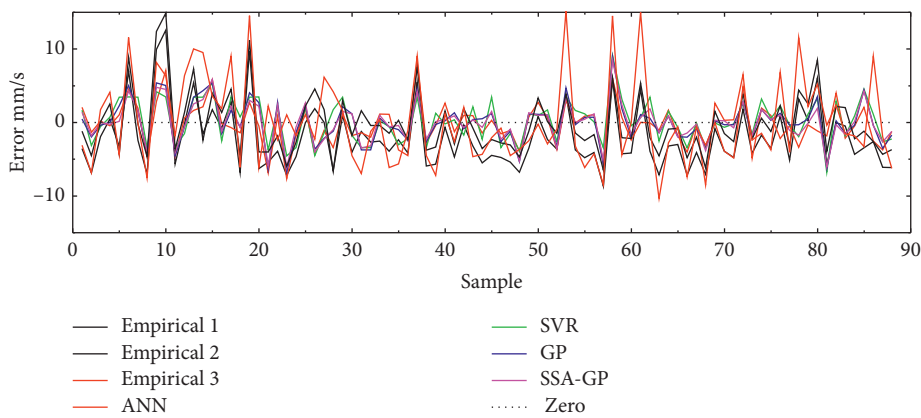


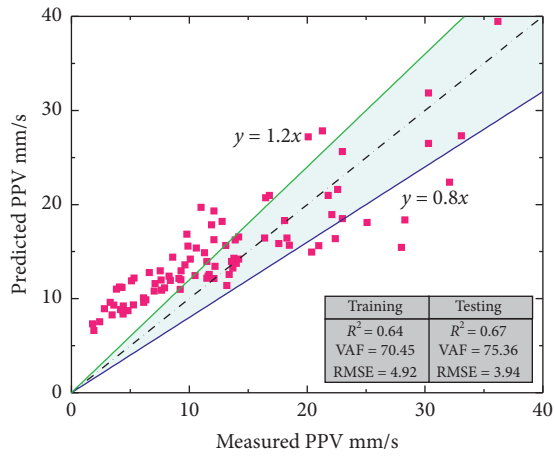
FIGURE 5: Errors between measured and predicted PPV values.

TABLE 1: Model performance of various models.

	Train			Test			Sum
	R^2	RMSE	VAF	R^2	RMSE	VAF	
Empirical 1	0.64	4.92	70.45	0.67	3.94	75.36	—
Empirical 2	0.70	4.44	70.44	0.75	3.43	74.74	—
Empirical 3	0.46	6.00	45.92	0.47	4.97	47.67	—
ANN	0.85	3.14	85.29	0.83	2.78	83.86	—
SVR	0.87	2.91	87.32	0.84	2.71	84.34	—
GP	0.86	3.00	86.46	0.87	2.43	87.40	—
SSA-GP	0.88	2.78	88.38	0.89	2.25	89.37	—
Empirical 1	2	2	3	2	2	3	14
Empirical 2	3	3	2	3	3	2	16
Empirical 3	1	1	1	1	1	1	6
ANN	4	4	4	4	4	4	28
SVR	6	6	6	5	5	5	33
GP	5	5	5	6	6	6	33
SSA-GP	7	7	7	7	7	7	42

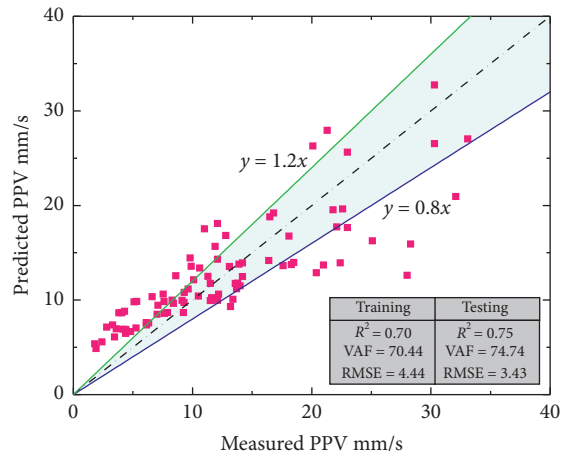
burden (T/B), and the distance between the monitoring station and blasting point (D). Normally, the distance between the monitoring station and blasting point (D) and the weight of explosive charge detonated per delay (W) were considered in the empirical prediction model, but the sensitivity analysis shows that more variables should be considered in future investigation.

3.9. *Superiority and Limitations.* After studying, a novel SSA-GP model was proposed and utilized to predict the blast-induced ground vibration caused by blast operation in Akdaglar Quarry. This method is inexpensive and has high precision, and the related modeling process of SSA-GP can guide the development of other hybrid models. Compared with three empirical prediction models, ANN model, and



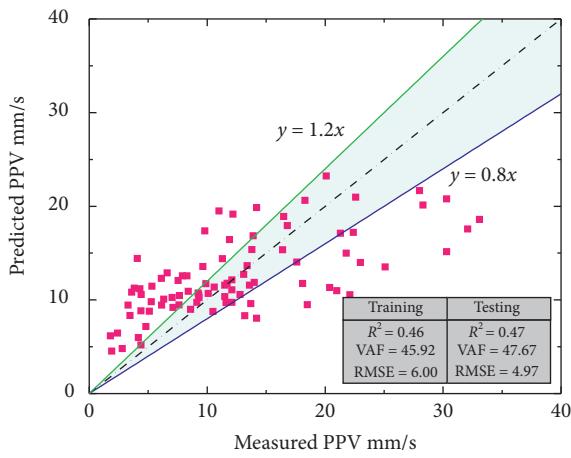
■ Empirical model
 - - - Ideal fit

(a)



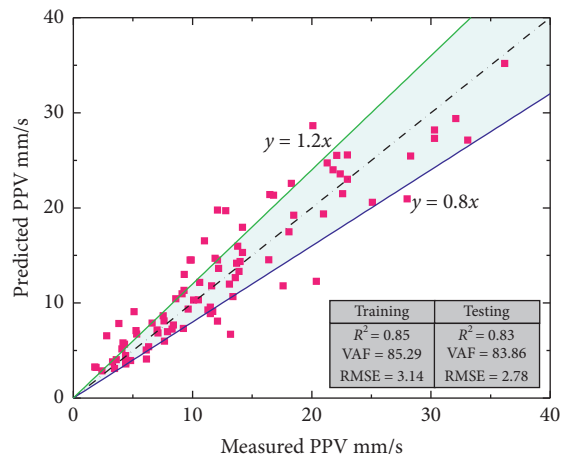
■ Empirical model
 - - - Ideal fit

(b)



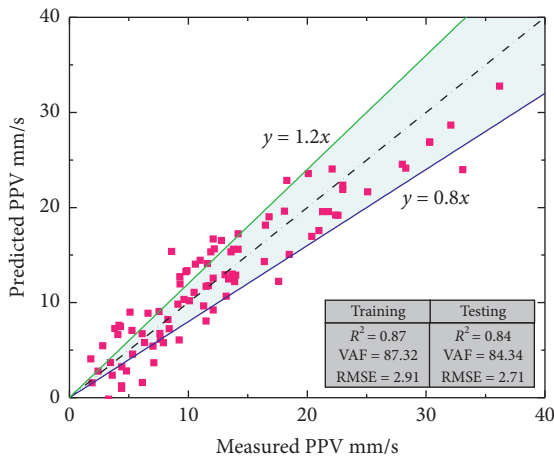
■ Empirical model
 - - - Ideal fit

(c)



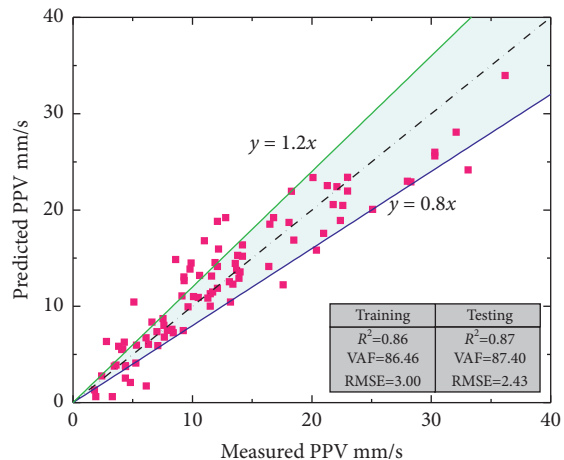
■ ANN
 - - - Ideal fit

(d)



■ SVR
 - - - Ideal fit

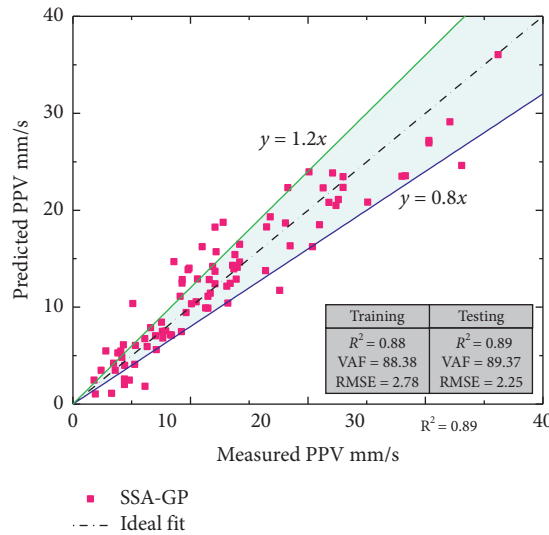
(e)



■ GP
 - - - Ideal fit

(f)

FIGURE 6: Continued.



(g)

FIGURE 6: Measured versus predicted PPV value: (a) empirical model 1; (b) empirical model 2; (c) empirical model 3; (d) ANN model; (e) SVR model; (f) GP model; and (g) SSA-GP model.

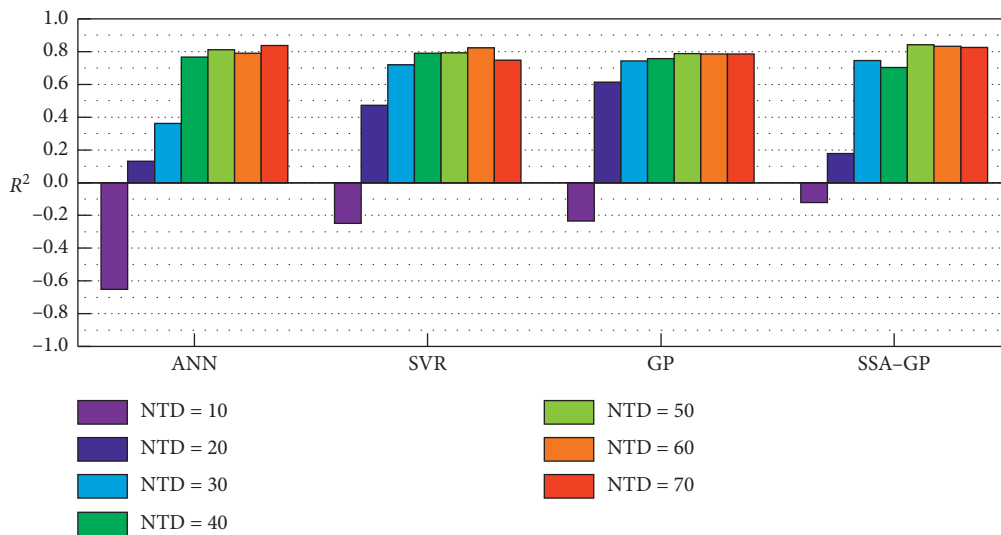


FIGURE 7: Performance dependency analysis results.

SVM model, the proposed SSA-GP model can accurately predict the blast-induced ground vibration, and the accuracy of that model can be easily improved by enlarging the collected database or collecting more variables.

Although some achievements have been obtained, some limitations were also found and should be considered in future investigations. First, the developed SSA-GP model in this study is a black box method and may be difficult for mining engineers when comparing with an explicit equation. Then, only a small database with 88 datasets and 9 variables was collected from the previous study, which may affect the precision of the developed model and the sensitivity analysis results. Meanwhile, the use of the ratio of two parameters and the lack of consideration of geology and explosive parameters may make the prediction a bias, so these

problems should be considered in future investigations. So, the collection of a bigger database with more datasets and more variables such as rock type and detonation delay time can be considered in future investigation. Also, developing an SSA-GP model needs more time when comparing with the ANN, SVR, and GP model, but it is meaningful. Last, only the GP model was optimized by the SSA in this paper. Although the SSA is a newly proposed metaheuristic algorithm and the optimization performance was proved when comparing with PSO, GSA, BA, FA, and GA, in the previous study, a more detailed comparison of using the SSA to optimize the hyperparameters of the prediction model such as the ANN, SVR, or RF or the comparison of using the different metaheuristic algorithm to optimize the GP model is meaningful.

As a machine learning model, the development of the prediction model is based on the collected database, so the developed SSA-GP model is only suitable for Akdaglar Quarry. But, the mining engineers in other mines can use the modeling process provided in this paper for developing their prediction model. Nevertheless, this study is a powerful supplement to the blast-induced ground vibration prediction and can be utilized to control the blast-induced hazard.

4. Conclusions

For an open-pit mine, blasting is a very important part of the mining process, and the quality of blasting has a significant impact on the mining economy. However, some unwanted effects, especially blast-induced vibration, can usually be found due to the wasting of explosive energy and lead to safety risks to the surrounding resident's lives and buildings. It is, therefore, stated that the high-precision prediction of peak particle velocity (PPV) is meaningful and can provide help for both mining engineers and the government.

For the easy-operated, inexpensive, and accurate blast-induced ground vibration determination, a hybrid SSA-optimized GP-based model, namely, SSA-GP, was proposed based on an 88-dataset database. During the model development process, the training datasets (70 datasets) were learned with the help of the 10-fold cross-validation method and SSA optimization method, then the testing datasets (18 datasets) were predicted, and the performance was checked using some performance metrics. Then, its performance was analyzed and compared with the empirical, ANN, SVR, and GP models. The comparison results show that the proposed SSA-GP yields the promising reliability with an R^2 of 0.88 and 0.89, RMSE of 2.78 and 2.25, and VAF of 88.38 and 89.37 for training and testing datasets and the smallest AIC and SBC value. Performance dependency analysis results show that the developed prediction model can provide a stable prediction performance when forecasting the unused datasets. Sensitivity analysis shows that more parameters should be considered in the future empirical prediction model development rather than the explosive charge of each delay and the distance from the blast block to the monitoring station. Through the acquired results, the superior optimization ability of the SSA was verified, and that algorithm has the potential to be applied in other prediction issues.

Data Availability

Previously reported data were used to support this study and are available at [10.1016/j.soildyn.2012.08.002]. These prior studies (and datasets) are cited at relevant places within the text as references.

Conflicts of Interest

The authors declare that there are no conflicts of interest regarding the publication of this paper.

References

[1] M. Khandelwal and T. N. Singh, "Prediction of blast-induced ground vibration using artificial neural network,"

- International Journal of Rock Mechanics and Mining Sciences*, vol. 46, no. 7, pp. 1214–1222, 2009.
- [2] M. Hasanipanah, M. Monjezi, A. Shahnazar, D. Jahed Armaghani, and A. Farazmand, "Feasibility of indirect determination of blast induced ground vibration based on support vector machine," *Measurement*, vol. 75, pp. 289–297, 2015.
- [3] M. Hasanipanah, R. Naderi, J. Kashir, S. A. Noorani, and A. Zeynali Aaq Qaleh, "Prediction of blast-produced ground vibration using particle swarm optimization," *Engineering with Computers*, vol. 33, no. 2, pp. 173–179, 2017.
- [4] H. Nguyen, X.-N. Bui, Q.-H. Tran, T.-Q. Le, N.-H. Do, and L. T. T. Hoa, "Evaluating and predicting blast-induced ground vibration in open-cast mine using ANN: a case study in Vietnam," *SN Applied Sciences*, vol. 1, p. 125, 2019.
- [5] K. A. L. Ramanathan and R. A. Abdullah, "Effects of quarry blasting towards the residential area at Kangkar Pulai, Johor, Malaysia," *Sains Malaysiana*, vol. 48, pp. 1583–1592, 2019.
- [6] Y. Azimi, S. H. Khoshrou, and M. Osanloo, "Prediction of blast induced ground vibration (BIGV) of quarry mining using hybrid genetic algorithm optimized artificial neural network," *Measurement*, vol. 147, Article ID 106874, 2019.
- [7] K. Taheri, M. Hasanipanah, S. B. Golzar, and M. Z. A. Majid, "A hybrid artificial bee colony algorithm-artificial neural network for forecasting the blast-produced ground vibration," *Engineering with Computers*, vol. 33, no. 3, pp. 689–700, 2017.
- [8] A. M. Rajabi and A. Vafae, "Prediction of blast-induced ground vibration using empirical models and artificial neural network (Bakhtiari Dam access tunnel, as a case study)," *Journal of Vibration and Control*, vol. 26, no. 7-8, pp. 520–531, 2020.
- [9] M. Khandelwal, "Blast-induced ground vibration prediction using support vector machine," *Engineering with Computers*, vol. 27, no. 3, pp. 193–200, 2011.
- [10] X. Zhang, H. Nguyen, X.-N. Bui et al., "Novel soft computing model for predicting blast-induced ground vibration in open-pit mines based on particle swarm optimization and XGBoost," *Natural Resources Research*, vol. 29, no. 2, pp. 711–721, 2020.
- [11] M. Saadat, M. Khandelwal, and M. Monjezi, "An ANN-based approach to predict blast-induced ground vibration of Gol-E-Gohar iron ore mine, Iran," *Journal of Rock Mechanics and Geotechnical Engineering*, vol. 6, no. 1, pp. 67–76, 2014.
- [12] J. Zhou, X. Li, and X. Shi, "Long-term prediction model of rockburst in underground openings using heuristic algorithms and support vector machines," *Safety Science*, vol. 50, no. 4, pp. 629–644, 2012.
- [13] J. Zhou, X. Li, and H. S. Mitri, "Classification of rockburst in underground projects: comparison of ten supervised learning methods," *Journal of Computing in Civil Engineering*, vol. 30, no. 5, 2016.
- [14] J. Zhou, X. Li, and H. S. Mitri, "Evaluation method of rockburst: state-of-the-art literature review," *Tunnelling and Underground Space Technology*, vol. 81, pp. 632–659, 2018.
- [15] K. Sevgen, G. Kocaman, Nefeslioglu, and Gokceoglu, "A novel performance assessment approach using photogrammetric techniques for landslide susceptibility mapping with logistic regression, ANN and random forest," *Sensors*, vol. 19, no. 18, p. 3940, 2019.
- [16] R.-P. Chen, P. Zhang, X. Kang, Z.-Q. Zhong, Y. Liu, and H.-N. Wu, "Prediction of maximum surface settlement caused by earth pressure balance (EPB) shield tunneling with ANN methods," *Soils and Foundations*, vol. 59, no. 2, pp. 284–295, 2019.

- [17] M. R. Moghaddasi and M. Noorian-Bidgoli, "ICA-ANN, ANN and multiple regression models for prediction of surface settlement caused by tunneling," *Tunnelling and Underground Space Technology*, vol. 79, pp. 197–209, 2018.
- [18] X. Zhou, D. J. Armaghani, J. Ye, M. Khari, and M. R. Motahari, "Hybridization of parametric and non-parametric techniques to predict air over-pressure induced by quarry blasting," *Natural Resources Research*, vol. 30, no. 1, pp. 209–224, 2021.
- [19] S. F. F. Mojtahedi, I. Ebtehaj, M. Hasanipanah, H. Bonakdari, and H. B. Amnieh, "Proposing a novel hybrid intelligent model for the simulation of particle size distribution resulting from blasting," *Engineering with Computers*, vol. 35, no. 1, pp. 47–56, 2019.
- [20] C. K. Arthur, V. A. Temeng, and Y. Y. Ziggah, "Soft computing-based technique as a predictive tool to estimate blast-induced ground vibration," *Journal of Sustainable Mining*, vol. 18, pp. 287–296, 2019.
- [21] M. Monjezi, M. Ghafurikalajahi, and A. Bahrami, "Prediction of blast-induced ground vibration using artificial neural networks," *Tunnelling and Underground Space Technology*, vol. 26, no. 1, pp. 46–50, 2011.
- [22] G. Li, D. Kumar, P. Samui, H. Nikafshan Rad, B. Roy, and M. Hasanipanah, "Developing a new computational intelligence approach for approximating the blast-induced ground vibration," *Applied Sciences*, vol. 10, no. 2, p. 434, 2020.
- [23] H. Sheykhi, R. Bagherpour, E. Ghasemi, and H. Kalhori, "Forecasting ground vibration due to rock blasting: a hybrid intelligent approach using support vector regression and fuzzy C-means clustering," *Engineering with Computers*, vol. 34, no. 2, pp. 357–365, 2018.
- [24] A. Rana, N. K. Bhagat, G. P. Jadaun, S. Rukhaiyar, A. Pain, and P. K. Singh, "Predicting blast-induced ground vibrations in some Indian tunnels: a comparison of decision tree, artificial neural network and multivariate regression methods," *Mining, Metallurgy & Exploration*, vol. 37, no. 4, pp. 1039–1053, 2020.
- [25] M. Iphar, M. Yavuz, and H. Ak, "Prediction of ground vibrations resulting from the blasting operations in an open-pit mine by adaptive neuro-fuzzy inference system," *Environmental Geology*, vol. 56, no. 1, pp. 97–107, 2008.
- [26] S. Wahyudi, H. Shimada, G. M. Simangunsong et al., "A review study of predictive model blast vibration attenuation equation by using neural network as an evaluator," *International Journal of Mining, Reclamation and Environment*, vol. 25, no. 1, pp. 69–85, 2011.
- [27] A. Das, S. Sinha, and S. Ganguly, "Development of a blast-induced vibration prediction model using an artificial neural network," *Journal of Southern African Institute of Mining and Metallurgy*, vol. 119, pp. 187–200, 2019.
- [28] W. S. Iramina, E. C. Sansone, M. Wichers et al., "Comparing blast-induced ground vibration models using ANN and empirical geomechanical relationships," *REM—International Engineering Journal*, vol. 71, no. 1, pp. 89–95, 2018.
- [29] M. Mohammadnejad, R. Gholami, A. Ramezanzadeh, and M. Jalali, "Prediction of blast-induced vibrations in limestone quarries using support vector machine," *Journal of Vibration and Control*, vol. 18, no. 9, pp. 1322–1329, 2012.
- [30] J. Huang, M. Koopialipoor, and D. J. Armaghani, "A combination of fuzzy Delphi method and hybrid ANN-based systems to forecast ground vibration resulting from blasting," *Scientific Reports*, vol. 10, pp. 1–22, 2020.
- [31] S. Mirjalili, A. H. Gandomi, S. Z. Mirjalili, S. Saremi, H. Faris, and S. M. Mirjalili, "Salp swarm algorithm: a bio-inspired optimizer for engineering design problems," *Advances in Engineering Software*, vol. 114, pp. 163–191, 2017.
- [32] E. Li, J. Zhou, X. Shi et al., "Developing a hybrid model of salp swarm algorithm-based support vector machine to predict the strength of fiber-reinforced cemented paste backfill," *Engineering with Computers*, 2020.
- [33] A. Kandiri, E. Mohammadi Golafshani, and A. Behnood, "Estimation of the compressive strength of concretes containing ground granulated blast furnace slag using hybridized multi-objective ANN and salp swarm algorithm," *Construction and Building Materials*, vol. 248, Article ID 118676, 2020.
- [34] F. Zhu, C. Xu, and G. Dui, "Particle swarm hybridize with Gaussian process regression for displacement prediction," in *Proceedings of the 2010 IEEE Fifth International Conference on Bio-Inspired Computing: Theories and Applications*, pp. 522–525, Changsha, China, September 2010.
- [35] Z. Yu, X. Shi, J. Zhou, R. Huang, and Y. Gou, "Advanced prediction of roadway broken rock zone based on a novel hybrid soft computing model using Gaussian process and particle swarm optimization," *Applied Sciences*, vol. 10, no. 17, p. 6031, 2020.
- [36] D. Fang, X. Zhang, Q. Yu, T. C. Jin, and L. Tian, "A novel method for carbon dioxide emission forecasting based on improved Gaussian processes regression," *Journal of Cleaner Production*, vol. 173, pp. 143–150, 2018.
- [37] T. Hudaverdi, "Application of multivariate analysis for prediction of blast-induced ground vibrations," *Soil Dynamics and Earthquake Engineering*, vol. 43, pp. 300–308, 2012.
- [38] E. Rovini, C. Maremmanni, A. Moschetti, D. Esposito, and F. Cavallo, "Comparative motor pre-clinical assessment in Parkinson's disease using supervised machine learning approaches," *Annals of Biomedical Engineering*, vol. 46, no. 12, pp. 2057–2068, 2018.
- [39] J. Zhou, E. Li, S. Yang et al., "Slope stability prediction for circular mode failure using gradient boosting machine approach based on an updated database of case histories," *Safety Science*, vol. 118, pp. 505–518, 2019.
- [40] J. Zhou, Y. Qiu, S. Zhu, D. Jahed Armaghani, M. Khandelwal, and E. Tonnizam Mohamad, "Estimating TBM advance rate in hard rock condition using XGBoost and Bayesian optimization," *Underground Space*, 2020.
- [41] W. I. Duvall and B. Petkof, *Spherical Propagation of Explosion-Generated Strain Pulses in Rock*, US Department of the Interior, Bureau of Mines, Washington, DC, USA, 1959.
- [42] W. I. Duvall and D. E. Fogelson, "Review of criteria for estimating damage to residences from blasting vibrations," Report Investigation, vol. 5968, p. 19, US Department of the Interior, Bureau of Mines, Washington, DC, USA, 1962.
- [43] B. Davies, I. W. Farmer, and P. B. Attewell, "Ground vibration from shallow sub-surface blasts," *Engineer*, vol. 217, pp. 553–559, 1964.
- [44] Indian Standard, Criteria for Safety and Design of Structures Subjected to Underground Blast, ISI Bull IIS-69226, 1973.
- [45] R. Schalkoff, *Artificial Neural Networks*, vol. 1, McGraw-Hill, New York, NY, USA.
- [46] H. Chen, P. G. Asteris, D. J. Armaghani, B. Gordan, and B. T. Pham, "Assessing dynamic conditions of the retaining wall: developing two hybrid intelligent models," *Applied Sciences*, vol. 9, 2019.
- [47] Z. Yu, X. Shi, X. Qiu, J. Zhou, X. Chen, and Y. Gou, "Optimization of postblast ore boundary determination using a novel sine cosine algorithm-based random forest technique and Monte Carlo simulation," *Engineering Optimization*, vol. 0, pp. 1–16, 2020.

- [48] Z. Yu, X. Shi, J. Zhou et al., "Prediction of blast-induced rock movement during bench blasting: use of gray Wolf optimizer and support vector regression," *Natural Resources Research*, vol. 29, no. 2, pp. 843–865, 2020.
- [49] Z. Yu, X. Shi, J. Zhou et al., "Feasibility of the indirect determination of blast-induced rock movement based on three new hybrid intelligent models," *Engineering with Computers*, 2019.
- [50] H. Nguyen and X.-N. Bui, "Predicting blast-induced air overpressure: a robust artificial intelligence system based on artificial neural networks and random forest," *Natural Resources Research*, vol. 28, no. 3, pp. 893–907, 2019.
- [51] J. Zhou, M. Koopialipoor, E. Li, and D.J. Armaghani, "Prediction of rockburst risk in underground projects developing a neuro-bee intelligent system," *Bulletin of Engineering Geology and the Environment*, vol. 79, no. 8, pp. 4265–4279, 2019.
- [52] M. Koopialipoor, A. Fallah, D. J. Armaghani, A. Azizi, and E. T. Mohamad, "Three hybrid intelligent models in estimating flyrock distance resulting from blasting," *Engineering with Computers*, vol. 35, no. 1, pp. 243–256, 2019.
- [53] P. F. Asl, M. Monjezi, J. K. Hamidi, and D. J. Armaghani, "Optimization of flyrock and rock fragmentation in the Tajareh limestone mine using metaheuristics method of firefly algorithm," *Engineering with Computers*, vol. 34, no. 2, pp. 241–251, 2018.
- [54] E. Ebrahimi, M. Monjezi, M. R. Khalesi, and D. J. Armaghani, "Prediction and optimization of back-break and rock fragmentation using an artificial neural network and a bee colony algorithm," *Bulletin of Engineering Geology and the Environment*, vol. 75, no. 1, pp. 27–36, 2016.
- [55] E. T. Mohamad, D. J. Armaghani, E. Momeni, A. H. Yazdavar, and M. Ebrahimi, "Rock strength estimation: a PSO-based BP approach," *Neural Computing and Applications*, vol. 30, no. 5, pp. 1635–1646, 2018.
- [56] A. Ebrahimabadi, M. Azimpour, and A. Bahreini, "Prediction of roadheaders' performance using artificial neural network approaches (MLP and KOSFM)," *Journal of Rock Mechanics and Geotechnical Engineering*, vol. 7, no. 5, pp. 573–583, 2015.
- [57] D. Jahed Armaghani, E. Tonnizam Mohamad, M. Hajihassani, S. V. Alavi Nezhad Khalil Abad, A. Marto, and M. R. Moghaddam, "Evaluation and prediction of flyrock resulting from blasting operations using empirical and computational methods," *Engineering with Computers*, vol. 32, no. 1, pp. 109–121, 2016.
- [58] G. Dreyfus, *Neural Networks: Methodology and Applications*, Springer-Verlag, Berlin, Germany, 2005.
- [59] W. Pedrycz, A. Sillitti, and G. Succi, "Computational intelligence: an introduction," *Computational Intelligence and Quantitative Software Engineering*, vol. 617, pp. 13–31, 2016.
- [60] P. G. Asteris, A. K. Tsaris, L. Cavaleri et al., "Prediction of the fundamental period of infilled rc frame structures using artificial neural networks," *Computational Intelligence and Neuroscience*, vol. 2016, Article ID 5104907, 12 pages, 2016.
- [61] M. Koopialipoor, D. Jahed Armaghani, M. Haghghi, and E. N. Ghaleini, "A neuro-genetic predictive model to approximate overbreak induced by drilling and blasting operation in tunnels," *Bulletin of Engineering Geology and the Environment*, vol. 78, no. 2, pp. 981–990, 2019.
- [62] K. O. Akande, T. O. Owolabi, S. O. Olatunji, and A. AbdulRaheem, "A hybrid particle swarm optimization and support vector regression model for modelling permeability prediction of hydrocarbon reservoir," *Journal of Petroleum Science and Engineering*, vol. 150, pp. 43–53, 2017.
- [63] F. Q. Cui, W. Zhang, Z. Y. Liu et al., "Assessment for thermal conductivity of frozen soil based on nonlinear regression and support vector regression methods," *Advances in Civil Engineering*, vol. 2020, Article ID 8898126, 12 pages, 2020.
- [64] B. Liu, R. Wang, Z. Guan et al., "Improved support vector regression models for predicting rock mass parameters using tunnel boring machine driving data," *Tunnelling and Underground Space Technology*, vol. 91, Article ID 102958, 2019.
- [65] Y. Li, "LIBSVM-faruto ultimate version: a toolbox with implements for support vector machines based on LIBSVM," 2009.
- [66] V. Vapnik, *The Nature of Statistical Learning Theory*, Springer, New York, NY, USA, 1995.
- [67] H. Nguyen, Y. Choi, X.-N. Bui, and T. Nguyen-Thoi, "Predicting blast-induced ground vibration in open-pit mines using vibration sensors and support vector regression-based optimization algorithms," *Sensors (Switzerland)*, vol. 20, p. 132, 2020.
- [68] C. C. Chang and C. J. Lin, *LIBSVM: A Library for Support Vector Machines*, ACM, New York, NY, USA, 2011.
- [69] A. A. Heidari, S. Mirjalili, H. Faris, I. Aljarah, M. Mafarja, and H. Chen, "Harris hawks optimization: algorithm and applications," *Future Generation Computer Systems*, vol. 97, pp. 849–872, 2019.
- [70] S. Mirjalili, S. M. Mirjalili, and A. Lewis, "Grey wolf optimizer," *Advances in Engineering Software*, vol. 69, pp. 46–61, 2014.
- [71] A. Dehghanbanadaki, M. Khari, S. T. Amiri, and D. J. Armaghani, "Estimation of ultimate bearing capacity of driven piles in $c-\phi$ soil using MLP-GWO and ANFIS-GWO models: a comparative study," *Soft Computing*, vol. 25, no. 5, pp. 4103–4119, 2020.
- [72] R. Storn, "Differential evolution—a simple and efficient heuristic for global optimization over continuous spaces," *Journal of Global Optimization*, vol. 11, pp. 341–359, 1997.
- [73] D. Whitley, "A genetic algorithm tutorial," *Statistics and Computing*, vol. 4, pp. 65–85, 1994.
- [74] H. Harandizadeh and D. J. Armaghani, "Prediction of air-overpressure induced by blasting using an ANFIS-PNN model optimized by GA," *Applied Soft Computing*, vol. 99, Article ID 106904, 2021.
- [75] P. A. V. Anderson and Q. Bone, "Communication between individuals in salp chains. II. Physiology," *Proceedings of the Royal Society of London. Series B*, vol. 210, pp. 559–574, 1980.
- [76] H. Faris, M. M. Mafarja, A. A. Heidari et al., "An efficient binary Salp swarm algorithm with crossover scheme for feature selection problems," *Knowledge-Based Systems*, vol. 154, pp. 43–67, 2018.
- [77] G. I. Sayed, G. Khoriba, and M. H. Haggag, "A novel chaotic salp swarm algorithm for global optimization and feature selection," *Applied Intelligence*, vol. 48, no. 10, pp. 3462–3481, 2018.
- [78] N. Henschke, J. D. Everett, A. J. Richardson, and I. M. Suthers, "Rethinking the role of salps in the ocean," *Trends in Ecology & Evolution*, vol. 31, no. 9, pp. 720–733, 2016.
- [79] C. K. Arthur, V. A. Temeng, and Y. Y. Ziggah, "Novel approach to predicting blast-induced ground vibration using Gaussian process regression," *Engineering with Computers- With the help of computer calculation, many problems including blast-induce*, vol. 36, pp. 29–42, 2020.
- [80] E. T. Mohamad, D. Jahed Armaghani, E. Momeni, and S. V. Alavi Nezhad Khalil Abad, "Prediction of the unconfined compressive strength of soft rocks: a PSO-based ANN

- approach,” *Bulletin of Engineering Geology and the Environment*, vol. 74, no. 3, pp. 745–757, 2015.
- [81] R. Hecht-Nielsen, “Kolmogorov’s mapping neural network existence theorem,” in *Proceedings of the International Conference on Neural Networks*, pp. 11–14, IEEE Press, San Diego, CA, USA, 1987.
- [82] J. Zhou, Y. Qiu, D. J. Armaghani et al., “Predicting TBM penetration rate in hard rock condition: a comparative study among six XGB-based metaheuristic techniques,” *Geoscience Frontiers*, vol. 12, no. 3, Article ID 101091, 2021.
- [83] W. S. Barham, S. R. Rababah, H. H. Aldeeky, and O. H. Al Hattamleh, “Mechanical and physical based artificial neural network models for the prediction of the unconfined compressive strength of rock,” *Geotechnical and Geological Engineering*, vol. 38, no. 5, pp. 4779–4792, 2020.
- [84] D. Guha Roy and T. N. Singh, “Predicting deformational properties of Indian coal: soft computing and regression analysis approach,” *Measurement*, vol. 149, Article ID 106975, 2020.
- [85] J. Zhou, Y. Qiu, S. Zhu et al., “Optimization of support vector machine through the use of metaheuristic algorithms in forecasting TBM advance rate,” *Engineering Applications of Artificial Intelligence*, vol. 97, Article ID 104015, 2021.
- [86] P. G. Asteris and V. G. Mocos, “Concrete compressive strength using artificial neural networks,” *Neural Computing and Applications*, vol. 32, no. 15, pp. 11807–11826, 2020.
- [87] P. G. Asteris and M. Nikoo, “Artificial bee colony-based neural network for the prediction of the fundamental period of infilled frame structures,” *Neural Computing and Applications*, vol. 31, no. 9, pp. 4837–4847, 2019.
- [88] B. Agoubi and A. Kharroubi, “Groundwater depth monitoring and short-term prediction: applied to El Hamma aquifer system, southeastern Tunisia,” *Arabian Journal of Geosciences*, vol. 12, pp. 1–10, 2019.
- [89] M. Phiri, Y. A. Shiferaw, and S. G. Tesfamichael, “Biome-level relationships between vegetation indices and climate variables using time-series analysis of remotely-sensed data,” *GIScience & Remote Sensing*, vol. 57, no. 4, pp. 464–482, 2020.
- [90] K. Zorlu, C. Gokceoglu, F. Ocakoglu, H. A. Nefeslioglu, and S. Acikalin, “Prediction of uniaxial compressive strength of sandstones using petrography-based models,” *Engineering Geology*, vol. 96, no. 3-4, pp. 141–158, 2008.
- [91] Y. Yang and Q. Zhang, “A hierarchical analysis for rock engineering using artificial neural networks,” *Rock Mechanics and Rock Engineering*, vol. 30, no. 4, pp. 207–222, 1997.

Research Article

Experimental Study on Thermal Expansion Behavior of Concrete under Three-Dimensional Stress

Zhipeng Yu,^{1,2} Fan Zhang ,¹ Xiao Ma,^{2,3} Fujian Yang,^{2,3} Dawei Hu ,^{2,3} and Hui Zhou^{2,3}

¹School of Civil Engineering, Architecture and Environment, Hubei University of Technology, Wuhan, Hubei 430064, China

²State Key Laboratory of Geomechanics and Geotechnical Engineering, Institute of Rock and Soil Mechanics, Chinese Academy of Sciences, Wuhan 430071, China

³University of Chinese Academy of Sciences, Beijing 100049, China

Correspondence should be addressed to Fan Zhang; fanzhang@aliyun.com

Received 26 January 2021; Revised 1 March 2021; Accepted 1 March 2021; Published 9 March 2021

Academic Editor: Chi Yao

Copyright © 2021 Zhipeng Yu et al. This is an open access article distributed under the Creative Commons Attribution License, which permits unrestricted use, distribution, and reproduction in any medium, provided the original work is properly cited.

Concrete is widely used in underground engineering and bears three-dimensional stress transmitted by overlying load. When a fire occurs, the thermal expansion of concrete structure under such stress state is different from that under stress-free state. For this purpose, a self-developed real-time high-temperature true triaxial test system was applied to investigate the thermal expansion behavior of concrete under three-dimensional stress state. The thermal expansion strain of concrete under the three-dimensional stress undergoes strain increasing and strain stabilizing stages. At 600°C, the maximum thermal expansion strain of concrete under the three-dimensional stress is 0.75%. The average coefficient of thermal expansion of concrete under three-dimensional stress condition was then calculated, and its value reaches the minimum of $8.68 \times 10^{-6}/^{\circ}\text{C}$ at 200°C and the maximum of $13.41 \times 10^{-6}/^{\circ}\text{C}$ at 500°C. Comparing the coefficient of thermal expansion of concrete under stress-free condition given by Eurocode, it is found that the three-dimensional stress has an obvious restraint on the thermal expansion of concrete. The research results can provide theoretical basis for the stability analysis of underground engineering concrete structures under high-temperature environment.

1. Introduction

Underwater and underground tunnels are widely employed in transportation due to their advantages of efficiency, punctuality, safety, and energy conservation. Concrete structure of these tunnels needs to bear three-dimensional stress transmitted by the overlying water, soil, or rock pressure and also occasional heating impact caused by fire accident. Under such condition of three-dimensional stress and high temperature, the concrete structure may generate additional deformation and stress due to thermal expansion, which will affect the safety and stability of the tunnel and threaten the normal operation of the equipment and the lives of personnel [1]. Different from thermal expansion behavior under stress-free condition, the thermal expansion behavior of concrete under three-dimensional stress condition is still not completely understood and is thus of great importance to study.

A large number of experimental studies [2–5] and numerical simulations [6, 7] have been performed on the coefficient of thermal expansion (CTE) of concrete materials. Loser et al. [8] proposed a method to measure the CTE of hardened cement-based materials and studied the effect of age on the CTE. Yeon et al. [9] performed in situ CTE test on concrete and found that the CTE of concrete increased slightly after a sudden decrease in a period of time and then tended to stabilize, and the value of CTE of the initial stage was about twice that of the stable phase. Childs et al. [10] developed a method for measuring the CTE of ultra-high-strength cement-based materials using optical fiber sensors. Siddiqui et al. [11] studied the CTE of concrete with different types of aggregates and cement paste volumes and proposed a method to optimize the CTE of concrete. Abdulkareem et al. [12] studied the thermal expansion behavior of geopolymer slurry at high temperature under different heating rates. Turcry et al. [13] studied the effect of temperature on

the autogenous shrinkage of cement slurry. Zhou et al. [14] established a model based on thermodynamic analysis to predict the CTE of concrete and found that the type of aggregate was the main influencing factor.

The studies mentioned above mainly consider the influences of concrete composition materials, age, water content, and heating rate on thermal expansion behavior. Thermal deformability of concrete is also conditioned by the curing conditions [15] and some of its properties [16]. However, the concrete structure of underwater and underground tunnels is often under three-dimensional stress condition, which is different from the stress-free condition. Joaquín et al. [17] argued that the applied volumetric compressive stress could significantly decrease the volumetric expansion rate of concrete caused by alkali silicate reaction (ASR). Moreover, stress seems to have a great influence on the thermal expansion behavior of other materials, for example, graphite, ceramic, and glass [18–21]. Therefore, it is highly important to investigate the thermal expansion behavior of concrete under three-dimensional stress condition.

In this study, a real-time high-temperature true triaxial test system is especially designed to perform thermal expansion tests on cubic concrete samples under triaxial stress condition, the thermal expansion strain is measured during the heating process, and the CTE under three-dimensional stress condition is analyzed and compared with that under stress-free condition.

2. Test Preparations

2.1. Test Equipment. The real-time high-temperature true triaxial test system (see Figure 1) is especially designed to investigate the thermal expansion behavior of geomaterial under triaxial compression stress. The system is mainly composed of three modules: true triaxial loading module, high-temperature control module, and servo control and data acquisition module [22]. The maximum and minimum principal stresses are, respectively, up to 1000 and 200 MPa at a real-time maximum temperature of 600°C. Meantime, the changes in displacement and stress in the three directions are continuously monitored by Linear Variable Differential Transformer (LVDT) during the loading and heating process. Four groups of detachable rigid heating components are employed for the achievement of real-time high temperature. Each group of heating components is composed of 1 electric thermocouple and 8 heating rods, which are inserted in the 4 corners of the thermoplastic mold steel. The mold steel is used as heat transfer medium to heat the sample, as shown in Figure 2. Therefore, the system can truly simulate the high-temperature and triaxial compression stress environment for the concrete in underground engineering.

2.2. Sample Preparation. According to the mixture proportions of the concrete (see Table 1), the concrete was poured into a cubic sample of 150 × 150 × 150 mm. After being cured for 72 hours, the sample was demolded and was

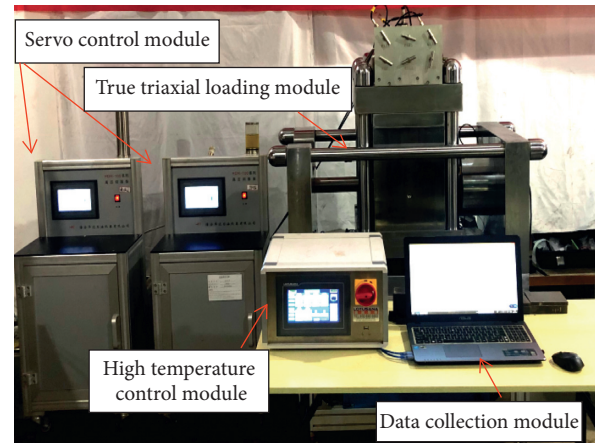


FIGURE 1: Photo of real-time high-temperature true triaxial test system.

placed in a special curing room for 60 days. The special values of the constant temperature and constant humidity for concrete curing are $20 \pm 2^\circ\text{C}$ and a relative humidity greater than 95%, respectively. The concrete specimens are put into water and submerged for long term. In order to prevent the concrete from being acidified, add a small amount of lime powder to the water. A quartz sample of $50 \times 50 \times 100$ mm was also prepared to calibrate test results.

In order to reduce the dispersion of test results induced by the heterogeneity of samples, a series of nondestructive detection methods, for example, density test, rebound strength test, and P-wave velocity measurement, were used for screening the samples [23, 24]. The value ranges of density, rebound strength, and P-wave velocity of the samples after detection methods are $2.423\text{--}2.639\text{ g/cm}^3$, 40.9–46.7 MPa, and 4328–4820 m/s, respectively. It is clear that there is only a small variation range and the prepared samples are thus considered to be relatively homogeneous. This could reduce errors caused by factors such as internal defects of the sample and improve the accuracy of data for subsequent test results.

2.3. Test Condition Setting. Immersed tube tunnel is increasingly used in traffic engineering and thus selected as a case to study. After the analyses of overlying loading on the tunnel [25, 26], a hydrostatic pressure of 0.5 MPa is determined and applied on the sample to simulate the three-dimensional stress condition.

When a fire occurs in an immersed tube tunnel, the temperature of inflammation point may rise to 1200°C. The concrete structure cannot withstand such high temperature, and the serious part is easy to collapse. However, considering that the strength loss of concrete is about 60–75% when temperature reaches 600°C [27, 28], a dual fire protection of “fire board + aluminum silicate fiber fire blanket” is thus often used in immersed tube tunnels and has the effect of fire prevention and heat insulation from inflammation point [29]. With the help of such protection, the maximum temperature of concrete structure in immersed tube tunnels is below 600°C. Therefore, it is considered to carry out the

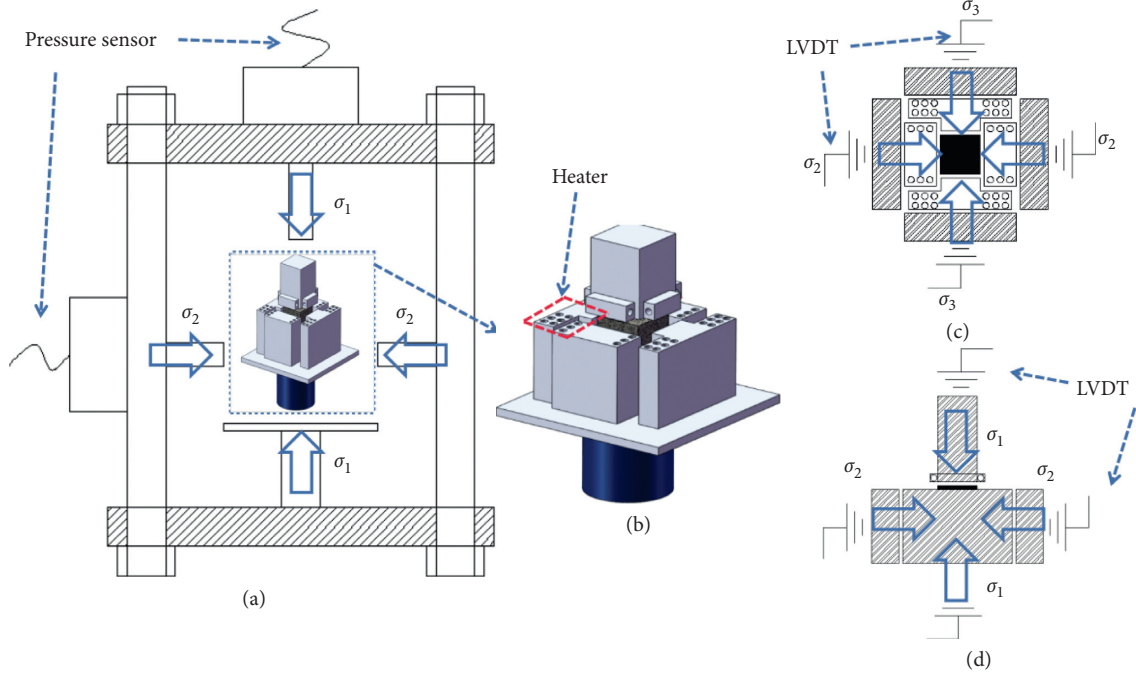


FIGURE 2: Schematic diagram of real-time high-temperature true triaxial loading system. (a) Real-time high-temperature true triaxial test system. (b) Interior layout drawing of real-time high-temperature true triaxial test system. (c) Schematic of the subsystem for the maximum and intermediate principal stress loading. (d) Schematic of the subsystem for the major principal stress loading.

TABLE 1: Mixture proportions of the concrete used in the experiment.

Strength grade	Cementitious material	Water cement ratio	Cement (%)	Fly ash (%)	Slag powder (%)	Sand rate (%)	Water reducing agent
C50	420 kg/m ³	0.35	45	25	30	43	1 kg/m ³

experiment in the range of 600°C, and 6 temperature levels of 100, 200, 300, 400, 500, and 600°C are selected for heating treatment.

2.4. Experiment Procedure. The displacement control is adopted for three-dimensional stress loading, and the loading rate is 0.001 mm/s. A hydrostatic stress of 0.5 MPa is applied on the samples to simulate the three-dimensional loading and held constant during the following thermal expansion deformation test.

After the load reaches the preset stress, the system is started to heat the sample from room temperature (RT) to the preset temperature T . The system should be kept for 2 h to ensure uniform heating inside the sample. The heating rate and the temperature relationship between heater and sample surface are shown in Figure 3.

During the heating process, a constant hydrostatic stress of 0.5 MPa is applied on the samples. Three sets of LVDT are arranged in each direction, and each set contains 2 transducers. The arrangement of transducers is shown in Figure 2. The system collects the displacement changes of the concrete in the three directions from the beginning of the temperature rising to the end of the constant temperature. In order to eliminate the error of the instrument itself during the heating process, a quartz sample is first used to calibrate the

results. Because the CTE of the quartz sample is about $5.5 \times 10^{-7}/^\circ\text{C}$, which is far lower than the CTE of concrete, and the thermal expansion of the quartz sample in the three directions can be ignored, the strains in the three directions in the cases of the quartz sample can be directly used as the thermal expansion strains of the instrument itself.

By eliminating the deformation of the instrument itself, the thermal expansion deformations of concrete under the three-dimensional stress condition can be obtained, and then the three-dimensional thermal expansion strains of the samples under three-dimensional stress condition are calculated.

Considering that the studied concrete is homogeneous and is subjected to a hydrostatic stress, an average value of the thermal expansion strains in the three directions is used to calculate the CTE of the samples under the three-dimensional stress condition. The formulas are written as

$$\varepsilon_n(T) = \frac{L_{n,T} - L_{n,S}}{L_{n,0}}, \quad (n = 1, 2, 3), \quad (1)$$

$$\alpha_C(T) = \frac{1/n \sum \varepsilon_n(T)}{\Delta T}, \quad (2)$$

where $\varepsilon_n(T)$ and $L_{n,T}$ are the thermal strain and thermal deformation of the concrete in the n direction at a

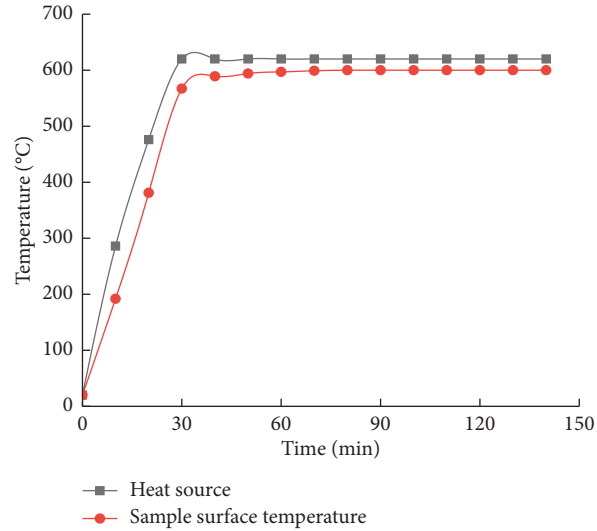


FIGURE 3: The temperature relationship between heater and sample surface.

temperature of T ; $L_{n,0}$ is the initial length of concrete in the n direction; $L_{n,S}$ is the thermal deformation of the quartz in the n direction at a temperature of T ; $\alpha_C(T)$ is thus the average value the CTE under three-dimensional stress; ΔT ($^{\circ}\text{C}$) is the temperature change of the samples.

3. Test Results of Thermal Expansion Deformations

3.1. Evolutions of Thermal Expansion Strain during Heating Process. Figures 4(a)–4(f) present the curves of the three-dimensional thermal expansion strains versus time under three-dimensional stress condition. In this study, the tensile strains produced by the thermal expansion of concrete are taken as positive. After heating to about 60 min, the thermal expansion strains enter the stable stage. At this time, the three-dimensional thermal expansion strains under three-dimensional stress condition basically reach the maximum. At 600°C , the maximum thermal expansion strain of the concrete under three-dimensional stress reaches 0.75%. The three-dimensional thermal expansion strains of the concrete under three-dimensional stress at various temperatures are summarized in Table 2.

3.2. Average CTE of Concrete under Three-Dimensional Stress Condition. The average CTE of concrete under three-dimensional stress condition is calculated according to Table 2 and equations (1)–(2), and the results are shown in Figure 5. The average CTE of concrete under three-dimensional stress condition presents an S-shaped trend with temperature changes. The CTE of concrete under three-dimensional stress condition presents a downward trend within 100 – 200°C , then an upward trend up to 500°C , and finally a downward trend within 500 – 600°C . The CTE of concrete under three-dimensional stress condition reaches its minimum of $8.68 \times 10^{-6}/^{\circ}\text{C}$ at 200°C and reaches the maximum of $13.41 \times 10^{-6}/^{\circ}\text{C}$ at 500°C .

4. Discussions

As mentioned above, the thermal expansion property of concrete is highly important for the structure stability analyses of underground and underwater tunnel subjected to fire accident. Previous study indicated that the thermal deformation of cement-based materials is closely related to temperature and stress state [30]. However, the CTE in most of existent standard of cement structures is usually measured under stress-free condition, and the calculation results of thermal deformation of concrete structures based on the CTE under stress-free condition may not be applicable in underground or underwater tunnels. Concrete structures are all subjected to three-dimensional stress. The thermal deformation of the structure is related not only to the temperature load but also to the stress. Using the CTE of concrete under the free-stress state to calculate the thermal expansion of the structure will be excessively exaggerated or small, and the calculation of the structural thermal stress is not accurate. In order to understand the difference between the thermal deformation of concrete under the three-dimensional stress condition and the stress-free condition, a typical CTE model of concrete under stress-free condition, which was suggested by the European Standards [31], is used to compare with the CTE measured in the present work.

To deal with the design of concrete structures for the accidental situation of fire exposure, a formula is suggested by the European Standards to calculate the thermal expansion strain of ordinary concrete and written as follows:

$$\Delta l/l = 2.3 \times 10^{-11}T^3 + 9 \times 10^{-6}T - 1.8 \times 10^{-4} \quad (20^{\circ}\text{C} \leq T \leq 600^{\circ}\text{C}). \quad (3)$$

The comparisons of the CTE of the concrete from the European Standards and the present work are shown in Figure 6. At 100°C , the CTE of concrete under three-dimensional stress is slightly larger than that given by the European Standards. After 200°C , the CTE of concrete under stress-free condition is about 1.07–1.47 times of the CTE

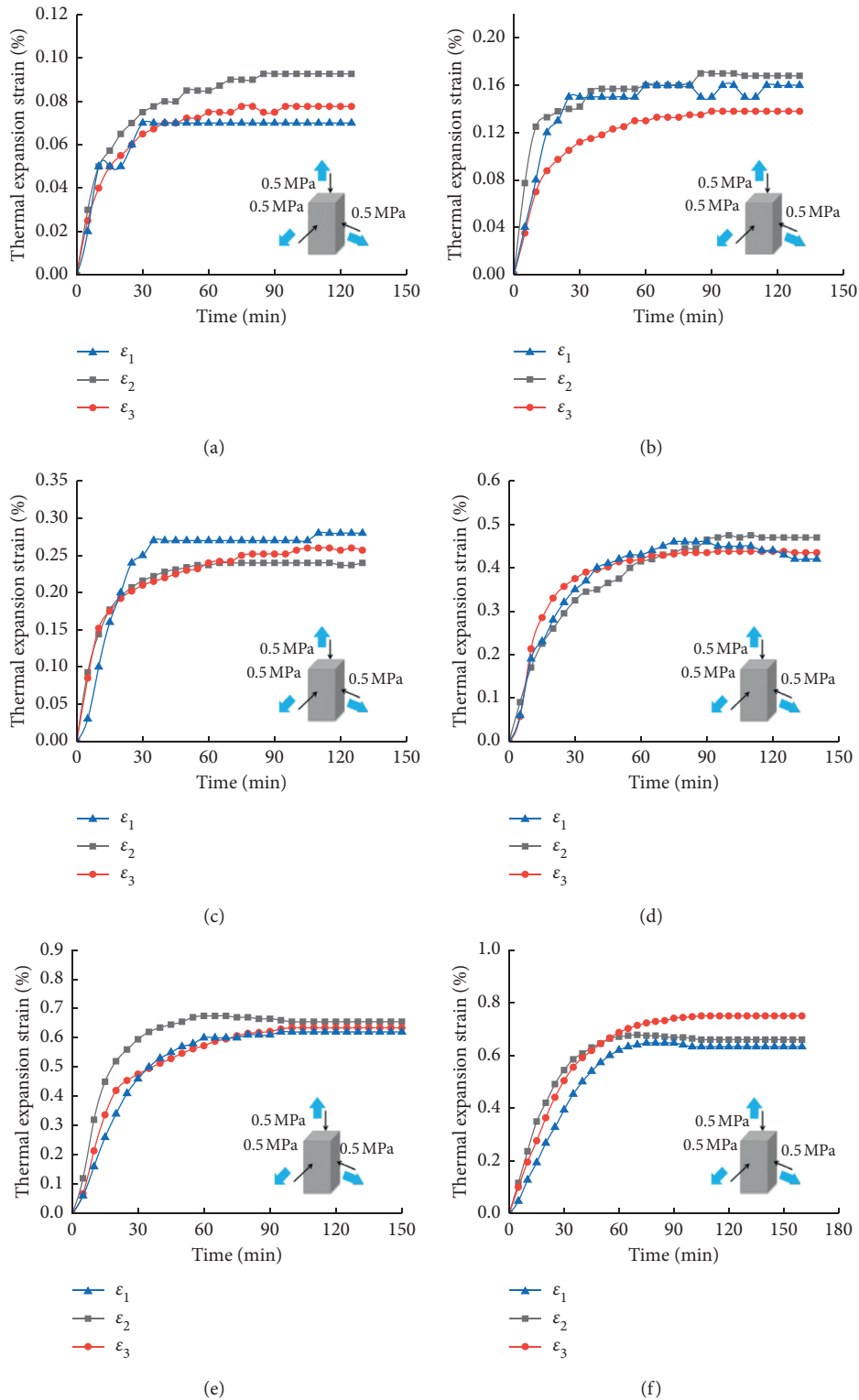


FIGURE 4: Thermal expansion strains of concrete under three-dimensional stress condition. (a) 100°C, (b) 200°C, (c) 300°C, (d) 400°C, (e) 500°C, and (f) 600°C.

under three-dimensional stress condition. In other words, the three-dimensional stress condition has obvious restraint effect on the thermal expansion of concrete. The effect of three-dimensional stress on the CTE of concrete could be

attributed to two mechanisms, that is, the compression deformation due to degradation of elastic modulus under high temperature [31–35] and restraint of thermal-induced microcracks [36–38]. Therefore, the CTE of concrete under

TABLE 2: Thermal expansion strains of concrete during heating under three-dimensional stress condition.

Parameters	Temperature (°C)					
	100	200	300	400	500	600
ε_1 (%)	0.070	0.160	0.280	0.460	0.620	0.647
ε_2 (%)	0.093	0.170	0.240	0.475	0.675	0.675
ε_3 (%)	0.078	0.138	0.260	0.438	0.634	0.750
ε_C (%)	0.080	0.156	0.260	0.458	0.643	0.691

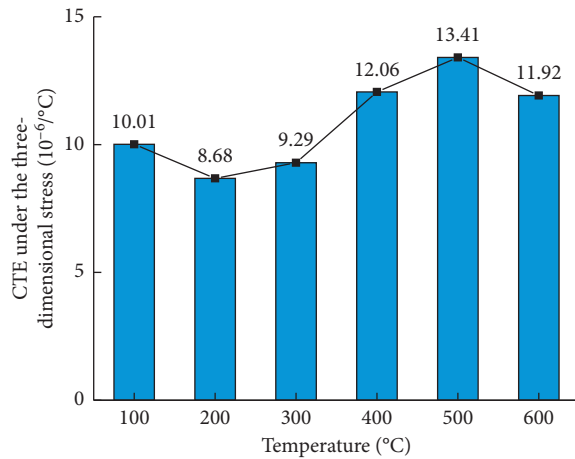


FIGURE 5: CTE of concrete under three-dimensional stress.

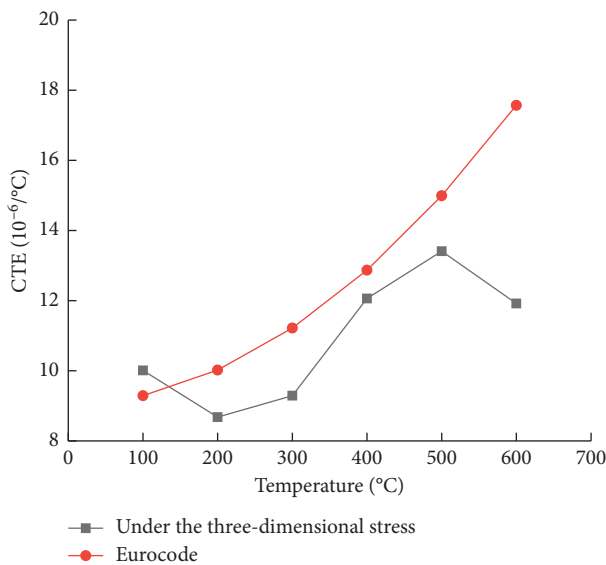


FIGURE 6: Comparisons of the CTE under different conditions.

three-dimensional stress condition is smaller than that under stress-free condition. A similar phenomenon has been also observed on rock materials [39, 40].

5. Conclusions

Six groups of concrete samples were screened out to perform thermal expansion tests at different temperatures under three-dimensional stress condition. The thermal

deformation behavior of the concrete under three-dimensional stress condition was investigated; the CTE was compared with that under stress-free condition. The thermal expansion strain of concrete under the three-dimensional stress undergoes strain increasing and strain stabilizing stages. At 600°C, the maximum thermal expansion strain of concrete under the three-dimensional stress is 0.75%. The average coefficient of thermal expansion of concrete under three-dimensional stress condition was then calculated, and its value reaches the minimum of $8.68 \times 10^{-6}/^{\circ}\text{C}$ at 200°C and the maximum of $13.41 \times 10^{-6}/^{\circ}\text{C}$ at 500°C. The average CTE of concrete under three-dimensional stress condition presents an S-shaped trend with temperature changes. The CTE of concrete under three-dimensional stress condition reaches its minimum of $8.68 \times 10^{-6}/^{\circ}\text{C}$ at 200°C and the maximum of $13.41 \times 10^{-6}/^{\circ}\text{C}$ at 500°C. By comparing the CTE of concrete under stress-free condition suggested by Eurocode, it is found that the three-dimensional stress has a significant restriction on the thermal expansion of concrete. The above research results can provide a theoretical basis for the stability analysis of underground concrete structures under sudden-fire and high-temperature environments.

Data Availability

The data used to support the findings of this study are available from the corresponding author upon request.

Conflicts of Interest

The authors declare that they have no conflicts of interest.

Acknowledgments

The work was supported by the National Key R&D Program of China (nos. 2018YFC0809600 and 2018YFC0809601), the National Natural Science Foundation of China (nos. 51779252 and 51479193), the China Geological Survey Bureau (no. DD20190128), and the Major Technological Innovation Projects of Hubei (no. 2017AAA128).

References

- [1] G. Wang, D. Barber, P. Johnson, and M. C. Hui, "Fire safety provisions for aged concrete building structures," *Procedia Engineering*, vol. 62, 2013.
- [2] V. Revilla-Cuesta, M. Skaf, J. A. Chica et al., "Thermal deformability of recycled self-compacting concrete under cyclical temperature variations," *Materials Letters*, vol. 278, 2020.
- [3] L. Zuda and R. Černý, "Measurement of linear thermal expansion coefficient of alkali-activated aluminosilicate composites up to 1000°C," *Cement and Concrete Composites*, vol. 31, no. 4, pp. 263–267, 2009.
- [4] B. Zahabizadeh, A. Edalat-Behbahani, J. Granja et al., "A new test setup for measuring early age coefficient of thermal expansion of concrete," *Cement & Concrete Composites*, vol. 98, pp. 14–28, 2002.
- [5] S. Ghabezloo, "Effect of porosity on the thermal expansion coefficient: a discussion of the paper "effects of mineral

- admixtures on the thermal expansion properties of hardened cement paste” by Z. H. Shui, R. Zhang, W. Chen, D. Xuan, *Constr. Build. Mater.* 24 (9) (2010) 1761-1767,” *Construction and Building Materials*, vol. 24, no. 9, pp. 1796–1798, 2010.
- [6] C. Zhou, X. Shu, and B. Huang, “Predicting concrete coefficient of thermal expansion with an improved micro-mechanical model,” *Construction and Building Materials*, vol. 68, pp. 10–16, 2014.
- [7] L. M. McCarthy, J. M. Gudimetla, G. L. Crawford, M. C. Guercio, and D. Allen, “Impacts of variability in coefficient of thermal expansion on predicted concrete pavement performance,” *Construction and Building Materials*, vol. 93, pp. 711–719, 2015.
- [8] R. Loser, B. Münch, and P. Lura, “A volumetric technique for measuring the coefficient of thermal expansion of hardening cement paste and mortar,” *Cement and Concrete Research*, vol. 40, no. 7, pp. 1138–1147, 2010.
- [9] J. H. Yeon, S. Choi, and M. C. Won, “In situ measurement of coefficient of thermal expansion in hardening concrete and its effect on thermal stress development,” *Construction and Building Materials*, vol. 38, pp. 306–315, 2013.
- [10] P. Childs, A. C. L. Wong, N. Gowripalan, and G. D. Peng, “Measurement of the coefficient of thermal expansion of ultra-high strength cementitious composites using fibre optic sensors,” *Cement and Concrete Research*, vol. 37, no. 5, pp. 789–795, 2007.
- [11] M. S. Siddiqui and D. W. Fowler, “A systematic optimization technique for the coefficient of thermal expansion of Portland cement concrete,” *Construction and Building Materials*, vol. 88, pp. 204–211, 2015.
- [12] O. A. Abdulkareem, A. M. M. A. Bakri, H. Kamarudin et al., “Effects of elevated temperatures on the thermal behavior and mechanical performance of fly ash geopolymer paste, mortar and lightweight concrete,” *Construction & Building Materials*, vol. 50, pp. 377–387, 2013.
- [13] P. Turcry, A. Loukili, L. Barcelo, and J. M. Casabonne, “Can the maturity concept be used to separate the autogenous shrinkage and thermal deformation of a cement paste at early age?” *Cement and Concrete Research*, vol. 32, no. 9, pp. 1443–1450, 2002.
- [14] C. Zhou, B. Huang, and X. Shu, “Micromechanical model for predicting coefficient of thermal expansion of concrete,” *Journal of Materials in Civil Engineering*, vol. 25, no. 9, pp. 1171–1180, 2013.
- [15] H. Y. Aruntas, S. Cemalgil, O. Simsek et al., “Effects of super plasticizer and curing conditions on properties of concrete with and without fiber,” *Materials Letters*, vol. 62, pp. 3441–3443, 2008.
- [16] Y. Sun, P. Gao, F. Geng, H. Li, L. Zhang, and H. Liu, “Thermal conductivity and mechanical properties of porous concrete materials,” *Materials Letters*, vol. 209, pp. 349–352, 2017.
- [17] J. Liaudat, I. Carol, C. M. López, and V. E. Saouma, “ASR expansions in concrete under triaxial confinement,” *Cement and Concrete Composites*, vol. 86, pp. 160–170, 2018.
- [18] L. Doojin and S. Soek, “Modeling the effects of elastic modulus and thermal expansion coefficient on the shrinkage of glass fiber reinforced composites,” *Composites, Part B Engineering*, vol. 146, pp. 98–105, 2018.
- [19] N. Khalili, A. Uchaipichat, and A. A. Javadi, “Skeletal thermal expansion coefficient and thermo-hydro-mechanical constitutive relations for saturated homogeneous porous media,” *Mechanics of Materials*, vol. 42, no. 6, pp. 593–598, 2010.
- [20] Y. Hirata, “Theoretical analyses of thermal shock and thermal expansion coefficients of metals and ceramics,” *Ceramics International*, vol. 41, no. 1, pp. 1145–1153, 2014.
- [21] H. Wang, X. Zhou, L. Sun, J. Dong, and S. Yu, “The effect of stress levels on the coefficient of thermal expansion of a fine-grained isotropic nuclear graphite,” *Nuclear Engineering and Design*, vol. 239, no. 3, pp. 484–489, 2009.
- [22] X. Ma, G. Wang, D. Hu et al., “Mechanical properties of granite under real-time high temperature and three dimensional stress,” *International Journal of Rock Mechanics and Mining Sciences*, vol. 136, 2020.
- [23] T. Y. Guo and L. N. Y. Wong, “Microcracking behavior of three granites under mode I loading: insights from acoustic emission,” *Engineering Geology*, vol. 278, 2020.
- [24] M. Alwash, D. Breyse, Z. M. Sbartai, K. Szilágyi, and A. Borosnyói, “Factors affecting the reliability of assessing the concrete strength by rebound hammer and cores,” *Construction and Building Materials*, vol. 140, pp. 354–363, 2017.
- [25] M. Wu, Q. Zhang, and S. Wu, “Risk assessment of operation period structural stability for long and large immersed tube tunnel,” *Procedia Engineering*, vol. 166, pp. 266–278, 2016.
- [26] Z. Zhang, W. Lin, H. Ji et al., “Layout and design techniques of cross section for the large immersed tunnel,” *Procedia Engineering*, vol. 166, pp. 37–44, 2016.
- [27] A. P. Mouritz and Z. Mathys, “Post-fire mechanical properties of glass-reinforced polyester composites,” *Composites Science and Technology*, vol. 61, no. 4, pp. 475–490, 2001.
- [28] F. H. Amundsen, “Studies of driver behavior in Norwegian road tunnels,” *Tunneling and Underground Space Technology*, vol. 9, no. 1, pp. 9–17, 1994.
- [29] J. Yao, H. Zhu, and Z. Yan, “Reviews and analysis on fireproof measures used for tunnel structure,” *Chinese Journal of Underground Space and Engineering*, vol. 3, no. 4, pp. 732–736+741, 2007.
- [30] H. Zhou, D. Hu, F. Zhang, and J. Shao, “A thermo-plastic/viscoplastic damage model for geomaterials,” *Acta Mechanica Sinica*, vol. 24, no. 3, pp. 195–208, 2011.
- [31] BSEN 1992-1-2, Eurocode 2, *Design of Concrete Structures. Part 1.2. General Rules, Structural Fire Design*, British Standards Institution, London, UK, 2004.
- [32] Y. Anderberg and S. Thelandersson, “Stress and deformation characteristics of concrete at high temperatures. 2. experimental investigation and material behaviour model,” *Lund Institute of Technology Bulletin*, vol. 54, 1976.
- [33] Q. X. Le, J. L. Torero, and V. T. N. Dao, “Understanding the effects of stress on the coefficient of thermal expansion,” *International Journal of Engineering Science*, vol. 141, pp. 83–94, 2019.
- [34] F. J. Ulm, O. Coussy, and Z. P. Bažant, “The “chunnel” fire. i: chemoplastic softening in rapidly heated concrete,” *Journal of Engineering Mechanics*, vol. 125, no. 3, 1999.
- [35] B. M. Luccioni, M. I. Figueroa, and R. F. Danesi, “Thermo-mechanic model for concrete exposed to elevated temperatures,” *Engineering Structures*, vol. 25, no. 6, pp. 729–742, 2003.
- [36] H. G. Zhang, L. Li, C. Yuan, and Q. Y. Wang, “Deterioration of ambient-cured and heat-cured fly ash geopolymer concrete by high temperature exposure and prediction of its residual compressive strength,” *Construction & Building Materials*, vol. 262, 2020.
- [37] F. Zhang, W. Hu, H. Q. Guo et al., “Nanoindentation tests on granite after heat treatment,” *Rock and Soil Mechanics*, vol. 39, pp. 235–243, 2018.

- [38] X. Cai, C. G. Shi, X. H. Chen et al., "Identification of damage mechanisms during splitting test on SFP at different temperatures based on acoustic emission," *Construction & Building Materials*, vol. 262, 2020.
- [39] W. Li, X. Miao, and C. Yang, "Failure analysis for gas storage salt cavern by thermo-mechanical modelling considering rock salt creep," *Journal of Energy Storage*, vol. 32, 2020.
- [40] T. T. Wang and T. K. Kwei, "Effect of induced thermal stresses on the coefficients of thermal expansion and densities of filled polymers," *Journal of Polymer Science PART A-2: Polymer Physics*, vol. 7, no. 5, pp. 889–896, 1969.

Research Article

Mechanical Properties of Sandstone Roof and Surrounding-Rock Control of Mining Roadways Subject to Reservoir Water Disturbance

Bin Ma,¹ Zaiqiang Hu ¹, Xingzhou Chen ², Lili Chen,² and Wei Du²

¹School of Civil Engineering and Architecture, Xi'an University of Technology, Xi'an 710077, China

²School of Architecture Civil and Engineering, Xi'an University of Science and Technology, Xi'an 710054, China

Correspondence should be addressed to Zaiqiang Hu; huzq@xaut.edu.cn

Received 14 December 2020; Revised 20 January 2021; Accepted 28 January 2021; Published 13 February 2021

Academic Editor: Faming Huang

Copyright © 2021 Bin Ma et al. This is an open access article distributed under the Creative Commons Attribution License, which permits unrestricted use, distribution, and reproduction in any medium, provided the original work is properly cited.

Sandstone-roofed roadways are susceptible to deformation and failure caused by reservoir-water-induced disturbances, thereby compromising human safety. Using rock-mechanics testing techniques, numerical simulations, and engineering principles, this study investigates the strength, deformation, and pore-structure characteristics of sandstone roofs as well as means to support the surrounding rock structure. The results obtained in this study reveal that the residual strain is proportional to the pore-water pressure, which, in turn, causes a significant reduction in the elastic modulus during the unloading phase. Furthermore, an increase in the pore-water pressure causes the shear failure of specimens in compression. The delay between crack initiation and specimen-volume expansion decreases. Moreover, the specimen demonstrates increased deformation and failure responses to changes in the confining pressure, thereby resulting in accelerated conversion. Changes in water inflow can be correlated to crack initiation, propagation, and fracture. This water inflow gradually increases with an increase in the osmotic pressure. Correspondingly, the volumetric strain required for maximum water inflow undergoes a gradual decrease. The increased water inflow can be considered a precursor to specimen failure. In addition, fractures in the surrounding rock structures are mainly caused by joint dislocations. The increase in pore pressure promotes the development of dislocation fractures in the deep surrounding rocks. Subsequently, these fractures overlap with their open counterparts to form large fractures; this increases the roadway-roof subsidence and layer separation of the shallow surrounding rocks, thereby further increasing the fracture count. Lastly, the use of high-performance rock bolts, cable-bolt reinforcements, and W-shaped steel bands is expected to ensure the stability of rocks surrounding sandstone-roofed roadways subject to water-pressure disturbances.

1. Introduction

The rapid development of mining technologies has resulted in an increased mineral-resource demand in China. However, these mineral resources, being nonrenewable, are prone to depletion [1, 2]. Therefore, the research on mining of resources that require complicated extraction process, especially those found under water bodies, such as reservoirs and rivers, has attracted significant attention in recent times [3]. Mining activities destroy existing rock-stress fields, thereby causing movement of the overlying strata and promoting the infiltration of surface water and water in aquifers into the ground. In particular, surface water

bodies—the main supplemental sources of mine water—significantly affect the safety of underground production activities. Therefore, the safe extraction of minerals from under water bodies is an important research topic from the rock-mechanics and engineering viewpoints.

Sun et al. [4] studied the overburden-failure process under reservoir mining conditions by performing physical and numerical simulations. They deduced the relationship between the maximum height of the water-conducting fissure development and coal-seam mining thickness. Dyke et al. [5] studied the relationship between rock strength and its sensitivity to water content. They revealed that a decrease in moisture content suppresses the onset of dilatancy and

microcracking. Colback et al. [6] analyzed the relationship between the compressive strength of South African quartzite and changes in water content. Subsequently, they discussed the quantitative effects of moisture on the compressive strength of rocks. Hadizadeh [7] analyzed the softening effect of water on sandstone. Risnes et al. [8] investigated the weakening and damaging effects of water on the microstructures of cretaceous rocks; they reported the water-weakening effect to be considerably reduced in high-ionic-strength solutions. Yao [9] investigated the physical and mechanical properties of water-enriched sandstones. They suggested the basic principle underlying the weakening of water-rich roadway roofs. Zhu et al. [10] analyzed the internal mechanisms related to the impact of water on the characteristic strength of saturated marble. They postulated that the mechanism influencing the fracture-initiation strength after rock-sample saturation is due mainly to the pore-water pressure and the “hindering force” of crack propagation. Zhu et al. [11] analyzed the influence of water pressure inside cracks on the compressive strength of rock masses. Moreover, they deduced equations to evaluate the initial rupture strength of rocks subjected to hydraulic pressures. Chen et al. [12] discussed macromechanisms underlying the changes in interactions between the water pressure and confining pressure on rocks. They revealed cases involving hydraulic unloading to demonstrate a significant impact on rock strength compared to those without hydraulic unloading. Tang et al. [13] analyzed the evolution patterns of the volume-expansion characteristics of sandstones with different moisture content. They reported that an increase in moisture content decreases the closure stress, initiation strength, damage strength, and peak strength of sandstone. Deng et al. [14, 15] investigated the effects of different pore-water pressures on the unloading deformation and failure characteristics of sandstone. They observed the lateral-expansion phenomenon to become obvious under high and low pore water and confining pressures, respectively. Xu et al. [16] performed pore-water pressures tests on saturated sandstones subjected to cyclic loading and unloading under constant triaxial confining-pressure settings. They reported the relationship between the residual strain and cyclic numbers to agree with the power of negative index under cyclic loading and unloading pore-water pressures. Wang et al. [17] experimentally studied the evolution characteristics of sandstone permeability based on the unloading path. They reported sandstone to sustain brittle failure and its lateral deformation and volume to expand significantly upon an increase in the initial confining pressure or unloading rate. Wang et al. [18] performed permeability tests on gritstones during deformation and failure under different confining-pressure conditions. They identified gritstone permeability as more sensitive to hoop-strain changes during rock-sample deformation and failure. Zhu et al. [19] studied the safety of coal mining under barrier lakes. They observed the coal-seam bedrock thickness to exceed the required dimensions of the safety waterproof pillar.

Most extant studies investigate the weakening of the physical properties of sandstone under the action water as

well as the overburden-failure characteristics of underwater mining activities. However, studies concerning the stability and control of roadway-roof mining under water-pressure disturbances are seldom undertaken. Underwater mining-roadway activities are classified as water-rock interactions. The mechanical properties of rocks surrounding these roadways inevitably deteriorate. Moreover, hydrophilic minerals in these surrounding rocks tend to swell and deform after water absorption, thereby adversely affecting the operational safety and maintenance of such roadways. For these reasons, the underwater mining roadway is considered in this study to perform engineering evaluations. This study analyzes the weakening trends and strength characteristics of sandstone roofs above roadways subjected to reservoir water disturbances. The corresponding results obtained were interpreted via unloading seepage tests, numerical simulations, and engineering assessments to determine the theoretical basis and practical significance of mining safety while considering reservoir water disturbances.

2. Experimental Preparation

2.1. Experimental System and Sample Preparation. The thermal-hydrological-mechanical-chemical (THMC) multifield coupling triaxial rheological testing system for rocks (Figure 1) was used in this study for the evaluations. The equipment is capable of automatically collecting data for changes in force and displacement during the loading process. The system working pressures were as follows: confining pressure of 0–100 MPa, axial pressure of 0–1500 kN, and osmotic working pressure of 0–60 MPa. A standard pressure/volume controller was used to collect the fluid from the upstream extremity.

The specimens used as the experimental materials were obtained from the sandstone roof of a coal mine roadway under a reservoir in the western part of China. According to the requirements of rock testing based on the relevant test standards and specifications, the YRD-2 CNC core cutting machine was used to prepare cylindrical specimens ($\phi 50 \text{ mm} \times L100 \text{ mm}$), with the roughness at both ends of the specimens controlled within $\pm 5 \text{ mm}$. The prepared samples are shown in Figure 2.

2.2. Experimental Methodology.

- (1) The obtained specimens were dried in an oven at 105°C for 24 h. Thereafter, saturated samples were obtained using the vacuum-extraction method, wherein specimens were placed in a vacuum de-aerator for forced saturation for 8 h and subsequently allowed to rest for 4 h. Sonic-wave tests were performed on the final saturated specimens, and specimens with similar wave velocities were selected as the samples to be used in the tests.
- (2) The stress environment of the sandstones was simulated using confining pressure according to the relation $P_0 = 0.013 \times H$, where P_0 denotes the horizontal in situ stress (MPa) and H denotes the

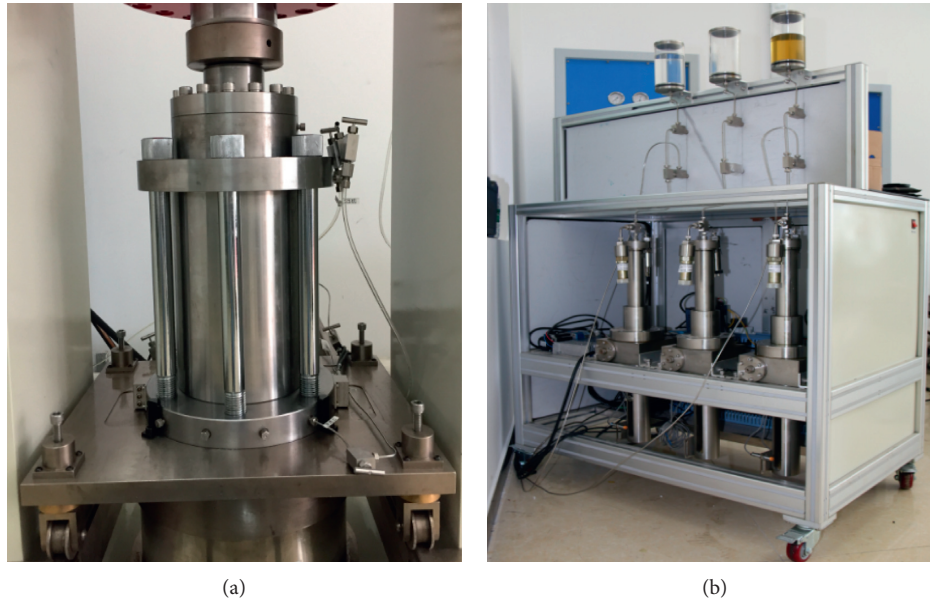


FIGURE 1: THMC multifield coupling triaxial rheological testing system. (a) Confining pressure chamber. (b) Servo unit for axial, confining, and pore pressures.



FIGURE 2: Sandstone specimens.

embedded depth (m) [20]. Combined with the actual site data of the embedded depth of the roadway of around 300 m, a confining pressure of 4.0 MPa was determined. The confining and axial pressures were thus increased to 4 MPa; subsequently, the confining pressure was maintained constant while the axial pressure was increased until the specimen fractured. The triaxial compressive strength was thus obtained as $\sigma_c = 32.5$ MPa, which provided the basis for the unloading test; the loading rate during the test was 0.2 MPa/min.

- (3) Five pore pressure gradients (0, 0.1, 0.2, 0.4, and 0.6 MPa) were applied to the sandstone samples during the triaxial unloading test to simulate the different water pressures resulting from changes in the reservoir water levels at specific embedded depths. The axial and confining pressures were

loaded as 4.0 MPa at a loading rate of 0.04 MPa/min. Simultaneously, when the confining pressure was greater than the predetermined osmotic pressure, the pore water pressure was applied. Then, the axial pressure was loaded with a predetermined value set to 70% of the conventional triaxial compressive strength (around 23 MPa). Finally, the confining pressure was unloaded at 0.1 MPa/min until the specimen fractured. The test plan and basic physical and mechanical parameters of the specimens are summarized in Table 1.

3. Experimental Results and Analysis

3.1. Analysis of Deformation Characteristics. To study the response patterns to excavation unloading of the sandstone under the effect of osmotic pressure, triaxial unloading tests were conducted under different pore pressure conditions, and the stress–strain curves corresponding to the entire deformation process were obtained, as shown in Figure 3.

Figure 3 reveals the axial and circumferential deformations to demonstrate linear growth trends during loading stage. Further, the pore-water pressure has a significant effect on sandstone deformation and failure. Under the case with pore water pressure, the deformation patterns were mostly identical during the initial stages of unloading; then, the deformation patterns differed during the failure stages for the different pore water pressures. Specifically, the osmotic pressure had a significant impact on the residual strain; when there was no effect of the pore water pressure, the specimens exhibited ductile failure. The increase in pore-water pressure causes the specimens to exhibit gradual brittle failure. During the unloading stage, the increase in the principal-stress difference with pore pressure is more rapid than without it. This can be attributed to the countersupport

TABLE 1: Basic physical parameters of specimens.

Test number	Test plan	Natural mass (g)	Natural density (g/cm ³)	Saturated mass (g)	Saturated mass (g/cm ³)	Saturated wave velocity (km/s)	Porosity (%)
S-1	Unloading without pore pressure	416.69	2.23	441.31	2.36	2.10	13.60
S-2	Unloading at 0.1 MPa pore pressure	410.53	2.25	434.73	2.38	2.23	13.51
S-3	Unloading at 0.2 MPa pore pressure	417.83	2.22	442.17	2.35	2.10	13.36
S-4	Unloading at 0.4 MPa pore pressure	420.77	2.23	446.25	2.36	2.13	14.00
S-5	Unloading at 0.6 MPa pore pressure	415.69	2.26	439.08	2.39	2.17	13.19

provided to the internal skeleton and sandstone particles by the internal water pressure under the action of the pore-water pressure. This is in line with the principle of effective stress proposed by Terzaghi [21].

Additionally, considering the concept of the unloading confining pressure ratio proposed in [22], the designated variable $\Delta\sigma$ was used to describe the unloading confining pressure ratio as

$$\Delta\sigma = \frac{\Delta\sigma'_3}{\Delta\sigma_3}, \quad (1)$$

where $\Delta\sigma'_3$ represents the measured confining pressure of the specimen before the stress reduction in the unloading process and $\Delta\sigma_3$ represents the unloading confining pressure of the specimen from the beginning of the unloading process until stress reduction.

Combined with the change rates of hoop and volumetric strains, the unloading stage can be divided into three stages as shown in Figures 3(b) and 3(c). When $\Delta\sigma \leq 30\%$, the change in strain is relatively steady and slow, which is the elastic compaction stage. For $30\% \leq \Delta\sigma \leq 60\%$, the unloading development stage, the strain increases rapidly, and circumferential deformation rate is noticeably higher than the axial deformation rate; tensile cracks are gradually initiated, and the trends in volumetric and hoop strains are identical, causing the specimen to gradually fracture. In particular, when the confining pressure is unloaded to around $\Delta\sigma = 50\%$ ($\sigma_1 - \sigma_3 = 21.5$ MPa), the deformation increases rapidly. For $60\% < \Delta\sigma \leq 90\%$, the circumferential deformation rate is relatively slow, and internal cracks gradually connect to form fractures until the stress reduces (specimen failure). Overall, it is observed that the deformation of sandstone is significantly affected by the circumferential deformation; further, after the fracture of sandstone (after the stress drops), the hysteresis effect can be seen in the hoop and volumetric strains owing to the low confining pressures of the experimental design. After the specimen fractures, the axial pressure compacts the specimen, resulting in a decrease in strain.

Rocks exhibit different deformation characteristics under different pore-water pressure conditions, and the resulting deformation characteristics include different residual strains and elastic modulus of each stage. Based on the above observation, the unloading seepage test was divided

into the loading, unloading (elastic, development, and propagation stages), and stress drop stages. Then, statistical analyses of the elastic moduli of the specimens for each of the five stages were performed to obtain the characteristic parameters of unloading seepage deformation shown in Table 2; this data was used to perform statistical regression analysis (Figure 4).

It is seen from Figure 4 that there is a good linear relationship between the residual strain and pore pressure; the greater the pore pressure, the greater the absolute value of the residual strain. After entering the unloading stage, the elastic modulus begins decreasing. Moreover, the elastic moduli at various unloading stages decrease significantly with the increase in pore pressure. During the unloading development and propagation stages, these reductions become more apparent, thereby indicating gradual specimen deformation and failure. This significantly affects the elastic modulus of the specimen causing it to deform and fail during the stress-drop stage. At this point, the elastic modulus reduces to approximately 35% of its corresponding loading-stage value.

3.2. Analysis of Strength Characteristics. Although the failure angles and fracture characteristics of the specimens under different pore water pressure states were considerably different, all the main cracks exhibited oblique shear or compression-shear characteristics (Figures 5 and 6). Under the condition of low pore-water pressure, failure occurred with a single dominant crack. When the pore water pressure reached 0.6 MPa, a “V” type failure occurred. With additional continuous increase in the water pressure, the corresponding peak deviatoric stress first increased and then gradually decreased as 22.79 MPa \rightarrow 23.16 MPa \rightarrow 23.15 MPa \rightarrow 22.93 MPa \rightarrow 22.41 MPa; the failure and deformation gradually shifted from shear failure to hybrid compression-shear failure and from a single dominant crack to multiple overlapping cracks. It was assumed that the reason for the emergence of this type of macrofracture characteristic was the shear stress that is inevitably generated in the crack initiation and propagation directions inside the specimen during the stress unloading process; thus, all specimens showed shear failure characteristics. Moreover, the hydromechanical coupling effect was not significant when the pore water pressure was low; when the

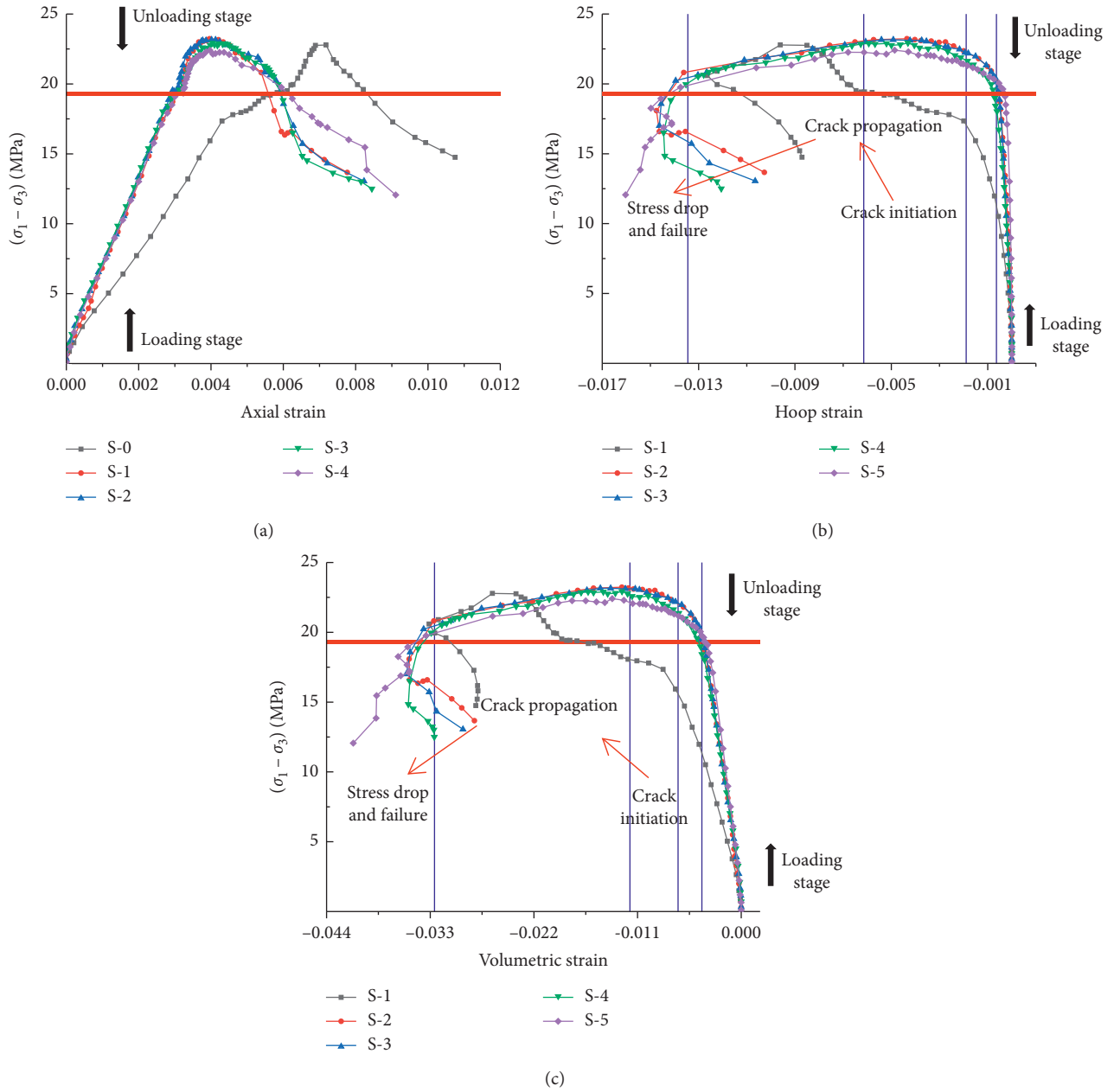


FIGURE 3: Stress–strain relationship curves for specimens used in this study. (a) Variation of $(\sigma_1 - \sigma_3)$ with ϵ_1 . (b) Variation of $(\sigma_1 - \sigma_3)$ with ϵ_3 . (c) Variation of $(\sigma_1 - \sigma_3)$ with ϵ_v .

TABLE 2: Characteristic parameter values during unloading seepage deformation.

Test number	Pore pressure (MPa)	Residual hoop strain	Residual axial strain	Loading stage, E (GPa)	Unloading stage (elastic), E (GPa)	Unloading stage (development), E (GPa)	Unloading stage (propagation), E (GPa)	Stress drop stage, E (GPa)
S-2	0.1	-0.0102	0.0078	7.76	6.86	6.67	5.68	2.59
S-3	0.2	-0.0106	0.0080	7.78	6.89	6.51	5.56	2.56
S-4	0.4	-0.0121	0.0085	8.07	6.90	6.14	4.53	2.12
S-5	0.6	-0.0160	0.0091	8.28	6.59	5.88	3.92	2.06

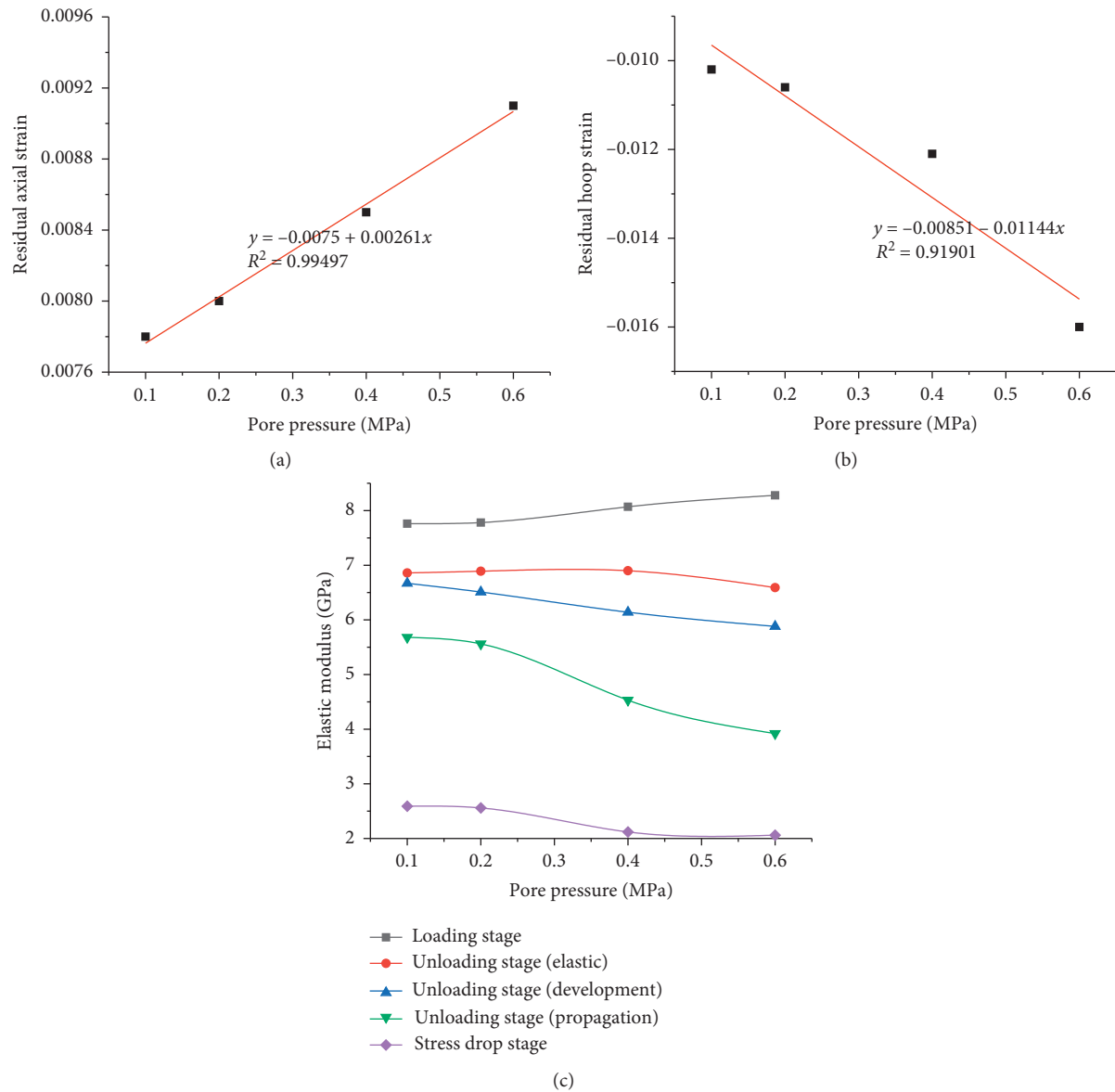


FIGURE 4: Variations in residual strain and elastic modulus with pore pressure. (a) Variation in residual axial strain with pore pressure. (b) Variation in residual hoop strain with pore pressure. (c) Variation in elastic modulus with pore pressure.

pore water pressure reached 0.6 MPa, the hydromechanical coupling effect gradually manifested, which promoted compression deformation of the specimen and formation of more compression cracks, showing compression-shear failure characteristics. The corresponding axial strain under the peak deviatoric stress changed as 0.392% \rightarrow 0.402% \rightarrow 0.404% \rightarrow 0.412%. This gradual increase can be considered as a verification. Additionally, owing to the small pore pressure gradient selected in this work, the change in axial strain was not apparent.

Cai et al. [23, 24] divided the stress-strain curves of rocks into four stages based on the state of development of the cracks within the rocks. Stage I is for closure and compression of the preexisting crack, Stage II is the linear elastic stage, Stage III is for stable crack growth, and Stage IV is the nonlinear growth stage. The end points of these stages

correspond to the crack closure stress σ_{cc} , crack initiation stress σ_{ci} , crack-damage stress σ_{cd} , and peak stress σ_c . Among them, the crack initiation stress σ_{ci} and crack-damage stress σ_{cd} are the two important parameters that characterize rock strength.

The damage stress σ_{ci} represents the starting point of stable crack growth in rocks, i.e., the crack initiation point. Thereafter, external loading is necessary to drive the propagation of cracks inside the specimens. The crack-damage stress σ_{cd} is the starting point of the nonlinear crack growth, i.e., the volume expansion point. A large number of cracks inside the specimen continue to grow and form larger cracks from the external force; this stage is not required to drive growth. In this work, the volumetric strain method was used to determine the characteristic strength and variation in characteristic strength of the unloading seepage of the

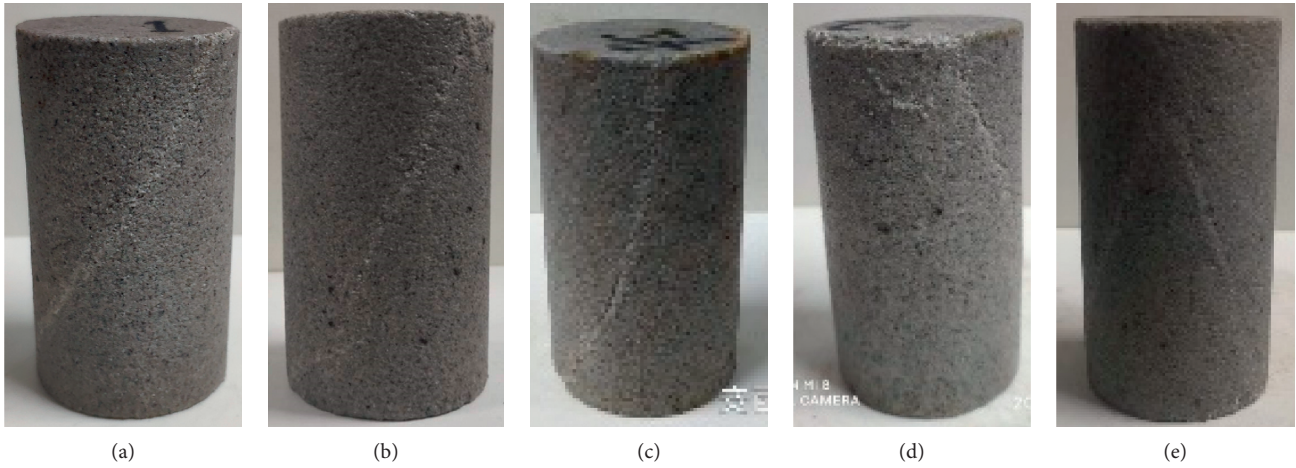


FIGURE 5: Typical specimen-fracture characteristics. (a) No pore pressure. (b) 0.1 MPa pore pressure. (c) 0.2 MPa pore pressure. (d) 0.4 MPa pore pressure. (e) 0.6 MPa pore pressure.

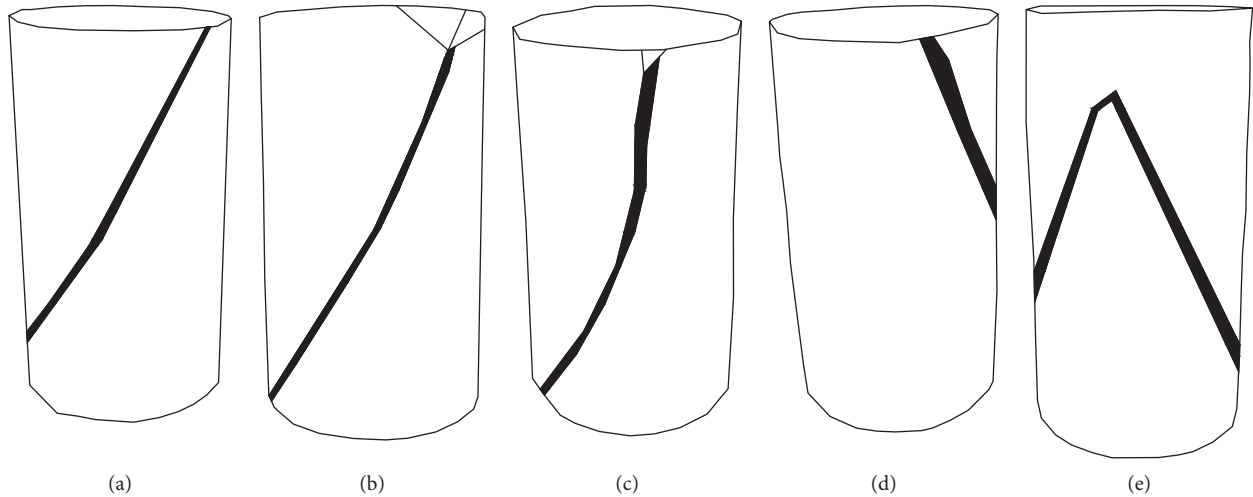


FIGURE 6: Sketch maps of specimen-fracture characteristics. (a) Pore pressure 0. (b) Pore pressure 0.1 MPa. (c) Pore pressure 0.2 MPa. (d) Pore pressure 0.4 MPa. (e) Pore pressure 0.6 MPa.

specimen under the action of pore water pressure. According to Figure 3(c), the characteristic values of the crack initiation stress σ_{ci} and crack-damage stress σ_{cd} are shown in Table 3, which are fitted and plotted in Figure 7.

It is seen from Table 3 that with the increase in water pressure, σ_{ci} and σ_{cd} gradually decrease, indicating that the crack initiation point of the specimen gradually decreases under the action of pore water pressure; i.e., crack initiation occurs in the rock at lower deviatoric stress values. In this experiment, the deformation and failure of the specimen were more sensitive to changes in the confining pressure with increase in water pressure, with more rapid responses. A small decrease in the confining pressure would thus cause initiation of cracks in the specimen. Besides, the difference between Stage III and Stage IV gradually decreases, indicating that the time between crack initiation and volume expansion reduces such that the conversion process is hastened. The pore water pressure will force the rock to

quickly go through the crack initiation stage and enter the crack propagation and growth stages under the same of in situ stress environment. The pore water pressure thus has a significant promoting effect on the deformation and failure of rocks. Therefore, problems related to water pressures in practical engineering scenarios in mine roadways necessitate countermeasures.

3.3. Analysis of Structural Characteristics of Pores. During the experiments, the water outlet was closed to form an environment with stable pore water pressure in the tank. When the pore structure in the specimen changed, the flow rate of the water inlet inevitably changes; ΔQ_m was defined as the change in the flow rate of the water inlet between time m and the start time:

$$\Delta Q_m = Q_m - Q_0, \quad (2)$$

TABLE 3: Strength characteristic values of unloading seepage.

Test number	Water pressure (MPa)	σ_{ci} (MPa)	σ_{cd} (MPa)
S-2	0.1	21.80	22.70
S-3	0.2	21.34	22.61
S-4	0.4	19.97	21.88
S-5	0.6	19.34	21.16

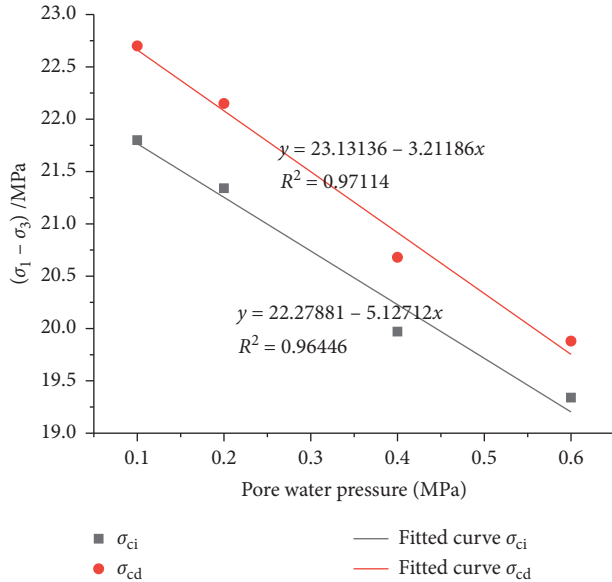


FIGURE 7: Strength characteristics of unloading seepage.

where Q_m denotes the flow rate at the water inlet at time m , and Q_0 is the flow rate at the water inlet at the start time.

When $\Delta Q_m > 0$, the pore structure is understood to expand and develop. When $\Delta Q_m < 0$, the pore structure is understood to shrink and close. The variation in ΔQ_m was therefore analyzed to characterize the changes in pore structures in the specimen. The relationship between the volumetric strain and water inflow at different pore pressure gradients can be plotted as shown in Figure 8.

Before failure, a four-stage evolution process of slow development \rightarrow rapid increase \rightarrow slight decrease \rightarrow sharp increase was observed in the specimen with change in the volumetric strain. Combined with the analysis of the stress path, it was observed that the change in water inflow was consistent with the variations in the deformation and strength characteristics. The change in water inflow was correlated with the process of initial microcrack compaction, stable crack growth, and crack propagation. Under various working conditions, the sandstone specimens exhibited noticeable linear elastic deformation characteristics in the loading and unloading elastic stages. During these phases, the specimens were close to being elastic bodies, and the water inflow first remained unchanged but slightly decreased later. In the stable and unstable crack propagation stages during the unloading process, the internal cracks grew and propagated rapidly, and the number and width of pore throats for seepage gradually increased, causing a gradual increase in the water inflow. At the stress drop stage, the

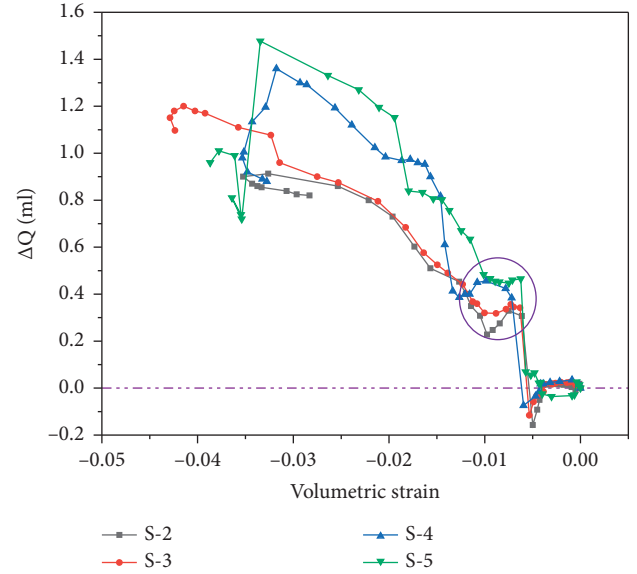


FIGURE 8: Curves demonstrating the relationship between sandstone seepage unloading and inflow.

“shrinkage” phenomenon occurred in the specimen after failure owing to axial pressure, which resulted in a decrease in the water inflow.

The water inflow of the specimens decreased after the stable microcrack development stage owing to gradual failure of the specimens after stable crack propagation, and the internal cracks entered the nonlinear development stage. The brittleness of the sandstone specimens was relatively apparent. Free water failed to diffuse to the crack tip in time, thus weakening the effect of the pore water pressure. Microfractures and pores that manifested in the specimens were compacted by the confining and axial pressures, resulting in a decrease in the fracture aperture and narrowing of the pore throats for seepage. Nevertheless, the duration of this process was short, and the specimens quickly entered the crack initiation and propagation stages, with rapid volume expansion. As the osmotic pressure increased, this phenomenon gradually became insignificant.

With the increase in osmotic pressure, the water inflow gradually increased. For example, the maximum change in water inflow was 0.91 mL when the osmotic pressure was 0.1 MPa, while it was 1.48 mL when the osmotic pressure was 0.6 MPa, showing an increase of 1.62 times. This is mainly because higher values of osmotic pressure weaken the radial inhibiting effect of the confining pressure on the specimen, and stronger hydromechanical couplings cause propagation and growth of cracks in the specimen, forming macroscopic fractures. The pore throats for seepage opened completely, leading to increased water inflow. After the maximum water inflow was attained, the specimen quickly entered the stress drop stage and failed, which can be considered as a precursor to deformation and failure. The osmotic pressure was inversely proportional to the volumetric strain required to reach the maximum water inflow; for instance, the volume strain rate was 0.35% at 0.1 MPa, while it was 0.33% at 0.6 MPa.

4. Numerical Simulation and Engineering Application

4.1. Numerical Simulation. In this study, mining extractions were performed in coal seam #16 in a mine located in western China. The seam had an average thickness of 8.8 m, an inclination of 8–18°, and a hardness coefficient $f \leq 3$. Between the coal seams and the water in the reservoir area, mainly the carboniferous system, Shiqianfeng formation, Shihezi formation, and Shanxi formation were noted. The lithology mainly included sandstone, shale, and sandy shale, with a thickness of around 300 m. The regional geological structure was relatively simple, with two waterproof strata and five water-bearing strata above the roof of the roadway. The local roof was relatively fragmented, and the fractures in the roof and floor as well as in the coal seam were relatively developed. The coal-mining methods used include the retreating longwall, fully mechanized top coal caving, and mining along the bottom while considering a 1:1.93 drawing ratio.

After the reservoir was filled, there was a hydraulic connection between the tertiary coal seam and the water in the reservoir area. The limestone in the northeast part of the mining area encounters the main coal seam owing to faulting (F2). The 60 m-thick fault-fracture zone F2 was exposed through the borehole; its bottom part was filled with a sandy material and had high water conductivity. The sandstones were thick and broadly distributed. The water in the reservoir area flowed into these water-bearing strata through the fault-fracture zone with high permeability and became the main source of water in the mining area. The schematic of the hydrogeological structure is shown in Figure 9(a). According to the diagram, a numerical calculation model was established using the UDEC simulation software (Figure 9(b)). Water pressures of 0.1/0.4/0.6/1.0 MPa were applied to the top of the model, and the Mohr–Coulomb constitutive model was adopted. The Bingham constitutive model [25, 26] was also adopted for diffusion and flow of water. The rock-mechanics parameters used are shown in Tables 4 and 5.

Survey lines were set up in the middle of the roadway roof to monitor the vertical displacement and relative separation of the surrounding rocks on the roof. The monitoring results are shown in Figure 10. It is seen from Figure 10 that as the water pressure increases, the subsidence of the roadway roof gradually increases, with changes proceeding in the order 16.1 cm \rightarrow 16.3 cm \rightarrow 25.1 cm \rightarrow 27.1 cm. In particular, when the water pressure increased from 0.4 MPa to 0.6 MPa, the roof subsidence increased significantly, indicating the existence of a certain water pressure threshold. Moreover, this phenomenon is consistent with the results of the unloading seepage test, where the deformation and failure of the specimen are more severe when the pore pressure exceeds 0.6 MPa. When the water pressure was low, the degree of separation of the shallow surrounding rocks (≤ 2 m) was significantly lower than that when the water pressure was high. In the transition to the deep surrounding rocks (3–7 m), the change in the relative separation of the surrounding rocks varied. In

general, this change was proportional to the water pressure. As the transition advances to the deep surrounding rocks (≥ 7 m), the change in the relative separation of the surrounding rocks was not noticeable, and the correlation with the change in the water pressure was weak.

Figure 11 shows the statistics of the joint development and development of fractures around the roadway, where the green line is the outline of the roadway, yellow represents the fracture area formed by joint opening, magenta represents the fracture area formed by joint dislocation, and red represents the mixed fracture area. It is observed that the fractures in the surrounding rocks are dominated by the dislocation fracture area. The number of joints gradually increases with the increase in water pressure. Nonetheless, when the water pressure is 0.6 MPa, the rate of increase drops significantly; at low water pressures (0.1–0.4 MPa), the two ribs of the roadway were mainly dislocation fracture areas, with unnoticeable fractures on the roof. At high water pressures (0.6–1.0 MPa), the dislocation fracture areas propagate from the two ribs to the top of the roadway, overlapping with the open fractures and forming mixed fractures, thereby forming a large area penetrated by fractures in the surrounding rocks of the roadway and resulting in significant shrinkage in the outline of the roadway. The roadway was thus severely deformed, affecting production safety. Hence, it is noted that the protection of the coal rib during roadway excavation under water disturbance is of critical importance.

The nephogram of the pore water pressure and survey line data of the surrounding rocks of the roadway are shown in Figure 12. It is seen from Figure 12 that with the increase in water pressure, the impact, the area of action of the water pressure gradually increases. Roof fractures develop in an intertwining manner, and fractures in the strata surrounding the upper part of the roadway roof are connected. The water flow was relatively free in this area, resulting in a reduction in the difference between various horizontal survey line data (Figures 12(c) and 12(d)). At a water pressure of 0.1 MPa, no pore water pressure was observed on the horizontal survey line at the coal seam of the roadway roof. However, when the water pressure was 0.6 MPa, the pressure of the horizontal survey line of the strata of the roadway roof approached 0.3 MPa, and the pore pressure inside various strata of the roadway roof gradually increased, resulting in enhanced water–rock coupling, thereby deepening and aggravating the disturbance to the rocks surrounding the roadway. The vertical survey line was analyzed, and it was observed to have sharply dropped within a certain range of the surrounding rocks above the roadway owing to excavation unloading. This can be considered as the range of roadway-roof disturbance caused by water pressure. By comparison, it was found that the roof disturbance changed as follows: 11.5 m \rightarrow 12.5 m \rightarrow 15 m \rightarrow 16.5 m, and the range of disturbance of the roof increased significantly. Furthermore, owing to the joint angles of the numerical model, water gathered to the left under the action of gravity, causing the pore pressure near the model boundary on the left side to be greater than that on the right side.

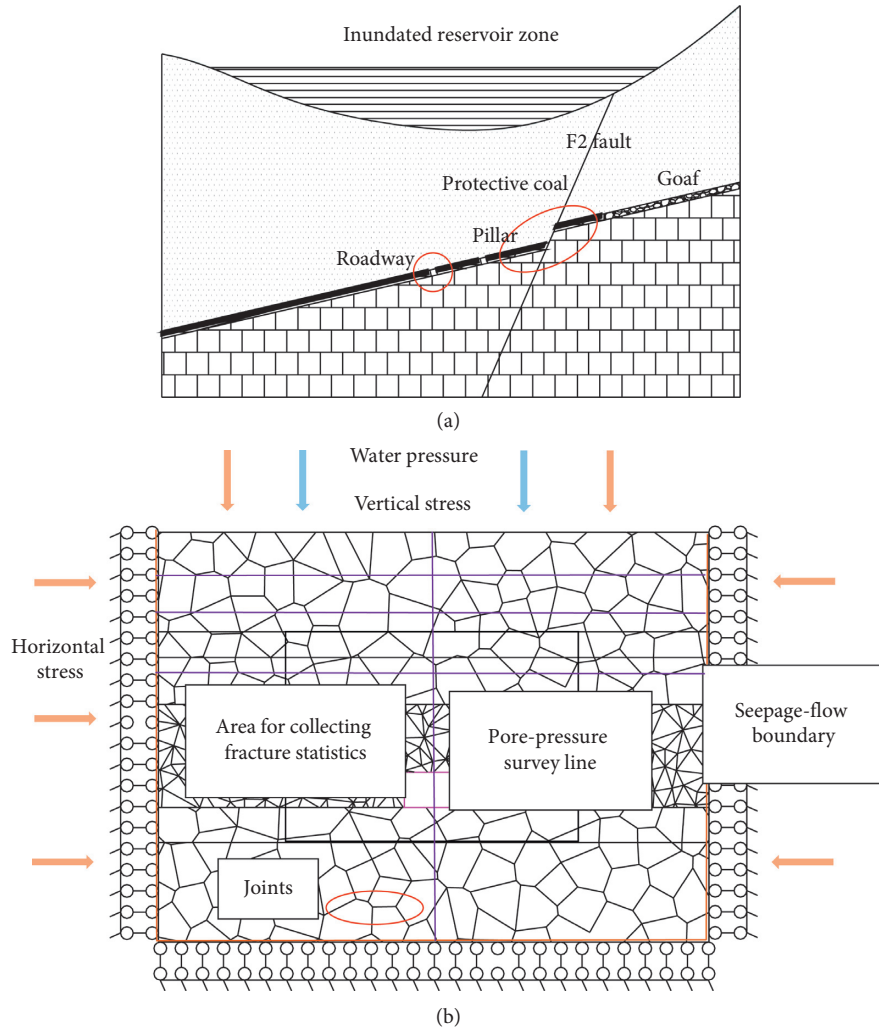


FIGURE 9: Hydrogeological and numerical calculation models. (a) Schematic of hydrogeological structure. (b) Numerical calculation model.

TABLE 4: Major parameters of rock mechanics.

Lithology	Density (kg/m ³)	Bulk modulus (GPa)	Shear modulus (GPa)	Cohesive strength (MPa)	Internal friction angle (°)	Tensile strength (MPa)
Fine sandstone	2500	0.85	0.4	1.87	30	2.15
Mudstone	1780	0.65	0.3	1.82	28	2.15
Coal	2450	0.4	0.2	1.71	28	1.69
Medium sandstone	2750	1.85	0.85	1.88	33	2.04

TABLE 5: Mechanical parameters of joint.

Lithology	Normal stiffness (GPa)	Tangential stiffness (GPa)	Cohesion (MPa)	Internal friction angle (°)	Tensile strength (MPa)
Fine sandstone	2.8	1.7	0.3	30	0.4
Mudstone	2.1	1.3	0.2	28	0.3
Coal	0.9	1.5	0.1	28	0.2
Medium sandstone	3.5	2	0.4	33	0.5

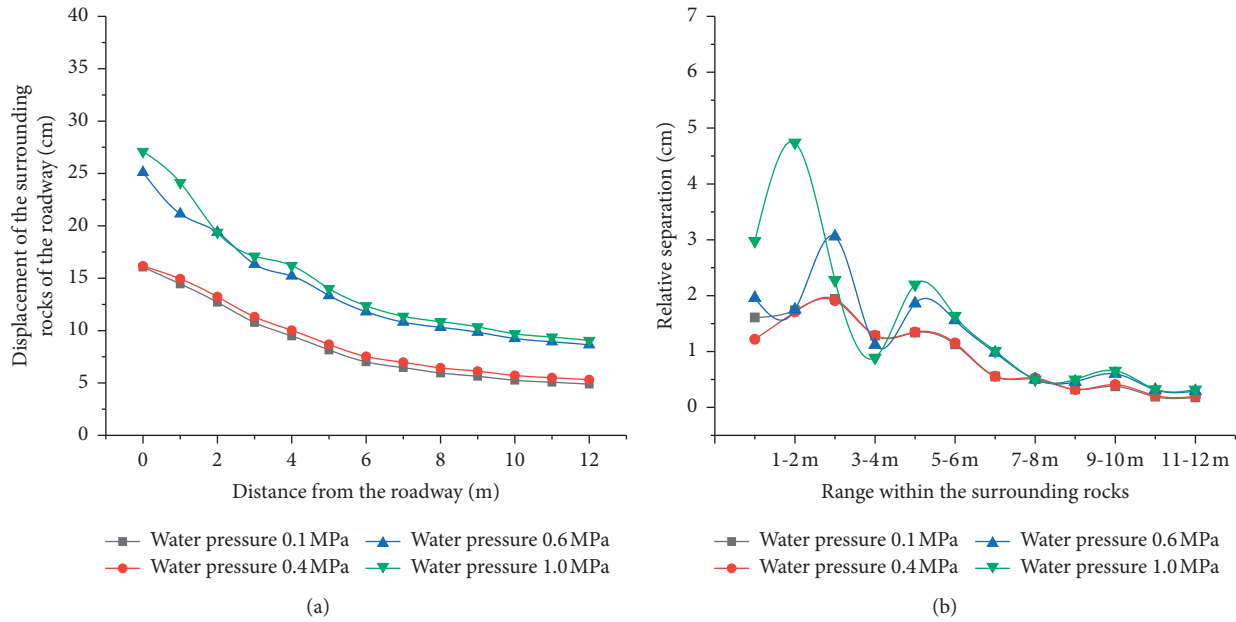


FIGURE 10: Variations in vertical displacement and relative separation of roof. (a) Vertical displacement of rocks surrounding the roof. (b) Relative separation of rocks surrounding the roof.

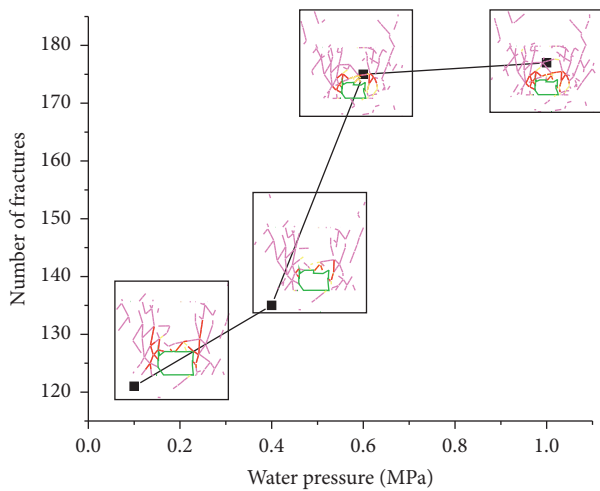


FIGURE 11: Roadway fracture development.

4.2. *Engineering Application.* Surface reservoirs, wherein noticeable water–rock interactions are observed, demonstrate a more significant effect of excavation unloading. This, in turn, results in increased roadway deformation, which causes rock-bolt breakage, steel-band falling, and roof subsidence, thereby affecting production safety. These failures are depicted in Figure 13.

In view of the specific conditions of mine roadways, the following support plan was specially developed. The roof and ribs were supported by high-performance rock bolts and reinforced with anchor cables. Diamond-shaped metal meshes combined with W-shaped steel bands were used for protection. Anticlockwise-rotating high-strength ribbed steel rock bolts without longitudinal ribs and dimensions $\phi 22 \times M24 \times 2000$ mm were used to support the roof and two

ribs. The intervals between the rock bolts were $700 \text{ mm} \times 700 \text{ mm}$. Each rock bolt was equipped with two extended anchorages of the Z2350 medium setting resin capsule. The dimensions of the steel strands of the anchor cables are $\phi 17.8 \times 6.8$ m. The boreholes were 6.5 m in depth, with intervals of $1.4 \text{ m} \times 1.4 \text{ m}$. Four sections of extended anchorages of the Z2350 medium setting resin capsule were used in each borehole. The pretightening force used was 120 kN, and the support plan is shown in Figure 14.

To explore the scientific nature of this support plan, three observation stations were set up in the north wing of the roadway. The borehole observation stations, which were all located in the middle of the roadway roof, were set up at distances of 160 m, 250 m, and 340 m from the excavation face, with a borehole depth of 10 m. The borehole observation videos were analyzed, and representative screenshots were selected for explanation, as shown in Figure 15.

It is seen from Figure 15(a) that uneven fractures and weak planes were distributed in the surrounding rocks within 1.4 m. The integrity of the surrounding rocks within the range of 1.4 m to 4.0 m was not high. The phenomenon of a fracture zone intersecting with multiple fractures occurred in some areas, while the strata were relatively intact, and no fractures were found in the remaining areas. It is seen from Figure 15(b) that over time, the surrounding rocks were relatively fractured within the range of 1.3 m. Within the range of 1.3 m to 2.4 m, the strata were relatively intact in the anchoring section, with no fractures, and the strata in the remaining areas were all relatively complete. It is seen from Figure 15(b) that two months after the construction of the observation station, the roadway has entered the phase of stable excavation, with the fracture zone and fractures of the surrounding rocks shifting towards the deep surrounding rocks. In summary, the stress of the roadway roof was

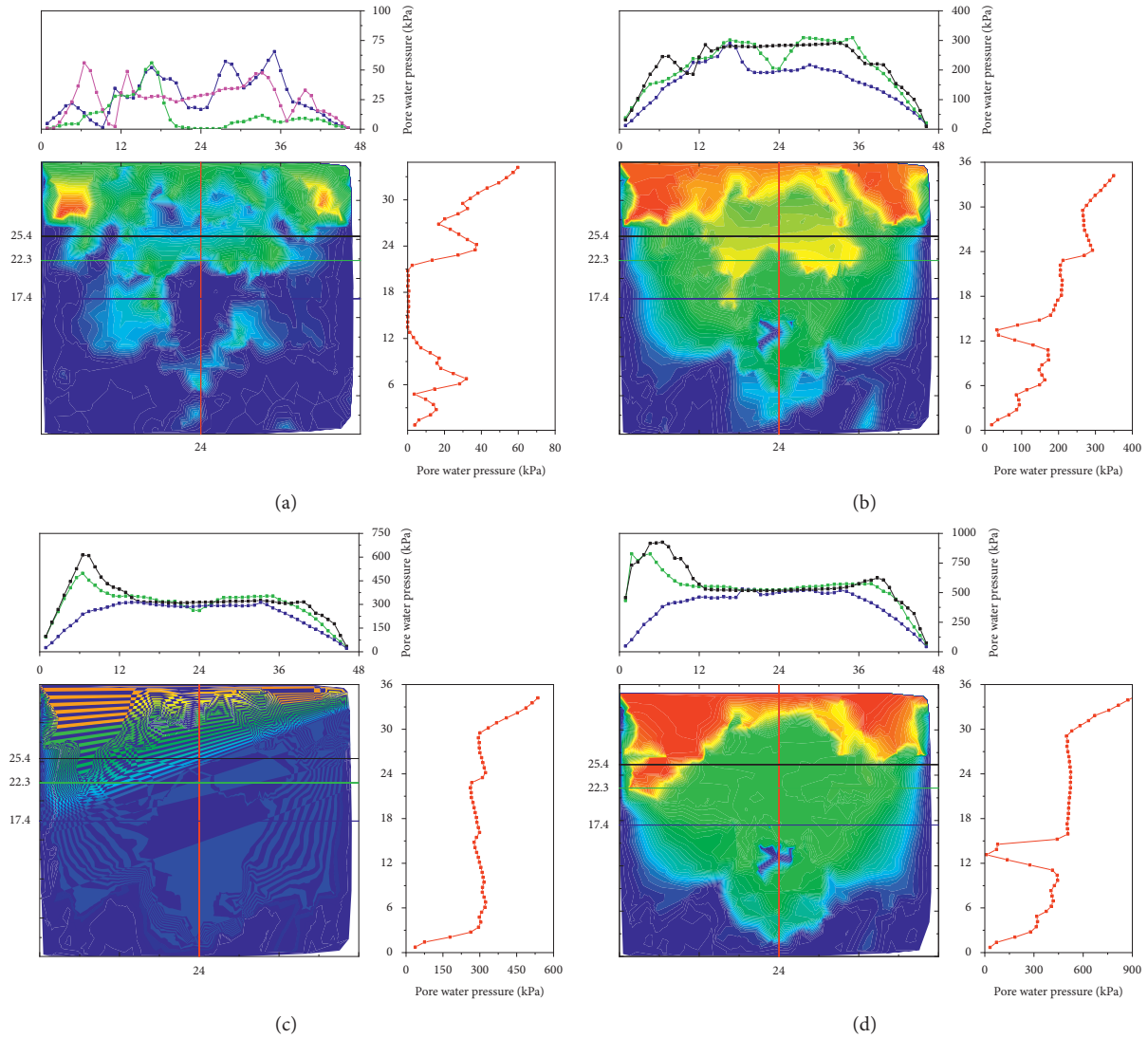


FIGURE 12: Nephogram of pore-water pressure and pore-pressure survey-line data. (a) 0.1 MPa water pressure. (b) 0.4 MPa water pressure. (c) 0.6 MPa water pressure. (d) 1 MPa water pressure.

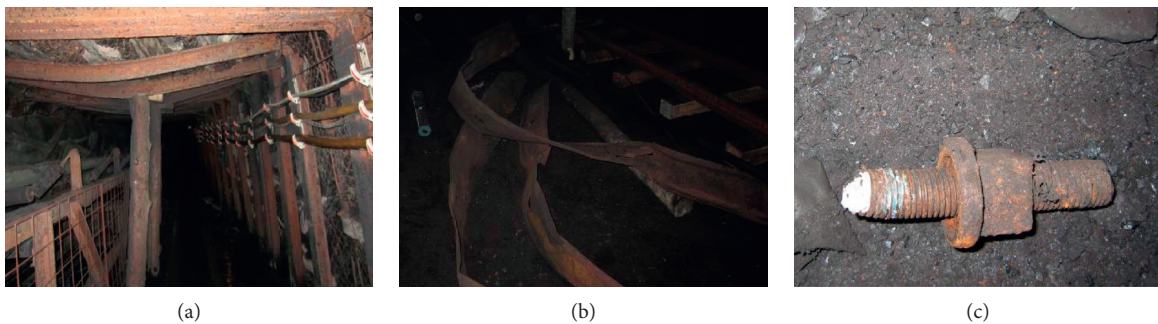


FIGURE 13: Current status of roadway support. (a) Roof subsidence. (b) Falling steel band. (c) Broken rock bolt.

redistributed at the initial stage of excavation, with separation and fracture occurring in the surrounding rocks within the range of 1.4 m. Over time, influenced by the overhead water body, reciprocal water–rock interactions caused the appearance of new fracture zones and

weak planes in shallow surrounding rocks, leading to separation and gradual propagation of the fractures towards deeper surrounding rocks. Overall, the general stability of the surrounding rocks of the roadway remained adequate.

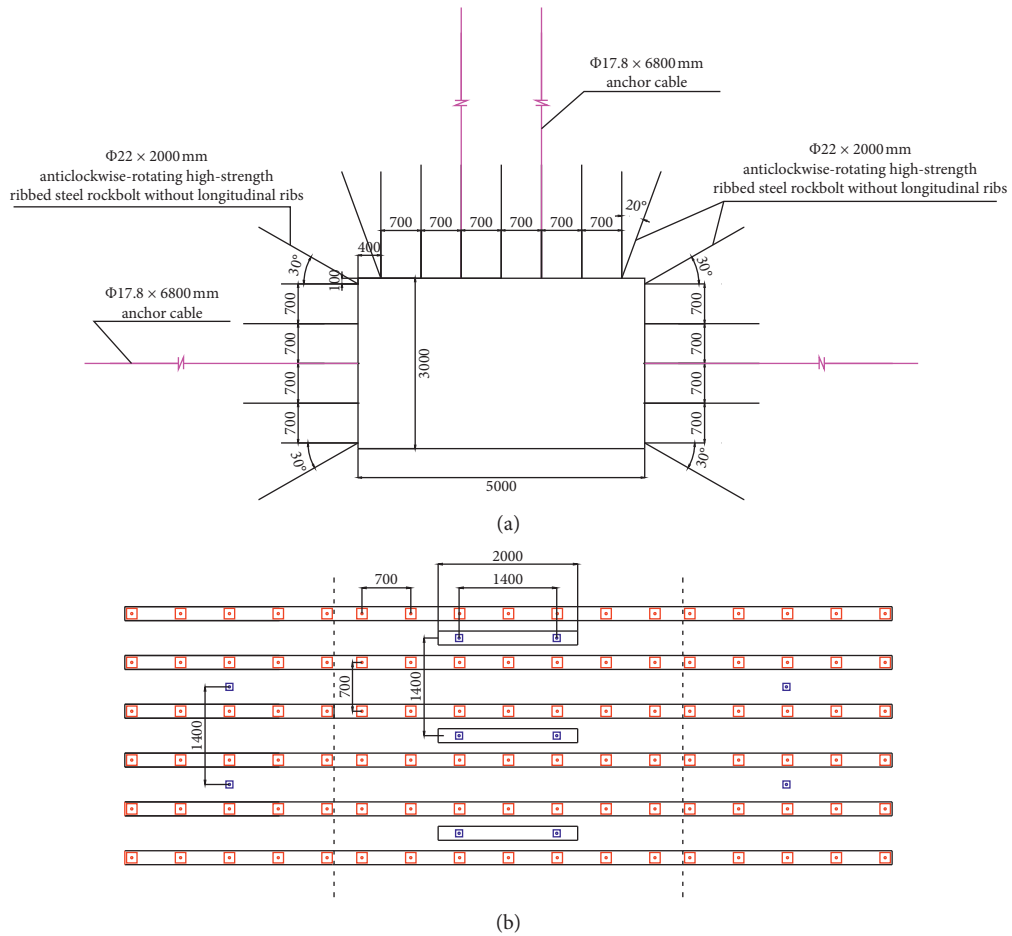


FIGURE 14: Roadway-support plan. (a) Cross section of support (unit: mm). (b) Expanded view of support (unit: mm).

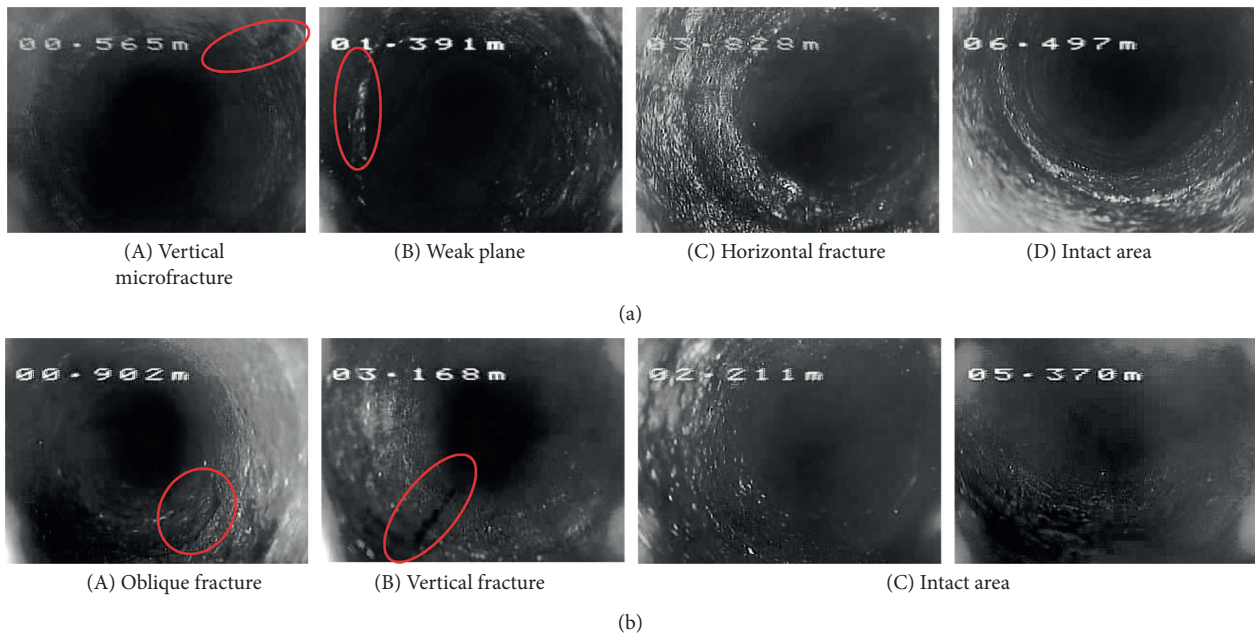


FIGURE 15: Continued.

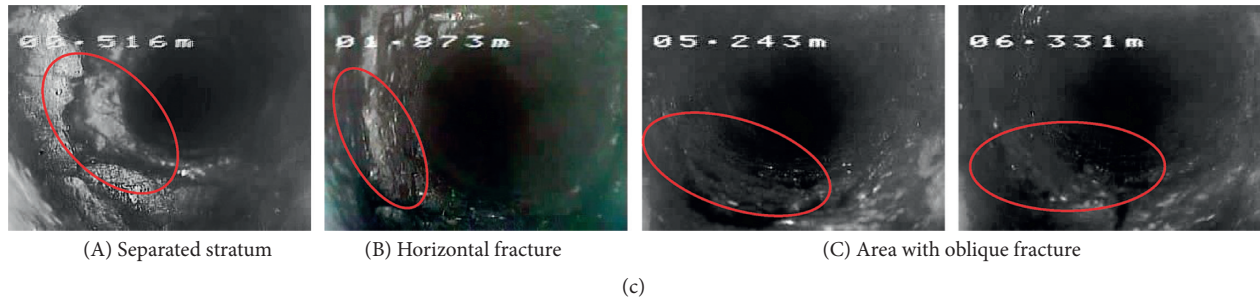


FIGURE 15: States of strata observed from boreholes at observation stations #1–3. (a) State of strata observed from borehole at observation station #1. (b) State of strata observed from borehole at observation station #2. (c) State of strata observed from borehole at observation station #3.

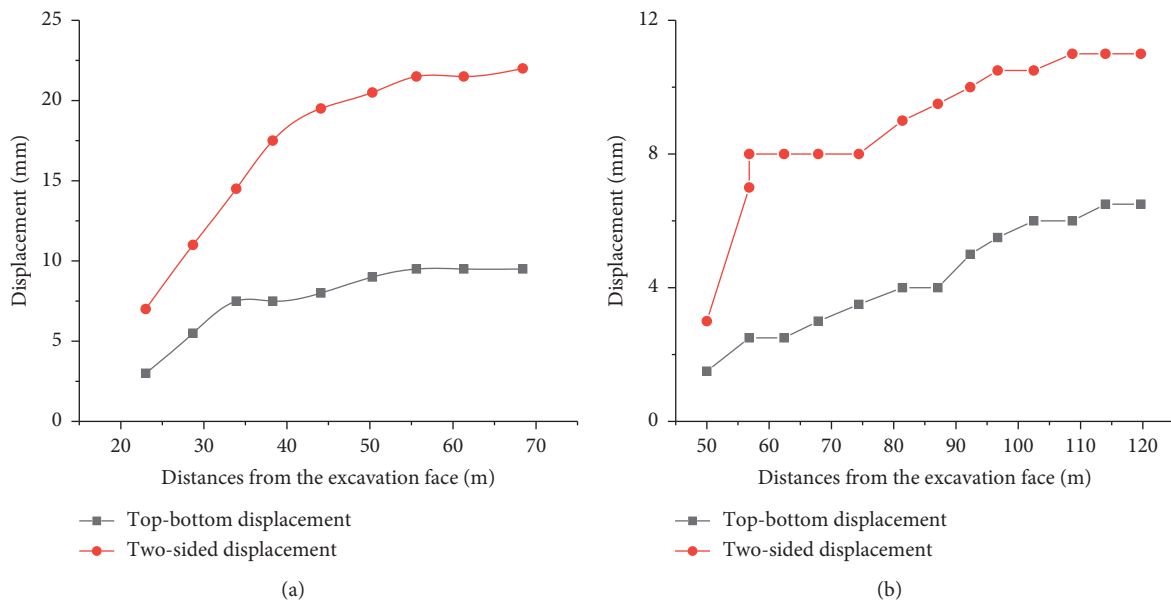


FIGURE 16: Roadway surface displacement. (a) 23 m away from excavation face. (b) 50 m away from excavation face.

All stations for surface-displacement measurement were located 23 m and 50 m away from the excavation face. The curves demonstrating the relationship between the relative distance between two roadway sides and that between the roof and excavation face are depicted in Figure 16. As can be seen, during the initial stages, the roadway deformation is dominated by the roof and floor movements. In contrast, during the later stages, the movement of the two sides dominates the said deformation. After excavation, the roadway becomes stable, and the surrounding rock, too, demonstrates good stability.

5. Conclusion

The proposed study investigates the deformation, strength, and pore-structure characteristics as well as surrounding-rock control of the mine-roadway sandstone roof subjected to water pressure. This investigation was performed using rock-mechanics testing methods, numerical simulations, and engineering principles. Major conclusions drawn from this study include the following:

- (1) The unloading confining pressure ratio was used in combination with the rate of change of strain to categorize the unloading stage as elastic compaction, unloading development, and unloading propagation stages. The residual strain was proportional to the pore pressure. The elastic moduli of the unloading development and propagation stages dropped significantly owing to the pore water pressure.
- (2) Shear failure was dominant in the specimen. However, with the increase in pore water pressure, the failure characteristics transformed from a single dominant crack to multiple overlapping cracks, and characteristics of the compression-shear failure manifested. The crack initiation point σ_{ci} and volume expansion point σ_{cd} were inversely proportional to the pore water pressure. Deformation and failure responses of the specimens to the changes in the confining pressure increased. The time between crack initiation and volume expansion reduced, and the conversion process was hastened.

- (3) The change in the water inflow correlated with the initial microcrack compaction, stable crack growth, and propagation of initiated crack. The water inflow gradually increased with the increase in osmotic pressure, and the volumetric strain required for the realization of maximum water inflow gradually decreased. The variation in water inflow can, thus, be considered a feature to detect specimen-failure occurrence.
- (4) As the water pressure increased, the effects of water–rock coupling were strengthened, enhancing the impact on the rocks surrounding the roadway and increasing the area of disturbance. The subsidence of the roadway roof gradually increased, and the separation of the shallow surrounding rocks (≤ 2 m) was relatively large, with a significant increase in the number of fractures. Fractures in the surrounding rocks of the roadway were mainly formed by joint dislocations and developed toward the top of the roadway to overlap with the open fractures. An area penetrated by fractures was formed in the surrounding rocks of the roadway, causing severe deformation of the roadway.
- (5) Combining experimental analysis, numerical simulation, and practical engineering evaluations, a support plan was developed where high-performance rock bolts, cable-bolt reinforcement, and W-shaped steel band protection were selected and applied to ensure stability of the roadway with a sandstone roof under changing water pressure, thereby providing effective protection for safe production in mines.

It is noteworthy that the unloading seepage-flow test was performed to exclusively investigate the specimen deformation and failure at a depth of approximately 300 m (confining pressure = 4 MPa). The surrounding rock structure as well as existing faults and other factors were not considered in the numerical simulations. Nonetheless, the results obtained in this study provide a ready reference to control the rocks surrounding mining-roadway roofs subjected to reservoir water disturbances. In future studies, the authors intend to consider such factors as the buried depth and goaf to investigate further to control the rocks surrounding the roadway roof under complex mining conditions and reservoir water disturbances.

Data Availability

The data used to support the findings of this study are available from the corresponding author upon request.

Conflicts of Interest

The authors declare that they have no conflicts of interest regarding the publication of this paper.

Acknowledgments

This project was supported by the Joint Funds of the National Natural Science Foundation of China (Grants nos. U1965107 and 51979218).

References

- [1] Y. Teng, D. Gao, W. Zhu et al., *Coal Mining Under Water*, Coal Industry Press, Beijing, China, 2012.
- [2] Y. Kang and B. Shen, *Coal Mining Under Water-Macroscopic Classification and Development Strategy*, Coal Industry Press, Beijing, China, 2012.
- [3] L. Fan, X. Ma, Z. Jiang, K. Sun, and R. Ji, “Review and thirty years prospect of research on water-preserved coal mining,” *Coal Science and Technology*, vol. 47, no. 7, pp. 1–30, 2019.
- [4] Y. Sun, Z. Xu, and Q. Dong, “Monito-ring and simulation research on development of waterflow wing fractures for coal mining under Xiaolangdi reservoir,” *Chinese Journal of Rock Mechanics and Engineering*, vol. 28, no. 2, pp. 238–245, 2009.
- [5] C. G. Dyke and L. Dobereiner, “Evaluating the strength and deformability of sandstones,” *Quarterly Journal of Engineering Geology and Hydrogeology*, vol. 24, no. 1, pp. 123–134, 1991.
- [6] P. S. B. Colback and B. L. Wiid, “The influence of moisture content on the compressive strength of rocks,” in *Proceedings of the 3rd Canadian Rock Mechanics Symposium*, pp. 65–83, Ottawa, Canada, October 1965.
- [7] J. Hadizadeh and R. D. Law, “Water-weakening of sandstone and quartzite deformed at various stress and strain rates,” *International Journal of Rock Mechanics and Mining Sciences & Geomechanics Abstracts*, vol. 28, no. 5, pp. 431–439, 1991.
- [8] R. Risnes, H. Haghighi, R. L. Korsnes, and O. Natvik, “Chalk-fluid interactions with glycol and brines,” *Tectonophysics*, vol. 370, no. 1–4, pp. 213–226, 2003.
- [9] Q. Yao, *Researches on Strength Weakening Mechanism and Control of Water-Enriched Roofs of Roadway*, China University of Mining and Technology. School of Mining Engineering, Xuzhou, China, 2011.
- [10] J. Zhu, J. Deng, Y. Huang, and Z. Yu, “Experimental study on the characteristic strength of saturated marble,” *Chinese Journal of Rock Mechanics and Engineering*, vol. 38, no. 6, pp. 1129–1138, 2019, in Chinese.
- [11] Z. Zhu, A. Zhang, and W. Xu, “Experimental research on complete stress-strain process seepage characteristics of brittle rock,” *Rock and Soil Mechanics*, vol. 23, no. 5, pp. 555–559, 2002, in Chinese.
- [12] X. Chen and L. Li, “Experimental study of unloading mechanical properties of rock under high confining pressure and high water pressure,” *Chinese Journal of Rock Mechanics and Engineering*, vol. 27, no. Supp. 1, pp. 2694–2699, 2008, in Chinese.
- [13] O. Tang, T. Li, and G. Chen, “Experimental study of the effect of moisture content on progressive failure process of sandstone,” *Journal of Experimental Mechanics*, vol. 13, no. 4, pp. 503–510, 2016, in Chinese.
- [14] H.-F. Deng, Z. Wang, J.-L. Li, Q. Jiang, and H.-B. Zhang, “Effect of unloading rate and pore water pressure on mechanical properties of sandstone,” *Chinese Journal of Geotechnical Engineering*, vol. 39, no. 11, pp. 1976–1983, 2017, in Chinese.
- [15] H. Deng, Z. Wang, J. Li et al., “Experimental research about influence of low pore water pressure on unloading mechanical properties of sandstone,” *Journal of Rock Mechanics and*

- Engineering*, vol. 36, no. Supp. 1, pp. 3266–3275, 2017, in Chinese.
- [16] J. Xu, H. Yang, S. Peng, Y. Jiang, and Y. Zhang, “Experimental study of mechanical property of sandstone under pore water pressure and confining pressure,” *Chinese Journal of Rock Mechanics and Engineering*, vol. 29, no. 8, pp. 1618–1623, 2010, in Chinese.
 - [17] R. Wang, B. Xu, W. Xu, W. Wang, Z. Lin, and J. Zhang, “Experimental study on influence of different unloading paths on permeability evolution of sandstone,” *Journal of Rock Mechanics and Engineering*, vol. 38, no. 3, pp. 467–475, 2019, in Chinese.
 - [18] X. Wang, G. Rong, and C. Zhou, “Permeability experimental study of gritstone in deformation and failure processes,” *Chinese Journal of Rock Mechanics and Engineering*, vol. 31, no. Supp. 1, pp. 2940–2947, 2012, in Chinese.
 - [19] W. Zhu and Y. Teng, “Study on the safety and mining influence of fully-mechanized caving mining with ultra-thick seam under barrier lake,” *Journal of Mining and Strata Control Engineering*, vol. 3, no. 1, Article ID 013525, 2021.
 - [20] B. Liu, Y. Ma, H. Sheng, H. Deng, Q. Han, and Y. Cao, “Experimental study on mechanical properties of cretaceous red sandstone under the freezing temperatures and confining pressures,” *Chinese Journal of Rock Mechanics and Engineering*, vol. 38, no. 3, pp. 455–466, 2019, in Chinese.
 - [21] D. Lu, X. Du, and C. Xu, “Analytical solutions to principle of effective stress,” *Chinese Journal of Geotechnical Engineering*, vol. 35, no. Supp. 1, pp. 146–151, 2013, in Chinese.
 - [22] K.-P. Zhou, Z.-X. Hu, F. Gao, M.-Q. Wang, and Z. Yang, “Study of marble damage evolution laws under unloading conditions based on nuclear magnetic resonance technique,” *Chinese Journal of Rock Mechanics and Engineering*, vol. 33, no. Supp. 2, pp. 3523–3530, 2014, in Chinese.
 - [23] M. Cai, P. K. Kaiser, Y. Tasaka, T. Maejima, H. Morioka, and M. Minami, “Generalized crack initiation and crack damage stress thresholds of brittle rock masses near underground excavations,” *International Journal of Rock Mechanics and Mining Sciences*, vol. 41, no. 5, pp. 833–847, 2004.
 - [24] Z. T. Bieniawski, “Mechanism of brittle fracture of rock,” *International Journal of Rock Mechanics and Mining Sciences & Geomechanics Abstracts*, vol. 4, no. 4, pp. 407–423, 1967.
 - [25] Itasca Consulting Group Inc, *UDEC (Universal Distinct Element Code) User’s Manual*, Itasca Consulting Group. Inc., Minneapolis, MN, USA, 2014.
 - [26] S. Pelliza and D. Peila, “Soil and rock reinforcements in tunneling,” *Tunneling and Underground Space Technology*, vol. 8, no. 3, pp. 223–233, 1993.

Research Article

Study on the Mathematical Model and Propagation Characteristics of AE Waveform Signals during Rock Fracture

Xun You ^{1,2}, Bin Gong ³, Xin Lv ⁴, and Longfei Hu ^{2,5}

¹Design & Research Institute of Masteel Engineering Technology Group Co., Ltd., Maanshan 243000, China

²Resources and Environment Engineering Institute, Jiangxi University of Science and Technology, Ganzhou 341000, China

³State Key Laboratory of Coastal and Offshore Engineering, Dalian University of Technology, Dalian 116024, China

⁴Modern Technology and Education Center, North China University of Science and Technology, Tangshan 063210, China

⁵Jiangxi Provincial Society of Engineering Blasting, Nanchang 330031, China

Correspondence should be addressed to Bin Gong; gongbin@dlut.edu.cn

Received 16 December 2020; Revised 22 January 2021; Accepted 28 January 2021; Published 9 February 2021

Academic Editor: Faming Huang

Copyright © 2021 Xun You et al. This is an open access article distributed under the Creative Commons Attribution License, which permits unrestricted use, distribution, and reproduction in any medium, provided the original work is properly cited.

Rock deformation or fracture is accompanied by the phenomenon of acoustic emission (AE). Due to the heterogeneity and anisotropy of rock materials as well as the complexity of their fracture, AE signals recorded by sensors at different positions have different characteristics. To explore factors influencing these differences, this study examines the effects of the physical properties of rocks, such as heterogeneity, anisotropy, and viscosity, on AE waveform signals from the perspective of the rock material and its fracture characteristics as well as the characteristics of the propagation of different AE waveform signals. The results show that the frequency (f) of the AE signals generated by rock fracture is inversely proportional to crack length (c) and directly proportional to the rate of crack growth (v). During signal propagation, the comprehensive effects of such factors as the heterogeneity, anisotropy, and viscosity of rocks as well as environmental noise weaken the energy of the signals and enhance the distribution of signal frequency. Each factor differently influences the time frequency of AE. A model for the propagation of AE signals was built and verified. Finally, as for on-site rock mass engineering, the low-frequency signals should be analysed prior to analysis in rock mass disaster monitoring.

1. Introduction

As a typical multiphase composite geological body, rocks are nonuniform, anisotropic, and viscous under the comprehensive action of materials (particles), structure (coupling between particles, diagenetic environment, and transformation), and boundary conditions (stress, temperature, water, and the free boundary) [1–3]. As the fracture of engineering rock mass becomes increasingly complex, the problem of the inaccurate prediction of failure precursors has become increasingly prominent. To simplify models for the analysis of large-scale rock mass failure on-site, the rock mass is regarded as an isotropic body [4, 5].

In the 1960s, Lekhnitskii [6] derived the general equation for the anisotropy and elasticity of rock mass from the generalized Hoek law, where this provided the theoretical

basis for examining the anisotropy and heterogeneity of rock materials. Methods of inverse analysis using the 3D finite element method (FEM), the Monte Carlo method, Bayesian analytical method, graphic discussion method under the Bragg condition, fractal measurements, and unit step increments in variation have been applied to measure the stress, strain, and displacement of rock media [7–10]. In terms of the anisotropy (including material and stress anisotropy), a certain correspondence has been noted between the velocity ratios of transverse and longitudinal waves and the lithology and geometric distribution of mesoscopic fracture in rocks containing moisture. The presence of moisture enhances the anisotropy of rocks [11–14]. The rate of loading, distribution of coupling, and direction of weak planes further increases the influence of anisotropy and heterogeneity on rock fracture behaviours and should thus

be considered in examining the engineering stability of rock or rock mass [15]. The separation between particles within rocks and particle fracture can lead to the phenomenon of disproportionation in the propagation of AE signals, such as in the reflection and refraction of the waves, and can even eliminate low-energy signals. Noise enhances the distribution of the frequency signals [16]. The existence of heterogeneity affects their propagation, and anisotropy makes the location of AE signals more difficult [17, 18].

The complexity of a rock medium and its rupture can distort the results of monitoring [19]. Research on factors influencing the mechanism of propagation of AE signals can promote the application of AE-based methods to identify rock fracture and can improve the accuracy of prediction of instability-induced fracture in the rock mass.

This study examines the effects of the heterogeneity, anisotropy, and viscosity of rocks as well as noise on their AE waveform. To this end, potential functions for transverse and longitudinal waves under different factors are formulated based on different wave equations in case of AE.

2. Influence of Rock Material and Its Fracture on Characteristics of AE Propagation

2.1. Typical Characteristics of Rock Materials

2.1.1. Anisotropy. The anisotropy of rocks can be divided into two types [20]. One is caused by the diagenesis of rocks and formed by the directional arrangement of particles and the mutual association among them. It is called material anisotropy. The other is caused by differences in the existence, arrangement, and distribution of microstructural planes, such as pores and microfractures in rocks, which change with the process of fracture. This is called stress anisotropy.

(1) *Material Anisotropy.* A rock is a typical anisotropic geological body. In the process of diagenesis, macroscopic anisotropy is caused by differences in the arrangement of mineral grains and fracture distribution at the microscopic scale.

(2) *Stress Anisotropy.* Assuming that the rock is composed of a series of hexahedrons, its stress tensor at any position can be decomposed into a spherical stress tensor with equal stresses in all directions and a deviant stress tensor. The spherical stress tensor causes the volumetric deformation of the rock material and the deviant stress tensor distorts it (deformation and fracture). Stress anisotropy is mainly caused by the deformation, expansion, and interpenetration of pores in rocks. With an increase in stress, the pores undergo a process of “compression → closure → expansion → interconnection.” The stress tensor is different in different parts of the rock, which leads to a difference in pore compression or deformation in six directions and leads to stress anisotropy.

Figure 1 shows the images of granite debris obtained by a scanning electron microscope with a magnification of 300x. The rock was a typical intrusive igneous rock formed by early

magmatic activity in Yanshan, and the direction of invasion determines its anisotropy. In rock fracture experiments, stress anisotropy is caused by fracture behaviour.

2.1.2. Heterogeneity. The rock is a collection of minerals with prominent heterogeneity [21]. The granite shown in Figure 1 was porphyritic, where the porphyry crystals were mainly potassium feldspar and quartz. The main minerals were potassium feldspar, plagioclase, and quartz as well as small amounts of biotite and amphibole. This type of granite is called weakly altered medium-to-coarse-grained porphyritic granite. Its mineral composition and corresponding contents are shown in Table 1. As a magmatic rock, granite is crystalline. It is deformed by a change in lattice bond length and its fracture is the rupture of this bond.

2.1.3. Viscosity. The rock is a typical viscous material [22]. The propagation of AE signals in it involves the mutual conversion of kinetic and potential energies due to the vibration of rock particles. For AE propagation, the rock prevents the reciprocal motion of particles which leads to a loss of AE energy. For lower energy waveforms, when the energy loss is too large, the component is easily lost. In particular, the high-frequency components of some AE signals have less energy and are prone to being lost during propagation.

2.2. Analysis of Influential Factors and Model Building. Under the action of deviating stress, the rock can be damaged and can even rupture. AE waveform signals generated by the fracture source are mixed with some reflected, refracted, and overlapping AE signals during propagation, which distorts them. Therefore, signals received by the sensors are divided into four types: (1) source signals of the fracture behaviour of rock, (2) signals distorted by anisotropy, (3) signals distorted by heterogeneity, and (4) signals distorted by noise jamming. According to the physical meaning of wave propagation and the influence of rock properties on wave propagation, equation (1) can be obtained and expressed as follows:

$$S(t) = (1 - \xi_4(t)) * (s_1(t) + s_2(t) + s_3(t) + s_5(t)), \quad (1)$$

where $S(t)$ represents the AE signals received by a sensor at time t , $s_1(t)$ is AE source signal caused by rock fracture at time t , $s_2(t)$ is the signal distorted by anisotropy at time t , $s_3(t)$ is the signal distorted by heterogeneity at time t , $\xi_4(t)$ is the signal attenuation coefficient caused by viscosity at time t , and $s_5(t)$ is noise jamming at time t . It is worth noting that $\xi_4(t)$ is a quantitative index that describes the signal attenuation during the signal spread through rock media and reflects the viscosity of rock media. Therefore, it can be determined by monitoring the attenuated signal during wave propagation tests.

The temporal sequence of AE reflects the law of energy dissipation during rock fracture and is determined by the size of the fracture as well as the energy stored and released by the rock. The AE frequency domain provides information

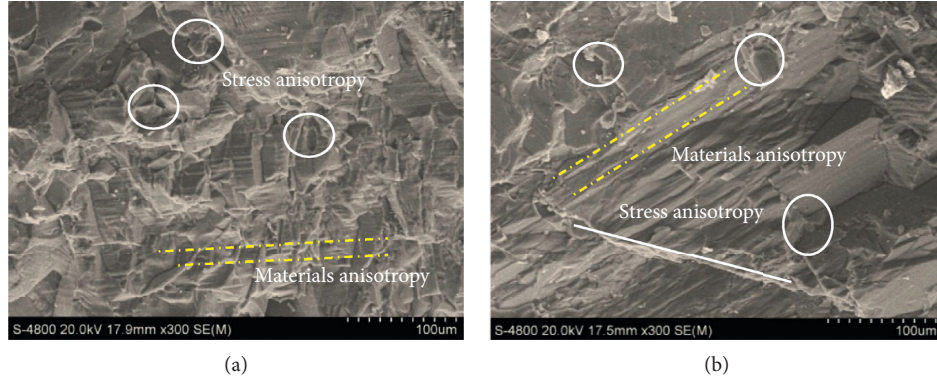


FIGURE 1: Images of granite debris obtained by a scanning electron microscope ($\times 300$). (a) Debris #1. (b) Debris #2.

TABLE 1: Composition and corresponding contents of the granite.

Composition	Content (%)	Features and structure	Particle size (mm)	Remarks
Potash feldspar	35~40	Granular	2~8	Slight kaolinization and sericitization; most of them are altered along the twin crystal lattices.
Plagioclase	25~30	Visible double crystal and ring band structure	0.5~3	Different degrees of kaolinization and sericitization; a few sericites are uncovered.
Quartz	30~35	Semiautomorphic to granular	1.5~8	—
Biotite	3~5	Flake	—	—
Amphibole	3~5	Long columnar	—	—

about the source of fracture, such as the size of the fracture, the energy dissipation, and the degrees of opening and closing of the fracture surface, especially for the classification and identification of crack patterns. It is one of the most accurate methods to represent the fracture source.

2.2.1. Time Sequence. Signal energy is the area of the signal envelope; that is, the AE signal is integrated there. The time sequence of AE is expressed from the perspective of energy as follows:

$$\int_{t-1}^t S(t)dt = (1 - f_{\xi_4}(t, l)) * \left(\int_{t-1}^t s_1(t)dt - \int_{t-1}^t s_2(t)dt + \int_{t-1}^t s_3(t)dt + \int_{t-1}^t s_5(t)dt \right) + \int_{t-1}^t R(n)dt. \quad (2)$$

Then,

$$\left. \begin{aligned} E(S_t) &= (1 - \xi_4(t)) * (E(s_1(t)) - E(s_2(t)) - E(s_3(t)) + E(s_5(t))) \textcircled{1} \\ E(S_t) &= (1 - \xi_4(t)) * (E(s_1(t)) - E(s_2(t)) + E(s_3(t)) + E(s_5(t))) \textcircled{2} \end{aligned} \right\} \quad (3)$$

where $E(S_t)$ is signal energy received by the sensor at time t and $E(s_1(t))$ is energy generated by the rupture at time t . $s_1(t)$ is the main component of the signals and is a positive number (+). $E(s_2(t))$ is the reduction in energy due to heterogeneity at time t and is a negative number (-); $E(s_3(t))$ is the reflection or refraction caused by anisotropy at time t . $\textcircled{1}$ When passing through an open fissure with a

degree of opening $D \geq$ wavelength (λ), the energy decreases (-). $\textcircled{2}$ When passing through a closed fissure or an open fissure with degree $D <$ wavelength (λ), the energy is superimposed (+). If the filling in the open crack is liquid, longitudinal AE waves cannot pass through and only transverse waves can. $\xi_4(t)$ represents signal attenuation due to viscosity at time t and is positively correlated with the

propagation distance at time t , <1 . $E(s_5(t))$ is energy carried by noise at time t and is a positive number (+).

2.2.2. Frequency Domain. We apply the Fourier transform to signal $S(t)$ to determine its frequency distribution:

$$F(w) = \int_{-\infty}^{\infty} S(t)e^{-iwt} dt = \int_{-\infty}^{\infty} s_1(t)e^{-iwt} dt + \int_{-\infty}^{\infty} s_2(t)e^{-iwt} dt + \int_{-\infty}^{\infty} s_3(t)e^{-iwt} dt + \int_{-\infty}^{\infty} s_5(t)e^{-iwt} dt = F_{s_1}(w) + F_{s_2}(w) + F_{s_3}(w) + F_{s_5}(w), \quad (4)$$

where $F(w)$ represents the frequency distribution of AE signals received by the sensor at time t , $F_{s_1}(w)$ represents the frequency distribution corresponding to rock fracture at time t , $F_{s_2}(w)$ represents signal distortion caused by rock heterogeneity at time t and the change of frequency due to reflection or refraction between crystals, $F_{s_3}(w)$ represents the change in frequency caused by signal distortion due to anisotropy at time t , and $F_{s_5}(w)$ represents the frequency corresponding to noise signals at time t and is a superposition effect.

(1) Rock Fracture Behaviour. Rocks of different scales are damaged or destroyed, and the frequency band of AE signals has a positive correlation with the scale of fracture [23, 24]. For large-scale damage at an engineering site, the frequency is generally distributed in lower band. Rock fracture in the

laboratory features small-scale cracks, and the frequency is generally distributed in the higher band. The relationship between the frequency of AE signals and the crack-related information they convey is as follows:

$$f \sim \frac{1}{[T + (c/v)(1 - (v/\beta)\cos\theta)]}, \quad (5)$$

where T is the time of crack closure, opening, or slippage, c is crack length, v is the speed at which a crack is formed, θ is the angle between the direction of signal propagation and the crack surface, $\theta \in [-\pi, \pi]$, and β is the rate of propagation of AE signals in a rock.

$\theta = -\pi$ or π is discussed below, and equation (5) can be changed to

$$f \sim \frac{1}{[T + (c/v)(1 - (v/\beta))]}, \quad \theta = -\pi \text{ or } f \sim \frac{1}{[T + (c/v)(1 + (v/\beta))]}, \quad \theta = \pi. \quad (6)$$

Equation (6) can be changed as follows:

$$\frac{1}{f} \sim \left[T + \left(\frac{c}{v}\right) \left(1 - \left(\frac{v}{\beta}\right)\right) \right], \quad \theta = -\pi \text{ or } \frac{1}{f} \sim \left[T + \left(\frac{c}{v}\right) \left(1 + \left(\frac{v}{\beta}\right)\right) \right], \quad \theta = \pi. \quad (7)$$

By inserting $c = v \cdot T$ into the above, we get

$$\frac{1}{f} \sim \left[T + T \left(1 - \left(\frac{v}{\beta}\right)\right) \right], \quad \theta = -\pi \text{ or } \frac{1}{f} \sim \left[T + T \left(1 + \left(\frac{v}{\beta}\right)\right) \right], \quad \theta = \pi. \quad (8)$$

We then make the following transformation:

$$\frac{1}{f} \sim T \left(2 - \frac{v}{\beta}\right), \quad \theta = -\pi \text{ or } \frac{1}{f} \sim T \left(2 + \frac{v}{\beta}\right), \quad \theta = \pi. \quad (9)$$

That is,

$$f \sim \frac{1}{(2T - c/\beta)}, \quad \theta = -\pi \text{ or } f \sim \frac{1}{(2T + c/\beta)}, \quad \theta = \pi. \quad (10)$$

According to equation (10), the frequency of AE signals generated by rock damage or fracture is related to T (the time it takes for a crack to close, open, or slip) and c (crack length). If a rock material is determined, then β is the rate of propagation of AE signals in a rock and can be regarded as a constant.

We can further transform equation (10), where $v = c/T$:

$$f \sim \frac{1}{c} \cdot \frac{1}{(2/v - 1/\beta)}, \quad \theta = -\pi \text{ or } f \sim \frac{1}{c} \cdot \frac{1}{(2/v + 1/\beta)}, \quad \theta = \pi. \quad (11)$$

According to equation (11), the frequency distribution of AE signals generated by rock damage or fracture is inversely proportional to c (the length of the crack); that is, the longer a crack is, the lower the frequency is. The frequency distribution of the AE signals is proportional to v (speed of crack propagation); that is, the faster crack propagation is, the lower the frequency is.

(2) *Signal Distortion Caused by Heterogeneity.* The rock material is a collection of minerals. As shown in Figure 2, suppose that there are three minerals in a rock: mineral 1, mineral 2, and mineral 3. The AE source/fracture source generates AE signals at point A, which propagate to sensors No. 1 and No. 2. Suppose that fracture point A occurs, and the AE signals received by sensor No. 1 are $F1 = S_{F1} + S_2 + S''_3$, that is, three superimposed composite signals. S_{F1} is the reflected signal when signal S_1 meets mineral 3, S_2 is the signal obtained directly from the fracture source A, and S''_3 is the signal of S_3 that has undergone two interfacial refractions through mineral 2. The AE signals received by sensor No. 2 are obtained by S_1 , which undergoes two interfacial refractions through mineral 3. Therefore, under the influence of heterogeneity, both S_1 and S_2 are distorted, and heterogeneity thus has a prominent influence on AE propagation.

(3) *Signal Distortion Caused by Anisotropy.* According to reasons for its occurrence, anisotropy can be divided into material anisotropy (rock body) and stress anisotropy (fracture). Material anisotropy is the physical property of the rock medium itself and so is not discussed here.

The existence of deviator stress leads to damage to or the destruction of the rock, which causes stress anisotropy. This leads to damage and fracture in various directions and with differences. Open cracks and sliding, staggered closed cracks are formed, which distort the AE signals. As shown in Figure 3, under the influence of anisotropy, if fracture occurs at point A, the AE signal received by sensor No. 1 is $F1 = S'_{F1} + S'_2$, which is a composite of two superimposed signals. S'_{F1} is the refraction of signal S_{F1} in an open crack that is obtained when S_1 is reflected in a shear-slip crack.

S'_2 is the refracted signal of S_2 in an open crack. The AE signal received by sensor No. 2 is $F2 = S'_1 + S'_{F2}$, where S'_1 is the refraction of S_1 through a shear-slip crack, S'_{F2} is S_2 that first undergoes interfacial reflection from an open crack and then is refracted through a shear-slip crack. In addition, when S_2 and S_{F1} pass through an open crack, they lose

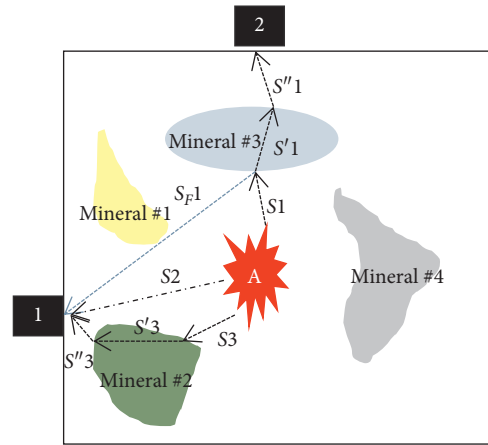


FIGURE 2: Schematic diagram of the influence of heterogeneity on AE signal propagation.

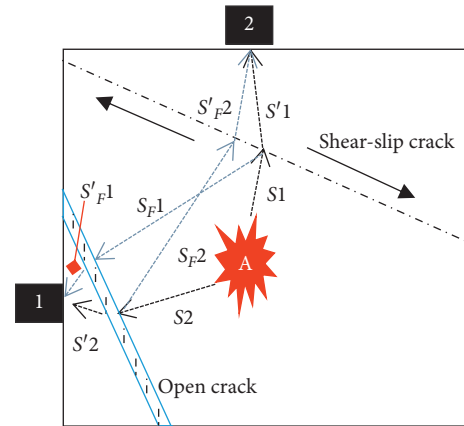


FIGURE 3: Schematic diagram of the influence of anisotropy on AE signal propagation.

energy, which leads to the loss of some high-frequency signals. Under the influence of the anisotropy of rock, the interfacial reflection and refraction of the fracture surface cause signal distortion and energy attenuation. Anisotropy thus has an impact on AE propagation.

(4) *Noise Jamming.* Noise jamming causes the superimposition of AE signals, which in turn increases the energy and complicates the frequency components. By analysing the noise signals, this interference can be eliminated. In addition, the energy stored in rocks is dissipated, caused by fracture, and some of it is used to overcome the damping force [25]. The viscosity of the rock reduces the energy carried by AE signals.

Assuming that AE signals travel a unit wavelength, the energy decreases by ξ . The factors influencing changes in the AE signals during rock fracture are summarised in Table 2: rock fracture behaviour and signal distortion caused by anisotropy, heterogeneity, viscosity, and noise jamming.

TABLE 2: Influential factors for and properties of AE signals during rock fracture.

Impact angle	Factor	Composition of influencing factor	Symbolic representation	Impact property
	Fracture behaviour	T (the time it takes for a crack to close, open, or slip) and c (the length of the crack). If the rock is determined, β is a fixed value	$S_1(t)$	Composition of a signal itself
Frequency domain	Heterogeneity	When AE signals pass through the boundary of mineral grains, intergranular reflection or refraction occurs	$S_2(t)$	Signal distortion
	Anisotropy	There are open cracks and sliding, staggered closed cracks that cause the reflection or refraction of AE signals	$S_3(t)$	Signal distortion
	Viscosity	Rock material itself	$S_4(t)$	Signal distortion
	Noise jamming	Signal superposition	$S_5(t)$	Complicated
Time sequence	Rupture behaviour	The energy dissipated during a rupture	$+E(S_1(t))$	Energy body
	Heterogeneity	The energy carried by reflected or refracted signals	$+E(S_2(t))$	Energy superposition
	Anisotropy	The energy carried by reflected or refracted signals. The energy decreases when the signal passes through an open crack	$\pm E(S_3(t))$	Energy superposition energy attenuation
	Viscosity	Rock material itself	$-E(S_4(t))$	Energy attenuation
	Noise jamming	Environmental factors	$+E(S_5(t))$	Energy superposition

2.3. *Analysis of Stages of Rock Fracture Behaviour.* The above models are used to explain the physical mechanism of changes in AE during rock damage and fracture.

- (1) In the initial stage (stage 1), only the closure of an original crack occurs inside the rock, and new cracks do not emerge. AE signals are generated by the closure of the original crack, and AE energy in terms

of time sequence is determined by its behaviour $E(s_1(t))$, heterogeneity $E(s_2(t))$, viscosity $\xi_4(t)$, and noise jamming $E(s_5(t))$. In the frequency domain, it is composed of crack behaviour $s_1(t)$, heterogeneity $s_2(t)$, and noise jamming $s_5(t)$.

$$\left. \begin{aligned} E(S_t) &= (1 - \xi_4(t)) * (E(s_1(t)) + E(s_2(t)) + E(s_5(t))) && \text{time sequence} \\ F(w) &= F_{s_1}(w) + F_{s_2}(w) + F_{s_5}(w) && \text{frequency domain} \end{aligned} \right\}. \quad (12)$$

- (2) The elastic stage: AE signals are caused by crystal deformation. AE energy in the time sequence is composed of heterogeneity $E(s_2(t))$, viscosity $\xi_4(t)$, and noise jamming $E(s_5(t))$. In the frequency domain, it is composed of heterogeneity $s_2(t)$ and noise jamming $s_5(t)$.

$$\left. \begin{aligned} E(S_t) &= (1 - \xi_4(t)) * (E(s_2(t)) + E(s_5(t))) && \text{time sequence} \\ F(w) &= F_{s_2}(w) + F_{s_5}(w) && \text{frequency domain} \end{aligned} \right\}, \quad (13)$$

- (3) The plastic stage: new cracks are formed in the rock. As the loading increases, the cracks penetrate one another to form a macroscopic shear-slip surface or open cracks. AE signals are jointly determined by the fracture behaviour, heterogeneity, anisotropy, viscosity, and noise jamming. It consists of rupture behaviour $E(s_1(t))$, heterogeneity $E(s_2(t))$, anisotropy $E(s_3(t))$, viscosity $\xi_4(t)$, and noise jamming $E(s_5(t))$ in terms of time sequence and is composed of rupture behaviour $s_1(t)$, heterogeneity $s_2(t)$, anisotropy $s_3(t)$, viscosity $\xi_4(t)$, and noise jamming $s_5(t)$ in terms of the frequency domain.

$$\left. \begin{aligned} E(S_t) &= (1 - \xi_4(t)) * (E(s_1(t)) + E(s_2(t)) \pm E(s_3(t)) + E(s_5(t))) && \text{time sequence} \\ F(w) &= F_{s_1}(w) + F_{s_2}(w) + F_{s_3}(w) + F_{s_5}(w) && \text{frequency domain} \end{aligned} \right\}. \quad (14)$$

- (4) Postpeak stage: the rock has failed due to instability and has lost its bearing capacity. The composition of AE signals at this time is similar to that in the plastic

phase and is also determined by fracture behaviour, heterogeneity, anisotropy, viscosity, and noise jamming. It is expressed as in the following equation:

$$\left. \begin{aligned} E(S_t) &= (1 - \xi_4(t)) * (E(s_1(t)) + E(s_2(t)) \pm E(s_3(t)) + E(s_5(t))) && \text{time sequence} \\ F(w) &= F_{s1}(w) + F_{s2}(w) + F_{s3}(w) + F_{s5}(w) && \text{frequency domain} \end{aligned} \right\}. \quad (15)$$

In short, changes in AE during rock damage and fracture evolution are complex, and factors influencing it in different stages are not the same.

3. Propagation Characteristics of AE Waveform Signals

3.1. Features of AE Waveform Signals. Under the action of external force, rocks with microscopic particles as a unit undergo mechanical movement and accumulate a certain amount of potential energy owing to elastic strain. The occurrence of deviatoric stress causes local deformation or even fracture, and the accumulated elastic strain-based energy is released in the form of elastic waves. The propagation of elastic waves is a process in which energy propagates from the fracture source to the surrounding media, that is, the propagation of AE signals. It can be described according to the theory of elastic waves.

A point in an elastic body and a section with an arbitrary normal direction can be decomposed into normal stress and shear stress in general. When the AE waveform passes through any position in the rock medium, the force affects the process of energy transfer. This effect can be divided into a spherical stress (normal stress) tensor and a deviatoric stress (shear stress) tensor. The spherical stress (normal stress) tensor appears as volumetric deformation and expansion and contraction along the direction of propagation. The form of the movement is a longitudinal wave (P-wave, expansion and contraction wave). The deviatoric stress (shear stress) tensor appears as shear deformation with a direction of propagation vertical to the direction of motion. It is a transverse wave (S-wave, shear wave). According to the orthogonal plane rule, it can be further divided into an SV-wave and an SH-wave (Figure 4).

According to differences in the modes of propagation of different AE wave signals, they can be divided into S-waves and P-waves (Figure 4). The direction of propagation of the S-wave is perpendicular to that of resonance and can be further divided into an SV-wave and an SH-wave that have a deviatoric stress effect and reduce energy. The direction of propagation of the P-wave is consistent with that of resonance, and it forms a spherical stress tensor to reduce energy.

3.2. Propagation Characteristics of AE Signals in Rocks

3.2.1. AE Longitudinal and Transverse Waves. In the same medium, the propagation of vertical and horizontal waves is determined by the wave equation, and the process of propagation of AE signals is shown in the following equation:

$$\left. \begin{aligned} \nabla^2 \varphi - \frac{1}{v_p^2} \frac{\partial^2 \varphi}{\partial t^2} &= 0 \\ \nabla^2 \psi - \frac{1}{v_s^2} \frac{\partial^2 \psi}{\partial t^2} &= 0 \end{aligned} \right\}. \quad (16)$$

The energy transfer mode of the transverse wave (S-wave, shear wave) is shear transfer, and its shape changes into that of a deviatoric stress tensor. The mode of propagation of rock materials is viscous and leads to a loss of energy during the propagation of the transverse wave. A longitudinal wave (P-wave, expansion and contraction waves) is compressed and expanded along the direction of propagation, which leads to a deformation of volume and has the effect of a spherical stress tensor. For this type of propagation, rock materials exhibit elastic characteristics; that is, the propagation of the longitudinal wave does not lead to the loss of energy.

3.2.2. Reflection Characteristics of the Free Interface on a Rock Boundary

(1) P-Wave. As shown in Figure 5, there is no other medium on the surface of the rock boundary, and the P-wave signal $\varphi_1(P)$ reflects only along the boundary between air or vacuum and the rock. When the P-wave encounters a rock boundary, it produces positive stress on the rock as well as tangential stress at a certain angle of incidence, which results in waveform conversion to form a reflected wave $\varphi_2(P)$ and a reflected wave $\psi_3(SV)$.

According to the law of propagation of the P-wave and S-wave in elastic media, we assume that the density of the medium is ρ , the longitudinal wave velocity is v_p , the transverse wave velocity is v_s , the incident angle is α , the

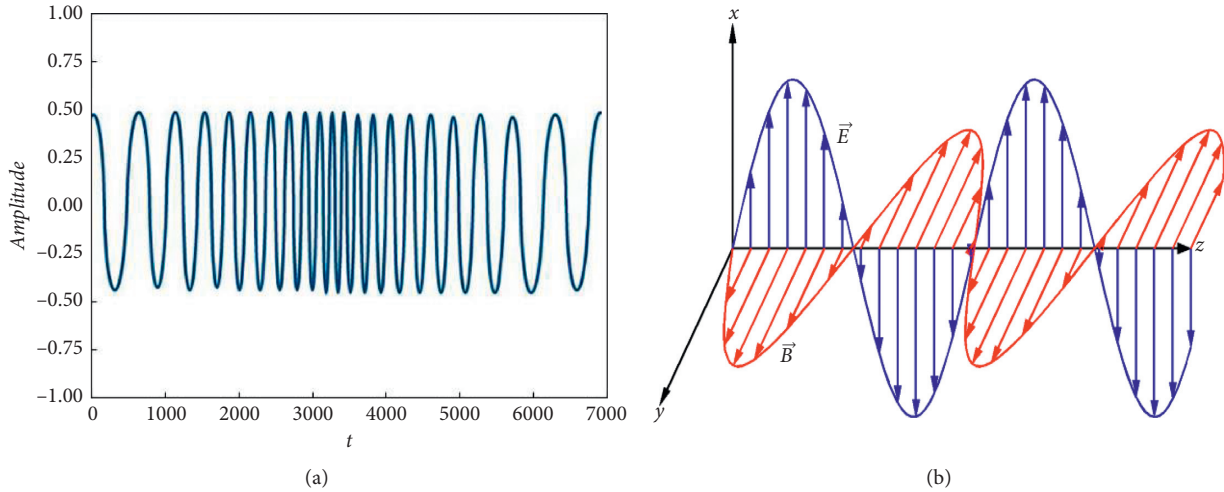


FIGURE 4: Classification of AE signal waveform. (a) Longitudinal wave (P-wave). (b) Transverse wave (S-wave).

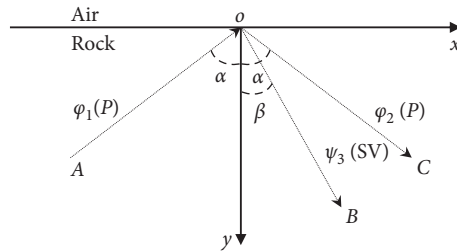


FIGURE 5: Propagation of acoustically emitted P-wave on rock boundaries.

reflection angle of the P-wave is also α , and that of the SV-wave is β . The potential functions of the P-wave, reflected P-wave, and reflected SV-wave are then as follows:

$$\left. \begin{aligned}
 \varphi_1 &= A_1 \exp \left[j\omega \left(t - \frac{x \sin \alpha - z \cos \alpha}{v_P} \right) \right] && \text{incident } P - \text{ wave} \\
 \varphi_2 &= A_2 \exp \left[j\omega \left(t - \frac{x \sin \alpha + z \cos \alpha}{v_P} \right) \right] && \text{reflected } P - \text{ wave} \\
 \psi_3 &= A_3 \exp \left[j\omega \left(t - \frac{x \sin \beta + z \cos \beta}{v_S} \right) \right] && \text{reflected SV - wave}
 \end{aligned} \right\} \quad (17)$$

The rock is a viscous medium. According to the propagation of the P-wave, the rock exhibits elastic deformation without energy loss. Due to the mode of propagation, the reflected SV-wave has the effect of deviatoric stress

accompanied by the loss of energy. Suppose that the incident P-wave is reflected at point O (x_O, y_O) on the rock boundary, forms a reflected SV-wave, and propagates to point B (x_B, y_B). The length of the journey is

$l_{OB} = \sqrt{(x_B - x_O)^2 + (y_B - y_O)^2}$ and the velocity of the SV-wave is v_{SV} ; then, the loss of energy is $\Pi_{SV} = l_{OB}/v_{SV}\xi$ and ξ is termed the damage factor. Moreover, ξ is a time-varying factor that describes the energy loss during signal propagation because of fracturing evolution.

The relationship between the energies carried by the incident P-wave, reflected P-wave, reflected SV-wave, and the attenuation of the SV-wave is as follows:

$$E_1 = E_2 + E_3 + \Pi_{SV}. \quad (18)$$

$$\left. \begin{aligned} \psi_1 &= B_1 \exp \left[j\omega \left(t - \frac{x \sin \beta - z \cos \beta}{v_S} \right) \right] && \text{incident SH - waves} \\ \psi_2 &= B_2 \exp \left[j\omega \left(t - \frac{x \sin \beta + z \cos \beta}{v_S} \right) \right] && \text{reflected SH - wave} \end{aligned} \right\}. \quad (19)$$

Assuming that the incident SH-wave propagates from the fracture source $A(x_A, y_A)$ to the rock boundary $O(x_O, y_O)$, the length of travel is $l_{AO} = \sqrt{(x_A - x_O)^2 + (y_A - y_O)^2}$. The reflected SH-wave propagates from point O to point $B(x_B, y_B)$, where the distance travelled is $l_{OB} = \sqrt{(x_O - x_B)^2 + (y_O - y_B)^2}$, and the velocity of incident SH-wave and the reflected SH-wave is v_{SH} . Then, the loss of energy is $\Pi_{SH} = \Pi_{\text{incident SH wave}} + \Pi_{\text{reflected SH wave}} = l_{AO}/v_{SH} + l_{OB}/v_{SH} = l_{AO} + l_{OB}/v_{SV}$.

The incident SH-wave propagates from point A to point O on the rock boundary, and the reflected SH-wave forms and propagates from point O to point B . The relationship between the energies carried by the incident SH-wave and the reflected SH-wave and the attenuation in the SH-wave is as follows:

$$E_1 = E_2 + E_3 + \Pi_{SH}. \quad (20)$$

(3) *Propagation Characteristics of the Wave along the Rock-Grain Boundary.* The important physical properties of rock minerals are their density, Poisson's ratio, and Young's

(2) *S-Wave.* As shown in Figure 6, the SH-wave ψ_1 (SH) is reflected only on the boundary. According to the propagation mode of the S wave, mode conversion does not occur, and only the reflected SH-wave ψ_2 (SH) exists.

Due to the law of propagation of the S-wave, suppose that the medium density is ρ , velocity of the transverse wave is v_S , and the incident angle and the reflection angle are both β . The potential functions of the incident and reflected SH-wave are then as follows:

modulus. Different mineral particles form rock materials through cementation or crystallization, and the rate of propagation of AE signals in different minerals is different. When it encounters mineral boundaries, the waveform is reflected or refracted. We discuss this separately for P-waves and S-waves.

P-wave: the signal $\varphi_1(P)$ of the P-wave is subjected to reflection, refraction, and waveform conversion, resulting in the reflected P-wave $\varphi_2(P)$, reflected SV-wave $\psi_3(SV)$, refracted P-wave $\varphi_4(P)$, and refracted SV-wave $\psi_4(SV)$ (Figure 7).

We assume that the density of mineral I is ρ_1 , its Poisson's ratio is λ_1 , the velocity of the longitudinal wave is v_{P1} , the velocity of the transverse wave is v_{S1} , the density of mineral II is ρ_2 , its Poisson's ratio is λ_2 , the velocity of the longitudinal wave is v_{P2} , and the velocity of the transverse wave is v_{S2} . Suppose that the incident angle of the P-wave is α , its reflected angle is also α , the reflected angle of the SV-wave is β , its refraction angle is α' , and the refraction angle of the SV-wave is β' . The relationship between the energies carried by the incident P-wave, reflected P-wave, reflected SV-wave, refracted P-wave, and refracted SV-wave is as follows:

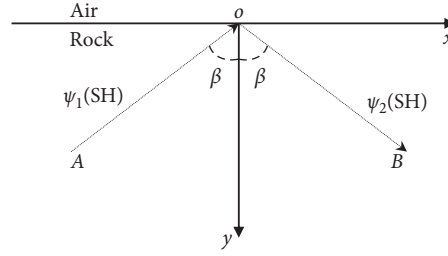


FIGURE 6: Propagation of acoustically emitted S-wave on rock boundaries.

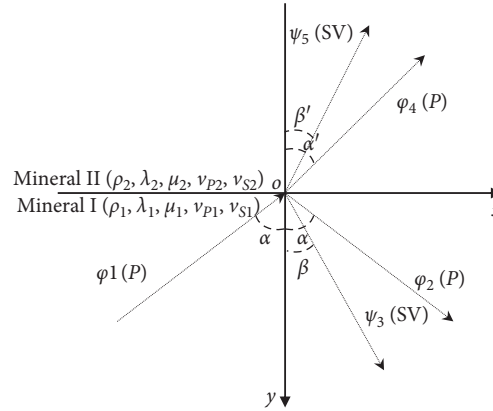


FIGURE 7: Propagation of AE P-wave on mineral boundaries.

$$\left. \begin{aligned}
 \varphi_1 &= A_1 \exp \left[j\omega \left(t - \frac{x \sin \alpha - z \cos \alpha}{v_{P1}} \right) \right] && \text{incident } P \text{ wave} \\
 \varphi_2 &= A_2 \exp \left[j\omega \left(t - \frac{x \sin \alpha + z \cos \alpha}{v_{P1}} \right) \right] && \text{reflected } P \text{ wave} \\
 \psi_3 &= A_3 \exp \left[j\omega \left(t - \frac{x \sin \beta + z \cos \beta}{v_{S1}} \right) \right] && \text{reflected SV wave} \\
 \varphi_4 &= A_4 \exp \left[j\omega \left(t - \frac{x \sin \alpha' + z \cos \alpha'}{v_{P2}} \right) \right] && \text{refracted } P \text{ wave} \\
 \psi_4 &= A_5 \exp \left[j\omega \left(t - \frac{x \sin \beta' + z \cos \beta'}{v_{S2}} \right) \right] && \text{refracted SV wave}
 \end{aligned} \right\} \quad (21)$$

According to rock viscosity, the reflected SV-wave and refracted SV-wave lose energy during propagation. Suppose that the incident P-wave is reflected and refracted at point $O(x_O, y_O)$ on the mineral boundary, the reflected SV-wave ψ_3 propagates to point $A(x_A, y_A)$, and the refracted SV-wave ψ_4 propagates to point $B(x_B, y_B)$. The length of the reflected SV-wave is $l_{OA} = \sqrt{(x_O - x_A)^2 + (y_O - y_A)^2}$ and that of the refracted SV-wave is $l_{OB} = \sqrt{(x_O - x_B)^2 + (y_O - y_B)^2}$; then,

the total loss of energy is $\Pi_{SV} = \Pi_{\text{reflected SV wave}} + \Pi_{\text{refracted SV wave}} = l_{OA}/v_{S1} + l_{OB}/v_{S2}$.

When the incident P-wave propagates to the AE source/fracture source and then to point O of the mineral boundary, reflected and refracted P-waves form, and the mode of conversion changes to a reflected SV-wave and a refracted SV-wave. The relationship of the total energy is as follows:

$$E_1 = E_2 + E_3 + E_4 + E_5 + \Pi_{SV}. \quad (22)$$

S-wave: according to the propagation characteristics of the S-wave, mode conversion does not occur. As shown in Figure 8, on the mineral boundary point O, the SH-wave is ψ_1 (SH), reflected wave is ψ_2 (SH), and refracted wave is ψ_3 (SH).

Assume that the density of mineral I is ρ_1 , its Poisson's ratio is λ_1 , the velocity of the longitudinal wave is v_{P1} , and

the velocity of the transverse wave is v_{S1} . The density of mineral II is ρ_2 , its Poisson's ratio is λ_2 , the velocity of the longitudinal wave is v_{P2} , and the velocity of the transverse wave is v_{S2} . Suppose that the incident angle of the SH-wave ψ_1 is β , the reflected angle of SH-wave ψ_2 is β , and the refracted angle of SH-wave ψ_3 is β' . The potential function of each wave component is then as follows:

$$\left. \begin{aligned} \psi_1 &= A_1 \exp \left[j\omega \left(t - \frac{x \sin \beta - z \cos \beta}{v_{S1}} \right) \right] && \text{incident S wave} \\ \psi_2 &= A_2 \exp \left[j\omega \left(t - \frac{x \sin \beta + z \cos \beta}{v_{S1}} \right) \right] && \text{reflected SH wave} \\ \psi_3 &= A_3 \exp \left[j\omega \left(t - \frac{x \sin \beta' + z \cos \beta'}{v_{S2}} \right) \right] && \text{refracted SH wave} \end{aligned} \right\} \quad (23)$$

Suppose that the incident SH-wave propagates from the fracture source/AE source point A (x_A, y_A) to the mineral boundary O (x_O, y_O), where its length is $l_{AO} = \sqrt{(x_A - x_O)^2 + (y_A - y_O)^2}$. The reflected SH-wave propagates from point O to point B (x_B, y_B) over distance $l_{OB} = \sqrt{(x_O - x_B)^2 + (y_O - y_B)^2}$, and the refracted SH-wave propagates from point O to point C (x_C, y_C) over distance $l_{OC} = \sqrt{(x_O - x_C)^2 + (y_O - y_C)^2}$. Then, the total loss of energy is $\Pi_{SH} = \Pi_{\text{Incident SH wave}} + \Pi_{\text{Reflected SH wave}} + \Pi_{\text{Refracted SH wave}} = l_{AO}/v_{S1} + l_{OB}/v_{S1} + l_{OC}/v_{S2}$.

The incident SH-wave propagates from point A to point O on the rock boundary, and the reflected SH-wave forms and propagates from point O to point B. The refracted SH wave propagates from point O to point C. The relationship between the energies carried by the incident SH-wave, reflected SH-wave, refracted SH-wave, and the attenuation of the SH-wave is as follows:

$$E_1 = E_2 + E_3 + \Pi_{SH}. \quad (24)$$

(4) *Propagation Characteristics of AE Signals through Cracks.* According to such physical phenomena as opening, closing, and filling, cracks can be divided into open cracks, open-filled cracks, and closed cracks. For these three types of cracks, the propagation of the P-wave and S-wave is discussed separately.

(i) Open cracks

Such cracks are not filled with any material. Assuming that the open surface of the crack is D , whether the AE waveform can pass through the crack is determined by its wavelength λ :

$$\left\{ \begin{array}{ll} \lambda \geq D, & \text{signals can pass through a crack,} \\ \lambda < D, & \text{signals cannot pass through a crack.} \end{array} \right. \quad (25)$$

(ii) Open-filled cracks

Such cracks have different effects on the propagation of the P-wave and S-wave according to the difference in the filling materials. If the filling is solid, it can be analysed using equation (3); if the filling is liquid, its shear modulus is zero, and it does not return to its original shape under shear stress; that is, it is not shear-resistant. In general, liquids cannot pass through transverse waves.

(iii) Closed fissure

The AE waveform is reflected and refracted here. In addition, the P-wave undergoes waveform conversion, and reflected and refracted SV-waves occur.

4. Discussion

The time-frequency characteristics of AE are determined here by using the stress or deformation of rocks. According to equation (11), the frequency distribution of AE signals is inversely proportional to c (crack length) and directly proportional to v (crack growth rate). This is why ultra-low-frequency seismic signals occur in case of ultra-large-scale fractures, such as in earthquakes [26, 27], low-frequency microseismic signals occur in case of earthquakes in mines that lead to rock failure, and higher-frequency signals occur in laboratory experiments [28, 29].

AE technology is an effective method for characterising rock damage or fracture. The material characteristics of rocks, such as heterogeneity, anisotropy, and viscosity, as well as the stages of crack evolution can distort the results of monitoring. The complexity of the rock medium and its fracture also lead to complex AE waveform propagation. In

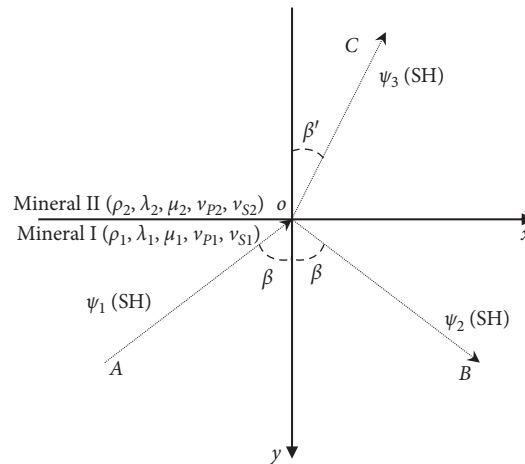


FIGURE 8: Propagation of AE S-wave on mineral boundaries.

addition, different boundary conditions lead to different AE signals.

The characteristics and transmission of AE during rock damage or fracture caused by multiple factors (damage fracture, loading condition, lithology, size, structure, and moisture) affect the results of analysis. Signals received by a sensor can still reflect the essential characteristics of rock damage and fracture.

5. Conclusions

In this study, the effects of the physical properties of rocks on AE waveform signals are examined from the perspective of the rock material and its fracture characteristics as well as the characteristics of the propagation of different AE waveform signals. The major findings and conclusions can be summarised as follows:

- (1) The time-frequency characteristics of AE show the complex rules during rock deformation or fracture and are affected by its heterogeneity, anisotropy, and viscosity as well as noise jamming. Meanwhile, they are also influenced by the fracture morphology and rock structure. The frequency (f) of the AE signals generated by rock fracture is inversely proportional to crack length (c) and directly proportional to the rate of crack growth (v).
- (2) The factors influencing the characteristics and propagation of AE signals are varied. Among them, the elastic phase is affected by heterogeneity, viscosity, and noise jamming. During signal propagation, the comprehensive effects of such factors weaken the energy of the signals and enhance the distribution of signal frequency.
- (3) A mathematical model has been developed for analysing the propagation of AE signals based on the fracture behaviour of rocks, and their anisotropy, heterogeneity, and viscosity as well as environmental noise jamming by considering the differences in the wave equation of its components. Namely, the AE wave can be divided into a transverse wave (S-wave,

shear wave) and a longitudinal wave (P-wave, expansion and contraction wave), and they can be considered, respectively, in the mathematical model.

Data Availability

The scanned images of granite debris and the composition data of the granite used to support the findings of this study are included within the article.

Conflicts of Interest

The authors declare no conflicts of interest.

Acknowledgments

This research was funded by the China Postdoctoral Science Foundation (Grant no. 2020M680950) and the National Natural Science Foundation of China (Grant no. 51627804).

References

- [1] S. Cherny, D. Chirkov, V. Lapin et al., "Two-dimensional modeling of the near-wellbore fracture tortuosity effect," *International Journal of Rock Mechanics and Mining Sciences*, vol. 46, no. 6, pp. 992–1000, 2009.
- [2] J. Wang, Y. Cao, G. Song, and H. Liu, "Diagenetic evolution and formation mechanisms of high-quality reservoirs under multiple diagenetic environmental constraints: an example from the paleogene beach-bar sandstone reservoirs in the dongying depression, bohai bay basin," *Acta Geologica Sinica-English Edition*, vol. 91, no. 1, pp. 232–248, 2017.
- [3] S. Hurwitz, K. L. Kipp, S. E. Ingebritsen, and M. E. Reid, "Groundwater flow, heat transport, and water table position within volcanic edifices: implications for volcanic processes in the Cascade Range," *Journal of Geophysical Research Solid Earth*, vol. 108, no. 12, 2003.
- [4] L. Haifeng, Y. Duoxi, L. Xiuyu, G. Liquan, and S. Dan, "Analytical solution of stress in a transversely isotropic floor rock mass under mining," *Chinese Journal of Underground Space and Engineering*, vol. 9, no. 5, pp. 1050–1056, 2013.

- [5] Z. Chen, "Base features of rock mechanics aspects of underground projects," *Journal of China Coal Society*, vol. 12, no. 4, pp. 1–7, 1986.
- [6] S. G. Lekhnitskii, *Theory of Elasticity of an Anisotropic Elastic Body*, Holdcn-Day Inc., San Francisco, CA, USA, 1963.
- [7] C. Wengui and Y. Ronggui, "Back analysis of stress measurement of anisotropic rock mass," *Journal of China Coal Society*, vol. 19, no. 2, pp. 122–130, 1994.
- [8] S. Xie and Z. Bao, "Fractal and multifractal properties of geochemical fields," *Mathematical Geology*, vol. 36, no. 7, pp. 847–864, 2004.
- [9] F. Tonon and B. Amadei, "Stresses in anisotropic rock masses: an engineering perspective building on geological knowledge," *International Journal of Rock Mechanics and Mining Sciences*, vol. 40, no. 7-8, pp. 1099–1120, 2003.
- [10] W. C. Zhu, M. S. Zhang, H. X. Zhang, X. Q. Guo, and G. Kai, "Numerical simulation for determining the size of representative element volume (rev) of jointed rock mass," *Chinese Journal of Geotechnical Engineering*, vol. 35, no. 6, pp. 1121–1127, 2013.
- [11] R. H. Tatham, "Vp/Vs and lithology," *Geophysics*, vol. 47, no. 3, pp. 336–344, 1982.
- [12] D. Y. Xi, Y. P. Liu, X. Y. Liu, Y. M. Shan, and W. G. Liu, "Influence of fatigue loading on physical mechanical characteristics of rock," *Chinese Journal of Geotechnical Engineering*, vol. 23, no. 3, pp. 292–295, 2001.
- [13] D. Y. Xi, B. Liu, and X. Y. Tian, "Anisotropy and nonlinear viscoelastic behavior of saturated rocks," *Chinese Journal of Geophysics*, vol. 45, no. 1, pp. 109–118, 2002.
- [14] T. Deng and L. D. Yang, "Characteristics of velocity ratio of P-wave and S-wave for anisotropic rocks," *Chinese Journal of Rock Mechanics and Engineering*, vol. 25, no. 10, pp. 2023–2029, 2006.
- [15] W. H. Shi, T. H. Yang, P. T. Wang, G. J. Hu, and P. Xiao, "Anisotropy analysis method for stability of open-pit slope rock mass and its application," *Chinese Journal of Geotechnical Engineering*, vol. 36, no. 10, pp. 1924–1933, 2014.
- [16] X. H. Huang, Y. B. Zhang, B. Z. Tian, and X. X. Liu, "Time delay estimation and acoustic emission source location of rock based on phase difference," *Rock and Soil Mechanics*, vol. 36, no. 2, pp. 381–386, 2015.
- [17] K. Mogi, *Study of Elastic Shocks Caused by the Fracture of Better O-Generous Material and its Relation to Earthquake Phenomena*, Vol. 40, Bull. of the Earthquake Res. Inst., Tokyo, Japan, 1962.
- [18] S. H. Wang, Y. B. Zhang, N. Zhang, and C. Lee, "Experimental study on acoustic emission measurement and source location for anisotropic rock failure process," *Journal of Northeastern University (Natural Science)*, vol. 28, no. 7, pp. 1033–1036, 2007.
- [19] D. Amitrano, M. Arattano, M. Chiarle et al., "Microseismic activity analysis for the study of the rupture mechanisms in unstable rock masses," *Natural Hazards and Earth System Sciences*, vol. 10, no. 4, pp. 831–841, 2010.
- [20] J. Tang and G. C. Wu, "Stress-dependent anisotropy of mudstone and shale with low porosity," *Chinese Journal of Geophysics*, vol. 8, pp. 2986–2995, 2015.
- [21] M. Menzies, "Alkaline rocks and their inclusions: a window on the Earth's interior," *Geological Society, London, Special Publications*, vol. 30, no. 1, pp. 15–27, 1987.
- [22] S. R. Pride, E. Tromeur, and J. G. Berryman, "Biot slow-wave effects in stratified rock," *Geophysics*, vol. 67, no. 1, pp. 271–281, 2002.
- [23] N. A. Haskell, "Total energy and energy spectral density of elastic wave radiation from propagating faults," *Bulletin of the Seismological Society of America*, vol. 54, no. 6A, pp. 1811–1841, 1964.
- [24] M. Ohnaka, "A physical basis for earthquakes based on the elastic rebound model," *Bulletin of the Seismological Society of America*, vol. 66, no. 2, pp. 433–451, 1976.
- [25] H. Xie, L. Li, Y. Ju, R. Peng, and Y. Yang, "Energy analysis for damage and catastrophic failure of rocks," *Science China Technological Sciences*, vol. 54, no. S1, pp. 199–209, 2011.
- [26] J. Chan and D. R. Schmitt, "Initial seismic observations from a deep borehole drilled into the Canadian Shield in Northeast Alberta," *International Journal of Earth Sciences*, vol. 104, no. 6, pp. 1–14, 2014.
- [27] G. R. Toro and R. K. Mcguire, "An investigation into earthquake ground motion characteristics in Eastern North America," *Bulletin of the Seismological Society of America*, vol. 77, no. 2, pp. 468–489, 1987.
- [28] C. W. Li, S. Fu, C. Guan, T. Wan, and B. Xie, "Characteristics and generation mechanism of ULF magnetic signals during coal deformation under uniaxial compression," *Journal of Geophysics & Engineering*, vol. 15, no. 4, p. 4, 2018.
- [29] X. Liu, L. Wu, Y. Zhang, Z. Liang, X. Yao, and P. Liang, "Frequency properties of acoustic emissions from the dry and saturated rock," *Environmental Earth Sciences*, vol. 78, no. 3, p. 67, 2019.